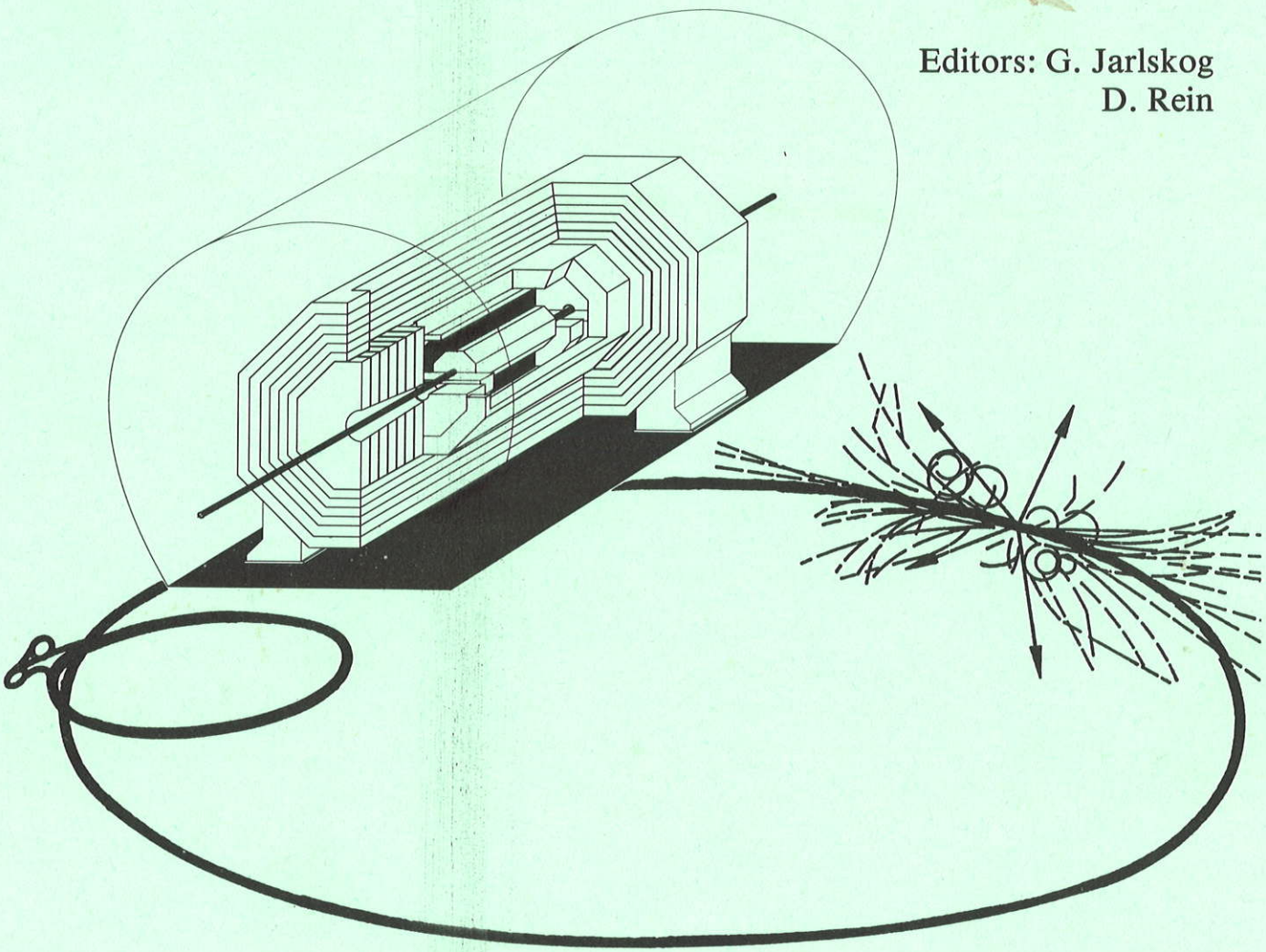
CERN 90-10
ECFA 90-133
Volume III
3 December 1990

EUROPEAN COMMITTEE FOR FUTURE ACCELERATORS

Large Hadron Collider Workshop

PROCEEDINGS
VOL. III

Editors: G. Jarlskog
D. Rein



Aachen, 4-9 October 1990



© Copyright CERN, Genève, 1990

Propriété littéraire et scientifique réservée pour tous les pays du monde. Ce document ne peut être reproduit ou traduit en tout ou en partie sans l'autorisation écrite du Directeur général du CERN, titulaire du droit d'auteur. Dans les cas appropriés, et s'il s'agit d'utiliser le document à des fins non commerciales, cette autorisation sera volontiers accordée.

Le CERN ne revendique pas la propriété des inventions brevetables et dessins ou modèles susceptibles de dépôt qui pourraient être décrits dans le présent document; ceux-ci peuvent être librement utilisés par les instituts de recherche, les industriels et autres intéressés. Cependant, le CERN se réserve le droit de s'opposer à toute revendication qu'un usager pourrait faire de la propriété scientifique ou industrielle de toute invention et tout dessin ou modèle décrits dans le présent document.

Literary and scientific copyrights reserved in all countries of the world. This report, or any part of it, may not be reprinted or translated without written permission of the copyright holder, the Director-General of CERN. However, permission will be freely granted for appropriate non-commercial use.

If any patentable invention or registrable design is described in the report, CERN makes no claim to property rights in it but offers it for the free use of research institutions, manufacturers and others. CERN, however, may oppose any attempt by a user to claim any proprietary or patent rights in such inventions or designs as may be described in the present document.

ISSN 0007-8328
ISBN 92-9083-031-X

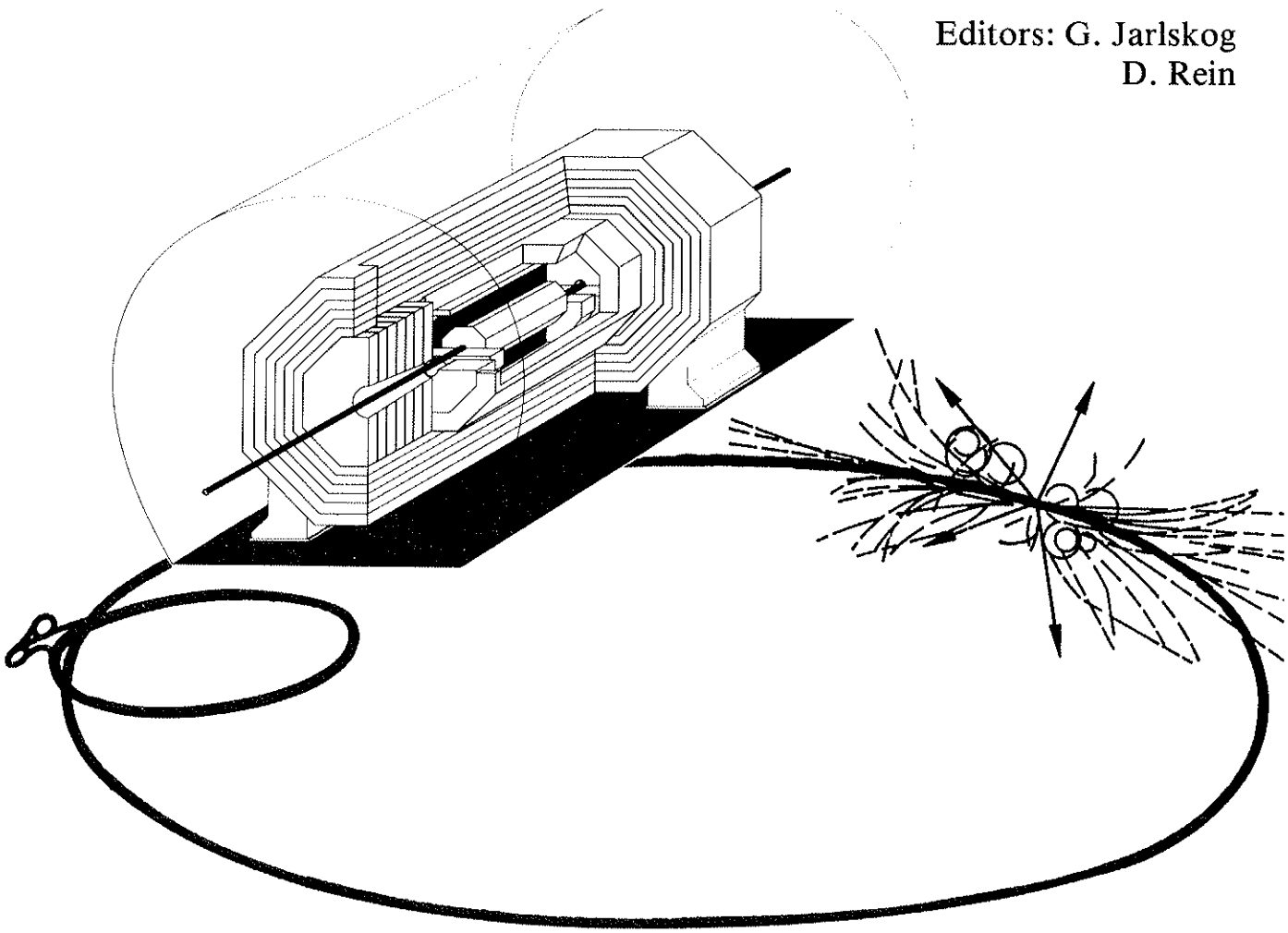
CERN 90-10
ECFA 90-133
Volume III
3 December 1990

EUROPEAN COMMITTEE FOR FUTURE ACCELERATORS

Large Hadron Collider Workshop

PROCEEDINGS
VOL. III

Editors: G. Jarlskog
D. Rein



Aachen, 4–9 October 1990



CERN–Service d'Information scientifique–RD/806–2500–décembre 1990

ABSTRACT

The aim of the LHC workshop at Aachen was to discuss the "discovery potential" of a high-luminosity hadron collider (the Large Hadron Collider) and to define the requirements of the detectors. Of central interest was whether a Higgs particle with mass below 1 TeV could be seen using detectors potentially available within a few years from now. Other topics included supersymmetry, heavy quarks, excited gauge bosons, and exotica in proton-proton collisions, as well as physics to be observed in electron-proton and heavy-ion collisions. A large part of the workshop was devoted to the discussion of instrumental and detector concepts, including simulation, signal processing, data acquisition, tracking, calorimetry, lepton identification and radiation hardness. The workshop began with parallel sessions of working groups on physics and instrumentation and continued, in the second half, with plenary talks giving overviews of the LHC project and the SSC, RHIC, and HERA programmes, summaries of the working groups, presentations from industry, and conclusions. Vol.1 of these proceedings contains the papers presented at the plenary sessions, Vol.2 the individual contributions to the physics sessions, and Vol.3 those to the instrumentation sessions.

SPONSORS

The workshop, which attracted roughly 500 participants including a sizeable group from industry, was organized by the European Committee for Future Accelerators and sponsored by the Commission of the European Communities, Deutsche Forschungsgemeinschaft, Deutscher Akademischer Austauschdienst, Bundesministerium für Forschung und Technologie, Philips Components, and CERN.



Volume I: Plenary Sessions
Volume II: Physics Working Groups

CONTENTS

Volume III

INSTRUMENTATION WORKING GROUPS

	Page
D1: Simulation and Software Engineering	1
A new geometry description for GEANT, *R. Brun et al.*	2
Status of simulation studies for fibre calorimetry, *V. Vercesi et al.*	14
Simulation of sampling calorimeters, *M. Nessi et al.*	23
Code management systems, *T. P. Shah et al.*	33
Programming languages at LHC, *I.E. Zacharov*	41
Standard interfaces between modules of event generators using dynamical common structures, *B. van Eijk et al.*	52
D2: Signal Processing, Trigger, and Data Acquisition	71
Trigger rates at the LHC, *S. Hellman et al.*	72
A digital solution to first level triggering using calorimetry at the LHC, *N. Ellis, J. Garvey*	80
Study of analog front-end electronics for supercollider experiments, *P. Jarron et al.*	84
A fast tracking level 1 muon trigger for high luminosity colliders using resistive plate chambers, *E. Petrolo et al.*	99
DSP review and applications, *D. Crosetto*	104
Data-acquisition and triggering with transputers, *J.C. Vermeulen*	112
A pedestrian approach to fast DAQ or How to outbus the buses, *R. Belusevic, G. Nixon*	116
Image processing in LHC detectors, *W. Krischer*	121
Ongoing approaches to the trigger problem using neural networks, *S. Amendolia, B. Denby*	129
Second-level muon trigger concept for the LHC, *G. Vesztergombi et al.*	136
A local/global architecture for level 2 calorimeter triggers, *J. Strong et al.*	145
A cluster finding analog network, *R. Bonino*	149
The TRD second-level trigger, *R.K. Bock, J. Pfennig*	154
Buses and standards for LHC, *H. Müller et al.*	159
SCI at LHC, *J.F. Renardy et al.*	165
Use of Fastbus at LHC, *D. Linnhofer et al.*	170
The "V"bus family, FUTUREBUS+ and SCSI, *W.G. Heyes et al.*	176
Report of the ECFA Working Group on fast data links, *M. Lomo, R. McLaren*	182
DAQ simulation for LHC, *J.-P. Porte et al.*	186
Digital front-end electronics for calorimetry at LHC, *G. Goggi, B. Lofstedt*	190
Fast electron triggers from a silicon track/preshower detector, *A. Poppleton*	201

D3 + D4: Vertex Detection and Tracking	207
Tracking with proportional chambers at LHC?, *T.C. Meyer*	208
Application of the microstrip gas counter in a LHC tracker, *F. Udo*	219
Further progress in the development of the microstrip gas chamber, *R. Bellazzini et al.*	222
A device for particle detection at future hadron colliders: the gaseous pixel chamber, *M.C.S. Williams et al.*	230
Conceptual design for a silicon tracker at the SSC, *K. O'Shaughnessy et al.*	234
Development of silicon pixel detectors for LHC, *E. Heijne et al.*	237
Calculations of pulse shape in silicon strip detectors, *S. Gadomski et al.*	241
GaAs detectors, *K.M. Smith et al.*	244
Monte Carlo simulations for central tracking with scintillating fibres, *U. Gensch, S. Schlenstedt*	248
Present status and future programme of scintillating fibres for central tracking, *C. D'Ambrosio et al.*	255
Opto-electronic delay tubes, *T. Gys et al.*	261
Topological trigger device using scintillating fibres and position-sensitive photomultipliers, *K. Kuroda et al.*	265
Top quark physics with B tagging at LHC, *F. Bedeschi et al.*	268
Study of an LHC detector with a central solenoidal field, *C. Daum*	273
Vertex detector electronics for LHC, *P. Seller*	277
HARP: Hierarchical analog readout processor with analog pipelining in CMOS, *F. Anghinolfi et al.*	284
Silicon tracking at high luminosity, *G. Tonelli*	285
Developments on Si detectors, *E. Focardi*	292
Effect of pile-up of minimum bias events on tracking in a magnetic field, *C.M. Buttar et al.*	297
D5: Calorimetry	299
Radioactivation in LHC calorimeters, *G.R. Stevenson*	302
Length of calorimeters and effect of absorbers in front of calorimeters, *J. Krüger*	306
Jet response of an ideal calorimeter, *D.E. Groom, E.M. Wang*	315
Combination of calorimeters with e/h = 1 but different samplig frequency, *J. del Peso, E. Ros*	320
Influence of calibration errors in the energy resolution of hadron calorimeters, *J. del Peso, E. Ros*	325
Scintillating fibers, *L. Poggioli et al.*	329
Calorimetry with warm liquids: Summary and prospects for LHC experiments, *E. Radermacher*	341
Warm liquid calorimeter project based on new materials, *J.P. Mendiburu*	348
Status report of R and D studies on warm liquid calorimetry by the WALIC collaboration, *B. Mansoulié et al.*	351
Liquid argon calorimetry, *D. Fournier at al.*	356
Study of liquid argon dopants for LHC hadron calorimetry, *V. Vuillemin et al.*	360
Software compensation for single particles and jets in the H1 calorimeter, *P. Schacht*	362

Liquid argon calorimetry with LHC-performance specifications, *D. Fournier et al.* 368
First results from the "Accordion" prototype, *D. Fournier et al.* 370
A fast and radiation hard crystal calorimeter for the LHC, *P. Lecoq, M. Schneegans* 374
New readout for BaF_2 calorimeters: gaseous detectors with solid photocathodes, *G. Charpak et al.* 384
Scintillating liquid xenon calorimeter, *M. Chen et al.* 389
Liquid xenon (krypton) calorimetry, *T. Ypsilantis et al.* 393

D6: Electron Identification 401

Electron detection in LHC calorimeters, *J.-P. Repellin* 402
Electron and photon identification with a barium fluoride electromagnetic calorimeter, *R. Zhu* 411
Tracking with scintillating fibres for electron identification at the LHC, *V. Cavasinni et al.* 424
Standard model physics impact on electron identification, *H. Plothow-Besch* 428

D7: Muon Identification 441

Muon rates at the LHC, *A. Nisati* 442
Punch through simulations, *H. Fesefeldt* 457
Muon trigger and identification, *M. Della Negra et al.* 467
Energy loss by muons in dense materials, *T. del Prete , C. Petridou* 477
A plastic foil chamber for large area muon detection, *F. Sauli* 485
New results on the blade chamber, *F. Bergsma* 489
The honeycomb strip chamber, *H. van der Graaf et al.* 498
Toroidal fields geometries for LHC muon spectrometers, *U. Goerlach* 504
An iron toroid for LHC, *G. Carboni* 513
Conceptual design of a muon spectrometer at hadron supercolliders, *G. Laurenti et al.* 520
Some aspects of toroid and solenoid design for LHC detectors, *C.R. Walters et al.* 532
The shaped solenoid for muon spectroscopy, *C.W. Fabjan* 538
Compact muon solenoid, *M. Pimiä et al.* 547

D8: Radiation Hardness 565

New dose calculations for LHC detectors, *G. Stevenson* 566
The radiation hardness test facility at RAL, *M. Edwards, D.R. Perry* 584
A neutron source for irradiation purposes, *B. Merkel* 596
Irradiation facilities at CERN, *M. Tavlet* 603
Ethanol-chlorobenzene dosimetry systems for high-dose dosimetry, *D. Razem* 606
Effects of radiation damage on scintillating fibre calorimetry, *A. Maio* 625
High and low dose rate irradiations of scintillators and wavelength shifters, *U. Holm et al.* 645
Radiation resistance of crystal scintillators. How to study it? How to improve it? The example of the BGO, *P. Lecoq* 651
Radiation damage and resolution loss in scintillation fibres calorimeters, *J. Badier* 661

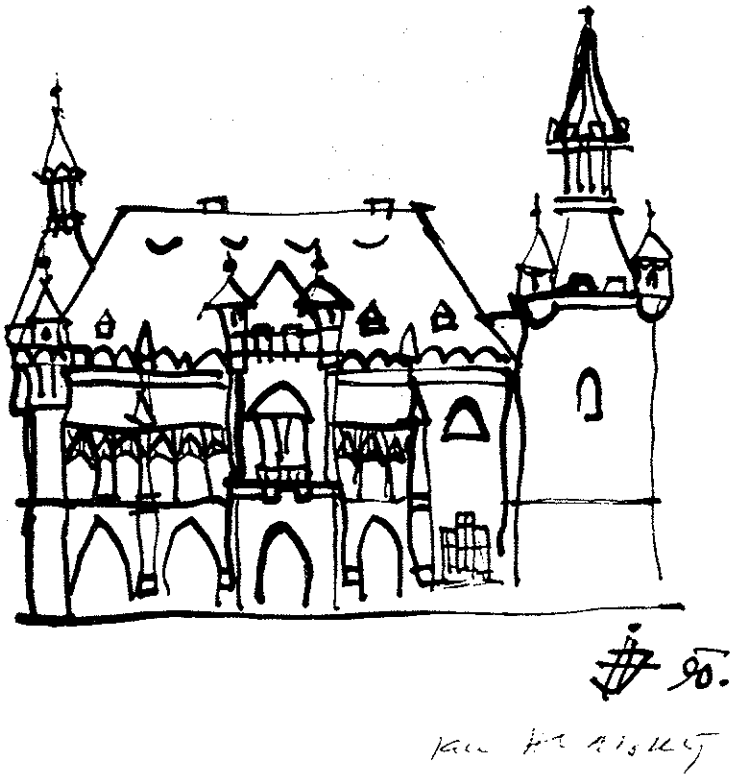
Silicon on insulator for ultra-hard applications – CEA SOI technologies *J.L. Leray et al.* 666
Rad hard and rad tolerant IC's developed to satisfy the extreme space and LHC requirements, *G. Durand, J.M. Maurel* 671
LPS radiation tests on service electronics, *H. Larsen, T. Massam* 677
Radiation-hard SOS-VLSI for detector electronics, *N. Bingefors et al.* 688
Radiation hard bipolar and CMOS front end electronics, *K. O'Shaughnessy et al.* 691
Radiation resistance of semiconductor detectors and associated electronics, *G. Hall* 693
Radiation damage of silicon detectors by monoenergetic neutrons and electrons, *G. Lindström et al.* 706
Study of operating condition of semiconductors for calorimetry, *C. Furetta et al.* 721
Results of radiation hardness tests of GaAs solid-state detectors, *S. D'Auria et al.* 725
Radiation testing of optical fibres and typical results, *H. Henschel* 732
Producing radiation hard all silica fibres: state of the art and future aspects, *H. Fabian et al.* 736
Radiation resistance of insulators and structural materials, *M. Tavlet, H. Schönbacher* 743
Radiation hardness of semiconductor detectors and read out electronics for the ALEPH minivertex detector, *P.W. Cattaneo* 749

D9: Experimental Areas 759

Experimental insertions for the LHC, *W. Scandale* 760
LHC interaction regions, *K. Potter* 765
Beam pipe size and impact parameter resolution, *F. Bedeschi* 769
LEP/LHC alternate operation and shielding, *H. Taureg* 770
Remarks on large magnets, *F. Wittgenstein* 778
L3+1 at LHC, *K. Freudenreich et al.* 791
Neutrino physics at LHC, *L. Camilleri et al.* 810
An e-p insertion for LHC and LEP, *A. Verdier* 820
e-p experiments in LEP/LHC interaction regions, *W. Bartel et al.* 824
Ion collisions at LHC, *P. Sonderegger* 833

Post-Deadline Paper 759

Fast muon tracking with resistive plate chambers, *R. Santonico* 838



The Organizing Committee takes pleasure in thanking one of the participants of this LHC Workshop at Aachen, Jan Hladky, from the Czechoslovakian Academy of Sciences (CSAV) at Prague, for the charming artist's sketches of various Aachen sites he contributed to these proceedings.

A new geometry description for GEANT

René Brun[1]
Federico Carminati[1]
Evgenij Chernyaev[2]
Victor Perevoztchikov[2]

November 23, 1990

Abstract

The GEANT3 program has been designed in 1981-1982 for the needs of the LEP collaborations and it has now become almost a standard for simulating the interaction of particles with matter in High Energy Physics detectors. To cope with the increased requirements imposed by the simulation of detectors for the next generation of experiments, improvements are now required in many areas of GEANT. This paper will focus on the work currently planned in the geometry description and detector data-base. Basic geometrical entities and composite volumes which can be handled by most CAD/CAM systems will be used to describe the detector. These are organised into a binary tree at initialization time to allow the utilization of new effective binary search algorithms for tracking. Elementary surface-point algorithms are used to take decisions at every bifurcation of the tree. The new description will feature a backward compatible user interface and enhanced functionality in many areas such as tracking performance, graphics, and detector design tools. In particular the new strategy will allow to exchange the detector description with CAD/CAM systems. This will represent a major advantage for physicists and engineers designing new detectors. The skeleton of a general event-viewing system will also be included, in an integrated environment together with detector design, physics simulation and event reconstruction.

1 Introduction

The GEANT3 [1] program has been designed at the beginning of the eighties with the LEP experiments in mind. It has now become almost a standard for detector simulation in High Energy Physics and it is also used in other fields such as cosmic ray showers, medical applications of synchrotron light or radio-dosimetry on space vehicles. Unlike many similar programs, GEANT does not require the user to find in which volume a particle is, but determines it from the detector geometry and the position of the particle all along the tracking process. The apparatus is

[1]European Laboratory for Particle Physics, CERN Geneva, Switzerland
[2]Institute for High Energy Physics, Serpukhov, (Protvino),USSR

built by the user during program initialisation via a set of FORTRAN calls which define and position objects in space. The modular design of the geometry and tracking/physics sub-systems and the simple and well-defined user interface have allowed to introduce enhancements and extensions without affecting significantly the users or changing the structure of the program.

The design has proven successful, and the complicated LEP experimental set-ups have been simulated within the original program structure. The detectors of the new generation appear more complex and costly than their predecessors. At the same time, the computing environment has dramatically changed to a much richer scenario facing the authors of software. This calls for a major improvement of the GEANT program, to be able to meet the new needs of the High Energy Physics community and provide a tool which can be used for the next decade or more.

Given the cost of a detector and the time taken to build and operate it, computer simulation is now absolutely necessary in the design stage to optimize the project with respect to many, and often incompatible, parameters. This calls for a closer collaboration among engineers designing the mechanical structure and physicists designing the functional part of the detector. Simulation MonteCarlos have traditionally been used to understand the behaviour of an existing apparatus. Today they are used also to predict its behaviour before it is built and to optimize its design. This optimization is typically realised via a design loop that involves several iterations during which the detector parameters must be exchanged between engineers and physicists in an efficient and reliable way.

The physicist optimising the detector functional design needs new tools to improve the efficiency of his work. These should be offered by an integrated interactive environment to design, modify, test and optimize a detector structure, and subsequently output a set of specifications which could be passed directly to the engineers' CAD system for the next iteration. High level 3D graphic interaction should be used where possible, while the program should be accessible also from low level, eventually even non-graphic terminals. To guarantee the possibility to simulate events interactively in the design phase and analyse interactively the result of a modification, performance must be substantially improved and the level of detail of the simulation must be tunable to the answer requested.

In the analysis phase the quality of the results depends also on the statistic available. Event simulation time in full shower development programs grows linearly with the energy of the collision. With the foreseen luminosity of the new detectors, the rule-of-thumb of two simulated events for every measured one, sets formidable CPU time requirements. More than half of the CPU time to simulate an event is spent in the geometrical calculations, which must therefore be optimized. In this sense a new geometrical structure should also be easy to optimize on advanced architectures, like parallel or vector computers. In view of the perspective of simulating larger and more complicated detectors, the availability of a more flexible and general way to describe new shapes is also desirable. At the moment new shapes can be introduced in GEANT, but at the price of a substantial programming effort prone to coding and logic errors.

The obvious advantages of an integrated and uniform environment should be extended also to the event viewing and reconstruction phase. The new structure will also serve as a base for a general event reconstruction and event viewing scheme.

2 Geometry data-base

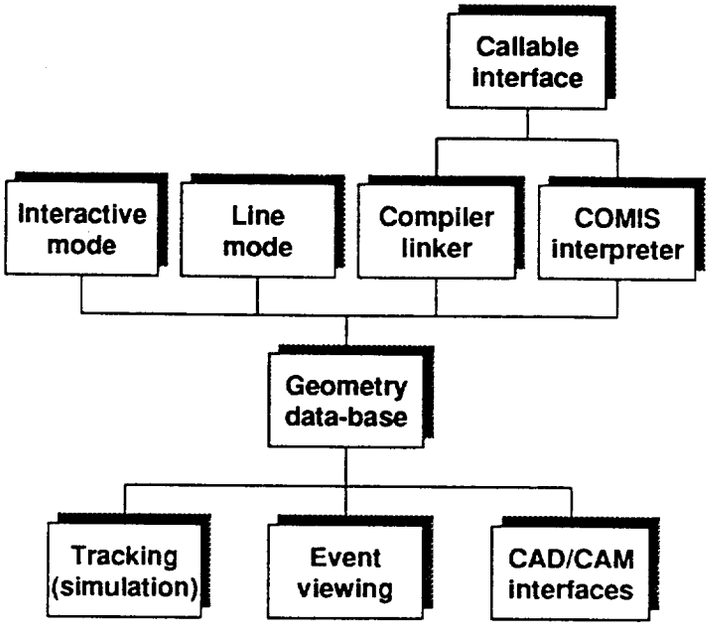


Figure 1: Data Base Structure for GEANT

The geometry data-base (fig 1) contains the structured geometrical description of the detector. The data-base contains only the *creation* history for each object, or otherwise said, the steps to define it from basic elements. The detector itself is really *built* in memory by the program accessing the data-base for particle tracking or detector visualisation.

The data-base has two front-ends: a user and an application interface. The user interface to the data-base has three different access modes: interactive, batch and via a program-callable interface.

Interactive mode In this mode the user will be able to access and modify the data-base via graphic input-output. This will provide for a very user-friendly access to the detector geometrical information, and will have its full functionality on advanced graphic workstations. A whole detector can be created, visualized and modified this way. Simple analysis tools to find for example

the volume or weight of the various detector components will be included. Facility to transparently access a remote data-base over network will be included. A menu mode will be provided via KUIP [2], which is currently being interfaced with toolboxes such as X-WINDOW/MOTIF. The detector graphic editor will be similar to the one featured by advanced CAD/CAM systems.

Command line mode A *line mode* interface will be provided to have access to a sub-set of the above functions via line commands. These will have the possibility to be grouped in macros (command files) to perform complex operations with one single command. This is the interface provided by the KUIP package, which will be the only one accessible from low-level graphic or alpha-numeric terminals, or from batch jobs.

Callable interface A callable interface will be provided to give access to the data base in order to include, modify, delete and visualize objects. This can be used in application programs, for example to convert from the GEANT geometry data base to different CAD/CAM systems representations. The callable interface can be used via the normal compile-link-and-run procedure or can be accessed interactively via the COMIS [3] FORTRAN interpreter.

The **application interface** has three main components:

Tracking This is of course the most important usage of the information of the geometry data-base. This module extracts the information from the data-base and identify a set of suitable surfaces. These are organized into a binary tree which is used at tracking time to determine the relevant information to propagate the particles through the detector. Given a point in space, the binary tree allows a very fast determination of which volumes this point is in. The information on the detector structure can also be passed to this module via a set of calls, in which case the data base need not be used as an input.

Detector/Event viewing This sub-system will allow the visualization of the detector components and of the events, both real and simulated ones. This modules will be used both in the event simulation and in the event analysis and reconstruction phases. This of course means the possibility to include, in the data-base (in some standard form) a description of real events and the possibility to visualise them together with the detector.

Communication with CAD/CAM This module is extremely important to optimize the design process of a detector. The structural design of a modern detector is done with CAD/CAM systems, and the exchange of the detector description with the engineering departments in a reliable and efficient way would represent a great step forward in the design process.

The basic tools to create and manage the data-base will be the ZEBRA memory manager with the RZ direct I/O sub-system. All the facilities currently available

in ZEBRA plus the ones which are planned for the future will be available for this database. This is particularly interesting for the inter-machine communication. Not only the data-base will be exportable in a transparent way over local and wide-area network via the ZFTP facility, but one single copy of the data-base will be accessible by many machines in a distributed and heterogeneous environment via the remote ZEBRA/RZ server. Another advantage deriving from the usage of ZEBRA/RZ is the possibility to store several versions of the detector and to retrieve a previous version from the data-base.

The data-base on disk is however not necessary. The present mode of operation of GEANT will be preserved. The geometry can be defined by a set of routine calls and the resulting detector description will be present only in the memory of the executing job. The tools described above will allow to optionally output this description in memory to generate a database which could be used as an input in subsequent runs.

3 Basic shapes

The detector description with the new geometry package is based on a constructive approach, where more complicated shapes are built from more simple ones (*basic shapes*) via an extended set of boolean operations. The main idea is that the basic shapes should be in limited number, easy to understand and able to describe an arbitrary object when combined via the allowed operations. Addition to the list of basic shapes should not be necessary even in case of very complicate objects. These goals can be reached thanks to the introduction of an extended set of operations which will include boolean operations. The definition of these shapes comes from an investigation of the basic shapes used in most CAD/CAM systems (EUCLID in particular).

We propose to introduce two sets of basic shapes:

Special shapes
These shapes have a somewhat fixed topology and set of parameters. The main motivation to introduce these shapes is that they are the most common in experimental set-ups and a substantial economy in programming effort can be realised if special routines are foreseen to define them rather than constructing them from general basic shapes. These shapes are (see fig 2): box, cylinder with hole, cone with hole, spheroid, paraboloid, trapezoid. This list could be increased if needed.

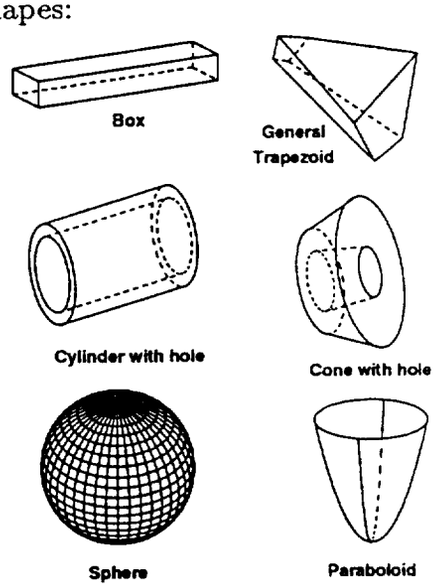


Figure 2: Special shapes

General (or constructive) shapes
These shapes cannot be described by a fixed set of parameters, but they are rather assembled from a set of even more elementary objects called entities. The entities composing a general shape must be defined before the shape is assembled. The basic entities (see fig 3) which we will use are:

1. set of points;
2. line (straight, joining two points);
3. polyline (joining a set of points);
4. contour (closed polyline);
5. face with holes (set of non-intersecting directed contours);

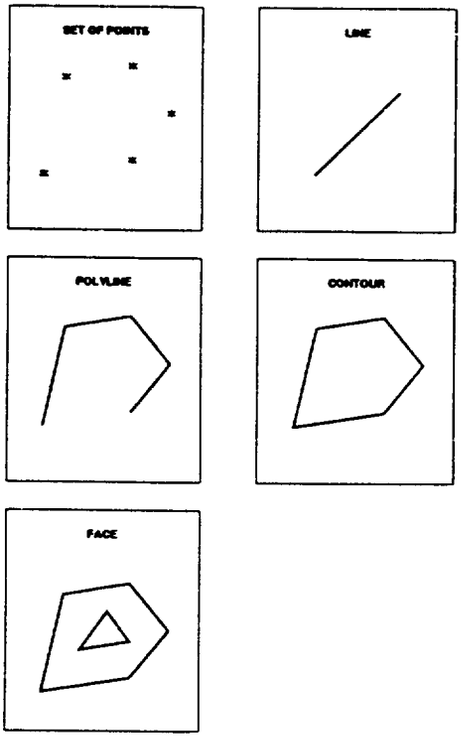


Figure 3: Basic entities

These basic entities can be assembled to form the following general shapes (see fig 4):

1. General prism – two faces with the same number of points, the points are orderly connected in pairs by straight lines;
2. Body limited by plane faces – closed set of faces. The body is the intersection of the semi-spaces on the positive side of the surfaces;
3. Convex body – for its description only the vertices coordinates are needed;
4. Body of revolution – face rotated around an axis. The rotation can be discrete (equivalent to the GEANT PGON shape) or continuous, to give a sector of a circle as a section;

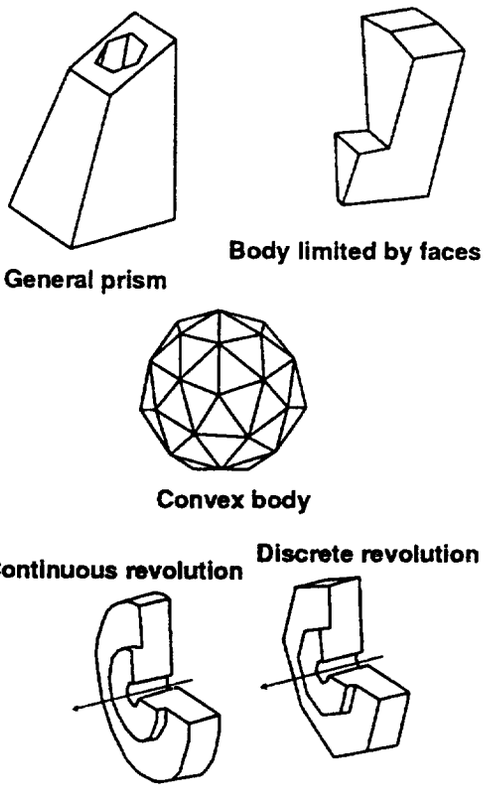


Figure 4: General shapes

In principle this is enough for most practical purposes, even if we could also add:

1. Kinetics bodies – a face is transported parallel to a polyline or a polyline is moved along the a contour;
2. Body defined by a set of its slices – set of faces;

As it will be explained in the next section, bodies can be translated, rotated or reflected. All boolean operations (union, subtraction and intersection) are possible (see fig 5). A special operation is defined for efficiency reasons, called GLUE. A GLUE operation is the union of two body which are touching each other.

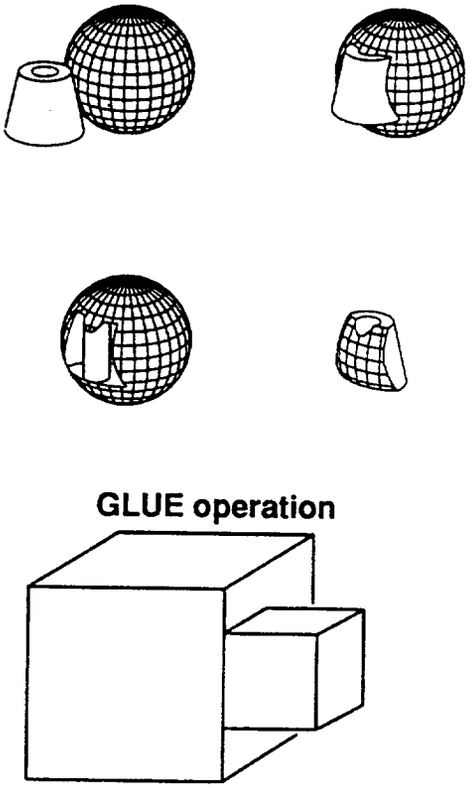


Figure 5: Boolean operations

Complex shapes are obtained by combination of basic shapes via boolean operations expressed by the following operators:

':' Links a shape to a transformation. '1:2' means shape 1 with tranformation 2 applied.

'+' Logical or of two shapes. '1+2' means union of shape 1 and shape 2.

'*' Intersection of 2 shapes. '1*2' means shape 1 intersected with shape 2.

'&' Glue operation. This can be used instead of + when two shapes have an intersection of dimensionality less than three.

'–' Difference. '1-2' means the portion of shape 1 which does not belong also to shape 2.

A typical example of a formula generating a complex shape is the following:

(1:2+3:5)*4&1:3

The current routines of GEANT to define the geometry will continue to work in the new scheme and it will be possible to mix them freely with the new ones.

4 Connection with CAD/CAM systems

The shapes described above are a subset of the shapes which are currently used in CAD/CAM systems. In this sense it will be rather easy to extract and transform the information of the geometry data-base in such a way that it will be understood by most CAD/CAM systems. The inverse operation may not be so trivial, because there are entities which are not included in our basic set, but are used by CAD/CAM systems, such as Bezier surfaces. The reason for not having a larger set of basic entities is that this would affect negatively the tracking time. In these cases most CAD/CAM systems are able to approximate curved surfaces via surfaces with planar facets to a given degree of accuracy. Unless these are used from the beginning in the CAD description, the export/import of a detector description from a CAD system would result in an object different from the original one.

5 Graphics

The *creation history* stored in the data-base constitutes also the starting point for graphics. A plane face description of the detector can be built starting from the constructive elements. Once this is done, extended boolean operations are applied to perform hidden line and hidden surfaces removal and provide a 3D representation of the detector. For this an extended version of the CG package introduced in GEANT in version 3.14 will be developed.

6 Tracking

6.1 Binary searching techniques

Searching algorithms can be classified in the following categories:

Linear searching It is the simplest one, time of searching is proportional to the number of objects.

Binary searching Time of searching is proportional to the logarithm of the number of objects. This technique requires a preliminary sorting of the objects to be searched.

Hash searching Time of searching is proportional to the number of objects but with a very small coefficient. This approach is possible only if searching keys are digitised.

The worst case of search used in the current version of GEANT is linear, with the possibility to introduce hashed search for selected volumes. Due to the very large number of volumes used to describe a modern detector, which is approaching 10^6, the linear algorithm becomes too expensive in CPU time.

We propose to replace the current algorithm by a binary search algorithm which we will call Binary Tree Technique. The main features of the new algorithm will be:

1. the current user interface to define the geometry will not change;

2. all the volumes currently described by GEANT will be described also in the new scheme by the same set of parameters;

3. the new structure will be faster than the current one to determine in which volume a point (x,y,z) is;

4. the speed of the Binary Tree Technique will have a rather weak dependence on the number of volumes at any given level of the tree. The dependence will be closer to a logarithmic one than to a linear one;

5. it will be no longer necessary to give explicitely the list of neighbours to optimize the tracking, because this will be automatically determined by the program;

6. it will be possible to check for overlapping volumes.

A possible drawback of this new structure is that the initialisation phase becomes much more complicated and costly in CPU time.

6.2 Basic definitions

All the volumes used may be considered sum of volumes V_i which are convex in the sense explained below. Each of the volumes V_i (i=1,...V) is defined by a set of intersecting surfaces S_{ij} (j=1,...S). The surfaces are defined using 2^{nd} degree polynomials in cartesian coordinates:

$$\begin{aligned} S(x,y,z) \;=\; & A_0 + A_x X + A_y Y + A_z Z + \\ & A_{xx} X^2 + A_{yy} Y^2 + A_{zz} Z^2 + \\ & A_{xy} XY + A_{yz} YZ + A_{zx} ZX \end{aligned} \qquad (1)$$

$$S(x,y,z) \begin{cases} < 0 & \text{the point (x,y,z) is on the } \textit{left} \text{ side of the surface} \\ > 0 & \text{the point (x,y,z) is on the } \textit{right} \text{ side of the surface} \\ = 0 & \text{the point (x,y,z) is } \textit{on} \text{ the surface} \end{cases}$$

A *convex* volume V_i is defined when it is possible to define for each surface S_{ij} the sign of the above expression when the point is inside the volume. We call this set of signs, which is the same for all the points inside the volume V_i the standard set of signs for that volume. In this way the answer to the question *is the point inside or outside the volume?* can be determined calculating the set of signs of the expression (1) for the given point with respect to all the surfaces S_{ij} and comparing it with the standard set of signs for the volume V_i. The standard sets of signs for all *convex* volumes is calculated at initialization time.

In this sense, *convex* means that the set of signs with respect to the surfaces defining the volume completely defines the position of a point relatively to it (inside or outside). The advantage of this internal representation of shapes is that it allows the definition of boolean operations among shapes.

To be able to answer the more general question *in which volume V_i is the point (x,y,z)?* we use a Binary Decision Tree. This tree, which consists of nodes and branches, is prepared during the initialization stage from the constructive description of the detector and it is subsequently used to take decisions during the searching procedure. Each node of the tree is a surface with one parent and two descendent links, pointing to the left and right branches originating from the node. Each of the descendent links can either be a parent link for a node or be a *leaf* i.e. a terminal element of the tree. Let P=(x,y,z) be a point and S the equation defining the surface associated with a particular node. If S(P) is negative, we will follow the left branch originating from the node, while if S(P) is non-negative we will follow the right branch. This procedure is continued until we reach a *leaf*, a link which does not have a descendent node. This identifies either a volume V_i or a *hole* or undefined shape.

In each step of the process we divide the space in two. All the volumes in the half which our point does not belong to, are automatically eliminated from the search. After some steps, the volume of the space in which we have to search decreases like $2^{-nsteps}$. In the special in which a single volume V_i is left we simply check the signs of all the surfaces S_{ij} not yet computed to determine if the point is inside it or not. The total number of surfaces for which we have to calculate the sign of S(P) is proportional to $\log_2(number\ of\ surfaces)$.

The optimal binary decision tree is the one where at each step the space is divided in two equal parts, in the sense that the number of volumes V_i in each part is the same. We are therefore left with the problem of building an optimal or near-optimal decision tree. Let V_0 be the volume containing a particular set of V_i (i=1,... N). All the V_i of this set are said to belong to V_0 which is called *mother volume* for the set. Let S_k (k=1,...) be the subset of S_{ij} which are unique inside V_0. Let P be a point in space. We now define the following relation among volumes V and surfaces S:

$$V_i \mathrm{in} V_0 \begin{cases} < S_j & \text{if, for all } P \in V_i, S_j(P) < 0 \\ > S_j & \text{if, for all } P \in V_i, S_j(P) > 0 \\ < S_j & \text{otherwise} \end{cases}$$

In case $V_i = S_j, S_j$ intersects V_i inside V_0. Now for each S_k we can define three numbers:

$$\begin{aligned} N^+ &= \text{number of } V_i > S_k \text{ inside } V_0 \\ N^+ &= \text{number of } V_i > S_k \text{ inside } V_0 \\ N^+ &= \text{number of } V_i > S_k \text{ inside } V_0 \end{aligned}$$

With the above definitions we can now describe the main algorithm for the creation of the binary tree. Let V_0 contain a set of volumes V_i and let S_{ij} be the corresponding set of surfaces. Let us now consider all the S_k as possible candidates for dividing the volume V_0 in two parts. The probability for a point P to be on the *left side* of S_k is proportional to $N^- + \frac{N^0}{2}$ while the probability to be on the *right side* is $N^+ + \frac{N^0}{2}$. The average number of discarded volumes is thus

$P^+N^- + P^-N^+$ where $P^{+,-}$ is the probability to be on one side.

$$P^{+,-} = \frac{N^{+,-} + \frac{N^0}{2}}{N^+ + N^- + N^0}$$

This gives us the following average number of discarded volumes:

$$Q = \frac{2N^+N^- + \frac{N^0(N^+ + N^-)}{2}}{N^+ + N^- + N^0}$$

We choose as node for the tree the surface S_k for which Q has maximum value. Then we assign all the volumes to two overlapping sets which are the two branches of the tree

$$Set1: \quad V_i \leq S_k$$
$$Set2: \quad V_i \geq S_k$$

A point P in V_0 is in Set 1 if $S_k(P) \leq 0$ and it is in Set 2 if $S_k(P) \geq 0$. Each group is subdivided into two subgroups using the same approach. This procedure is repeated until either the current V_0 is entirely contained into a V_i or it does not contain any more volumes, in which case it is said to be a *hole*. This completes the preparation of the decision tree.

The convex volumes needed to build the binary tree are called *caves*. The first operation for the construction of the binary tree is the creation of caves from volumes. The splitting of the standard shapes into caves is part of the definition of the binary tree and it is hidden from the user. There is a special routine for every shape to do this job. The only operation required to introduce a new shape in the system it to write a routine to split this shape into caves. All the other operations are absolutely independent from the kind of shape used.

6.3 Calculation of distances

The calculation of the distance (R) from a point to a surface can be performed with the following formulae (summation over repeated indices is implicit). Let:

$$S(x) = A_0 + A_iX_i + A_{ij}X_iX_j$$
$$G_i = \frac{dS(X)}{dX_i} \text{Gradient of S(X) in } X_0$$

S(X) is normalized so that $G_1^2 + G_2^2 + G_3^2 = 1$.

$$A_{gg} = |A_{ij}G_iG_j|$$
$$A_{ij}^2 = A_{ij}A_{ij}$$
$$S_0 = |S(X_0)|$$

The distance from the point X_0 to the surface S is:

$$R \geq \frac{2S_0}{1 + \sqrt{1 + 4S_0\left(A_{gg} + \sqrt{A_{ij}^2 - A_{gg}^2}\right)}}$$

This formula is exact for planes, cylinders and spheres. For other 2^{nd} degree surfaces the error tends to zero with the distance. This means that for points near to the surface the value returned is close to the exact distance and for points far from the surface the value is smaller than the actual distance.

6.4 Distance along the trajectory

When the trajectory is a straight line the calculation is very simple because all the surfaces are 2^{nd} degree surfaces. In the case of a charged particle in a magnetic field, the trajectory is an helix and to calculate the distance along it we would need to solve transcendental equations. An approximation to the second order (sin(x) replaced by x and cos(x) replaced by $1 - \frac{x^2}{2}$ leads to an approximate solution. The accuracy of the solution can be estimated easily. If the resulting distance is greater than the accuracy, then the accuracy is taken for the step. Then the distance is calculated again. For most particles one iteration is enough, while for slow tracks no more than 15 iterations are needed.

References

[1] R.Brun, F.Bruyant, F.Carminati, M.Maire, A.C.McPherson, P.Zanarini, GEANT3, CERN Program Library Long Writeup W5013

[2] R.Brun, P.Zanarini, KUIP - Kit for an User Interface Package, CERN Program Library Long Writeup I202

[3] V.Berezhnoi, R.Brun, S.Nikitin, Y.Petrovykh, V.Sikolenko, COMIS COmpilation and Interpretation System, CERN Program Library Long Writeup L210

Status of Simulation Studies For Fibre Calorimetry

V.Vercesi
A.Dell'Acqua G.Fumagalli
INFN Sezione di Pavia, Pavia - Italy

Abstract

In this paper we present the current status of simulation studies for a sampling calorimeter using lead as absorber and scintillating fibres as active medium. The simulations have been done using the prerelease of the GEANT 3.14 programme. Results are presented for electrons, muons and pions and are compared with experimental data obtained on test beams by the Spacal Collaboration at CERN. All results are to be considered preliminary. A reasonably good agreement is observed for electrons and muons, whilst the hadronic part need more work to be fully understood.

1 Introduction

The scintillating fibre calorimeter technique has been developed to meet the requirements for detectors at future high energy colliders. The experimental project currently known as Spaghetti Calorimeter (or in short: Spacal) was initiated after it was theoretically predicted [1], and subsequently proven experimentally [2], that a lead/plastic-scintillator sampling calorimeter can be made compensating, a feature which until that moment was believed to be a unique property of uranium devices. In order to make such a device compensating, the detector should have a small sampling *fraction*, a factor of 4 smaller then typical values, which implies that sampling fluctuations tend to dominate the energy resolution. This can be counterbalanced by using a high sampling *frequency*, hence the choice of fibres as active material rather then the traditionally used scintillator plates.

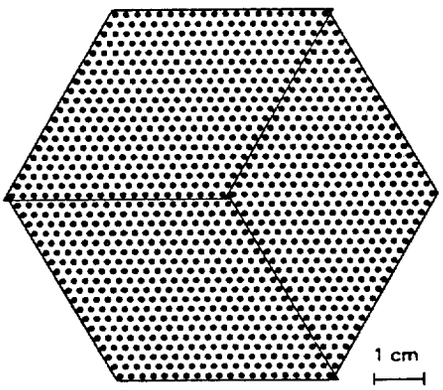


Fig.1 : View of one hexagonal module

As a consequence, this kind of calorimeter technique has some notable properties which make it very interesting as an object of simulation studies: comp

linearity, good resolution for electromagnetic and hadronic showers, uniformity of response as a function of impact point and angle. All these items address problems of fundamental physics, involving the detailed description of both electromagnetic and hadronic showers.

2 Geometry of the Fibre Calorimeter

The implementation of this technique by the Spacal Collaboration is made through the construction of hexagonal modules of 4.3 cm to the side and of 2 meters length. Each module consists of a lead matrix with 1141 cilindrical fibres of $\sim$1 mm diameter arranged as in Fig. 1. Fibres are made of polystyrene doped with SCSN-38 and are built by the company Kiowa in Japan. Modules are assembled at CERN by stacking extruded lead foils and fibres, layer by layer. The final setup is made of 155 such hexagonal modules, in a honeycomb structure as shown in Fig. 2. The resulting detector, a 20-ton integrated electromagnetic and hadronic calorimeter, has been exposed to pion, muon and electron beams. Particles were entering the calorimeter at a small angle with respect to the front face: a full angular scan has been made from 0^o to 10^o, and deviations from a gaussian response have been observed if $\theta_{inc} < 3^o$. Hence most of the data have been taken for an incidence angle of 3 degrees, and to those data we will be referring in the rest of the comparison.

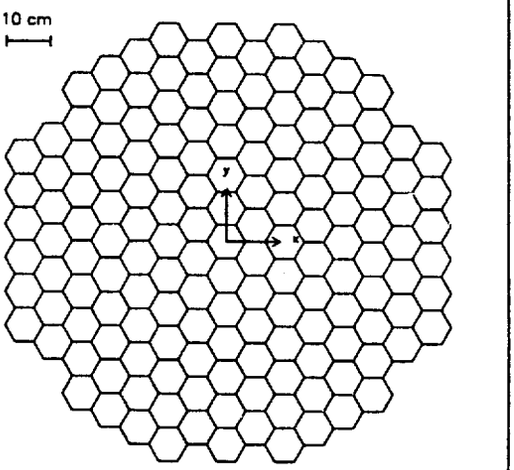


Fig.2 : Experimental simulated setup

Simulating this kind of geometry in an efficient way is not a trivial task. Unfortunately the present version of GEANT does not include any elementary shape which could be used fruitfully to describe this kind of "hexagon with holes", and it is obvious that positioning 1141 fibres per hexagon will immediately lead to astonishing values of CPU time/event. To overcome this problem, and waiting for a more general description of shapes inside GEANT we took the following steps:

1. each hexagon is divided (by positioning) into three overlapping rhomboidal shapes (see Fig. 1) made of lead

2. we exploit the division technique of GEANT along the x and y axis of each rhombus to build efficiently the search tree

3. into each division a "hole" of 1.1 mm diameter is positioned to account for the fact that we have typically a 50 micron air-gap between the lead and each fibre

4. iside the hole we put a fibre and the division automatically replicates this pattern over all the hexagon

5. we then position 155 copies of the module built in that way, to create the final detector setup

As it is clear from this description, the geometry is optimized by using the division technique whenever possible, and positioning only the few elements which are really necessary at each stage. In this way, for a single module, we obtain a reduction factor of 10 in CPU time.

3 Physics Simulation

It is worthwhile mentioning that even with the geometrical solution adopted above this kind of simulation has anyhow an high degree of complexity: we are confronted with thin layers of materials (typically 1 mm of fibre and 2 mm of lead) and we need to apply the lowest possible cutoffs for the physical processes we are interested about. This stems from the fact that fibres are particulary sensitive to the low-end part of the Compton and photoelectric spectrum, and missing these contributions will necessarily result into a poor description of the properties of this calorimeter.

The other consequence is that the parameters specifying the step size, the maximum energy deposition per step in the energy loss mechanism and the maximum displacement for multiple scattering become very tangled. This is due to the rapidly changing characteristics of the medium in all spatial directions and to the small thickness of both fibre and lead. For example, a crude treatment of δ-rays in the scintillator will reduce the dE/dx contribution, and a gaussian approximation for the multiple scattering distribution is completely insufficient to describe this process: those phenomena are clearly correlated and need to be treated in a coherent way.

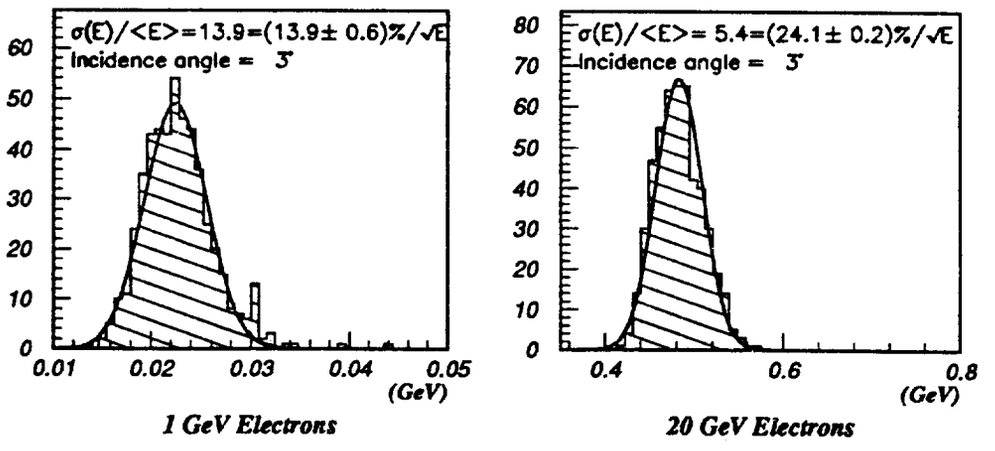


Fig.3 : Resolution for electrons

In this respect the major help which is contained in GEANT version 3.14 [3] is the introduction of the automatic calculation for all these parameters. This calculation is done after the GPHYSI routine is invoked, and takes into account the correlations

between the geometry description and all the different physical processes activated with (in principle) different cutoffs. In this way the only parameter which is left free to the user is the boundary check parameter ϵ, which is the tolerance on the border between different volumes (set to 1.E-3 cm in this simulation). The introduction of this automatic calculation allows for more efficient studies of the performance when changing geometrical or physical parameters, and exploits the GEANT capabilities of a detector designing tool in high energy physics (see the proceedings of R. Brun at this conference for a complete description of all the changes made in version 3.14).

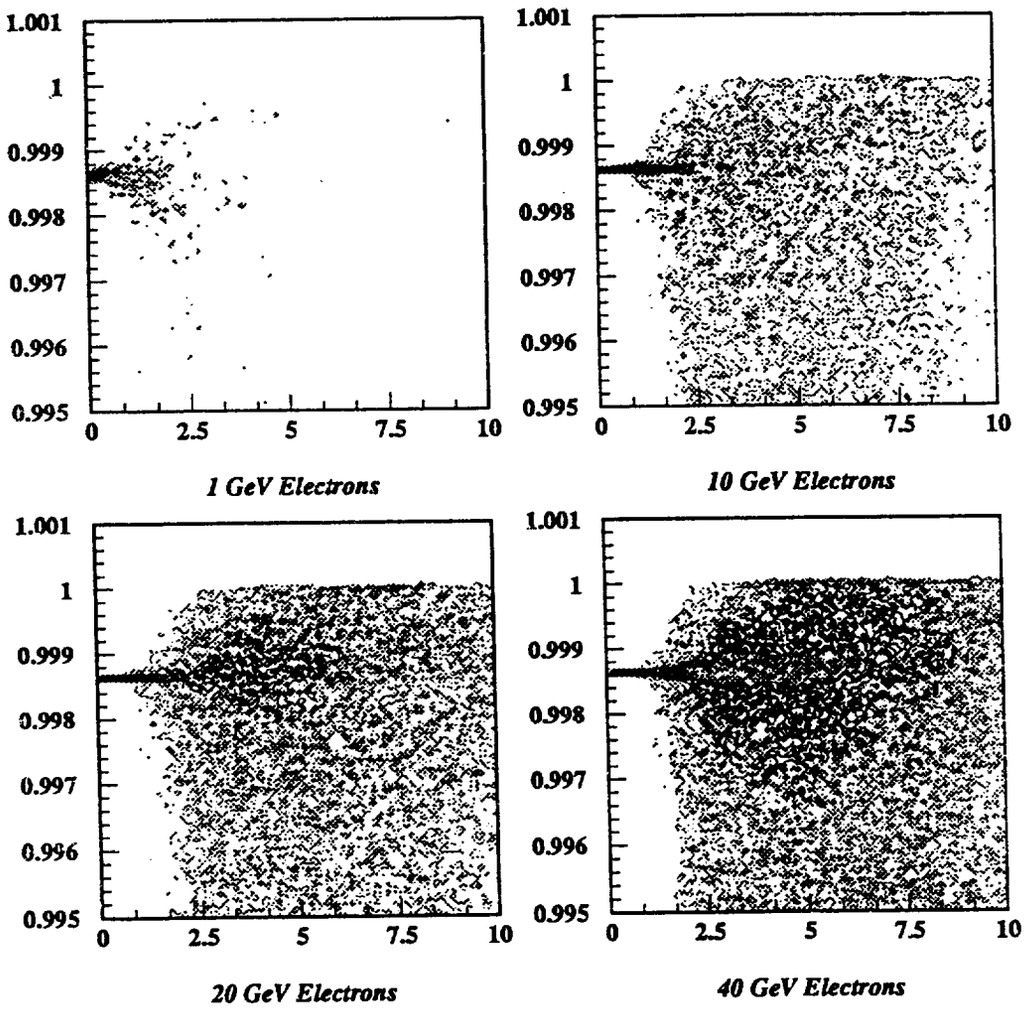


Fig.4 : Cosθ versus Z shower developments

The results presented in the next sections have been obtained using the following framework:

- all the cutoffs for the physical processes set to 10 KeV
- inclusion of the Birk's law for the saturation of local charge deposition, as measured for the used scintillator type (see Ref. [1])

- inclusion of the attenuation length of the fibres, as measured directly by the Spacal Collaboration
- no photofission effect in lead
- beam generation according to the experimental gaussian distribution in the transverse coordinates

The simulation was run on RISC machines of the series Apollo DN10000 or DEC 5400 (some of them partecipating in the SHIFT [4] project) and on the CRAY 1-X/MP. Typical values for the CPU time on CRAY are 8 seconds/GeV/event for electrons and 6 seconds/GeV/event for pions: the gauging factor (taking CRAY=1) was found to be 0.75 for the DN10000 and 0.45 for the 5400. Electrons and pions have been simulated at 1,5,10,20,40,80 and 150 GeV and muons at 150 GeV only.

3.1 Electron simulation

Fig. 3 shows the resolution obtained for electrons at 1 GeV and 20 GeV: a striking feature is that while at 1 GeV the σ is of the order of $13.5\%/\sqrt{E}$ (which is very close to the experimental value), at 20 GeV it increases at approximately $25\%/\sqrt{E}$. From purely statistical considerations one should expect the resolution computed with a *Montecarlo* to behave like $a/\sqrt{E}$, but this result seems to indicate the presence of an additional *constant*, a feature which is normally present only in *experimental* data where several terms originate this behaviour. We found a possible explanation of this phenomenon by studying the details of the shower developement in this type of calorimeter. When a particle enters the calorimeter at θ=3°, that is a small angle with respect to the fibre direction, the evolution of the shower depends slightly on whether it enters the fibre or the lead. In fact, the bremsstrahlung and pair production processes generate particles at angles of order $\frac{m}{E}$, where m is the electron mass and E the energy of the generating particle. This means that the first part of the cascade will *remember* the direction of the parent particle, and the generated particles will spend more time in the same fibre, giving a dE/dx larger then for the late part of the shower. Since the rate for those processes increases with the energy of the particle, one should expect this phenomenon to become more and more important as the energy increases. Fig. 4 illustrates this effect by plotting the cosine of the angle of particles in the shower (with respect to the fibre direction) versus the depth in the calorimeter. The shading is proportional to the energy deposited. One can easily see that the importance of "black" zones increases with energy and that their localization is correlated with the direction of the incident particle. We checked that, for example, this behaviour is completely absent at 90°. We are not able now to give a full quantitative extimation of this effect, and more studies are needed. In the rest we will simply fit the resolution values versus the energy to a function of the type $a + b/\sqrt{E}$, a being the *constant* term. A thoroughful investigation is under way, because this constant term, apperaring in the simulation, represents the contribution of geometrical effects to the constant term in the experimental data. We are trying to disantangle this part from all the other systematic contributions present in the data.

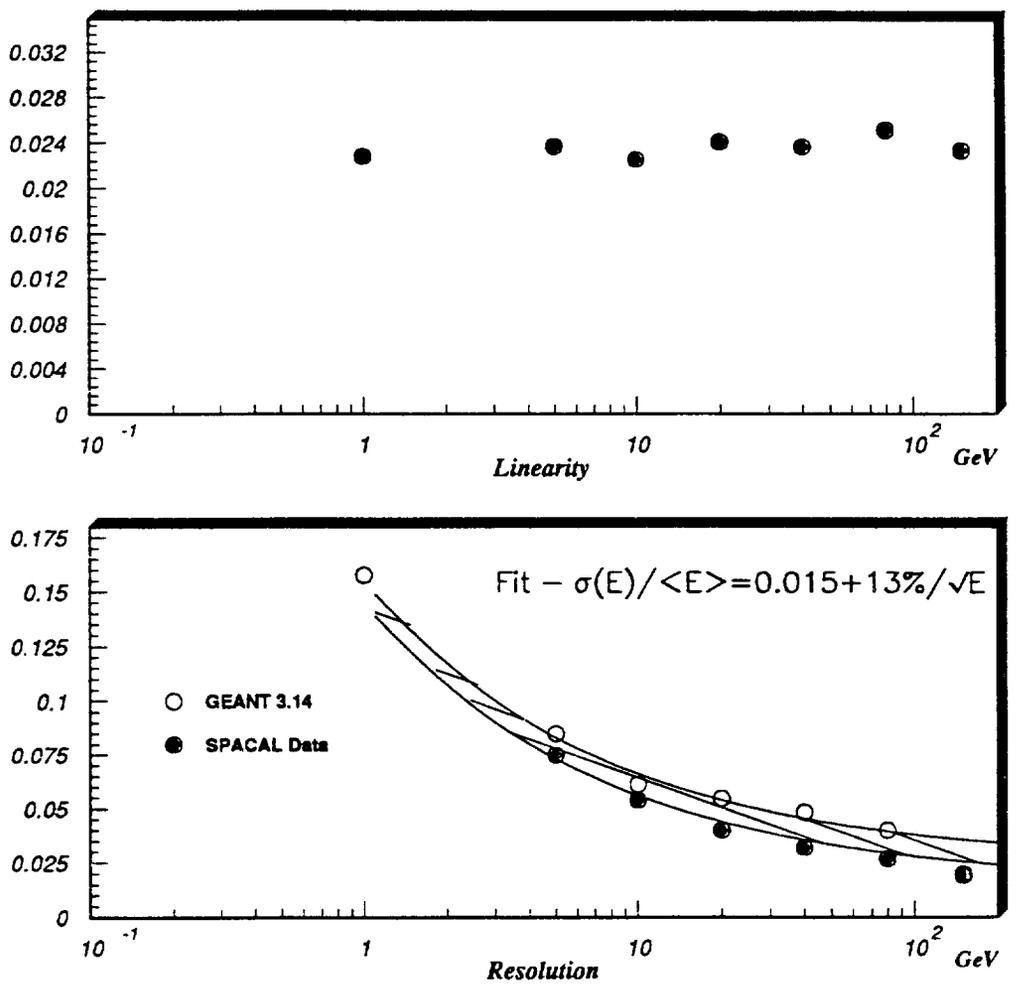


Fig.5 : Sampling fraction and resolution vs. energy for e

Fig. 5 shows the sampling fraction, i.e. the fraction of the energy of the incident particle deposited in the active medium, and the resolution versus the energy of the simulated electron beam. From this we can conclude that the simulation of the fibre calorimeter displays a perfect linearity and that the resolution agrees with the experimental points to within half a percent.

3.2 Muon simulation

No full simulation of muon response inside the fibre calorimeter has been done, also because of lack of a complete analysis of the experimental data. One particular and important example is anyhow given in Fig. 6. The Spacal group took a set of muon

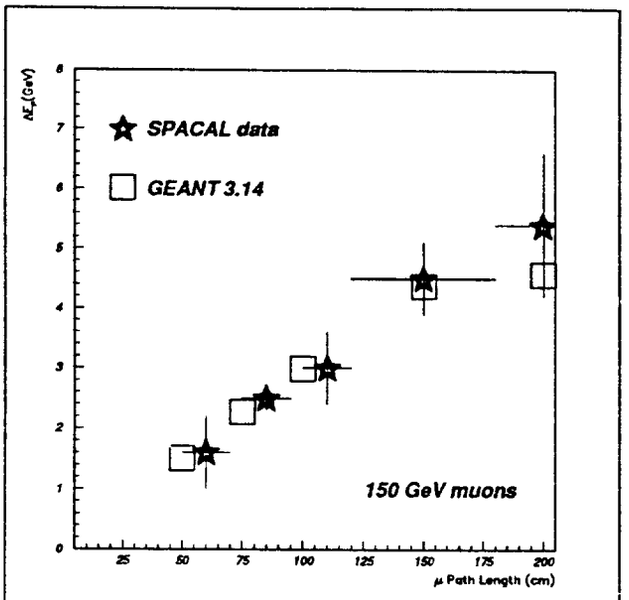


Fig.6 : Energy loss by muons vs. muons path length

data in order to verify the linearity of the calorimeter for minimum ionising particles. The geometrical pathlength of muons inside the module was varied (this was done by moving the impact point of the beam on the front face at fixed angle) and the observed energy rescaled assuming a e/mip ratio of 0.6. If the only mechanism is the ionization loss, one should expect the total energy loss to be directly proportional to the total path inside the module. On the Montecarlo side both quantities can be measured directly without any *a priori* assumption: the good agreement between data and simulation shows a very good linearity and that the assumptions for the e/mip ratio is reasonable. This study could be pursued to determine a general method for evaluating the e/mip ratio.

3.3 Pion simulation

The corner of the hadronic simulation has always been less rewarding then the electromagnetic one. Notwithstanding the enormous efforts which have been put on this item by several people, we are still lacking a complete description of the hadronic shower mechanisms, in particular at very low energies, where the tangling between energy loss and hadronic production reactions becomes very important. Nevertheless we attempted a simulation of the pions data collected by the Spacal Collaboration, using the same setup as for electrons. Two different simulations were developed, one using the GHEISHA package, the other using the new NUCRIN package. No particular difference has been found between the two approaches, although the NUCRIN package should be in principle more adequate for describing the hadronic evolution in the low energy range ([0,5] GeV). It must be stressed however that the results presented here are very preliminary and that more studies are needed to fully understand the origin of the discrepancies between data and simulation.

A hadronic shower develops in a completely different way from an electromagnetic one. In particular the angular sensistivity which was seen in simulating electrons is not present here, because the shower extends longer in depth and does not exhibit simmetry properties which are peculiar to the electromagnetic cascade. For these reasons we fitted the resolution curve to a function of the form $a/\sqrt{E}$, and we unfolded the *experimental* constant term (as measured in [5]) from the data points in the following comparison.

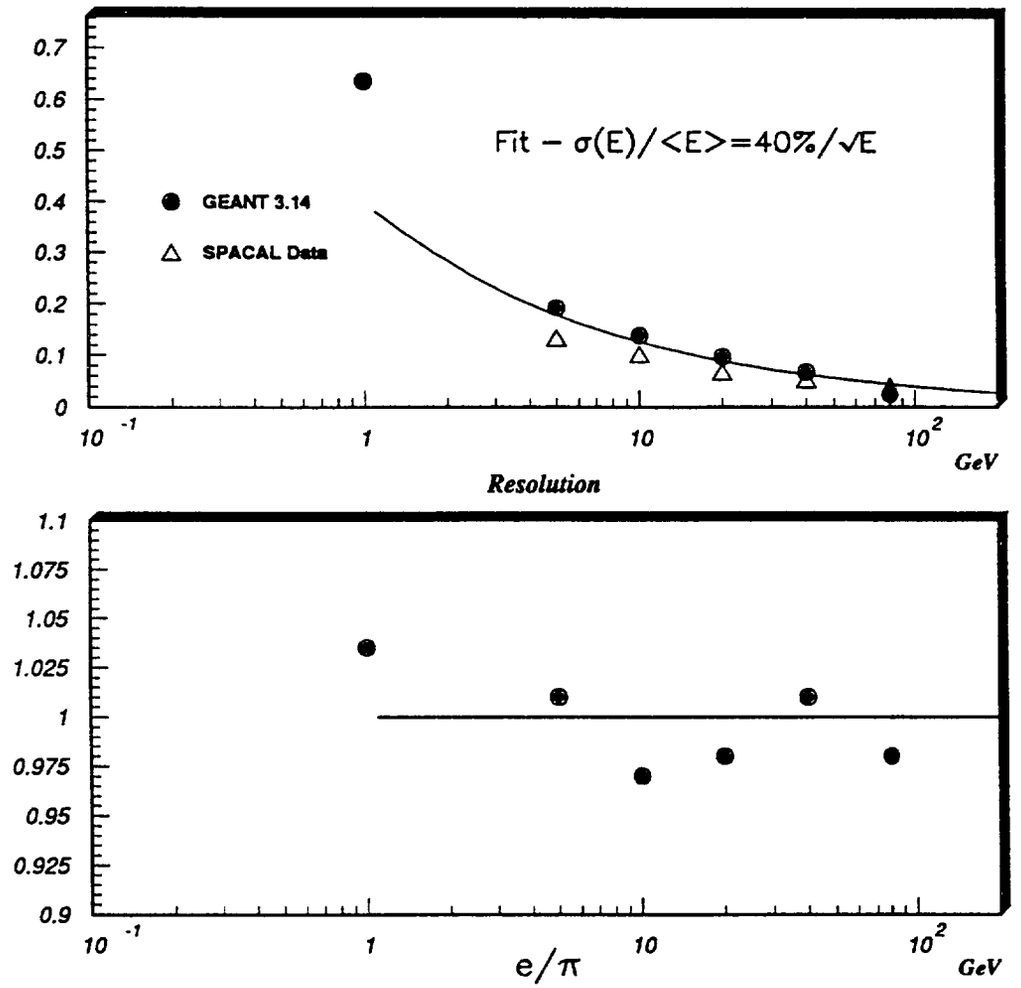


Fig.7 : Resolution for pions and e/h ratio

The simulated points (see Fig. 7) fit to a value of $40\%/\sqrt{E}$, which has to be compared to experimental value of $30\%/\sqrt{E}$: it is clear again that more work is to be done to complete this part of the simulation. It is however an important result that the e/h ratio is nicely close to one for all the energies: this imply that the compensation properties of this type of calorimeter are fully reproduced (on the average) by our simulation.

4 CONCLUSIONS

We have presented some results about the simulation of the Fibre Calorimeter prototype built by the Spacal Collaboration at CERN using the GEANT Montecarlo programme. The electron data are, to a great extent, reproduced by our simulation, and we have indications that we can acheive also a better understanding of some

specific geometrical properties which are present in the experimental results. The muon results show that minimum ionising particles are properly simulated, and they might be helpful in defining a method to extract an e/mip value from the data. Pions need certainly much more work to be fully understood, but first attempts seem at least encouraging. In particular we find that the compensation properties which are predicted for this type of calorimeter are reproduced by the Montecarlo. Finally it should be stressed that, given the non negligible amount of CPU time which is necessary to pursue these studies, we are looking forward to find a parametric description of the shower evolution properties. Work on this subject has also started, together with the authors of GEANT. Once a complete agreement between simulated and experimental data is reached, we intend to use this framework to address the problems of building a projective prototype, e.g. for optimizing the geometrical configuration and the performance of the detector.

References

[1] R.Wigmans, NIM A259 (1987) 389.

[2] E.Bernardi et al, NIM A262 (1987) 229.

[3] R.Brun et al., GEANT - CERN Program Library W5013.

[4] J.P.Baud, J.Bunn, D.Foster, F.Hemmer, E.Jagel, J.Joosten, O.Martin, L.Robertson, B.Segal, R.Többicke, SHIFT Scalable Heterogeneous Computing Facility Testbed Design Study and Implementation Proposal, CN Division CERN, Version 1, July 25, 1990.

[5] The Spacal Collaboration, CERN/DRDC/90-23.

Simulation of sampling calorimeters

M.Nessi,
P.Jenni, F. Nessi-Tedaldi
CERN, Geneva (Switzerland)

1 Introduction

In this report the results of several simulation studies of electron, hadron and jets in sampling calorimeters are presented. The aim of these investigations was first to set up and then test a tool for simulations of different, also hybrid, calorimeter configurations for LHC detector studies. First simulation of calorimeters with LHC performance characteristics are also presented.

The topics to be studied are

- The signal ratio for electrons versus hadrons as well as the resolution and the linearity for electrons, hadrons and jets in different calorimeter configurations;
- the study of hybrid configurations;
- the tuning of compensation for the achievement of optimum resolution for jets.

2 Simulation of existing calorimeters

At the start of this project, a decision had to be taken about the package to be used. Differently from simulation work done in the past no defined calorimeter setup existed which had to be simulated in detail and then compared with experimental data and even further, no test beam results were available to strengthen the consistency of the simulation models with the data through parametrizations, as had been done in the past. On the other hand, a generalized package like GEANT3.13 was available, which had already shown in many applications great versatility and reasonable results. Along with our first simulations aiming to reproduce existing data from other experiments testing in particular electromagnetic and hadronic shower simulations, a new version of GEANT3 was developed, with improved showering, in a mutual attempt to obtain a simulation package to be used reliably for future studies of new calorimeter configurations and geometries. In the simulation results presented here the tools which were adopted are simulations of electromagnetic and hadronic barrel calorimeters based on the new version, GEANT3.14 [1]. The user interface to define the geometry was implemented via

simply steerable datacards. These allow to input the geometry parameters for combined electromagnetic and hadronic sampling calorimeters, so that different configurations can easily be used for similar simulations without that the user has to worry about setting up the geometry definition himself. While the GEANT3.14 package allows to develop electromagnetic and hadronic showers via its own implementation of the EGS tables and GHEISHA, the production of jets was achieved interfacing the LUND-Monte Carlo package of Jetset72 [2] to our simulation. As a calorimter signal, the energy deposited in the active medium was used, where saturation effects affecting the correlation between signal output and energy deposition was taken into account reducing the calculated energy deposition by a quadratic expression of the Birks law [3] both for scintillator and, empirically, also for Liquid Argon. However, before to investigate with simulations the properties of new configurations, it was important to test the tools to be used in comparing the results with measurements for existing calorimeters. The following "test benches" were used:

1. *Lead-Scintillator* → ZEUS test propotype of Ref. [4]
2. *Lead-Liquid Argon* → H1 test prototype [5]
3. *e/mip studies*

2.1 Lead-Scintillator

The simulation of a fully compensating calorimeter is of particular interest, since this allows to test against each other the calculated electromagnetic and hadronic responses. The prototype used in the test measurements consisted of a squared configuration of 3×3 modules with a sandwich structure of 10 mm Lead and 2.5 mm Scintillator (SCSN-38) plates, 5 interaction lengths (λ) deep for a total of 81 layers, where the first interaction length belonged to the electromagnetic section (i.e 29 X_o) while the other 4 λ constituted the hadronic section. The light was collected by wave length shifting plates running along the left and the right side of each module. In the simulation the same sampling, 10 λ deep, was used in a barrel configuration with inner radius 1.5 m, were similar results are expected for particles at $\theta = 90°$. Details of the geometry like the presence of wave length shifting plates and spacers (in the form of PVC) rods were neglected.

The simulation results (see Fig. 1) show a mean e/π ratio for particle energies between 3 GeV and 100 GeV compatible with the measured value 1.04 ± 0.05 with no apparent energy dependence, as expected. The electromagnetic resolution in simulation is

$$\frac{\sigma}{E} = \frac{(24.0 \pm 0.8)\%}{\sqrt{E}} \oplus 0.5\%$$

while the data yield

$$\frac{\sigma}{E} = \frac{(23.5 \pm 0.2)\%}{\sqrt{E}} \oplus (1.2 \pm 0.2)\%.$$

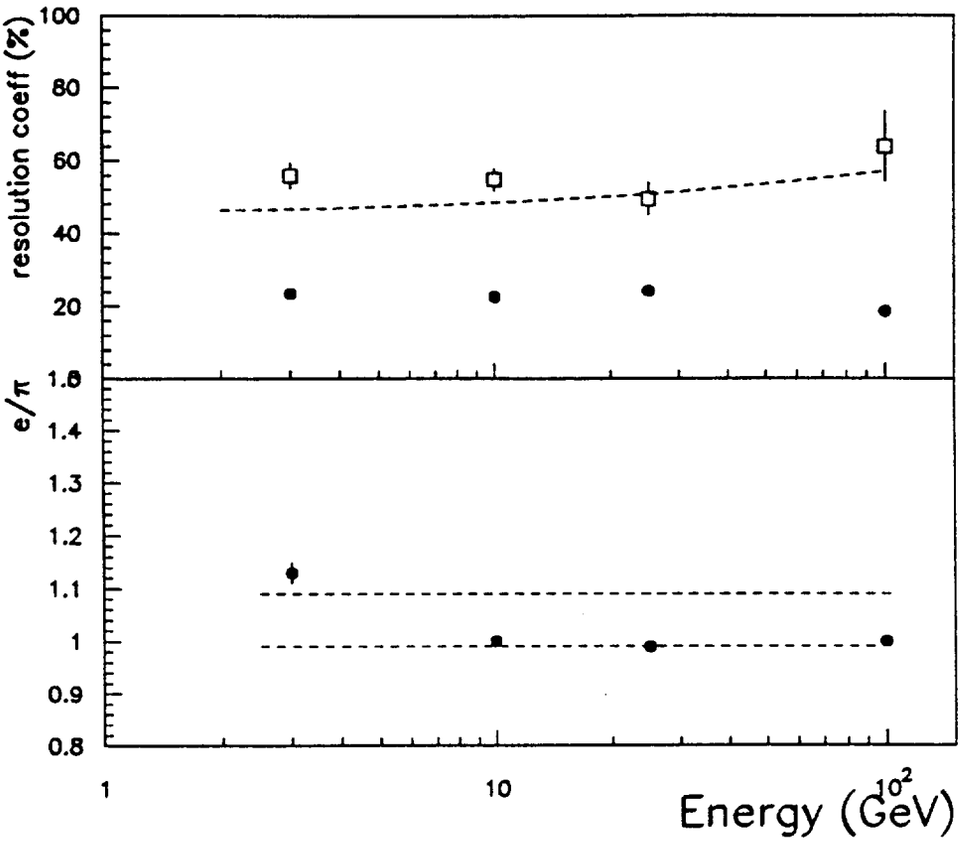


Figure 1: Results of the simulation for a sampling calorimeter consisting of 10 mm lead plates and 2.5 mm scintillator plates, compared to experimental data of Ref. [4] (dashed line resp. band). Top: Resolution coefficient R (%) (where $\sigma/E = R/\sqrt{E}$ with E in GeV) for electrons (black circles) and hadrons (white squares). Bottom: e/π ratio.

For hadrons, one obtains a resolution

$$\frac{\sigma}{E} = \frac{(50.9 \pm 3.8)\%}{\sqrt{E}} + (0.3 \pm 0.9)\%$$

with E in [GeV], which is compatible within errors with the experimental value of $(44.2 \pm 1.3)\%/\sqrt{E}$. The agreement is resonably good, taking into account that some details of the setup (see above) have been neglected. However, the simulated resolutions results are systematically somewhat higher with respect to the measured values.

2.2 Lead-Liquid Argon

Lead-Liquid Argon calorimetry represents an example of non-compensated response. In this kind of calorimeters, the electromagnetic resolution can be accurately calculated. This has been confirmed even in simulation of complex configurations like the "accordion" geometry, as can be seen in Ref. [6]. To check the

simulation of the hadronic response, the H1 test setup [5] was available, which consists of following elements:

- An electromagnetic section of 26 X_o Lead plates of 2.4 mm and 2.8 mm Lar gaps.
- A hadronic section, 6 λ deep, consisting of 5 mm Cu plates and 2×1.5 mm Lar gaps.

The same sampling was simulated again in a barrel geometry [7], where plastic readout boards and Kapton foils present in the setup were also simulated, with all plastics taken as density 1 materials with C-H composition. In combining the two different samplings, the same definition of e/π was used as in the experiment. The results for 30 GeV pions are as follows: An e/π ratio of $1.22 \pm 0.02 \pm 0.04$ from the simulation, to be compared with the measured value 1.24 ± 0.01. The resolution for hadrons in the simulation is $11.3\% \pm 0.3\%$ for a measured value of 11.0%. The good agreement not only leaves us confident in extrapolating to other configurations with liquid Argon as the active medium, but it also confirms the procedure used for combining different calorimeters.

2.3 e/mip studies

The ratio of electron over minimum ionizing particle signals e/mip is of special interest in view of an attempt to tune the electron response suppression in non-compensating calorimeters through cladding techniques (local hardening / filtering) or through an appropriate choice of the Z-ratio between active and passive media (migration effect) [8]. In Figure 2 the ratio e/mip is shown for a Lead-Scintillator configuration where the thickness of the active material is fixed to 5 mm and the one of the absorber is varying from 0.2 mm to 100 mm. The solide line is a fit to an EGS4 calculation (white circles, from Ref. [9]), while the the black points are the results of our calculation [10]. These points were calculated using a tracking step precision of 1/100 of each material thickness. The same tracking step parameter was also applied in the EGS4 calculations in order to meet the experimental results (black triangle, Ref. [11]). Our simulation lies systematically lower with respect to the EGS4 calculation by about 7%. The disagreement is bigger if the simulation is performed using the standard tracking parameters corresponding to the "AUTO 1" option of GEANT3.14. Part of the discrepancy may also be due to some details in the material composition which were not reproduced in our simulation. The sudden drop at thicknesses above $\sim$ 30 mm is due to the fact that the electron deposits most of its energy in the first absorber layers. The region below, between a few 1/10 mm and 10 mm in Lead thickness is the "migration effect" region, where some tuning is possible.

Calculations were also performed with liquid Argon as the active medium. While the shape of the absorber-thickness dependence of e/mip remains, the effective drop due to the migration effect is smaller than 5%. No substancial effects are therefore expected and compensation through electron signal suppression will hardly be tunable through the thickness ratio of Lead and liquid Argon.

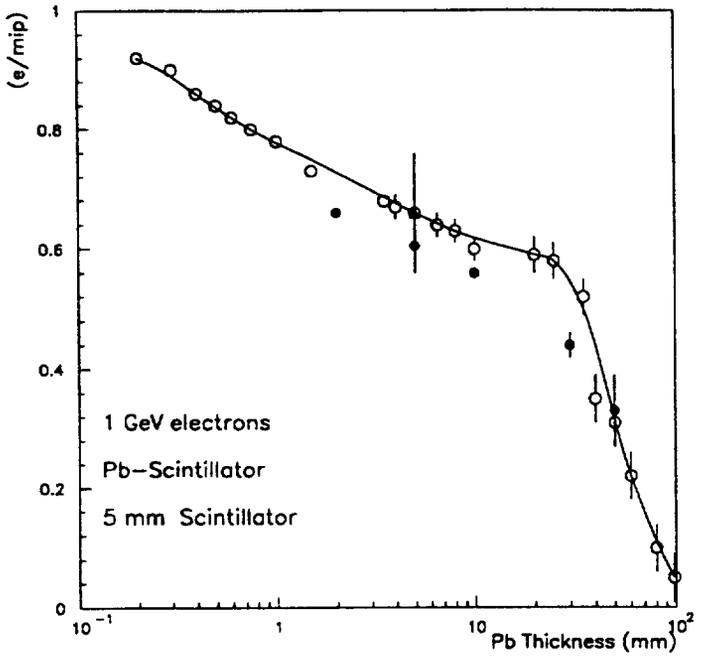


Figure 2: e/mip for a sampling consisting of 5 mm scintillator plates and Pb plates of variable thickness (black circles), compared to an EGS4 calculation from Ref. [9] (white circles) and to experimental data(black triangle).

3 Extrapolation to possible LHC configurations

After some confidence had been gained in the reliability of the available simulation tools, calculations were performed to extrapolate our knowledge to possible LHC calorimeter configurations. Performance requirements for an LHC calorimeter are set to a resolution around $50\%/\sqrt{E}$ for hadrons and to better than $10\%/\sqrt{E}$ for electrons, with a very small constant term, if the decay $H \rightarrow \gamma\gamma$ for $50\ GeV < m_H < 150\ GeV$ shall be reconstructable [12]. A few calorimeter configurations were investigated here, with homogeneous sampling and also with two different sections, aiming at resolutions comparable with the required ones. Results are presented here for three configurations all having a Lead-liquid Argon EM calorimeter. Good resolution for electromagnetic showers in sampling calorimeters requires a very fine sampling, which is difficult in the case then scintillator is used as active medium.

Simulations were performed with the following three different sampling configurations:

1. *Calorimeter with identical sampling for EM and hadronic compartment*

   - A "cryostat", 0.7 X_0 Fe and 4 cm Air at $R = 150\ cm$, followed by
   - 10λ of alternating layers of 3 mm Pb and 4 mm LAr (522 double layers, up to $R = 521\ cm$.

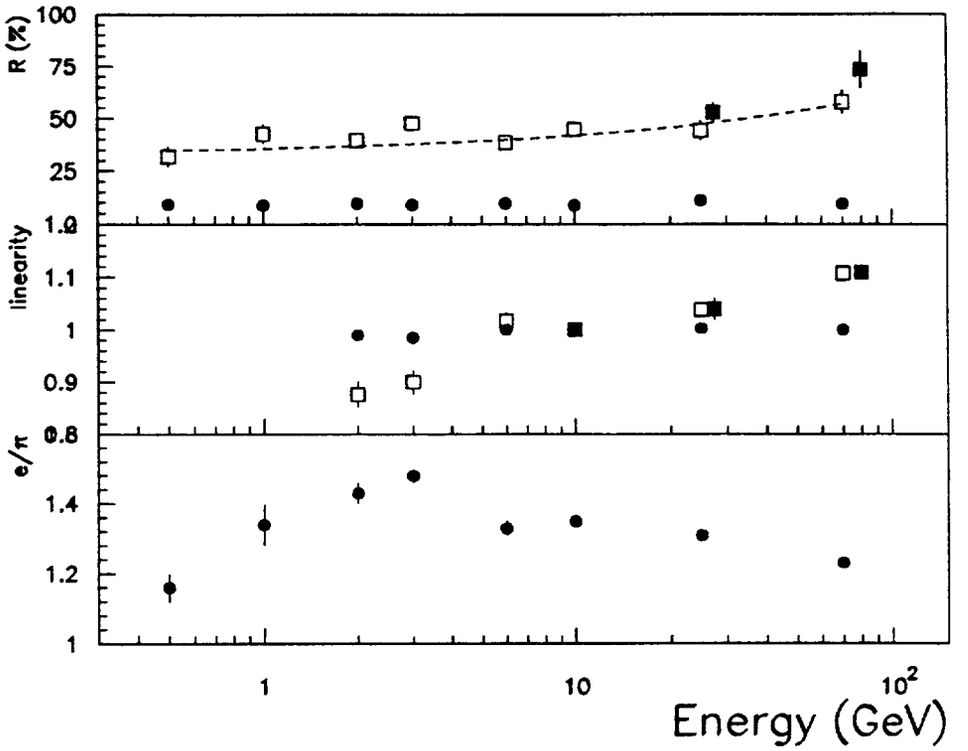


Figure 3: Results for a calorimeter with 3 mm Lead and 4 mm liquid Argon layers. Top: Resolution coefficient R (%) (where $\sigma/E = R/\sqrt{E}$ with E in GeV) for electrons (black circles), hadrons (white squares) and jets (black squares). Center:Linearity for electrons (black circles) and hadrons (white squares) calculated with respect to 10 GeV data. Black squares give the linearity for jets with respect to 10 GeV pions. Bottom: e/π ratio.

2. *Liquid Argon Calorimeter with different sampling for EM and hadronic compartments*

   - A "cryostat", 0.7 $X_\circ$ Fe and 4 cm Air at $R = 150$ cm, followed by
   - 27 $X_\circ$ of alternating layers of 3 mm Pb and 4 mm LAr for the EM compartment.
   - 10λ of alternating layers of 10 mm Pb and 4 mm LAr for the hadronic compartment.

3. *Hybrid Calorimeter*

   - A "cryostat", 0.7 $X_\circ$ Fe and 4 cm Air at $R = 150$ cm, followed by
   - 27 $X_\circ$ of alternating layers of 3 mm Pb and 4 mm LAr for the EM compartment.

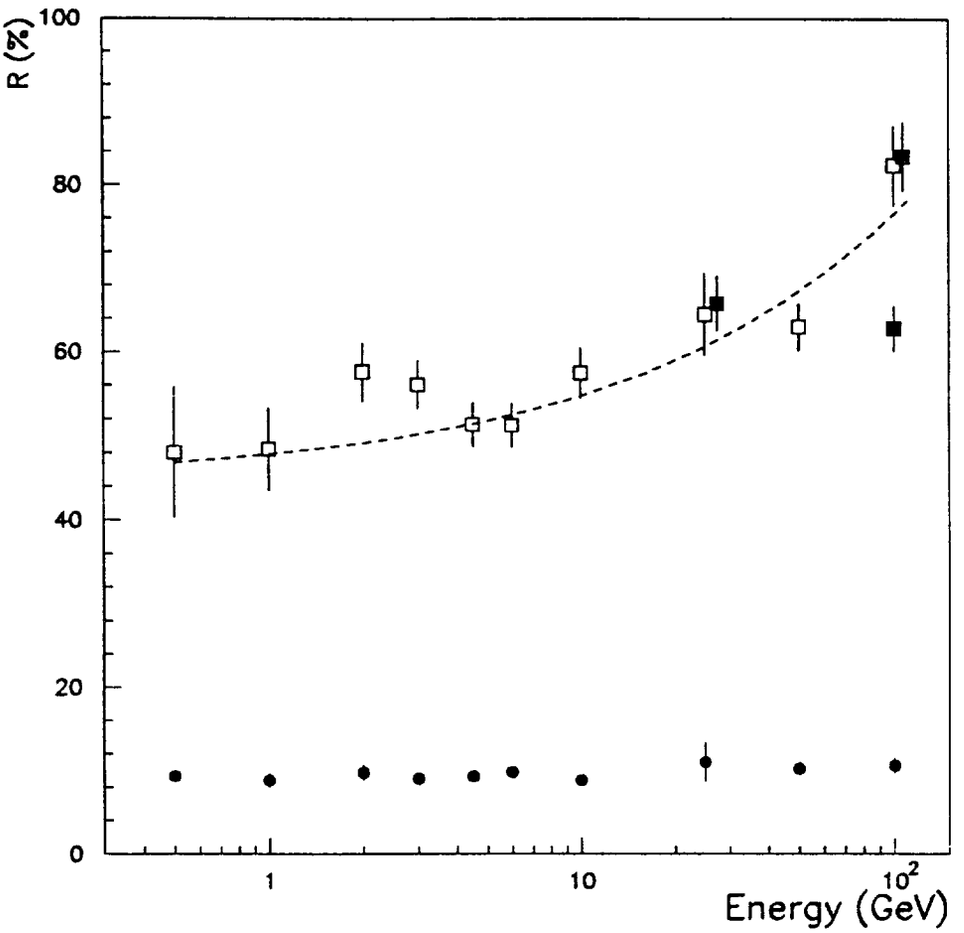


Figure 4: Resolution coefficient R (%) for electrons (black circles), hadrons (white squares) and jets (black squares) in a calorimeter with EM sampling as in Fig. 3 and hadronic sampling with 10 mm Pb and 4 mm liquid Argon layers.

- A "back cryostat", 2.5 cm Fe and 10 cm Air at $R = 150$ cm, followed by
- 10λ of alternating layers of 10 mm Pb and 2.5 mm scintillator for the hadronic compartment.

For the calorimeters with two different samplings, a calibration factor α was determined, to combine the signals of the two sections for hadrons:

$$S_{TOT} = S_{EM} + \alpha \cdot S_{HAD}$$

where S_{TOT} is the signal that provides the particle energy measurement, S_{EM} and S_{HAD} are the energy deposition signals in the EM and hadronic sections.

The results for resolution, linearity and e/π ratio of the homogeneous sampling calorimeter are shown in Fig. 3. The e/π ratio is > 1, particularly pronounced at

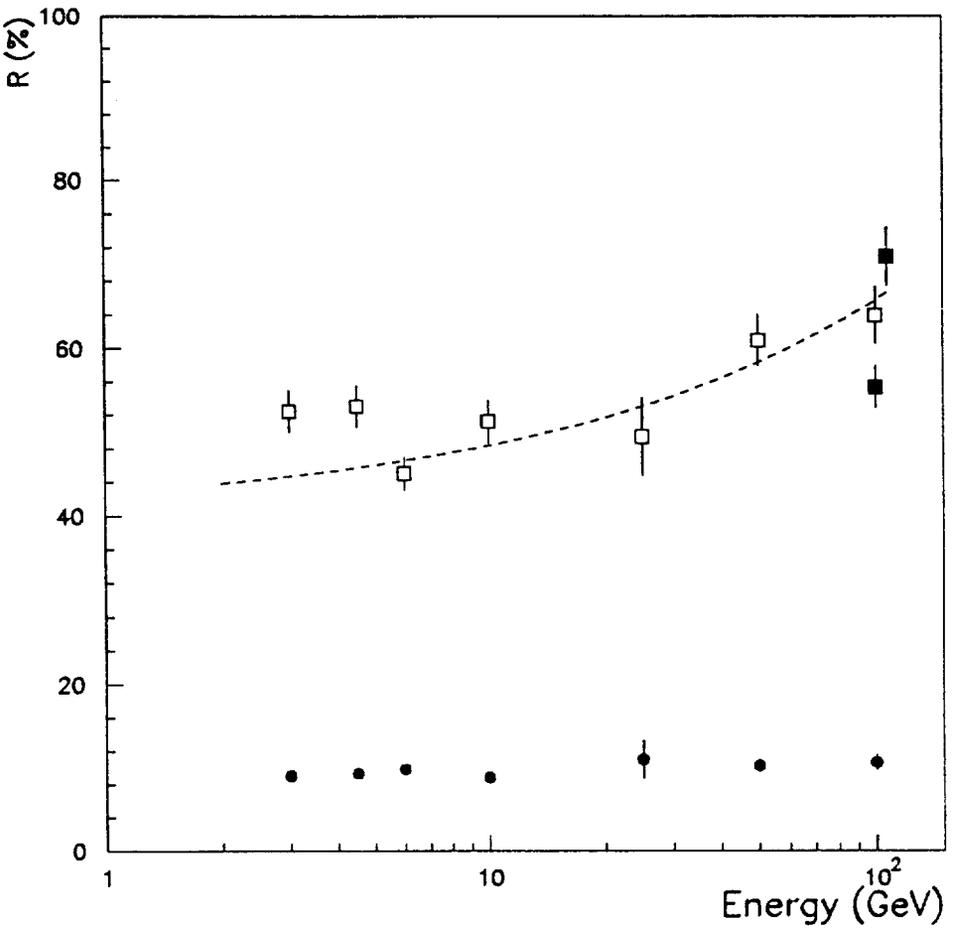


Figure 5: Resolution coefficient R (%) for electrons (black circles), hadrons (white squares) and jets (black squares) in a calorimeter with EM sampling as in Fig. 3 and hadronic sampling with 10 mm Pb and 2.5 mm scintillator layers.

low energies. This affects the jet energy resolution, because jets have a substancial electromagnetic fraction (1/3 in average) and the particles in a jet carry only a fraction of its original energy. The resolution for hadrons is in the expected range, worsening at high energy ($\geq 70\ GeV$) where also the linearity and e/π are noticeably changing again. The resolution shown for hadrons corresponds to

$$\frac{32.7 \pm 4.2}{\sqrt{E}\%} + (2.9 \pm 1.0)\%$$

as indicated by the curve in Fig. 3, while for electrons it is

$$\frac{9.0 \pm 0.5}{\sqrt{E}}\% + (0.1 \pm 0.1)\%.$$

Jets show a somewhat worse energy resolution than single charged pions, using however the α coefficient determined for hadrons. The construction of such a calorimeter is very unrealistic, because of the huge radial space required.

For the inhomogeneous sampling (Fig. 4) we show the resolution coefficient , which for hadrons can be described by

$$\frac{44.6 \pm 3.2}{\sqrt{E}}\% + (3.2 \pm 0.6)\%.$$

The resolution for jets is comparable to that for hadrons. If however a calibration

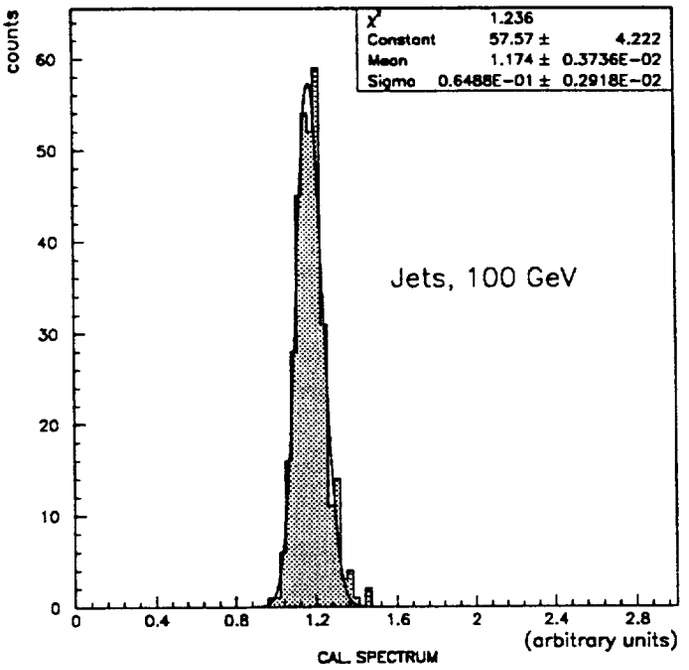


Figure 6: Spectrum of 100 GeV jets in hybrib calorimeter.

factor α is determined for jets, the resolution improves dramatically, as indicated by the lower jet point in Fig. 4 at 100 GeV.

The hybrid configuration, for which resolution results are shown in Fig. 5, exhibits properties similar to those of the LAr calorimeter with inhomogeneous sampling. For hadrons, the energy resolution corresponds to

$$\frac{40.3 \pm 2.5}{\sqrt{E}}\% + (2.5 \pm 0.5)\%.$$

All the quoted simulation results were obtained with limited statistics, of 100-200 generated events at each incident particle energy. Electromagnetic as well as hadronic shower development were followed down to a 11 keV cut on all particle energies. The jet energy resolution shows similar results, with a considerable improvement (by $\sim 20\%/\sqrt{E}$) if, instead of the calibration factor α for hadrons, the one for jets themselves is used.

Due to the fact that the energy deposition of jets in the EM section of a calorimeter is due to a different spectrum of processes than the energy deposition of hadrons, the calibration coefficient α, as mentioned, is not expected to be the

same for hadrons and jets. The improvements in jet energy resolution achieved with a jet calibration were already shown above. For illustration purposes, we show in Fig. 6 the spectrum for 100 GeV jets in the hybrid calorimeter configuration. The resolution obtained using a "jet" calibration factor is $(55.3 \pm 2.5)\%/\sqrt{E}$ at 100 GeV and $(69.7 \pm 22.2)\%/\sqrt{E}$ at 300 GeV, where the large error is due to limited statistics. In these first jet simulations we obtain that the linearity between 100 GeV and 300 GeV jets is better than 1% while the resolution results can be parametrized as $35.6\%/\sqrt{E} + 2.0\%$.

4 Conclusions

Simulations based on GEANT3.14 have been verifyed to reproduce reasonably well the performance of some existing Lead-Scintillator and Lead-Liquid Argon calorimeters. First studies show that conventional sampling calorimeters can be realized with LHC performance specifications.

References

[1] R. Brun, this conference; R. Brun *et al.*, GEANT3.14, CERN Computer Newsl. **200** (1990) 13.

[2] T. Sjöstrand and M. Bengtsson, JETSET, Comp. Phys. Comm. **43** (1987) 367.

[3] J. B. Birks, "The theory and practice of scintillation counting" (Macmillan, New York, 1964).

[4] E. Bernardi *et al.*, Nucl. Instr. Meth. **A 262** (1987) 229.

[5] H1 Collab., W. Braunschweig *et al.*, Nucl. Instr. Meth. **A 265** (1988) 419 and Nucl. Instr. Meth. **A 275** (1989) 246. H1 Collaboration, to be published in Proc. XXV Int. Conf. on High Energy Physics, Singapore (1990), Eds. K.K.Phua and Y. Yamaguchi.

[6] M. Lefebvre *et al.*, Int. Report CAL-NO-002 of the LHC working group on calorimetry (CERN); M. Nessi *et al.*, to be published in Proc. Int. Conf. on "Calorimetry in High Energy Physics", Batavia (USA) 1990.

[7] D. Cavalli, L. Perini, M. Sciamanna, Internal Report ECFA subgroup on Liquid Argon Calorimetry.

[8] H. Brückmann *et al.*, Nucl. Instr. Meth. **A 263** (1988) 419.

[9] J. deL Peso and E. Ros, DESY 90-045.

[10] L. Malgeri *et al.*, Int. Rep. ECFA subgroup on Liquid Argon Calorimetry.

[11] E. Bernardi *et al.*, Desy Internal Report FI-87-01.

[12] J. P. Repellin, this conference.

Code Management Systems

V.Innocente*, C.Onions
CERN, Geneva, Switzerland
and
T.P.Shah
Rutherford Appleton Laboratory, Chilton Didcot, U.K.

Abstract

We discuss various aspects of Code Management Systems: their necessity and the attributes they should possess. The existing systems in use are briefly reviewed and compared.

1 Introduction

High Energy Physics experiments involve complex detector systems and generate a large amount of data which have to be usually processed in a large variety of machines in different countries. The software to handle this processing is developed at various sites and then merged together at a central distribution centre. The life of this software is of the order of ten years and during this time it would normally evolve to take into account new algorithms and upgraded detectors etc. A computer based system which facilitates the task of code development, maintenance and distribution is of vital importance in such an environment. A code management system is needed to meet some of the following specific requirements:

- For inserting common sequences shared by several routines in the appropriate places.
- For organising the source code into decks or modules and defining a set of modules which would make up a production program.
- For code distribution to collaborating institutions and maintaining parallel versions at different sites.
- For generating different program versions (e.g. to handle the inevitable machine dependent code).
- For maintaining a history of code changes and for providing the means of recovering an earlier version.

*permanent address: INFN, Sezione di Napoli, Napoli, Italy

In the following sections we list the desirable attributes of a modern code management system and then review some of the existing systems in use in the HEP community. Finally, in the concluding section we give a summary table of what each system provides and we speculate on the factors that would ultimately govern one's choice of a code management system in the LHC era.

2 Desirable Features

We list below the requirements a modern code management system should satisfy in order to provide the functionality needed in the context of a modern large HEP experiment where the software development and processing is distributed over many institutions and computing systems.

1. Because modern HEP experiments tend to be large collaborations, and the software is developed at different sites, the code manager has to be able to maintain parallel versions on different computer systems. Hence the code management system has to be portable.
2. It should be easy to use with a user-friendly interface. The code to be modified should be quickly accessible and any editing should be possible using the local editor without leaving the environment.
3. The code manager should provide the same interface to the user on different platforms (i.e. he/she should be able to use the same commands).
4. The code manager must support the inclusion of macros such that common code can be expanded when required (e.g. to produce object libraries).
5. The code manager must be able to handle conditional code in a flexible way (eg. machine dependent code, generating different program versions).
6. It should provide a history of the code development with a facility for recreating an older version if needed.
7. It should be possible to obtain the differences between two versions and, optionally, it should be possible to generate a correction deck (a delta file) to update an earlier version.
8. Comments on why a new version was produced should be required (e.g. who made the change and why).
9. The organization of the source code or macros should be in decks or modules and it should be possible to define a group of modules which logically belong together.
10. The code manager should provide some control over simultaneous changes to a module by means of a warning or a lock.
11. It should be possible to merge variant versions of a module (although this cannot be done in a fully automatic way and care would always need to be exercised in any merging operation).

12. The code management system should have facilities for the distribution of code to outside institutions, i.e. a transportable format should be provided. However, in order to make the transfer quick over wide area networks, updating with delta files should be possible. The delta file should only be able to modify the unique file to which it applies.

13. Finally, the code manager should allow multiple source code libraries with no arbitrary limit on the number of lines of code.

3 Review of some existing Code Managers

In this section we review some existing code managers, particularly those which have been adopted by sections of the HEP community. We start with PATCHY which is the oldest and has probably been used by more HEP people than any other code manager. Then we look briefly at other products (mostly commercial): SCCS, VAX CMS, HISTORIAN, CMZ and Codebase.

3.1 PATCHY

PATCHY [1] was developed at CERN around 1965 at a time when programs were fed to the computer via a card reader. By maintaining the source code in a PATCHY Master file (PAM) on tape and using a small cradle of update cards the user was freed from the burden of reading in a trayful of cards ! It reads in and acts upon several sequential files by means of cards. PATCHY, because of its origins, is not an interactive program at all. Because it accesses the data sequentially PATCHY is necessarily slow or cumbersome in those facilities best provided by random access.

PATCHY handles common sequences well and conditional code can also be managed but in a slightly more complicated manner. History of code development can only be maintained if all changes are made via correction decks at the start of the PAM file. In particular, if source code is modified directly using the local editor then no history is available (unless done manually by way of a comments deck at the start); there is no automatic way of going back to an earlier version in this case. The updating process cannot be controlled or monitored in any way. PATCHY is very good for distributing code to other sites on tape and correction decks can be circulated for the PAM files in other centres but no guarantee that they would apply to the correct version(s) of the PAM file. PATCHY, as already mentioned, has been the most widely used code manager in the HEP community.

3.2 Unix SCCS

This system is not used in HEP but we mention it as a reminder that the problems and solutions relating to code management are not unique to our community. The Source Code Control System, SCCS [2] maintains a record of versions of a file containing software, a program or documentation. It is supposed to keep track of each set of changes, who made them, why and when. Changes can be merged and control is exercised to ensure that two people do

not edit the same file at the same time. It also allows old versions to be recovered. There does not, however, seem to be provision for the transfer of files to other sites. Also the notation is a little too succint !

3.3 VAX CMS

This is a commercial product which is derived from or inspired by Unix SCCS. VAX CMS [3] provides sophisticated facilities for maintaining a history of code development. Code can be modified using the local full-screen editor. The system controls simultaneous updating of code and provides a way of merging variant versions arising from a common ancestor. However there are no facilities for handling conditional code and common sequences can only be handled using the Fortran INCLUDE. Code distribution is also not foreseen. These limitations arise because this system is for VAX use only. It has been used by the CDF experiment and they have written a pre-processor to solve the problems of conditional code and common sequences handling. Users of VAX CMS are very pleased with it, particularly its speed and robustness.

3.4 HISTORIAN

This is another commercial product and was originally intended as a replacement for PATCHY at CERN. It is marketed by OPCODE Inc. based in Texas. The HISTORIAN PLUS system [4] consists of a batch sub-system and an interactive sub-system. In the batch mode, updates are applied to code stored in the library and either a new library, the "source" code, "compile" code or a so-called "compatible" library for export can be produced. The interactive mode uses HISTEXTRACT to extract the code to be modified, which can be edited using any local editor and a correction set generated, or the library updated, interactively using HISTGEN. Typically, users generate correction sets which are sent to a library manager for inclusion in a new release. The new library which is produced contains a history of updates and thus permits the recovery of earlier versions. HISTORIAN does not allow variant versions but old versions are recoverable. Note that the version number is a function of the library as a whole and not of the individual decks. Control of updates is minimal. HISTORIAN handles conditional code and common sequences very well, in particular allowing nested conditions and automatic propagation of common deck changes. Code distribution via "compatible library" is possible but usually these libraries tend to be rather large. A useful feature, which is not found in other code managers, is the unique identifier given to each record in the file. If a record is deleted, then attempts to modify the record in a later run are flagged with a warning. In other code managers, a different record would be modified without any warning at all. At the time of writing, CERN has negotiated a new contract with OPCODE such that the company will only maintain the current version; no further development or installation on new machines is foreseen. HISTORIAN has been used by several experiments (e.g. ALEPH,CHARM2,NA31,UA2..) at CERN and generally the users have been quite satisfied with it.

3.5 CMZ

CMZ (Code Management system using Zebra) [5] was developed by CodeMe S.A.R.L. This is also a commercial product which is about to be officially supported by CERN and it runs on any computer on which the CERN library does. CMZ sets out to provide a code manager which is fully PATCHY compatible and provides for interactive code modification and development using the local system editor. From within the CMZ environment it is possible to compile and link Fortran and C programs, import or export C, Fortran, "text" or PAM files and generate correction sets by comparing two PAM cycles. It also provides several tools to check and tidy Fortran code, such as statement relabelling and indenting, checking for undefined variables etc. It handles common sequences and conditional code as PATCHY does but allows the inclusion of conditional code also in sequence definitions. In CMZ, when a deck is modified and then saved, a new RZ cycle is created; multiple copies enable history to be maintained. A mechanism to handle versions is provided, but multiple lines of developments are not allowed. CMZ does not provide any enforced control of changes but a history of all changes applied to the deck is kept in comment lines at the top of the deck itself. The organization of the source is such that PATCHY PATCHes become RZ directories and the decks then are within this directory. The code distribution is done using CARD images of the CMZ files (which are PATCHY compatible) or correction decks.

The appeal of CMZ is clearly for those who wish to make a smooth transition from PATCHY to a more modern product. Its functionality is however somehow constrained by its design aim of being completely compatible with PATCHY. It has been used at CERN by the L3 collaboration who use it in the code development phase (using Apollos) but code stability for production is maintained by PATCHY mainly for historical reasons. Code distribution to outside laboratories is also done using PATCHY; correction sets are distributed regularly to keep production libraries in collaborating institutions up to date. The L3 collaboration has experienced some problems with the integrity of the CMZ library files (they get corrupted from time to time). These problems are supposed to be solved by a new version of the Zebra RZ package. CMZ has also been chosen by the H1 HERA collaboration at Desy.

3.6 Codebase

This is a commercially available code manager developed originally to the specifications drawn up by the Zeus experiment at HERA [6,7]. It is marketed by BASE GmbH. Its design aim was to provide a portable code manager which would have the functionality of VAX CMS but cater also for common sequences and conditional code handling. Written entirely in C it is supposed to provide a common interface on various platforms (VAX, IBM/VM, IBM/MVS, GOULD etc.). It stores the decks as modules with a prefix (equivalent to a directory). These modules can be extracted for modification, edited using the local editor, expanded for compilation and testing and saved as new versions in the Codebase library. This new version, or any earlier version of

this module (note that version number applies to the module), can be extracted from the library. The Codebase system allows common code handling and powerful conditional code handling using Boolean expressions allowing logical operators AND:, OR: and NOT:. Every time a module is saved in the library a comparison is made between the original and edited versions and corrections are appropriately inserted. Comments on changes are also recorded and a full history of all changes to a module can be obtained by requesting a special annotated listing. Codebase also controls the updates that can be performed on a module simultaneously by means of "locks".

Codebase is a very new system which is now beginning to be used seriously by the Zeus experiment on the HERA machine at DESY. Potentially it is rather powerful but, at the time of writing, not all the advertised features work on all platforms. It has so far been most extensively tested on the VAX and IBM/MVS systems. Its response time for some commands is still considered rather slow and it is not yet felt to be robust enough.

4 Summary and Conclusions

In the table below we give a list of desirable attributes (Features) and what the different systems have to offer (the more stars the better it is). Common Sequences are supported by all code managers except VAX CMS; only Codebase and CMZ allow these sequences to reside in any library (note that PATCHY can also emulate this but rather painfully !). Similarly Conditional Code is handled by all except VAX CMS and SCCS for reasons discussed above. The Multiple Versions feature is either through a single line of development or via variant versions. The latter are supported only by VAX CMS and Codebase. Control of Changes refers to the possibility of several people modifying the same module simultaneously; again VAX CMS, Codebase and SCCS issue some warnings and have "locking out" features. Documentation of changes means that at least it provides a way to document who modified the code. Organization refers to how the code is structured. Distribution refers to the availability of a transport format for distributing code and/or update decks. Multiple language asks what sort of languages are supported by the code manager. Interactivity refers to the power of the interactive version and to its speed. Utility stands for tools other than the one used for the code management itself, like code checking and tidying tools. Size refers to the size of the library for the same code. Portability refers to the present availability of the code managing program itself on various computers. We conclude by giving a rough guide of relative cost to the user: CERN products tend to be "free" (ignoring manpower costs) whereas commercial products not distributed through some general licencing agreement through CERN would cost "real" money.

The final choice of system depends on the weight that one gives to the different desirable features. Of course the best code management system is one which costs nothing and offers all the features we want and works so well that its existence is hardly noticed ! In practice this utopian situation cannot be attained and the choice must depend on what one can afford and what

is likely to be most acceptable to the user community in the experiment. If PATCHY compatibility is a must then CMZ would seem to be a good choice; if, on the other hand, you want a powerful system which can handle merging of variant versions then a Codebase-like system could be the answer; VAX CMS would be a good solution if the code was likely to be developed and maintained on the VAX machines exclusively. It could also be the case that in the future, with Unix systems being the norm everywhere, there will be a sufficiently portable and powerful but user-friendly Unix based product !

A good code manager should facilitate both the development and maintenance of code. Portability, robustness and speed are very important features. Code managers with these qualities, which also address the particular needs of distributed computing, will clearly be needed in the LHC era.

5 Acknowledgements

We would like to thank the following people for providing us with useful input for this paper: J.C.Hart, H.Kowalski, P. Palazzi, S. Fisher.

References

[1] PATCHY Reference Manual, CERN Program Library, March 1988.

[2] See for example: R. Morgan and H. McGilton "Introducing Unix System V", McGraw-Hill Book Company, pag 540.

[3] Guide to VAX DEC/Code Management System, May 1989, Digital Equipment Corporation,Maynard, Masachussets.

[4] HISTORIAN Plus User's Manual CERN/DD/US/101.

[5] CMZ User's Guide and Reference Manual, CMZ Version 1.35, September 1990.

[6] Codebase User's Guide, Release 1.10, 1990.

[7] Requirements for a Code Management and Distribution Facility, ZEUS-Note 88-005,H. Kowalski., February 1988.

Table 1: Features of various Code Management Systems

Feature	PATCHY	SCCS	VAX CMS	HISTORIAN	CMZ	Codebase
Common Seq						
One Lib.	***	?	?	***	***	***
> 1 Lib.	*	?	?		***	***
Cond. code	**			***	**	***
Multi Vers						
unique line of dev.	?	?	***	***	***	***
Variant versions		?	***		*	***
Control of changes		***	***		*	***
Docum. of changes		***	***		***	***
Prop. of changes				**	***	
Organization						
Deck/Module	***	?	***	***	***	***
Patch/Group	***	?	***	***	***	***
Set/"Class"		?	***	***		***
Distribution						
Transport Format	***	?	?	**	***	***
Multiple Languages	*	?	**	**	**	**
Interactivity		**	***	*	***	*
Utilities					***	
Speed	*	?	**	**	***	*
Size	***	?	**	*	***	***
Portability	***	**		**	***	**
Cost	***	**	**	*	*** ?	*

The star rating is our assessment of how well a feature is catered for: * means feature is available, *** means it is well implemented or is rather complete, a blank means it is not supported and a '?' means that we are unsure of this feature (or rating) for this product.

Programming languages at LHC

I. E. Zacharov
CERN
1211 Geneve 23, Switzerland

November 23, 1990

1 Introduction

With LHC a few years away, now is the time to (re)define the programming support CERN can offer for future experiments. The background for the rethinking process are the difficulties with the software experienced by the HEP community and the software crisis in general.

Therefore it is essential for the success of future LHC experiments to plan carefully their software development. CERN can bring out some recommendations in this area, and based on a general agreement it has to decide which libraries, data bases and packages it will offer to the physics community. Especially important is the decision on which programming languages CERN will support.

It is clear to the majority of the programmers that software written in the FORTRAN 77 programming language tends to be less reliable than what would be reasonably expected from another, strongly typed language. Therefore, despite the popularity FORTRAN 77 has among the physics community, it would be desirable to write the code in a programming language offering support for modern software engeneering methods. An important criterion for a new language is the level of data abstraction it can offer to the programmer.

One attractive choice as a modern programming language seems to be Fortran 90, a successor to FORTRAN 77. It is now in its last stages of formal standardization. Another attractive possibility is the C++ programming language, which is already available on most platforms. This report lists arguments in favour of each of these programming languages, considering the features of both languages and the environment in which they will be used.

The ADA programming language is not discussed in this report. From the software engeneering point of view Fortran 90 offers the same possibilities as ADA, avoiding most of its heavy constructs. On the other hand ADA does not have the class inheritance mechanism like of C++, therefore it is not an object oriented language either. At the moment there is no appealing reason to use ADA for the HEP programming. However, not everybody would reject ADA so readily. The discussion in this report can be viewed as a comparison of a powerful, computational, procedural language (like Fortran 90) with an efficient object oriented language (like C++).

This comparison of the programming languages is not a comparison of the semantics. It is rather the comparison of the underlying philosophy; a decision about the programming style leads to the choice of a programming language supporting it. Boundary conditions have to be taken into account, however, which might inhibit certain choices of programming languages.

The report is organized as follows. We consider the Computational Model and the Computational Environment of the 90's in the next chapter. Chapters 3 and 4 discuss respectively Fortran 90 and C++; chapter 5 expands on the concept of the inheritance.

2 The Computational Environment

A computer program is never selfsufficient: it needs interaction with the Operating System (OS), e.g. I/O. Moreover, it has to be aware of the underlying hardware architecture to some extent, as big run time savings can be achieved with programs exploiting hardware capabilities.

2.1 The Computational model

The prefered hardware organization of the 90's is a collection of loosely coupled processors (Workstations) with tape and file server(s) on the network. There might be a powerful central processor or several special purpose processors coupled to this network as well. This model is imposed by the evolution of the hardware.

In such an environment the Communication and the Naming Service, Resource Allocation, Remote Procedure Calls (RPC) and the associated with it Location Broker (just to mention a few concepts) obtain crucial importance. Moreover, it is a multivendor environment in which standardization is the only way to achieve connectivity.

In fact, this Computational model is already a reality today, and it will be enhanced in the future:

- with the introduction of faster networks (FDDI, HIPPI, etc.)
- yet more powerful workstations (20 Mips workstations are available today)
- an adequate distributed programming support (especially improving the cpu utilization in a loosely coupled environment)

It is estimated that on the timescale of two years (in 1992/1993) this Computational model will be dominant in the HEP environment.

2.1.1 Note on the Distributed Processing

Generally speaking there are two ways to use a system of loosely coupled processors:

- As a pool of processors for batch work; a well established method.
- Execution of tasks on several processors in parallel on behalf of a single program.

The HEP programming can profit from the well known method of automatic program parallelization using the explicit data parallelism (assuming events are independent), that serves both methods of processor utilization. The parallel task execution on behalf of a single program can be programmed using RPC.

It is important to emphasize that the RPC or any other remote task execution method needs an explicit interface definition, so that stubs can be generated automatically for the client and the server. Therefore this Computational Model demands a strongly typed programming language with explicit interface definitions.

2.2 The Operating System

The Operating System of the 90's is UNIX. Although introduced initially on small machines, nowadays UNIX is supported on the most powerful mainframes (Amdal, nCube, just to mention a few; IBM is moving in that direction).

There is a considerable number of flavours of the UNIX Operating System on the market. It should be emphasized, however, that the differences between the UNIX flavours are more important for system programmers than for "normal" users. It is much more easy to move an application between different UNIX platforms than from VMS to MVS for example. Usually vendors support something called AT&T sys5.3 with BSD4.3 enchancements.

From the many flavours of UNIX two main streams are emerging right now: the "Open Software Foundation" (OSF) type of UNIX (supported by DEC, IBM, HP, etc., about 250 vendors) and the "UNIX International" (UI) type (most notably AT&T, Sun and Amdal, about 200 vendors). Many vendors are members of both, OSF and UI and will support both flavours in their products.

Programs running in the UNIX environment request OS services via a call to a standard library, passing parameters packaged in structures. This model requires the programs to be written in a programming language which supports derived data types. The programming language in the UNIX environment is C. Fortran (77 and 90) is intrinsically incompatible with UNIX and demands a special binding standard to be able to access OS services. For the UNIX interface to the FORTRAN 77 programming language the standardizing committee will go to ballot this year (1990) (the IEEE 1003.9 FORTRAN bindings: a library of fortran callable routines).

2.3 The Programming Base

There is a huge investment in software written in the FORTRAN 77 programming language. Therefore, whatever new programming language is adopted by the HEP community, it should allow a smooth transition from the present situation. Also the investment in training and experience is important.

However, it is not entirely clear that the investment in software is as big as it seems to be. New experiments will develop software (almost) from scratch. The memory management systems as we know them today (e.g. ZEBRA, etc.) might not be needed in their present form and will be partially replaced by the programming language constructs.

The balance between rewriting and reusing existing code is not found yet, and it will depend very much on the choice of the programming language.

2.4 Software Engeneering

There will be a huge amount of data to be processed in the LHC experiments. Therefore, the software must be designed for efficiency. Yet, it is of enormous importance to increase the reliability of programs and to decrease the development time. The reusability of code is an important issue in this context.

Instrumental in this approach is the employment of modern programming methods. We do not claim that the drawing of Data Flow Diagrams is a panacea. What is important is the software development policy enforced by the compiler, that would automatically block the appearence of certain bugs in the system. For example, if the data is hidden, you are sure nobody except a well defined routine can modify them. If there is a subroutine interface, nobody can pass an invalid parameter. Data which describes itself can signal an inconsistent usage. If these (and some other) concepts are part of the programming language (i.e. they are enforced by the compiler), more reliable programs will be produced in shorter time.

2.5 Summary

To summarize, the computing environment of the 90's demands a programming language with strong typing, explicit call interfaces, derived data structures, dynamic memory management and efficient computational support. As a matter of policy the concepts of loose module coupling, data hiding, self describing data should be enforced by the compiler.

3 Fortran 90

There are a few excellent books on the Fortran 90 standard (see e.g.[1]). Without attempting to be complete we will try to give a flavour of programming possibilities in Fortran 90. Another example is constructed by M. Metcalf in a recent article, see[2].

3.1 Module Coupling

It is well known that the tight coupling between modules introduced by fortran common blocks is a source of bugs in programs. In Fortran 90 the common block construct of FORTRAN 77 can be replaced by the MODULE declaration. We illustrate it with an example of the Standard Common Block proposed for the Monte Carlo (M.C.) program construction[3]. The most important F77 code is as follows:

```
PARAMETER (IEVMAX=2000, IEVSIZ=23, IEVDIM=IEVMAX*IEVSIZ)
COMMON /HEPEVE/ IEVRUN,IEVNUM,NEVTOT, particle_record, HEP(IEVDIM)
EQUIVALENCE (HEP(1),QHEP(1))
```

Here, the particle_record is a collection of 23 variables, which can be filled by the M.C. programmer with the values of the generated particle properties (momentum, spin, etc.). Then, with the CALL HEPHIS(N,'S') they are transfered into the array HEP at position N. Equivalently, if the array has been filled from a M.C. output, the CALL HEPHIS(N,'G') will set the particle record variables to the parameters of particle N. Potential bugs can enter the programs if users wish to access the HEP array directly, without the HEPHIS routine. For example the HEP/QHEP confusion is very common. The array boundaries are not protected either: outside HEPHIS the check NEVTOT.LE.IEVMAX cannot be enforced.

In Fortran 90 the construction might be as follows (note, that Fortran 90 is case insensitive; here we write the Fortran 90 keywords with capital letters for clarity):

```
MODULE hepeve                ! in line comments; names can be up to 31 characters
  INTEGER ievrun, ievnum     ! the M.C. run and event number
  INTEGER nevtot             ! number of particles generated so far
  TYPE  particle_record      ! user defined data type
    INTEGER status, pdg, mother1, mother2, daughter1, ... (not all listed)
    REAL px, py, pz, energy, mass, x_vertex, y_vertex, z_vertex,  ...
  END TYPE particle_record
  INTEGER, PRIVATE, PARAMETER :: ievmax = 2000 ! not visible outside the module
  TYPE(particle_record), ARRAY(ievmax) :: ihep
END MODULE hepeve
```

This module (defined in a separate file) can be included in a user's program. Every routine which USEs a MODULE shares the public variables and the operators in it.

```
USE hepeve, ihep => myhep ! optionally resolving potential name conflicts
IMPLICIT NONE             ! this useful setting is now a part of the standard
  myhep(n)%pdg = 20       ! structure elements are accessed
  myhep(n)%mass = ...     ! with the % qualifier
  print*, myhep(n)%energy ! such code removes the IHEP/QHEP confusion
  etc.
```

An array boundary check can be enforced by making the ihep array PRIVATE and defining the HEPPAR interface:

```
MODULE hepeve
  ... (up to the array declaration as before)
  TYPE(particle_record), ARRAY(ievmax), PRIVATE, TARGET :: ihepx ! private data
  TYPE(particle_record), POINTER :: ihep => ihepx(1)
  INTERFACE heppar
    MODULE PROCEDURE hephis
  END INTERFACE heppar
  CONTAINS
    FUNCTION hephis(n) ! here is the subprogram body
      TYPE(particle_record), POINTER :: ihep
      INTEGER, INTENT(IN) :: n            ! contains particle index
      IF(n <= 0 .OR. n >= ievmax) THEN
         IF(nevtot >= ievmax) CALL error  ! no more room in the array
         nevtot = nevtot + 1              ! add a new particle in free space
         n = nevtot
      ENDIF
      hephis => ihepx(n)  ! associate pointer with the n-th particle record
    END FUNCTION ihep
    SUBROUTINE error    ! internal entry, not visible outside of the module
      PRINT*, 'no more room for additional particles'
      STOP              ! could allocate some more space in reality
    END SUBROUTINE error
END MODULE hepeve
```

Now the user is forced to use the code myhep=>hephis(n) before the assigment.

For simplicity, we did not make the array dynamic here (the ALLOCATABLE attribute). The standard solution is to declare a private array of pointers. Fixed size memory chunks are allocated and assigned to the next free pointer, when the previously allocated memory is full. Since pointer arrays are not supported in Fortran 90, the escape is to define a new data type containing a pointer as a member and to declare an array of that type.

Note, that the data type particle_record and the function to fill in the particle array realize a simple form of data abstraction.

3.2 Data Abstraction

Data abstraction is the way to bundle together (to encapsulate) data and meaningful operations on that data. Data abstraction is a very powerful concept, since is seems to represent more closely a mathematical representation of algorithmic problems. An example of data abstraction for an integer SET data type is shown in ref.[1]. Here we construct an example of a Lorenz vector space.

The intrinsic Fortran 90 operations on vectors and matrices use the euclidian metric. The lorenz metric is defined by the inner product $s = (x^0)^2 - (x^i)^2$, where $x^i, i = 0, ...3$ are the 4-vector components. The operations on 4-vectors should follow the Lorenz metric:

```
USE lorenz
TYPE (vector_4) :: a, b, c, p, q, r
REAL c, s, mass
...
p = q          ! assignment component by component
a = c * p      ! augmentation of 4-vector by real value
b = p + r      ! addition component by component
s = p * r      ! F77: s = SQRT(p(0)*r(0)-p(1)*r(1)-p(2)*r(2)-p(3)*r(3))
mass = p * p   ! i.e. p**2
c = a.boost.b ! transform a into the lorenz frame of b to obtain c
```

The calculus in this example follows closely what is usually written on the paper. The details of the operations are hidden in the module, which is USEd at the beginning of the program. The functions in the module are called each time the compiler detects the operations on the derived data type which match the argument types in the functions.

Note the special array constructs in this example. Since the vector operations are explicit, compilers will be able to take advantage of the vector machines and the long-instruction-word machines. There are more array constructions available [1] than shown here.

```
MODULE lorenz
  TYPE vector_4
    REAL x0, x(3)
  END TYPE vector_4
  INTERFACE OPERATOR(*)       ! overload the * operator: type of the arguments
                              ! determine uniquely the function to be called
    MODULE PROCEDURE vtimesv ! dot product between two lorenz vectors
    MODULE PROCEDURE ctimesv ! augment lorenz vector by a scalar
    MODULE PROCEDURE vtimesc ! idem, other sequence of the arguments
  END INTERFACE OPERATOR(*)  ! all argument types have been covered
  INTERFACE OPERATOR (+)
    MODULE PROCEDURE vplusv  ! add two lorenz vectors
  END INTERFACE
  INTERFACE OPERATOR (.boost.)    ! a new operator:
    MODULE PROCEDURE boostme      ! lorenz transformation
  END INTERFACE OPERATOR (.boost.)
  CONTAINS
    FUNCTION vtimesv(a, b)    ! dot product between two lorenz vectors
    REAL vtimesv
    TYPE(vector_4) :: a, b
      vtimesv = a%x0 * b%x0 - a%x * b%x  ! array operation
    END FUNCTION
    FUNCTION ctimesv(c, a)    ! augment lorenz vector by a scalar
    TYPE(vector_4) :: ctimesv, a
    REAL c
      ctimesv%x0 = c * a%x0
```

```
      ctimesv%x  = c * a%x          ! array operation
    END FUNCTION
    FUNCTION vtimesc(a, c) ! operators on derived types are not abelian
    TYPE(vector_4) :: vtimesc, a
    REAL c
        vtimesc = ctimesv(c, a)
    END FUCTION
    FUNCTION vplusv(a,b)  ! add two lorenz vectors
    TYPE(vector_4) vplusv, a, b
        vplusv%x0 = a%x0 + b%x0
        vplusv%x  = a%x  + b%x      ! array operation
    END FUNCTION
    FUNCTION boostme(a,b)
    TYPE(vector_4) :: boostme, a, b
    REAL u(4), v(4), x(4) ! temporary to hold the 4-vectors
       u(1) = a%x0
       u(2:4) = a%x                 ! array operation
       v(1) = b%x0
       v(2:4) = b%x
       CALL lorenz4(v,u,x)  ! call cernlib routine U101 for simplicity
       boostme%x0 = x(1)    ! but could be trivially rewritten
       boostme%x = x(2:4)           ! array operation
    END FUNCTION
END MODULE lorenz
```

This type of programming has also some disadvantages. It is difficult to move between different programming languages, for instance the program above cannot be reused outside of the Fortran 90 environment. Another consideration concerns specifically Fortran 90. Operations have to overload for each combination of argument types, even those that have a trivial conversion (e.g. integer to float; a = c * p in the example above would not work if c is an integer). It is trivial to cover basic types in the operator interfaces. However, a user can define unlimited numbers of derived types that might logically still be handled by the operations already declared, but would not be accepted by the compiler, because they are not mentioned in the interface. For example, consider creating a new type called named_vector_4 with the same properties as vector_4, but having a string in addition. Logically, this addition would not change the inner product, but all the operations have to be redefined. In Fortran 90 this problem can not be solved in general and caution must be applied in creating new data types with operators.

In the object oriented languages this problem is solved by the inheritance mechanism, discussed in chapter 5.

3.3 Library interfaces

To illustrate a possible way to use libraries in F90 programs we take as an example one of the CERN programming library entries. When a library is defined in Fortran 90, its calling sequences are made explicit with an interface definition and the correct usage is enforced by the compiler:

```
MODULE kernlib
  INTERFACE D509   ! find the minimum of a function of one variable
```

```
    SUBROUTINE minval(x, y, r, eps, step, maxf, a, b, f)
      REAL, INTENT(INOUT) :: x ! estimate of the abscissa of a minimum of f
      REAL, INTENT(OUT) :: y, r
      REAL, OPTIONAL, INTENT(IN) :: eps, step, a, b
      INTEGER, OPTIONAL, INTENT(IN) :: maxf
      INTEGER, EXTERNAL :: f    ! user function to be minimalized
    END SUBROUTINE minval
  END INTERFACE
END MODULE
```

This routine can be used in a variety of ways:

```
call minval(x, y, r, myfunc)
call minval(x, y, r, eps=1.e-6, myfunc)
etc.
```

There is a possibility to create optional arguments (attribute OPTIONAL). In the body of the subroutine the presence of the optional arguments (e.g. eps) is detected with the statement IF(PRESENT(eps)) ...

There is no way to enforce the correct calling sequence of the user function f at compile time. This is due to the fact that Fortran 90 does not have the notion of a pointer to a function. The compiler cannot check if myfunc has in fact the correct type and number of arguments in the user's program.

However, the calling semantics of the user function f can be checked at run time with the following piece of code in the body of minval:

```
USE kernlib    ! include the interface for compilation of the minval code
   SUBROUTINE minval(x, y, r, eps, step, maxf, a, b, f) ! subroutine body
... (entity declarations as in the interface, including the external function)
      INTERFACE f
         INTEGER FUNCTION f(ifu, xfu)
            INTEGER, OPTIONAL, INTENT(IN) :: ifu
            REAL, OPTIONAL, INTENT(IN) :: xfu
      END INTERFACE f
C executable code follows
      IF(.NOT.PRESENT(ifu)) CALL error
      IF(.NOT.PRESENT(xfu)) CALL error
      ... (etc., doing the actual function minimalization)
```

Note that since the interface to a library entry is defined explicitly, the actual call can be replaced by a stub call (e.g. with a preprocessor), making the processing on a remote machine transparent for the user.

3.4 Preliminary conclusions on Fortran 90

The Fortran 90 constructs allow us to write code in a modern programming style, making the programs more powerful and more reliable.

In addition, FORTRAN 77 programs will compile under Fortran 90. There are some restrictions on mixing the constructs of the two languages in the same program. However, there will be F77/F90 translators to make the transition to the next standard easier.

Nevertheless, Fortran 90 is not a universal programming language:

a) Fortran 90 pointers are not usable for low level and on-line programming. There are no pointers to functions – a prerequisite for error recovery and asynchronous processing.

b) Except for some (optional) status variables there is no error handling.

c) There is no asynchronous processing.

d) There is no inheritance (see next chapter).

e) Fortran 90 is too late for the interface builders based on X. The Fortran 90 compilers from major vendors are expected in 1992/93 (IBM, DEC, HP); Cray promises for 1991, but in general the compilers will arrive in 1 to 3 years from now. The development of user interfaces based on the X-Window protocol definition has already started (using C/C++).

f) Fortran (90 and 77), by itself, is intrinsically incompatible with UNIX OS.

As pointed out in chapter 2, a special binding standard is required to be able to access the OS functions from Fortran programs. It is expected that the same working group that has standardized the FORTRAN 77 UNIX interface will do the Fortran 90 UNIX bindings in 1991/92. This will dramatically improve the Fortran/UNIX situation, but the points a) to e) still hold. The main conclusion here is that if Fortran 90 is adopted by the HEP community, several languages (at least two) have to coexist (i.e. for the off-line and the on-line programming; for user interfaces). Therefore, the following point is important in this discussion:

g) The Fortran 90 standard does not define interfaces to other languages.

4 C++: an (object oriented) extension to C

The definition of the C++ programming language comes from Bjarne Stroustrup [5]. It is (almost) compatible with the ANSI C programming language definition in the sense that an ANSI C program can be compiled by a C++ compiler. In fact, many C++ compilers are just preprocessors to a C compiler. C++ has the advantage of much more rigorous code validation by the compiler, as compared to plain C. The C programming language is popular in the on-line programming, since it allows pointer manipulation and asynchronous processing. The additional features of C++ make it a serious candidate also for off-line programming.

The following strong points of Fortran 90 apply also to the C++ language:

- derived data types
- operator overloading
- internal procedures
- module (object) interfaces

The examples of the Fortran 90 code can be trivially rewritten in C++ semantics. There is a difference in operator overloading: Fortran 90 allows the creation of new operators .op.; C++ can overload only existing operators. On the other hand C++ overloads array references and pointer dereferences (the so called "smart pointers"). Also the notion of a pointer to function is very powerful in C++.

The ANSI C and C++ have the concept of the function call template, therefore floating operations do not have to be converted to double, as it is done in plain C. This makes the

floating point arithmetic more efficient. C++ does not have a powerful set of mathematical functions defined in the language, these have to be supplied from outside, but can be made indistinguishable from the intrinsics. A programmer's effort must go into optimizing the library, since the vector constructs are not explicit for the compiler.

The main difference between C++ and Fortran 90 is the presence of the inheriting class concept in the former.

4.1 The standardization of C++

A new committee has been formed under ANSI X3 to standardize the C++ programming language. The first meeting of this committee will take place in spring 1991.

Most features of C++ version 2.0 are already quite stable and will presumably be fixed as they stand today. There might be exception handling and parametrized types in addition.

5 Application of Inheritance in HEP

Data abstraction is a very powerful concept. It can be limited, however, by the necessity to write out all possible usage of the operators explicitly and by the proliferation of the data types.

Thus, the next step is to define an abstraction of the data abstraction. This step identifies the collection (classes) of objects, grouped by their operations (behaviour). The proliferation of operations is called inheritance. From abstract classes concrete classes are built in class hierarchies. Workable systems have been already demonstrated in the HEP environment, but they are still not large enough to convince everyone of the validity of this approach.

Since the classes are grouped by their common behaviour, the behavioural analysis is instrumental in the analysis of the system[6].

The analysis of the off-line software was concentrating so far on data modeling. It seems, that the data modeling (e.g. Entity-Relationship analysis) is only a part of the story. It is equally important to realize how the data is going to be used. This approach naturally leads to the data abstraction. It is possible to group data by their behaviour, therefore it leads also to the abstraction of the data abstraction.

At the conceptual level, there seems to be no escape from this approach. If so, the programming language of chose should allow for the inheritance to be able to take advantage of abstract classes.

More practical research is needed to validate this approach.

6 Conclusions

The computing environment of the next generation HEP experiments will consist of network of workstations running UNIX. The Fortran 90 environment is adequate to program the off-line analysis systems. Moreover, the layer of libraries necessary in the present systems programmed in FORTRAN 77 will be reduced and otherwise can be made looking like a native Fortran 90 system with the data abstraction mechanism. However, if the abstraction of the data abstraction is found to be practical, next step to an object oriented language like C++ is necessary.

References

[1] M. Metcalf, J. Reid, "Fortran 90 Explained", Oxford University Press, Oxford and New York, 1990.

[2] M. Metcalf, "A derived-data type for data analysis", CERN-CN/90/21, October 1990. (Submitted to Computers in Physics).

[3] F. Carminati, O. Di Rosa, B. van Eijk, I. Zacharov, D. Hatzifotiadou, "Standard Interface between Modules of Event Generators using dynamical Common Structures", CERN-ECP/xx/90. (DRAFT)

[4] "Fortran 90" X3J3/S8.114 (January 1990) working document.

[5] B. Stroustrup, "The C++ Programming Language", Addison-Wesley, 1986.

[6] E. Gibson, "Objects - Born and Bred", BYTE, October 1990.

Standard Interfaces between Modules of Event Generators using dynamical Common Structures

F. Carminati, O. Di Rosa*, B. van Eijk*,**, I. Zacharov
CERN, Geneva, Switzerland

D. Hatzifotiadou
World Laboratory / HED Project, Lausanne, Switzerland

Abstract

Modularity in High Energy Physics Monte Carlo event simulation programs allows to combine physics models involved in different programs in one. To interface parts of the programs to each other it is necessary to standardise the data formats. Based on the identification of the information needed in the different phases of the event generation chain, we propose a set of simple commons allowing different program units to have access to the same data in a standard way.

---

* LAA Project, CERN, Geneva, Switzerland

** Also supported by the 'Netherlands Organization for Scientific Research (NWO)', The Netherlands

1. Introduction

At recent meetings of the ECFA working group on physics and detector simulation for future colliders, LHC in particular, the necessity has been stressed to introduce a standard recording of event history, particle properties data and particle decay tables. This to ease the exchange of information between different program units (modules) of different event generators in High Energy Physics (HEP). A step towards standardisation for Monte Carlo (M.C.) programs has been the proposal of the M.C. particle numbering scheme by the Particle Data Group (P.D.G.) [1, 2]. It constitutes a coding convention for particle identification essentially based on their "elementary particles" content. Further proposals have been presented notably by T. Sjöstrand et al. [3] and B. van Eijk [4]. T. Sjöstrand et al. have mainly been concerned with the standardisation of event generator output formats. In particular, they indicated a simple solution to store the main features of simulated events via a FORTRAN data structure - a Common - to allow future analysis programs to input in an unique way output data from various generators. This paper describes a more general approach to standardisation of HEP data. Our implementation of Event, Particles and Decay records is also based on simple FORTRAN commons. The choice of the variables therein is based on the quantities which the physicist as a user of a Monte Carlo event generator needs to know or store, and the relationship between them. It is based on the design of a modular M.C. system and aimed to meet the expectations of the M.C. user community in and outside CERN.

2. Contents of the proposal

In a run of an event generator a varying number of events may be produced, each providing many "entries" (i.e. a particle, a cluster, or any other system you may want to describe). The description of an event is the description of the entries thereby produced.

Let us first briefly recall which information the already established event commons [3] *HEPEVT* and *HEPSPN* foresee before describing the proposed commons. *HEPEVT* records for each event: its particle content, the event history, momenta, and the production vertices coordinates:

```
PARAMETER  (NMXHEP  =  2000)
COMMON  /  HEPEVT  /  NEVHEP,  NHEP,  ISTHEP(NMXHEP),
IDHEP(NMXHEP),  JMOHEP(2,NMXHEP),  JDAHEP(2,NMXHEP),
PHEP(5,NMXHEP),  VHEP(4,NMXHEP)
```

Here the different parameters, variables and arrays have the following meaning:

NMXHEP	maximum number of entries per event.
NEVHEP	the event number.
NHEP	number of entries (particles) in current event.
ISTHEP	status code for current entry.
IDHEP	particle identity (standard).
JMOHEP	pointer to mother.
JDAHEP	pointer to daughter.
PHEP	energy-momentum.
VHEP	production vertex position.

The second existing standard common *HEPSPN* contains the spin four-vector from which polarization information may be calculated. The detailed explanation of the variables of both commons is given in [3]. Some of the authors of major M.C. programs have already adopted these commons in their programs [5,6,7,8]. We notice that in the original proposal [3] only the event information was covered.

Our current proposal offers the possibility to handle particle properties, particle decays and naming in addition to the event information. The color connection information of the particles produced is now provided within the event common, and the spin has been included in the same commons rather than being in a separate one. The main improvement of the present proposal is that memory layout is continuous without unnecessary empty spaces. This has two advantages: a) memory access is optimized, since all information related to one particle is kept in adjacent memory locations; b) the length of the commons can be changed locally without the need of recompiling all the other modules referencing the common (dynamical -).

It is noted that this introduces a somewhat less transparent way to access the information. Therefore we propose and provide a set of routines to handle data structures within the commons. Alternatively, the data relative to one particle can be accessed via symbolic *offsets* (index). The index to a given particle can be found via a simple arithmetic calculation or via a statement function. We propose the following set of commons to be filled at different levels in the event simulation chain:

a) *HEPEVE*, HEP EVEnt, to record any phase of an event during the simulation chain.

b) *HEPPPR*, HEP Particle PRoperties, used for general Particle Properties.

c) *HEPPDE*, HEP Particle DEcay, used to describe the particle decays.

d) *HEPPNA*, HEP Particle NAme, used to store the particle character names.

The structure and the usage of the common is discussed in the following chapters. Appendix A shows a symbolic chart of a modular event generator illustrating the use of these commons.

3. The Event common

The layout of the new event common is shown in Fig. 1.

```
C  HEPEVT definitions...
   INTEGER IEVMAX, IEVSIZ, IEVDIM
   PARAMETER (IEVMAX = 2000, IEVSIZ = 23)
   PARAMETER (IEVDIM = IEVMAX*IEVSIZ)
   INTEGER IEVRUN, IEVNUM, IEVTOT, IEVSTA, IEVMCC, IEVMT1,
   IEVMT2, IEVDT1, IEVDT2, IEVCOM, IEVACM, IEVCOD, IEVACD, IHEP(IEVDIM)
   REAL EVMOMX, EVMOMY, EVMOMZ, EVENER, EVMASS, EVXVER, EVYVER, EVZVER,
   EVTVER, EVSPI1, EVSPI2, EVSPI3, EVSPI4, QHEP(IEVDIM)
   COMMON / HEPEVT / IEVNUM, IEVRUN, IEVTOT, IEVSTA, IEVMCC, IEVMT1,
   IEVMT2, IEVDT1, IEVDT2, IEVCOM, IEVACM, IEVCOD, IEVACD, EVMOMX,
   EVMOMY, EVMOMZ, EVENER, EVMASS, EVXVER, EVYVER, EVZVER, EVTVER,
   EVSPI1, EVSPI2, EVSPI3, EVSPI4, IHEP
   EQUIVALENCE (IHEP(1), QHEP(1))
   LHEP(NPHIS) = (NPHIS-1)*IEVSIZ
```

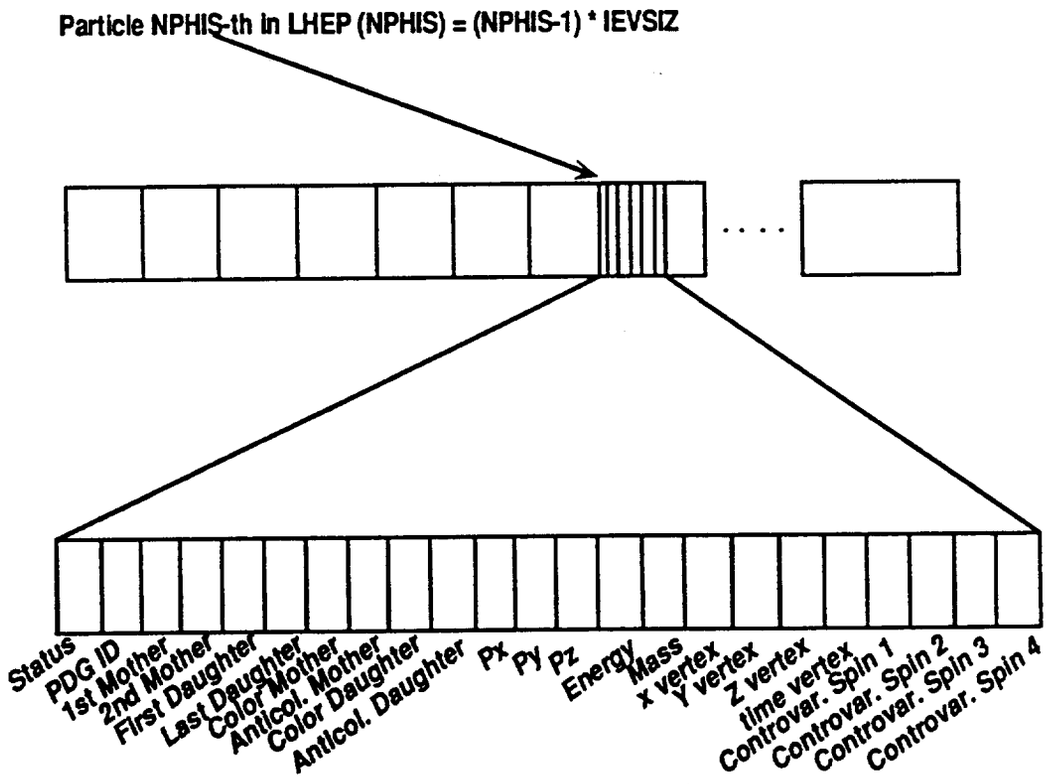


Fig. 1 The dynamical event common

Here the parameters are:

`IEVMAX`	maximum number of entries per event.
`IEVSIZ`	number of parameters characterizing one entry in the common.

`IEVRUN` is the user defined run number, `IEVNUM` is the current event number. `IEVTOT` is the total number of entries in the current event. The particles are counted from 1 to `IEVTOT` and introduced into the common in that sequence. The subsequent (23) variables, from `IEVSTA` to `EVSPI4`, hold the record of the last produced or accessed entry. Entries with their attributes are stored in the array `IHEP` contiguously (starting from position 27 in the common) in *particle records*. The particle record contains information on one particle as illustrated in Fig. 1. The array index `J` of one specified record is found from the count `NPHIS` of the particle ("n^{th} particle in the history") inside the event via a simple arithmetic operation or via the statement function `LHEP: J = LHEP(NPHIS)`. The structure is the following:

`IHEP(J+1)`	status code for the particle;
`IHEP(J+2)`	identification P.D.G. code of the particle;
`IHEP(J+3)`	number of the first mother of the particle;
`IHEP(J+4)`	number of the second mother of the particle;
`IHEP(J+5)`	number of the first daughter of the particle;
`IHEP(J+6)`	number of the last daughter of the particle;
`IHEP(J+7)`	color mother of the particle;
`IHEP(J+8)`	anticolor mother of the particle;
`IHEP(J+9)`	color daughter of the particle;
`IHEP(J+10)`	anticolor daughter of the particle;
`QHEP(J+11)`	X-component of the 4-momentum of the particle;
`QHEP(J+12)`	Y-component of the 4-momentum of the particle;
`QHEP(J+13)`	Z-component of the 4-momentum of the particle;
`QHEP(J+14)`	energy of the particle;
`QHEP(J+15)`	mass of the particle;
`QHEP(J+16)`	X-coordinate of the production vertex;
`QHEP(J+17)`	Y-coordinate of the production vertex;
`QHEP(J+18)`	Z-coordinate of the production vertex;
`QHEP(J+19)`	time of the production vertex;
`QHEP(J+20)`	first spin component of the particle;
`QHEP(J+21)`	second spin component of the particle;
`QHEP(J+22)`	third spin component of the particle;
`QHEP(J+23)`	fourth spin component of the particle.

A more complete description of these variables is given in appendix B.

The following fragment of code shows how to calculate the combined mass of the decay products of particle number `NPHIS` and to check that it remains below the limit of the mass of the particle `NPHIS`:

```
   HEPEVE definitions
```

```
.
.
J=LHEP(NPHIS)
EVMASS  =  QHEP(J+15)
IEVDT1=IHEP(J+5)
IEVDT2=IHEP(J+6)
PXTOT=0.0
PYTOT=0.0
PZTOT=0.0
ENTOT=0.0
DO  10  JDAUG=IEVDT1,  IEVDT2
      J=LHEP(JDAUG)
      PXTOT=PXTOT+QHEP(J+11)
      PYTOT=PYTOT+QHEP(J+12)
      PZTOT=PZTOT+QHEP(J+13)
      ENTOT=ENTOT+QHEP(J+14)
10 CONTINUE
   HMCOM=SQRT(ENTOT**2-PXTOT**2-PYTOT**2-PZTOT**2)
   IF  (HMCOM.GT.EVMASS)  THEN
   WRITE(6,*),"CHECK  FAILED"
   STOP
   ENDIF
```

Using the *HEPEVE* definition "box" as above we can handle up to 2000 entries / event. To extend the allowed number of entries we change the parameter **IEVMAX** only in the main program and there is no need to modify and recompile the other routines referencing the *HEPEVE* common. An "automated" way to fetch (or store) information about a particle **NPHIS** is provided with the subroutine **HEPHIS(NPHIS, CHOPT)**, which copies the particle record from (to) **IHEP** array to (and from) the first 23 words in front of it in the common. The "direction" of copy is specified by the **CHOPT** parameter:

CALL HEPHIS (NPHIS, CHOPT)

NPHIS number of the particle in the history (input INTEGER)

CHOPT character describing to the routine the action to take (input CHARACTER):

'G' GET, retrieve the parameters of particle number NPHIS;
'S' SET, set the parameters of particle number NPHIS. If NPHIS < IEVTOT and NPHIS≥ 0, a new entry is added and IEVTOT is increased by 1.

The following fragment of code shows how to calculate the combined mass of the products of particle number NPHIS calling HEPHIS (under the assumption that daughters of a particle are all recorded sequentially in the IHEP vector):

```
   HEPEVE definitions
.
.
CALL  HEPHIS  (NPHIS,  'G')
PXTOT=0.0
PYTOT=0.0
PZTOT=0.0
ENTOT=0.0
JDAUG1  =  IEVDT1
JDAUG2  =  IEVDT2
DO  10  JDAUG  =  IDAUG1,  JDAUG2
     CALL  HEPHIS  (JDAUG,  'G')
     PXTOT=PXTOT+EVMOMX
     PYTOT=PYTOT+EVMOMY
     PZTOT=PZTOT+EVMOMZ
     ENTOT=ENTOT+EVENER
10 CONTINUE
   HMCOM=SQRT(ENTOT**2-PXTOT**2-PYTOT**2-PZTOT**2)
   IF  (HMCOM.GT.EVMASS)  THEN
   WRITE(6,*),"CHECK  FAILED"
   STOP
   ENDIF
   .
   .
```

4. The Particle Properties Common

The Review of Particle Properties [2] which is published every two years in Physics Letters

by the Particle Data Group lists all the experimental results on the properties of particles. These properties include masses, widths or lifetimes, decay modes and so on. Where feasible, it provides a suggested "best value" for each parameter, based on their judgment using the best available data. It also provides an extensive summary of searches for hypothesized particles in the form of mass limits under specified assumptions. There is a collaboration of the Monte Carlo Simulation Laboratory group and the P.D.G. group aiming to provide a file containing a summary of the particle information needed by the M.C. programs. This file will be available at CERN and will be updated more frequently than the Review of Particle Properties itself, i.e. every year. In the meanwhile, the various event generators use values for the particle properties either coded in the program (e.g. in block data statements) or read from some file, provided by the M.C. author. When the value of one of these quantities is not experimentally well established, it is common practice by M.C. authors to adopt some theoretical estimate for it.

```
C   HEPPPR definitions...
    INTEGER IPPMAX, IPPSIZ, IPDIME
    PARAMETER (IPPMAX = 2000, IPPSIZ = 11)
    PARAMETER (IPDIME = IPPMAX*IPPSIZ)
    INTEGER NPARPS, IPPCOD, IPPPAP, IPPDEC, IPPFDP, IPPFDA,
    IPART(IPDIME)
    REAL PPCHAR, PPMASS, PPLMAS, PPUMAS, PPLIFE, PPFWHM,
    QPART(IPDIME)
    COMMON / HEPPPR / NPARPS, IPPCOD, PPCHAR, IPPPAP, PPMASS,
    PPLMAS, PPUMAS, PPLIFE, PPFWHM, IPPDEC, IPPFDP, IPPFDA,
    IPART
    EQUIVALENCE (IPART(1), QPART(1))
    LPART(IPAPSD) = (IPAPSD-1)*IPPSIZ
```

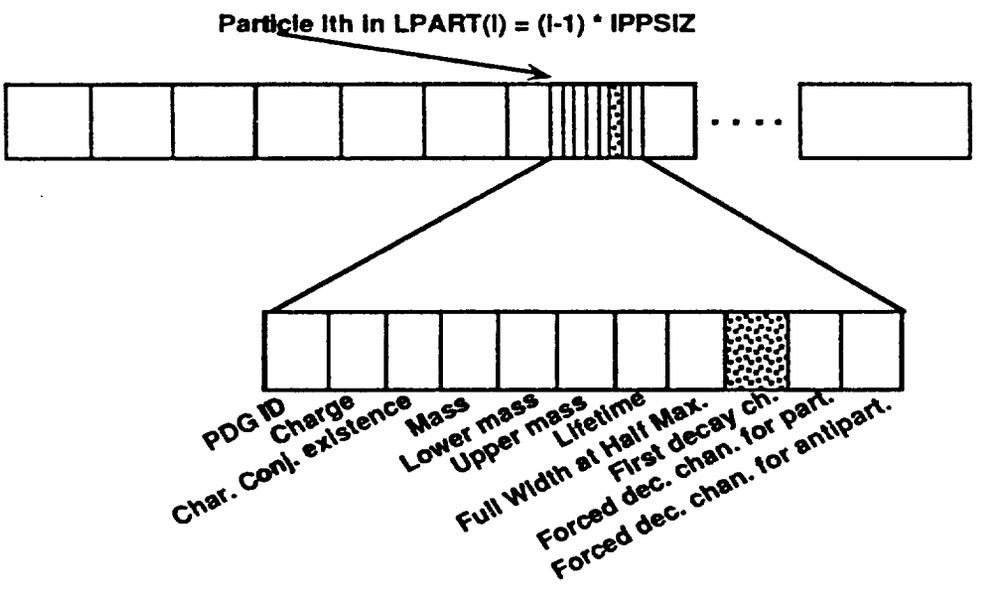


Fig. 2. The structure of the particle properties common

Different guess values for various particle properties are also used in M.C. simulation by different users. We propose to use standard commons for the particle properties, the decay channels and the particle names. At initialization, M.C. programs will read particle data (e.g. from a file) and will fill these commons (vectors IPART and IDEC) as proposed below, so that the data can be used by all program modules of the simulation chain.

The structure of the Particle Properties standard common is shown in Fig.2.

IPPMAX	maximum number of particles at initialization.
IPPSIZ	number of parameters characterizing one particle in the proposed common.

NPARPS is the total number of particles described in the common. The subsequent (11) variables, from IPPCOD to IPPFDA, hold the record of the last updated or accessed particle. Particle properties are stored in the array IPART contiguously (starting from position 13 in the common) in records of particle properties. The array index of one specified record J is found from the particle number IPAPSD inside the common by the statement function LPART. If J is the index to the record describing particle IPAPSD, then J = LPART(IPAPSD) and the structure of the record is the following:

IPART(J+1)	Monte Carlo Standard code, according to P.D.G.
QPART(J+2)	charge
IPART(J+3)	flag indicating the existence of charge conjugate; 1 if it exists
QPART(J+4)	mass
QPART(J+5)	lower mass limit
QPART(J+6)	upper mass limit
QPART(J+7)	life time
QPART(J+8)	full width at half maximum in the mass distribution
IPART(J+9)	pointer to the first decay channel (0 for stable particles)
IPART(J+10)	pointer to the forced decay channel for particle
IPART(J+11)	pointer to the forced decay channel for antiparticle

It is sufficient to give the standard identification code of a given particle to store or to fetch the particle data. The particle number IPAPSD, is derived from its standard identification code, IDPDG, by a translation routine (function LOCPNS) based on the original approach by G. Lynch (P.D.G., Berkeley). If we have a particle with code IDPDG and we want to find the mass and charge, the following sequence of code could be used:

```
HEPPPR definitions
```

```
.
.
JPART=LPART(LOCPNS(IDPDG))
.
.
```

Alternatively, there is a routine to fetch (and store) the particle record from (to) the first 11 words of the common:

```
CALL  HEPPAR  (IDPDG,  CHOPT)
```

IDPDG — the standard particle code in the M.C. coding scheme (input INTEGER)

CHOPT — character describing to the routine the action to take (input CHARACTER):

- 'G' GET: retrieve the parameters for a particle given its P.D.G. code
- 'S' SET: set the parameters for a particle given its P.D.G. code

The following fragment of code shows how to increase by 10% the mass of a particle with P.D.G. code IDPDG:

```
HEPPPR definitions
```

```
.
.
CALL  HEPPAR  (IDPDG,'G')
PPMASS=PPMASS*1.10
CALL  HEPPAR  (IDPDG,'S')
```

5. The Decay table common

One of the "properties" of particles are their decays. The third common proposed is the one containing the decay table for particles. Normally particles have more than one modes of decay with different probabilities. The Particle Properties common described in the previous

```
C  HEPPDE Definitions...
   INTEGER IPDMAX
   PARAMETER (IPDMAX = 20000)
   INTEGER IPDCOD, IPDMXE, IPDMLT, IPDNEX, IPDPRO(10), IDEC(IPDMAX)
   REAL PDBRAT, QDEC(IPDMAX)
   COMMON / HEPPDE / IPDCOD, IPDMXE, PDBRAT, IPDMLT, IPDNEX, IPDPRO, IDEC
   EQUIVALENCE (IDEC(1), QDEC(1))
C  The value of the pointer to the next decay channel is:
C  IDEC(J) = J+5 + IDEC(J-1), if that is not the last channel
C  IDEC(J) = 0, if this is the last decay channel
C  Notice that the pointer to the first channel is known from the
C  common / HEPPPR /
```

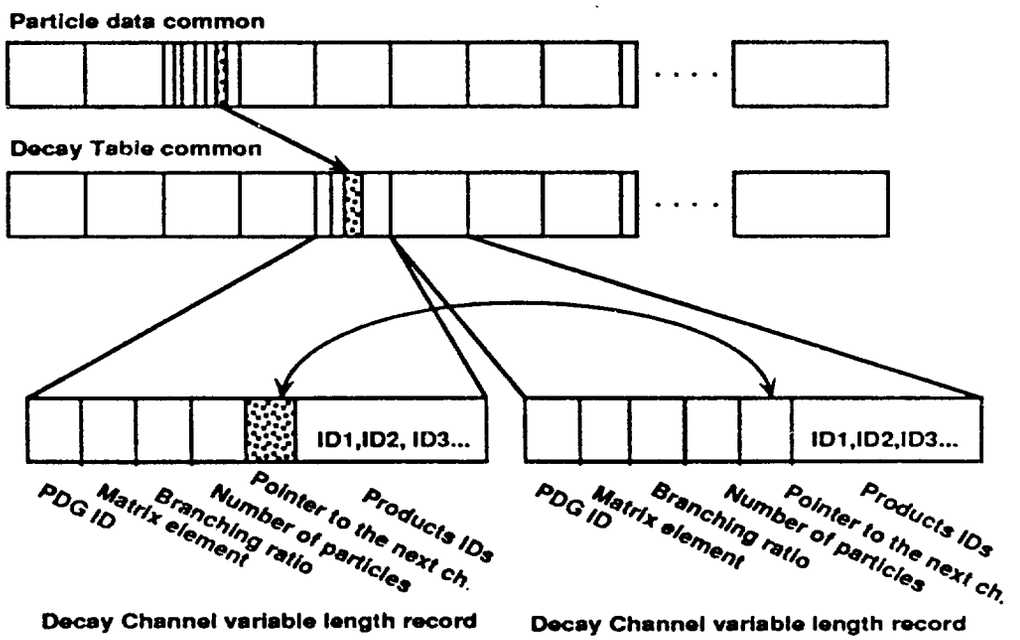


Fig. 3 The Decay Table Common and its structure linked to the particle properties common.

chapter contains a pointer to the "first" decay channel. This pointer is just an array index of the record of this decay channel in the Decay Table common. Therefore, the two commons are linked, as shown in Fig. 3. The variable **IPPDEC** in the **HEPPPR** common points to the variable **IPDNEX** in the *HEPPDE* common. The **IPDNEX** variable contains the index of the next decay channel, which in turn points to the next, and so on (see fig. 3). When the last decay channel of the particle is reached the pointer is set to 0.

The tables describing the decay of the particles are stored contiguously in the array **IDEC**. Analogously to the previous cases 5 variables and one array at the beginning of the common are filled with the information referring to the current channel. If **J** is the pointer to a decay channel, then the structure of the related information in the common is the following:

IDEC(J-4)	P.D.G. code of the parent particle
IDEC(J-3)	matrix element for the decay
QDEC(J-2)	branching ratio for the current channel
IDEC(J-1)	number of products **(IPDMLT)** in this decay channel
IDEC(J)	pointer to the next decay channel for the current particle; last decay channel if 0
IDEC(J+1)	P.D.G. code of the first product for the current decay channel
.	
.	
IDEC(J+IPDMLT)	P.D.G. code of the last product for the current decay channel

The following fragment of code shows how to choose a decay channel for a particle with P.D.G. code **IDPDG**:

```
   HEPPPR definitions
```

```
  HEPPDE definitions
```

```
.
.
CALL  HEPPAR  (IDPDG,'G')
RAN=RNDM(Q)
CBRAT=0.0
JDECCH=IPPDEC
10 CONTINUE
CBRAT=CBRAT+QDEC(JDECCH-2)
```

```
JDECCH=IDEC(JDECCH)
IF(CBRAT.LT.RAN.AND.JDECCH.NE.0)  GO  TO  10
.
.
```

A routine to fetch or to store the information in the particle decay table common is proposed:

`CALL HEPDEC (IDPDG, J, CHOPT)`, with

`IDPDG` P.D.G. code of the parent (input INTEGER)

`J` on input, either pointer to a decay channel or -1, on output either pointer to the next decay channel (zero if none) or to the current one, according to the value of `CHOPT` (input/output INTEGER)

`CHOPT` character describing to the routine the action to take (input CHARACTER):

- `' '` blank, retrieve the decay channel pointed to by `J`. If `J=-1` the first decay channel is retrieved. On output `J` points to the next decay channel, or is zero if the last one has been retrieved;
- `'G'` GET, retrieve the decay channel pointed to by `J`. If `J=-1` the first decay channel is retrieved. On output `J` points to the current decay channel;
- `'A'` ADD, add the given channel to the decay table for particle P.D.G.. On output `J` points to the new decay channel. If `J=-1` there is no more space in the decay table to store a new decay channel. The branching ratios are renormalized automatically;
- `'D'` DELETE, delete the decay channel pointed to by `J`. If `J=-1` the first decay channel is deleted. On output `J` points to the next decay channel;
- `'S'` SET, set the decay channel pointed to by `J`. If `J=-1` the first decay channel is set. On output `J` points to the current decay channel.

The following fragment of code shows how to choose a decay channel for a particle with P.D.G. code `IDPDG` using `HEPDEC`:

```
HEPPDE definitions
.
.
RAN=RNDM(Q)
CBRAT=0.0
JDECCH  =  -1
10 CALL  HEPDEC  (IDPDG,  JDECCH,  '  ')
CBRAT=CBRAT+PDBRAT
IF   (CBRAT.LT.RAN.AND.JDECCH.NE.0)  GOTO  10
.
.
```

6. The Particle Names Common

The use of the P.D.G. particle numbering scheme makes it possible to refer to a particle unambiguously. Nevertheless, it may be practical sometimes to name a particle. We therefore introduce one more common to record the particle names. Sixteen characters are foreseen for the full name and four for the abbreviated name, which is preferred in some applications. The proposed structure is included with the *HEPPPR* common:

```
CHARACTER*20  CPNAME
CHARACTER*16  FPNAME
CHARACTER*4   APNAME
COMMON  /  HEPPNA/  FPNAME,  APNAME,  CPNAME(IPPMAX)
```

In this scheme, **FPNAME** and **APNAME** are the full and the abbreviated name of the current particle. **CPNAME** is the array containing name and short name of all the particles. The index J of the current particle is still found from the IDPDG code via the usual function LOCPNS and the content of **CPNAME(J)** is the following:

```
CPNAME(J)  (1:16) full name
CPNAME(J)  (17:20)  abbreviation for that name.
```

In order to fetch and store particle names given the particle ID, we use **HEPPAR** as illustrated in chapter 6.

7. Summary and outlook

The aim of the paper is to define the minimum information needed to allow a User to construct his own simulation chain based on different modules from different Monte Carlo event generators. The current proposal is optimized from the point of view of memory space allocation and use and, more in general, as far as software engineering is concerned (within the framework of possibilities of FORTRAN77; tailoring to FORTRAN90 will be fully supported). It is also complete in its physics contents (as far as event, particle properties and decays are concerned). It gives flexibility, maintainability and it is still very easy to use. The set of dynamic commons and related handling routines are proposed as a standard to achieve modularity in

the various steps of Monte Carlo simulation. Working software has been developed and is available in C.E.R.N. libraries.

We have clearly profited from earlier work by T. Sjöstrand.

The facility for interfacing different program modules which has been described so far will be used in the COSMOS project [4, 9]. This project provides the "support environment" for the organization and the interface of different simulation packages and tracking programs, together with a user interface. A file containing the P.D.G. particle properties is available at C.E.R.N.. This file can be used to fill the *HEPPPR*, *HEPPDE* and *HEPPNA* commons.

References

[1] G.R. Lynch and T.G. Trippe, "Particle I.D. Numbers, Decay Tables, and Other Possible Contributions of the Particle Data Group to Monte Carlo Standards", LBL-24287, Proc. of the Workshop on Detector Simulation for the SSC, Argonne, Illinois (USA), August 1987.

[2] M. Aguilar Benitez et al., Particle Data Group, Phys. Lett. B 204 (1988) 1.

[3] G. Altarelli, R. Kleiss and C. Verzegnassi, "Z Physics at LEP 1", Vol. 3, CERN 89-08, 21 September 1989.

[4] B. van Eijk, Proposal for the C. & C. Huygens Research Fund, 'Netherlands Organization for Scientific Research (NWO)', The Netherlands (1988),
B. van Eijk et al., COSMOS, 'COmprehensive Super MOntecarlo System', in preparation.

[5] F. Anselmo and B. van Eijk, EUROJET version 3.1, in preparation,
A.Ali and B.van Eijk, EURODEC version 2.5, CERN Pool Program W5048, March 12, 1990.

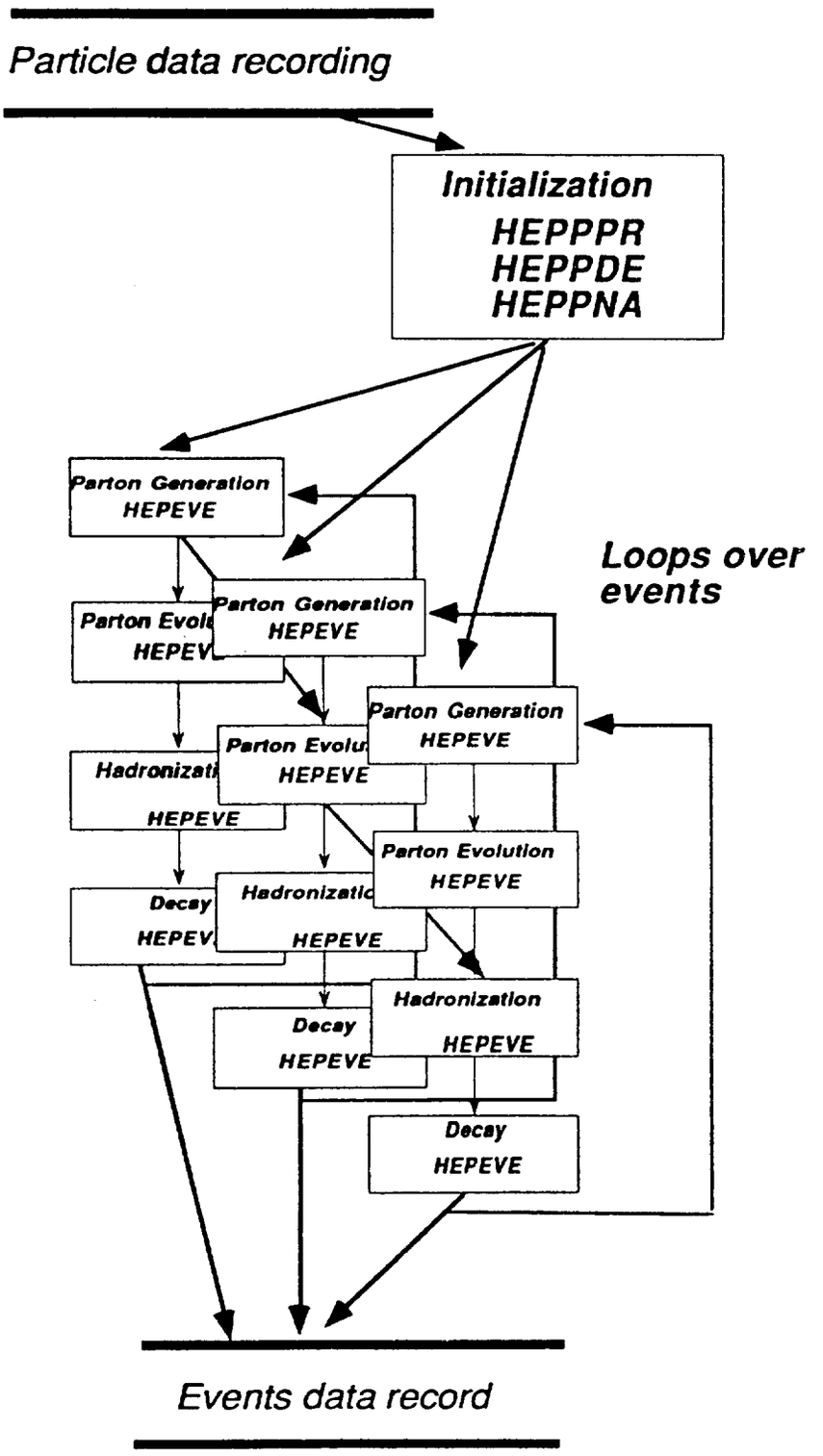
[6] The Lund Monte Carlo Programs, CERN Pool Program W5035/W5046/W5047/ W5048 long write-up, 3 April 1987, and references therein,
H.U. Bengtsson and T. Sjöstrand, Comput. Phys. Commun. **46** (1987) 43.

[7] G. Marchesini and B.R. Webber, HERWIG version 4.2, CERN Pool Program W5037, February 1990.

[8] R. Odorico, Comput. Phys. Comm. **59** (1990) 527.

[9] J.M. Alberty et al. , "An integration of Physics Packages, Data Modelling and Human Interface", to appear in the Proceedings of the International Workshop on Software Engineering, Artificial Intelligence and Expert Systems for High Energy and Nuclear Physics, Lyon / Villeurbanne (France), March 1990.

Appendix A
Modularity in Event Generators with the Standard HEP common blocks



Appendix B

Detailed description of the variables used in the *HEPEVE* common.

IEVRUN the run number as user-defined (input/output INTEGER)

IEVNUM the event number as user-defined (input/output INTEGER)

IEVTOT the actual number of entries produced and stored in current event. These are found in the first **NPART** positions of the history vector **IHEP** in the common. Index **NPHIS**, $1 \leq$ **NPHIS** $\leq$ **NPART**, is used to denote a given entry (output INTEGER)

IEVSTA status code with following meanings (input/output INTEGER):

- **0** null entry;
- **1** an existing entry, which has not decayed or fragmented. This is the main class of entries which represents the *final state* given by the generator;
- **2** an entry which has decayed or fragmented and therefore is not appearing in the final state, but is retained for event history information;
- **3** a documentation line, defined separately from the event history. This could include the two incoming reacting particles, etc;
- **4-10** undefined, but reserved for future standards;
- **11-20** at the disposal of each model builder for constructs specific to his program, but equivalent to a null line in the context of any other program. One example is the cone defining vector of HERWIG, another cluster or event axes of the JETSET analysis routines;
- **21-** at the disposal of users, in particular for event tracking in the detector;

IEVMCC particle identity, according to the Particle P.D.G. Group standard (input/output INTEGER)

IEVMT1 particle number of the first mother. The value is 0 for initial entries (input/output INTEGER)

IEVMT2 particle number of the second mother. The value is 0 for initial entries (input/output INTEGER). Normally only one mother exists, in which case the value 0 is used. In cluster fragmentation models, the two mothers would correspond to the q and qbar which join to form a cluster. In string fragmentation, the two mothers of a particle produced in the fragmentation would be the two end-points of the string (with the range in between implied); (input/output INTEGER)

IEVDT1 particle number of the first daughter. If an entry has not decayed, this is 0; (input/output INTEGER)

IEVDT2 particle number of the last daughter. If an entry has not decayed, this is 0. This pointers are specially useful under the assumption that the daughters of a particle (or cluster or string) are stored sequentially, so that the whole range **IEVDT1** to **IEVDT2** contains daughters. Even in cases where only one daughter is defined (e.g. K°->K°S) both values should be defined, to make for a uniform approach in terms of loop constructions (input/output INTEGER)

IEVCOM color mother of the particle

IEVACM anticolor mother of the particle

IEVCOD color daughter of the particle

IEVACD anticolor daughter of the particle

EVMOMX momentum in the X direction, in GeV/c (input/output REAL)

EVMOMY	momentum in the Y direction, in GeV/c (input/output REAL)
EVMOMZ	momentum in the Z direction, in GeV/c (input/output REAL)
EVENER	energy, in GeV (input/output REAL)
EVMASS	mass, in GeV/c**2. For space-like partons, it is allowed to use a negative mass, according to **AMASS=-SQRT(-m^2)** (input/output REAL);
EVXVER	production vertex x position, in mm (input/output REAL)
EVYVER	production vertex y position, in mm (input/output REAL)
EVZVER	production vertex z position, in mm (input/output REAL)
EVTVER	production time, in mm/c (= 3.33*10^{-12} s) (input/output REAL)
EVSPI1	spin first component of the particle
EVSPI2	spin second component of the particle
EVSPI3	spin third component of the particle
EVSPI4	spin fourth component of the particle.

Trigger Rates at the LHC

Sten Hellman, Livio Mapelli and Giacomo Polesello
CERN, Geneva, Switzerland

Presented by Sten Hellman

This contribution presents a first attempt of a global estimate of first level trigger rates at the LHC, based on a compilation of relevant studies. In most cases the inclusive rates have been taken directly from the individual studies. In some cases it was necessary to extrapolate or 'interpret' the inclusive studies, as for instance when computing expected background rates or when comparing different studies. We try to credit the original authors of these studies and to point out the cases where we have manipulated their results.

In general we have tried to identify thresholds giving rates of the order of 1 - 10 kHz at $\mathcal{L} \approx 10^{34}$ cm^{-2}s^{-1}.

1 Inclusive Muon Rates

Inclusive muon rates have been determined by A. Nisati. The method used is described in detail in reference [1]. Briefly, ISAJET is used to generate the muon spectra from the following sources:
c,b $\rightarrow \mu$ X, W $\rightarrow \mu\nu$, t $\rightarrow \mu$ X (m_t = 130 GeV), Z $\rightarrow \mu\mu$, Drell-Yan production of $\mu\mu$ and backgrounds from decay of π and K

In addition reference [1] also considers the background from hadron punch-through. The study assumes muon coverage within $|\eta|<3$. For the punch-through a total absorber thickness varying from 10 to 20 λ, depending on polar angle, is assumed. More details on rates from hadronic decays and punch-through can be found in ref. [2,3].

In the range $p_t > 10$ GeV, the dominant contribution to the muon rate is prompt muons, the contribution from decays and punch-through being negligible. The prompt muon rates above a given p_t-threshold, p_t^{th}, are shown in table 1 for single muons and muon pairs, where the softest muon is required to have $p_t > p_t^{th}$. We conclude that at $\mathcal{L} \approx 10^{33} cm^{-2} s^{-1}$ one can expect

p_t^{th}	Single Muon Rates	
	Rate at 10^{33}	Rate at 10^{31}
20 GeV	200 Hz	2 kHz
30 GeV	50 Hz	500 Hz
40 GeV	20 Hz	200 Hz
	Dimuon Rates	
20 GeV	3 Hz	25 Hz

Table 1: Inclusive Single Muon Rates Above p_t^{th}, from ref [1]

a trigger rate of a few hundred Hertz for single muon triggers down to a p_t^{th} of 20 GeV, rising to a few kHz at $\mathcal{L} \approx 10^{34} cm^{-2} s^{-1}$. The dimuon rate at the same threshold gives a few Hertz at $\mathcal{L} \approx 10^{33} cm^{-2} s^{-1}$ and around 25 Hz at $\mathcal{L} \approx 10^{34} cm^{-2} s^{-1}$.

2 Inclusive Electron Rates

Electron trigger rates based on calorimeter information will depend critically on what rejection against hadronic backround can be achieved. The large QCD production cross sections for hadronic jets implies that even a small fraction of these missinterpreted as electrons will give overwhelming rates. Two studies address these questions:
One is made by N. Ellis [4] who used ISAJET to produce two-jet events. The calorimeter is modelled with a grid in $\eta \times \phi$ space, extending to $|\eta| < 3$. Each tower is divided into one electromagnetic and one hadronic compartement. Electromagnetic particles deposit their energy in one electromagnetic cell, whereas hadrons share their energy between the electromagnetic and hadronic compartements of one tower. This longitudinal sharing is described by a parameterisation made from complete simulations of the UA1 U/TMP calorimeter.

In a second study J. P. Repellin [5] uses 2-jet events generated with PYTHIA. For calorimeter modelling he uses a GEANT simulation in a homogenous cylinder of "lead", inside $|\eta| < 2$, which has been defined as having half the density of lead. Separate studies [6] have shown that this procedure gives lateral shower extensions which agree with a full GEANT simulation of a complete sandwich of absorber/sampling medium. After the GEANT swimming the energy is ascribed to calorimeter cells with smearing for detector resolution.

Initial rejection against hadrons is obtained by requiring transverse energy above some given threshold, E_t^{th}, deposited in one electromagnetic cell. In reference [5], for E_t^{th} of 20 GeV and cell size 0.1×0.1 a rejection against hadron jets ~55 is found. In table 2 we show the rejection factor obtained in reference [4] [1] .

	E_t^{th}				
$\phi \times \eta$	10 GeV	20 GeV	30 GeV	40 GeV	50 GeV
0.1 × 0.1	~10	~10	~65	~140	~120
0.2 × 0.2	~30	~30	~40	~60	~90

Table 2: Rejection, as defined in text, by demanding one em cell fired, from ref. [4]

In addition to this cut one can require isolation of the candidate electromagnetic showers, and cut on the hadronic leakage of the showers. In [4] these cuts have been combined by considering the energy in a matrix of 4×4 cells, centered on the electron candidate. Defining E_t^{Σ} as the sum of the energy in the 12 electromagnetic cells surrounding the 4 cells centered on the electron candidate and the 16 hadronic cells immediately behind, one typically finds additional rejection factors of 3-5 (2-3) for cell sizes 0.2×0.2 (0.1×0.1) by requiring $E_t^{\Sigma} < 5$-10 GeV.

Tighter cuts are applied in [5], where only the case of E_t^{th} >20 GeV is considered. Requiring less than 2 GeV of E_t seen in the hadronic cell with cell size 0.2×0.2 behind the electromagnetic cell gives a rejection of ~6. The isolation criteria are applied by demanding that the additional energy in the neighbourhood of an electron candidate is less than 4.5 GeV. 'Neighbourhood' is defined as the em and hadronic compartments in a matrix 0.2×0.2 centered on the em cell of size 0.1×0.1. This cuts give an additional rejection factor of 2-3. The combined rejection from isolation and leakage is thus in the range 15 to 25.

Comparing reference [4] with reference [5] one finds the expected increase in rejection with smaller cell size. The rejection at the first trigger level will depend on the granularity used in the trigger, and exactly how the isolation and leakage cuts can be implemented in the trigger. To obtain an estimate of trigger rates under varying conditions we give three numbers; The

[1] The rejection factors shown in table 2 were computed as the inverse of the fraction of jets with $E_t > E_t^{th}$ that passed the cut

rate expected by requiring one em-cell over a given threshold E_t^{th}as given in [4], and the rate assuming an additional rejection after isolation/leakage cuts of 5 and 20 respectively [2]

For the di-electron case we only give the rates as computed by demanding two em cells being above E_t^{th}. There will be additional rejection from requirements on isolation and hadronic leakage. For di-electron events one can probably not assume the square of the rejection for single electrons, due to correlations between the two electrons. From the numbers presented in

	Cell Size 0.1×0.1			Cell Size 0.2×0.2		
E_t^{th}	Cell above p_t^{th}	R = 5	R = 20	Cell above p_t^{th}	R = 5	R = 20
20 GeV	230 kHz	45 kHz	12 kH	310 kHz	65 kHz	16 kHz
30 GeV	35 kHz	7 kHz	2 kHz	53 kHz	11 kHz	3 kHz
40 GeV	6 kHz	1.2 kHz	300 Hz	14 kHz	3 kHz	750 Hz
50 GeV	3 kHz	600 Hz	150 Hz	4 kHz	800 Hz	200 Hz

Table 3: Inclusive Single Electron Rates at $\mathcal{L}$ =10^{31}, from ref. [4]

E_t^{th}	Cell Size 0.1×0.1	Cell Size 0.2×0.2
10 GeV	100 kHz	260 kHz
20 GeV	10 kHz	36 kHz
30 GeV	1 kHz	2 kHz

Table 4: Inclusive Di-Electron Rates at $\mathcal{L} = 10^{31}$, from ref [4]

tables 3 and 4 one concludes that even with cellsizes 0.2×0.2 and rather modest assumptions on the additional rejection from isolation and hadronic leakage cuts, the single electron rate at $\mathcal{L}\approx 10^{31} cm^{-2}s^{-1}$ could be brought down to $\leq$ 10 kHz for E_t^{th}<40 GeV. Di-electron rates will be in the kilohertz range if requiring E_t^{th}>20 GeV for both electrons.

3 Inclusive Jet Rates

3.1 The effect of pile-up

Since the cross section for QCD jet-production is a steep function of p_t one has to consider the effect of pile-up at high luminosities. A study by T Sjöstrand [7] investigated the effect of pile-up from PYTHIA generated minimum bias event on jets. The jet energy was collected in cones with $\Delta R > 0.5$ ($\Delta R = \sqrt{\phi^2 + \eta^2}$). He found that the additional energy collected in such a cone from pile-up of minimum bias events could be parametrized as <n>·$\frac{8}{5}$ GeV, where <n> is the average number of minimum bias events seen by a detector. A detector with a memory time of 3 bunch crossings, for example, would have <n>≈32 at $\mathcal{L}\approx 10^{31} cm^{-2}s^{-1}$, giving an additional 20 GeV of transverse energy in a jet cone defined as above. Given the jetalgorithm used in reference [7] we do however consider this number to be pessimistic. Attempts to design "luminosity-hard" jet algorithms have been made, resulting in jet definitions which do seem to be less sensitive to pile-up effects. To loosely cover for this we have assumed, in what follows, that pile-up effects at $\mathcal{L}\approx 10^{31} cm^{-2}s^{-1}$will contribute ~10 GeV to the jet energies. Rates above a given p_t-threshold have been computed using the cross section for (p_t-10) GeV.

[2]Note that these rate-estimates is based on ISAJET or PYTHIA predictions for the 2-jet rate at p_t as low as 20 GeV, where the uncertainty might be almost one order of magnitude.
There are also additional uncertainties in the rejection from leakage and isolation cuts due to uncertainties in the fragmentation models used in the Monte Carlos. These questions, and the sensitivity of these results to the longitudinal shower profile modelling are under study.

A second effect of pile-up might be the seen 4-jet rate caused by random pile-up of two 2-jet events. Using the 2-jet cross section given by [8] and $\sigma_{inel.}$ of 80 mb one obtains a faked 4-jet rate, using jet definitions as below, of less than 100 Hz at a luminosity of 10^{31}. Thus one concludes that topological pile-up does not represent a major problem at the trigger level even at the highest projected luminosities.

3.2 Multi-jet rates.

The most relevant study available is made by P. Lubrano, reported in [8], who ran a multi-jet Monte Carlo based on the calculation of [9]. One result of this study is the integrated cross sections for different topologies, demanding that the softest jet in each event has $p_t > 50$ GeV, assuming η-coverage extended to 3, and that the angular separation between jets is larger than 30^o. At $\mathcal{L} \approx 10^{31} cm^{-2} s^{-1}$ we then obtain the rates shown in table 5

n=	2	3	4	5
rate	240 kHz	11.5 kHz	1.3 kHz	150 Hz

Table 5: Inclusive Jet Rates Above p_t^{th}, from ref. [8]

For 2- and 3-jet topologies we have used the differential cross-sections to determine p_t-thresholds yielding rates $\sim$10 kHz at $\mathcal{L} \approx 10^{31} cm^{-2} s^{-1}$. We have estimated the increase in seen cross section caused by the addition of 10 GeV from pile-up.

With the same jet-definitions as above one obtains, at luminosities of 10^{31}, rates of about 10 kHz for two-jet events demanding the softest jet to have $p_t > 160$ GeV. For three-jet events the rate is $\approx$1 kHz at a threshold of 130 GeV.

4 Inclusive Missing Transverse Energy Rates

The inclusive missing transverse energy trigger is possibly the most difficult to model. A large fraction of these triggers could be caused by instrumental effects, for which simulations are less well developed, rather than by physical processes. Here we will address the importance of the pseudorapidity-coverage, the range and resolution of trigger electronics and detector cracks. One topic not covered is machine induced backgrounds.

4.1 Pseudorapidity-coverage of Calorimeter

N. Ellis [4] has investigated the $\not\!\!E_T$ spectrum created by insufficient η-coverage by generating two-jet events with ISAJET ($p_t^{hard} > 30$ GeV) and measured $\not\!\!E_T$ with the same type of calorimeter simulation as described in section 2. As can be seen in figure 1 coverage out to pseudorapidities equal to 5 should be sufficient, whereas it seems desirable to reach out beyond 4.5. This latter agrees well with several physics studies.

4.2 Calorimeter Electronics

In a somewhat statistics limited study N Ellis also studied the effect of limited resolution and dynamic range in the ADCs used in the trigger electronics. He found that even with rather modest perfomance; 1 GeV/bit and 8 bit dynamic range, the rate for $\not\!\!E_T > 50$ GeV (>100 GeV) is $\sim$300 Hz ($\sim$25 Hz) at $\mathcal{L} \approx 10^{31} cm^{-2} s^{-1}$. This particular contribution to the $\not\!\!E_T$ trigger rate is thus acceptable at the first level trigger.

4.3 Cracks

This source of $\not\!\!E_T$ is obviously very difficult to study in a realistic manner. An attempt has been made by P Sphicas in a study also described in [10]. His study can be summarized in the following steps: First he uses the PAPAGENO Monte Carlo to generate 3-, 4- and 5-jet events [3] with the correct matrix elements. These parton level jets are then 'dressed' to jets. This is achieved by using parametrisations of the E_t flow around the jet axis as a function of E_t and ΔR obtained by running ISAJET. These jets are then sent into a calorimeter with the same geometry, including cracks, as the CDF calorimeter. Energy falling in the sensitive part of the calorimeter is resolution smeared, while energy falling in the crack region is considered lost. Figure 1 shows the obtained differential cross-section in $\not\!\!E_T$ requiring three jets with $p_t >$ 150 Gev, for two different values for the resolution smearing, viz. $\Delta E/E = 10\ \% / \sqrt{E}$ and $= 80\ \% / \sqrt{E}$ respectively. From this study one would tend to conclude that the contribution to the $\not\!\!E_T$-rate from this effect is of the order of 1 kHz for $\not\!\!E_T > 100$ GeV.

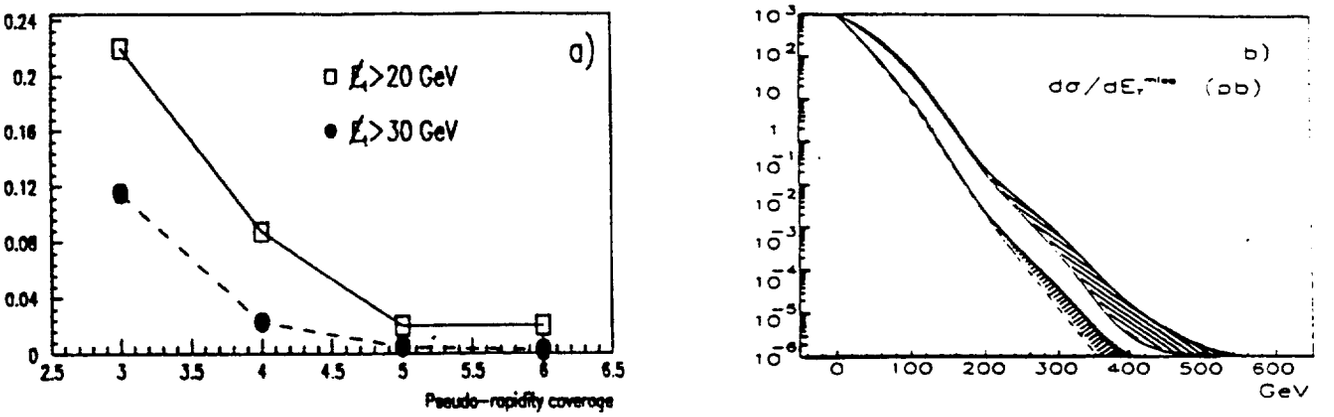


Figure 1: a) $\not\!\!E_T$ induced by limited pseudorapidity coverage. The curves show fraction of jets with $\not\!\!E_T$ over threshold. b) $\not\!\!E_T$Induced by Cracks. The curves show the effect for two different assumptions on calorimeter resolution, see text. The width of the bands show the statistical uncertainty from simulation.

5 Three Examples of Physics Triggers

In this section we use three physics signatures to demonstrate the feasibility of first level triggers which give acceptable rates, and good efficiencies for the physics signals. In section 5.1 we draw much of the material from [11], while section 5.2 use material from [12].

5.1 Top

We consider three possible channels for a top search at LHC: $t\bar{t} \rightarrow$ (e or μ) + 3 Jets, $t\bar{t} \rightarrow$ e + μ + X and W g $\rightarrow t\bar{b}$

1. Three Jets and a Lepton (e or μ): In this channel it is necessary to reach a p_t threshold of 40 GeV, both for the charged lepton and for the three jets. *Muons:* For a cut at p_t^{th} >40 GeV the inclusive rate at 10^{31} is ~200 Hz. Most muons of that p_t come from the decay of b- and c-quarks, and W production. If in addition one requires three jets above 10 GeV,

[3] The most abundant source of $\not\!\!E_T$, QCD two-jet events is thus **not** included. The conclusions based on this study are thus valid only to the extent that this particular topology is vetoed

the rate reduces to a few Hertz. *Electrons:* Depending on the assumptions for the rejection by isolation/leakage cuts, one expect inclusive electron rates of 0.5-5 kHz for E_t^{th}=40 GeV. The main background is multi-jet events, in which one jet is misidentified as an electron. Using σ (4 jets: p_t> 40 GeV, $|\eta^{jet}| < 2$) ≈200 nb, [11] and the above estimate of topological overlap the 4-jet rate will be ≈2.5 kHz at $\mathcal{L}$=10^{31}. Assuming a conservative rejection factor of 10^2 per jet gives rates ∼100 Hz, taking combinatorics into account.

2. Electron and Muon: In this search one can accept p_t-thresholds of 50 GeV for both leptons. At this p_t-cut the inclusive muon rate is ∼100 Hz, dominated by b- and c-quark decays. The inclusive electron rate above p_t^{th}=50 GeV is in the range 20-400 Hz, depending on cell sizes and which additional rejection factors one assumes. Combining the two signals leave $b\bar{b} \rightarrow \mu$ + fake electron as the principal background. With $\sigma(b\bar{b}$: p_t^{μ} >50 GeV, $|\eta^{\mu}|$<2, p_t^{b} > 50 GeV) ∼ 3 nb, [11] the rate is roughly 0.3 Hz at 10^{31} assuming a jet rejection of 10^2. Pile-up might boost this rate slightly, but it will still stay within reasonable limits.

3. W-gluon Fusion: In this channel, relevant for the search for a very heavy top, one would require one electron or muon with p_t > 40 GeV, and 2 jets, also with p_t > 40 GeV. *Muons:* The inclusive muon rate above p_t= 40 GeV is of the order of 200 Hz at 10^{31}. If in addition one requires 2 jets with p_t > 40 GeV the rate reduces to the few Hertz range. *Electrons:* for electrons the main background is 3-jet events, where one jet fakes an electron. Using σ (3 jets; p_t>40 GeV, $|\eta^{jet}|$< 5)= 3 μb, [11] we are left with a rate of just below a kHz, again assuming hadron rejection factors of 100. Clearly electron identification will not be available over this pseudo-rapidity range which will reduce the rate of faked electrons [4], we estimate the surviving rate to be of the order of 300 Hz.

5.2 Higgs

For the Higgs searches we consider two scenarios requiring four leptons in the final state, and one requiring a lepton, 2 jets and $\not{E}_T$

1. H → ZZ/Z$^{(*)}$Z* → 4 leptons, 170<M$_{Higgs}$ <300 GeV: The search for a Higgs in this mass window could start from a requirement of 2 electrons or 2 muons with p_t larger than 20 Gev. *Muons:* The inclusive di-muon rate above 20 GeV gives rates around 25 Hz at 10^{31}. *Electrons:* The di-electron rate cutting at p_t of 20 Gev will be 10-30 kHz at 10^{31}, before applying isolation and leakage cuts. Assuming that these cuts will bring a further rejection of a factor 5-20 on each leg will bring the rate down to 25 Hz - 1 kHz. Pile up will push up this rate slightly [5] while the requirement of a third lepton with p_t> 10 GeV will reduce it. We estimate that the rate for this combined signature will be in the 100 Hz range.

2. M(Higgs) >300 GeV: For a search in this mass range the requirement of 2 leptons with p_t> 30 GeV will give sufficient efficiency for the signal. *Muons:* The di-muon rate above 30 GeV will be ∼ 10 Hz, dominated by $Z \rightarrow \mu\mu$. *Electrons:* Before the rejection from isolation/leakage the rate will be ∼ 100 Hz. Applying these cuts will bring the rate down almost to the 10 Hz from Z decays.

3. Higgs to 2 W → $\ell^{\pm}\nu$+ 2 jets: This channel, which is of interest for the very high mass range for Higgs, would require a charged lepton with p_t > 100 GeV. *Muons:* With this rather high p_t cut the inclusive rate at $\mathcal{L}$≈$10^{31} cm^{-2} s^{-1}$ is down to ∼10 Hz, most of which is from the decay of top and W. Clearly this poses no rate problem for a first level trigger. *Electrons:* The electron rate will be dominated by background from QCD jets. Using σ(incl. jets: p_t > 100 GeV, $|\eta^{jet}|$< 2) = 3 μb, [12] and assuming that the rejection at cell level

[4] Since jets with 3<|η|<5 will not contribute to the "fake" electron rate

[5] Note though that the probability to fake electrons of a given p_t increases slower than the increase of jet-rates, since the additional energy in a cone from pile-up effects will cause the jet to rarely pass isolation/leakage cuts

flattens out at ~100 at large p_t and that isolation/leakage cuts still give a rejection of 3, this would lead to a rate of about 100 Hz at first level trigger.

5.3 Supersymmetry

For SUSY we consider two possible signatures: $\tilde{g}\tilde{g} \rightarrow \not{E}_T$ + multijets and $\tilde{g}\tilde{g} \rightarrow$ Z Z jet jet $\tilde{\gamma}\tilde{\gamma} \rightarrow$ 4 electrons + jets + $\not{E}_T$.

1. Multijets and $\not{E}_T$: One test case [13] is the pair production of $\tilde{g}$ with $m_{\tilde{g}}$=300 GeV. In this case one would require 3 jets with p_t above 200 GeV and $\not{E}_T$> 200 GeV. As seen in [8] the inclusive rate for 3 jets with p_t> 200 GeV is ~200 Hz at $\mathcal{L} \approx 10^{31} cm^{-2} s^{-1}$. The 'crack'-study [10] indicates that with these cuts on $\not{E}_T$ and p_t of the jets, the rate should be a few Hertz. The main physics background at this level is $t\bar{t}$, which for a top-mass of 150 GeV will have a rate of a few Hertz. First level triggering thus looks feasible with these thresholds.

4 leptons and $\not{E}_T$: In this channel one would require 2 charged leptons with $p_t$above 30 GeV at level one. This would result in rates of 10-100 Hz as described in section 5.2 , and does not pose serious problems.

6 Conclusions

In table 6 we summarize the examples given above. The following points can be made starting from table 6:

	Inclusive		Combined	
Process	Signature	Rate	Combination	Rate
Top				
3J + lepton	μ, p_t>40 GeV	40-200 Hz	+ 3 Jets > 40 GeV	a few Hz
	electron, p_t> 40 GeV	0.5-5 kHz	+ 3 Jets > 40 GeV	$\leq$ 20 Hz
electron + μ	μ, p_t>50 GeV	100 Hz	e + μ, p_t' , p_t'' >50 GeV	~1 Hz
	electron, p_t> 50 GeV	20-100 Hz	e + μ, p_t' , p_t'' >50 GeV	~1 Hz
2 jets + lepton	μ, p_t>40 GeV	200 Hz	+2 jets, p_t> 40 GeV	a few Hz
	electron, p_t>40 GeV	0.5-5 kHz	+2 jets, p_t> 40 GeV	300 Hz
Higgs				
leptons				
(int. mass)	2μ, p_t>20 GeV	25 Hz	third lepton	10 Hz
	2 electrons, p_t>20 GeV	0.1-1 kHz	third lepton	~100 Hz
(high mass)	2 μ, p_t>30 GeV	10 Hz		
	2 electrons, p_t>30 GeV	100 Hz	isolation/leakage cuts	10-30 Hz
2 jets, lepton, $\not{E}_T$	μ, p_t>100	10 Hz	+2 jets	a few Hz
	electron, p_t>100 GeV	100 Hz	+2 jets	a few Hz
SUSY				
$\not{E}_T$	3 jets, p_t>200 GeV	200 Hz	$\not{E}_T$>200 GeV	1-100 Hz
4 leptons + $\not{E}_T$	2 μ, p_t>30 GeV	10 Hz	+third lepton	a few Hz
	2 electrons, p_t>30 GeV	100 Hz	+ third lepton	a few Hz

Table 6: Examples of Physics Trigger Rates

• At the first level there is a large overlap between the various suggested prompt triggers. In fact five level 1 conditions would cover all the examples shown here; a charged lepton (electron

or μ) with p_t> 40 GeV, a lepton pair with p_t> 20 GeV and 3 Jets, all with p_t> 200 GeV would give adequate acceptance for the three searches considered here.

• The most critical prompt triggers are the ones requiring electrons. To obtain acceptable rates it seems imperative either to use relatively small cell sizes already at the first trigger level, or to achieve a rejection factor >5 from isolation and leakage criteria in the first level trigger.

• As a final caveat we remind the reader that the rates presented have been computed assuming sharp thresholds. In practice the trigger efficiency will rise from 0 to 1 over some finite $p_t$or $E_t$interval. To estimate how much thresholds need to be raised because of this one would need more precise information on the final detector configurations. Prompt muon triggers will be sensitive to this effect, some initial studies seem to indicate that thresholds would need to be raised by the order of 10-15 GeV to get the same rate as for an infinitely sharp threshold. Similar considerations apply to jet thresholds, which will be smeared by detector resolution. To estimate the effect here one will need definite assumptions on resolution and also pulse shaping times, to estimate effects of pile-up.

• Assuming that thresholds can be kept reasonably sharp it seems possible to provide prompt triggers with sufficient acceptance for physics giving level one output rates ~10 kHz. A more detailed study of threshold effects needs to be performed as soon as realistic parameters become available, in particular for muon triggers.

• Given these prompt rates it appears to be relatively straightforward to combine further trigger requirements beyond the simple cuts on inclusive rates to bring the rates down to a few hundred Hertz.

• At the level of these combined triggers the largest expected rates are again coming from the electron triggers. Another trigger which might prove marginal is the "SUSY" trigger based on jets and $\not\!\!E_T$. Clearly such a trigger is very sensitive to instrumental effects, creating large $\not\!\!E_T$ values. In addition the rate estimates for multijets are sensitive to both structure functions at low x, and to assumptions in the Monte Carlo programs on fragmentation effects.

References

[1] A.Nisati, Muon Rates at the LHC, these proceedings.

[2] M. Della Negra, Muon trigger and identification, these proceedings.

[3] H. Fesefeldt, Punch Through Simulations, these proceedings.

[4] N.Ellis, Communication to study group on experimentation at LHC.

[5] J.P.Repellin These proceedings

[6] D.Froidevaux, private communication.

[7] T.Sjöstrand, Communication to study group on experimentation at LHC.

[8] P.T.Cox et al., Jets at the Large Hadron Collider, these proceedings.

[9] H.Kuijf, Multiparton Production at Hadron Colliders. Ph.D. Thesis, university of Leiden, the Netherlands. Unpublished.

[10] P Sphicas, Communication to study group on experimentation at LHC.

[11] G Unal, Communication to study group on experimentation at LHC.

[12] D Froidevaux, Communication to study group on experimentation at LHC.

[13] C.Albajar et al. Experimental Aspects of SUSY Searches at the LHC, these proceedings.

A Digital Solution to First Level Triggering using Calorimetry at the LHC

N. Ellis and J. Garvey
University of Birmingham, UK

1. Introduction

One of the most challenging problems for experiments at the LHC is to make sophisticated selections using calorimeter information which are fast enough to be used as a first level trigger. One would like to be able to trigger on high transverse-momentum (p_T) electrons (or photons), jets and large missing transverse energy. The possibility of demanding, in addition, that the electrons be isolated is desirable. We believe that a digital trigger processor offering all of these capabilities could be built for an experiment at the LHC. Using our experience from building digital first level calorimeter trigger processors for the UA1 experiment [1], and exploiting recent developments in custom VLSI chip design, we have initiated a programme of research and development for experiments at the LHC.

We believe that digital trigger processors offer many advantages compared to triggers based on analogue sums and discriminators. The algorithms which a digital processor can evaluate may be quite complex and, after the initial digitization has been made, no precision need be lost. It is these powerful features that allow one to make isolation requirements on electromagnetic clusters and to do a full missing transverse energy calculation. A high degree of flexibility can be built into the system through programmable thresholds and control words. The calibration is easy to apply using look-up tables to convert from raw ADC counts to transverse energy (in addition to applying pedestal, gain and geometry factors, one has the possibility to correct for any non linearity). Finally, monitoring is straightforward since the hardwired trigger algorithm can be exactly reproduced by software simulation.

2. Trigger Requirements for the LHC

The requirements of a trigger for the LHC are very severe as discussed in Ref. [2]. The interval between beam crossings is only 15ns and the trigger must be able to analyse new events with this period. In order to limit the size of pipeline memories used to store data from all the detector channels during first level trigger processing, the trigger must be as fast as possible. A decision time (latency) of ~1μs is generally assumed for the first level trigger. Triggers much faster than this are ruled out by the long cable delays required to gather together trigger information from the whole detector in a single place and to distribute the trigger decision to the front end electronics – for a typical LHC detector the cable delays will be at least ~0.4μs.

While the rate at which the trigger must handle events is extremely high and the latency is short, the trigger must be very selective. At the anticipated luminosities of $>10^{34}$ $cm^{-2}s^{-1}$, the total interaction rate will be ~10^9 Hz, corresponding to more than ten interactions every beam crossing (i.e. every event that the trigger analyses will contain many interactions). It is generally believed that the first level trigger rate should not exceed 10^4–10^5 Hz so that programmable devices can be used in the second level of triggering – hence, the trigger must not select more than about one interaction in 10^5.

The signatures of a wide range of physics channels which are of interest at the LHC and the backgrounds to these signatures have been studied in this workshop [3]. For electron triggers based on calorimeter clusters, the background rate, due to high-p_T jets, depends on the window size used to define the clusters. While calorimeters with very fine granularity (typically with a cell size in pseudorapidity–azimuth space of $\Delta\eta x\Delta\phi = 0.02x0.02$) are under consideration, our studies suggest that a coarser granularity of $\Delta\eta x\Delta\phi = 0.2x0.2$ with just one electromagnetic (EM) and one hadronic (HAD) sampling will be sufficient for the first level trigger.

3. Architecture of a Digital Trigger

A block diagram of the architecture of a digital trigger processor is shown in Fig. 1a. One makes an analogue sum of a small number of calorimeter channels before digitizing using a fast ADC; the analogue sum is required to match the fine granularity of the calorimeter to the coarser granularity used by the trigger. Since the EM and HAD parts are digitized separately, any calibration differences between the calorimeters can be corrected; this may be important for the resolution of jet and missing transverse energy triggers.

Having digitized signals from the detector, a look-up table is used to convert to transverse energy units. This is shown in more detail in Fig. 1b, where the latches shown after the ADC and after the look-up table are memory registers which synchronize the flow of data. Every 15ns the data from a given beam crossing move downwards from one latch to the next under the control of synchronization (clock) signals – this is called pipelined processing. Thus, the digital transverse energy value is available 30ns after the signal was presented to the ADC. Note that flash ADCs operating at 100MHz (for 8-bits) and RAMs with 15ns access times are standard items.

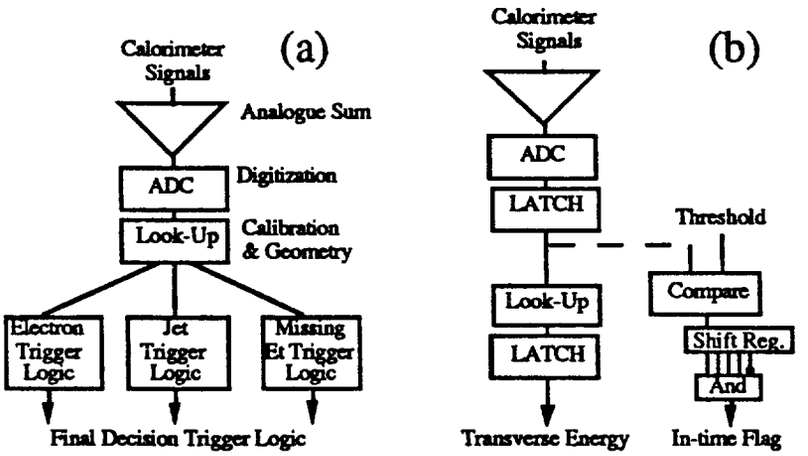


Fig. 1 (a) Block diagram of a digital processor for a first level calorimeter trigger; (b) conversion from analogue signals to digital transverse energy values with (optional) bunch crossing identification logic.

It is worth noting that a more ambitious approach [4] is to fully digitize all channels from the calorimeter before the first level pipeline memory. If this were done, separate digitization for the first level trigger would be unnecessary and the trigger would use information from the detector calibrated channel by channel, using digital addition to form sums over areas corresponding to the granularity used by the first level trigger.

A complication which we anticipate is that the pulses coming from the calorimeter will be slow compared to the bunch crossing period of 15ns. We note that it is possible to include leading-edge timing analysis in our design by adding a digital comparator after the ADC as shown in Fig. 1b. The comparator threshold must be large enough to ensure that (pile-up) noise is very unlikely to fire the comparator, and low enough to ensure that for the large pulses of interest the signal level has already risen above the comparator threshold in the first 15ns. The history of the comparator output, retained in a shift register, is used to flag in-time pulses making use of the constant delay between the leading edge and the pulse maximum. In the example shown in Fig. 1b, a leading-edge to pulse-maximum delay of four beam crossings (60ns) is assumed.

The digital transverse energy values from the look-up tables are input to hardwired electronics which searches for small (isolated) clusters in the electromagnetic calorimeter (electrons), larger clusters in the electromagnetic plus hadronic calorimeters (jets), and calculates the missing transverse energy. While, in Fig. 1a, we have shown these as

independent entities, in practise it is more efficient to integrate them for the first stages of the calculation. In the following, we illustrate the trigger processor electronics using the electron trigger as an example. The jet trigger is simpler because no isolation calculation is needed – we envisage an algorithm based on overlapping sliding windows. The missing transverse energy calculation is implemented in a straightforward way with adder trees, using look-up tables to obtain the components of the energy vectors before addition.

The logic for the electron trigger is shown as a block diagram in Fig. 2; in Fig. 3 we show in more detail part of the logic. For each EM trigger cell the algorithm forms two sums; a vertical sum where the cell is added to the adjacent cell above it (ϕ), and a horizontal sum where the cell is added to the adjacent cell to its right (η). Each of the sums of adjacent cells is compared to a threshold. The summation of pairs of cells is necessary in order to have good efficiency for electrons where the shower traversed a cell boundary. The sums are made separately in η and in ϕ so that the area over which the sum is made is still small compared to the typical jet size thereby minimizing the background rate. Isolation is defined by considering a 4-by-4 area in the EM calorimeter and the corresponding area in the HAD calorimeter behind it. The transverse energy is summed in this 4-by-4 area (EM+HAD), excluding the central 2-by-2 area in the electromagnetic calorimeter containing the electron candidate. (The coordinates shown in Fig. 3 refer to the location of the trigger cell on the 4-by-4 grid as shown.) Our simulation studies suggest that this definition of isolation has good efficiency for isolated electrons while giving a large rejection against the background from jets.

Note that the all electronics which is illustrated in Fig. 2 is repeated for every electromagnetic trigger channel (~1000 channels). Such a block of electronics would probably be implemented on only one or two custom chips – this has advantages in terms of speed, density of logic and also cost! In Fig. 3, only one operation (add, subtract, compare, etc.) is done in each 15ns step. This speed is achievable using existing CMOS technology; it might be possible to do more per step by the time a processor for LHC had to be built.

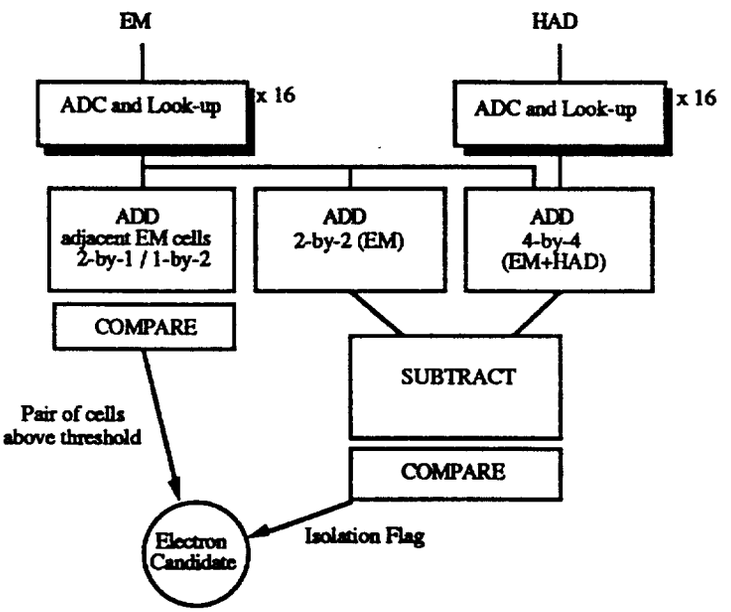


Fig. 2 Block diagram of electron trigger.

4. Feasibility

Simple calculations based on counting the number of pipeline steps give a calculation time (excluding cable delays and signal shaping time) of less than 400ns which is acceptable for LHC experiments. As mentioned above, the electron logic would be implemented on one or two custom chips, and existing CMOS circuits have the required speed. It is worth noting that

recent technological advances make custom chip design much more accessible to us than a few years ago and that the cost is now quite affordable.

Until one knows more about the calorimeters, it is not possible to decide where the trigger electronics should be located (on or off the detector). This issue has implications for permissible power dissipation and radiation hardness. Also of crucial importance is the routing of cables – even with care, the cable delays will be comparable with the trigger processor decision time! One must also address the problem of how to synchronize a pipelined processor distributed over a large area. This is a rather general issue since the pipeline memories used to store data during the first level trigger processing must also be synchronized.

It should be made clear that we are not presenting a detailed design – the optimal implementation will look different to the one we have presented here even if it has the same functionality. We also point out that the design could be extended to include information from other detectors (e.g. a preshower detector) provided the data are available sufficiently early.

In conclusion, our initial studies of digital processors for a first level calorimeter trigger at the LHC look encouraging and we are pursuing our programme of research and development.

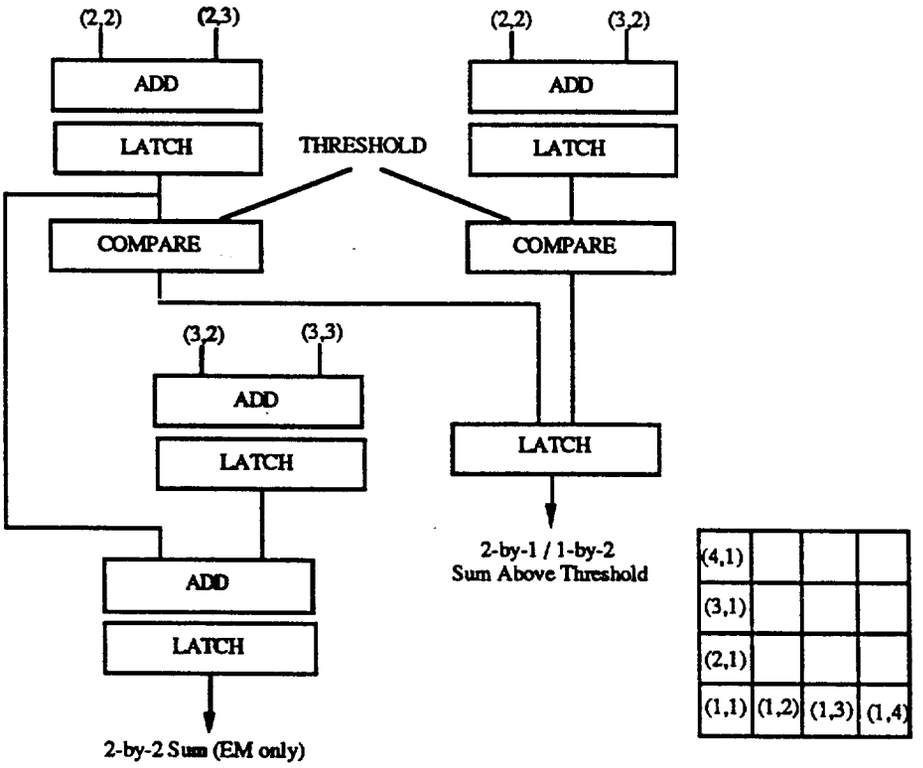


Fig. 3 Example of logic for pipelined processing. Adjacent pairs of EM cells are added in η and in ϕ and the sums are compared with a threshold; a sum is also made over a 2-by-2 area in the EM calorimeter for subsequent use in the isolation calculation. The logic shown contains two pipeline steps, corresponding to a delay of 30ns.

References

[1] N. Bains et al., Nucl. Instrum. Methods A292 (1990) 401.
[2] N. Ellis, S. Cittolin, L. Mapelli and P. Sharp, "Signal processing, triggering and data acquisition", presented at this workshop.
[3] S. Hellman, "Trigger rates at LHC", presented at this workshop.
[4] G. Goggi and B. Lofstedt, "Digital front end for calorimeters at LHC", presented at this workshop.

We would like to acknowledge useful discussions with the following people: P. Sharp, M. French, B. Lofstedt and P. Jovanovic.

STUDY OF ANALOG FRONT-END ELECTRONICS FOR SUPERCOLLIDER EXPERIMENTS

Francis Anghinolfi, Paul Aspell, Michael Campbell, Erik Heijne, Pierre Jarron and Gerrit Meddeler
CERN, CH-1211 Geneva 23, Switzerland

ABSTRACT

The potential of new analog signal processing techniques and readout approaches made in monolithic circuits for front-end electronics at LHC experiments are presented. The optimisation of the preamplifier with the detector characteristics is discussed. Experimental results of analog memory and signal processing VLSI circuits are presented: a fast current amplifier, a current sampling integrator and an analog pipeline. The signal peaking time for low capacitance detector elements is less than 15 ns, the sampling rate of the pipeline element in the 1.5 μm CMOS technology reaches 66 Mhz for at least 10 bits precision. An advanced readout architecture, based on this approach, with sparse data scan and on-chip ADC is presented.

1. INTRODUCTION

The large number of detector elements producing a vast quantity of data at the high interaction rate expected in the LHC experiments will require a new approach to detector readout architecture. Advanced signal processing techniques will play an important role in the implementation of these architectures. The Italian-funded CERN–LAA R & D project was specifically conceived to initiate efforts on such new basic architiectures.

Figure 1 represents the detector readout system of a conventional particle physics experiment. Usually, analog signals from the detector element are amplified and transmitted via cable to a remote electronic DAQ system located in the "counting room". Such a scheme could be difficult to apply in the LHC experiments because of the large volume of cables required. With advances in technology, it appears that the power dissipation in the analog line drivers at the required bandwidth would be comparable to the power needed for local ADCs. An obvious alternative is then to install flash ADCs inside the experiment and to transmit digital data to the DAQ system, as shown in fig. 2. For digital data transmission one could use high speed optical fibre links, which are very compact but would still require high power drivers. Added to the power dissipation of the ADCs this would result in the need for an efficient cooling system at the detector.

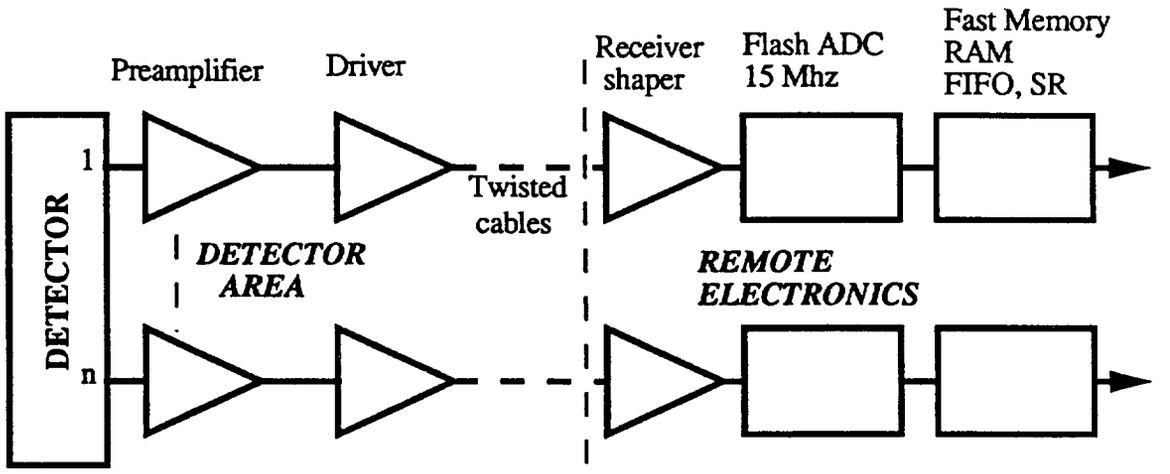


Fig. 1 Conventional detector readout via analog signal transmission using cable. Often, the cable acts also as signal delay element.

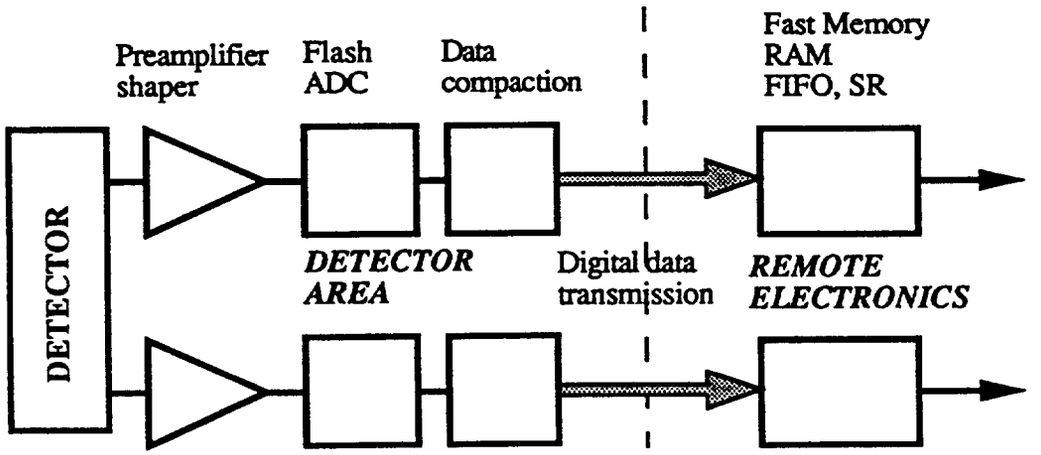


Fig. 2 "Brute force" method consisting in digitization of all signals inside the detector, and transmission of compacted digital data. The delay function is achieved after digitizer in the digital memory in the remote electronics area.

Application Specific Integrated Circuits (ASICs) designed in full custom offer the possibility of considerably increasing the complexity and the local intelligence of the front end electronics, thus significantly reducing the amount of data to be transmitted and the power dissipation of the electronics in the experiment. Based on this approach, we have developed a new readout concept, named "Hierarchical Analog Readout Pipeline Processor" (HARP) which is shown in fig. 3. Under this scheme, analog information is stored locally until a trigger decision enables the readout system to digitize only the analog signals which belong to the triggered sampling time.

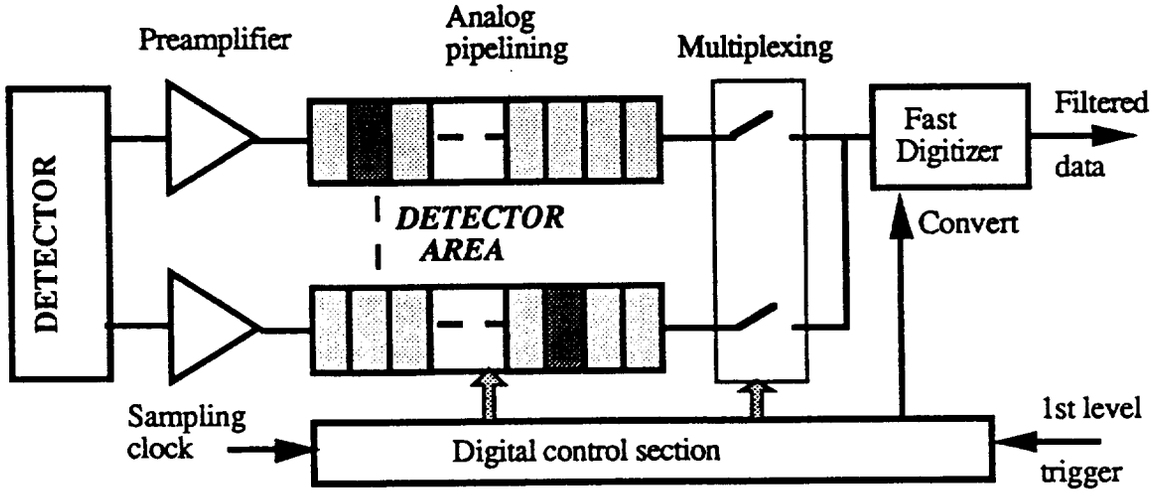


Fig. 3 New approach uses analog pipeline inside the detector as signal delay element. Only data selected in this first level trigger are digitized, also inside the detector, and the data filtered by level 1 trigger are transmitted in digital form to the remote electronics area.

This paper describes in detail our efforts on the various circuits needed in the HARP scheme. Section 2 discusses preamplifier optimisation and a fast amplification technique using the current conveyor principle is explained; preliminary experimental results on a chip fabricated in 1.5 µm CMOS technology(*) are presented. The analog pipeline storage technique is described in section 3 and experimental results of the analog pipeline circuit SAPE

(*) Mietec N.V. Oudenaarde, Belgium.

(Simultaneous write/read Analog Pipeline Element) fabricated in a 1.5 μm CMOS process are presented in section 4. An important new feature of this device can be the absence of dead time usually occuring in a readout cycle. Section 5 discusses the complete HARP implementation comprising preamplification, analog pipeline, sparse data scan and digitization.

2. THE PREAMPLIFIER

2.1 Detector characteristics and signal preamplification technique

The ultimate speed limitation of the detector readout is determined by the transfer time of the signal charge on the detector to the preamplifier. For detectors with a short collection time (e.g. silicon detectors and scintillating fibres), the acquisition time of the analog signal can be as short as one or two bunch intervals of the LHC (15-30ns).

For detectors with a longer collection time (e.g. cold or warm liquids in calorimeters), only a fraction of the detector charge can be measured in one or two LHC bunch intervals. Consequently, signal pile-up might occur at sensors of this kind of detector. Moreover, multiple events per bunch crossing and high channel occupancy will add considerably to the intrinsic detector pile-up. Pile-up will further occur in the charge sensitive preamplifier which is traditionnally used. One approach to solve this problem is the use of a pulse shaper with bipolar or tripolar characteristics after the charge amplifier, in order to obtain a signal baseline at zero [1]. The pile-up in the charge preamplifier can be avoided by using a current preamplifier as shown in fig. 4, followed by a monopolar or a bipolar pulse shaper. This circuit avoids the pile-up effect of the charge amplifier and thus, only the detector pile-up must be dealt with.

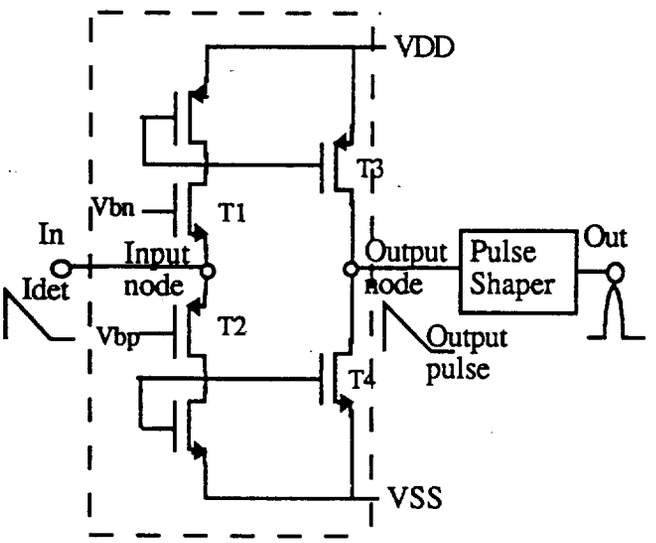


Fig. 4 Analog front end channel employing a CMOS current sensitive amplifier based on the current conveyor technique. The input MOS transistors T1 and T2 are matched for equal transconductance (g_m) and are in the common gate configuration to obtain a low input resistance of $1/2g_m$. Transistors T3 and T4 are in common source configuration with a high output resistance and a low output capacitance. The detector current is copied from the low impedance input node to the high impedance output node.

To investigate this approach, we have designed a current sensitive amplifier using the current conveyor principle. A test chip has been fabricated in 1.5 μm CMOS. Preliminary experimental results are given in table 1 and the waveform of the output signal is shown in fig. 5. This amplifier circuit has been designed to keep a signal peaking time compatible with LHC event rate of 15 ns for a detector capacitance of less than 50 pF. Nevertheless, this circuit design approach could be adapted to a larger detector capacitance at the expense of an increase in the power consumption.

most important design criteria .Therefore, each kind of detector needs a dedicated design in order to obtain a good overall optimisation of the analog front end. The ASIC approach offers the opportunity to achieve this goal, provided that in the coming years radiation hard VLSI technologies are made available to cope with the high level of radiation expected in the high luminosity collider environment [2, 3].

Signal peaking time	8 ns
Noise ENC @ Cin=10pF	2000 r.m.s. e
Noise slope	50 e/pF
Gain	770mV/pC
Input impedance	100 ohm
Dynamic range	± 2 V
Power consumption	1.5 mW

Table 1
Experimental results of the current sensitive amplifier based on the current conveyor principle.

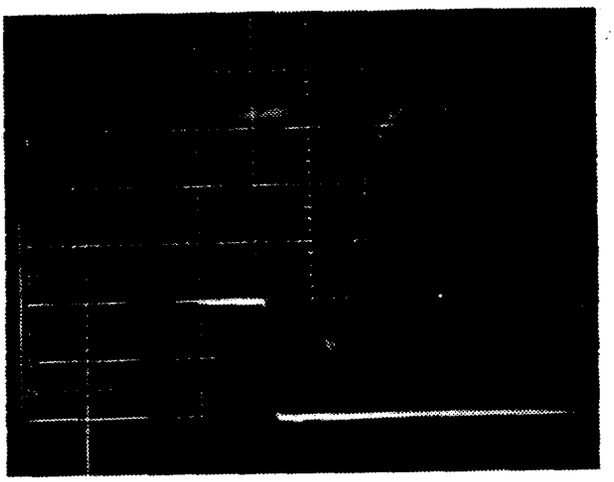


Fig. 5 Output response of the current amplifier circuit fabricated in a 1.5 µm CMOS technology. The lower trace represents the input step voltage of 10 mV applied to the input the current amplifier via a test capacitor of 1.8 pF. The upper trace is the output response of the current amplifier. The horizontal scale is 20 ns/division and the vertical scale is 5 mV/division.

2.2 Preamplifier optimisation and power dissipation

The trade-off between speed, noise, and power, at a given detector capacitance C_{det}, is the crucial point in the preamplifier design for detectors located in the inner collider region (vertex, tracker, preshower detector) because of the lack of available space for efficient cooling. The transconductance g_m of the input transistor biased at the current I_b ideally obtained in a bipolar input transistor is expressed by

$$g_m = qI_b/kT \quad . \tag{1}$$

The minimum of power P_{dmin} is then

$$P_{dmin} = U_b\, g_m\, kT/q \quad , \tag{2}$$

where U_b is the supply voltage, k is the Boltzman constant, T is the absolute temperature and q is the electron charge. The minimum Equivalent Noise Charge (ENC_{min}) achievable for triangular pulse shaping with peaking time t_M can be expressed [4] by

where U_b is the supply voltage, k is the Boltzman constant, T is the absolute temperature and q is the electron charge. The minimum Equivalent Noise Charge (ENC_{min}) achievable for triangular pulse shaping with peaking time t_M can be expressed [4] by

$$ENC^2_{min} = 2\,k\,T\,C_{det}^2/(g_m\,t_M)\ . \qquad (3)$$

Thus, eqs (1), (2) and (3) determine the minimum power necessary in the preamplifier to obtain the desired speed and noise performances for a given detector capacitance. For instance with C_{det} = 10 pF, t_M = 15 ns, and ENC = 1400 rms e, the transconductance g_m must be 1 mA/V. This gives a power consumption of the input transistor branch of 250 μW. This result is the best possible figure and it is valid for any kind of transistor technology and feature size: junction FET, gallium arsenide FET, CMOS and bipolar on silicon.

2.3 Detector segmentation

In most particle physics experiments the detector segmentation is determined by practical considerations of the detector construction and by the physics requirements. Nevertheless, it is useful also to take into account the consequence of detector segmentation on the optimisation of the monolithic preamplifier.

For a total detector capacitance C'_{det} segmented in n elements of capacitance C'_{det}/n, the preamplifier geometry and current biasing can be scaled down by the same segmentation factor n. The resulting impact on the preamplifier performance has been studied, e.g. by Krummenacher [5]. For constant preamplifier speed and density of power dissipation, the effect of the scaling is:

- an increase by a factor n of the DC voltage amplification A,
- a decrease of the noise (ENC) by a factor $\sqrt{n}$.

Therefore, higher detector segmentation yields higher sensitivity and lower noise of the preamplifier. But it increases the number of channels and the complexity of the readout system. Consequently, the detector segmentation should be taken into account for the preamplifier performance and the system complexity.

3 ANALOG STORAGE

Charge Coupled Devices (CCDs) are well known analog signal processing elements [6]. Their precision is usually limited to about 8 bits, which may not be sufficient for many applications in physics experiments. Data stored on a CCD can in general be read serially, when the transferred charge reaches the end of the pipeline, and it is difficult to make a radiation hard CCD.

The switched capacitor technique offers the possibility of storing analog signals on good quality capacitors without transfering charge. The advantage is that analog signals stay in place on the storage capacitors whilst the memory addressing is done by read and write pointers driven by digital shift registers. Using this technique analog signals can be stored with 11 or 12 bit precision [7, 8] and data can be randomly accessed through addresses or pointers.

3.1 Simultaneous read and write operation

Signals from detector elements, after amplification if necessary, are passed into a switched-capacitor analog pipeline memory which allows storage for the time T1 needed to build the first level trigger decision. The memory can be organised in such a way that reading and writing can be performed simultaneously, thus eliminating system dead time.

The principle is illustrated in fig. 6 for a matrix of memory cells. The write and read operations use separate addressing registers, bus lines, switches and amplifiers. The delay time

T1 between write and read can be adjusted to the latency of the level 1 trigger. This delay ensures that a memory location cannot be addressed in write and read at the same time. A simplified circuit scheme of the addressing of the memory cells is shown in fig. 7 for a 3 cell array. Each cell consists of a capacitor C_S, a write switch and a read switch. The write shift register WSR addresses the write switch defining the cell to be charged while the read shift register defines the cell to be read out. Both operations can be carried out within the same clock cycle.

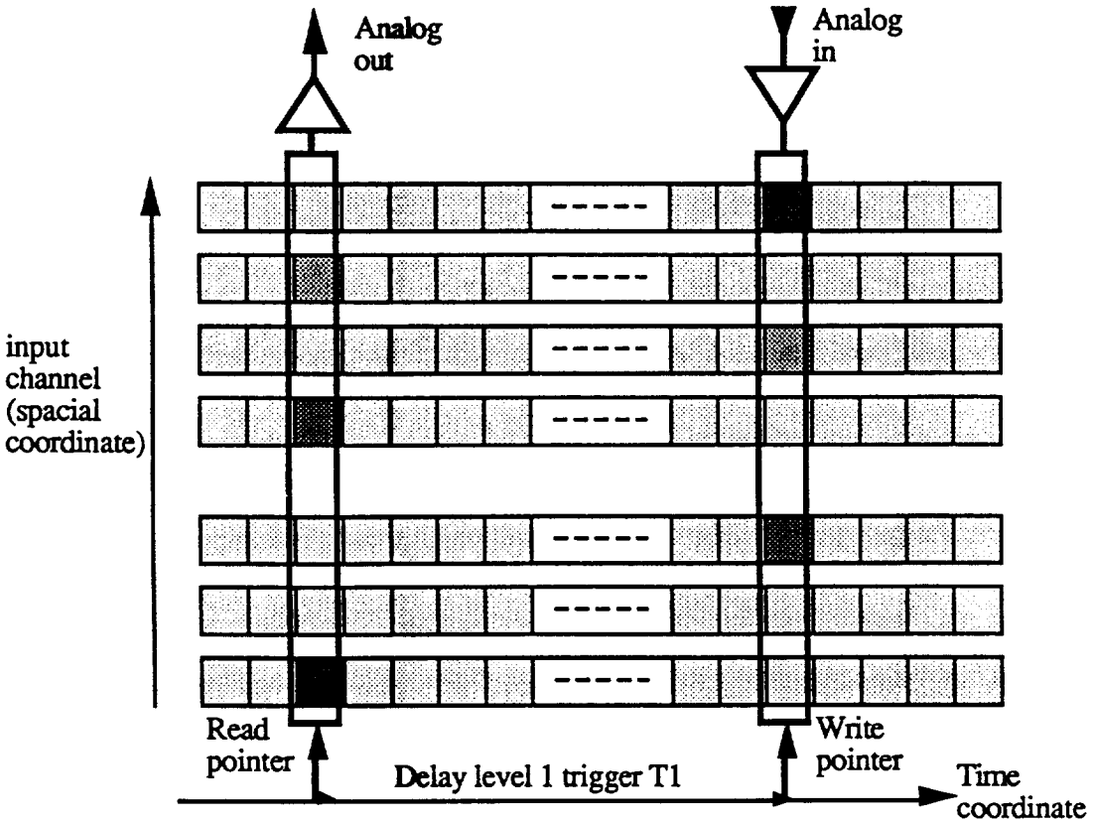


Fig. 6 Matrix of analog signal storage cells. Each row contains the consecutive data from a single detector element. The signal of the present event is being written in the column of cells indicated by the write pointer. At the same time data from an event, loaded T1 seconds ago, indicated by the read pointer, can be read out if selected by the trigger.

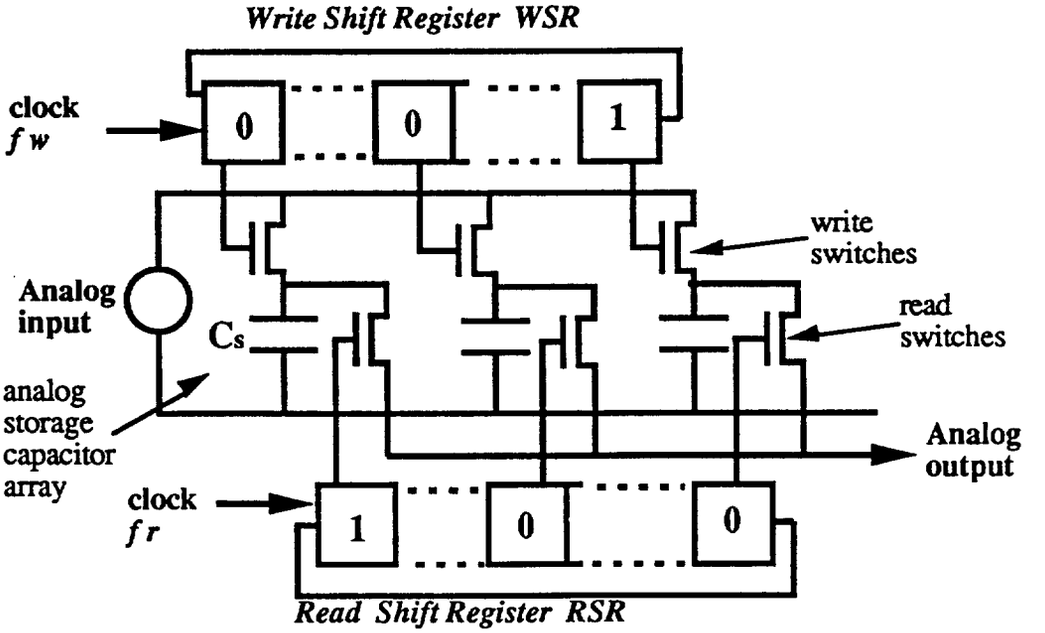


Fig. 7 Schematic of the a circuit which allows to write and read simultaneously in different storage capacitors.

3.2 Voltage sampling and charge sampling technique

The input to the analog memory can be configured as either a voltage sampler or a current integrating sampler. These configurations are illustrated in figs 8 and 9 for a 3 capacitor array. The voltage sampling technique of fig. 8 is the most widely used. The write amplifier W_{amp} in the voltage follower configuration simply stores the instantaneous input voltage on capacitor C_{s1} while the write switch is closed. In this example C_{sn} is simutaneously read by the amplifier R_{amp}, and C_{si} is disconnected.

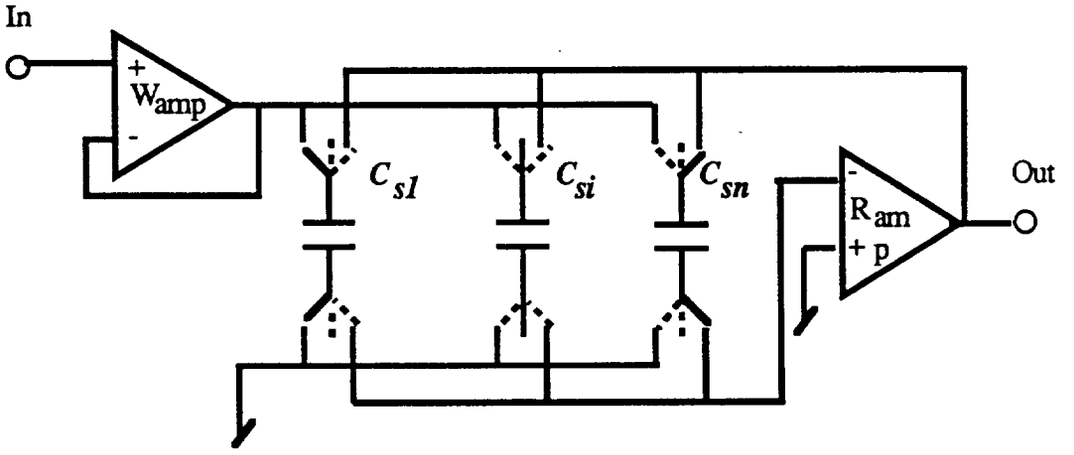


Fig. 8 Voltage sampling input circuit

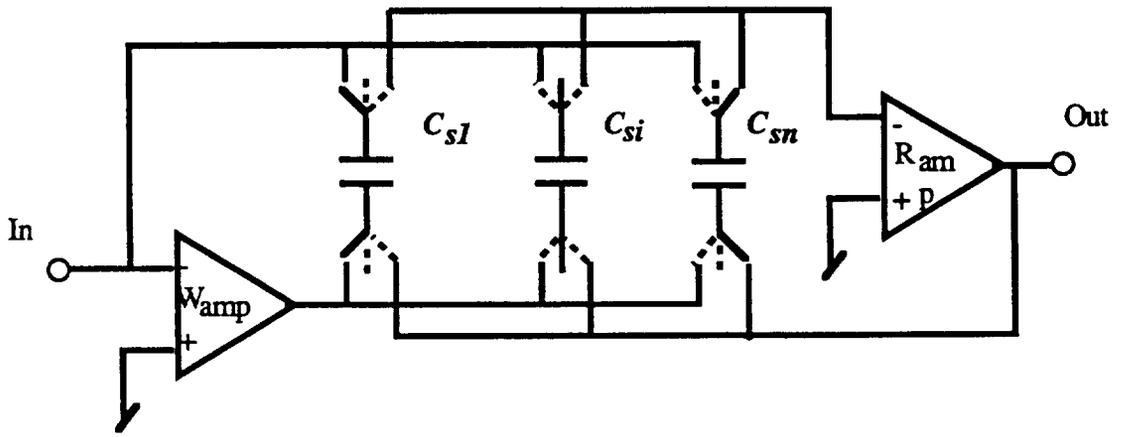


Fig. 9 Current sampling input circuit.

The current integrating configuration of fig. 9 uses memory capacitor C_{si} as a feedback capacitor of the write amplifier W_{amp} so that this circuit operates like a traditional charge amplifier. The resulting voltage on the capacitor is proportional to the integral of the input signal current from the detector during the sampling interval. We call this circuit configuration the Current Sampling Integrator (CSI).

In particle physics detector applications, the CSI configuration has several advantages over the voltage sampling technique, mainly because the charge is the relevant information of most particle detectors based on ionization. In LHC the detector signal may spread over several clock periods of 15 ns. Assuming there is no pile-up, the simple sum over several cycles would yield the detector charge. To obtain this using voltage sampling with a low number of samples requires a knowledge of the pulse shape. Moreover, for a 10 ns pulse width, the analog pulse shape may well be sensitive to local variations. The detector geometry may lead to different input capacitances, and the charge collection speed may vary, e.g. after radiation damage.

The current sampling integrator has the sensitivity of the charge amplifier, thus it may turn out to be superfluous to have a preamplifier between detector and analog pipeline circuit. Also, the CSI circuit acts as a gated integrator equivalent to a time variant filter on each sampling period, followed by a time invariant filter consisting of the transfer function of the write amplifier. In principle, no further analog signal processing should be needed to enhance the signal to noise ratio.

In order to reduce clock feedthrough effects identical write and read switches are placed symmetrically on the two nodes of the storage capacitor as illustrated in fig. 10. The Analog Memory Element (AME) is completed by a reset switch which discharges the capacitor C_S after reading, when all other switches around the capacitor are turned off. The injected charge is then equally distributed to both capacitor nodes.

The total Equivalent Noise Charge (ENC) of the CSI circuit is expected to have three dominant noise contributions. First the ENC of the gated integrator W_{amp} can be calculated following the approach of Radeka for signal filtering for Ge detectors [9]. Second is the kT/C noise caused by the reset switch, which is 64 μV for C_S = 1pF. The third contribution is the noise voltage of the read amplifier. Further analysis is expected to show that the gated integration is the dominant noise contribution, at least in the ideal case.

One limitation of the CSI circuit is the mismatch between capacitors in a single pipeline channel which may cause a gain spread. If double polysilicon capacitors are used, the spread may be limited to 0.5–1%. If a higher precision gain is needed the voltage sampling configuration may be more appropriate.

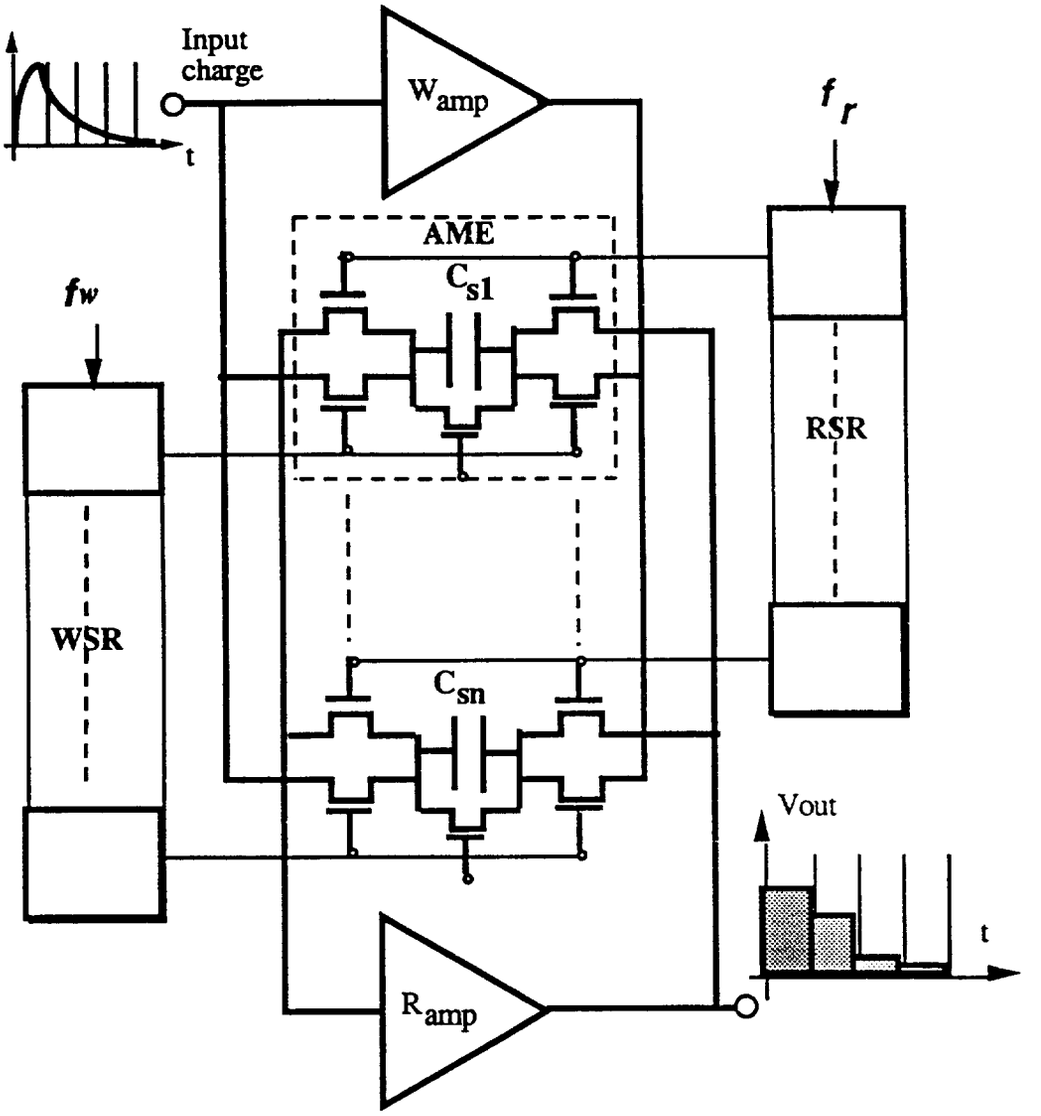


Fig. 10 Schematic diagram of the analog memory elements (AME) in the current sampling integrator circuit. The symmetric write and read switches are actuated by their respective shift registers WSR and RSR.

4. EXPERIMENTAL ANALOG PIPELINE CIRCUIT

A double pipeline prototype, called SAPE,with four channels has been designed using a 3 μm n-well CMOS technology with double polysilicon. A description and experimental results are reported elsewere [10]. The sampling speed reached 20 Mhz which is not sufficient for the event rate expected at the LHC. The speed limitation came from the logic controlling the transfers of data between the first and the second analog pipeline elements. Therefore, we have developed a single pipeline simultaneous read/write circuit in the MIETEC N.V. 1.5 μm double polysilicon, double metal process. The block diagram in fig. 11 shows the pipeline structure with 64 memory cells. The chip photograph is shown in fig. 12.

The circuit consists of 4 parallel channels with 2 voltage samplings and 2 CSI inputs. The write and read amplifiers, using differential folded cascode OTAs, are designed with p-channel transistors at the input and n-channel as the cascode devices to obtain settling time less than 10 ns. Unity gain bandwidth is 220 Mhz with 0.8 pF load. Power consumption is 5 mW. The value of the storage capacitor of 0.4 pF is a trade off between accuracy and noise on one hand and the speed and silicon area on the other hand. The shift registers WSR and RSR act as

to the storage capacitors to be written or read. The size of each AME cell is 100 μm × 38 μm. The total length of each channel is 3150 μm.

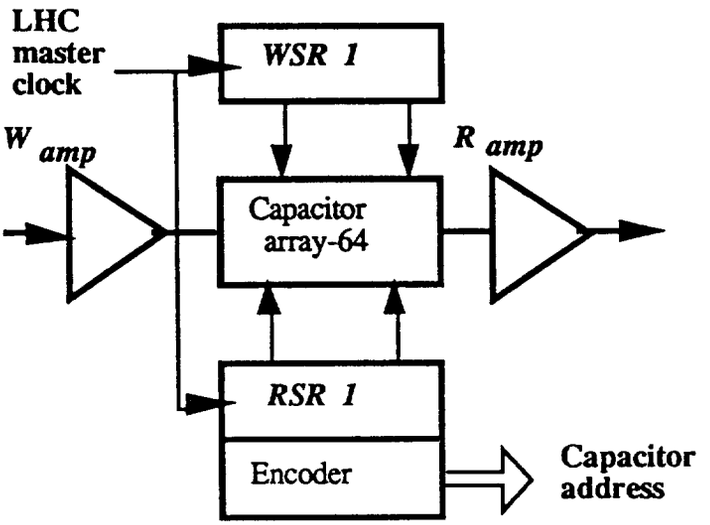


Fig. 11 Block diagram of the SAPE circuit.

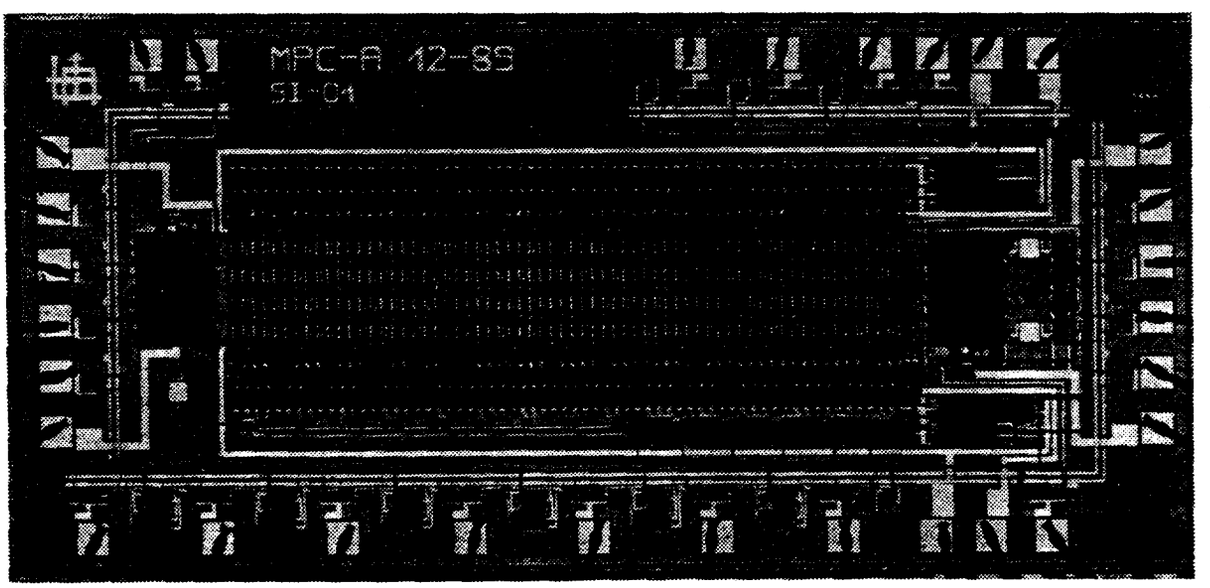


Fig. 12 Photograph of the SAPE chip. The dimensions are 4 mm × 2.5 mm.

The operation of the circuit as a waveform analyser is shown in figs 13 and 14. In these tests, the analog pipeline is firstly filled at a write frequency of 70 Mhz, and read out at a frequency of 1 Mhz. Figure 13 illustrates the response of the voltage sampling channel while fig. 14 shows the CSI output. The preliminary results suggest a precision of 11 bits. However, at present our measurement setup does not yet allow digital acquisition to fully characterize the precision.

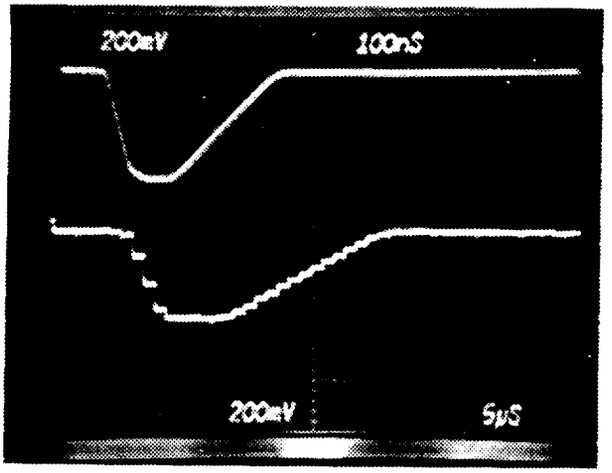


Fig. 13 Oscilloscope picture of the operation of the SAPE circuit as waveform recorder in voltage sampling mode. The input pulse (upper trace), is stored in the SAPE at the write frequency (sampling) of 67 Mhz and at a lower readout frequency is 1 Mhz (lower trace).

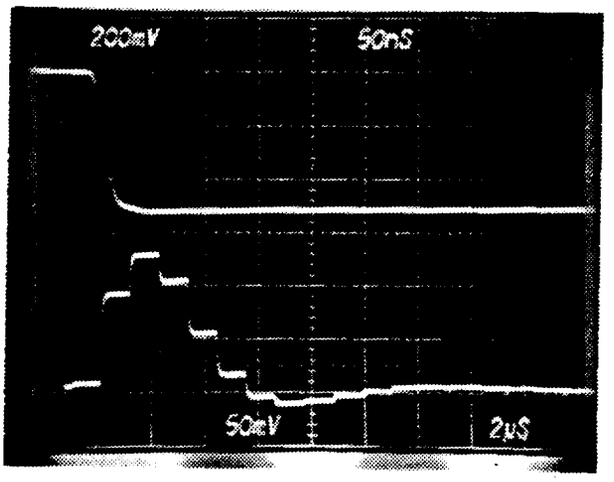


Fig. 14 Oscilloscope picture of the operation of the SAPE circuit as waveform recorder in current sampling integrator mode. The input step voltage (upper trace), injects a charge at the input of the circuit via a test capacitor of 4.8 pF. The input charge is sampled at 67 Mhz.The impulse response is readout at a frequency of 1 Mhz (lower trace). The sum of the samples read at the output is the image of the input charge. The waveform of the output response is determined by the write amplifier impulse response.

The sensitivity of the CSI circuit channel (fig. 15) is 2.29 mV/fC and the linearity extends from –0.7 pC to + 1 pC. A 2 MIP signal-equivalent in a Si detector, corresponding to a charge of 8 fC, is visible in one of the cells in fig. 16. This proves that the circuit can operate even without an external front-end amplifier. The pedestal distribution of the 64 memory elements is plotted in fig. 17. The mean value is –1.28 V and is related to the offset voltage of the source follower amplifier used to measure the output of the read amplifier. The variance of the pedestal non-uniformity is 2.4 mV and also the variance of the output signals for a single memory element is in this range (2.6 mV) with a sampling clock of 70 Mhz and a readout clock of 1 Mhz. At present we are studying which are the limiting factors and it would be premature to regard these fluctuations as being the noise performance of the circuit.

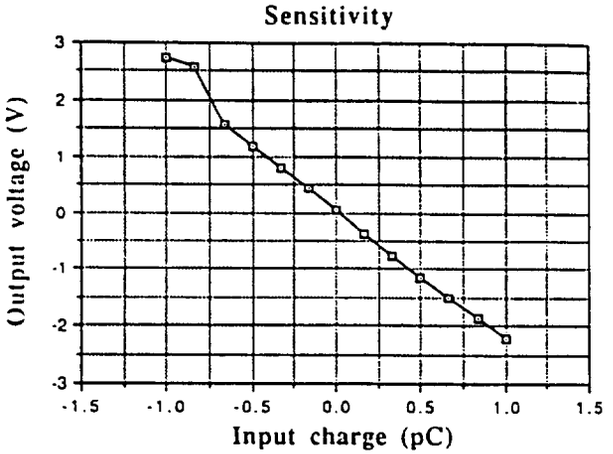


Fig. 15 Graph of the output voltage of SAPE as a function of the input charge, measured at 1 MHz.

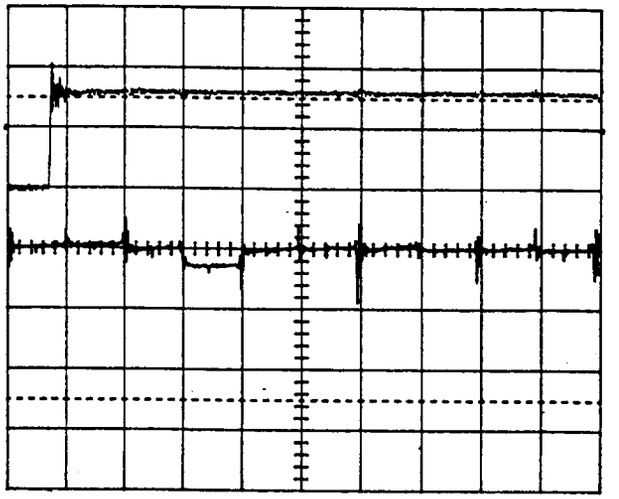


Fig. 16 Two graphs from a digital oscilloscope. The upper trace is the voltage signal injected via a 1.8 pF test capacitor to CSI input which is equivalent to a charge of 50 000 electrons. The output (lower trace) from the cells without signal remains stable, but the 4th cell shows the signal above the pedestal.

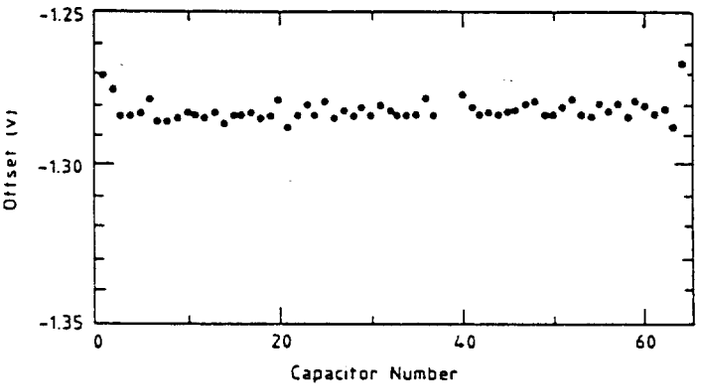


Fig. 17 Plot of the pedestal values of the 64 memory elements of SAPE, current sampling integrator channel.

5. PIPELINE ARCHITECTURE WITH SPARSE DATA SCAN

In the previous section an architecture was discussed which enables data reduction in the time domain using local analog storage and the information supplied by the level 1 trigger. Due to the very large number of channels operating in the high event rate conditions of the LHC, it is also useful to exclude from the readout the channels which did not receive any hit in a given triggered event.

Analog multiplexing of the channel outputs with zero suppression is proposed as an additional feature in the front-end chip [11]. This scheme can tremendously reduce the readout time and the amount of data by triggered event, if the channel occupancy is low ($\leq 1\%$).

In view of the Tracker /Preshower R & D development for the LHC [12] a readout architecture is shown in fig. 18. The principle is based on the HARP scheme with a sparse data scan feature which employs a data driven analog multiplexer. The multiplexing is obtained by using the digital information provided by a discriminator array by comparing analog signals from the preamplifier array outputs with a threshold voltage. The information from discriminators is then stored in a digital memory DRAM. The write and read operations in the digital memory use the same addressing signals as the analog memory. When the level 1 trigger selects one event to be read out (that is one column of the analog memory ADRAM), at the same time the corresponding column of the digital memory presets the hit pattern multiplexer.

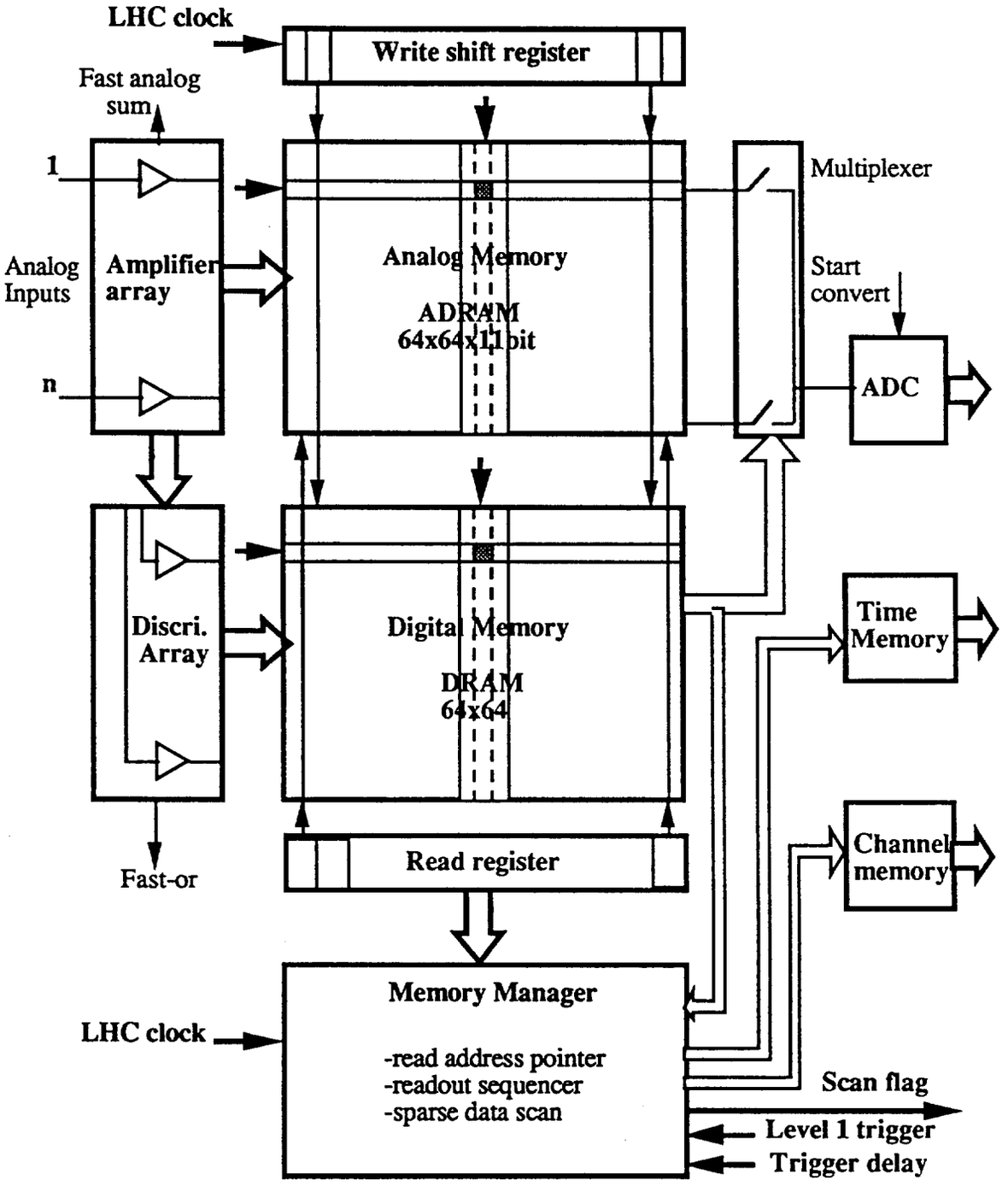


Fig. 18 Analog front end electronics with analog and digital local storage, multiplexing with sparse data scan and digitization.

Digitization is made with on-chip ADCs on only analog information which were selected both by level 1 trigger and the data driven multiplexer. Depending on the final readout architecture, multiplexed ADCs with sampling rate of 10 MHz or less could be sufficient. An experimental 1 MHz sampling rate ADC in 3 μm CMOS technology has already been developped and is reported elsewhere [13]. It operates with a very low power consumption of 12 mW by using a pipeline architecture.

The following information accompanies each digitized data during the readout:

- a "Time Memory" identifies the trigger event to which the digitized data belongs;
- an "Address Memory" is giving the channel address, and eventually the capacitor address for gain and pedestal equalisation.

6. CONCLUSIONS

The high event rate at the LHC requires the development of customised fast front-end electronics using radiation-hardened microelectronic technologies, such as Silicon On Insulator (SOI) or gallium arsenide. Vertex, tracker and preshower detectors, each with millions of detector elements, will need very compact, low-noise and low-power front-end electronics placed closed to the point of collision.

Preliminary results on the operation of functional building blocks for the HARP processor have been described. In particular, the SAPE building block made in 1.5 μm CMOS technology performs already very satisfactorily at 70 Mhz both in voltage sampling and in current sampling for a power consumption of less than 10 mW/channel. This shows promise for use at the LHC. The key features of this readout architecture are local analog storage, for level 1 filtering with simultaneous write and read operation without dead time.

The further development of the HARP architecture will bring discriminators and ADCs on chip. This readout system will perform amplification, analog delay, signal discrimination, time stamping, digitization and data compaction functions. This development will be serving various detector developments for use at the future LHC.

REFERENCES

[1] C.W. Fabjan, Signal processing for detectors at high luminosity hadron colliders, CERN–EP/90-85.

[2] G. Stevenson, New dose calculation for LHC, these proceedings.

[3] J.L. Leray, Silicon on insulator for ultra rad hard applications, these proceedings;
C. Terrier, ASIC in rad hard SOI process, these proceedings;
G. Durand, Rad hard IC's developed to satisfy LHC requirements, these proceedings;
T. Davies, The Marconi range of rad hard products in silicon on saphire, these proceedings;
N. Bingefors and T. Ekelöf, Radiation hard SOS, these proceedings.

[4] P. Jarron, Fast silicon detector systems for high luminosity hadron collider experiments, ECFA proceedings Barcelona, (1989) 287.

[5] F. Krummenacher, Pixel detector with local intelligence: an IC designer point of view, Pixel detector Workshop, Leuven (1990), to be published in NIM.

[6] H. Anders et al., Feasibility study for a charge coupled device (CCD) as a multiplexing signal processor for microstrip and other particle detectors, CERN/EF 85–10.

[7] K. Matsui et al., CMOS video filters using switched capacitor 14 Mhz circuits, IEEE journal of solid-state circuits, vol. sc–20, No 6, dec. 1985, 1096.

[8] J. Moschen et al., High-speed analog CMOS pipeline system, NIM A288 (1990) 180-186.

[9] V. Radeka, Trapezoidal filtering of signals from large germanium detectors at high rates, IEEE Trans. Nucl. Sci. NS–16 (1972).

[10] F. Anghinolfi et al., HARP: Hierarchical Analog Readout Processor with Analog Pipelining in CMOS, CERN ECP to be published.

[11] P. Seller, Vertex detector for the LHC, this proceedings.

[12] D. Munday et al., A proposal to study a Tracking/Preshower Detector for the LHC; CERN/DRDC/90–27; DRDC/P3.

[13] F. Anghinolfi et al., 1 MHz sampling rate low-power Analog-to-Digital Converter for data processing in particle detectors, to be published in Nuclear Physics B.

A FAST TRACKING LEVEL1 MUON TRIGGER FOR HIGH LUMINOSITY COLLIDERS USING RESISTIVE PLATE CHAMBERS

F. Ceradini, F. Cesaroni, F. Lacava, A. Nisati,
E. Petrolo, L. Sorrentino, S. Veneziano.
Istituto Nazionale di Fisica Nucleare e Uviversita' "La Sapienza" - Roma

presented by
Emilio Petrolo

ABSTRACT
A system for a fast LEVEL1 muon trigger for high luminosity colliders is presented. The system, based on the use of a fast detector, will be able to extract the T_0 bunch crossing machine. The electronic scheme of a possible implementation is also given.

1 INTRODUCTION

We propose to build a fast tracking muon trigger for high luminosity proton-proton colliders with momentum cut-off. The cut will depend on the magnetic configuration.

The trigger will provide the muon multiplicity, for each bunch crossig, within a delay off ~200 ns, including cables delays. It also will give informations on the direction of muon candidates, that can be provided very fast as input to other detectors.

The Resistive Plate Chambers (RPC) [1], that we plan to use as trigger detectors, have a time resolution shorter than the machine bunch crossing period. With RPC's is possible to cover easily very large areas, since they are chip and easy to build.

The geometry of the read-out electrodes on the detector plane can be adapted to different needs: pads, strips, rings, etc. In the following we assume a read-out with strips of width 1 cm $< \Delta x <$ 3 cm. The trigger is not synchronized and a track is recognized without the need of a beam crossing time gate.

Since the RPC, at the state of the art, don't give an adequate space resolution for precision measurement, we decided to separate the two functions of precision measurement ad fast triggering.

2 THE RESISTIVE PLATE CHAMBERS

The choice of the RPC was influenced by many factors. The most important factor is that they have a time resolution < 10 ns and they are easy to build and inexpensive. They also are robust (no wires inside them), and stables (no photomultipliers for their read-out). The electronic of the read-out is very simple and the power consumption is low because there is no need for preamplifiers .

The fig. 1 shows a double RPC chamber. There is a gas mixture (argon, freon and butane at normal pressure) beetwen two resistive plates separated by spacers. When a particle hits the chamber a discharge is generated in the gas under the action of an electric field of ~4kV/mm. The discharge produces an induced signal on the pick-up strip-line.

The charge collected from the strip is ~100 pC. The signal has a duration of 10 ns (FWHM) and a rise time of ~3 ns. The detection efficiency is 98%, limited by the dead area of the spacers beetwen the resistive plates.

The discharge in the gas is produced over an area of ~10 mm^2 that will remain inactive for ~1 ms: this impose a limit of 100 Hz/cm^2 on the maximum flux tolerated by the chamber.

3 THE TRIGGER

In the following example we assume a toroidal configuration in iron. The trigger is based on the detection of muon tracks through 3 layers of RPC chambers. The layers are separated by two meters of magnetized at 1.8 T iron (fig.2) .

The fig.4 shows the expected muon flux versus the angle respect to the beam direction, for an apparatus whose geometrical dimensions are showed in fig.3. We can see that the muon flux is larger than 100 Hz/mm^2 only in the forward region. The total muon rate is showed in fig.5 [4].

As already said, the detection of tracks is made by 3 layers of chambers. The basic principle of detection of a track is illustrated in fig.6. Each strip hit, on the first layer, opens a path of possible hits on the subsequent layers. The width of the path depends on the magnetic configuration and on the momentum cut-off. In the example, a "road" of 3 strips is opened, by each strip of the first layer, on the subsequent layer. If a track is found in the road a trigger signal is generated.

A possible way of implementation of this scheme is presented in fig.7. The switches A and B provide the momentum cut-off control. This scheme has the disadvantage that, due to the OR on the 2nd layer, we loose the information on where the track is passed in this layer; we only know that the track is passed in the "cone". As consequence, the path of the cone on the 3rd layer must be rather large. To avoid this problem the scheme of fig.8 can be used. In this scheme two small cones, one from layer1 to layer2 and one from layer2 to layer3 are opened. Adopting this scheme the gallim-arsenide gate-array must be larger.

Fig.9 shows the width of the cone on the 2nd layer, versus the coordinate (vertex of the cone) of the strip on the 1st layer, for 3 cm pitch strip. Fig.10 shows the width of the cone on the 3rd layer, versus the coordinate of the strip on the 2nd layer for the same pitch strip. The plot takes into account the bending of the tracks due to the multiple scattering in the iron and the width of the interaction region. The cut on P_T is fixed at 20 GeV/c.

4 THE TRIGGER

As said the detection of a track is made by means of two GaAs gate-arrays each on a chamber layer. Since the gate delay of a GaAs chip is very short (~100 ps) [6] , we can assume that the time needed for the detection of a track on one layer is zero. Under this conditions the timing of the system is presented in fig.11. From this figure we can see that the signal coming from the layer2 reaches the layer3 in coincidence with the particle. This means that the track is recognized in "real-time" mode and no pipeline is needed at the level of the chambers.

The timing of fig.11 does not take into account the different propagation delays of the signals on the strip. The equalization if this delay is the most critical part of the system. If necessary, to mantain the coincidence beetwen the arrival of the particle and the arrival of the signal from the previous layers, the duration of the signal can be made larger (max 12-14 ns since the beam crossing period is 16 ns) or the strip can be made shorter (1.6 m - 1.8 m).

The information from the different sectors of the apparatus are sent to the Main Control Logic, that will process the whole event (fig.12 and fig.13). Note that the synchronization with the beam crossing comes only at the end.

5 CONCLUSIONS

Using RPC it seems to be possible to build a LEVEL1 muon trigger for high luminosity p-p colliders, able to extract the T_0 machine crossing. The system, implemented with the use of ultra-fast electronic technologies, will give an answer for each beam crossing in ~200 ns.

REFERENCES

[1] R.Santonico, R.Cardarelli, NIM 187,377,1981.
[2] R. Cardarelli et al., NIM A263, 20, 1988.
[3] M.Bertino et al., NIM A283, 654, 1989.
[4] A.Nisati, "Muon Rates at LHC", proceedings of this workshop.
[5] A.J.Lankford, "Issues fo Trigger Processing at High Luminosity Colliders", proceedings of the ECFA Study Week, Barcelona 14-21 september 1989.
[6] GBL, GaAs IC Data Book & Designer's Guide. B

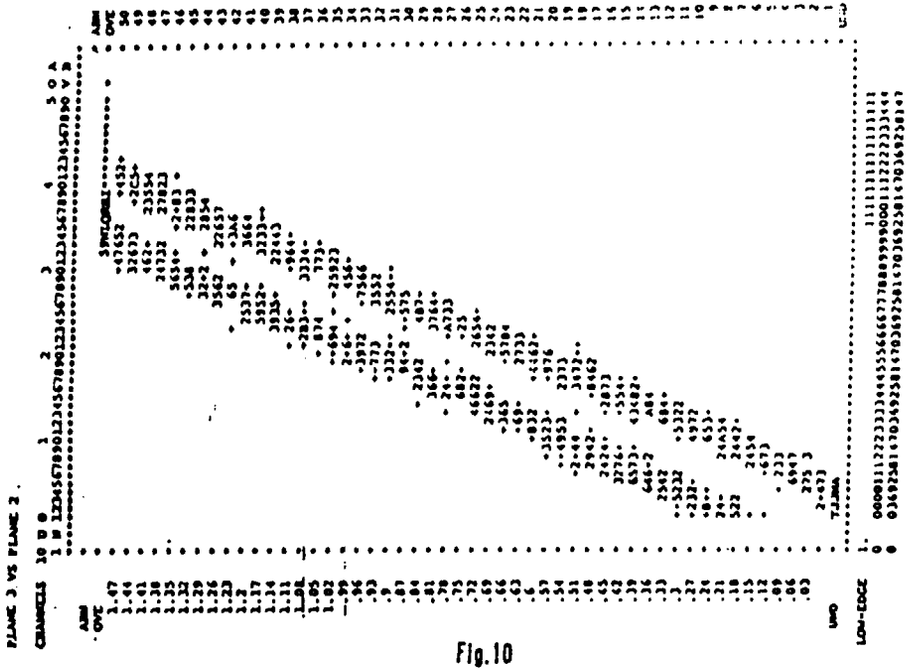


Fig.10

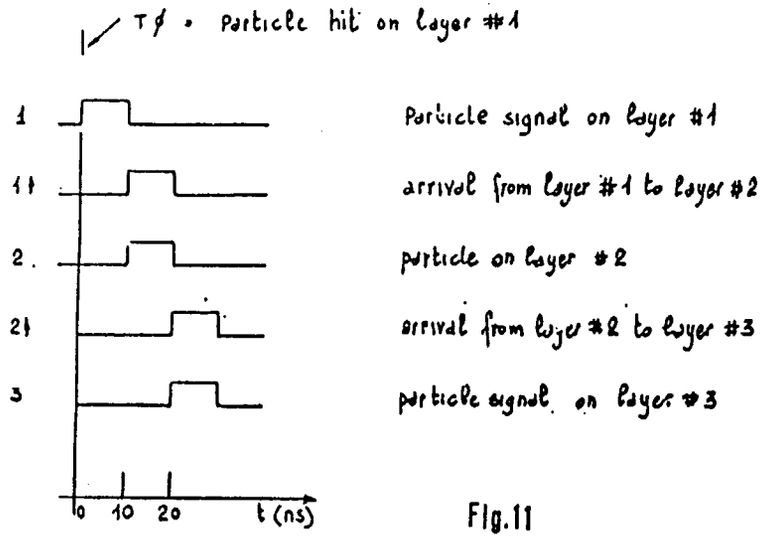


Fig.11

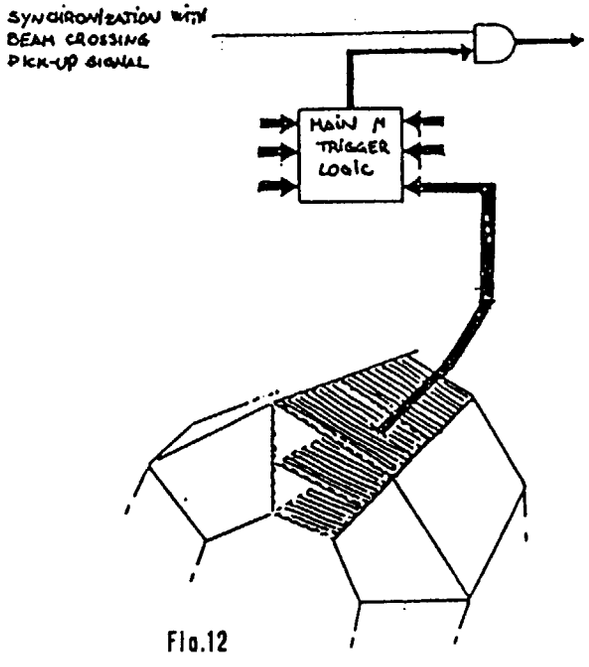


Fig.12

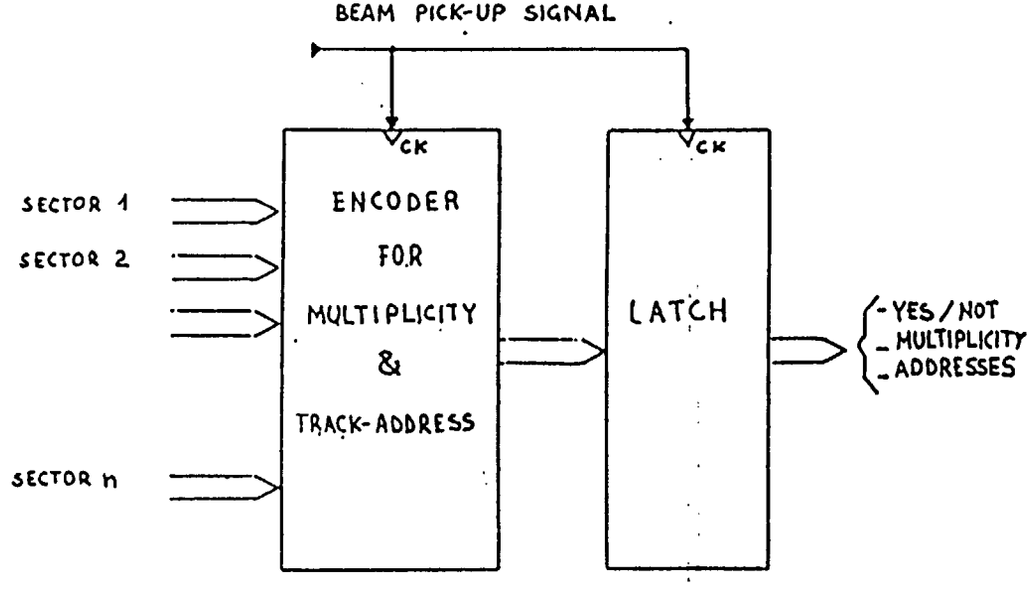


Fig.13

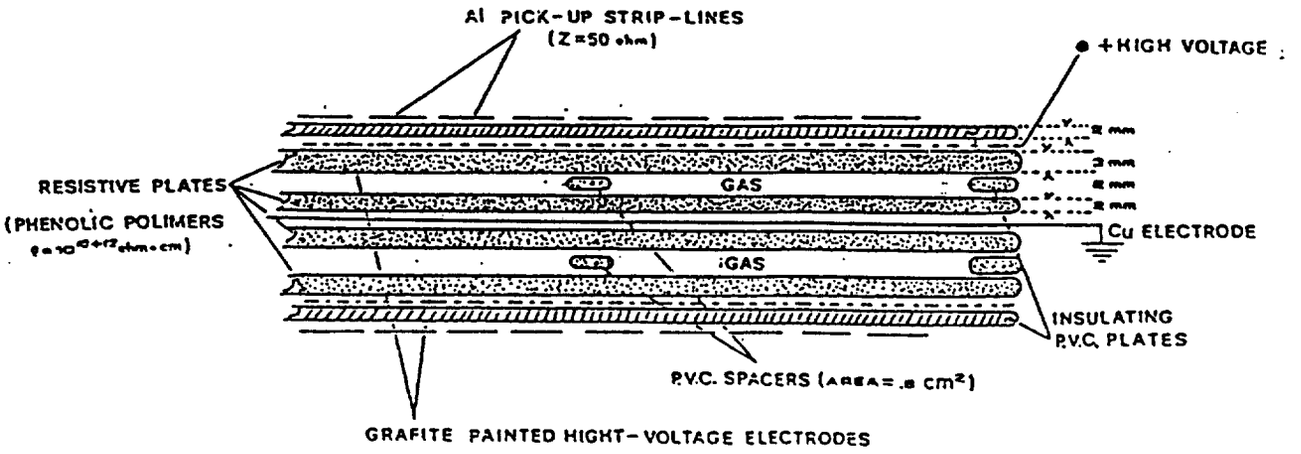


FIG.1

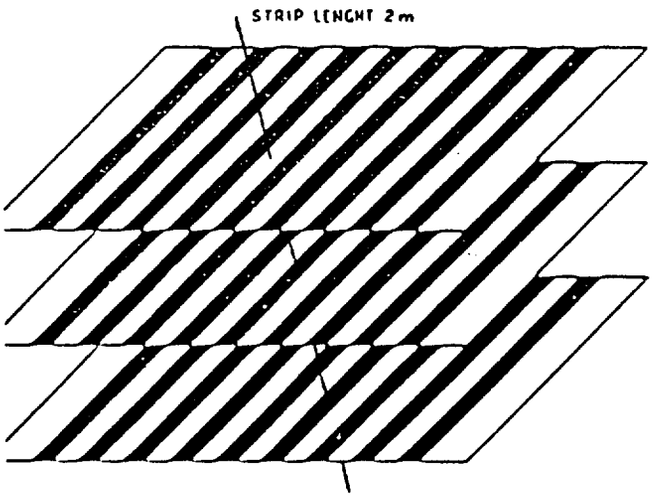


fig.2

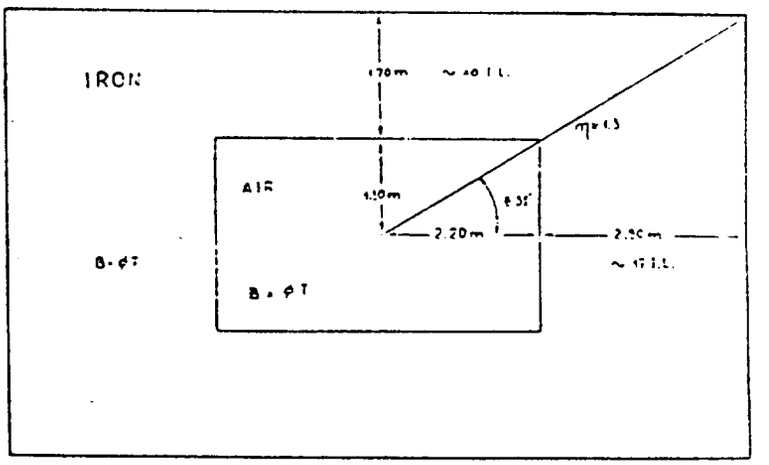


Fig.3

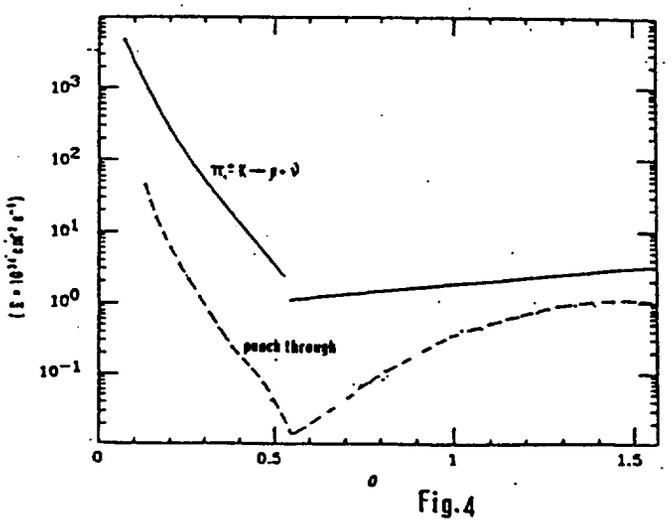


Fig.4

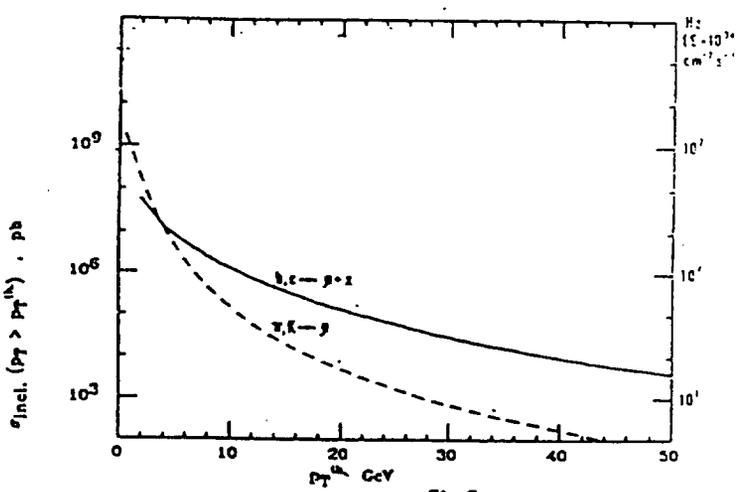


Fig.5

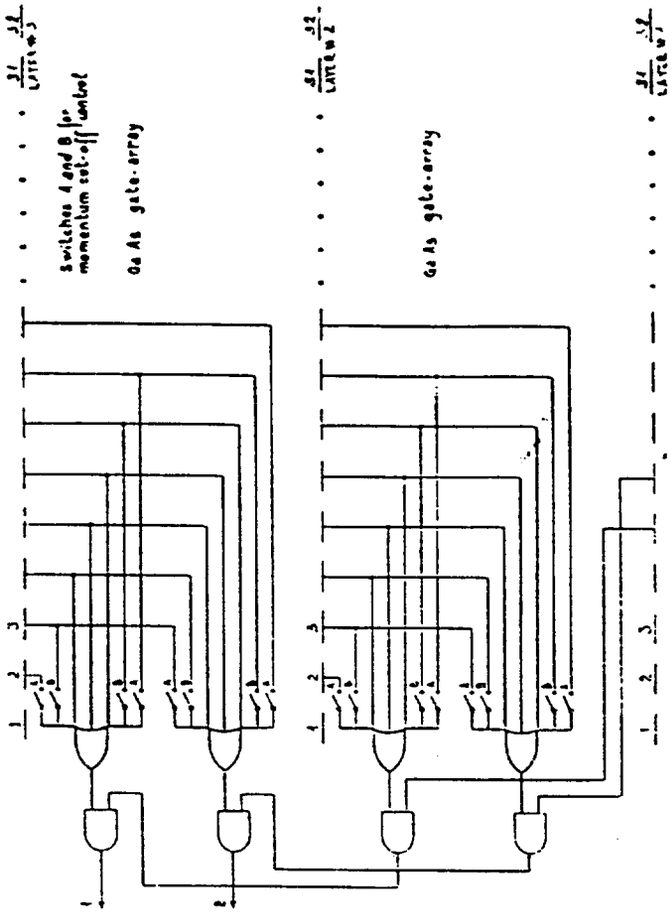


Fig.7

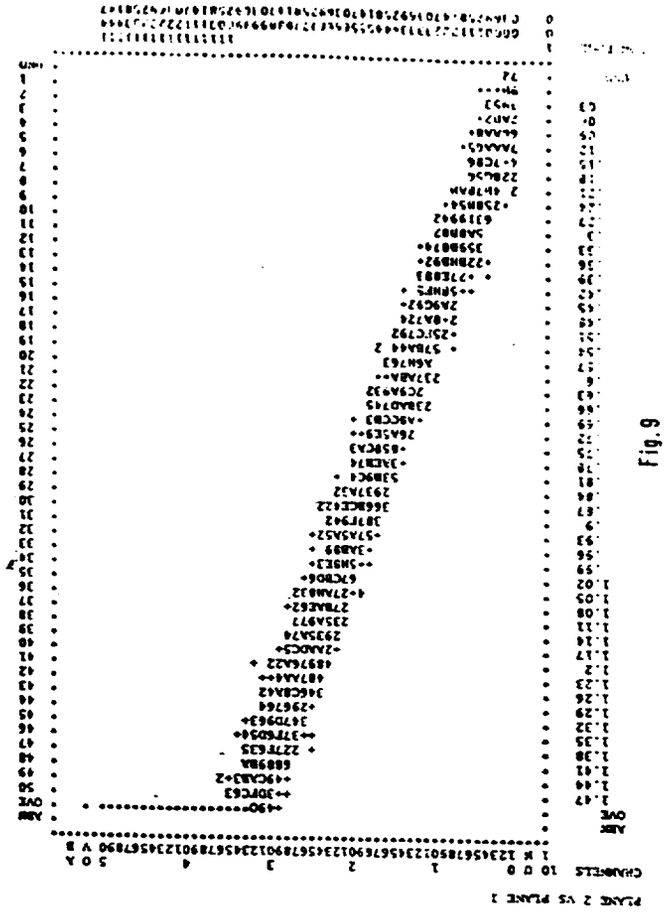


Fig.9

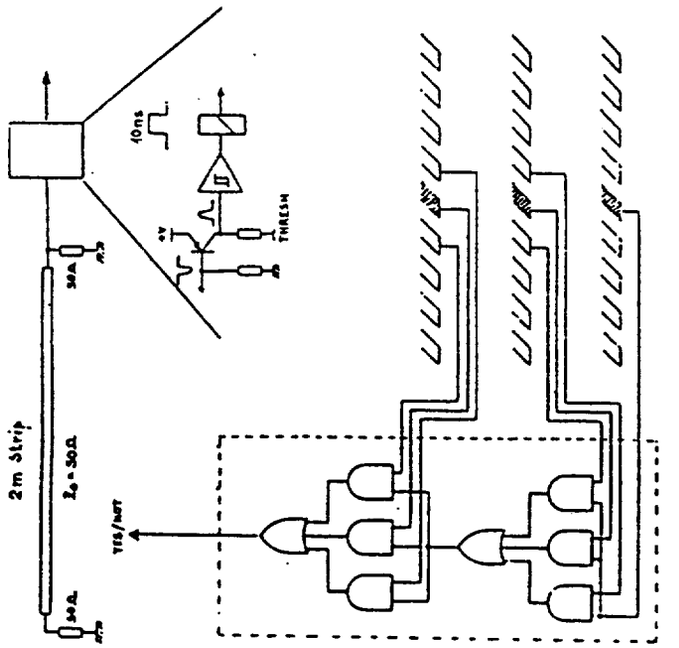


Fig.6

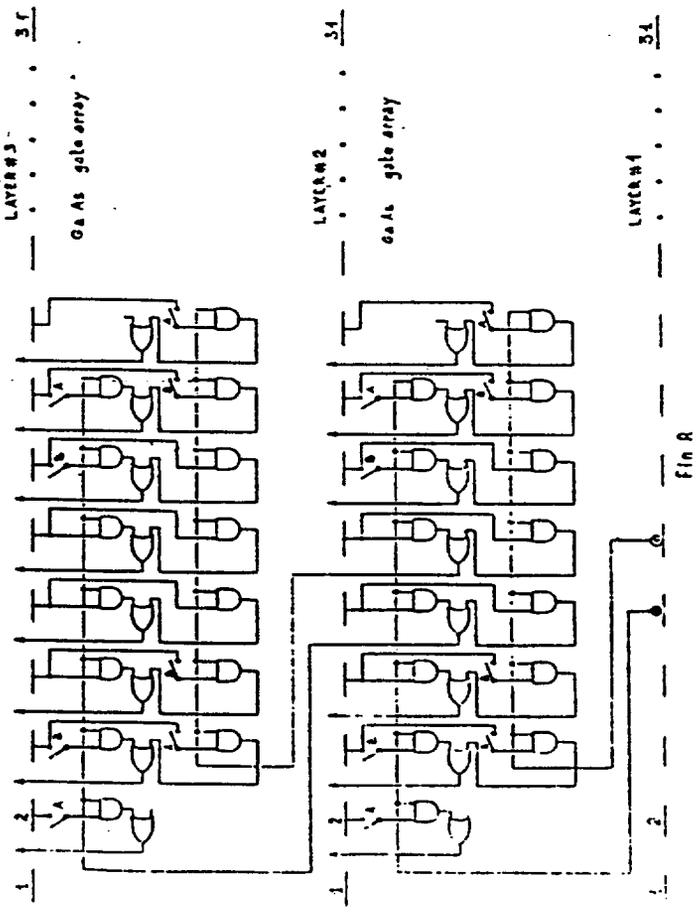


Fig.8

DSP review and applications
D. Crosetto
INFN - Torino, Italy

1. DIGITAL SIGNAL PROCESSORS (DSP).

Digital Signal Processors are special purpose microprocessors optimized for the execution of digital signal algorithms. They are traditionally designed for performance, not extensive functionality nor programmer convenience.

In the beginning most DSP's were distinguishable from other microprocessors due to their characteristics of:

1) Harvard architecture (separation between Program and Data memories)
2) internal and very small Program and Data memory area
3) small instruction sets, and mostly executable in one cycle, e.g multiply-accumulate (for this reasons similar to RISC)
4) special hardware units for treatment of digital signals (such as: parallel multiply, barrel shifting, auxiliary registers for single cycle manipulation of data tables, etc.)

- After performance comparison with other components it will become clearer why the DSP is more suitable for several types of applications.
- The most important thing to do in selecting a component in a certain application is to know the characteristics of all the components that can solve the same problem in order to make balanced judgement.

1.1. Characteristics of DSPs.

- In recent years we see that the characteristics of the DSP's are improving very rapidly. No one features of the past was dropped **(hardware multiplier, special instructions,** etc.) but in addition today's DSPs use **extensive pipelining, several independent memories with large address capability, hardware "do loop", parallel function units (one cycle floating point instruction), and hardwired design** (not microprogrammed).
- Applications in this field are increasing so rapidly that at present a classification among the hardware of the DSPs must be made (section 1.7).
- Some of the characteristics that make DSP's particularly suitable to treat discrete signals are found in its instruction set.

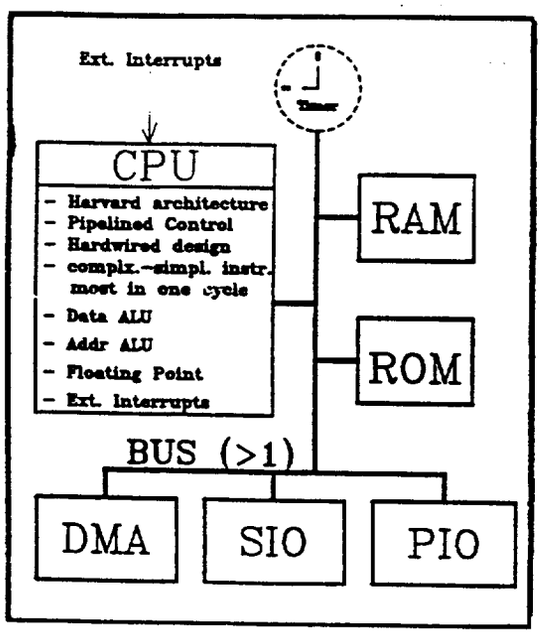


Figure 1. Simplified block diagram of a General Purpose DSP.

1.2. MICROCONTROLLERS versus DSP

- A "microcontroller" contains all the necessary components of a complete system on one piece of silicon (E.g. Intel 8051, Motorola MC6804, MC6805, MC68HC11, etc.).

The microcontroller has less performance than a DSP, has 4, 8, 16-bit, has an instruction set more like CISC processor (using more then one cycle per instruction). Some extra programmable peripherals on chip, like A/D converters are not available on DSP. It is not designed to build concurrent systems but it is intended to be used for economical applications in embedded systems where is necessary only to have the capability of one of the most common 8-bit or 16-bit microprocessor instruction sets.

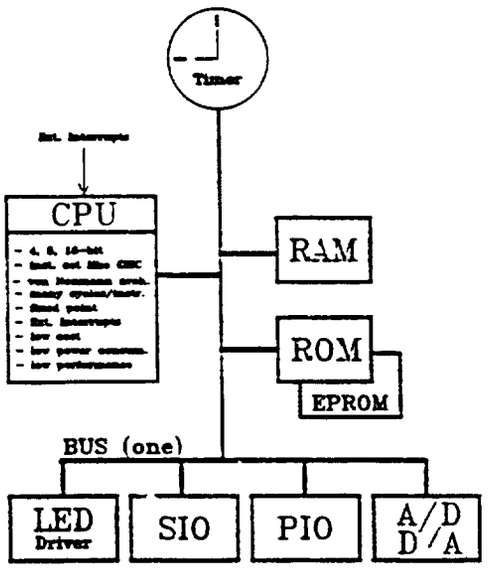


Figure 2. Simplified Block diagram of Microcontroller versus DSP.

1.3. TRANSPUTER versus DSP.

- Transputer is designed as a programmable component to implement a system with much higher degree of concurrency then is currently common, The formal rules of Occam provide the design methodology for this family of concurrent systems. Special instructions divide the processor time between the concurrent processes, and perform interprocessor communication.

DSPs have a performance of 20 to 40 Mflops, the T800 Transputer have 4.5 Mflops.

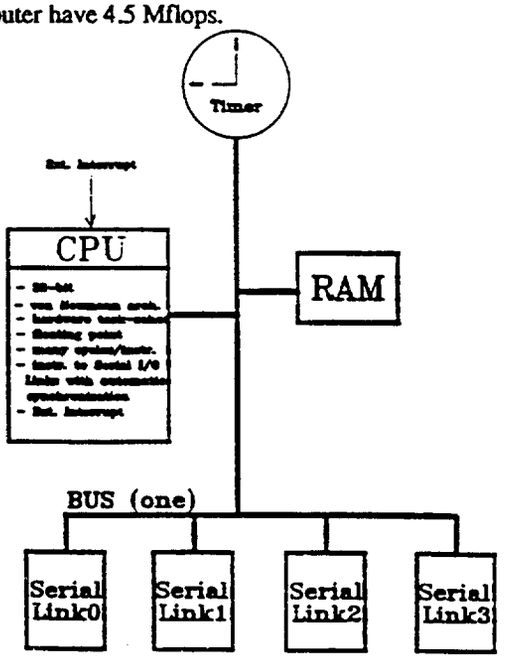


Figure 3. Simplified block diagram of Transputer versus DSP.

1.4. RISC versus DSP.

- Initial simple concepts of a register-intensive cpu design from Seymour Cray in 1960 for CDC 6600
- modern notion of RISC architectures emerged from John Cocke's project at IBM in 1970.
- Cocke's team goal was to design the best CPU architecture for an optimizing compiler, the machine should be register-to-register with only load and store accessing the memory, the architecture eliminated microcode and microsequencers in favor of simple, hardwired, pipelined, one-instruction-per cycle CPU design.
- RISC technology created an almost insatiable demand for memory speed. The answer to this problem comes with high performance memory hierarchy, including general purpose registers and cache memories, the instruction set is regular and simple with few addressing modes: indexed and PC-relative.

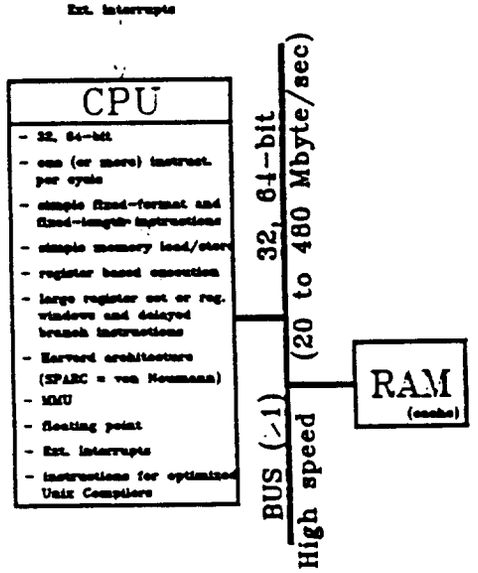


Figure 4. Simplified block diagram of RISC versus DSP.

1.5. CISC (CRISP) versus DSP

- CISC (Complex Instruction Set Computer) architecture use a large amount of hardware complexity to provide high degree of instruction set capability. They are characterized by a large instruction set with some very complex instructions. The length and execution time of instruction can be different from one another. Instructions can manipulate bit, byte, word and long word. The dynamic bus interface allows for simple, highly efficient access to devices of different data bus width. The latest components of this technology support, directly via BUS Monitoring, Multimaster and Multiprocessor applications.

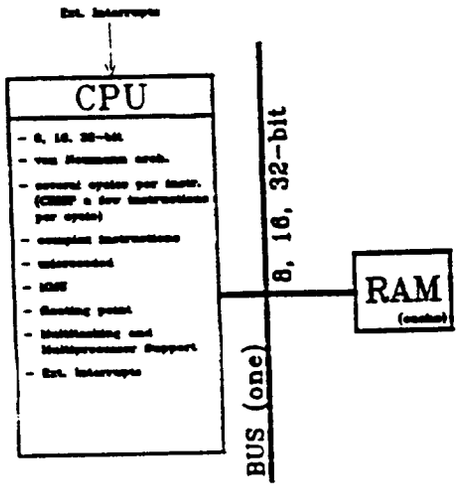


Figure 5. Simplified block diagram of CISC versus DSP.

1.6. High performance EMBEDDED CONTROLLERS versus DSP.

This architecture (new since 1990) has been designed to meet the need of embedded applications such as machine control, robotics, process control, avionics, and instrumentation.

- These type of applications require high integration, low power consumption, quick interrupt response time and high performance.
- Since time to market is critical, embedded processors need to be easy to use in both hardware and software design.

The newest chips on these family are from Intel and Motorola with some differences in their characteristics.

- Intel chips (80960) are based on a RISC core architecture. Each processor in the series will add its own special set of functions to the core to satisfy the need of a specific application or range of applications in the embedded market. For example, future processors may include DMA controllers, timers, or an A/D converter.
- other characteristics are: large register set, Fast instruction execution, load/store architecture, simple instruction format, overlapped instruction execution, integer execution optimization.
- The Motorola MC683xx family combines the high performance of M68000 family microprocessor with intelligent data-handling peripherals on a single chip.
- In one chip (32-bit) besides the CPU, there are: DMA controller, a timer module, a serial I/O module, a system interface module, and a 16-bit data port. Instructions are similar to the M68000 Family and need several cycles per instruction.

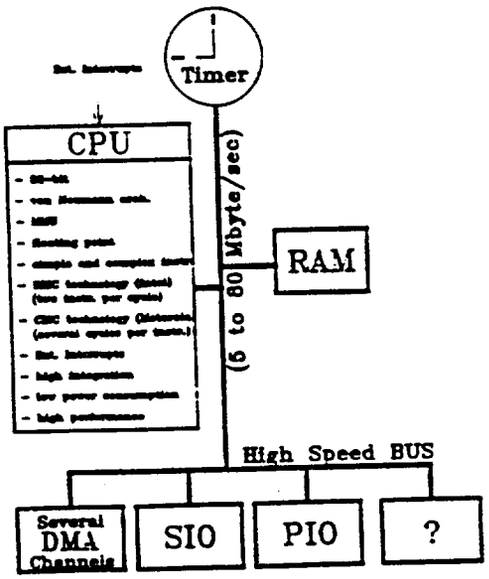


Figure 6. Simplified Block diagram of High performance Embedded Controllers versus DSP.

1.7. Classification of DSP hardware.

Among all the DSP chips available on the market, there are four main classification of the hardware:

1.7.1. High performance general purpose DSP.

These processors have an architecture similar to an MPU/MCU, but in addition may include on chip multiplier, RAM, ROM, DMA, peripherals I/O, hardware Do-loop, pipelining and several internal and external busses.

Some examples of these DSP types are:

- AT&T DSP16, DSP16A, DSP32, DSP32C
- Motorola DSP5600x, DSP9600x
- Texas TMS320Cxx
- Analog Devices 2100.

1.7.2. Algorithm specific DSP.

The architecture is configured for the optimum processing of a specific algorithm.

Among the DSP types designed for executing digital filter algorithms (FIR, IIR) there are: INMOS A100, LSI64240, Motorola DSP56200

Among the DSP types designed for executing FFT there are: TRW2310, HDSP66110, UT69532, Zoran ZR34161.

1.7.3. Application specific DSP.

This type of DSP's are designed to implement specific applications such as a modem or voice encoder/decoder.

1.7.4. Building blocks

Multiplier, adder, registers, RAM, ROM, I/O peripherals, etc. can be used as building block components to configure a complete DSP system with very high performance but with higher costs. (E.g. MaxVideo graphic processor)

2. APPLICATION EXAMPLE USING DSPs AND TRANSPUTERS.

2.1 A suitable on-line configuration and corresponding algorithms for cluster analysis.

The principal reason for testing a new Fast Digital Parallel Processing (FDPP) module, with data obtained with a highly granular scintillating fibre calorimeter, is to find the best on-line configurations and corresponding algorithms for different calorimeter types (hexagonal or square elements) and sizes by comparing FDPP output with more sophisticated off-line analysis programs. Even if the real-time procedures are simpler, the comparison should yield similar qualitative results so that it is possible, for example, find cluster structures, calculate energies, separate pions from electrons, with the confidence needed for higher-level trigger decisions and real-time data compaction.

2.1.1. Aim of the tests.

The Fast Digital Parallel-Processing (FDPP) [1] system is a modular system in which each node consists of one DSP tightly coupled to one Transputer. Any number of nodes can be interconnected using the four serial links (1.2 Mbyte/sec) provided by the Transputers, while any data source can communicate with the DSP at 10 Mbyte/sec.

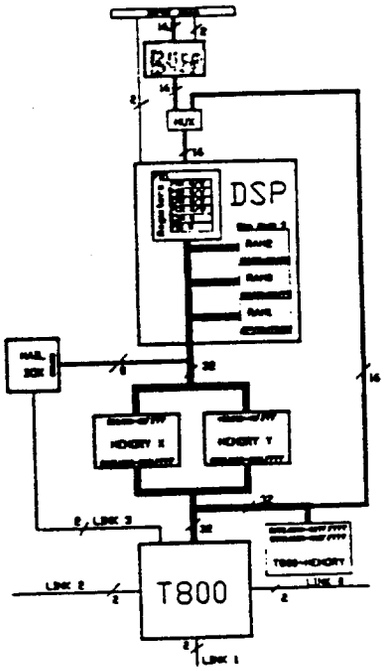


Figure 7. Block diagram of the Fast Digital Parallel Processing module (FDPP).

The system is scalable in the sense that several DSPs can be used in parallel.

Tests done on SPACAL experimental data were aimed at:

- checking the flexibility of the FDPP system
  - for off-line analysis by loading data through Transputers serial links at 1.2 Mbyte/sec,
  - for on-line analysis by loading data through the DSP parallel I/O port in DMA at 10 Mbyte/sec;
- checking the performance, in order to evaluate its cost, of a scalable FDPP system suitable for data compaction, for finding clusters within 42 to 48 μs (An array of Data-driven processors could do this task more efficiently), calculating their energies and their shape factors (I/C, O/C, sect. 2.3), on different calorimeter structures (hexagonal or square) within 15 μsec.

The test have been carried out as follows:

A feasibility study of parallel processing based on FDPP has been made for real-time algorithms for second-level trigger decisions and data compactions, as needed for hexagonal and square calorimeter structures (Figs 7 and 8).

A series of algorithms has been selected, coded in DSP32C assembly code and executed directly on the FDPP as they would be executed during on-line data taking.

After having executed the real-time algorithms on the FDPP, qualitative results (clusters identification, energy calculation, cluster-shape factors) have been compared with the off-line analysis processed on the IBM 3090.

The results given below show the time required to execute the different algorithms on 3000 different events from the SPACAL test runs on a 155 module fibre calorimeter prototype in June 1990 (jets, pions and electrons) together with results of cluster identification and cluster-shape factors.

2.2. Flexibility of the FDPP system.

2.2.1.Off-line/on-line interchangeability.

As shown in Fig. 7 and Fig. 8 the Digital Signal Processor DSP32C at each node of the parallel processing system, is the same basic element used in both platforms for on-line (real-time) and off-line analysis, capable of testing the same algorithms on the same data at real-time speed. In one case data will be loaded from the DSP I/O port at 10 Mbyte/s in DMA, while in the other case data will be loaded from the Transputer at 1.2 Mbyte/s.

2.2.2. Scalability for any calorimeter size.

Figures 7, 8 and 9 show how a parallel-processing system based on FDPPs can be configured for different calorimeter sizes. Figure 7 shows the detail of the FDPP module.

The general problem to solved is that of edges regions of processing activities, which have to overlap in order to achieve homogeneous coverage.

Figure 9 shows the detail of a 10 x 10 calorimeter channels area (processed by one FDPP node); the nodes are overlapping in order for each calorimeter channel to be analysed by only one FDPP node.

Figures 10, 14, 15 and 17 show that each described algorithm needs two values from nighboring elements in all directions for each channel analysed; this implies an overlap of four channel values between neighbouring FDPP modules.

Any segmentation of the calorimeter can be done. The overall performance of the system will change for different assignments of the number of channels to be analyzed by each FDPP. If first level trigger processing is capable of giving information of the calorimeter region of interest of the data that has to be transferred, a substantial reduction of the number of FDPP parallel processing nodes can be achieved.

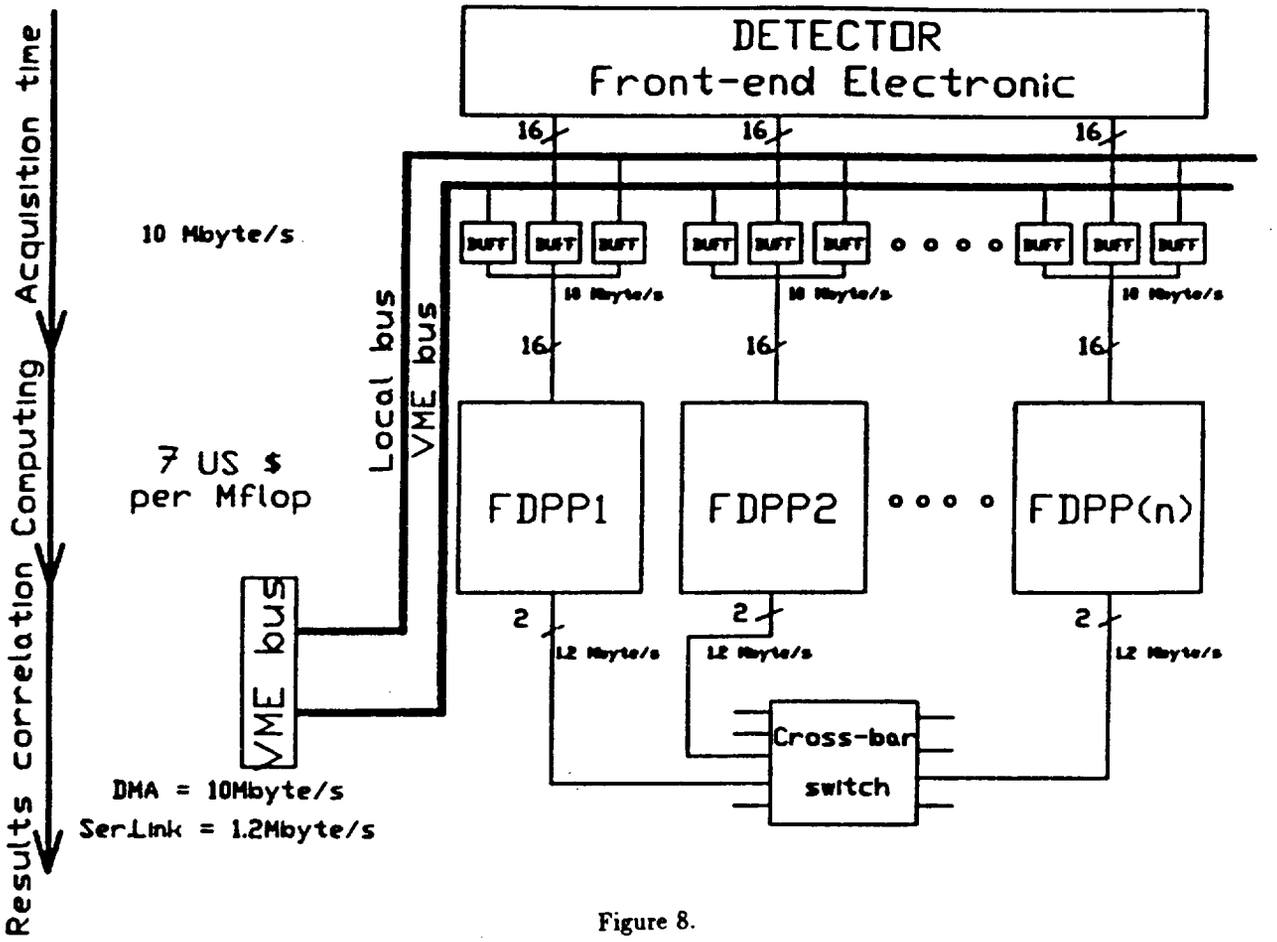


Figure 8.

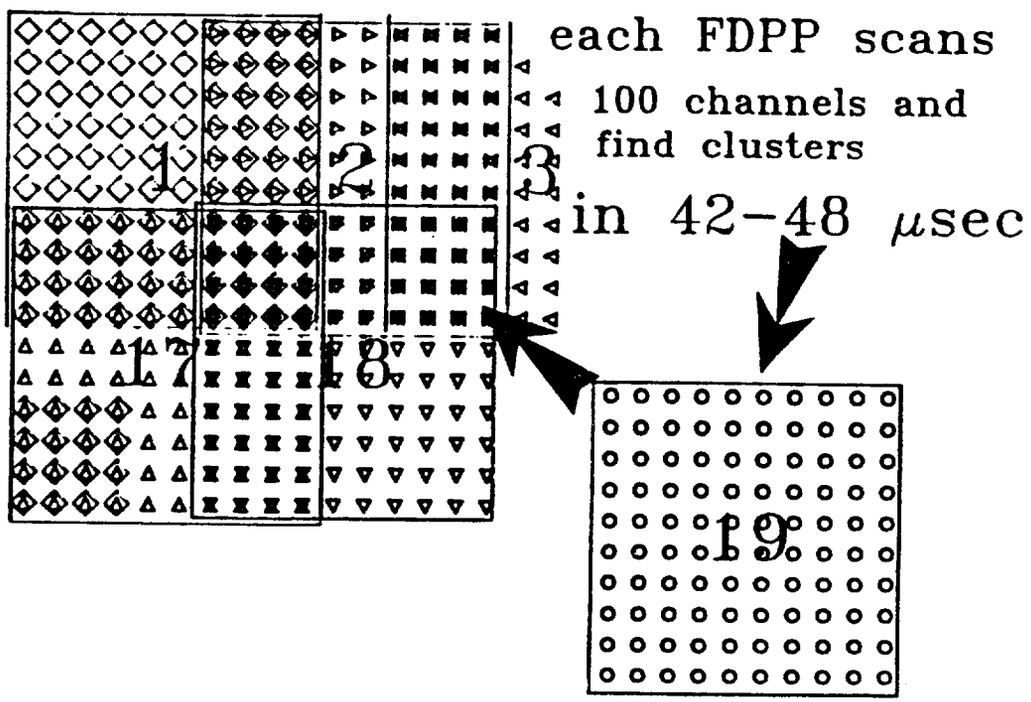


Figure 9.

2.2.3. Adaptability of the FDPP for different calorimeter structures.

Algorithms 1,3,4 are examples of real-time analysis coded in DSP32C assembly code for hexagonal calorimeter element structures. The algorithms are directly applied to the hexagonal structure without requiring transformation to a square matrix structure, thus giving more precise calculations.

Algorithm 2 is an example of real-time analysis executed by the DSP on a square calorimeter structure.

2.3. Performance of the FDPP system on different real-time algorithms.

Tests on a series of real-time algorithms [3], [5] were performed with one FDPP module using SPACAL data from the 155-channel prototype. Electron, pion and "jet" data were used.

A multi-FDPP parallel configuration will achieve a similar performance for a granularity of 100 channels/FDPP, irrespective of the complexity of the entire system (except that the I/O problem will be more complicated).

The detailed timing for algorithm 1 (Fig.12a) with a granularity of 100 channels/FDPP is:

- to scan channels and find local maxima 42 - 48 μs.
- to calculate E, I/C, O/C or Rp 15 - 17 μs.

The performance of the FDPP parallel processing system is 25 Mflop per unit at the cost of 7 US $ per Mflop.

The FDPP system will fulfill the requirements of the Zeus readout as presented at the conference on Transputer Applications at Southampton [6], offering serial link communication, extended Transputer data-bus connection; in addition, it will add 25 Mflop floating-point capability at each node at very low cost.

2.3.1. Test results from algorithm 1.

Algorithm 1 (fig. 10) applied to the hexagonal-element structures consist of the following phases:

(a) find all local maxima in the calorimeter and set a flag in an image array (42 to 48 μs),

(b) for all local maxima compute, the total energy (sum of 19 elements within 5 μs),

(c) for all local maxima compute, in floating point, I/C and O/C (fig. 10), where a local maximum is defined as a calorimeter channel with a value grater of the neighbors (10 μs).

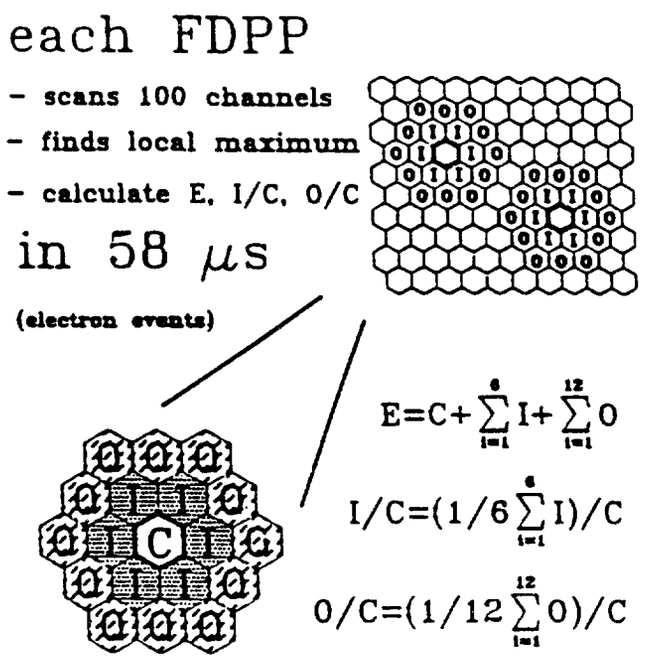


Figure. 10. Algorithm 1

Figure 11 compares the energy distributions of 600 electron events at 40 GeV, obtained by using the complete off-line analysis algorithm executed on IBM 3090 (fig. 11a) and obtained by using the simplified on-line real time algorithm executed on the FDPP in 5 μs (Fig. 11b). It should be noted that the results are comparable qualitatively, even if the off-line analysis algorithm is more complete, and therefore more precise in energy calculation: the on-line algorithm on the FDPP module provides, in a short time (10 μs), an information that is sufficiently precise and reliable to identify particles (pion/electron) for trigger decisions.

Figure 12a and 12b shows the distributions of I/C and O/C, respectively, for electron events at 40 Gev, while figs 13a and 13b show the same distribution for jet events; both were obtained from algorithm 1 executed on the FDPP.

The results of fig. 12a and 13a show a very good separation between the electron and pion distribution at I/C = 0.016, while the same separation can be found at O/C = 0.0006. Figure 13b shows that for jet-event run examined, only three jet events over 1474 passed the criteria defining electrons (misidentification fraction 2×10^{-3}).

2.3.2. Test results from algorithm 2.

Algorithms 2 (fig. 14) applied to the square-matrix element structure (conversion from hexagonal to a square matrix-matrix structure has been made by applying the criteria described in [4]), consists of the following steps:

(a) find all local maxima in the calorimeter and set a flag in an image array (42 to 48 μs),

(b) for all local maxima compute, in floating point, the total energy (sum of 25 elements within 6 μs),

(c) for all local maxima compute, in floating point, I/C and O/C (10 μs).

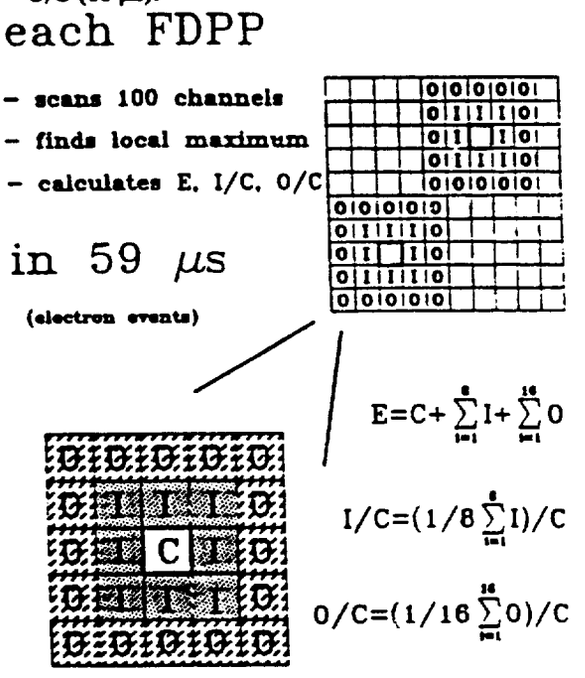


Figure 14. Algorithm 2.

2.3.3. Test results from algorithm 3.

Algorithms 3 (fig. 15) applied to the hexagonal-structure consists of the following steps:

Two types of local maxima are sought. A local maximum of type 1 has a value which is grater than that of any of its neighbors by at least a constant parameter. A local maximum of type 2 is a set of three neighboring elements having values within a given interval.

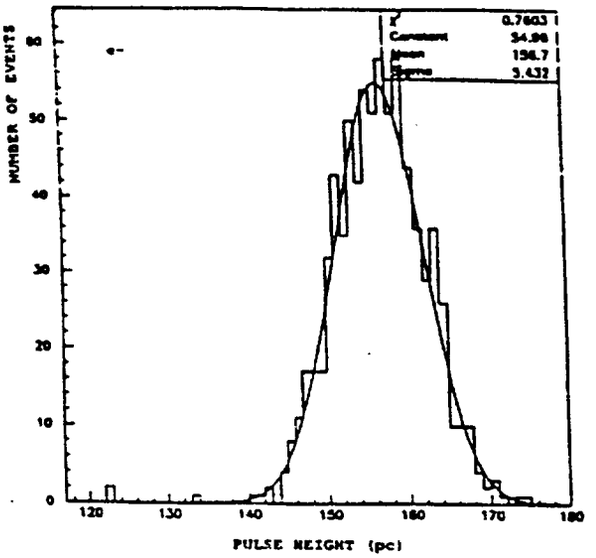


Figure 11a.

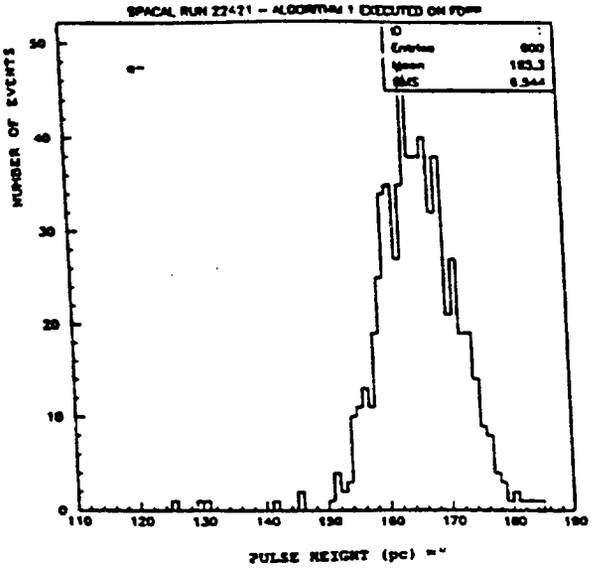


Figure 11b.

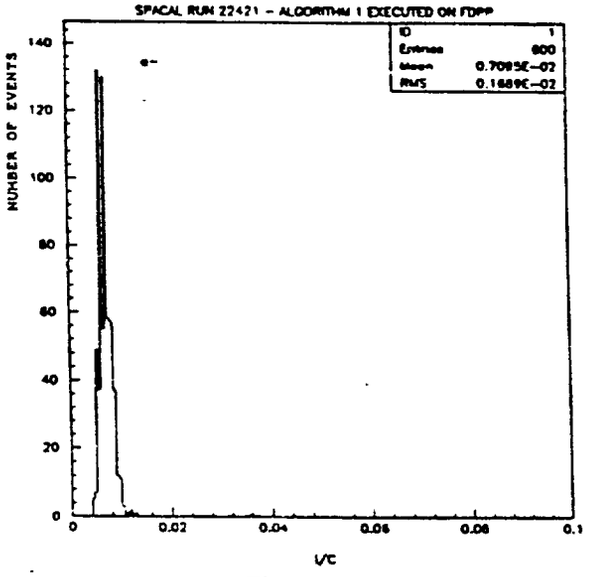


Figure 12a.

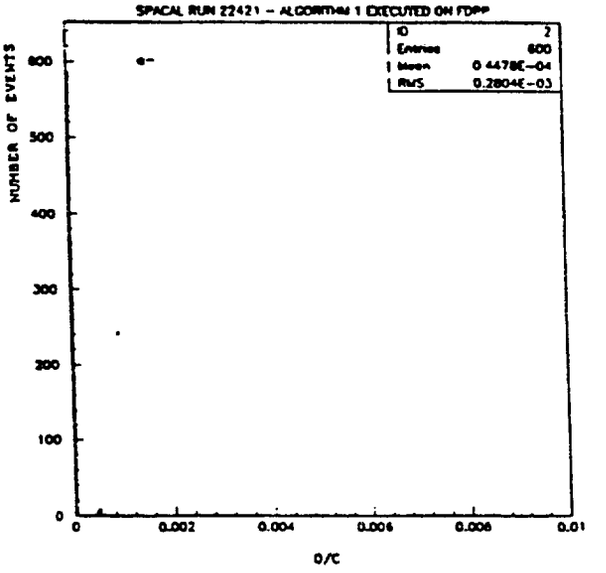


Figure 12b.

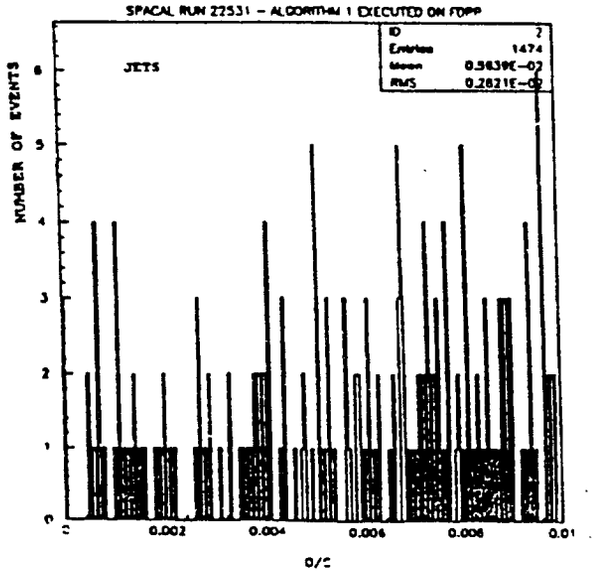


Figure 13a.

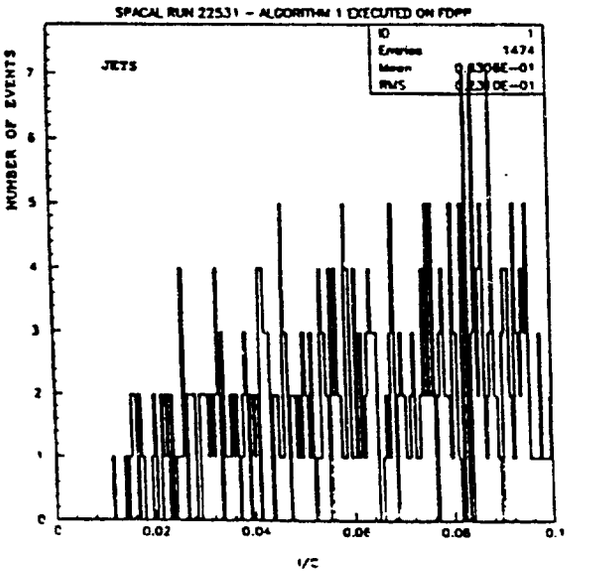


Figure 13b.

(a) Find all local maxima in the calorimeter and set flag 1 (flag 2) in an image array for local maxima of type 1 (type 2) Time required = 43 to 49 μs.

(b) For all local maxima, compute, in floating point, the total energy (sum of 19 elements for type 1 and 27 elements for type 2). Time required = 5 to 6 μs.

(c) For all local maxima, compute, in floating point, I/C and O/C (10 to 11 μs).

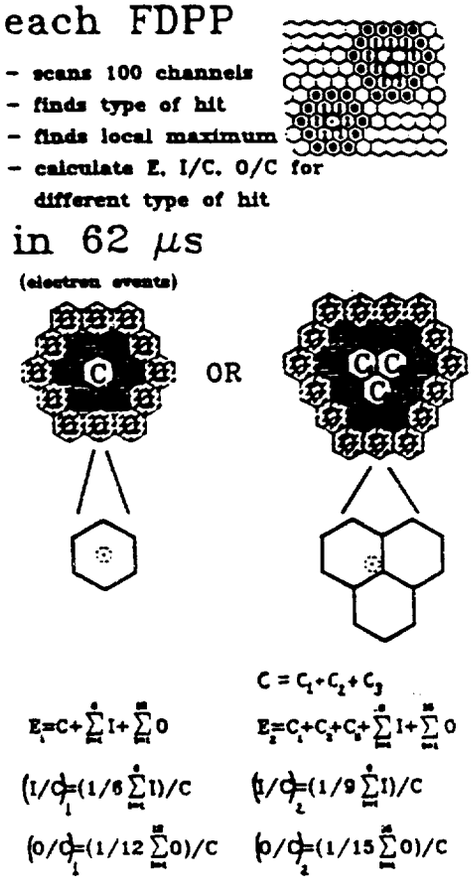


Figure 15. Algorithm 3.

The same event N. 31 from RUN 22531 on SPACAL (1990)	
E_1 = 26 Gev	E_2 = 31.5 Gev
I/C_1 = 0.4047	I/C_2 = 0.2152
O/C_1 = 0.3333	O/C_2 = 0.075

Figure 16 compares results of the same jet event with type 1 and type 2 hit-point calculations.

2.3.4. Test results from algorithm 4.

Algorithm 4 (fig. 17) applied to the hexagonal structure, consists of the following steps:

(a) find all local maxima in the calorimeter and set a flag in an image array (42 to 48 μs),

(b) for all local maxima, compute Rp in floating point as reported in fig. 17, where a local maximum is defined as a calorimeter channel with a value greater than that of its neighbors (15 μs)

Figure 18 shows the execution time for algorithm 4 for 40 GeV electron events (fig. 18a) and the time (fig 18b) to find one local maximum and two local maxima from "jet" events at 40 GeV. Figure 19a shows the distribution of Rp for electron events, while fig. 19b shows the distribution of Rp for jet events, both calculated [5] with off-line analysis programs.

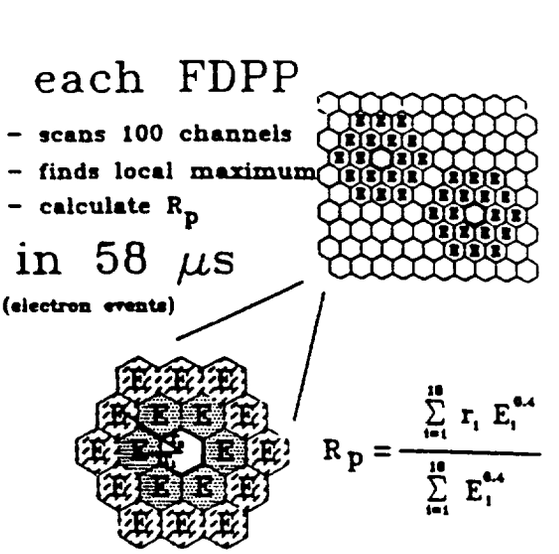


Figure 17. Algorithm 4.

Figures 20a and 20b show the same results obtained from algorithm 4 executed on the FDPP.

Observing the results of Fig. 20a and 20b for the calculation of Rp, one can see that there is a very good separation between electron and pion.

Acknowledgement.

I wish to thank the experimental physicists of the SPACAL collaboration for making their data available for these tests, as well as S. Cittolin who suggested performing them.

Additional support through a felloship from the ASP (Associazione per lo sviluppo Scientifico e tecnologico del Piemonte) for a physics student collaborator S. Buono is gratefully acknowledge.

For the entire FDPP project I wish to acknowledge the initial support of the DD Advance Computing Group and the continuing support of the Electronic Computing in Physics Division, especially that of P. G. Innocenti

For stimulating discussion and clarifying interactions with the text, I wish to thank A. Werbrouck.

References:

[1] D. Crosetto. "Fast Digital Parallel Processing module" FDPP CERN - DD/89 - 33 (AC)

[2] SPACAL Collaboration, Proposal: "Scintillating fibre calorimetry at the LHC" CERN/DRDC/90-23

D. Acosta et al., Nuclear Instrument and Methods, A294 (1990) 193.

[3] R.K. Bock et. al.: Benchmarking computer architectures for HEP real-time algorithms, CERN - LAA/RT/88-08.

[4] R.K. Bock et. al.: Algorithms and image processing architecture for on-line electron identification from lateral profiles in SPACAL, CERN - LAA RT/90-01 May, 1990.

[5] D. Acosta et al., Localizing particles showering in Spaghetti Calorimeter, preprint CERN-PPE/90 (1990); submitted to Nuclear Instrument and Methods.

[6] D.J. Pritchard and C.J. Scott Application on Transputers 2. IOS Press 1990 Amsterdam.

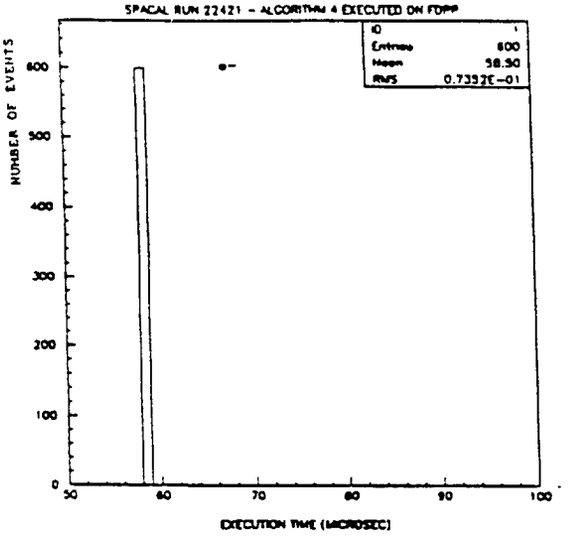


Figure 18a.

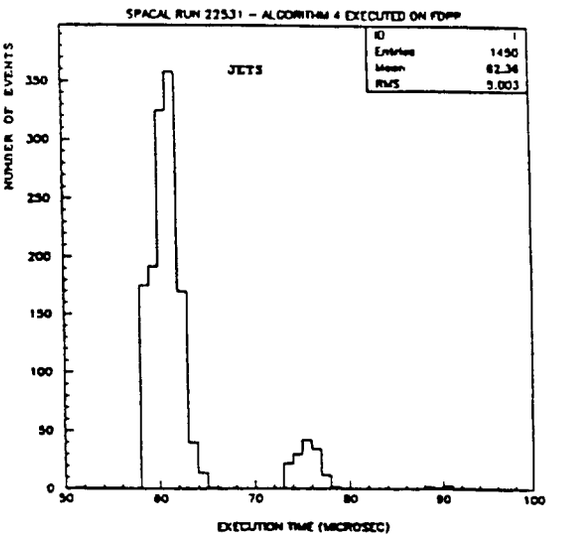


Figure 18b.

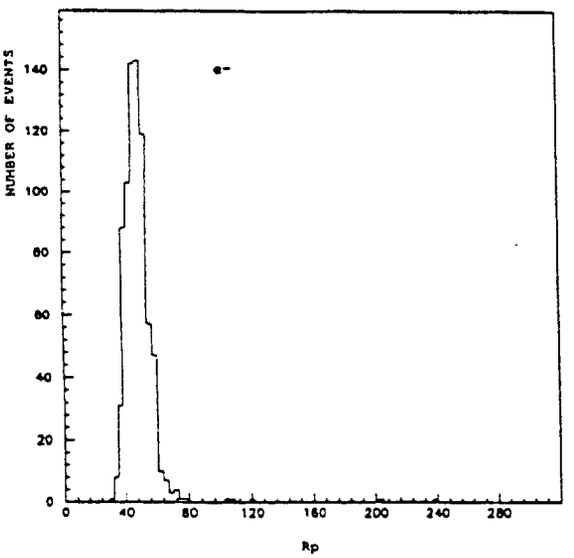


Figure 19a.

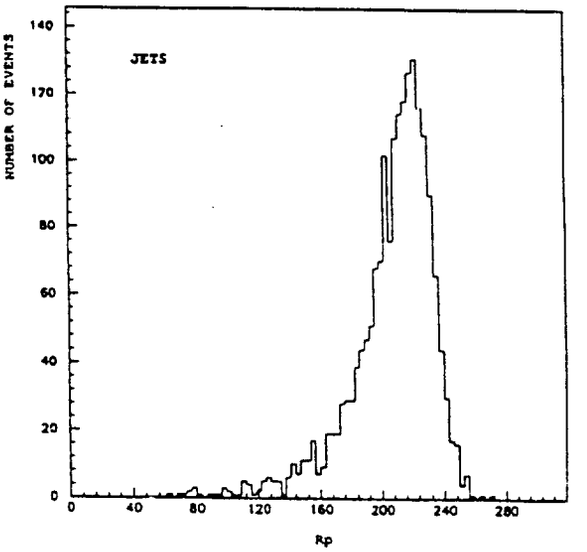


Figure 19b.

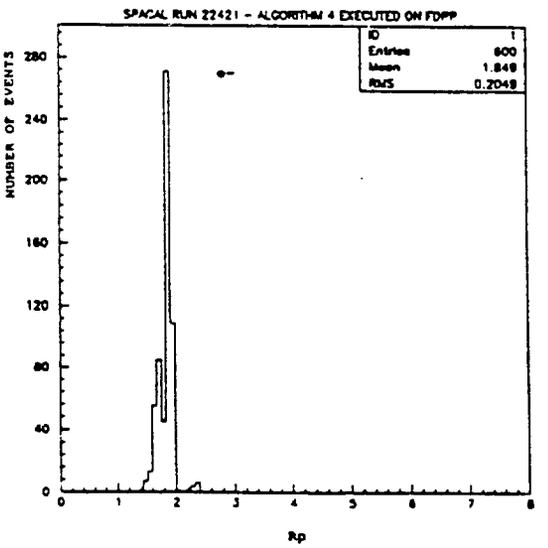


Figure 20a.

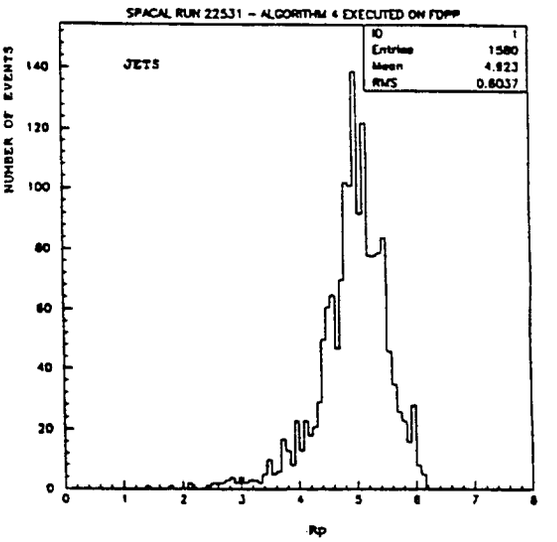


Figure 20b.

Data-acquisition and triggering with transputers

J. C. Vermeulen
NIKHEF-H, P.O.Box 41882, 1009DB Amsterdam

Properties of the transputer

A transputer of the current generation (1) is an integrated circuit with a 16 or 32-bit CPU, a fast on-chip memory (2 or 4 kByte) and interfaces for 4 bi-directional serial 20 Mbit / s point-to-point links with DMA support. Each link consists physically of two wires. All links can be used simultaneously. Each link can transport data in both directions simultaneously. The throughput per link per direction is of the order of 1 MByte / s (1.77 MByte / s at maximum). The micro-code of the CPU contains a two priority level multi-tasking kernel. It provides support for process scheduling, inter-process communication and descheduling of processes while waiting for timers or for an external signal. The communication mechanism is synchronous: a process is descheduled when attempting to communicate with another process and is made executable again when data transmission (by the CPU when both processes run on the same transputer, or under DMA control via a link) is completed. The 32-bit CPU's computing power is comparable to that of a Motorola 68020 CPU for integer operations. Some transputer types have a floating point unit with a performance of about 1 million floating point operations per second. Task switching takes at maximum 4 μs. A transputer has a 16-bit address / 16-bit data or 32-bit address / 32-bit data external bus interface for connecting external memory and interfaces. Transputers can be programmed in occam (2), a language with support for multi-tasking and inter-process communication, or a.o. in a parallel dialect of C or FORTRAN.

Systems can be built from single transputers - which may be equipped with external memory and / or dedicated interfaces - by connecting them together via the links. The links provide not only inter-processor communication, but also a boot path, as a transputer can be booted after a reset via one of its links. The links are fast enough for many present high-energy physics on-line applications. It has been shown to be possible to make them 100 m long, when using balanced drivers and receivers and high-quality twisted pair cable.

The functionality of systems built from transputers can be augmented with 32 by 32 crossbar switches for links, which are available from INMOS as single integrated circuits. Also available are integrated circuits for interfacing a transputer link to a parallel microprocessor bus. These devices are functionally comparable to simple conventional interfaces for asynchronous serial links ("ACIA's"). Finally, at NIKHEF-H an uni-directional fan-out circuit for links has been developed, that can be used for broadcasting messages to up to 16 destination transputers.

Present applications of transputers in high-energy physics

At present three high-energy physics experiments are or will be using transputers for data-acquisition and / or triggering:

- The JETSET experiment at LEAR, starting data taking, applies three transputers for event building (3). The transputers communicate with VALET-PLUS systems via the parallel bus to link interfaces mentioned earlier,
- The UA6 experiment, also starting data taking, uses about 60 transputers for data read-out, event building and third-level triggering (4). Third-level triggering is not done using the conventional farming approach, i.e. assigning the data of one event to a single transputer, the data of the next event to the next transputer, etc. . In stead different transputers execute different parts of the algorithm, while the data is distributed accordingly,
- The ZEUS experiment at HERA, scheduled to start data taking in August 1990, is the largest scale application with an estimated total of about 550 transputers, which will be used for data read-out, second-level triggering and event building (4, 5). About 400 of the transputers will be residing in VME-crates in so-called 2TP-VME modules. This type of module has been developed at NIKHEF-H and contains a.o. 2 transputers, which both can access the VME-bus. The systems of ZEUS will be partially dynamically reconfigurable. For data-acquisition the crossbar switches will be used for multiplexing data from many links onto a few links. In the event-builder crossbar switches are used to route the data to the correct third level crates. In all cases the crossbar switches are controlled by 16-bit transputers, with parallel bus to link interfaces attached to the external bus. Every transputer that needs to output data via the crossbar switch has a direct link to one of the interfaces for sending switch requests to the 16-bit transputer and for receiving messages acknowledging that the switching has been done. The NIKHEF-H broadcast circuit will be used a.o. for distribution of trigger decisions.

Programming of these transputer systems is done mainly in occam.

For a newly proposed high rate experiment at the CERN SPS it is intended to use transputers for event-building and third-level triggering and for interfacing (via SCSI) to digital audio cartridge tape drives (6). Other projects, not directly connected to an experiment, consist of the development of a DSP + transputer combination (7), the development of a combination of an Intel 860 processor, an Intel 960 communication engine and a transputer (8), and work on embedding transputers in the Fastbus environment (9).

These applications prove that transputer technology makes it possible to construct high-energy physics data-acquisition and trigger systems in a modular and natural way on account of the transputer links and the synchronous communication mechanism, supported by the on-chip multi-tasking kernel. The synchronous communication is very helpful in the data-driven environment of a data-acquisition system. There is no need for complicated interrupt or handshake schemes, as a process sending data to another process, that could be located in another processor, will only continue when the data is received (time-outs can be provided, if necessary). The on-chip multi-tasking kernel furthermore facilitates to run monitoring processes as background processes.

The new generation of transputers

In 1991 Inmos intends to start marketing a new type of transputer with code name H1 (10). This device is expected to offer 5 - 10 times the computing power of the present 32-bit transputers and to have a peak performance of 20 million floating point operations per second. The instruction set is a superset of the instruction set of the present T805. There are again 4 bidirectional links, but now physically consisting of 4 wires. The throughput per link and per direction should be 10 MByte / s. It will be possible to couple present transputer links via protocol converters to H1 links. The internal memory is increased to 16 kByte and can also be configured as cache memory. The on-chip real-time kernel will be somewhat extended, so that the implementation of a multi-level scheduler on top of the existing facilities will be eased. There will be some form of memory management. An important innovation, illustrated in fig. 1, is the introduction of hardware support for "virtual channels". Consequently it will be possible to define communication channels between any arbitrary pair of processes, regardless on which transputers they are executing. The hardware will take care of multiplexing several "virtual channels" on a single physical link, if necessary, and will also take care of routing the messages. For routing a method is used that is known as "wormhole routing". A path between source and destination is opened by the first packet of a message. This path is also followed by all subsequent packets of that message. The last packet closes the path again. With this technique no buffering of data at intermediate nodes is needed. A packet contains 32 bytes. However, the last packet of a message can be smaller. A handshake mechanism (one acknowledge per packet in stead of one acknowledge per byte as is used in the present transputer generation) guarantees that the synchronous communication model is obeyed. It is possible to randomize the route taken to a certain extent in order to avoid the occurrence of "hot spots".

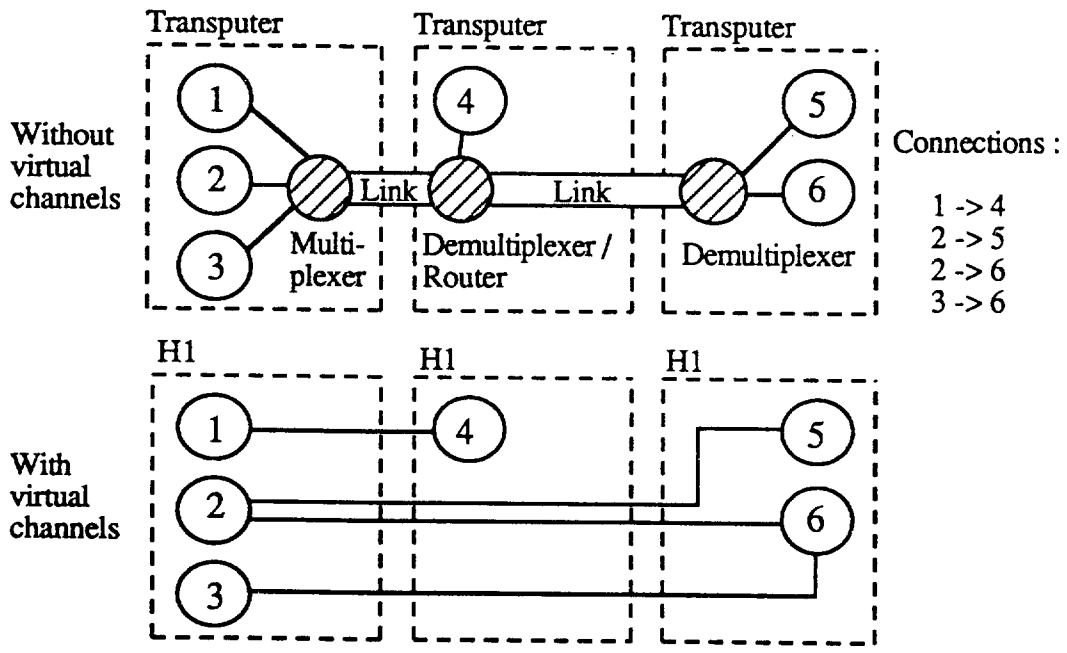


Fig. 1: For the present generation of transputers multiplexer, demultiplexer and router processes have to be applied to make communication possible between processes executing on arbitrary processors. The programmer of a system of H1's can make use of virtual channels between any pair of processes, i.e. the hardware takes care of any muliplexing, demultiplexing and / or routing needed.

After the introduction of the H1, it is expected that a new 32 by 32 crossbar switch will become available, which also will provide hardware support for routing. Only when starting up the information necessary for the routing of messages has to be loaded in the device, i.e. there is no need for a transputer controlling the switching actions of it. By combining the new crossbar switches with H1's it becomes possible to construct large systems with relatively high bandwidth and low latency inter-processor communication between arbitrary processors in the system.

The new generation of transputer hardware thus supports at the level of the application software a transparent mechanism for inter-processor communication. Point-to-point links in combination with the new routing crossbar switches guarantee an efficient use of the available bandwidth and also a low latency. These properties are very desirable for data-acquisition and trigger systems for LHC experiments.

Concluding remarks and outlook

The transputer is characterized by the integration of communication engines and a CPU - with a multi-tasking kernel in micro-code, which supports synchronous inter-process(or) communication - on a single chip. Its use for data-acquisition and triggering in three high-energy physics experiments demonstrates that its properties satisfy the requirements of these experiments in a natural and scalable way. Next year an order of magnitude faster transputers with extended functionality can be expected to be available. Especially the support for "virtual channels" is of interest. On basis of their functionality, the H1 and also the new crossbar switch are attractive components for applying in LHC experiments. As the H1 will be 1991 technology, even more advanced devices featuring faster operation, higher data transfer rates and perhaps also a further extension of functionality may be expected to become available during the design phase of these experiments. A recipe for implementing a functionally equivalent alternative is not simple. It would consist of building a transputer-like device, probably from one or more powerful CPU / CPU's, capable of fast task switching, and coupling it / them to suitable intelligent interfaces, capable of autonomous data transfers, to fast point-to-point connections. Also autonomous transfers between interfaces in one device, necessary for the implementation of virtual channels, should be possible. Furthermore a suitable multi-tasking kernel should be applied. This of course can all be done, but does not seem to be an attractive approach when sufficiently powerful real transputers are commercially available.

References

(1) INMOS, The transputer databook, second edition, 1989.
(2) INMOS Limited, occam® 2 Reference Manual, Prentice Hall, 1988.
(3) A. Bogaerts et al. , "The JETSET event builder", paper presented at the workshop on on-line applications of transputers in nuclear and high-energy physics, 2 March 1990, CERN.
(4) R. W. Dobinson, J. L. Pagès and J. C. Vermeulen, Particle World, to be published.
(5) L. W. Wiggers and J. C. Vermeulen, Comp. Phys. Comm. 57(1989) 316 - 320 .
(6) G. D. Barr et al. , CERN/SPSC/90-22.
(7) D. Crosetto, CERN-DD/89-33.
(8) R. Belusevic et al. , these proceedings.
(9) B. Martin, "Transputers in Fastbus", paper presented at the workshop on on-line applications of transputers in nuclear and high-energy physics, 2 March 1990, CERN.
(10) Dick Pountain, Byte, April 1990, "Europe and World" supplement, p. 3 - 12.

A pedestrian approach to fast DAQ
or
How to outbus the buses

R. Belusevic **G. Nixon**

Department of Physics & Astronomy, University College London
London WC1E 6BT, U.K.

The future high luminosity accelerators will be characterised by enormous data rates - as many as 100 million collisions every second! - compared to present-day machines (see Table 1). This will require a new approach to detector technology, in particular data acquisition electronics. With this in mind we have designed two general-purpose readout controllers capable of the highest data transfer rates and processing power currently attainable, while keeping the complexity of hardware and operating software to a minimum. We have also demonstrated the feasibility of data compaction and trigger processing within these systems by developing appropriate software.

Table 1: High luminosity colliders

Machine	Luminosity cm^{-2} sec^{-1}	Inelastic cross section	Bunch spacing	Events per second
LHC/SSC	10^{33}	100mb	25/16ns	100 million
		100nb [W,Z]		100
		0.1nb [$M_H \leq 2M_W$]		0.1
		5nb [$M_{t\bar{t}} \leq 2M_W$]		5
LEP	10^{31}	30nb [Z^0]	22μs	0.3
HERA	2×10^{31}	50μb	96ns	1K
TEV1	2×10^{30}	50mb	1μs	100K
		10nb [W,Z]		0.02

In our approach we were guided by what we believe to be the most important requirements a future data acquisition system must satisfy:

- Data transfer speed of about **100 Mbytes/s**, including real-time overheads;
- **Processing power** to match it;
- **Concurrency** with respect to data transfer and processing to increase the overall system throughput;

- **Versatility** (independence of detector and crate type);
- **Simplicity** of hardware and operating software, which leads to increased reliability and reduces heat dissipation and cost;
- **Data compaction** and trigger processing before readout by the crate controller.

To achieve the above goals we found it essential to implement the following hardware and software solutions in the two designs:

- Reduce **interfacing logic** and eliminate **bus arbitration** by using:
  a) special **on-chip hardware** for data handling,
  b) **single** controlling microprocessor with an advanced instruction set and simple operating software which supports **multitasking**,
  c) **dual-ported** memories throughout the system;
- Reduce **real-time overheads** by means of clever tricks with hardware;
- Provide **easy access to data** for the most powerful microprocessors;
- Use fast (1 Gigabit/s) intercrate **serial links**;
- Form a **pipeline of reduced data** (using DSPs or "superscalar" microprocessors for data parameterisation and compaction) on the readout cards, which results in a better utilisation of board space and avoids the transfer of unwanted data.

The first readout system consists of a transputer-based crate controller (CC), which includes an Intel i860 microcomputer, and of a set of readout cards (RC), each containing a digital signal processor (DSP) for fast data parameterisation and compaction. The reduced data is written into a dual port memory (DPM), where it can be accessed concurrently by the transputer and transferred to a common DPM on the CC card. A crateful of data thus assembled at one place can further be processed by the powerful i860 microcomputer. Address generators (simple binary counters) are included on the crate controller and each readout card to enable direct memory access (DMA) operations, resulting in a considerable increase in data transfer speed (maximum 80 Mbytes/s; see fig.1). The use of a transputer as the sole controlling processor, in conjunction with DPMs, renders bus arbitration unnecessary leading to very simple interfacing logic and operating software. The four high speed serial links of the transputer greatly facilitate downloading of programs and intercrate communications. This scheme also enables easy bootstrapping of the embedded microprocessors, without the need for EPROMs. Fast intercrate data transfers in the DMA mode are accomplished by connecting the DPMs directly to a 1 Gigabit/s serial link. The operating software is written in the Occam language, which was specially developed for programming concurrent systems based on transputers.

The block diagram showing the system's main components and data flow within a crate, indicating also intercrate communication links, is in fig.2. A paper describing hardware and software aspects of essentially the same design will appear shortly in NIM.

The second system (see fig.3) differs from the one described above in two ways. The crate controller contains two address generators: one for the local dual port memory and one for the DPMs on the readout cards, thereby reducing the amount of hardware per crate. Furthermore, we have replaced the binary counters by versatile single-chip sequencers, in order the keep the "glue logic" on the crate controller as simple as possible and to increase flexibility of the data transfer hardware (to be submitted to NIM).

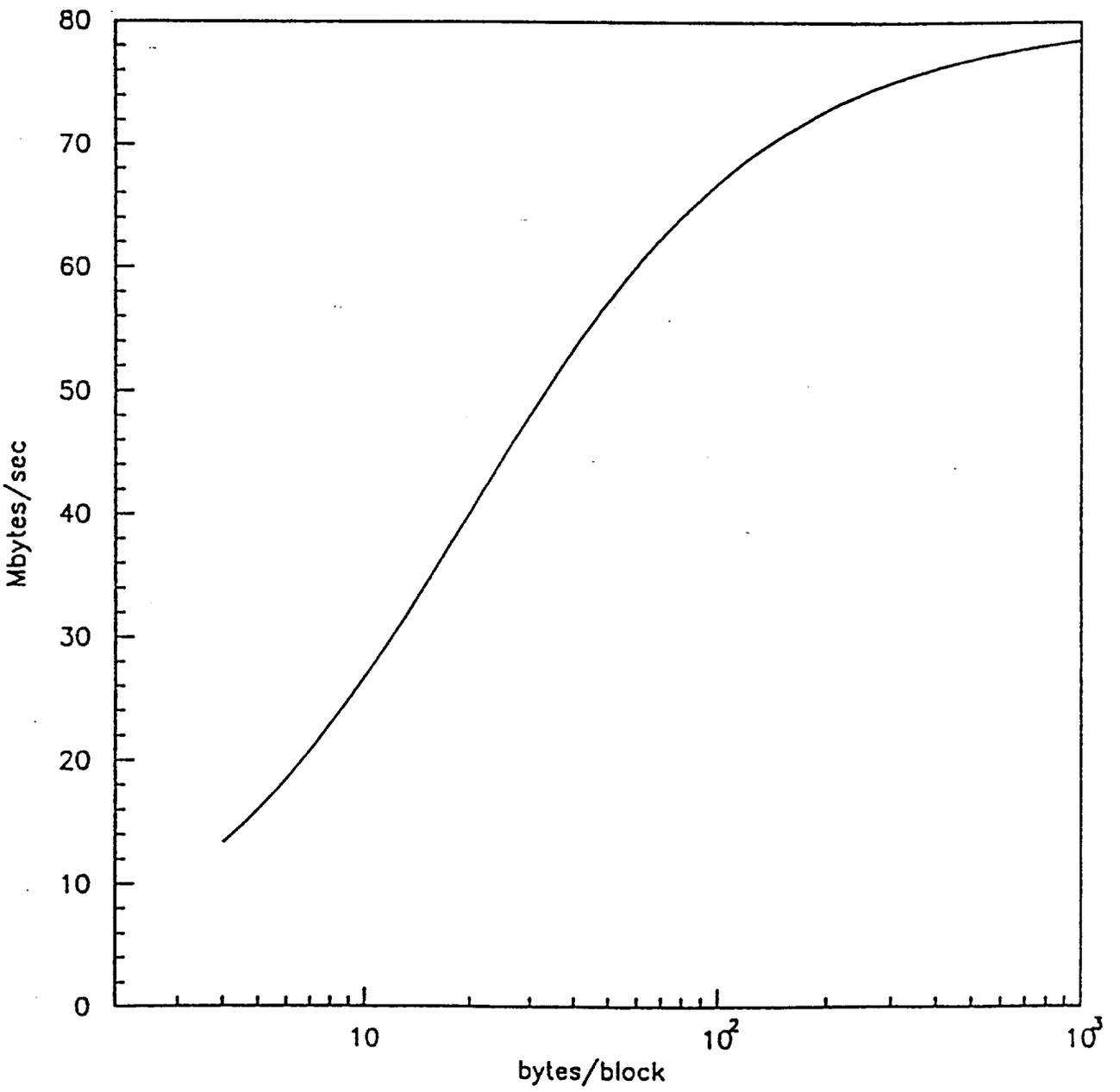


Fig. 1

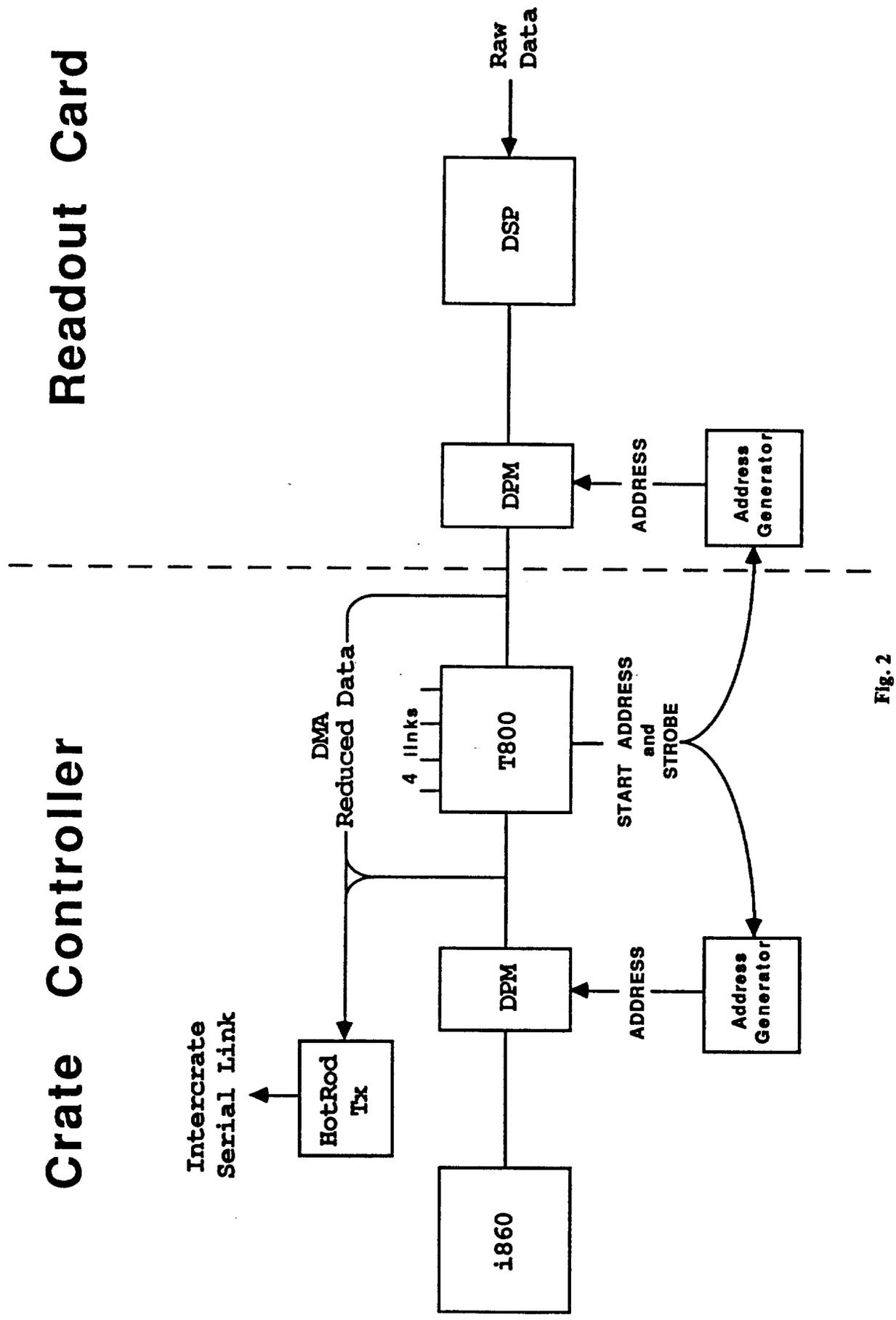

Readout Card
Crate Controller
Raw Data
DSP
DPM
ADDRESS
Address Generator
DMA
Reduced Data
4 links
T800
START ADDRESS and STROBE
DPM
ADDRESS
Address Generator
Intercrate Serial Link
HotRod Tx
i860

Fig. 2

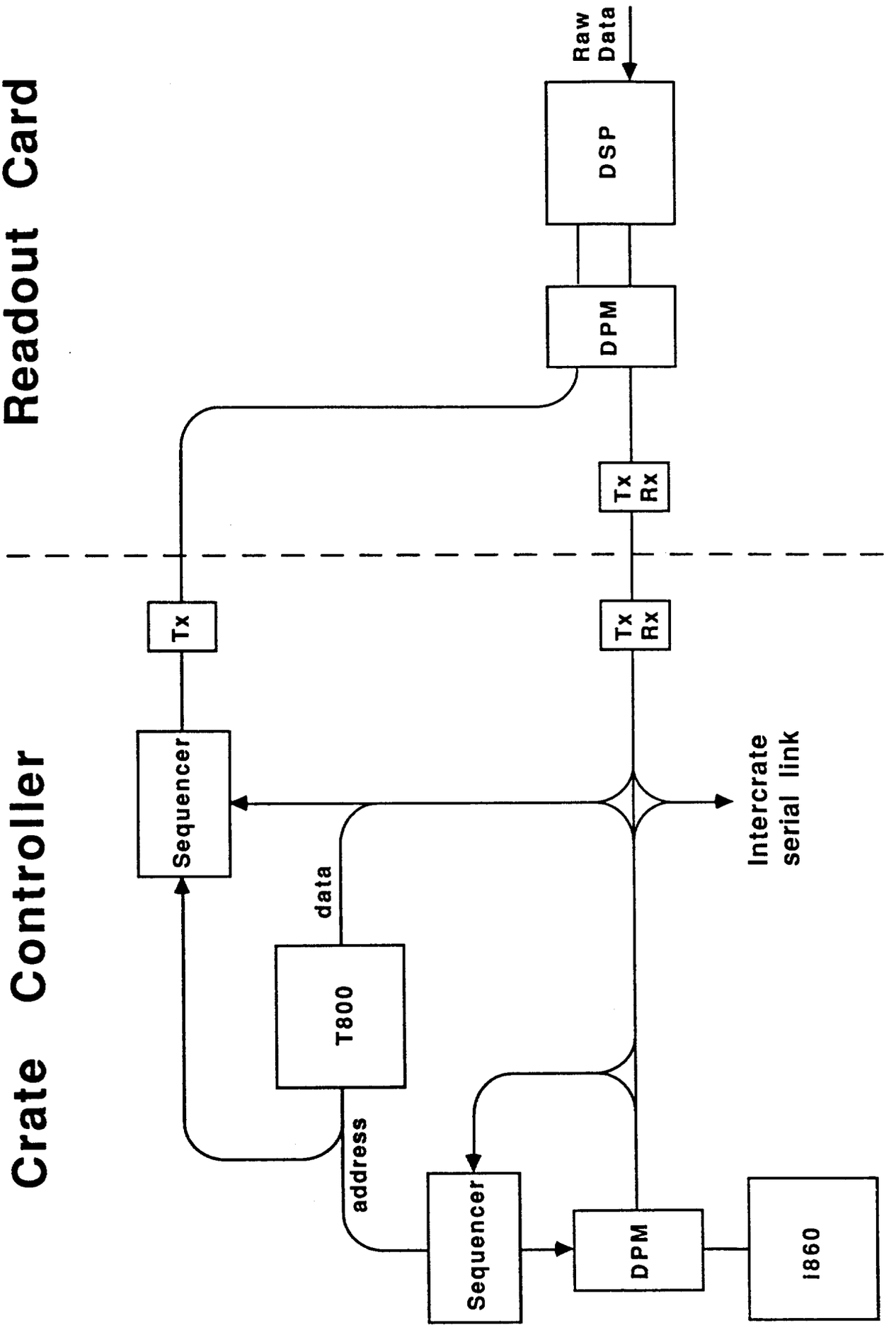

Readout Card
Crate Controller
Raw Data
DSP
DPM
Tx Rx
Tx
Tx Rx
Sequencer
Intercrate serial link
data
T800
address
Sequencer
DPM
i860

Fig. 3

Image processing in LHC detectors

Werner Krischer
CERN / ECP

INTRODUCTION

Detectors at LHC will be faced with a formidable problem : The bunch separation will be 15 ns and we have to expect multiple collisions per bunch crossing ($\geq 10^8$ events/second). (The corresponding figures for LEP or UAi are 22 or 3.8 μs and 0.3 or 50000 events/sec, respectively). After an analog trigger reduction of ~ 1000 : 1 the average decision frequency for the second level trigger is assumed 100 kHz. Per recorded event we expect ≥1 megabytes of data. This increased data volume is due partly to the larger dimensions of the future detectors, but mostly to the finer resolution in space and grayvalue. The detector output will look more like an "image". If executed today on commercial fully programmable processors, trigger algorithms are too slow by a large factor. The speed-up of several orders of magnitude over present-day on-line systems can not be expected only from improvements in IC fabrication, new technologies, algorithms and/or programming techniques. It has to come mainly from using adequate parallel architectures, properly integrated in the data flow. Our aim is therefore to understand the existing parallel architectures to be able to embed suitable ones later in future readout systems.

A judgement of architectures depends completely on the classes of algorithms one wants to run, and on finding a balance between total throughput and latency, important in real-time. In [1] we have identified some typical algorithms, that we used as benchmarks for triggering and data compaction. The purpose of these tests was to find out which architecture matches best which algorithm and not to find one architecture that performs equally well on all algorithms. Some algorithms ran a million times faster than on a VAX 8300. Their analysis led us quite naturally to a certain algorithmically specific architecture, a pipelined image processing system, which we will describe here in some detail. We also tried out several Single Instruction Multiple Data [SIMD] processor arrays. There are two further talks at this conference ([2]) on the most successful SIMD architecture of our benchmark, the Associative String Processor. We will therefore restrict ourselves here to a description of our model of a pipelined image processing system. We will repeat here the reasons that led us to this choice not only with the same algorithms but we prefer to do this mainly with some recent work done for the lead / scintillating fibre calorimeter (SPACAL) [3].

TYPICAL ALGORITHMS AND IMPLEMENTATION ON PIPELINED IMAGE PROCESSORS

PEAK FINDER

A frequently recurring algorithm is the reduction of a graylevel image (e.g. 8 bits/pixel) to a binary one (1 bit/pixel) or to a list of x's, y's (and grayvalues). Simple thresholding is usually not sufficient. We have chosen a two-dimensional peak finder. A centre pixel is considered a peak if the 3 following conditions are fulfilled :

1. The centre pixel C is bigger than the average XAV of its 4-connected neighbours X.

```
 O
OXO
```

2. XAV is bigger than the average of the 8 next outer neighbours O.

```
OXCXO
OXO
```

3. The centre pixel is a maximum in a 3*3 neighbourhood.

```
O
```

The computation of the grayvalue difference of 2 groups of pixels like in the conditions 1 and 2 can be interpreted as a convolution. Testing if these differences exceed certain constants is a typical point operation on one image. Finding the maximum in a neighbourhood is one of the most basic morphological operations in image processing. Producing the x,y - list is the feature extraction task. Fig. 2 shows a possible configuration for the peakfinder algorithm.

TRACK FINDER

A list of x's and y's (< 256) of straight tracks coming from a known vertex is given. The tracks should be found by an angular histogram. This can be interpreted as the logical "AND" - operation between the binary image to which the x's and y's belong and a mask containing the histogram bin-numbers. The only non-zero pixels of the resulting image have a grayvalue equal to the bin-number at

the original (x,y) - position. The tracks can then be found from a graylevel histogram. Another way of looking at this problem is to store the x - and y - **addresses** in separate images and perform a table lookup on the combined 16 - bit image. This algorithm will therefore take on a system with Region Of Interest (ROI) - capability 256*256*100 ns = 6.5 ms, if the 2 images are "AND" - ed, and only 130*1*100 ns = 13 μs for the given 130 addresses, which we had to process. Fig. 3 shows configurations for these two cases, the so called "iconic" and the "symbolic" one.

CLUSTER ANALYSIS IN A CALORIMETER

We have recently worked on the development of cluster finding algorithms for the SPACAL calorimeter [4]. Our test data came from beam exposures in December 1989 and June 1990. We mapped the hexagonal structure of these 20 or 155 tower modules onto a rectangular pixel memory in such a way, that a space invariant operation on the hexagonal array remains space invariant after the mapping on the rectangular array. For interactive algorithm development, we mapped several thousands of test events into big images like in Fig. 1 (top right). Fig. 1 (bottom right) shows zoomed parts of it. A pseudocolour scale was used for displaying the energy values. One notices the qualitative difference between electron (e) triggers on the bottom (occupying few pixels), and pion (π) triggers at the top (much more extended clusters). Our goal was to express this difference in lateral spread into an e/π - discrimination algorithm. Instead of developing algorithms for the isolated grayvalues given, we approximated the real trigger situation by using no a priori information about cluster position, and developed algorithms for such big images, built up of many small events. The detection of the pixel with beam impact, i.e. of local maxima, therefore obviously had to be one of the processing steps (this corresponds to no pointer information from a first level trigger!).

We extracted from the original image some different features, e.g. total energy , local maximum, sum of the inner or outer neighbours, the sum of the 3 biggest values, the peak of the paraboloid $z = a + b(x^2+y^2) + cx + dy$ calculated through the 2 biggest grayvalues and their closest neighbours, etc. We then made two-dimensional histograms from these features, and chose the pair of variables that gave the best cluster separation in this "feature space" and thus allowed to produce an optimal classification algorithm. Fig. 1 (top left) shows such a two-dimensional histogram. One sees how one can interactively define a discriminant in the feature space. It should be noted here that simply comparing local maxima with inner and outer neighbours as in the peakfinder above did not work at all on this data because the resolution of this calorimeter was not fine enough. We got the best results by going to subpixel precision. The dynamic range in the original files extended from 0 to about 700. We reduced it to 0 - 255 in our simulation using several different compression scales, e.g. sinusoidal, piece-wise linear, logarithmic. The triggering algorithm's discrimination power can be substantially improved by choosing the appropriate transformation function. A logarithmic LUT turned, e.g. in the case of the plot of the fitted maximum against the inner neighbours, a completely useless histogram into an optimal one. It should be noted that a very local neighbourhood has been used here, which eases implementation and allows for minimal isolation criteria, i.e. is most robust against pileup in high-luminosity situations.

A highly simplified possible implementation of our algorithms on a pipelined image processing system could look like in Fig. 4. The input image is first passed through a look-up table, which accomplishes the nonlinear transformation, apart from a dynamic range adjustment. The chosen features consist essentially of simple neighbourhood operations like convolutions or minimum/maximum determinations, and can be easily implemented by commercially available neighbourhood processors with several parallel data paths. Their outputs (the features) are then combined at the input of a big look-up table, in which all the decisions are coded. The at present available 16 - bit look-up tables allow 2-dimensional numerical classification in real time.

Our simulation program allows to see immediately the effect of different input-LUT's, features and discriminants in the feature space and it produces the contents of the input- and output- LUT.

AN ALGORITHMICALLY DEDICATED PIPELINED ARCHITECTURE

Among the systems on the market, that perform exactly the type of algorithms we have described earlier, we have chosen for our tests the MAXVIDEO - family from DATACUBE, Peabody(MA) (see [5]). This is sold as a family of (at present) about 40 very powerful VME - compatible boards. A flexible and expandable bus-system (MAXbus) allows to define the data paths between the different modules. A single output port can drive up to 10 input ports. Any input port can be physically connected to two output ports. Switching can be done on a pixel-by-pixel basis. We can thus design practically any single or multiple parallel processing pipelined architecture. At present data is transferred between I/O ports at a rate of 10 or 20 Mbytes/sec. Regions Of Interest (ROI) can be specified from 1 to 4096*4096 pixels and the processing time is proportional to the number of pixels. Examples of interesting modules

are the triple ported Region Of Interest memories (ROI's) from 512*512 * 16 bits to 8 Megapixels, cascadable up to 16384*16384 * 8 bits. Convolvers exist from 3*3 up to 16*16 arbitrary coefficient kernels and a large kernel convolver for 2*256*64 with 2 coefficients only. This corresponds to a processing power of 180, 5120 and 320000 million arithmetic operations per second, respectively. A systolic neighbourhood processor can be used for nonlinear processing, e.g. morphological operations (erosion, dilation) or minimum/maximum finding in a 3*3 neighbourhood. Other examples are programmable crosspoint switches, pointwise ALU's, a module to count the occurences of many different events and to extract the coordinates of a specific event, MIMD - or SIMD - like configurable DSP's to fill the gap between special purpose hardware modules and more general software solutions. Many modules contain look-up tables (from 256 * 8 bits to 65536 * 16 bits, i.e. an arbitrary function F(X,Y) can be performed on two 8- bit images X and Y).

Fig. 5 shows in a simplified form the complete system we have put together for most of our algorithms. This configuration could today be replaced by a single board that works at a 20 MHz rate.

SOFTWARE

Whereas general purpose computers fetch, process and store data under the tight control of a processor, pipeline processors operate on a continuous flow of pixel data. Their control is set up prior to the operations of the pipe. DATACUBE supports UNIX and OS/9 development systems. Another company has been founded to interface to non VME-bus and other operating systems. Some relatively high level software (MAXWARE) had been provided as C - source code. It allows to call functions like "read red LUT" , "convolve with coefficient bank nr. i", etc, but it leaves you e.g. the worry about the pipeline delays! A new object oriented "IMAGEFLOW" software is advertized to allow you to "program pipelines and not image processing hardware". An ASCII - configuration file defines the hardware set-up parameters, an Application Programmers Interface hides all the hardware details and there is no loss of real time performance.

FURTHER EXAMPLES OF SIGNAL PROCESSING ACTIVITIES

Apart from our belief that digital signal processing in general will play a more and more important role in our data acquisition systems (e.g. [3],chapter 3.2.3), there are certain domains of very active research in the international digital signal processing (in particular the HDTV) community that are of particular interest in the context of processing and/or storage of signals from our sensors.

IMAGE CODING

We usually threshold the signals from our detectors and record for every track hit their coordinates, maximum, integral, etc. If for some reason we cannot or do not want to define a threshold or if, because of real-time constraints, it is not possible to extract the whole information on-line, we may be forced to use standard signal coding techniques that have been developed for the storage and transmission of digital images (facsimile, digital television,...). Fig. 6 shows one of the many techniques (see e.g. [6]), we have tried on our signals. One sees how perfectly this particular one "fits" our signals. It preserves the essential information, only smoothes the background and reduces the 128 time samples of this example to 13 transform samples. We have used here the fastest of all known unitary transforms, the HAAR - transform, which seems particularly well suited to represent the signals of our electronic detectors.

ADVANCED SIGNAL PROCESSING ALGORITHMS AND ARCHITECTURES ([11])

We have mentioned above the calculation of a paraboloid through 4 points in the SPACAL example. Although a least squares fit through more points was not superior for SPACAL we would like to ask the question if an on-line least squares fit of some function z(u,v) is conceivable or not. A least squares fit of a paraboloid $z_i = a + b(u_i^2 + v_i^2) + cu_i + dv_i$ ($i = 1, m$) through the m points u_i, v_i, z_i can be written as the general linear least squares problem $|| Ax - z ||_2 = \text{minimum}$, where the matrix A(m,n) and the vector z(m) are known and usually $m > n$. In our case $n = 4$ and $x^T = (a,b,c,d)$. The method of normal equations $x = (A^T A)^{-1} A^T z$ is not stable [7]. If we used algorithms like the orthogonal triangularization $A = QR$ with $x = R^{-1} A^T z$ we could use the "systolic" architecture of Fig. 7 (derived in [8]) and a linear one for the backsubstitution. Here the circular boxes compute the coefficients of the Givens rotation and the square ones perform the rotation. In [9] a "systolic"

architecture is described that produces immediately the residuals of such a fit. Several different processors have been used to implement this type of algorithm. The DATAWAVE processor ([10]) would be ideally suited for this type of application. This is just one example of the type of problems that have been solved - theoretically and in practice - by the signal processing and/or HDTV community.

TECHNOLOGY OUTLOOK

Our present model of a pipelined system is the MAXVIDEO system. It represents the state of the art in image processing. Parallelism is used at all levels : at the task, image, neighbourhood and the pixel-bits level. For control and communication the industry standard VME - bus is used. The MAXbus used for data has an expandable bandwidth of at present 10 Mbytes/sec per pipeline. The **open** architecture, based on modularity and communication, allows to improve the functionality (bandwidth and processing power) at any moment by adding more hardware of existing or novel architectures and technologies, off-the-shelf or home-built. DATACUBE announces for ~ 1992 a 100 MHz version. Other companies sell 100 MHz versions today, but without a ROI feature and with none of the extremely powerful neighbourhood processors (a convolution with a n^2 mask needs n^2 passes through the system). Intermetall GmbH , Freiburg im Breisgau , from the ITT semiconductor group announced recently a completely programmable single chip video processor [10] with a 125 MHz clock rate and a peak performance of 4 Gops. The sustained throughput rate is supposed to be 750 Mbytes/sec. The price of the chip for large quantities could be in the range of 30 - 40 $. The chip is executed in 0.8 μ technology. They extrapolate this for 1993 in 0.4 μ technology to a 250 Mhz clockrate and a peak performance of 32 Gops. This processor has been designed for HDTV applications e.g. to save silicon area by having only one programmable processor for the treatment of all television standards.

Together with the possibility to process regions of interest defined by the first level trigger all these systems are very hot candidates for second level triggering.

CONCLUSION

A speed-up of several orders of magnitude in intelligent computing over today's on-line systems will be needed to make use of fine-grain detectors in future hadron colliders. This speed-up will have to come mainly from progress in architectures. We have analyzed representative triggering and data acquisition algorithms as low level image processing tasks. Sequential von Neumann computers can not exploit the parallelism in these algorithms. Fortunately we can benefit from the work of the very large international signal (image) processing and HDTV community and their commercial products. During the last decades they have solved many problems in the development of highly parallel signal (image) processing algorithms and architectures. Some of these systems are now (or in the near future) commercially available. They seem to deliver the necessary computing power and will certainly have an important role to play in the design of future triggering and data compaction systems.

ACKNOWLEDGEMENTS

I want to acknowledge the continuous support of A. Zichichi, LAA project leader, and would like to thank my colleagues R. K. Bock, V. Buzuloiu, A. Gheorghe.

REFERENCES

[1] S.Lone,R.K.Bock,Y.Ermolin,W.Krischer,C.Ljuslin,K.Zografos : Fine-grain parallel computer architectures in future triggers - NIM A288 (1990) pp. 507-516
R.Bock,W.Krischer,S.Lone : Benchmarking computer architectures for HEP real-time algorithms CERN-LAA/RT/88-08
[2] J.Pfennig : TRD trigger (this conference), G.Vesztergombi : Muon trigger (this conference)
[3] The SPACAL Collaboration : Scintillating fibre calorimetry at the LHC - CERN/DRDC/P1,1990
[4] R.K.Bock,V.Buzuloiu,W.Krischer : Algorithms and an image processing architecture for on-line electron identification from lateral profiles in SPACAL - CERN LAA RT/90-01.

[5] DATACUBE : MAXVIDEO User's Manual
[6] A.K.Jain,P.M.Farrelle,V.R.Algazi : Image Data Compression in Digital Image Processing Techniques
(editor M.P.Ekstrom)-ACADEMIC PRESS 1984
[7] G.H.Golub,C.F.van Loan : Matrix computations, John Hopkins Press, Baltimore, 1983
[8] W.M.Gentleman and H.T.Kung : Matrix triangularization by systolic arrays,
SPIE Vol. 298 Real-Time Signal Processing IV (1981), pp. 19-26.
[9] J.G.McWhirter : Recursive Least Squares Minimisation using a systolic array
Proc. SPIE, Vol. 431, Real-Time Signal Processing VI (1983), pp. 105-112.
[10] U.Schmidt,K.Caesar,T.Himmel : Data driven single chip video processor
IEEE Transactions on Consumer Electronics 8/90
[11] K.Bromley (editor) : Highly Parallel Signal Processing Architectures
SPIE Critical Review of Technology Series 19,vol. 614,1986
K.Bromley,H.J.Whitehouse : Signal Processing Algorithms,Architectures and Impl.s,SPIE : O-E/LASE 1986
S.Y.Kung : VLSI Array Processors - Prentice Hall 1988
H.T.Kung , C.E. Leiserson : Systolic arrays for VLSI
in DUFF,Stewart (eds.) : Sparse Matrix Proceedings 1979, SIAM 1979 ,pp. 256-282
H.T.Kung : Why systolic architectures ? IEEE Computer,vol.15, 1982 ,pp.37-46.

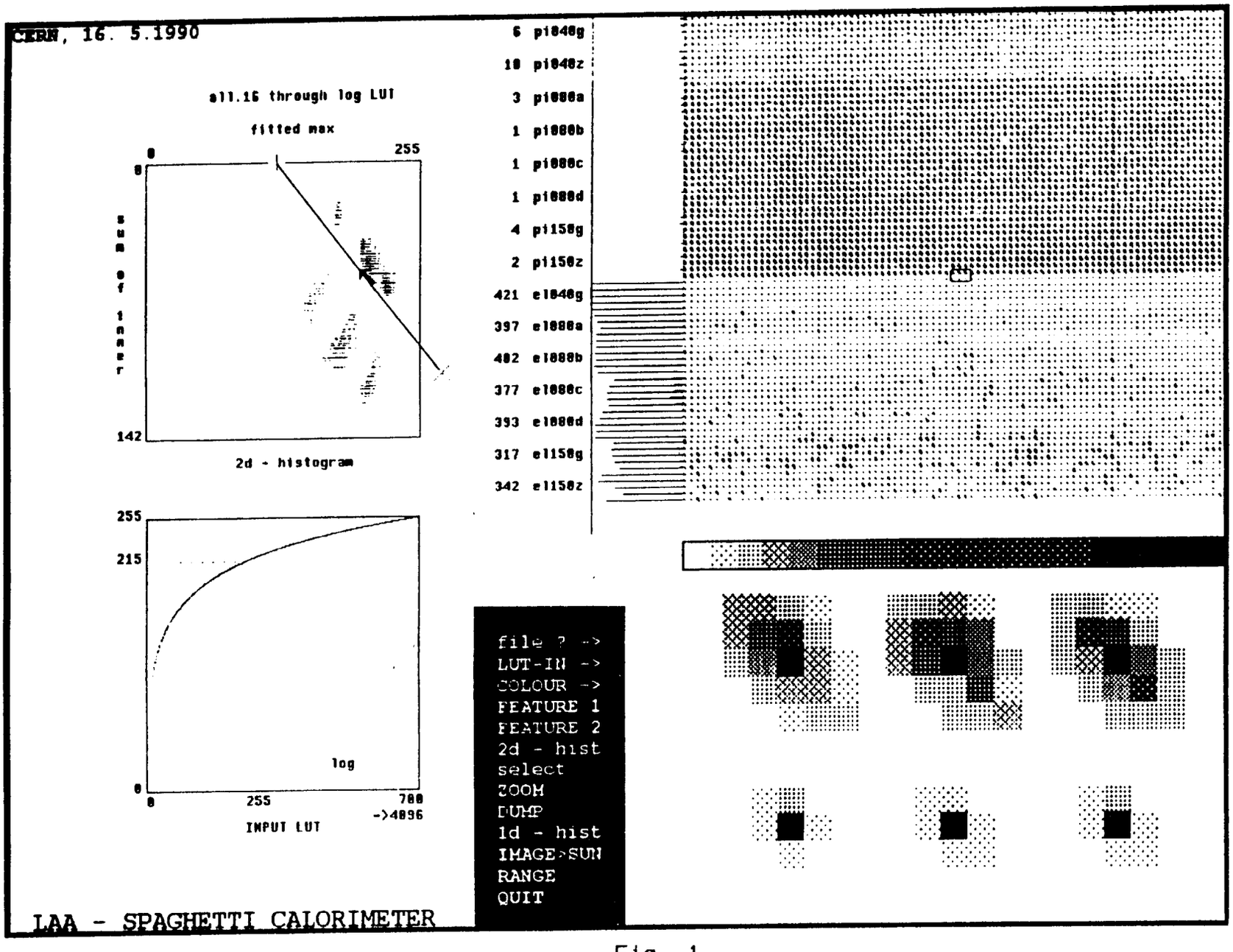

CERN, 16. 5.1990
all.16 through log LUT
fitted max
0
255
0
142
2d - histogram
255
215
0
0
255
700
->4096
log
INPUT LUT
6 pi040g
10 pi040z
3 pi080a
1 pi080b
1 pi080c
1 pi080d
4 pi150g
2 pi150z
421 el040g
397 el080a
402 el080b
377 el080c
393 el080d
317 el150g
342 el150z
file ? ->
LUT-IN ->
COLOUR ->
FEATURE 1
FEATURE 2
2d - hist
select
ZOOM
DUMP
1d - hist
IMAGE>SUN
RANGE
QUIT
LAA - SPAGHETTI CALORIMETER

Fig. 1

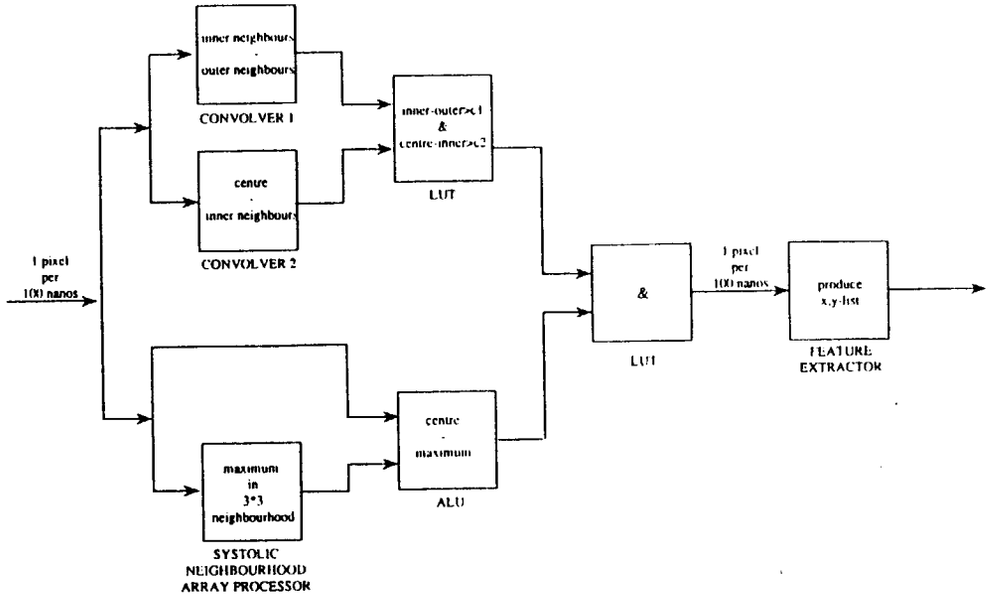


Fig. 2

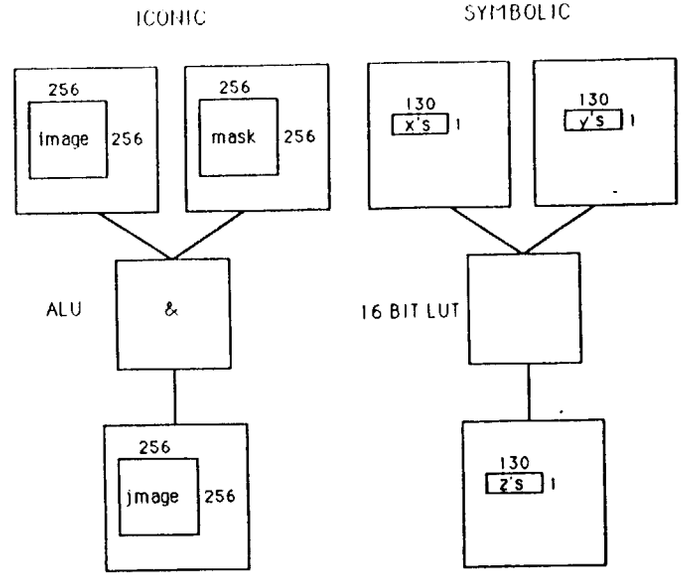


Fig. 3

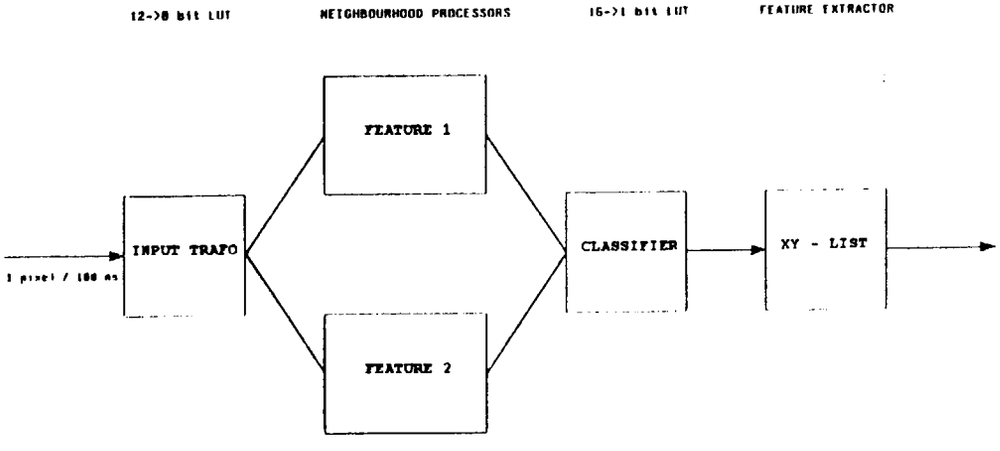


Fig. 4

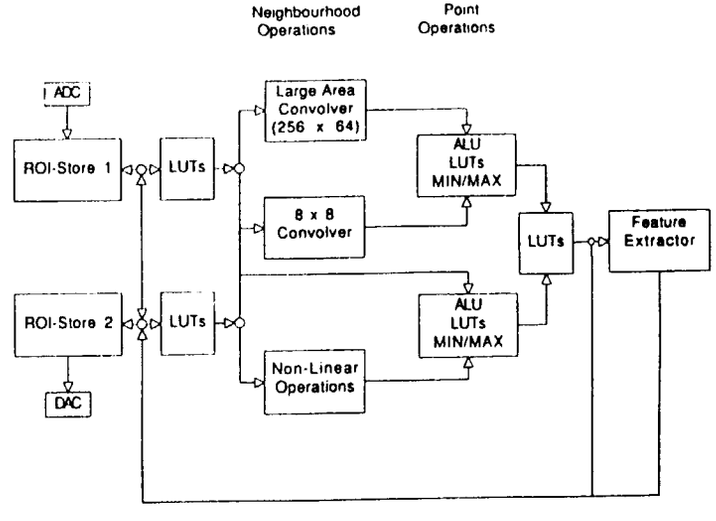


Fig. 5

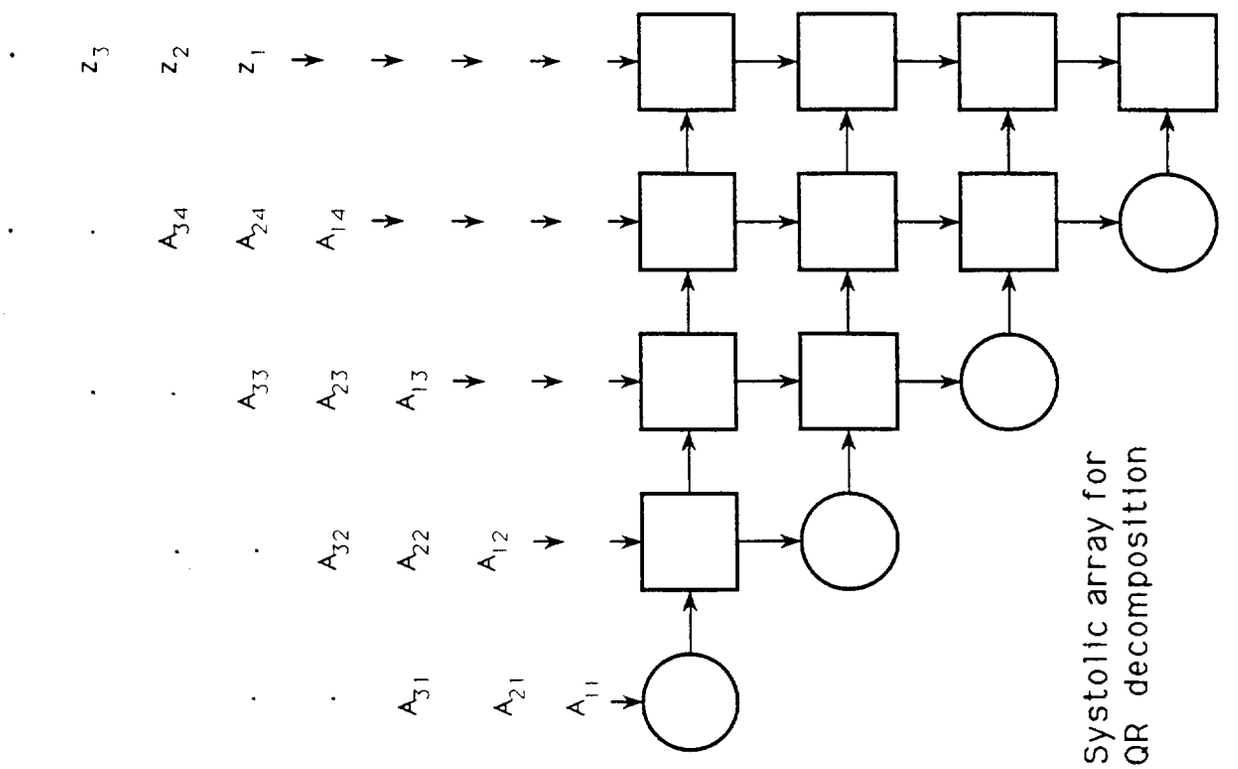

A_{11}
A_{21}
A_{31}
A_{12}
A_{22}
A_{32}
A_{13}
A_{23}
A_{33}
A_{14}
A_{24}
A_{34}
z_1
z_2
z_3
Systolic array for
QR decomposition

Fig. 7

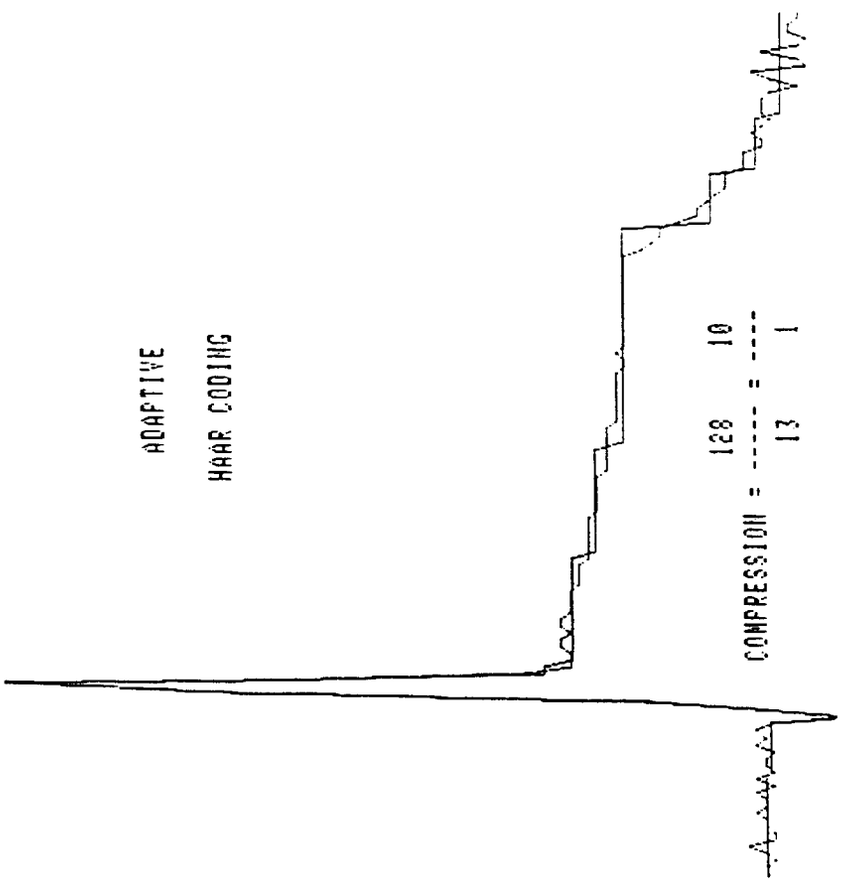

ADAPTIVE
HAAR CODING
COMPRESSION = 128 / 13 = 10 / 1

Fig. 6

Ongoing approaches to the Trigger Problem using Neural Networks

S.R.Amendolia
University of Sassari and INFN Pisa - Italy
and
B.Denby
Fermilab, Batavia, Il 60510,USA

Abstract

A possible way of implementing fast triggers for the future accelerators, where exceedingly high rates combine with a remarkable complexity of the event structure, relies on the use of Neural Networks. Their intrinsic parallelism, together with their natural pattern recognition and associative memory capability, are briefly discussed, and some applications currently being developed in the field are presented, in order to give a convincing proof of the potential strength of this approach.

1. Introduction

It is well known that the trigger problem in complex experimental environments, like those expected for very high energy interactions at the Large Hadron Collider, results in a remarkably difficult pattern recognition task, where high multiplicity events must undergo a reconstruction process already at the early trigger stages. The experience collected in the field of Neural Networks can be used to design a dedicated "neural" machine which can perform this task in a very short time possible, something quite demanding using conventional computing techniques.

2. Neural Networks

2.1 Definitions and Properties

A Neural Network is a large network of simple interconnected processing elements called *neurons*. (Fig. 1) [1]. The interconnection between any two neurons i and j is characterized by a coupling constant w_{ji} (*the weight*). If the analog output of a neuron i is called $(output)_i$, the input signal to neuron j is a linear combination of the output of the neurons connected to it, namely:

$$(input)_j = \Sigma_i \, w_{ji} * (output)_i$$

Each neuron operates on the input signal it receives and produces an output which is a well defined function of the input: $(\text{output})_j = f\ [(\text{input})_j]$. The function f is called the *activation function*, and its form depends on the kind of network being implemented. One of the most commonly used activation functions (Fig. 1) is the sigmoid: its non linearity allows the network to behave in a more efficient way than just a linear associator, still preserving the possibility of computing the values of the weights in an analitical way .

This model of the elementary neuron originates from the studies on the structure of the brain: here millions of neurons interact via a chemical excitatory-inhibitory mechanism, mediated by axons and synapses. Hardware implementations of such a structure as an electrical circuit are today limited to few hundred neurons, which limits the scope of the task one can envisage to perform.

Neural Network are programmed by determining the type of activation functions, the number of neurons needed, and the values of the weights between neurons. For the latter operation *programming techniques* exist, while there is no definite tool to evaluate a priori the best architecture for the network, which is done on a trial and test basis.

Information storage inside the network can be either *local* , when each neuron represents a single datum (i.e. it is associated with a specific parameter of the problem), and the weights, representing the relation between any two data, can in some cases be imposed from the outside; or *distributed* , when the information is shared among neurons, and the weights carry a much more complex meaning, their values having to be determined through a so-called *learning process.*

A fundamental property of Neural Networks is that they can discriminate higher than linear relations between input data, thus behaving more powerfully than conventional techniques used for cathegoryzing data structures (e.g. the discriminant analysis). This property depends strictly on the behaviour of the single neuron (its non linear activation function) and on the structure of the network (the way in which neurons are connected).

Two kinds of problems are particularly well suited to the Neural Network approach: the Pattern Classification (including the Associative Memory capability, i.e. the ability at reconstructing underlying structures even in presence of incomplete input data), and the Function Minimization (even in the case of NP-complete problems).

2.2 Basic Examples

One type of network widely used to perform Pattern Classification deserves a special mention: the Feed Forward Network. Here the information flow has a defined direction, from the set of input neurons (into which the input data are fed) to the set of output neurons, via one or more sets of hidden layers' neurons; a neuron in a layer can communicate only with neurons in the subsequent one. This allows to implement a

special supervised learning algorithm, called the backpropagation method, in which the network is fed with several training patterns, and for each of them the network output is compared with the expected result (the target output associated to that training input): the weights are modified accordingly, attempting at minimizing the quadratic error function

$$E = \Sigma_{p,i} \mid target_{p,i} - output_{p,i} \mid^2$$ where index p ranges on the training patterns' set and i ranges on the output neurons' set

In order to perform Function Mimimization, Neural Network architectures in which all the neurons are connected to each other are used (recurrent networks, with feedback capabilities). The network can be regarded as a dynamical system, described by a set of general coordinates (the state of each neuron). A point in state space represents the instantaneous condition of the system, and the equations of motion of the system describe the flow in state space. An *energy* function is associated to the states of the system such that trajectories in state space lead to a global minimum point of the function. If the energy function is directly related to the cost function of an optimization problem, then the system architecture describes the problem, the initial conditions of the network determine a problem instance, and the net evolves in time seeking a global minimum, i.e. a better solution to the problem. The study and the description of these networks (seen as many-interacting-element systems) greatly exploits the parallel which can be estabilished with statistical mechanics methods.

3. The trigger

In a High Energy Physics experiment, the trigger system has to select events from background, relying on their physical signature and/or content. This has to be achieved in an environment affected by detector's noise, systematic errors and inefficiencies. Quite often this cannot be obtained just using first momenta of the distributions of physical variables (like the multiplicity), but requires advanced computations of parameters (like track finding, event topology description, etc.).

What is required is a feature extraction , i.e. the capability of classifying a set of interrelated elements (hits, pulse heights, computed parameters) as representing the physical content of the event, which is so tagged as belonging to a pre-determined cathegory.

Summaryzing, to build up a trigger one needs Function Minimization, Associative Memory capability (because of noisy or incomplete data) and Pattern Classification , all of which can be obtained using Neural Networks.

4. Ongoing approaches

4.1 Calorimetry based B-triggers

Beauty events selection in a 4π-collider experiment has been tested with the help of a Feed Forward Neural Network [2]. The CDF electromagnetic calorimeter towers were used to feed data (pulse heights) into such a network: given the two towers with the highest signal in an event, two squared regions of 64 towers surrounding them in the η-Φ space constituted the 128 input pattern to the network. The latter was trained to recognize B-jet events, via the backpropagation method, using a set of real background CDF events, and a set of Montecarlo produced b-bbar events. Several configurations for the hidden neurons' layers were tried; preliminary results account for a 65% B-events recognition coupled with a 95% background events rejection.

4.2 Track finding

A study on straight track finding in a straw tube arrangement has been carried out using a Feed Forward Network configuration [3]: 14 input neurons received the drift time information form 14 straw tubes packed into a four-layer arrangement (Fig.2). The network, featuring a 25-neuron hidden layer, was able to reconstruct the incoming straight track angle with a r.m.s. error of 0.5 ° (straw tubes "pitch" was 6.0 °).

Another approach attempts at finding tracks, bent by an axial magnetic field, in a central detector environment [4,5]. Hits in the R-Φ projection are used. The system exploits a recurrent network configuration, where a neuron represents the link (i.e. a segment of track) between any two hits. A link has to exist (that is a neuron has to produce a "high" output value) if its two hits belong to the same track. Neurons interact with each other via an externally computed weight function which favours the "reinforcement" of neurons sharing a hit, and at a smooth relative angle: starting from an all-neurons-high initial state, the network evolves, after few iterations, toward a state in which only meaningful links survive, describing tracks in two-dimensional space (Fig.3).

4.3 Vertex trigger

A similar approach is being used in the study of a trigger on secondary vertices in collider and fixed target configurations. The aim is to separate Beauty events from background looking at the secondary vertex structure of the event [6]. Secondary vertices are produced in B events by direct B-mesons decay, and by possible subsequent charmed mesons decays.

Assuming that track finding is performed beforehand, one can describe tracks as points in D-Φ space, where D is linked to the impact parameter and Φ is the production angle at

vertex. Tracks coming from a secondary vertex at distance R from the primary one obey the relation

$$D = - R \sin [\Phi - \text{arctg}(y_v/x_v)] \qquad \text{where } x_v, y_v \text{ are the vertex coordinates}$$

Then primary vertex tracks lie on a quasi horizontal straight line, while secondary vertex tracks lie on negatively bent lines (Fig.4). In the network, configured as a recurrent one, neurons represent secondary vertex candidates (i.e. links between any two points in the D-Φ track plot). An externally determined weight function governs the interaction of neurons with each other, favouring the survival of neurons which lie outside the primary vertex line, and are aligned to form a secondary vertex structure in D-Φ space. Due to differences in the event topology between collider and fixed target environments, the D-Φ plots look different in the two cases, but the network (tried in a preliminaryb study on Montecarlo data) seems to be able to tag B-events and background events with remarkable performance (50% B acceptance and 1:10,000 background rejection for the fixed target case, Fig.5).

5. Conclusions

What we reported here is a partial review of works still in their preliminary phase. We are encouraged by the success of these approaches in so many differents domains of the trigger pattern recognition problem. The simplicity of the Feed Forward Networks facilitates their implementation on existing hardware chips, which will allow to perform the task in times of the order of a microsecond, as required by trigger applications.
The intrinsic parallelism of the recurrent networks is another major advantage: just simulating such networks on a sequential computer, without going to hardware chips, has proved to be more effective than using conventional algorithms, when applied to offline analysis problems.

References

[1] D.E.Rumelhart, J.L.McClelland "Parallel Distributed Processing" MIT Press, 1986

[2] B.Denby, M.Campbell et al. "Neural Networks for Triggering" Fermilab prep. Conf-90/20, Submitted to IEEE Trans. on Nucl. Sci.

[3] B.Denby, E.Lessner,C.S.Lindsey "Tests of Track Segment and Vertex Finding with Neural Networks" Fermilab-Conf-90/68

[4] B.Denby "Neural Networks and Cellular Automata Algorithms" FSU-SCRI-88-141, Florida State University

[5] C. Peterson "Track Finding with Neural Networks" NIM, A279 (1989) 537b

[6] S.R.Amendolia and B.Denby, NAxx Collaboration, to be published

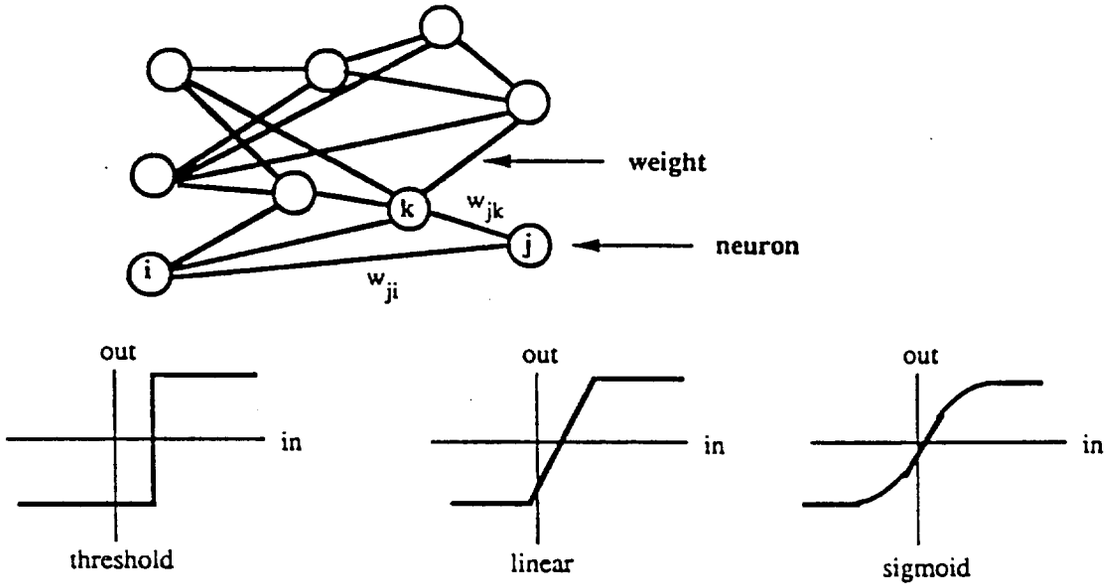


Fig.1 - Sketch of Neural Network architecture and some activation functions

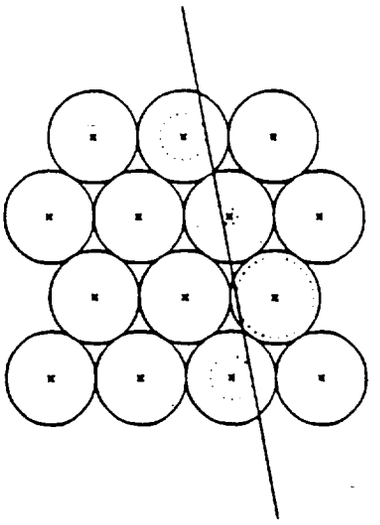


Fig. 2 - Straw tubes arrangement

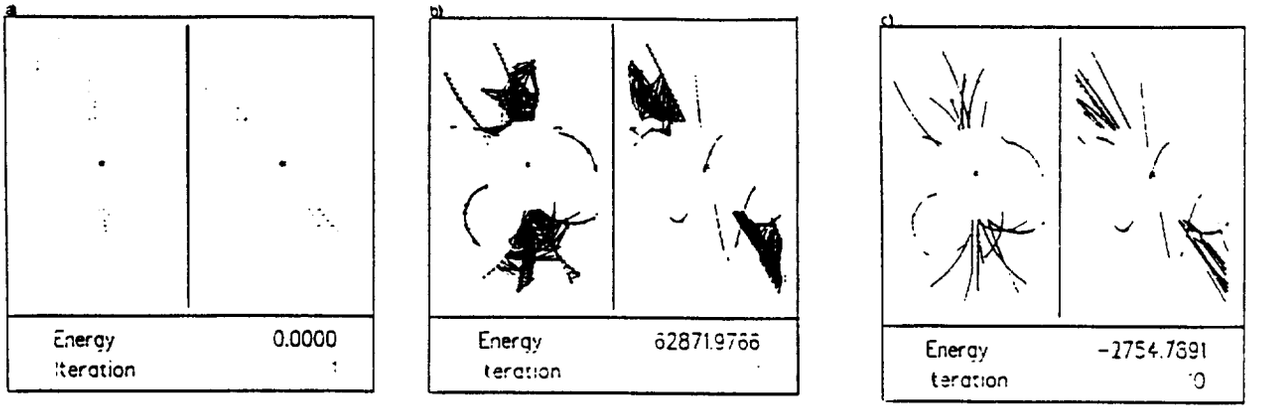


Fig. 3 - Track finding on simulated Delphi events - a) hits . b) all links possible . c) after setting. (from Ref. 4)

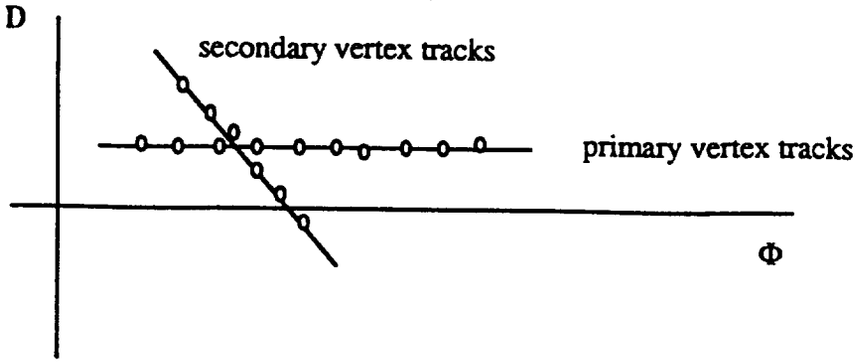


Fig. 4 - D-Φ plot for primary and secondary vertex tracks

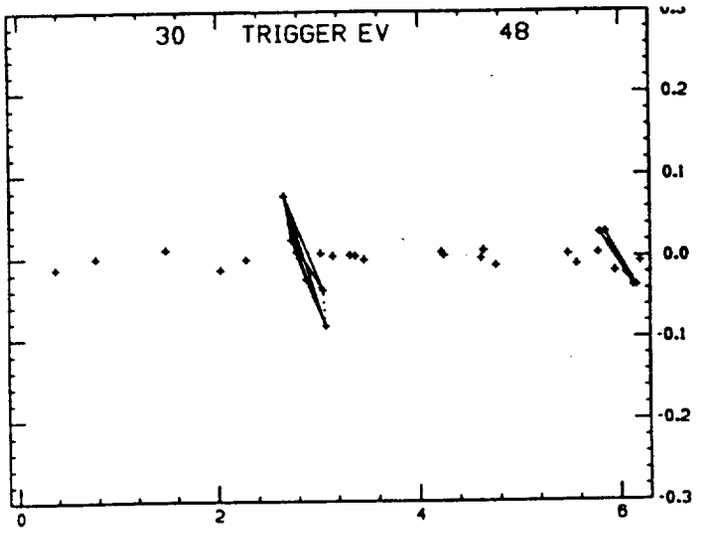
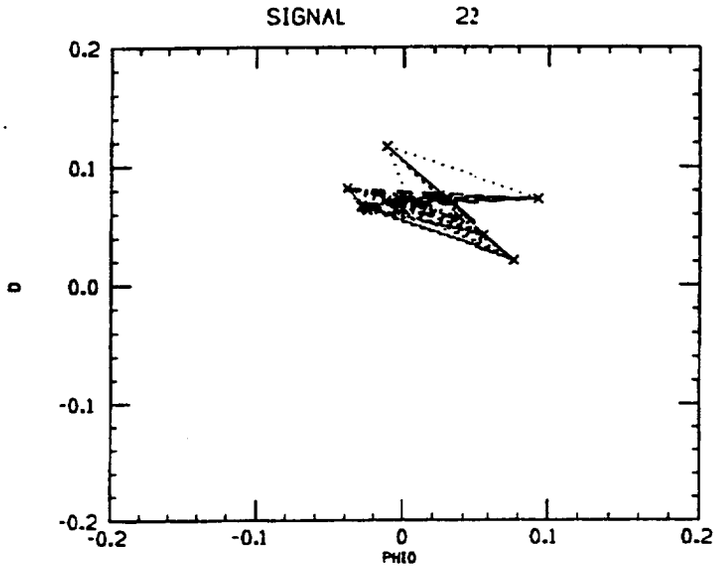


Fig. 5 - D-Φ plot for collider and fixed target environments



SECOND-LEVEL MUON TRIGGER CONCEPT FOR THE LARGE HADRON COLLIDER

G. Odor(*) and F. Rohrbach
CERN, Geneva, Switzerland

G. Vesztergombi(*)
Max-Planck-Institute, Munich and CERN

ABSTRACT

A scheme for second-level muon trigger is proposed for high luminosity LHC detector. Massively parallel processor system based on ASP architecture is being built in the frame-work of MPPC project. The basic ideas for the triggering algorithm are presented here.

1. DETECTOR CONCEPT

At the expected extremely high luminosities ($> 10^{34}$ cm^{-2}s^{-1}) at LHC muons offer an advantage over other particles since the trigger can be performed after a thick absorber where the particle flux is low. Therefore single and di-muon triggers will play a crucial role in such experiments as the search for the Higgs-boson through the

$$H \rightarrow \mu\,\mu\,\mu\,\mu \text{ and/or } H \rightarrow \mu\,\mu\,e\,e$$

decays. In order to be more specific in describing the proposed 2-level trigger scheme we adopt the so called "Compact Muon Solenoid" detector concept [1]. It consists of a high field superconducting solenoid surrounded by an iron muon filter, magnetized by the return flux (fig. 1), the first 10 λ absorption length is provided by the calorimeter put inside the solenoid. Ring shaped muon chambers are positioned at radii:

$r_0 = 3.5$ m (inner solenoid radius)

$r_1 = 4.0$ m (outer solenoid radius)

$r_2 = 5.0$ m (middle of the iron-filter)

$r_3 = 6.0$ m (outer filter radius)

$r_4 = 6.5$ m (outer edge of the detector)

(*) On leave of absence from Central Research Institute for Physics, Budapest, Hungary.

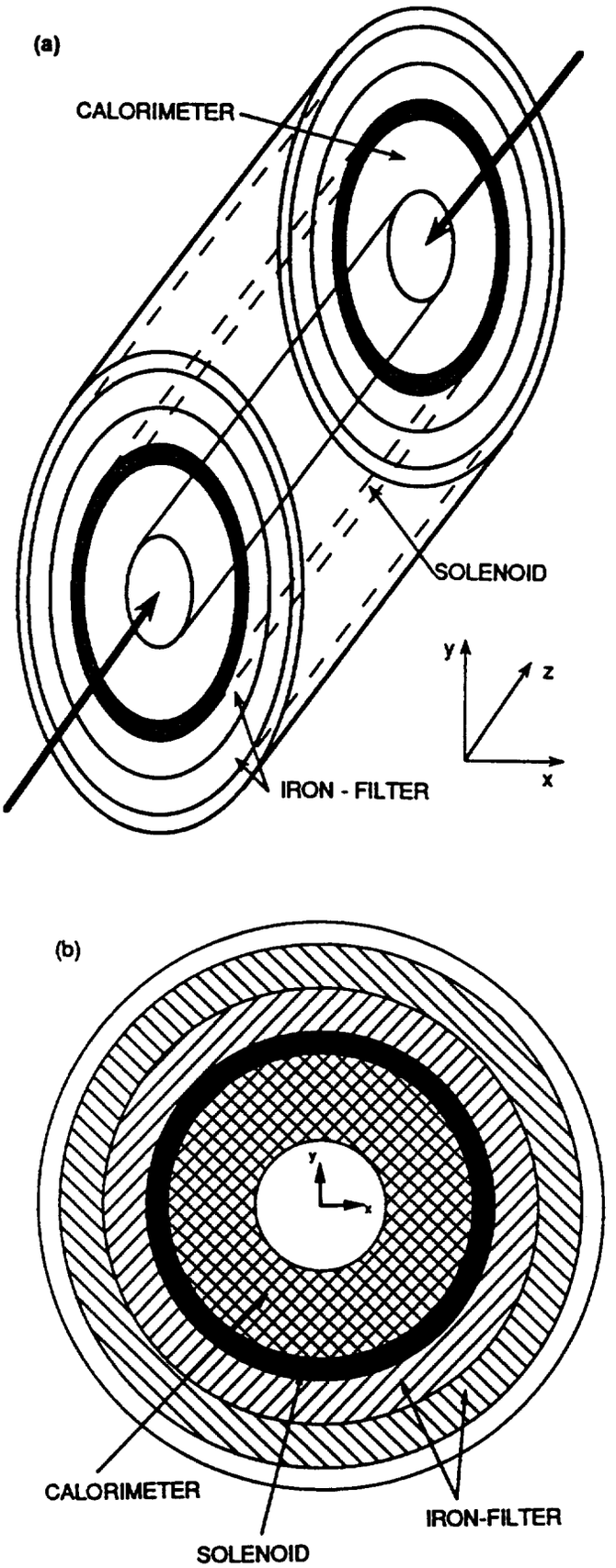


Fig. 1 (a) "Compact Muon Solenoid", (b) (x,y) projection

The magnetic field is assumed to be: $B_{inside} = +4$ Tesla; $B_{outside} = -2.3$ Tesla

In the next we shall deal with the barrel-part of the detector, recording only the (r, ϕ) projection of the particle trajectories (numbers are quoted only to indicate the scales, there is not existing any definite detector design yet).

The trigger is assumed to be worked out on two levels:

(a) the "hard-wired" 1-level trigger expected to cut the rate down to the 10^5 Hz level;
(b) a more sophisticated 2-level "soft" trigger will select high P_t single or di-muon events according to the adjustable threshold values.

In this talk the 1-level decision is taken to be granted and the 2-level trigger logics will be discussed only.

2. PRINCIPLE OF PARALLELISM

The solenoid field and the fact that the interaction vertex is known with extreme precision (±10 microns) in the plane transverse to the beam provides a highly symmetric arrangement. In the frame-work of data processing this inherent CIRCULAR-SYMMETRY can be converted into highly PARALLEL-ALGORITHM. In the (r, ϕ) plane the particle trajectories are defined by 2 parameters: emission angle ϕ_{emi} and transverse momentum P_t. We are interested in only the rather "stiff" tracks which experience modest deflection even in this strong magnetic field, therefore they are not curling up and will cross the muon-chambers at

$$(r_0, \phi_0), (r_1, \phi_1), (r_2, \phi_2), (r_3, \phi_3), (r_4, \phi_4)$$

points consecutively. In case of 2 tracks with identical P_t but different emission angles ϕ_{emi}^A and ϕ_{emi}^B the angular differencies relative to the innermost chamber:

$$C_i = \phi_i^A - \phi_0^A = \phi_i^B - \phi_0^B \quad \text{for} \quad i = 1, 2, 3, 4$$

are independent of the emission angle. This invariance can be exploited by applying a massively parallel processor which is able to search for all muons in a given (P_t, $P_t + \Delta P_t$) bin simultaneously for each emission angle, reducing the 2-dimensional (r, ϕ) problem into a single one. One can pre-calculate for each P_t bin the relevant {C_1, C_2, C_3, C_4} so called TRACK-CODE combinations. The proposed 2-level trigger logic makes an exhaustive search in a way described in the subsequent sections for all 5-point combinations having TRACK-CODES corresponding to muon trajectories above a preset $P_t^{Threshold}$.

3. ASSOCIATIVE STRING PROCESSOR

We are proposing to work out the 2-level trigger by the massively parallel processor developed in the frame-work of the MPPC project [2]. This Associative String Processor

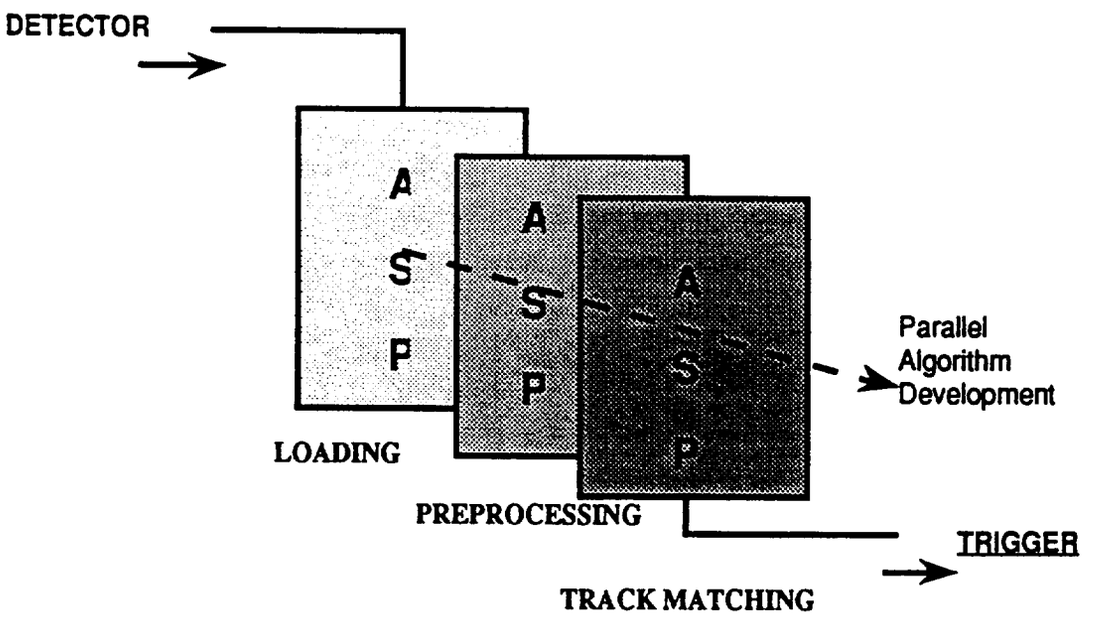
(ASP) is based on the concept of parallel processing, providing high performance through the simultaneous operation of MANY comparatively LOW performance processing elements [3]. It belongs to the single instruction, multiple data (SIMD) class of parallel processors. These machines apply one instruction at a time to a large number of processing elements (which are called APEs in case of ASP), each storing a different data item, but capable of performing the same operation on these data simultaneously. In this way a SIMD machine exploits the opportunity for parallelism inherent in all repetitive computation.

In our case the phrase LOW performance processing element really should be taken literally. APEs possess only 64 + 6 bits of inside the processor "addressable" memory in the DATA and ACTIVITY REGISTER; calculations are executed by a 1-bit CPU. What makes them extremely efficient is the COMPARATOR, which transforms these simple "1-bit adders" into Associative Processing Elements (APE), enabling content addressable associative computing.

The communication between APEs is provided along a linear chain (here comes the STRING in the name ASP). Out of the many possible features provided by the very flexible ASP architecture we rely mainly on two basic ones. Depending on the instruction in a given moment the whole system can be regarded as an ASSOCIATIVE MEMORY: each APE representing a memory cell; or in an other moment as a single-bit SHIFT-REGISTER logically connecting into a string one given bit of each APE.

4. "ICONIC" MAPPING

The principle of the proposed trigger can simply be illustrated by the following symbolic sketch:



From the detector the loading of the hit pattern into ASP is done in a special way in order to minimize the **loading** time to a few μs for the full detector. Then the **preprocessing** is performed generating the "master-points" of the hit pattern. Finally the **track matching** search occurs for finding all muons according to their sign and P_t. In the next as an illustration for ASP programming we concentrate only on the track matching algorithm.

Generally the bottle-neck in massively parallel systems containing several thousands of processing elements arises in the communication network when data movement is required between many processors at the same time. In order to avoid the occurrence of such situations for efficient programming the data movements should be kept at the absolute minimum level. This can be achieved if from the beginning each data item is positioned as near as possible to the locations where it will be used. In case of 2-dimensional geometrical problems (like our muon tracks) the most natural way is to store the hit pattern in a BIT ARRAY which faithfully represents the topological relations between the points as it is seen in the graphical image. This so called "ICONIC" MAPPING can be achieved in two logical steps:

(a) The rotational symmetry of the detector is transformed to "translational symmetry modulo (2 π)" under the condition that the wire pitch in the chamber rings is proportional to their radii i.e:

$$\Delta\phi = \text{fix} \qquad \text{for all } r_i \qquad i = 0, 1, 2, 3, 4.$$

(of course, these are only symbolical wires. In our terminology the value of φ digitized in Δφ steps is called "wire", as if it were the wires of a cylindrical MWPC. The really measured coordinates can be transformed to them by using e.g. Look-Up-Tables during data loading).

(b) Mapping onto the BIT ARRAY realized by bits of the APE Data Register is performed by setting to 1 the BIT # i in APE # k if the WIRE # k was hit in CHAMBER # (i-1) as it is shown in fig. 2.

5. TRACK-CODE SEARCH

The above iconic mapping assures that identical "wires" from different chambers are stored in the same APE [4]. To emphasize this fact each APE has this wire number as a label, prestored in bits #33–#48.

There is a special class of tracks, the very stiff ones (track "A" in fig. 2) which are going straight through the detector despite the strong magnetic field. They possess the unique TRACK-CODE = {0, 0, 0, 0}. By definition, the 5 hits belonging to such tracks will be stored in a single APE. In the ASP it is trivial to identify those APEs which has this bit combination. It behaves as an ASSOCIATIVE MEMORY, when the "content-addressing" is

performed through BITS #1–#5 and the memorised data retrieved from BITS #33–#48. If there are more than one such very high momentum muon with {0, 0, 0, 0} code, then the read-out is performed sequentially along the string. As it was mentioned in the introduction there are only few tracks which can reach the outer rings of the detectors, therefore it is unprobable that 2 or more track produces a false code match by conspiracy.

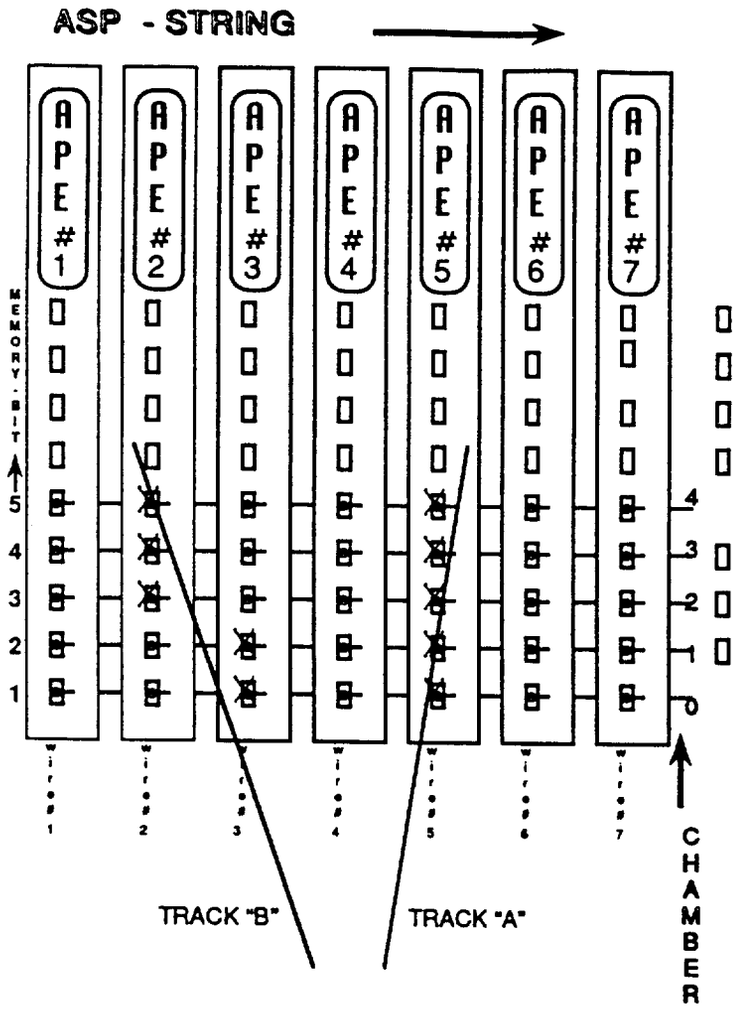


Fig. 2 Iconic mapping of muon-data on ASP

The {0, 0, 0, 0} code is identical for positive and negative muons, but in all other cases to each positive code corresponds a distinct negative one. Here we discuss only positive codes but it is understood that there is a parallely running logic for negatives with reversed codes.

Any $\{C_1, C_2, C_3, C_4\}$ code can be reduced to {0, 0, 0, 0} by shifting BIT COLUMN #(i+1) by C_i steps reducing the problem to the previously solved one. Column shifting is well adapted for ASP because in some sense it can be regarded as a 1-bit SHIFT-REGISTER along the communication STRING.

As an example a possible TRACK-CODE list is reproduced in table 1. for muons with $P_t > 10$ Gev/c assuming wire spacing corresponding to 2 mrad angular resolution. The list is shown in ascending order starting from {0, 0, 0, 0} and finishing at the "most curved" track with {14, 31, 35, 35} code. As the ascending order is preserved in almost every step digit by digit, that is generally $C_i^k \leq C_i^{k+1}$, the total number of shift steps is approximately equals to

$$N_{step} \cong C_1^{last} + C_2^{last} + C_3^{last} + C_4^{last} = 115 \ .$$

Of course, these numbers are only for illustration. For real detector the r_i positions, angular resolution, P_t threshold etc. should be appropriately adjusted. The message of this simple example, however, is clear in the sense that one expects on the order of 100 TRACK-CODES.

	C_1	C_2	C_3	C_4
TRACK-CODE # 1	0	0	0	0
TRACK-CODE # 2	0	0	1	1
TRACK-CODE # 3	0	1	1	1
TRACK-CODE # 4	0	1	2	2
TRACK-CODE # 5	1	1	1	1
TRACK-CODE # 6	1	1	2	2
TRACK-CODE # 7	1	2	2	2
TRACK-CODE # 8	1	2	3	3
TRACK-CODE # 9	1	3	3	3
TRACK-CODE # 10	1	3	4	4
TRACK-CODE # 11	2	3	4	4
TRACK-CODE # 12	2	4	4	4
:				
TRACK-CODE # 51	7	16	19	19
TRACK-CODE # 52	8	16	19	19
TRACK-CODE # 53	8	17	19	19
TRACK-CODE # 54	8	17	20	19
TRACK-CODE # 55	8	17	20	20
TRACK-CODE # 56	8	18	20	20
TRACK-CODE # 57	8	18	21	21
TRACK-CODE # 58	9	18	21	21
TRACK-CODE # 59	9	18	22	21
TRACK-CODE # 60	9	19	22	22
TRACK-CODE # 61	9	19	23	22
TRACK-CODE # 62	9	19	23	23

	C_1	C_2	C_3	C_4
:				
TRACK-CODE # 92	14	29	33	33
TRACK-CODE # 93	14	29	34	33
TRACK-CODE # 94	14	29	34	34
TRACK-CODE # 95	14	30	34	34
TRACK-CODE # 96	14	30	35	34
TRACK-CODE # 97	14	30	35	35
TRACK-CODE # 98	14	31	35	35

Table 1 Fragments of TRACK-CODE list for $P_t > 10$ GeV/c, $\Delta\phi = 2$ mrad

6. PERFORMANCE SCALING

Assuming that the processing of a given TRACK-CODE (shift + search) takes about 200 ns, then for an exhaustive search of 100 codes the response time will be 20 μs. There are ways, however, to speed up this process. Due to the fact that the codes are exclusive one can test any segment of the ordered TRACK-CODE list separately. The price of this speed-up is that one should have an additional parallel substring for each of these list segments. Each substring has its own starting code $\{C_1^{ini}, C_2^{ini}, C_3^{ini}, C_4^{ini}\}$ using the so called "associative list loading" the data can be preshifted to this position during the loading procedure, therefore the number of shifts required for a given segment will be reduced to

$$N_{seg} = (C_1^{out} - C_1^{ini}) + ... + (C_4^{out} - C_4^{ini})$$

steps, where the "out" index is referring to the last code included in the segment. In our previous example a simple doubling the number of APEs would reduce the processing time to the 10 μs range. The total number of APEs would be in this case $N_{APE} = 2 * 6284$, where the factor 2 takes into account the parallel system for negatives, which is well within the capacity of the first MPPC machine with 16 k APEs.

In case of our TRACK-CODE algorithm there is a simple scaling law between performance and number of APEs. N times greater speed is achieved by N times more processing elements or N times finer angular resolution (which generates approximately N times more TRACK-CODEs) requires N times more APEs to preserve the same speed. Though, at first glance, these perspectives look frightening, in reality the APEs are representing the cheapest part of the project. In mass production one expects a price of about 1 $/APE thus even a the total amount of one million APEs seems to be modest sum compared to the cost of a

whole LHC detector. In our case we are really very lucky that the ASP through this algorithm provides performance which is proportional to n, the number of processor elements, because in practical cases generally only log(n) behaviour is observed in performance increase as function of n. This "second order" substring parallelism makes our ASP algorithm rather fast, flexible and cost effective.

7. CONCLUSION

We have shown that the circular symmetry inherent to the CMS detector can be exploited for parallel tracking algorithm. It is demonstrated that the TRACK-CODE search method reduces tracking calculations to simple bit-shift operations. Speed-up by "second order" parallelism (i.e. installing parallel running additional substrings) promises fast response times in the range of ≤ 10 μs. As the search for **all** muons is executed in parallel, therefore on can get an effective **multi-muon** trigger.

One should remark that the TRACK-CODE search represents only part of the tracking program executed by the ASP. In reality the simple muon-chambers assumed so far are multi-layer detectors. For them one needs a clustering algorithm which produces the so called "master-points" for the subsequent tracking. This master-point algorithm is based on the local hit pattern associations which are ideally suited for the ASP architecture and does not produce significant overhead on the trigger response time.

The relative cheapness and fault-tolerant architecture makes ASP attractive for large scale applications. The first **on-line** ASP system is expected by the end of 1991 from the MPPC project.

REFERENCES

[1] K. Eggert et al., ECFA talk , this conference.

[2] F. Rohrbach et al., Proposal–MPPC project, CERN/EF/MPPC 89–1.

[3] R.M. Lea, IEEE Micro, (1988) 10–29.

[4] G. Vesztergombi , Computer Physics Communications, 57 (1989) 290.

A local/global architecture for level 2 calorimeter triggers

D. Crosetto INFN Torino Italy
N. Ellis University of Birmingham Birmingham U.K.
G. Mornacchi CERN Geneva Switzerland
J. Strong R.H.B.N.C. Egham Surrey U.K.

Introduction

A major problem in triggering and data acquisition at LHC is the quantity of data which must be moved and stored at each stage of the selection process. The architecture proposed here, see Fig.1, restricts the data flow to manageable rates and allows sufficient time for programmable devices operating sophisticated algorithms to process data for a level 2 trigger. Using the example of a calorimeter based isolated electron trigger we present some initial results of a system simulation.

For a first level trigger, most proposals [1] assume that data are stored in a pipeline with a depth of at least 64 elements. This allows approximately 1 μs for the collection of the trigger information, its processing by hardware units and distribution of the accept /reject signal to all parts of the experiment. The level 1 system must produce a decision for each machine bunch crossing i.e. at intervals of 15 ns. It is believed that the rate for level 1 acceptance can be restricted to about 10^5 Hz at the highest luminosities proposed for LHC while keeping a high efficiency for retaining 'interesting' physics events. Level 2 is required to reduce the acceptance rate by at least two orders of magnitude.

In order to achieve the very short decision time at level 1, information is grouped with a granularity significantly larger than the detector basic cell size. For our estimates we have considered an electromagnetic calorimeter with a basic cell size of 0.02 in phi (ϕ) by 0.02 in pseudorapidity (η) with 2 depth samples and 2.10^5 channels. Based on Isajet studies [2], a level 1 trigger calorimeter granularity of 0.2 by 0.2 in $\phi\eta$ space with no electromagnetic depth information appears capable of providing a satisfactory trigger rate while maintaining the number of electronic channels and stages in the trigger to a feasible level.

If level 2 is to produce a substantial reduction in the level 1 trigger rate then, where appropriate, information must be processed at the basic cell size, additional information on depth or timing profiles added and more sophisticated algorithms

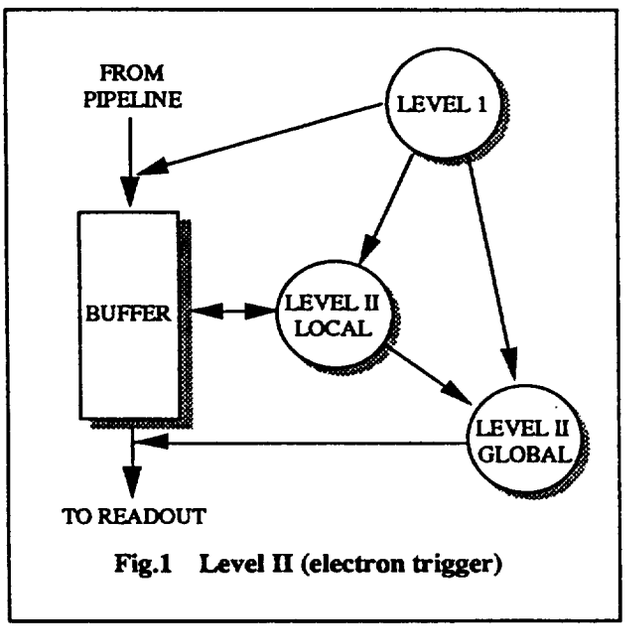


Fig.1 Level II (electron trigger)

used to evaluate the data. Total energy, jet and missing P_t triggers are formed at level 1 using large granularity and relatively coarse energy bins and only marginal improvements can be made in these triggers at the second level by making use of finer details. For the isolated electron trigger, however, a significant improvement can be obtained by using more detailed information. Where possible, data from several detectors should be correlated but, for this exercise, we have only considered the problems associated with analysing calorimeter data.

Local and global processing

For the calorimeter described above and assuming that the data from each channel has been formed into a digital word of two bytes, the calorimeter data occupies 4.10^5 bytes and transferring this data to level 2 processors would require a bandwidth of 4.10^{10} bytes/s. Zero suppression could be used to reduce the transfer requirements but would result in a more complex data format and a concomitant increase in processing time.

We propose to use the level 1 information to indicate areas of interest in the calorimeter and to transfer data only from those areas to level 2 processors. Allowing for edge effects, an isolated electron trigger at level 1 specifies the position of a cluster to an area of about 0.3 by 0.3 in $\phi\eta$ space. For each cluster, only data from 0.2% of the calorimeter, about 1 kbyte, need be transferred to level 2 for validation, and the data transfer rate has been reduced to 10^8 bytes/s/cluster.

Sustained transfer rates of a few 10^8 bytes/s are possible but not trivial and are unnecessary if data are transferred to a processor connected to a restricted part of the calorimeter i.e. a local processor. For a local processor covering an area of 0.3 by 0.3 in $\phi\eta$ space, the local trigger rate is about 200Hz and the local data transfer rate is only 2.10^5 bytes/s. Under these circumstances, transfer rates of only 10^7 bytes/s and processing times approaching 1 ms can be considered. Note that, when overlaps are taken into account, about 1000 local processor are needed at level 2.

To correlate information from several areas and to add information, from other detectors, which cannot be supplied to the local processor, global processors are used. The volume of data to be transferred from the local to the global processor can be limited to a few words providing, for example, the position of the cluster, its energy and fit quality. The accept/reject decision is made at the global processor level (see Fig.2). Because memory uses silicon efficiently, front end storage of data for long level 2 decision times is not a serious problem. In the multi-chip module design of Goggi and Löfstedt [3], a derandomizing buffer, a memory for data storage and all the level 2 and readout interface logic has been included on the

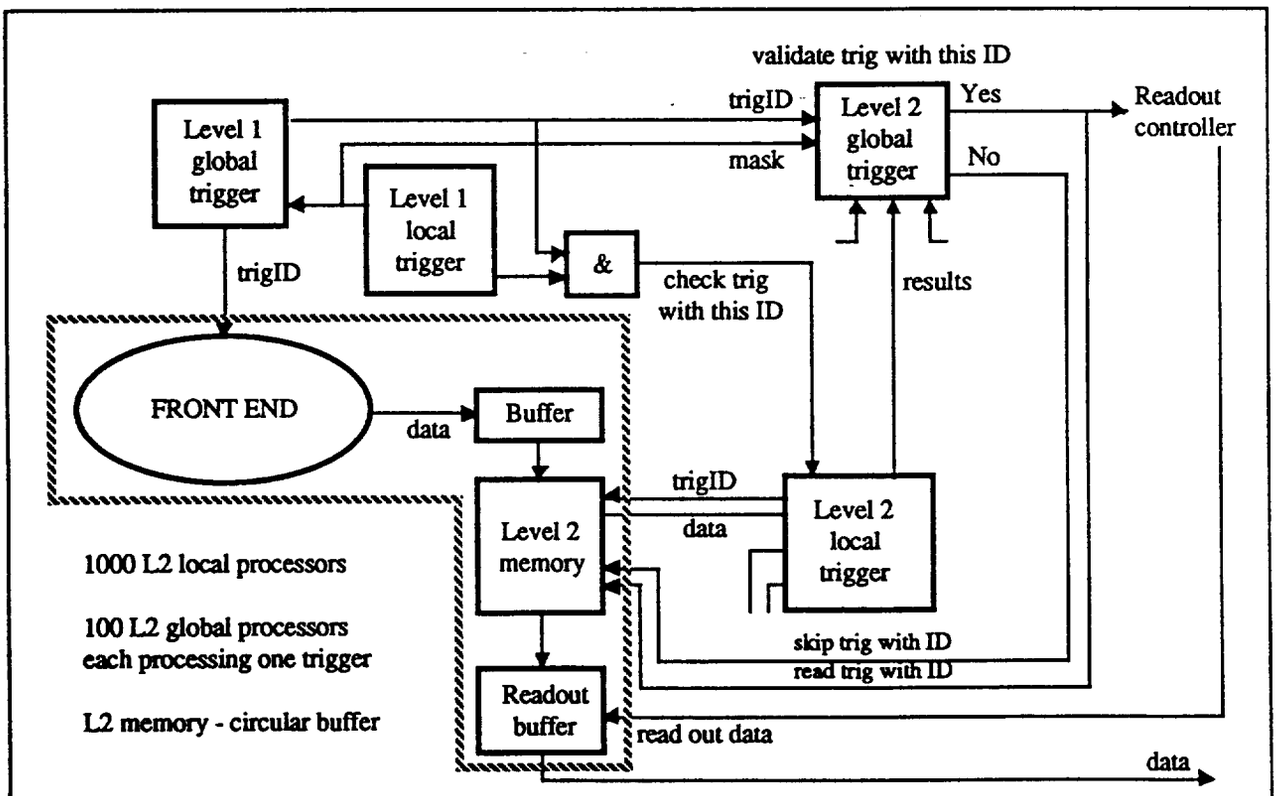


Fig.2 An architecture for Level 2 calorimeter triggers

front end card. In Fig.2 all the items inside the hashed line are incorporated onto the front end card. Only 2 kbytes of memory are needed to store data from 10 channels for 100 level 1 triggers.

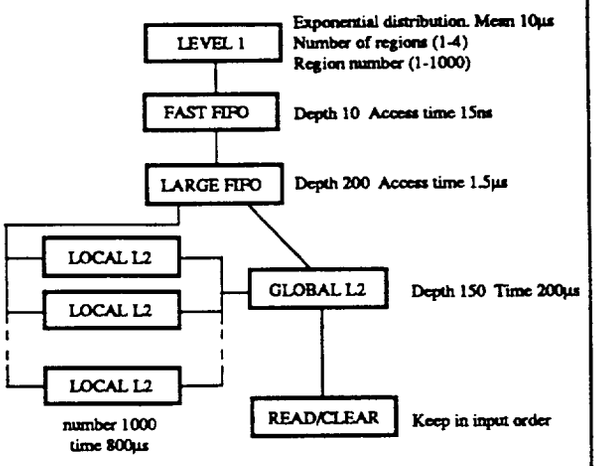


Fig.3 Local / global system model

Simulation

Data loss due to dead time is acceptable if the loss is kept small but, with significant quantities of data held in buffers, it is important that no part of the trigger system saturates. If saturation occurs, data taking must be stopped until the blockage is cleared and queued data in front of the blockage must be flushed. Returning the system to a coherent state after saturation is time consuming and wasteful and results in an unacceptable level of dead time. As well as designing a system which has the correct size buffers to minimize dead time, it is important to incorporate into the design the ability to inhibit global level 1 triggers before saturation occurs.

We have modelled [4] the performance of a level 2 system with local and global processors using SIMSCRIPT [5]. The performance of the system has been evaluated for a range of values of selected parameters. Fig.3 shows the model used and standard parameter values.

A level 1 rate of 10^5 Hz is assumed with an exponential distribution in time between triggers which are locked to the LHC bunch separation of 15ns. The fast FIFO and the large FIFO correspond to the buffer and level 2 memory of Fig.2. Local level 2 processors are assigned on the basis of information provided by level 1 but, as they are assigned randomly, global processors share a common queue. To simplify the electronic reality, the level 2 memory is assumed to be a circular buffer and, therefore, the read/clear operations must be kept in input order. This requirement is imposed on the simulation by not releasing the global processor for an event until all previous events have been completed.

Running on a SUN SLC the program takes about 11 minutes to process 10^5 triggers i.e. 1 second of data taking. A summary is produced for each run giving the overall performance and showing where resources have become saturated as well as their average utilization. Fig.4 shows results obtained from runs varying the number of global processors and the local level 2 processing time but keeping the total level 2 time constant at 1 ms; other parameters were kept at their default

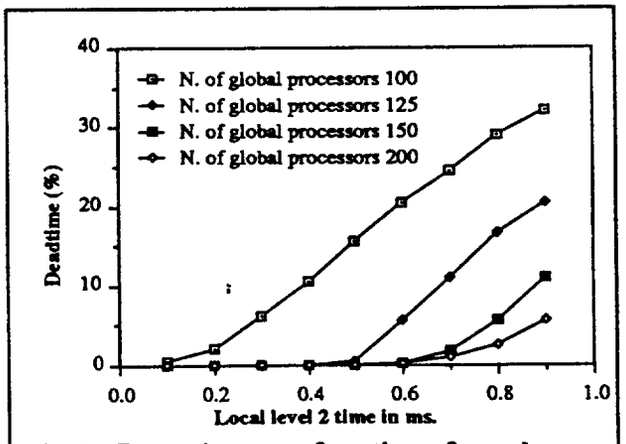


Fig.4 Dead time as a function of number of global processors and local level 2 time.

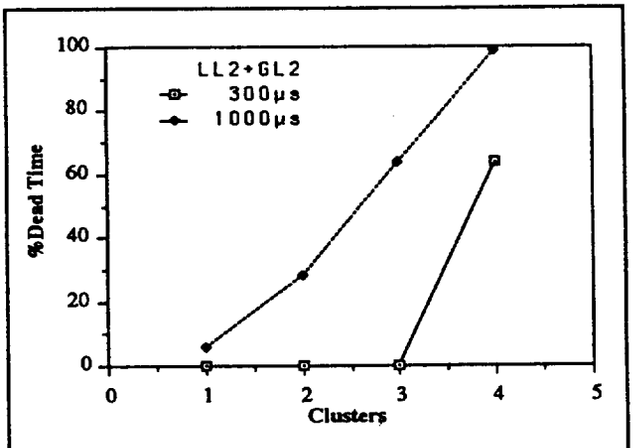


Fig.5 Dead time v. number of clusters

values. Dead time becomes significant only when the number of global processors is reduced below 125 or the local processing time is greater than 500 μs. Fig.5 shows the effect of varying the number of clusters for total level 2 processing times of 300 μs and 1 ms. For the shorter processing time, the dead time only becomes unacceptable when the 4–cluster trigger rate approaches 10^5 Hz, but the longer processing time can operate successfully only on one cluster triggers at that rate.

Implementation

As shown in Fig. 2 and discussed above, the data buffers and level 2 interface, can be incorporated into the front end card [3].

Several possibilities exist for the local and global processors. Tests have been made on an FDPP module [6] used as a local processor connected to 100 channels. Using data from the SPACAL test calorimeter [7] and standard benchmark algorithms [8] the module finds the position of maxima in 42 μs; total energy and width parameters take another 15 μs for each cluster. Allowing for data transfer times, the total local level 2 latency would be less than 100 μs.

For clusters which straddle boundaries to be treated correctly, it is necessary to have fixed connections and local processing areas which overlap or to build in the facility to select the information to be sent to the local processor. The second option could be accomplished using HIPPI links [9] and crossbar switches. Such a system allows local transfers of 1 kbyte of information in about 12 μs. Similar links or a bus system could be used to transfer data from local to global processors.

Conclusions

We have shown that a level 2 trigger is feasible using current technology. Simulation languages make it possible to asses the performance of a system at an early stage and system models can be easily and rapidly changed to accommodate new ideas on architectures. We intend to develop our model to include greater detail on proposed implementations of level 2 architectures. A considerable amount of work, at both the physics and detector simulation level, is required before estimates of the efficacy of the isolated electron second level trigger can be obtained.

References

1) Ellis N., Proceedings, ECFA Large Hadron Collider Workshop, Aachen 1990
2) Hellman S., Proceedings, ECFA Large Hadron Collider Workshop, Aachen 1990
3) Goggi G. and Löfstedt B., Proceedings, ECFA LHC Workshop, Aachen 1990
4) Fumagalli G., INFN, Pavia, Private communication
5) SIMSCRIPT, CACI Products Division
6) Buono S. and Crosetto N., CERN/ECP 90–6
7) SPACAL Collaboration, Proposal, CERN/DRDC/90–23
8) Bock R. et al., CERN–LAA/RT/88–08
9) High Performance Parallel Interface, ANSI X3T9.3/88–023

A cluster finding analog network

R Bonino CERN/PPE

Abstract

The use of resistive networks as the support for an array of analog processors for fast clustering is described Applications to preshower clustering and calorimeter triggers are presented

Introduction

Triggers (e.g. in calorimetry) are often based on threshold cuts of the total energy deposited in a cluster of contiguous cells within a detector This problem is usually solved extracting the information from the detector and reconstructing the pattern of the event through appropriate processing.

An alternative would be to treat the information locally, associating a processor to each cell of the detector. Each processor, connected to it's nearest neighbours, should then perform a simple calculation based on the energy deposited in the corresponding cell and the information received from the rest of the network. This approach has the advantage that the event topology is never lost and the network operates directly on the pattern of the energy distribution. In applications where the main constraints come from connectivity, speed and data flow rather than from precision in the calculation, as for a fast level1 trigger, analogue processors could be more appropriate that digital ones.

The next section describes an array of analogue elementary processors connected through a resistive network. The input to the system is the energy distribution in a detector and, at the output, only processors corresponding to a cluster's peak are active and carry the information of the total energy deposited in the cluster. In the following sections applications of this network for fast triggering are discussed.

The clustering network

Resistive networks

As an example consider the linear resistive network shown in Fig 1. Injecting into each node i of the network a current I_i, the voltage V_k at node k will be(1):

$$(1) \qquad V_k = \frac{1}{2G_0} \sum_n I_n \Gamma^{|n-k|}$$

Where:

$$G_0 = \sqrt{\frac{G}{R}} \sqrt{1 + \frac{1}{4L^2}}$$

$$\Gamma = 1 + \frac{1}{2L^2} - \frac{1}{L}\sqrt{1+\frac{1}{4L^2}} \qquad L = \sqrt{\frac{G}{R}}$$

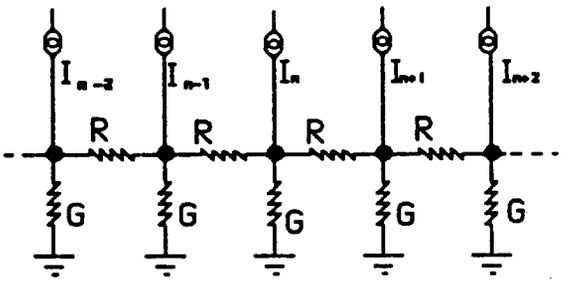


Fig 1 Linear resistive network.

The voltage at each node represents the local average of the current distribution with a smoothing effect that depends on the factor R/G : the voltage distribution broadens when the resistance to ground is increased. The height of the distribution is determined by the total impedance of the network and the R/G smoothing factor.

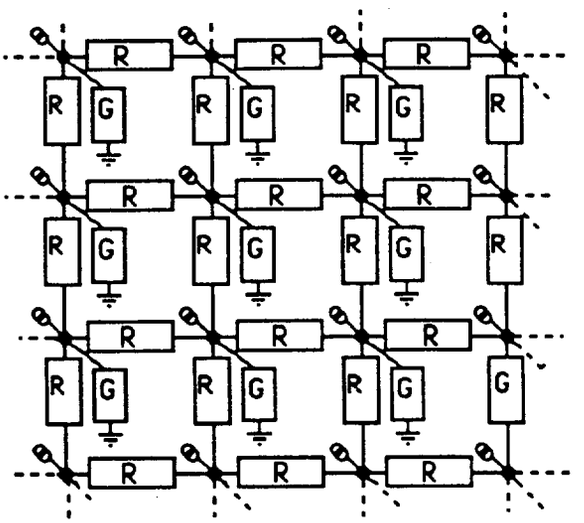


Fig 2: Two dimensional resistive network.

Consider now the case of a two dimensional network (Fig 2). A current I at node (l,m) of an infinite network generates a voltage $V_{(i,j)}$ at node (i,j) :

$$V_{(i,j)} = I \; f_{(i-l,j-m)}$$

where the function f depends on the R/G ratio and has a maximum at (0,0)

In general for a current distribution $I_{(l,m)}$

$$V_{(i,j)} = \sum_n \sum_m f_{(i-l,j-m)} \; I_{(l,m)}$$

Injecting a 1 μA current in one node of a 20kΩ/20kΩ network generates a 5mV signal voltage on the node itself, 1.3 mV on the 4 neighbour nodes and 0.6 mV on the 4 diagonal neighbour nodes not connected directly.

Detector Interface

This network can be interfaced to a pad detector or a calorimeter sampling plane, each node of the network receiving a current proportional to the energy deposited into the corresponding detector cell as illustrated in Fig 3.

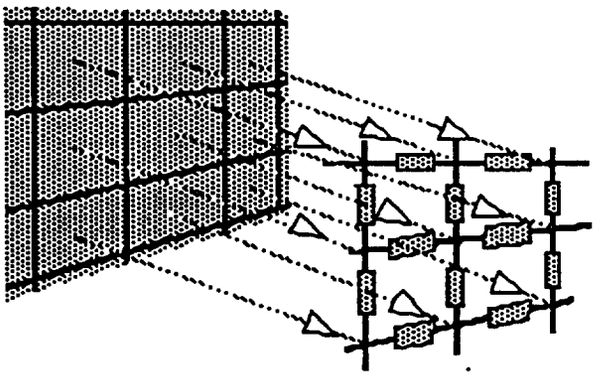


Fig. 3: Interfacing the network to a detector.

The total energy deposited in a cluster is proportional to the sum of the currents injected into the nodes by the active cells. The width of the voltage distribution generated on the network depends on the dimensions of the cluster itself and on the smoothing factor. A peak in this voltage distribution corresponds either to the cell with the maximum energy deposited or to some kind of 'centre of gravity' for large area clusters.

Peak finding and Isolation cut

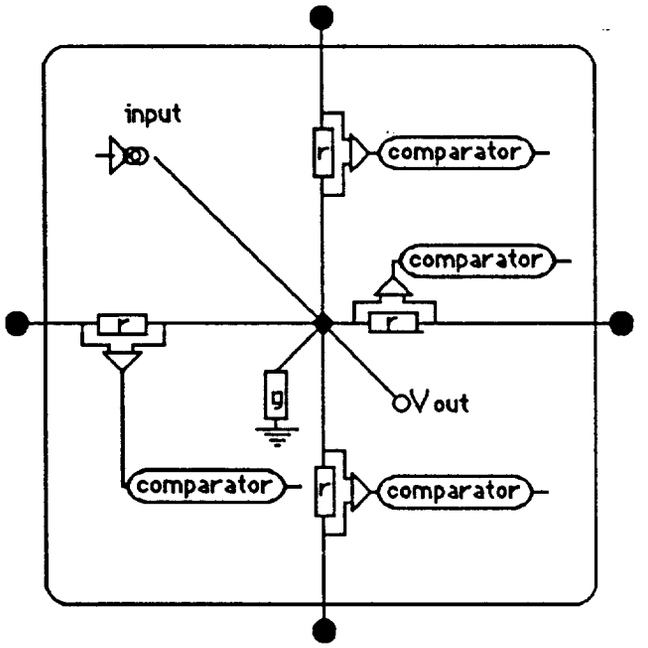


Fig.4: Elementary cell r=R/2 g=G/2.

To determine the presence of a cluster and identify the centre of the energy deposition, each node is implemented with comparators to monitor the 4 voltage drops to the neighbour nodes (Fig 4). A peak is identified when all comparators show a positive voltage difference . If one or more of the voltage differences is below the comparator threshold the cluster is not detected.

Now consider two distributions with the same peak voltage but different widths. In the broader distribution voltage differences from node to node are smaller than in the sharper one, therefore reducing the efficiency to detect large area clusters: the processors perform an effective isolation cut. This effect will be illustrated in more details in the following sections.

Energy measurement

For n cells receiving a current I_0, I_1, I_n...we can rewrite the voltage at the peak as the sum of the contribution of all the active nodes:

$$(2) \qquad V_{peak} = \sum_{k=1}^{n} f_{(\Delta i,\Delta k)}\, I_k$$

Where Δi and Δk are the x and y distances from the cells to the peak cell and the function f decreases with the distance.

If the cluster involves a limited number of cells a rough estimate of the total current I_{tot} injected, and therefore of the energy of the cluster E, is provided by the peak voltage itself:

$$(3) \qquad E = K\, I_{tot} = K \frac{V_{peak}}{f_{(0,0)}}$$

where K is a factor relating the energy deposited and the current injected. The precision obtained with (3) decreases with the area of the cluster since the energy deposited in cells away from the peak contributes with a factor $f_{(\Delta i,\Delta k)}/f_{(0,0)}$

It is possible to improve the energy measurement at least for clusters with cross sectional area smaller than the size of a cell: in this case the energy is usually distributed in 1 or 2 cells and only rarely in 3,4 or more. Call δ the sum of the voltage differences from peak node to neighbours and $\Sigma 1$ and Σ_2 the sum of the currents injected into the nodes located respectively at the side and diagonally to the peak. If $\Sigma_2 << \Sigma_1$ we write:

$$V_{peak} = a_i\, I_{peak} + a_\Sigma\, \Sigma_1$$
$$\delta = b_i\, I_{peak} + b_\Sigma\, \Sigma_1$$

where a's and b's depend on the $f_{(\Delta i,\Delta k)}$ and V and δ are known and we want to reconstruct:

$$I_{tot} = \alpha\, I_{peak} + \Sigma_1$$

Solving for I_{peak} and Σ_1:

$$(4) \qquad E = K\, I_{tot} = K \frac{V_{peak}}{f_{(0,0)}} (1+\alpha A)$$

$$(5) \qquad A = 4 - \frac{f_{(0,1)} - f_{(0,0)}}{f_{(0,0)}} \frac{\delta}{V_{peak}}$$

where A is a measurement of the dimension of the cluster weighted by the energy deposition and A=0 if there is only 1 cell activated. Expression (4) is exact for energy distributed in two cells side by side and, at least in principle, can be used for the energy measurement.

Time evolution

An Hspice simulation of the network was written to study the time evolution of the voltages at the nodes for various input configurations and parasitic capacitances.

Fig 5 shows the waveform of the peak voltage (thick line) of a 10KΩ/2.5KΩ network when two neighbour cells (side by side) are activated by triangular currents peaked at 7ns with maximum value 75 and 15 μA. The network includes parasitic capacitances of 1pf from node to node and 2 pF from node to ground. The triangular curve shows the peak voltage for the same network without parasitic capacitances . The thin lines show the voltage differences from the peak to the 4 neighbour nodes, some curves being superimposed because of the symmetry of the voltage distribution around the peak The response of the network itself is extremely fast and would allow operating at LHC rates .

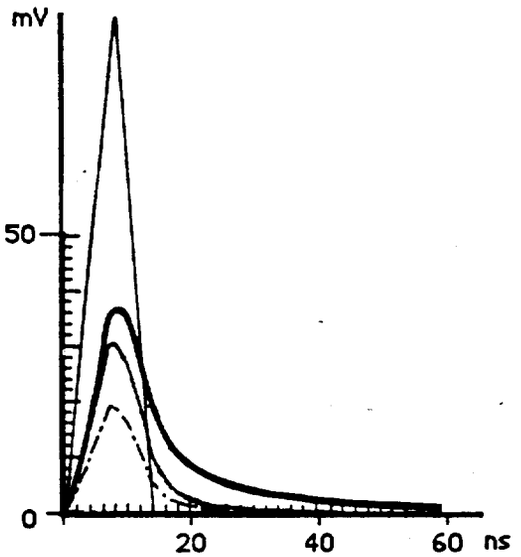


Fig 5: Hspice simulation of 10KΩ/2.5KΩ resistive network

Preshower energy reconstruction

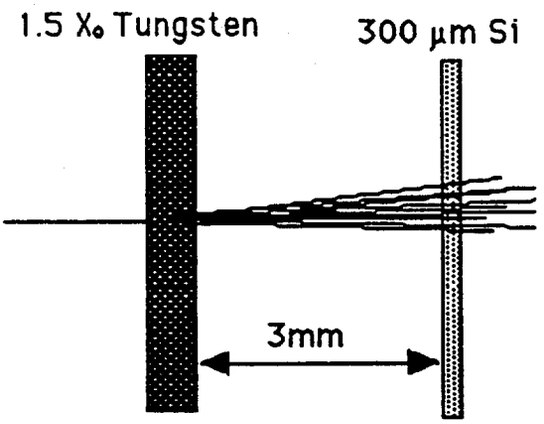


Fig 6: Silicon preshower set-up.

This section shows the results of a GEANT simulation of the set-up illustrated in Fig 6. Clusters are generated by 10 GeV electrons hitting a 1.5 X_0 tungsten converter and are detected by a 300 μm silicon plane divided in cells of 24x24 mm (2).

For each event the energy deposited in each cell is calculated, a current of 4μA per Mip deposited is injected into the corresponding node of the network (with a maximum of 200 μA) and the network response is determined. The effect of noise and resistor spread is not taken into account but is probably not negligible.

Sensitivity

In Fig 7 the minimum of the four voltage differences between the peak node and it's four neighbours is plotted for each event to illustrate the effect of the voltage threshold cut in identifying clusters .

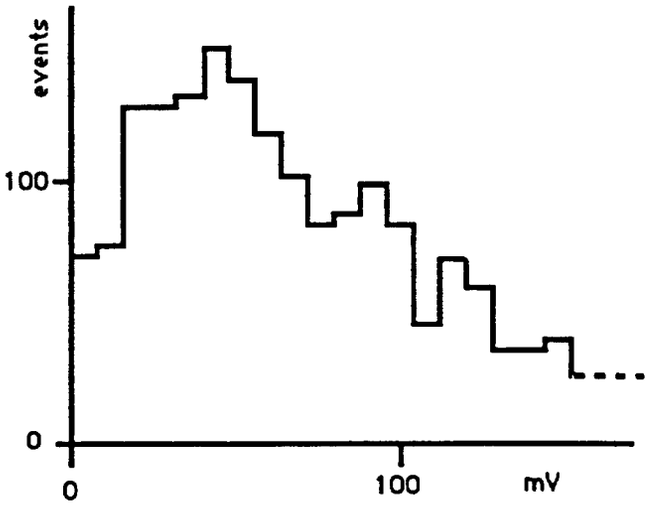


Fig 7: Minimum of the four voltage differences at the peak node

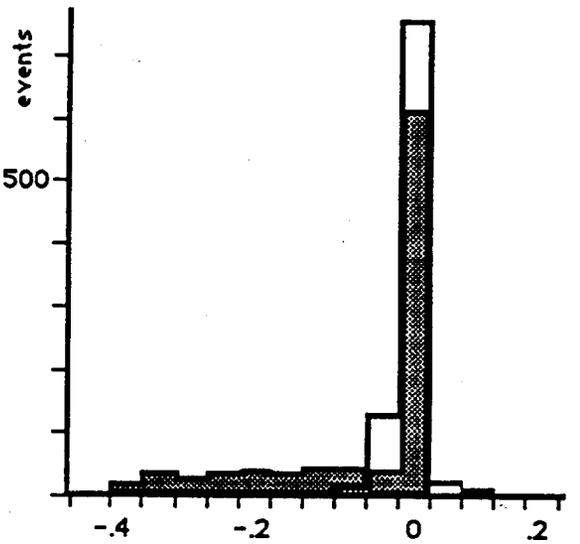


Fig 8: Resolution for energy measurement.

Assuming that comparators cannot detect voltage differences of less than 2 mV, less than 1% of the clusters would be missed. In addition in some cases (2-3%) a single cluster with energy deposited essentially in 2 cells that are at the corner of each other is separated in two clusters.

The shaded distribution in Fig 8 shows the resolution ($\Delta E/E$) of the network for the energy measured as defined in (2) compared to the total energy deposited in the cluster. The tail on the left side comes from events where a substantial amount of energy is deposited in more than one cell. Fig 9

shows how the resolution relates to A (as defined in (5)) for clusters of more then one cell. The thick curve in Fig 9 shows the results of using (4) to calculate the energy deposited.

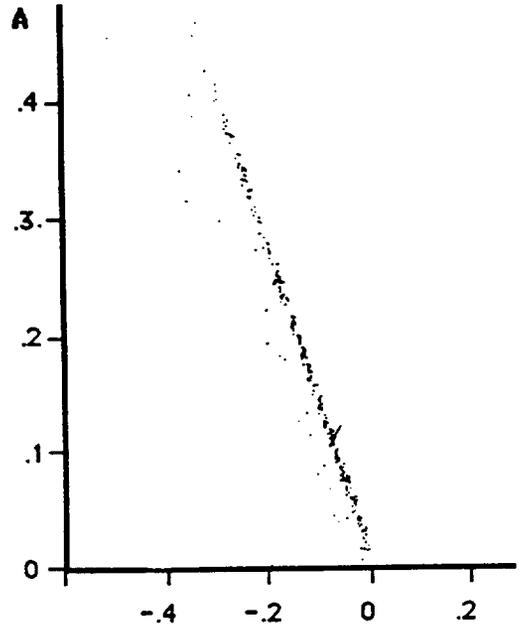


Fig 9: Resolution as a function of A

Varying the R/G ratio from 20KΩ/10KΩ to 20KΩ/40KΩ gives more weight to the contribution from cells away from the peak and the rms of the energy resolution, for clusters with more than 1 cell, improves from 0.13 to 0.09. On the other hand an increase of the smoothing effect, while keeping fixed the total impedance of each node, generates a reduction of the voltage differences from node to node and a degradation of the efficiency. The distorsion due to background and noise, not simulated here, would increase as well if a larger area is considered to define the cluster energy. If one applies formula (4) for the energy, the resolution does not depend on the smoothing factor and has a constant value of 0.02

Calorimeter trigger processor

It is also possible to apply clustering networks in a calorimeter trigger processor. For each plane to be analysed two networks are needed :

- A fine granularity network connected to individual calorimeter cells to identify electron clusters. This network is insensitive to jets because of the effective isolation cut described before
- A coarse granularity network connected to larger cells obtained with the analogue sum of elementary cells to identify jets.

To avoid double counting of the electrons their energy must be subtracted from the appropriate sum before the coarse network is operated. This gives the schematics shown in Fig 10.

A program has been written to simulate the response of such a trigger processor with the following algorithm:

1 Determine the response of the clustering network connected to the high granularity cells
2 Identify electrons as em clusters if there is no substantial hadronic energy deposition .
3 Add up the energy deposited in cells above a threshold to make low granularity cells. Subtract the energy of previously identified electrons .
4 Determine the response of the clustering network connected to the low granularity cells.
5 Identify jets from em clusters
6 Add hadronic energy of corresponding hadronic clusters

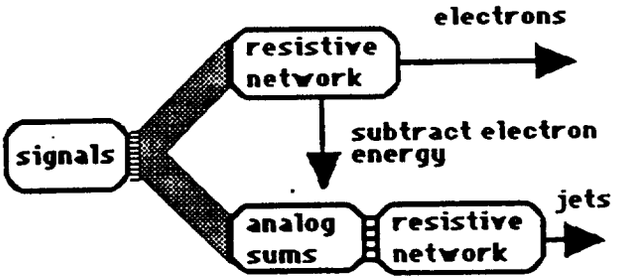


Fig 10: Calorimeter trigger flow-chart.

Comparison with standard cluster search

This algorithm has been compared with a standard cluster finding algorithm based on a 5 GeV seed and isolation cuts in $\sqrt{(\Delta\eta^2\Delta\phi^2)}$ of .5 and 1. for electrons and jets respectively The two algorithms have been run on a simple simulation of a cylindrical calorimeter extending from -5 to 5 in η and divided into 128 cells in η and 256 cells in ϕ . The energy of incoming particles is deposited in the cell that is hit and smeared longitudinally in the electromagnetic and hadronic sections, but not laterally. The results shown come from 100 Pythia events of :

Higgs (200GeV) ->ZZ -> e e jet jet

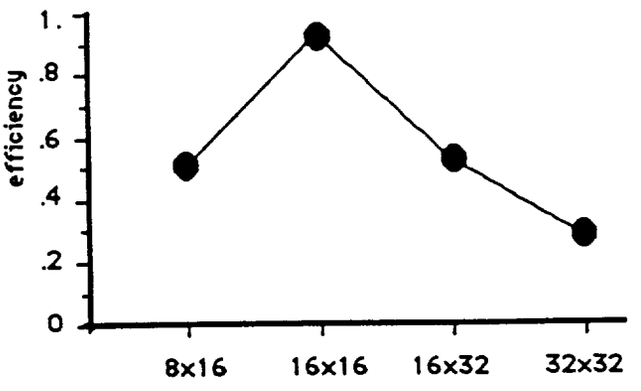


Fig 11: Jet efficiency vs cell size

Since the electron energy is deposited in a single cell, in this simulation it is not realistic to use the resistive network for electron identification. However it is reasonable to assume that, for a calorimeter of similar cell size, the electron

response should be analog to what was obtained in in the preshower simulation .

Fig 11 shows the efficiency of the network in finding jets respect to the standard algorithm varying the number of elementary cells (n cells in η x m cells in ϕ) added up to make a large cell . If the coarse cells are made too small the efficiency is low since the network is not able to detect clusters that extend on a large number of cells. On the other hand if the cells are too big two clusters may not be resolved, reducing again the efficiency. This results in an efficiency peak for sums of 16x16 elementary cells corresponding to $\Delta\eta x\Delta\phi.=0.6x0.8$

Fig 12. shows the effect of the smoothing factor using the optimum $\Delta\eta x\Delta\phi.=0.6x0.8$ cell dimension. The open squares and circles represent the efficiency and resolution($\Delta E/E$) of the network algorithm itself compared to the standard cluster finding algorithm.

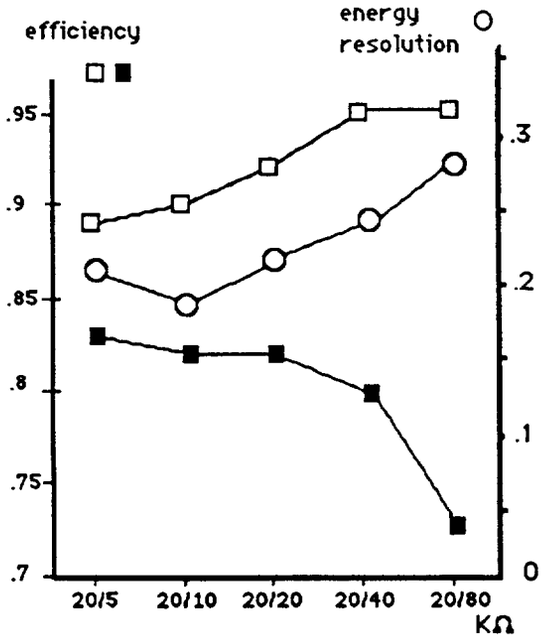


Fig 12: Resolution and efficiency for $\Delta\eta x\Delta\phi.=0.6x0.8$ cells.

When the smoothing factor is increased the contribution of cells away from the peak is given more importance and the efficiency improves. On the other hand the resolution degrades because more energy coming from cells not belonging to the cluster is added up. The solid squares show that if one applies a sensitivity cut of 2mV, normalizing the total impedance to the 10KΩ/10KΩ network, the efficiency degrades since more and more cluster peaks have at least one voltage difference below threshold. The energy resolution does not sensibly depend on the cut.

In general in the jet case clusters are broader than just 2 cells side by side and the correction for the energy measurement (4) is no longer valid and brings little or no improvement. The resolution for a 20KΩ/20KΩ network interfaced to $\Delta\eta x\Delta\phi.=0.6x0.8$ cells is shown in Fig 13. The ϕ and η resolution correspond to the cell dimensions.

Superimposing on each event 15 minimum bias background events degrades the performances : the efficiency for a 20KΩ/20KΩ network reduces to .8 and the resolution degrades to 0.3.

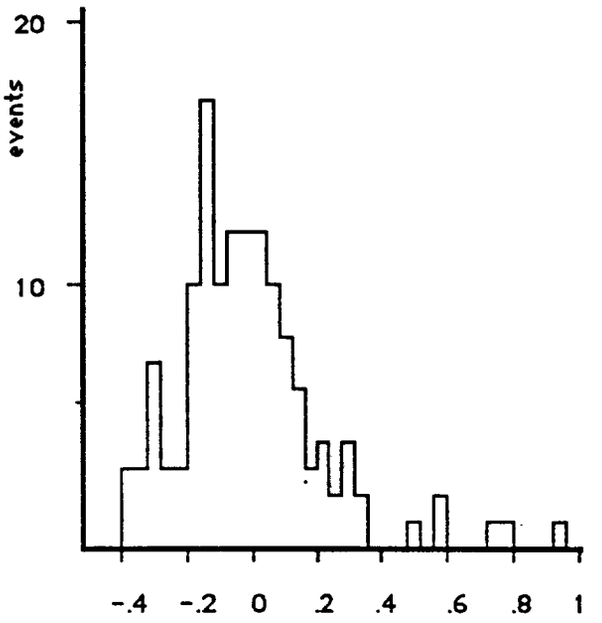


Fig 13: Energy resolution for 20KΩ/20KΩ net.

Summary and conclusions

I presented an analog network that can be used in identifying and measuring energy clusters. The system shows >95% efficiency and a resolution that can be reduced to 2% for clusters with dimensions smaller than the cell side .

A sketch of a calorimeter trigger processor was also presented and compared with a classical jet finding algorithm. The efficiency for finding jets in events with two jets superimposed on a minimum bias background is 80% and the energy resolution 0.3. The performances of the network can still be improved by additional optimization of the parameters and should then be compared to other level1 trigger simulations rather than an offline algorithm.

It would also be interesting to use networks where each node is connected to 6 or 8 neighbours. Such a configuration would provide a better monitoring of the voltage distribution and should result in better resolution and efficiency.

Acknowledgments

Many thanks are due to P Jarron for countless discussions and suggestions on the networks, to A Cester who, as a summer student with P. Jarron, wrote the Hspice network simulation and to S. Hellman from whom I borrowed the calorimeter simulation and cluster finding algorithm used as a test bench for the network results.

References

(1) C. Mead. "Analog VLSI and Neural systems". Addison-Wesley 1989

(2) D. Munday et al. "Proposal to study a Tracking/Preshower Detector for the LHC". CERN/DRDC/90-27 2-Aug-1990

The TRD Second-level Trigger

R.K.Bock (CERN), J.Pfennig (CERN)
(presented by J.Pfennig)

1. The problem definition

For use in a future LHC detector, a transition radiation detector has been proposed [1] whose capability in e/hadron discrimination can be put to use in real time. In this contribution, we discuss the data handling aspects of this device, characteristic for a class of triggering devices at LHC.

We use as a TRD model the straw configuration called 'halo model' in [1]; it is schematically shown in fig.1. Straws are arranged between 70 and 120 cm of radius around the beam pipe, in multiple planes (a total of about 900), and about 580 straws to a plane. In order to get optimal tracking capabilities from this detector, every alternate plane carries the straws in a reverse arrangement, thus allowing full stereo views. Note that some multitrack ambiguities can arise in such a tracking arrangement, but due to the non-parallelism of straws they are minimized.

Readout of the roughly 500 000 straws (on outer end only) is proposed to be largely centralized off the detector, to avoid the various problems encountered by on-detector intelligence: radiation, obstruction, and power dissipation. For the intended trigger, this siting issue is secondary, except that full access to all channels must be possible. We assume that the front-end readout takes care of signal extraction for individual bunch crossings, and remains passive until a (calorimeter-based) signal for a given time slice is received, indicating both that the corresponding bunch crossing establishes one or more electron candidate(s), and where these candidates are to be found ('pointer'). The assumption is made that such bunch crossing candidates do not occur more frequently, on average, than every 10 μsec., i.e. the first-level trigger reduces from the bunch crossing rate by a factor of 1000. It has become customary to term this kind of reduced-rate/fine-grain/full-precision/simple-algorithm/local trigger a 'second-level' trigger, for obvious reasons.

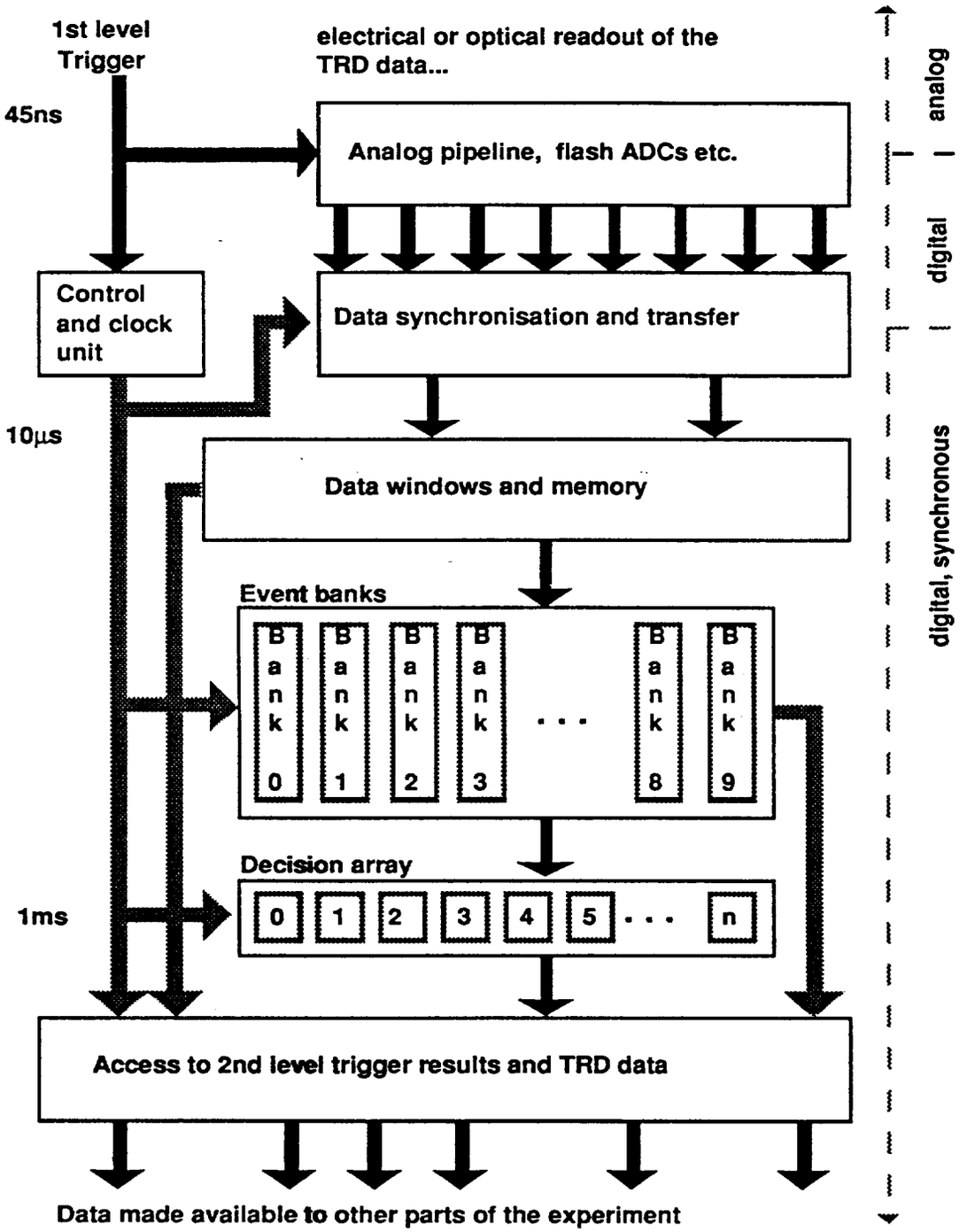
We have chosen the halo model for straws because it shows the typical second-level trigger problems in an extreme form: bandwidth of transmission, locality of algorithms, component performance for both low- and high-level aspects of the algorithm.

2. The triggering algorithm

The basis of discriminating electrons from hadrons in a TRD is a statistical analysis of pulse heights of all digitizings belonging to a track, so that a measure for the probability of X-ray emission (and detection) can be determined. This probability is a function sensitive to the Lorentz factor γ of the track. Hence the finding of a (stiff) track pointing towards the calorimeter cell signalling an electron candidate is a first local step, its (statistical) pulse height analysis a second local step, and a decision taking into account correlations of (multiple) signals, physics cuts, etc., is a concluding global step of the algorithm. All computations have to be preceded, for practical reasons of bandwidth and performance, by a data selection step under control of the first-level pointers.

3. *Data flow through the TRD trigger*

Due to the fact that tracks can pass through roughly one quarter of the longitudinal extension of the detector and due to the statistical nature of track detection, a single algorithm running in a single hardware unit is conceivable only in a serial von Neumann machine. We are interested in parallelizing and/or pipelining the process, hence we propose to subdivide the 2nd level trigger into three phases, each of them implemented on a different type of hardware and running a dedicated algorithm. The following sections will expand on the proposed practical solutions, as we envisage them at this early state of design.



3.1 Phase I algorithm: data distribution

All data belonging to bunch crossings that passed the 1st level trigger selection, will first be synchronized and then transported from the experiment site to the main trigger electronics in a counter house. The synchronization has been introduced to allow simple point to point communication between the readout logic and the trigger, as well as between the phases of the trigger. The TRD trigger, internally, will operate synchronously.

At the input side the full data rate is 100 GBit/s. All incoming data will be kept during a period of some msec in public addressable memory, to allow other components of the experiment to monitor the TRD and the 2nd level trigger performance. The data transport at this level could be based on the HPPI standard [2].

Only a fraction of the data is relevant for tracking in the trigger. Using the 1st level trigger information and limiting the number of electron candidates to four (independent calorimeter candidates), one sixth of the data will be mapped into 4 data windows that will undergo further processing. Next the data is mapped from the TRD specific straw representation into plane rectangles of pixels. The plane contains the beam axis and the firing calorimeter cell, and for each potentially interesting track such a plane containing all space points belonging to it can be constructed.

Data mapping and selection are based on loadable Look-Up tables, where the data packing is handled by DSPs or similar hardware (no buses, but of the order of 512 local point-to-point connections).

3.2 Phase II algorithm: searching for information

Every 10 μsec (one time slot) the data of 4 to 8 planes (depending on the calorimeter resolution) generated from each of the 4 data windows is sent to the phase II hardware. This is acomplished using the same type of HPPI links mentioned above.

The phase II processors are divided into 10 groups, called banks, to work in parallel on different time slots, and that are used in a pipelined fashion. This is required in order to extend the interval that is availlable for processing from 10 to 100 μsec. Each time slot is assigned to a processor bank on a round-robbin schedule. On the input side, the data can be further reduced by requiring digitizings to be inside of roads defined by the calorimeter information from the first-level trigger.

For processing of phase II, a massively parallel architecture can be put to use. A solution that has been studied so far is the SIMD 'associative string processor' (ASP) [3]. An ASP implementation of phase II would use 10 Fastbus crates with a total of about 640.000 processing elements, on 80 boards, as well as 40 controller/road-builder boards. The processing power of this solution allows to check for about 128 plane areas, each one covering a trapezoid of 16 TRD slices out- and 32 TRD slices inside (per time slot).

In our present thinking, the track finding algorithm is based on shifting (distorting) the trapezoid and histogramming in parallel. The shift (angle) for the highest value is saved for each bin, and should, in an ideal case, coincide with a track. Note that a balance has to be found between calorimeter tower size, vertex area, and histogram bin size.

3.3 Phase III algorithm: decision taking

As a result of Phase II the n (about 64) best peaks would be read out (still under control of the ASP Hardware) and transferred to n corresponding processors in the phase III hardware. Processors in phase III are assumed to be conventional RISCs, programmed under C in a real time operating system environment. It will be at this level that sensitive physics- or luminosity-dependent cuts and limitations are introduced.

The interface of the second-level trigger to other components of the detector is via public addressable memory. The 3rd level trigger, for example, polls for the second-level status and data, and can therefore be treated as completely asynchronous. Assuming this interface to be implemented in buses like SCI [4], even the complete TRD raw data could be read out occasionally without affecting the trigger operation. The total latency is expected to lie below 4 msec, and raw data can safely be kept available for a time span of 20 msec.

4. Highlighting some of the innovative ideas

The discussion above contains a number of ideas not currently found in detector readout systems. We want to highlight them briefly in this section.

The internally *synchronous operation* of the entire second-level trigger facilitates hardware implementations enormously. At least phases I and II can readily seen to be operating in fixed time frames (i.e. time does not depend on the data). Abandoning thresholding of data for compression ('zero-suppression', not very effective at the TRD's high occupancy), and data-independent algorithm execution are a prerequisite for this.

The *separation of data and control* flows is made possible by the synchronous operation and the use of simple point-to-point connections. As fixed-size data blocks are transmitted, block transfers can be initiated. Control information, on the other hand, is low in volume and needs broadcasting, hence can be carried by buses.

The data is kept in *distributed memories*: no internal data collection is required. The availability of buses like SCI will, nevertheless, allow access to the full data set for monitoring and testing, albeit at a reduced rate.

Due to the complexity of the architecture and the vital impact of trigger functioning on physics, a *self-testing mechanism* must be built into the system. We foresee to use the idle time slots, invariably occurring as a consequence of synchronous operation, when a no-trigger situation occurs, to inject sets of test patterns instead of real data. A clever way of testing all parts of the trigger will have to be devised.

5. Conclusion

We have discussed above a possible architecture for executing the TRD trigger algorithm at a frequency of 100 KHz, using a number of innovative ideas not all restricted to this particular detector, and based on architectural components available in 1991. The evolution of technology will make solutions of 1993 or 1995 simpler and cheaper, and may also favor alternative architectures. We are thus confident that the TRD, even in its most complicated form, can perform its triggering task in real time, if the device performance and the physics environment turn out to be as predicted today.

We consider it our task in the coming two or three years to demonstrate the various parts of our solution in hardware, emulating as closely as possible the expected situation at the LHC.

6. References

[1] Integrated High-Rate Radiation Detector and Tracking Chamber for the LHC, Proposal, B.Dolgoshein, spokesman, CERN - DRDC/90-38

[2] HPPI, High-Performance Parallel Interface, Specifications, ANSI X3T9.3/88-023 (February 1990)

[3] M.Lea, ASP: A Cost-effective Parallel Microcomputer , IEEE Micro Oct.1988, and MPPC, Progress Report, to be submitted to the DRDC.

[4] SCI Scalable Coherent Interface, IEEE P1596.

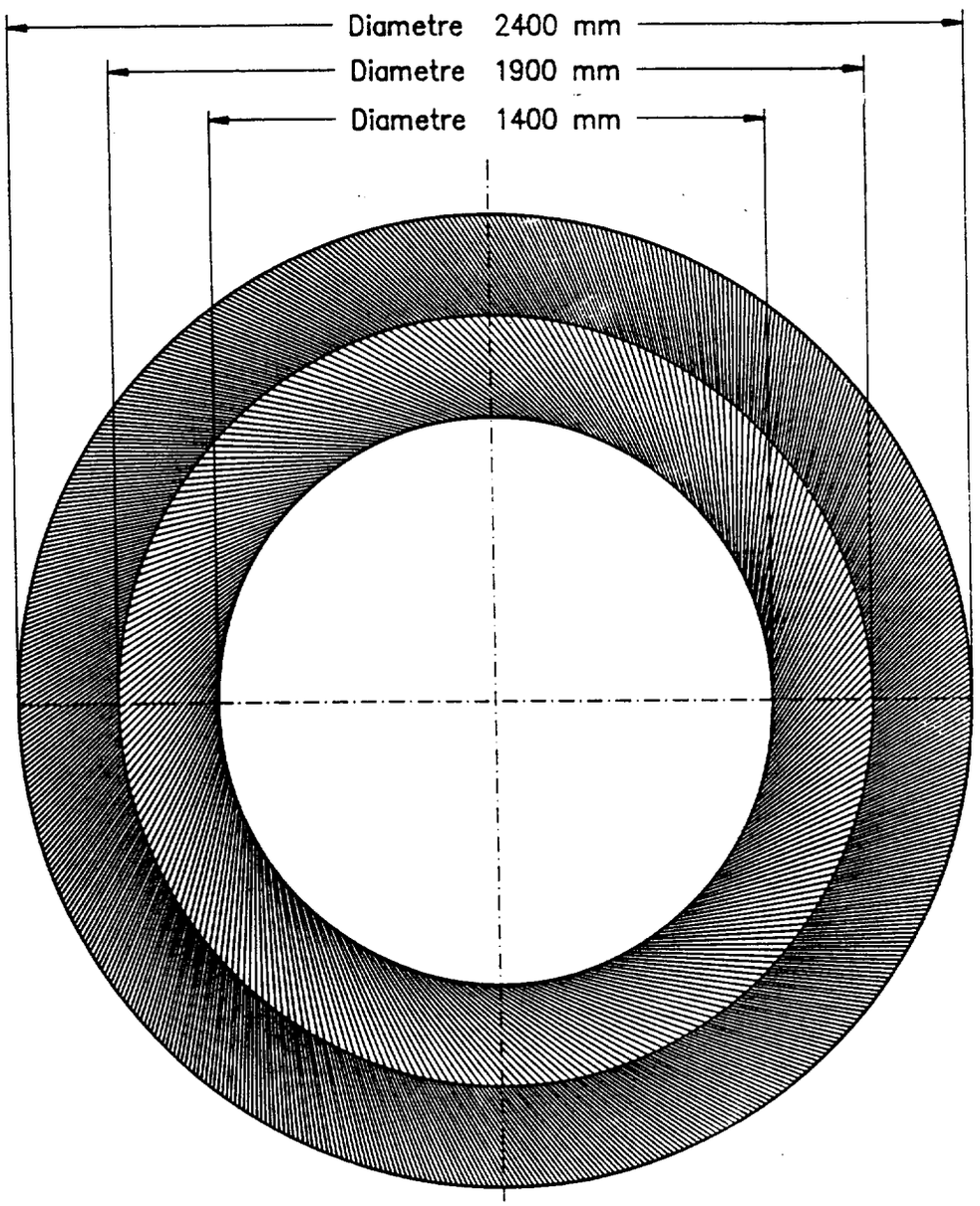


Fig 1:
TRD Halo Model

Buses and Standards for LHC

H.Müller[1] J.Belleman[1] A.Bogaerts[1] D.Burckhart[1] R.Divià[1]
H.Döbbeling[4] C.Eck[1] G.Heyes[1] D.Linnhöfer[2] R.McLaren[1]
C.Parkman[1] M.Pentney[1] J.Petersen[1] P.Ponting[1] J.F.Renardy[3]

Abstract

The ECFA sub-working group on 'standards and buses' has investigated the role of both conventional and new buses for LHC. Three working teams present their results in specialized companion papers. This summary paper compares the use of Fastbus, SCI, VME-family buses and Futurebus+ using a common model of a LHC data acquisition system. The different buses were investigated for their capabilities to be used in the various areas our standard model LHC system, and the results are shown in a survey table.

1 Standard buses at LHC

The question whether standard buses, such as Fastbus (IEEE960), VMEbus (IEEE1014) VXI and VME64 (IEEE1155), Futurebus+ (IEEE896) or SCI (IEEE1596) can be used in a future LHC data acquistion system has been investigated by the ECFABUS team. A cross reference paper [2] describing bus parameters in comparable terms has been published by us for reference. All ECFABUS papers use **a common model of a digital LHC data acquisition system** which is based on LHC parameters provided by the working group on Trigger and Data Acquisition [5]. Specific bus implementations are described in three companion papers of this workshop [3] [1] [4].

[1] CERN/ECP, CH-1211 Geneva 23
[2] Institut für Hochenergiephysik, ETH Zürich
[3] Saclay, France
[4] PSI, Villingen, Switzerland

Both the model and the major conclusions are presented here. The most general conclusion is that buses *will have an important future in LHC data acquisition experiments.* The following paragraphs give an explanation.

Why standard buses Though any model of LHC can only have significant uncertainties, several global problems can be identified for which the use of standards and buses provides a most reasonable solution: *Massive connectivity of up to* 10^7 *channels, extremely large event sizes of* 10^7 *bytes/event and very high throughput of* $10^{10} - 10^{11}$ *bytes/s.* This will require:

- Uniform transmission properties of data paths
- No crosstalk and EMF sensitivity
- Unique addressing schemes for single and multiple access.
- Minimal, very well defined read-write protocols.
- Minimal, very well defined access protocols (arbitration) for fan in units in a data driven environment
- Error detection and recovery
- Live insertion and removal of parts
- A modular, mechanical framework which allows for replacement, renewal and maintenance.

- A very reliable power supply and cooling environment

All these points are obviously reasons why bus standards were created.
It will require very innovative ideas and high investments into verification in order to replace the standard bus solutions by chip I/O specs, capton-foil systems, or meshes of private links. System-level specifications, available for most of the standard buses will need to be invented, and imposed for such systems.

Standards: An important feature of buses is the attribute *standard* which can be translated as: ***things fit together and have guaranteed and very well defined properties.*** It also means that ***industry will supply standard components, ready to fit into a system.*** In very large systems like LHC, 'standards' should therefore provide a safe environment for the chip- and board-level designer as well as for the system architect.

Are buses too slow ? The role of standard buses for LHC is frequently seen together with performance in existing HEP experiments, in particular LEP. The overall performance in LEP's data acquistion systems is much less than the bandwidth of the buses in use. An extrapolation of the use of standard buses to the very high bandwidth requirement in LHC seems therefore a priori excluded. It is however true that a 'close to bus bandwidth' performance is a question of implementation. Particular choices of architectures and software as well as economy considerations strongly influence performance. With careful implementation choices, even conventional buses can be pushed to 40 - 100 Mbytes/s.

New, powerful bus generations are evolving, driven by interest from high end computing industry, to provide performance and interconnectivity much beyond the limits of conventional buses. Examples:

- VME64 practically doubles the performance of VMEbus
- Futurebus+ may achieve 3.2 Gbyte/s on 256 bit backplanes
- SCI, a point-to-point cable bus will have a performance of 1 Gbyte/s/node

Other buses like Fastbus could also be able to increase significantly their real performance if investments into better implementations are made.

2 How to use buses

Neither Fastbus, nor VME are used in HEP experiments at even half of their backplane bandwidth limit. The overall performance of large Fastbus LEP systems is even far from the bandwidth limit: though a performance of 150 Mbytes/s was achieved and published [7], LEP experts quote typically 10-20 Mbytes/s as peak performance! Responsible for the discrepancy are 'implementation choices' which either should be avoided for LHC, or the bandwidth requirement should generally be multiplied by a factor of 2 or 4.

Implementation choices: The ECFABUS team uses unscaled bandwidth figures and therefore assumes that implementation choices will be taken with highest priority for performance: *A loss of performance can be due to:*

- embedded 'de-luxe' software
- no parallelism for the sake of economy
- not making use of data driven concepts where applicable
- curing of 'flakey' implementations by slow speed operation
- general purpose designs with inferior performance than specific purpose
- module design with functionality specs rather than performance

Areas for new buses: The new bus standards stretch their bandwidth well into the 1 Gbyte/s range. Assuming we know how to make good use of it, the new buses **promise to be excellent candidates for an LHC data acquisition system** in the areas of the **3 main data streams:**

- global trigger level 2 decision complex
- level 3 trigger processing farm
- data logger

These streams require bandwidth in the order of $10^8 - 10^9$ bytes/s (see Fig. 1) and are therefore problematic for conventional buses.

Bus layers: Buses will be specialised for certain layers of future systems, i.e there will be **'no unique, single bus'**. Special attention is required for the interfaces between different bus layers. *Conventional backplane buses* are more likely to be found around the local trigger level 2 area, while *new buses* are required for the global trigger 2, trigger 3 and event building stage.

Conventional buses: Buses like like Fastbus or VME are applicable wherever new buses are neither required nor economical. They are both an economical as well as a 'safe-ground' choice for the areas where data from many input channels is stored and locally processed. The max. bandwidth requirements here are typically 100 Mbytes/s.

Backplane buses: Buses like like Futurebus+ VME64 or Fastbus provide, via their short and well defined backplanes, very high speed local interconnections. This is the optimal environment for local processing and includes the physical framework for housing high density, power-hungry modules in a well defined, standard way. The interconnection between backplanes can be based on point-to-point buses or links, if the standard does not already provide it. Most backplane bus standards provide upgrade path from a conventional bus into a new bus.

Point-to-Point buses: The SCI Scalable Coherent Interconnect provide a novel way of interconnecting processor and memory nodes at very high speed which is largely independent of the number of nodes. Any node may send or receive data or commands to other nodes in the network. Topologies of interconnected ringlets can be easily changed by changing the cabling. Standard interconnections between commercial processors and backplane buses like VME are expected to become available soon together with the node chips for specific memory interface designs. SCI presents a very promising solution for the main data steams in LHC as described above.

New features of new buses: The availability of new features like *caching, split transactions, virtual memory access* will allow for better performance, more throughput and new data acquisition concepts. Further studies in connection with test-setups and system simulation are however required. Companion specifications like the CSR specification allow for merging of bus layers and permit to use the same software for different layers. CRC checking, available for SCI, will considerably improve error detection.

3 The ECFABUS model

The ECFABUS model (see Fig. 1) can only serve as a rather crude assumption. Its main purpose is to **provide a common denominator for terms used within the ECFABUS teams**. This model divides the LHC data acquisition into 3 crude areas:

- *detector level* including the trigger level 1
- *bus level*, situated further away from the detector receiving zero-suppressed data from detector channels after trigger 1 'Yes'
- *link level* where high bandwidth is required to link different parts of the detector for global triggers and event building

The Detector level: Due to confinement in space and analog signals this part is unlikely to be implemented using buses. We have therefore excluded, *with the exception of VXIbus* the use of standard buses in this area.

The Bus level: Backplane buses are required in the local trigger-2 data concentrator

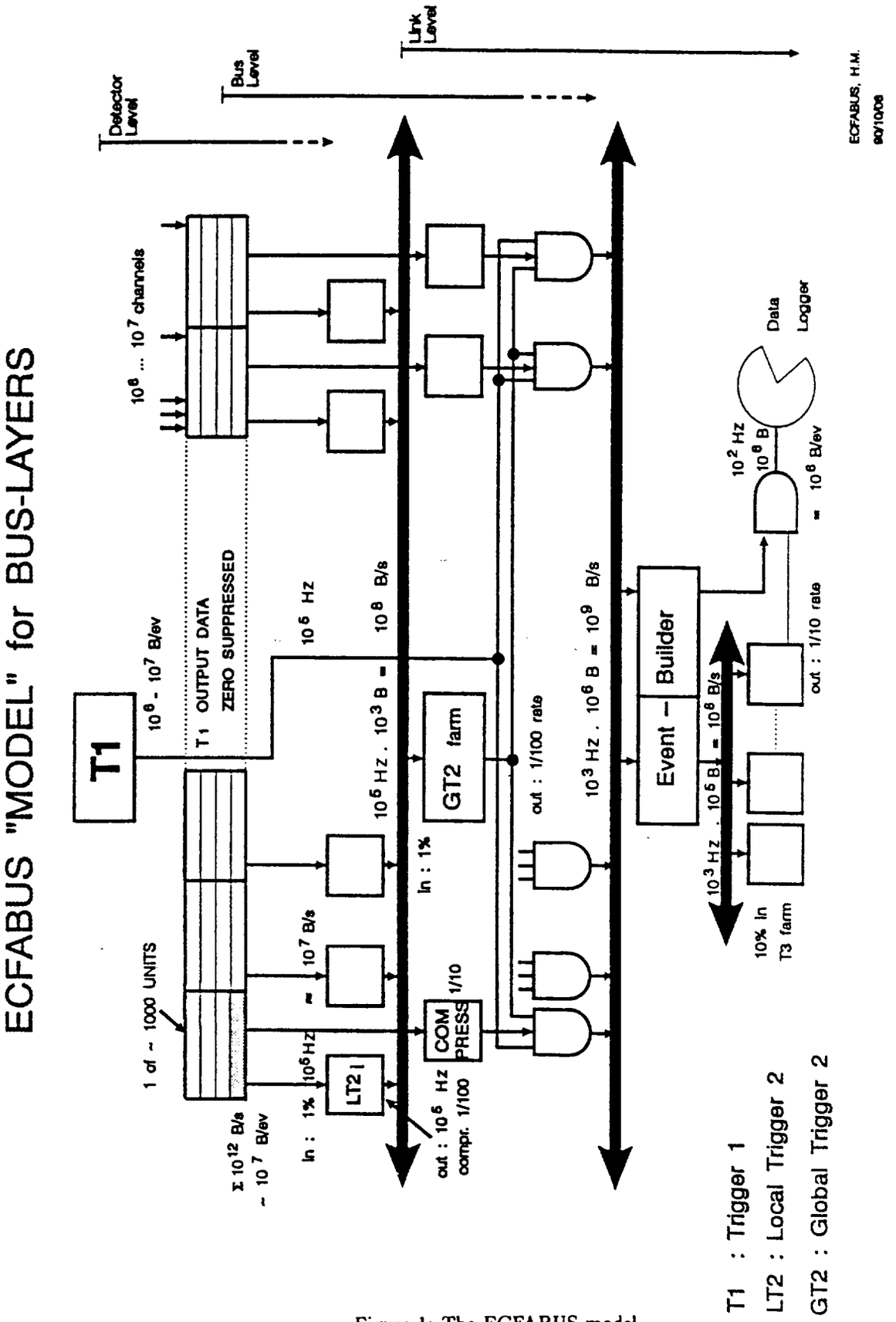


Figure 1: The ECFABUS model

units which in our model, receive digital derandomized and zero suppressed data from the detector.

Units: ECFABUS uses the term *unit* for independent and uniform channel concentrators, receiving data after trigger level 1 'Yes'. They require internal buses in order to be able to act as data concentrators via embedded, fast hardware processors. Event-data is queue-stored in memories, directly accessible from both the local processors and from the output port of the unit. Each unit is independently concerned with local processing such as compaction and formatting. *We assume that 1000 parallel units would be required for* 10^6 *LHC channels* however this number may be scaled.

The local trigger processing performed within the units is assumed to access only 1 % of the data. At 10^5 Hz input, the required unit-internal bandwidth is 10^7 B/s. Such requirements can be met either by conventional backplane buses (like Fastbus, or VME64) or new backplane buses. We conclude that units can be implemented using standard buses with the additional advantage of being economic and modular.

The Link level: The area is concerned with interconnection and routing of data. Since each unit has only very few (ideally one) output channel, the downstream part in our model consists of 1000 channels which need to be interconnected for the 3 data steams: global trigger 2, trigger 3 and data logger. In our model, this will require a total integrated bandwidth of 10^8 bytes/s for each of them.

The global trigger 2: The input rate for this global trigger is equal to the unit's input rate of 10^5 Hz since local processing cannot reduce the rate. Assuming a compression by 1/100 and access to only 1% of date from global trigger2, the total bandwidth required for a global trigger 2 decision is estimated as 10^8 bytes/s.

The event builder: Outputs from n units needs to be combined into one trigger 3 processor and, after a trigger 3 'Yes' into the data logger. Assuming a processor farm with n processors the eventbuilder is 1000 by n switching network. Such problems have undergone intensive SSC studies [6]. We are here only interested in an estimate of the required bandwidth. Bus-specific solutions are described in the companion papers [3] and [1].

In conventional event builders, full data is copied to the trigger processors, however only a 10 % fraction may be used for the trigger 3 decision. We assume that data residing in the units is further compressed by a factor of 10. With a global trigger 2 decision filter factor of 1/100, the estimated bandwidth is 10^8 bytes/s on the input of the trigger 3 processors.

The data logger: Assuming that trigger 3 reduces the input rate by 1/10, data is written at 10^2 Hz with an event size of 10^6 bytes/event. This requires a bandwidth of 10^8 bytes/s and contributes to the load of the event builder network. It is unlikely that the data logging requires explicit use of buses. Commercial computers may be using buses like SCSI (or successors) for tape writing.

4 Applicability survey

A summary table (Fig. 2) has been established, showing our results on applicability of standard buses for the different areas of the LHC data acquisition model. The classifications are based both on the information presented in the companion papers [1] [3] [4] and the bus cross-reference paper [2] and are shown as 4 graduated steps:

- - not applicable
- 0 possible
- + adequate
- ++ best choice

The best choice conclusions are presented in more detail in [5]

	FAST-BUS	FUTURE BUS+	SCI	VME	VXI	SCSI	MAX. CONSTRAINT
T1	-	-	-	-	+	-	SPECIAL FAST ANALOG
T1 -> T2	-	-	-	-	(0)	-	10^6-10^7 Simple
BUFFERING + Loc. T2	++	+(+)	0	+	+	-	10-100 Ev. 10^4-10^5 Hz 1/100 Compr.
LT2 -> GT2	+	+(+)*	++	-	-	-	10^8 B/S from 1000 LT2 units
Buffer -> Ev. Builder	0	+(+)	++	-	-	-	10^9 B/S from 1000 units
Event - Building	0	+(0)**	++	-	-	-	1000 x n -> farm
Ev. Build. T3	0	++	++	-	-	-	10^8 B/S
T3 D. Logger	+	++	++	0(?)	-	-	100 MB/S
-> MASS - STORAGE	-	-	-	-	-	++	4 x 10 MB/S

Figure 2: Survey table ECFABUS

5 Acknowledgments

This work is a group effort of the ECFABUS team.
Special thanks also to: P. LeDu, J. R. Hansen, E. Kristiansen, D. Gustavson, C. Bee, H.Von der Schmitt, S. Cittolin and L. Mapelli as well as to all others who showed interest in our discussions.

References

[1] J.F.Renardy et al., *SCI at LHC* in these proceedings

[2] CSI buses and links group *Buses Cross Reference version 1.0* ECFABUS team, edited by C.Parkman, CN division CERN

[3] D.Linnhöfer et al., *Fastbus at LHC* in these proceedings

[4] G.Heyes et al., *VMEbuses and Futurebus+ at LHC* in these proceedings

[5] L.Mapelli, *Data Acquisition at LHC* Plenary talk in these proceedings

[6] E. Barsotti et al., *Effects of various event building techniques on Data Acquisition Architectures* Proceedings, Computing for High Intensity and High Luminosity Santa Fe 1990

[7] E.Siskind, *Experience with a Fastbus based Data Acquisition System*.. IEEE Trans. Nucl. Sci. Vol NS31., No. 1 Febr. 1984

SCI at LHC

J.F. Renardy J. Belleman A. Bogaerts R. Divià H. Döbbeling
D. Linnhöfer H. Müller R. Mclaren P. Ponting

1 Abstract

SCI, the Scalable Coherent Interface is a draft standard (IEEE P1596) for large multiprocessor systems. It provides bandwidth beyond the capabilities of conventional backplane buses. Its performance is independent of the number of nodes which can reach 65536. Data acquisition systems for LHC experiments are likely to contain thousands of embedded processors and to require a bandwidth of up to 1 GByte/s. SCI is one of the candidates providing this performance. The SCI standard and a model for an SCI based data acquisition system for LHC are described.

2 SCI Basics

Physical/Logical layer The SCI standard [1] defines a point to point connection between nodes which are processors and memories. In practice the physical connection is based on unidirectional rings of flat cables or optical fibres. Each node has one input and one output port. A large SCI system may consist out of several ringlets which communicate through bridges. Throughput, latency and fault tolerance can be optimised by choosing a suitable topology. The distance between neighbouring nodes is limited to tens of meters. The optical fibre companion standard can be used for larger distances at a reduced performance of 1 Gbit/s.

On a SCI cable, 16 bit symbols are transmitted synchronously at 500MHz giving a 1 Gbyte/s throughput for each node. These symbols can be either part of information packets or idle symbols. A packet contains target address (16 bit), command, source address, control and internal address (48 bits), followed by 0, 16, 64 or 256 bytes of data and checksum. New packets can be inserted between circulating packets by the originating node at any time until the ring is saturated to its bandwidth limit. The destination node echoes a truncated packet which is removed by the sender. Idle symbols are generated in exchange for deleted symbols.

An SCI transaction is split in two subactions: a request and a response packet. In a write transaction, data is in the request packet. In a read transaction data is in the response packet. More complex transactions are defined, for instance lock and cache coherence primitives.

Use of SCI SCI has been primarily designed as an interconnect for shared memory and multiprocessor systems providing support for cache coherence. Memory read/write operations are translated by the processor interface into an SCI request packet, which is sent to the memory node. The response packet is used by the SCI interface to complete the processor read/write.

SCI is located between the cache and the main memory and is completely transparent

to the processor.

Cache Coherence in SCI SCI uses a particular cache coherence scheme based on directories distributed in the nodes. This system has been chosen to allow the directory size to scale with the number of nodes and to avoid potential contention which might arise if the directory were located in a single node. The memory node maintains, for each of its cache lines, a directory of all the nodes with a cached copy organised as a distributed linked list. The size of the cache line is 64 bytes. The SCI transactions implementing the cache coherence protocol are divided into several sets. The common part is called base coherence and implements the minimum set of transactions. Performance optimisations are possible by using extra transactions.

3 How to use SCI

A possible application of SCI in an LHC experiment is presented, starting with assumptions about data acquisition. An SCI based architecture is described followed by a discussion of unresolved issues.

3.1 The data acquisition model

The basic parameters such as trigger rates, event sizes and data volumes are taken from the common data acquisition model [2]. The architecture is based on a hypothesis about the segmentation of the detector readout electronics, a possible implementation of the level 2 trigger, and on some assumptions about level 3 trigger processing and data recording.

Segmentation We assume a segmentation in $\approx$ 1000 independent units each collecting data from one sector of a detector (central tracker, calorimeter, muon identifier). We assume that each unit contributes approximately an equal amount of data and has a uniform interface to the readout system. Data in each unit has already been compressed and formated for further trigger processing and recording. Units contain enough storage to buffer events during the trigger decisions.

3.2 Physical layout

Detector channels can be linked in various ways to these units, which may be far away from the detector. Optical fibres will very likely be used to cover the long distance. Short SCI cables may be used to interconnect the outputs of these units (if they are grouped together) with further stages of the system.

level 2 trigger Following the proposal of [3], the second level trigger needs only to process data held by a small fraction (1%) of the units, as marked by the first level trigger decision. The trigger process can be split in a local part, requiring data from a single unit, and a global part requiring the combined output of the local trigger processors. The bandwidth for each local trigger processor is 10^7 bytes/sec, which is well in reach of standard buses. The output of each local trigger processors is estimated to be 10^3 bytes, which gives an integrated data rate of 10^8 bytes/sec into the global trigger 2 processor. This bandwidth exceeds the capacity of existing backplane buses but is well within the capabilities of SCI. The output data of each trigger processor may be buffered locally and accessed directly by the global level 2 trigger processor, thus avoiding data copying and recombination. Alternatively, data can be copied and sent from the SCI nodes of the local trigger processors to a global trigger 2 memory. This data driven approach permits to exploit the full bandwidth of SCI. We assume that, as a result of the local level 2 processing, data may

be further compressed by a factor ten, e.g. by converting channel values in such physical parameters as track coordinates, momenta and energies. The level 3 trigger and data logger will then use compacted data.

Level 3 trigger The level 3 trigger is a software decision based on data of a complete event similar to the level 2 trigger but with more processing time available. From experience of previous experiments (UA1 and ALEPH), it can be assumed that trigger decisions need on average only 10% of the data. One reason for this is that events may be rejected at an early stage of the analysis when only a small fraction of the data has been examined. The same mechanisms provided by SCI for trigger level 2 can be used. In particular, a traditional event builder may be avoided if data is accessed directly. It should be noted that the integrated bandwidth required by an event builder amounts to 10^9 bytes/sec. of which only two times 10^8 bytes are used.

Data recording The event recording requires data to be copied from the unit memories to the data logger, but at a rate very much reduced by the level 3 trigger decision. The data recording rate still amounts to 10^8 bytes/sec.

3.3 SCI model

Rates In the ECFABUS standard model one can identify three data streams: trigger data for the global level 2 trigger, partial events for the level 3 trigger and full events for the data logger as illustrated in Fig. 1. This traffic can be handled by an SCI network with a proper topology.

Topology The topology of the system is illustrated in Fig. 2. It is based on a hierarchy

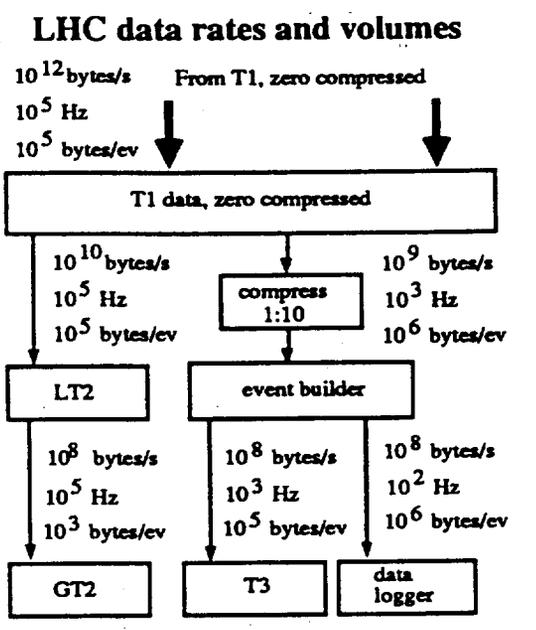


Figure 1: Data rates and volumes.

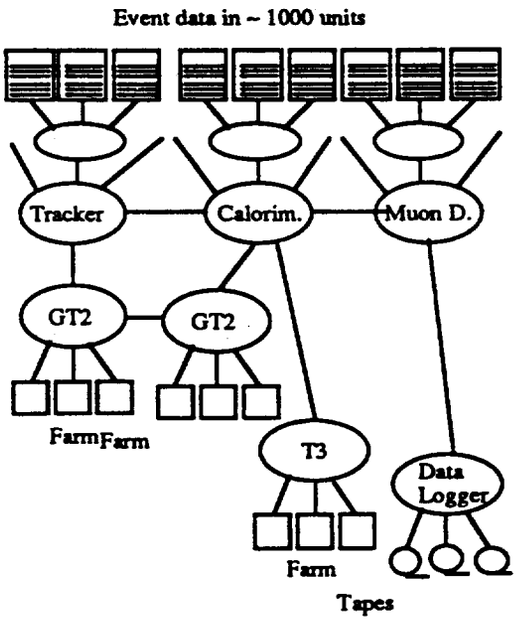


Figure 2: SCI network topology.

of three layers of SCI-rings each containing ten to twenty nodes. Some of these nodes are interconnecting bridges.

Typically $\approx$ 16 units are grouped together in ringlets which form the first layer. Ringlets of the first layer are further grouped making up the second layer. The choice of the grouping of the secondary ringlets may reflect the natural structure of detectors or may be matched to data rates. The ringlets on the third layer correspond to processor farms (the global level 2 and level 3 trigger) and the data logger. Scalability can easily be achieved by adding more layers, rings or bridges if required by data rates or latencies.

Data access The data which is distributed over 1000 memory units is seen by each processor as part of its own memory. SCI protocols allow to access only that part of the data which is used by the processor. A virtual memory scheme may help in simplifying the software required for each of the processors. Repeated access to data is improved by local caching. The SCI cache coherence should be exploited to provide a synchronisation mechanism between the memory units and the global processors.

3.4 Pending questions

There are many issues not yet evaluated in the standard data acquisition system model. Some of these questions require simulation. The important issues are:

- Mapping of event data in the address space of processes. This depends on the implementation of the virtual memory in both the hardware and the system software of the processor.
- Methods used to control the data flow.
- Evaluation of the memory size. The amount of memory required is dominated by the trigger decision time.
- Choice of data structures.
- Optimisation of the SCI network topology.

4 Schedule for commercial SCI

The Standards Committee is proposing a final draft which is expected to be approved before the end of 1990. Some complementary protocols are still evolving, and specific protocol enhancements are expected after the first use of SCI.

The implementation of SCI basic protocols in silicon has started. A VME based starter kit containing a node chip (ECL) is expected to become available during the second half of 1991. The node chip is being designed by Dolphin A.S., Oslo, Norway and will be produced by National Semiconductors, Inc. The chip will be made available in the early stages to developers for US $1000. Commercial implementations of SCI based products are expected to reach the market after 1992.

5 What needs to be done

The first step is to refine the standard data acquisition model. This should be followed by modeling and simulation of alternative architectural configurations to calculate data throughput, latency, deadtime and memory requirements for various detectors. If bottlenecks are encountered, it may be necessary to resort to the optional part of the protocol. This task can be completed by the end of 1992.

Simultaneously, action should begin with a VME based starter kit to get real experience

with SCI, in particular the interfacing of processors and memories. The first tests can be started with a two node system. By the end of 1992 a working system with tens of nodes interfaced to VME should exist. Software aspects, such as the influence of data structures and the mapping of data into virtual memory, needs also to be studied. This should provide sufficient insight to be able to take a decision about the suitability of SCI for the data acquisition system of an LHC experiment by the end of 1992.

6 Conclusions

SCI is expected to become a standard interconnect in high end multi-computer systems. SCI is a commercial standard. It provides bandwidth beyond the capabilities of backplane bus systems. Its scalability and perceived applicability as an interconnect between memories and processors, make SCI an attractive candidate for the three data streams of an LHC data acquisition systems beyond the first level trigger. The SCI protocols contribute significantly to a simplification of the architecture, both in hardware and in software. The schedule for the commercial development of SCI matches the time scale for LHC experiments.

7 Acknowledgements

The proposals in this document are the result of a collective contribution of members of the ECFABUS working groups. Special thanks are due to: C. Bee, D. Burckhart, S. Cittolin, C. Eck, J.R. Hansen, G. Heyes, E. Kristiansen, P. leDu, L. Mapelli, C. Parkman, M. Pentney, J. Petersen, and H. v.d.Schmitt.

References

[1] D.B.Gustavson, "Applications for the Scalable Coherent Interface", AIP Conference Proceedings of Computing for High Luminosity and High Intensity Facilities, Santa Fe, NM 1990

[2] H. Muller, "Buses and Standards for LHC" in these proceedings

[3] J. Strong, "Local/Global scheme" in these proceedings

[4] J.F. Renardy, "Introduction to cache coherence", to be published by the CSI group, CERN, ECP division

Use of Fastbus at LHC

D.Linnhöfer J.Belleman D.Burckhart R.Divià
H.Döbbeling H.Müller M.Pentney P.Ponting
J.F.Renardy

Abstract

The possible use of FASTBUS as a standard in data acquisition systems for experiments at the planned CERN hadron collider LHC is investigated. In a model data acquisition system for LHC the advantages of using FASTBUS are described. It is shown that FASTBUS is a very good choice for certain stages of such a data acquisition system, whereas its use in other stages requires further development.

1 The FASTBUS standard

FASTBUS [2] is an IEEE standard tailored for the use in data acquisition (DAQ) and control systems. The standard itself defines hardware characteristics as well as a set of software routines. FASTBUS modules have slave and/or master capabilities. FASTBUS is a multiplexed bus: 32 data lines (ECL) are used for addresses as well as for data transfer. The address space of each module consists of two different parts: a well defined register part, which has an internal 32-bit address space, and a data part, which also has a 32-bit wide internal address. The register at internal (secondary) address 0 is mandatory for identification and enabling of the module. Physically FASTBUS systems are composed of independent, interconnected segments. Those segments are either backplanes or cables, which interconnect backplane segments. As each segment is independent of each other, data transfers can go on in parallel as long as they do not cross segment boundaries. The Segment Interconnect module (SI) is part of the specification. The primary address (which may be physical, logical or geographical) of any module also contains information about the destination segment which is required for routing the data through the system. A completely automatic connection from the sending module to the destination is provided via lookup route tables in the SIs. For the user the system configuration is transparent. As the SIs are software configurable any topology can be built and the system can be reconfigured by software according to special needs.

FASTBUS provides a lot of additional features which are essential for the successful implementation of DAQ systems. Special broadcast functions

allow to perform very efficient access to distributed data via a sparse data hardware protocol. The distributed arbitration avoids system deadlocks. The large board size, the high power supplies and the well proven cooling systems allow to integrate up to 96 digitizing ADC/TDC channels [3] on one board. A system of modest size (one crate) can hold up to 2400 digitizing channels. Commercial interfaces which connect FASTBUS to a wide variety of computers (PCs, workstations, hosts) and to other buses (CAMAC, VME) are available.

Large FASTBUS systems are currently in use at the LEP experiments and have collected hundreds of Gigabytes of data. Practical bandwidth reached in these experiments in handshaked block transfers is in the order of 40 Mbytes/s. As these limitations are imposed by the current implementations of modules and higher numbers have been reported [4], we expect the typical bandwidth to go up to 80 Mbytes/s in the next years.

2 DAQ model architecture

In order to judge whether the use of FASTBUS is still possible at LHC experiments we have to use an imaginary model [1] of a "typical" DAQ system (see figure 1) and we also have to use rough estimates about the rates. It is certain that the raw data from the detector (about 10^6bytes at 10^5Hz after the first level trigger [6]) cannot be transferred by any conventional bus-based system. So our considerations start with the memories which hold and process these data. Those memories (we need about $O(10^6)$ channels [6]) would occupy a very large number of crates. We imagine a local level-2 trigger acting on a single crate or on a subset of the input data (to look at one specific detector element, or simply to compact the data). Those local results (or compacted data) then are transferred to a second step of the level-2 processor where all results are collected and a decision is made. Depending on that decision the event is either discarded or transferred to the third level of trigger.

3 Implementation in FASTBUS

The modules which receive data from the frontend (after first level decision) need to have many channels on one board in order to get a system of manageable physical size. This is an ideal place to use FASTBUS. As it is now possible to put more than 2000 digitizing channels in one crate it should also be possible to put about the same number of memory channels in one FASTBUS crate. This high density of channels requires for about 10^6 input channels only a system of 500 crates which is a factor of three bigger than the system currently in use by the DELPHI experiment [5]. Also the data rate handled by the local T2 processors seems to be manageable: the data from 2000 channels with an occupancy of at most 10^{-2} [6] have to be read

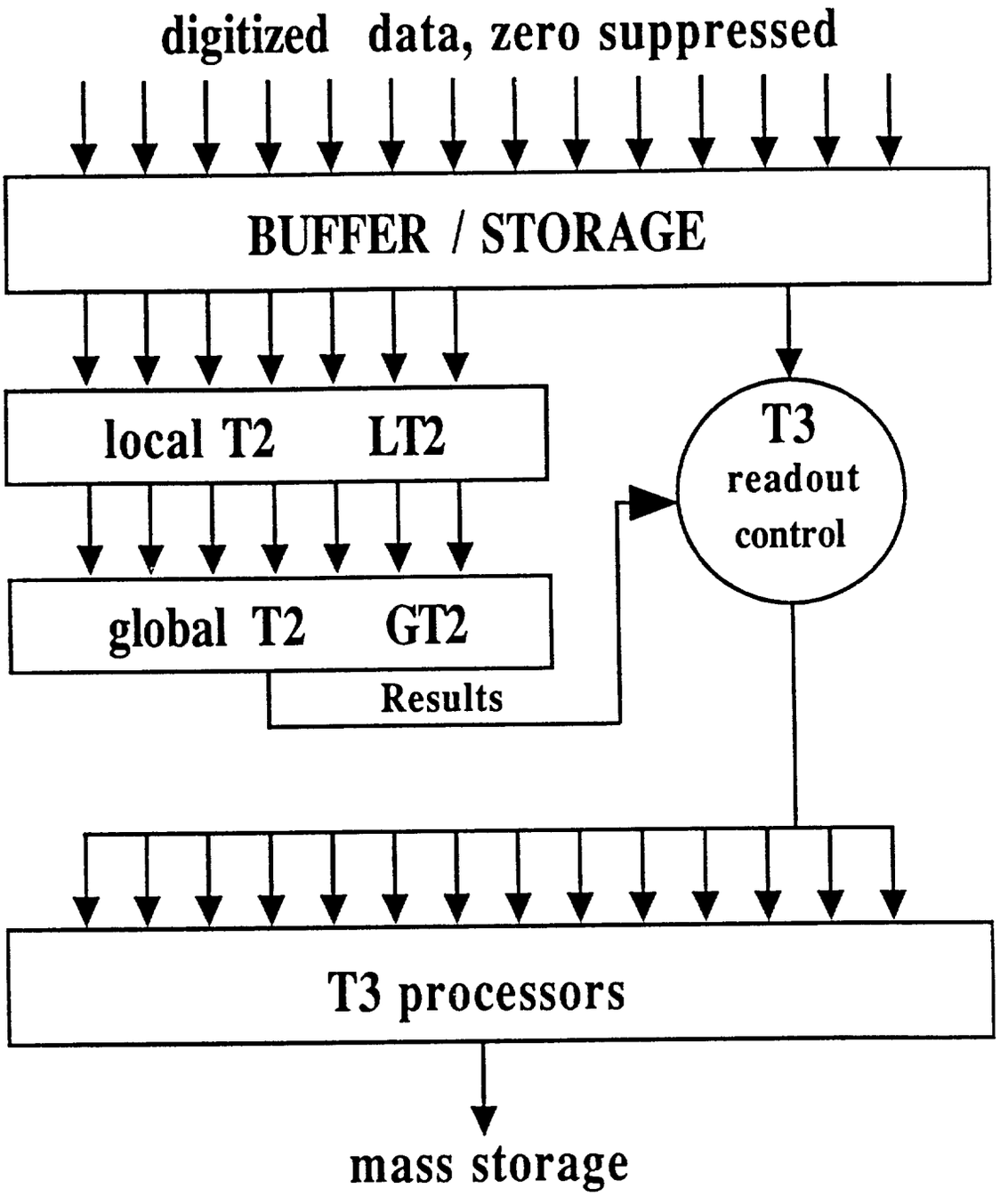


Figure 1: A possible DAQ architecture for LHC

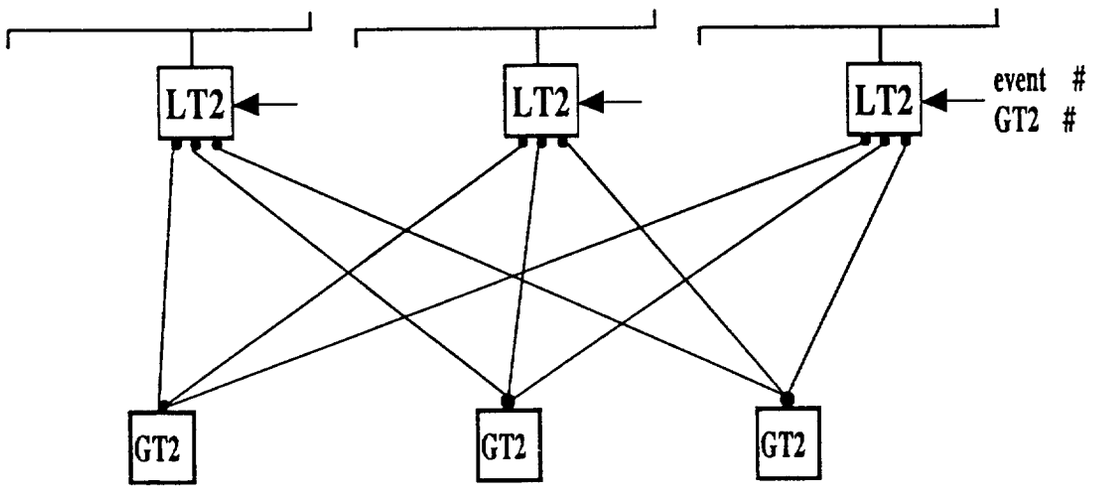


Figure 2: Network for GT2

in about 10 to 100 μs ($\sim$ 1Mbyte/s). This data flow can be easily handled by FASTBUS even if the local T2 works on a cluster of several crates.

On the other hand there is a bandwidth problem as soon as the compacted data from all local processors are combined into one global processor. Here the bandwidth required is about 100 Mbyte/s, which excludes (according to our experience with LEP) the use of a single FASTBUS segment. A possible way to implement this is to use parallelism (see fig.2). The development of new FASTBUS chips [7] will open up the possibility to connect one module to several FASTBUS cable segments. These cable segments can be used as point to point links. Figure 3 shows the same setup as figure 2 but redrawn in FASTBUS terminology. If one of the segments is occupied, the local T2 may send a different event on a different segment. This has another implication: some special (but simple) hardware has to assign to each event one processor to ensure the synchronisation of events. The number of parallel segments is limited by connector space on a module; probably not more than ten are possible. This limits the bandwidth reachable with such a parallel concept to about 1 Gbyte/s.

For the third level trigger there are two problems: the first one is to put the data into the processors and the second one to transfer the accepted events to mass storage. The second step is easy to implement in FASTBUS, as the expected data rates are below 100 Mbyte/s. A data driven event builder concept would require a total bandwidth in the order of 1 Gbyte/s. The solution with several parallel links would also allow the implementation in FASTBUS.

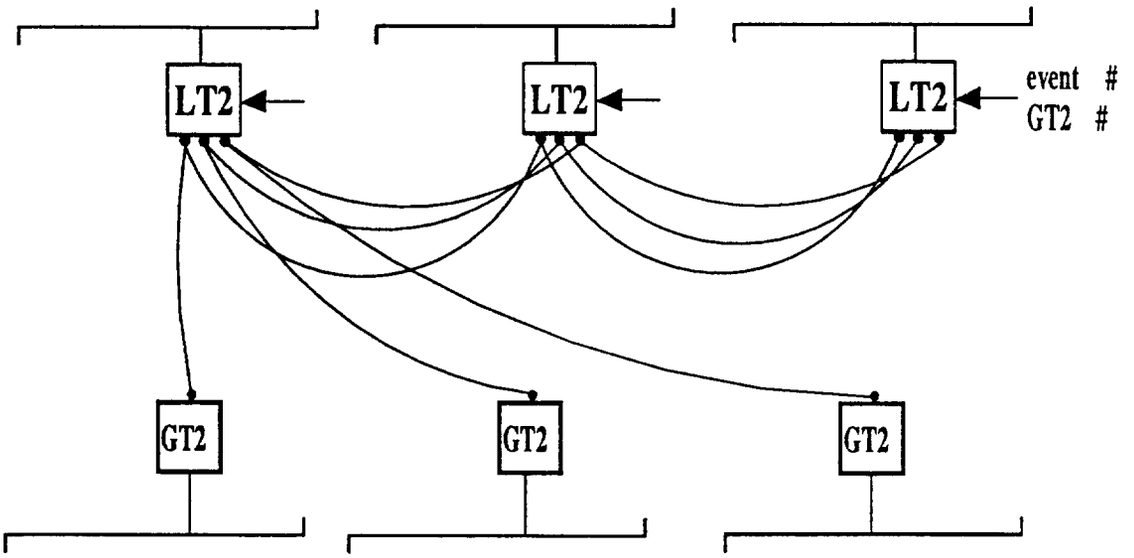


Figure 3: FASTBUS implementation for GT2

4 Conclusions

It has been shown that FASTBUS, due to its board size and high power supply, is well suited to house and readout the memories which hold the level-1 accepted data. The FASTBUS bandwidth is adequate to implement local triggers which work only on a subset of data. The implementation of a global level-2 trigger and of the third level trigger in FASTBUS is possible, but requires very careful considerations and is probably at the limit of what can be done using this standard. In order to use FASTBUS at the planned hadron collider it is necessary to continue developments in FASTBUS. The implementation of reliable, high speed optical cable segments and the development of chips, which integrate all necessary functions to drive a cable segment, are vital for the application of FASTBUS in high bandwidth areas of LHC.

References

[1] H.Müller, Buses and Standards for LHC, this conference

[2] IEEE Standard FASTBUS Modular High-Speed Data Acquisition and Control System
Hardware: IEEE Std.960-1989
Software: IEEE FASTBUS Standard Routines, IEEE Std. 1177-1989

[3] see for example TDC 1879 (LeCroy), ADC 1880 (LeCroy)

[4] Eric.J.Siskind et al., IEEE Trans. Nucl. Sci. NS-32, No.1, 209-211

[5] Delphi uses more than 200 FASTBUS crates, private communication, DELPHI DAS group

[6] L.Mapelli, Data Acquisition, this conference

[7] Product preview by SSI, Los Alamos, NM

The "V"bus family, FUTUREBUS+ and SCSI.

W.G.Heyes, C.F.Parkman,J.A.Bogaerts, J.Petersen, J. von der Schmitt.

Abstract

The ECFA working group on buses was initiated with the task of reviewing the present and short term future situation regarding the standards for buses with a view to making recommendations on the suitability of their use in a general LHC data acquisition system. This report treats the VMEbus, VSB, VXIbus, VICbus, FUTUREBUS+ and SCSI buses.

Introduction

In the general design of a data acquisition system there is a requirement for four varieties of bus, the system bus, the sub-system bus, the cable or interconnect bus and the peripheral bus. A data acquisition system is composed of of functional modules which will typically be micro-processor systems with specific tasks within the overall system. The micro-processor systems physically take the form of a 19 inch rack mounting "crates" and are interconnected by either point-to-point links or an interconnect bus. An interconnect bus is chosen if information available to several systems must be shared between them for example in trigger processing or event building. The boards forming a particular "system" within a crate are connected by the system bus which provides inter-board communication and resources such as clocks and power supplies. Both VMEbus and FUTUREBUS+ are specifications for system buses. The physical format of the bus is one or more rigid backplanes extending the width of the crate. The electronic characteristics of the backplane limit the rate at which information can be distributed between boards to of the order of one hundred million transfers per second. A high data transfer rate can be obtained by transferring several bytes in parallel. The VMEbus has a maximum word width of 32bits (extendible to 64-bits in the latest revision which allows multiplexed

transfers) while for FUTUREBUS+ this value is 256-bits. The data transfer rate for FUTUREBUS+ is of the order of 1 G.byte.S^{-1} so that FUTUREBUS+ is to be recommended where high data transfer rates are required. In some situations, for example trigger processing, it is necessary to connect devices with requirements which are outside the bus specification for example ECL logic or analogue electronics. The VXI bus is an extension to the VMEbus specification which provides standard mechanisms for additional power supplies, well defined analogue and digital signal paths, and RF shielding and so on.

Within a system, because of the finite bandwidth of the system bus it is often necessary to connect two or more boards without resorting to use of the system bus. The VSBbus is a sub-system bus for VMEbus systems which allows the sub-grouping of boards within a VMEbus system.

The SCSI bus is a peripheral bus which provides a mechanism for connecting commercially available "standard" peripherals such as printers, disks and tapes to a system. It is included here for completeness.

The detailed characteristics of the buses treated here is treated in detail elsewhere.[1]

The VMEbus.

The VMEbus specification IEEE-1014 has been extremely successful and is widely accepted commercially. The number of VMEbus manufacturers is numbered in the hundreds and the products in the thousands. VMEbus has for many years been one of the highest performance buses for the construction of modular computer system. This reason and the commercial availability of modules has lead to its use in many high energy physics experiments.

A VMEbus system consists of up to 21 modules in a 19 inch rack mounting crate. The bus is implemented using two 96 way backplanes one of which provides the minimal 16-bit bus with 24-bit addressing while the second provides extension to 32-bit data and address. The second backplane also provides 64 connector pins which are not covered by the specification and are free for user definition or use by the VSBbus. For a 32-bit implementation most bus masters commonly used support block transfer rates of around 10-20M.Byte.S^{-1}. The bus

supports multiple masters on three priority levels and a seven levels of interrupt. Block transfers are supported. The VMEbus specification does not provide high level guide-lines on how to implement a system, such as inter-processor communication and error recovery protocols. The power supply specifications for VMEbus do not easily support analogue or ECL logic on a board.

The VSBbus.

The VSBbus is a sub-system bus designed solely to complement VMEbus, it uses the 64 user definable pins of the VMEbus P2 connector and takes the form of a rigid backplane with between 2 and 6 connectors which plugs onto the back of the VMEbus P2 backplane. The bus provides 32-bit multiplexed address and data, it supports multiple bus masters, interrupts and block transfers. As a complement to VMEbus VSBbus is well matched in performance. The drawbacks of the bus are those of the VMEbus, a lack of system level specification and the board size limit.

The VXIbus.

The VXIbus is a specification for an instrumentation bus which uses the VMEbus specification as a basis. Four board formats are specified. Formats A and B are equivalent to the VMEbus specification for 16 and 32-bit modules, in the case of format B the 64 user definable pins of the VMEbus are completely specified by VXIbus as additional power supplies, clocks, analogue and digital lines. Format C extends the boards area of format B by lengthening the board from 6.3 to 9.2 inches. With format D a third backplane is added and the board size is increased to 14.4 by 13.4 inches. The VXIbus slot width for formats C and D is 1.2 inches (compared with 0.8 for VMEbus) which allows for electromagnetic screening between boards. The VXIbus specification allows commercial VMEbus boards to be used if they do not make any assignments to the outer rows of pins of the P2 connector.

VXIbus is in use in nuclear physics, commercial and military applications were the large board size and provision for ECL and low level analogue signals make it an ideal instrumentation bus. VXI was intended as a successor to GPIB and is rapidly gaining popularity.

The VICbus.

The VICbus is a specification for an interconnect bus for use with buses such as

VMEbus. Interfaces to several buses have been implemented so that a mixed system can be implemented. Physically VICbus is a cable bus with several systems connected at intervals along the cable by master or slave interfaces. It provides 32-bit memory mapped or buffered transfers between tested at at a rate of 3 M.Byte.S^{-1}. Multiple masters are allowed and interrupts can be transmitted by slave interface to the master.

VICbus is a true bus allowing transparent memory mapped transfers between up to 31 devices on cables up to 100m long.

FUTUREBUS+.

FUTUREBUS+ is a specification, in an advanced stage of preparation, for a system bus. A specification for an interconnect bus is being prepared. The bus is will support the technology which it is expected will be developed by the start of the 21st century but but can be realised now. The backplane system bus suffers from the usual theoretical transfer rate limitations but by allowing a scalable data word size of up to 256-bits in parallel it is possible for 2.3G.Byte.S^{-1} transfer rates to be realised with currently available technology. The bus contains specifications for multiple bus masters, interrupt handling as well as specifications for high level system features such as cache coherence across the bus.

The first FUTUREBUS+ products are to be expected by the end of 1991 which is within the timescale of any LHC projects.The draft specification for the bus is already available. Its expected characteristics put FUTUREBUS+ in the performance range which can handle the main data stream from an LHC experiment. The specification of a high speed interconnect bus would allow FUTUREBUS+ to be used in areas such as the event builder where a high degree of connectivity is required.

SCSI.

SCSI, small computer system interface, is designed to provide access to peripherals such as tape and disk drives, printers and so on. It is the most widely used interface for personal computers and workstations but is becoming increasingly used in data acquisition. Cartridge tape drive systems driven from VMEbus via a SCSI interface are available which will handle rates of 3-4 M.bytes.S^{-1}. An update to the specification provides for either an increased word width and/or improved protocol to increase throughput. A

system of several tapes writing in parallel could be implemented with current technology to handle the expected data rate for an LHC experiment. It is likely that a system of this type will be used to provide data logging in LHC experiments.

CONCLUSIONS.

The ECFABUS working group has proposed a simple standard model for a LHC data acquisition system. [2] Based upon these assumptions an estimate of the usefulness of the bus standards described here can be made.

The data transfer rate for VMEbus although adequate for applications in current generation experiments is an order of magnitude too low for VMEbus to be used in the main data stream of a typical LHC experiment. The extension to 64-bits goes some way to relieving this problem but VMEbus still falls short in performance. The VMEbus could still find uses in the data acquisition at those points where the more performant but also more expensive systems would not be required, in particular the monitoring of data samples, control and data logging. However, VMEbus still has a role to play since it is cheap and widely available it is likely that it will be used for medium speed data acquisition, for example monitoring and on-line event analysis where only a sample of the data stream is treated. VMEbus may also have a valuable role to play in control of the overall system and downloading of software especially as the internal bus of workstations.

In a LHC environment VXIbus could perhaps find application in the trigger where the availability of a large board area, ECL supplies and bus lines would be useful. As an instrumentation bus VXIbus could find an application in what is currently called slow control. In LHC it will be necessary to provide information on hardware failure in real time to allow for dynamic reconfiguration without stopping data taking.

By the time the first LHC experiment comes on line FUTUREBUS+ will be able to provide the required performance for handling the main data stream. It is also likely that FUTUREBUS+ hardware will be available during the early planning stage when prototypes are required. However the cost of FUTUREBUS+ hardware may mean that at stages where massive parallelism is required a different solution will be required.

Finally it is likely that the data from a LHC experiment will be recorded on a high speed recording medium by drives interfaced via SCSI bus to dedicated VMEbus or FUTUREBUS+ data logging systems.

Acknowledgements

The content of this document is the result of a collaborative effort on behalf of the members of the ECFABUS working groups.

References

[1] "Summary of backplane bus characteristics", Editor C.F.Parkman, (to be published by the CSI group), and references therein.

[2]"Standards and buses for LHC",, H.Muller, in these proceedings.

Report of the ECFA working group on Fast Data Links

Edited by M. Lomo and R.A. McLaren

The members of the working group were:-

Jacques Anthonioz-Blanc (CERN), Adolfo Fucci (CERN), Ian Kenyon (University of Birmingham), Morten Lomo (CERN), Robert McLaren (CERN), Emilio Petrolo (INFN/Rome), Esko Pietarinen (University of Helsinki), Jean Francois Renardy (SACLAY).

The working group decided, from the outset, to concentrate on individual projects and interests rather than to aim for a complete "state of the art" report. There was, for example, no attempt within the working group to review available components or to compile lists of price and performance data. There was also no attempt to compare the use of buses and links in different architectures, as this was felt to be outside our mandate.

Gigabit optical links are starting to appear on the market. Major computer manufacturers including IBM, DEC and Hewlett Packard all have working prototypes. Components to build these links are also now available from companies like Gigabit Logic, Vitesse, and BT&D.

Roberto Cardarelli working at INFN (Rome) has gained considerable experience with these components in building STARNET. In the STARNET topology, the stations are connected to a passive star coupler and to the central controller using asynchronous and point-to-point channels. The central controller optimizes the traffic using a Request-to-send Clear-to-send protocol and hardware timing control depending on fixed parameters (relative distances, guard times, response times) and variable parameters (length of data packets) Final tests will be carried out before the end of this year. The Data link channel is realized using GaAs technology.

Emilio Petrolo and Paulo Cennini have developed, for the UA1 experiment, the largest optical data transmission system presently in use in HEP. The system, installed in 1987, is composed of approximately 420 data links and is based on the PArallel TRansmission Optical Link (PATROL) component. In this component the data are loaded and received as a 16 bit parallel word at 16.6 Mbit/s. A 100 Mbit/s version of PATROL system, using discrete components, has also been prototyped.

The INFN R&D board has financed, in FY 1991, a project for the development of a transreceiver chipset for optical data suitable for HEP applications. The link will work at 1 Gbit/s and the project will be developed in Rome (INFN/Roma1 E. Petrolo and INFN/Roma2 R. Cardarelli).

Ian Kenyon and his colleagues at Birmingham University, have an opto-electronics program whose objectives are to investigate opto-electronic

solutions to the problems posed by high rate and high luminosity at LHC for DAQ and triggering.

Last year, they completed work on a simple FDDI fiber test link using the AMD Taxi chipset. This revealed the difficulties of testing systems at full speed and the necessity of a dedicated bit error rate tester.

A project for a 10 Km, 1 Gbit/s. optical link between the L3 online and offline computer is also under way. The project team is drawn from Birmingham University, CERN, and Hewlett Packard Laboratories in Bristol. The project should be completed within two years.

Birmingham has also compiled a market survey of available chipsets and opto-electronic components. The Vitesse chipset, plus some Gigabit Logic components offers capability at above 1 Gbit/s. A design based on these components has begun.

Adolfo Fucci and Morten Lomo are in contact with the USA Naval Air Development Center that has developed a high speed, serial, fiber optic switched network. They offer a prototype for 40/60 days evaluation. The link can run up to 1 Gbit/s.

The prototype includes a cross-bar switch. The encoder/decoder section has been fabricated in gallium arsenide. The 4B/5B encoder accepts 8 or 16-bit parallel words which are serialized. The decoder reverses this process so that the network is completely transparent to the user. Communication is completely asynchronous. The handshake protocol is via a simple DATA READY/ACK scheme, and the network may also transmit a small number of command words.

There is a danger in looking at the components for links that one forgets that the link must connect to a memory or bus system. With this in mind, **Jean Francois Renardy** is looking at the possibility of using the Scalable Coherent Interface Protocol as a simple link. This work is covered in his SCI paper.

Jean Francois is also investigating SONET, (Synchronous Optical NETwork). This is the new PTT network which will eventually be implemented worldwide. Basic specifications were agreed in 1988 and the final standards will be approved in 1992. Already, many manufacturers (AT&T, GTE, Alcatel, Siemens, Ericson...) propose SONET compliant equipment. HEP may not need SONET switches and control centers, but SONET links can be used for our point-to-point digital connections.

SONET modems for transparent bit streams have been designed for the initial deployment of the network: any PTT link can have its specific modems replaced by the SONET ones without disruption. If one chooses one of the PTT bit rates, HEP applications can use easily these modems . The optical fiber and transmitter/receiver for short distance are described in G652.

Robert McLaren is looking at the HIPPI and Fiber Channel. HIPPI is currently under review by ANSI and a completed standard is expected this year. The standard has also been proposed to ISO. HIPPI is a 32 bit parallel, point to point link which transfers data in one direction (simplex) at 100 or 200 Mbyte/s. It runs over 25 meters of twisted pair cable (there is 1 cable for the 100 Mbyte/s version and 2 cables for the 200 Mbyte/s version). Flow control across HIPPI is distance independent and it is possible to build fiber optic "extenders" which run at full bandwidth. Error detection is provided by byte parity on the 32 bit data words and a checksum at the end of every (256 word) burst of data. The protocol on the HIPPI is very simple using only Request, Connect, Packet, Burst and Ready signals.

Fiber Channel is a draft ANSI proposal for a network which would transport IPI, SCSI and HIPPI protocols. The standard defines Fiber Channel as running at 1.0625 Gbit/s over single mode optic fiber. Up to 2 Kms between stations is envisaged with an error rate of better than 10^{-15}.

It may, or may not, be possible to directly use these standards in data acquisition systems. However the components which they generate are very relevant. For example the circuits being designed for the High Definition TeleVision standard have the performance and functionality required by DAQ systems of the future.

The use of 1 Gbit/s links is at present expensive and it is not certain that there will be enough commercial applications to drive the price down. There is therefore an interest in using multiple, 100 Mbit/s links made of cheaper components.

Esko Pietarinen has designed a VMEbus inter-crate module (VMExi) using the TAXI chipset from AMD. The chipset components are a transmitter and a receiver which are both cheap and simple to use. The transmitter accepts 8-10 bits of parallel information which it encodes and serializes. At the receiver, the serial data is then reconverted back to the original 8-10 bits. TAXI chips run at 175 Mbit/s. The serial output of the TAXI chips is ECL, this means that a Electrical/Optical convertor is required for transmission over optical fiber. A new series of components, known as FOXI, integrates the TAXI chips and the convertor on a single hybrid. This component is currently being tested.

Esko is also committed to the development of a low cost, parallel, fiber optic connection to replace the copper connections. He is collaborating with Tampere University and companies in Finland. The aim is to integrate the electronics, optics and the interconnection components .

Morten Lomo is using the VMExi in connection with the PPCS project, a joint venture between IBM and CERN on parallel computing. The idea is to be able to run the applications which now run from the local host, also from a remote host. Communication drivers for the optical link, and modifications to the software drivers at the host, are now being implemented.

The VMExi link will be used in two transfer modes: window and DMA. The window mode makes transparent VMEbus accesses into the remote crate, it is used primarily for commands and transfer of messages. The DMA mode is used mostly for fast data block transfers.

Jacques Anthonioz-Blanc is working on the Fiber Distributed Data Interface (FDDI) which is a 125 Mbit/s standard used for networks. Presently FDDI is used as a backbone for the CERN network. All the Ethernet segments are interconnected via translating MAC level bridges to the backbone. The FDDI ring is made of bridges and wire concentrators from the same vendor. The FDDI stations from various vendors could be included in the backbone if they are fully compliant to the standard. When a new FDDI station is proposed it is first tested in a so called "test" ring before insertion. The LEP experiments will have their own FDDI rings in the near future probably connected to the backbone ring when FDDI to FDDI bridges will be available. FDDI can be used for a point to point link connection.

Buses and links will certainly co-exist in the future. We must now work to understand how best to combine the two. In addition there is the topology of the interconnecting "fabric" to consider. There are two possible directions: hands-on experience and simulation.

Simulation provides a tool which allows us to investigate new components and architectures. Erik van der Bij and Marina Passaseo, amongst others, have simulated the use of a crossbar switch to build events. This work is now being continued in the INFN (Rome) by Mary Censa Ferrer and Jinyuan Wang.

To conclude, some recommendations:-

We must understand how the wide choice of "building blocks", which includes processors, links, buses, switches, etc., can be used together in future data acquisition systems. These activities should be organized in the framework of one, or several, of the proposed DRDC projects.

A fiber optic laboratory should be set up within the HEP community. This would provide test equipment for analog and digital transmission at speeds up to 2 Gbit/s. In addition it should investigate "new applications" which would include the use of fiber optics to bring data from the detectors and their use as sensors of temperature, pressure etc.

DAQ Simulation for LHC

G.Fumagalli, G.Mornacchi, J-P.Porte

Verilog, a C like hardware description language already used at CERN for electronic design and gate level simulation, has been used to study statistical behavior of some DAQ architecture (M.Passaseo, E.van der Bij, L.Zanello). Meaningful results were obtained but there we had some concern about the overkilling complexity of Verilog for flexible evaluation of hardware architectures. We have tried to find a tool which would not require much expert help and could be used by the designers of DAQ architectures with minimal training.

After some preliminary investigations and discussions with people with experience in simulation (notably M.Botlo, now at SSC, and J.F.Renardy) we have focussed on products from CACI, a company with a long experience in the field.

Several specialized packages are available, but they are not extensible and, although they may offer a much faster solution in some cases, we feel that they cannot be recommended for general use. Our main effort of evaluation has been focussed on two simulation languages **MODSIM** and **SIMSCRIPT**.

MODSIM a modern Object-Oriented language, similar to Modula-2, is still in development. It may become in the future, with an iconic interfaces, one of the best tool for the type of simulation we are looking for. At the time being, we feel it would not be easy to use by engineers and physicists not yet enough acquainted with the object-oriented techniques.

SIMSCRIPT, an old classic, easy to use by non-professional programmers, was extensively evaluated and is now installed at CERN on a SUN SLC.

The choice of SIMSCRIPT as the best tool for a first step in systematic simulation of data acquisition and readout architecture must not preclude other solutions for the future, besides MODSIM.

New modern products like SES/***workbench***, an iconic simulation and design tool, linked to some of the major CASE systems now available or in development, is being investigated at SSC.

It must also be remembered that if very high efficiency is required nothing is going to beat general purpose languages like **FORTRAN** or **C**.

Other "general purpose" languages like **SMALLTALK** should be well adapted to simulation studies.

We must also watch **VHDL**, the emerging standard for hardware description.

A quick overview of SIMSCRIPT

This language has been designed for discrete, process-oriented simulation. It has evolved over 20 years, many of its features were added as a result of user feed-back.

The documentation is very good, large but well organized, several books and many articles describe the language and its applications.

During our evaluation, we found SIMSCRIPT quite easy to use. It was possible to do useful things quickly with a small subset of the language after reading only a small fraction of the documentation.

Programs written in SIMSCRIPT are easy to read. If special care is taken when they are originally written, they may even be made understandable by non-programmers field specialists, who are then able to check the conditions of the simulation and to make minor modifications.

The built-in statistical tools are powerful and easy to switch-on.

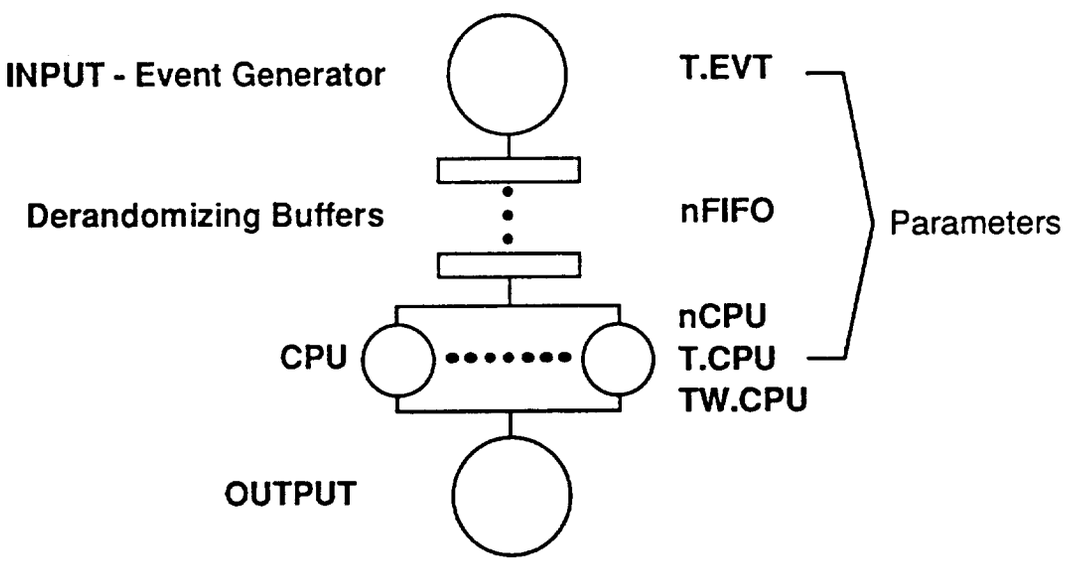
The library is well adapted to simulation (e.g. extensive choice of random distributions).

Animated graphics, are easy to plug-in an existing SIMSCRIPT program.

FORTRAN and C routines can be called directly from SIMSCRIPT. The compiler produces intermediate C code which can be modified if needed.

Sketch of a SIMSCRIPT program

Let us demonstrate the use of SIMSCRIPT on the simple following example:



A SIMSCRIPT program is divided in
- a PREAMBLE to declare processes and resources and define statistics
- a MAIN routine to set up the environment and start up the simulation
- processes to be activated at various points in time by the simulation engine

In our example **EVT**, the most important process, describes the fate of an event in the read-out setup.

```
PREAMBLE
  processes include GENERATOR, EVT
  resources include FIFO, CPU
...
''tell SIMSCRIPT to gather statistics on number of busy FIFO and CPU
  accumulate ABUSYF = average and MBUSYF = maximum of N.X.FIFO
  accumulate ABUSYC = average and MBUSYC = maximum of N.X.CPU
  accumulate CPUBUSY.HIST (0 to 99 by 1) as the histogram of N.X.CPU
...
MAIN
... define parameters:  nEVT, T.EVT, nFIFO, nCPU,T.CPU,TW.CPU
... (by reading a data file or by typing them interactively)
  create every FIFO(1), CPU(1)
  U.FIFO = nFIFO  U.CPU = nCPU  "tell SIMSCRIPT how many FIFO & CPU
  activate a GENERATOR now
  START SIMULATION
...
PROCESS  GENERATOR
  for ievt = 1 to 10000000  do ''(simulation will be stopped in EVT)
    activate an EVT
    wait EXPONENTIAL.F(T.EVT,1) microsec  ''wait before next event
    loop
...
PROCESS  EVT
  if U.FIFO = 0   add 1 to nLOST   go to 'EndEvt'   always
  request 1 FIFO

  request 1 CPU
  relinquish 1 FIFO
  wait NORMAL.F(T.CPU,TW.CPU,2) microsec

  relinquish 1 CPU

'EndEvt'  add 1 to nTHRU   if nTHRU < nEVT return   always

''End of Event Generation
... print run statistics nLOST, nTHRU and compute dead-time etc...
... print statistics of FIFO occupancy:  ABUSYF and MBUSYF
... print statistics of CPU  occupancy:  ABUSYC and MBUSYC
... print histogram of CPU occupancy:    CPUBUSY.HIST
END
```

Notes:
- "..." replaces parts of the program not essential for our purpose
- the construct "if...always" is equivalent to the FORTRAN "if...endif"
- different random streams are used for event generation and CPU time
- U.rrr and N.X.rrr are internal SIMSCRIPT variables automatically associated with declared resources

DAQ simulation exercises performed so far

Cross bar switch event builder (VERILOG)
a rather complex simulation of ~1000 lines,
took one week to implement by a team of physicists + Verilog expert

A simplified TRD 2nd level trigger (VERILOG, SIMSCRIPT)

A simple DAQ block (VERILOG, SIMSCRIPT, MODSIM)

Simplified UA2 acquisition

- VERILOG	1200 lines of code	
		1000 sec for 10^5 events (SUN SLC)
- SIMSCRIPT	450 lines	
		more statistics available
		about 10 times faster (as implemented !)
- MODSIM	850 lines	
		more statistics available
		twice slower than SIMSCRIPT

(in all cases ~200 lines for parameter definition & printout)

2nd level calorimeter trigger scheme for LHC (J.Strong)
the first actual simulation study for LHC using SIMSCRIPT
estimated implementation time 3 days, assuming some experience

. parameter definition & printout	300 lines
. generator	100 lines
. event flow	150 lines

11 minutes on SUN SLC for 10^5 events (1 sec data taking)

Digital Front-end Electronics for Calorimetry at LHC

G. GOGGI
CERN, Geneva, Switzerland
Pavia University and INFN, Pavia, Italy

B. LOFSTEDT
CERN, Geneva,Switzerland

Abstract

Front-end signal processing for calorimetric detectors is a necessary ingredient to achieve adequate selectivity in the trigger functions of an LHC experiment. Furthermore, data identification and compaction before read out is mandatory in the harsh, high-rate environment of a high-luminosity hadron machine. Another crucial consideration is the extremely wide dynamic range requirements for this type of electronics. These requirements are best met by an early digitalization of the detector information, followed by on-chip DSP and buffering functions at both the Level 1 and Level 2 trigger latencies. In this paper we propose a fully digital approach to the front-end electronic chain suitable for all classes of calorimeter performance.

1. Introduction.

Front-end electronics for calorimetry at LHC has to meet simultaneously a number of very stringent requirements. It must be capable of providing fast information to the first-level trigger chain at the 66 MHz frequency of the collider without dead-time, exploiting the signal speed and resolution of the detector over an extremely wide dynamic range. Also it must store, or pipeline, the input signals at the bunch crossing frequency for a period corresponding to the first-level trigger latency.

Both analog and digital approaches to this problem are possible. In the former, the complete analog information must be preserved with full resolution in the storage process before conversion. In the latter, only digital storage is required, which allows the most stringent demands on the electronics chain to be concentrated at the converter stage. A fast digital approach offers in addition a unique flexibility, in allowing a certain amount of programmable digital signal processing (DSP) to be integrated in the very early stages of the acquisition chain. It therefore lends itself to the integration of the conversion, filtering, control and readout functions into the logical and physical structure of the detector.

In the first part of this paper, we discuss the basic parameters of A/D conversion in digital front-end calorimeter electronics. The parameters are completely specified in terms of signal speed, bunch crossing frequency and detector resolution and represent the basic input for a realistic implementation. It is to be noted that the same considerations apply, but for speed considerations, to the A/D converter stage of any LHC calorimeter electronics irrespective of its location in the data acquisition chain. In the second part of the paper we propose a possible architecture for a digital front-end and readout chain in terms of the basic functions in each separate stage and of the overall system performance, including data reduction, readout and control functions.

The proposed scheme, which requires sampling rates at or above the bunch crossing frequency, can be based on Flash A/D converters, complemented by digital correction and signal processing circuits. Taking advantage of the digital pipeline structure, transversal filters (FIR) can be directly integrated into the structure. The necessary derandomizing and buffering of the data before final readout can be implemented locally. A local energy sum information for the first level trigger process can be extracted from the filter functions and the second level trigger process can randomly access the buffered data.

The majority of the above mentioned functional blocks can be implemented with today's standard ASIC technology. However, the A/D converter must be developed since nothing exists on the market that fulfils the required specifications. Such an item is feasible today at the laboratory level[1-4]. A careful extrapolation of the advancement in production technologies makes us to believe that within one or two years industrial production of such a device could be a reality.

2. Dynamic range and Resolution.

The dynamic range necessary for calorimetry at LHC is mainly dictated by physics and detector requirements for electron detection. At the high end of the energy spectrum, basic considerations are the maximum electron energy and detector granularity. Lateral calorimeter segmentations of the order of the Moliere radius, which optimize both energy and position resolution, correspond to deposits of up to 80-90% of the electron energy in a single cell. At the low end of the spectrum, energy isolation criteria for the identification of electrons in a hadronic environment require adequate sensitivity down to the level of the noise generated by event pileup and electronics. Therefore, assuming a maximum detectable mass of an hypothetical Z' boson of about 4 to 5 TeV, and a "noise" level between 50 and 100 MeV per cell, the required dynamic range turns out to be about 15 bits.

The resolution of the A/D conversion and the characteristics of the preceding (nonlinear) (analog) transfer function are determined by the energy resolution of the detector and by the requirement that quantization noise contribute in a negligible way to the overall resolution of the system.

If f(E) is the fractional energy resolution of the calorimeter,

$$f(E) = a/E \oplus (b/\sqrt{E} + c) \tag{1}$$

a quantization matched to the detector resolution implies,

$$LSB(E) \leq \sigma(E)/k \tag{2}$$

where $\sigma(E)$ is the energy resolution and k a constant. Using the relation (3a), eq.(2) translates into a bound (3b) on the transfer function n(E) of the converter,

$$dn(E)/dE = (LSB(E))^{-1} \tag{3a}$$

$$dn(E)/dE \geq k/E\ f(E) \tag{3b}$$

The value of k is set by the contribution of σ_n, the s.d. of the quantization uncertainty, to the overall resolution:

$$\sigma_n = \sigma(E)/k\sqrt{12} \qquad \sigma_{tot}(E) = \sigma(E) \oplus \sigma_n(E) \tag{4}$$

For instance, assuming an upper limit of 8%:

$$R = \sigma_{tot}(E)/\sigma(E) - 1 \leq 0.08 \tag{5}$$

yields

$$k \approx 1/\sqrt{2}$$

Eqs. (3a) and (3b) can be used in two ways. On one side, for any given detector resolution f(E), eq. (3b) and its integral yield a lower bound on the transfer curve and its derivative, to be compared with realistic hardware implementations. On the other side, any arbitrary choice of n(E), both in functional form and total

resolution, can be compared through (3a) to the matching condition given by eq.(2).

Fig. 1 shows the minimal transfer function, $n_{min}(E)$, as a function of energy for two detector resolutions. Case A corresponds to the measured performance of a scintillating fibre calorimeter[5] (b=0.13, c=0.01), whereas case B (b=0.08, c=0.007) shows the sensitivity of this analysis to a substantial improvement in detector performance. In both cases we assume a=0.05 (GeV). As an example, the minimal transfer functions are compared to simple logarithmic functions having a resolution of 9, 10 and 11 bits respectively. All transfer curves are normalized to two counts at E=0.1 GeV.

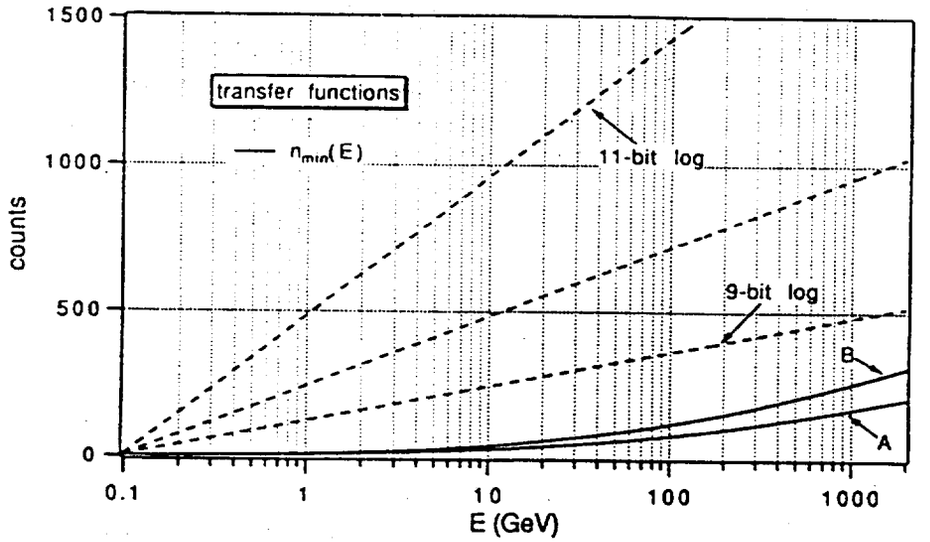


Figure 1

It may appear from fig. 1 that a 9-bit logarithmic curve already exceeds the required resolution for both types of detectors. However, the condition given by eq.(2) becomes dominant at high energies. This is shown in fig. 2, in which the LSB values corresponding to the three logarithmic curves are compared to the maximum values allowed by eq. (2) (with $k = 1/\sqrt{2}$).

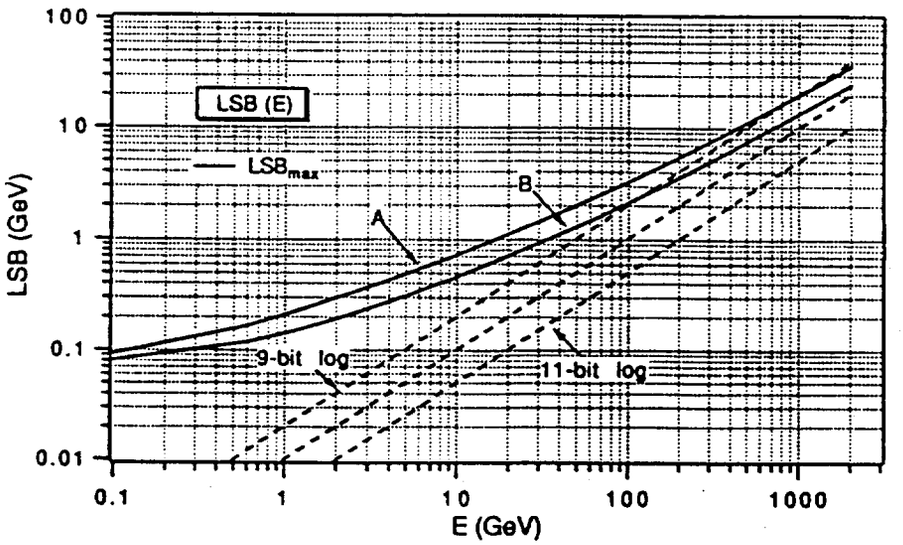


Figure 2

It is to be noted that this comparison rests on the value of k, which sets the scale of the effect on the overall resolution introduced by the matching condition (2). In order to assess this effect independently of k and with realistic transfer functions, the quantity R (eq.(5)) has been computed for the three logarithmic transfer curves. The results for the two detector models A and B are shown in figs. 3 and 4 respectively.

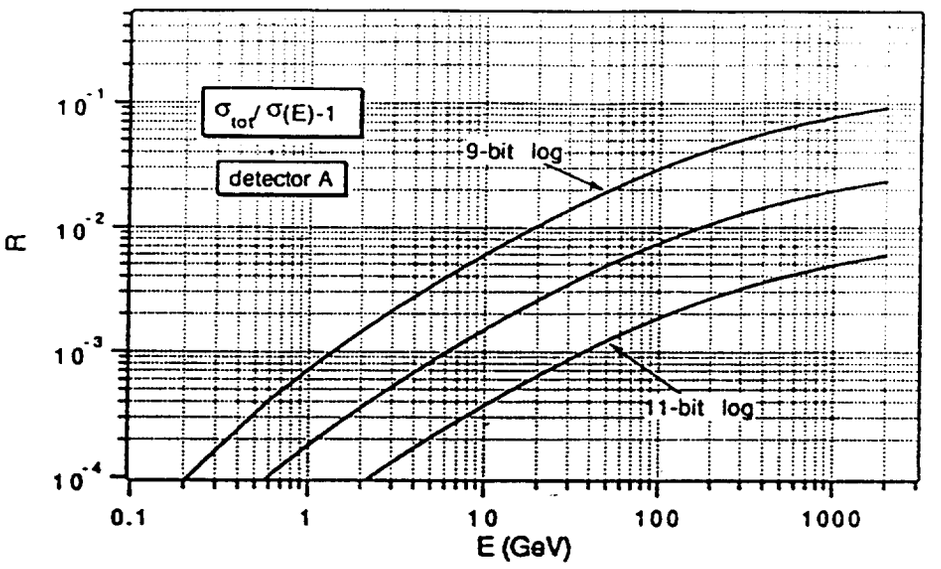


Figure 3

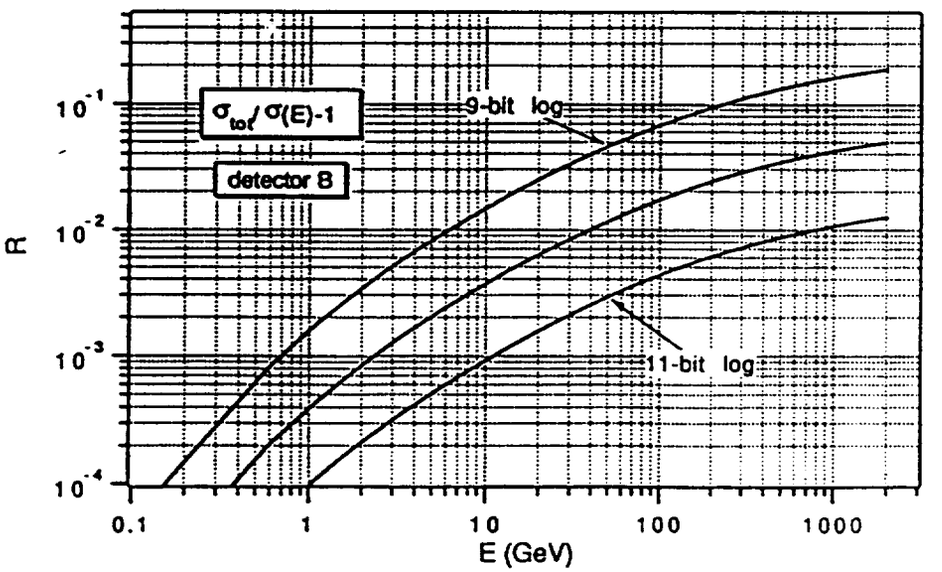


Figure 4

A 9-bit logarithmic response seems adequate for case A since the worst-case effect on the resolution does not exceed 10% and only at the highest energy, where the absolute effect is minimal ($\approx 10^{-3}$ at E = 2 TeV). For case B, a 9=bit resolution would worsen the constant term c from 0.007 to about 0.008 at the highest energy,while the 10-bit resolution would have a negligible effect on c. A third family of calorimeters, typically consisting of homogeneous scintillating crystals, has resolutions with parameters $b \approx 0.02$ and $c \approx 0.005$. More complex transfer functions (e.g. "broken log") can match the requirements of this type of detector within the 10-bit resolution range.

It can be concluded that, with purely logarithmic transfer functions and taking into account the imperfections of the A/D converter, resolution of at most 10 bits is adequate for most calorimetric detectors in the LHC energy range. However, approximations other than logarithmic to the transfer function can make more efficient use of the resolution of the converter, eventually leading to the choice of a 9-bit converter. The only condition that such curves must meet is to have a monotonic behaviour over the entire dynamic range.

3. Sampling speed and Shaping.

The sampling frequency, (f_s), typically equal to the LHC bunch crossing frequency (f_{co}), could be chosen as a (sub)multiple of f_{co} depending on the nature of the signal to be digitized. A realistic range of f_s would be 0.5 f_{co} to 3 f_{co}.

A minimum of shaping and filtering must be applied to the signal before conversion. The shaping of the signal must be tailored to the requirements of the detector, i.e. to achieve a signal-to-noise ratio that allows the measurement to be done with the required accuracy. The frequency spectrum of the signal must not extend above 0.5 f_s. If the spectral content of the signal applied to the A/D converter exceeds this limit, the energy which lies above 0.5 f_s will be folded back into the passband (0 to 0.5 f_s) and be seen as noise. The required attenuation depends on the resolution of the A/D converter and should be such that this energy becomes a negligible contribution to the total electronic noise (i.e.<1 LSB).

A possible solution could be a staggered set of partial integrators with a time constant equal to a multiple of the time between bunch crossings[6].

4. Architecture of the electronics.

A digital implementation of a readout chain aimed at calorimetric detectors easies the problems related to the storage of information having a large dynamic range (≈15 bits). The use of noncritical nonlinear transfer functions (see § 2) simplifies the design of the preamplifier and of the A/D converter. The global transfer function is linearized after the A/D converter, at the point where the data is transferred to the pipeline. The retrieved information, trigger sum, total charge and time information are all created by transversal filters which are an integral part of the pipeline.

Figure 5 shows how a number of such readout channels, together with a CPU and the necessary control and interface functions can be implemented as a hybrid

device, either using classical technology or as a "silicon on silicon" micro system hybrid which can be mounted directly on the surface of the detector.

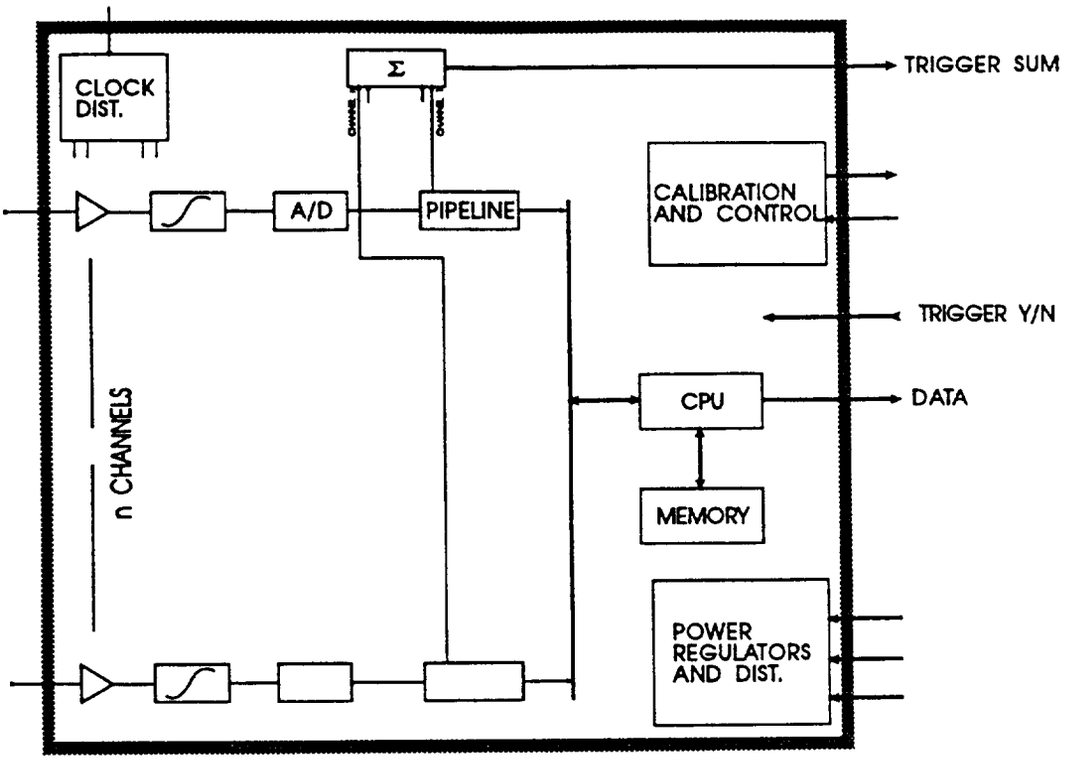


Figure 5

4.1. Preamplifier and A to D conversion.

Each individual calorimeter has its own requirements on the preamplifier and the filter/shaping functions. The parameters of the amplifier must be matched to the detector in terms of capacitance, noise etc., and the filter/shaper function must assure that the signal applied to the A/D converter fulfils the requirements outlined above. To provide a solution which is as general as possible the preamplifier and the shaper/filter stages should be implemented as individual items. The short interconnections between the different items eliminates the need for power consuming output driver stages.

An interesting solution, among others, to the A/D converter is a 2-step approach with a resolution of 10 bits and implemented in a "5 plus 5" architecture. The advantage of this solution is that such an converter only needs 64[3] or 32[7] comparators, compared to 1024 in a "classic" FADC. Also the power consumption will be much lower as a result of the small number of comparators. The main disadvantage is that such a converter needs two clock cycles to convert one sample, but this is largely outweighed by the simplicity of the circuit. Current developments[2] show that conversion speeds of 100 to 150 MS/s should be feasible with circuits implemented in a CMOS sub-micron technology.

The transfer characteristic of the preamplifier and of the A/D converter is, as

discussed above, nonlinear. As a first approximation a logarithmic function can be used, but the final choice will be dictated by the actual hardware implementation. Any function, as long as it is monotonic and inside the limits discussed in § 2, is acceptable.

4.2. Pipeline memory and filter.

The data, after A/D conversion, is passed through a Look-up table to retrieve data in a linear format. This table, 1024 words of 15 bits for 10-bit resolution and 15-bit dynamic range, not only contains the constants needed to convert the data into a linear format but also allows the compensation of any error introduced by non-ideal transfer curves. It will also compensate for differences in gain between individual channels. This means that the data applied to the input of the pipeline is absolute, i.e. no compensation or calibration constants have to be applied later. The only other parameter that must be controlled is the pedestal value which is set by a DAC as described in § 4.4.

To extract the information of interest, filter functions can be integrated into the pipeline. These filters make use of the existing delay (pipeline) elements to form three filter functions to retrieve; (i) a (coarse) energy value for the Level 1 trigger, (ii) a precise total charge value and (iii) a bunch crossing identification for synchronization purposes. However, this does not necessarily mean that there will be three individual filters as shown in fig.6. Each filter function is fully programmable for what concerns both constants and length in order to adapt this design to variety of detector characteristics.

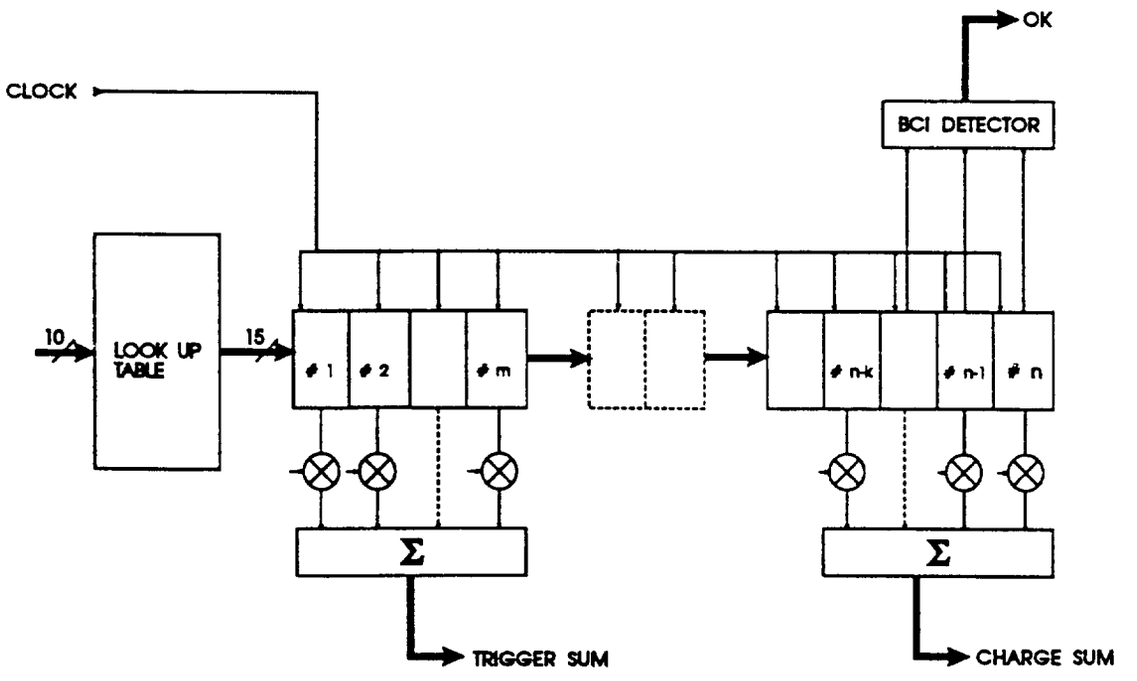


Figure 6

There are two different solutions to the pipeline-filter complex, either, as in fig.6, to carry the "raw" data through the complete pipeline or to extract the information at an early point and pipeline the results. The final decision will emerge from ongoing simulations of these functions. Whatever solution is adopted it can be implemented in existing ASICs of the gate array type[8].

4.3. Data identification and Reduction (Filtering).

Each bunch crossing in the LHC will create a number of events and the Level 1 trigger will identify the crossings containing interesting events. A typical signal from a calorimeter will have a length (in time) that covers more that one bunch crossing interval, thus making it necessary to identify each signal as originating from a particular crossing. This is done by one of the filter functions described above and the information is added to the information in the pipeline.

A carefully designed data reduction function is required to allow the readout system to handle the information from the detector. There are two levels of decisions, Level 1 and Level 2, which give a reduction of 1000 and 100 respectively (current estimation). The data enters the pipeline at twice the bunch crossing rate ($f_s = 2f_{co}$) and is extracted in case of a positive Level 1 decision, i.e. at an average rate of 66 KHz. However, the peak rate can be equal to 66 MHz, and to cope with this fact the data passes a derandomizer before it is written into a set of rotating buffers which

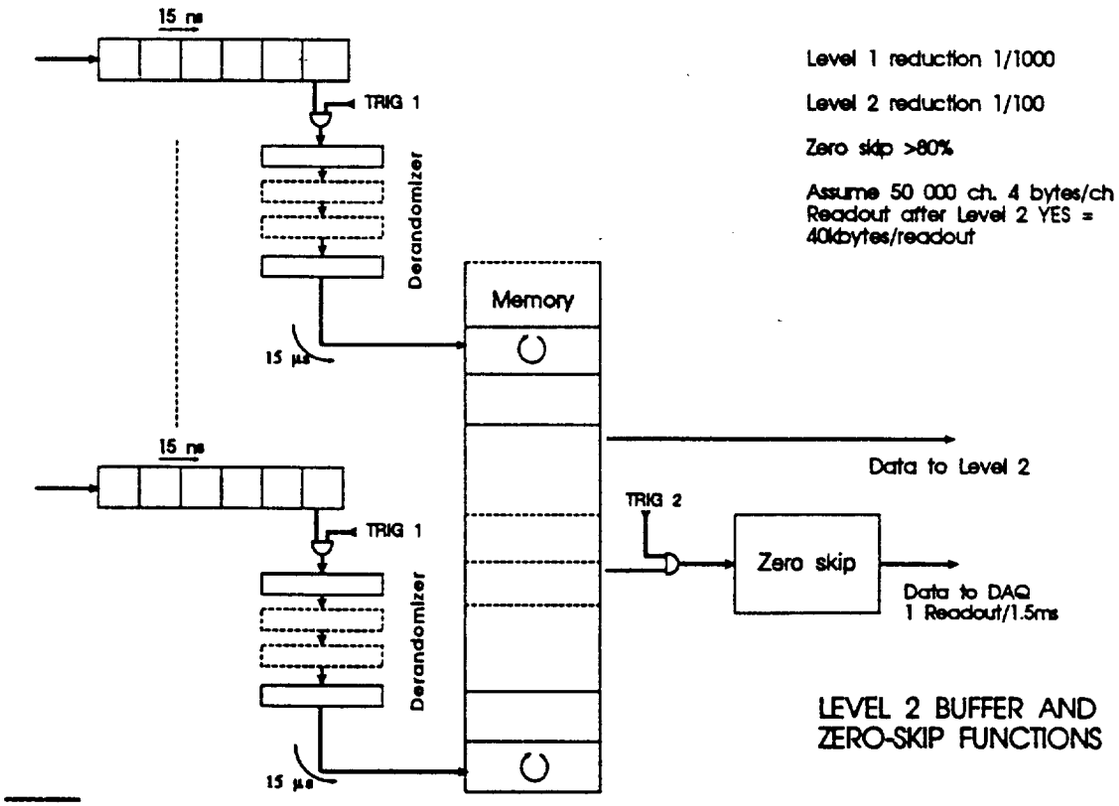


Figure 7

are physically part of the memory function. Figure 7 shows a possible implementation of these functions.

The Level 2 processes have "random" access to the data stored in the buffers and extract the information needed for subsequent decision. When the Level 2 result is positive the internal CPU generates a block of data that contains the valid information acquired by its readout channels. A very high level of data compaction can be achieved at this stage by using a "Zero-suppression" mode, with a fully transparent mode remaining possible for monitoring purposes. A conservative estimate is that only <20% of the channels contain valid data. Assuming a detector with 50000 channels, each generating 4 bytes per bunch crossing, the data volume to be extracted after the above defined reductions is 40 Kb each 1.5 ms, requiring a transfer bandwidth of only 26.5 Mb/s.

4.4. Calibration and Control functions.

In order to handle the large numbers of readout channels of a LHC detector it is important to have powerful but simple means of testing and calibrating the electronics. As a basic criterion, all channels must have identical response to avoid the application of calibration constants at a later stage. As a consequence the information to the Level 1 and 2 triggers become as precise as possible.

There are three different compensations to be applied to each channel, pedestal value, full scale value ("gain") and corrections to the transfer curve.The pedestal value is set by injecting a DC level at the input of the A/D converter with a DAC having a resolution of 6 bits. The individual pedestal values of the individual A/D converters can be set within a range of ± 10 LSB with a resolution of 0.3 LSB. This setting is meant to equalize all channels and has nothing to do with data reduction. Corrections for gain and nonlinear transfer curves are computed locally and loaded into the Look-up table. This operation requires a precise calibration voltage to be distributed to all channels of the detector. One way is to distribute a DC level and let the local CPU control the generation of the required calibration pulse. Also the pedestal adjustments are done locally.

All digital storage devices must have a read/write function or special test features must be added to the circuit. The filter functions must be totally programmable which includes the possibility to make them transparent both for test purposes and during the computation process of the constants to be loaded into the Look-up table and the DAC registers. Finally, the circuit must have the appropriate interface to the protocols (to be defined) used to distribute the trigger decisions and the one used by the DAQ system to transport the readout data.

5. Packing technologies.

There are different technologies available for the assembly of the individual items. However, the most promising one seems to be the "Silicon on Silicon" solution, proposed by both European and US assembly houses. This technique is similar to the well known hybrid technique but uses a substrate of silicon where all support functions are buried. The substrate, being of the same material as normal integrated

circuits, can be seen as an (primitive) integrated circuit containing voltage regulators, input-output protection, buses and other common circuitry.

The individual building blocks can be changed to adapt the unit to a particular application, thereby generating a family of detector readout solutions with the same basic components.

6.Power consumption, Radiation hardness.

The power dissipation of the proposed device can only be obtained after a more detailed design evaluation. However, in view of the available outer surface of a calorimeter, where this device is to be mounted, this should not be a major issue. In fact, the dissipation of the on-detector electronics is distributed over a surface of typically 50 to 100 m^2.

A hermetic calorimeter of adequate resolution being inherently a self-shielding device, the radiation level at the outer surface of such a detector is by definition low compared to the levels considered for the inner detectors. Calculations of radiation levels at various depths of typical detectors are in progress.

References.

(1) J. Yuan and C. Svensson, "High-Speed CMOS Circuit Technique", IEEE J. Solid-State Circuits, Vol 24, pp 62-70, Feb. 1989.

(2) C. Svensson, K. Chen, and J. Yuan, "A 6-bit 200 Mhz FADC", unpublished.

(3) A. G. F. Dingwall and V. Zazzu, "An 8-MHz CMOS Subranging 8-Bit A/D Converter",IEEE J. Solid-State Circuits, Vol SC-204, pp 1138-1143, Dec. 1985

(4) P. R. Gray, Univ. of California, Berkeley, Private communication.

(5) F. G. Hartjes and R. Wigmans, Nucl. Instr. and Meth. A277 (1989) 379.
R. DeSalvo *et al.*, Nucl. Instr. and Meth. A279 (1989) 467.
D. Acosta *et al.*, Results of prototype studies for a Spaghetti Calorimeter, CERN-EP/90-37 (1990).

(6) R. Sundblad, SiCon AB, Linköping Sweden, Private communication.

(7) S. Hosotani, T. Miki, A. Maeda and N. Yazawa, "An 8-bit 20-MS/s A/D Converter with 50-mW Power Consumption", IEEE J. Solid-State Circuits, VOL 25, pp 167-702, Feb. 1990.

(8) Some very interesting work is being done in the field of HDTV development. HDTV uses a sampling frequency of 54 MHz, close to the 66 MHz of the LHC. One example is the MULAC8 "High Speed Transversal Filter Processor" from CNET, Grenoble.

Fast electron triggers from a silicon track/preshower detector

presented by A. Poppleton, CERN

1 Introduction

The SIlicon Tracker/Preshower device (SITP) [1] is under study as a complementary detector to a fine grained electromagnetic calorimeter, mainly for the purpose of distinguishing electrons from the background of QCD jets (including direct photons and π^0's from jet fragmentation) that fake the calorimeter signature for electron identification [2]. Existing collider experience indicates that the detector response should be very fast to minimise the overlap of signals from different bunch crossings, and that a highly granular space-point readout (pads) is desirable for adequate pattern recognition. It is evident that there is a formidable data acquisition problem presented by operating this device at the 67MHz LHC bunch crossing frequency, with its large number of channels ($\sim 25 \times 10^6$) each needing a reasonably precise pulse height measurement. A possible solution, relying on a sophisticated front-end chip mounted on the detector in the style currently used at the UA2 experiment [3], is outlined below. In this scenario the full SITP data would be available to the 2nd level trigger processors after $\sim 30\mu$s, enabling a substantial enrichment of the electron signal at this level. There would be no deadtime introduced under the assumption of an average 1st level rate of 50kHz.

2 Expected electron trigger rates at LHC

The program PYTHIA [4] has been used to simulate inclusive QCD jet production in the central rapidity region ($|\eta| \leq 2$) at a centre of mass energy $\sqrt{s} = 16$ TeV. The same program has been used, with jet fragmentation functions consistent with data at $\sqrt{s} = 630$ GeV and $\sqrt{s} = 1.8$ TeV, to estimate π^0 production. In addition, the cross-section for direct photon production has been estimated [5], together with the inclusive production of electrons from the two most prolific sources, namely $pp \rightarrow b\bar{b} + X$, with the b or $\bar{b}$ decaying semi-leptonically to yield non-isolated electrons [6], and $pp \rightarrow W + X$; $W \rightarrow e\nu$ producing isolated electrons [7].

These integrated cross-sections per unit central rapidity interval are shown as a function of transverse momentum (P_T) threshold in GeV/c in figure 1. It can be seen that if a jet threshold of order $P_T > 20$GeV/c, efficient for studying W/Z production, is retained at the highest LHC luminosity ($L \approx 4 \times 10^{31}$ cm^{-2} s^{-1}), then the jet rate will approximately equal the 67MHz bunch crossing frequency and very little rejection will be obtained from the calorimeter threshold alone. Additional calorimeter constraints on lateral and longitudinal shower development will mainly select isolated π^0's, photons and electrons with a reduction of $\sim 1/1000$ from the jet rate. Since isolated electrons, principally from W and Z decays, occur at $\sim 10^{-5}\times$ the jet rate, true electrons will represent $\sim 1/100$ of the electromagnetic showers identified by the calorimeter.

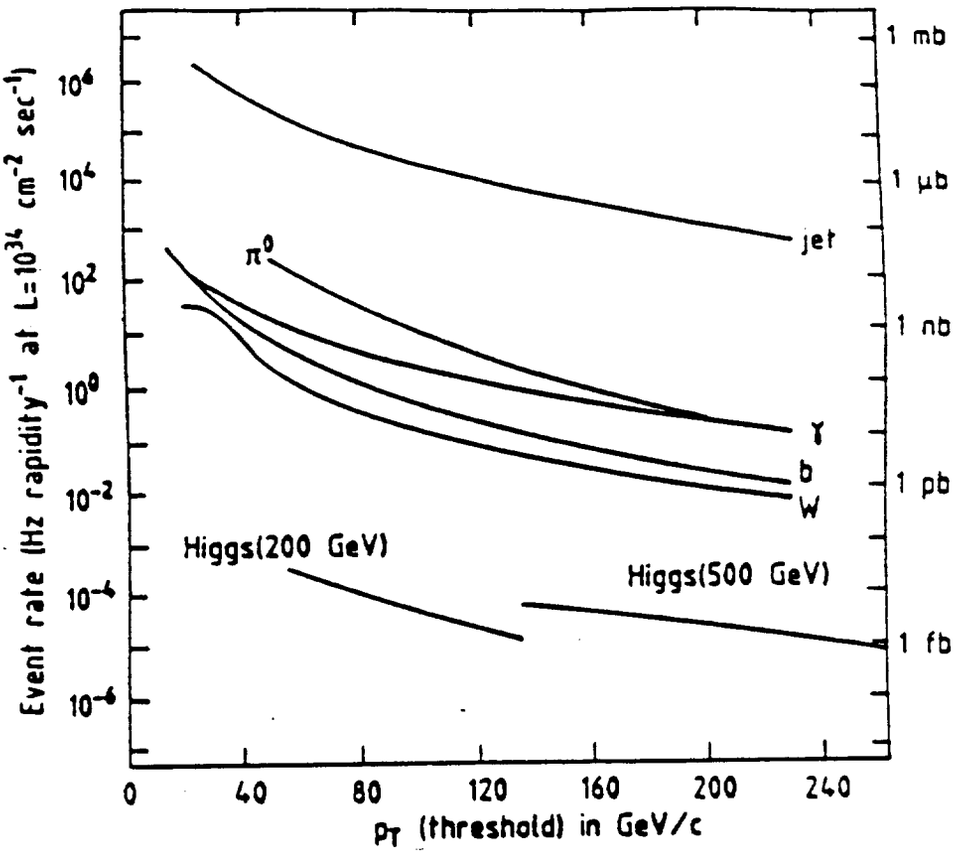


Figure 1: Expected rates from Pythia for the inclusive production of QCD jets, π^0's and photons as a function of the P_T threshold given for a luminosity $L = 10^{34}$ cm^{-2} s^{-1}. Also shown are the expected inclusive electron rates from b-quark, W and Higgs decay. The centre of mass energy is 16 TeV.

Although most physics topics involve additional lepton(s), neutrino(s) or jet(s) in the final state, which allows rejection factors to be compounded, interesting channels containing electrons occur at a rate higher than can be supported by conventional data acquisition systems. Thus to exploit the available luminosity there is a clear requirement that an electron identification system should be able to remove fake electrons to below the true electron rate at the earliest possible trigger level.

In practice a realistic high luminosity assumption is that the calorimeter will provide a 1st level trigger rate at or below 50kHz for multilepton final states, but that an inclusive electron trigger will require either a raised P_T threshold or additional trigger information. At later trigger levels the SITP should reduce the data rate to essentially the true electron rate.

3 SITP detector and rejection power

The preliminary SITP design has 3 tracking and 3 preshower layers of silicon pads. Arranging these layers as concentric cylinders enables mechanical rigidity to be combined with ease of access while leaving space for the necessary cooling system. The 9mm^2 pad area is a compromise giving radiation hardness, low electronic noise and low occupancy with a size that matches the attached electronics. The 24 × 24mm^2 silicon crystal dimension is chosen as the optimum for manufacturing quality control, thus each crystal consists

of 64 pads. These crystals are grouped onto printed circuit boards, currently with 64 crystals/board to give a convenient board size of 20cm×20cm. The boards slightly overlap to reduce acceptance cracks; each detector layer would consist of $\sim$ 1000 boards to cover the central rapidity region. More details can be found in reference [1].

At the highest luminosity there will be $\lesssim$ 1000 tracks/bunch crossing in the central region from underlying events. From previous collider experience there will also be a large number of 'extra' hits which cannot be assigned to tracks. A realistic assumption is for a board occupancy of $\sim$ 4 hits/crossing equivalent to a pad occupancy of $\sim$ 0.001 hits/crossing. Pile-up should not be a problem at pad or even crystal level.

The device aims to provide an electron signal/background ratio of 10:1, corresponding to an additional rejection of 10^3 after calorimeter selection. Table 1 illustrates that adequate rejection is available against the principle backgrounds, which have been listed in order of importance. However this rejection can only be obtained after an analysis of the signal observed in all six layers of the device. For a fast (1st level) trigger it is very complicated to provide all the layer interconnects necessary for this analysis, so it is worth considering the rejection power available from a single layer. Since $\sim$ 90% of π^0's produce an associated preshower hit, it is more profitable to look for hits in the tracking layers. The most frequent track source comes from a π^0 conversion in the upstream material. A multilayer pulse height analysis is required to distinguish this. Since the dimensions of a silicon crystal approximately match the lateral cell size of a highly granular calorimeter ($\Delta\eta \approx \Delta\phi \approx 0.03$), the relatively simple requirement of a hit crystal in the innermost layer will provide a rejection of $\lesssim$ 10 limited by the conversion rate (assuming 5%X_0 material in front of the detector). However the high output bandwidth/board needed to transfer this to the 1st level trigger is expensive :

67MHz *(crossing frequency)* × 64bits *(crystal pattern)* = 536Mbyte/s *(transfer rate)*

4 Front end chip

The large number of channels and high data rate make data compaction (including pedestal subtraction) a necessity on the front-end read-out chip. An initial design is for one chip per crystal (64 channels). There is also a need to combine a low power dissipation ($\lesssim$ 5mW/channel) into the restricted central space, together with radiation hardness in order to operate in the LHC environment (SOI technology).

Principle backgrounds	Track stub rate	Preshower rate	Additional rejection to track×preshower rate
Conversion ($\pi^0 \rightarrow \gamma\gamma$ 5%X_0 before stub)	0.1	1.0	100 from double ionisation track stub
Dalitz ($\pi^0 \rightarrow \gamma e^+ e^-$)	0.01	1.0	> 10, two close electrons or as above
Soft $\pi^\pm$ overlaps π^0	$\lesssim$ 0.01	0.9	$\sim$ 10, precise track/preshower match
$\pi^\pm$ charge exchange	1.0	0.05	> 100, charge exchange cross-section

Table 1: SITP rejection against principal e/m calorimeter backgrounds

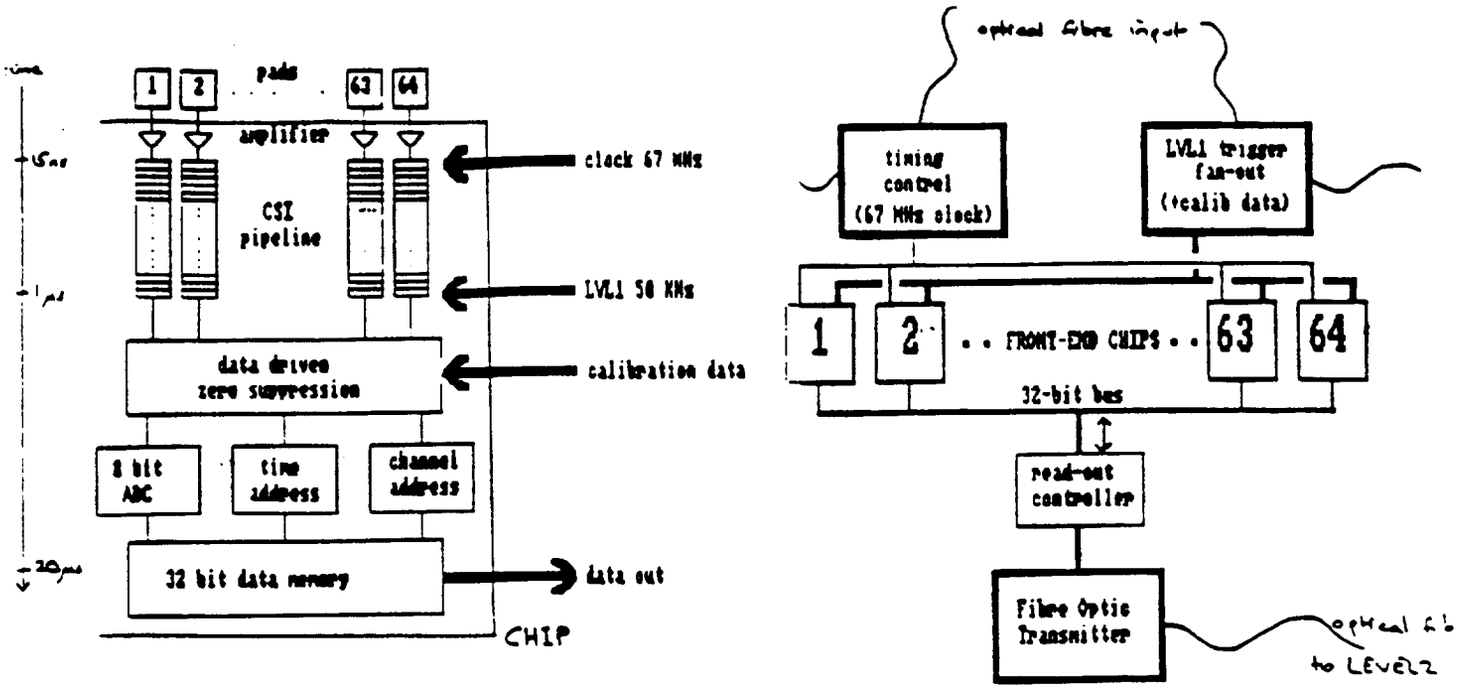


Figure 2: (left) schematic front-end chip, (right) board schematic

A schematic chip configuration is shown in figure 2. A charged track will deposit a primary ionisation of $\gtrsim 16000$ e-h pairs into a silicon pad. For each pad the signal is read out via a fast low noise amplifier (gain ~ 8, peaking time ~ 15ns) into a dedicated CSI pipeline [8, 9] clocked at the bunch crossing frequency (67MHz). This stores the analogue data until the arrival of the 1st level trigger decision currently assumed to be after $\sim 1\mu$s. Then the triggered data is digitised into an on-chip buffer memory using a data driven zero suppression scheme with pedestal subtraction from downloaded calibration data. This digitisation is expected to have a latency time of $\sim 20\mu$s. The whole system is designed to handle an average 1st level trigger rate of 50kHz with no deadtime. Each hit requires 32 bits of memory data to encode its time and channel addresses plus an 8 bit pulse height. It is clear that a significant data compaction can be achieved :

$$50\text{kHz}\ \textit{(1st level)} \times \frac{4}{64}\ \textit{(occupancy)} \times 32\text{bits}\ \textit{(data)} = 12.5\text{kbyte/s}\ \textit{(output data rate)}$$

5 Data acquisition and 2nd level trigger

Each detector layer consists of ~ 1000 boards which could communicate through optical fibre data links. The crystal data would be multiplexed at board level via a 32 bit bus and read-out controller to give an average 800kbyte/s output data rate. A standard 20Mbyte/s fibre connecting each board to a 2nd level processor would allow a safety margin adequate for extreme jet core multiplicities i.e. ~ 100 hits/20μs (1st level rate). In this scheme additional optical fibres would be used to input the 67MHz clock signal to the board timing control unit, download the calibration data and feed the 1st level trigger fan-out. These would be daisy chained to reduce installation complexity. Thus it is feasible to provide full data read-out to a 2nd level trigger processor about 30μs after a bunch crossing.

It is assumed that the 2nd level processors will handle data arranged in logical towers consisting of some segment of the calorimeter with the boards from all six layers facing this. In the case when the calorimeter segment contains an electromagnetic cluster, then track stub and preshower finding will be performed, otherwise the processors have only to buffer the SITP data awaiting the 2nd level decision. The trigger algorithm should be rather fast (a few $\times$ 10μs) as the pattern recognition is simple (an advantage of pads), 1-dimension clustering should suffice (this may even be implemented at the front-end to reduce noise), and to reject conversions it is sufficient to demand a pulse height above 0.6mip in the innermost tracking layer with a minimum track pulse height below 1.6mip.

An alternative solution is available in the massively parallel 2nd level scheme under consideration for the calorimeter (with $\sim$ 1000 towers) [10]. Then only the SITP data facing calorimeter clusters triggering at 1st level would be read out in time to be used at the 2nd level. This would require less output bandwidth, but an additional buffer memory would be needed to keep the data on each board until the 2nd level decision was made.

In either scheme difficult cases, such as bad pads or acceptance cracks, would be deferred until the 3rd trigger level. Assuming the deferral rate to be $\sim$ 2% and the signal $\sim$ 1%, then the trigger rate would be reduced by 1/30. A full detector readout to the 3rd level will also permit searches for additional electrons, or direct photons, or confirmation of muon tracks through a singly ionising track stub.

References

[1] D. Munday, presentation to vertex detection and tracking session at this workshop.

[2] A. Weidberg, presentation to electron identification session at this workshop.

[3] R. Ansari et al., Nucl. Inst. Methods A 288 (1990) 240.

[4] Pythia 4.8: H-U. Bengtsson, T. Sjostrand, LU TP 87-3, and revision 5.3 (November 1989).

[5] P. Aurenche et al., Nucl. Phys. B286 (1987) 509.

[6] A. Nisati, private communication.

[7] T. Matsuura, H. Plothow-Besch and D. R. Wood, private communication.

[8] F. Anghinolfi, presentation to vertex detection and tracking session at this workshop.

[9] P. Jarron, presentation to signal processing, trigger and data acquisition session at this workshop.

[10] J. Strong, presentation to signal processing, trigger and data acquisition session at this workshop.

TRACKING WITH PROPORTIONAL CHAMBERS AT LHC?

Thomas C. MEYER
PPE Division
CERN, Geneva, Switzerland

ABSTRACT:

This article is a review of the present state of the art in gaseous tracking techniques designed for high resolution operation in a very high radiation environment, such as the future large hadron collider (LHC) at CERN. The possible performance of these devices will be reviewed with special emphasis on LHC related problems and constraints, such as cell occupancy and detector ageing due to radiation.

INTRODUCTION:

The concept of a new generation of high energy proton colliders with demands on highest achievable luminosities seemed to mark the end of an era in central tracking techniques for particle physics using the classical multiwire proportional chamber (MWPC), the drift chamber, and hybrids of both.

New detection methods based on silicon and scintillating fiber technologies now offer far superior performance in terms of speed and position resolution, but still suffer from problems such as radiation damage, high cost and poor reliability.

However, with the advances made in the development of VLSI electronics, and in view of the presently inherent drawbacks of the silicon and fiber detectors, progress has also been made in the field of MWPCs and drift detectors, which are now able to meet the challenging requirements for a central tracker in an LHC experiment. After sufficient research and development work, these new devices may, in the long run, outperform their more recent and modern competitors made of silicon or scintillating fibers.

WHY GASEOUS DETECTORS?:

They:
a) are relatively cheap;
b) rely on well understood technologies and physics;
c) are very flexible owing to the inter-play of several operational parameters, such as E, p, gas type, geometry;
d) are comparatively radiation hard; indeed they are totally insensitive to radiation damage when in standby mode, i. e. H.V. off;
e) deliver large signals from gas amplification;
f) offer various methods to obtain space points for ease of pattern recognition: cathode readout, charge division, stereo angle;
g) allow for electron identification via transition radiation, when filled with Xenon.

However, even if properly designed for high rate operation at LHC, these detectors are still subject to limitations such as:

a) long memory time due to slow electron drift in counting gases;
b) degradation of resolution and efficiency due to large drift angles (*figure 1*) in the presence of strong magnetic fields (E x B effect);
c) inferior spatial resolution compared to other technologies (Si, etc..);
d) the inevitable safety hazard when using flammable gases.

The step from the well known MWPC's and drift chambers with geometrical dimensions of the order of cm or more to new detector concepts with sub-millimeter electrode spacing is a non-continuous process imposed by the future experimental environments, which are orders of magnitude more demanding than present scenarios.

Only via rigorous downsizing and shrinking of all geometrical parameters can these new chambers possibly cope with the speed of the new colliders and avoid the positive charge accumulation due to large radiative backgrounds. Together with the proportional gain, this sets an upper limit on the rate capability of the detectors [1], before gain reduction and field distortions render them inoperable.

WHAT ARE THE CHALLENGES?:

1.) Physics

Today's physics constitutes the background at the 100 mb level, while "for every interesting event at the p-barn level there will have been 10^{11} other events"[2].This also sets the scale in credibility for finding new physics amidst a vast background of minimum bias events.

2.) Radiation Damage

In an article by D. Groom [3], radiation damage can be seen as "collision products which strike the detector at a rate which is equivalent to the accidental loss of one beam into the apparatus every 6 days" (for the SSC), or every 5 hours for the LHC. Compared to the present CERN p-p accelerator, radiation levels induced by beam collisions will be a factor of $>10^4$ higher at LHC.

3.) Crossing Rates

Current accelerators operate with a moderate number of particle bunches and as a result, relatively long inter-bunch spacings allow sufficient time for particle tracks to drift over large distances. In LEP for example, imaging drift chambers and time projection chambers with drift times as long as tens of μsec are used, which still leave enough time before the next bunch interaction occurs.

In contrast, to obtain the necessary luminosity, the proposed new colliding beam machines must run with a maximum number of bunches. For LHC and SSC this leads to very short bunch interval times of ≤15 nsec, corresponding to electron drift distances of approximately 1 mm. However, an active detector gas volume with only 1 mm thickness will prove highly inefficient due to clustering effects in the primary ionization process. Thus, any gaseous chamber to be run at better than 80% efficiency must have a correspondingly larger drift volume, and consequently be sensitive to more than one bunch crossing.

4.) Interaction Rates

In addition to the high crossing rates, detectors have to cope with an unusually high charged particle rate, which results from the high luminosity and a substantial interaction cross section (86 mb) at the proposed machine energy. Assuming the top luminosity of LHC will be 4×10^{34} cm^{-2} sec^{-1}, the charged particle rate into a small counter with area dA is:

$$dN/dA \approx 2.4 \text{ GHz}/r_t^2$$

where r_t is the distance from the beam line in cm.

These fluxes, characteristic of the fierce radiation environment at LHC, combined with the relatively long resolving time of gaseous counters, pose serious limitations on the use of these detectors at LHC. These two constraints have led to the concept of occupancy, which will be discussed later in the text.

TRACKING CHAMBERS FOR LHC

1.) THE INDUCTION DRIFT CHAMBER [4]

Originally designed as a vertex detector for HERA and proton colliders, this chamber has the ability of observing high counting rates and has excellent spatial resolution. Wire spacing is such that a single cell measures only 600 μm x 2 mm in sensitive volume on either side of the detection plane (*figure 2*).

It should be noted that the term "drift" chamber is misleading, for no use is made of the drift time information. Rather the position of the particle tracks is obtained from the measurement of:

a) the total charge on the sense wire;

b) the induced charge on the neighboring cathode or potential wires

Counting hits only on the sense wires is the 'cheap' way to measure track coordinates, but at the expense of poor resolution (σ = 179 μm). A more precise position measurement is obtained by an interpolation method in which the difference of the induced signal on the potential wires is exploited. Test measurements result in a resolution of σ = 26 μm, which is limited only by electronic noise.

Note that the induced charge measurement via the potential wires is made with a gate of 100 nsec, although the maximum drift time in one cell for most types of drift gases is less than this. If shorter integration times are used, not all of the ionization clusters are collected, thereby reducing the signal to noise ratio and hence the spatial resolution.

PERFORMANCE CHARACTERISTICS:

SPATIAL RESOLUTION:	26 μm (179 μm)
TWO TRACK RESOL.:	not measured
RATE CAPABILITY:	10^8 events/cm^2 sec
CELL BUSY TIME:	100 nsec

2.) THE MICROSTRIP CHAMBER [5,6,7,8]

Replacing the wires of the induction drift chamber with thin metal strips fixed on a suitable substrate led to the development of the microstrip (avalanche) chamber (*figure 3*). By means of photolithography, very precise (± 0.2 μm !) thin strips are produced on an insulating surface to act as anodes and cathodes similar to MWPCs. Very uniform gas amplification is generated primarily between neighboring strips rather than between the anodes and the drift cathode plane. This results in an energy resolution superior to that of MWPCs.

Compared to the induction drift chamber, cell size is smaller by a factor of three with no apparent improvement in spatial resolution. This is probably due to lower ionization statistics of tracks leading to an inferior signal to noise ratio. Similarly, track coordinates are determined by measuring the total charge on the anode strips (which gives poor resolution), and/or the charge sharing on the cathode strips. The latter leads to a position resolution of σ = 39 μm using Xenon-DME (Di-Methyl-Ether) gas mixtures.

PERFORMANCE CHARACTERISTICS:

SPATIAL RESOLUTION:	39 μm
TWO TRACK RESOL.:	250 μm
ENERGY RESOLUTION:	15% @ 5.9 keV ^{55}Fe photons
RATE CAPABILITY:	$\geq 10^7$ events/cm^2 sec
CELL BUSY TIME:	50 nsec

3.) THE MULTIDRIFT TUBE [9]

The Multidrift tube (400 or 800 mm long at present) containing 70 independent drift cells of hexagonal geometry represents a modular approach to a high speed, high resolution tracking detector. Unlike the previous devices, this detector derives the track coordinate from a drift time measurement in a single cell having a radius of only 1.45 mm. This helps to achieve high granularity with good multitrack resolution and short drift times of the order of 40 nsec. Modules can be stacked and assembled around the intersection region, while each element is a self contained unit being easily replaceable in case of failure. Inspite of a non-linear correlation between drift time and real coordinate, impressive localization accuracies are achieved; i.e. 65 μm radially. High gains also allow good longitudinal position resolution via charge division (~1% of wire length). Furthermore, extensive studies on wire ageing have been made, and depending on gas quality, integral charges of up to 1 Coul/cm, equivalent to 1 Mrad of radiation, can be absorbed with no loss in performance.

PERFORMANCE CHARACTERISTICS:

SPATIAL RESOLUTION:	65 μm
TWO TRACK RESOL.:	500 - 1000 μm
LONGITUDINAL RES.:	0.9% of wire length
RATE CAPABILITY:	10^6 events/cm^2 sec
AGEING LIMIT:	0.5 - 1 Coul/cm
CELL BUSY TIME:	30 - 40 nsec

4.) THE STRAW TUBE CHAMBER [10]

Instead of a cell defined by several cathode wires with a central sense wire, the "straw tube" is made of a continuous cylindrical cathode surface of 4 or 6 mm diameter. It was found that this approach would introduce no more absorber than an open wire chamber and could have less material than the conventional design. An enclosed cathode system would isolate wire breakage and provide better immunity to noise and ageing. Straws can be built in lengths up to several meters, with supports to prevent the sense wire from sagging. This limits their use under extreme conditions such as the high luminosity forseen at LHC.

Total drift and recovery time in a 4 mm straw amounts to 42 nsec, still in line with the charge collection time of the previous detectors. Position resolution at present is ~ 100 μm, while the two track resolution is basically defined by the straw size itself (4 mm).

PERFORMANCE CHARACTERISTCS:

SPATIAL RESOLUTION:	105 μm
TWO TRACK RESOL.:	~ 4 mm
CELL BUSY TIME:	42 nsec (for 4 mm straw)

CELL OCCUPANCY:

Due to the mismatch in bunch crossing and cell resolving time of the detector, the occupancy of the detection cell can be defined as:

$$O = \text{resolving time/average time between hits}$$
$$= \text{busy time x rate/cell}$$

Note that the rate corresponds to the charged particle activity in a particular cell depending on cell size and distance from the beam. Furthermore, the resolving time of the individual counting channel is determined by the **total** time that the cell is busy; i.e. the drift period of primary electrons plus any signal processing (shaping), etc.

It will be shown that, in order to overcome the problem of long busy times, small cell sizes must be chosen for the detectors to keep occupancies at a tolerable level. While the induction drift chamber and microstrip chamber easily fulfil this demand because of their inherently small cell sizes (typically 5-10 cm x anode pitch), the long (40 - 200 cm) multidrift tubes and straw tubes cannot be considered as contenders for an LHC environment. For the purposes of comparison in terms of occupancy, the four detectors discussed above have had their cell **length** normalized to 10 cm in *Figure 4*.

Setting an arbitrary but reasonable occupancy limit of 10%, straw tubes of 10 cm length can do adequate tracking at 70 cm distance from the vertex or more. The microstrip detector, on the other hand, remains efficient as close as 15 cm to the interaction region.

DETECTOR AGEING:

Radiation damage in MWPCs, also known as wire ageing, is a subject of much debate and has received growing attention in the context of the new super colliders. There is little doubt however, that the various phenomena of wire ageing are attributed to the total charge absorbed per unit length of electrode (wire). Hence, the rate of ageing in MWPCs will depend on the amount of primary ionization per track and the level of proportional wire gain chosen,

typically between 10^3 and 10^4. In one case (multidrift tube), ageing has been studied in detail, however, since a general understanding of the ageing mechanism is still lacking, no universal prediction of the ageing rate can be made.

Figure 5 shows the absorbed charge per unit length of wire for one year of LHC operation as a function of distance from the interaction vertex. The multidrift- and straw tubes receive higher radiation doses owing to their larger cell **width**, independent of cell **length**.

It is reasonable to assume that with a minimum of constructional precautions, chambers may, in general, be safely operated up to an integrated charge exposure equivalent to say 0.1 Coul/cm (note, however, that multidrift tubes have been tested successfully to ten times this conservative limit). From this, one can then estimate the lifetime of the detector, when operated at various distances from the beam. This is shown in *figure 6*.

CONCLUSIONS AND FUTURE PROSPECTS:

The question of whether the new MWPCs and drift chambers will successfully work in an LHC tracking detector, cannot be entirely answered in this report. However, we have shown that, within the scope of two crucial LHC issues, i.e. occupancy and radiation damage, some of these new chambers favourably compete with Silicon and fiber detectors. The ultimate limitation to any tracking device will be its survival time and hence, its long term reliability within an LHC experiment.

Microstrip chambers, which are structurally similar to Silicon microstrip detectors, can offer comparable performance with yet higher reliability and lower cost. Apart from **E** x **B** effects, they are as much subject to other technical and constructional constraints as solid state and fiber detectors. **E** x **B** effects can partly be offset or compensated for by proper choice of gas and geometrical arrangement. Nonetheless, other more general problems remain to be solved such as curling tracks in a magnetic tracker, which will further increase channel occupancy and radiation risks, and alignment of tens of thousands of subdetectors with tight control of systematic errors is still an open issue, as are the electronics and triggering.

The new generation of proportional gas and drift chambers offers promising performance and reliability in an LHC experiment, although their development in this direction has only just begun.

REFERENCES:

[1] A. H. Walenta, Nuc. Instr. Mthds. A217 (1983), 65

[2] J. S. Russ, Nuc. Instr. Mthds. A279 (1989), 29

[3] D. E. Groom, Nuc. Instr. Mthds. A279 (1989), 1

[4] E. Roderburg et al., Nuc. Instr. Mthds. A252 (1986) 285

[5] A. Oed, Nuc. Instr. Mthds. A263 (1988) 351

[6] F. Udo, NIKHEF-H Amsterdam, Sept. 1990

[7] F. Hartjes et al., NIKHEF-H Amsterdam, April 1990

[8] F. Angelini et al., INFN PI/AE 90/1

[9] R. Bouclier et al., Nuc. Instr. Mthds. A283 (1989) 509

[10] SSC Detector Subsystem Proposal, G. Hanson - spokesman

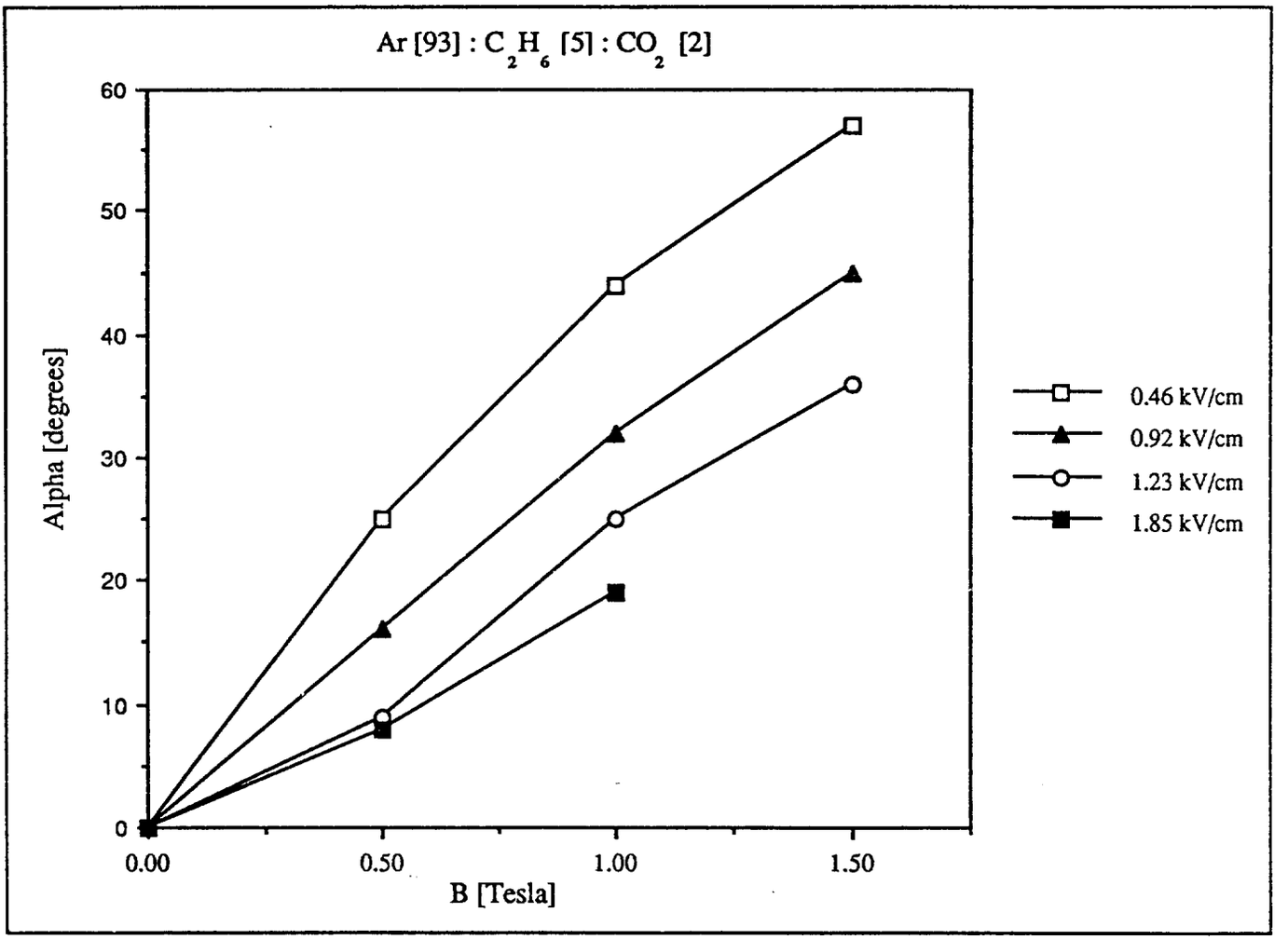


FIG. 1 Drift Angle versus Magnetic Field

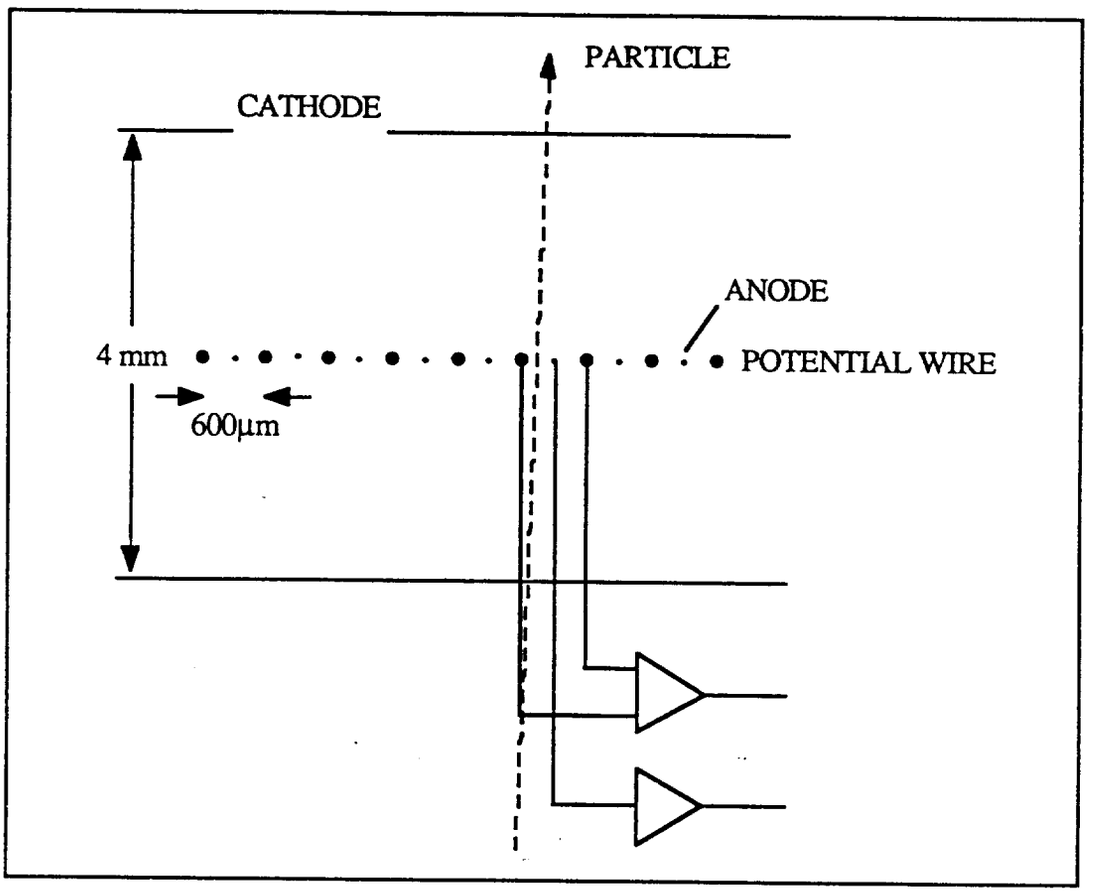


FIG. 2 The construction of the induction drift chamber

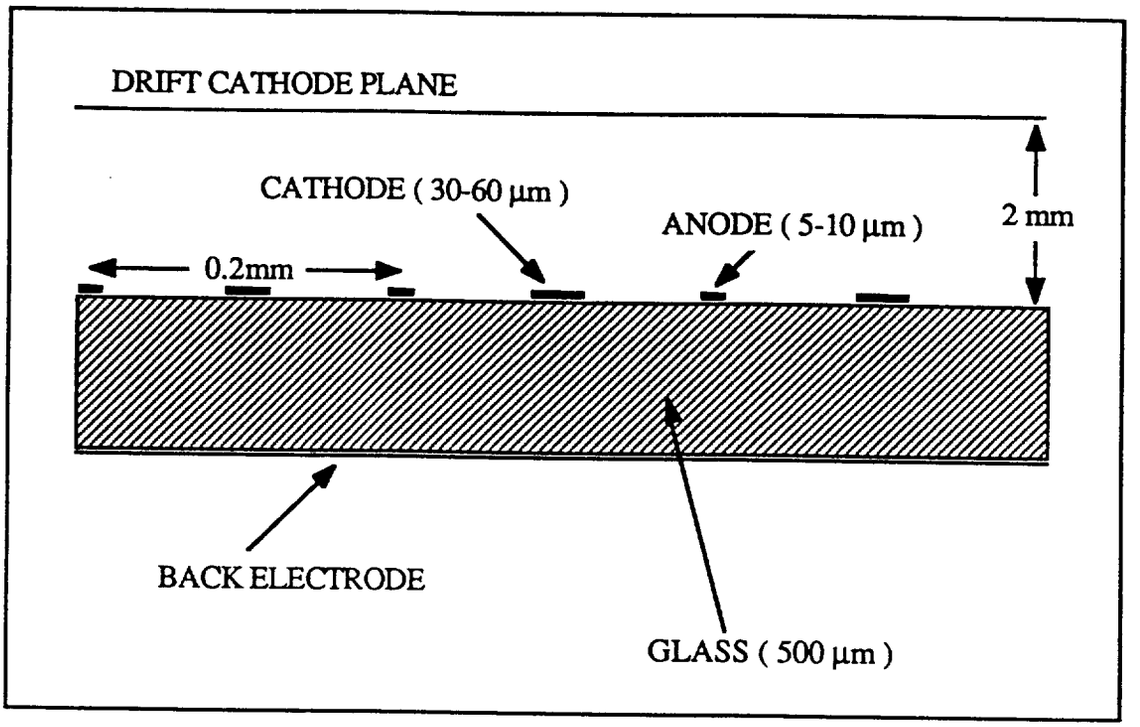


FIG. 3 The construction of the microstrip (avalanche) chamber

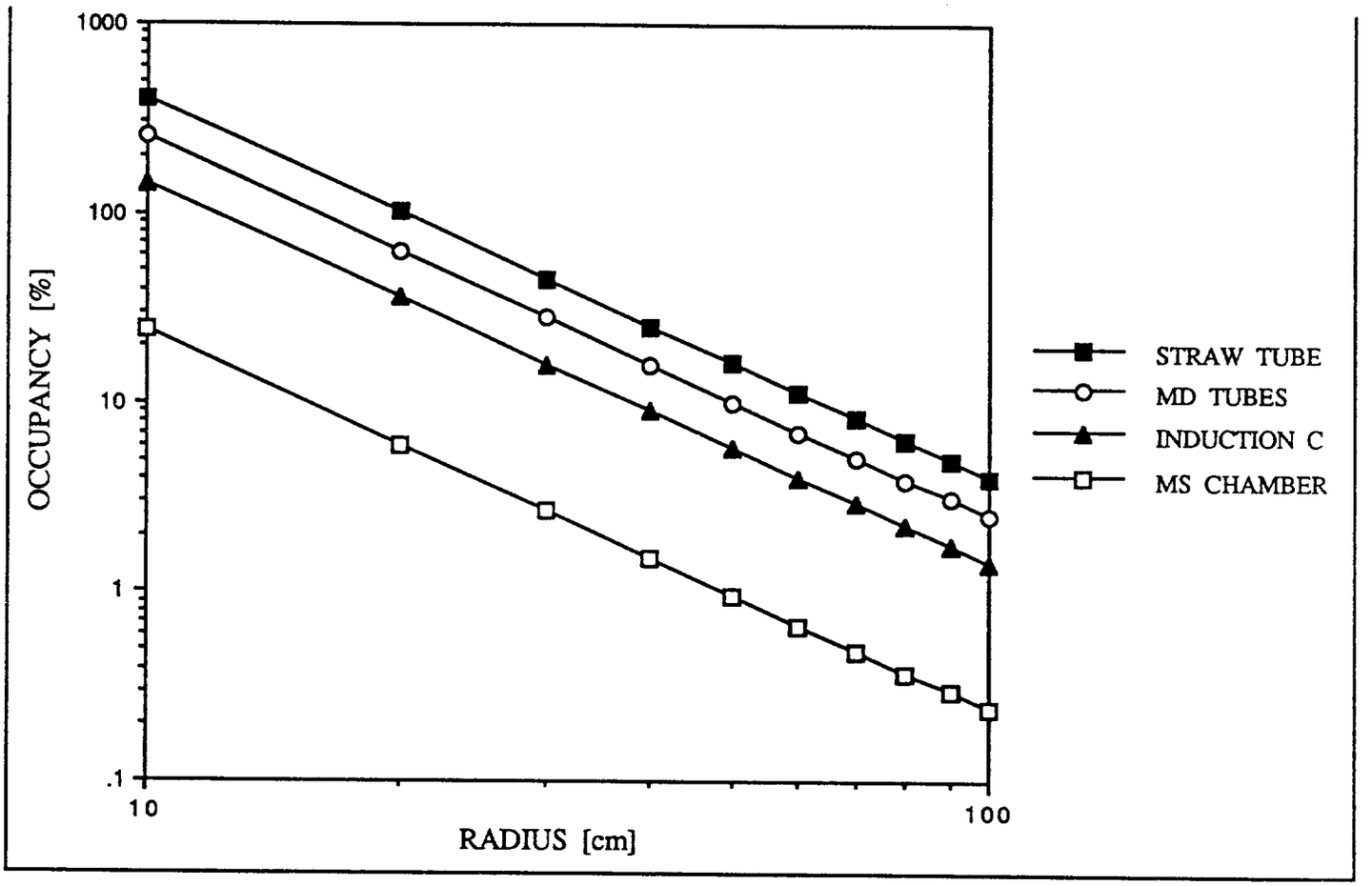


FIG. 4 Occupancy At LHC Normalised To 10cm Detector Cell Length

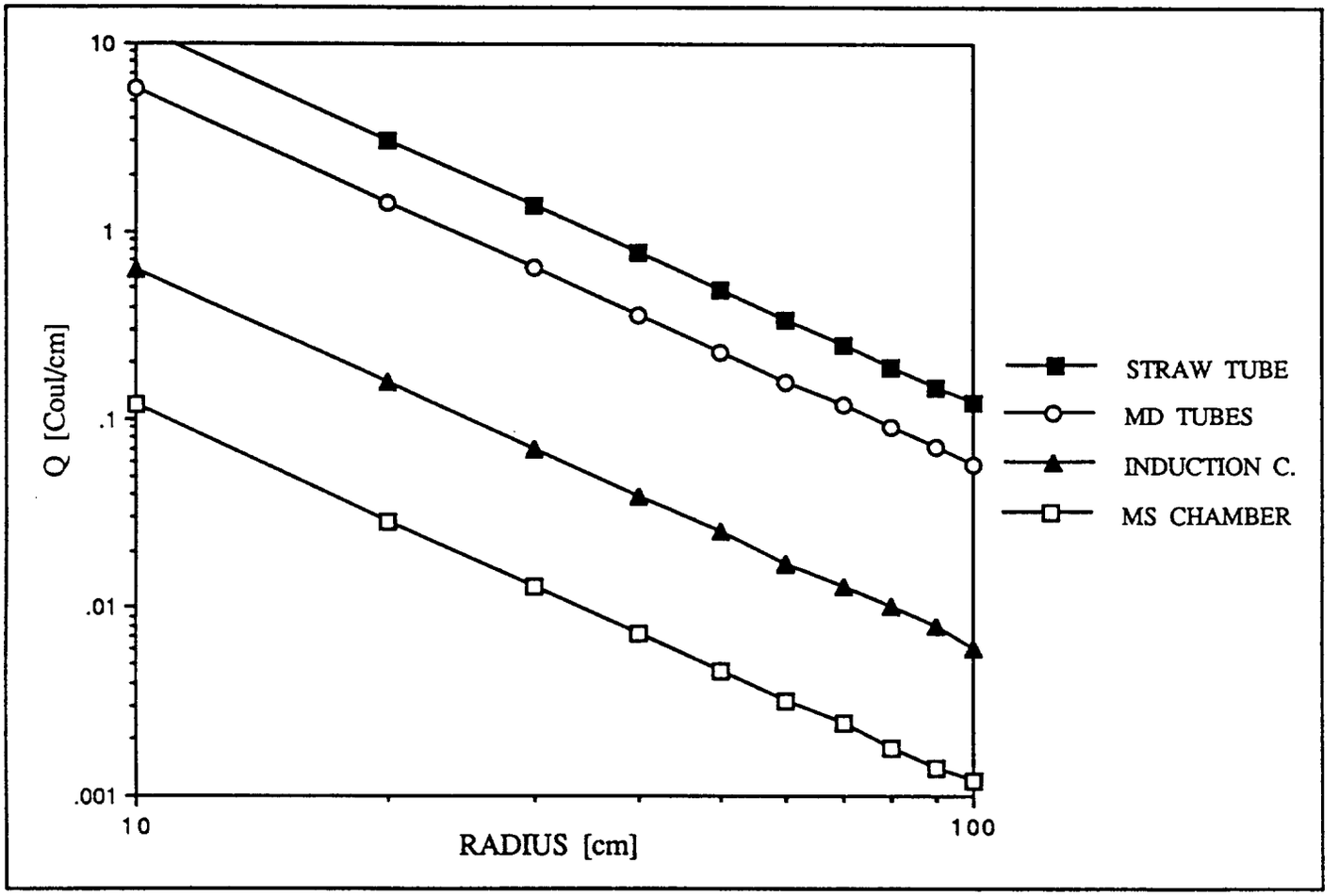


FIG. 5 Charge Accummulated Per cm Of Wire In One Year

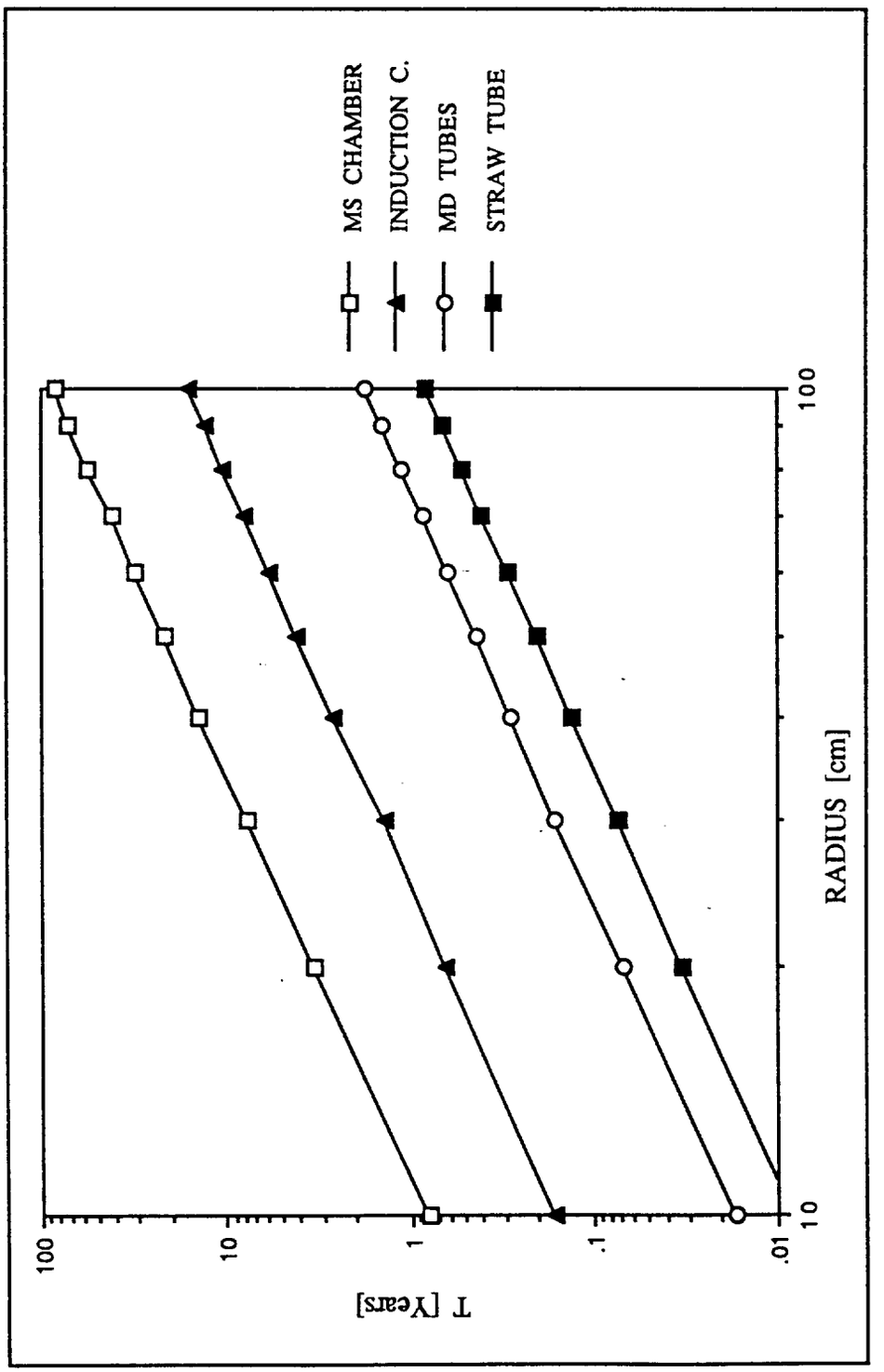


FIG. 6 Estimated Survival Time With 0.1 Coul/cm Maximum

Application of the microstrip gascounter in a LHC tracker.

F.Udo
NIKHEF-H Amsterdam.
Sept. 1990.

The paper discusses a LHC tracker constructed with microstrip gas counters (ref1) in a solenoidal field of 4 Tesla. Figure 1 shows a cross section of a microstrip gas counter (MSGC). The position determination of the track follows from the projection on the strip surface of the electrons liberated along the track. This projection should not be smeared over too many strips.This leads to two requirements for the correct operation of the tracker: the tracks to be measured need to be perpendicular to the substrate surface in the plane shown in figure 1 and the presence of a magnetic field should not deviate the drift of the electrons too much from the vertical.These requirements dominate the design parameters of the tracker . The minimum radius (40 cm) is determined by radiation and occupancy at a luminosity of 10^{34} cm^{-2}.

The detrimental effects of the magnetic field on the operation of the MSGC can be avoided if the detectors are oriented such, that the electric driftfield and the magnetic field are parallel. This implies a vertical position of the detectorplanes which is the natural choice in the small angle region. Continuing this philosophy forward one arrives at a design as sketched in figure 2. The detectorplanes are tilted 20^{o} in the central part of the tracker, while the strips are oriented radially in the discs measuring the (r,ϕ) coordinate.This tilt is varied with the scattering angle. The result is, that the tracks cross the detectors and thus the gasgaps under a small angle, but parallel to the strips. In this way one assures, that the tracklength in the gas is everywhere longer than the gasthickness, so the gasgap can be reduced to 1.5 mm. The application of this principle in the forward direction is limited as we have to keep the angle between the drift direction and the magnetic field below 20^{0} to limit the Lorentz angle to less than 10^{o} even at a field of 4T.

The tracker shown contains about 16000 detectors of 10x10 cm^2. The total displacement due to the Lorentz angle effect is reduced to less than 300μm and the maximum drifttime to 15 nsec. A particle from the interaction region will cross at least 12 detector gaps.The thickness of the tracker as seen by a particle can be estimated to be .12 L_r taking into account a substrate of 150μm thick, the angular effects and some extra material.

The charge collection time will be around 15 nsec, so it is certainly possible to sample the output voltage every 16 nsec and assign the signals to a bunch crossing. The interaction region is about 15 cm long along the beam direction, so a resolution of 1 mm in z is sufficient to disentangle the truly simultaneous vertices. A few small angle stereo layers can do this.

The arrangement of counters and strips as described above leads to another desirable effect: the tracker can be made insensitive to low momentum particles. These particles are bent over large angles or loop around, so their ionisation projection spreads over many strips. The result is, that starting at a certain bending angle the pulseheight per strip falls under a preset value so the track is not seen. This reduction in pulseheight is a factor 15 for loopers as they cross at right angles to the strips (they cross 0.2mm instead of 3mm gas per anode strip).

If we assume that the efficiency starts to drop at an angle of incidence where the projection of the

track spreads over more than 3 strips, than the effiency of the tracker starts to drop below a momentum of 1.7 GeV/c at a radius of 40 cm. This certainly excludes the omnipresent mass of low momentum particles from detection. Detailed simulations have to show the effects more in detail, but surely a picture without loopers or heavily bent particles is attractive.

Some essential questions about any tracker at the LHC are:

1 Can it stand the rate?

2 How long can it survive?

3 Can one disentangle the resulting patterns?

Q1.

The particle flux at a luminosity $L=10^{34}cm^2$ and a total crosssection of 100mb (10^9 interaction/sec) at r=40cm is $7.5*10^5$ $sec^{-1}cm^{-2}$ (ref2). Fluxes in excess of 10^7 particles per cm^2 per sec can be handled by the MSGC, so this flux is within the capacity of the detector. The strips are 10cm long and cover 0.2mm anode spacing,, hence the flux per strip is $1,5*10^5sec^{-1}$. This leads to an occupancy of 1.5% per channel for a pulselength of 50nsec, as every particle is seen by about 2 strips. Here we neglect the fact that the projected length of the strips is about a factor 2 lower than the 10cm assumed and we neglect the reduction obtained by the directional effect, which might be as much as a factor 4.

Q2.

If the gasgain is 3000, then each passing particle produces $1.5*10^5$ electrons on the strips. At 40cm from the beam the charge per year per cm strip is $4*10^{-3}$Coulomb . A charge of 0.1C per cm seems reasonable to assume for the radiation hardness of the strips, so the lifetime of the detectors at r=40cm and $L=10^{34}$ cm^{-2} seems no problem. We cannot apply the reduction argument here as the unseen particles still produce ionisation.

The dose at r=40 cm is 250 Krad/year . Several people (ref3,4) have reported radiation hardnesses of preamplifiers above 1 Mrad, so this problem can most probably be solved.

Q3.

G.Hanson et al. (ref5) have simulated a tracker for the SSC made with classical MWPCs, so each channel had 100 times the sensitive area of a MSGC. With an occupancy exceeding 10% they remain optimistic about analysing it all, so as long as our expected occupancy remains a factor 10 below this value we can be confident, that even with a modest number of points on a track one can do a good job in pattern recognition.The report of C.Daum (ref6) discusses momentum resolution and multiple scattering effects of a similar tracker.

References.

1. Angelini et al. Proc. ECFA studyweek on instrumentation for high luminosity colliders. Barcelona, Sept 1989 page 465.
   F.Hartjes et. al. Ibid. Page 455.
2. G.R.Stevenson. Ibid. Page 96.
3. Sadrozinski et al. Ibid. Page 153.
4. G.Steenvoorde. TNO Delft Private communication.
5. G.G.Hanson et al. Ibid. Page 413.
6. C.Daum. Study of a LHC detector with a solenoidal field. Submitted to this conference.

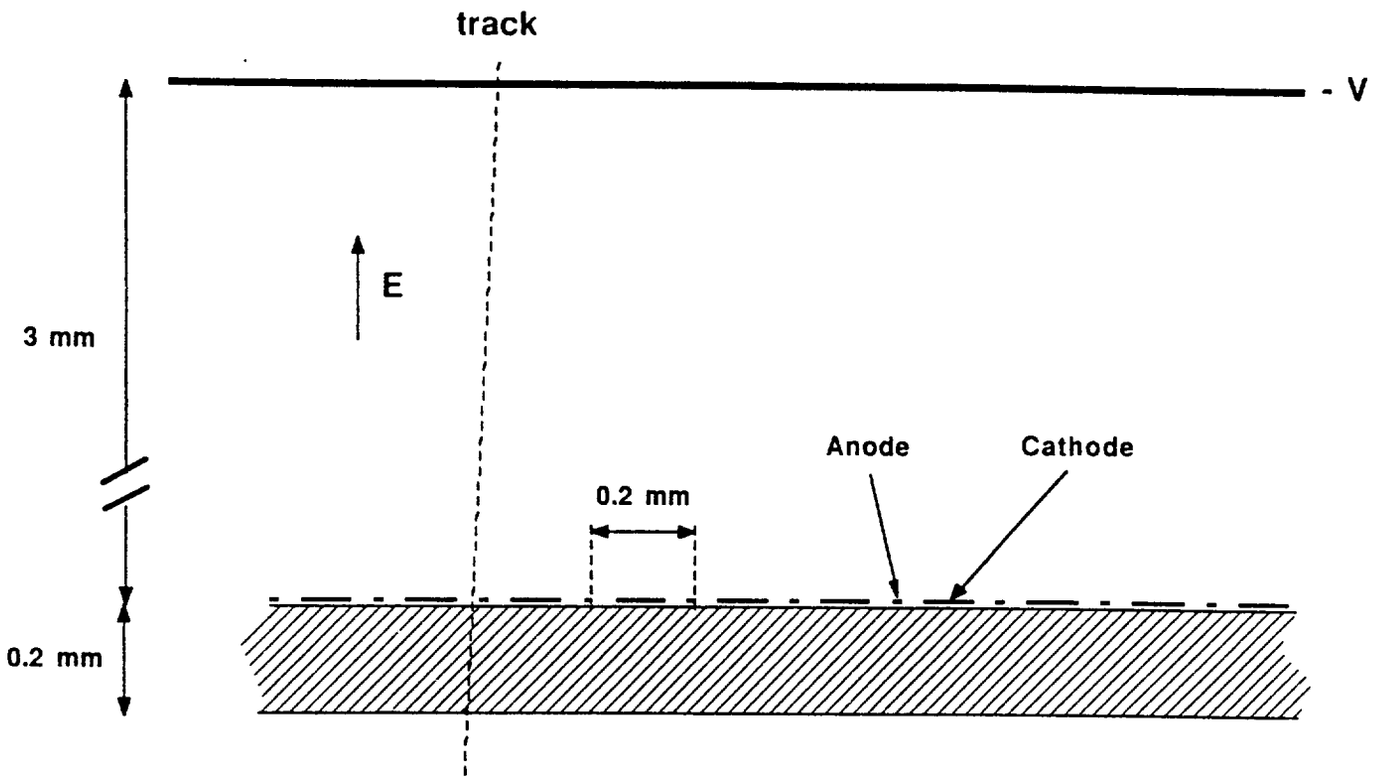


Figure 1. Cross section of a microstrip gas detector. Both the thickness of the substrate and the size of the gasgap are taken from an actual prototype. The track inclination in the tracker proposed here is 90^{o} in this projection.

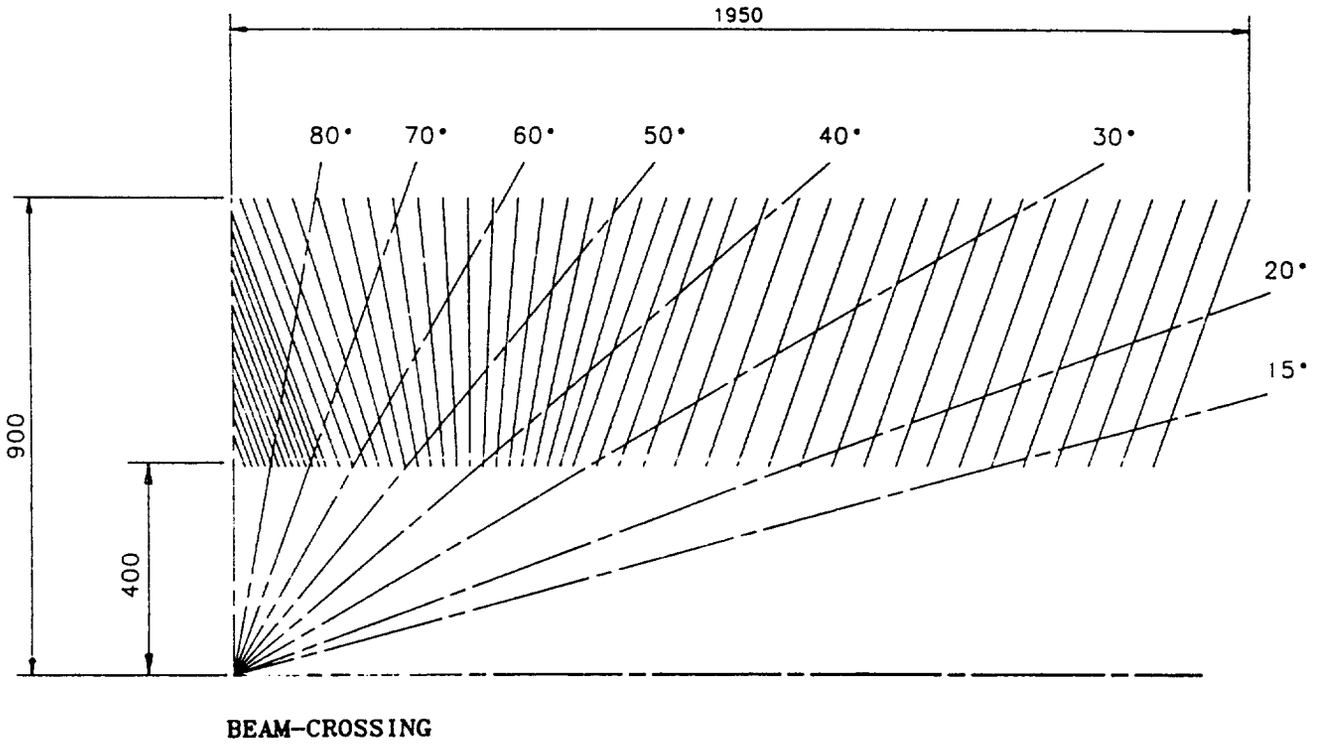


Figure 2. :Design of a tracker optimised as described in the text. The dimensions are in mm.

FURTHER PROGRESS IN THE DEVELOPMENT OF THE MICROSTRIP GAS CHAMBER

F.Angelini, R.Bellazzini, A.Brez, E.Focardi, T.Lomtadze, M.M.Massai, G.Spandre and M.R.Torquati,
INFN and University of Pisa, via Livornese 582, 56010 S.Piero a Grado, Pisa, Italy

R.Bouclier, J.Gaudaen and F.Sauli.
CERN, Geneva, Switzerland

A.Perret.
CSEM, Neuchatel, Switzerland

We describe the operating principles of the microstrip gas chamber and the main results of measurements realized with several prototype devices in the detection of X-rays and charged particles. Detectors with 3, 5 and 10 μm anode widths and 125 or 200 μm pitch have been successfully tested. A gas gain of 10^4 and an energy resolution of 11% fwhm at 6 KeV have been measured. A localization accuracy for minimum ionizing particles of 30 μm rms, a two track resolution of 250 μm and a high rate capability (above $2 \cdot 10^7$ $cm^{-2}s^{-1}$) make the device a good candidate for tracking at high luminosity colliders. Tests of survivability and of operation of the detector with fast gas mixtures have been performed.

1. STRUCTURE OF THE DETECTOR

The microstrip gas chamber was introduced some time ago in an attempt to reproduce the field structure of multiwire chambers, at a much smaller scale [1,2]. It consists essentially in a sequence of alternating thin conductive anode and cathode strips placed on an insulating support; a drift electrode defines a region of collection of charges, and application of the appropriate potentials on anodes and cathodes create a proportional gas multiplication field.

Fig.1 shows the computed field lines in the multiplying region at typical values of the operating voltages [3]. One can understand the operation of the device as follows: drift lines connecting the upper cathode to the anode strips concentrate on the anodes, even more so due to the high potential difference between anode and cathode strips; the high electric field in the neighbourhoods of the anodes results in gas amplification. The major part (>70%, according to fig.1) of the positive ions created during the avalanche process, drift back to the close cathodes along the field lines, inducing signals on both anode and cathode strips.

For the measurements described in this report, we have used several detectors having cathode strips widths between 30 and 60 μm and anode strips between 3 and 10μm, at a 200 μm pitch (see fig.2). A detector having a 125 μm anode pitch has been also successfully tested.

Three kinds of glass have been used as substrate differing mainly for their surface resistivity (10^{10}-$10^{13}\Omega/\square$). The surface resistivity affects the gain drift which is observed in the first minutes after voltage switch on. The lowest resistivity glass showed an overall gain drift of ≈8%.

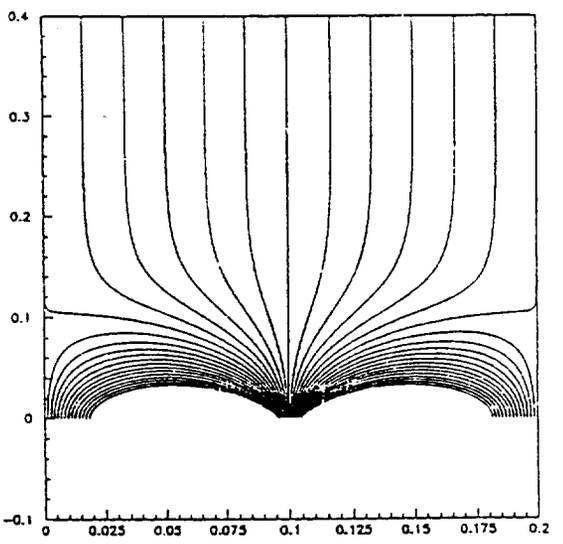


FIGURE 1
Field lines of one cell of the microstrip gas chamber.

The detectors are made using a microelectronics technology, namely electron beam lithography for the mask scribing and photolithography and thin film deposition to engrave 2μm thick aluminium strips onto a 500 μm thick glass substrate. The intrinsic accuracy of this kind of technology is 0.1 μm. The active area of the devices was 80×80 mm^2, although only a limited number of strips were actually readout. A conductive electrode on the back plane slightly influences the operating gain; conveniently stripped, it can be used to obtain a second coordinate of the avalanche. Drift gaps between 2 and 6 mm were used in the detectors, the shorter gaps being favoured for detection of charged particles (since they imply a better time resolution).

In the case of cathode readout, all the anodes were connected together and to the (positive) high voltage, while the cathode strips were connected to the virtual ground of a low input impedance charge sensitive amplifier. In the case of anode readout, all the cathode strips were connected together and to the (negative) high voltage, while the anode strips were individually readout. In a new detector that is now under test, the anode strips are connected to high voltage through individual 2MΩ current limiting resistors which are directly built on the substrate. This opens the possibility of having at the same time both anode and cathode readout. The double readout could improve substantially the position resolution.

2. GAS GAIN, ENERGY RESOLUTION AND RATE DEPENDENCE.

Fig.3 shows the gas gain as a function of anodic voltage obtained with a detector having a 5 μm anode width and a 200 μm pitch. The gas filling was Argon-Ethane (90-10). Proportional gas gain around 10^4 can be safely reached with several fillings [4,5] when working with detectors with 3, 5 or 10 μm anode widths and 200 μm pitch. The detector with a pitch of 125 μm and a 5 μm anode width had a proportional gain limited to 10^3. For the same gas gain the operating voltages were correspondingly lower for the 3 and 5 μm anode widths in comparison with the 10 μm anode width (for example, 400 Volt versus 500 Volt anode cathode potential difference for 3 and 10 μm widths respectively). The best energy resolution was obtained with the thinnest anode strip (3μm).

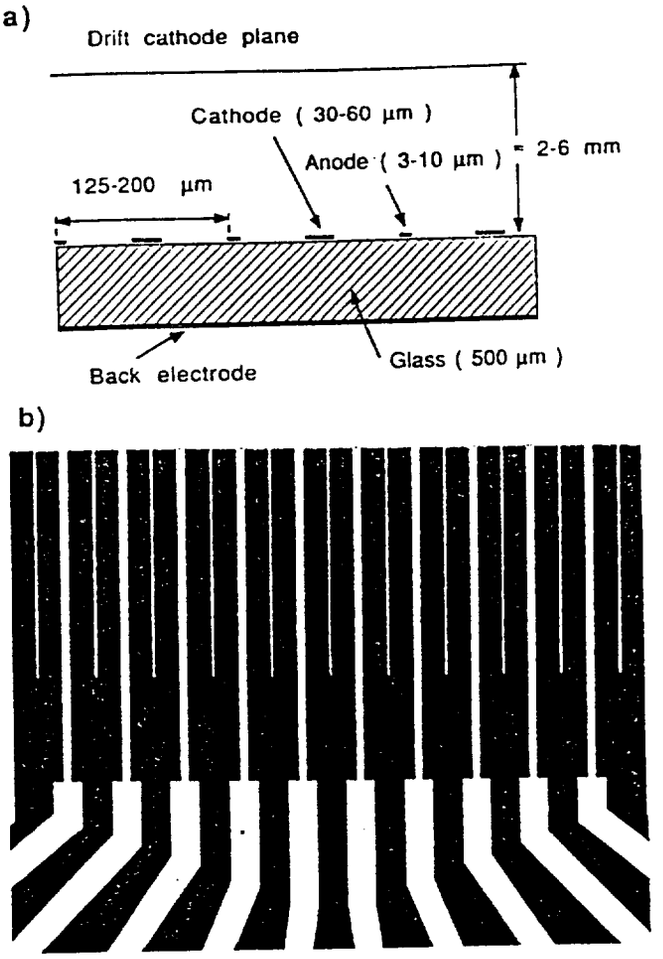


FIGURE 2
a) A cross section of the detector
b) A microphotograph of the anode-cathode structure and of the cathode fanout

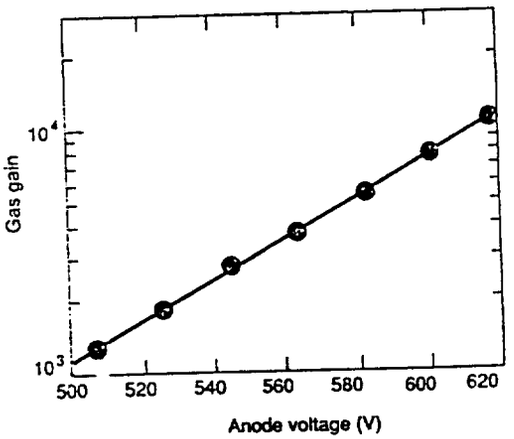


FIGURE 3
The gas gain as a function of anodic voltage

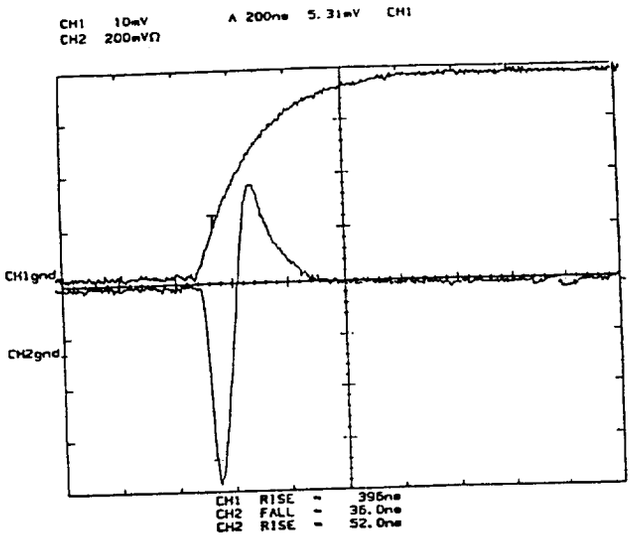


FIGURE 4
Upper trace: the charge signal (single shot) observed on a digital oscilloscope (differentiation time constant $\tau = 200$ μs) Lower trace: the same signal after amplification and fast differentiation ($\tau = 30$ ns).

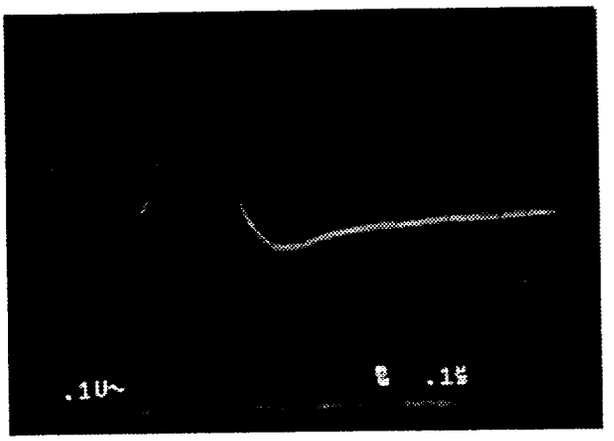


FIGURE 5
The anode signals with ^{55}Fe illumination.

The upper trace of fig.4 shows the charge signal (single shot) as a function of time observed on a digital oscilloscope (200 μs differentiation time constant). The interesting feature is the fast collection time (≈400 ns) of positive ions to the close cathodes which are only 60 μm apart in this case. The lower trace shows the same signal after amplification and fast differentiation (τ=30 ns).The signal to noise ratio is > 100.

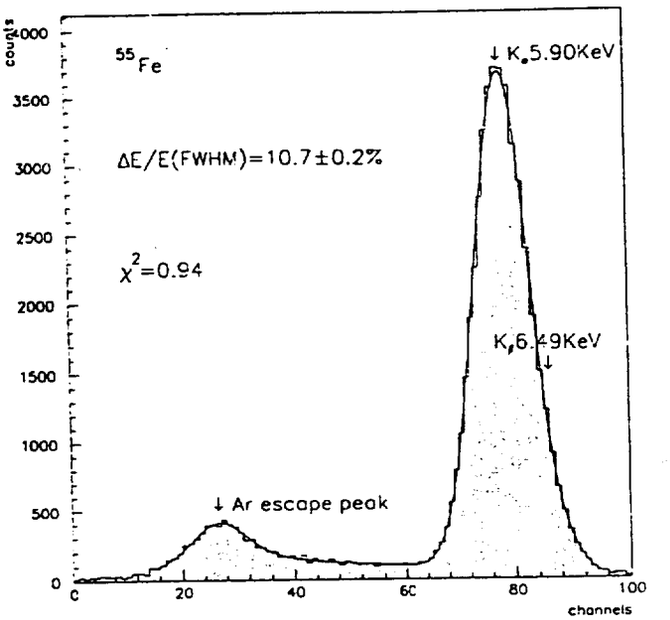


FIGURE 6
Pulse height spectrum of the ^{55}Fe signals shown in fig.5; bin width = 56 eV, fwhm at 5.95 KeV = 10.7±0.5%.

Fig.5 shows an analog oscilloscope picture of several pulses coming out of the detector with a 3 μm anode, working with an Argon-Ethane (90-10) gas mixture. The corresponding pulse height spectrum measured on a group of anode strips for 5.9 KeV x-rays is shown in fig.6; it is rather uniform over the sensitive area of the detector, with a fwhm of 10.7±0.5%. This resolution is remarkably good when compared to typical results obtained in multiwire proportional chambers and it is very close to the statistical limit for this gas mixture.

While a gas gain of 10^4 is probably high enough when the primary ionization is > 100 e^-, it could become a limiting factor when the primary ionization is quite lower as when using very thin detectors (2 - 3 mm) at atmospheric pressure. Thin detectors are needed, for example, at the next high luminosity hadron colliders (LHC, SSC) to reduce the detector memory (i.e. the electron drift time). For tracking at LHC or SSC a higher gas gain could therefore be desirable . Because no more gain could be obtained from the amplification process around the thin anode strips, we have tried to get a further stage of gain from the drift region (5 mm thick) which is in

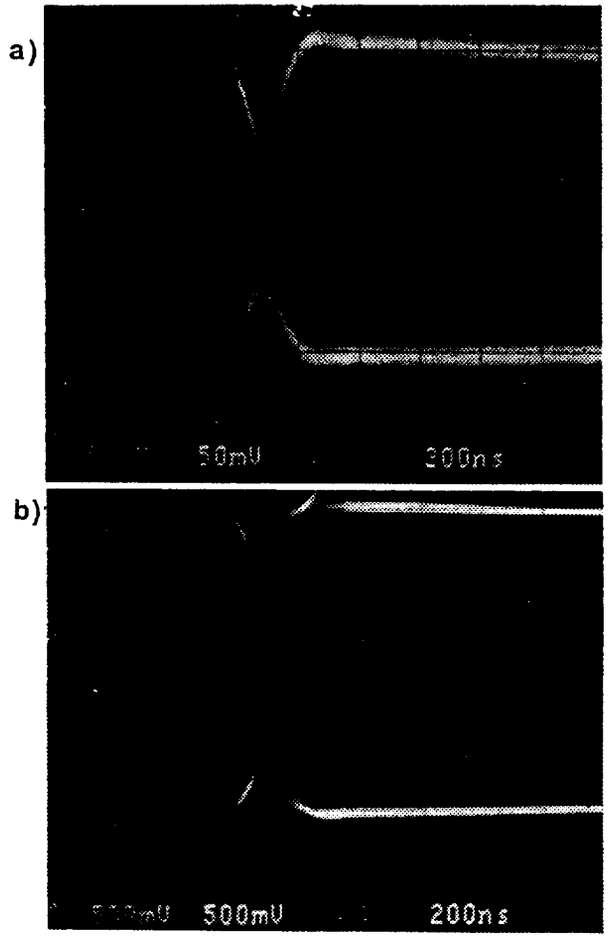


FIGURE 7

a) cathode (upper trace) and anode (lower trace) ^{55}Fe signals observed when the detector works without gas gain from the drift region;
b) the same of a) but with a contribution to the gain coming also from the drift region.

front of the amplification region [6]. The electric field was originally set to 2 kV/cm which is below the threshold for gas multiplication in an Argon-DME mixture (90-10). By reducing the quencher fraction to 5 %, and by increasing the field to 6 kV/cm, we succeeded in starting the multiplication process already in the uniform field region. A 6 kV/cm field is rather modest and quite comfortable. Fig.7a) and fig.7b) show the ^{55}Fe signals obtained from the anodic and cathodic strips when operating the chamber in the two different regimes, i.e. with or without amplification in the drift region . When all the gain comes from the anodic strips (fig.7a) the signals show the

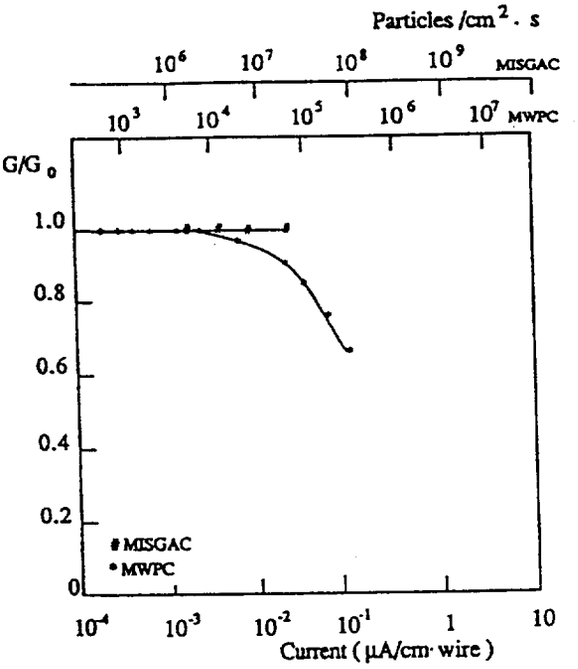


FIGURE 8

The relative gas gain versus the wire current and versus the incoming flux for a standard MWPC (*) and a microstrip gas chamber (#).

classical ^{55}Fe line (gain independent of the conversion point) , while when working with two stages of gain the signals show an almost continuous spectrum typical of a parallel plate operation (gain dependent on the conversion point , $G(x) = e^{ax}$, where x is the drift path of the photoelectrons). Note the change of vertical scale of a factor 10. This regime has been used for the 125 μm anode pitch detector whose proportional gain was limited to 10^3.

To check the rate dependence of the proportional gain, the chamber was exposed to an x-ray generator with controlled variable flux; the largest fraction of detected x-rays corresponds to the 8 KeV Cu line. At increasing values of the flux, the current, counting rate and pulse height spectrum were recorded on the cathode strips at fixed operating potentials. The result of the measurement is summarized in fig.8, providing the normalized gain as a function of the detector current per unit length of strip; a typical result obtained in a multiwire chamber is also shown for comparison [7]. As one can see, in the microstrip detector

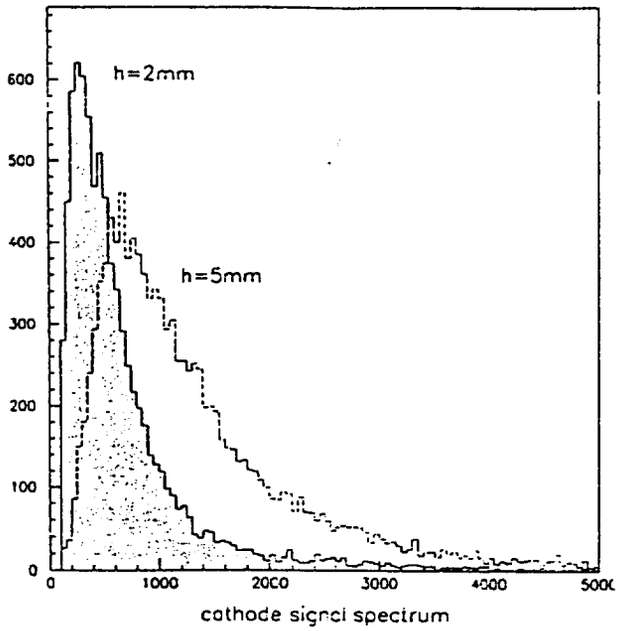


FIGURE 9
Pulse height spectrum of the sum of cathodic signals produced by minimum ionizing particles (Xe-DME) with 2 and 5 mm of drift gap.

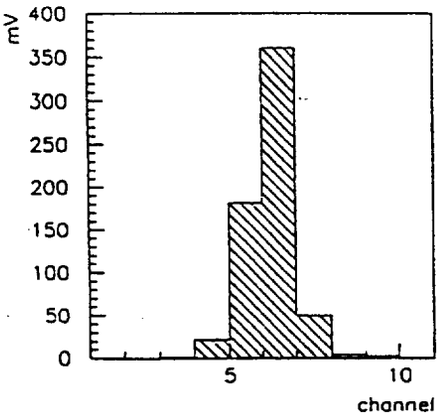


FIGURE 10
An example of cathode charge distribution

the gain is unchanged at currents an order of magnitude larger than in a MWPC; taking into account the reduction in pitch (at least by a factor of ten), one expects a rate capability in the microstrip chamber more than two orders of magnitude larger than in a MWPC, as shown by the upper scale in the figure. An actual measurement in a high intensity minimum ionizing particles beam has however still to be performed.

3. LOCALIZATION ACCURACY AND MULTITRACK RESOLUTION.

Localization in the direction perpendicular to the strips can be performed by recording the induced charge profile on the cathode strips and computing event per event the corresponding center of gravity. Preliminary measurements realized with a ^{55}Fe x-ray source indicated a localization accuracy in this case better than 80μm rms, limited by the collimator width [2].

For a measurement of efficiency and localization accuracy for minimum ionization particles, a microstrip chamber was installed in a high energy test beam at CERN, using as reference the space coordinates provided by a pair of silicon strip detectors [8]. For each event, the induced charge profile on 10 adjacent cathode strips was recorded, thus covering a 2 mm region;the gas filling for these measurements was Argon or Xenon with about 10% Dimethylether (DME) as quencher. Xenon was used in order to increase the energy loss and reduce their primary ionization fluctuations in the thin (5 mm thick) drift gap constituting the sensitive volume of the detector.

Fig.9 shows an example of pulse height spectrum for the Xe-DME mixture, integrated over the cathode strips, and fig.10 a typical induced charge profile for a single track. A scatter plot of the coordinate measured in the gas microstrip chamber, as a function of the position provided by the silicon strip detectors, is shown in fig.11 : it shows a good linearity and a dispersion of about 40 μm. rms; this is better seen in the projected histogram of fig.12. Taking into account the estimated dispersion of the silicon strip detectors, one can infer an intrinsic localization accuracy for the microstrip gas chamber of around 30 μm rms. The measurements in Ar-DME provide, as expected, a slightly worse space resolution.

The multitrack resolution depends on the rms of the induced charge profile. Fig.13 shows this quantity measured for minimum ionizing particles in Xe-DME. It has an average value of 125 μm; assuming that two tracks can be resolved if the corresponding induced pulse profiles are at least two standard deviations apart, we infer a multitrack resolution of 250 μm.

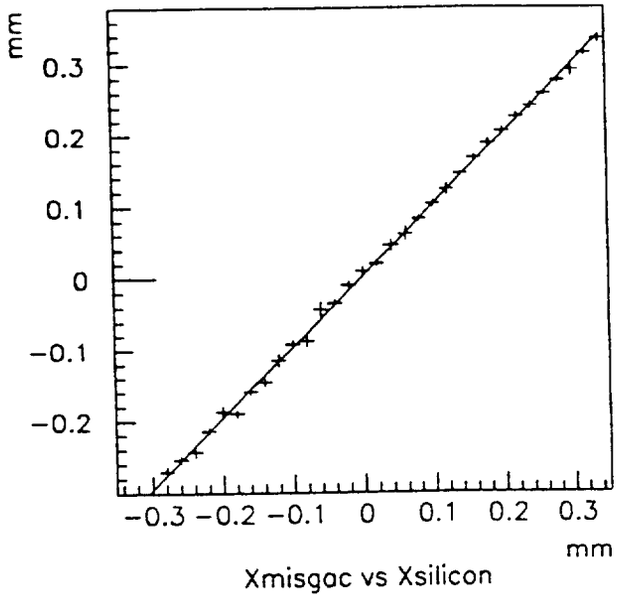


FIGURE 11
The correlation between the coordinates measured by the silicon detectors and the microstrip gas chamber.

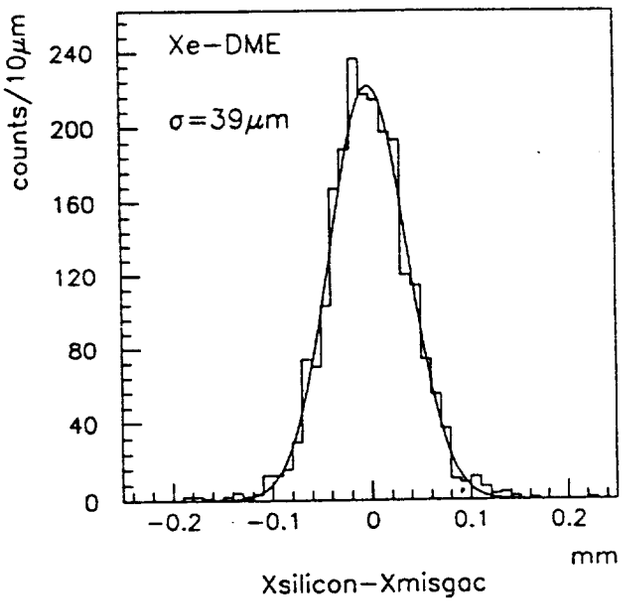


FIGURE 12
Distribution of the differences between the coordinates measured with the silicon detectors and the microstrip gas chamber.

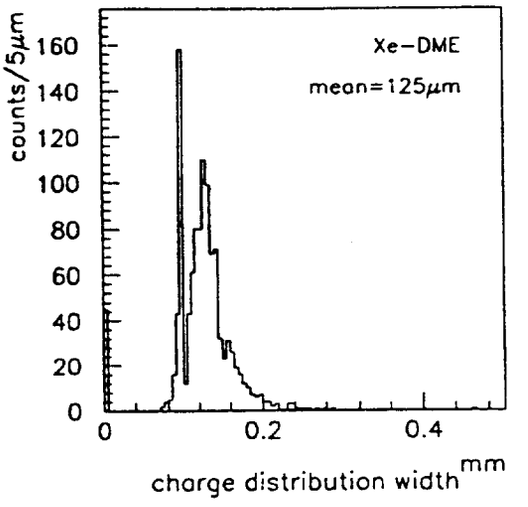


FIGURE 13
The width (rms) of the charge distribution

4. OPERATION OF THE DETECTOR WITH CF_4 BASED GAS MIXTURES..

Any detector aiming to work at SSC or LHC has to be fast to reduce the memory time and therefore the cell occupancy. Fast, in this case, means that the charge collection time which defines the pulse leading edge, has to be in the few ns range to be comparable with the bunch crossing separation. Standard, Argon based, gas mixtures are relatively slow (v_{drift}≈20 ns/mm) and the gas thickness has to be large because of the low ionization density of Argon (≈20 clusters/cm). CF_4 is a very fast (v_{drift}≈10 ns/mm), very dense (≈50 clusters/cm) new gas recently proposed for gas detectors. Furthermore it seems to have etching properties of the polymerization products which are at the origin of the ageing process.

We have successfully operate a 2 mm thick microstrip gas chamber with a CF_4 (80)-Isobutane(20) gas mixture. Fig.14 shows the average pulse observed on a single strip with a ^{90}Sr β source. It is a very fast pulse (13 ns rise-time) having a total duration of ≈50 ns. This is a suitable pulse for a tracker at the high luminosity hadron colliders (≤1% occupancy at 20 cm from the LHC beam axis). Fig.15 shows the pulse height spectrum of the anode OR observed when illuminating the detector with a ^{90}Sr source. The acquisition was triggered by a central cathode strip to be sure that the β ray is within the detector active region. The spectrum is completely apart from the pedestal distribution (left peak).

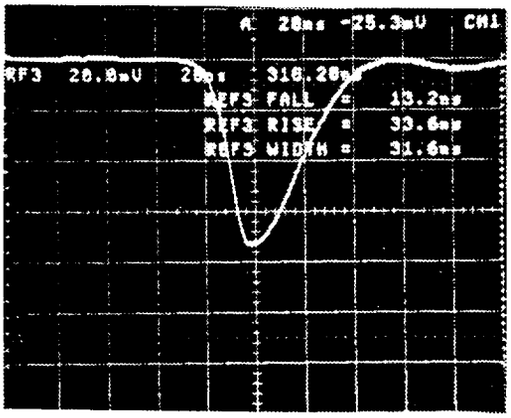


FIGURE 14

Average pulse from a single strip with a ^{90}Sr β source, observed on a digital oscilloscope.

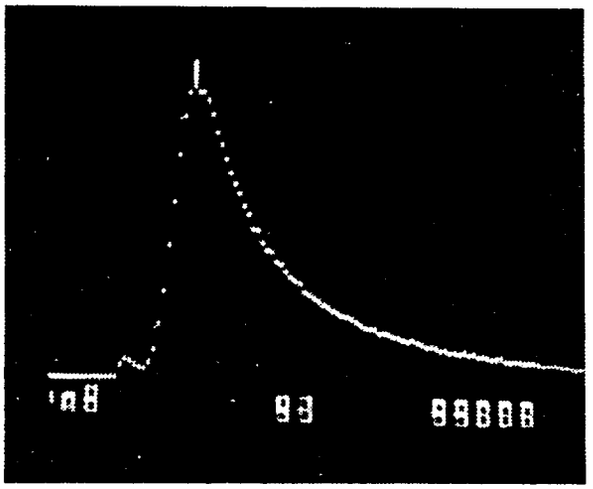


FIGURE 15

Pulse height spectrum of the anode OR with a ^{90}Sr β source.

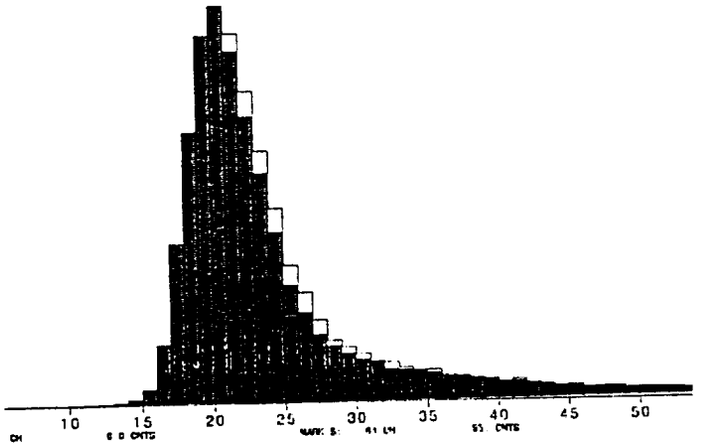


FIGURE 16

Landau distributions measured in two 100 ms time windows at the beginning and at the end of the spill of the NA-34 (Helios) intense proton beam at CERN.

5. TEST OF SURVIVABILITY OF THE DETECTOR IN A HIGH-RATE ENVIRONMENT.

The test beam studies were performed with a low rate charged particle beam (10 KHz). To study the survivability of the detector in the much more severe experimental and environmental conditions expected at the SSC or LHC, we moved the detector in the most intense beam existing today at CERN, which is the NA-34 (Helios) proton beam. This beam has, at focus, a flux of $\approx 10^7$ protons/mm^2◊s. We placed the detector a few meters out of focus where the flux is reduced to $\approx 10^6$ protons/mm^2.s, which is very close to the most stringent requirement at LHC. We left the detector in the beam for three weeks, monitoring the Landau distribution from the OR of anode strips (gas filling Ar 80-Methane 20). No significant change was observed during this period. The integrated fluence was $\approx 10^{12}$ particles/cm^2. To study if there is any substrate charging at this very high rate, the Landau distribution was taken also in two different 100 ms time windows, one at the beginning of the beam spill and the second at the end of the spill. The spill duration was 2.4 s. No noticeable difference between the two distributions was observed (see fig.16), indicating that no charging process occurred at this rate.

6.CONCLUSIONS.

The microstrip gas chamber has been shown to allow fast and accurate detection of both soft x-rays and minimum ionizing particles. Its performances compare rather well to those obtained with solid state microstrip detectors; the advantages seem to be however a higher radiation resistance, a lower cost and a larger signal/noise ratio, this last point rather interesting in that it could lead to the use of cheaper and/or faster electronics readout.

Work is in progress to improve the operating characteristics of the device, the angular dependence of the localization accuracy and to study its long term stability. Use of small gaps and fast gases has been studied to take full advantage of the rate capability of the detector.

ACKNOWLEDGMENTS

We would like to thank C.Magazzù and G.C.De Carolis for the technical assistance.

REFERENCES

1. A.Oed et al. Nucl.Instr. and Meth A263 (1988) 351

2. F.Angelini et al., Nucl. Instr. and Meth. A283 (1989) 755.

3. P.Astier, Private communication.

4. F.Angelini et al. Particle World vol 1., n.3 (1990) 85

5. H.Hartjes et F.Udo, Proceedings of ECFA study week on Instr. Tech. for High-Luminosity Hadron Colliders, Barcelona (1989), CERN 89-10, 455.

6. F.Angelini et al., A microstrip gas avalanche chamber with two stages of gas amplification, to be published on Nucl. Instr. and Meth.

7. F.Angelini et al., Proceedings of ECFA study week on Instr. Tech. for High-Luminosity Hadron Colliders, Barcelona (1989), CERN 89-10, 465.

8. F.Angelini et al., Proceedings of the 1989 IEEE Symposium on Nuclear Science, San Francisco, January 1990.

A Device for Particle Detection at future Hadron Colliders: The Gaseous Pixel Chamber (*)

D. Antreasyan, Y. Liu, D. Mattern, M.C.S. Williams and A. Zichichi
CERN, Geneva, Switzerland

(*) The work presented here is supported totally by the LAA project

1. Introduction

The Gaseous Pixel Chamber is a new type of particle detector with a unique combination of features. All its essential building parts come on the surface of two pc-boards or foils. It is easy to build as it needs only the cheap standard materials and fabrication processes of a printed circuit workshop. The precision of the final product is not influenced by extra mechanical work such as the positioning of a stretched wire. It is governed by the accuracy of the film used to produce the etched pattern. Signals are big since the device, we use at present, works in limited streamer mode. This detector works reliably at high rates. Since this detector is pixel in conception, it does not suffer from the occupancy problems usually found with gaseous detectors in the central region.

2. Device description

Figure 1 shows the design of the anode/cathode foil that we use at present. We build a 'standard' chamber by mounting a second 'roof' foil 8 mm above the anode-cathode foil. This roof foil is for field shaping. The design of the roof foil is similar to the anode-cathode foil except it has big anode areas. We have also tried other materials and techniques to fabricate this chamber. Using thick film technology we have printed the structure on alumina ceramic. This avoids hole drilling. This ceramic chamber also works but has not yet reached the excellent performance of the Kapton based chamber.

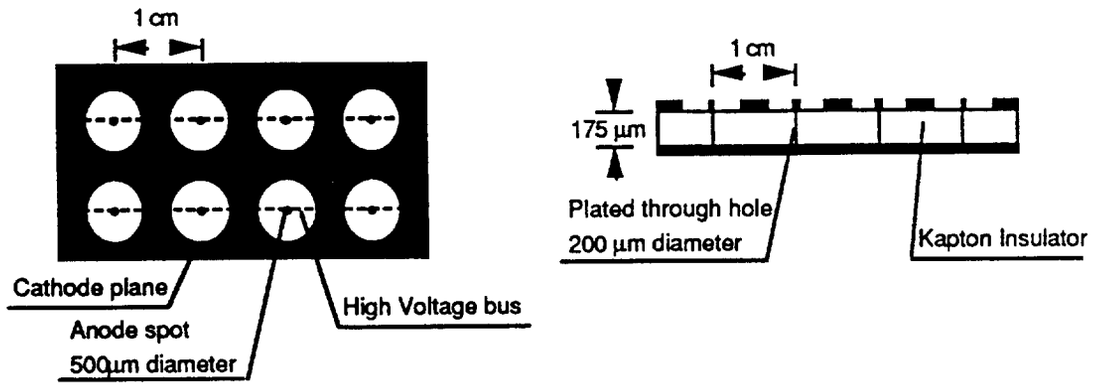


Figure 1: Schematic view of 'standard' foil

3. Results

We have tested various foils with minimum ionizing particles in a beam at the CERN-PS. Results have been reported elsewhere (ref. 1-5). A brief overview of the more recent results is given here. Figure 2 shows the performance of foils having thicker Kapton base material (dielectric of 325 μm). The beam was set to an intensity of 20 kHz/cm^2. The measurements were taken with the first 1000 particles of each beam spill. When we integrated over three beam spills the efficiency was lower (90 % compared to 96 %). The voltage of the knee of the plateau is lower and the maximum working voltage is extended in comparison with the standard thickness foil.

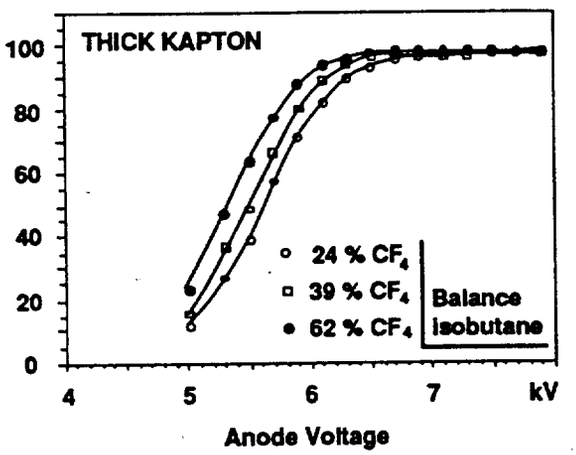


Figure 2: Detection efficiency for 6 GeV/c pions (see text)

The rate behaviour of the standard thickness Kapton chamber up to 100 kHz/cm^2 is reported in ref. 2. The thick Kapton chamber also works with an extended Argon content of up to 33 % Argon in Isobutane. At this Argon concentration the knee voltage is reduced by around 500 V. In pure Isobutane the maximum safe working voltage is extended to 7.4 kV. We investigated the role of the thicker dielectric further by printing solder mask onto the standard chamber in the region between anode and cathode. The efficiency is improved to 100 %.

We also measured the position resolution of our chamber. The readout was such that the anode spots were bussed together in rows, while pads on the roof board were bussed in columns. Therefore we could identify individual pixels. The distance of the track going through to the nearest anode was measured with external driftchambers. The drifttime to this anode was then used to lookup the radius in a space-time table. Figure 3 shows the distribution of the residuals. We have an upper limit of 320 μm sigma . We expect this to improve a lot when we work with much smaller cells and smaller anodes.

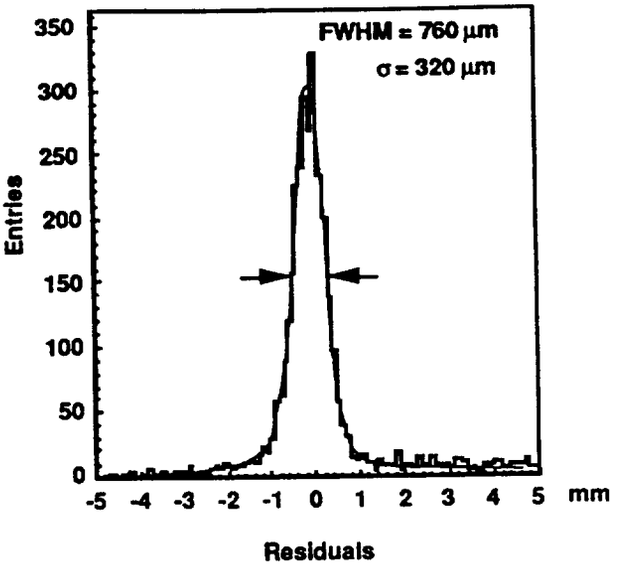


Figure 3: Distribution of residuals for the radial distance

In the future we want to reduce the size of the anode by at least a factor ten. This will also allow us to reduce anode voltage and the cell size. A reduced cell size gives us automatically a better resolution and a shorter drifttime. First studies were with chopped 50 μm wires in the anode holes. This test looked very promising. It was possible to increase the Argon content to 96 % and get the chamber fully efficient at around 1.2 kV anode voltage. With this modification we were able to resolve multi particles firing more than one pixel by looking at the sum signal of all anodes. This is shown in figure 4. We are now investigating various advanced laser technologies for punching small diameter holes into Kapton foils. We have just received first Kapton foil samples with laser ablated holes throughplated from Siemens AG, Munich. These have been tested successfully in the laboratory with an ^{55}Fe source.

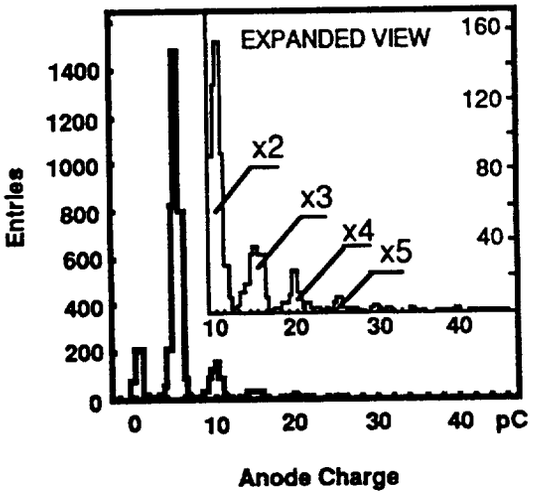


Figure 4: Charge spectrum of pixel chamber with chopped wires

They operate at a lower high voltage (~2 kV) than the standard foil. These foils have holes of 50 μm and an anode pitch of 5 mm. Work is in progress to reduce these values even further. We can also double the actual pixel density and reduce drifttime by using two foils offset by half a cell facing each other with the gas in between.

Computer simulations of the electric field in this chamber have been done. The geometry essentially calls for 3D-programs including the treatment of dielectric materials. Local effects around the anode are studied with the assumption of rotational symmetry. The line feeding the anode voltage to the pad on top and the arrangement of the pixels on a rectangular 2D-lattice break this symmetry. Work is in progress.

4. Applications at a future hadron collider

We can foresee various applications of this type of chamber at future colliders. One of which are large area chambers for muon detection. With the thick Kapton chamber we are already very close to that goal. Another possibility would be to arrange the anodes on a curved line. Therefore we could build some special trigger and tracking chambers in the forward direction of the standard toroidal design. In the central region a simple jet trigger could be built that just demands a certain track density in a given detector region. An interesting application arises from the mechanical flexibility of the foils. We could build a thin and simple z-chamber for an additional tracking information. We could simply warp our foils around for example a scintillating fiber tracker. The anodes would be arranged like rings on a barrel in this case. We hope to soon have this gaseous pixel detector working in proportional mode. This will allow us to build preshower counters for calorimeters.

5. References

1. D. Mattern and M.C.S. Williams, Green Report CERN 89-10, ECFA 89-124 (1989) 435-439
2. D. Mattern, M.C.S. Williams and A. Zichichi, CERN/ECP 90-4, submitted to Nuclear Instruments and Methods in Physics Research
3. D. Mattern, M.C.S. Williams and A. Zichichi, CERN/PPE 90-147, contributed paper to the 2nd London Conference on Position-Sensitive Detectors, 4-7 September 1990, London, England, to be published in Nuclear Instruments and Methods in Physics Research
4. D. Antreasyan et al., Contributed paper to the 12th Workshop of the INFN Eloisatron Project, Erice-Sicily: 15-20 September 1990
5. D. Antreasyan et al., Proposal to the CERN Detector Research and Development Commitee, CERN/DRDC/90-60, DRDC/P14, 31st October 1990
6. F. Bachmann, Eximer lasers in a fabrication line for a highly integrated printed circuit board, CHEMTRONICS 4 (1989) 149-152
7. D. Mattern, Calculation of 3D-electrostatic problems with dielectrics using a commercial finite element program, to be published.

Conceptual Design for a Silicon Tracker at the SSC

K. O'Shaughnessy, B. Hubbard, D. Pitzl, A. Seiden
Santa Cruz Institute for Particle Physics
University of California, Santa Cruz, CA 95064
A. Weinstein
California Institute of Technology
Pasadena, CA 91125
J. Hylen, J. Matthews
Johns Hopkins University
Baltimore, MD 21218

We present a conceptual design for a silicon tracking detector to be used at the SSC. The goals for the detector are to provide excellent pattern recognition, excellent vertex resolution for high p_t tracks and momentum resolution that is good in a stand-alone mode and excellent when combined with an outer tracker

The proposed design is shown in Figure 1 and consists of a 10 layer barrel section and 14 planes in each of the forward and backward regions, giving tracking capability out to a rapidity of 2.5. The individual silicon strip detectors are double-sided, with strips on

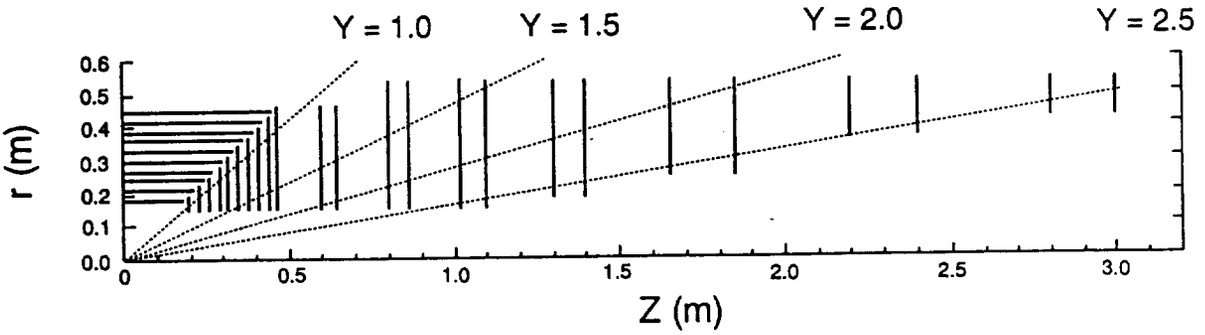


Figure 1: Layout of the silicon tracking system used for the study.

one of the sides having a small (5 mrad) stereo angle. The pattern recognition uses a local linking of hits within two adjacent layers, giving a local track tangent vector. These vectors are later joined to form tracks [1].

An estimate has been made of the performance of the silicon tracking system both alone and with an outer tracking system. For the purposes of this study, an outer system with 64 measurements at radii from $0.7^{\mathrm{mto}}1.8^{\mathrm{m}}$ and position resolution of 150 μm was used. The momentum resolution of the silicon and an outer tracker is 10%p at 1 TeV and meets the level needed to reconstruct the Higgs boson mass (for masses between 300 and 800 GeV) in the benchmark process $H^0 \rightarrow Z^0Z^0 \rightarrow 4\ell$ with a resolution less than the natural width

of the H^0. The impact parameter resolution of the silicon system is 50 μm for momenta above 1 GeV and drops to 15 μm if an outer tracker is included.

A software package has been written that will simulate hits in the silicon tracker from events generated by ISAJET[2]. The hit generation accounts for multiple scattering, energy loss and a spread in the z vertex positon of the interaction of 7 cm. Not included are photon conversions, random noise, strip inefficiencies and effects of misalignments. An option for adding tracks from multiple minimum-bias events is also available. After the hits are generated, a track-finding routine and a track-fitting routine produce tracks. The package has been used to study the track-finding efficiency for several physics processes: the decay $H^0 \rightarrow Z^0 Z^0 \rightarrow e^+e^-\mu^+\mu^-$, jets with p_t from 50 GeV/c to 2 TeV/c, and b quark jets from $t\bar{t}$ decays.

The analysis of the Higgs decay was the most thorough, examining the efficiency of reconstructing the lepton tracks, the quality of the reconstruction and the invariant mass of the lepton pairs (to compare with the Z^0 mass). In addition, minimum-bias events were added to mimic multiple interactions per crossing. The efficiency for finding these isolated tracks was approximately 95% and did not depend on the number of minimum-bias events added. This is shown in Figure 2a. Figure 2b and 2c show the efficiency after requiring that the reconstructed momentum be within a factor of 2 of the generated momentum and then that the dilepton invariant mass be within 5 GeV of M_Z. The overall efficiency for

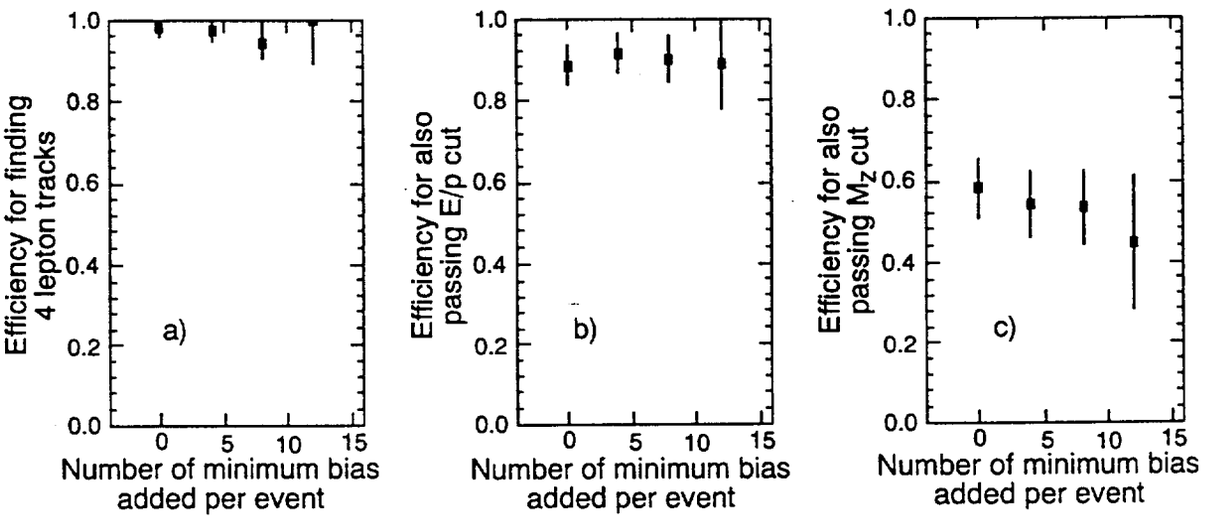


Figure 2: Efficiencies for the Higgs boson analysis as a function of the number of minimum-bias events added. The efficiency for finding the 4 lepton tracks is shown in a), and b) and c) show the efficiencies as the E/p cut and the dilepton invariant mass cut are applied.

these types of events is roughly 55% and has only a slight dependence on the number of interactions per crossing.

Track-finding within jets is a much more difficult problem and optimization of the algorithm parameters is necessary. The efficiency is strongly dependent on the p_t of the jet and, for a standard configuration and set of parameters, typical numbers were 97% (for a jet p_t of 100 GeV/c), 88% (500 GeV/c) and roughly 78% (1TeV/c).

The potential of the silicon and outer system for tagging b quark jets was studied. The algorithm employed was simple and consisted of counting the number of tracks in a jet direction above a p_t cut (*e.g.* 1 GeV/c) that have impact parameters inconsistent with the

primary vertex. With this algorithm, the efficiency for recognizing a b jet with $p_t > 30$ GeV/c is approximately 50% (or 65% if a 3-layer pixel device is included). For a top mass of 150 GeV/c^2, this translates to a 50% efficiency for tagging one or both b-jets in a $t\bar{t}$ event where the top quarks decay semi-leptonically.

From these studies one can conclude that the silicon tracking system as proposed is capable of fulfilling the tracking requirements outlined above. Further studies must be performed with a more realistic simulation to optimize the design and determine engineering constraints.

References

1. J. Hylen *et.al.*, SCIPP 90/24.

2. F. Paige and S. Protopopescu, *Proceedings of the Summer Study on the Physics of the SSC*, Snowmass, Colorado, 1986, R. Donaldson and J. Marx, eds., p. 320.

DEVELOPMENT OF SILICON PIXEL DETECTORS FOR LHC

pixel detector collaboration
CERN, Collège de France, CPPM Marseille, EPFL, ETHZ, IMEC, INFN Bologna, INFN Genova, INFN Milano, INFN Pisa
spokesman: Erik H.M. Heijne

Introduction, why pixel detectors ?

The use of silicon diode microstrip detectors, introduced about 10 years ago[1], has become widespread because they combine several crucial properties: particle localization with ≥ 5 μm precision in one coordinate, double hit separation better than 100 μm, geometrical precision better than 1 μm, signal charge collection in less than 20 ns, bias voltage below 100 V, easy installation and reliable operation. The production of silicon detectors is based on microelectronics planar manufacturing technology. Progress in this technology is driven by considerable economic interests and ever smaller, more sophisticated electronic structures are becoming feasible. Therefore, it is now realistic to consider as a natural extension to the microstrip detectors the development of unambiguous two-dimensional particle detector arrays which incorporate signal processing electronics in an area equivalent to the detecting area. Following the terminology developed for optical imaging devices, the basic cell (picture element) in an array is called a 'pixel', whence 'pixel detectors'. Chips which have signal processing as well as a certain degree of data reduction can be called **micropattern detectors**[2]. Such detectors should produce unambiguous two-dimensional position information for selected events only.

The primary application of semiconductor micropattern detectors will be vertex detection and tracking inside experiments at LHC, in particular at small radii where the track density in LHC precludes the use of any other type of detector. Physics arguments for the use of pixel detectors will be developed elsewhere in these proceedings by Bedeschi (b-tagging), Tonelli, Quercigh (heavy ions), a.o. Experience in NA32 and UA2 as well as simulations show the clear advantages of true two-dimensional detection for event selection, improvement of the background and reduction of analysis time. In the USA, Pfeiffer [3] has made a study of the use of pixel detector data for the first level trigger.

The combination of 1 or 2 silicon pixel planes with a projective detector consisting of Si microstrips or scintillating fibers might be the most efficient approach to inner tracking, given the high multiplicity and taking into account the cost of pixel detectors

Serial vs. parallel readout of pixels.

Photodiode arrays and Charge Coupled Devices (CCD) are already used as pixel detectors for electronic imaging, but the speed required for most optical applications allows serial scanning of the array, and the on-chip signal processing (e.g. Correlated Double Sampling) can be restricted to a single output channel. In a CCD the signal charge is physically transferred to the output node by shifting through a row and a column of pixels whereas in Direct Readout Devices (DRO) the pixels are serially addressed and readout via a bus, as in a Random Access Memory (RAM). In either case the readout time is of the order of ms for e.g. a 500 x 500 pixel matrix.

Serial readout is inadequate for the high luminosity hadron colliders, and for the high rate environments new, parallel signal processing structures and information readout architectures have to be developed. A sophisticated signal processing circuit must be integrated with each pixel element. It should contain a preamplifier, shaper, peak detector, comparator and analog and digital memory elements. The first experimental readout chip following this concept [4] has been developed in the framework of the LAA detector R&D program, in a collaboration with ETHZ and EPFL. This version did not contain analog signal storage but the next version is planned to include this feature. Digital circuitry in the pixel or at the edge of the matrix should allow time stamping of pixels hit in order to associate their data with a positive trigger.

Monolithic and hybrid pixel detectors.

In a monolithic pixel device the detector function as well as the signal processing are built into a single silicon chip. In one approach the readout circuits are located in an ion-implanted well [5] or directly in the high resistivity substrate [6], which acts itself as detector. It is not straightforward to create the desired detector segmentation without losing detector efficiency. Another approach uses the Silicon On Insulator (SOI) technology, in which the processing circuits are separated from the detecting part of the silicon wafer using an oxide layer. There exist several ways of creating such SOI structures, and we propose to evaluate the SIMOX technology in which a 0.4 μm thick oxide layer is formed at 0.2 μm below the surface by implantation of oxygen ions. Monolithic detectors are elegant, present minimal material thickness, are easier to assemble and possibly cheaper in the manufacturing. However, the technological development is likely to be considerable.

Hybrid pixel detector construction is more flexible because one can separately optimize the detector part and the readout electronics. Connections are made by using a bump-bonding technique. The metal bumps may add a significant amount of high-Z material to the detector, however. The readout circuit reported in our previous paper [4] is intended for hybrid mounting. Using a similar approach, Jernigan et al. [7] presented recently the first results for alpha particle detection using a simpler, charge integrating hybrid pixel array.

Pixel size.

The granularity of the pixel detector has to be chosen to fulfill a number of contradictory requirements. Detection precision and double track resolution are dictated by the experimental application. The occupancy in the high luminosity environment, in conjunction with the time needed for the first level trigger decision, determine the probability for a single pixel to be hit twice. Smaller pixels have a smaller double hit probability. If multiple hits may occur, the electronics has to be more complex, which will increase its size. Therefore, smaller pixel area may be desirable.

An important aspect of the pixel detectors is the power dissipation. It has been remarked already on several occasions,e.g. by Jarron[8], that a finer segmentation leads to lower power consumption in the analog front-end part, for a given noise performance. Again, this pleads in favour of small pixels. Obviously, the digital control part increases in size and in power and a trade-off has to be made.

The size of the pixel, the detector thickness and the connection pad determine the effective input capacitance and thereby the noise of the input amplifier circuit. The lower this noise, the thinner the active detector layer can be. A chip thickness of 150 μm is probably at the limit of handling possibilities for hybrid fabrication. A 150 μm thick Si detector delivers a signal of ≈12000 e-h pairs per minimum ionzing particle and has a geometric capacitance of 7×10^{-7} pF per μm^2 or 2 fF for a 30 μm x 100 μm pixel. The capacitive contribution to the noise will in this case be dominated by stray capacitances.

In the presently proposed hybrid devices the pitch is determined by the size of the electronics circuit, and the existing experimental chip has a 200 μm pitch, whereas the next circuit could reach a 75 μm pitch. A final consideration for the pixel size comes from the expected leakage current degradation due to the high dose irradiation in LHC [9] which is discussed in the next section..

Detector degradation by radiation effects.

Radiation damage is a major concern for the application of semiconductor detectors in supercolliders[10]. The effects are: increase of leakage current, carrier removal which modifies the effective material resistivity, and signal charge trapping. We adopt here for the current increase the same numbers as in [11], i.e. 10^{-17}A cm^{-1} for minimum ionising particles (mip), and 10^{-16}A cm^{-1} for albedo neutrons. No definitive agreement exists as yet on these numbers: the number for minimum ionizing hadronic particles may be slightly higher and the neutron number lower, see the contribution by Lindström et al. in these Proceedings. The effects of the same dose of high energy electrons or muons may not equivalent, and certainly photon dose gives several orders of magnitude lower current increase. In a pixel volume of 30 μm x 100 μm x 150 μm a radiation induced leakage current of 100 nA will then be reached after ≈ $2\ 10^{15}$ neutrons/cm^2 or 550 Mrad of ionizing mip radiation, which are accumulated in LHC after ≈ 10 years of operation. The signal processing circuit can be made tolerant to such a current level. Note that this current would correspond to 3 mA at 60 V bias or ≈ 0.2 W per cm^2. Eventually, the power dissipation in the

detector will become equal to that in the electronics readout. The current increase in a detector element can be limited by lowering of the temperature, by chosing a smaller pixel size or by using a higher bandgap semiconductor, e.g. GasAs.
The modification of the detector resistivity, eventually even the reversal from n-type Si to p-type Si has to be taken into account from the outset, probably by providing channel stops between the pixel elements. The signal charge trapping has not been studied sufficiently to determine if it represents a problem for fast detector operation. Increase of bias voltage may be sufficient to counter the trapping effect.

The radiation effects in the readout electronics are thought to be manageable, given the extensive experience in this field in specialized industry, as shown in various contributions in these Proceedings.

Development of signal processing circuits.

In a preliminary feasibility study it has been concluded that fast (10 MHz) circuits can be designed within the power and space budgets [12]. Subsequently, an experimental direct readout circuit has been designed and tested up to 10 MHz[4]. The properties of this existing circuit are described in table 1, and a comparison is made with the projected characteristics of a micropattern detector for high luminosity colliders.

Table 1 Characteristics of a silicon micropattern detector.

parameter	[4]LAA experimental DRO chip	vertex detector collider
pixel size	200 μm x 200 μm	30 μm x 100 μm
array size	9 x 12	256 x 128
functionality	comparator,digital memory	comp., analog+digital memory
readout	external	sparse,time-stamps
chip size	2 x 2.5 mm^2	15 x 15 mm^2
technology	3 μm SACMOS	<1 μm GaAs or SOI
typical input charge	10 000 e^-	10 000 e^-
clock frequency	synchronous, 10 MHz	70 MHz
signal peaking time	30 ns	5 -10 ns
analog memory time		10 μs
memory dynamic range		10 000 e^-
comparator response time	100 ns	20-30 ns
power supply voltage	3 V	3 V
power dissipation per pixel	30 μW	30 μW

The development in signal processing electronics has to focus on the design of faster circuits which still achieve low noise and low power consumption. At present, a 2 μm or 3 μm technology still can be used, but eventually rad-hard, sub-micron processing will have to be adopted. New ideas for the signal processing electronics were recently presented by Krumennacher [13].

The choice of combined analog-digital or pure digital signal processing depends on the objectives of the experiments, the actual feasibility of treating the amount of analog data in off-line analysis and the capability of the circuit designers to compact all circuitry into the small space available. In the first experimental circuit [4] only digital output has been implemented and no peripheral digital controls were included.

Interconnections.

In the development of hybrid pixel devices the interconnection technique is a critical point, because practically no experience exists with such techniques applied to particle detectors. Preliminary discussions have been conducted with the Tape Automated Bonding (TAB) department of EM Microelectronic-Marin SA in Neuchatel, with the Centre for Manufacturing Technology CFT of

Philips in Eindhoven, with the Allen Clark Research Centre of Plessey Research, Caswell [14] and with Thomson TMS in Grenoble, who commercializes an indium bump process developed by LETI. Several more European companies may also have experimental bump bonding processes, because it is the interconnect technology needed for flat screen displays. In the USA the technology has been developed mainly for military applications in sensors, and Hughes Aircraft Cy. is working on a hybrid silicon pixel device [15], in the framework of a SSC development contract.

Can it be done ?

The first steps towards the realization of prototype pixel detectors have been made, in Europe as well in the USA. Once some practical aspects like bump-bonding have been developed, one will focus on the functional performance of the devices. Threshold uniformity control and reliability may be primary concerns. The radiation damage issues will have to be settled in the course of 1991 as well as possibilities of detector cooling and realistic limits to the overall power dissipation. It seems worthwile to spend a serious effort on these developments in view of the benefits for high precision tracking in the high luminosity colliders, in particular LHC.

References

[1] E.H.M. Heijne, et al., A silicon surface barrier microstrip detector designed for high energy physics Nucl. Instr. & Meth. 178 (1980) 331.

[2] E. Heijne, P. Jarron, A. Olsen and N. Redaelli, The silicon micropattern detector : a dream? Nucl. Instr.& Meth. A273(1988)615

[3] C. Pfeiffer, Design study of real time processing of silicon tracker hits for particle momentum and vertex determination, to be published in Proceedings of SSC Symposium, Fort Worth, 1990

[4] M. Campbell et al., A 10 MHz micropower CMOS front-end for direct readout of pixel detectors Nucl. Instr. & Meth. A290(1990)149.

[5] G. Vanstraelen, et al., Fully integrated CMOS pixel detector for high energy particles Nucl. Instr. & Meth. A275 (1989) 574

[6] S. Holland and H. Spieler, A monolithically integrated detector-preamplifier on high-resistivity silicon IEEE Trans. Nucl. Sci. NS-37 (1990) 463

[7] J.G. Jernigan et al., Performance measurements of hybrid PIN diode arrays, SLAC-PUB 5211

[8] P. Jarron, Fast silicon detector systems for high luminosity hadron collider experiments Proc. ECFA study week 1989, CERN 89-10, Vol.I p. 287

[9] G. Stevenson, New dose calculations for LHC, These Proceedings

[10] E. Beuville et al., Measurements of degradation of silicon detectors and electronics in various radiation environments, Nucl. Instr. & Meth. A288 (1990) 68

[11] A. Clark and C. Goessling c.s., A proposal to study a tracking/preshower detector for LHC CERN/DRDC/P3

[12] E.A. Vittoz, Tradeoffs in low-power CMOS analog circuits for pixel detectors Nucl. Instr. & Meth. A275 (1989) 472 (Proc. Int. Workshop Silicon Pixel Det. 1988, Leuven)

[13] F. Krummenacher, Pixel detectors with local intelligence : An IC designer point of view to be published in Nucl. Instr. & Meth. A (Proc. Int. Workshop Silicon Pixel Det. 1990, Leuven)

[14] D.J. Pedder, Flip-chip solder bonding for advanced device structures Plessey Research Review 1989 , p.69

[15] O. Barkan et al., Development of a customized SSC pixel detector readout for vertex tracking, to be published in Proceedings of SSC Symposium, Fort Worth, 1990

Calculations of pulse shape in silicon strip detectors

S. Gadomski, M. Turala, A. Zalewska
Institute of Nuclear Physics, Kraków Poland
W. Dabrowski
Institute of Nuclear Physics and Techniques, Kraków, Poland

Abstract

The shapes of current pulses from silicon strip detectors have been calculated using numerical methods [1]. The simulation was performed for detectors of 300 μm thickness and pitch of 25 and 50 μm having depletion voltage of 60 V. The pulses on the strips collecting charges as well as on the neighboring ones were computed for p and n-sides and for operating voltages of 66 and 100 V. The calculations took into account potential distributions, drift and diffusion. The knowledge of the shapes of original pulses will help in the designing of detectors for the future high rate accelerators.

1 Calculations of potential distributions

A schematic drawing of the silicon strip detector considered in our simulation is shown in Fig. 1a. The analytical solution of the Poisson equation for such a structure is not possible so the numerical overrelaxation method has been used. To perform the calculations only in two dimensions[1] we assumed, that the potential distribution does not change along the strips. Potentials in the implanted (diffused) parts were used as boundary conditions. For the $Si - SiO_2$ interface on the p-side an extra boundary condition $\frac{\partial V}{\partial y} = 0$ (where y axis is perpendicular to the boundary) was applied to simulate the influence of the accumulation layer. This condition means that the equilibrium has been reached and no more electrons are attracted to the accumulation layer. The case of the $Si - SiO_2$ interface on the n-side is different, because the accumulation layer joints the n+ strips. This connection can be broken by putting a voltage on specially designed electrodes placed on the top of the oxide and this way depleting the accumulation layer underneath [2]. It was assumed that the voltage near the interface surface was almost equal to the one on n+ strips. An example of calculated potential distributions is shown in Fig. 1b.

2 Calculations of pulse shapes

2.1 Ramo's Theorem – The Weighting-Field Concept

Signal induced on the electrode by a moving charge may be calculated using the weighting field concept [3]. Let us have electrodes arbitrary placed in space and kept on arbitrary voltages. Let us also have a charge q in a point $\vec{r}$ moving with the velocity $\vec{v}$. The current induced by this charge on electrode number k is equal:

$$i_k = q\vec{v} \cdot \vec{E}_m(\vec{r}) \tag{1}$$

[1] in our case the calculations were performed on an IBM AT compatible computer which already after optimization took a few hours of computing time per a single case

$\vec{E}_w$ is called a weighting-field. It is equal to a negative gradient of a potential which would exist in our system under the following conditions: voltage on the electrode number k is equal to unity, voltages on all the other electrodes are zero and there are no charges in space outside the electrodes. The weighting-field is in units of m^{-1}.

2.2 Signals from a strip detector

The potential distribution inside a detector in most of the bulk depends only on the distance from the detector surface and resembles the one dimensional analytical solution. Only near the strips it depends also on the coordinate parallel to the detector surface (x). The grid used to simulate the evolution of the charge distribution inside a detector crossed by a particle was two-dimensional near the strips and one-dimensional deeper in the bulk. The program calculates the pulse shape in two phases. During phase one the time step dt is chosen. For each grid node the drift of a single charge originating at this node is accurately simulated during the time interval dt. Coordinates of the resulting shift and the average value of the current induced by our single charge are stored. In the phase two $2.4 * 10^4$ electron-hole pairs, simulating a track of an ionizing particle, are uniformly distributed along the y axis at selected position x. The iterations, each corresponding to the time interval dt, are performed and the values earlier stored for every grid point are used to calculate the evolution of the charge density and the total induced current. The charges flowing from one-dimensional grid zone into the two-dimensional one are distributed in the x direction in the shape of gaussian to simulate diffusion in this direction. The width of this gaussian is proportional to $\sqrt{t}$. The diffusion in y direction is taken into account by applying the discrete form of the diffusion equation.

The calculated pulses for the p-side strip are shown in figure 2, for the n-side one in figure 3. On the left there are pulses for the tracks passing at the distance 0, $\frac{1}{2}$ and 1 strip pitch. On the right there are pulses for the distances 1, $1\frac{1}{2}$, 2, $2\frac{1}{2}$ and 3 strip pitches.

Acknowledgements

This work was stimulated in large fraction by discussions with dr. H. Sadrozinski from UC Santa Cruz.

References

[1] S. Gadomski, M.S. thesis at the Jagiellonian University, Kraków, May 1990

[2] B. S. Avset et al. CERN-EP/90-11 January 23rd, 1990

[3] G. Cavalleri et al. Nuclear Instruments and Methods 92 (1971) 137-140 V. Radeka, Ann. Rev. Nucl. Part. Sci. 38, 217 (1988)

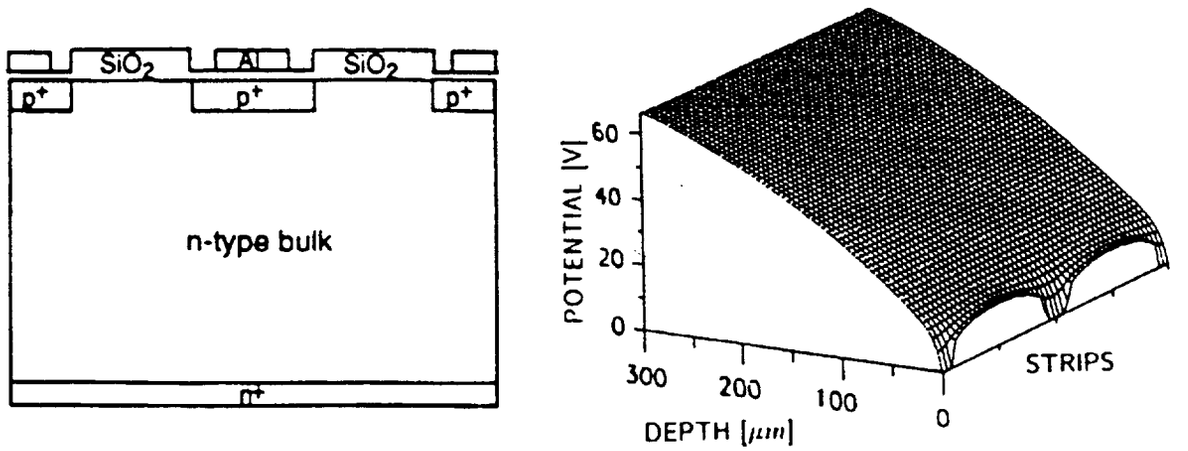


Figure 1: The schematic cross-section of the detector taken for analysis (left) and the potential distribution for detector with 50μm pitch operating at $V_{bias} = 66V$ (depletion voltage $V_{depl} = 60V$) (right)

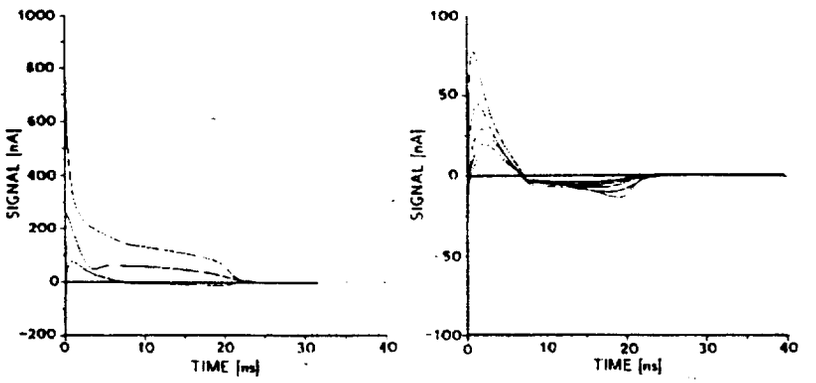


Figure 2: Current signals from the p+ strips of a detector of 300 μm thickness and 50 μm pitch operating at $V_{bias} = 100V$ ($V_{depl} = 60V$) for the cases when a particle traverse the detector in the region of the strip (left) and under the neighboring strips (right); the different curves are for different distances of generated tracks from the strip center

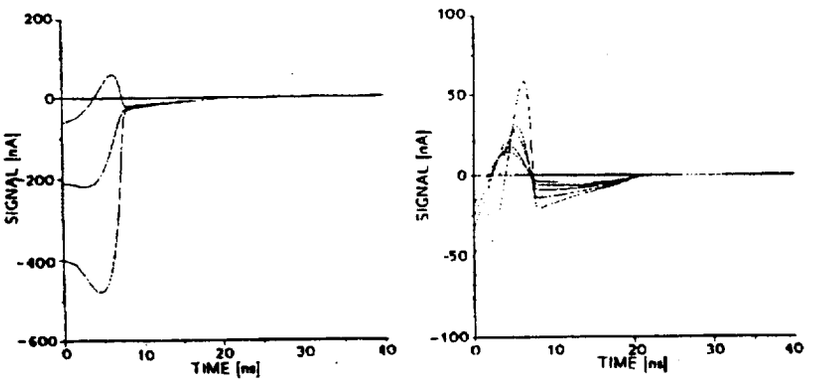


Figure 3: Current signals from the n+ strips of a detector as above for the cases when a particle traverse the detector in the region of the strip (left) and under the neighboring strips (right); the different curves are for different distances of generated tracks from the strip center

GaAs Detectors

presented by K.M.Smith[5]

S.P.Beaumont[4],R.Bertin[2],S.D'Auria[1], C.del Papa[1], M.Edwards[6],F.Fiori[1],
J.G.Lynch[5],B.Lisowski[1],M.Nuti[3],V.O'Shea[1], P.G.Pelfer[3],C.Raine[5],
I.O.Skillicorn[5],K.M.Smith[5],R.M.Turnbull[5], and A.Zichichi[2]
1 - Dipartimento di Fisica dell'Universita' and INFN Bologna, Italy
2 - CERN, Geneva, Switzerland
3 - Dipartimento di Fisica dell'Universita' and INFN Florence, Italy
4 - Dept. of Electrical and Electronic Engineering, University of Glasgow, U.K.
5 - Dept. of Physics and Astronomy, University of Glasgow, U.K.
6 - Rutherford Appleton Lab., Chilton, Didcot, U.K.

Abstract

This report describes results obtained on GaAs Schottky diode charged particle detectors by the Glasgow and CERN-based LAA groups. Their radiation hardness and potential speed, more than competitive with silicon detectors, make GaAs detectors attractive for applications in high radiation environments.

Introduction

We first discuss the choice of semi-insulating GaAs as a detector material, the manufacture of our Schottky diodes [1], and the response of the diodes to alpha, beta and gamma radiation and to test beam pions. Results are presented of gamma - and neutron - irradiation effects on GaAs diodes, and of measurements of the speed of response of the diodes using laser pulse excitation. The report concludes with a summary of our current understanding of GaAs diode detectors.

The advantages of GaAs

GaAs is a direct band-gap semiconductor, with a band-gap of 1.43 eV. The radiation length is 2.3 cm, (four times shorter than silicon), but this is partly compensated by the higher specific ionisation loss of 5.6 MeV/cm. GaAs wafers are generally prepared by the LEC (Liquid-encapsulated Czochralski) method. Higher purity may be achieved by Molecular Beam Epitaxy, (MBE), but this is limited to layers of at most a few tens of microns in thickness by the slow rate of deposition. Vapour Phase Epitaxy (VPE) may overcome the latter limitation in the future [2]. Liquid Phase Epitaxial growth, (LPE), formerly employed for pure and doped GaAs wafers, has now been largely superseded by MBE and VPE for most applications.

The best results obtained in the early 1970's [3] with LPE GaAs diode detectors were difficult to reproduce but established that good energy resolution for X- and gamma-rays was possible. While development in LPE detectors has been inhibited by the variability of the wafer material, improvements in LEC commercial crystal growth techniques [4] have resulted in more uniform wafers of higher purity and mechanical strength, and with a greatly improved surface quality.

Finally, the high electron mobility in GaAs devices, (almost six times that of silicon at best), offers the prospect of high speed particle detection and signal processing.

Diode Manufacture and Electrical Tests

Diodes of 500, 300 and 125 microns thickness and 1 and 3mm contact diameter were manufactured in the University of Glasgow Department of Electrical and Electronic Engineering by evaporating a Ti - Au Schottky barrier onto one side of a semi-insulating GaAs chip and an ohmic contact of Ni - Ge - Au onto the other. No attempt was made to deposit a passivating layer on the surface of the diodes. Typical diode reverse bias leakage currents, shown in Figure 1, and in Figure 2 for an array of diodes on one chip, are significantly higher than that for typical silicon detectors. Measurements on diodes with a guard ring electrode surrounding the Schottky contact suggest that the leakage is not predominantly due to surface effects, but probably more to bulk generation.

Tests with Radioactive Sources and Beam

A typical diode response to alpha-, beta- and gamma ray sources is shown in Figure 3. The charge released by each was known from the energy required to generate an electron-hole pair in GaAs, namely 4.2 eV. The measured charge collection efficiency increased with bias voltage as shown in Figure 4.

The inefficiency is interpreted as due to very rapid trapping of the holes released by the ionising particles, the observed signal being due to the electrons migrating to the collecting electrode. This interpretation is supported by comparing the pulse height spectrum with an alpha source next to the ohmic contact with that obtained with the source at the Schottky electrode. Simulation of the charge

trapping by a simple model gave the predicted charge collection efficiency variation also shown in Figure 4, (cf. [1], [5]). The variation in leakage current, charge collection efficiency and signal/noise ratio among the diodes of an array on one chip is given in Figure 5. Figure 6 shows the pulse height spectrum obtained in a 6 GeV/c pion test beam [1].

Speed of Reponse

The picosecond laser facility at the University of Florence was used to excite a GaAs diode with a 1.5 picosecond pulse. The output signal from the diode, observed using a high speed oscilloscope, is shown in Figure 7. The very fast initial pulse is followed by a tail of around 4 nanoseconds in length, thought to be due to trapping effects in the charge transport mechanism. Simple simulation of the trapping/de-trapping gives the pulse shape also shown in Figure 7. More detailed studies of the trapping and de-trapping process may lead to better understanding of the charge collection inefficiency discussed above.

Radiation Hardness

Several diodes, subjected to gamma irradiation up to a total dose of 17 MRad, showed only a very small change in leakage current, and the response to radioactive sources was almost completely unaffected. A set of diodes was also subjected to neutron irradiation by a fluence of $7.10^{14} n/cm^2$ at the R.A.L. test facility in the ISIS accelerator [6]. A comparison is given in Figure 8 of the pulse height spectrum obtained with a collimated Ru-106 source, (equivalent to minimum ionising particles), before and after the neutron irradiation. The GaAs diode has clearly deteriorated, but the signals are still easily resolved, and the detector continues to be usable.

Alternatives to Semi-insulating material

We have concentrated on diodes made from semi-insulating GaAs, the cheapest available material. Previously, L.P.E. GaAs diodes have been used successfully for gamma ray spectroscopy. More recently, high purity V.P.E. GaAs wafers have been produced at growth rates exceeding 100 microns per hour [2]. The density of trapping centres in L.P.E. and V.P.E. materials is reported to be less than in semi-insulating wafers, so that the charge collection efficiency may be higher in epitaxial diodes. We hope to test samples of both these alternative materials within the next few months.

GaAs Read-out Electronics

GaAs FET pre-amplifiers operating at low temperatures have recently been used in a liquid argon calorimeter read-out system, [7]. In addition, a SPICE analysis of a GaAs bipolar pre-amplifier design predicts noise and power consumption figures which are significantly lower than corresponding values for silicon, [8]. The expected higher radiation resistance of the GaAs circuits make this a worthwhile study. Integration of optical read-out onto the semi-insulating wafer could offer useful advantages in particle physics, which we intend to investigate further.

Summary of Results Obtained to Date

In summary, GaAs Schottky diodes work satisfactorily as charged particle detectors, with essentially 100% detection efficiency for minimum ionising particles. They tolerate radiation loads at the level expected in several years of running at a radial distance of only a few cm. from the intersection point of the SSC at nominal luminosity. The output signal of only a few nanoseconds is very satisfactory for the new colliders. While these results are already encouraging, further study of the charge trapping which we have observed in semi-insulating GaAs may enable further improvements in the performance of diodes manufactured in this material.

References

[1] R.Bertin et al., *A Preliminary Study of GaAs Solid-State Detectors for High Energy Physics*, Nucl. Instr. and Methods A294, (1990), 211

[2] K.Gruter et al., *Deposition of high quality GaAs films at fast rates in the LP-CVD system*, Jour. of Crystal Growth 94, (1989), 607

[3] J.E.Eberhardt, R.D.Ryan and A.J.Tavendale, *High-resolution nuclear radiation detectors from epitaxial n-GaAs*, Appl. Phys. Lett. 17, (1970), 427

[4] R.N.Thomas et al., *Status of device-qualified GaAs substrate technology for GaAs integrated circuits*, Proc. I.E.E.E.76, (1988), 778

[5] C. del Papa, C. Raine, *New Results on GaAs Solid-State Detectors for High Energy Physics*, Contributions to the 4th San Miniato Topical Seminar on Experimental Apparatus for High Energy Physics and Astrophysics, June 1990. (To be published)

[6] M.Edwards and D.R.Perry, *The radiation hardness test facility* , R.A.L. Report RAL-90-065, August 1990

[7] A.Alessandrello et el., *Gallium-arsenide charge-sensitive preamplifier for operation in a wide low-temperature range*, Nucl. Instr. and Meth. A289, (1990), 426

[8] P.H.Sharp, *Developments in VLSI*, Proceedings of the Eloisatron Workshop on New Technologies for 200TeV Physics, Erice, September 16-20th, 1990

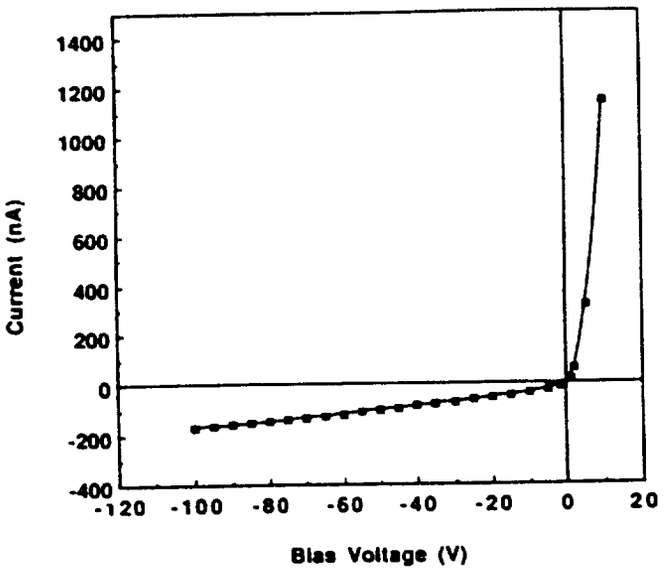


Figure 1: Typical diode I-V characteristic.

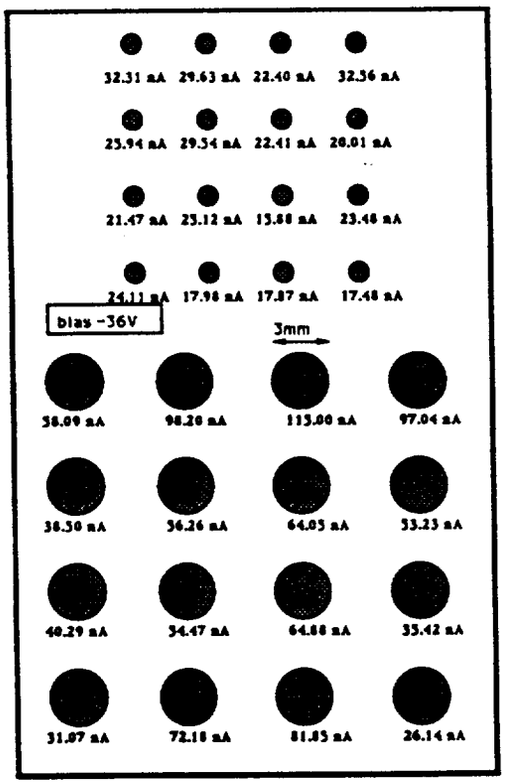


Figure 2: Leakage currents for diodes in an array on one chip.

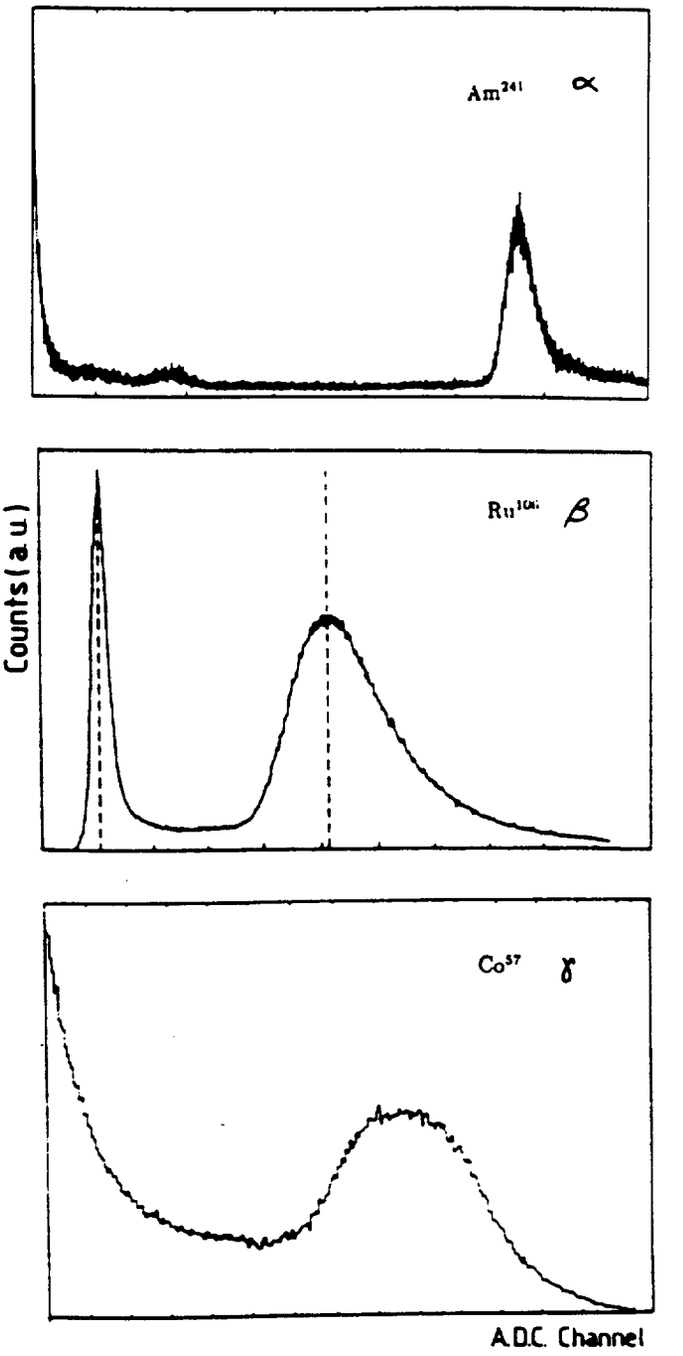


Figure 3: Pulse height spectra from radioactive sources.

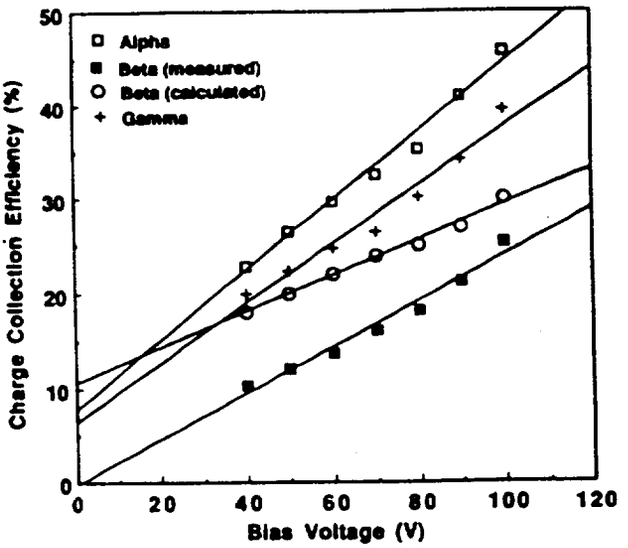


Figure 4: Charge collection efficiency variation with bias voltage, for alphas, betas and gamma rays.

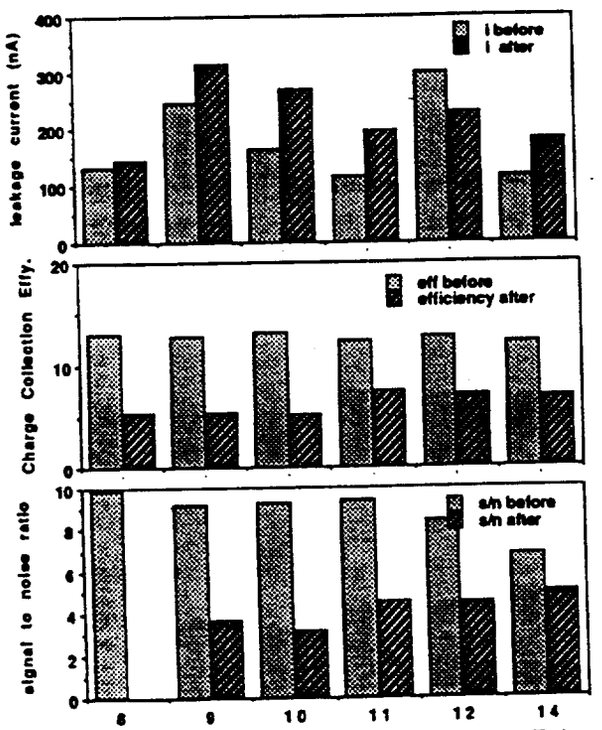


Figure 5: Leakage current, charge collection efficiency and s/n variation for the diode array, before and after neutron irradiation by $7.10^{14} n/cm^2$.

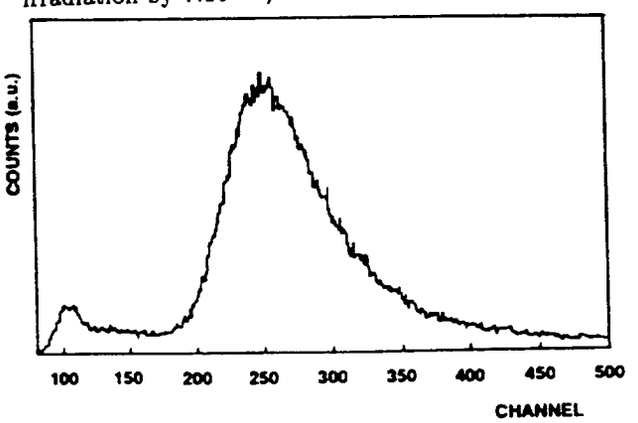


Figure 6: Pulse height spectrum obtained in a GaAs detector with 6GeV/c pions.

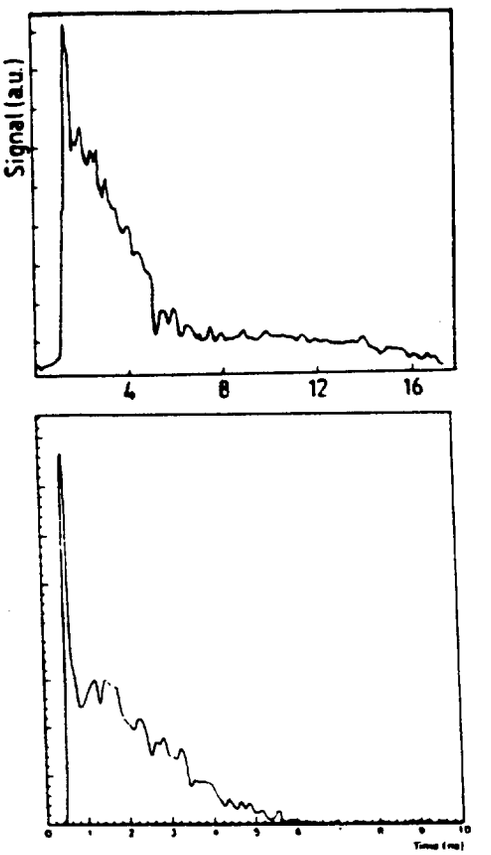


Figure 7: Oscilloscope trace of GaAs detector response to a 1.5 picosecond laser excitation pulse. The lower trace is the result of a simulation, with trap cross-section $10^{-13} cm^2$ and de-trapping time 245 psec.

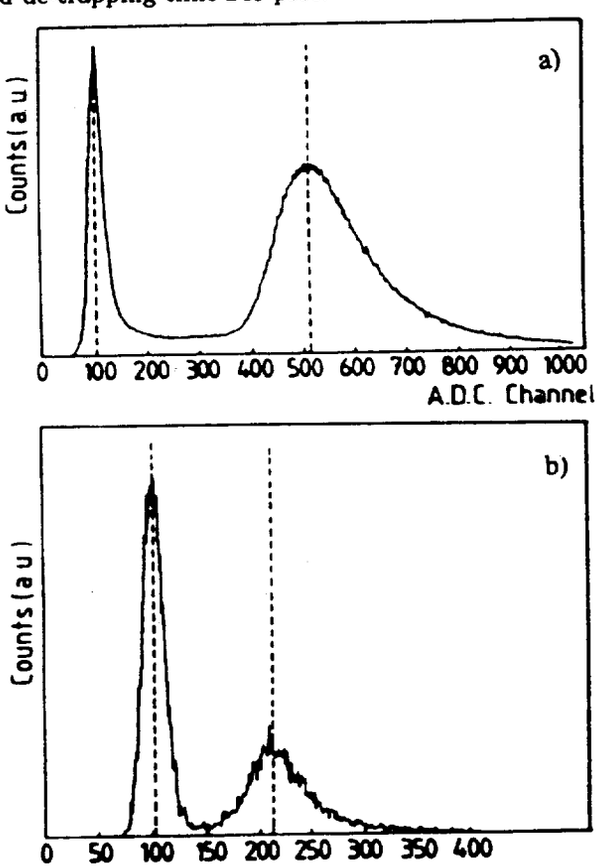


Figure 8: Pulse height spectrum from Ru-106 source, corresponding to minimum ionising particles, before(a) and after(b) irradiation of the GaAs detector by $7.10^{14} n/cm^2$.

Monte Carlo Simulations for Central Tracking with Scintillating Fibres [1]

U.Gensch(Speaker), S.Schlenstedt

Institut für Hochenergiephysik
O-1615 Zeuthen,Germany

ABSTRACT

Aspects of central tracking in a LHC experiment are discussed. The tracker consists of concentric shells surrounding the beam pipe. Each of the shells is composed of coherent scintillating fibre layers arranged in z-u-v-z-directions in order to measure (z, ϕ) coordinate pairs. The tracker works inside a magnetic field. The performance of the tracker is studied for a luminosity of about $10^{34}\ cm^{-2}s^{-1}$. It is shown that scintillating fibres are well suited for central tracking in a LHC detector.

1 Introduction

In this contribution a central tracker is considered as part of a general purpose detector, i.e. tracking is being discussed at medium luminosities and in the presence of a magnetic field. In comprehensive reviews on the tasks of tracking it was pointed out that experiments at future super colliders without a central tracking device will be incomplete [1,2] : the performance of the detector will be reduced and the physics possibilities will be limited. Here we just summarize issues for which central tracking is vital :

- improving the momentum resolution for stiff tracks
- applying isolation cuts
- estimating the z-position of the primary vertex in order to improve detector performance and reject multiple interactions
- enabling secondary vertex (b-tagging) tagging by linking reconstructed tracks downwards to a vertex detector

[1]The work reported here is part of the LAA-project

In addition, the tracking information can be used to build up topological trigger decisions in order to reject minimum bias events.

To reach these goals a tracker has to fulfil specific requirements as high granularity to reduce the occupancy and to guarantee the required spatial resolution. Furthermore the detector has to be sufficiently radiation hard and finally the readout has to meet the drastic timing constraints of the LHC. The hardware realisation of the tracker is sketched in sect. 2 where also the event samples used for the Monte Carlo simulations are described. In sect. 3 the results of our simulations are presented. The aim of this contribution is to demonstrate that a detector using scintillating fibres can take the part of a central tracking device in a LHC experiment.

2 Detector layout and event samples

The simulations were performed for a central tracker consisting of five cylindrical shells. They are located concentric around the beam pipe at radii between 15 and 100 cm. Each of the shells is composed of four coherent scintillating fibre layers arranged in z-u-v-z directions. Fig.1 displays the r,z- and r,ϕ-projections of the detector. For each of the five shells the half length of the fibres (L/2) is marked and the radius at which the shell is located is also given. As the granularity of the detector has to be high to keep the occupancy low the diameters of the fibres have to be appropriatly chosen : the values are 30, 60, 90, 150 and 300 μm (from the innermost to the outermost shell). The detector covers the central part of the kinematic range of the pp interactions, its acceptance is confined to $\mid \eta \mid < 1.7$ at $\sqrt{s}$=16 TeV , η being the pseudorapidity. The opto-electronic readout chains are not shown, they are arranged in between the fibre shells. Detailed descriptions of the hardware realisation of this detector can be found in ref. [3,4,5].

The fibre diameters are small, therefore the fibres can not be handled individually. They are packed into multibundles within each layer. The thickness of each layer is 2.5 mm. The presence of two spaced z-layers increases the efficiency and eases pattern recognition. The fibres orientated along z (beam direction) determine the polar angle ϕ, whereas the z coordinate is provided by the u-v-pair. The actual value of the stereo angle α between the z-fibre and the u- (v-) fibres has to be chosen with care. A compromise has to be found between precision of the z-measurement ($\delta z \sim 1/\sin\alpha$) and confusion in finding the z-u-v stereo tripletts. For this study calculations were done with α = 4 or 8 degrees. The values of the precisions of the z-measurements vary between between 0.22 and 2.2 mm for α = 8 degrees.

The performance of such a detector was demonstrated in beam tests with tracker shell prototypes. Bundles consisting of 30 μm fibres were exposed to a pion beam. The precision reached

is 35 μm and the two track resolution is measured to about 83 μm [3].
To perform the simulations of the tracker perfomance pp interactions at $\sqrt{}$ s=16 TeV were generated with PYTHIA 5.3 [6]. Three different event classes were considered : top production (m_{top} = 90 GeV/c), Higgs production (m_{Higgs} = 200 GeV/c) and minimum bias interactions enabling a comparison with the always present background. In order to calculate occupancies and to estimate efficiencies for the track reconstruction these MC-events were tracked through GEANT [7] with a model of the scintillating fibre detector incorporated. In the simulation of particle tracking through the fibre detector interactions of the particles were taken into account, also included are γ-conversions, δ-rays, multiple scattering, bremsstrahlung and energy loss. One tracker shell represents 2.4% of radiation length and 1.8% of interaction length [3]. In table 1 we give for the three event categories the total charged multiplicities ($< n >$) and the multiplicities calculated for charged tracks within in detector acceptance ($< n >_{acc}$). The numbers of charged tracks (in acceptance) with transverse momenta larger than 1 or 2 GeV are also shown.

events	$< n >$	$< n >_{acc}$	$< n(p_T > 1GeV) >_{acc}$	$< n(p_T > 2GeV) >_{acc}$
Higgs	176	62	24.4	13.4
top	182	68	27.5	15.8
min.bias	75	15	1.4	0.3

Table 1: event characteristics

The characteristics of both "physics" processes, Higgs and top production, are similar : the values obtained for the multiplicities and the number of "high" p_T-tracks almost agree, therefore we present in this contribution only simulation results obtained for events with top production. The experimental problems caused by the minimum bias events are not negligible, although their charged multiplicity is relatively small : the fibre detector will be traversed by more than 200 additional charged particles beside those from the triggered "physics" event if the experiment is running at a luminosity of about $10^{34}\ cm^{-2}s^{-1}$ corresponding to 15 multiple pp interactions per bunch crossing.

3 Simulation results

In this section calculations of the fibre occupancy are presented and the reconstruction of tracks is discussed. In table 2 are collected the fibre occupancies, i.e. the percentages of exposed fibres for shell 1 (r=15 cm) and shell 5 (r=100 cm). The values are given for single top events, top events overlayed with 10 or 20 minimum bias events (mb) and single minimum bias events. To study the influence of looping tracks on the results the occupancies are calculated

for several values of the magnetic induction B.

B , T	shell	top	top + 10 mb	top + 20 mb	mb
0	1	0.20	0.61	1.01	0.06
	5	0.45	1.38	2.46	0.01
1	1	0.22	0.65	1.01	0.08
	5	0.36	1.02	1.71	0.01
3	1	0.24	0.83	1.25	0.11
	5	0.22	0.54	0.78	0.02

Table 2: fibre occupancy (%)

The effect of "loopers" is clearly seen as the occupancy for fibres at the first shell increases with B. At the contrary a decrease of the occupancy with increasing B is observed at the outermost shell demonstrating the sweeping effect of the magnetic field [8].

A simple pattern recognition algorithm was developed to study the tracking ability of the detector. We limited this to high p_T tracks as they represent the easiest case and are very frequent in top and Higgs final states but rare in minimum bias events. We start the track search at shell 5 for a specific p_T within an appropriate sagitta corridor. A general demand for tracks are hits in both z-layers per shell to reject spurious hits due to slow electrons, gamma conversions and δ-rays. For every hit on shell 5 we calculate with a hit on shell 4 and the beam position the actual curling radius for this hit combination (see Fig.2). Now we check if we find on shell 3,2,1 within a corridor of 10 fibre diameters a hit on the predicted position on this curling radius. The second condition applied on the track candidates is $|\theta_{i+1} - \theta_i| < \delta\theta_{i+1,i}$, i=1,2,3 (i being the shell number), i.e. the slope change of tracks in the r-z-plane is small. θ is given by $tan\theta = \triangle r/\triangle z$ with the radial and z - difference on neighboured shells. $\delta\theta_{i+1,i}$ is related to the precisions of the z-measurement on the shells $i+1$ and i. In Fig.3a are shown the reconstuction probabilities obtained under different conditions. Highest values are obtained for a low magnetic field. For a magnetic induction of 3 T the reconstruction probabilities are shown for single top events and for top events overlayed with 10 minimum bias events. The differences between both cases are small. The probability to get falsely reconstructed tracks, i.e. combinations of hits from different tracks (from same event or from different events) is at the percent level.

As illustration, running the experiment at 1 T about 12 tracks from a top event with a p_T of at least 2 GeV are reconstructed enabling a determination of the vertex position. The vertices of the overlayed minimum bias events are distributed over the interaction region and the number of "high" p_T-tracks in these events is negligible.

Finally we discuss the possibility to use the information of fibre detector to form a fast trigger

decision. The idea is very simple and can be derived from the numbers given in table 1. Accepting only interactions with a certain fraction of "high" p_T rejects minimum bias events. But a fast trigger cannot be realised with the foreseen optical readout via delay tubes and CCD's and the large number of readout channels. In a scenario enabling both high precison tracking and fast triggering the fibres will be read out on one side via the dedicated optical readout. On the opposite side a fast readout of the bundles has to be realised matching the timing constraints, e.g. avalanche photo diodes. The number of channels will be drastically reduced considering 1 mm^2 fibre bundles. The perfomance of such a trigger was checked applying our track recognition procedure but using hits derived from bundles. The efficiencies obtained are displayed in Fig.3b. More than 80 % of the tracks are reconstructed for transverse momenta larger than 2 GeV. The price of the lower resolution is the fraction of about 30 % of falsely reconstructed tracks but most of them do not point to the vertex.

To conclude, scintillating fibres are well suited for central tracking in a LHC experiment. Occupancy will cause no severe problems for a fibre tracker with fine granularity. Applying a simple pattern recognition algorithm it was demonstrated that the majority of the high p_T-tracks will be reconstructed. Such a detector can fulfil the task of tracking even in a typical LHC environment of 10 to 20 pp interactions per bunch crossing. In addition, the information provided by the tracker can be used to get a fast trigger decision in order to reject minimum bias events.

References

[1] D.H.Saxon, The Tasks of Tracking and Vertex Location at Future Hadron Colliders, ECFA study week Barcelona, CERN 89-10.

[2] G.G.Hanson,M.C.Cundy,A.P.T.Palounek,Nucl.Instr. and Meth. A289(1990)365.

[3] H.Leutz, Central Tracking of Particles with Scintillating Fibres, ECFA study week Barcelona, CERN 89-10.

[4] C.D'Ambrosio, contribution to this proceedings.

[5] T.Gys, contribution to this proceedings.

[6] The event samples used were generated by F.Anselmo, member of the LAA-SMC-group.

[7] R.Brun et al.,GEANT3, CERN-Program Library.

[8] C.Buttar,T.Sloan,I.ten Have, contribution to this proceedings.

Figure Captions

Fig.1: r, z- and r, ϕ-projections of the scintillating fibre tracker (1/4 of the detector shown). The radii of the shells and their half lengthes are given in cm.

Fig.2: Sketch of the first part of the pattern recognition algorithm: starting from shell 5 calculate the curling radius with every hit on shell 4 (within the sagitta defined by $p_T{}^{max}$) and look on shells 3,2,1 for hits on the predicted position.

Fig.3: Track reconstruction probability vs. p_T.

a) fibre detector with full granularity
(▲) B = 1 T without multiple interactions, (△) B = 3 T without multiple interactions and (o) B = 3 T, with 10 overlayed min. bias events.

b) trigger scenario: 1 mm^2 fibre bundles and search corridor of ±1 mm.
Shown are the results for good (o) and false (□) tracks for B = 1 (full) and 3 (open) T.
10 min. bias per events are overlayed.

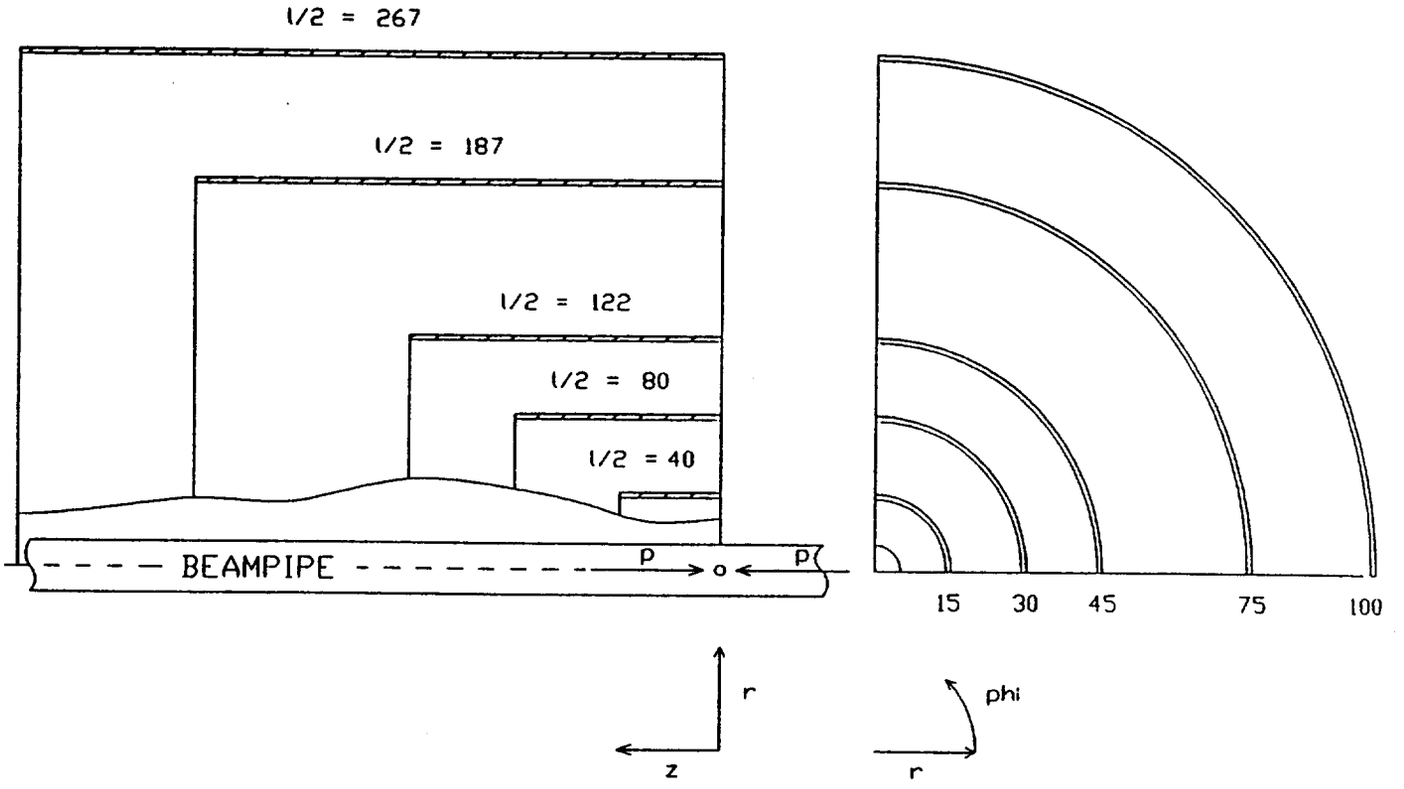


Figure 1: $r-z$ and $r-\phi$ view

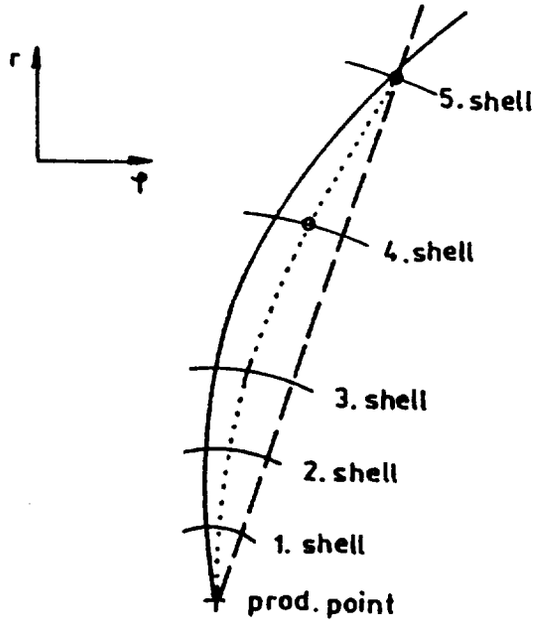


Figure 2: Pattern recognition algorithm

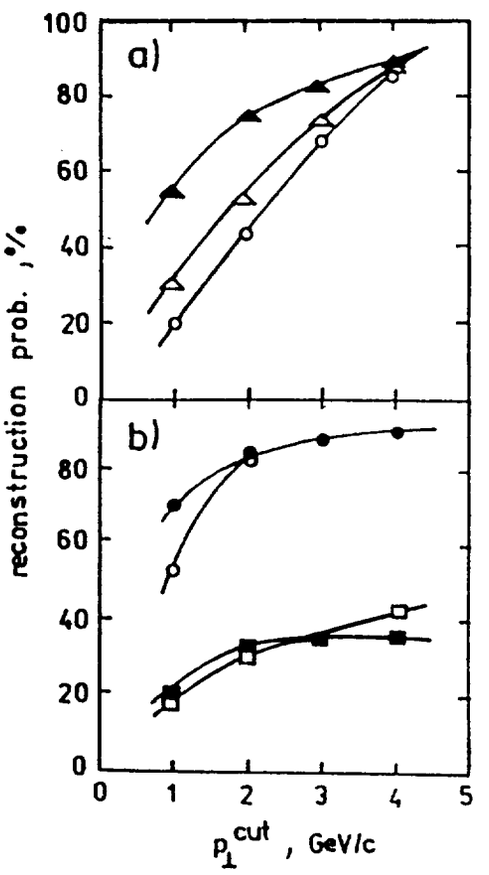


Figure 3: Track reconstruction probability

PRESENT STATUS AND FUTURE PROGRAMME OF SCINTILLATING FIBRES FOR CENTRAL TRACKING(*)

C. D'Ambrosio (speaker), H. Leutz, S. Tailhardat and M. Taufer
CERN, Geneva, Switzerland

1. INTRODUCTION

In view of the expected luminosities and particle multiplicities of future pp colliders, a central tracker must provide time resolutions ≤ 10 ns and 2-track resolutions ≤ 100 μm associated with excellent spatial precision. In addition, low occupancy of the detector elements will be vital and visual pattern recognition via CCD pixels will reduce considerably the number of read-out channels.

These advantages are inherent to the scintillating fibre technique, provided we can meet the following conditions (for all of these topics, a more exhaustive discussion can be found in ref. [1]):

- production of small diameter coherent fibres in multibundles,
- reduction of light losses due to absorptions and multiple reflections,
- prevention of cross talk to neighbouring fibres,
- delay of track patterns to enable coincidences with the first-level trigger,
- sufficient radiation hardness.

In sect. 2 a scenario for a central tracker made of scintillating fibres is discussed with reference, in particular, to the process of local emission of light in small diameter fibres and to beam tests.

In sect. 3 we describe some spectroscopic properties of four new dopants with large Stokes shifts, which have been synthesized and studied by our group. Finally, in the conclusions, some relevant aspects for future developments will be discussed.

2. CENTRAL TRACKING WITH SCINTILLATING FIBRES

Several scenarios for a scintillating fibres tracker are feasible, one of which is presented in fig. 1 as an example. The beam pipe is surrounded by concentric cylindrical shells, each between 10 and 20 mm thick and composed of coherent fibre layers. These superlayers are arranged in Z–U–V–Z directions to provide r, ϕ (via the Z-strands) and Z-coordinates (via the stereo angle between the U and V-strand). Since thin fibres with diameters smaller than ~ 250 μm cannot be manipulated individually, we arranged them as

(*) The work reported here is part of the LAA project.

square multibundles of edge dimensions between 0.5 and 1.5 mm, which provide still enough flexibility for convenient winding.

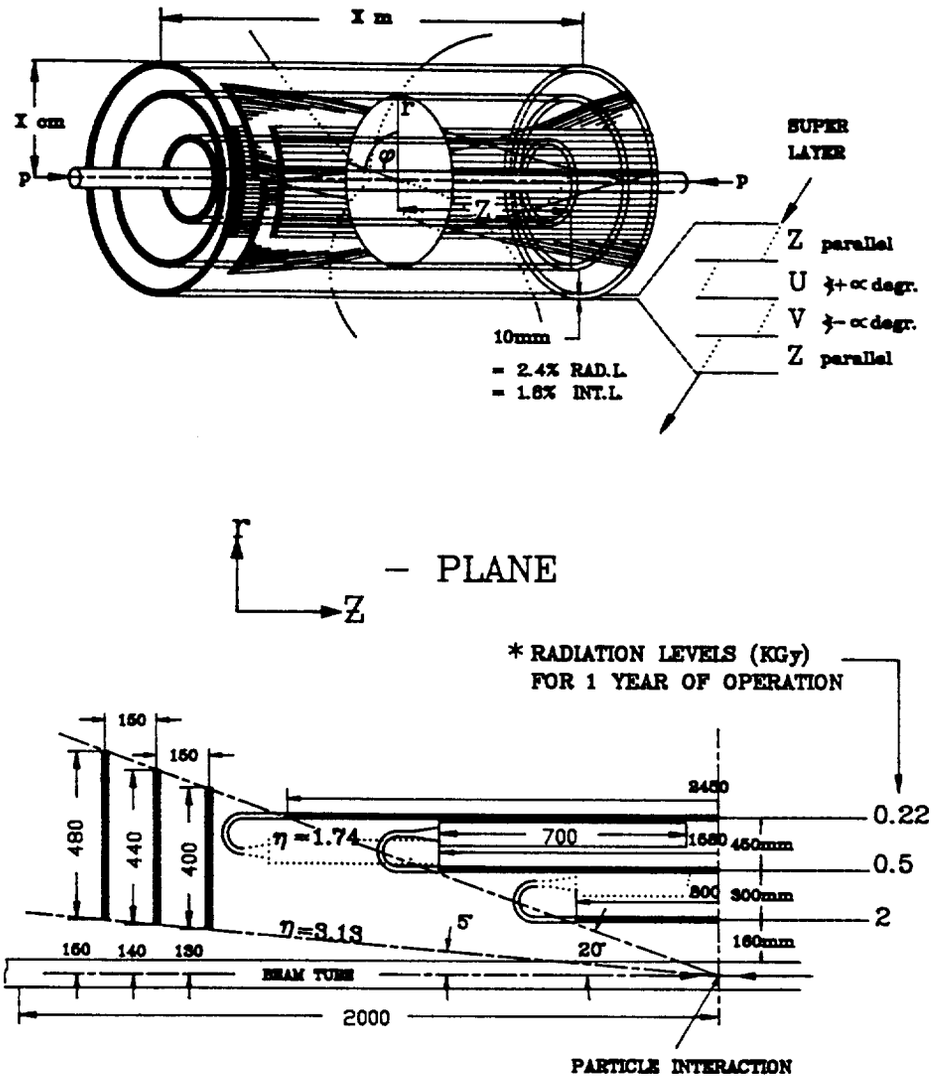


Fig. 1 An example of a central tracker based on scintillating fibres. The rapidity of 1.74 can be increased to 3.13 by adding three fibre screens to subtend the forward–backward particle production.

Depending on its edge dimensions and the individual fibre diameter, it contains hundreds of hexagonal fibres each surrounded by a 3 μm thick cladding. As a result of the production process, each multibundle represents a compact fiber-strand with excellent coherency. Read-out is made by using an optoelectronic chain, details of which are found in [2].

In order to achieve the maximum obtainable spatial precision and two-track resolution, cross talk of scintillation light to the neighbouring fibres must be avoided.

To understand this process we look at fig. 2. The energy loss of an ionizing particle is transferred to the basic matrix of the fibre core, in most cases polystyrene (PS). Since the quantum yield of PS is rather poor, it must be enhanced by adding a scintillator, in most cases p-Terphenyl. The energy transfer between the basic matrix and the added scintillator occurs, depending on the scintillator concentration, in two competitive ways: non-radiative (Förster transitions) or radiative via photon exchange (low concentration). For both mechanisms an overlap of the respective absorption and emission bands is necessary (fig. 2). Since p-Terphenyl emits at around 340 nm, normally a second dopant must be added, whose emission matches the transparent region of the basic matrix and the sensitivity of suitable photocathodes. Since absorption and emission bands of such wavelength shifters overlap considerably (fig. 2(a)), their concentrations must be kept low to achieve a reasonable light transmission through the scintillating fibre. We have therefore radiative energy transfer between scintillator (p-Terphenyl) and wave shifter (POPOP in fig. 2(a)). The absorption length of the wave shifter is in the order of 300 to 500 μm.

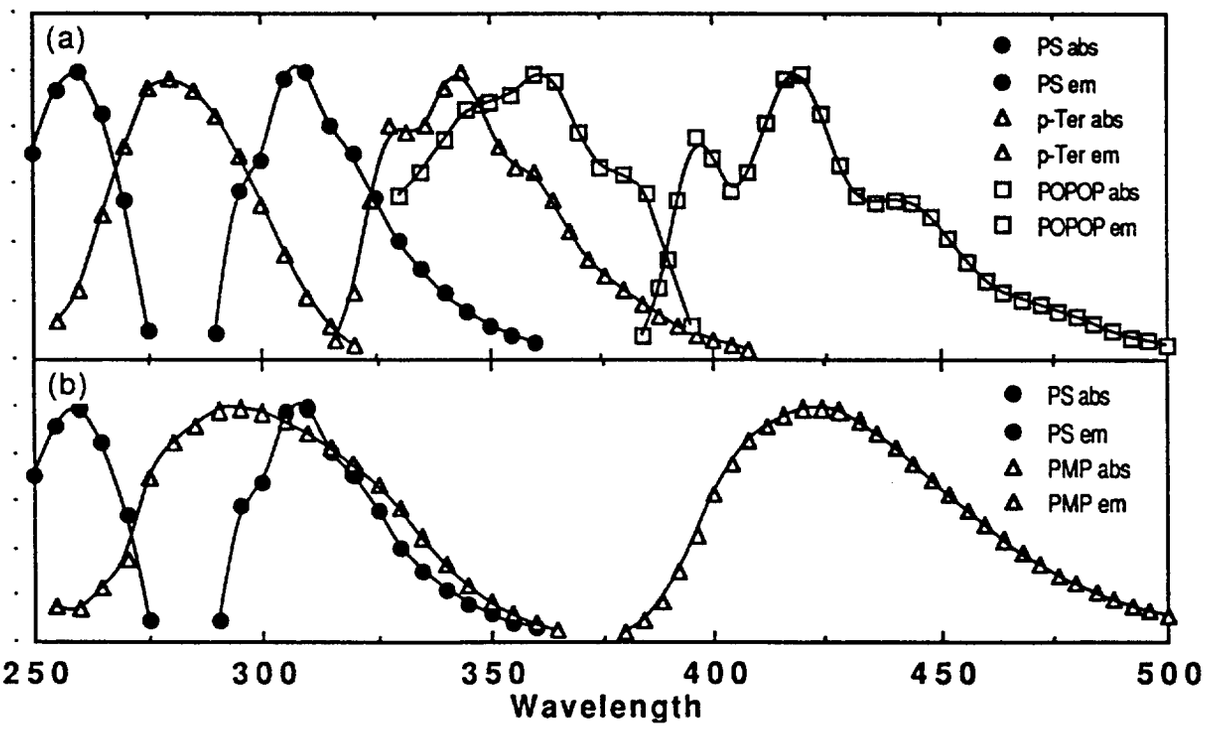


Fig. 2 Absorption and emission bands of polystyrene doped with: (a) p-Terphenyl and POPOP as a wave shifter and (b) PMP, (the spectra are not to scale).

In applying PMP as a scintillator, the addition of a wave shifter is not necessary. Due to its large Stokes shift, the PMP absorption band overlaps conveniently with the PS emission band and the PMP emission peaks at 420 nm. Due to the small overlap between

absorption and emission, we can apply PMP concentrations high enough to ensure non-radiative transitions between PS and PMP. Therefore, no primary light escapes even from very small diameter fibres. This can be seen from fig. 3, which shows the light emissions of two fibre bundles, one with PMP and the other with traditional doping; both bundles are excited in the same way by a Nd:Yag laser at 265 nm. Whereas the PMP bundle emits only from the first excited fibre layer, the bundle with a wavelength shifter shows clearly the cross talk of primary light over several fibre layers.

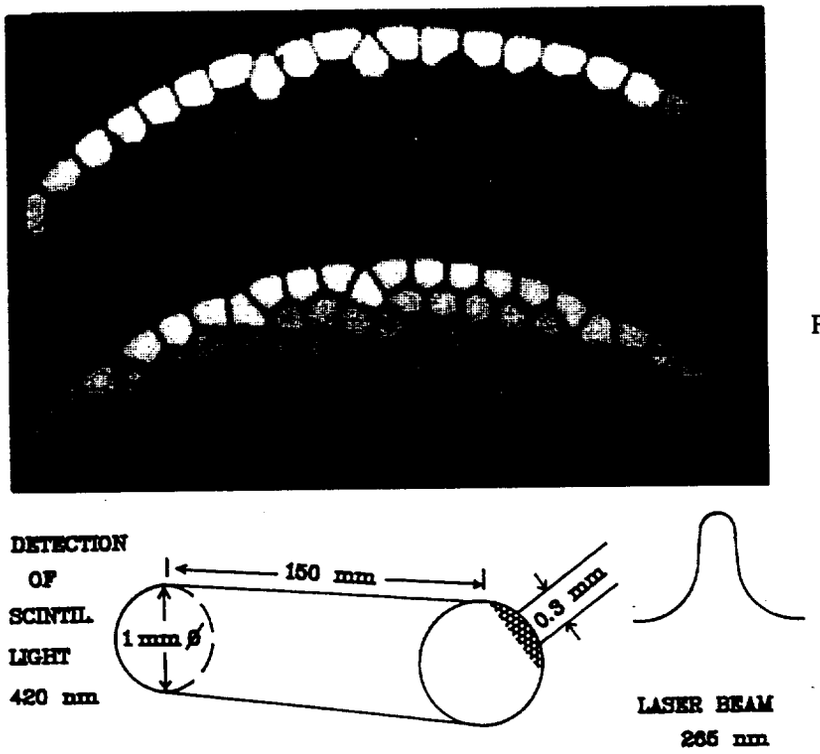


Fig. 3 Excitation of differently doped multibundles by a Nd:Yag laser at 265 nm. The PMP-doped bundle (up) emits only from the first directly excited layer. The bundle with a wave shifter (down) shows cross talk over several fibre layers.

For beam tests, fibre bundles of 1 mm × 1 mm cross section and with 30 μm diameter of individual fibres have been assembled (fig. 4) to simulate a 10 mm thick tracker shell over a width of 5 mm and a length of 200 mm. They were exposed to a 20 GeV π^- beam at the CERN PS. Figure 4(a) shows a resulting track at a distance of ~ 150 mm from the bundle ends facing the first photocathode of the optoelectronic chain and fig. 4(b) shows the bundle configuration. Figure 5 shows a histogram of the residuals of 272 tracks with 83 mm FWHM (two-track resolution) and a sigma (precision) of 35 mm.

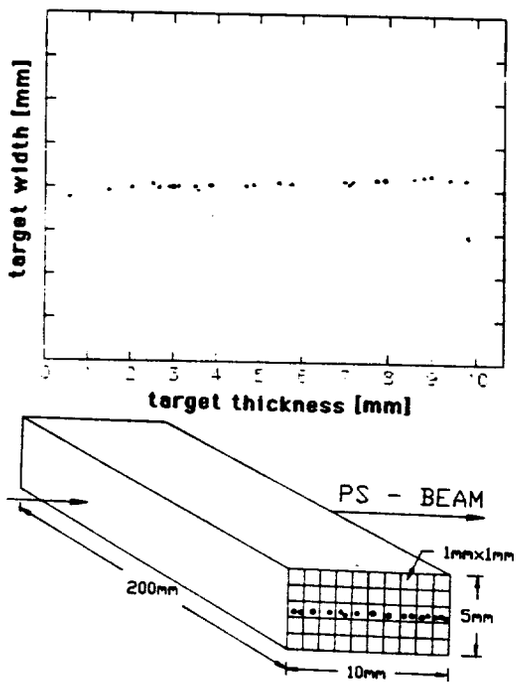


Fig. 4 Beam exposure of a 200 mm long target. The tracks show 24 hits along 10 mm.

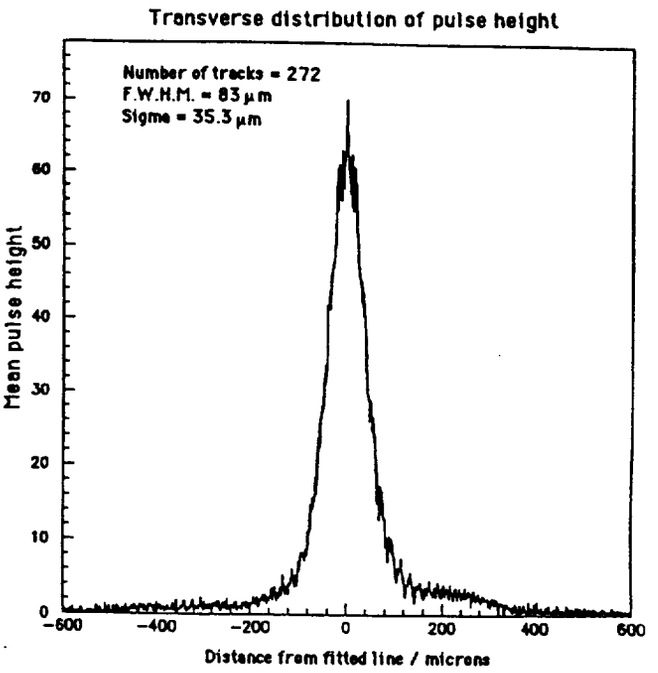


Fig. 5 Histogram of the residuals of 272 beam tracks.

3. NEW DOPANTS

Recently, we synthesized four new organic scintillators with large Stokes shift [3]. They are similar to PMP(*) and have spectra with emission maxima ranging from 430 to 460 nm.

In table 1, their spectroscopic properties when diluted in toluene are shown in comparison with POPOP, p-Terphenyl and 3-HF.

It is worth noting the big Stokes shift of the PMP derivatives and 3-HF compound with p-Terphenyl or POPOP. On the other hand, 3-HF exhibits a lower light yield compared to all PMP derivatives.

(*) Which, in the table 1, is named PMP420.

Table 1 Spectroscopic properties of the investigated scintillators in toluene at 0.025 molar solutions

Scintillator	Absorption maximum [nm]	Emission maximum [nm]	Stokes shift [cm^{-1}]	Light[(a)] yield	Range of absorption[(b)] length [m]
PMP 420	295	422	10 200	1	0.02 → 9.0
PMP 430	295	432	10 750	0.90	0.03 → 3.0
PMP 440	305	440	10 060	0.85	0.008 → 3.0
PMP 450	300	448	11 012	0.70	0.08 → 10.0
PMP 460	309	458	10 528	0.60[(c)]	0.1 → 2.0[(c)]
3–HF	338	528	10 650	0.20	2.0 → 3.0
p-Terphenyl	275	344	7 295	2.30	
POPOP[(d)]	352	418	4 485		0.0001 → 2.0

(a) Excited at 240 nm (surface excitation) and normalized to PMP 420.
(b) Across full width at half maximum of the emission band.
(c) 0.01 molar solution.
(d) 0.0025 molar solution.

CONCLUSION

Tracking with scintillating fibres appears feasible for a LHC detector. First computer simulations for luminosity up to ~ 10^{34} cm^{-2} s^{-1} confirm this conclusion [4].

However, improvements in the basic features of scintillating fibres are needed:

- Hit densities for small diameter fibres can be improved by lowering the refractive index of the fibre cladding, increasing therefore the fraction of trapped light.
- Light transmission can be improved both by finding new dopants with large Stokes shifts and small overlap between absorption and emission spectra, and by improving the quality of the core-cladding interface.
- Aluminium coating of the free-fibre end will improve considerably the hit density for an event in the region away from the photocathode.

REFERENCES

[1] H. Leutz, Central tracking of particles with scintillating fibres, proceedings of ECFA Study Week on Instrumentation for High-Luminosity Hadron Colliders, 14–21 September 1989, Barcelona, Spain (and related contributions).

[2] T. Gys, Optoelectronic Delay Tubes, these proceedings.

[3] C. D'Ambrosio, H. Güsten, H. Leutz and M. Taufer, New organic scintillators with large Stokes shift, to be published in Applied Spectroscopy.

[4] U. Gensch and S. Schlenstedt, Monte Carlo simulations for central tracking with a scintillating fibres detector, these proceedings.

OPTO-ELECTRONIC DELAY TUBES(*)

T. Gys (speaker), J. Dupont, J.P. Fabre, J.L. Garavel, P. Nappey and D. Piedigrossi

CERN, Geneva, Switzerland

ABSTRACT

This paper describes a scale model prototype of an opto-electronic pipeline for the read-out of a scintillating fibre tracker. It also presents preliminary results on the capability of this device to delay optical images and select them by external trigger signals.

1. INTRODUCTION

Within the framework of the LAA Project [1], we have designed an optoelectronic delay line for the read-out of a scintillating fibre tracker [2–4]. The principle of this delay device has been discussed in detail in previous papers [5–6]. It represents an electromagnetically focused image intensifier with sufficient drift space for low-energy photo-electrons, in order to provide an image delay of ~ 1 μs. The functions of delay, selection and amplification of optical images are ensured by adequately applying electric fields in the different tube sections separated by high-transparency grids (fig. 1).

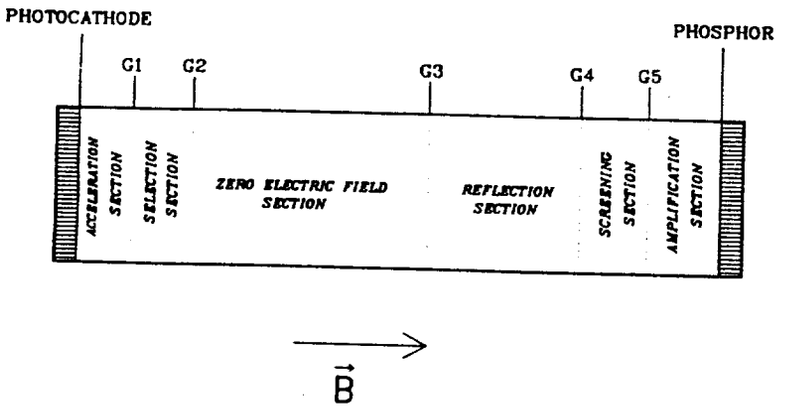


Fig. 1 Basic scheme of the delay tube

(*) The work reported here is part of the LAA Project

The choice of this solution for an analog pipeline has the following advantages:

- it is an imaging device by itself, and thus simplifies the overall data analysis;
- it preserves both excellent time resolution (within the bunch crossing period) and space resolution (within the microfibre diameter);
- it can perform parallel processing of up to 1 million channels (1 channel = 1 microfibre). As a consequence, it yields a low cost per channel;
- it has a low power consumption (of the order of 1 W per tube) and thus minimizes heat production;
- it represents only a few percent of a radiation length;
- it is expected to be radiation hard.

With a first simplified prototype built by EEV Ltd (England), we have already demonstrated our ability to delay optical images for some hundreds of nanoseconds with an excellent space resolution (25 μm) in a moderate magnetic induction (0.7 T) [6]. This device, however, was not equipped to perform the selection of an image.

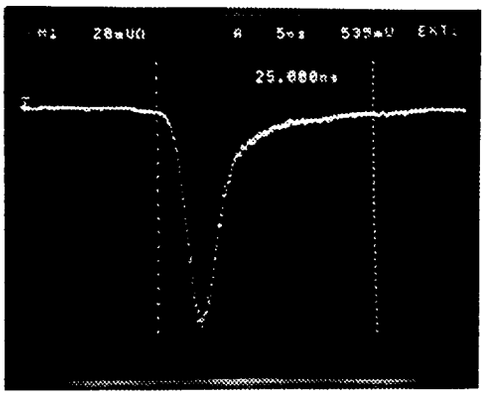
2. THE SCALE MODEL PROTOTYPE AND THE IMAGE SELECTION

A 300 mm long prototype (scale 2:1) has been manufactured by DEP B.V. (The Netherlands) and delivered at CERN in July 1990. It includes all the elements schematically depicted in fig. 1. With this device, optical signals have been delayed by up to 500 ns, selected by appropriate grid pulsing, and amplified by a phosphor screen.

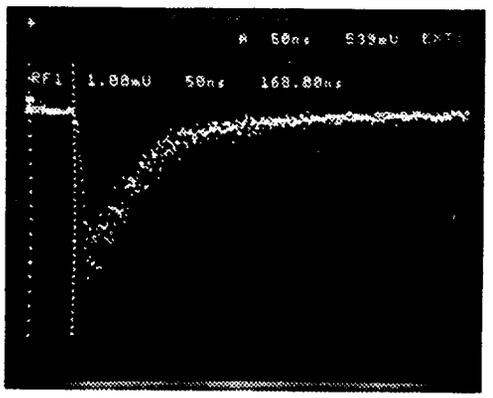
The selection performances of the tube are illustrated in fig. 2. For timing measurements, the tube can work in a magnetic induction limited to 0.03 T. It is fed by a short light-pulse from a blue LED (fig. 2(a)). Figure 2(b) displays the output signal obtained by supplying all the tube grids at +7.5 V DC, the cathode being at ground, and the phosphor at +6 kV. In this mode where all photo-electrons drift through the tube without being reflected in the reflection section, a delay of only 170 ns is obtained and no image selection is possible.

If the tube works in the image elimination mode [5,6], grids Gl, G2, G3 and G5 are at +7.5 V and grid G4 at –1 V so that every image is now reflected and delayed by 400 ns. The selection of an image is realized by pulsing G1 with

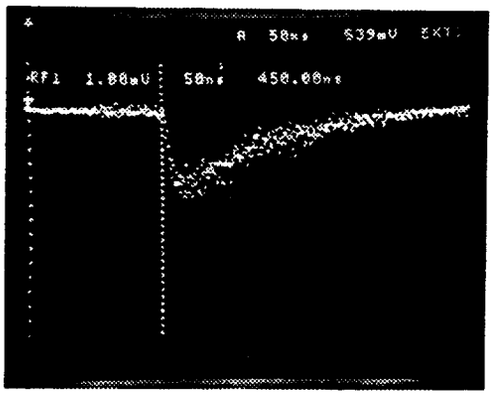
a short negative pulse (triangular shape –200 V in amplitude, 3 ns fall time, 5 ns rise time). The resulting phosphor signal is displayed in fig. 2(c).



(a) Averaged blue LED light-pulse feeding the tube photocathode (time base: 5 ns/div., cursor separation: 25 ns).



(b) Averaged phosphor-light signal obtained when the tube grids are at the same potential of +7.5 V. The rise time of the signal is given by the decay time constant τ of the phosphor screen (we use a P47 screen so that $\tau \sim 60$ ns (time base: 50 ns/div., right cursor position: 168 ns)).



(c) Averaged phosphor-light signal obtained when the tube is working in image elimination mode while a negative pulse is applied on grid G1 in order to select an image (time base: 50 ns/div., right cursor position: 450 ns).

Fig. 2

3. CONCLUSIONS

We tested a prototype of an opto-electronic delay line. Preliminary results show encouraging performances in terms of signal delay, selection and amplification capabilities.

We are currently investigating in detail the time resolution of the device. In the next future, we envisage to test the selection of a wanted image out of several consecutive images separated by 15 ns. We intend also to study the noise performance of the tube.

Acknowledgements

We thank Dr G. Stefanini from CERN for having made a magnet available, in order to perform several delay tube experiments.

REFERENCES

[1] A. Zichichi, The LAA project, ICFA Instrum. Bull., 3 (1987) 17.

[2] H. Leutz, Central tracking of particles with scintillating fibres, and related contributions, Proc. of the ECFA study week on instrumentation technology for high-luminosity hadron colliders, Vol. 1, E. Fernandez and G. Jarlskog Eds, Barcelona (Spain) 14–21 September (1989) 176.

[3] C.d'Ambrosio, H. Leutz, S. Tailhardat and M. Taufer, Present status and future programme of scintillating fibres for central tracking, these proceedings.

[4] U. Gensch and S. Schlenstedt, Monte Carlo simulations for central tracking with a scintillating fibre detector, these proceedings.

[5] J.P. Fabre et al., Conceptual design for an opto-electronic delay line, Rev. Phys. Appl. 24 (1989) 1019.

[6] T. Gys et al., Opto-electronic delay for the read-out of particle tracks from scintillating fibres, Proc. of the ECFA Study Week on Instrumentation Technology for High-Luminosity Hadron Colliders, Vol. 1, E. Fernandez and G. Jarlskog Eds, Barcelona (Spain) 14–21 September (1989) 255.

TOPOLOGICAL TRIGGER DEVICE USING SCINTILLATING FIBRES AND POSITION-SENSITIVE PHOTOMULTIPLIERS

V.Agoritsas[1], N.Akchurin[2], J.Dufournaud[3], R.Giacomich[4] , A.M.Gorin[5] , K.Kuroda[3], A.P.Meschanin[5], C.Newsom[2], S.B.Nurushev[5], Y.Onel[2], N.Oshima[6] , G.Pauletta[4], A.Penzo[4], V.E.Rakhamatov[5], V.L.Rykalin[5], G.Salvato[4], P.Schiavon[4], D.Sillou[3], V.L.Solovyanov[5], F.Takeutchi[7] , A.N.Vasiliev[5], V.G.Vasil'chencko[5], A.Villari[4], R.Yamada[6] and T .Yoshida[8]

An approach to a high quality of the Level-1 Trigger is investigated on the basis of a Topological Trigger Device (TTD). It will be realized by using scintillating fibres (SciFi) and position-sensitive photomultipliers (PSPM), both of which are considered as potential candidates of new detector-components thanks to their excellent time characteristics and high radiation resistance. The device is characterized in particular by its simple concept and reliable operation supported by the mature technologies emploied.

1. CONCEPTUAL DESIGN AND EXPECTED PERFORMANCES.

A conceptual structure of the TTD is shown in Fig.1. It consists of two cylindrical hodoscopes, RH1 and RH2, with the radii of 50 cm and 100 cm respectively, covering a rapidity range $-1.5 \leq \eta \leq 1.5$. Each hodoscope is a triplet of SciFi layers (U-V-Z) made of 0.5 mm ø SciFis coherently aligned along a stereo-angle ($\sim$ 15°) with respect to the Z-axis. For the reason of high resolving time required for such a trigger device each RH is divided at the central plane ($\eta = 0$) into two parts which are less than 2 m in length. Hence, the maximum transit time of light is less than 10 ns.

---

[1]CERN, Geneva, Switzerland
[2]Iowa Univ., Iowa, USA
[3]LAPP, Annecy, France
[4]INFN, Messina-Trieste-Udine, Italy
[5]IHEP, Serpukhov, USSR
[6]FNAL, Batavia, USA
[7]Kyoto-Sangyo Univ., Kyoto, Japan
[8]Osaka City Univ., Osaka, Japan

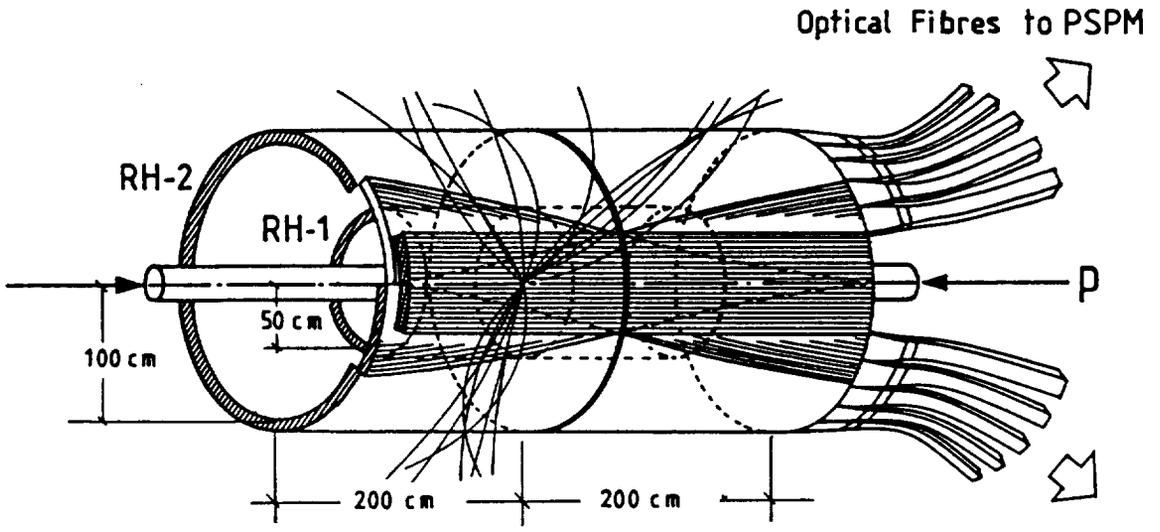


Fig.1 Conceptual structure of the TTD

Table 1 : Expected performances of TTD

Spatial resolution :	$\sigma_{\phi} \simeq 150$ μm/sublayer, $\simeq 90$ μm/triplet, $\sigma_z \simeq 400$ μm
Number of equivalent pixels :	2.8×10^7 in RH1, 1.1×10^8 in RH2
Two-hit resolution :	$\simeq 0.7$ mm
Resolving time/hit :	$\simeq 0.5$ ns
Total time spread :	< 10 ns
Occupancy at $L = 10^{34}$ cm^{-2}sec^{-1} :	~ 5 % in RH1, ~ 1 % in RH2

Table 1 presents expected performances of the TTD based on commercially available PSPM (~1200 tubes of Type R2486-Hamamatsu).

2. ORIGINAL ROLES OF THE TOPOLOGICAL TRIGGER DEVICE.

The PSPM together with a real-time digitizer (RTD), such as developed in our collaboration[1], will afford an elegant solution to meet the requirements of high flux density of charged particles under the LHC environment :

1) The RTD is capable to reject low $p_\perp$ particles travelling through a strong solenoid field of the vertex detector. Fig.2 presents preliminary results of a Monte Carlo simulation showing how the low $p_\perp$ tracks of the minimum-bias events are rejected by a cut on the incident angle θ_{in} onto RH1 and RH2.

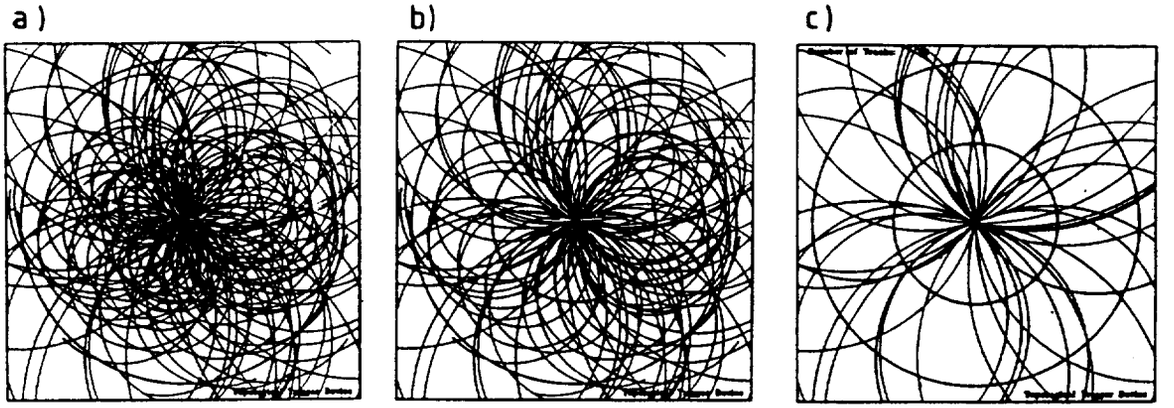


Fig.2 Rejection of low $p_\perp$ tracks by RTD ;
a) Superposition of 15 min.-bias events produced in pp collision at $\sqrt{s}$ = 16 TeV (ISAJET),b) Cut on RH1 ($\theta_{in} > 40°$), c) Cut on RH2 ($\theta_{in} > 40°$) ; B = 2 Tesla.

2) A selection of high $p_\perp$ tracks, such as lepton pairs or jets produced by Z^o or $W^\pm$, is also possible with the aid of a local coincidence between RH1 and RH2. The level of false coincidence due to the min.-bias events should, a priori, be very low taking into account a high segmentation of the local coincidence, in particular in η, which is foreseeable with the resolving time of $\sim$ 0.5 ns/hit.

3) Another interesting feature of the TTD is a possibility of measuring the time structure of hits along the SciFi layers. This redundancy in Z coordinate will help much ;
- linkage between U-V layers, and
- Elimination of "out-of-time" events including loopers.

3. CONCLUSION.

The real-time selection of events, such as mentioned in 1) and 2), can be combined with the calorimetric information to define a "Hybrid" Leven-1 Trigger, which should play an essential role, in particular, in the search for rare events at the LHC. On the other hand, the map of "in-time" events, as mentioned in 3), will serve to pin up, in a higher level trigger or in off-line, "good" tracks and showers among the backgrounds accidentally observed in the relevant devices of the complex of vertex detector.

REFERENCE.

[1] K.Kuroda et al., CERN-EP/90-90, 29 June, 1990.

Top Quark Physics with B tagging at LHC

F. Bedeschi, G. Bellettini, G. Punzi, H. Wenzel

Presented by
F. Bedeschi
INFN - Pisa

Abstract

We discuss the importance of b tagging in events containing the top quark. In particular we focus on its effectiveness in improving the signal to background ratio, the determination of the top mass and the study of deviations from the minimal Standard Model. We then estimate the efficiency for tagging b's, assuming a "reasonable" vertex detector and outer tracking, based on an extrapolation of the CDF experience.

The top quark is postulated in the Standard Model as the weak isospin doublet partner of the bottom quark. Despite many indirect evidence of its existence [1], however, the top has not as yet been discovered [2]; probably due to its high mass, which prevents production in existing e^+e^- Colliders, and implies rather low cross sections (in the 1 to 100 pbarn range) at the present highest energy Hadron Colliders. Though it is not unlikely that the top quark will eventually be discovered at the Tevatron, provided the mass is not too high, it is only at the high luminosity Hadron Colliders of the future (LHC, SSC) that a detailed study of its properties will be possible with good statistics. In this paper we shall describe how the tagging of b quarks associated with the top decay can help in these studies as well as strengthening the signature of events with top. We will later discuss what requirements are imposed on the tracking system to achieve reasonable b tagging efficiencies and what kinds of efficiencies are to be expected.

Top quarks are typically produced in pairs, mostly through gluon fusion diagrams. Each top quark then decays into a W (real) and a b quark; there are therefore 2 b-jets and 2 W's in the event. The W's in turn can decay either hadronically (2 jets) or semileptonically. This gives rise to three possible event topologies:

a. $t\bar{t} \rightarrow 6jets$	B.R.=45%
b. $t\bar{t} \rightarrow 2l^{\pm} + 2\nu + 2jets$	B.R.= 5% (excluding τ's)
c. $t\bar{t} \rightarrow 1l^{\pm} + 1\nu + 4jets$	B.R.=30% (excluding τ's)

The fully hadronic mode, though having the highest branching ratio, is very hard to detect, due to the extremely high QCD background. On the contrary the di-lepton mode (b) is very clean and should be easy to detect, if the production rate is not a problem and non physical backgrounds can be kept under control. We do not expect therefore that b tagging will be particularly helpful in this mode except for strengthening the top signature. The lepton + jets mode (c) has a high branching ratio and is not as clean: from the CDF experience we expect a signal to background ratio (S/B) in the order of 1 to 1 [3], mostly due to W + jets production, with the W decaying semileptonically. Since the jets produced in association with the W are essentially gluons from initial state radiation, we

expect a substantial improvement in S/B by tagging the b's in this particular mode. The upper limit in the improvement factor being due to b's produced by gluon splitting in the gluon jets. Assuming an average b content in gluon jets in the order of 3%, we expect to have b's in about 11% of the W + jets events. This implies that tagging 1 of the 2 b's in the event would allow to improve S/B by a factor $\approx$10. Tagging both b's the improvement could be substantially larger, since we can use the angular correlation between the two b's to discriminate between those originating from gluon branching and those from top decay.

If the Tevatron and $Sp\bar{p}S$ experiences and the Standard Model cross sections can be realistically extrapolated, detecting the top quark in the mode (b) at LHC should be rather straightforward. It is important, however, to have also a clean measurement of the mode (c), in order to measure the semileptonic branching ratios of the top and possibly test deviations from the minimal Standard Model. In the simplest extension of the standard Higgs sector, there are two Higgs doublets and consequently both charged and neutral Higgs bosons [4]. If the charged Higgs has a mass smaller than the top mass, there are scenarios where the decay mode $t \rightarrow H^+b$ can compete with the mode $t \rightarrow W^+b$. The semileptonic branching ratios of the top could, in this case, be quite different than what predicted by the Standard Model, as shown in fig.2 for a specific model. In particular we notice that for small values of $tan\beta$, the ratio of the vacuum expectation values of the 2 neutral Higgs fields, the semileptonic B.R. of the top could be quite small.

Measuring with good accuracy the mass of the top quark is going to be an important task of the future hadron Colliders. Many different methods have been proposed so far, all having some kind of systematic uncertainty and/or model dependence. Among these the most appealing consists in the direct measurement of the invariant mass of the 3 jets in which the top decays, in the lepton + jets event sample. Here the main sources of systematic errors are the combinatorial background (4 jets in the final state) and the jet energy scale. All these effects can be greatly reduced by tagging the b's in the event. Indeed after tagging of the b jets, the remaining 2 can be associated to the W. The constraint of the W mass can be used to calibrate the jet energy scale and the combinatorics is greatly reduced. The remaining systematic error is expected to be in the 5% range. In fig.1.a and fig.1.b we show the W mass spectrum from the jet-jet invariant mass and the top mass distribution from the 3 jet invariant mass, as obtained in a study performed by the SDC collaboration [5].

In conclusion, tagging the b's allows a large improvement of the S/B in the selection of top events in the lepton + jets mode, a better determination of the top semileptonic branching ratios, which are sensitive to deviations from minimal Standard Model behaviour, and a model independent direct way to measure the top mass.

Tagging b's with good efficiency implies several constraints on the tracking system (vertex detector and outer tracker) at LHC:

i. *large acceptance.* Due to the higher center of mass energy a tracking coverage within $|\eta| \leq 2$ is needed for top masses in the 100$\div$200 GeV range.

ii. *good impact parameter resolution.* A measurement accuracy in the 10 μm range is needed, given the typical impact parameter scale in the order of a few hundred microns. This resolution in practice is significantly degraded by multiple scattering contributions at low momentum. It is therefore important to place the first layer of measurement as close as possible to the beam line to reduce the lever of arm, and to have momentum measurement to estimate the precision of the measurement on a track by track basis. Large backgrounds from badly measured low p_t tracks could arise otherwise.

iii. *redundancy.* Given the complexity of the events, an outer tracker with a good sampling and double track resolution is needed. Some redundancy in the vertex detector is also useful to ensure an efficient matching with the outer tracker.

A typical impact parameter resolution curve as calculated for CDF with the inclusion of the Silicon Vertex Detector is shown in fig.3. We have used this curve and a tracking acceptance of $|\eta| \leq 2$ to estimate the b tagging efficiency in top events at LHC. A b is assumed to be tagged if at least 3 charged prongs from its decay are contained in the tracking volume and have impact parameters which are at least 3 times their calculated error. Correlations between the impact parameters and the directions of the tracks are taken into account to reduce the rate of error to a negligible level. The results displayed in the following table show, for various top masses, the efficiency for tagging at least 1 b and both b's in the assumption of perfect (σ_D=0) impact parameter resolution. In this case only the B branching ratios and the acceptance contribute.

M_{top}	100 GeV	150 GeV	200 GeV
$Eff_{\geq 1B}$	64%	75%	78%
Eff_{2B}	18%	27%	30%

When detector resolution effects are turned on the efficiency is somewhat decreased as shown in the table below.

M_{top}	100 GeV	150 GeV	200 GeV
$Eff_{\geq 1B}$	32%	47%	52%
Eff_{2B}	3.4%	7.8%	10.5%

At LHC, even with a luminosity $\sim 10^{33} cm^{-2} \cdot sec^{-1}$, several millions of $t\bar{t}$ pairs will be produced. Given the above efficiencies, the physics studies outlined in the first part of the paper are quite feasable, even with the more costly double b tag, if a tracking system with the features we have described can be reliably built and operated.

References

[1] G. L. Kane and M. Peskin, Nucl. Phys. **B195**, 29 (1985)
A. Bean et al., Phys. Rev. **D35**, 3533 (1987)
W. Bartel et al., JADE collab., Phys. Lett. **146B**, 437 (1984)
H. Albrecht et al., Argus collab., Phys. Lett. **192B**, 245 (1987)
M. Artuso et al., CLEO collab., Phys. Rev. Lett. **62**, 142 (1989)

[2] F. Abe et al., CDF collab., Phys. Rev. Lett. **64**, 2233 (1989)
F. Abe et al., CDF collab., Fermilab-PUB-90/137-E, July 1990,
Submitted to Phys. Rev. D

[3] Fermilab Top Studies group, CDF Note 1157, July 1990

[4] J. J. Gunion et al., "The Higgs Hunter Guide", Addison Wesley (1990)

[5] Reply by the Solenoidal Detector Collaboration to questions from the Program Advisory Committee, 12 July 1990

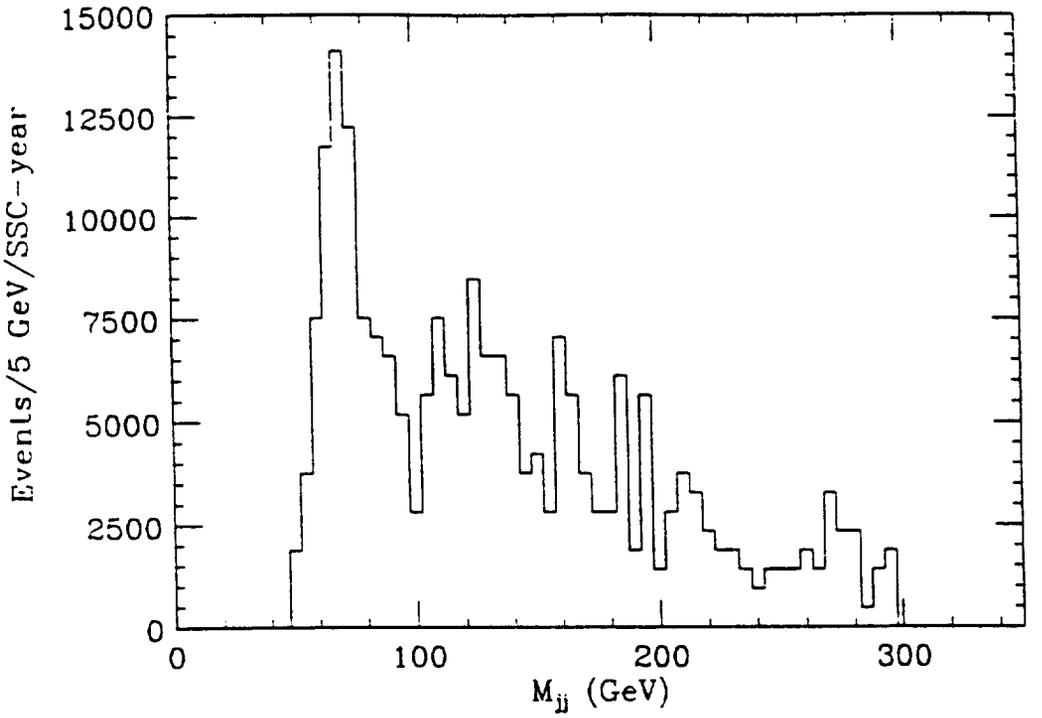


Fig. 1.a. The distribution in the invariant mass of the dijet system composed of any two jets not tagged as b's in $t\bar{t}$ events, where one of the top quarks decays semileptonically. $M_{top} = 250GeV$.

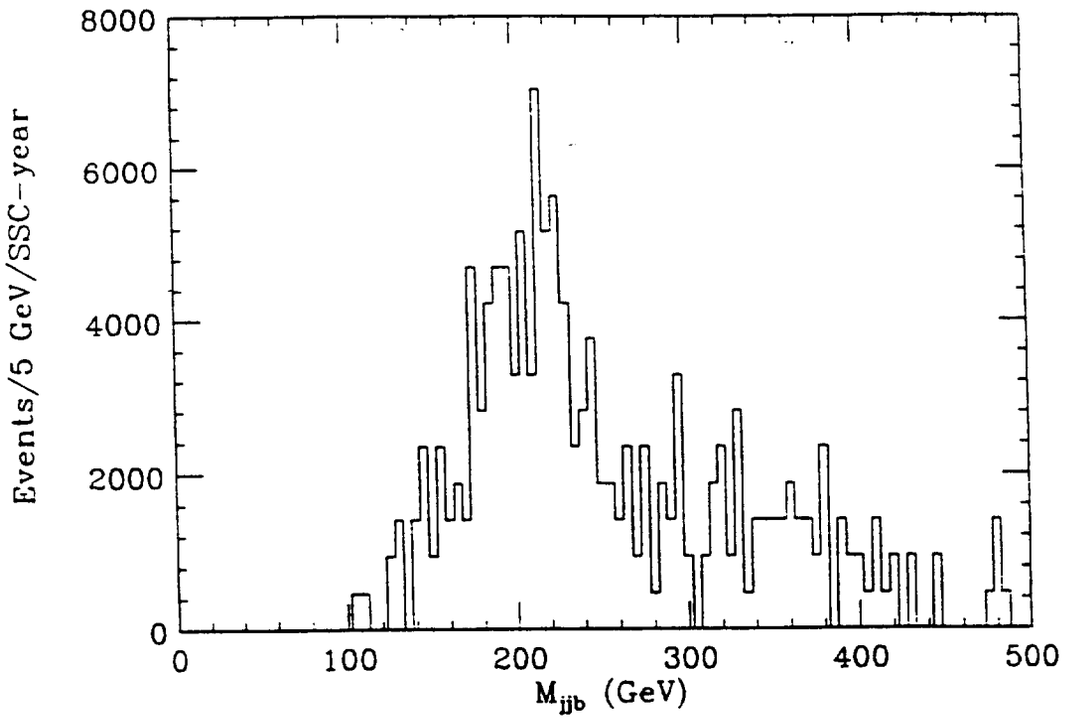


Fig. 1b. The invariant mass of the system comprising the dijet pair from fig. 1.a and a tagged b jet.

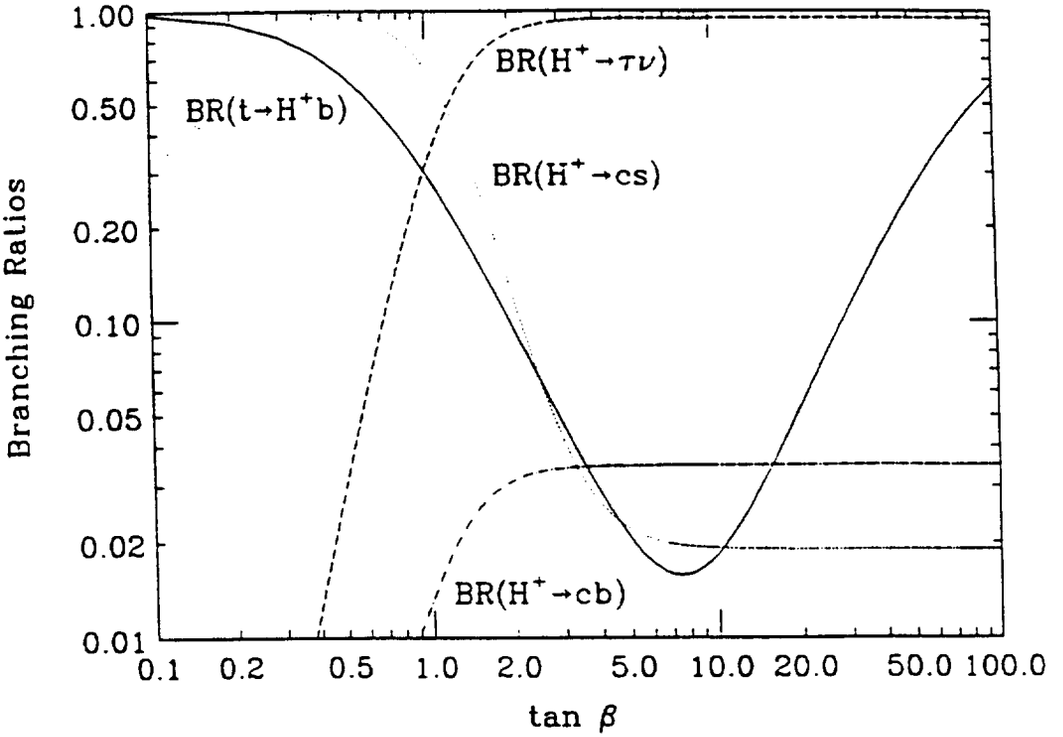


Fig. 2. Branching fractions for the reactions $t \rightarrow H^+b$ and $H^+ \rightarrow \tau\nu, c\bar{s}$ and $c\bar{b}$ as a function of the parameter $tan\beta$.

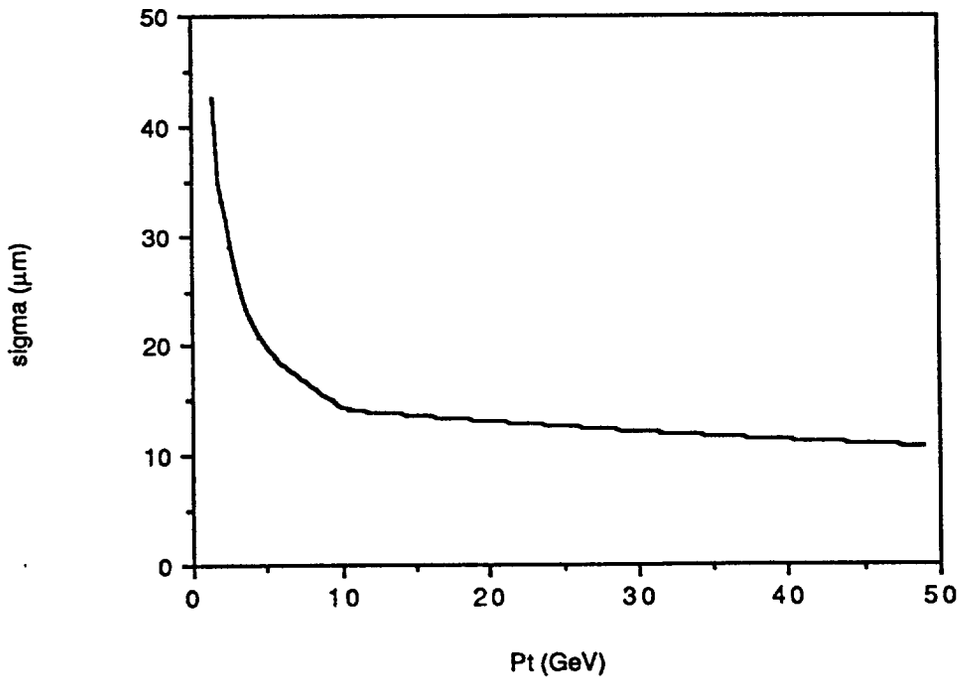


Fig. 3. Impact parameter resolution as a function of the particle p_t as expected for the CDF vertex detector.

STUDY OF AN LHC DETECTOR WITH A CENTRAL SOLENOIDAL FIELD

C. Daum, NIKHEF-H, Amsterdam

A study is made of a selection procedure of parameters of a central solenoidal field of radius R and central field B and a central detector with resolution ε for an LHC detector.

Relevant criteria are:
1) the error on momentum due to resolution and multiple scattering,
2 the synchrotron radiation loss for electrons,
3) the stored energy of the magnetic field,
4) the hoop stress of the coil and the thickness of the support cylinder.

The motion of a particle of momentum p (GeV) and unit charge originating from the point (x,y,z) = (0,0,0) on the axis of the solenoidal uniform magnetic field B (T) is a helix of constant radius of curvature ρ (m) and constant pitch angle λ, while the axis of the helix coincides with the axis if the solenoidal field. I get

$$p \cos\lambda = 0.3\, B\, \rho = \frac{0.3\, B}{k},$$

where k is the curvature of the particle track, and λ is the angle with respect to the plane normal to the z - direction (along the beam) at the point (0,0,0).

Particles originating from the point (0,0,0) on the axis escape from the cylinder, if $2\rho \geq R$. The cutoff occurs at $2\rho = R$, at which

$$p_{Tcut} = 0.15\, BR\ .$$

I introduce a parameter

$$\xi = \frac{p_{Tcut}}{p_T} = \frac{R}{2\rho} = \sin\frac{\alpha}{2}\ .$$

Here, α is the bending of the particle trajectory from the axis to the edge of the field, and the projected track length in the bending plane is

$$L' = \rho\alpha\ .$$

The parameter ξ is used over the range 0 ($p_T = \infty$) to 1 ($p_T = p_{Tcut}$).

The errors δk_{res} and δk_{ms} in the curvature due to the measurement resolution and multiple scattering, respectively, and similarly the errors $\delta\theta_{res}$ and $\delta\theta_{ms}$ in the measurement of the polar angle are conveniently expressed as functions of B, R, ξ (α), ε, and the coil length L_m , using the formalism of R.L. Glückstern (NIM 24 (1963) 381 - 389).

I calculate now the momentum resolution of charged particles and the synchrotron radiation loss of electrons for values of the pseudorapidity η = 0,1,2,3 and 4 for a configuration with B = 4T, R = 1 m, ε = 20 μm, and a track detector with a total thickness of 0.12 radiation length (e.g. for microstrip chambers which are expected to operate well in a high magnetic field, F. Udo). The length of the coil is determined by the

pseudorapidity range from 0 to η which is completely covered by a tracking region of radius R = 1 m. Table 1 shows the corresponding values of L_m of η.

Table 1

η	tan (θ/2)	θ	L_m	R	pTcut
		rad	m	m	GeV
				L_m = 4 m	B = 4 T
0	1.0000	1.571	0.00	1.000	0.600
1	0.3679	0.705	2.36	1.000	0.600
2	0.1353	0.269	7.22	0.551	0.331
3	0.0498	0.099	20.2	0.200	0.120
4	0.0183	0.037	54.1	0.073	0.044

A reasonable choice of the useful length is L_m = 4 m for which the range $0 \leq \eta < 1.44$ is entirely contained within the tracking region up to R = 1 m. Table 1 also shows the corresponding values of R and p_{Tcut} as function of η. Fig. 1 shows the resolutions for η = 0, 1, 2, 3, and 4. These parameters yield a resolution dp/p ≈ 0.10 p (TeV) for large p compared with dp/p ≈ 0.33 p (TeV) for a field of 1.63T. For the range $0 \leq \eta \leq 2$ this resolution at B = 4 T is better than that of an electron calorimeter with dE/E = 0.01 + 0.17/$\sqrt{E}$ up to 200 GeV and that of a hadron calorimeter with dE/E = 0.01 + 0.35/$\sqrt{E}$ up to 300 GeV. The relative synchrotron radiation loss -dW/E of electrons in this field is less than the energy resolution of above electron calorimeter up to E = 400 GeV.

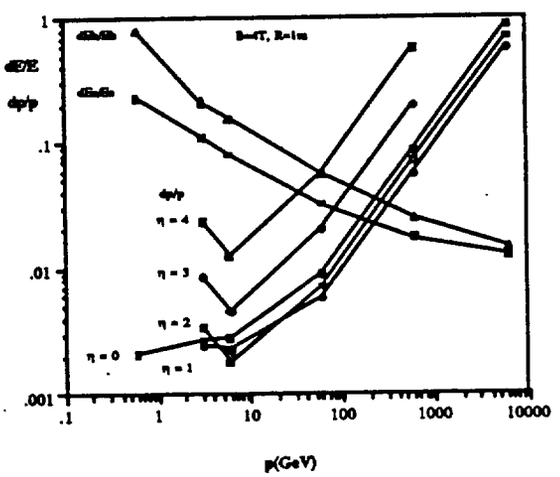


Fig. 1 Momentum resolution for electrons, muons and hadrons for various values of η. The curve dEe/Ee is the energy resolution for an electron calorimeter with dE/E = 0.01 + 0.17/$\sqrt{E}$. The curve dEh/Eh is the energy resolution for a hadron calorimeter with dE/E = 0.01 + 0.35/$\sqrt{E}$.

The synchrotron radiation loss for electrons on a trajectory of curvature $\rho(\theta)$ over one revolution is derived below. On a trajectory of curvature $\rho(\theta)$ over one revolution

$$\Delta W_e = -0.0882 \cdot 10^{-3} \frac{\beta^3}{\rho(\theta)} E^4 \text{ GeV} .$$

The radius of curvature is

$$\rho(\theta) = \frac{\rho}{\sin\theta}$$

The relative energy loss over the path length L is

$$\frac{\Delta W_e}{E} = -0.0948 \cdot 10^{-6} \frac{B^3 R^{'2}}{\sin^2\theta\ \xi^2} \alpha \ .$$

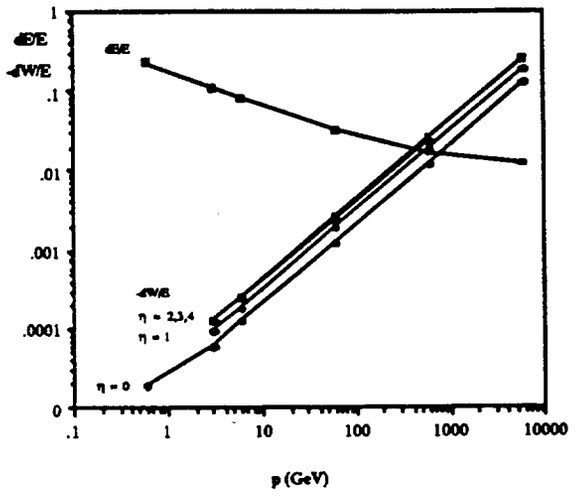


Fig. 2 The synchrotron radiation loss dW/E for electrons in a field of 4 T with a radius of 1 m. The curve dE/E is the energy resolution for an electron calorimeter with $dE/E = 0.01 + 0.17/\sqrt{E}$.

The stored energy W_s of a magnet with a field of B 4 T, a radius R = 1 m, and a length L_m = 4 m within an iron return yoke is about 104 MJ.

The main limiting factor in the choice of field and radius is the hoop stress described below using Fig.3.The axial field is

$$B\ (T) = \mu_0 nI\ (At/m) = \frac{4\pi\ nI\ (At/m)}{10^{-7}} \ .$$

The Lorentz force per unit length on windings of solenoid is

$$\vec{F} = \vec{I} \times \vec{B} \ \Rightarrow\ F\ (N/m) = I\ (A)\ B\ (T) \ .$$

The radially outward magnetic pressure on n windings per meter

$$P_m\ (Pa) = nI\ B = \frac{B^2}{\mu_0} \approx 0.8 * 10^6\ B\ (T)^2 \ .$$

The outward pressure on the surface of the cylinder stretches the circumference of the cylinder and causes a hoop stress in the cylinder which is

$$\sigma_2\ (MPa) = P_m \frac{R}{t} \approx 0.8 \frac{B\ (T)^2 R\ (m)}{t\ (m)} \ .$$

Existing superconductive solenoids consist e.g. of a cryostat made of Al ($t_{cry} \approx 0.4\ X_0$), the coil (mainly Al stabiliser, $t_{coil} \approx 0.3\ X_0$), and a support cylinder made of Al ($t_{cyl} \approx 0.3\ X_0$). For Al , I have X_0 = 0.089 m, and the allowed hoop stress for Alis $\sigma_{all} \approx 80$ MPa at 293 K, and $\sigma_{all} \approx 120$ MPa at 4.2 K. Only t_{cyl} = 0.0267 m contains the hoop stress.

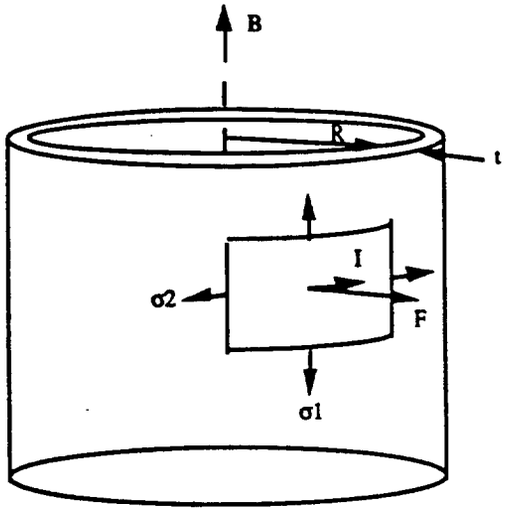


Fig.3. Definition of the hoop stress σ_2.

With σ_2 = 80 MPa, I get $B^2R = \sigma_2 t / 0.8 = 80 * 0.0267 / 0.8 = 2.67\ T^2m$, which yields for R = 1 m, B = 1.63 T. E.g. for B = 4T, and R = 1m I need $t_{cyl} = 0.160$ m = 1.8 X_0. Using the same t_{cry} and t_{coil}, t_{total} = 2.5 X_0 which is too large if the coil is followed by a calorimeter. In practice t_{coil} also will depend on B. Existing solenoids are limited to fields of < 1.8 T by the hoop stress in the Al support cylinder

I can design a solenoid with a thin outer support cylinder using for the support cylinder a low Z material of high tensile strength T for which we may take optimistically $\sigma_{all} \approx 0.5$ T for reduction of the total radiation length of the coil and for increasing σ_{all} and thus B for a given radius R. Various materials exist : HT graphite yarn (Z = 6), Boron (Z = 5) fibre with W (Z = 74) core or SiC (Z = 14 and 6) core, Al (Z = 13) Li (Z = 3) alloy (~4:1), Al (Z = 13) and C (Z = 6) fibre composite. For example, using HT1000 graphite yarn (~67 %) in epoxy matrix with T ≈ 7000 MPa and thus σ_{all} = 3500 MPa = σ_2 (from C. Hauviller, CERN), $\rho \approx 1.55$ g cm^{-2}, and $X_0 \approx 0.275$ m I obtain $t_{cyl} \approx 0.05$ $X_0 \approx 0.0275$ m, $B^2R = \sigma_2 t / 0.8 \approx 60\ T^2m$, and for R = 1 m I get B ≈ 7.8 T. This leaves 0.1 - 0.2 X_0 for an Al cylinder, perhaps on the inside of the coil for carrying the He cooling tubes, providing sufficient heat conductivity between He tubes and coil, and quench stability. The thickness of this solenoid would be less than 1 X_0.

The proposed coil design might be used in an Economic Compact Universal LHC detector. A small coil with B = 4 T, R = 1 m and L_m = 4 m is surrounded by an electron and hadron calorimeter which is then situated in a field of up to 0.27 T. The thickness of the coil will depend on the field due to the linear increase of the number of ampereturns with B, and to the decrease of the critical current with B. The calorimeter is surrounded by an iron return yoke instrumented for muon detection. The iron return yoke can have coils for additional excitation, if required for momentum determination of muons (e.g. at large η). The smallness of the coil keeps all other instrumentation Compact and thus such a Universal detector may be relatively Economic.

VERTEX DETECTOR ELECTRONICS FOR LHC

P.Seller, Rutherford Laboratory, Chilton, Oxon, England

INTRODUCTION

It is unclear whether a vertex detector is useful in the LHC environment (REF 1) if the highest luminosity is to be used. On the one hand the multiple interactions per beam crossing make it difficult to do tracking while on the other hand the very same complex multiple events will require the highest precision detectors to perform adequate separation. This said the constraints upon the electronics needed can be identified and used to investigate what possibilities exist. The constraints are numerous and can best be summarized in a table (Table 1)(REF 2). The most notable features are the enormous number of channels (10e7) requiring low power for each channel (1-2mw complete level 1 and level 2) in order to have acceptable total power consumption and also the extreme radiation hardness (REF 3,4) requirements for this type of electronics (1Mrad/yr and 10e14 N/cm2/yr). Whilst enduring this the electronics must take data at 66MHz and be ideally dead time free. There are several detector types proposed (REF 5) but there are generic features within these different detectors which can be recognized. In addition to the two levels of triggering discussed in this paper the data can also be zero-suppressed in a simple fasion because only 1% of the channels are non-zero in any crossing.

PREAMPLIFIERS.

The preamplifiers will obviously be specific to the type of detector used and whether analogue or digital data is required from the elements. For instance it has been shown (REF 6) that signals can be extracted from silicon pixel or short strip detectors within the 16ns crossing time. This electronics can be built at the density required and with sufficiently low power dissipation.

LEVEL 1 LEVEL 2 ARCHITECTURES.

Obviously the amount of data coming from the front end devices will have to be reduced on line. The perceived route to doing this is to have a two level filtering system with a level 1 trigger produced within approximately1us to filter the data once. This good level 1 data is held for a further length of time (20us-50us) in a level 2 buffer until a level 2 trigger is produced in order to filter the data for transmission out of the detectors. One of the first and simplest architectures build (Ref7) to do this data reduction is A1 (Fig1) "CLOCK DRIVEN DATA, POINTER ADDRESSED LEVEL 1, POINTER ADDRESSED LEVEL2". This shows some general features of these level 1,level 2 systems. In this case the data stored is analogue values from each detector element in comparison to other tracking systems which take only digital data allowing data coding techniques to be used for storage. This architecture is clock driven implying data is stored every beam crossing as opposed to a data driven system which stores data only on useful data existing in a channel (pixel) or group of channels (pseudo pixel). Clock driven systems obviously have to store more data but are intrinsically simpler. A third feature is the two buffers which requires successful L1 data to be passed to the L2 buffer. This can be a power hungry, complex procedure and a source of error which is difficult to account for with calibration. Several systems allow the data to remain stationary while pointers or addresses are used to index into the data circumventing the above problem. It is assumed in these architectures that the level 1 trigger (T1) comes back at a fixed time interval (1us) after the event is written into the buffer.This allows the data to be accepted or rejected. The level 2 trigger (T2) is allowed to come back at any time (10us-50us) after the T1 but it must be in the correct chronological order and there must be a T2 decision, good or bad for every T1. It is typically expected that there will be 10e2 to 10e3 fewer T1s than beam crossings and 10e2 fewer good T2s than T1s (REF 8). This quickly gives the L1 and L2 buffer lengths and L2 output reading speed.

With architecture A2 (Fig2) "DATA DRIVEN DATA, STAMP ADDRESSED L1, POINTER ADDRESSED L2" data is stored only when one of the channels in a pseudo pixel has good data. This is achieved with the 'ored' discriminators shown. Because many time slots will not contribute data, a time stamp is stored in a Content Addressable Memory (CAM) along side the data. This stamp address is used to address data for read out at the appropriate T1 time. If the occupancy is less than 1/m in each channel then there would be a decrease in the buffer length but at the expense of providing the CAM. This system is useful in low occupancy systems. A3 (Fig 3) is a similar structure but has a stamp for each channel and only stores the stamp if there is a hit on a channel. If this matches the stamp produced at the L1 delay time then a hit is passed to one of two types of L2 buffers. This system can only be used for digital data. As with the L1 data from A2 this L1 data may not contain hits for the time slot that is currently being passed to L2. S1(Fig 4) generates nullwords to pack out the L2 buffer whereas S2 (Fig 5) only stores good data but keeps account of the number of nullwords between good data items. With S1 the data read out is simple but with S2 data has to be unpicked on return of the good and bad L2 triggers.

A4 (Fig 6) "CLOCK DRIVEN MIXED L1/L2 DATA, STAMP ADDRESSED WITH FIFO FREE LISTS" introduces the idea of keeping the data stationary during L1 and L2 and using pointers into this mixed buffer. Fifo0 is first filled with all the addresses from 1 to d0. The addresses are used to address the L1/L2 buffer for writing data. After being used for writing data, each address is taken from Fifo0 and passed to Fifo1 rippling down Fifo1 until at the appropriate T1 time a decision is made to pass it to Fifo2 or if the data is rejected the address is passed back to Fifo0. After a T2 delay the address which has rippled down Fifo2 is used to address the data buffer to readout the good data and the address is returned to Fifo0 for future use. In this system the address of the storage location is available at the time of readout

which allows the system to be calibrated. The disadvantages with this system is that long addresses must be transferred around the system at the full 66MHz rate.
A5 (Fig 7)"CLOCK DRIVEN MIXED L1/L2 DATA, POINTER ADDRESSED L1, POINTER ADDRESSED L2, COINCIDENT POINTERS" is prima facia a schematically elegant system which has one data buffer and a pointer which moves continuously through the buffer at the beam crossing rate. Several functions are performed while the pointer is at each location. Firstly it is ascertained whether this location is being used by interrogating the L1 Sequence Buffer (L1SB) location. If T2 is active the appropriate cell is read out and released for future write operation. The cell released is the cell with the lowest nonzero sequence number in L1SB (this will be 1). At the same time a flag is set to decrement all sequence numbers in L1SB. The second stage is to skip used cells. The third stage occurs if T1 is active and involves the sequence number being written into L1SB and incrementing the sequence number. The forth stage is to write new data into an unused location. This architecture puts a simple constraint on T2 that it comes back synchronized toT1 (modulus the L1 delay) and also relies on the fact that the pointer returns to the first location after this delay time rather than going to the end of the buffer. This aligns the pointer for T1 and T2 processing. The obvious drawback of this system is that four operations have to happen in one crossing time however this problem might be alleviated with A8. Other problems involve decrementing the sequence numbers quickly and synchronizing this with new level 1 triggers so that erroneous numbers are not stored. A6 (Fig 8)"CLOCK DRIVEN MIXED L1/L2 DATA, POINTER ADDRESSED L1, SEQUENCE ADDRESSED L2" involves a very similar scheme but in this case the Write, Read and T1 pointers are separate and operate autonomously. This makes the time to perform the functions more relaxed but still has the sequence number decrementation problems.
A7 (Fig 9) "CLOCK DRIVEN MIXED L1//L2 DATA, POINTER ADDRESSED L1, DIRECT ADDRESSED L2, " is a system with many advantages. The Write, Read and T1 pointer move independently. The Write pointer is driven by the 66MHz clock, skipping cells flagged as used cells by the L1 Used Buffer (L1UB). L1UB simply stores a list of " Used Flags".These are just 1s and 0s not sequence numbers as in A5. The T1 pointer moves at the appropriate delay after Write, skipping used cells and storing a new Used Flag in L1UB on a good T1 decision. The location of the pointer at this time is also stored in a Read Pointer Location Buffer (RPLB). T2 returns good and bad decisions. On a bad decision the next location address in RPLB is discarded. On a good decision the read pointer uses this address to move to the appropriate location and data is read out. The read pointer location put in RPLB can be generated either by counting "Writes" modulo the number of cells in the data buffer or by encoding the position directly. Likewise the read pointer can be moved either by a clocked pointer or addressing it directly.
A8 (Fig11) "BLOCK MULTIPLEXED SYSTEM" is a system the can be overlaid onto any of the architectures A5, A6 and A7. This system multiplexes the input data into four (for example) buffers in turn. These buffers work in an identical fasion to the architectures above but at a quarter of the speed and also there are a quarter of the number of storage cells connected to the output of a preamplifier at any time.
TECHNOLOGY FOR IMPLIMENTATION
It would advantageous to fabricate the preamplifiers, pipelines, and ADC elements on one chip in order to lower interconnection capacitance, increase reliability and to make construction easier. This means the technology must support low noise amplifier design, switched capacitor techniques and be very radiation hard. Several technologies have been identified (REF 3). The choice will be either a rad hard bulk CMOS process like UTMC, if the technology can be exported from the US or a rad hard SOI or SOS process like the Pessey/MEDL process. If the preamplifiers can not be made fast enough in CMOS maybe a hybrid version with bipolar preamplifiers will be used but as no rad hard BiCMOS technology is available this will have a great overhead in bonding complexity.
The bonding technology itself needs consideration as there are at least 2*10e7 bonds to be made compared to 3*10e7 seconds in a year. A fast, reliable bonding technique will be needed. Wire bonding will be too slow so that a technique like the UA2 conductive rubber or 'flip chip' solder bump bonding should be used (REF 9). Solder bump technology has the advantage that it could form the mechanical support as well as the electrical connection to the detectors. Studies are being conducted on this at RAL using the Plessey bonding process.
REFERENCES
1. The task of tracking and vertex location at future hadron colliders. D.Saxon ECFA Barcelona NOV 89. CERN 89-10
+ Tracking issues. D. Saxon. LHC track and vertex working group CERN June 90 . LHC Workshop.(Transparencies.)
2. Table generated from many sources. Gosling, Leutz, Cittolin.
3. Electronic components in high dose environments. F.Wulf. ECFA. Barcelona.
+ Status of rad hard electronic devices in Europe. F.Wulf H.Schonbacker. ECFA WG7. Radiation hardness.
+ Test of rad hardness of CMOS test structures in neutron and proton beams ECFA Barcelona.
4. Radiation levels in detectors at SSC. D.Groom ECFA Barcelona
5. Detector concepts and limitations for vertex detection and tracking. H.Leutz CERN June 90 LHC Workshop.
6. Fast silicon detector systems for high luminosity hadron collider experiments. P.Jarron ECFA Barcelona.
7. High speed analogue CMOS pipeline system. J.Moschen NIM A288 March1990.
+ Development of CMOC circuits and silicon pixel detectors in the CERN-LAA project. Sept 89. CERN 89-14
8. Trigger, signal processing and DAQ overview. S.Cittolin CERN June 90 LHC Workshop.
9. Flip chip solder bonding for microelectronic applications. D.J.Pedder. Hybrid Circuits (ISHM-UK) Jan 1988

TABLE 1

a) 2 * 10e7 detector elements.
b) Mean occupancy 1% worst case.
c) Single bucket time resolution required.
d) Level 1 trigger rate 100KHz maximum.
e) Level 2 trigger rate 1KHz maximum.
f) Time for level 1 trigger data preparation 200ns.
g) Time for level 1 data readout 16ns.
h) Time for level 2 trigger data preparation and readout 8us
i) Level 1 trigger, synchronous, latency 1us, accurate 2ns.
j) Level 2 trigger decision time 10us to 50us, decisions returned for good and bad decisions in order of level 1 triggers.
k) Readout time less than 20us with mean less than 1us. T2 total rate has to equal T1 rate.
l) Power less than 2mW per channel for preamp and level 1 level 2 including ADC at readout.
m) Signal pipeline path must be recoverable off-line for calibration,
n) 8 bit dynamic range for analogue information.(detector dependent).
o) ADC after level 2 pipeline.(trigger dependant)
p) 66MHz operation deadtime free.
q) Area of electronics less the area of detector. Low radiation length.
r) Reliable quick interconnection technology to detectors. (e.g. solder bump technology) (There are 3 * 10e7 sec/yr and 2 * 10 e7 bonds).
s) 1M Rad/yr ionizing radiation and 10e14 Neutrons/cm**2/yr.
t) Minimum number of control signals into a segment (assume 20).

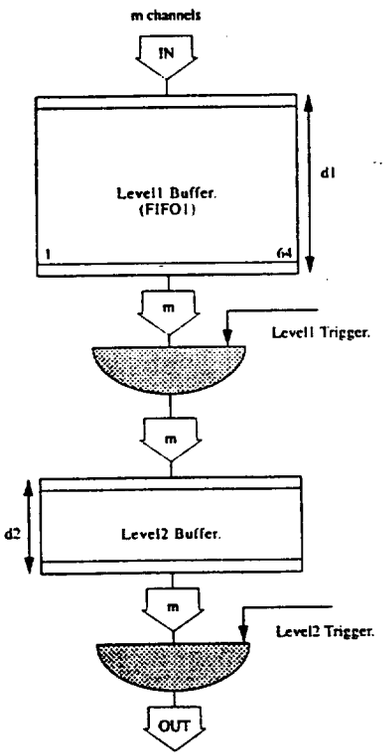


Fig 1 Architecture 1

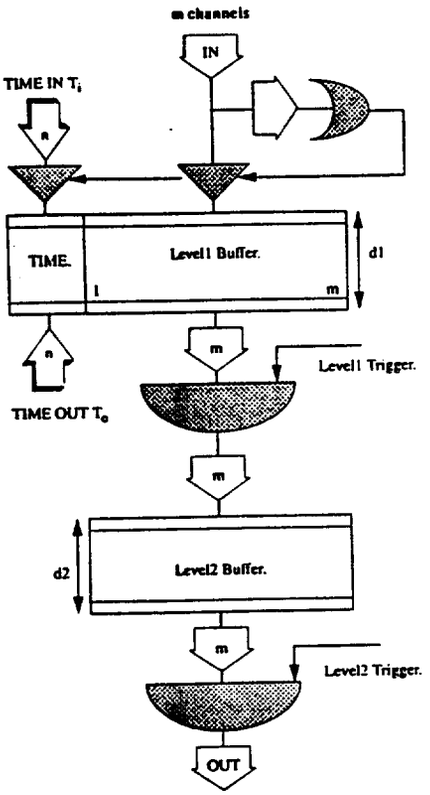


Fig 2 Architecture 2

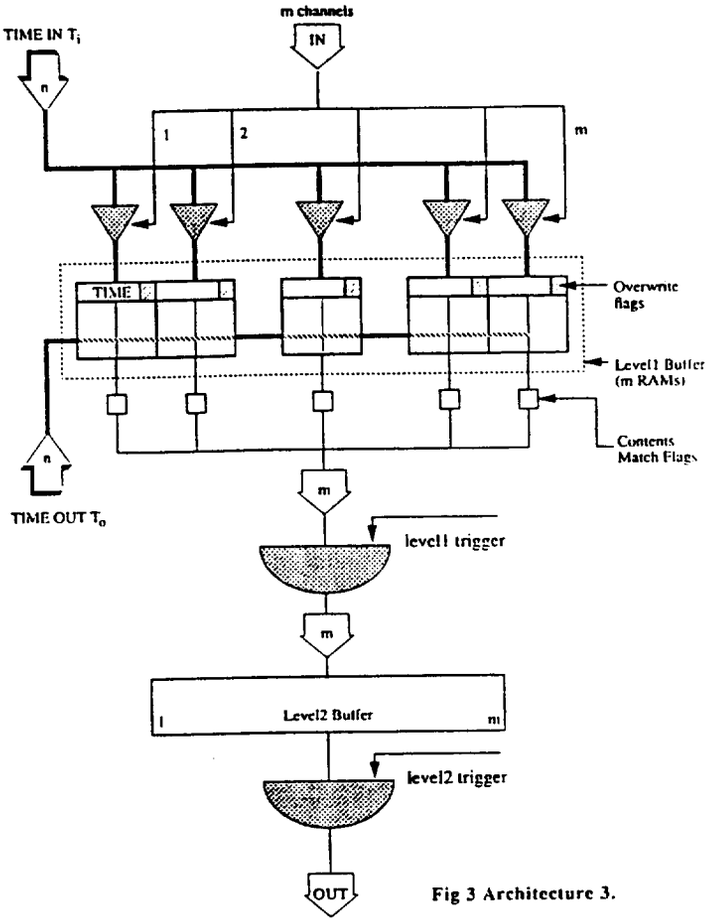


Fig 3 Architecture 3.

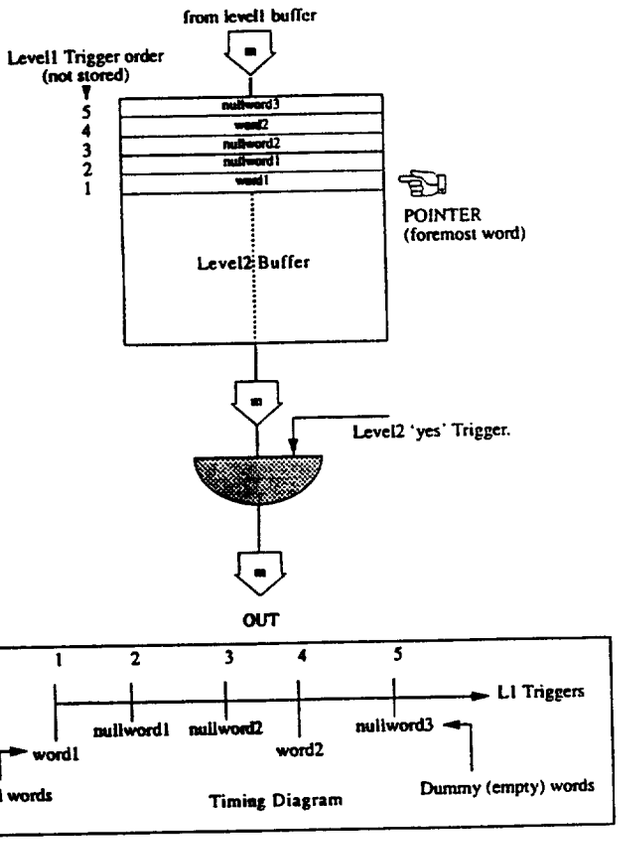


Fig 4 Structure 1 for Level2 Buffer.

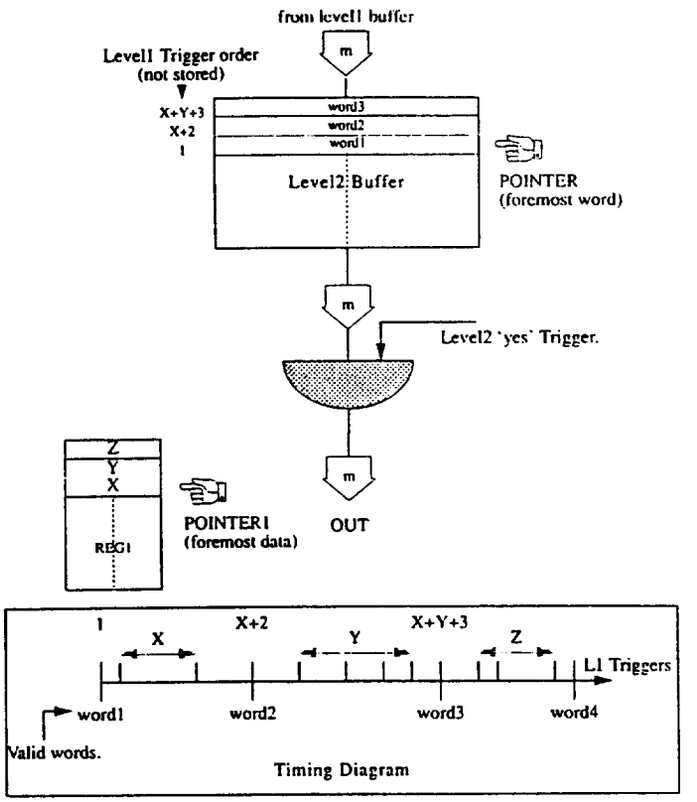


Fig 5 Structure 2 for Level2 Buffer.

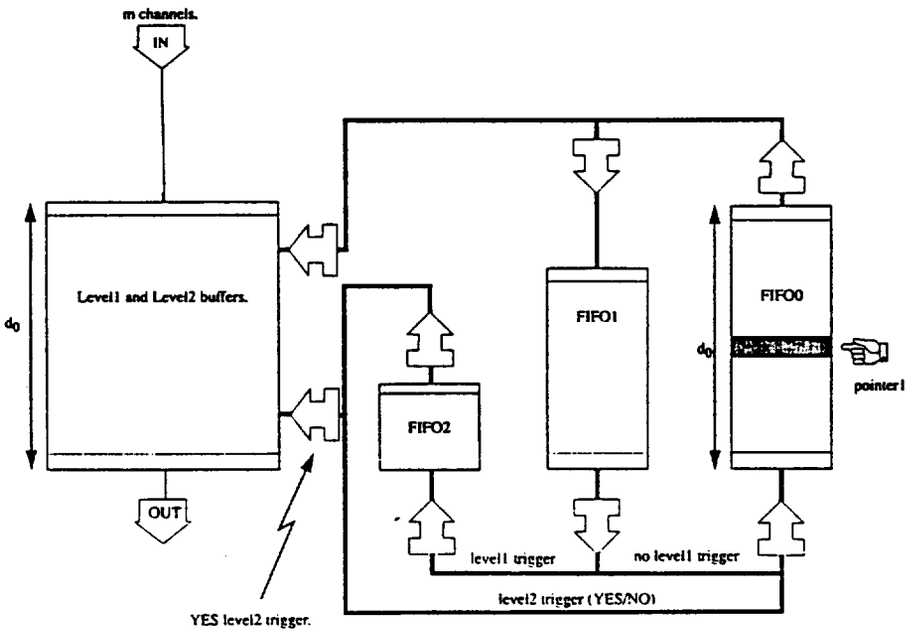


Fig 6. Architecture 4.

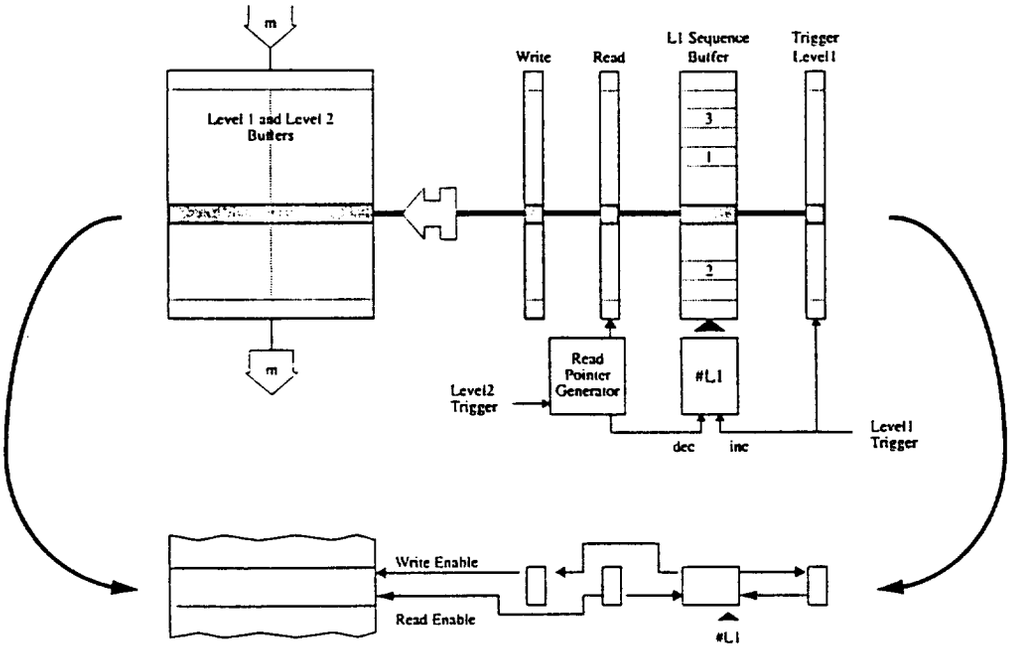


Fig 7. Architecture 5.

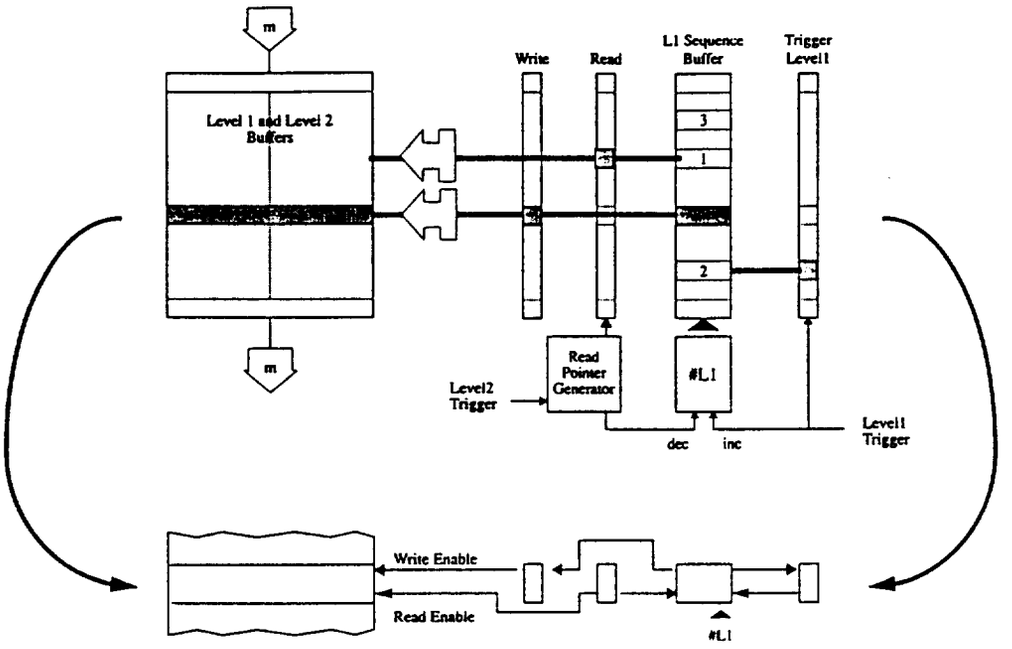


Fig 8. Architecture 6.

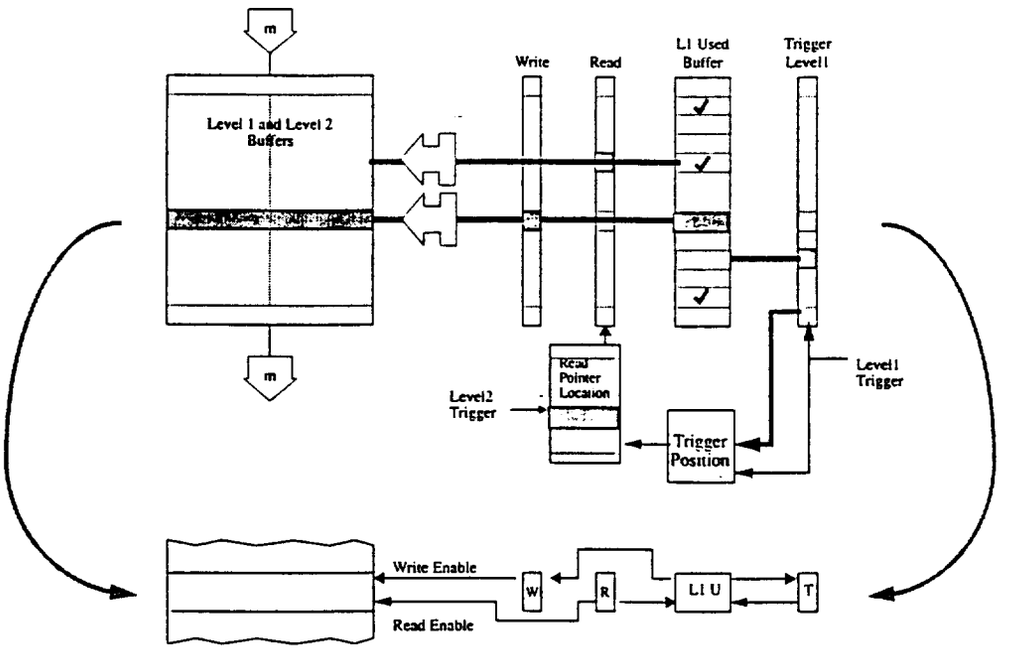


Fig 9. Architecture 7.

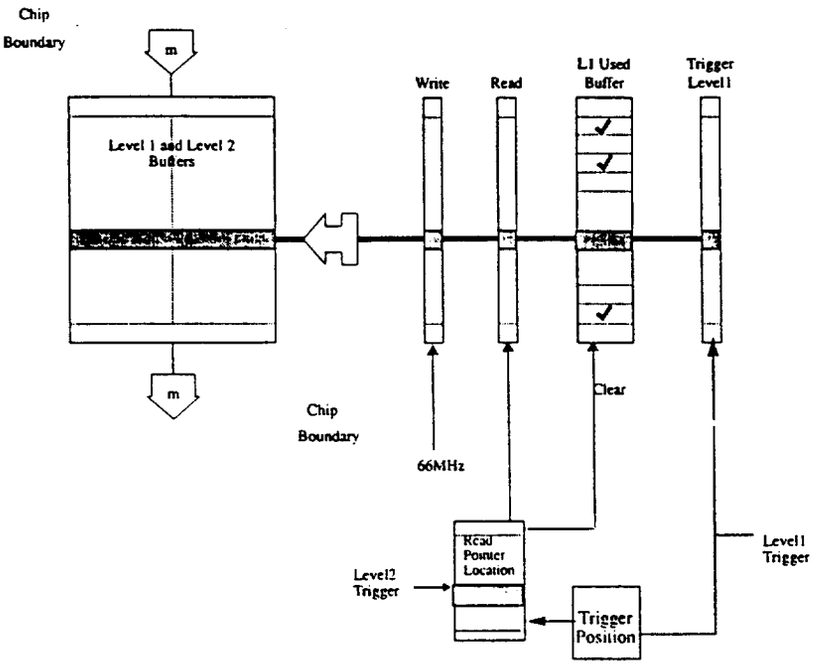


Fig 10. Architecture 7.

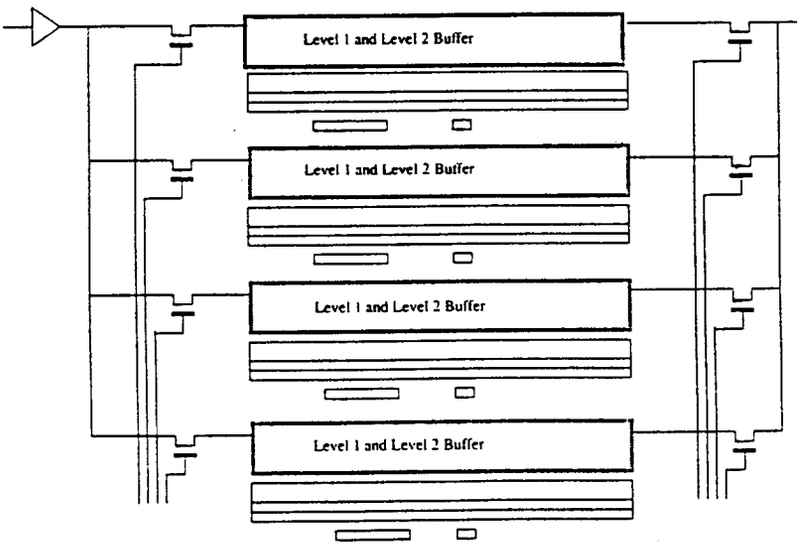


Fig 11. Architecture 8.

HARP : HIERARCHICAL ANALOG READOUT PROCESSOR WITH ANALOG PIPELINING IN CMOS

Francis Anghinolfi, Paul Aspell, Michael Campbell, Erik Heijne, Pierre Jarron and Gerrit Meddeler

CERN, CH-1211 Geneva 23, Switzerland

ABSTRACT

The potential of new analog signal processing techniques and readout approaches made in monolithic circuits for front-end electronics at LHC experiments are presented. The optimisation of the preamplifier with the detector characteristics is discussed. Experimental results of analog memory and signal processing VLSI circuits are presented: a fast.current amplifier, a current sampling integrator and an analog pipeline. The signal peaking time for low capacitance detector elements is less than 15 ns, the sampling rate of the pipeline element in the 1.5 μm CMOS technology reaches 66 Mhz for at least 10 bits precision. An advanced readout architecture, based on this approach, with sparse data scan and on-chip ADC is presented.

The text of this article is published in these proceedings, Signal Processing, Trigger and Data Acquisition Session, under the title:

STUDY OF ANALOG FRONT-END ELECTRONICS FOR SUPERCOLLIDER EXPERIMENTS

Francis Anghinolfi, Paul Aspell, Michael Campbell, Erik Heijne, Pierre Jarron and Gerrit Meddeler

CERN, CH-1211 Geneva 23, Switzerland

Silicon Tracking at High Luminosity.

Guido Tonelli

INFN Sezione di Pisa, Universita' di Pisa, (Italy).

ABSTRACT

The role of silicon devices in charged particle tracking at high luminosity machines is discussed. The sketch of a possible silicon tracker at LHC/SSC is proposed with a discussion of the main limitations and expected performance.

1. Introduction.

High luminosity machines are currently being discussed both for reaching the highest possible collision energy and for producing vast quantities of interesting particles at lower energies. The former is the case of proton colliders like LHC and SSC ($\mathcal{L} = 10^{33} \div 10^{34} cm^{-2} s^{-1}$ at $\sqrt{s} = 16$ and 40 TeV respectively); the latter is the case of storage rings at energies between 1 and 11 GeV, specialized as particle factories to allow precision studies of b, c, τ, k etc. Although for high energy proton colliders, namely for LHC, the ultimate luminosity is expected to be $3.8 \div 5.0 \times 10^{34} cm^{-2} s^{-1}$, the average luminosity $< \mathcal{L} >$ is usually several times smaller than the peak luminosity, so, in the following, I shall consider $10^{34} cm^{-2} s^{-1}$ as a reference $< \mathcal{L} >$.

The use of silicon detectors to perform precision tracking at these interaction rates is a very challenging option in any case, but overall, the LHC requirements are the most difficult ones to achieve. What can be used in proton-proton collisions at $10^{34} cm^{-2} s^{-1}$ is eventually suited for everything else, so in this paper I shall restrict my considerations to the former case.

2. Physics Goals at LHC and Impact on Tracking.

The research program of experiments at LHC can be arbitrary split into two fields: 1) search for new, very massive particles, like Higgs, Z', W' etc. (where the cross sections grow like $\sqrt{s}$ and the signals are very small with important background), and 2) precision studies (in b physics: rare decays and possibly CP violation; the measurement of the mass, branching ratios and decay modes of the top quark if $m_t \leq 200$ GeV/c^2) where the cross sections are very large but the background is overwhelming. As an example consider that already at $\sqrt{s}$= 1.8 TeV the inclusive $b\bar{b}$ production cross section is about 10 μb but the QCD background is many orders of magnitude larger; the same considerations apply, on another scale, for $t\bar{t}$ production, where the inclusive cross section at 16 TeV is expected to be of the order of 1 nb.

The role of a good tracking system in searching for new particles is crucial: let us consider, as an example, the Higgs search with $m_H \leq 800$ GeV. Due to background from $t\bar{t} \rightarrow W^+W^-b\bar{b}$ the decay $H \rightarrow W^+W^-$ is very difficult and one is restricted to $H \rightarrow Z^oZ^o \rightarrow 4$ leptons final state with any possible combinations of two pairs of leptons e^+e^-, $\mu^+\mu^-$,$\tau^+\tau^-$. Since the production cross section is expected to be low (between 0.5 and 5 pb), the selection of a cascade of low branching ratio decay modes reduces heavily the amount of visible candidates and even at an integrated luminosity of 10^{41} cm^{-2}, after acceptance and analysis cuts to remove the physics and instrumental backgrounds, only a few tens of events are expected.

With an event rate so low, acceptance problems become crucial and the role of a good tracking system can be very important to increase the sample of good candidates or to consider all possible channels. For example $Z^o \rightarrow e^+ e^-$ can be measured in principle with calorimeters only, but in practice a good tracking is essential to reject backgrounds. In particular the tracking information is crucial to assess that the four leptons come from the same event vertex, to trigger on high p_t leptons, to match momentum for muons and electrons, to explore the channels with tau's looking for a few highly collimated tracks.

For b physics the acceptance problems are not so critical since more than 10^{13} b's are produced at an integrated luminosity of 10^{41} cm^{-2}. In this case efficiency in b tagging may be low (say 10%) providing that background rejection be extremely efficient ($\sigma_{b\bar{b}}/\sigma_{tot} \approx 1/500$). The study of rare b decays like $B \rightarrow K^* \gamma$, which is expected to have a branching ratio 10^{-5}, or $B_d \rightarrow \pi^+\pi^-$ (B.R.$\approx 5 \times 10^{-5}$) would be possible with a number of b's between 6×10^6 and 2×10^8. If 10^{10} produced $b\bar{b}$ were available, the study of CP violation in the b system would also be possible. By using semileptonic decays of both b's and by selecting high p_t electrons and muons, the standard quantity which is sensitive to CP violation can be measured:

$$\frac{\sigma(B\bar{B} \rightarrow l^+l^+) - \sigma(B\bar{B} \rightarrow l^-l^-)}{\sigma(B\bar{B} \rightarrow l^+l^+) + \sigma(B\bar{B} \rightarrow l^-l^-)} \sim 10^{-3}$$

By using hadronic final states of the b's, like ΨK_s or $\pi^+\pi^-$ the same study can be performed with a smaller number of b's ($\approx 10^8$ $b\bar{b}$ pairs), but, in any case, a good tracking system, aimed particularly to identify secondary vertices, plays a key role in experiments of this kind.

Finally I would mention the importance of b tagging to perform high statistics studies of the top as has been recently proposed. In this case anyway, since double tagging is needed, efficiency in reconstructing secondary vertices must be as high as possible [1].

3. Expected Performance of a Silicon Tracking System.

A tracking system based on silicon detectors in high luminosity colliders should provide various information: 1) the matching of individual particles trajectories to energy deposit in calorimeters and particle tracks in the outer tracking systems. This allows a good E/p measurement, the identification of isolated electrons and muons and provides information on the jet axis; 2) the reconstruction of the z coordinate of the primary vertex to allow the identification of multiple pp interactions within a single bunch crossing; 3) the detection of secondary vertices (s, c, b or τ ; single point resolution ≈ 10 μm)

To accomplish these requirements it seems very useful to couple an inner silicon system to a large central tracking chamber and to have the central tracker imbedded in a strong magnetic field. Let us assume a solenoidal field B= 2 Tesla and a good central tracker with at least 30 measurement points, 1.5 m radius, single point resolution σ = 150 μm.

The main tasks of a magnetic tracking system would be to provide a trigger for stiff tracks; allow a first momentum measurement and provide track roads to look for matched hits in the silicon tracking system; help pattern recognition; provide rough z information at a level of a few millimeters.

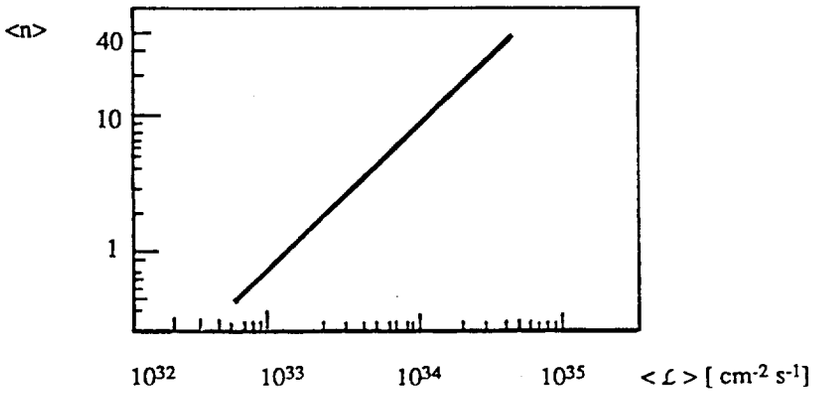


Fig.1 Average number of interactions per bunch crossing at LHC .

Coupled with the redundancy and the big lever arm provided by a large tracking system, the high precision of silicon devices installed in the innermost region can be fully exploited and the overall dimensions of the silicon tracker can be reasonably small. On the other hand in the central region around the interaction spot the system must handle a very large number of tracks coming from hadron interactions at high energy.

Fig.1 shows the average number of interactions per bunch crossing expected at LHC energies assuming $\sigma_{inel} \approx 60$ mb and $\Delta t = 15$ nsec.At high luminosity up to 40 interactions per bunch crossing are expected on average, therefore it is necessary to identify multiple events in the same bunch crossing using the fact that they are spread for several centimeters in z depending on the machine parameters.

Fig.2 shows, for different luminosities, the fraction of events with another vertex within 1mm distance in z.

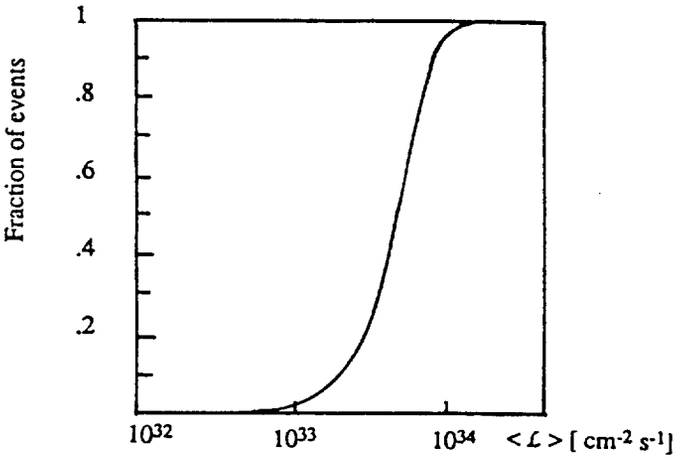


Fig.2 Fraction of events with another vertex within 1 mm vs luminosity at LHC .

To disentangle these events σ_{vz}, the longitudinal resolution on the primary vertex, is required to be « 1mm.

For $|\eta| < 2$, $dN/d\eta \approx 5.5$ and $\langle n \rangle = 40$ we expect about 1000 charged tracks in the average minimum bias event and an additional number of spirals due to low momentum particles. Assuming a cylinder of silicon detectors surrounding the interaction region at R = 10 cm, without any z information all events pile-up in the r-ϕ view and we have an average track density of 1.5 tracks/mm. The z information will reduce strongly this density which is, nevertheless, the "natural environment" for silicon detectors with granularity ≈ 50 μm.

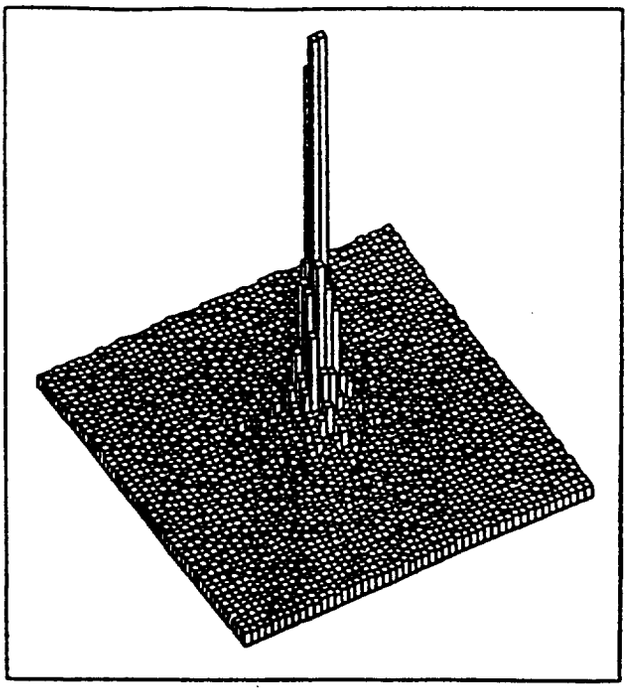


Fig. 3. Track density for 1 TeV jets, Pithia 4.8.(from ref. 2)

The situation can be more complicated for highly collimated jets of particles where the problem of ambiguities can be more severe. Fig. 3 shows the result of a simulation where many jets with p_t larger than 1Tev hit the same point in the middle of an array 1cm x 1cm placed at a radial distance of 10 cm from the interaction region of a p-p collider at SSC energies [2].The bin size of the Lego plot is 200 μm. The typical jet core multiplicity at this distance is 12/cm^2 with tails up to 30 particles/cm^2. The mean angular track separation is 0.5 mrad; jet angular width, $\theta/2$ = 10 mrad; p_t of tracks in the jet core is 50 GeV.

Aiming at an efficiency in track reconstruction in high p_t jets ≥ 90%, a real xyz information on track impact point is necessary. Table I summarizes the main features of a silicon tracking system at LHC/SSC.

4. The Building Blocks: Pixel and Double-Sided Microstrip Detectors.

The ingredients to cope with these requirements are very sophisticated devices with a single point resolution of about 10 μm and the ability to withstand very high rates.

At R ≤10 cm from the beam, only pixel devices can be used. They provide true spatial points with a resolution $\sigma \approx d/\sqrt{12}$ where d is the pixel size, and a two track separation ≈ d. The probability of having ambiguity or overlap even in high p_t jets is low for pixel size 50 μm ≤ d ≤ 200 μm. Fig. 4 shows that the fraction of fully resolved events in high p_t jets above 1 TeV is around 90% for d = 100 μm and about 99% for d = 50 μm, for perpendicular incidence and R=10 cm [2].

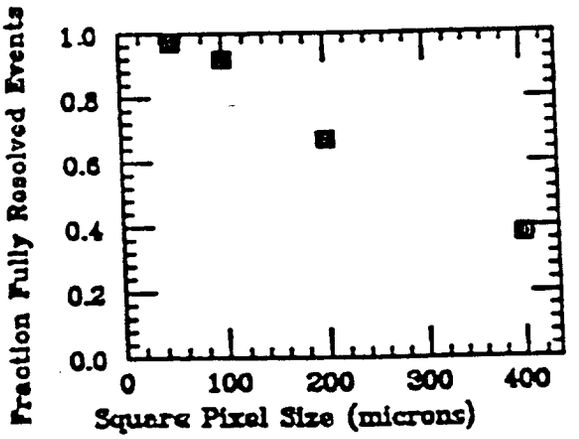


Fig. 4 : Fraction of fully resolved events vs pixel size in jets with $p_t \geq 1$ TeV, at SSC energies, R=10 cm, perpendicular incidence (from ref.2)

Pixel detectors are ideally suited to cope with the requirements we are dealing with but, unfortunately, they are still in development. A big effort is under way in many laboratories to provide smart solutions to the problem of fast readout of a large number of channels concentrated in a small region [3].

Double-sided microstrip detectors can provide xy projections with point resolution σ ≈ 10 μm and two track separation ≈ 100 μm. They are available and have already been used in large experiments (namely ALEPH) ; the r-ϕ, r-z views can be combined with the information of the other tracking systems to give an impact parameter resolution below 100 μm for stiff tracks [4]. The r-z information can be used to identify the z coordinate of the primary vertex with a resolution easily better than 1 mm.

Both devices, to be used in high luminosity hadron colliders, require some local intelligence to perform zero suppression, some form of analog fast pipelining to match the high frequency of interactions, low power consumption etc. Here we assume that progress in microelectronics will be such in the next five years that the most of these problems will be solved.

5. Radiation Damage.

The weakness of silicon devices in high radiation environments is well known and a lot of effort is put in looking for more radiation resistant processes, primarly for electronics but also for detectors.

It is generally accepted that standard microstrip detectors can stand up to 4 x 10^{12} mip/cm^2. This means that useful information (the released charge) is collected on each readout element with a signal to noise ratio still acceptable ($\geq$ 10:1). Since the standard dimensions of read-out elements in this case are 2.5 x 10^{-2} cm^2 (5 cm long strips times 50 μm readout pitch) we can equivalently say that silicon detectors can stand a maximum number of mip per readout element : (4 x 10^{12} mip/cm^2)x(2.5 x 10^{-2} cm^2) = 10^{11} mip/readout element; or, assuming 1 year = 10^7 sec, the maximum rate per readout element becomes: 10^4 mip/sec·readout element. Here we assume that the overall damage is proportional to the volume of the wafers so, as a first approximation, by subdividing the damage into more readout elements the overall radiation resistance is increased. Increasing the granularity as far as the detectors are closer to the beam becomes necessary not only to reconstruct particles which are highly collimated but also to stand radiation effects.

In Table II a comparison among different devices (pad detectors, daisy-chained microstrip devices, small sized microstrip and pixel detectors) is shown to give an idea of the intrinsic different radiation resistance of the various detectors.

Fig. 5 shows the charged particle flux vs radial distance from the beam at different luminosities in hadron colliders at 90°. On the right axis is shown the minimum density of readout elements which can be used to safely withstand a given flux and the device corresponding to this granularity. As an example of the use of this figure one can see that below 10 cm, at 10^{34}, only pixel detectors can be used but it comes out quite surprisingly that a pad detector (i.e. 1 cm^2 for pre-shower sampling) at 2 meters distance is much more critical than a pixel device at 5 cm.

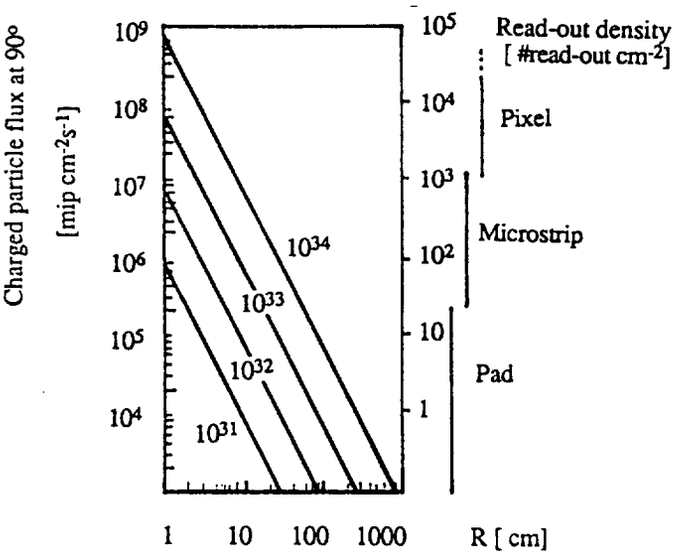


Fig 5: Charged particle flux at 90° vs radial distance to the beam axis for various luminosities.

Obviously these are very simplified considerations which do not take into account many factors; surface effects are not considered; radiation damage due to neutrons will reduce the useful lifetime of devices; a possible inversion of the starting material is not considered; other sources of radiation are not included (beam injection, beam gas and beam pipe interactions ecc.); on the other hand also other effects, which can increase the radiation resistance, are not considered like a reduction in integration time, AC coupling, the use of absorbers for low energy neutrons.

6. A Possible Sketch.

According to the previous considerations a possible sketch of a Silicon Central Tracking system is shown in fig. 6. Three planes of silicon detectors are installed around the interaction region with two endcaps assembled in circular rings.The first layer is made out of pixel devices (100μm x 100 μm) installed at 4 cm distance from the beam line where the flux of particles from interactions only is expected to be 10^8 mip/cm^2 s; the density of readout elements is correspondingly large (10^4/cm^2). A second layer, made out of small double sided microstrip devices, is positioned at 10 cm distance; the strips are, as usual, on a 50 μm pitch but the detectors are only 1 cm long.

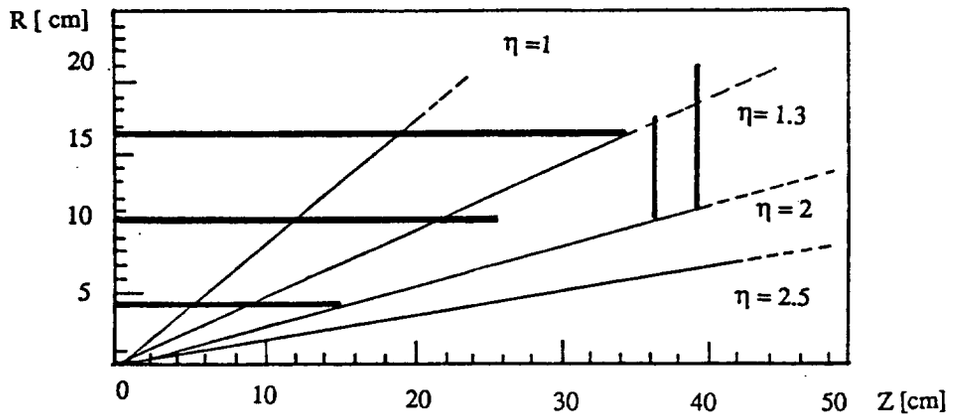


Fig. 6. Sketch of a central silicon tracking system.

This is needed to allow a readout density of about 200/cm^2 which is necessary to stand fluxes > 10^6 mip/cm^2 s. The same small-size detectors are used to equip the endcaps that cover a large fraction of rapidity. The third plane is made out of standard double-sided 25 cm^2, 50 μm pitch.

Table III gives the number of readout elements of the whole system which adds up to 10^7 channels. In principle this number is on a linear extrapolation of the trend of the last 10 years; the complexity of the silicon systems used in high energy physics has increased by about two orders of magnitude every 5 years in the past (from ~ 10 read-out elements in NA1 in 1980 to ~ 1,000 channels in fixed target experiments in 1985, to ~100,000 in Aleph in 1991. So to gain two more orders of magnitude in the next 5 years does not seem completely inconceivable. In practice a complete new set of problems must be solved. For example the heating up of the whole system due to power consumption of electronics and detectors. With the actual values for analog preamplifiers (around 0.5 mW/channel) we end up immediately with an astonishing 5 kW which is clearly not manageable. On the other hand more speed in read-out means more power consumption and it seems actually difficult to imagine read out elements at 66 MHz clock and power consumption in the range of ~ 10 μW/channel.

Finally Table IV shows the expected occupancy of the whole system for minimum bias events.

Conclusion

Silicon tracking at high luminosity can now be conceived since some basic blocks already exist (double-sided detectors) and an increase in granularity could be the right approach to face radiation problems for detectors. Pixel devices will be crucial for tracking in future hadron colliders. The increase in radiation resistance of both detectors and electronics is one of the main goals to achieve. Detectors will work if high density, low power, 15 nsec readout electronics with sparse readout will be available soon. A strong R & D effort must be concentrated on these items.

References.

[1] F.Bedeschi's talk in these proceedings.

[2] SSC Detector R&D Proposal LBL, July 8, 1987.

[3] E.Hejine's talk in these proceedings.

[4] E.Focardi's talk in these proceedings.

Table I

Position resolution	10 μm
Two track separation	100 μm
Impact parameter resolution	20 μm for p >10 GeV
Z vertex resolution	100 μm
Angular coverage	$\eta \leq 2$
Momentum resolution	$\sigma_{p_t}/p_t \leq 20\ \%\ p_t$
Efficiency for high p_t isolated tracks	> 90 %
Efficiency in b tagging	> 10 %
Occupancy	~ 1%
Radiation length at 90°	< 2%

Table II

Device (Dim. of readout el.)	**Read-out density** (# readout·cm^{-2})	**Maximum flux** (mip·cm^{-2} s^{-1})
Pad detectors (1 cm^2)	1	10^4
Daisy-chained μstrip (50 μm x 20 cm)	10	10^5
Small size μstrip (50 μm x 1cm)	4×10^2	4×10^6
Pixel detectors (100 μm x 100 μm)	10^4	10^8

Table III

Device (Dim. of readout el.)	**Read-out density** (# readout·cm^{-2})	**Active area** (cm^2)	**# Channels**
Pixel detectors (100μm x 100 μm)	10^4	~ 750	~ 7.5×10^6
Small size double sided (25 μm x 1 cm)	400	~3, 000 (x 2)	~ 2.4×10^6
Standard double sided (50 μm x 5 cm)	40	~7, 000 (x 2)	~ 5.6×10^5
Endcaps	200	~1, 000 (x 2)	~ 4.0×10^5
Total		~ 12 m^2	~ 1.1×10^7

Table IV

Occupancy from real tracks (including spirals, conversions etc.)	~10, 000 / crossing	
Noise hits:		
Pixels (S/N > 100:1)	~ 7,000 / crossing	
Small size double sided (S/N >30:1)	~ 10,000 / crossing	
Standard microstrips (S/N > 20:1)	~ 5,000 / crossing	
Total occupancy	~ $3 \cdot 10^4$ /crossing	< 1%

DEVELOPMENTS ON Si DETECTORS

E. Focardi

INFN and Scuola Normale Superiore, Pisa, Italy

ABSTRACT

The status of the art of the developments on Si detectors made in Pisa is described. Emphasis is put on the results of the tests performed in the laboratory and the application of double sided Si strip detectors in the LEP collider, including some preliminary results from the 1990 LEP run. In the meantime, some effort has been put in the development of pixel structures, several of which have already been built.

1.INTRODUCTION

The development of double-sided Si strip detectors has started in Pisa several years ago when small diodes 1 cm^2 have been fabricated to test the working principle. The basic idea to isolate n^+ strips in the ohmic side is to insert p^+ blocking strips between them, fig.1, ref 1; in this way the electron accumulation layer can be interrupted and the ohmic side segmentation can be used. Then 5x5 cm^2 detectors have been built to test the fabrication process for larger area devices.
By using the punch-through effect between two p^+ junctions, the juction side biasing scheme has been studied. A tuning of the ohmic side accumulation layer has been made by choosing a suitable pattern of p^+ blocking strips between bonding pads and guard ring. An external AC chip has been developed to prevent current going from the detector to the amplifier. These detectors have been installed as part of the ALEPH Si vertex detector for 1990 LEP running; the high spatial resolution of these devices improves the method of tagging decay vertices among the collision products of e^+e^- interactions.

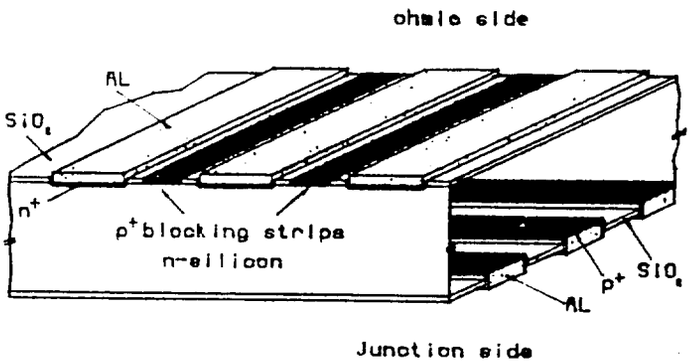


Fig.1: Schematic view of a double sided Si strip detector.

2.DOUBLE SIDED Si STRIP DETECTORS

The fabrication process of double sided Si strip detectors has been already described in detail elsewhere, ref.2; here I will give the main characteristics of the detectors. 4 " n-type high resistivity (>4 KΩ cm) 300 μm thick Si wafers from Wacker have been used, they were polished on both sides to allow precise processing steps. 5x5 cm^2 double sided Si strip detectors have been fabricated in the central region of the wafer, around this several test structures have been built to study the most significant parameters of the process.

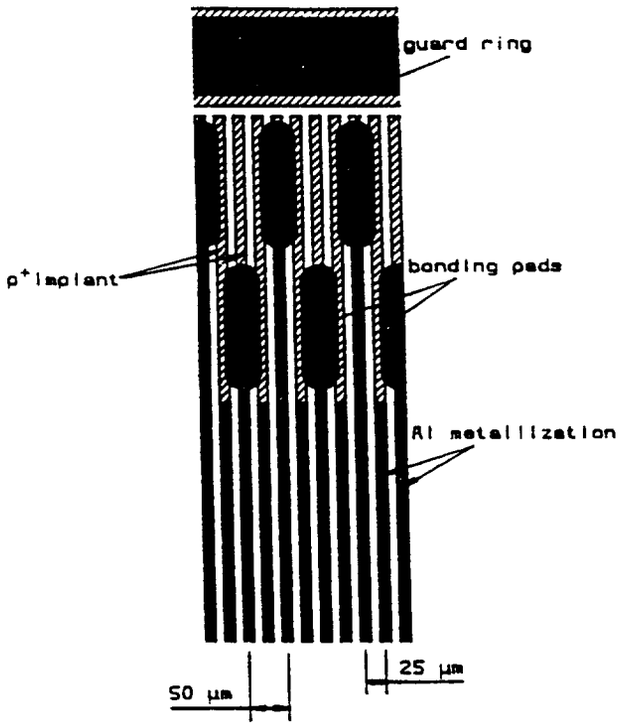


Fig.2: Strip pattern on the junction side.

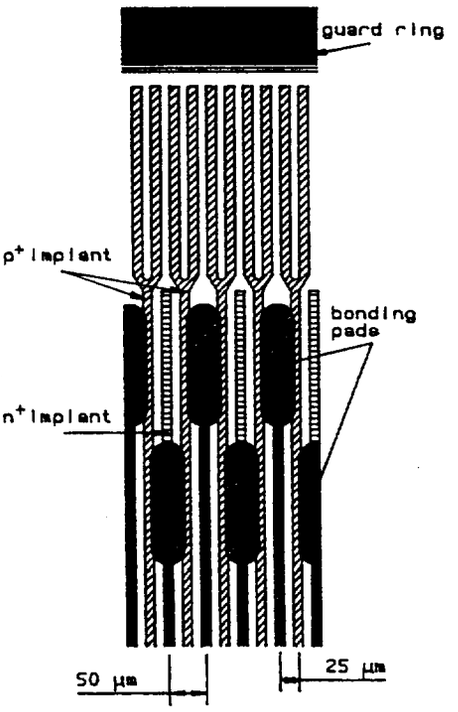


Fig.3: Strip pattern on the ohmic side.

On the junction side (p side) there are p^+ implanted strips with 25 µm pitch, and there are bonding pads every 50 µm, fig.2. Very high interstrip resistance (several GΩ) prevents the strips from floating and using properly the charge partition between them. To avoid this problem the punch-through effect between two close p^+ implants has been used to bias the strips: the distance between the guard ring and the p^+ strips is small (few microns) and such that the voltage difference between guard ring and strips is a few Volts and constant in equilibrium conditions.

On the ohmic side (n side) there are n^+ implant strips with 50 µm pitch interleaved with p^+ strips. The scheme to interrupt the electron accumulation layer and allow for individual strip readout has been widely studied in test structures; the effect of implant dose and geometry of the p^+ 'blocking strips' has been tuned. In particular a 'channel stop' is needed at the edge of the readout strips to prevent low resistance among the strips and the guard ring, fig.3.
Fig.4 shows a typical interstrip resistance as a function of the reverse bias voltage.

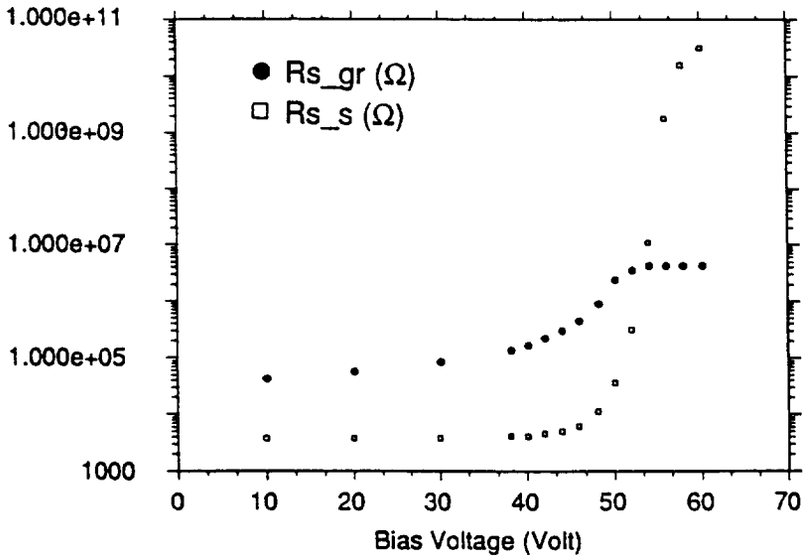


Fig.4: R_{S_S},interstrip resistance on the ohmic side
R_{S_gr}, resistance between strips and guard ring.

The total leakage current of these detectors is in the range of few hundred nA, with this value measured at a bias voltage >1.5 times the depletion voltage. Fig. 5 shows the distribution of leakage current for all detectors produced so far: out of 120 detectors produced, 7 have a reverse current larger than 10 μA and are not shown in the plot. Detectors with leakage current above 2 μA are rejected. A scanning of the leakage current for each strip on the p-side is performed; if necessary the same scanning is done on the n-side to check for local problems. Typical strip leakage current is 100 pA, most detectors have no strips with I>10 nA. After cutting a stability test is done, the leakage current is monitored over several hours; detectors showing instabilities are rejected. After these selection criteria a yield of 75% is obtained.

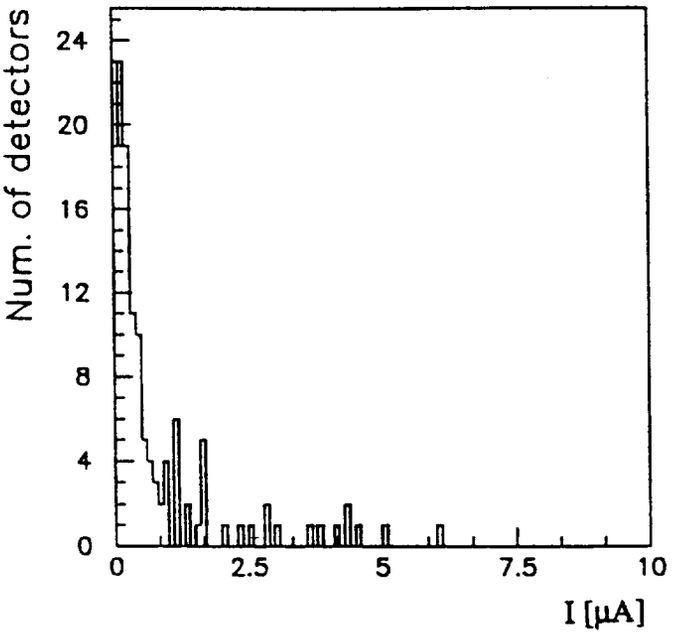


Fig.5: Distribution of the total leakage current for all detectors produced in the last two years.

3.VERTEX DETECTORS APPLICATION

These double sided Si strip detectors have been developed for the ALEPH vertex detector (VDET), ref.3; they have been installed as part of this detector for the LEP 1990 run, ref.4. Fig.6 shows a sketch of a 'face' made of two 'modules'.

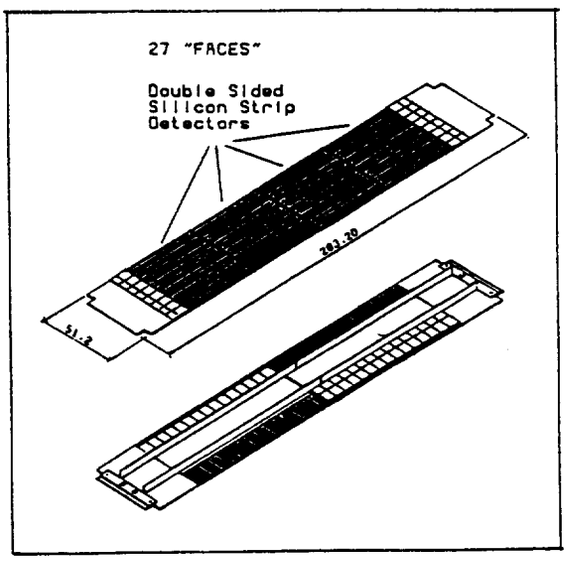


Fig.6: Sketch of one face: top, r-ϕ wiew up; bottom, r-z view up.

A module is the elementary unit of the detector, it consists of 2 double sided Si strip detectors and 2 ceramic fan-outs used as mechanical support and as support for the front-end electronics. To prevent saturation caused by leaky strips or different dc input levels in the charge sensitive preamplifier, a capacitive coupling between strips and preamplifier is used. An external AC chip has been built with capacitors (210 pF) made by double polisilicon; the pitch is 100 μm, same as the electronics; to reduce the stray capacitance a quartz substrate has been chosen. Before the installation in Aleph some modules were put in a test beam at Cern SPS; as a preliminary result a spatial resolution of 15 μm in the r-ϕ projection (100 μm readout pitch) and 24 μm in r-z projection (200 μm readout pitch) were obtained.

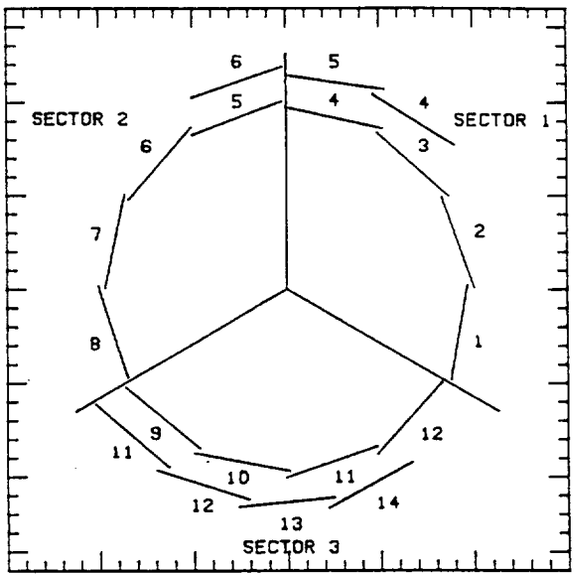


Fig.7: Faces installed in Aleph for 1990 LEP run.

19 faces were installed in Aleph in Feb '90, fig.7; 150 K hadronic Z^0 were collected with VDET by the end of the run. After a crude alignment, a preliminary exercise in the impact parameter has been made: the primary vertex is calculated on an event by event basis, then the tracks hitting the vertex detector are forced to pass trough the corresponding VDET hit keeping the same momentum p as determined by TPC. In these conditions the impact parameter resolution in the r-ϕ plane for $p>p_0$ is shown in fig.8.

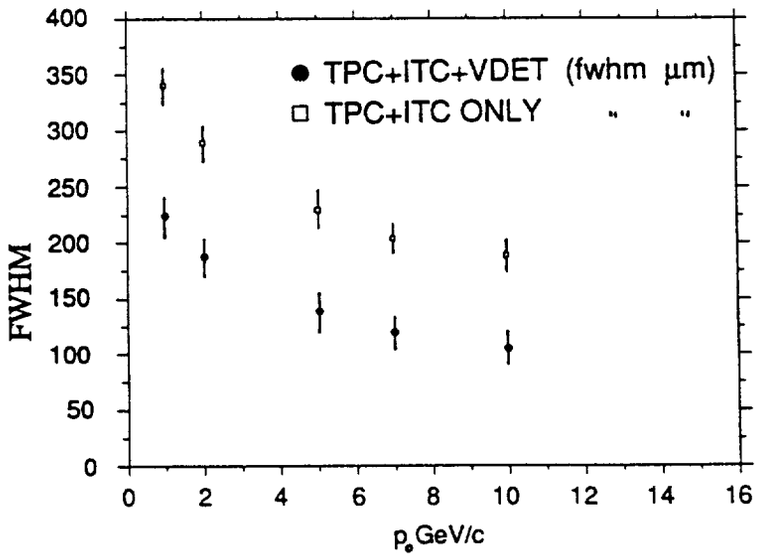


Fig. 8: Impact parameter resolution in r-ϕ plane for $p>p_0$

4. PIXEL DEVICES

For the next generation of high luminosity hadron colliders (SSC, LHC), events with highly collimated tracks inside jets can prevent the use of double sided Si strip detectors; in fact space ambiguities due to multiple hits in the same wafer can be left unresolved, if the signal to noise ratio is too small there is no way to use the pulse height correlation between the two projections to solve this kind of ambiguity. If a Si pixel device is used a true 2-dimensional space information can be provided. The time ambiguity has also to be solved: events rate approching 100 MHz are foreseen, up to now no electronics work in this range. The problem is to store the information of interested pixels in a pipeline until a decision about the interest of the event has been taken. The first level trigger may arrive .5 μsec after the event, in this case a pipeline of 50 events is required.
The last problem is the high radiation level in the next hadron colliders where a flux of fast neutrons of 10^{13} n/cm^2 at $L = 10^{33}$ cm^{-2} sec^{-1}, r=10 cm, is expected. Several linear (100 μm pitch) and square (380 μm pitch) arrays of pixels have been built to test combined low capacitance detectors and suitable electronics. These structues will then be irradiated to study the effect of high level radiation doses.

5. CONCLUSIONS

After several years of development, the double side readout Si strip detectors can now be fabricated with high level of reliability. The first results in the Aleph Si vertex detector show that they are suitable devices to cope with the requirements of vertex detectors in general. Tests have to be done to understand the radiation resistance of these detectors and eventually improve it. The effort in understanding how the sensitive element area reduction can improve the use of Si detectors in the next generation of high luminosity hadron colliders has started.

REFERENCES

1. G.Bagliesi et al., " A double side readout silicon strip detector. A new device for vertex detection in high energy experiments", INFN PI/AE 86/10
   G.Batignani et al., Nuclear Instruments and Methods **A273**, 677 (1988)
2. G.Batignani et al., to be published in Nuclear Physics B, paper presented by G. Tonelli at the "2nd International Conference on Advanced Technology and Particle Physics, Como, Italy, 11-15 June, 1990"
3. P.Holl et al., Nuclear Instruments and Methods **A253**, 587 (1987)
4. G.Batignani et al., to be published in Nuclear Physics B, paper presented by E. Focardi at the "2nd International Conference on Advanced Technology and Particle Physics, Como, Italy, 11-15 June, 1990"

EFFECT OF PILE-UP OF MINIMUM BIAS EVENTS ON TRACKING IN A MAGNETIC FIELD

C.M. BUTTAR[3], T.SLOAN[2], I. TEN HAVE [1]
1) *Dept. of Physics and Astronomy, Glasgow University.*
2) *Dept. of Physics, Lancaster University.*
3) *Dept. of Physics, Sheffield University.*

The pileup of minimum bias events in a tracking detector at the LHC has been simulated for a luminosity of $4 \times 10^{34}\text{cm}^{-2}\text{s}^{-1}$. The effect of the magnetic field on tracking and muon isolation in top quark production has been studied and shown not to be large.

At LHC energies the inelastic cross-section is around 100mb and so at the highest LHC luminosities ($4 \times 10^{34}\text{cm}^{-2}\text{s}^{-1}$) there will be on average 60 minimum bias events in a single bunch crossing. As the particles have a soft momentum spectrum, the large number of low momentum tracks which spiral in the magnetic field lead to a large number of hits in tracking detectors.

We studied the effect of these soft tracks on tracking in a 4T magnetic field. Four-vectors were generated using EUROJET and the UA5 Monte Carlo, GENCL, and tracked through the magnetic field. The number of tracks and their hits on a cylindrical detector covering $|\eta| \leq 2$ at various radii are shown in figs. 1 and 2. There are a large number of hits per track at small radii due to the spiralling of the tracks in the magnetic field. However at radii above about 1.0m the number of hits per track <1 because the tracks spiral inside the detector. The discrepency between the GENCL data and the EUROJET data is due to the lack of tuning of EUROJET. The GENCL generator had been tuned to reproduce UA5 minimum bias data at various energies and then used to generate minimum bias events at 16 TeV.

To assess the effect of the minimum bias tracks on a physics process , we looked at the number of extra hits within 10cm of a decay muon from a 100 GeV t-quark. The muon isolation, defined in this way, is shown as a function of radius using EUROJET events in fig. 3. Again there is a rapid drop with radius and for radii above 1.0m the muon is very isolated.

We also studied the dependence on the magnetic field strength for a detector of radius 0.7m. The results for EUROJET events are shown in figs. 4,5 and 6. At low fields there are only a few hits per track as the tracks hit the calorimeter before spiralling. At medium fields there are many hits per track because of the tracks spiralling. At high field the number of hits per track falls again as the tracks spiral inside the detector radius. The muon isolation does not significantly depend on the magnetic field.

The effect of minimum bias events on magnetic tracking is not significant for detectors of radii >0.7m. A strong magnetic field is an advantage as it confines the spiralling tracks to inside the detector radius. The effect of pileup on the isolation of muons is not significant for radii >0.7m and is effectively independent of magnetic field.

We would like to thank R. Dewolf for providing the GENCL events.

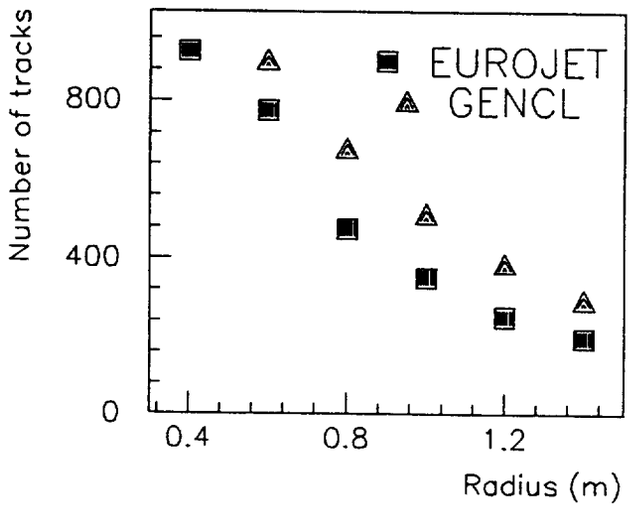


Fig.1

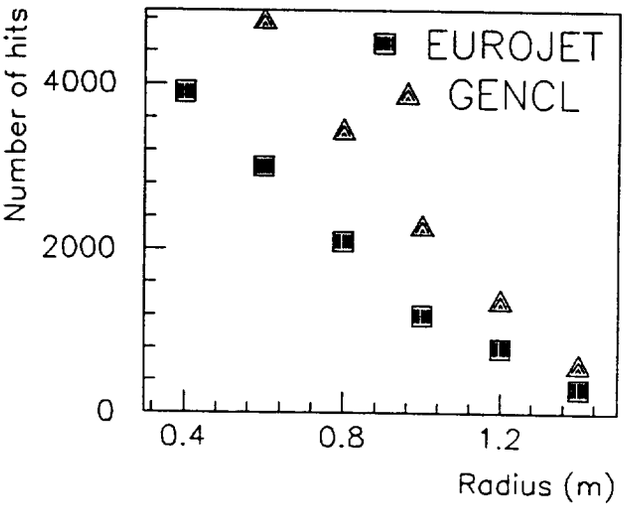


Fig.2

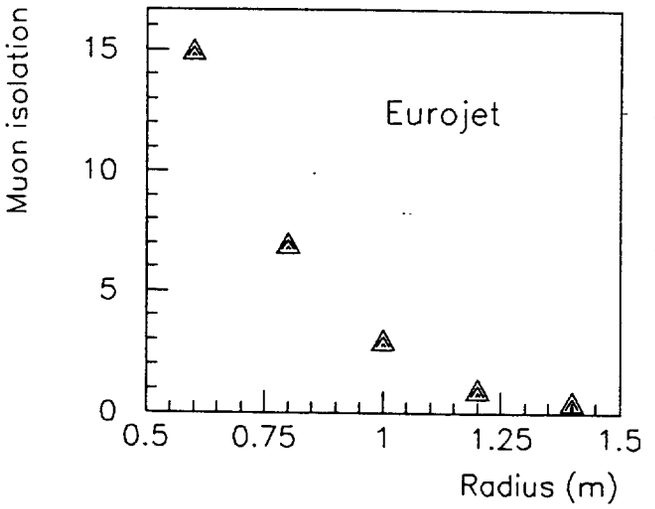


Fig.3

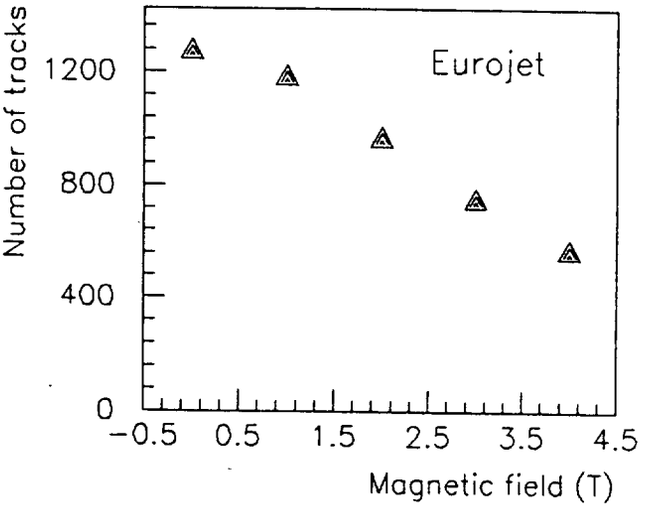


Fig.4

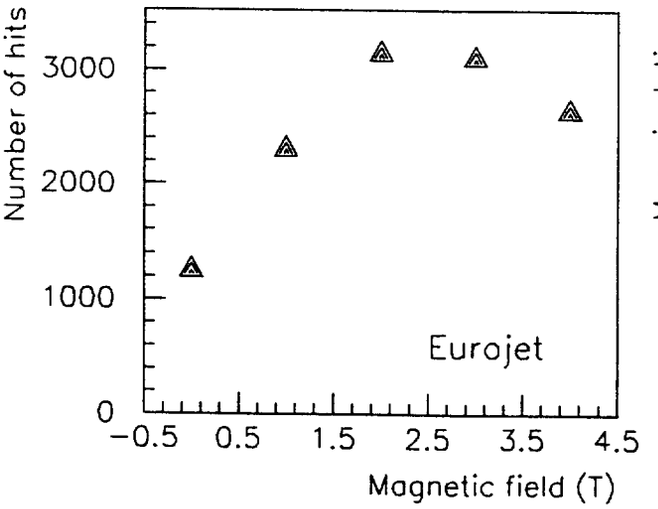


Fig.5

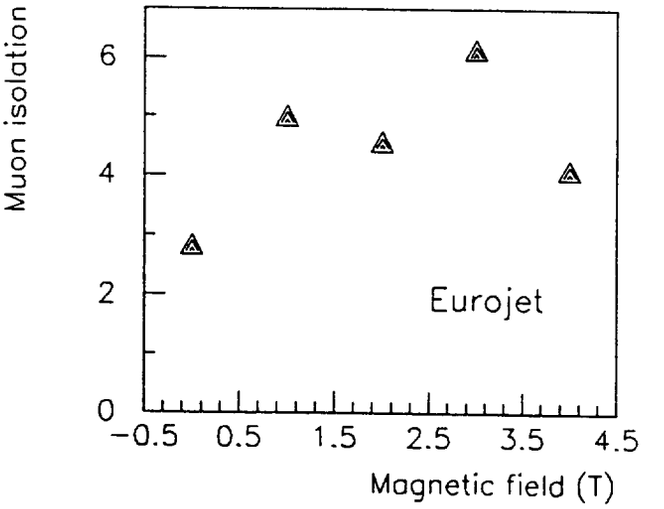


Fig.6

RADIOACTIVATION IN LHC CALORIMETERS

G. R. Stevenson
CERN, Geneva, Switzerland
10 October 1990

Abstract

This paper shows how inelastic hadron collision (star) densities in an LHC calorimeter structure can be used to determine other quantities of interest such as the distribution in concentration of a particular radio-isotope, the contact dose rate from remanent radioactivity or the current pedestal in a detector embedded in the calorimeter material due to this induced remanent radioactivity. Specific examples relating to expected LHC performance are given for an idealized spherical lead calorimeter.

1 Introduction

Monte-Carlo calculations of the cascade generated by secondary particles from proton-proton collisions at 8+8 TeV within a spherical lead shell are described elsewhere in these proceedings [1]. In addition to determining the energy deposition in the spherical shell, these calculations also gave the density of inelastic hadron interactions (stars) averaged over various rapidity and depth intervals. The results of these determinations of star densities are given in Table 1. The purpose of this note is to show how these star densities can be

Table 1: Star density in cm^{-3} per collision

η interval	0.0 - 1.0	1.0 - 2.0	2.0 - 3.0	3.0 - 4.0	4.0 - 5.0
Radius (m)					
2.000 - 2.025	0.519E-05	0.233E-04	0.278E-03	0.947E-03	0.629E-02
2.025 - 2.050	0.366E-05	0.219E-04	0.339E-03	0.118E-02	0.889E-02
2.050 - 2.075	0.302E-05	0.199E-04	0.335E-03	0.133E-02	0.996E-02
2.075 - 2.100	0.243E-05	0.185E-04	0.360E-03	0.151E-02	0.108E-01
2.100 - 2.150	0.161E-05	0.169E-04	0.376E-03	0.161E-02	0.108E-01
2.150 - 2.200	0.115E-05	0.145E-04	0.366E-03	0.157E-02	0.109E-01
2.200 - 2.300	0.594E-06	0.109E-04	0.311E-03	0.138E-02	0.915E-02
2.300 - 2.400	0.293E-06	0.790E-05	0.245E-03	0.109E-02	0.707E-02
2.400 - 2.600	0.111E-06	0.468E-05	0.162E-03	0.688E-03	0.421E-02
2.600 - 2.800	0.280E-07	0.214E-05	0.759E-04	0.331E-03	0.201E-02
2.800 - 3.000	0.729E-08	0.102E-05	0.390E-04	0.154E-03	0.101E-02
3.000 - 3.400	0.135E-08	0.317E-06	0.133E-04	0.513E-04	0.319E-03
3.400 - 3.800	0.591E-10	0.604E-07	0.249E-05	0.100E-04	0.848E-04
3.800 - 4.200	0.000E+00	0.153E-07	0.553E-06	0.305E-05	0.388E-04
4.200 - 4.600	0.000E+00	0.289E-08	0.162E-06	0.959E-06	0.185E-04
4.600 - 5.000	0.000E+00	0.663E-09	0.434E-07	0.492E-06	0.118E-04

used to determine other quantities of interest such as the distribution in concentration of a particular radio-isotope, the contact dose rate from remanent radioactivity or finally the current pedestal in a detector embedded in the calorimeter material due to this induced remanent radioactivity. A general description of rules of thumb for dealing with induced radioactivity at high-energy proton acccelerators is to be found in [2]; more detail is given in [3].

It should be noted that the lead sphere has an inner radius of 2 metres for these calculations and that there is no material within the cones of $|\eta| > 5$.

2 Partial Cross-sections

From the above star densities it is possible to calculate the production of any other isotope in lead whose partial cross-section is known. It is also possible to calculate the production in another material embedded in the lead but which does not perturb the hadron cascade in the lead, e.g. in a silicon detector or in liquid argon. The number of atoms produced per unit volume, N, is given by:

$$N = \frac{n_{tar} \cdot \sigma_{partial}}{n_{Pb} \cdot \sigma_{Pb-incl}} \times S_{Pb}, \quad (1)$$

where n_{tar} is the density of target atoms in the material of interest, n_{Pb} is the density of lead atoms, $\sigma_{partial}$ is the cross-section for the required reaction, $\sigma_{Pb-incl}$ is the star-production cross-section in lead and S_{Pb} is the star density in lead. Thus for ^{24}Na production in lead where n_{tar} is equal to n_{Pb}, and with $\sigma_{Pb-incl} = 1850$ mbarns and $\sigma_{partial} = 10$ mbarns, for a star production rate of 1 cm^{-3}.s^{-1} the saturation activity A_{sat} is given by

$$A_{sat} = \frac{10}{1850} \approx 5 \times 10^{-3} \text{ Bq/cm}^3 \quad (2)$$

3 Remanent Dose Rates

A simple formula, deriveable directly from simple energy conservation relates the dose rate at the surface of a semi-infinite slab to the concentration of a photon emitter which is uniformly distributed in the slab:

$$D = 2.9 \times 10^{-7}\ a\ E \text{ Sv/h}, \quad (3)$$

where a is the specific activity of the photon emitter measured in Bq/g and E is the sum of the photon energies emitted per disintegration in MeV. Semi-infinite means approximately 5 cm deep for iron or lead. For iron, a star production rate of 1 cm^{-3}.s^{-1} corresponds to a saturation activity of 0.12 Bq/g, and so, using the information that the mean photon energy from irradiated iron is 0.8 MeV, for an infinitely long irradiation with no cooling time the surface dose rate close to a slab will be:

$$D = 2.9 \times 10^{-7} \times 0.12 \times 0.8 = 2.8 \times 10^{-8} \text{ Sv/h}. \quad (4)$$

It is traditional to refer dose rates to an irradiation time of one month and a decay time of one day, which is lower by about a factor of three than the dose rate after an infinite irradiation and no cooling time in the case of iron. This dose rate from unit star density is referred to in the literature as the ω-factor, which as the above argument shows, will have a value of 10^{-8} Sv/h for iron. ω-factors for other materials have been determined by Hoefert [4] and are listed in Table 2.

Table 2: Conversion factors

Material	ω-factor $Sv.h^{-1}/(cm^{-3}.s^{-1})$
Iron	1.0×10^{-8}
Copper	1.0×10^{-8}
Stainless steel	1.3×10^{-8}
Aluminium	2.0×10^{-9}
Lead	1.5×10^{-8}
Tungsten	1.1×10^{-8}
Normal Concrete	3.0×10^{-9}
Marble	6.0×10^{-10}

To summarize, the γ dose rate close to the surface of a semi-infinite slab in which there is a uniform density of inelastic interactions is given by:

$$\text{Dose Rate in Sv/h} \quad = \quad \omega \text{ factor} \times \text{Star Density prod. rate in } cm^{-3}.s^{-1} \qquad (5)$$

The star densities listed in Table 1 have been multiplied by the ω-factor appropriate to Lead; the resulting dose rates assuming a luminosity of 10^{31} $cm^{-2}s^{-1}$ and a p-p inelastic cross-section of 60 mbarns are given in Table 3.

Table 3: Remanent dose-rate in Sv/h

η interval	0.0 - 1.0	1.0 - 2.0	2.0 - 3.0	3.0 - 4.0	4.0 - 5.0
Radius (m)					
2.000 - 2.025	0.467E-01	0.210E-03	0.250E-02	0.852E-02	0.566E-01
2.025 - 2.050	0.330E-01	0.197E-03	0.305E-02	0.106E-01	0.800E-01
2.050 - 2.075	0.272E-01	0.179E-03	0.301E-02	0.120E-01	0.897E-01
2.075 - 2.100	0.218E-01	0.167E-03	0.321E-02	0.139E-01	0.969E-01
2.100 - 2.150	0.145E-01	0.152E-03	0.339E-02	0.145E-01	0.976E-01
2.150 - 2.200	0.103E-01	0.131E-03	0.329E-02	0.141E-01	0.981E-01
2.200 - 2.300	0.534E-05	0.982E-01	0.280E-02	0.124E-01	0.824E-01
2.300 - 2.400	0.264E-05	0.711E-01	0.221E-02	0.980E-02	0.636E-01
2.400 - 2.600	0.100E-05	0.421E-01	0.146E-02	0.619E-02	0.378E-01
2.600 - 2.800	0.252E-06	0.193E-01	0.683E-03	0.300E-02	0.181E-01
2.800 - 3.000	0.656E-07	0.919E-05	0.351E-03	0.138E-02	0.910E-02
3.000 - 3.400	0.121E-07	0.285E-05	0.120E-03	0.462E-03	0.287E-02
3.400 - 3.800	0.532E-09	0.544E-06	0.224E-01	0.902E-01	0.764E-03
3.800 - 4.200	0.000E+00	0.137E-06	0.498E-05	0.274E-01	0.349E-03
4.200 - 4.600	0.000E+00	0.260E-07	0.146E-05	0.863E-05	0.167E-03
4.600 - 5.000	0.000E+00	0.596E-08	0.390E-06	0.443E-05	0.107E-03

It should be noted that these dose rates are those that would be obtained by splitting the "calorimeter" open to expose that star densities at the positions shown. They are also relevant to the idealized 2 m internal radius calorimeter used in the calculations. Whereas the dose rate to be expected close to the inner face of the barrel part of a real calorimeter will be close to the 40 μSv/h value to be found in the first line of the second column of Table 3, the dose rates in contact with the forward part of the forward calorimeter will be reduced by inverse-square law arguments from the 0.1 Sv/h level indicated in the Table to several mSv/h. Even so, these levels will entail that all work on the inner and forward parts of the detector structure must be carried out by registered dosimeter holders and that care must be taken not to exceed the specified working limits of accumulated dose (at CERN) of 15 mSv/year. All material inside the inner part of the detector must also be considered as radioactive with consequent restrictions on the movement and manipulation of the detector assemblies.

4 Current Pedestals

The γ dose rates given in Table 3 can also be used to estimate the current pedestal that would be given by a detector embedded in the calorimeter absorber material. Firstly the dose rates should be doubled because one is now considering "infinite" rather than "semi-infinite" geometry. Again the dose rate should be further doubled to allow for the extra dose rate from β-activity in the material. The pedestal can then be estimated simply using the following identity which is contained in the definitions of dose and dose equivalent for photons and electrons.

$$1 \text{ Sv/h} = 1 \text{ Gy/h} = 1 \text{ J/(kg.h)} = 1.7 \text{ TeV/(cm}^3\text{s)} \quad (6)$$

References

[1] G. R. Stevenson, *New dose calculations for LHC detectors*, Proceedings of this conference.

[2] G. R. Stevenson, *Activation at accelerators*, CERN Divisional Report TIS-RP/90-10/CF (1990).

[3] R. H. Thomas and G. R. Stevenson, *Radiological safety aspects of the operation of proton accelerators*, Technical Report Series No. 283, IAEA Vienna (1988).

[4] M. Hoefert and A. Bonifas, *Measurement of radiation parameters for the prediction of dose rates from induced radioactivity*, CERN Internal Report HP-75-148 (1975).

LENGTH OF CALORIMETERS AND EFFECT OF ABSORBERS IN FRONT OF CALORIMETERS

Jürgen Krüger

II. Institute for Experimental Physics, Hamburg University,
Luruper Chaussee 149, D-2000 Hamburg 50, Germany

October 1990

ABSTRACT

A detailed analysis of the longitudinal hadron shower development was performed with the longitudinally finely segmented WA78 calorimeter at CERN (5–210GeV). The shower containment studies allow an optimization of the depth of hadron calorimeters and a reasonable extrapolation for particles and jets to very high energies (≈1TeV).

The effect of absorbers in front of calorimeters on hadrons, electrons and jets was studied systematically with the FCAL calorimeter prototype at CERN (0.5–100GeV).

1. LENGTH OF CALORIMETERS

1.1 INTRODUCTION

The optimum length of a hadron calorimeter is directly related to the longitudinal development of hadron showers.

Longitudinal shower profiles have been measured for single particles and jets with the WA78 hadron calorimeter at CERN in the energy range from 5GeV to 210GeV [1],[2].

A detailed analysis on the shower containment and the influence of dead material (PM-boxes) inside the calorimeter was performed in particular with respect to the optimization of the depth of the high resolution ZEUS uranium scintillator calorimeter ($\sigma_h/E \approx 35\%/\sqrt{E}$) and extrapolations to higher energies.

1.2 THE WA78-H1-ZEUS CALORIMETER TEST

The WA78 hadron calorimeter (Fig. 1) consists of two parts with different absorber material, upstream uranium layers (60 x 60 x 1 cm^3) and downstream iron layers (60 x 60 x 2.5 cm^3). The 1. part (5.4λ) was operated with 12 modules of depleted uranium (10mm)/scintillator (5mm), 4 elements per module (0.45λ) and the 2. part (8λ) with 13 modules of iron (25mm)/scintillator (5mm), also 4 elements per module (0.62λ).

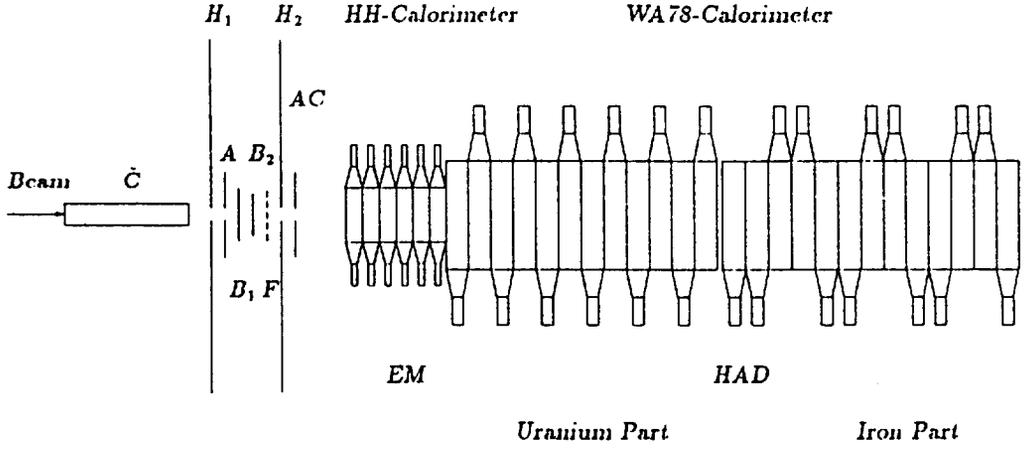


Fig. 1 The Experimental Set Up of the WA78-H1-ZEUS Test

1.3 LONGITUDINAL HADRON SHOWER DEVELOPMENT AND SHOWER CONTAINMENT

The WA78 calorimeter has the advantage of a fine longitudinal segmentation and in addition the measurements allow a reasonable extrapolation to higher energies ($\approx$ 1 TeV).

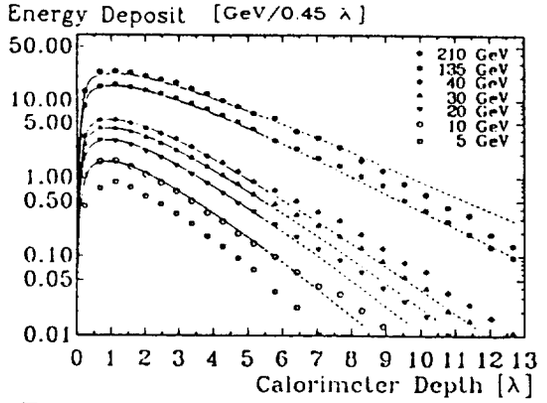


Fig. 2 Longitudinal Shower Profiles for Hadrons between 5 to 210 GeV for all Events

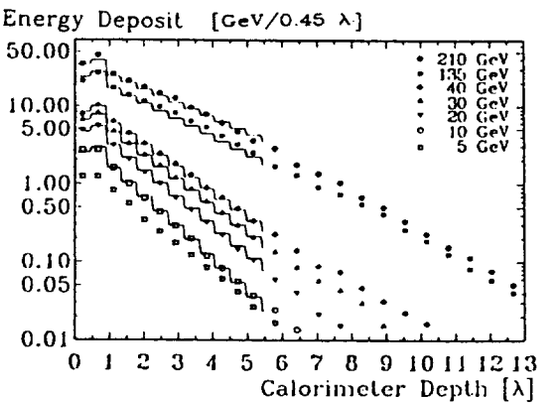


Fig. 3 Longitudinal Shower Profiles for Hadrons between 5 to 210 GeV for Events with Shower Vertices in the First Module

Figure 2 shows the longitudinal hadron shower profiles from 5 to 210GeV for all hadrons (= single hadrons) as function of the calorimeter depth in units of nominal interaction lengths λ. Figure 3 is similar to Fig. 2, but for events with shower vertices in the first module (0.45λ) of the calorimeter. These events are considered to behave like jet-like objects and are also called jets in the following.

A phenomenological function has been fitted to the data. The curves are overlayed and in good agreement with the data for energies above 10GeV.

The parametrization of the energy deposit dE/dx(x) (Fig. 3) as function of the distance x in interaction lengths from the shower vertex is:

$$\frac{dE}{dx}(x) = E_0 \left\{ \alpha \frac{b^{a+1}}{\Gamma(a+1)} x^a \, exp\,(-bx) + (1-\alpha)\, c \, exp\,(-cx) \right\}$$

where E_0 is the incident energy, a=3, $b[\lambda^{-1}]$=19.5, α=0.13$\pm$0.02 and $c[\lambda^{-1}]$=(0.67$\pm$0.03)-(0.166$\pm$0.003) ln(E_0[GeV]/50) .

The shower distributions measured from the front end of the calorimeter (t) for all hadrons are given by the convolution of dE/dx(x) with the shower vertices:

$$\frac{dE}{dt} = \frac{1}{\lambda_\pi} \int_0^t exp\,(-\frac{x}{\lambda_\pi}) \frac{dE}{dx}\,(t-x)\,dx$$

where $\lambda_\pi = 1.11$ represents the interaction length of the incoming hadrons.

In order to determine the optimum length of a calorimeter the fraction of events with a certain shower containment has to be known. The fractions of all hadrons and jets with a shower containment of 95% in the calorimeter as function of the calorimeter depth are presented in Fig. 4 and 5. The criterium for the depth of the ZEUS calorimeter was for example that 90% of the jets are contained in the uranium scintillator calorimeter with 95% of their energy [3].

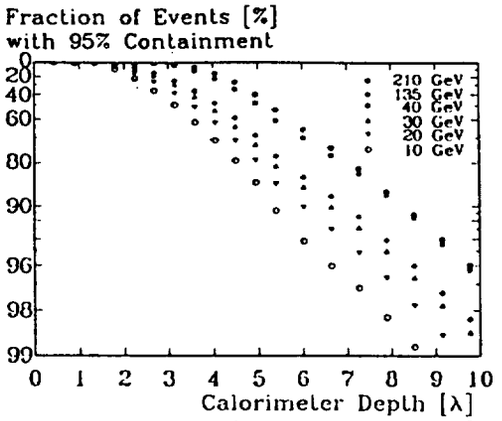


Fig. 4 Fraction of Events with 95% Energy Containment as a Function of the Calorimeter Depth for all Hadrons

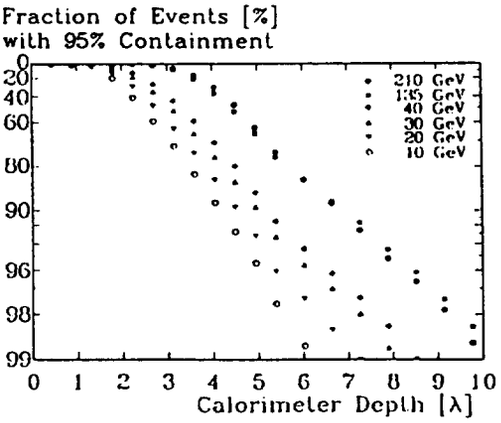


Fig. 5 Fraction of Events with 95% Energy Containment as a Function of the Calorimeter Depth for Events with Shower Vertices in the First Module

1.4 LEAKAGE DUE TO DEAD AREAS

The data offers also the possibility to investigate the influence of dead material, such as PM boxes, at various places inside the calorimeter [1].

The influence on the resolution due to the shower energy lost in the dead material of 0.6λ behind 5.4λ has been studied for 40GeV jets and behind 7.2λ for 135GeV jets. The chosen calorimeter configuration is presented in Fig. 6. It consists of a high resolution hadron calorimeter (a) plus (veto readout section (necessary only for very high energies) (b),) dead material (PM boxes) (c) and a coarser backing calorimeter (d).

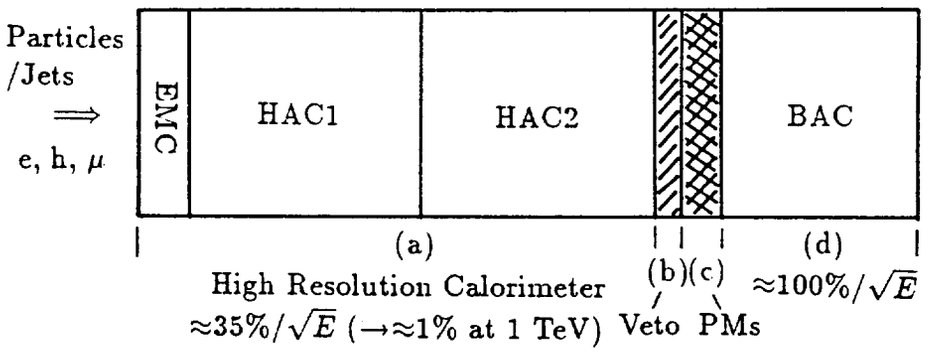


Fig. 6 Calorimeter Design of a High Resolution Calorimeter (a), (Veto Readout Section (b),) PM Boxes (c) and Backing Calorimeter (d)

The fraction of events contributing to nongaussian tails due to the energy lost in the dead material (PM boxes) is measured in units of the calorimeter resolution for hadrons (σ_h/E=35%/$\sqrt{E}$=σ_{35}) as function of the calorimeter depth. This is shown for jets in Fig. 7 and 8 if less than 2% of the shower energy is deposited in the backing calorimeter (E_{BAC} < 2%, valid for about 90% of the events).

With a calorimeter depth of 5.4λ about 2.6% of the 40GeV jets are shifted additionally outside $1\sigma_{35}$ and 0.6% outside $2\sigma_{35}$.

For a corresponding investigation with a calorimeter depth of 7.2λ and 135GeV jets about 3% are additionally outside $1\sigma_{35}$ and 0.6% outside $2\sigma_{35}$.

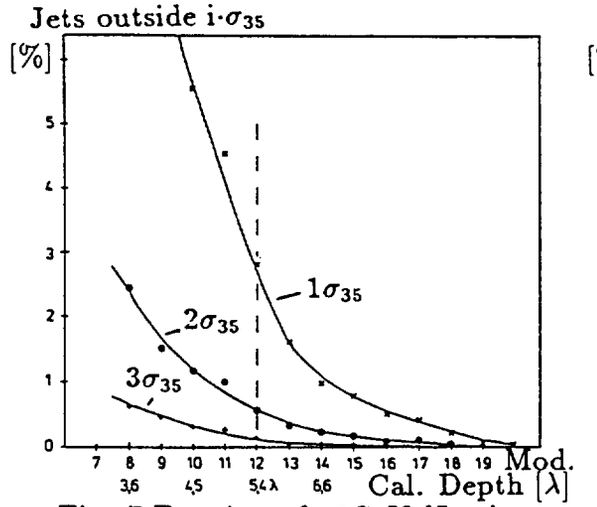


Fig. 7 Fraction of 40GeV 'Jets' outside i·σ_{35} as Fct. of the Calorimeter Depth and E_{BAC} < 2% of the Shower Energy

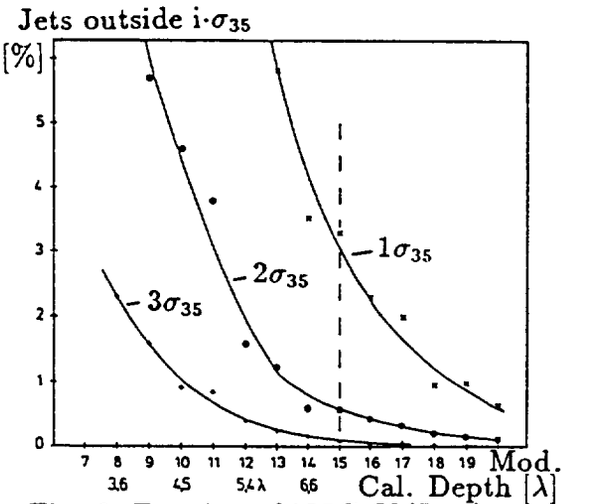


Fig. 8 Fraction of 135GeV 'Jets' outside i·σ_{35} as Fct. of the Calorimeter Depth and E_{BAC} < 2% of the Shower Energy

1.5 EXTRAPOLATION TO 1 TEV PARTICLES AND JETS

As already mentioned a reasonable extrapolation to higher energies is also possible with these data [4].

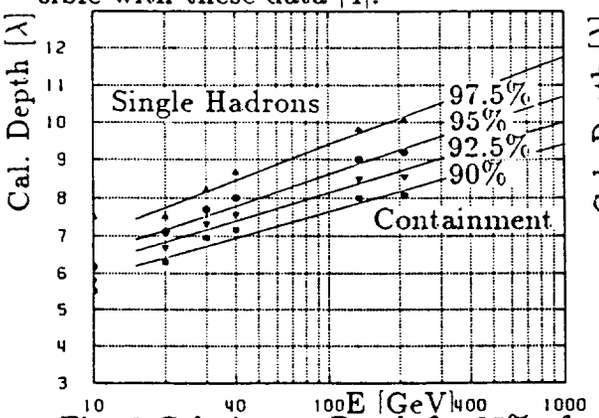


Fig. 9 Calorimeter Depth for 95% of Single Hadrons as Function of the Energy

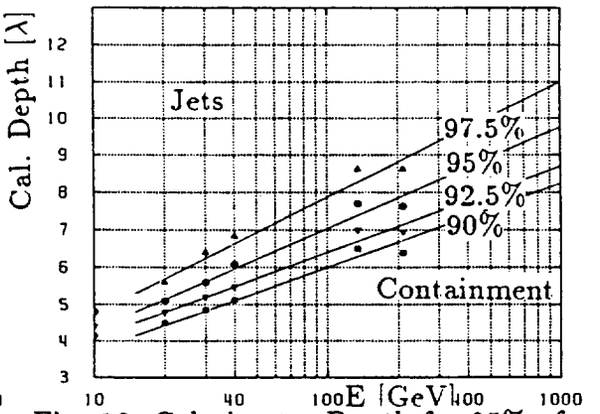


Fig. 10 Calorimeter Depth for 95% of Jets as Function of the Energy

The calorimeter depth needed for a certain shower containment (90%, 92.5%, 95%, 97.5%) as function of the energy is presented for 95% of single hadrons in Fig. 9 and for 95% of jets in Fig. 10. An extrapolation to 1 TeV is also indicated.

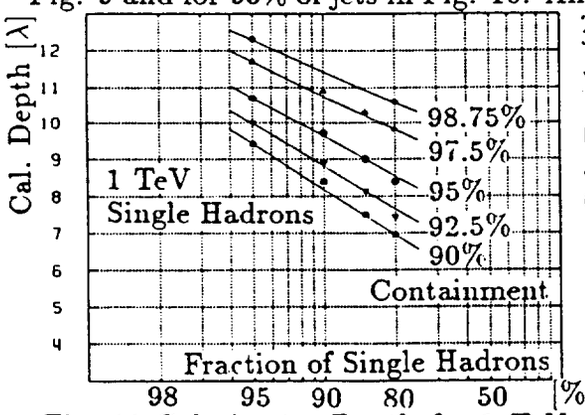


Fig. 11 Calorimeter Depth for 1 TeV Single Hadrons as Function of the Fraction of Single Hadrons

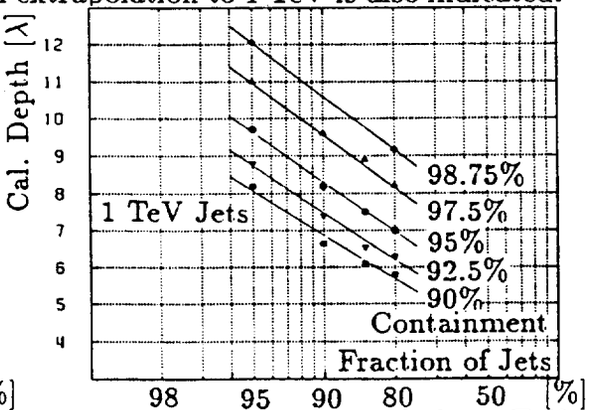


Fig. 12 Calorimeter Depth for 1 TeV Jets as Function of the Fraction of Jets

Figure 11 and 12 show the calorimeter depth necessary for 1 TeV single hadrons and jets (extrapolations) with a certain shower containment as function of the fraction of single hadrons and jets.

For 85% - 90% of the 1 TeV jets with a shower containment of 98.75% a calorimeter depth of about 10λ is needed or correspondingly for 95% of the 1 TeV jets with a shower containment of 95% also a calorimeter depth of about 10λ is necessary.

At 1 TeV the relative energy resolution of a high resolution hadron calorimeter with $\sigma_h/\mathrm{E} \approx 35\%/\sqrt{E}$ approaches 1% .

In order not to lose this excellent energy resolution at very high energies due to energy lost in the dead material of the PM boxes a very promising solution is to install an additional readout section in front of the dead material as veto counter to select events fully contained in the high resolution calorimeter as indicated in Fig. 6.

2. EFFECT OF ABSORBERS IN FRONT OF CALORIMETERS

2.1 INTRODUCTION

Very often tracking chambers, a magnet coil and various mechanical constructions are installed in front of a calorimeter. For example the material in front of the high resolution ZEUS uranium scintillator calorimeter is over a wide range about 1–1.5 radiation lengths X_0. But there are also narrow peaks up to 4 X_0 at a few small regions where mechanical constructions are necessary. This material degrades the measured signal and the energy resolution of the calorimeter.

2.2 MEASUREMENT PROGRAM WITH THE FCAL PROTOTYPE

Systematic measurements with various thicknesses of absorber (Al) in front of the ZEUS forward calorimeter (FCAL) prototype [5] have been performed at CERN in the energy range from 0.5 to 100GeV to determine quantitatively the effect of absorbers [6],[4].

The FCAL prototype (Fig. 13) consists of four modules with a front area of 80cm x 80cm (4 x (20cm x 80cm)), a depth of 2m (7λ) and 192 PMs [8].

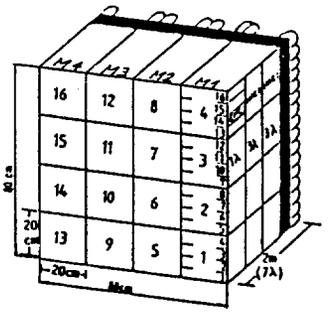


Fig. 13 The Module, Tower and Longitudinal Structure of the FCAL Prototype

The experimental set up used at CERN consisted of the scintillation beam counters B1, B2, B3 and B4 defining the beam, two Cherenkov counters C1 and C2 and the FCAL prototype calorimeter itself (Fig. 14).

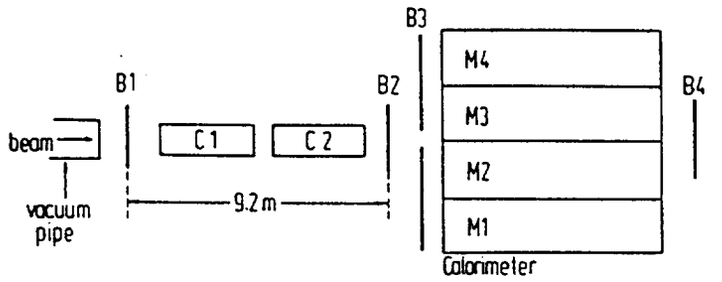


Fig. 14 The Experimental Set Up with the FCAL Prototype at CERN

Without material in front of the prototype the energy resolution is $\sigma_h/\mathrm{E}=35\%/\sqrt{E}$ for hadrons and $\sigma_e/\mathrm{E}=18\%/\sqrt{E}$ for electrons.

The main points of the measurement program are listed in the following:

Hadrons and Electrons

Absorber in front:	Aluminium	0cm, 9cm, 18cm, 27cm (= 0, 1, 2, 3 X_0)
Energy:	at CERN PS:	0.5, 1, 2, 3, 5 GeV
	at CERN SPS:	10, 20, 30, 75 GeV

Hadrons and Interaction Trigger - Jets

Absorber in front:	Aluminium	0cm, 4cm, 10cm
Energy:	at CERN SPS:	50, 100 GeV

2.3 EXPERIMENTAL RESULTS

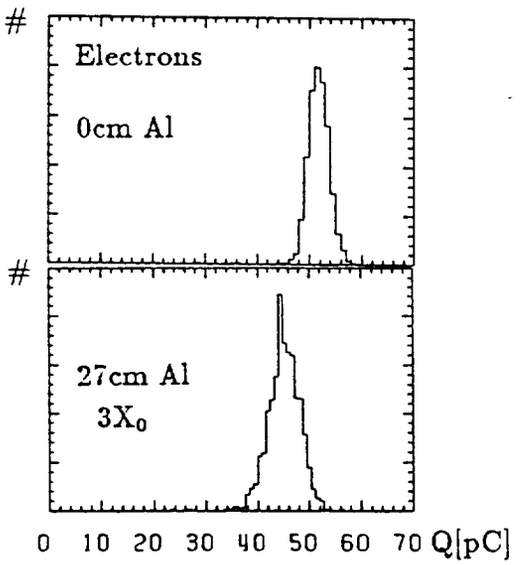


Fig. 15 Pulse Height Spectra for 30GeV Electrons without and with 27cm Al in Front of the Calorimeter

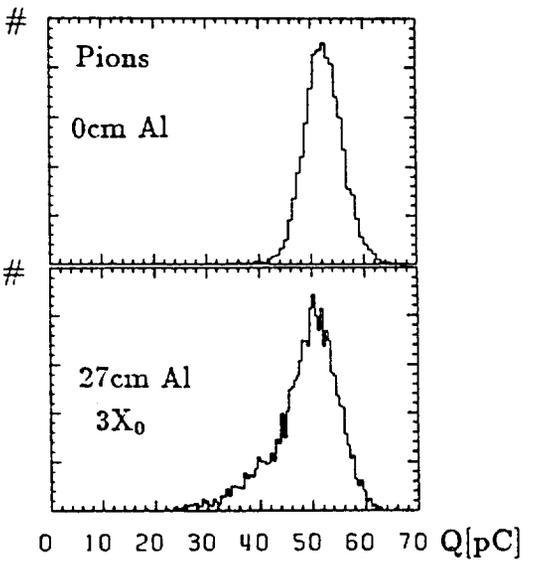


Fig. 16 Pulse Height Spectra for 30GeV Pions without and with 27cm Al in Front of the Calorimeter

Figure 15 and 16 show the pulse height spectra for electrons and pions at 30GeV without and with 27cm Aluminium absorber ($3X_0$) directly in front of the prototype. With absorber in front the mean values of the spectra are shifted significantly to lower values and the widths of the distributions increase.

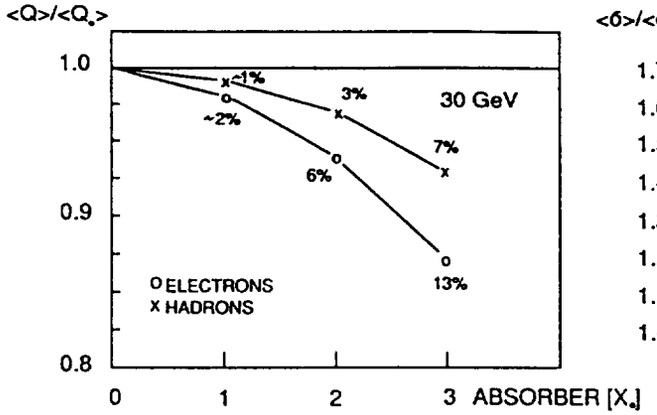


Fig. 17 Ratio of the Mean Signal Height with Absorber (<Q>) and without Absorber (<Q_0 >) as Function of the Absorber Thickness

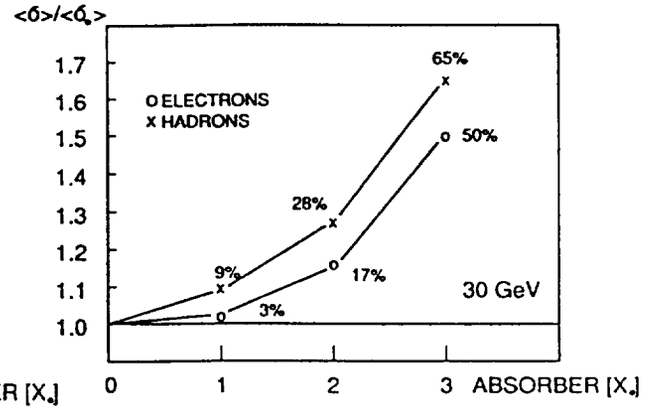


Fig. 18 Ratio of the Standard Deviation with Absorber (< σ >) and without Absorber (< σ_0 >) as Function of the Absorber Thickness

Figure 17 and 18 show for electrons and hadrons at 30GeV the ratio of the mean signal height and the standard deviation with material (< Q >, < σ >) and without material (< Q_0 >, < σ_0 >) as function of the absorber thickness in front of the calorimeter. For 1 X_0 material in front the mean value is reduced by about 1% for hadrons and 2% for electrons and decreases significantly in particular for electrons with increasing absorber thickness. The widths increase with absorber material in front and are for 1 X_0 by about 3% larger for electrons and 9% for hadrons.

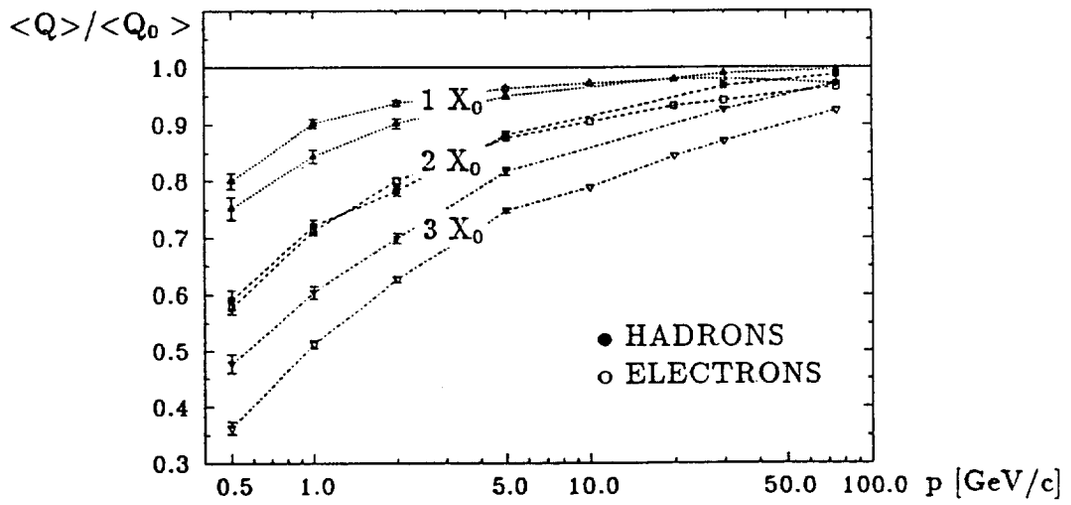


Fig. 19 Ratio of the Mean Signal Height with Absorber (<Q>) and without Absorber (<Q_0 >) as Function of the Momentum

The ratio <Q>/<Q_0 > for 9cm, 18cm and 27cm Aluminium absorber as function of the particle momentum is shown in Fig. 19. The deviation from 1 is large at low momenta and is decreasing with increasing momentum. Monte Carlo simulations have been performed and a similar behaviour has been found [7].

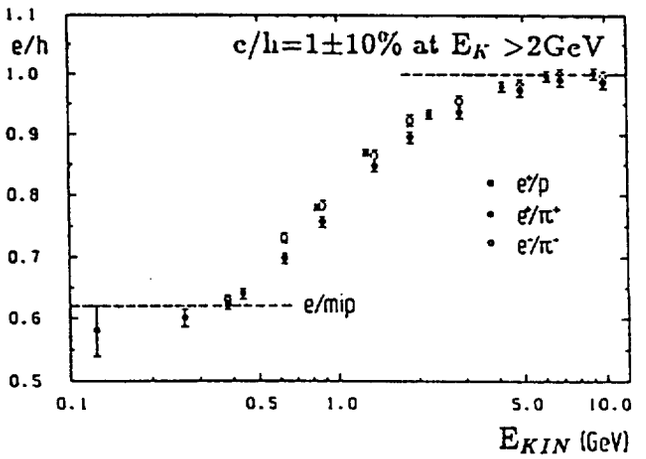


Fig. 20 e/h as Function of the Kinetic Energy E_{KIN} for p, π^+, π^-

Figure 20 shows the e/h ratios at equal kinetic energies E_{KIN} for π^+, $\pi^-$and p [5]. e/h is the same for π^+, π^- and p and depends in first approximation only on the kinetic energy E_{KIN}, the energy available for particle production and energy deposit in the calorimeter. At low energies hadrons lose more and more of their energy via dE/dx and give the sampling fraction of a minimum ionizing particle (mip). Thus e/h approaches e/mip, which is 0.62 in the present calorimeter. Due to the fact that the electron response e corresponds essentially to the kinetic energy the ratio $<Q>/E_{KIN}$ shows with absorber in front less deviations from 1.

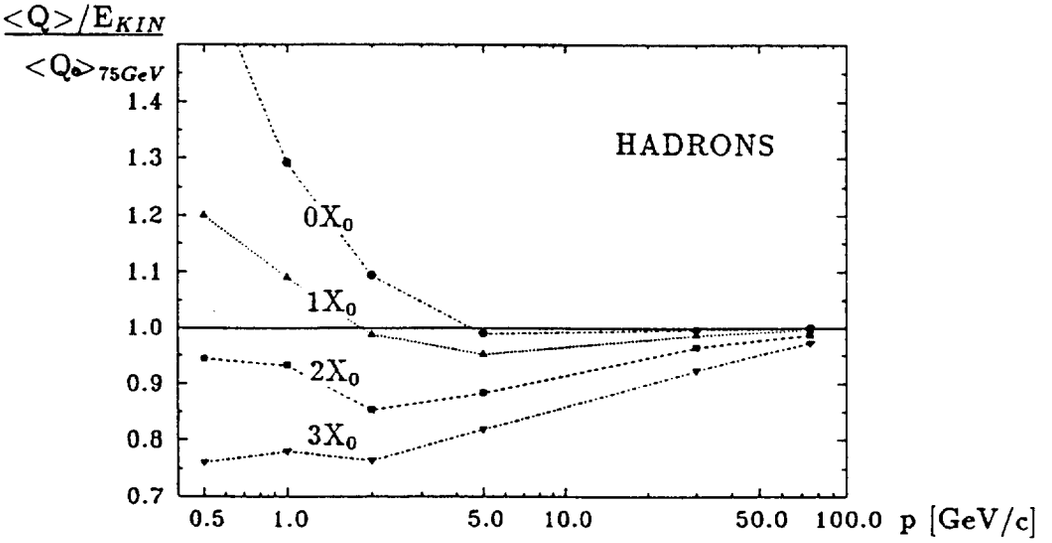


Fig. 21 Ratio of the Mean Signal Height ($<Q>$) and the Kinetic Energy E_{KIN} as Function of the Momentum

The normalized ratio $<Q>/E_{KIN}$ is shown in Fig. 21 for hadrons as function of the momentum. The different curves show the dependence of the absorber thickness. The deviation from $<Q>/E_{KIN} = 1$ is significantly reduced compared to $<Q>/<Q_0>$.

The analysis of the data taken with the interaction trigger in front of the FCAL prototype is in progress [8].

REFERENCES

1. Krüger, J., "Shower Development in a Uranium/Scintillator Calorimeter (WA78) and the Requirements for the Hadron Calorimeter of the ZEUS Detector", DESY, ZEUS Note 86-019 (1986)
2. Catanesi, M.G. et al., "Hadron, Electron and Muon Response of a Uranium-Scint. Calorimeter", Nucl. Instr. and Meth. A260 (1987) 43-54
3. The ZEUS Detector, Technical Proposal, DESY, March 1986
   The ZEUS Detector, Status Report 1987, DESY, September 1987
   The ZEUS Detector, Status Report 1989, DESY, March 1989
   Wolf, G., "HERA: Physics, Machine and Experiments", DESY 86-089
4. Krüger, J., "The ZEUS Uranium Scintillator Calorimeter ... ", Hamburg, DESY, in preparation
5. Behrens, U. et al., "Test of the ZEUS Forward Calorimeter Prototype", DESY 89-128 (1989)
   Andresen, A. et al., "Response of a Uranium-Scintillator Calorimeter to Electrons, Pions and Protons in the Momentum Range 0.5 - 10 GeV/c", DESY 89-149 (1989)
6. Fürtjes, A., Diploma Thesis, Münster (1990), DESY F35-90-02
7. W.R. Nelson, H. Hirayama and D.O. Rogers, EGS, SLAC-265 (1985)
8. Kröger, W. et al., "The Interaction Trigger ...", DESY, in preparation

JET RESPONSE OF AN IDEAL CALORIMETER*

D. E. Groom and E. M. Wang
Lawrence Berkeley Laboratory, Berkeley CA 94720, USA

Abstract

The response of a large calorimeter with uniform structure to an incident hadron with energy E, relative to that for an incident electron or photon with the same energy, is adequately described by $R_h/R_e = [1-(1-\epsilon_h/\epsilon_e)(E/E_0)^{m-1}]$. Here $m \approx 0.86$, $E_0 \approx 1$ GeV, and ϵ_e/ϵ_h is essentially the "intrinsic e/h" introduced by Wigmans. In a jet with energy E_J the hadron spectrum is described by a fragmentation function $D(z)$, where (for particle energy $E \approx p_{\|}$) $E = zE_J$. The calorimeter response to a jet may be found by integrating the single-hadron response over this distribution:

$$R_J/\epsilon_e = E_J\Big[1-(1-\epsilon_h/\epsilon_e)(E_J/E_0)^{m-1}\int_0^1 z^m D(z)dz\Big]$$

The response to a jet is the same as that to a single hadron only if the integral is unity. For $D(z)$ obtained from published DELPHI and CDF data and for ISAJET jets at $\sqrt{s} = 40$ TeV, the integral lies between 0.92 and 1.06, with significant uncertainties concerning low-z behavior and the nonelectromagnetic energy fraction. Even for a low-energy jet in a very noncompensating calorimeter ($\epsilon_e/\epsilon_h = 1.3$), the error in jet energy determination is less than 2%. Such errors are likely to be small compared with those resulting from the clustering algorithm, the low-z cutoff imposed by a possible solenoidal magnetic field, and the effects of dead material in front of the calorimeter.

1. Introduction

Not all jets are created equal. Calorimeter response, measured in a test beam with incident hadrons, can be thought of as the response to the "jet" produced in the first collision of the hadron with a heavy nucleus in the calorimeter—or in a convertor out front, as is often done in test beam simulations of jet response. However, the incident jet might consist of just a few energetic particles, for example from the decay of a high-energy W or Z. At the other extreme, a high-energy jet from the primary collision at the SSC contains a large number of very soft particles. If the calorimeter is noncompensating, there is no guarantee that the response to these different kinds of jets with same energy will be the same.

We report a study of the effect of differences in jet composition, as given by a range of fragmentation functions, on the response of an ideal calorimeter. By "ideal" we mean the calorimeter is large, in the sense that leakage effects can be ignored, and "uniform," in the sense that the structure is the same throughout—if there is a plate structure, it is the same front-to-back.

* This work was supported by the U. S. Department of Energy under Contract No. DE-AC03-76SF00098.

2. Response to a single incident hadron

The response of a calorimeter to an incident hadron with energy E may be written as[1]

$$R_h = \epsilon_e E\left[1-(1-\epsilon_h/\epsilon_e)(E/E_0)^{m-1}\right], \quad (1)$$

where R_h is the response of the calorimeter to an incident hadron, ϵ_e is the efficiency with which electromagnetic energy deposition is converted to output signal, ϵ_h is the efficiency with which energy deposition by low-energy hadrons is converted to output signal, E_0 is a scale energy (approximately 1 GeV), and $m \approx 0.85$–0.87. In practice, only the product $(1-\epsilon_h/\epsilon_e)E_0^{1-m}$ can be measured. The ratio ϵ_e/ϵ_h is very close to Wigmans' "intrinsic e/h."

The response to an electron or photon is taken to be linear:

$$R_e = \epsilon_e E \quad (2)$$

The ratio R_e/R_h ("e/π") is asymptotically unity, and the "linearity" R_h/E is proportional to its reciprocal.

3. Response to an ensemble of particles

A jet with energy E_J consists of photons from π^0 decay and "stable" hadrons. (In the present analysis, we ignore energy carried away by muons and neutrinos.) We need only to sum the responses of all of these particles to obtain the

response to a jet. If R_e^j is the response to the jth π^0 in the jet (with energy $E_{\pi^0}^j$) and R_h^k the response to the kth stable hadron (with energy E_h^k), then the response to the jet is given by

$$R_J = \sum_{j=1}^{N_{\pi^0}} R_e^j + \sum_{k=1}^{N_{\rm had}} R_h^k \,. \qquad (3)$$

Using Eqs. (1) and (2) to evaluate R_h^k and R_e^j, this reduces to

$$R_J = \epsilon_e E_J \Big[1-(1-\epsilon_h/\epsilon_e)(E_J/E_0)^{m-1} \times \sum_{k=1}^{N_{\rm had}} (E_h^k/E_J)^m\Big] \,. \qquad (4)$$

Alternatively, the spectrum of "stable" hadrons (those which reach the calorimeter without decaying) can be described by a fragmentation function $D(z)$, where z is the hadron's momentum parallel to the jet direction, scaled by the jet's momentum. In the present study we treat z as the fractional energy, *i.e.* $z \approx E_{\rm had}/E_J$. The arguments leading to Eq. (4) can then be repeated to obtain

$$R_J = \epsilon_e E_J \Big[1-(1-\epsilon_h/\epsilon_e)(E_J/E_0)^{m-1} \times \int_0^1 z^m D(z) dz\Big] \,. \qquad (5)$$

If the summation in Eq. (4) or the integral in Eq. (5) is evaluated with for $m = 0$, the stable hadron multiplicity ($N_{\rm had}$) is obtained. If $m = 1$, the result is the nonelectromagnetic fraction of the jet's energy ($F_{\rm had}$). The desired integral, with $m \approx 0.86$, is in some sense an interpolation between the two.

If the correction factor given by the sum or integral is unity, then the calorimeter has the same response for a jet as for an incident hadron. Imposition of this requirement for the "jet" from the first hadronic collision in the calorimeter results in recovery of the relationship between m, the mean multiplicity, and the average hadronic energy fraction in a single collision which was given in Ref. 1. If the factor is not unity, then the compensation of the calorimeter appears to be different for jets than for single hadrons. The dependence of the effective compensation factor as a function of the correction factor is shown in Fig. 1.

In using either experimental or Monte Carlo distributions to evaluate the sum or integral, special treatment of the very low-z region is necessary, as is normalization to an appropriate $F_{\rm had}$.

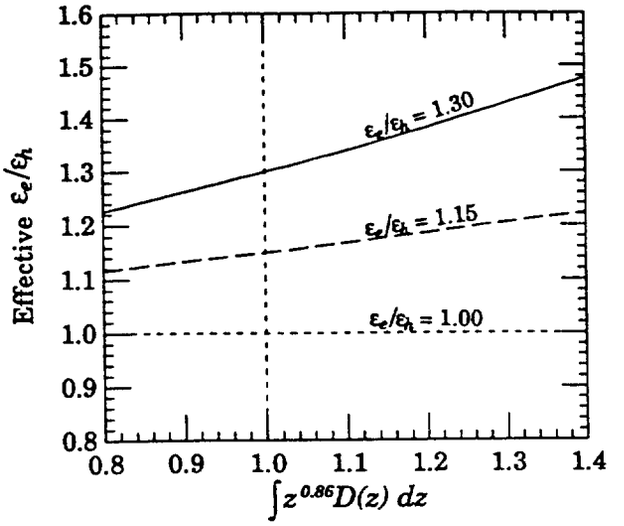


FIG. 1. Effective ϵ_e/ϵ_h for representative values of ϵ_e/ϵ_h as a function of the correction factor $\int z^{0.86} D(z) dz$ (see Eq. 5.)

4. Examples

We evaluate the integral in Eq. (6) for four representative cases:

Two experimental results, both with jet energies at or near $M_Z/2$. Since the measurements are for *charged* hadrons, the distributions must be renormalized to include the contributions of such particles as Λ's and K_L's.

1. Jets from Z decay, as measured by the DELPHI collaboration at LEP[3]. The published fragmentation function is for the entire event, so we have normalized the function downward by a factor of two to describe the individual jets. Data were read from their Fig. 3(b) and extrapolated to $z = 0$.

2. CDF charged fragmentation function at $\sqrt{s} = 1800$ GeV[4]. $z dN_{\rm ch}/dz$ was extrapolated to $z = 0$ to force $\langle F_{\rm ch}\rangle = 0.65$, their reported value. (Since some of the energy is carried by neutrals, this value is probably too high for consistency with isospin conservation.)

Two samples of TWOJET ISAJET events at $\sqrt{s} = 40$ TeV. In both cases, all hadrons other than π^0's are used:

3. 3226 events with p_t (hard scatter) > 40 GeV/c, and 100 GeV < M_{JJ} < 200 GeV. The mean jet momentum is 73 GeV/c, and the mean non-π^0 hadronic multiplicity is 26.
4. 3042 events with p_t (hard scatter) > 400 GeV/c, and 1000 GeV < M_{JJ} < 2000 GeV. The mean jet momentum is 677 GeV/c, and the mean non-π^0 hadronic multiplicity is 70. The z distribution for these events is shown in Fig. 2.

The results are summarized in Table 1. In all cases, there is ambiguity because of uncertainty in $F_{\rm had}$ (or $F_{\rm ch}$, in the the experimental results). For $I = 1$ pion production one would expect $F_{\rm had}$ = 2/3, but the value should be somewhat lower because of $I = 1/2$ states. Some of the bias can probably be removed by normalizing $\int zD(z)dz$ to 0.67 (entries in parentheses). As can be seen, the integral is slightly less than unity for the similar low-energy LEP and Tevatron functions, and is slightly greater than unity for simulated high-energy SSC jets. Values lie between 0.84 and 1.15 before normalization, and 0.92 to 1.06 after normalization. The integrals change by about 0.03 if m is changed by 0.01, introducing an additional uncertainty of perhaps 6%. Given the various uncertainties, we conclude that the correction factor for jets at the SSC will be between 0.85 and 1.15, and will depend upon the kind of jet. In the following discussion, we treat the limits as 0.9 and 1.2, in part to avoid confusion between the lower limit and the value of the exponent m.

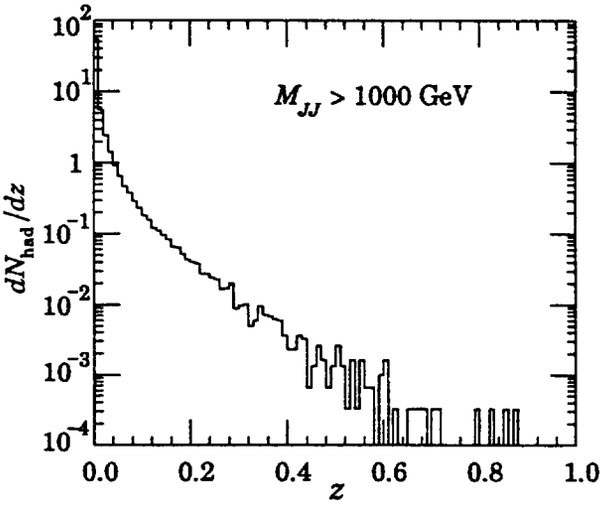


FIG. 2. Distribution in z for ISAJET TWOJET events at $\sqrt{s}$ = 40 TeV, for 1000 GeV < M_{JJ} < 2000 GeV.

Table 1

Integrals over representative fragmentation functions. Numbers in parentheses are calculated for the nonelectromagnetic energy fraction normalized to 0.67. In the case of the DELPHI and CDF results, the unrenormalized energy fraction is for charged hadrons only.

Source	Process	$\int_0^1 D(z)dz$	$\int_0^1 z^{0.86}D(z)dz$	$\int_0^1 zD(z)dz$
DELPHI	$Z \rightarrow jet\ jet$	11.0(12.1)	0.84(0.92)	0.61(0.67)
CDF	$\sqrt{s}$ = 1.8 TeV	17.8*(19.9)	0.94(0.97)	0.65(0.67)
ISAJET	40 TeV, $\langle p_J \rangle$ = 73 GeV/c	26.2(25.2)	1.04(1.00)	0.69(0.67)
ISAJET	40 TeV, $\langle p_J \rangle$ = 677 GeV/c	69.8(64.7)	1.15(1.06)	0.72(0.67)

*The extrapolated low-momentum part of the function contributes 10 to this total.

It is also interesting to look at the *distribution* of corrections for a given jet energy. This is shown for the $M_{JJ} \approx$ 100 GeV ISAJET events in Fig. 3. The width of the distribution is large compared to the slight offset of the mean given in Table 1. For a noncompensating calorimeter this distribution results in a small resolution degradation. However, its origin is in fluctuations in π^0 content, which is not sensibly different for a jet than for the first-collision products for an incident single hadron. It is just the famous "constant term" in the resolution[2].

5. Effect of low-z cutoff

It can be seen from Fig. 2 that most of the particles in a typical jet have z < 0.01. The z dependence of the various integrals of interest in this study is shown in Fig. 4 for our higher-energy ISAJET sample, where 80% of the particles

have $z < 0.01$. These carry 17% of the energy. The other fragmentation functions have similar behavior. We observe that:

a) While the curves for $a = 0.86$ and $a = 1.00$ change rapidly with the cutoff in z, their *ratio* does not. This means that when the integral for $a = 0.86$ is normalized to a given hadronic energy fraction, as is done for the entries in parentheses in Table 1, the compensation correction factor obtained in this way is not terribly sensitive to the cutoff.

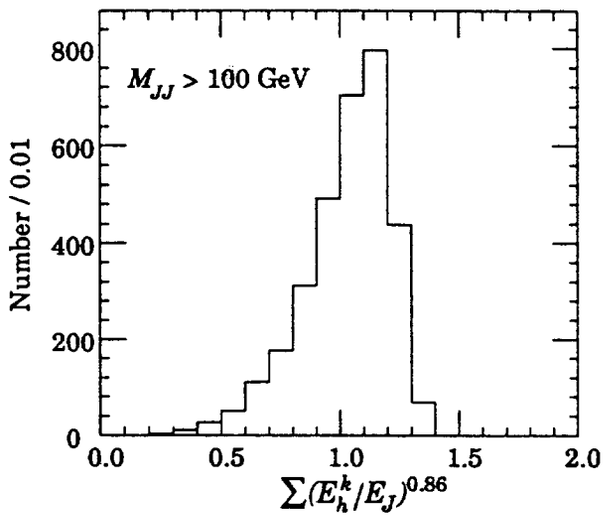


FIG. 3. Distribution of $\sum(E_h^k/E_J)^{0.86}$ for a sample of ISAJET TWOJET events at $\sqrt{s}$ = 40 TeV with 100 GeV $< M_{JJ} <$ 200 GeV.

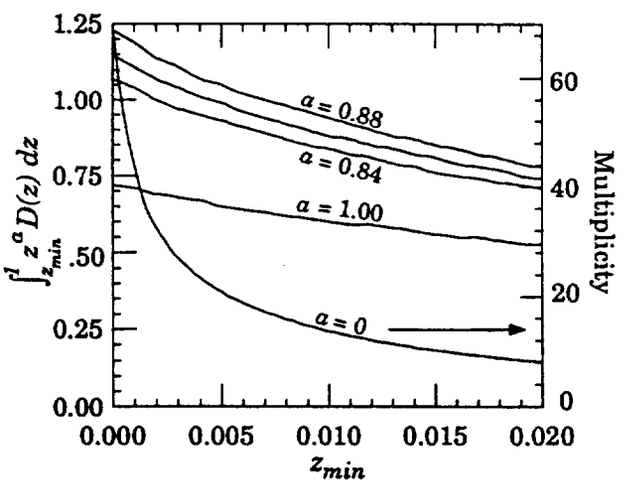


FIG. 4. Behavior of $\int_{z_{min}}^1 z^a D(z)dz$ for the 1000 GeV $< M_{JJ} <$ 2000 GeV ISAJET sample for small z, for $a = 0$ (multiplicity; axis on right), $a = 1$ (hadronic energy fraction), $a = 0.84$, $a = 0.86$ (unlabeled), and $a = 0.88$.

b) A substantial fraction of the energy is carried by very soft particles, and these preferentially deposit their energy in any dead material in front of the calorimeter.

c) For a 100 GeV jet in our ISAJET simulation, at least 3% of the energy is carried by particles with $p < 600\text{MeV}/c$, which is the cutoff transverse momentum in the solenoidal field of the proposed SDC detector. Somewhat more energetic particles reach the calorimeter, but may not be within the $\Delta\eta\Delta\phi$ region defining the jet.

Table 2

Energies found for jets with correction factors 0.90 and 1.20 on the basis of single-hadron calibration R_h in a calorimeter with ϵ_e/e_h = 1.30. Energies and responses are in GeV.

E	R_h	$E_{0.90}$	Error	$E_{1.20}$	Error
10.0	8.3	10.2	1.95%	9.6	−3.91%
20.0	17.0	20.3	1.74%	19.3	−3.49%
50.0	43.3	50.8	1.51%	48.5	−3.02%
100.0	87.9	101.4	1.35%	97.3	−2.70%
200.0	178.0	202.4	1.21%	195.1	−2.43%
500.0	451.7	505.3	1.05%	489.5	−2.11%
1000.0	912.3	1009.5	0.95%	981.0	−1.90%
2000.0	1840.8	2017.1	0.85%	1965.8	−1.71%

6. Implications for calibration and compensation

The only reasonable way to calibrate a calorimeter is in terms of equivalent electron response, so for purposes of this section we take the first factor on the right of Eq. (1) as unity, and measure the response in GeV. The corresponding energies determined for jets in our $\epsilon_e/\epsilon_h = 1.30$ calorimeter are shown in Table 2. For example, if $E_0 \approx 1$ GeV, then a 1000 GeV pion produces a response of 912.3 GeV. Conversely, if a 912.3 GeV signal is observed for an incident hadron, Eq. (1) can be inverted to find $E_h = 1000$ GeV. For an incident jet, Eq. (4) or (5) must be used instead. If the correction factor is 0.90 and if the energy scale has been calibrated in a hadron test beam, then a 1000 GeV jet will appear to have 1009.5 GeV. The percentage errors shown in the table for the two limiting cases are plotted in Fig. 5, along with

similar results for a calorimeter with $\epsilon_e/\epsilon_h = 1.15$. (A lead–liquid argon calorimeter with fast readout might have $\epsilon_e/\epsilon_h = 1.30$, and 1.15 might be obtained for a poorly-designed metal-scintillator calorimeter.) The error is 4% in the worst case at 10 GeV, and decreases with energy and with the degree of compensation. We emphasize again that the correction factor limits used in this figure are nearly twice those indicated by the data and simulations.

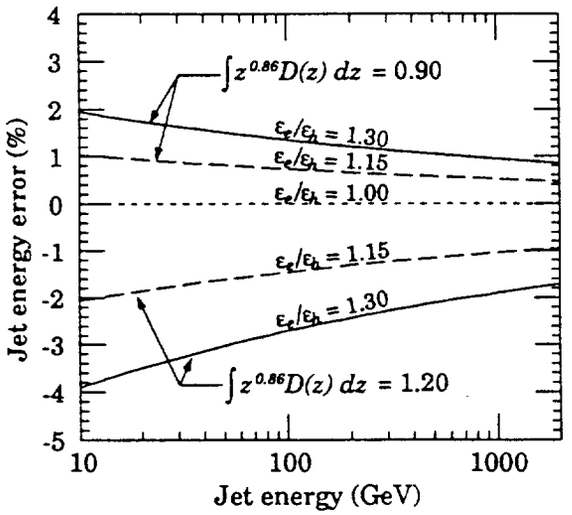


FIG. 5. Energy determination error as a function of jet energy for representative values of ϵ_e/ϵ_h, for the two extreme case of the correction factor: 0.90 (top curves, for hard, low-multiplicity jets) and 1.20 (bottom curves, for soft, high-multiplicity jets).

These errors, related to noncompensation, are likely to be small in comparison with errors associated with a possible solenoidal field (as discussed above), those connected with jet definition in a cluttered event (*via* some clustering algorithm), and dead matter in front of the calorimeter. In addition, the hadrons which reach the calorimeter tend to interact earlier than those in a single-hadron cascade, and in a real calorimeter the early part (electromagnetic section) might be different than the rest. Further studies of these effects are planned.

References

1. D. E. Groom, "Energy Scaling of Low-Energy Neutron Yield, the e/π Ratio, and Hadronic Response in a Calorimeter," in *Proc. of the Workshop on Calorimetry for the Supercollider*, Tuscaloosa, Alabama, 13–17 March 1989, ed. R. Donaldson and M. G. D. Gilchriese, World Scientific (June 1990), 59–75.
2. D. E. Groom, "Contributions of Albedo and Noncompensation to Calorimeter Resolution," Solenoid Detector Collaboration Note SDC-90-00083 (1990), and in *Proc. 1990 DPF Summer Study on High Energy Physics*, Snowmass CO (to be published).
3. P. Aarnio *et al.*, Phys. Lett. **240B**, 271 (1990).
4. F. Abe *et al.*, Phys. Rev. Lett. **65**, 968 (1990).
5. F. E. Paige and S. D. Protopopescu, in *Physics of the Superconducting Supercollider*, ed. by R. Donaldson and J. Marx (Snowmass CO, 1986), 320.

COMBINATION OF CALORIMETERS WITH e/h = 1 BUT DIFFERENT SAMPLING FREQUENCY

J. del Peso
DESY
E. Ros
Hamburg University, II Institut
(Representing the ZEUS Calorimeter Group)

INTRODUCTION

The e/h and energy resolution of hadron sandwich calorimeters is closely related to the thickness of absorber and readout layers [1]. In fact the e/h ratio depends essentially on the ratio of thicknesses, which has to be fixed, but it is still possible to play with the sampling frequency to improve the energy resolution. However most of the energy of jets is deposited in the front part of calorimeters. In this note we would like to discuss the possibility of combining a thin layer front calorimeter with a thick layer one, without degrading significantly the combined energy resolution.

CALORIMETER AND DATA

The measurements were performed with an uranium-scintillator sandwich calorimeter built to investigate compensation and energy resolution properties of uranium, which has been described in detail elsewhere [2,3].

The calorimeter consisted of 4 separate but identical modules (fig. 1a). Each module, 1.5 λ deep, contained 45 layers of 3.2 mm thick uranium and 3.0 mm thich scintillator plates. An additional module, 1 λ deep, was used as tail catcher. The total cross-section perpendicular to the beam was 60x60 cm^2. In the vertical direction the scintillator plane was segmented into 12 strips, 5 cm high each, in order to provide information on the lateral development of the shower. The light from each strip was transmitted to PMs via wave length shifter bars and plexiglass light guides. These light guides were bent such that two modules could approach each other without leaving any significant dead space between them. Graded filters were also introduced between the scintillator and the WLS to compensate for the attenuation along the WLS material.

The measurements were performed in the X5 test beam of the CERN-SPS in the energy range from 10 to 100 GeV. The calibration procedure made use of the uranium natural radioactivity in addition to beam signals (electron and muons). The precision of this calibration can be estimated to be at the 1% level (see [2] for more details).

The odd scintillator plates on the left side (L) of the calorimeter and the even scintillator plates on the right side (R) were covered with black paper (see fig. 1b and ref. [3]). Therefore a fine sampling calorimeter (calorimeter 1) was obtained by summing R and L side PMs, while a coarse one (calorimeter 2) was obtained by summing only R or L side PMs. A combined calorimeter (calorimeter 3) with fine sampling in the front part and coarse sampling in the back part could be obtained by summing R and L signals in the first module (1.5 λ deep) and only R or L signals in the other modules.

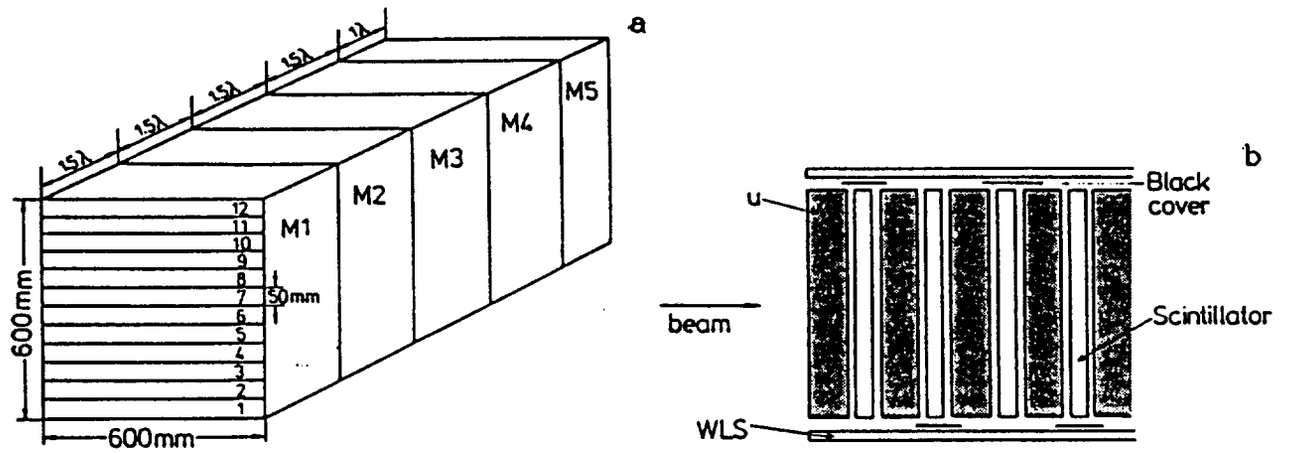


Figure 1: a. *Segmentation of the uranium-scintillator calorimeter.* b. *Layer structure of the calorimeter. Each scintillator plate can be read out only on one side.*

EXPERIMENTAL RESULT

In fig. 2a, 2b and 2c we show the 50 GeV hadron energy distributions for calorimeters 1, 2 and 3 described in the previous section. In first approximation they are all gaussian distributions with however some tails, which are more significant for the calorimeters 2 (coarse sampling) and 3 (combined case).

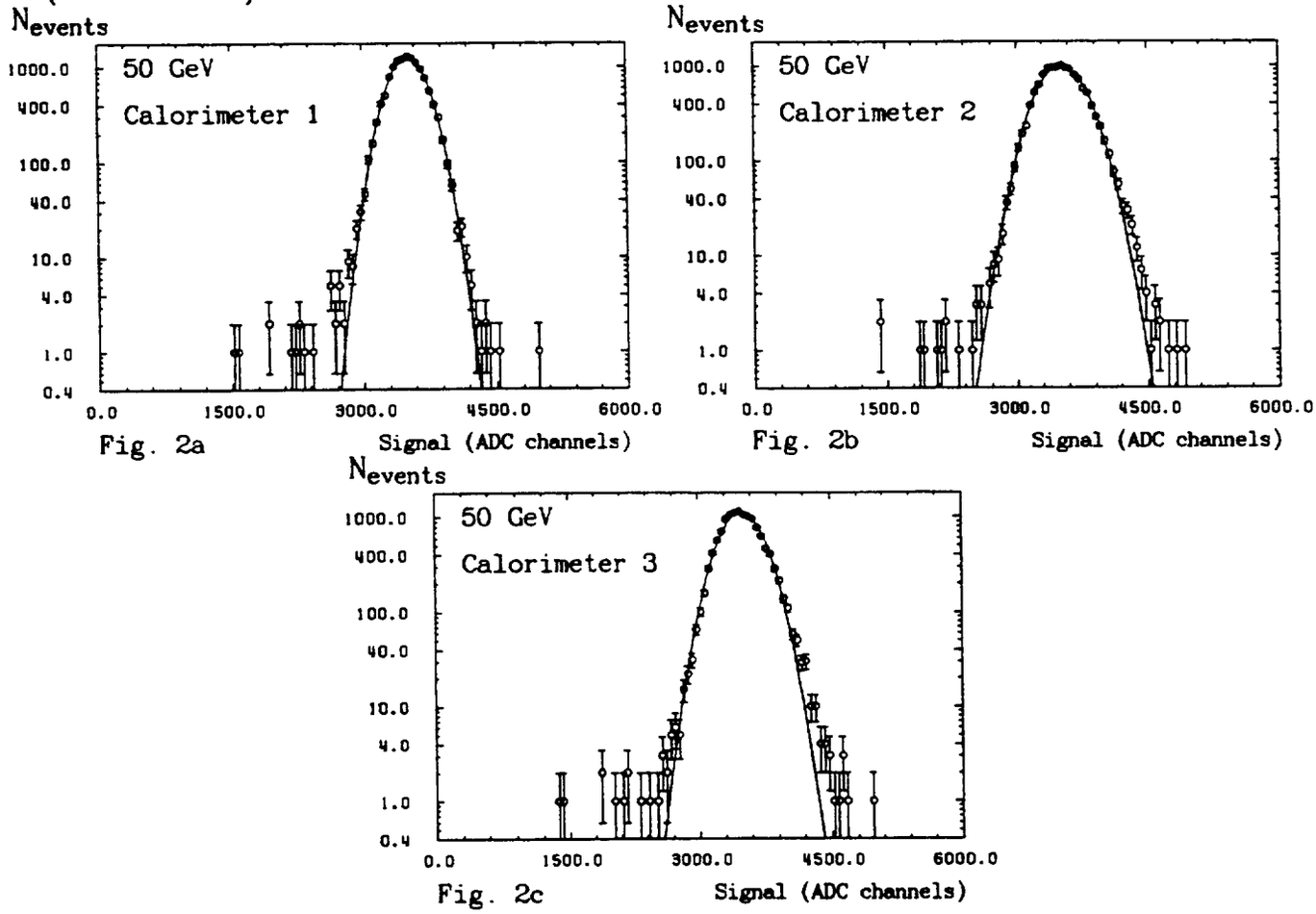


Figure 2: *Distribution of the calorimeter signal at for an incident energy of 50 GeV.* a. *Calorimeter 1 (fine sampling).* b. *Calorimeter 2 (coarse sampling).* c. *Calorimeter 3 (combined sampling).*

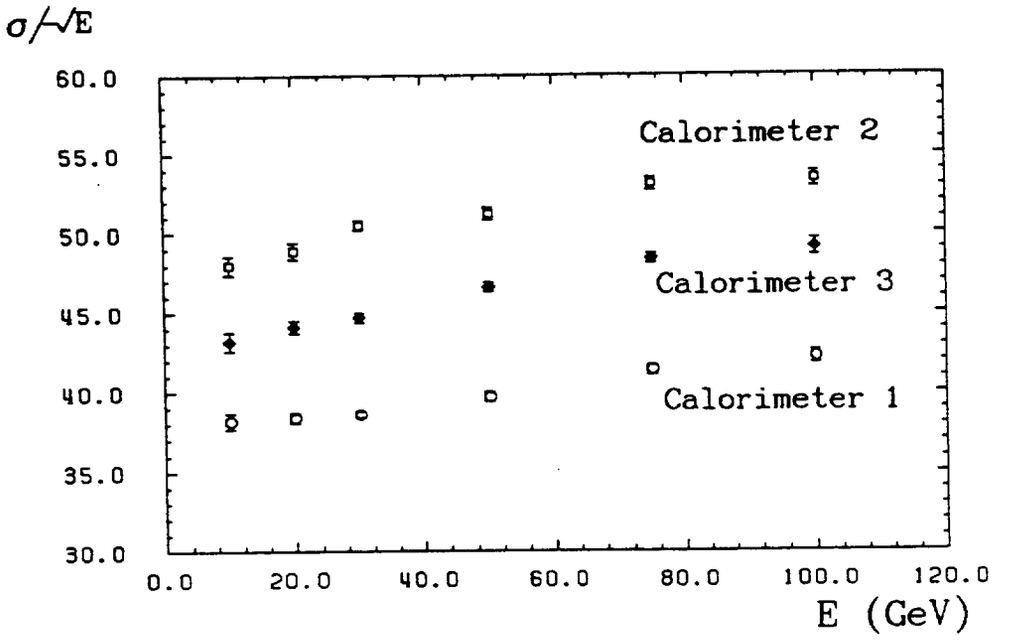


Figure 3: *Energy resolution versus the incident energy for the three calorimeter configurations.*

In fig. 3 we display the energy resolution of the three calorimeters versus the beam energy. The coarse sampling calorimeter has a resolution worse than the fine sampling one by a factor of about $\sqrt{2}$ (in fact smaller than $\sqrt{2}$ due to intrinsic fluctuations), while the energy resolution of the combined calorimeter lies in between as expected. At 50 GeV, for example, calorimeter 1 has a resolution of $39.7\%/\sqrt{E}$, calorimeter 2 gives $51.2\%/\sqrt{E}$ and the combined one $46.6\%/\sqrt{E}$. All 3 calorimeters show a constant term in the energy resolution with the values 2.1 ± 0.1, 2.2 ± 0.2 and 2.6 ± 0.1 for calorimeters 1, 2 and 3 respectively. This constant term receives contributions from the beam momentum spread, the leakage at the rear of the calorimeter and intecalibration errors between the different modules. In the case of the combined calorimeter this constant term is slightly enhanced.

DISCUSSION OF THE RESULT

In our experimental measurements the length of the front part of the calorimeter, with a fine sampling, could not be varied in a continuous way. However we could select samples of events with a different fraction of energy (f) contained in this front part. In fig. 4 we plot the energy resolution as a function of f for the three calorimeters at 50 GeV. We observe that this energy resolution is roughly constant for calorimeters 1 and 2, as expected. The energy resolution of calorimeter 3 can be explained by the formula (full line in fig. 4)

$$\sigma_3 = \sqrt{f\sigma_1^2 + (1-f)\sigma_2^2} \qquad (1)$$

where $\sigma_1, \sigma_2, \sigma_3$ are the energy resolutions (σ/E) of calorimeters 1, 2 and 3 respectively and f is the average fraction of energy in calorimeter 1. This formula predicts at 50 GeV an energy resolution of $45.4\%/\sqrt{E}$ for the combined calorimeter, in good agreement with the measured value of $46.6\%/\sqrt{E}$ (we note that $f = 50.2\%$ at this energy). This formula can be derived by a simple theoretical model (see appendix).

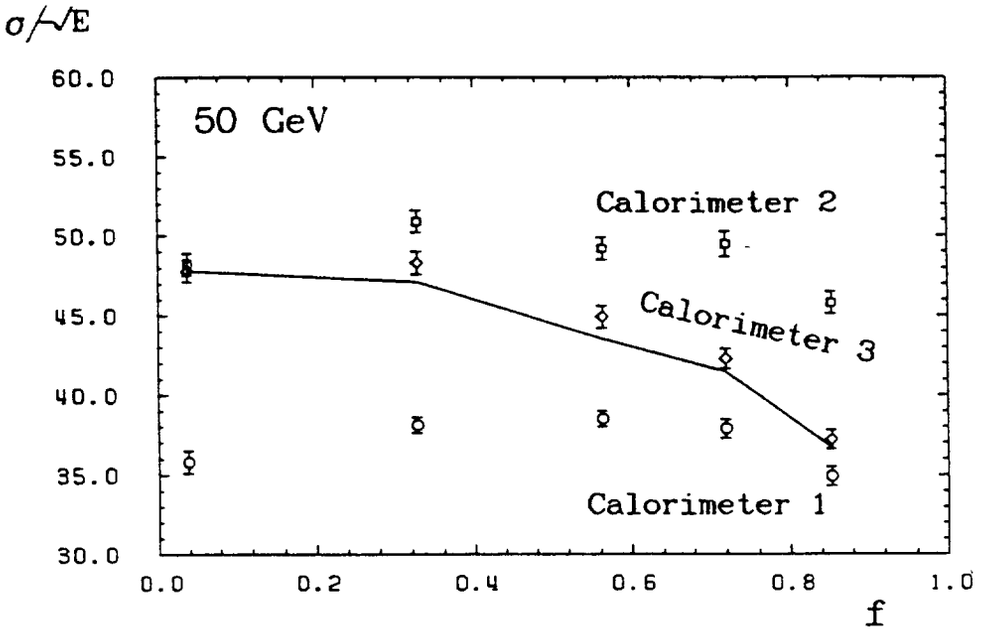


Figure 4: *Energy resolution as a function of the energy fraction in module 1 for the three calorimeter configurations. The full line corresponds to the prediction given by formula (1).*

SUMMARY

The energy resolution of a hadron sampling calorimeter obtained by combining a fine sampling front calorimeter with fractional energy resolution σ_1 and a coarse sampling back part with fractional energy resolution σ_2 can be described by

$$\sigma_3 = \sqrt{f\sigma_1^2 + (1-f)\sigma_2^2}$$

f being the average fraction of the total energy deposited in the front part.

This formula agrees with experimental data obtained with a uranium-scintillator calorimeter.

APPENDIX

The visible energy in a calorimeter consisting in two parts with sampling fractions h_1 and h_2 is:

$$E_{vis} = h_1 E_1 + h_2 E_2 = hE$$

E_1 and E_2 being the energies deposited in each part and E the total energy $E = E_1 + E_2$. The fluctuation of the visible energy is:

$$\Delta E_{vis} = (\Delta h_1)E_1 + (\Delta h_2)E_2 + h_1 \Delta E_1 + h_2 \Delta E_2$$

where the first 2 terms account for fluctuations in the sampling fractions and the last 2 terms for fluctuations in the deposited energies. If we assume the same sampling fraction for both calorimeter parts we obtain:

$$h_1\Delta E_1 + h_2\Delta E_2 = h(\Delta E_1 + \Delta E_2) = h\Delta E = 0$$

since the incident energy is fixed. The energy fluctuation of parts 1 and 2 is such that:

$$\frac{\sigma(h_i)}{h_i} = \frac{\sigma_i}{\sqrt{E_i}}, \quad i = 1,2$$

and they can be considered uncorrelated. Therefore:

$$\frac{\sigma_{vis}}{E_{vis}} = \frac{\sqrt{E_1}}{E}\sigma_1 \oplus \frac{\sqrt{E_2}}{E}\sigma_2 = \frac{1}{\sqrt{E}}(\sqrt{f_1}\sigma_1 \oplus \sqrt{f_2}\sigma_2)$$

f_1 and f_2 being the average energy fractions in parts 1 and 2.

Finally:

$$\sigma_3 = \sqrt{f_1}\sigma_1 \oplus \sqrt{f_2}\sigma_2$$

ACKONWLEDGEMENTS

We would like to thank R. Klanner for helpful discussions.

REFERENCES

[1] C.W. Fabjan and R. Wigmans, Rep. Prog. Phys. 52(1989)1519
[2] G. d'Agostini et al., NIM A274(1989)134
[3] G. Drews et al., NIM A290(1990)335

INFLUENCE OF CALIBRATION ERRORS IN THE ENERGY RESOLUTION OF HADRON CALORIMETERS

J. del Peso
DESY
E. Ros
Hamburg University, II Institut
(Representing the ZEUS calorimeter group)

INTRODUCTION

The fractional energy resolution of hadron sampling calorimeters is usually parametrized in the following way [1]:

$$\frac{\sigma_E}{E} = \frac{a}{E} \oplus \frac{b}{\sqrt{E}} \oplus c \qquad (1)$$

where E is the energy of the incoming particle (electron or hadron) and the symbol $\oplus$ means a quadratic sum. The first term (proportional to $1/E$) is the contribution of noise, the second term (proportional to $1/\sqrt{E}$) is the contribution of sampling and intrinsic fluctuations and the third term appears due to effects like calibration errors and non-uniformities in the calorimeter response [1]. In this note we want to estimate the contribution to c of calibration errors. This estimation is based on experimental data taken with a prototype of the ZEUS high resolution hadron calorimeter [2].

CALORIMETER AND DATA

The measurements were performed with an uranium-scintillator sandwich calorimeter built to investigate compensation and energy resolution properties of uranium, which has been described in detail elsewhere [3,4].

The calorimeter consisted of 4 separate but identical modules (fig. 1). Each module, 1.5 λ deep, contained 45 layers of 3.2 mm thick uranium and 3.0 mm thich scintillator plates. An

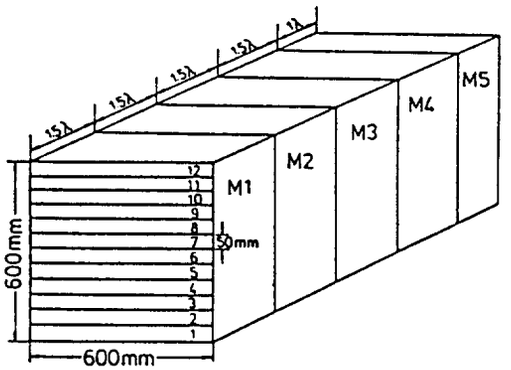


Figure 1: *Segmentation of the uranium-scintillator calorimeter*

[1] For non-compensating calorimeters ($e/h \neq 1$) an additional contribution to c from intrinsic fluctuations has to be considered

additional module, 1 λ deep, was used as tail catcher. The total cross-section perpendicular to the beam was 60x60 cm^2. In the vertical direction the scintillator plane was segmented into 12 strips, 5 cm high each, in order to provide information on the lateral development of the shower. The light from each strip was transmitted to PMs via wave length shifter bars and plexiglass light guides. These light guides were bent such that two modules could approach each other without leaving any significant dead space between them. Graded filters were also introduced between the scintillator and the WLS to compensate for the attenuation along the WLS material.

The measurements were performed in the X5 test beam of the CERN-SPS in the energy range of 10 to 100 GeV. The calibration procedure used the uranium natural radioactivity in addition to beam signals (electrons and muons). The precision of this calibration can be estimated to be at the 1% level (see [3] for more details).

EXPERIMENTAL DETERMINATION OF C

To study the effect of calibration errors in the energy resolution we have generated random calibration errors in each cell of the calorimeter in the following way

$$E_\delta = \sum_{cells} E_i(1+\delta_i) \tag{2}$$

E_δ being the total hadronic energy, E_i the energy deposited in each cell and δ_i a random number generated according to a Gaussian distribution centered at 0 and with a width δ. The random numbers δ_i were changed in each event in order to simulate a scan across the complete calorimeter [2]. The fractional energy resolution obtained in this way is displayed versus incident energy in fig. 2a for $\delta = 0$ (σ_0) and $\delta = 5\%$ (σ_δ). As expected, the resolution is worse in this second case and the following relation is satisfied:

$$\frac{\sigma_\delta}{E_0} = \frac{\sigma_0}{E_0} \oplus c \tag{3}$$

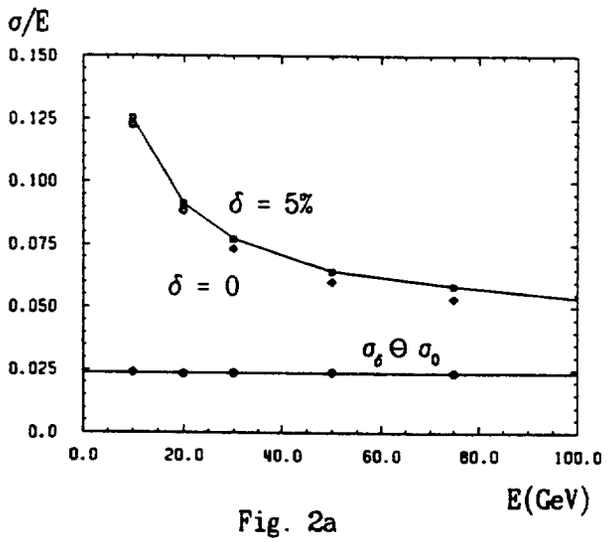


Fig. 2a

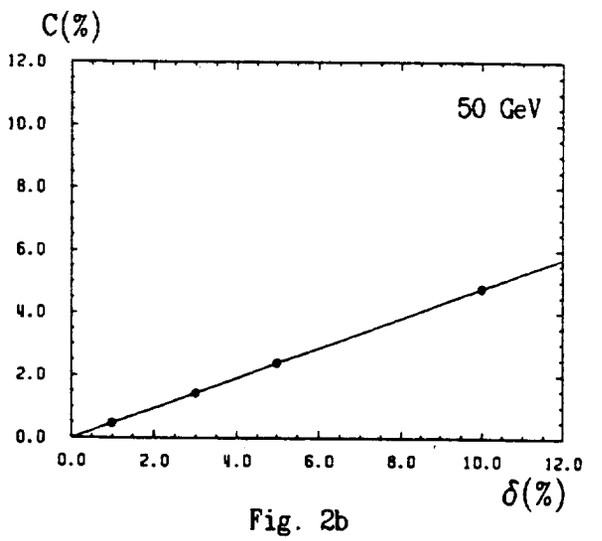


Fig. 2b

Figure 2: a: *Energy resolution as a function of the incident energy for a calibration error of 5% (upper curve), no calibration error (curve in the middle) and the quadratic difference (lower curve). b: Constant term (C) in the energy resolution versus the calibration error*

[2] In the data the beam was incident at the center of strip number 7

where c is an energy independent constant and E_0 the calorimeter energy. In particular $c = 2.4\%$ for $\delta = 5\%$. We have also found a linear relation between c and δ as shown in fig. 2b.

DISCUSSION OF THE RESULT

The constant term c generated by calibration errors is of the same order of magnitud than the calibration error δ, but smaller due to the segmentation of the calorimeter. A simple theoretical model (see appendix) leads to the following formula

$$c = \delta \sqrt{\sum_{cells} (\overline{f_i}^2 + \sigma_{fi}^2)} \tag{4}$$

where $\overline{f_i}$ is the average fraction of the total energy in the calorimeter deposited in cell number i and σ_{fi} its r.m.s. fluctuation. We notice that if all the energy is deposited in a single cell (this could be the case for electrons), we have $\overline{f_i} = 1$ and $\sigma_{fi} = 0$ and therefore $c = \delta$. In the case of hadrons the values of $\overline{f_i}$ and σ_{fi} measured with our calorimeter are plotted in fig. 3a and 3b. We observe that the maximum value of $\overline{f_i}$ is about 0.3. The factor $\sqrt{\sum_{cells}(\overline{f_i}^2 + \sigma_{fi}^2)}$ is equal to 0.5 and rather energy independent, thus explaining the experimental result presented in the previous section.

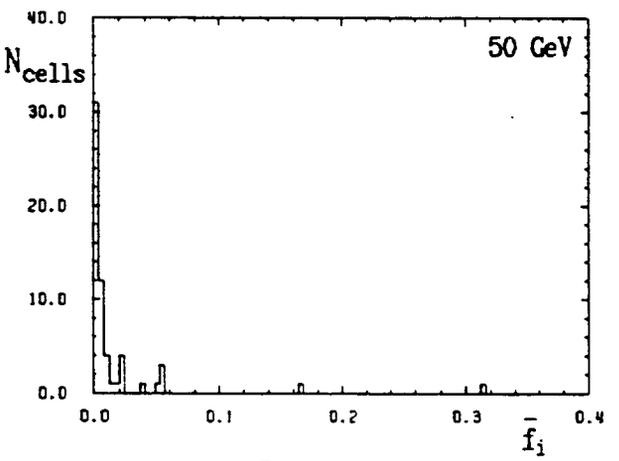


Fig. 3a

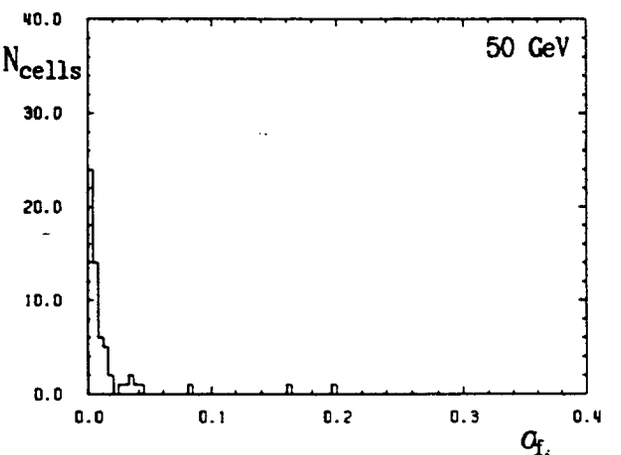


Fig. 3b

Figure 3: a: *Distribution of the average energy fraction in cells.* b: *Distribution of the r.m.s. energy fraction in cells.*

SUMMARY

Calibration errors introduce a constant term in the energy resolution (σ/E) of hadron calorimeters. This constant term is proportional to the calibration error but usually smaller. The exact relation depends on the segmentation of the calorimeter. The experimental data can be described by the formula

$$c = \delta \sqrt{\sum_{cells} (\overline{f_i}^2 + \sigma_{fi}^2)}$$

where c is the constant term in the resolution, δ the calibration error, $\overline{f_i}$ the average fraction of the energy deposited in cell number i and σ_{fi} its r.m.s. fluctuation.

APPENDIX

The total calorimeter energy smeared by calibration errors is, for a given event,

$$E_\delta = \sum_i E_i(1+\delta_i)$$

where the sum runs over all calorimeter cells and the gaussian distributed random numbers δ_i vary in each event. The deviation from the average energy E_0 is

$$\Delta E = E_\delta - E_0 = \sum_i E_i\delta_i \implies (\Delta E)^2 = \sum_{i,j} E_iE_j\delta_i\delta_j$$

By averaging over the random numbers δ_i we obtain

$$\overline{(\Delta E)^2} = \delta^2 \sum_i E_i^2$$

since $\overline{\delta_i\delta_j} = \delta^2\delta_{ij}$.

The energy resolution can be obtained by averaging over all events

$$(\sigma_\delta/E_0)^2 = \delta^2 \sum_i \overline{f_i^2} = \delta^2 \sum_{cells} (\overline{f_i}^2 + \sigma_{fi}^2)$$

where $f_i = Ei/E_0$.

Finally

$$\sigma_\delta/E_0 = \delta\sqrt{\sum_{cells}(\overline{f_i}^2 + \sigma_{fi}^2)}$$

ACKNOWLEDGEMENTS

We would like to thank R. Klanner for helpful discussions.

REFERENCES

[1] C.W. Fabjan and R. Wigmans, Rep. Prog. Phys. 52(1989)1519
[2] The ZEUS detector, Status Report 1989, DESY (March 1989)
[3] G. d'Agostini et al., NIM A274(1989)134
[4] G. Drews et al., NIM A290(1990)335

SCINTILLATING FIBERS

Presented by L. Poggioli

Contributions from : R. De Salvo, A. Henriques, L. Linssen, M. Sivertz, and R. Wigmans

We report on the use of scintillating fibers in calorimetry for LHC. We will first review the major advantages of combining lead and fibers, then look at the different approaches, with emphasis on the one used by the SPACAL group at CERN. We will present the most significant results (SPACAL), and finally review what is needed to move to a full LHC calorimeter.

1 Conceptual designs

1.1 Choice of lead and fibers

Between the two possibilities for a dense absorber, i.e. lead or uranium, the first has many advantages with respect to the LHC requirements. Lead in association with scintillators can provide compensation [1,2], it is faster than uranium (the neutrons thermalizing primarily via elastic scattering off protons, which is a fast process), and the neutron yield is 3 times less than in uranium, which greatly reduces the radiation damage caused by neutrons. Moreover, lead is rather cheap, abundant, and easy to machine. Finally, used with scintillators, it is as compact as uranium (if one requires compensation).

Using fibers leads to the well known advantages of scintillators, with some specific additional features : fibers allow a very fine sampling, which can provide good energy resolution, and arbitrarily fine granularity. Most importantly one does not need external wave length shifters or light guides, hence the use of fibers provides fast signals, significant light yield ($\simeq 10^3$ photoelectrons per incident GeV), and an almost perfect hermeticity. This implies having the fibers run approximately in the direction of the incident particles.

If clearly this association can reach most of the requirements for a LHC calorimeter, it raises some difficult problems : non-gaussian response at low incidence angles, uniformity problems due to fiber-to-fiber fluctuations and finite attenuation length, difficulty achieving longitudinal sampling, and the need for radiation hardness.

1.2 Different approaches

To tackle these problems different approaches are being tested, mainly in the US and at CERN. Since the Americans (grouped into the funded subsystem proposal PC-020) are still at an early stage, we will concentrate on the SPACAL approach at CERN, under the direction of Richard Wigmans.

The basic design consists of a matrix made up of extruded lead plates which are soldered together with tin, in which $1\,mm$ diameter fibers are embedded. At

this stage of the project, the modules are hexagonal (side $43.3mm$), the distance between fibers (center-to-center) being $2.2\,mm$. The lead to fiber ratio in volume is set to 4 : 1 to achieve compensation.
This leads to the following parameters, which give a very compact calorimeter, a radiation length $X_0 = 0.75\,cm$, and an interaction length $X_{int} = 21\,cm$.

Among the various prototypes which have been tested, the most recent consisted of 155 modules, each $2\,m$ long ($\simeq 9.5\,X_{int}$), representing a effective volume of $13.3\,tons$ ($2\,mX2\,mX1\,m$).
For these tests, SCSN-38 fibers from Kyowa Gas Company (Japan) were used. Each fiber was equipped with an aluminium mirror (sputtering technique), with a very good reflection coefficient ($R = 85\%$).
The fibers, sticking out at the end, were bunched together, then coupled via an hexagonal light guide to a photomultiplier. A yellow filter was also used, which in conjunction with the mirror increased the effective attenuation length λ_{att} to about $8\,meters$.
A schematic description of this approach can be found in Fig. 1.

2 Performances

2.1 Major results (SPACAL)

We review here the most significant results on uniformity, electron and hadron response.
Fig. 2 shows the results of a electron scan across 2 modules. The electron signal is more sensitive to fiber-to-fiber fluctuation than with hadrons, since less fibers are involved in the shower development. One observes a uniformity of better than 1% (2% between the modules).

Fig. 3 shows the electron resolution versus the shooting angle θ_z, assuming an expression $\sigma/E = a + b/\sqrt{E}$. One obtains a scaling term of the order of 13%. The constant term, much more sensitive to θ_z, is as low as 1%, for angles around $3\,degrees$, which does not spoil the projectivity.

Fig. 4 gives the impact point resolution for electrons and pions, using traditional barycenter methods. At $80\,GeV$, the average resolution is of $1.6\,mm$ in each direction for electrons, which is quite satisfactory, with regard to the bad granularity of the prototype for electrons. For pions, the average resolution is around $5\,mm$ in each direction.

Fig. 5 shows the energy resolution for individual hadrons in the range $5 - 150\,GeV/c$ (preliminary). Assuming the same expression as for electrons leads to a scaling term of 29% and a constant term of 2.6%. This rather high constant term reflects first a very short attenuation length in the fibers close to the photomultiplier coming from light propagating in the cladding and affecting deeply penetrating hadrons only. This effect is under study and can be easily corrected. Second, the finite attenuation length in the fiber, which affects the uniformity in depth, also contributes. Anyway, this effect should be less important for jets. It seems that one could bring this constant term down to the 1% level.

We move now to the time structure and speed of the signals. Fig 6 gives the resolution for electrons and hadrons versus the integration time (preliminary). One can clearly use a very short gate length (of the order of $30\,ns$) to get a satisfactory response. The same holds for the e/h ratio (Fig. 7), which also shows that the calorimeter is slightly undercompensating ($e/h \simeq 1.05$. Preliminary).

An other important highlight of this technique is its extreme compactness as shown in Fig. 8, where one sees that an integration radius of $30\,cm$ is sufficient to provide a stable hadronic response.

2.2 Electron-pion separation

In this section, we discuss different ways of separating electrons from *isolated* pions. What is relevant for the LHC is the separation from jets and is under study.

A first method exploits the high speed of the signals and their intrinsic time structure [3]. As shown in Fig. 9, measuring the width of the signal at $20\% - 20\%$ yields a rejection factor of 800 for an electron efficiency of 99% at $80\,GeV$. This method could be easily used at a first level trigger.

A more conventional method based on lateral profile of the shower leads to (in conjunction with a preshower detector) a rejection factor of 5000 at $80\,GeV$ for an electron efficiency of 98%. This method could also be implemented at a first level trigger.

Due to the very fine granularity of the calorimeter for hadrons, it is possible to identify an electron (with 95% efficiency), for a hadron misidentification of 10^{-3}, when the 2 particles are as close as $4.3\,cm$.

All these results can be found in more detail in [4,5,6].

2.3 Radiation damage

This crucial issue is being studied by many groups [7], in particular in the SPACAL group [8]. The goals are manifold : with studying different types of fibers, with different types of irradiation (neutrons, photons, electrons), in different atmospheres (air, oxygen, nitrogen).

If one parametrizes the light emission of a fiber as a function of the distance d to the photomultiplier, by the expression : $I(d) = I_0 e^{-d/\lambda_{att}}$, the radiation has 2 effects . First, it affects the emission I_0, i.e. a 20% decrease after $10 Mrad$ (this stands for 3HF+PTP fibers), and second the transmission which is less critical. Fig. 10 shows a typical response for 2 kinds of fibers to non-homogeneous irradiation in depth, simulating the damage due to π^0's.

Using actual characteristics of the fibers these effects lead to a degradation of the order of 1.5% on calorimeter performances, as evaluated by Monte-Carlo (on electron linearity, electron resolution).

Considering now what it means for a calorimeter in a LHC environment, one should concentrate on the damage due to π^0's, which is dominant and very localized in depth. The damage caused by charged hadrons is less important since it is spread

over the full length of the fibers. The damage caused by neutrons is almost negligible (with minimal neutron yield for the Pb/fiber combination, and electronics sitting after $10\,X_{int}$).
In conclusion, $10\,Mrad$ corresponds to 4 years running at a rapidity of $\eta = 2.8$, for a luminosity of $10^{34}\,cm^{-2}s^{-1}$, at a distance of $4\,meters$ from the vertex. The situation is not critical, but still requires a lot of effort, mainly to find a solution for rapidities larger than 3.

3 Towards a real LHC calorimeter

The question is what still has to be done in order to be ready to start building a full calorimeter for LHC in about 2 years.

A major issue concerns calibration, the aim being to work at the 1% level. The problem at LHC will be made more critical because it will be difficult to calibrate modules in test beams, and because of the eventual shifts in performance caused by radiation. Of course one should take advantage of the experience from previous experiments (UA2, CDF, ZEUS).
A lot of work has to be done on this point.

Concerning radiation damage issues, more tests are needed with new fibers and in conditions closer to an LHC environment (long fibers in lead put in real beams). Once more one has to emphasize the necessity to find a solution for rapidities greater than 3.

Concerning the production of modules, even though the current extrusion technique is quite promising (SPACAL), it needs to be improved in order to be mass produced ($\simeq 10^5$ modules).
Moreover, one has to move to projective modules for a final configuration. This will lead to a better matched granularity for electrons, and could provide longitudinal sampling, if one can read out separately long and short (i.e. starting after roughly $30\,X_0$) fibers.

As for light detection devices, photomultipliers are not optimal, mainly because of their limited dynamic range and power consumption ($\simeq 1W$). In that respect, a new device has been developed in the SPACAL group, the Hybrid Photo Diode (Fig. 11). This device provides a good dynamic range (10^5), low power consumption ($\simeq mW$), and allows for anode segmentation to match the required granularity for electrons. This is under study. The behavior in a magnetic field has to be investigated.

A lot of effort has to be directed towards trigger and acquisition issues. Since most of these aspects are not specific to the fiber technique, one should concentrate on its unique features (electron identification at prompt trigger level).

A last point which needs work is full-scale engineering. One needs to maintain a projective structure of about 10^4 tons, without spoiling hermeticity. This problem is being undertaken by many groups (by EMPACT and TEXAS in The United States and SPACAL at CERN).

We describe here a basic design (SPACAL). The detector is divided into indepen-

dent structures called "super-rings" (Fig. 12) to give easier handling and better access to the central part of the detector. Each "super-ring" is in turn made out of rings, themselves built out of pyramidal modules. All these elements are maintained together using glue and iron skirts, and reinforced by a honeycomb structure. CAD studies are in progress.

In parallel, robots for inserting the fibers into the modules are being developed. A different solution is under study for the very forward region.

4 Conclusions

The fiber technique for calorimetry at hadron colliders was introduced around three years ago. It is already very advanced, many non trivial problems having been already solved (mainly in the SPACAL group).
Up to now, no problem looks impossible to solve, but a big effort on *R&D* is still needed (mechanics, calibration).

We conclude with two remarks :
The scintillating fiber technique provides an integrated electromagnetic AND hadronic calorimeter.
With its features (fast, hermetic, uniform, good electromagnetic and hadronic resolution, granularity), this calorimeter can provide valuable and unbiased information (for electrons, jets, missing E_T) already at the first level trigger, which will be of crucial importance for extracting the physics at the LHC.

References

[1] R. Wigmans, Nucl. Instr. and Meth. **A259** (1987) 389.

[2] E. Bernardi et al., Nucl. Instr. and Meth. **A262** (1987) 229.

[3] R. DeSalvo at al., Nucl. Instr. and Meth. **A279** (1989) 467.

[4] D. Acosta et al., Results of prototype studies for a spaghetti calorimeter, Nucl. Instr. and Meth. **A294** (1990) 193.

[5] D. Acosta et al., Electron-pion discrimination with a scintillating fiber calorimeter, CERN/LAA/HC 90-008, to be published in Nucl. Instr. and Meth.

[6] D. Acosta et al., Localizing particles showering in a spaghetti calorimeter (in preparation).

[7] Proceedings of the Workshop on Radiation Damage of Plastic Scintillators, Tallahassee (1990).

[8] D. Acosta et al., Effects of radiation damage on scintillating fiber calorimetry (in preparation).

Figure Captions

1. An electromagnetic module. (SPACAL)
2. Uniformity scan for $80\,GeV$ electrons across modules (SPACAL)
3. Electromagnetic resolution versus the shooting angle θ_z (SPACAL).
4. Position resolution for $80\,GeV$ electrons and pions versus distance from the center of a module (SPACAL).
5. Energy resolution for $5 - 150\,GeV\pi^-$. Preliminary results (SPACAL).
6. Electromagnetic and hadronic energy resolution as a function of the gate width. Preliminary results (SPACAL).
7. e/h ratio as a function of the gate width. Preliminary results (SPACAL).
8. Hadronic resolution for isolated π^- versus the integration radius. Preliminary results (SPACAL).
9. Distribution of the widths, measured at 20% of the amplitude, of e.m. and hadronic shower signals at $80GeV$ (SPACAL).
10. Response of 2 kinds of fibers to different irradiation doses. The dose is non-homonogeneous in depth to simulate the damage from π^0's.
11. Layout of a Hybrid Photo Diode with anode segmentation (DEP Company & SPACAL).
12. Layout of a full coverage fiber calorimeter with projective geometry, organized in "super-rings" (SPACAL).

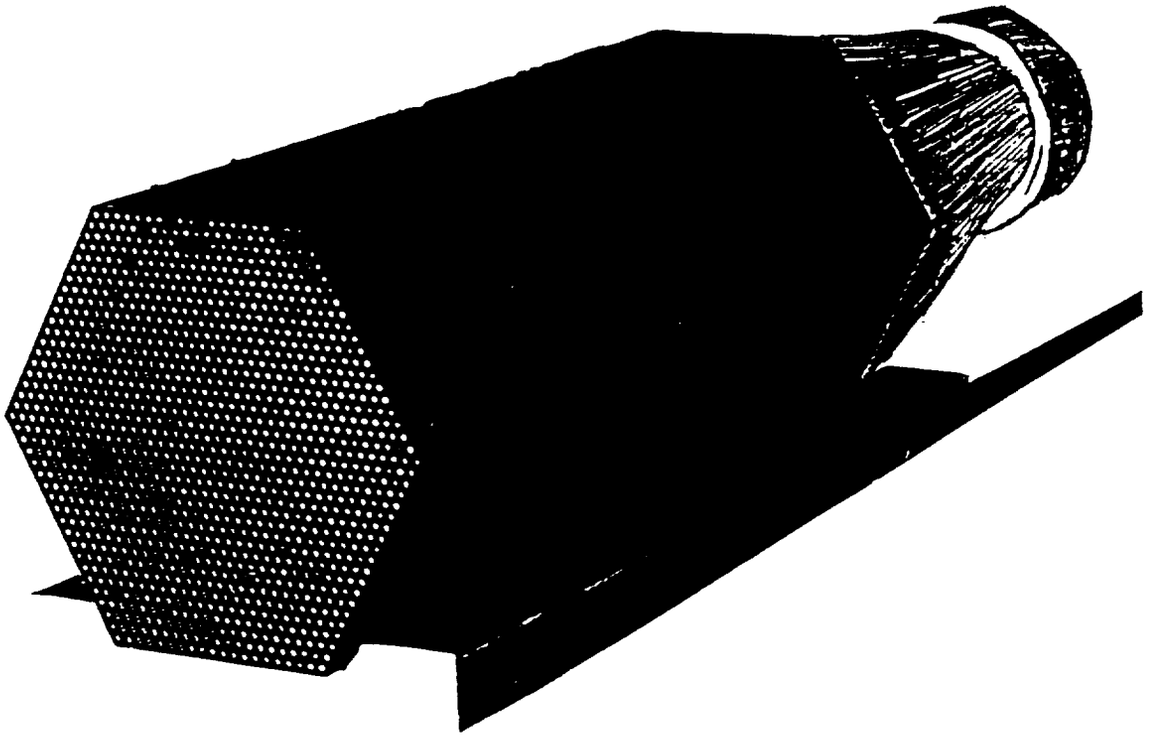


Fig. 1

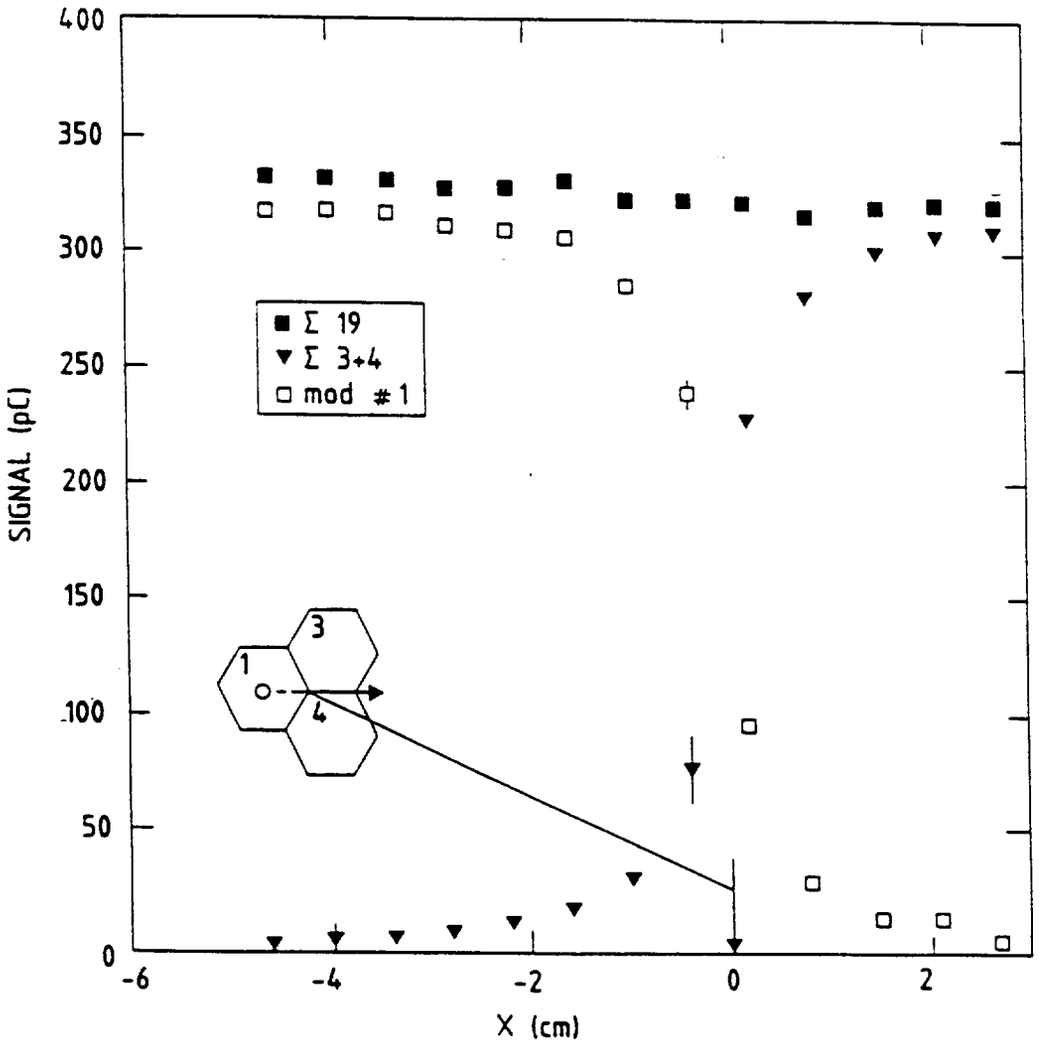

400
350
300
250
200
150
100
50
0
SIGNAL (pC)
Σ 19
Σ 3+4
mod #1
1
3
4
-6
-4
-2
0
2
X (cm)

Fig. 2

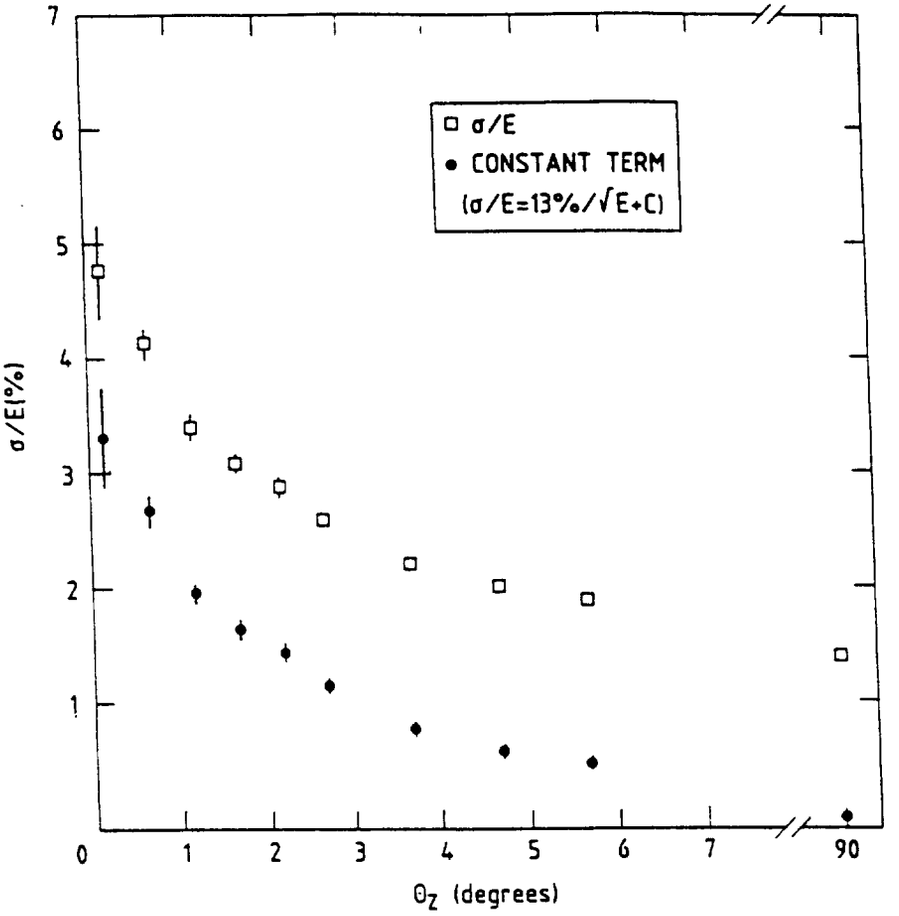

□ σ/E
• CONSTANT TERM
(σ/E=13%/√E+C)
σ/E(%)
θz (degrees)
0
1
2
3
4
5
6
7
90

Fig. 3

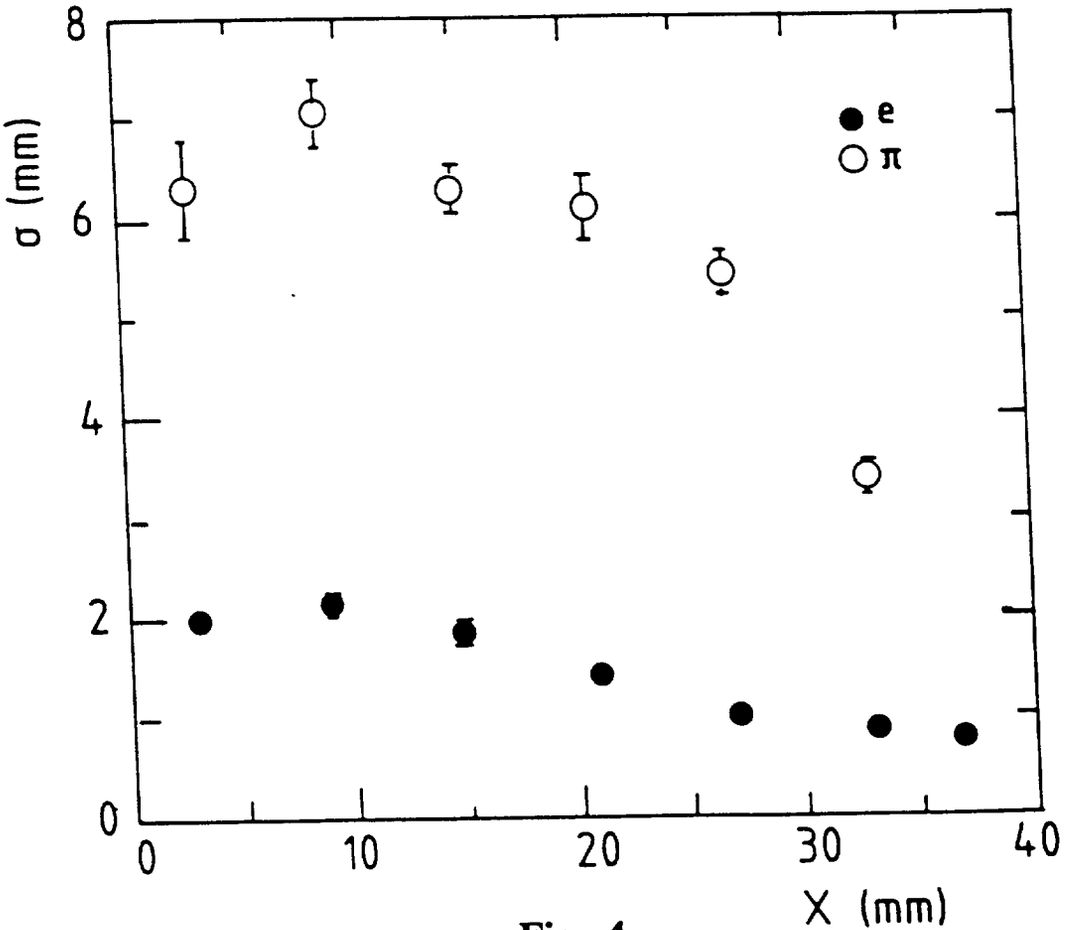

σ (mm)
e
π
X (mm)
0
2
4
6
8
0
10
20
30
40

Fig. 4

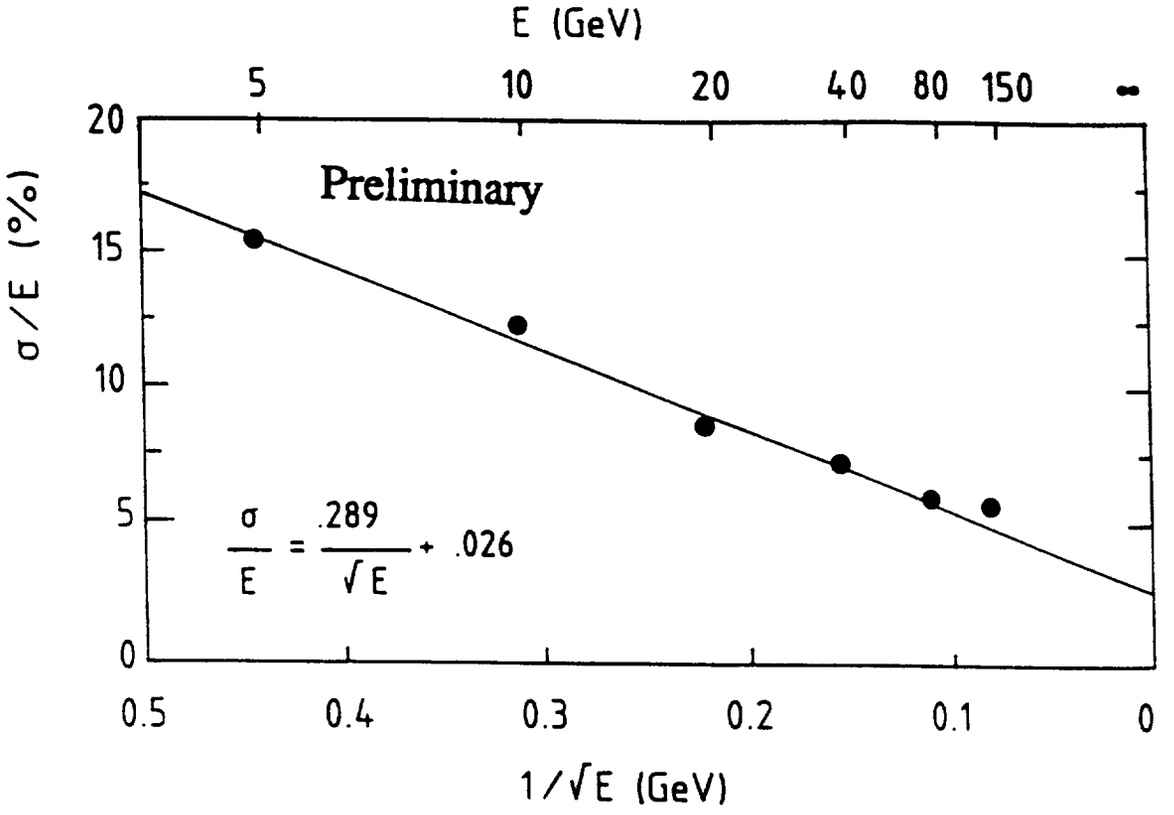

E (GeV)
5
10
20
40
80
150
∞
Preliminary
σ/E (%)
20
15
10
5
0
σ/E = .289/√E + .026
0.5
0.4
0.3
0.2
0.1
0
1/√E (GeV)

Fig. 5

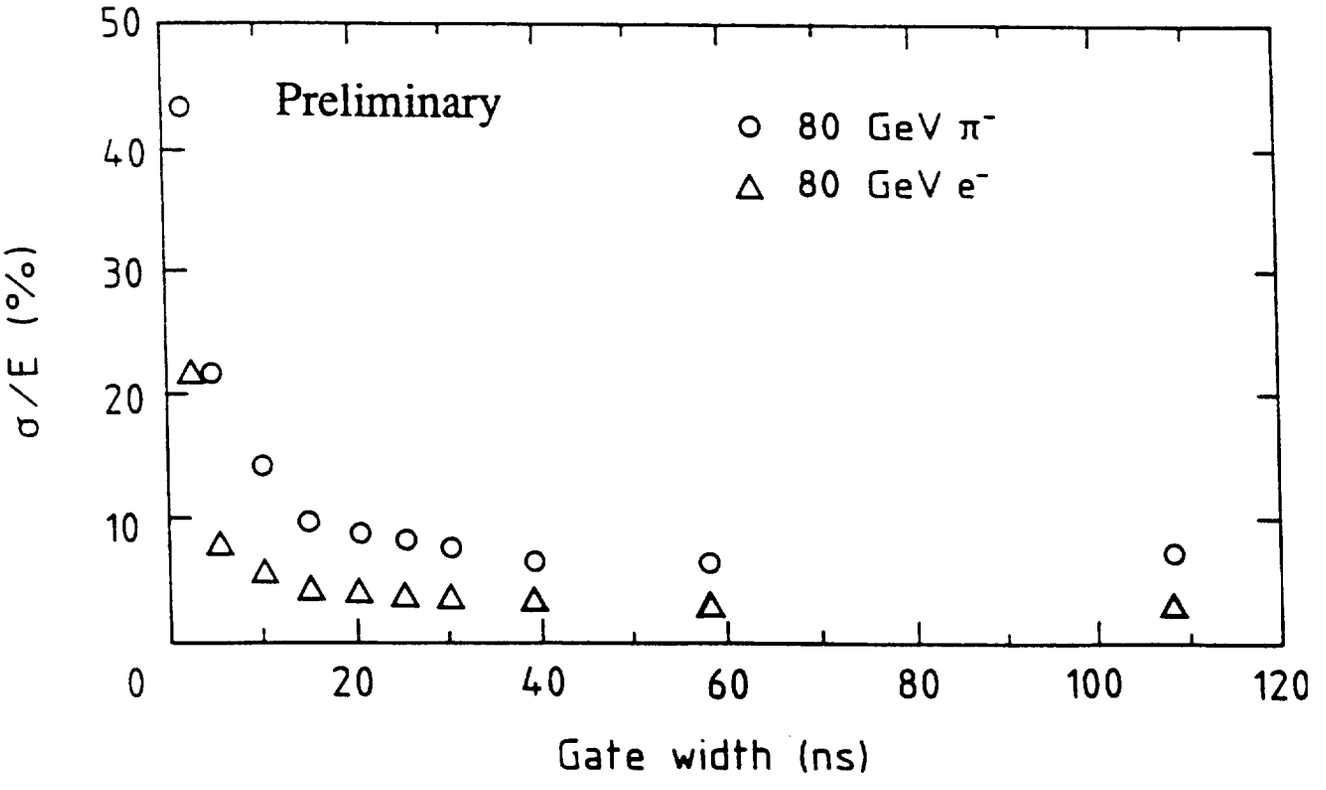

Preliminary
80 GeV π⁻
80 GeV e⁻
σ/E (%)
50
40
30
20
10
0
20
40
60
80
100
120
Gate width (ns)

Fig. 6

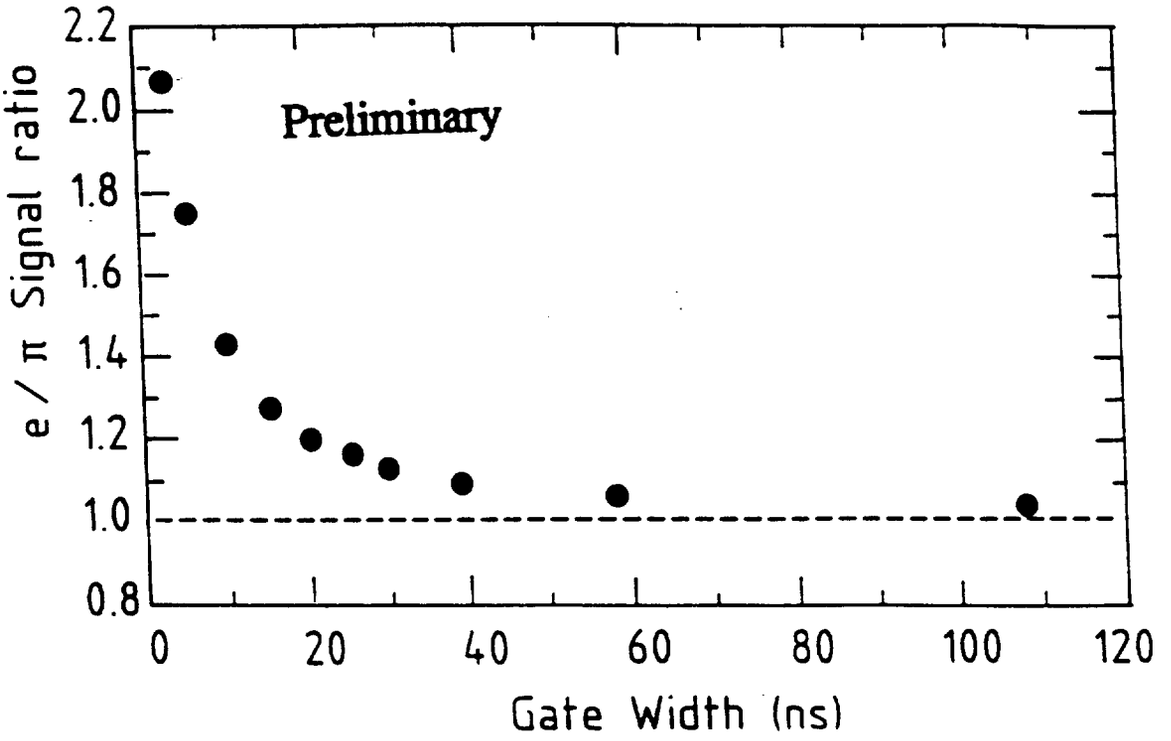

Preliminary
e / π Signal ratio
2.2
2.0
1.8
1.6
1.4
1.2
1.0
0.8
0
20
40
60
80
100
120
Gate Width (ns)

Fig. 7

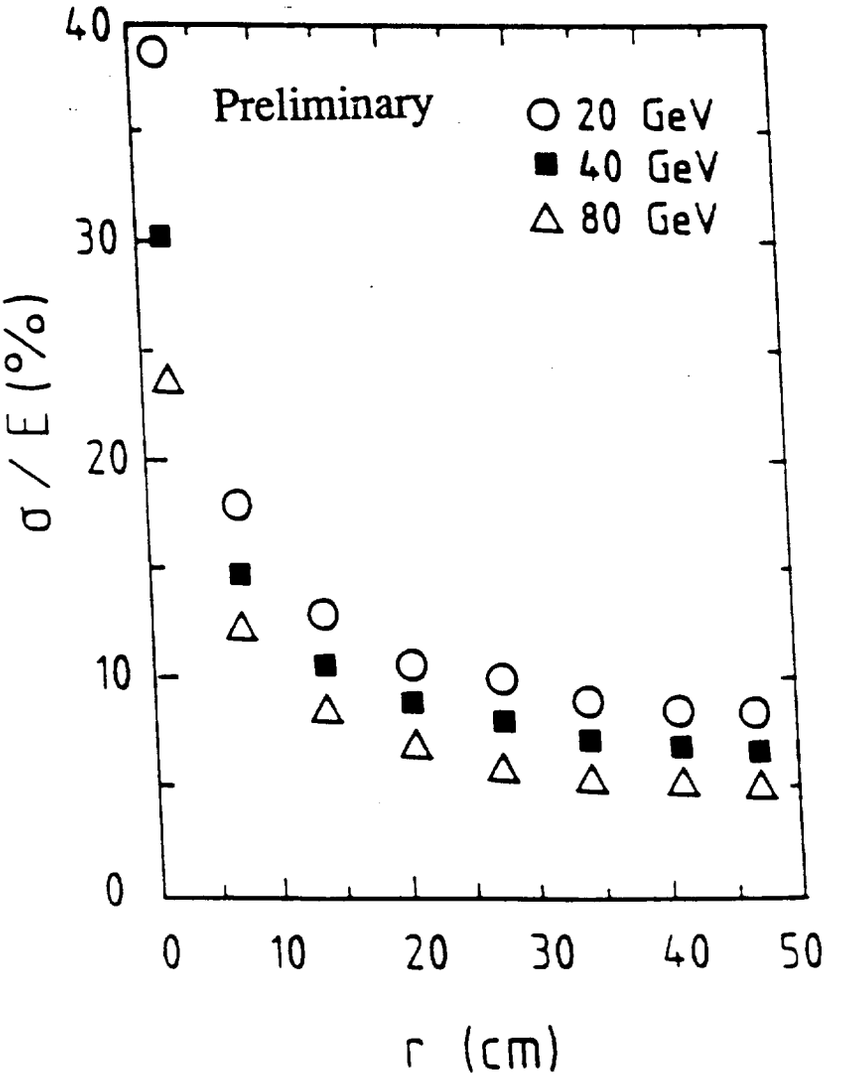

Preliminary
20 GeV
40 GeV
80 GeV
σ / E (%)
40
30
20
10
0
0
10
20
30
40
50
r (cm)

Fig. 8

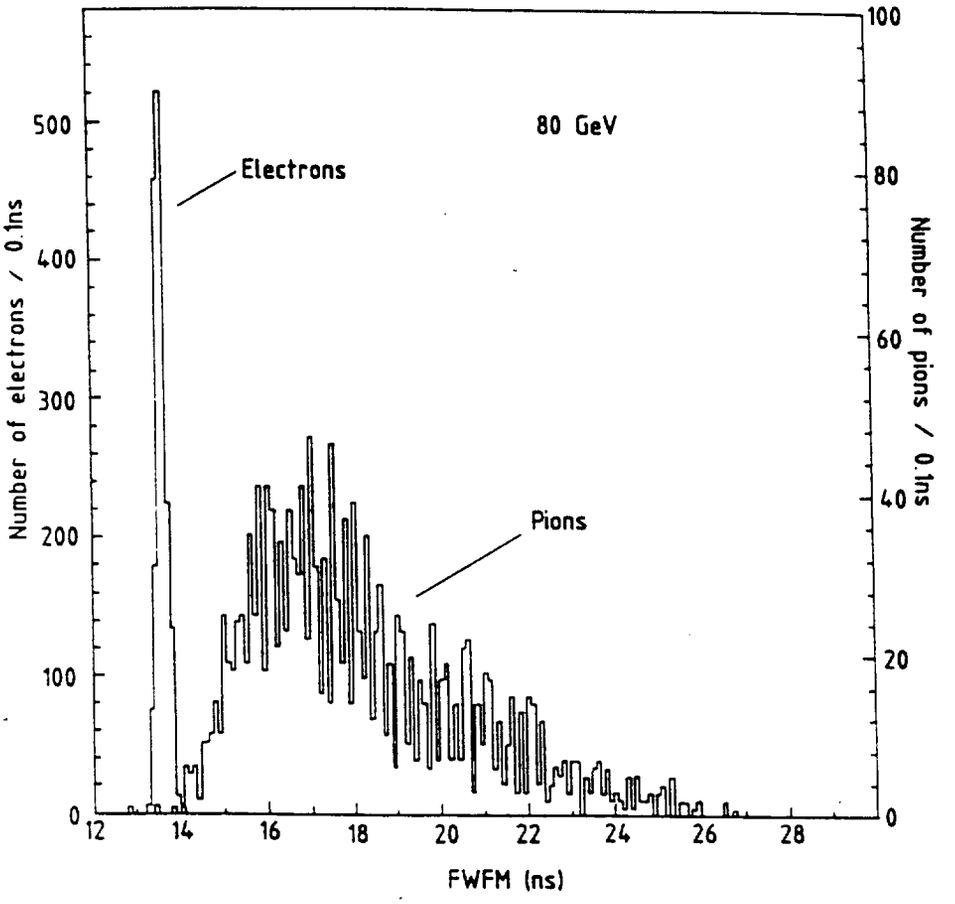

80 GeV
Electrons
Pions
Number of electrons / 0.1ns
Number of pions / 0.1ns
FWFM (ns)
0
100
200
300
400
500
20
40
60
80
100
12
14
16
18
20
22
24
26
28

Fig. 9

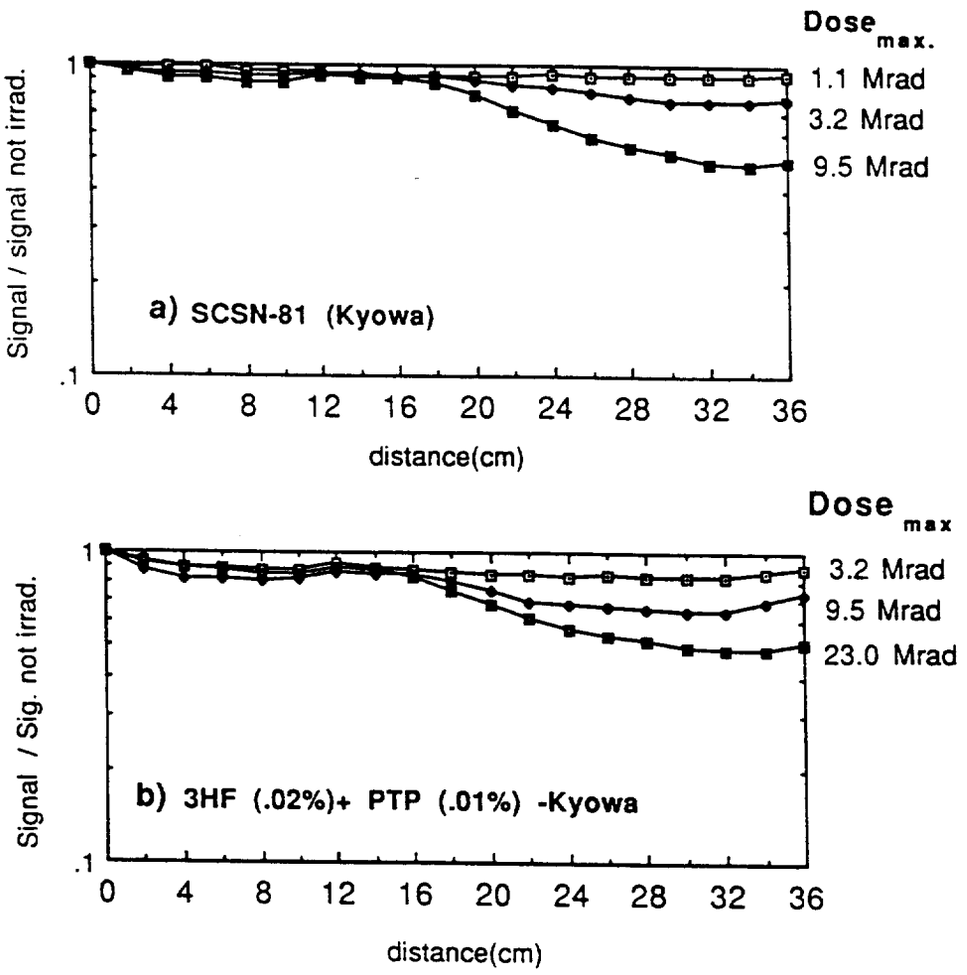

Dose max.
1.1 Mrad
3.2 Mrad
9.5 Mrad
Signal / signal not irrad.
a) SCSN-81 (Kyowa)
distance(cm)
Dose max
3.2 Mrad
9.5 Mrad
23.0 Mrad
Signal / Sig. not irrad.
b) 3HF (.02%)+ PTP (.01%) -Kyowa
distance(cm)

Fig. 10

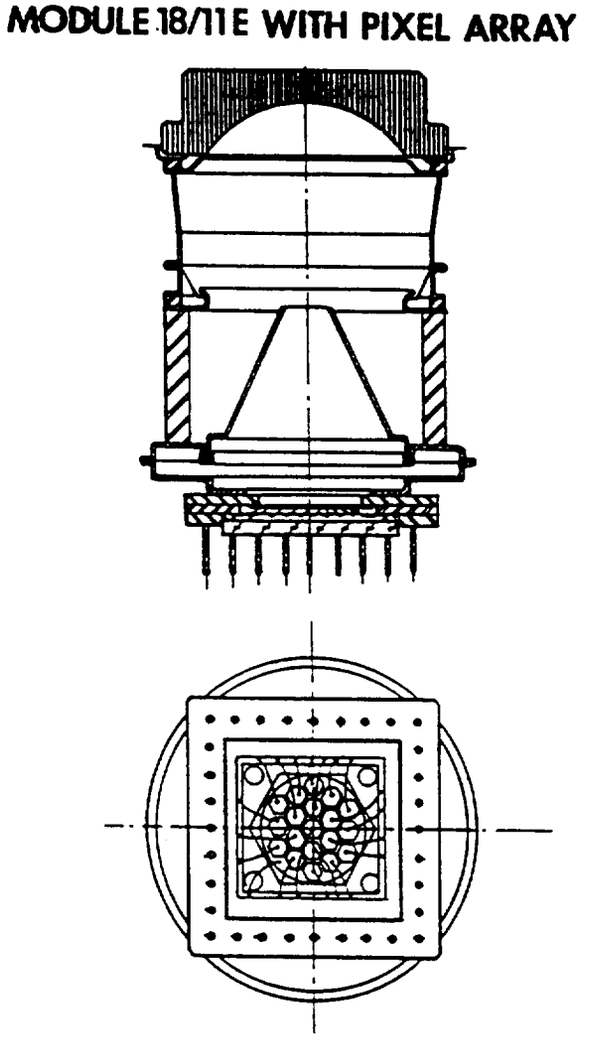


Fig. 11

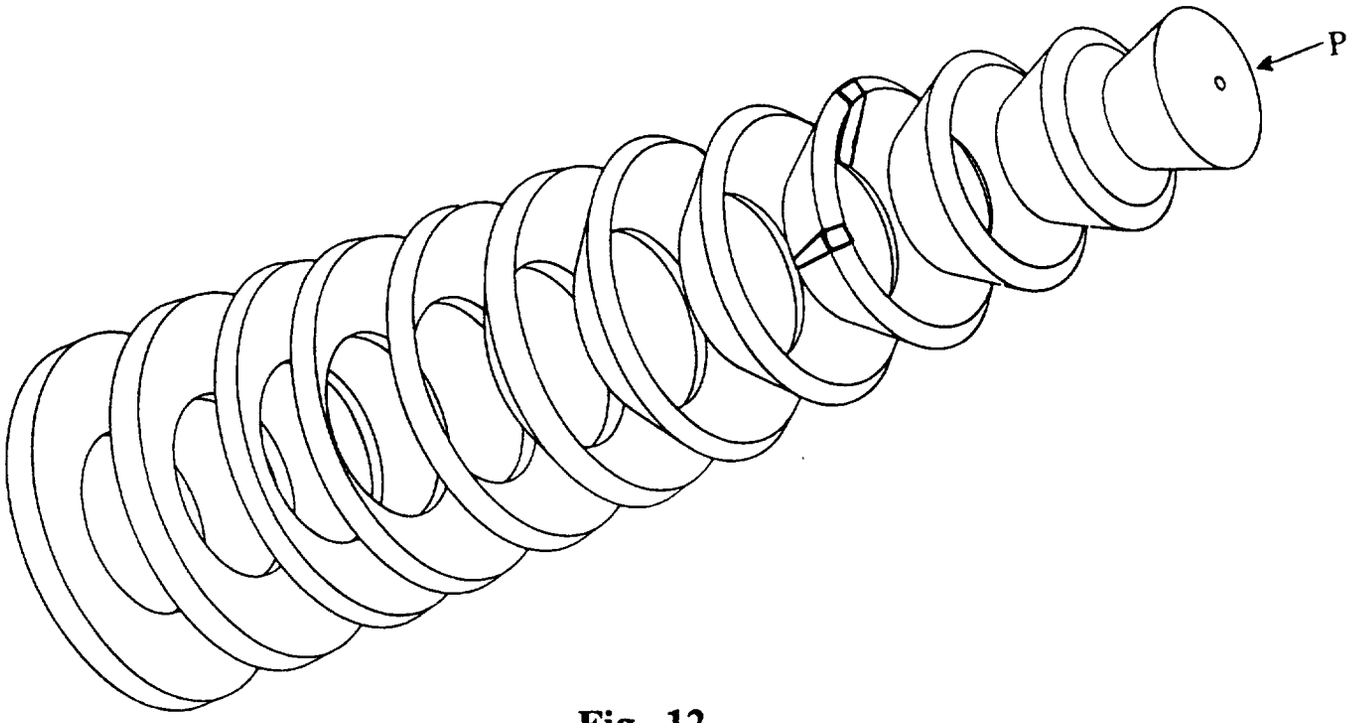


Fig. 12

CALORIMETRY WITH WARM LIQUIDS: SUMMARY AND PROSPECTS FOR LHC EXPERIMENTS

E. Rademacher
CERN, Geneva, Switzerland

1. INTRODUCTION

There are several reasons for which calorimeters based on a liquid detecting medium with high mobility are of considerable interest for a LHC detector, namely the direct relation between charge and energy deposition, the ease of accurate calibration, the possibility of fine transverse and longitudinal segmentation and the possibility to obtain maximum hermeticity and e/π compensation.

In the past several liquids have been studied [1] and the relevant properties are given in table 1.

Table 1 : Characteristics of warm liquids.

	TMP	TMSi	TMGe	TMSn
Formula	C_9H_{20}	$C_4H_{12}Si$	$C_4H_{12}Ge$	$C_4H_{12}Sn$
Density [g / cm^3]	0.72	0.645	1.006	1.314
Dielectric constant	1.98	1.92	2.01	2.25
Radiation length [cm]	62.3	52.2	18.2	9.2
dE / dx [MeV / cm]	1.58	1.36	1.78	2.09
Mobility μ_e [cm^2 / V.sec]	30	100	90	70
Drift time t_d [nsec] at 50 kV / cm for 1 mm gap	74	23	23	24
Ion pair yield G_{fi} (0) per 100 eV at zero field	0.75	0.63	0.61	0.63
Flashpoint [°C]	7	-18		21
Boiling point [°C]	123	27	43	78
Vapor pressure [Torr] at 20 °C	15	650		

The important parameters are the drift time t_d (fig.1) and the ion pair yield $G_{fi}(E)$ (fig. 2), which has been calculated [2] using Onsager's theory [3].

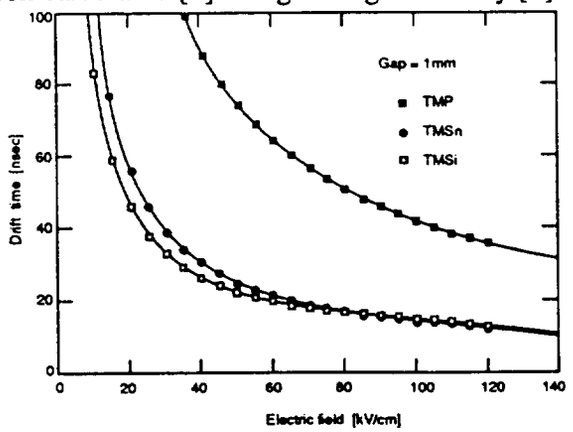


Fig. 1 : Drift time in TMP, TMSi and TMSn as a function of the electric field applied to a 1mm gap ionization chamber.

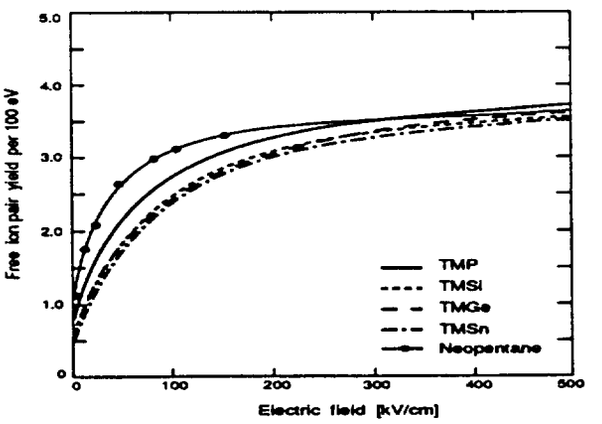


Fig. 2 : Ion pair yield per 100 eV in TMP, TMSi, TMGe, TMSn and Neopentane as a function of the electric field. The dotted points are experimental values.

Tetramethylpentane (TMP) and tetramethylsilane (TMSi) have been investigated intensively in the development of the UA1 calorimeter project [4,5]. Especially, the production of large volumes of ultrapure liquids giving electron life times of the order of several hundred microseconds is now well established, as well as the cleanliness of containers and ionization chambers [6,7]. For a LHC calorimeter TMP and TMSi will be considered as candidate liquids. Tetramethylgermane (TMGe) and tetramethyltin (TMSn) are excluded for the moment because of their price and toxicity.

2. RESULTS FROM EXISTING CALORIMETER MODULES

In this session results from two groups have been presented. The first group [8] reported results on the response to electrons and pions from one TMSi filled ionization chamber placed between Uranium or Lead plates of different thickness. Actually they are testing a prototype calorimeter with 40 ionization chambers. The second group [9] reported on first results of a prototype calorimeter from the WALIC collaboration. It consists of 34 ionization chambers of the UA1 type filled with TMP and interleaved with Lead plates. Results obtained in a FNAL beam on the response to muons and the electron energy resolution were reported. It remains to review here the results of the UA1 U/TMP calorimeter modules performed in a test beam at CERN.

Several large U/TMP calorimeter modules have been constructed and intensively tested in a beam [7]. They are operated at electric fields between 8 and 15 kV/cm and perform well as a combined electromagnetic and hadronic calorimeter. The energy resolutions for electrons and pions were measured and are found to be in agreement with expectation from Monte Carlo studies. The resolution for electrons (fig. 3) is given by :

$$(\sigma(E) / E)^2 = (0.12 / \sqrt{E})^2 + (0.009)^2$$

and for pions (fig. 4) one obtains without correction for lateral shower escape, but unfolding the noise distribution:

$$(\sigma(E) / E)^2 = (0.581 / \sqrt{E})^2 + (0.068)^2$$

This resolution is for one U/TMP module ($\lambda = 2.3$) operated at an electric field of 8 kV/cm combined with the UA1 Iron/scintillator calorimeter ("C" module, $\lambda = 4.5$).

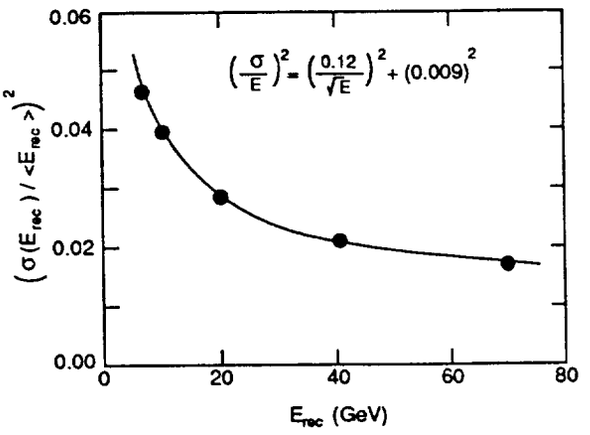


Fig. 3 : Electron resolution of a UA1/TMP calorimeter module as a function of the reconstructed beam energy.

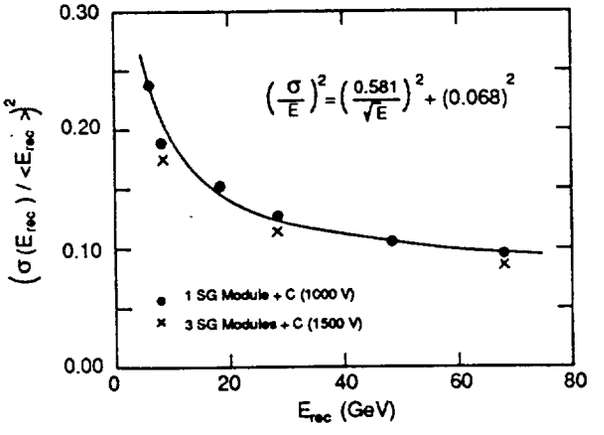


Fig. 4 : Hadronic resolution of UA1/TMP calorimeter modules as a function of the reconstructed beam energy for two running conditions.

Three U/TMP modules mounted on top of each other to avoid lateral shower escape were measured in the same configuration as described above. The result obtained for the hadronic resolution (fig. 4) is:

$$(\sigma(E) / E)^2 = (0.47 / \sqrt{E})^2 + (0.078)^2$$

The improvement in resolution is due to the higher electric field (12 kV/cm) as well as to the lateral containment of the shower. This energy resolution can also be written in linear form to allow more easily direct comparison with quoted results of other calorimeters:

$$\sigma(E) / E = 0.36 / \sqrt{E} + 0.055$$

Due to this calorimeter configuration, namely the combination of the two types of calorimeters, a sizable constant term is present in the pion energy resolution. The hadron resolution improves significantly

with increasing electric field whereas the electron energy resolution varies only slightly. The impact point of the electrons is measured in a position detector [10] located at a depth of 3.4 radiation lengths. The spatial resolution in the position detector for single electromagnetic showers approaches 1.0 mm for energies greater than 30 GeV.

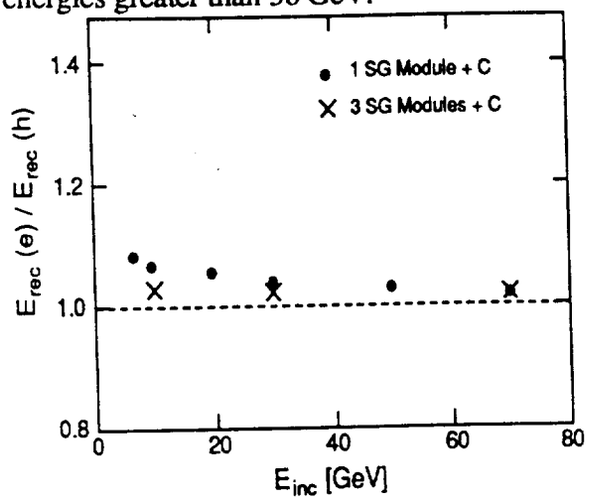


Fig. 5 : Ratio of the reconstructed electron to pion energies for the UA1/TMP calorimeter as a function of the incident particle energy for two running conditions.

The electron/pion ratio of the U/TMP module followed by the "C" module is found to be close to 1 (fig. 5). This implies that compensation is observed in a non-uniform sampling calorimeter without sacrificing linearity and electron resolution.

The signal to noise ratio averaged over the six samplings of the UA1 modules is 4.4 using 70 GeV muons. The tower to tower uniformity is better than 1%. For energies greater than 50 GeV one finds an e/π rejection ratio of 10^{-4} for an electron identification efficiency of 90% [7].

16 of the modules described above will be assembled to form one Supergondola structure.This structure will be installed in the UA1 magnet in order to test noise and cross-talk in real environment. Cosmic ray runs will allow to control the calibration under several conditions over a long period of time.

3. PARAMETERS FOR WARM LIQUID CALORIMETRY AT LHC

From the results mentioned above it is evident that this type of calorimeter is also adequate at LHC energies. However, for the application of this technology to the environment of the Large Hadron Collider several factors become important.

Due to the high luminosity and the repetition rate of 15 nsec of the LHC, it is desirable to collect the full charge in about the same time. By increasing the voltage and decreasing the gap, a drift time comparable to the bunch crossing time can be achieved. TMSi is therefore a more suitable choice than TMP since its drift time is roughly three times shorter (fig. 1). In such a way the overlap of events due to pile-up will be considerably reduced. Nonetheless the problem of positive ion accumulation remains to be studied at high luminosities.

At present ionization chambers use only stainless steel and ceramics. Future designs may require the use of other metals and insulating materials. Studies of radiation effects on suitable materials and their interaction with the calorimeter liquid are necessary. First results [11] were reported at this workshop. It seems that an insulating material called VECTRA can be used for calorimeter cells.

A compromise has to be found between the size of the cells and their number. In order to keep the pile-up small the cell size in the electromagnetic part should be chosen in first approximation between 3 and 5 Molière radii which in the case of an Uranium calorimeter is approximately 5 cm. This reduces the capacitance of the electrodes by a factor of 4 compared to the ones of the UA1 calorimeter. The size of the electrodes for the hadronic calorimeter can be made larger.

In order to fully contain electromagnetic showers the length of the first part of the calorimeter has to be 30 X_0. For the same reason the depth of the hadronic section should be at least 7 interaction lengths.

The radiation doses at LHC will be several orders of magnitude higher than those at the $p\bar{p}$ collider. Over a period of several years the total accumulated dose received by the chambers is expected to reach 10 Mrad (100 kGy) [12]. Radiolytic decomposition of the liquid is expected and the interaction of these radiolytic products with molecules adsorbed on the electrodes and walls may have an influence on the electron lifetime and ion pair yield (see § 6).

4. DESIGN OF TEST CHAMBERS AND MODULES

Three designs have already been presented in this session . The first design [8] describes an U/TMSi hadronic calorimeter with individual ionization chambers having a pad read out. The WALIC collaboration [9] proposes for SSC a "swimming pool" design where absorbers and electrodes are mounted in one

volume filled with TMP or TMSi. In the third design [11] individual ionization chambers are moulded out of VECTRA with subsequent metallization to obtain the electrodes. The chambers will have a 2 mm gap, filled with TMSi and operated at a high electric field. In the following we present a design which is part of a proposal submitted to the DRD Committee [13].

The idea is to construct small gap chambers to keep the operating voltage below 10 kV and to collect the charge within 15 nsec. High electric fields ensure high electron yields since the recombination is reduced. Positive ion effects are reduced as well since the ion drift velocity is higher. One intends to build test chambers with a multigap structure made of successive metallic grids in one liquid volume. The absorber will be outside the liquid containing chambers. The use of metallic grids leads to a reduced surface of the electrodes and will allow - beside other effects which we mention later - easy pumping during bake out. In addition the capacitance of the cells will also be some 15 to 20% smaller than for cells with sheet electrodes.

In the final design of a calorimeter the liquid is contained in rigid boxes in order to avoid microphonic effects. Initially one plans to build small boxes to study the high field behaviour of the liquid in the desired configuration.

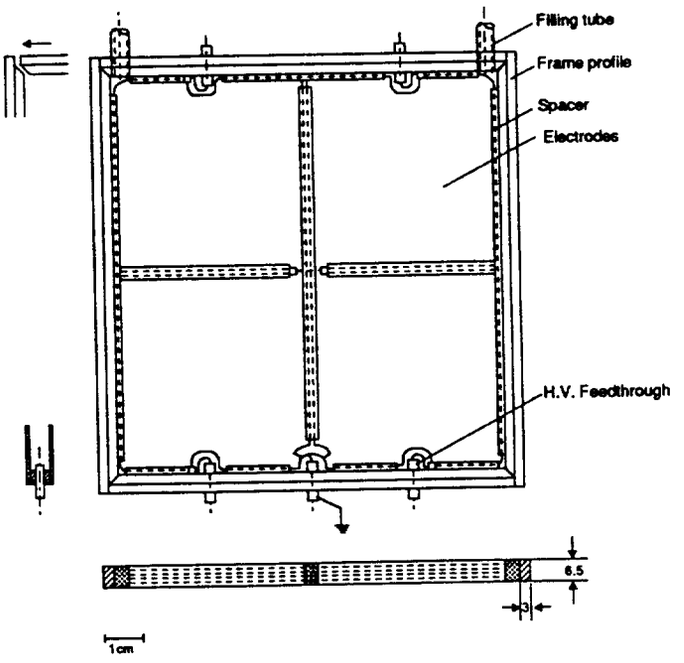


Fig. 6 : Layout of an ionization chamber.

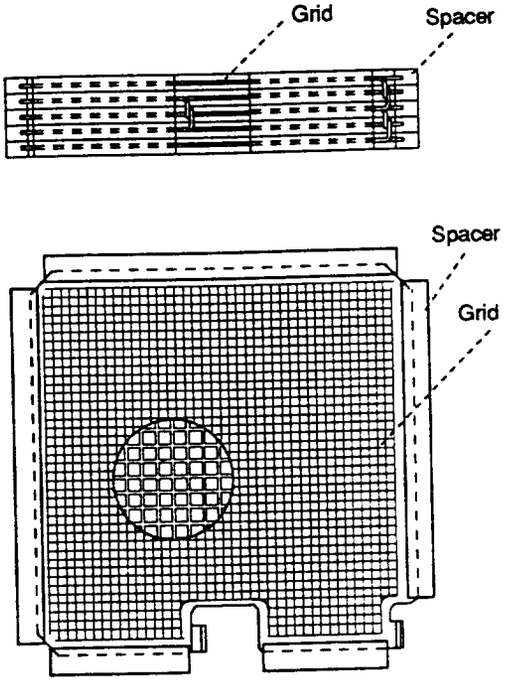


Fig. 7 : Grid electrodes with insulating spacers.

Each of these test boxes (fig. 6) is made of a stainless steel picture frame unit of 3 x 6 mm^2 profile. The two covers of 0.5 mm stainless steel are laser-welded on the frame. Inside the box are four multigap structures of 5 grids each. These grids are separated by 1 mm, are 5 x 5 cm^2 in size and 0.1 mm thick (fig. 7). They can be either stainless steel or Copper-Beryllium produced by photoetching or even metallized ceramic plates. Their flatness guarantees a constant gap width over the whole surface.The grids are held by insulating spacers which can be made out of ceramics, as a first step. It is the intention to try other insulating materials which can stand the bake out temperature of 250 °C and are radiation resistant to avoid pollution of the liquid. With these first boxes all relevant parameters will be studied.

One further step will be the construction of a small calorimeter by assembling 45 boxes with 2 mm Uranium plates, equivalent to 30 radiation lengths, for beam tests. The number of free electrons expected from minimum ionizing particles in one of the 4 mm multigap chambers is given by :

$$N_e = 1/2 \times 10^{-2} \times d \times G_{fi}(E) \times dE/dx \quad \text{[electrons]}$$

where d is the gap and $G_{fi}(E)$ is the free ion pair yield as calculated [2] according to the Onsager theory [3]. In the case of TMSi one obtains for an electric field of 100 kV/cm applied to the 4 mm multigap chamber approximately 7000 electrons which corresponds to a charge of 1.12 fC.

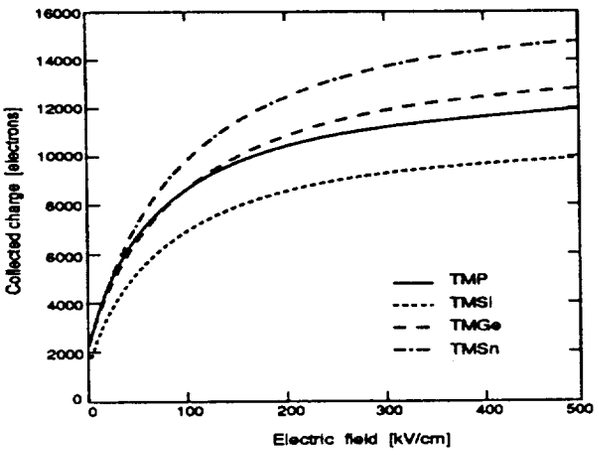


Fig. 8 : Number of electrons in TMP, TMSi, TMGe and TMSn as a function of the electric field in a 4 mm multigap chamber.

Fig. 8 shows the number of electrons N_e as function of the electric field for a gap of 4 mm for the liquids of table 1.

The next step is the construction of a full scale calorimeter prototype module. Actually one considers an electromagnetic section of about 30 radiation lengths and a hadronic one of approximately 7 interaction lengths. This depth ensures that more than 95 % of the energy of a 150 GeV shower is absorbed [14].

In the UA1 design, one of the reasons to choose Uranium as absorber was its compactness. The test beam results [7] show that Uranium in association with TMP gives an e/π ratio close to unity as well as a good hadronic energy resolution without affecting the electron energy resolution. Furthermore the lateral dimensions of the shower are a factor two smaller with respect to Lead.

Extrapolating from these results one expects for 1 mm thick Uranium plates as absorber an electromagnetic resolution of

$$\sigma(E) / E = 0.09 / \sqrt{E}.$$

In order to minimize the constant term in the hadronic resolution an absolutely uniform hadronic calorimeter has to be built. Presently one plans to use 5 mm Uranium plates. In order to avoid overcompensation the number of Uranium plates has to be determined. With the proposed multigap ionization chambers one aims to reach a hadronic resolution comparable to the one from the UA1 calorimeter modules, namely

$$\sigma(E) / E \approx 0.3 / \sqrt{E}.$$

A small constant term due to the stepping from 1 to 5 mm between the electromagnetic and hadronic sections may remain. Other materials like Copper-Tungsten composites or Molybdenum will be included in the research programme. It is expected that the test calorimeter will have a 0.5 x 0.5 m^2 cross section with several hundred detector planes.

An additional feature of the calorimeter will be the built-in tracking detector. In contrast to the UA1 calorimeter which has only one position detector one plans to insert several position sensitive detectors, similar in construction to the one used in the UA1 calorimeter, to measure the shower direction.

One aim of the R&D programme is to study by simulation the interplay of these parameters in order to reach the best possible configuration. Presently, the UA1 U/TMP calorimeter has been simulated in detail using the Monte Carlo programme GEANT 3.14. A good agreement with the experimental data has been observed, especially on the variation of the e/π ratio with the electric field [15]. The same Monte Carlo programme will be used to simulate the behaviour of the proposed calorimeter. To achieve the best possible resolution and compensation, the simulation studies must also optimize the choice of the absorber material, its thickness, the cell size of the ionization boxes and the sampling fraction. Simulation studies using GEISHA [16] indicate for instance that for a TMSi calorimeter the optimum sampling is reached with Iron with a fraction of 1 : 1. Using 0.5 cm Fe and 0.5 cm of TMSi may lead to a hadronic resolution of $\approx$ 30 % / $\sqrt{E}$ with an e/π ratio near to one, the electron energy resolution being of course not very good.

5. ELECTRONICS FOR A WARM LIQUID CALORIMETER

At TeV energies and high luminosities the amplifiers must withstand very high counting rates maintaining simultaneously excellent stability and very large dynamic range. A relevant paper [17] has discussed the " *limit to the counting rate posed by the time required to transfer the charge from the electrodes into the amplifier* ". This time is essentially a function of the length of the connection between the electrode and the amplifier.

There are two possibilities to improve the charge transfer time [18]. One way is to reduce the input resistance of the preamplifier. This requirement is difficult, nevertheless for the design of § 4 one believes that a suitable charge integrator can be made taking advantage of the new components coming from the growing market of consumer electronics (HDTV). In order to maintain a reasonable signal to noise ratio and to take full advantage of the short charge collection time one has to increase considerably the

transconductance/bandwidth ($f_t = k \times g_m/C_{in}$). Moreover, the mechanical structure of the proposed detector will allow the mounting of the amplifiers close to the feedthroughs in order to minimize transit time effects.

On the other hand it is planned to develop wide-band voltage amplifiers which elaborate the signal obtained by the current integrated on the anode of the detector itself, hence producing an output signal of similar shape as the current pulse in the chamber. Simulation of this type of amplifiers has already been done. The results are promising and one believes that amplifiers with gain-bandwidth product of the order to 10^9 can be obtained. Nevertheless the noise charge level will be such that the muon calibration of the calorimeter will be difficult to perform. Therefore one is presently investigating the possibility of using the integrated cathode current for this purpose. The amplifiers of the UA1 U/TMP calorimeter seem adequate for this approach.

The second way to improve the charge transfer time is to reduce the detector capacitance, i. e. reducing the cell size or the number of cells per sampling. In both cases the number of preamplifiers may increase to larger numbers. A possible alternative will be the connection in series of the cells within one sampling. This is called the electrostatic transformer (EST). Tests on models and simulation studies have already been performed [18]. A similar approach by decoupling the chamber capacitances with an additional capacitance has been presented in this workshop [11].

6. RADIATION HARDNESS OF THE LIQUIDS

Although there has been a special presentation in this workshop [19] concerning the radiation damage of warm liquids we will briefly mention the important aspects of it.

Radiation energy absorbed by the liquid is converted into ionization and excitation. In a liquid most ion pairs are generated in close spatial correlation and they undergo geminate recombination after a very short half life time. The recombination energy is converted into excitation as well, which is responsible for the breakage of chemical bonds. The main results of bond breakage is the formation of radicals R. Radicals are chemically reactive species with a limited life time. They disappear either by reaction with molecules of the liquid or by reaction with each other.

The **radiolysis** process describes this breakage of chemical bonds by the absorbed radiation energy and the subsequent formation of radicals. Usually many products are formed and it is only possible to detect the most prominent ones. The main products which interest in the present context are gases like hydrogen and methane, high molecular weight compounds and radicals which are chemically reactive species with a limited life time.

In presence of a vapour space a higher concentration of hydrogen will develop in the vapour space leading to an increase in pressure. For 10 Mrad the resulting **pressure increase** would be 3.7 bar in the vapour space if one includes the contribution from the methane generated.

In absence of a vapour space, the equivalent pressure exerted by the H_2 molecules is 330 mbar. It is possible that the hydrogen remains dissolved in the liquid without forming a vapour phase and will take part in the radiolysis reactions.

The **electron life time** is limited by the concentration of electronegative substances present in the liquid. Although the liquid will have a very low level of these compounds, radiation chemical effects may transport substances adsorbed at the electrodes and the walls into the liquid. Hydrogen and methane may form OH^- or H_2O with the oxygen layers on the surface of the walls. These, in turn, may react with the hydrocarbon radicals to form electronegative impurities reducing the electron life time, mobility and yield. It is this one of the main reasons to use grids instead of solid metal electrodes, since their surface is increased by a factor 20 compared to grids.

The formation of high molecular weight compounds may influence the **electric properties** of the ionization chamber. Charge transfer from parent positive ions to dimer or polymer ions reduces the overall mobility of the positive species. This effect may be detrimental to the fast clearing of the gap from positive charges. By drift, the polymer ion is transported to the cathode where it is deposited. An electrically insulating layer may be the result.

In order to study the influence of high radiation doses on warm liquids one foresees to build special stainless steel containers. In order to avoid pressure increase due to gas pockets, care has to be taken that no gas volume is on top of the liquid, especially close to the valve. The first test consists in measuring a possible pressure increase due to the formation of hydrogen during the irradiation. Next, the irradiated liquid will be transferred into a special counter with double grids where the ionization electrons will be produced with the help of a Laser light irradiating the cathode. The electrons will drift to the anode and the total charge will be measured. Comparing this charge with the one obtained from non irradiated liquid gives directly the decrease in life time due to the radiation.

7. CONCLUSION

From the present knowledge of the warm liquid calorimetry one may conclude that this kind of detector is very adequate for the LHC since good resolutions and natural compensation can be achived. Nevertheless the radiation hardness of the liquids, the possibility of a fast read out and the achievement of high electric fields has to be studied.

8. ACKNOWLEDGEMENT

I would like to thank all participants of the working group which contributed with presentations or in discussions to this summary.

9. REFERENCES

[1] W. F. Schmidt, Can. J. Chem. **55** (1977), 2197.
T. G. Ryan and G. R. Freeman, J. Chem. Phys. **68** (1978), 5144.
H. Jungblut and W. F. Schmidt, Nucl. Instr. and Methods **A241** (1985), 1128.
J. Engler, H. Keim and B. Wild, Nucl. Instr. and Methods **A252** (1986), 29.
H. Faidas, L. G. Christophorou, D. L. McCorkle and J. G. Carter, Nucl. Instr. and Methods **A294** (1990), 575.
S. Geer, R. A. Holroyd and F. Ptohos, Nucl. Instr. and Methods **A287** (1990), 447 and BNL 44709, June 1990.
I. Lopes and W. F. Schmidt, Z. Naturforsch. **45a** (1990), 832.
[2] G. Ambrosini and F. Cavanna, UA1 TN/90 -19 (1990)
[3] L. Onsager, Phys. Rev. **54** (1938), 554.
[4] M. G. Albrow et al., Nucl. Instr. and Methods **A265** (1988), 303.
[5] C. Bacci et al., Nucl. Instr. and Methods **A292** (1990), 113.
[6] A. Gonidec, C. Rubbia, D. Schinzel and W. F. Schmidt, CERN - EP/88 -36.
[7] R. Apsimon et al., to be published.
[8] K. Shmakov, these proceedings.
[9] B. Mansoulié, these proceedings.
[10] K. Ankoviak et al., Nucl. Instr. and Methods **A279** (1989), 83.
[11] J. P. Mendiburu, these proceedings.
[12] G. R. Stevenson and H. Schönbacher, CERN 88-02 (1988), 39.
[13] E. Geulig et al.,*"Warm Liquid Calorimetry for LHC"*, Proposal submitted to the DRD Committee, CERN/DRDC/90-50, DRDC/P 11, October 5, 1990.
[14] M. Abolins et al., Nucl. Instr. and Methods **A280** (1989), 36.
[15] A. Givernaud, Proceedings of the ECFA study week on Instrumentation Technology for High-Luminosity Hadron Colliders, Barcelona September 1989, CERN 89-10, Vol. 2, 551.
[16] H. Fesefeldt, private communication.
[17] V. Radeka and S. Rescia, Nucl. Instr. and Methods **A265** (1988), 228.
[18] J. Colas, Proceedings of the ECFA study week on Instrumentation Technology for High-Luminosity Hadron Colliders, Barcelona September 1989, CERN 89-10, Vol. 2, 563.
[19] E. Geulig and W. Wallraff, these proceedings.

WARM LIQUID CALORIMETER PROJECT BASED ON NEW MATERIALS

Jean Pierre Mendiburu
Collège de France and CERN

1 / INTRODUCTION

This paper reports on the feasability of building a warm liquid sampling calorimeter using a new plastic (VECTRA) for the general frame, lead for absorber, and TMS for ionization medium.

2 / THE R&D ON NEW MATERIALS

Since 1986, the WALIC collaboration has made a systematic effort to find substitutes for the materials currently used to contain the warm liquids (Stainless Steel and Ceramics), that should be easier to handle and to assemble on the scale of a large calorimeter for LHC.

For this compatibility test,we retained only materials having adequate properties : Either very low (metals) or very high electrical resistivity (plastics, glasses etc.), strong mechanical resistance, low density, very low porosity, resistance to ultra cleaning and bake out, radiation hardness, simplicity for industrial management (ability to be molded, extruded, metalized etc.),possibility to be assembled by soldering or gluing etc. The results of this R&D is summarized in figure 1.

The search for the best choice has led us to new plastics.

Several qualities make VECTRA, an optimized mixture of NDA ($C_{12}H_8O_2$), DHN ($C_{10}H_8O_2$) and HNA ($C_{11}H_8O_3$), the most promissing candidate.
Its mechanical hardness is between aluminium and stainless steel,but with lower interaction and radiation lengths (λ_r = 21.7 cm, λ_a = 62.7 cm, d=1.57 g/cm^3); it has a low porosity, even at high temperature (10^{-8} mbar.l / s at 100 º c) and can be baked out at 250º c ; It can be molded, extruded, machined, metalized, glued and welded ; It is an excellent insulator (Volumetric Resistivity = 10^{15} Ω / cm, Rigidity = 43 Kv /mm), its dielectric constant is 4.1 at 1 KHz and it is also extremely radiation hard (no observable modification after 500 Mega rads of Co_{60})
The VECTRA is also fire-proof ; it is auto-extinguishable.
The R&D prouved that the VECTRA , even metallized, is compatible with TMS.

3 / THE CALORIMETER PROJECT

The strategy of this project is to build a very simple and cheep element that can be duplicated as many times as necessary to make a large calorimeter.

The basic element has a parallelepipic shape with a hole in the middle, which will contain a sheet of absorber, introduced like a drawer ; little metalized basins in the upper and in the lower part, when joined to the corresponding upper and lower parts of the neighboring elements will form the ionization gaps; A vertical chimney is foreseen , between the two half basins to allow general cleaning, the pump out and allow vertical liquid circulation.

Figures 4 shows a lay out of the different parts of a sampling unit.

Monte Carlo simulation of such a calorimeter, with 2 mm of TMS and 2 mm of lead shows an electromagnetic resolution of 11%/√E and a hadronic resolution of 50%/√E ; further work on this topic is still in progress .

4 / FRONT END ELECTRONIC

We have adapted the Electrostatic transformer idea, taking advantage that the electrodes are isolated one another, from the ground and from the absorber.
The gaps of a same sampling unit are connected by strong linking capacitances added between the cathode of a gap and the anode of its neighbor. The usual loading high

voltage resistances are split in two, one between the cathode and the power supply and a second one between the anode and the ground .

The charges produced are transferred through these linking capacitances and the gap capacitances to the unique preamplifier of the sampling unit .

The Figures 2 and 3 show the electronic equivalent schema and the computer simulation of the response to a charge induced in the first gap and in the last gap ; as expected, the impedance seen by the amplifier is reduced and no charge is lost during the transfer. A test module is being constructed at Collège de France to measure the behavior of the system, in terms of its speed of response and noise.

5 / CONCLUSIONS

In 1991, we want to test the technical solutions and the different steps of the construction up to a prototype of 9 towers, of 10 modules each.

We want to measure the electronic behavior of this set up and quantify its performances in a test beam.

REFERENCES

1 Speed and noise ....S. Radeka and S. Rescia NIM A 265-1988-228

2 Speed of response... J.Colas Barcelona proceedings CERN 89-10-563

3 A Charge Transfer Device .. JP Mendiburu CDF 90 48

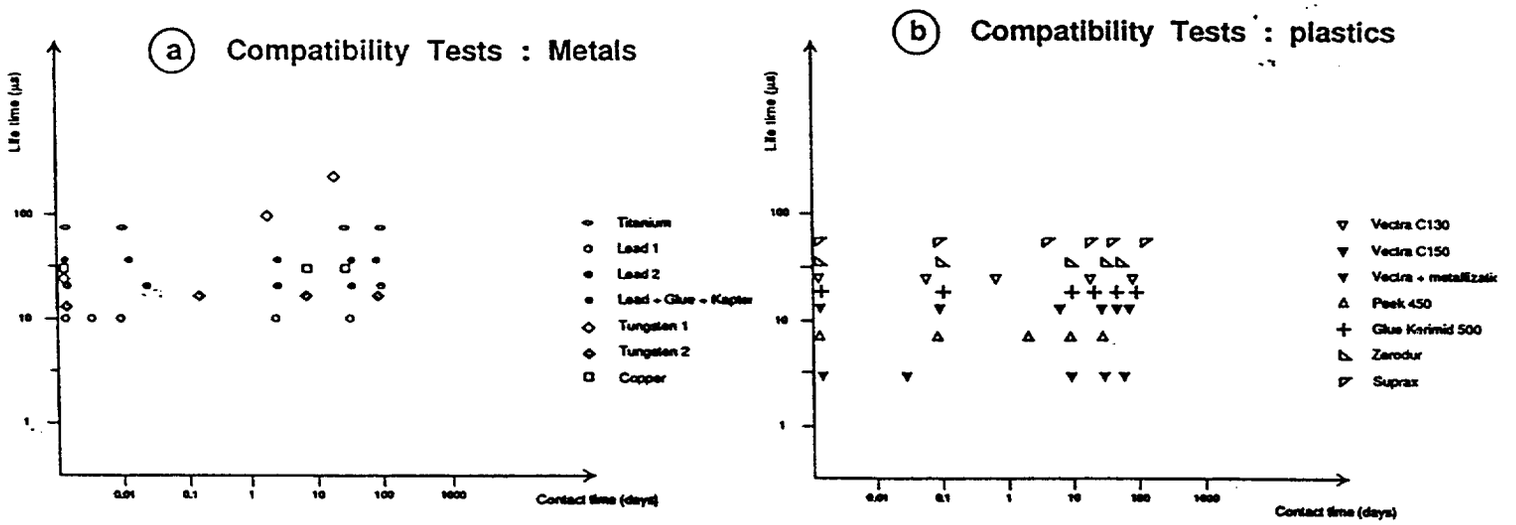


Figure 1 : Isolating materials and Metals compatibility with warm liquids

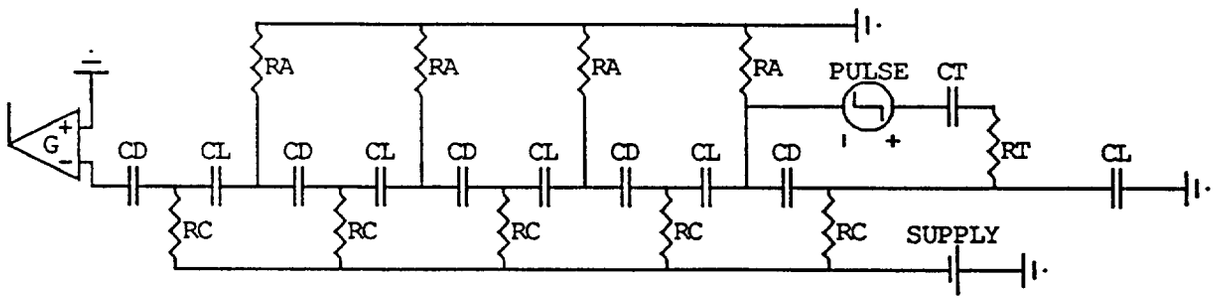


Figure 2 : Electronic equivalent schema of CTD

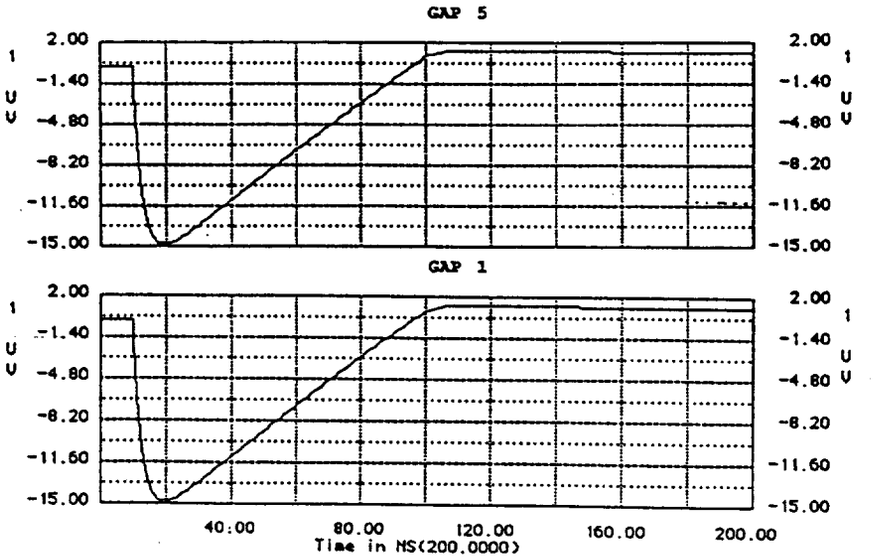


Figure 3 : Response of the preamplifier to the closer and the furthest gap

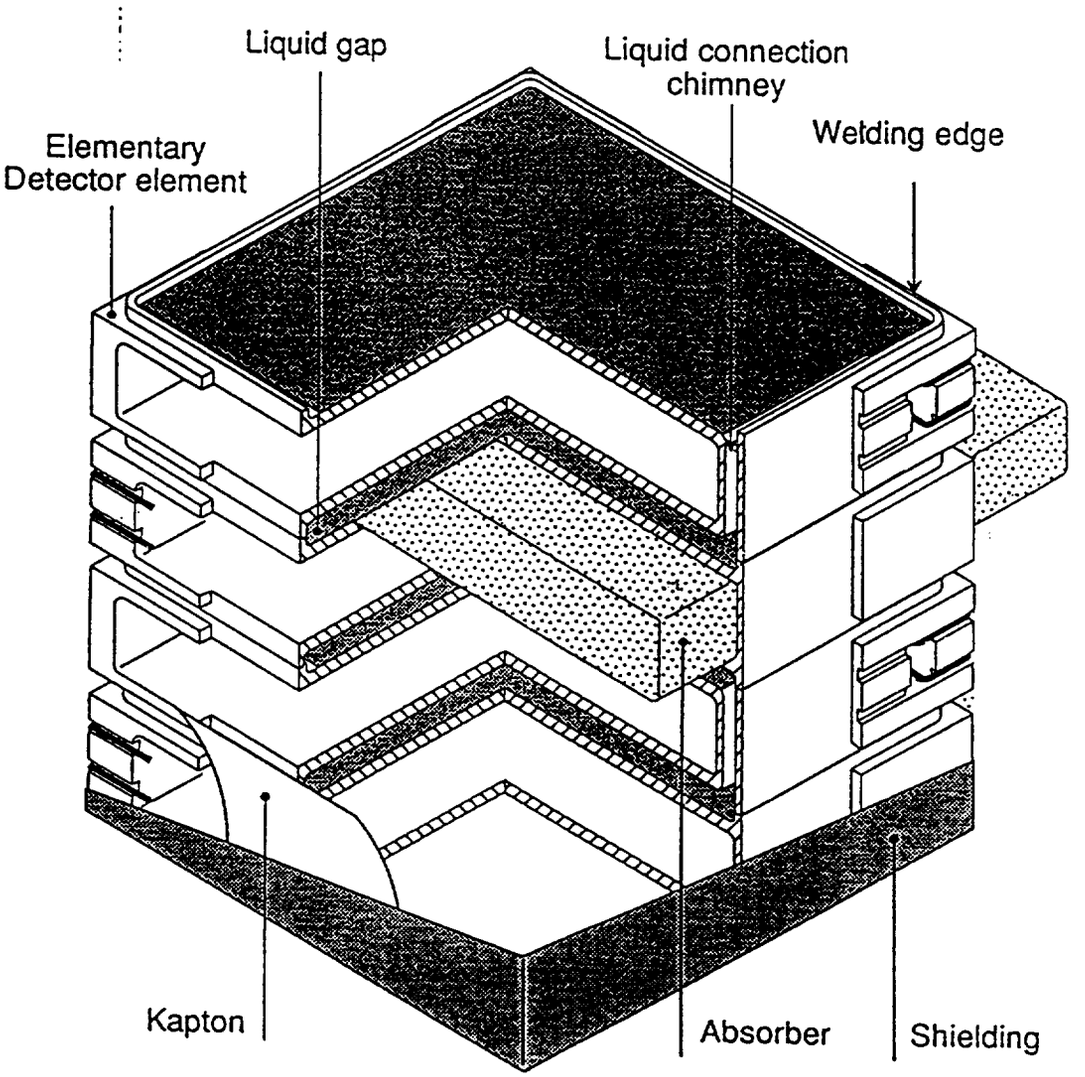


Figure 4 : Design of Plastic Calorimeter : Lay out of a sampling unit

Status Report of R and D studies on Warm Liquid Calorimetry by the WALIC collaboration

(DPhPE Saclay, LAPP Annecy, LBL Berkeley, LPC Collège De France Paris)*
Presented by B.Mansoulié

1) Introduction

The goal of the WALIC collaboration is to study the use of ambient temperature organic liquids (so-called "warm liquids", such as tetra-methyl-pentane (TMP) , tetra-methyl-silane (TMS), etc..) for ionization calorimeters at the LHC and SSC. It follows two main lines of research :

- Generic studies on liquids and their use in calorimeters, such as:
  . Saturation measurements (Birks'constant) at CERN SC, (published in NIM A286 (90) 147)
  . materials compatibility
  . mechanical schemes
  . read-out schemes (e.g. the "Electro-Static Transformer) and electronics.
- Extensive study of the e/pi ratio of response, with a totally modular calorimeter prototype (experiment E795 at FNAL).

This report presents preliminary results obtained with this prototype from the first data taken during the summer of 1990.

2) The modular calorimeter prototype (Fig. 1)

The prototype calorimeter consists of a mechanical structure on which independent planes can be hung, either absorber planes or detector planes, allowing for any desirable combination. Its front cross-section is 60 by 60 cm^2 . It is entirely enclosed in a Faraday cage to reject any pick-up noise.

A detector plane is made by two ionization chambers filled with TMP (similar to the ones used by UA1). The chamber is a thin stainless-steel box (30 cm x 60 cm) with an electrode in the middle, which makes two 1.25 mm liquid gaps. The central electrode is divided in four independent read-outs (30 cm x 15 cm) across the area of the chamber.

After a thorough cleaning procedure, a chamber is filled with purified TMP with a life-time always in excess of 60 micro-seconds, and sealed to make an autonomous detector. It is then enclosed in an aluminum "folder" consisting of two 1 mm plates, for better geometry and handling.

The read-out electronics consists of low noise pre-amplifiers located inside the Faraday cage , shapers with a peaking time of 1.2 micro-seconds, and LeCroy 2280 type ADC's. Each electrode is read-out separately and the electronics noise is 2300 electrons for an electrode capacitance of 1 nf.

* Other labs from the U.S. and Japan joined later.

The absorber planes used for this running period were 6.35 mm lead plates. Only 34 TMP planes were available at that time (the final set-up will have 70 planes). Data were taken with the following absorber/TMP planes configurations:

- "Electromagnetic" configuration : 26 x [1 TMP plane, 1 lead plane]
- 4 different "hadronic" configurations :
  - . 34 [TMP / lead / CH_2 / lead / CH_2 / lead / CH_2] (6.5 absorption lengths λ)
  - . 34 [TMP / 3 lead] (6.5 λ)
  - . 6 [TMP / 4 lead] + 28 [TMP / 6 lead] (7.8λ)
  - . 6 [TMP / lead / 3(CH_2 / lead)] + 28 [TMP / lead / 5(CH_2 / lead)] (7.8λ)

The "CH_2" planes are polyethylene planes with the same nuclear content as the TMP planes (in particular hydrogen) in order to achieve the same shower development as if TMP planes were used .

The chambers were operated with a voltage of 845 V, i.e. an electric field in the liquid of 6.5 kV/cm, and a total collection time of 600 ns.

3) Results

a) Muons.

Fig. 2 shows the energy measured in the liquid for 175 GeV incident muons in a tower of 34 planes with one electrode per plane, together with the pedestal noise for this tower. The r.m.s. noise is 3.0 MeV, and the muon signal peaks at 12.2 MeV, thus the signal to noise ratio is 4.1 .

b) Electrons, measured in the "electromagnetic" configuration.

Fig. 3 shows the profile of the electromagnetic shower for 5, 25, and 150 GeV electrons. Each bin stands for one detector plane, which sample the shower every 1.2 radiation length; the bin height is proportional to the energy measured in this plane. The data are well described by the Geant Monte-Carlo simulation (full lines).

Fig. 4 shows the linearity of the response of the calorimeter and Fig. 5 the energy resolution, as a function of the electron beam energy from 5 to 150 GeV.

The resolution can be parameterized as follows :

$$(\sigma / E)^2 = (1.3 \pm 1\%)^2 + (16.3 \pm 1\%)^2 / E + (.3 / E)^2 \quad \text{(with E in GeV)}$$

from "constant ", sampling, noise terms

c) Hadrons

The analysis on the hadron data is still in progress. Fig. 6 shows the profile of a 25 GeV pion shower in the first hadronic configuration, together with the profile of a 25 GeV electron shower. The sampling is every 4.5 radiation length or 0.2 absorption length.

4) Conclusions.

The operation of the modular calorimeter prototype has begun successfully. Data taken with muons and electrons show a good performance of the system in terms of noise and linearity. The modularity allows to change the configuration of the prototype in one or two days, and results are expected soon about the e/pi ratio for four different hadronic configurations.
Purification of the liquid and filling of the chambers is continuing smoothly and the set-up will be completed before the next running period early in 1991.

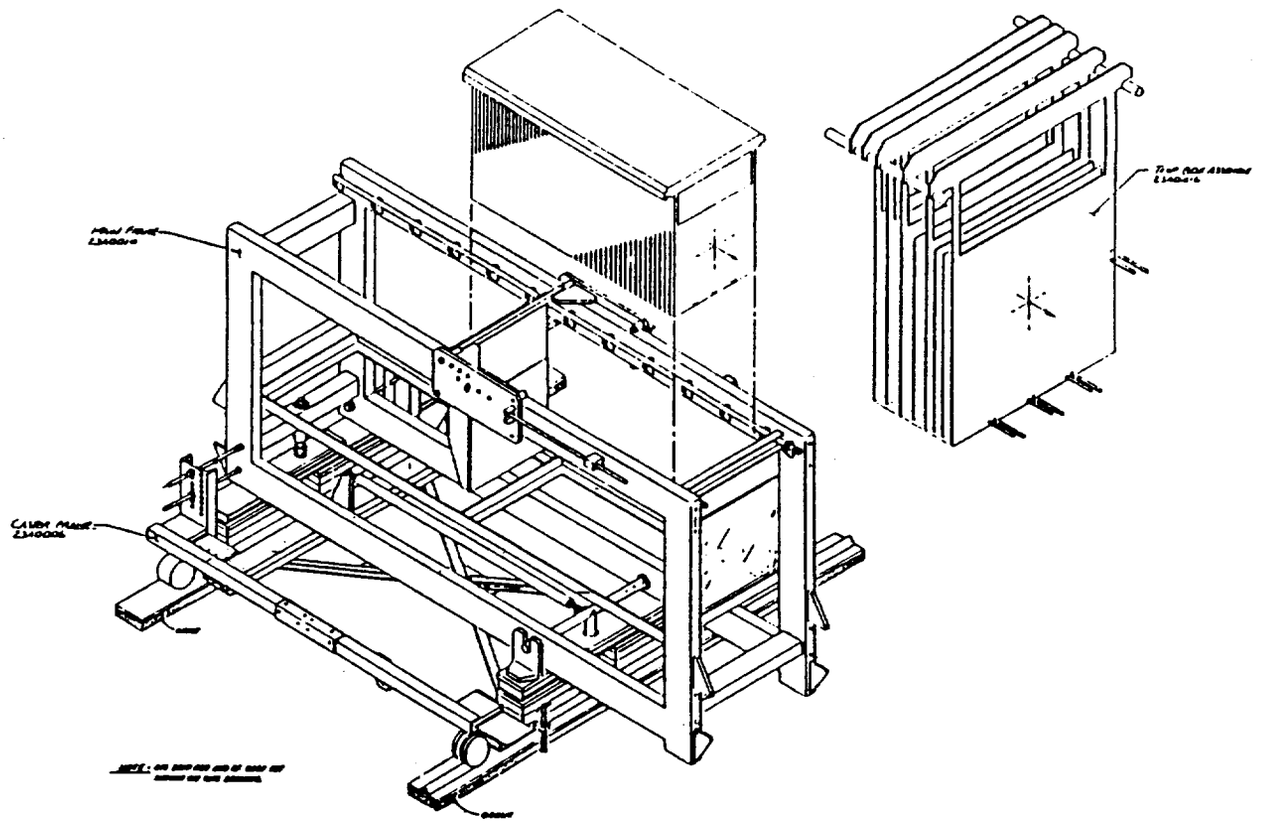


Fig. 1 : Mechanical structure of the modular prototype calorimeter (E795)

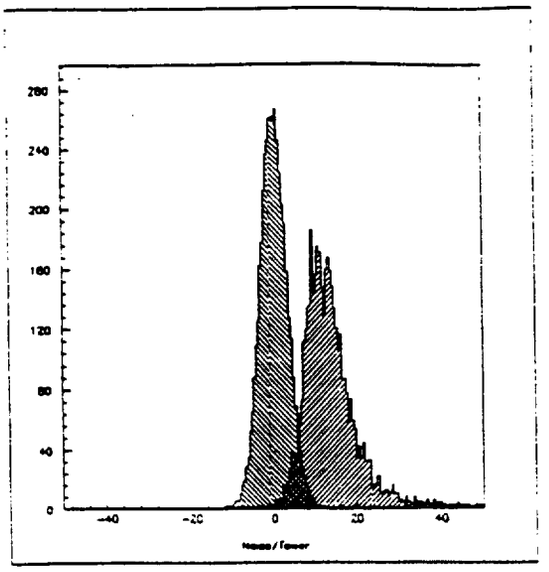


Fig.2 : Muon signal and pedestal signal for a 34 plane tower.

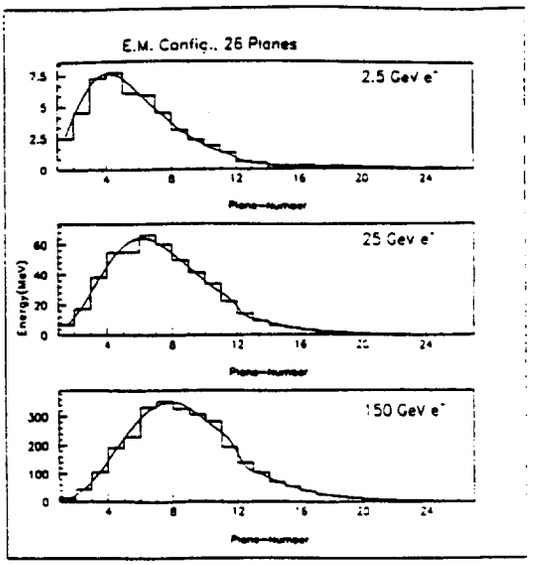


Fig. 3 : Profiles of electron showers in the 26 planes e-m configuration.

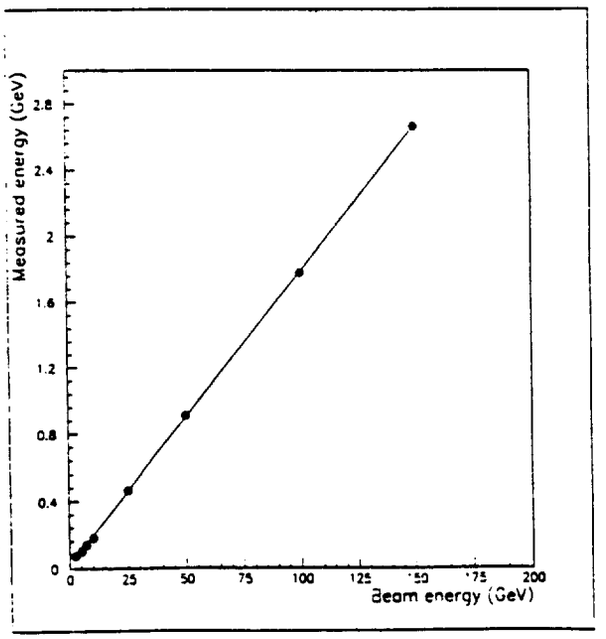


Fig. 4 : Response to electrons of the 26 planes e-m configuration.

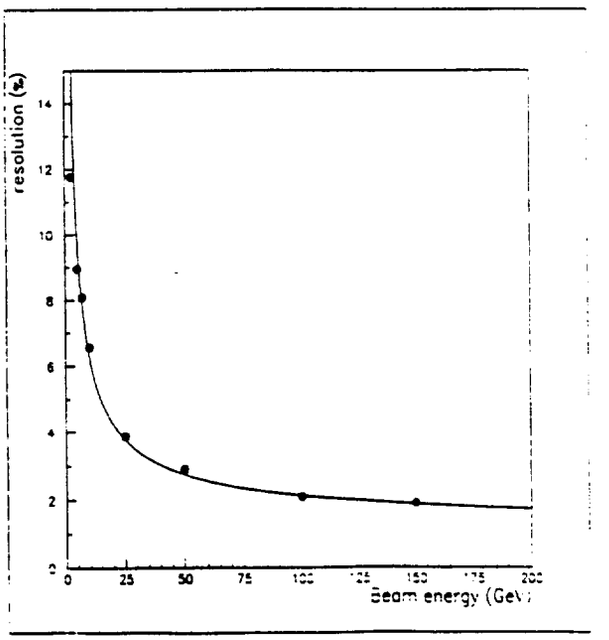


Fig. 5 : Energy resolution for electrons 26 planes e-m configuration. Solid line as described in text.

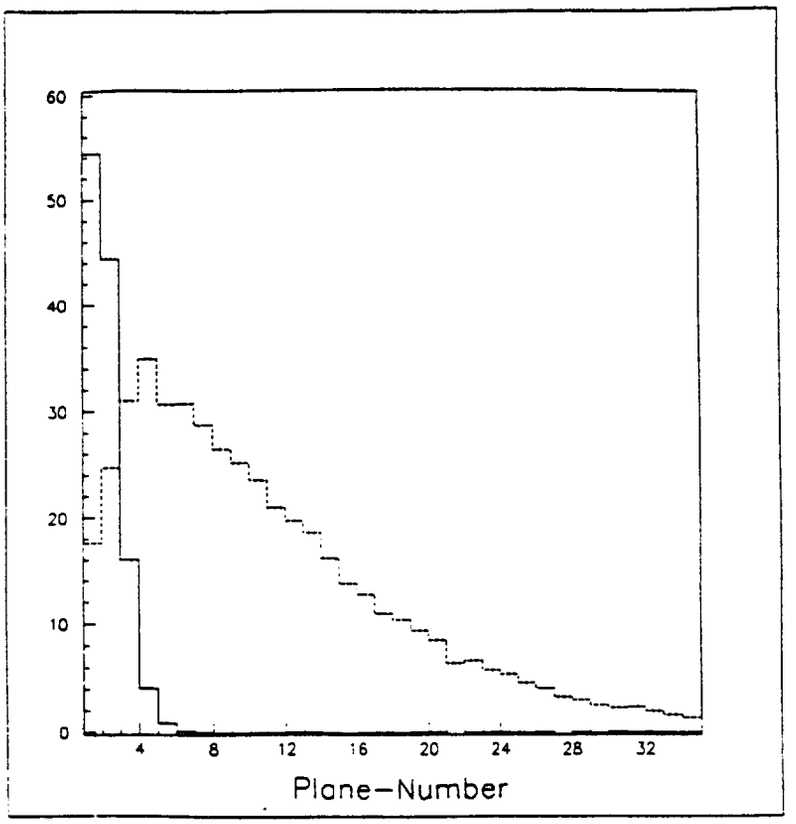


Fig. 6 : Profile of electron (solid) and hadron (dashed) showers in the 34 planes hadronic configuration (hadron data scaled by a factor 5).

LIQUID ARGON CALORIMETRY

Convener: D. Fournier
LAL Orsay and PPE Division – CERN, Geneva

Liquid argon calorimetry has been widely used in the last 15 years, both in fixed target experiments (including precision experiments like NA31) and at electron colliders (MARK II, Cello, SLD), hadron colliders (D0) and ep colliders (H1). In these experiments, the calorimeters are operated as ionization chambers: the charge signal is built up by integrating the whole ionisation current circulating between the electrodes (see Fig. 1). In these circumstances, the speed of response is governed by the distance between electrodes (typically 2 mm) and is therefore rather slow (τ_D = 400 ns to integrate the whole charge over 2 mm, occupation time $\approx$ 4 t_D after shaping)..

An alternative approach consists in using the initial current i_0 as signal (Fig. 1), which in practice is measured by integrating i(t) over a time τ much shorter than t_D. In this case, using suitable shaping, the critical time is τ and no longer t_D. The main limitation then becomes a signal to noise problem and no longer a speed problem.

Obviously, this last approach is the one relevant for the high rates and high energies of LHC (or SSC) [1]. Progress in speed of response is related to progress in cold electronics [2]. Minimisation of the time constant associated to the circuit formed by the calorimeter cell and its connections to the preamplifiers [3] is also a critical issue. To solve this point, a new 'accordion' geometry has recently been proposed (see R&D Proposal [3]).

For a given calorimeter geometry, the initial current i_0 is proportional to the electron drift speed. Dopants, like methane, which increase the speed by a factor ~ 2 are obvious

candidates to improve correspondingly (for a given electronic chain) the signal to noise ratio. This is addressed in the talk about dopants by V. Vuillemin.

On the subject of hadron calorimeters, a major issue is compensation. With liquid Argon as a detecting medium, compensation has been demonstrated only with Uranium as a converter (HELIOS, D0). However, using uranium causes so many difficulties that one would like to achieve compensation –even if approximate– by other means [3]. Three ways are presently being investigated:

– enhancement of signal from heavily ionising fragments using photo–sensitive dopants [4] (see talk by V. Vuillemin);
– reduction of π^o signals by laminating the heavy converter plates with foils of light materials [5];
– software reduction of the π^o components of jets using fine longitudinal and transverse segmentation and appropriate weighting (see talk by P. Schacht).

Another important point for an LHC calorimeter is hermiticity [3]. This addresses specific design of forward calorimeters and the effect of residual cracks between modules, specially at the limit between barrel and end caps [7].

Not yet mentioned is the problem of radiation hardness. The high levels of radiation at LHC place severe constraints on the calorimeter techniques to be used, especially for rapidities ≥ 2. The materials used in liquid argon calorimeters, and the liquid itself (if pure – see the contribution of V. Vuillemin) are thought to be stable well above the levels of concern at LHC ($\approx$ 10 MRads) [3]. The only weak element is the preamplifier, which by necessity of fast response should be in the cold, as close as possible to the modules, and therefore fully exposed to radiation. Progress in radiation hard electronics is, however, quite fast. For example, an exposure of a few GaAs preamplifiers of the same type as used in the accordion prototype test (see last contribution) has shown a $\approx$ 20% degradation of performance (gm decreases, noise increases) when exposed (at room temperature) to 10 MRads or 10^{14} n/cm^2 [6]. Thus there is good hope here to meet the necessary requirements on the time scale of LHC.

This brings us to the last point mentioned here, calibration: this is one of the strong points of the existing liquid argon calorimeters: after calibration of the electronics, only one number is needed for the whole calorimeter to have the calibration available at a given time. This rests on the fact that the liquid is homogeneous within the calorimeter and assumes there is no mechanical deformation within the stacks. This overall sensitivity is better obtained from particles irradiating the experiment. At LHC, $Z^o \rightarrow e^+e^-$, is a preferred candidate for

the EM calorimeter. The relatively high rate of this reaction (~ 5 Hz at 10^{34}) is probably enough to look for long or medium range non uniformities, possibly associated to the large dimensions necessary for an LHC calorimeter.

During the course of the present ECFA studies, two meetings were organized to complement the work presented below. One was about mechanics, cryogenics and hermiticity [7]. The second one was about front end electronics [8]. No written version of the presentations exist but copies of transparencies can be made available on request.

The written contributions following below are:

V. Vuillemin: presentation of R&D Proposal P6 on dopants
P. Schacht: Software compensation for single particle and jets in the H1 calorimeter
P5 – Liquid Argon Calorimetry with LHC Performance Specifications (Proposal Summary)
D. Fournier: First results from P5

References

[1] C. W. Fabjan in 'Feasibility of Experiments at High Luminosity at the Large Hadron Colliders; E. Fernandez and G. jarlskog ed., CERN 89–10 (1989) 69.

[2] V. Radeka and S. Rescia, Nucl. Instr. and Methods A265 (1988) 228.

[3] B. Aubert et al., Liquid Argon Calorimetry with LHC–Performance Specifications; CERN/DRDC/90–31, DRDC/P5 (1990).

[4] P. Cennini et al.. Study of Liquid Argon dopants for LHC Calorimetry

[5] A. Angelis et al.. CERN–EP/90–73

[6] D. Camin, R&D work in the framework of Ref. [3].

[7] Cryogenics and hermiticity, presentations by
M. David (Saclay H1)
P. Lottin (Saclay H1)
H. Gordon (BNL – Empact)

[8] Front–end electronics, presentations by
H. Oberlack (Munich – Cold electronics option for H1)
P. Cennini (CERN – ICARUS frontend)
D. Camin (Milano – GaAs preamp)
B. Chase (Orsay – 'Only one common gate transistor in the cold')
C. de la Taille (Orsay – A bench test for preamplifiers)
E. Beuville (Saclay – Radiation hard frontend).

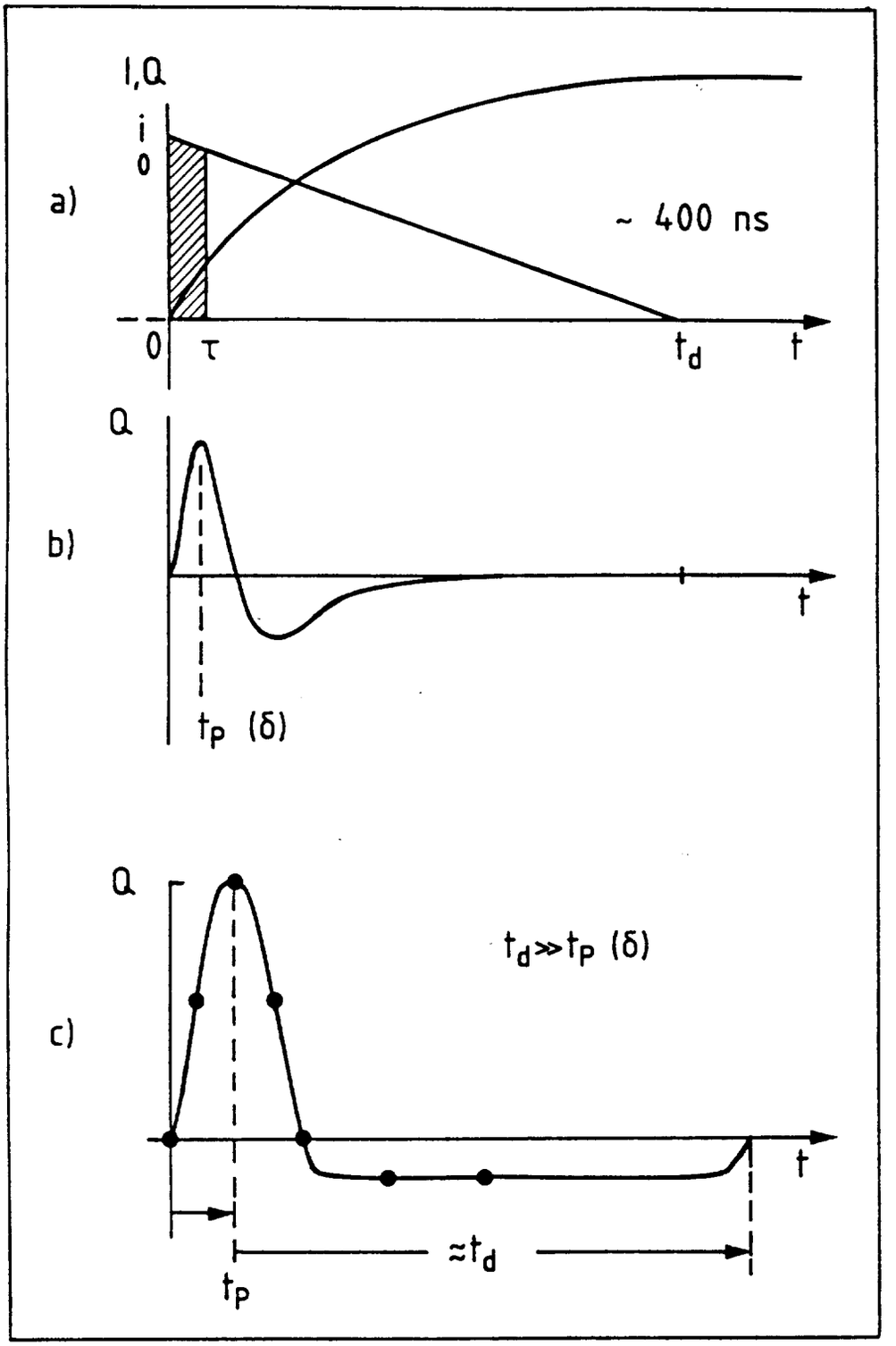


Fig. 1

a) Current and integrated charge as a function of time. t_D is the total drift time in the gap.

b) Response of the shaping network to a short current pulse (δ).

c) Response of the shaping network to the current form of a). Dots show where beam crossings would appear (every 16 ns) for t_p (δ) ≈ 20 ns.

Study of Liquid Argon Dopants for LHC Hadron Calorimetry.

P.Cennini , C.W.Fabjan , A.Gonidec , D.Lacarrère , D.Schinzel , W.Seidl , V.Vuillemin
CERN , Geneva , Switzerland

P.Carlson , W.Klamra , Th.Lindblad , B.Lund-Jensen
Manne Siegbahn Institute of Physics , Stockholm , Sweden

ABSTRACT

Hadron calorimetry based on the Liquid Argon Ionisation Chamber technique is one of the choice techniques for LHC-experimentation. We propose to study in a systematic way the effect of dopants to LAr to improve on driftspeed ("Fast Liquid Argon ") and on its response to densely ionising particles (" Compensated Liquid Argon "). We describe the measurements and monitoring of the critical parameters, including the use of IR absorption spectroscopy.

We intend to carry out a systematic study of selected dopants on Liquid Argon (LAr) with the aim to achieve an improvement on[1] :

(i) search and study of dopants to increase the drift velocity. It has been already shown that CH_4 added at a fraction of one percent increases the drift velocity by a factor of two or more

(ii) search and study of dopants to increase the response to densely ionising particles, resulting in improved compensation, such as photosensitive dopants.

Monitoring of the parameters involved in understanding the response of a calorimeter is essential. In case of doped LAr, the charge yield, the non-saturated drift velocity and the electron lifetime in the liquid should be precisely and simultaneously monitored as they all vary with the level of dopant concentration and with the amount of impurities dissolved in the liquid.

In order to measure these parameters, we consider three solutions : radioactive sources, photoproduction of free electrons in the drift gap by a UV Laser and as far as impurity and dopant concentrations are concerned, IR spectroscopy. The effect of the dopants as a function of the ionization density can be evaluated with α and β-particles. For the present test set-up we plan to use both sources, ^{241}Am for α-particles and ^{207}Bi for electrons, placed in the same volume of liquid. The amount of recombination, the dE/dx-saturation properties and the charge gain due to photosensitive substances can be measured by direct comparison of the charge responses from α and β-particles. In addition, use of an UV Laser extracting free electrons from a photocathode facing the drift gap has the advantage of providing a much higher number of primary electrons permitting sensitive pulse-shape studies.

The set-up is shown in Fig.1. Double-grid chambers are used for the observation of induced electrons by UV Laser and ^{241}Am α-particles. The drift time separating the two grids provides a direct measurement of the drift velocity for a given electric field and the ratio between the charges collected at the cathode and the anode is a measurement of the lifetime of the charge in the liquid. The electric field will be approximately 10 kV/cm to approach as much as possible the real conditions of an LHC calorimeter in terms of speed, charge and recombination.

In parallel we will pursue an investigation of the time dependance of the LAr luminescence intensity in the presence of additives such as dopants or LXe and its correlation with ionization signals.

We intend to build a small argon and dopant purification system using Ti-getter and molecular sieves. After purification, the dopant can either be mixed with argon in a special reservoir before liquefaction or transferred directly into the cell. Temperatures of the test cell around liquid argon will be obtained inside a specific cryostat including a non-acoustic noise cooling system.

Measurement of the lifetime of the liquid mixture is certainly sensitive to dissolved impurities, however it provides no information on the types of impurities such as oxygen, carbon mono- and dioxyde or halogens. Monitoring of the amount of dopant and of its

possible decomposition during an irradiation test could be a unique tool in evaluating the behaviour of such substances under the LHC radiation environnement. This kind of monitoring has to be performed in situ, namely with the same liquid in the test cell. IR absorption spectroscopy allows to perform such an analysis under this constraint. A cell including IR windows on both sides will be added to the test cell and to the lower part of the cryostat. The set-up for IR absorption spectra measurements in shown in Fig.2.

The present ionisation chambers and luminescence test cells as well as the set-up designed for IR absorption spectra studies are general and could also be used for later studies involving LKr or LXe.

[1] P.Cennini et al., CERN / DRDC / 90-34, DRDC proposal P6, August 23, 1990

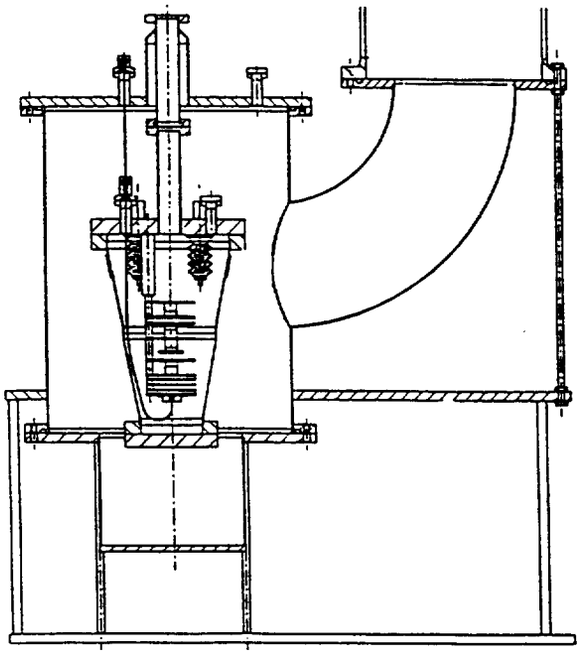


Figure 1 :

Schematics of the ionisation chambers test cell inside the cryostat. The bottom parts of the test cell and cryostat will be instrumented with special IR windows to accomodate the pass of a IR parallel beam through the cryogenic liquid.

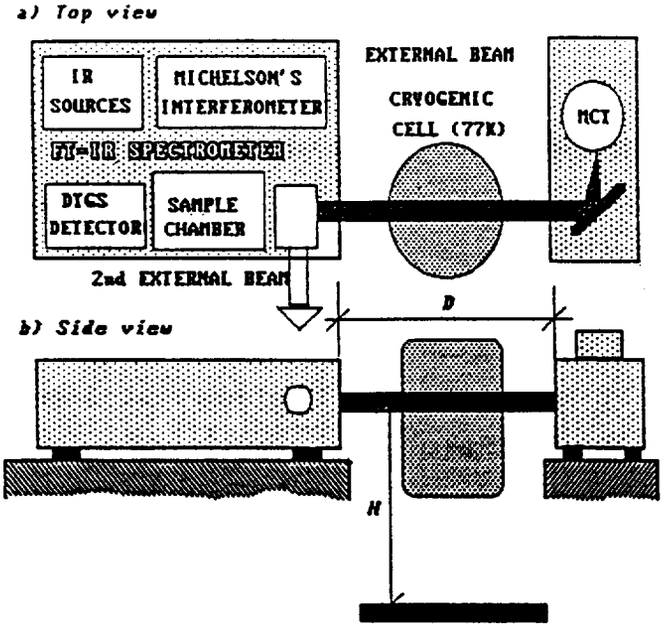


Figure 2 :

Diagram of the IR spectrometry set-up. The spectrometer is equipped with additional optics allowing the extraction of an external parallel beam. A high sensitivity detector, coupled to the spectrometer, is situated on the other side of the cryogenic cell and measures IR absorption spectra of dissolved impurities and additives.

Software Compensation for Single Particles and Jets in the H1 Calorimeter

H 1 Calorimeter Group

presented by P.Schacht

Max-Planck-Institut für Physik und Astrophysik, München, Germany

The H1 calorimeter group has studied the π^0-weighting technique in detail for single particles using beam calibration data of the H1 calorimeter prototype or standard modules [1,2,3,4]. Typically a hadronic energy resolution of (45 - 50) % / $\sqrt{E}$ has been achieved even though the H1-calorimeter - a lead/stainless steel liquid argon calorimeter - is intrinsically non-compensating. One of the crucial questions is, to which extent these results can be transfered to ep events at HERA, where the calibration of jets rather than for single particles is the issue of primary importance.

This question has been studied using final state particles from the fragmentation of u-quark jets generated with the LUND code [5]. To simulate the response of electromagnetic particles the EGS4 code [6] has been used, which yields a good description of the data. On the other hand the hadron simulation programs used so far did not describe the single pion data at the level of accuracy required to extract the weighting constants. Therefore the response of the hadronic particles in the jet has been taken from the single particle measurements done at CERN.

The lateral segmentation of the 1987 test set-up calorimeter has been used, which was not yet the final one used in the H1 calorimeter, even though rather similar. To have a reasonable angular coverage for jets, this calorimeter structure has been extended horizontally and vertically up to a size of 2 × 2 m, with the interaction vertex being 2 m in front. Thus jets have been simulated in an angular region corresponding to the forward region (i.e. proton direction) in the H1 calorimeter.

To obtain the pion response at different energies and impact angles, we had to scale between the energies, where beam data were available, and rotate the single pion event relative to the normal impact angle (90°) used in the beam. To do so, a scaling and rotation algorithm [7] has been developed, which preserves the charge fluctuations in the pads. This algorithm has been extensively tested with MC events. From the comparison of directly simulated MC events and MC events obtained via the identical interpolation and rotation algorithm as used for the test data, we get good agreement in longitudinal and lateral charge distributions for hadronic showers up to rotation angles of 35° and down to energies of 10 GeV.

The main difference between single particles and jets is the larger fraction of elec-

tromagnetic energy in the jet. This leads to a significant different e/π-ratio in the e.m. calorimeter as can bee seen in Fig. 1. This larger amount of e.m. energy yields also a better energy resolution even without any weighting (Fig. 2). Assuming $\frac{\sigma}{E} = \sqrt{A^2/E + B^2}$ one obtains for jets $A = 0.535 \pm 0.035$ GeV$^{1/2}$ and $B = 0.034 \pm 0.002$ and for pions $A = 0.604 \pm 0.004$ GeV$^{1/2}$ and $B = 0.064 \pm 0.001$.
As shown previously [1,2,3,4] the charge deposited in a single channel offers the possibility to identify the underlying showering process: E.m. showers deposit locally more charge than hadronic showers. A non-linear dependence $E(Q)$ of the energy on the charge deposited in an individual channel, which takes into account both the e/π-ratio and the tagging efficiency for charge deposits from electromagnetic particles will effectively compensate for the different e and π response and thus improve the energy resolution.
The functional form of $E(Q)$ can be extracted directly from the data. Each individual charge bin Q_i for the e.m. and hadronic calorimeter is multiplied by a separate calibration constant a^i to obtain the total energy E:

$$E = \sum_{i=1}^{N_{EM}} a^i_{EM} Q_i + \sum_{i=1}^{N_{HAD}} a^i_{HAD} Q_i$$

The parameters a^i_{EM} and a^i_{HAD} are determined from a least square fit by minimizing the energy resolution. They yield the optimal numerical values $E(Q_i)/Q_i$ of the calibration function at a given value Q_i. This distribution is shown in Fig. 3 for pions and jets at two different energies for the e.m. and hadronic calorimeter. With the larger amount of e.m. energy deposited in the e.m. calorimeter, the difference between jets and pions is mainly pronounced in the electromagnetic calorimeter: Jets require a substantially softer weighting function than pions. The strong impact of the e.m. energy fraction f_{em} in a jet on the weighting function has to be considered in the ansatz. With $f_h = 1 - f_{em}$ and using an estimator for f_{em} [7,8] based on the charge deposited in the e.m. calorimeter, we arrive finally at the following ansatz for the weighting function [7,8]:

$$\frac{E_{EM}(Q)}{Q} = < C^e_{EM} > + f_h[A \cdot e^{-(\alpha_1 \cdot f_h + \alpha_2) \cdot Q} - 1]$$

$$\frac{E_{HAD}(Q)}{Q} = < C^e_{HAD} > + f_h[B \cdot e^{-(\beta_1 \cdot f_h + \beta_2) \cdot Q} - 1]$$

$< C^e_{EM} >, < C^e_{HAD} >$ are the calibration constants for electrons for the e.m. and hadronic calorimeter respectively. The parameters α_1, α_2, β_1 and β_2 are almost energy independent. They have been determined from a fit minimizing the energy resolution in a similar way as described in ref. [4].

Using this ansatz we have studied the energy normalization and energy resolution for jets. The resulting deviation $\Delta = (E_R - E)/E$ from the nominal jet energy and the resolution $\sigma/\sqrt{E}$ are shown in Figs. 4a and 4b. The maximum deviation from the jet energy is 0.5 %. The energy resolution varies from 37 $\%/\sqrt{E}$ to 46 $\%/\sqrt{E}$ in the energy range studied.

A detailed study of the dependence of the energy normalization and energy resolution on other jet variables like particle multiplicity or thrust did not reveal any significant variation [7, 8].

In conclusion, the π°-weighting technique, used so far for single particles, has been applied to jets. Only the e.m. fraction f_{em} of jet energy has an impact on the weighting function. The incorporation of an estimator for f_{em} into the weighting ansatz yields results on energy normalization and energy resolution similar to the results obtained for single particles.

REFERENCES

[1] W. Braunschweig et al., Nucl. Instr. and Meth. **A265** (1988), 419

[2] W. Braunschweig et al., Nucl. Instr. and Meth. **A270** (1988), 334

[3] W. Braunschweig et al., Nuclear Instr. and Meth. **A275** (1989), 246

[4] W. Braunschweig et al., DESY 89-022 (1989)

[5] T. Sjöstrand, Computer Physics Communication **39** (1986), 347 - 407

[6] R.L. Ford, W.R. Nelson, SLAC-Report **210** (1978)

[7] H. Greif, Ph.D. thesis, Munich 1990

[8] Study of Software Compensation for Single Particles and Jets in the H1 Calorimeter, H1 Calorimeter Group, Contributed paper to the XXV International Conference on High Energy Physics, Singapore, 1990

FIGURE CAPTIONS

1. e/π ratio for pions and jets
2. Energy Resolution $\sigma/\sqrt{E}$ for pions and jets (no π°-weighting)
3. Distribution of $a^i = \frac{E(Q_i)}{Q_i}$ for pions and jets
4. Deviation from the nominal jet energy (a) and energy resolution for jets (b) using π°-weighting (see text)

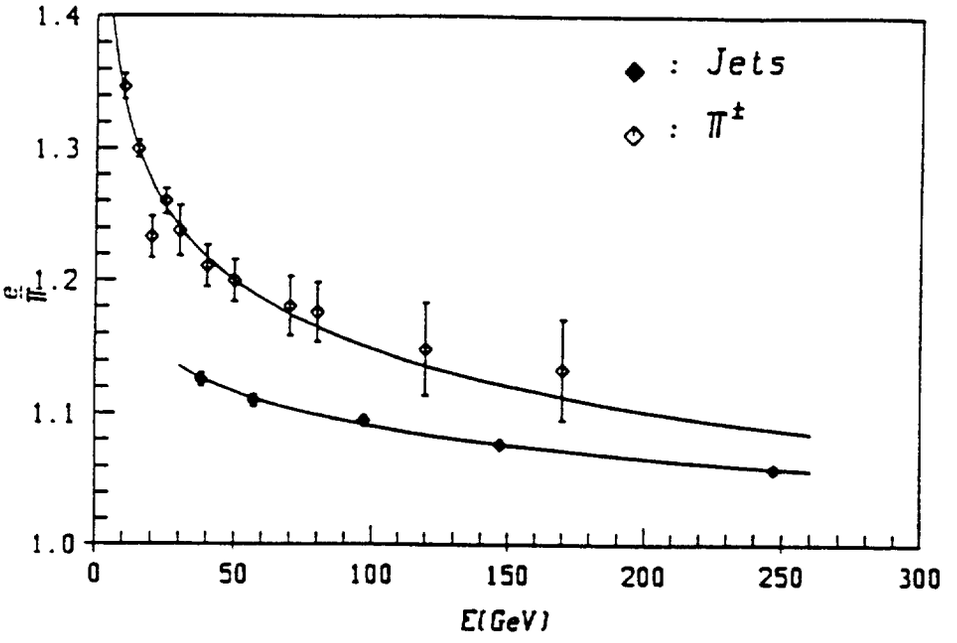


Fig. 1

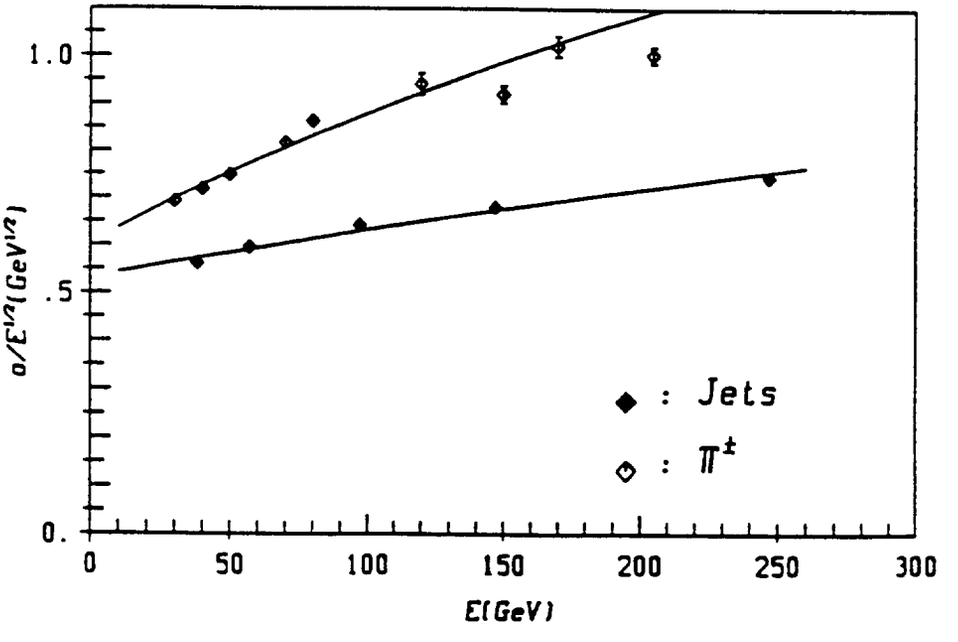


Fig. 2

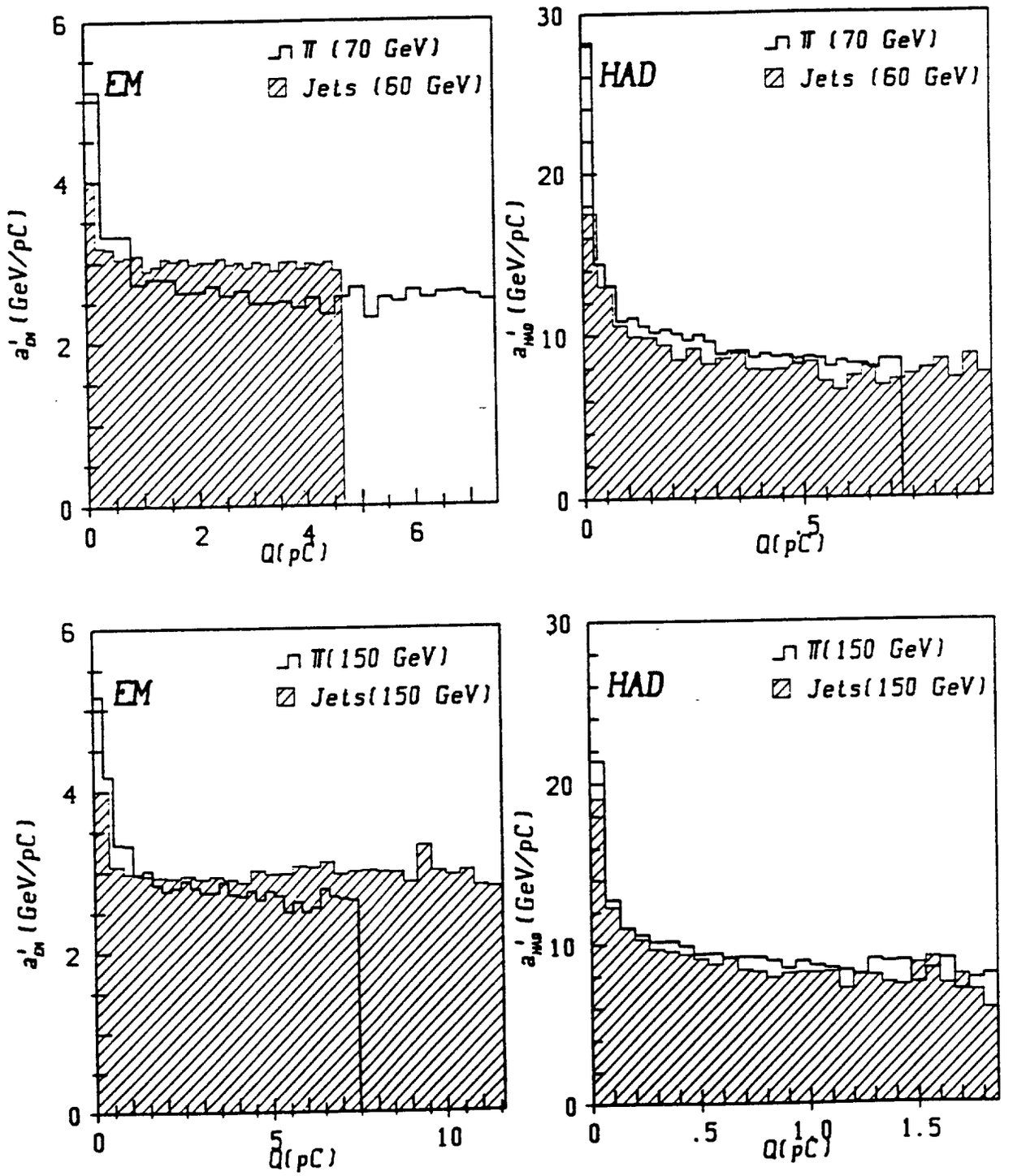

EM
π (70 GeV)
Jets (60 GeV)
HAD
π (70 GeV)
Jets (60 GeV)
EM
π(150 GeV)
Jets(150 GeV)
HAD
π(150 GeV)
Jets(150 GeV)
Q(pC)
GeV/pC

Fig. 3

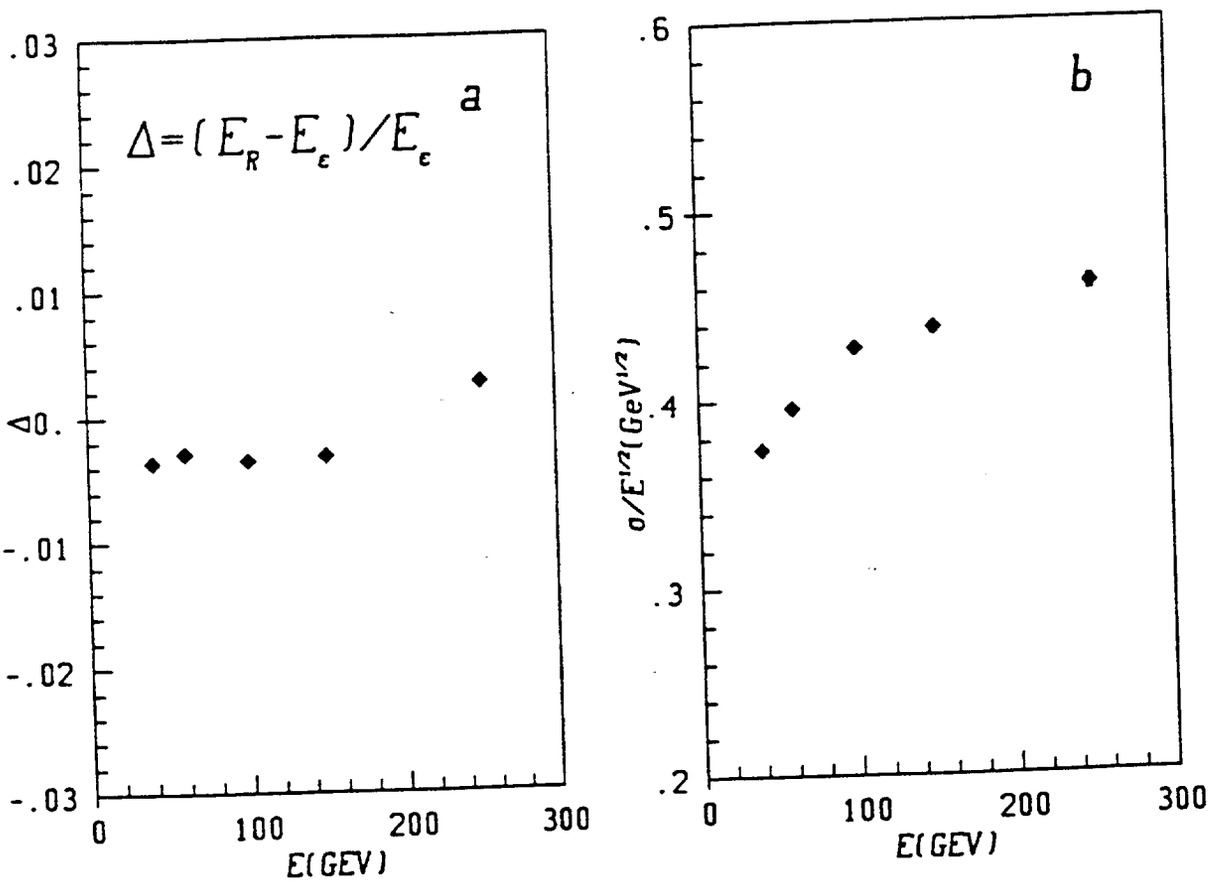

a
$\Delta=(E_R-E_c)/E_c$
.03
.02
.01
Δ0.
-.01
-.02
-.03
0
100
200
300
E(GEV)
b
.6
.5
.4
.3
.2
σ/E^1/2(GeV^1/2)
0
100
200
300
E(GEV)

Fig. 4

R&D PROPOSAL

LIQUID ARGON CALORIMETRY WITH LHC–PERFORMANCE SPECIFICATIONS

B. Aubert, B. Beaugiraud, F. Cavanna, J. Colas, A. Daba, M. Maire, J.P. Vialle
LAPP, Annecy, France

H.A. Gordon, V. Polychronakos, V. Radeka, D. Rahm, S. Rescia, I. Stumer
Brookhaven National Laboratory, Upton, USA

C.W. Fabjan[2], O. Gildemeister, P. Jenni, M. Lefebvre, M. Nessi,
F. Nessi-Tedaldi, M. Pepe, G. Polesello, G.R. Stevenson, W.J. Willis
CERN, Geneva, Switzerland

P. Lavocat, B. Mansoulie, J.P. Meyer, J.F. Renardy, J. Teiger, H. Zaccone
DPhPe-CEN Saclay, Gif-sur-Yvette, France

C. Battistoni, C. Birattari, D. Camin, D. Cavalli, G. Costa, A. Ferrari,
F. Gianotti, L. Mandelli, M. Mazzanti, L. Perini
Dipartimento di Fisica dell'Università e Sezione INFN, Milano, Italy

E. Augé, J.C. Chollet, C. de la Taille, L. Fayard, D. Fournier[1], J.M. Gaillard,
G. Guilhem, A. Hrisoho, L. Iconomidou-Fayard, B. Merkel, J.M. Noppe,
G. Parrour, P. Pétroff, J.P. Repellin, A. Schaffer, N. Seguin
LAL, Orsay, France

C. Fuglesang
Manne Siegbahn Institute, Stockholm, Sweden

Summary

Good electomagnetic and hadronic calorimetry will play a central role in an LHC detector. Among the techniques used so far, or under development, the liquid argon sampling calorimetry offers high radiation resistance, good energy resolution (electromagnetic and hadronic), excellent calibration stability and response uniformity. Its rate capabilities, however, do not yet match the requirements for LHC.

The aim of this proposal is to improve the technique in such a way that high granularity, good hermiticity and adequate rate capabilities are obtained, without compromising the above mentioned properties. To reach this goal, we propose to use a novel structure, the 'accordion', coupled to fast preamplifiers working at liquid argon temperature. Converter and readout electrodes are no longer planar and perpendicular to particles, as usual, but instead they are wiggled around a plane containing particles (see Fig 1). Cutting the readout electrodes in longitudinal strips "automatically" brings signals equivalent to a tower readout to the front or back face of the calorimeter. With a charge preamplifier directly connected there, the most favourable situation is reached for low inductance and low capacitance, resulting in low noise, high speed and reduced cross–talk.

1) Spokesperson, 2) Contactperson

A first prototype was built to test these ideas. It uses lead converter plates cladded with stainless steel, multilayer kapton boards for the readout electrodes, and two different sets of cold preamplifiers, one based on Si-technology, and the other one on GaAs. The "tower" size is 2.5 by 2.8 cm. A simulation with GEANT of electron showers in this device predicts a resolution of $8.3\%/\sqrt{E}$ with a constant term smaller than 1%. Data taken with this prototype at the SPS, during a short first test, are presently being analysed.

The electonic noise has been measured to be about 4 MeV per channel with a shaped response peaking at 120 ns. The purpose of the next beam test (1991) is to operate this same prototype with fast electronics giving a peak response at 30 ns. This requires the development of new shapers. Work will also continue to improve the preamplifiers, in both the Si and the GaAs approaches.

Meanwhile, a mechanical study of a complete electromagnetic calorimeter using the accordion structure will be undertaken. Working dimensions are a cylinder of 1.3 m internal radius and 10 m length with segmentation of typically 0.02 to 0.03 in both azimuth and rapidity. This study will be followed by the construction of a module which could be considered a 'preprototype' of a sector (typically 80cm by 80cm) of this calorimeter.

For the hadronic calorimeter, proposed studies are centered on two aspects: the first one concerns compensation with the aim of avoiding the use of uranium while maintaining acceptable e/h ratio and a small constant term in jet energy resolution (for example using different cladding materials to reduce the response of electrons relative to pions). The second one is devoted to mechanics. The first scheme to be studied incorporates the accordion structure coupled to an 'electrostatic transformer' readout (Fig. 2).

After completion of these studies, the aim is to build a module of full thickness (9 interaction lengths) covering the same solid angle as the electromagnetic sector. We plan to have both prototypes ready for the fixed target period of 1992.



Fig. 1: Display of a 40 GeV electron shower in the accordion structure. Only charged tracks above 10 MeV are shown.

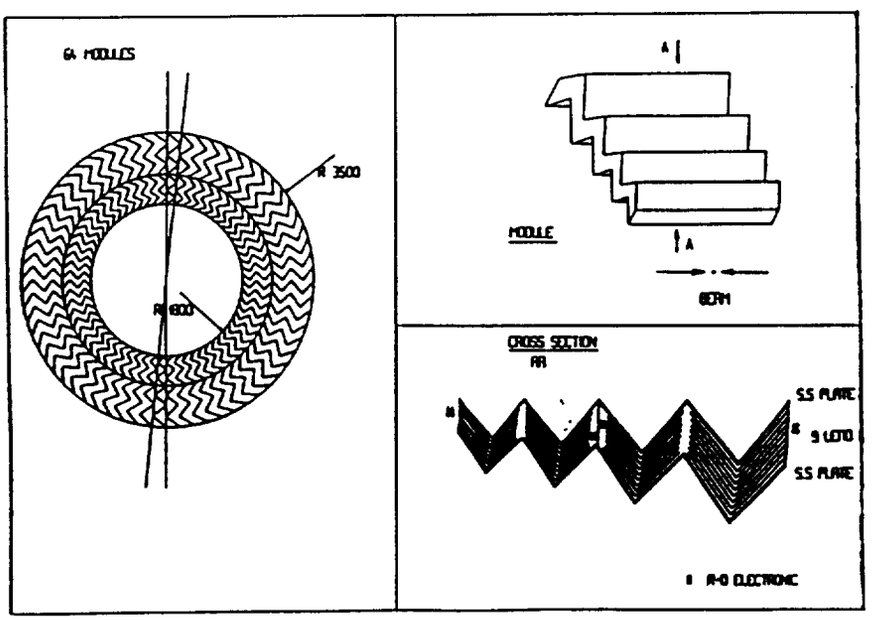


Fig. 2: A possible layout for the barrel hadronic calorimeter, using the accordion and electrostatic transformer concepts.

First Results from the "Accordion" Prototype

Annecy-BNL-CERN-Milan-Orsay-Saclay-Stockholm[1] Collaboration

presented by D. Fournier

A first prototype of an Electromagnetic calorimeter using the "accordion geometry (see preceding talk) has been built and exposed for a short test period to a high energy beam of pions, electrons and muons.

The transverse size of the prototype is about 40 x 40 cm. Its thickness about 26 X_o. The "accordion" folds are vertical. Read-out proceeds in "towers" of 2.5 cm (vertical) x 2.7 (horizontal) cm. There is a twofold segmentation in depth (2 x 13 X_o). This prototype calorimeter is followed (in the same cryostat) by 2 stacks from the Helios Uranium Liquid Argon Calorimeter which represent about 3 interaction lengths.

Electronic calibration is done via capacitances, of 22 pF, measured to 0.1 pF and selected. The peaking time of the bipolar shapers is $\simeq$ 100 ns for a short current pulse (δ) and 140 ns for a signal similar to the ionisation current in the chamber. Readout uses 12 bit ADC, with a sensitivity of about 16 MeV per count. Dedicated runs for muons were also taken with a sensitivity of 8 MeV and 1 MeV per channel.

A telescope of two x/y chambers allows to calculate the position of the beam particle on the front face of the calorimeter with an accuracy of about 500 μ (σ) in both directions. Trigger uses a coincidence of 2 counters of 10 x 10 cm and of a small counter (S3) of 2 x 2 cm. For the muon runs S3 was removed from the coincidence and instead we used a coincidence with a counter 30 x 30 cm downstream of 2 m of iron following the calorimeter set-up.

The detector was installed in the H6 beam line of the SPS north area at CERN. The beam was transported under vacuum except for 2 CEDAR detectors and a space of about 10 m length, 30 m upstream of the calorimeter where a cascade of three tests of silicium detectors was installed. Those devices represented in total between 0.5 and 1 radiation length.

Electron data were taken at 30, 60, 90, 125 and 150 GeV. At 90 GeV and above, electrons are separated from pions by synchrotron radiation energy loss in a set of bending magnets following the momentum slit. Below 90 GeV the beam is unseparated and contains about 30% electrons. Those are separated from pions using the signal given by the hadronic calorimeter. Above 90 GeV no such separation is necessary.

To form a calorimeter signal, energy is collected in a set of 3 x 3 (or 5 x 5) towers around the extrapolated point.

Energy resolution is obtained by fitting a gaussian to the energy distribution, over an interval of $[-1\sigma, +2\sigma]$ around the peak. The low limit (-1σ) is chosen so as to limit the effect on the measured resolution of the bremsstrahlung tail due to parasitic materials.

The energy resolution obtained in this way is plotted as a function of $1/\sqrt{E}$ in figure 1. The fit of a straight line gives

$$\frac{\sigma}{E} = (10.1 \pm 0.6)\ \%\ /\sqrt{E} + (0.0 \pm 0.1)\%$$

or, with a possible constant term added in quadrature

$$\frac{\sigma}{E} = (10.3 \pm 0.4)\ \%\ /\sqrt{E} \oplus (0.2 \pm 0.2)\% \ .$$

The terms varying as $1/\sqrt{E}$ is somewhat larger than the Monte Carlo simulation value (8.3%) for a fixed point [1]. Taking into account (in Monte Carlo) the residual modulation associated with the geometrical structure (0.6% at 40 GeV) one computes a resolution at 40 GeV of 1.45% which is quite close from the value (1.6%) interpolated between measurements.

Using the centre of gravity calculated from the calorimeter signals in the x and y directions, one can estimate, by comparison with the extrapolated impact point, the position resolution of the calorimeter. The difference ($x_{COG} - x_{extr}$), obtained in this way, is shown in figure 2 for 125 GeV electron data. A gaussian fit to this distribution gives a width (σ) of 680 microns. By unfolding the uncertainty on the extrapolated point, one estimates a calorimeter resolution of about 450 microns. Using harder cuts on the beam chambers and scintillator signals, even better resolution have been obtained (down to $\simeq 300\ \mu$). In the y direction this calorimeter behaves as a "normal" calorimeter with 2.5 cm towers. In particular, a correction on the position of up to 2 mm has to be applied to correct for the bin width effect. After such a correction the position accuracy is also quite good ($\lesssim 700\ \mu$).

The muon data, analysed in a similar way, show the same features even clearer. In the horizontal direction the centre of gravity (reconstructed from 2 cells) is unbiased and give a position accuracy of the muon impact point of 2 mm [fig. 3]. In the vertical direction only the cell number is accessible.

In 1991, the same prototype, but with faster electronics, will be exposed again to high energy beams. The aim is to check that similar performances can be obtained with a speed adequate for LHC.

[1] B. Aubert et al., "Liquid Argon Calorimetry with LHC-performance specifications, CERN/DRDC/90-31.

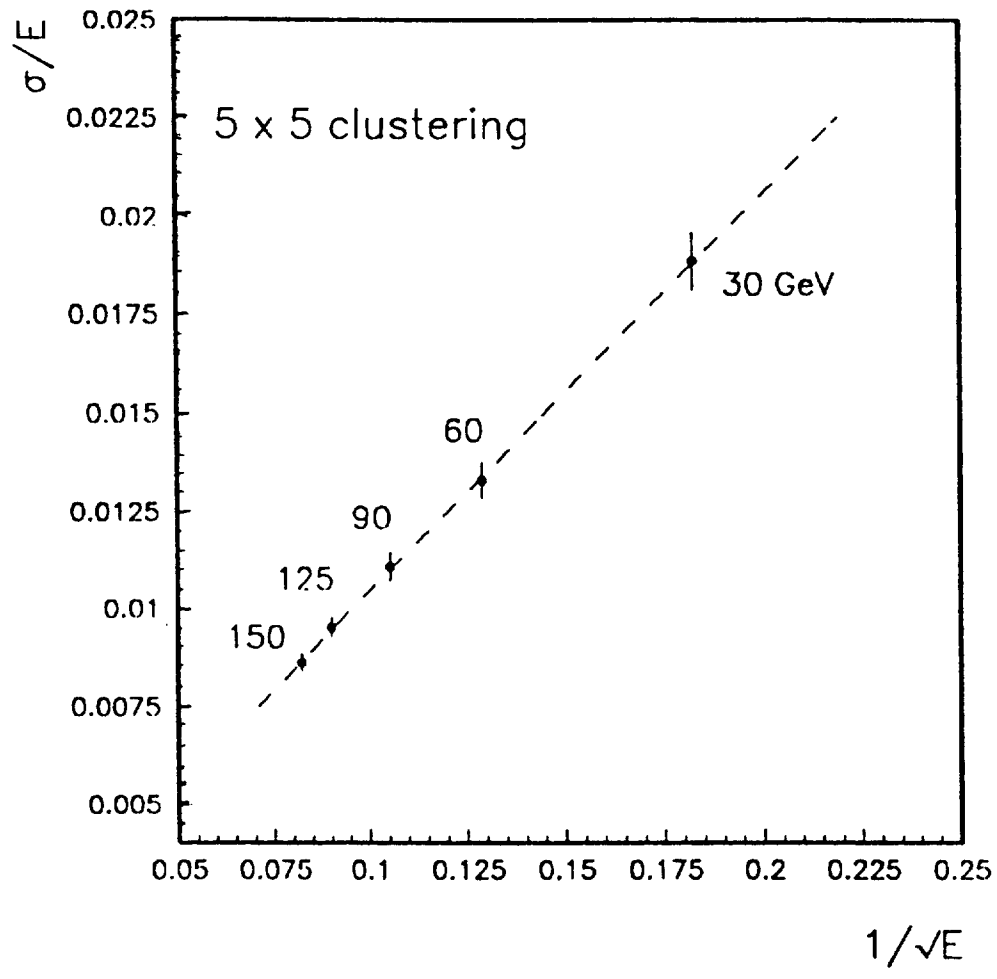


Figure 1 Energy resolution for electron showers as a function of $1/\sqrt{E}$.

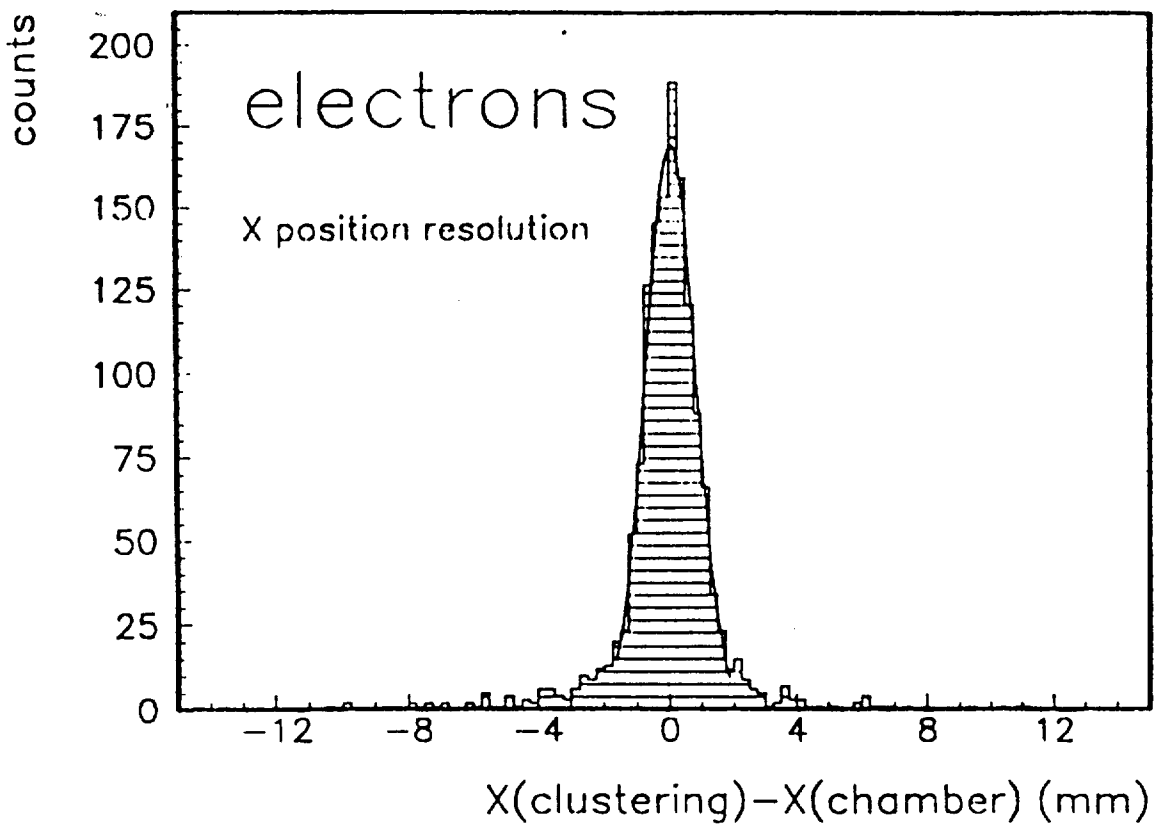


Figure 2 Distribution of the difference between the extrapolated position and the position measured from the calorimeter (horizontal directions) for 125 GeV electrons.

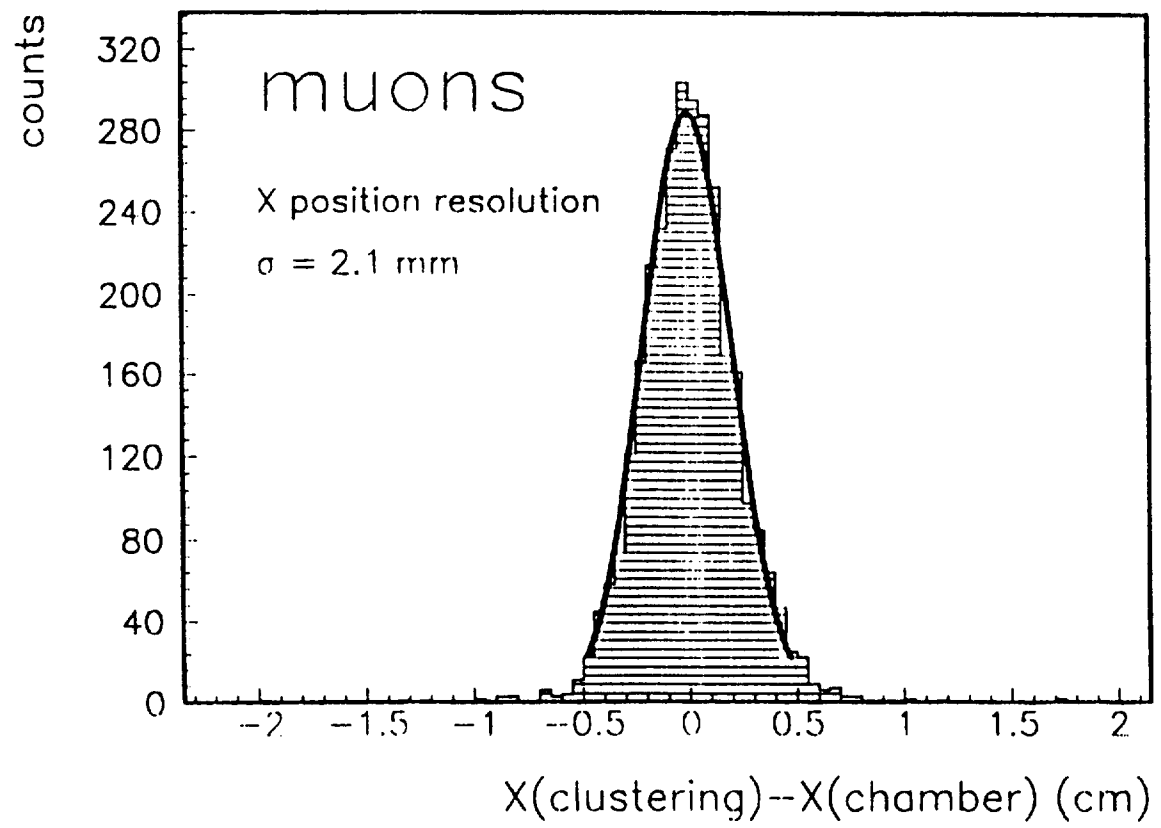


Figure 3 Distribution of the difference between the extrapolated position and the position measured from the calorimeter (horizontal directions) for ≃ 100 GeV muons.

A FAST AND RADIATION HARD CRYSTAL CALORIMETER FOR THE LHC

P.Lecoq CERN / PPE , M. Schneegans LAPP

Abstract

Homogeneous crystal calorimeters are so far the best in terms of energy resolution and compactness . Large scale detectors have been built for several experiments and the engineering problems are well understood . One of these crystals , BaF_2 , is already well known as a fast and radiation hard scintillator . From our systematic studies of scintillation properties and radiation damage mechanisms of several scintillators , we believe that a complete family of fluorides crystals or glasses should behave like BaF_2 , but with shorter radiation lengths and no slow component . A scheme , based on CeF_3 , is presented for a possible calorimeter configuration at LHC.

1- Physics goal :

The leptonic decay mode is certainly the cleanest way to study heavy bosons and Higgs particles at the LHC . Access to the e^+e^- and $\gamma\gamma$ channels will complement the traditional 4 μ channel , increasing the statistics and offering a cross check with different backgrounds and systematics [1,2] ; the $\gamma\gamma$ channel will also offer the only possible way to detect the Higgs , if its mass is in the 80 - 140 GeV/c^2 range .

In fact , as was confirmed by the work of the ECFA/LHC groups at this workshop [3] , two channels have a chance to be observed for Higgs masses between 80 and 180 GeV/c^2:

$$pp \Rightarrow H^\circ + X \quad \text{and} \quad pp \Rightarrow H^\circ + W^\circ$$

$$\downarrow \qquad\qquad\qquad \downarrow \quad \downarrow$$

$$2\gamma \qquad\qquad\qquad 2\gamma \quad e(\mu)+\nu$$

In this mass range , the Higgs width is of the order of 10 MeV , and a very high resolution calorimeter with high density and small granularity will be needed to reconstruct the Higgs mass above the large background .

For the H° –> 4 leptons channel in the intermediate mass range (140 GeV ≤ M_H ≤ 180 GeV) , the decay products of the virtual Z° can have an energy of a few GeV only . Therefore a high resolution is necessary down to low energy , particularly to reduce the background from the semileptonic decay of heavy quarks .

At higher Higgs masses , the reconstruction of the two real Z^0 from their leptonic decay will give the signature for the Higgs production . A good electron resolution in this mass range is essential for a precise measurement of the width of H^0 –> $e^+e^-e^+e^-$, as well as for the selection of electron events in the Z^0 mass peak in order to control the background .

It is also very important to have a fast signal from the em calorimeter which can be used in a first level trigger , since at present , compensating calorimeters must have a too long integration gate , and only fast scintillators can be efficiently used for fast trigger information at the rates of the LHC .

2. Crystals for a calorimeter at LHC :

So far , crystal calorimeters have the best possible energy resolution with a small constant term , compactness , homogeneity and very good hermiticity .

Several large scale crystal calorimeters have been built in the past (Crystal Ball with NaI(Tl) , Cleo II and Crystal Barrel with CsI(Tl), L3 with BGO) , and a lot of experience already exists about mechanical structures, light collection , monitoring and calibration of such detectors . From this point of view , a crystal calorimeter can be considered as a conservative approach, which is a valuable argument considering the short time scale to design and build a detector for the LHC .

Several fast and radiation hard candidates are already known like BaF_2 [4] , pure CsI , CsI/CsBr [5] , and some others look very promising (CeF_3 , LaF_3 , PbF_2 [6]) . From our systematic investigations on the luminescence and radiation damage mechanisms of BGO and BaF_2 during the last five years [7,8,9] , it is more than likely that several fluoride crystals must behave like fast and radiation hard scintillators .

The intense intrinsic luminescence of ionic crystals is generally attributed to the non localized emission of relaxed excitons (for instance e^- trapped by V_K centres) . This luminescence is often intense , but intrinsically

slow and temperature dependant . On the other hand , a newly discovered scintillation mechanism is observed in several bialkali-earth halide compounds like BaF_2 . The fast UV light emission is attributed to a cross luminescence mechanism which involves localized transitions from the deep outercore electronic states of the cation (Fig 1) . This process is necessarily fast and temperature independent . Moreover , for these cross luminescent scintillators , adding a third heavy component in a binary compound should not affect the optical properties of the crystal , as it has been verified on BaY_2F_8 and $KMgF_3$. This opens a new field of investigations for materials having the same nice features as BaF_2 , but with a much shorter radiation length and no slow component . For instance the family $LiYF_4$, $ErYF_4$, $TmYF_4$, $HoYF_4$ deserves a particular interest .

For the same reasons , it seems that heavy fluoride glasses can have characteristics similar to their crystalline brothers . Quaternary compounds with densities in the range of $8g/cm^3$ already exist , and the economical interest of such materials is evident .

Some dense crystals or heavy glasses (PbF_2 , KRS-6) are known to be efficient Cherenkov radiators . Doped with some fast scintillators (TbF_3 or CeF_3) they open a new way for off line hadron compensation , using the ratio of the Cherenkov to the scintillation signal , to correct the energy on an event by event basis .

A R&D proposal has been submitted to CERN for the systematic study of these scintillators [10] , including the understanding of mass production problems and costs . A similar program , more specifically on BaF2 , was proposed by Newman et al. for the SSC [11] ; a first array of 7 x 7 BaF2 crystals should be available mid 91 and tested in front of a compensating hadron calorimeter prototype .

3- Calorimeter design considerations :

The overall dimensions depend largely on the crystal choice , but not the design principle . The example of the CeF_3 (X_0 = 1.68 cm , R_M = 2.6 cm) will be taken in the following ; it is clear that the crystal length scales with the radiation length .

The very high rate at the maximum LHC luminosity , with the pile up of 10 to 30 events in the same bunch crossing , will make the background rejection by isolation cuts difficult . Moreover , for the $H^\circ \rightarrow \gamma\gamma$ channel , the

assignment of the 2 γ to one of the vertices in the z coordinate ($\sigma_z \approx 5.5$ cm) will be difficult , and the associated error on the 2γ opening angle will affect the H° mass resolution as well as the π° identification .

To fight against the LHC severe conditions and guarantee good Higgs mass resolution , a measurement of the photon angles is desirable . This can be achieved with active preshower counters , the crystal converters being readout for instance by parallel plate chambers with CsI or CsI / TMAE photocathodes as proposed by Charpak et al. [12] .

Another way , which be propose here , is to longitudinally segment the crystals into 2 pieces (C1 and C2) in the ratio of approximately 1/3 ; 2/3 (to be optimized by Monte Carlo) . In the first segment C1 , the photon conversion efficiency will be high and some development of the shower will yield a position measurement by barycentric method .To take advantage of the small shower radius in this segment , a granularity better by a factor of 4 than in the second segment is proposed , as shown on Fig 2 . All the crystals are readout independantly . Similarly , a barycentric method will give the position of the shower axis in the second segment C2 .

With this configuration , resolutions of respectively $\approx$ 0.5 mm and $\approx$1mm are expected in the first and second segments above 10 GeV , which should yield $\approx$ 0.3° angular resolution and $\approx$ 5 mm accuracy in reconstructing the z position of the vertex at $\theta = 90°$ (2 cm at $\theta = 30°$) . This should in general give unambiguous determination of the event vertex and thus precise 2γ opening angles for Higgs and π^0 as well as reduction of the combinatorial background in case of superposed events . The small lateral development of showers in the first segment will also improve particle and shower separation , and both segmentation and granularity will help in rejecting the hadrons . This design will also allow some e/γ discrimination in a magnetic field , by using the constraint of the vertex in the R/Φ plane .

The proposed detector geometry is based on a cylinder + cone design , having in mind the following considerations :

- all crystals should have a length corresponding to about 25 radiation lengths . Their sections should be as square as possible and large or sudden variations in transversal dimensions should be avoided .
- the coverage should be continuous from $|\eta| = 0.0$ to $|\eta| = 2.5$; as confirmed by recent studies presented at this workshop [3] , our main physics goal are satisfied by this coverage ; higher rapidities should be handled in a dedicated forward plug , if necessary .

- the internal radius should be large enough to allow good particle separation , taking into account the Moliere radius of the crystal , the pile-up expected at high luminosity [13] and the total volume of crystals , the radiation problem being crucial only at the highest rapidities .

- keep as much as possible a constant $\Delta\eta \times \Delta\phi$; this is satisfied by a cylinder of infinite length on which all crystals are nearly square with equal front areas . To limit the crystal volume , the cylinder should be stopped at some angle, and the inner radius progressively reduced , keeping the number of crystals in ϕ constant . This results in a slow crystal dimension decrease up to $\eta = 2.5$.

We propose an inner radius of the cylinder of 80 cm for the crystal front (reasonable compromise between performance and cost) , a granularity : $\Delta\eta \times \Delta\Phi = 0.02 \times 0.02$ for C1 and 0.04×0.04 for C2 and a maximum decrease of the crystal dimensions by a factor of 2 , which leads to the parameters listed in Table 1 . The large distance (z = 245 cm to the crystal front) at $\theta = 10°$ helps to keep the maximum radiation level to a "tolerable level " of a few Mrads / year at $L = 10^{34}$ / cm^2xs . The choice of the transition point from cylinder to cone (here at $\theta = 30°$, $\eta = 1.33$) has some effect on the crystal volume , but can be chosen according to the central tracker needs . An internal radius of the cylinder of 1 m , would yield a total crystal volume less than 50% larger .

The readout of the scintillation light is also crystal dependant . For crystals like CeF_3 , having a fast component in the visible range and no slow component , the use of photodiodes will probably offer a " cheap " solution . For the fast UV component of BaF_2 (or other similar crystals) , parallel plate chambers with TMAE adsorbed on CsI photocathodes [12] could be used . Another solution is to use a photocell with solar blind Cs-Te or a newly developed K-Cs-Te photocathode , which strongly suppresses the slow component (Fig 3) .

The crystals can be supported by a carbon composite mechanical structure (Fig 2) , similar to the one built for the L3 BGO detector , and to the one proposed for L* at SSC [11] .

4- Conclusion :

Crystal calorimetry offers a unique and conservative way to study the leptonic decay modes of heavy particles at LHC , and particularly the $\gamma\gamma$

decay mode of the Higgs . From the recent progress in understanding the radiation damage and scintillation mechanism of crystal scintillators , several dense , fast and radiation hard scintillators can be selected or developed . A few of them have been identified in the recent years , and the studies for large scale production and cost reduction are already well on the way .

References :

[1] J. Gunion et al. "The Higgs Hunter's Guide" , UCD preprint , 89-4 (1989).

[2] M. Chen et al. , Proc. of the Summer Study on High Energy Physics , Snowmass , 1988 , p.806 .

[3] See for instance : communications at this workshop from Seez , Froidevaux and Altarelli .

[4] L* Expression of Interest to the SSC by the L* collaboration .

[5] D. Renker , communication at this conference

[6] D.F. Anderson , E.J. Ramberg , "Recent developments in high speed , non sampling electromagnetic calorimetry " , Fermilab-Conf-90 / 46

[7] C. Laviron , P. Lecoq ,"Radiation damage of bismuth germanate crystals" NIM 227 (1984) 45-53 .

[8] P.Lecoq , P.J. Li , B. Rostaing ,"BGO radiation damage effects : optical absorption , thermoluminescence and thermoconductivity " L3 internal report # 746 . To be published in NIM .

[9] H. Newman , R.Y. Zhu , private communication .

[10] P.Lecoq et al. " Proposal for a fast and radiation hard crystal calorimeter at LHC " , CERN / DRDC / 90-25 / P2

[11] H. Newman et al. " A precision BaF2 crystal calorimeter for the SSC " R&D propsal at the SSC

[12] Charpak et al. , Proceedings of the ECFA study week in Barcelona , CERN 89-10 , Vol 2 , p593

[13] J.Colas et al. Report on Calorimetry at this workshop

Table 1 : Preliminary parameters of a CeF_3 crystal calorimeter for LHC

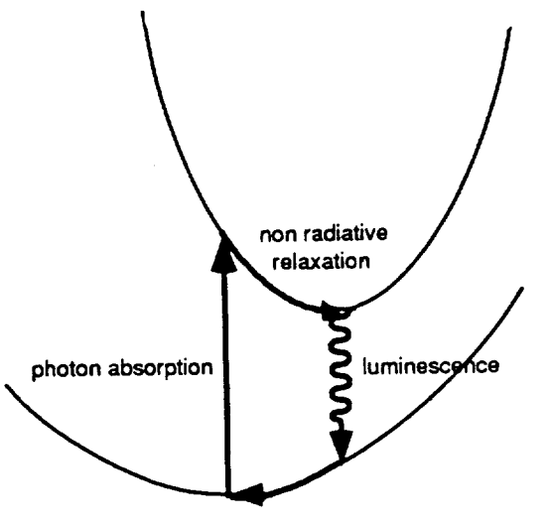
	Cylinder	Cone
Geometry (crystals only)	r=80 cm , R=122 cm , z=±139 cm	r= 40 cm , z =±245 cm at θ = 9.4°
Angular acceptance	30° < θ < 150°	9.4° < θ < 30° 150° < θ < 170.6°
Pseudorapidity accept.	$\|\eta\| < 1.33$	$1.33 < \|\eta\| < 2.5$
Crystal longitudinal segmentation	L1 ≈ 8 RL = 13 cm L2 ≈ 17 RL = 29 cm	L1 ≈ 8 RL = 13 cm L2 ≈ 17 RL = 29 cm
Granularity C1 : $\Delta\eta$ x $\Delta\phi$	.02 x .02	.02 x .02 down to η=2 *
crystal front face	1.6 x 1.6 cm^2	1.6 x 1.6 cm^2 to 1.2 x 1.2 cm^2 *
Granularity C2 : $\Delta\eta$ x $\Delta\phi$	.04 x .04	.04 x .04 up to η=2.5
crystal front face	3.6 x 3.6 cm^2	3.6 x 3.6 cm^2 to 1.8 x 1.8 cm^2
Number of crystals : C1	43520	≈ 24000 *
: C2	10880	9920
N_θ x N_ϕ	2 times 160 x 34	2 times 160 x 31
Total crystal number	54400	≈ 34000
Total crystal volume	7 m^3	2.9 m^3

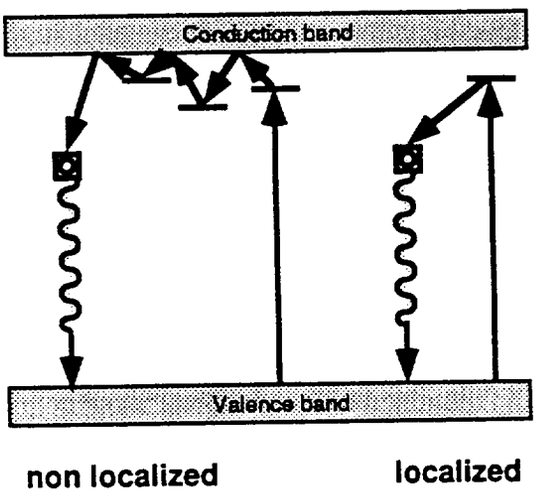
* The division of C1 in 4 crystals can be stopped above η = 2.0 , since the crystal dimensions are already small compared to the Moliere radius .

P. LECOQ / CERN

LUMINESCENCE MECHANISMS IN INORGANIC SCINTILLATORS

Luminescence : • emission of relaxed excitons
• in general large Stokes shift
• localized ⇨ fast
temperature independant
generaly weak
• non localized ⇨ slow
temperature dependant
more light





Cross luminescence : • Most of the alkali-earth halide binary compounds
• Fast UV
• Temperature independant
• Optical structure not much modified
by addition of a third heavy component

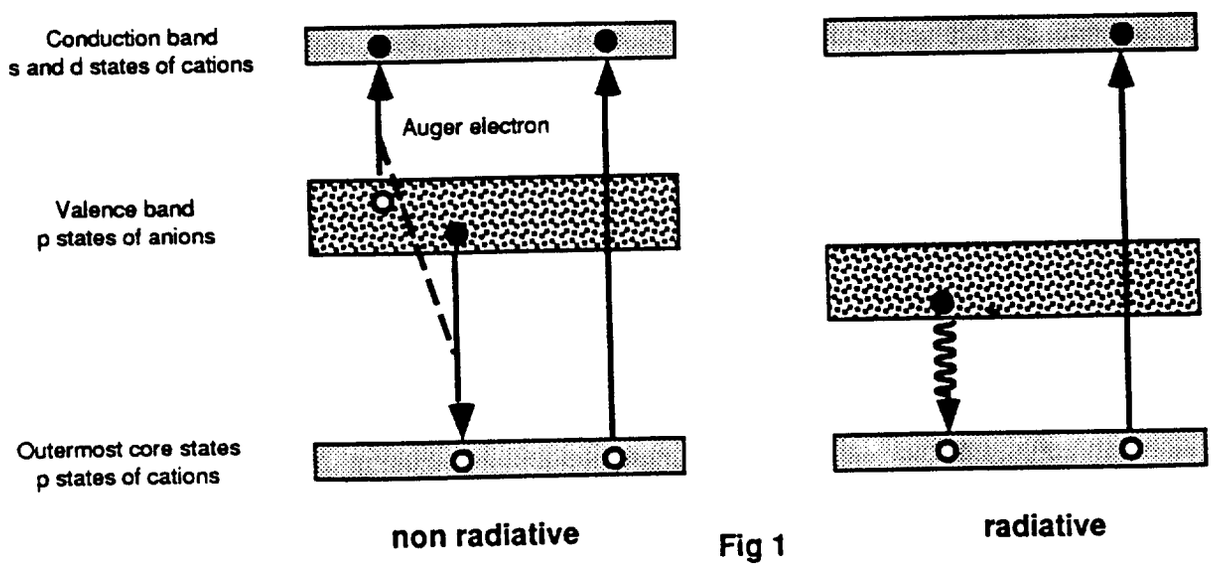
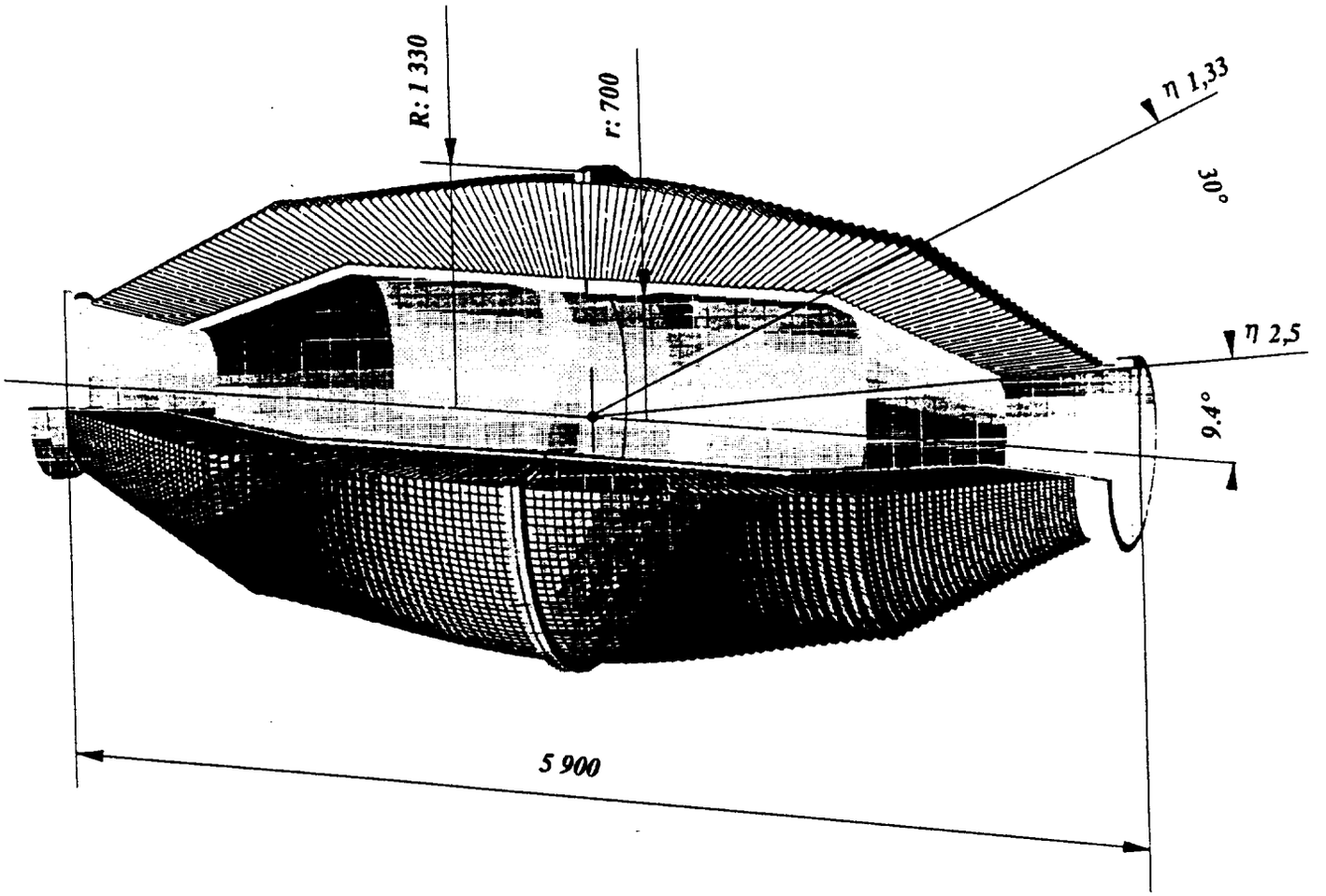


Fig 1


R: 1 330
r: 700
η 1,33
30°
η 2,5
9.4°
5 900

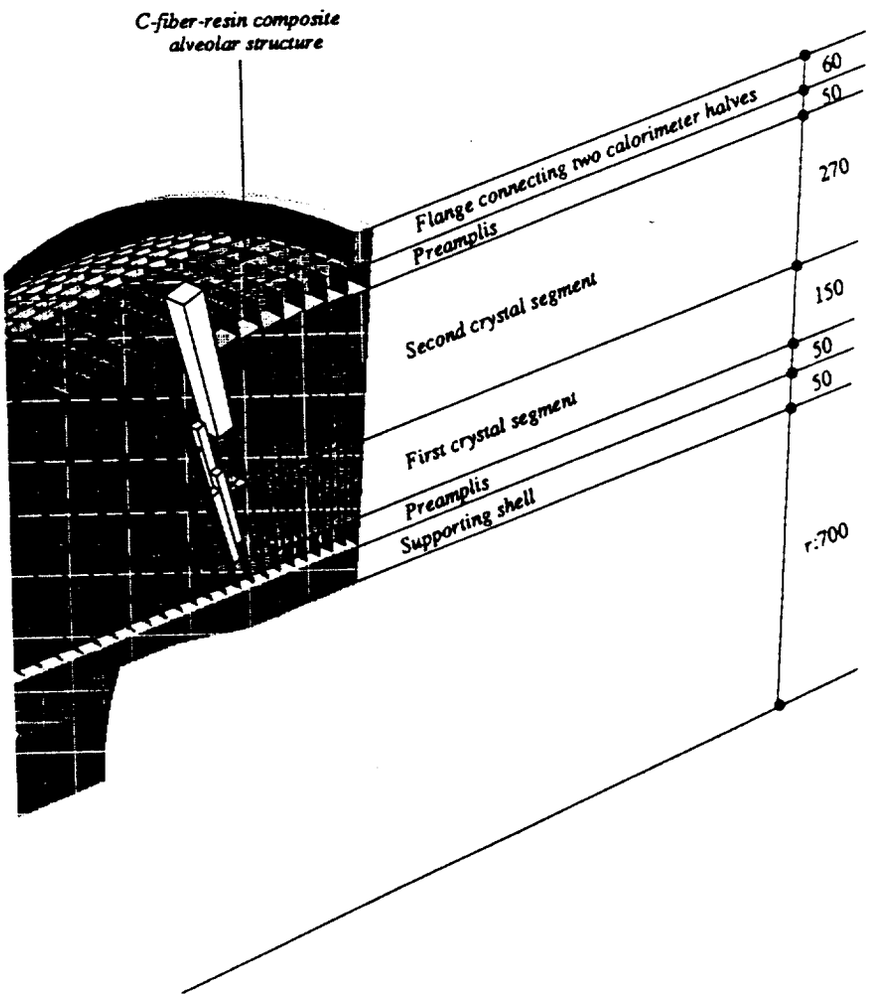
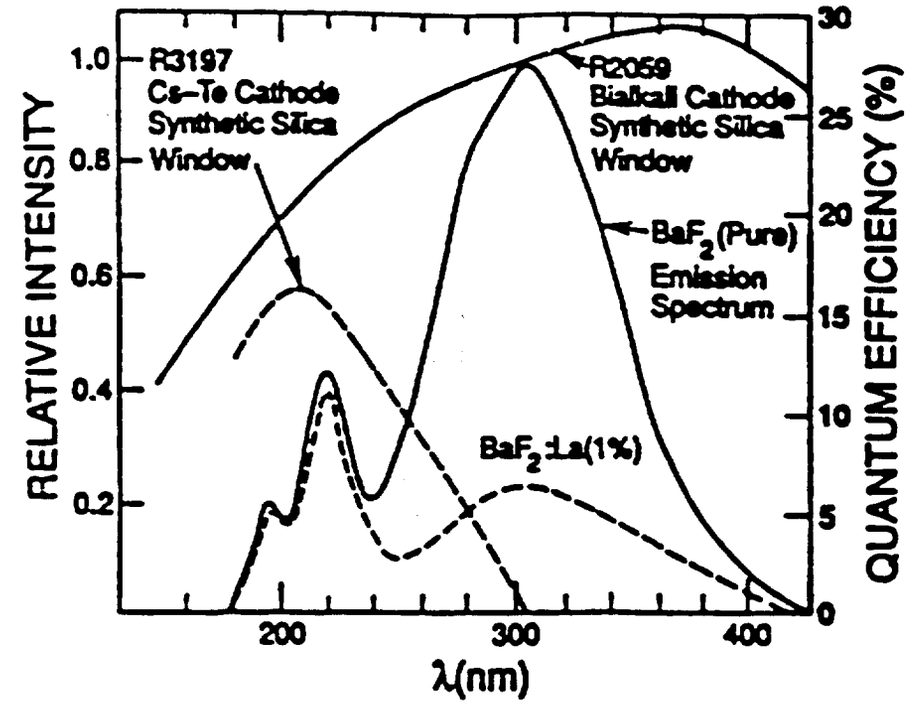

C-fiber-resin composite
alveolar structure
Flange connecting two calorimeter halves
Preamplis
Second crystal segment
First crystal segment
Preamplis
Supporting shell
60
50
270
150
50
50
r:700

Fig. 2


RELATIVE INTENSITY
QUANTUM EFFICIENCY (%)
λ(nm)
R3197
Cs–Te Cathode
Synthetic Silica
Window
R2059
Bialkali Cathode
Synthetic Silica
Window
BaF2 (Pure)
Emission
Spectrum
BaF2:La(1%)
1.0
0.8
0.6
0.4
0.2
30
25
20
15
10
5
0
200
300
400

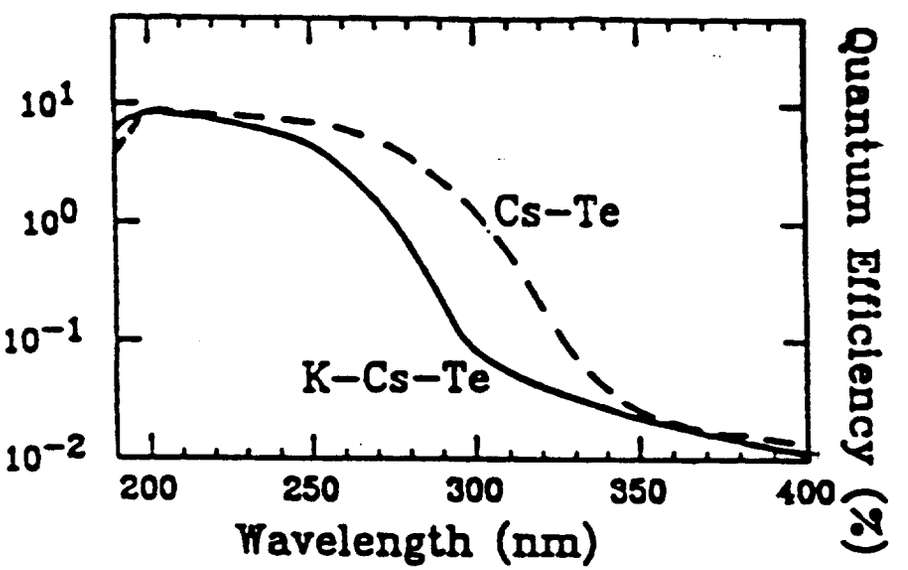

Quantum Efficiency (%)
Wavelength (nm)
Cs–Te
K–Cs–Te
10¹
10⁰
10⁻¹
10⁻²
200
250
300
350
400

Fig 3

New readout for BaF_2 calorimeters: gaseous detectors with solid photocathodes

G. Charpak,V. Peskov and D. Scigocki

ABSTRACT

Our latest results concerning the development of BaF_2 calorimeters for experiments at the future large hadron colliders (LHC, SSC) are presented. We are elaborating electromagnetic calorimeters made of BaF_2 crystals preceded by layers of low-density VUV scintillators, such as $KCaF_3$, to separate e and γ, and by a BaF_2 preshower counter with a high granularity. The readout of these scintillators is done with parallel-plate avalanche chambers combined with photocathodes. For the BaF_2 calorimeter, we have tested new readouts using gaseous ionization chambers with photocathodes, which have advantages regarding good stability, good energy resolution and radiation hardness.

1 Introduction

It is commonly acknowledged that the main requirements for the electromagnetic calorimetry to be used at future colliders such as the LHC or SSC, are a high speed (15 ns bunch crossing), a high radiation resistance (up to 0.1 MGy), a good energy resolution, and the best possible hermeticity. Calorimeters made of dense inorganic scintillators were considered to be one of the best options, and a promising candidate is BaF_2. The question concerning BaF_2 calorimeters, which is still under active discussion, is : What is the best choice for the readout? Different types of readout have been investigated. The first readout used in BaF_2 calorimetry consisted of low-pressure multiwire proportional chambers (MWPCs) filled with a photosensitive vapour [e.g. tetrakis(dimethylamine)-ethylene (TMAE)]. An energy resolution of about $3.9\%/\sqrt{E}$ (GeV) was measured with a good linearity, a position resolution close to 1 mm, and an e/π rejection factor of 10^{-3} at 5 GeV [2]. A time resolution of better than 1 ns was also obtained [2]. However, this readout is not attractive because of the rapid ageing effect caused by polymerization of the TMAE in MWPCs.

Another solution, developed by Lorenz et al. [3], is to read out BaF_2 crystals by means of solid (Si) photodiodes, which are simple and very compact. An energy resolution of about $2\%/\sqrt{E}$ (GeV) was measured between 2 and 40 GeV by recording the fast and slow components of the BaF_2 emission. Such photodiodes have no gain, which greatly simplifies the long-term stability problem, but their use is limited by the high capacitance of the large devices needed in calorimetry. In addition, these standard photodiodes are sensitive to the BaF_2 slow component (600 ns decay time), which may induce an important pile-up in the high rates expected at the future high-luminosity hadron colliders. Recently Zhu [4] proposed to use vacuum photodiodes for the BaF_2 readout. But such

photodiodes are still sensitive to the slow component and magnetic field, and are rather expensive.

The last readout candidate for BaF_2 calorimetry is a photomultiplier (PM) [5]. A PM is a fast device, but it occupies a lot of space. This does not permit high granularity, and PMs are sensitive to magnetic fields.

We have developed a new approach to the readout of BaF_2 crystals, either by parallel-plate avalanche chambers (PPACs) [6], or ionization chambers [7], combined with photocathodes that are sensitive only to the BaF_2 fast emission.

2 An ionization chamber with CsI photocathodes

Among the photocathodes already investigated, the best result was obtained with pure reflective CsI photocathodes, with a measured quantum efficiency of about 10% below 190 nm [8]. This result was verified by Dangendorf et al. [9].

This year, a systematic study has been made by Séguinot et al. [7] of the properties of CsI photocathodes, in ionization chambers under very clean gas conditions: a stainless-steel vessel and tubes, Oxisorb absorbers, and so on. The observed quantum efficiency achieved at $\lambda = 193$ nm was much higher than in previous measurements, about 30%. This efficiency is so high that is was possible to record VUV scintillation light from the BaF_2 by an ionization chamber combined with a pure CsI photocathode (see Fig. 1 [7]), and to observe an energy resolution better than $4.5\%/\sqrt{E}$ (GeV) [10]. In addition the quantum efficiency increases again by a sizeable factor when vapours of TMAE are adsorbed on the CsI [7].

The ionization chamber has many advantages over other types of readout. Large surfaces can be obtained at a low price because no window is needed between the BaF_2 crystal and the ionization chamber. These detectors can be flushed, and even if the photocathode is damaged, full recovery is possible after flushing with a gas mixture containing the same photosensitive vapour (TMAE or EF (ethylferrocene)[6]) as the one initially deposited on the CsI photocathode. Without any gain in the chamber, the needed mechanical tolerances are reduced, and a gain monitoring is no longer necessary. Since the photocathode is not damaged by feedback from the positive ions [11], the long-term stability of the chamber, which depends on the behaviour of the photocathode only, should be good. In addition, the ageing caused by polymerization due to the charge density in the avalanche does not exist since there is no gain [11]. The influence of direct ionization is still negligible because of the small required gap width (about 0.5–1 mm), particularly with a gas mixture based on helium. For all these reasons, we consider the ionization chamber with CsI or CsI+TMAE or EF photocathodes as an attractive readout for future BaF_2 calorimeters.

3 PPAC with CsI photocathodes

The measurements with the CsI photocathode described above were done in the ionization-chamber mode only. We have studied the same photocathodes with

high multiplication gaps [6], which are necessary for BaF_2 preshower counters. The results, presented here, are encouraging.

The set-up is similar to the one described in Ref. [12], with a single-wire counter used in the proportional mode, with high gain (up to 10^5). The CsI layer (500 nm thick) was evaporated onto the metallic cathode, which was then placed in the detector. A gas mixture of argon (91%) + methane (9%) was flushed into the detector through a bubbler of liquid EF or TMAE, so as to form the adsorbed layer on the CsI photocathode. With EF + CsI, the quantum efficiency was about 15% at 193 nm; with TMAE + CsI, it was 20%. We have observed that when the CsI is coated with an EF adsorbed layer, it can stay at least one hour in contact with air without any modification of the quantum efficiency, as was first observed with TMAE [7]. Because of this property, it is probably not necessary to keep the CsI photocathode permanently in contact with the EF or TMAE vapours. Therefore CsI + EF or TMAE photocathodes can be used with gases chosen for their excellent ageing properties. These photocathodes are simple and easy to manipulate, and we consider them to be very promising for a preshower counter. We have made a preliminary beam test of a small prototype BaF_2 calorimeter with such a photocathode. The composition of the calorimeter prototype is shown in Fig. 2. It consists of a BaF_2 crystal, $\sim$ 20 cm long and $\sim$ 5 cm in diameter, coupled to a PPAC with a CsI photocathode. The PPAC was formed by a mesh, touching the crystal, and by the CsI photocathode itself. The gap between the electrodes was about 4 mm. The chamber was flushed with He + 10% CH_4 at a pressure of 1 atm. In order to simulate the real experimental conditions, no special precautions were taken to ensure that the system was clean. Also, because of a mishap, the chamber had sprung quite a big leak. Nevertheless the chamber worked in a stable fashion up to a gain of $\sim 10^3 - 10^4$, and we were able to see, at the same voltage on the PPAC, signals obtained with 5 GeV deposited by electrons and 130 MeV by pions.

4 Low-density VUV scintillators with a PPAC and solid photocathodes for γ rejection

The efficiency of all the photocathodes which we have studied increases greatly in the wavelength region below 200 nm. This means that SSPCs using these photocathodes will be much more efficient with scintillators emitting in this region and thus achieve better energy resolution. In the case when PPACs are used with CsI photocathodes, a separating window is not needed between the scintillator and the chamber. This allows the detection of short-wavelength emission spectra (120–200 nm) from some VUV scintillators, such as $KCaF_3$, $KMgF_3$ and so on (see for example [8]). The number of primary photoelectrons produced in such detectors by traversing minimum ionizing particles will be about one hundred in a crystal of a few millimetres thickness.

On the other hand the γ absorption will be negligible because the radiation length of these scintillators is about 7–8 cm. It is thus possible to use these low-density VUV scintillators, coupled with PPACs and photocathodes, for e/γ separation when they are placed in front of a BaF_2 calorimeter.

5 Conclusions

In studying the coupling of BaF_2 and low-density scintillator crystals to gaseous detectors, we have made some progress in the construction of BaF_2 high-granularity preshower detectors and electromagnetic calorimeters with properties matching the requirements of future colliders: fast timing, radiation hardness, and good granularity and energy resolution. We are developing an homogeneous electromagnetic BaF_2 calorimeter composed of low-density VUV scintillators ($KCaF_3$) for γ rejection and a BaF_2 preshower counter with high granularity, read out by PPACs and solid photocathodes, followed by a few layers of BaF_2 crystals, coupled to photosensitive ionization chambers.

REFERENCES

1. E. Fernandez and G. Jarlskog (eds.), Proc. ECFA Study Week on Instrumentation Technology for High-Luminosity Hadron Colliders, Barcelona, 1989 (CERN 89–10, ECFA 89–124, Geneva, 1989), 2 vols.

   T.J. Gourlay and J.G. Morfin (eds.), Proc. Symp. on Particle Identification at the High-Luminosity Hadron Colliders, Batavia, 1989 (Fermilab, Batavia, 1990).

   Proceedings of the Conference on Very High Resolution Electromagnetic Calorimetry, Sigtuna (Sweden), 1989.

2. R. Bouclier et al., Nucl. Instrum. Methods **A267** (1988) 69.

3. E. Lorenz, G. Mageras and H. Vogel, Nucl. Instrum. Methods **A249** (1986) 235.

4. R.Y. Zhu, A high resolution BaF_2 calorimeter, R & D report CALT–68–1656 (1990).

5. M. Murashita et al., Nucl. Instrum. Methods **A243** (1986) 67.

6. G. Charpak, V. Peskov and D. Scigocki, preprint CERN–EP/90–41 (1990).

7. J. Séguinot et al., preprint CERN–EP/90–88 (1990).

8. G. Charpak et al., Proc. Batavia Symposium, *in* Ref. [1], p. 295.

9. V. Dangendorf, A. Breskin and R. Chechik, A gas-filled UV photon detector with CsI photocathode for the detection of the xenon light, Weizmann Inst. report WIS–89/52 (1989).

10. I. Giomataris, V. Peskov, J. Séguinot and T. Ypsilantis, paper in preparation.

11. G. Charpak et al., liquid and solid photocathodes for fast detectors, paper presented at the Second Conf. on Position-Sensitive Detectors, London, 1990.

12. V. Peskov et al., Nucl. Instrum. Methods **A269** (1988) 149.

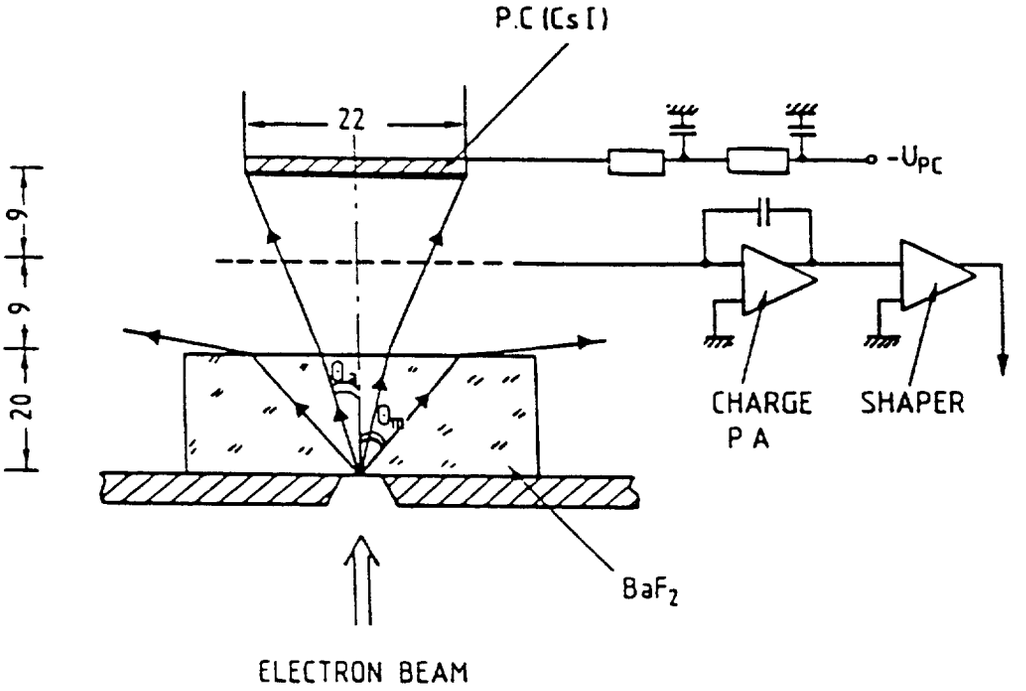


Fig. 1 A schematic view of the BaF_2 scintillator, the CsI reflective photocathode, the collection mesh, the charge-sensitive preamplifier, and the 0.8 μs shaper.

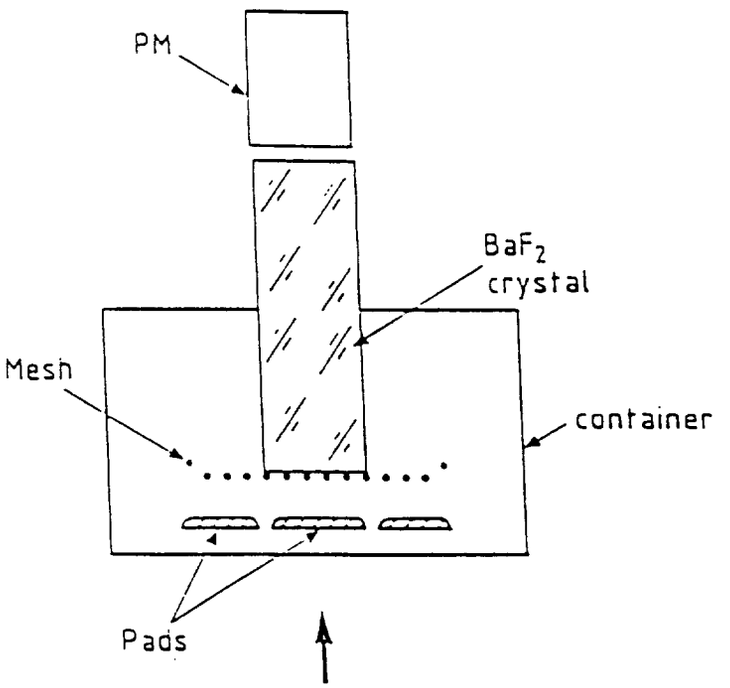


Fig. 2 Prototype of a BaF_2 calorimeter with a PPAC.

M. Chen et al.[1]

Scintillating LXe EM Calorimeter

A Introduction

Liquid Xenon (LXe) is radiation hard and its scintillation light for electrons/photons is fast (decay time 20 ns, cf. [1]) and intense (4×10^7/GeV at 170 nm, cf. [2]). The inherent large signals naturally result in excellent total energy ($\sigma(E)/E < 0.5\%$) and dE/dx measurements.

The scintillation signals from nuclear spallation (e.g. slow protons) produced in hadron-nucleus inelastic scattering, are yet faster (decaytime of a few ns) and more intense (7×10^7/GeV)([2]) than that of an electron. It is thus possible to use a short gate (about 15 ns) to enhance the π signal relative to the electron signal to compensate the nuclear binding energy loss and achieve e/π=1.

Using three layers of thin photodiodes and fast amplifiers submersed in LXe, one can use 3-D shower profiles to determine a photon vertex of $\sim$ 0.7 cm. This is useful in selecting the correct vertex of photons at high luminosities when multi-events occur in a single crossing. The longitudinal shower profile is also a measurement of the rear energy leakage thus can be used to improve the energy resolution by adding a correction term, dependent on the back/front energy ratio, $E_3/(E_1 + E_2)$ (Figure I.1). The total energy and the pre-shower (first layer) measurements together can yield a π/e suppression better than 10^{-4}.

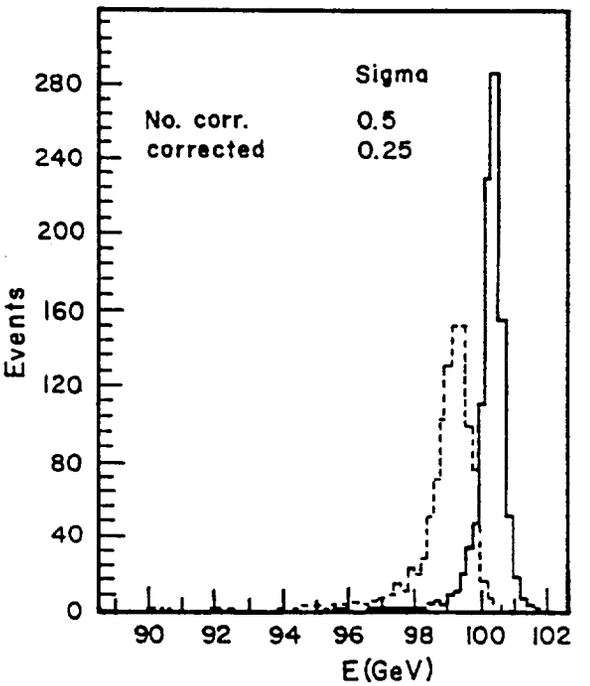


Figure I.1: Distribution of the total energy for 100 GeV electron showers in 22 X_o of LXe. The dashed histogram is the sum of energy of 3 diodes (0.5% σ and 1.2% rms), while the solid includes the correction due to back/front energy ratio (0.25% σ and 0.7% rms). Similarly, for 100 GeV photons, the resolutions are 0.6% σ and 1.9% rms without correction and 0.3% σ and 1% rms with correction.

B LXe EM Calorimeter

Using multi-layers of UV-photodiodes and fast amplifiers submersed directly in LXe to measure the scintillation light from LXe, one can thus detect photons and electrons with an EM energy resolution of < 0.5%; as well as a photon vertex determination of $\sim$ 0.7 cm and a spatial resolution of their impact points to $\sim$ 1 mm by measuring their three dimensional shower profiles.

Such a detector could contains $\approx 2 \times 10^4$ LXe cells. A typical cell of the xenon EM shower counter contains photodiodes, UV reflectors, and amplifiers as described in the following:

[1]M. Chen, D. Luckey, D. Pelly, S. Shotkin, K. Sumorok, B. Wadsworth, X.J. Yan, C. You, X. Zhang, Laboratory for Nuclear Science, MIT, Cambridge, MA, USA; E.G. Chen, M.P.J. Gaudreau, D.B. Montgomery, J.D. Sullivan, Plasma Fusion Center, MIT, Cambridge, MA USA; W. Wallraff, I. Physikalisches Institut, RWTH Aachen, D-51 Aachen, Germany; M. Vivargent, Laboratoire de Physique des Particules, LAPP, Annecy, France; Manfred Mutterer, Dept. of Physics, Technische Hochschule, Darmstadt, Germany; A. Bolozdynya, V. Chernyshev, P. Goritchev, V. Khovansky, A. Kouchenkov, A. Kovalenko, V. Lebedenko, V.A. Vinogradov, V. Epstein, S. Zeldovich, ITEP, Moscow, USSR; R. Krasnokutsky, R. Shuvalov, IHEP, Serpuchov, USSR; E. Aprile, R. Mukherjee, M. Suzuki, M. Moulsen, Dept. of Physics, Columbia University, New York, NY, USA; S. Sugimoto, K. Okada, Dept. of Physics and OULNS, Osaka University, Osaka 560, Japan; T. Fujino, T. Matsuda, M. Miyajima, Nat. Lab. for HEP, KEK, Tsukuba, Ibaraki 305, Japan; T. Doke, J. Kikuchi, A. Hitachi, T. Kashiwagi, Y. Nagasawa, H. Ichinose, N. Ishida, T. Nakasugi, T. Ito, Science and Eng. Res. Lab., Waseda University, Tokyo 162, Japan; K. Masuda, E. Shibamura, Saitama College of Health, Saitama 338, Japan; T. Takahashi, Riken, Saitama 351, Japan; H.S. Chen, H.W. Tang, K.L. Tung, Institute of High Energy Physics, Beijing, China; H.L. Ding, Institute of Atomic Energy, Beijing, China.

B.1 UV photodiodes

We have developed large windowless UV sensitive silicon solid-state photodiodes covered by gold meshes, which are insensitive to magnetic fields and have a quantum efficiency > 50%. The diodes are 400 μm thin so that < 0.1% of the signal of an EM shower is due to particles passing through the diodes. This makes hermetical calorimeters with 3-D shower measurement possible.

The leakage current from the diodes is less than 10 nA at −108°C. It may increase by three orders of magnitude after heavy doses of radiation and the noise due to leakage current is still negligible.

B.2 Fast amplifiers

Fast amplifiers operate in LXe directly and have a peaking time of 10 ns for the largest size diode (5 cm diameter). The detector yields < 0.5% energy resolution for 2.5 GeV ^{27}Al ions. The fast amplifiers can be positioned behind the largest diode, attached to the cooling lines outside the active xenon region.

B.3 UV reflecting cell walls

We have constructed 3 x 3 UV reflectors using 100 μm aluminum foils, welded flat piece by piece using electron guns, and then expanded into shape. These metal reflectors also serve as Faraday shields for individual cells to reduce cross talk and noise.

Assuming a reflectivity of 0.88 at 170 nm, which was achieved by large system of Al coated mirrors [8], Monte Carlo studies show excellent uniformity (see Figure I.2) for the following configurations:

1. Using a single photodiode and darkening the nearest ~ 1 cm of the reflector, the signal corresponds to 40% light collection.

2. Using two photodiodes, S_1 and S_2, at either end, The composite signal, $\frac{S_1 S_2}{S_1+S_2}$, corresponds to ~ 60± 1.5% light collection efficiency over the full section. The uniformity of this configuration is insensitive to the exact values of reflectivity or attenuation length used.

The resultant uniformity is better than the average of the L3-BGO crystals, which has been proven to have excellent energy resolution. Reflectivity of mirrors is currently measured using a VUV spectrometer at Osaka University.

C Results from Tests on Prototype Detector

The properties of prototype scintillating liquid xenon detectors using diodes and amplifiers developed at Waseda/MIT are described in the following sections and summarized in Table I.1.

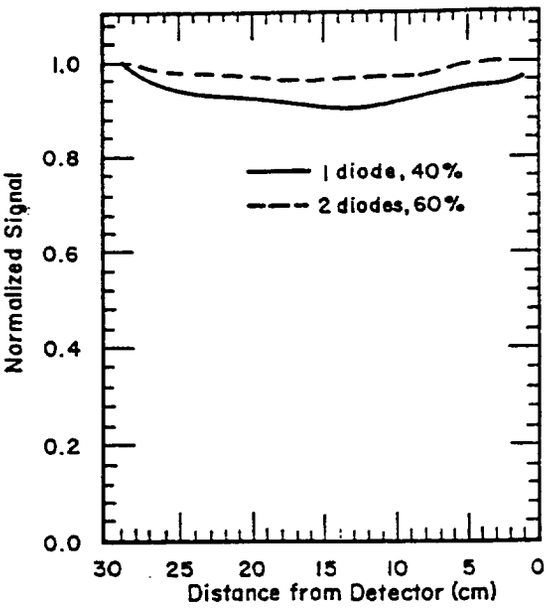


Figure I.2: Monte Carlo studies of the signal uniformity as a function of distance from the large end of a 30 cm long section of a 66 cm long, truncated pyramid reflector cell with a normal reflectivity of 0.88.

Table I.1: Physical properties of liquid xenon with our diode/amplifiers

photoelectrons/GeV	10^7, including Q.E. and acceptance
calibration	5.49 MeV α
saturation	100 times higher than NaI
$\sigma(E)/E$	< 0.5% for E > 2.5 GeV

D Calibration using α Particles in situ

We determine the photoelectron yield and study calibration methods for LXe detectors using 5.49 MeV α's [3]. The measured pulse height of photoelectrons corresponds to 4×10^4 electrons with a resolution, dominated by the electronic noise of the amplifier, of 6.6% (slow) and 17% (fast amplifiers). The temperature dependence of the scintillation yield, in the temperature region between −110°C and −75°C, was about −0.4%/°C, three times smaller than that of the BGO.

When α's are allowed to stop directly in the diode, the width of the pulse height distribution is 0.5% with 3 μs gate time and 1.5% with 20 ns [4]. This high resolution demonstrates the excellent uniformity of the photodiodes, both home made and from Hamamatsu. Both diodes and amplifiers work well at low temperature.

The α spectra are very stable and, therefore, can serve as a reliable calibration for the experiments. One can use two α sources, (one situated in LXe and the

other on the diode), and cosmic μ for calibration, after the detectors have been calibrated in beams Figure I.3.

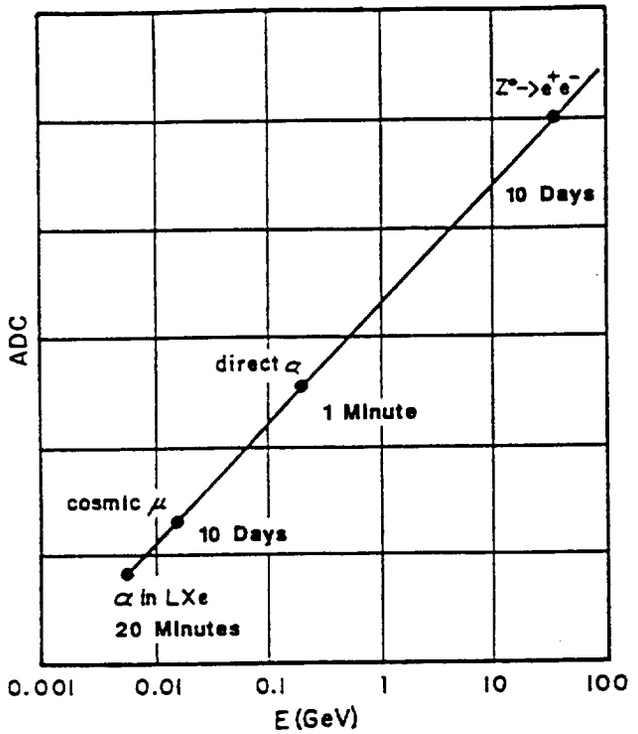


Figure I.3: Calibration of liquid xenon detector using α particle in LXe and direct on the diodes, cosmic μ's, based on our measurements, and monitored by the expected $Z \rightarrow ee$ events. Estimated time needed to reach 0.5% calibration accuracy is indicated for each data set.

E Energy Resolution measured with Heavy Ion Beams

We determine the intrinsic energy resolution of a scintillating LXe detector equipped with full size (5cm diameter) silicon photodiodes using heavy ion beams from the Ring Cyclotron at Riken, Japan. The observed energy resolution was 0.6% RMS for 1.64 GeV ^{14}N, and 0.68% for 2.65 GeV ^{40}Ar. The charge observed is 2.91×10^7 for 2.65 GeV ^{40}Ar.

To estimate the intrinsic resolution of LXe detectors, and to test the reliability of the detectors, we baked the same diode used for the above measurements until the quantum efficiency of the diode has dropped to 50% of its previous value. We repeated the measurement using 2.47 GeV ^{27}Al ions 2 months after the previous Ar ion tests. Indeed the charge observed is reduced to 1.36×10^7 electrons. The measured energy resolution without corrections improves slightly to 0.5% with 40 ns gate, due to better beam collimation.

(Figure I.4)

These results demonstrate that the measured energy resolution is mainly due to beam energy spread, not electronics or intrinsic photon statistics: the actual intrinsic energy resolution of LXe detectors is still much better than what are quoted above.

F Purification System

Ypsilantis (cf. [1]) showed that the attenuation length of LXe is >> 20 cm. We have studied the effect of impurity by filling up two full size scintillating liquid xenon cells with commercial grade xenon and found that scintillation works well even without any purification. We have built an 65 cm long single cell, completed with UV reflector, full size diodes and fast amplifier to be tested in heavy ion beam in order to determine uniformity and attenuation length.

G Xenon Availability

Four commercial companies: Air Liquide, Matheson, Spectra Gases and Union Carbide, have submitted letters that each of them can produce up to 15 m^3 of new LXe by 1999 at a price of about 2.5 M\$/m^3 of LXe.

H Future Beam tests

The present development program is aiming at the measurements of fully contained high energy electron showers using a 5 x 5 LXe cells in 1991, and (with a hadron calorimeter behind) fully contained 100 GeV pion showers using an 11 x 11 LXe cells in 1992, in order to:

- determine e/π ratio,
- determine the energy resolution, uniformity, linearity of xenon detectors with both electron and π beams,

I Conclusion

We summarize our recent results in the following:

- photodiodes: α and heavy ion tests with home made full size photodiode and amplifiers submersed in LXe, show:
  1. quantum efficiency > 50%
  2. 10 ns peaking time
  3. $\sigma(E)/E$ < 0.54% at E > 2.5 GeV.

  Therefore 3-D shower measurement becomes possible.
- Calibration: LXe detectors have large output (> 10^7 photo-e/GeV) and thus can be calibrated using α's in situ. This calibration method has been verified using heavy ion beams.
- Uniformity: Monte Carlo studies show high uniformity can be achieved.

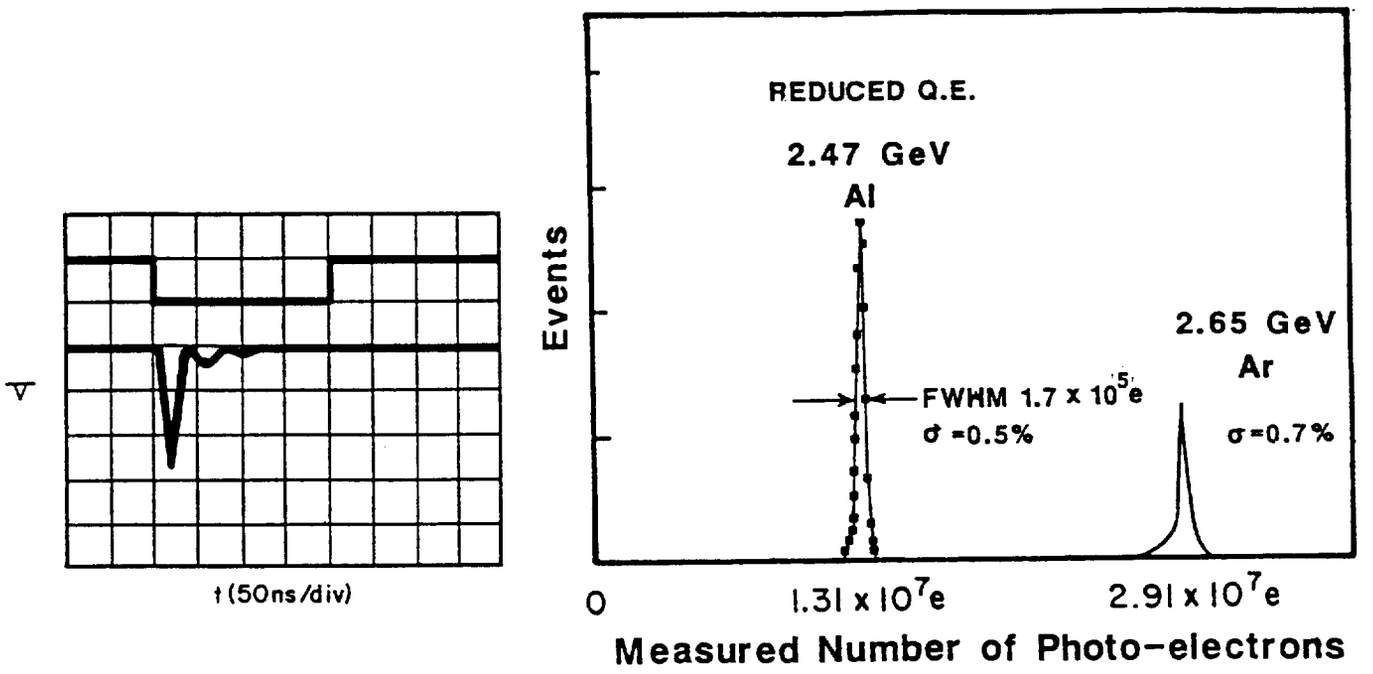


Figure I.4: a. Output pulse shape from a full size diode and fast amplifier; b. Measured photo-electrons for 2.65 GeV Ar ions and 2.47 GeV Al ions with 50% reduced quantum efficiency, showing the measured resolution is limited by beam energy spread.

- The potential new production of xenon is sufficient.

References

[1] T. Ypsilantis, ECFA/LHC Meeting on Detector R&D, Aachen, October 1990; and LAA Progress Report, CERN 90/1.

[2] M. Chen *et al.*, ECFA Workshop, CERN 89-10, vol.2, 1989.

[3] M. Chen *et al.*, The Xenon Prototype Detector Subsystem Proposal, 1989 and 1990.

[4] M. Gaudreau *et al.*, MIT-LNS Tech. Rep. # 174, 1990;
T. Doke *et al.*, MIT-LNS Tech. Rep. #175, 1990;
and S. Sugimoto *et al.*, OULNS 90-2, Osaka Univ., May 1990.

[5] M. Gaudreau *et al.*, OULNS Rep. 90-01, May 1990;
S. Sugimoto *et al.*, OULNS Rep. 90-02, May 1990;
T. Doke *et al.*, private communication.

[6] M. Miyajima *et al.*, Japanese Physical Society Meeting at Osaka, March, 1990.

[7] S.Sugimoto, M.Miyajima, S.Sasaki, and H.Tawara, Osaka Univ. OULNS 90-8, June 30, 1990.

[8] Mean reflectivity of the 300 RICH counters used by DELPHI at LEP, P. Baillon et al., Nucl. Instr. & Meth. A276 (89) 492 and 277 (89) 338.

[9] Note: $0.6 = \sqrt{0.1^2 + 0.15^2 + 0.57^2}$.

[10] L3 collaboration, B. Adeva *et al.*, Nucl. Instr. and Meth. A 289 (1990) 35.

[11] K. Masuda *et al.*, NIM 188 (1981) 629.

[12] D. Nachreiner, SSC Detector R&D Workshop, October 1990.

LIQUID XENON (KRYPTON) CALORIMETRY. Presented by T. Ypsilantis [1].

1. INTRODUCTION

Liquid Xenon is desireable as the sampling and showering medium of a totally active electromagnetic (em) calorimeter because it is a fast ($\tau \leq$ 20 ns) and efficient scintillator ($3 \cdot 10^4$ photons/MeV) and an efficient ionizer ($6.8 \cdot 10^4$ electrons/MeV). Drift of ionization electrons can provide sensitive positional information. It's relatively short radiation length of 2.8 cm allows a totally active calorimeter ($28X_0$) in length 78.4 cm.

Observation of either ionization or scintillation gives an excellent measure of energy ($\approx$1%) but simultaneous observation of both will give even better resolution because the anticorrelation of these quantities allows suppression of the Landau-like fluctuations.

Accurate position determination ($\sigma_x \approx$ 0.1mm) is obtained in 15 mm drift cells and directional sensitivity ($\sigma_\theta \approx$1 mr) through depth sampling. Direction and position determinations are made without referance to the vertex origin of the photons hence these quantities may be used to determine this point, along the z axis of the collider.

Its slow drift velocity (v=3 mm/μs) represents a difficulty at high luminosity hadron colliders since the maximum drift time t=5 μs. Doping with 3% methane increases v to (20 mm/μs) and reduces t to 750 ns. Even with this long integration time, double hits in the same cell can be unambiguously resolved because the fast scintillation signal provides an amplitude tag for the position sensitive (but slow) ionization signal.

Since cost and availability of Xenon are important factors in this project we intend to also construct and test a liquid Krypton calorimeter, following the methods developed for Xenon. Doping Krypton with ($\approx$ 5%) Xenon supresses the slow scintillation component. Krypton has the longer radiation length of 4.6 cm hence a totally active $28X_0$ calorimeter will require 128.8 cm. This longer length may be acceptable in a dedicated Higgs search experiment, via photon and electron decay modes.

This continuing work has been carried out during the past two years within the CERN-LAA project.

2. THE CALORIMETER CONCEPT

A front view of the unit calorimeter cell is shown in fig. 28, vol.1. It has 29 quartz readout wires strung between two C fiber readout posts with tranverse photocathode walls and a floor for mechanical rigidity and field shaping. The cell is oriented so that the axis of the electromagnetic shower is parallel to the wires. The photocathode walls are also parallel to the wire array. Each cell has a depth of two radiation lengths (56 mm) and fourteen such cells constitute a tower which extends the full ($28X_0$) length. The transverse cell size is $\Delta x = \Delta y$=30 mm and 10x10x14 such cells ($10.7X_0$ by $10.7X_0$ by $28X_0$) make up the prototype calorimeter. The totally active liquid Xenon makes up $\approx$99% of the calorimeter mass. Monte Carlo simulations (GEANT3.14, EGS4) of e.m. showers show that the inactive material of this calorimeter contributes only a small term to the energy

resolution ($\sigma_E/E \approx 0.2\%/\sqrt{E}$). The sensitive Xenon (Krypton) volume will be about 70 (312) liters which will require a total volume of 100 (400) liters weighing 308 (976) kg.

The transverse walls are coated with a 500 nm thick CsI reflective photocathode. A fast signal is generated when Xenon scintillation photons impinge onto the CsI surface to create photoelectrons which are injected into the liquid. The signal waveform is a current step function with amplitude proportional to the electron drift velocity and the total tower energy. Differentiation gives a fast signal for a first level energy trigger.

A uniform electric field of about 10 KV/cm is applied between the photocathode wall (at 15 KV) and the collection wires (at earth). The ionization charge and the injected photoelectrons are drifted up to and through the Frisch decoupling grid and collected on the wire array. The Frisch grid is made of an electroformed metal mesh with 90% optical transparency, located 1.5 mm before the wire plane. Each quartz wire runs the full length of the calorimeter but is metalized in 54 mm sections with a 2 mm bare gap, to match the cell pitch of 56 mm. As the wire enters a readout post, it is soldered to a resistive carbon fiber wound helically around the post. The unmetalized gap allows each of the cells (along the wire) to be readout independantly. Wave form digitizers (or flash ADC's) at each end of the resistive fiber determine the deposited charge distribution along the y (wire array) direction by charge division and along the x (drift) direction by timing. Thus the readout gives the position (x_i, y_i) of deposited charge (q_i) at the cell of depth (z_i) .

The scintillation signal is identified as the charge which arrives exactly 750 ns after the trigger because photo-injection is isochronous and time diffusion is small (σ_t=7 ns for 15 mm drift). Because the ionization and scintillation amplitudes are correlated, the ionization charge (which is produced in the same beam crossing as the trigger) is amplitude tagged. An example of this logic is shown in fig. 1. Assume that a (t=0) trigger is initiated (in part) by a 25 GeV photon which enters a particular tower at a position (say) 10 mm to the left of the wire array. Its ionization signal therefore arrives at t=500 ns and the photoinjected signal at t=750 ns. A second (say t=550 ns) trigger initiated (in part) by a 50 GeV photon which hits the same tower at a position (say) 3 mm to the right of the wires causes an ambiguity because its ionization signal arrives at t=700 ns, before the first event is entirely collected. The photoinjected scintillation signal arrives at t=1300 ns, after 750 ns drift. The pulse at t=750 ns is identified as the scintillation signal due to the first trigger and it tags the iso-amplitude pulse at t=500 ns as the corresponding ionization signal. Similarly, the pulse at 1300 ns is identified as the scintillation signal due to the second trigger and identifies the iso-amplitude pulse at t=700 ns as the corresponding ionization signal. In a real detector, the ionization and scintillation signals will not be necessarily of equal amplitude but are proportional hence the preceeding argument remains valid. Left-right ambiguities are

resolved from the amplitudes of the fast tower signals which are proportional to the solid angle subtended by the source hence distiguish left from right.

At LHC the beam crossing time will be 15 ns with ≈18 interactions per beam crossing [at high luminosity ($2 \cdot 10^{34}/cm^2 \cdot s$)] and about 10 high energy photons (E ≥ 25 GeV) per interaction. Integrating this rate over 50 beam crossings (750 ns) leads to a pileup of 9000 such events during one calorimeter driftout time. A spherical calorimeter with 1 m inner radius and 900 mm^2 cell area will have about 14 thousand towers hence a tower occupancy 0.64 (high energy photons per 750 ns) assuming an isotropic photon distribution. This is only an order of magnitude estimation but amplitude tagging can cope with this occupancy and probably to a level five times higher. In the above example (occupancy 2) the signals can be correctly identified unless the two showers have identical energies.

A minimum ionizing hadron loses only 30 MeV in traversing a cell hence 420 MeV per tower. A fast scintillation threshold of 10 GeV would require at least 20 hadrons per tower which seems improbable. Further discrimination is possible through the depth profile of an e.m. shower.

2.1 THE EXPECTED PERFORMANCE

A Monte Carlo simulation of a shower (GEANT 3.14), z integrated over a cell depth, shows extremely fine (x_i, y_i) distributions (especially in the first three or four cells). The energy centroid gives a precise determination of the shower position and many such determinations, in depth, give a precise determination of the vector direction of the shower.

A spherically symmetric calorimeter was assumed with a 1 m inner radius and radial normals. From simulated data (EGS4) the directional resolution σ_θ for (25, 10, 1) GeV electrons was calculated from the energy weighted centroid points (x_i, y_i) at depth z_i, weights $(\sigma_{xi}, \sigma_{yi})$ were obtained from the width of these distributions. Directional errors σ_θ of (0.9, 1.4, 12.4) mr, respectively were found. The projected position coordinate ρ (at the interaction point) was found with errors σ_ρ of (1.0, 1.5, 12.8) mm, respectively. The error along the beam axis $\sigma_z = \sigma_\rho / \sin\theta$ is good enough to resolve multiple interaction vertices if the photon energy E ≥ 25 GeV and the polar angle $\theta \geq 19^0$ (i.e. $\sigma_z \leq 3$ mm for $\eta \leq 1.8$). Since the photons of interest in Higg's searches are almost always greater than 25 GeV the only limitation will be in the rapidity range. This feature of the calorimeter can reduce the $H \text{---} \gamma + \gamma$ combinatorial background by several orders of magnitude at LHC where high luminosity operation will produce about 18 interactions per crossing in a ≈200 mm length (i.e. ≈10 mm vertex spacing). The position errors σ_ρ' at the inner face of the calorimeter are (50, 90, 640) μm, respectively.

The energy resolution of this calorimeter will be of the form $\sigma_E/E = aE^{1/2} + b$ with a ≤ 0.5% because detection of both ionization and scintillation will allow supression of Landau-like fluctuations (probably due to the highly ionizing δ-rays of the shower). The constant term is

estimated as b ≈ (0.2-0.3)% due to calorimeter leakage. The smallness of (a, b) will permit excellent resolution at both high and low energies.

It is believed that the combination of unexcelled energy and angular resolution with the asociated vertex finding capability of this device will be of decisive value for Higg's searches and other new physics at LHC. In addition, the two-gamma shower separation capability of ≤ 1 mm will allow excellent off-line π^0 rejection.

3. EXPERIMENTAL RESULTS

3.1 SCINTILLATION DETECTORS

Two different in-situ photosensors have been developed and/or tested and shown to be viable. They are a reflective CsI photocathode and a Silicon strip photodiode.

3.1.1 THE CsI REFLECTIVE PHOTOCATHODE.

A CsI reflective photocathode has been made by vacuum deposition onto a stainless steel substrate. After rinsing the film (by flow of pure methane gas over the surface) the reflective quantum efficiency was measured as shown in fig. 2. A quantum efficiency of 32% has been attained at the Xenon scintillation wavelength of 175 nm.

3.1.2 THE SILICON STRIP PHOTON DETECTOR.

The quantum efficiency of a large area (6 x 3) cm^2, high resistivity Silicon strip detector (DELPHI) has been measured as a function of photon wavelength λ, in collaboration with P. Weilhammer of CERN. The UV quantum efficiency (fig. 2) is extremely high in the UV region (≥ 100%) even including the reflection and absorption losses. This indicates that collection is efficient and more than one electron per photon is produced.

3.2 THE PULSED 100KV ELECTRON ACCELERATOR.

A pulsed 100 kV electron accelerator is the source of excitation energy injected into the liquid Xenon. A light beam from a hydrogen flash lamp (FWHM=15ns) is focused onto a CsI vacuum reflective photocathode to produce the photoelectrons which are subsequently accelerated. This device can deliver as little as 1 MeV (400 electrons each with 2.5 keV) or as much as 1 TeV (10^7 electrons each with 100 keV) of excitation energy per pulse into the liquid, permitting investigation of scintillation and ionization over a wide range of total energy and specific ionization. Low energy behaviour is of interest even for high energy calorimetry because δ rays are continuously produced and because a large fraction of the shower energy is eventually degraded into low energy electrons and photons.

3.3. CRYOSTAT, CONDENSER AND CLEANER

A cryostat, condenser and cleaning system was built without high-vacuum specifications (i.e. a stainless steel vessel pumpable to high vacuum with bakeout at 300 ^{0}C) using materiels which make construction of the calorimeter practical but with enough cleaning power to remove impurities by continuous closed gas circulation. It contains Ceramics, Boron Nitride, Viton O rings, metals (all cleaned and degassed before assembly) and a circulation pump with a neoprene diaphragm. The gas

which evaporates from the test cell (due to the heat load) is forced by the circulation pump through an oxisorb cartridge and molecular sieves (13X and 4A at -80 ^{0}C) and then recondensed in a heat exchanger, cooled to the desired temperature by feedback controlled flow of liquid nitrogen.

Xenon gas (Carbagas N45) was initially injected and liquid was condensed. Electron drift was rapidly observed with a lifetime (τ=100 ns) which increased to (τ=4 μs) after 5 days of circulation and cleaning.

Improved lifetime was obtained by injecting Xenon gas (of USSR origin) which had been precleaned (to τ =160 μs) with high vacuum technology by D.Schinzel and A.Gonidec of CERN. The initial electron lifetime was low (due to contamination in transfer) but increased to (τ $\approx$100 μs) after 5 days of circulation and cleaning.

These data show that a calorimeter can be constructed of Ceramics, Boron Nitride, Viton O rings, rubber and metals without high vacuum technology. To obtain the required long lifetime it suffices to inject pure gas followed by continuous circulatation and purification through filters.

3.4 XENON LIQUID SCINTILLATION

3.4.1 LIFETIME

First observation of the scintillation with a vacuum photomultiplier (PM) showed a 20 ns pulse width (lamp pulse width=15 ns hence the quadrature difference=13 ns). No recombination tails were observed.

3.4.2 YIELD AND LIQUID TRANSPARENCY

The scintillation yield of $3 \cdot 10^4$ photons/MeV was measured. The energy required to produce one photon is, therefore, 33 eV about twice as large as the ionization energy of W=15.6 eV. The liquid transparency was measured and an absorption length $\geq$10 cm was found, hence light collection in the unit cell (3x3) cm^2 will not be limited by absorption.

3.4.3 ENERGY RESOLUTION

A linear PM response was observed versus total deposited energy. The energy resolution σ_E/E was limited by the photoelectron statistics $1/\sqrt{N_{pe}}$. The small solid angle of the PM was imposed by the cell geometry however future detectors (CsI or Silicon strip) will not be so limited. Even so, the resolution scaled correctly and was 1.5% at 20 GeV/c.

3.5 XENON LIQUID: IONIZATION AND SCINTILLATION

These measurements were made in a Xenon cell with a Silicon photodiode replacing the PM and a drift gap to collect the ionization electrons. The ionization and the scintillation signals were measured as a function of the electric field, for a fixed incident energy of 9 GeV/c. The ionization (I) increased and the scintillation (S) decreased with electric field, as expected, if an anticorrelation mechanism is operative. The scatter plot (fig. 3) of the ionization versus scintillation clearly shows the anticorrelation. Improvement in energy resolution will be obtained by using the specific linear combination of the signals (I+αS) which projects the points onto an axis perpindicular to this anticorrelation line.

3.6 XENON LIQUID: IONIZATION

3.6.1 CHARGE COLLECTION EFFICIENCY AND FREE ELECTRON YIELD

An ionization drift gap only was mounted in the Xenon cell and the charge Q was observed versus the electric field E_d (fig. 4) for electron beams of (15, 37, 67) keV with total energy of (0.64, 1.97, 4.02) GeV. The data are fit to the formula $Q=Q_0 \ln(1+\xi)/\xi$ where $\xi=K/v=(K/\mu)/E_d$. Fit values are K/μ=(3.8, 2.9, 2.1) kV/cm and Q_0=(1.74, 4.51, 8.93)$\cdot 10^7$e, respectively. The corresponding W values are (37, 44, 45)eV/e, which are considerably larger than the min. ion. value of 15.6 eV/e. The fit values of K/μ imply that drift fields of (95, 72, 53) kV/cm respectively, are required to collect 98% of the charge. Methane doping increases the drift velocity by a factor 7 and decreases the field needed by the same factor. This points out a basic problem of liquid Xenon ionization detectors related to the (1-100 keV) δ rays : 1) the W value is ($\approx$3 times) larger than for min. ion. and 2) a large electric field is needed to collect the charge. Simultaneous detection of scintillation may compensate for these fluctuations.

This increased W value for δ ray energies is probably intrinsic for high density Xenon, but perhaps not for lower density Krypton. An approximately normal value (W=27 eV) was measured for liquid Argon.

3.6.2 ENERGY RESOLUTION

The energy resolution from ionization was also measured as shown in fig. 5. The variation of the incident energy was effected by changing the incident electron energy (2.5 to 84) keV with the corresponding total energy deposit going from 250 MeV to 8.6 GeV. The observed energy resolution (fig. 5) is fit to the form $\sigma_E/E=aE^{1/2}+b$ with a=0.3% and b=1.1%. The constant term is thought to be due to as yet uncontrolled fluctuations in the electron beam flux. In several runs, under the best conditions, a high energy resolution of 0.8% was attained. This allready excellent result was obtained from ionization of (2.5 to 84) keV electrons which suffer most from recombination fluctuations and low free electron yield. It will indeed be surprising if the correlated scintillation measurement does not improve on this result.

[1] J.Seguinot, J.Tocqueville and T.Ypsilantis. College de France, Paris, France. M.Bosteels, A.Gougas, G.Passardi, J.Tischhauser and A.Zichichi. CERN, Geneva, Switzerland. Y.Giomataris, World Laboratory, Lausanne, Switzerland.

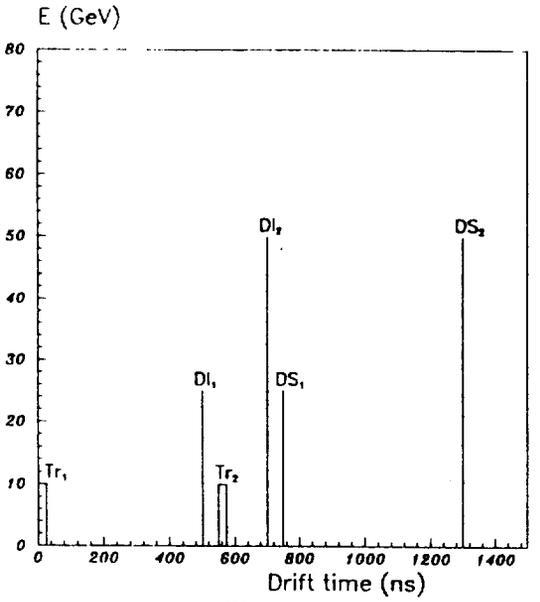


Fig. 1

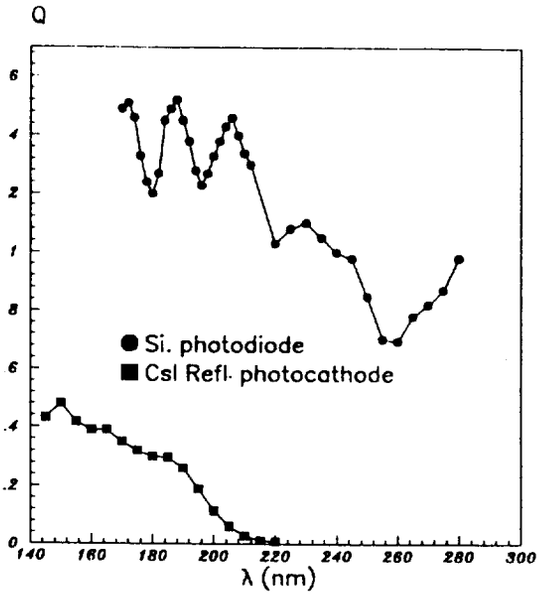


Fig. 2

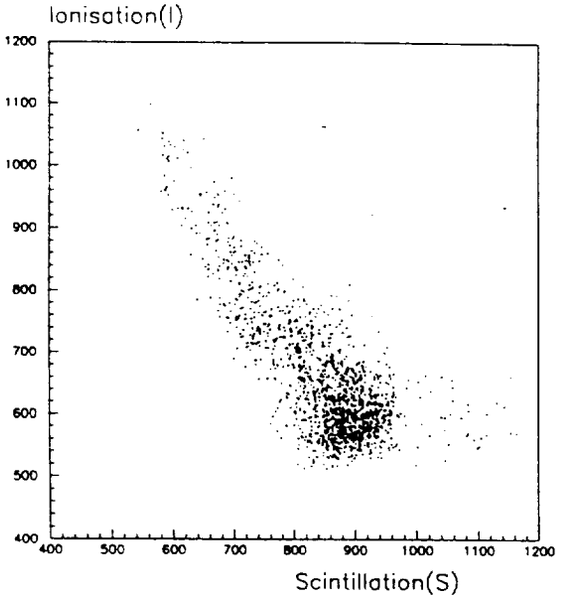


Fig. 3

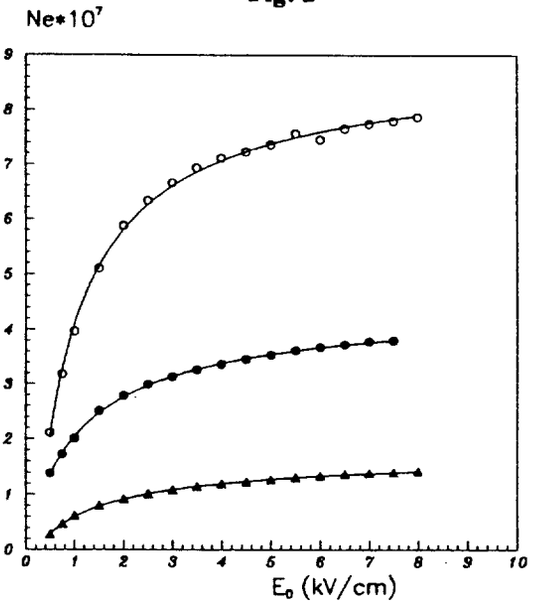


Fig. 4

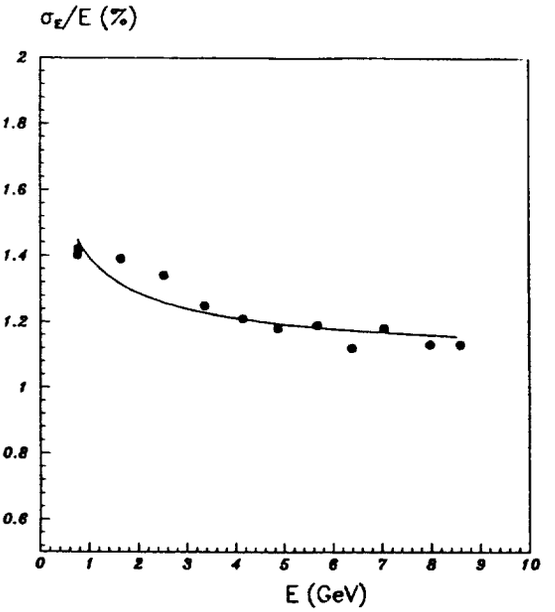


Fig. 5

Electron Detection in LHC Calorimeters

Jean Paul Repellin
L.A.L. Orsay

1. Introduction.

Many physics studies presented at this workshop have stressed the prime importance of lepton detection at LHC as a signature of the production of new heavy particles and of dynamic studies involving W and Z leptonic decays [1].

This report sumarizes a study of a simulation of some properties of the electron detection which can be expected in LHC calorimeters.

The following points are considered :

- Electron and photon trigger
- shower position and electron identification

The performances of a calorimeter on these points are studied as a function of

- calorimeter segmentation
- event pile up noise and calorimeter speed
- thermal noise (example of a liquid argon calorimeter).

2. Simulation frame work.

The energy response to electrons, jets and minimum bias of a simplified calorimeter are used. This response has been obtained with a GEANT simulation [2]. The calorimeter model is a cylinder of 1 m internal radius and covering $\pm$ 3 units of rapidity.

It is segmented in towers of transverse dimensions $\Delta\phi = 0.021$, $\Delta\eta = 0.02$. The towers are pointing to the mean interaction vertex and are segmented into an electromagnetic part 25 radiation length deep followed by a hadronic part of 8 interaction lengths.

This calorimeter model is made of homogeneous active lead with a density scaled by one half. This extreme simplification dictated by computing time limitations is a good approximation for this study as well as for others using the same simulated data. The most critical points relevant to the study reported here are the correct simulation of

- the transverse extension of the electromagnetic showers. The lead density factor was chosen to reproduce the transverse profile of showers in a realistic calorimeter made of lead sheet absorbers and liquid argon active medium.
- the longitudinal extension of hadronic showers. It was checked that the distribution of the electromagnetic to hadronic response simulated for 50 GeV jets is in fair agreement with other GEANT detailed simulations of jets.

The GEANT program version used is 3.13 with 1 MeV cut off values. Some simulations have also been made with higher cut off values of 100 MeV to speed up the generation of jets by a factor of 5. Comparison will be given later.

The following events have been simulated :

- electrons with a fixed transverse momentum of 20 GeV and randomly distributed over ± 2 units of rapidity (300 events, low cut off)
- two jet events generated with Pythia at a central rapidity of ± 0.05 and with p_T larger than 20 GeV (1900 events, low and high cut off) and p_T larger than 50 GeV (4000 events high cut off)
- Pythia minimum bias events which are used to simulate the pile-up (low cut off).

The energy deposition simulated in all the cells is smeared by $10\% /\sqrt{E} \times 1\%$ when originating from electromagnetic showers and $50\%/\sqrt{E} \times 2\%$ when originating from hadronic showers.

The effect of pile up in a fast response calorimeter at a luminosity of 2×10^{34} cm^{-1} s^{-1} is simulated by adding the contributions of an average number of 19 minimum bias events.

The pile-up in a slow calorimeter is also studied with the example of a liquid argon calorimeter with the time response shown in Fig. 1. A peaking time of about 50 ns has been chosen as a reasonable guess of how fast a liquid argon calorimeter could be.

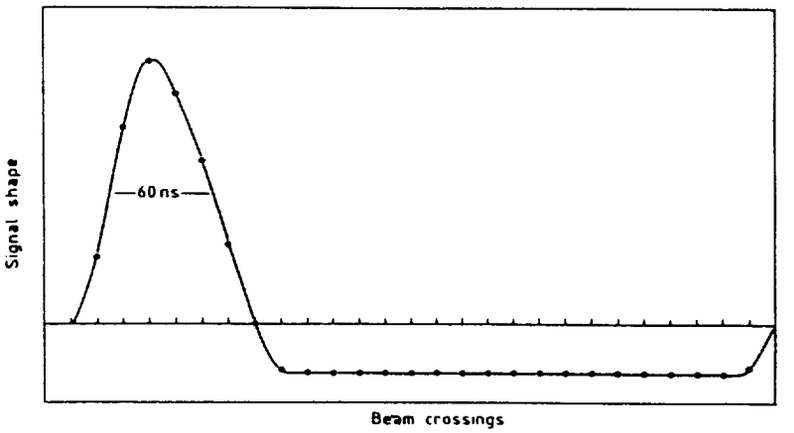


Fig. 1 Bipolar response of the liquid argon calorimeter

The energy spectrum deposited by pile-up at 10^{34} cm^{-2} s^{-1} over an area $\Delta\phi$ $\Delta\eta$ of 0.21 x 0.20 is shown in Fig. 2a) for the fast calorimeter and 2b) for the liquid argon calorimeter.

The effect of the thermal noise of a liquid argon calorimeter with such a short shaping time is also included. Typical r.m.s.values of 70 MeV and 140 MeV are used for the electromagnetic and hadronic individual towers.

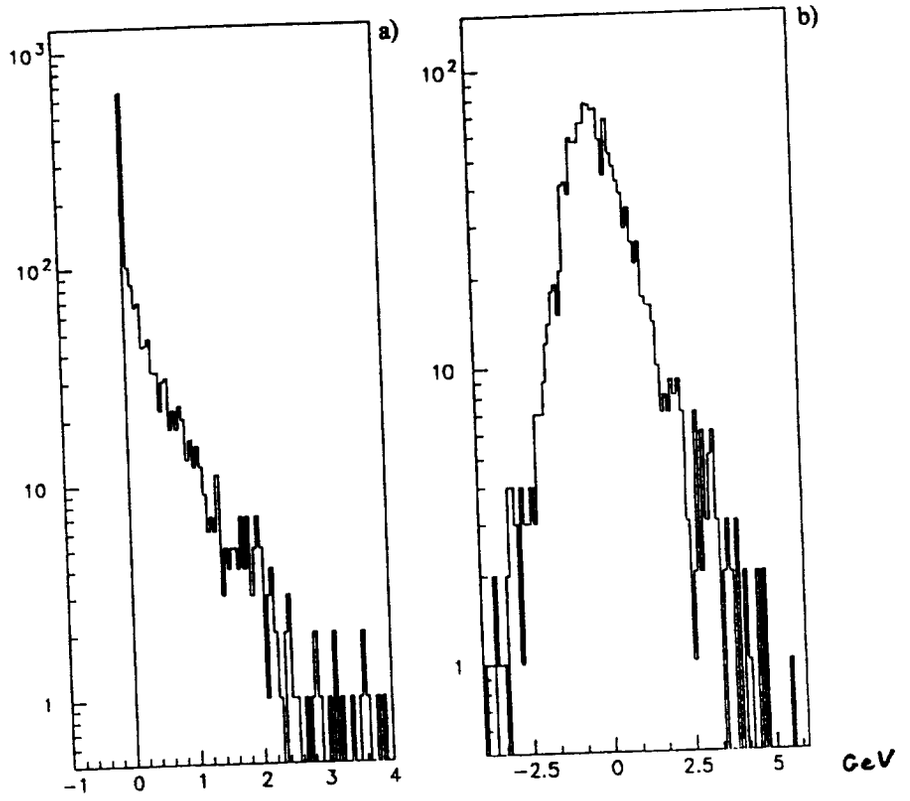


Fig. 2 Energy pile-up in 0.21 x 0.20 towers at 10^{34} cm^{-2} s^{-1} luminosity

3. Electron and photon trigger.

The electron or photon trigger considered here is done in the usual three steps.

The first is to require a minimum transverse energy E_T deposited in the electromagnetic part of the calorimeter over a chosen $\Delta\phi$ $\Delta\eta$ area containing the core of electromagnetic showers.

The second step is to veto this first step threshold trigger when there is a large energy leakage observed in the hadronic compartment behind the trigger cell over a larger area : typically 4 x $\Delta\phi$ $\Delta\eta$.

The third step completes the previous condition into an isolation criteria by requiring that the energy deposited in the electromagnetic calorimeter cells surrounding the triggering cells is less than a fixed value. This isolation applies to a core size of typically 4 x $\Delta\phi$ $\Delta\eta$.

Most of the energy of a single electromagnetic shower is collected over an area of 3 x 3 unit cells in the calorimeter model used in this study (6 x 6.3 cm).

Starting from this minimal collection area three different segmentations are considered and summarised in Table 1 (column 1 and 2).

Table 1

Segmentation	em	had	trigger	had leakage isolation
Fine	.021x.02	.063x.06	.063x.06	.19x.18
medium	.042x.04	.084x.08	.084x.08	.17x.16
coarse	.063x.06	.13x.12	.13x.12	.25x.24

The trigger column gives the area over which the energy is collected. For the fine segmentation the nonet of individual cells (size 0.02^2) is centred on the cell with the maximum electromagnetic energy. For the medium and coarse segmentation the quartet of individual cells (size ~ 0.04^2 and ~ 0.06^2) with the maximum local electromagnetic energy is chosen.

The last colum indicates the size over which the hadron leakage and the energy isolation criteria are applied. For simplicity the same size is assumed for both.

The rejection against 20 and 50 GeV p_T jets is measured with the three calorimeter segmentations described above. The corresponding transverse energy thresholds are fixed at 20 and 50 GeV respectively.

The hadron leakage and isolation cuts are chosen such that the loss of efficiency for 20 GeV p_T electrons does not exceed 5% for the fast calorimeter and 10% for the liquid argon calorimeter. These inefficiencies include the effect of pile-up from Pythia minimum bias events at a luminosity of 2×10^{34} cm^{-2} s^{-1}.

The cuts chosen here, for hadron leakage and isolation respectively, are given below in GeV for the three segmentations :

1.5 /7.0 1.5/5.0 2.0/5.0 for the fast calorimeter

3.5/7.0 3.0/5.0 5.0/5.0 for the liquid argon calorimeter.

The rise of the hadron leakage cut beween fast and slow calorimerter is mostly due to the effect of the thermal noise. The hadronic part of a liquid argon calorimeter could possibly be segmented in depth and the effectivness of the hadron leakage cut could then be improved.

The larger value of the isolation cut in the fine segmented calorimeter allows for the small fraction of the electron energy which spills outside of the trigger cell, mostly in the rapidity direction. This widening in the rapidity direction results from the fact that the towers are pointing on the centre of the apparatus and not on the event vertex distributed along the beam.

The results of the trigger simulation are summarized in Figs. 3 and 4. Figure 3a) gives the inefficiency to 20 GeV p_T electrons and Fig. 3b) gives the efficiency to trigger on 20 GeV p_T jets, both for the fast calorimeter. Figure 4a and 4b give the equivalent results for the liquid argon calorimeter.

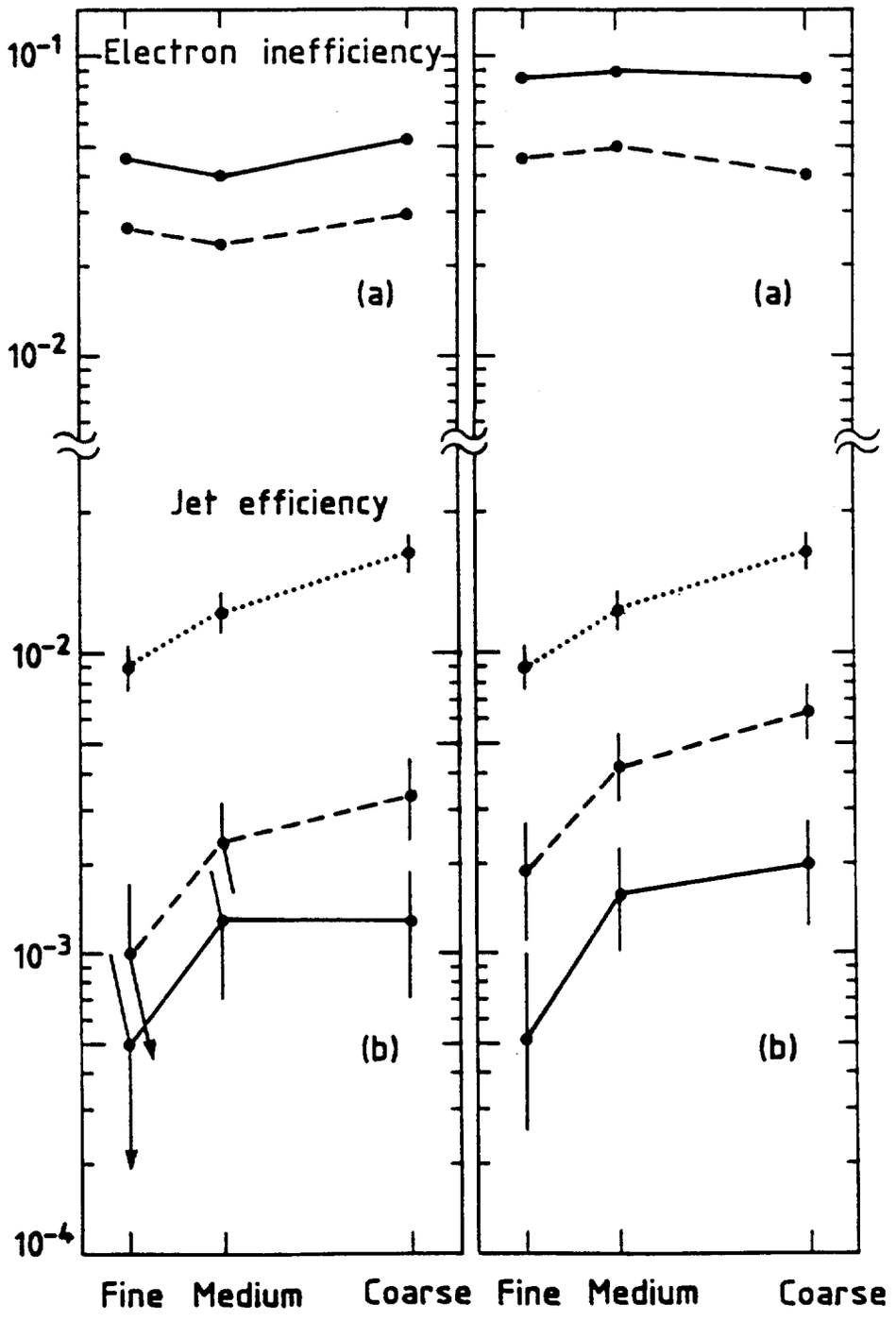


Fig. 3 Fig. 4

Electromagnetic triggers for 3 calorimeter segmentations

The dotted curves indicate that rejection factors of 50 to 100 can be achieved with the energy trigger depending on the segmentation (about linearly with $\sqrt{(\Delta\phi \cdot \Delta\eta)^{-1}}$. Note here, that to measure the jet rejection, no pile-up of minimum bias events are added. Including the pile-up would have some effect on the threshold trigger since the probability to deposit more than 1 GeV in a trigger cell of 0.20^2 is about 11% for a fast calorimeter and about 16% for a slow calorimeter (see Fig. 2) at a luminosity of 10^{34} $cm^{-2}s^{-1}$. Further studies are necessary to evaluate the size of this effect on the threshold and isolation triggers.

The dashed curves show the electron inefficiency and the jet acceptance resulting from the hadron leakage cut. The full curves show the final result including the energy isolation requirements.

The full rejection against jets is seen to range from 500 to 2000 depending on the segmentation, similar for the fast and the slow calorimeter, but at the price of a worsening of a factor of 2 in the electron inefficiency for the slow calorimeter.

The rejection variation as a function of the segmentation is rather weak, besides the statistics are very poor since only a few events survive the combined cuts, even if they originate from the same simulation sample. Further work is neccessary to study the nature of the events surviving in the medium segmentation selection and failing in the fine one. The fine segmentation approaches the photon separation coming from a 20 GeV p_T π^0.

Very similar results are observed for 50 GeV jets simulated with the high cut offs. They confirm with twice the statistics of the 20 GeV jets the improvment of about a factor of 4 in the rejection obtained when going from the coarse to the fine segmentation.

A comparison with the GEANT simulation made at 20 GeV with high cut offs indicates a small variation of the jet rejection (at most a factor 2 worse for the coarse segmentation after isolation).

The dependence of the results on the jet fragmentation and on the calorimeter modelling has not been studied..

4. Shower position measurement.

Electromagnetic showers have a typical transverse radius of 2 radiation lengths and the use of the energy profile in a segmented calorimeter provides a measurement of the shower position. Here a crude calculation of the centre of gravity of the energy simulated in a nonet of cells is used to determine the shower position. An ad hoc correction is used to suppress the non-linearity induced by the energy profile segmentation.

The purpose of this study is to compare the resolution of the position measurement for two segmentations of the electromagnetic calorimeter (cell sizes 2.1 x 2.0 mm^2 and 4.2 x 4.0 mm^2) and to estimate the degradation which results from pile-up at luminosities of 2 x 10^{34} cm^{-2} s^{-1} in the fast and the liquid argon calorimeters as simulated in section 2.

The effect of the thermal noise of the latter is also evaluated. Three examples of the distributions of the distance Δt between the reconstructed shower position and the extrapolated electron trajectory in the Rϕ plane are shown in Fig. 5 for the calorimeter with the 4.2 x 4.0 mm^2 granularity. The mean shower position in depth is assumed to be 6 cm on average from the front face of the calorimeter.

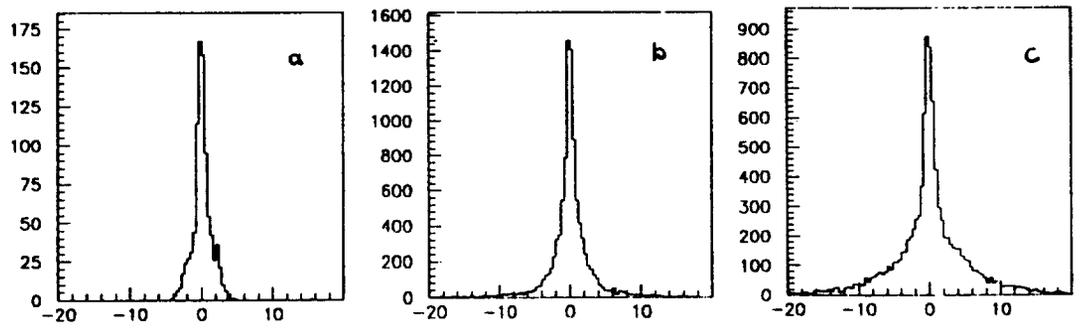


Fig. 5 Transverse position measurements in mm

At the level of the simulation, the Δt distribution is close to a gaussian (Fig. 5a). When the pile-up is superimposed, this gaussian sits on a larger distribution which results from the finite probability of an accidental energy deposition in the cell nonet. Figures 5b) and 5c) correspond to the fast and the slow calorimeter respectively.

The results are summarized in Table 2 for the r.m.s. of the distributions in mm, σ_t is the r.m.s. of the Δt distribution and σ_z is the r.m.s. of the distribution along the rapidity axis.

Table 2

$\Delta\phi$ $\Delta\eta$	0.021x0.20		0.042x0.040	
	σ_t	σ_z	σ_t	σ_z
GEANT	0.6	1.2	1.2	2.3
Thermal noise Liq. Arg.	0.7	1.2	2.5	3.0
Pile-up fast	0.7	1.25	2.9	3.4
Pile-up + noise Liq. Arg.	0.9	1.35	4.3	4.6

The value of 0.6 mm found for σ_t with the fine segmentation can be compared to real measurements. For example a resolution of 0.4 mm with 100 GeV electrons has been obtained in a test of a new liquid argon calorimeter presented at this workshop [3]. In any case the more important question addressed in this report is the degradation of the position measurement and not so much its abssolute value.

In Table 2 it appears that σ_z is larger than σ_t. This results from the distribution of the vertex along the beam direction approximated with a gaussian of 5.5 cm r.m.s., and from the fluctuations of the shower development in depth.

The fine segmentation clearly gives a better measurement, and since the measurement involves an area which is 4 times smaller, it is much less sensitive to pile-up than the medium segmentation.

In a detector with no central magnetic field a precise measurement of the shower position is particularly effective in the electron identification by the requirement of its matching with the track measured in a tracking device. The matching suppresses the background resulting from the accidental presence of a low energy charged particle in front of the cells hit by a high energy π^0 (overlap background).

The overlap background scales nearly like D^2, the square area of the matching distance cut, D. Figure 6 shows the inefficiency of an electron signature as a function of the cut on the distance D, Figs. 6a) and 6b) correspond to the fine and medium segmentations. The 4 curves are labelled according to the following conditions 1 isolated electron, 2 isolated electron with the liquid argon calorimeter (thermal noise), 3 pile-up in the fast calorimeter, 4 pile-up in the liquid argon calorimeter.

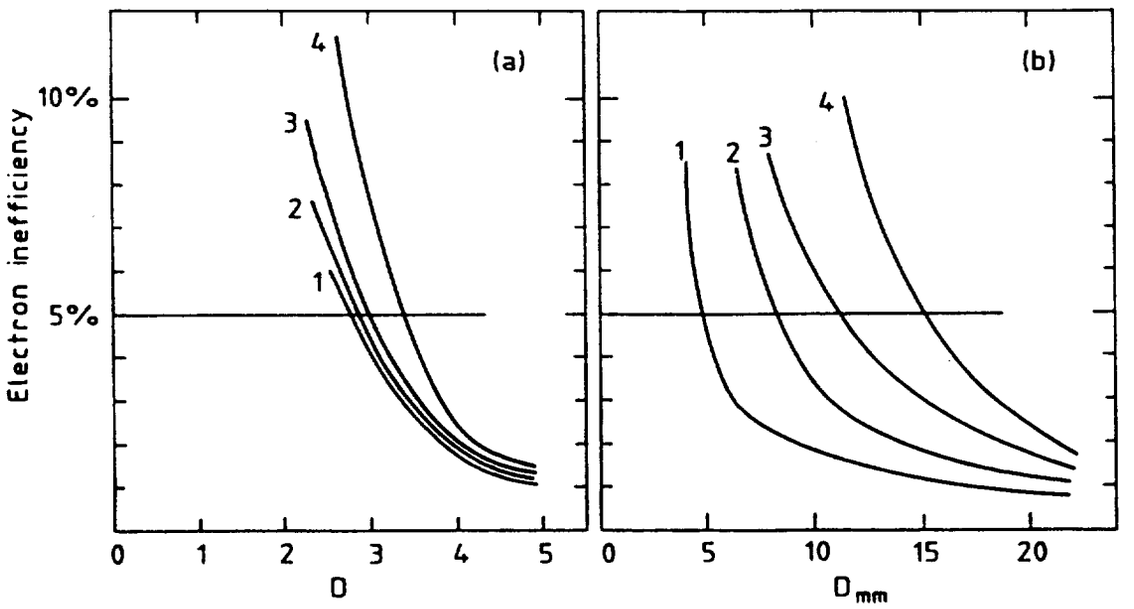


Fig. 6 Loss of electron efficiency as a function of the track calorimeter matching

These curves confirm the better performance of the fine segmentation. A cut at 4 mm loses only about 3% of the electrons, while the cut must be increased to 15 or 20 mm for the medium segmentation, namely an increase of a factor of about 20 of the overlap background. One should remember that preshower detectors can achieve better performances [4].

5. Conclusions.

A barrel calorimeter with a granularity better than 0.06 (0.12) radians in azimuth and 0.06 (0.12) units in rapidity for its electromagnetic (hadronic) part can provide an adequate electron trigger at LHC. If it can be achieved, a finer granularity (of a factor 2 to 3 in the cell sizes) can provide an improvment of the same order of magnitude on the jet rejection especially at luminosities of 2×10^{34} cm^{-2} s^{-1}.

If a further electron identification requires the measurement of the position of the electromagnetic shower in the calorimeter, then the fine granularity is necessary at high luminosity.

REFERENCES

[1] D. Denegri Standard Model Physics Working Group, Vol. 1.these proceedings.

F. Pauss .Beyond Standard Model Physics Working Group, Vol. 1 these proceedings.

[2] Simulation done by D. Froidevaux and G. Unal.

[3] D. Fournier Liquid Argon Calorimetry Working Group, Vol. 3 these proceedings.

[4] A. Weidberg Electron identification Working Group, Vol. 3 these proceedings.

Electron and Photon Identification with a Barium Fluoride Electromagnetic Calorimeter

Ren-yuan Zhu[1]
Lauritsen Laboratory
California Institute of Technology
Pasadena, CA 91125

1 Introduction

It has been recognized recently that a precision measurement of electrons and photons at the LHC/SSC is extremely important for searching rare and unexpected phenomena [1]. In order to use the potential of these machine effectively, however, it is necessary to separate out the electron and photon signals from a background of ~60 MHz hadronic events. For this reason, an electromagnetic calorimeter designed for an LHC/SSC experiment has to meet the following criteria:

- Good radiation resistance to survive in a high radiation environment. Ideally, long term shifts should be 10% or less per year, at a particle flux of $10^{15}/\text{year}/r_\perp^2$ at an average luminosity of $10^{33}/\text{cm}^2/\text{sec}$, where $r_\perp$ is the distance from the beam in cm. This corresponds to doses of up to 10^7 Rads per year at small angles with respect to the beam.
- Fast response time of ~16 nsec or less, to cope with the high interaction rate by allowing the detector to be gated in a single bunch crossing.
- Linear response over a large dynamic range, to allow precision measurements of electrons and photons in a range from a few GeV to a few TeV.
- High granularity, to ensure that electromagnetic particles can be isolated, and precisely constructed, even when they are near to hadronic jets.
- Relatively short radiation length and Moliere radius, to fully contain the longitudinal shower development and to limit the lateral spread of high energy showers. This factor must be combined with good granularity to ensure that particles in jets can be resolved, and that electromagnetic showers can be reconstructed precisely.

[1]Work supported in part by U.S. Department of Energy Contract No.DE-AC03-81-ER40050.

Among all these criteria, the high resolution is very important, as demonstrated in the search of intermediate mass Higgs boson through $H^0 \rightarrow \gamma\gamma$ decay [2,3]. Once the electrons and photons are identified, suppressing the remaining backgrounds from conventional physics depends on the high energy resolution and the good angular resolution of the calorimeter. The experience of L3, as well as the earlier work of the Crystal Ball, CUSB and CLEO, has shown that the highest resolution may be obtained reliably with calorimeters composed of large, single-crystal, inorganic scintillators, which divide the sphere into $\sim 10^3$ to more than 10^4 cells. The L3 BGO calorimeter, for example, has achieved a resolution of $1.3\%/\sqrt{E} + 0.5\%$ [4].

In this report we present Monte Carlo studies on electron and photon identification based upon an electromagnetic calorimeter made by barium fluoride (BaF_2) crystals. A brief description of the BaF_2 detector is given in section 2. Sections 3 presents the ability to distinguish an isolated electron from a single charged hadron. The rejection of a hadron jet in electron or photon identification is discussed in sections 4 and 5.

2 Barium Fluoride Calorimeter

Figure 1 shows the conceptual design of the BaF_2 calorimeter, which includes two parts:

- A central barrel calorimeter with an inner radius of 75 cm and an outer radius of 140 cm, covering a rapidity range of $|\eta| \leq 1.45$ ($26° \leq \theta \leq 154°$).
- Two endcaps, located at z=$\pm$ 150 cm, covering a rapidity range of $1.45 \leq |\eta| \leq 2.87$ ($6.7° \leq \theta \leq 26°$ and $154° \leq \theta \leq 173.3°$).

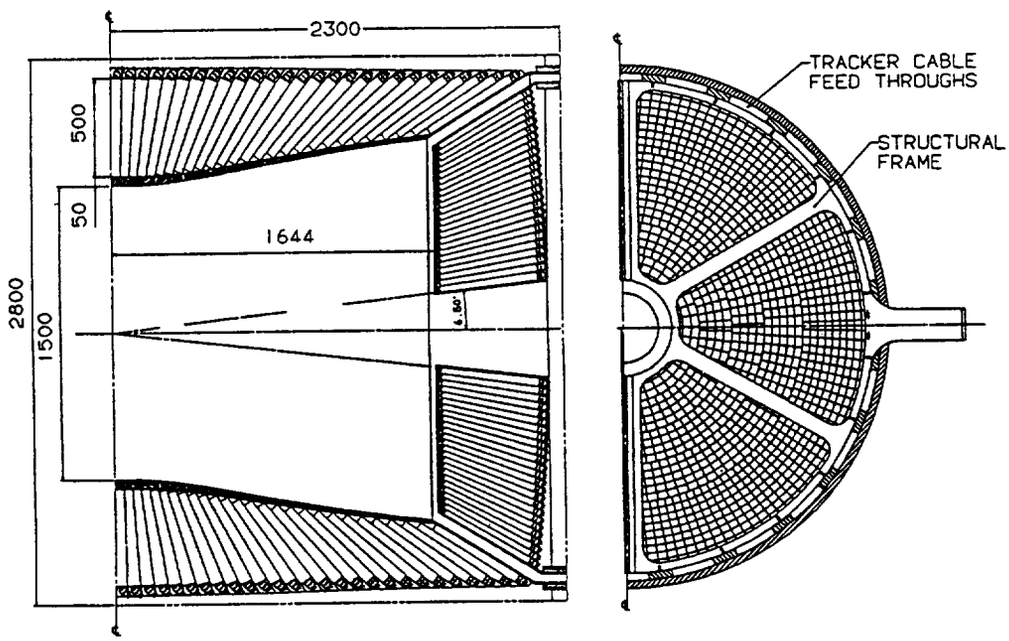


Figure 1: The side and end views of the BaF_2 calorimeter.

Table 1: Features of the BaF_2 Calorimeter.

Barrel ($\mid \eta \mid \leq 1.45$)	
Crystal Front Face (cm^2)	3 × 3
Crystal Rear Face (cm^2)	5 × 5
Crystal Length (cm)	50
Total Crystal Number	10,944
Total Crystal Volume (m^3)	9.9
Total Crystal Weight (Tons)	48.4
Two Endcaps ($1.45 \leq \mid \eta \mid \leq 2.87$)	
Crystal Front Face (cm^2)	2.3 × 2.3
Crystal Rear Face (cm^2)	3.1 × 3.1
Crystal Length (cm)	50
Total Crystals Number	7,100
Total Crystal Volume (m^3)	2.7
Total Crystal Weight (Tons)	13.1

The total crystal volume of the BaF_2 calorimeter is 12.6 m^3, with a total crystal weight of 61.5 tons. Table 1 shows the basic parameters of the BaF_2 calorimeter.

The calorimeter has the following features [5,6]:

- **Speed:** gating time is less than 16 nsec ;
- **Energy Resolution:** $\Delta E/E = (1.3/\sqrt{E} + 0.5)\%$;
- **Position Resolution:** Δx and $\Delta y \approx 1$ mm at the surface of crystals
- **Segmentation:** $\Delta\eta \approx \Delta\phi \approx 0.04$;
- **e/π, γ/jet, and e/jet Separation:** $\sim 10^{-4}$;
- **Radiation Resistance:** $\geq$ 10 MRads.

3 π/e Separation

Because of the high uniformity and fine granularity of the BaF_2 calorimeter, one can use the detailed lateral shower information to distinguish an electron from a charged pion. The ability to match the momentum measured in the central track detector, or the energy measured in the hadron calorimeter, with the energy measured in the electromagnetic calorimeter provides an additional powerful rejection.

The main mechanism of a charged pion faking an electron in the electromagnetic calorimeter is the charge exchange process, which produces an energetic π^0 from an incident charged pion. The charge exchange cross-section, however, decreases with increasing energy. In the energy region relevant to the LHC/SSC, i.e. > 5 GeV, rejection against pions at the level of $\sim 10^4$ may be obtained by using the following cuts:

- Since the shower from a hadron which interacts in the electromagnetic calorimeter tends to spread more laterally than an electron shower, a lateral shower development cut is used to reject hadrons:

$$\frac{\sum_{3\times3} E_{EM}^{cell}}{\sum_{5\times5} E_{EM}^{cell}} > S_{cut} \Rightarrow \textbf{ Reject}$$

where the sum is over the 3×3 and 5×5 group of cells centered on each cell in the electromagnetic calorimeter (EM). S_{cut} is slightly energy dependent, and was determined using a GEANT simulation: S_{cut} = 0.95, 0.96, 0.965 for E_{EM} = 10, 100, and 1000 GeV respectively.

- Matching the energy measured in electromagnetic calorimeter (E_{EM}) and the momentum measured in central tracking detector (P_{trk}):

$$|E_{EM} - P_{trk}| > 3\sigma \Rightarrow \text{ Reject}$$

where

$$\sigma = \sqrt{\sigma_{E_{EM}}^2 + \sigma_{P_{trk}}^2},$$

$$(\sigma_E/E)_{EM} = 1.3\%/\sqrt{E_{EM}} + 0.5\%, \text{ and}$$

$\sigma_{P_{trk}}$ is parameterized as a function of polar angle (θ):

$$\sigma_{P_{trk}}/P_{trk} = \text{ X\% } \sin\theta \; P_{trk} \text{ (in GeV)}$$

with X = 0.13, 0.22, 0.29, and 0.65 for θ in the range of
(26°, 154°), (22°, 26°) or (154°, 158°), (17°, 22°) or (158°, 163°)

- Since the nuclear interaction length of BaF_2 is much longer than its radiation length, a hadron shower penetrates much deeper than an electron shower. A veto on the energy in the hadron calorimeter (HCAL) can be used to reject high energy pions:

$$E_{HCAL} > E_{EM} \times H_{cut} \Rightarrow \textbf{ Reject}$$

where H_{cut} is slightly energy dependent, and was determined using a GEANT simulation: H_{cut} = 0.025, 0.025, 0.040 for E_{EM} = 10, 100, and 1000 GeV respectively.

A GEANT (full shower) simulation was carried out to obtain the π/e rejection ratio as a function of energy. The simulation was done by injecting electrons and pions uniformly at the front surface of the center crystal of a BaF_2 matrix composed with 13 × 13 crystals. A layer of aluminum of 0.12 radiation length thick in front of the BaF_2 array, and the 250 μm thick carbon fiber walls between crystals were

included in the simulation. The energies deposited in each crystal, in the carbon fiber walls between crystals, in the aluminum sheet, and leaking out sideways were recorded. The full resolution of the electromagnetic calorimeter in measuring electromagnetic energy ($1.3\%/\sqrt{E} + 0.5\%$), the resolution of the hadron calorimeter in measuring hadronic energy, and the momentum resolution of the tracker as a function of angle, were taken into account in the simulation. The rejection power of each cut is illustrated in Figures 2, 3 and 4.

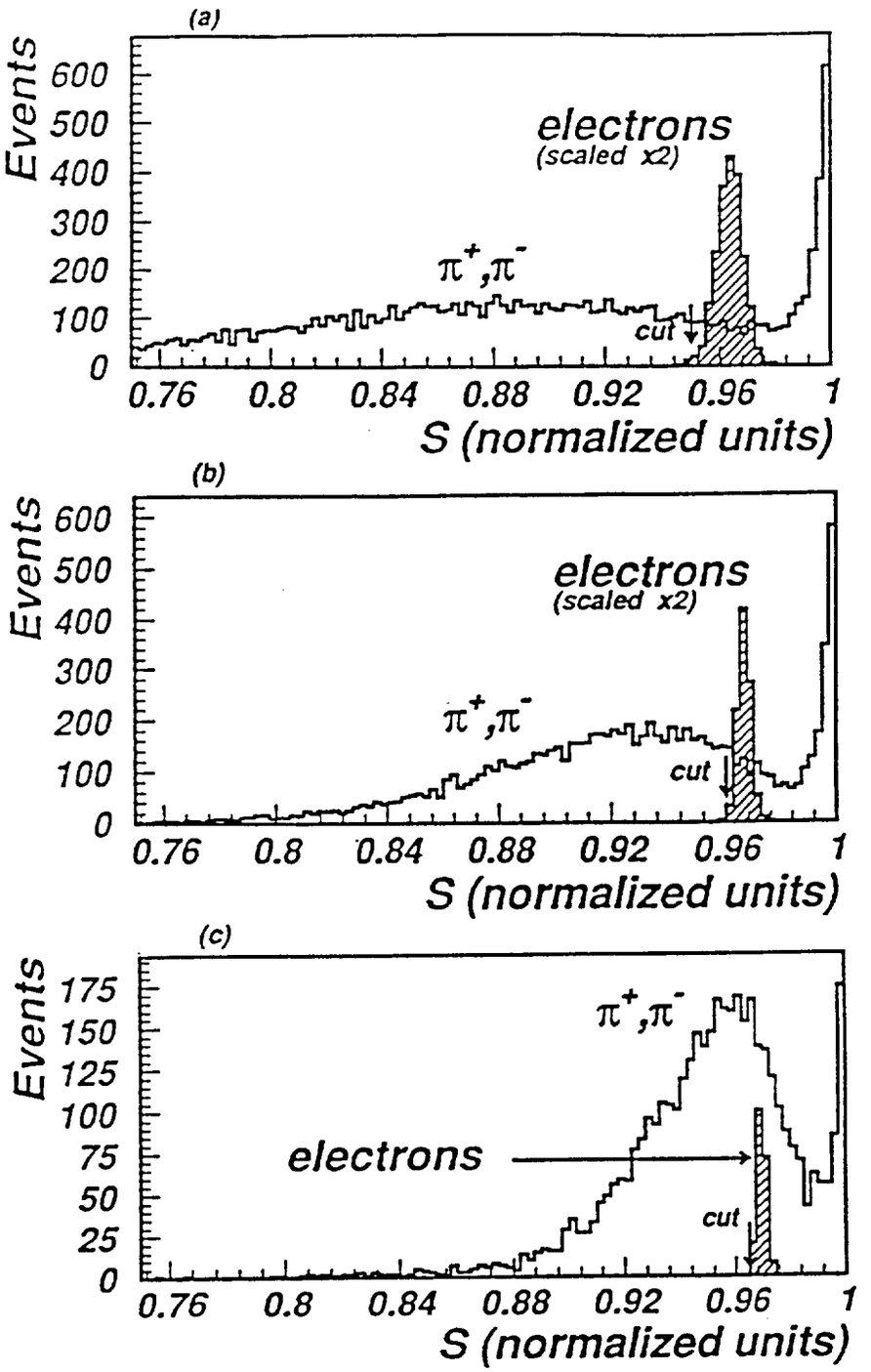


Figure 2: The lateral shower distribution as function of S$\equiv \sum_{3\times3} E_{BaF_2} / \sum_{5\times5} E_{BaF_2}$, for electrons and charged pions at (a) 10 GeV, (b) 100 GeV and (c) 1 TeV.

Figure 2 shows that the rejection power of the cut on $\sum_{3\times3} E_{EM}^{cell} / \sum_{5\times5} E_{EM}^{cell}$ stems from the fact that this ratio is a narrow peak in a high resolution calorimeter coupled with the fact that many of the surviving pions do not interact in the electromagnetic calorimeter.

Figure 3 shows that after the cut on the lateral shower shape, no pions at 10 GeV, and few at 100 GeV, have enough energy deposited in the electromagnetic calorimeter to match the momentum measured in the tracker.

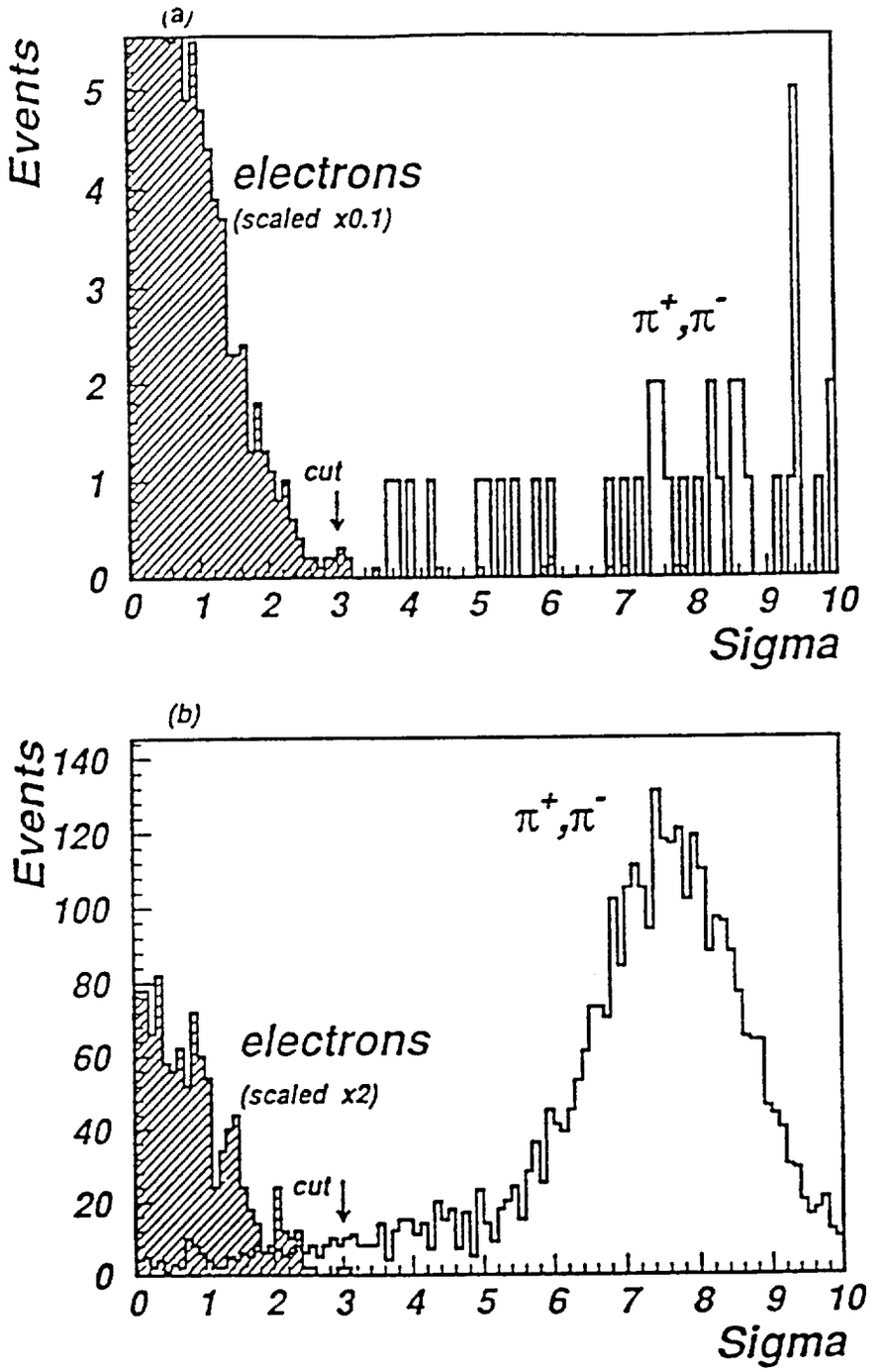


Figure 3: The $|E_{BaF_2} - P_{trk}|$ distribution in units of σ after lateral shower shape cut, for electrons and charged pions at (a) 10 GeV and (b) 100 GeV.

Figure 4 shows that all of the remaining pions (down to the 10^{-4} level deposit a large part of their energy in the hadron calorimeter. The rejection power of the HCAL veto cut (Figure 4) increases with an increasing π energy.

The results of the simulation are summarized in Table 2. As seen in the table, combining a tracker and hadron calorimeter the BaF_2 calorimeter will be able to separate isolated electrons and pions with a rejection of $\sim 10^{-4}$.

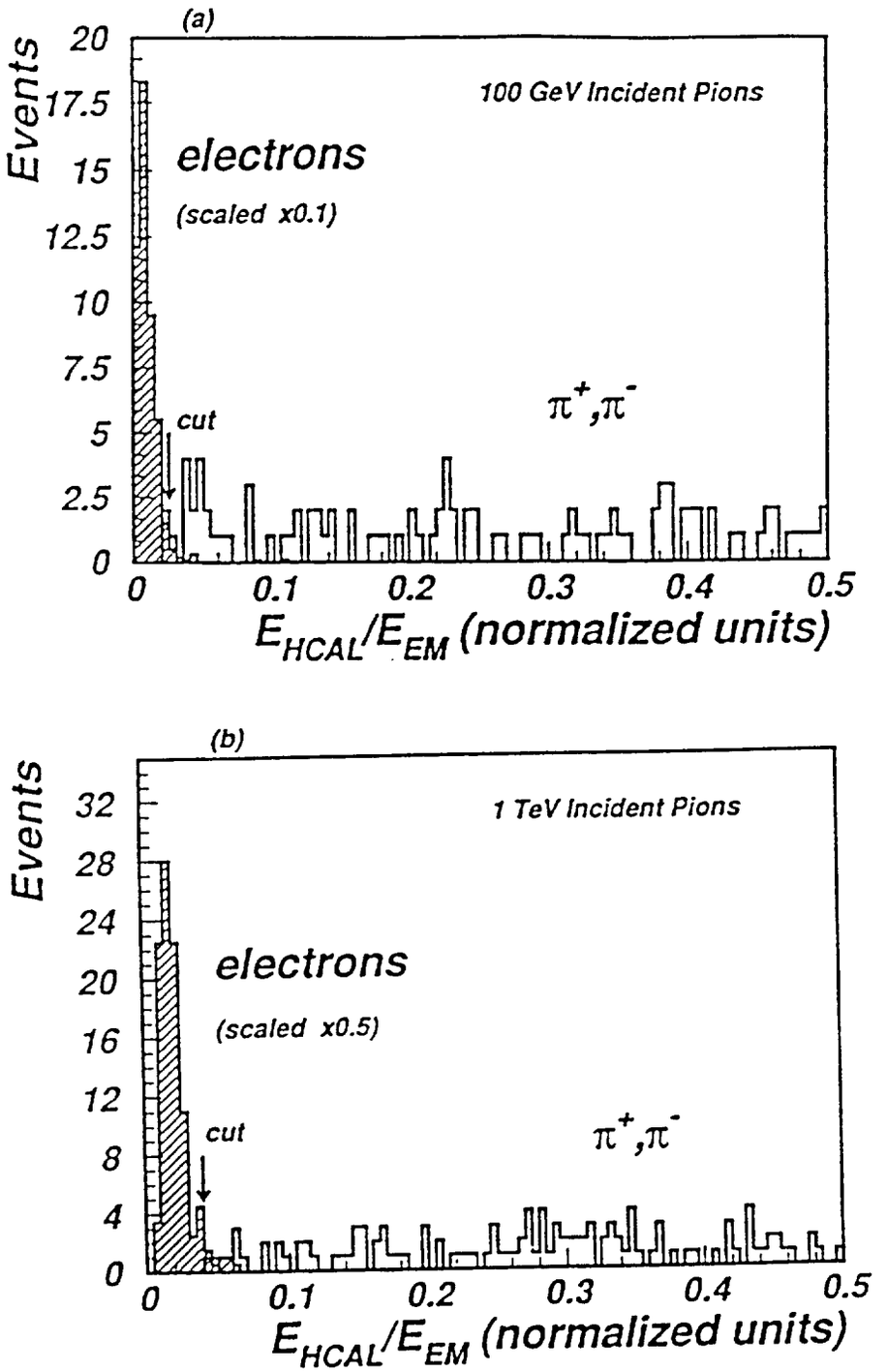


Figure 4: The E_{HCAL}/E_{EM} distribution after the other two cuts, for electrons and charged pions at (a) 100 GeV and (b) 1 TeV. None of the pions survived the first two cuts in our simulations at 10 GeV.

Table 2: π/e Separation of BaF_2 Calorimeter

E (GeV)	10	100	1000
After Lateral Shower Cut:			
π acceptance (10^{-2})	32.6 ± 0.4	34.7 ± 0.5	39.4 ± 0.7
e acceptance (%)	99.3	99.5	99.5
After E_{BaF_2} and P_{trk} match (10° - 90°):			
π acceptance (10^{-3})	< 0.1	12.3 ± 0.9	388 ± 7
e acceptance (%)	97.3	99.2	99.5
After HCAL Veto:			
π acceptance (10^{-4})	< 1	2.0 ± 1.4	< 2.2
e acceptance (%)	97.3	96.4	95.0

4 Jet/Electron Separation

The identification of isolated electrons is important for many physics processes, such as $H^0 \rightarrow e^+e^-e^+e^-+X$, $Z' \rightarrow e^+e^-+X$ and $W' \rightarrow e+X$. A QCD jet, however, may fake an isolated electron because of:

- genuine electrons may be produced by heavy quark decays and π^0 Dalitz decays: $\pi^0 \rightarrow \gamma e^+e^-$;
- charged pions may fake an electron, with the probability calculated in the previous section;
- a photon from π^0 decay and a charged particle may both hit a single calorimeter cell.

Simulation shows that the dominant background which produces a fake 'electron' is from a photon overlapping with a charged particle. To eliminate a jet faking an isolated electron, we employ an isolation cut on the sum of transverse energies in a cone surrounding the candidate electron with R=0.3 ($R=\sqrt{\Delta\eta^2 + \Delta\phi^2}$), and we require that the electron criteria described in the previous section are satisfied.

Following process were used in our analysis to implement the isolation cut:

- Generate QCD 2 jets using the PYTHIA program [7];
- Assume electrons and photons deposit all their energies in BaF_2 calorimeter, and assume that charged hadrons deposit their energy in BaF_2 according to a distribution generated with a GEANT (full shower) simulation.
- Define the sum of the transverse energy in BaF_2 from all particles hitting one cell (ΣE_T) as E_T^{cell};

- Starting with the largest E_T^{cell}, if there is no charged track hitting the cell or more than one charged track hits the 3 × 3 cells centered on this cell, the central cell is rejected;

- Define the sum of E_T^{cell}'s in the 3 × 3 set of cells centered on each cell surviving the above cuts as $E_T^{electron} = \sum_{3\times3Cells} E_T^{cell}$.

- Require that the sum of the transverse energy in a cone of radius R=0.3, excluding all energy in the 3 × 3 matching cells in both BaF_2 and hadron calorimeter, is less than 10% of the $E_T^{electron}$ plus an isolation energy cut (E_T^{cut}):

$$\sum_{R<0.3} E_T - \sum_{3\times3cells} E_T > E_T^{cut} + 0.1E_T^{electron} \Rightarrow Reject,$$

- If a charged pion passed above cuts, we weight it by its probability of faking an electron, i.e. by 2×10^{-4} as shown in the previous section;

- Continue this process for all cells;

- Define the probability (F) of a jet faking an isolated electron as the sum of the weights of all cells passing all above cuts, normalized to the number of jets generated.

Table 3 lists the probability of a jet faking an isolated electron (F) as a function of the electron P_T. It is clear that a 10^{-4} jet/electron rejection ratio may be obtained by using the isolation cut described in this section.

Table 3: Probability (10^{-4}) of a Jet Faking an Isolated Electron

E_T^{cut} (GeV)	5	10	15	20
$E_T^{electron} > 10$ GeV	1	3.8	6.5	9.0
$E_T^{electron} > 20$ GeV	0.25	0.5	1.3	1.5

5 Jet/Photon Separation

There are copious π^0's, and thus photons, produced at the LHC/SSC. A Monte Carlo program PYTHIA is used in our study of jet/photon rejection. Our study includes the effects of leading π^0's which could (in rare cases) produce a jet which fakes an isolated high energy photon. An isolation cut, on the same token as discussed in previous section, is used to reject the jet background.

The following procedure was used in our analysis to implement the isolation cut:

- Generate QCD jets;
- Search through BaF_2 cells to identify all cells hit by photons only. Define the sum of the transverse energy of all photons hitting one cell (ΣE_T^{γ}) as E_T^{cell};
- Starting with the largest E_T^{cell}, if there is a charged track hitting the 3 × 3 cells centered on this cell, the cell is rejected;
- Define the sum of E_T^{cell}'s of these 9 cells ($\sum_{3\times3cells} E_T^{cell}$) as the E_T^{photon}.
- Require that the sum of the transverse energies in a cone of radius R=0.6 (R=$\sqrt{\Delta\eta^2 + \Delta\phi^2}$), excluding the E_T^{photon}, is less than 10% of the E_T^{photon} plus an isolation energy parameter (E_T^{cut}):

$$\sum_{R<0.6} E_T - E_T^{photon} > (E_T^{cut} + 0.1E_T^{photon}) \Rightarrow Reject,$$

- Continue this process for all identified cells which were hit by photons only;
- Define the probability (F) of a jet faking an isolated photon as the number of photons passing all above cuts normalized to the number of jets generated.

Table 4 lists the calculated probabilities of a jet faking an isolated photon (F) with $P_T > 20$ GeV as a function of E_T^{cut}. By using this isolation cut, the rate of a jet faking an isolated photon is reduced to 10−4. Note, a further reduction of the fake photon rate may be obtained if detailed shower shape analysis, as described in section 3, were performed to the photon candidate.

Table 4: Probability of a Jet Faking an Isolated Photon as a Function of E_T^{cut}

E_T^{cut} (GeV)	5	10	15	20
Probability (10^{-4})	1	3	6	10

6 Electron and Photon Trigger

A crucial issue in electron and photon study is to make a Level-1 trigger decision in a ~60 MHz beam crossing enviroment. A Monte Carlo study was carried out to determin an electron photon trigger strategy which will survive physics signal while rejecting the huge QCD background. With a fast calorimeter, such as BaF_2, we assume that the Level-1 trigger decision may be performed for each beam crossing by using coarse tower sums from calorimeters. The goal of the Level-1 trigger is to reduce the rate from ~60 MHz to less than 200 kHz, i.e. a 5 μsec decision.

With ~200 kHz input, the Level-2 trigger will be able to provide finer tower sums from the calorimeters. By using a rough isolation cut, the data rate will be further

reduced to less than 1 kHz. The Level-3 trigger will then apply event selection cuts to the full reconstruct events using digitized data. The informations from the central tracker and other detectors will also be available in this level. A detailed isolation cut, as described in previous sections, will be performed. By using parallel computing techniques, we hope the rate accepted by Level-3 will be reduced to ~10 Hz.

6.1 The Level-1 Trigger

The Level-1 trigger for electrons and photons is based on sums of transverse energies in groups of cells in the electromagnetic calorimeter (EM), with a typical group covering 0.2 × 0.2 in $\Delta\eta \times \Delta\phi$, i.e. 5 by 5 BaF_2 crystals. Each group of EM cells is matched with an overlapping hadron calorimeter 'tower' (a group of HCAL cells) behind it. An HCAL veto, requiring that the sum of the transverse energies measured in the matching HCAL tower is less than 10% of the sum of the transverse energy in the EM cell-group, is used to reject the huge QCD background.

A Monte Carlo simulation was carried out to calculate the Level-1 trigger rate by using PYTHIA program [7]. The response of the electromagnetic calorimeter and hadronic calorimeter was computed for each particle in the jets by assuming:

- electrons and photons deposit all of their energy in the electromagnetic calorimeter;
- hadrons deposit a fraction of their energy which is distributed according to the predictions of the GEANT (full shower) simulation.

The total response of each EM and HCAL group was obtained by summing the responses to the individual particles in the jets, event by event.

The strategy used in Level-1 trigger is as follows:

- N electromagnetic clusters (EMC) with transverse energy larger than E_{Tcut}^N in $|\eta| < 3.8$, i.e.

  $$E_T^{cluster} > E_{Tcut}^N,$$

  where E_{Tcut}^N equals 50, 15 and 5 GeV for N = 1, 2 or 3, and >3 respectively;
- the sum of the transverse energies in the matching hadron calorimeter tower E_T^{tower} is less than 10% of the sum of the transverse energy in the electromagnetic cluster, i.e.

  $$E_T^{tower} < 0.1 \times E_T^{cluster}$$

The numerical values of these cuts were chosen after extensive preliminary studies, and were cross-checked to insure that the cuts are loose enough to allow all of

the interesting physics events, such as $H^0 \rightarrow \gamma\gamma$ and $H^0 \rightarrow e^+e^-e^+e^-$, to survive. Table 5 lists the acceptance of $H^0 \rightarrow \gamma\gamma$ (80 GeV) and $H^0 \rightarrow e^+e^-e^+e^-$ (150 GeV) processes as a function of the number of EMC's.

Table 5: Level-1 Acceptance (%) for $H^0 \rightarrow \gamma\gamma$ and $H^0 \rightarrow e^+e^-e^+e^-$

N (EMC)	1	2 or 3	> 3	Total
$H^0 \rightarrow \gamma\gamma$ (M_H=80 GeV)	40	77	9.7	85.0
$H^0 \rightarrow e^+e^-e^+e^-$ (M_H=150 GeV)	52	49	87	98.4

Table 6 lists the calculated trigger rates from QCD jets as a function of the number of EMC's. The total Level-1 trigger rate is ~35 kHz.

Table 6: Level-1 EM Trigger Rate (Hz) from QCD Jets, After HCAL Veto

N (EMC)	1	2 or 3	> 3	Total
QCD Jets (kHz)	7.1	14.3	17.6	35

6.2 The Level-2 Trigger

At the Level-2 trigger, isolated electromagnetic clusters are selected by requiring that the transverse energy of the electromagnetic cluster ($E_T^{cluster}$) is larger than E_{Tcut}, and the sum of all transverse energies in a cone of radius R=0.3, excluding the electromagnetic cluster, is less than an isolation energy cut (E_{Icut}). After analyzing the results of the simulations, we chose $E_{Tcut} = 20\ GeV$ and $E_{Icut} = 10\ GeV$, i.e.

$$E_T^{cluster} > 20\ GeV,\ and$$

$$\sum_{R<0.3} E_T - E_T^{cluster} < 10\ GeV.$$

The total Level-2 trigger rate from QCD jets is reduced to ~135 Hz. The Level-2 reduction of the acceptance is less than 1% for $H^0 \rightarrow \gamma\gamma$ (80 GeV) and $H^0 \rightarrow e^+e^-e^+e^-$ (150 GeV).

6.3 The Level-3 Trigger

The Level-3 trigger applies the cut on matching charged track momenta with the energy in each electromagnetic calorimeter cluster, and then performs the physics event selection cuts. The QCD process is expected to be reduced to a negligible level.

7 Acknowledgements

I am grateful to my collaborators: Drs. H. Newman and A. Gurtu for their support and collaboration. Mr. M. Chen and D. Kirkby at Caltech carried out part of the Monte Carlo simulations described in this report.

References

[1] J. Colas, *A Summary Talk of Calorimeter Working Group*, in these proceedings.

[2] R.Y. Zhu, *A High Resolution Barium Fluoride Crystal Calorimeter*, **CALT-68-1656**, March 1990, will be published in *"Super Collider II"*, Plenum Press, edited by McAshan.

[3] T. Virdee and C. Seez, in these proceedings.

[4] L3 Collaboration, L3 Technical Proposal, May 1983;
J. Bakken *et al.*, Nucl. Instr. and Meth. **A254** (1987) 535 and **A228** (1985) 294.

[5] L* Collaboration, *Expression of Interest to the Superconducting SuperCollider Laboratory*, May 1990.

[6] Caltech *et al.*, *A Precision BaF_2 Crystal Calorimeter for Superconducting SuperCollider*, a subsystem R&D proposal submitted to the SSCL, September 1990.

[7] H. Benson and T. Sjostrand, *A Manual to the Lund Monte Carlo for Hadronic Processes*, PYTHIA version 5.4, June, 1990.

Tracking with scintillating fibres for electron identification at the LHC

C. Angelini, A. Cardini, V. Cavasinni, V. Flaminio,
E. Iacopini, S. Lami and D. Lucchesi

Dipartimento di Fisica, INFN, and Scuola Normale Superiore, Pisa, Italy.

G. Stefanini
CERN, Geveva, Switzerland

Abstract

We discuss the capability of a tracking performed with scintillating fibres in a solenoidal magnetic field, for electron identification at the LHC.

1 Introduction

Electron identification at the LHC will require rejection factors against non–electron background (hadrons and direct photons, and from π^0/η decay) that are larger than 10^5. A tracking in a magnetic field provides a measurement of the momentum of the charged particle, independently of the calorimeter's determination of its energy. The combined measurements, via the E/p matching, can improve the electron identification by a factor greater than 10^2 (even at a low field, say 3 kG).

If the field is strong (say 5 T), a measurement of the electron and muon momentum is possible up to $\sim$ 1 TeV, increasing substantially the physics capabilities of the detector.

We propose to use scintillating fibres (SciFi) of 0.5 mm diameter for a large-volume tracking. These fibres have already proved their suitability as a device for preshower tracking in the UA2 experiment at the CERN $p\bar{p}$ Collider [1], and they are also being considered for experiments at the SSC [2]. The advantages of a SciFi device can be summarized as follows [3]:

1) it is a fast detector: the typical time response is 3–8 ns;
2) it has good two-track resolution: as small as the fibre diameter;
3) it is radiation hard ($\leq 10^5$ Gy);
4) there is no power dissipation in the sensitive area;
5) it is insensitive to the magnetic field and to RF and beam-induced noise;
6) it is a low-cost device.

However, since fibres are a projective device, a careful design of the geometry (number of layers and stereo views) is needed. Probably the easiest solution for safe pattern recognition (especially at $L = 10^{34}$ cm^{-2} s^{-1}) is to use them in conjunction with a pad detector with coarse spatial resolution to solve ambiguities [1]. Moreover, a compact, fast (ideally, the readout should occur every 15 ns), and cheap solution for the front-end readout, allowing also a trigger decision within $\sim$ 1 μs, is still to be found.

2 Tracker geometry

The geometry of the proposed SciFi tracker is shown in Figs. 1a and 1b. It consists of two superlayers (superimposed layers of fibres) positioned at a radius of 0.5 m and 1 m. They subtend a rapidity range $|\eta| < 1.7$, and this range implies a length of 1.3 m and 2.6 m for the inner and outer superlayer, respectively. The cross-section of a superlayer[1] is given in Fig. 1b: four layers of fibres of 0.5 mm diameter are staggered, each relative to the other, by 1/4 of this diameter; the same four-layer structure is repeated after a 5 cm spacer. In this way, each superlayer provides a point in $R \times \phi$ and a particle direction pointing to the next superlayer (track stub method). The uncertainty in the transverse plane position provided by four layers of staggered fibres of diameter $D = 0.5$ mm is

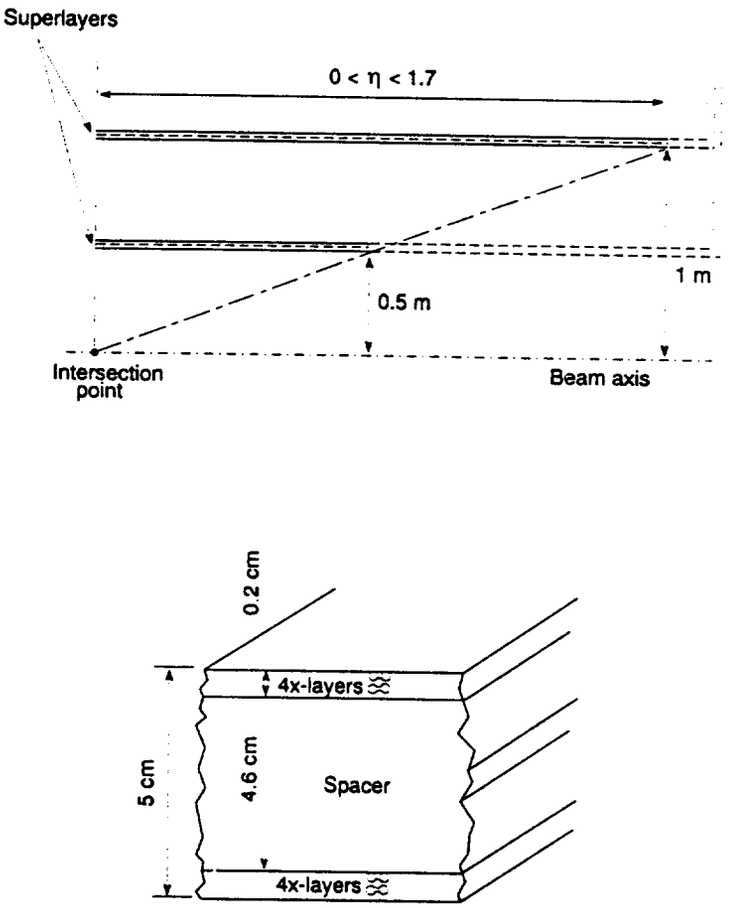


Figure 1: Schematic view of the geometry of the scintillating-fibre tracker: a) Longitudinal view; b) Cross-section of a superlayer.

[1]This geometry of a superlayer was first proposed by experiment SDC at the SSC.

$$R \times \sigma_\phi = \frac{D}{4\sqrt{12}} = 36\ \mu\text{m} \tag{1}$$

or

$$\sigma_\phi = \frac{36 \times 10^{-4}}{R\ (\text{cm})} \ .$$

This implies a r.m.s. uncertainty in the particle direction σ_θ given by a superlayer (4+4 layers),

$$\sigma_\theta = \sqrt{2}\ \ \frac{R\sigma_\phi}{\Delta} = 1.2\ \text{mrad}\ \ , \tag{2}$$

where Δ is the spacer thickness.

The fibre occupancy from primary charged particles at the maximum LHC luminosity ($L = 4 \times 10^{34}\ \text{cm}^{-2}\ \text{s}^{-1}$) is estimated to be 3.2% and 1.6% for the superlayers at $R = 0.5$ and $R = 1$ m, respectively. The multiple scattering is negligible, as is the contribution to occupancy by δ rays.

3 Tracking in a 5 T solenoidal field

The curvature radius R in a magnetic solenoidal field is given by

$$R = \frac{p_\text{T}}{3 \times 10^{-4} B}\ \ , \tag{3}$$

where R is in metres, p_T in TeV/c, and B in tesla. Particles with $p_\text{T} < 0.375$ (0.75) GeV/c loop inside the inner (outer) superlayer. Using PYTHIA Monte Carlo [4] we estimated this 'automatic' rejection to be $\sim 50\%$ and 75% for the inner and outer superlayer.

We can use the transverse vertex position and the inner superlayer particle direction resolution σ_θ, defined in Eq. (2), to cut low-p_T particles: in fact,

$$\frac{\delta p_\text{T}}{p_\text{T}} = \frac{2}{3} \times 10^4 \frac{p_\text{T}}{BL^2}\sigma_\theta = 3.2 \times 10^{-3}\ p_\text{T}\ (\text{GeV}/c)\ , \tag{4}$$

where L is the transverse track length. For a 30 GeV/c particle, we get a resolution of 10%.

For a high-p_T particle we use the sagitta (S) method and the vertex position to get

$$p_\text{T}\ \ =\ \ 37.5\ \ \frac{BL^2}{S}, \tag{5}$$

$$\frac{\delta p_\text{T}}{p_\text{T}}\ \ =\ \ \frac{\delta S}{S} = 5.3 \times 10^{-3}\ \ \delta S\ \ \ p_\text{T}\ , \tag{6}$$

where p_T is in TeV/c, and S and δS are the sagitta and the error on its measurement (in μm). Using the inner and outer superlayers and the transverse position of the vertex, we get $\delta S = 40\ \mu$m, i.e.

$$\frac{\delta p_\text{T}}{p_\text{T}} \approx 20 \times 10^{-2}\ p_\text{T}\ \ . \tag{7}$$

Therefore we measure the momentum of a 1 TeV/c particle at 20% relative error, allowing for a safe determination of its charge.

In a high magnetic field, special attention should be paid to particles that are trapped inside the detector and loop in the sensitive area, thus deteriorating the pattern recognition

of the event. We estimated this effect in the following way. A particle is trapped for only a time τ:

$$\tau \approx \frac{\ell}{2v_L} = \frac{\ell}{2}\frac{m\gamma}{p_L} \quad , \tag{8}$$

where ℓ is the detector length, m is the mass of the particle, and v_L and p_L are its longitudinal velocity and momentum, respectively. The phase of the helix of the particle in the magnetic field $\phi(t)$ is given, when $t = \tau$, by

$$\phi(t) = \frac{eB}{m\gamma c}t = \frac{eB\ell}{2cp_L} = \frac{3.75}{p_L(\mathrm{GeV}/c)} \quad \mathrm{rad} \quad , \tag{9}$$

i.e. for $p_L < 500$ MeV/c, particles perform one loop in the detector (two loops for $p_L < 250$ MeV/c etc.). In addition to this condition on p_L, we require the radius of curvature of the particle to be $0.25 < R < 0.5$ m, which translates into $0.375 < p_T < 0.75$ GeV/c. Using PYTHIA Monte Carlo, we have evaluated the fraction of particles with p_L and p_T within $0 < p_L < 500$ MeV/c and $375 < p_T < 750$ MeV/c, and we found this to be only 4%.

4 Tracking in a 3 kG solenoidal magnetic field

The 'modest' bending power provided by a 3 kG magnetic field can be used also to reject 'low'-p_T charged particles. In this case, from Eqs. (5) and (6) we get

$$\frac{\delta p_T}{p_T} = \frac{p_T}{37.5BL^2}\,\delta S = 3.5 \times 10^{-3}\; p_T\;(\mathrm{GeV}/c) \quad . \tag{10}$$

For example, for $p_T = 10$ GeV/c $\delta p_T/p_T = 3.5\%$, which allows for an easy momentum cut. Again with PYTHIA, we calculated that a cut at $p_T = 10$ GeV/c would provide a hadron rejection factor of $\sim 10^2$.

5 Conclusions

Fibres seem to constitute a suitable detector for tracking at the LHC. A fibre tracking in a magnetic field (even a weak one) can improve electron identification by several orders of magnitude.

For an optimized tracking detector, we have to make a better study of
1) particle occupancy as a function of luminosity;
2) its use in conjunction with other detectors;
3) readout options.

REFERENCES

1. J. Alitti et al., Nucl. Instrum. Methods **A279** (1989) 364.

2. See the letters of Expression of Interest for an SSC experiment, submitted by the TEXAS and SDC Collaborations.

3. For a general discussion on scintillating-fibre characteristics, see the sessions devoted to tracking and radiation hardness (these Proceedings).

4. H.U. Bengtsson and T. Sjöstrand, Comput. Phys. Commun. **46** (1987) 43.

STANDARD MODEL PHYSICS IMPACT ON ELECTRON IDENTIFICATION

H. PLOTHOW-BESCH
CERN - PPE, CH - 1211 Genève 23, Switzerland

1. INTRODUCTION

At LHC or SSC energies ($\sqrt{s}$ = 16 TeV or 40 TeV, respectively) the production of single standard $W^{\pm}$'s and Z^0's proceeds at a very high rate (i.e. ~ 10^9 W's are produced for one year of data-taking at peak-luminosities of $\mathcal{L} = 10^{34}\,cm^{-2}s^{-1}$ including the branching fraction for W decay into leptons). Because of this high rate the production of standard $W^{\pm}$'s and Z^0's tends to be more important as a serious background to other interesting physics processes than as a signal for use in detailed physics studies. On the other hand, detailed studies of W^+W^-, $W^{\pm}Z^0$, Z^0Z^0, $W^{\pm}\gamma$ *and* $Z^0\gamma$ *pair* production are particular interesting as a test of the structure of the electroweak theory. A study on the observability of these processes at the LHC has been performed for $W^{\pm}Z^0$ (see Ref. [1]) and for $W^{\pm}\gamma$ (see Ref. [2]) pair production. In the following, we shall briefly describe some theoretical motivations (Section 2), signal rates and background estimates are discussed in Section 3 and the impact for a potential LHC detector on lepton identification is presented in Section 4.

2. GAUGE BOSON PAIR PRODUCTION

The physics potential of studies of electro-weak *gauge-boson pair* production was recognized long time ago [3]. At present colliders the process of gauge boson pair production is unfortunately below the kinematical limit. Therefore the rates of these potentially very interesting events resulting from Vector Boson self-interactions predicted by the standard electroweak theory are too low to be observed. The present study of electroweak gauge boson pair production was triggered by some publications from the authors of Ref. [4] and [5]. These Vector Boson self-interactions are a manifestation of the non-abelian gauge symmetry on which the electroweak theory is based. In the Standard Model (SM) there are important cancellations in the amplitudes for W^+W^-, $W^{\pm}Z^0$ and $W^{\pm}\gamma$ production which depend on the gauge structure of the WWV trilinear couplings ($V = Z^0$ or $V = \gamma$). The Z^0Z^0 and $Z^0\gamma$ reactions are *not* sensitive to these trilinear couplings, but could test non-standard interactions (i.e. compositness of the gauge bosons). In addition, the rate of $W^{\pm}\gamma$ production is sensitive to the magnetic moment of the W boson. The lowest

order Feynman diagrams for gauge boson pair production (W^+W^-, $W^\pm Z^0$, Z^0Z^0 and $W^\pm\gamma$) from $q\bar{q}$ annihilation are shown in Fig. 1.

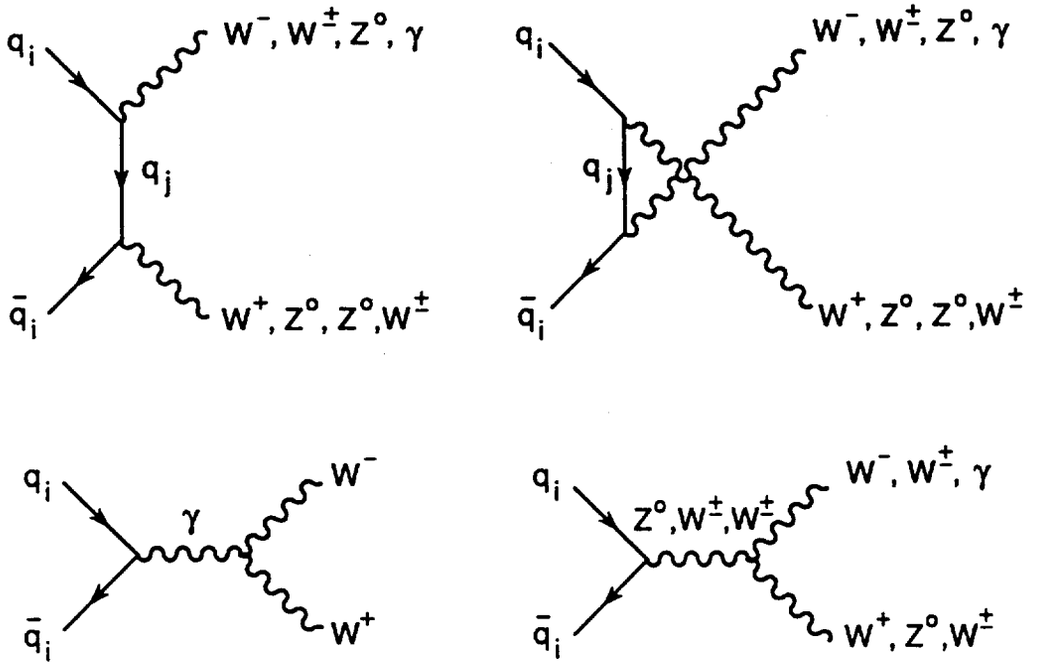


Figure 1
Lowest order Feynman diagrams for gauge boson pair production

In the approximation that the Vector Bosons are coupled to massless fermions the effective Lagrangian can be parametrized in terms of seven free parameters in case of $W^\pm Z^0$ production, which are g_1, κ, λ, g_4, g_5, $\tilde{\kappa}$ and $\tilde{\lambda}$, and in terms of four free parameters in case of $W^\pm\gamma$ production, which are κ, λ, $\tilde{\kappa}$ and $\tilde{\lambda}$,

$$\begin{aligned}\mathcal{L}_{WWV} = -e\cot\theta_W \{ & i g_1 (W^\dagger_{\mu\nu} W^\mu V^\nu - W^\dagger_\mu V_\nu W^{\mu\nu}) \\ & + i\kappa W^\dagger_\mu W_\nu V^{\mu\nu} + \frac{i\lambda}{M_W^2} W^\dagger_{\lambda\mu} W^\mu{}_\nu V^{\nu\lambda} \\ & + i\tilde{\kappa} W^\dagger_\mu W_\nu \tilde{V}^{\mu\nu} + \frac{i\tilde{\lambda}}{M_W^2} W^\dagger_{\lambda\mu} W^\mu{}_\nu \tilde{V}^{\nu\lambda} \\ & - g_4 W^\dagger_\mu W_\nu (\partial^\mu Z^\nu + \partial^\nu Z^\mu) \\ & - g_5 \varepsilon^{\mu\nu\rho\sigma} (W^\dagger_\mu \overleftrightarrow{\partial}_\rho W_\nu) Z_\sigma \},\end{aligned}$$

where V^μ represents either the Z or the photon fields, W^μ are the W^- fields, θ_W is the electroweak mixing angle and e is the proton charge. The following abreviations are used: $W_{\mu\nu} = \partial_\mu V_\nu - \partial_\nu W_\mu$, $V_{\mu\nu} = \partial_\mu V_\nu - \partial_\nu V_\mu$, $\tilde{V}^{\mu\nu} = \frac{1}{2}\varepsilon_{\mu\nu\rho\sigma} V^{\rho\sigma}$ and $(A \overleftrightarrow{\partial}_\mu B) =$

$A(\partial_\mu B) - (\partial_\nu A)B$. Within the SM the couplings g_1, κ and λ respect the discrete symmetries C and P, $\tilde{\kappa}$ and $\tilde{\lambda}$ are odd under P and even under C, g_4 respects P but is odd under C and, g_5 is odd under C and P, therefore within the SM $g_1 = \kappa = 1$ and $\lambda = \tilde{\kappa} = \tilde{\lambda} = g_4 = g_5 = 0$. In case of $W\gamma$ production g_1 is always fixed to unity by the electromagnetic gauge invariance and g_4 and g_5 are forbidden, the κ and λ terms are related to the magnetic dipole μ_W and electric quadrupole Q_W moments of the W, while $\tilde{\kappa}$ and $\tilde{\lambda}$ are related to the electric dipole d_W and magnetic quadrupole $\tilde{Q}_W$ moments.

Any deviation of SM couplings, i.e. anomalous Vector Boson self-interactions leads to amplitudes which grow with energy. Therefore, deviations from the SM are more apparent at higher invariant masses of gauge boson pairs. To avoid violation of the unitarity bound anomalous couplings should not be assumed to be constant but have to be introduced as a form factor c which decreases at high invariant masses. This form factor $c(\hat{s}, q_W^2, q_V^2)$, which is a function of the square of the four-momenta of the three gauge bosons (WWZ or WWγ) is parametrized [4,5] as

$$c(\hat{s}, q_W^2 = M_W^2, q_V^2) = \frac{c_0}{(1 + \hat{s}/\Lambda^2)^n}$$

with $q_V^2 = M_Z^2$ (WZ) or $q_V^2 = 0$ (Wγ), where n is chosen as the minimal value compatible with unitarity and Λ represents the scale at which new physics becomes important in the weak-boson sector, e.g. due to a composite structure of the W boson. The form factor c vanishes when any of the four-momenta becomes large. The parameters of the form factor c has to be chosen such as to allow for an additional increase in the total cross section due to resonances in the vincinity of $\sqrt{\hat{s}} = \Lambda$, without conflicting with unitarity. In the following $n = 2$ and $\Lambda = 1\ TeV$ have been used throughout.

The total cross section for Vector Boson pair production at lowest order has been calculated for the W^+W^-, Z^oZ^o (see Ref. [6]) and $W^\pm Z^o$ (see Ref. [1]) channels using the DFLM set of structure functions with $\Lambda_{QCD} = 260$ MeV. The result is shown in Fig. 2 as a function of the centre-of-mass energy, $\sqrt{s}$.

For *W^+W^- pair production* a total cross section of $\sigma_{Tot}(W^+W^-) = 93.3$ pb at LHC and of 325.7 pb at SSC energies has been obtained. This channel is sensitive to the interplay in the s-channel among γ and Z^o exchange and in the t and u channel to quark-exchange contributions. The absence of the Z^o exchange term would give a strong rise of the total cross section with $\sqrt{s}$. LEP II will produce W^+W^- pairs close to its threshold ($\sqrt{s}$ = 180 to 200 GeV) and can test anomalous couplings if the deviations from the standard couplings are sufficiently large. This channel is very difficult to be seen at LHC or SSC energies, because it will be swamped by $t\bar{t}$ production followed by the subsequent decay of $t \rightarrow Wb$ which produces real W's at a 50 times higher rate (i.e. $\sigma(t\bar{t}) = 4.4$ nb for $m_{top} = 150$ Gev/c^2).

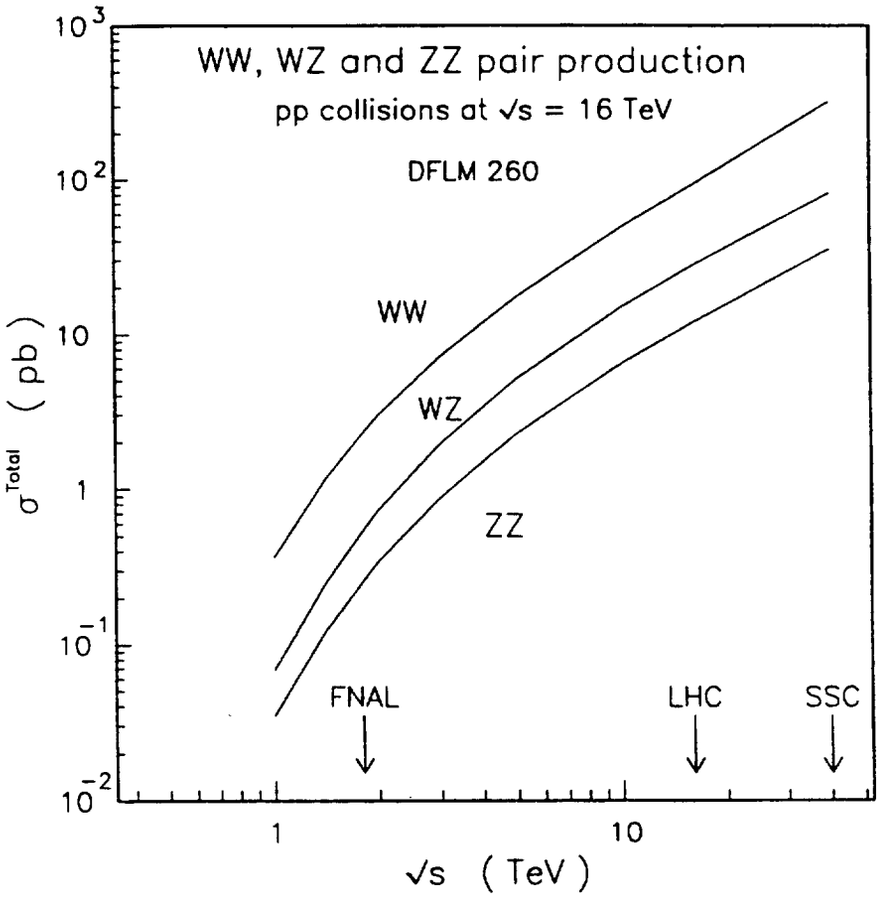


Figure 2

Total W^+W^-, Z^oZ^o and $W^{\pm}Z^o$ pair production as a function of $\sqrt{s}$

The *Z^oZ^o pair production* occurs at a rate of $\sigma_{Tot}(Z^oZ^o) = 12.0$ pb at 16 TeV and of 35.8 pb at 40 TeV. This channel is mostly interesting as a background process to the production and decay of a heavy Higgs boson. The yield of Z^oZ^o pairs is smaller by about a factor 8 to 10 compared to W^+W^- pairs.

For *$W^{\pm}Z^o$ pair production* a total cross section of $\sigma_{Tot}(W^{\pm}Z^o) = 27.9$ pb at LHC and of 82.4 pb at SSC energies has been obtained. This channel is particular interesting (see next Section), because it is easy to isolate compared to WW pair production, it is clean for testing the anomalous Vector Boson self-interactions and it allows to study the WWZ vertex alone (there is no contribution from a WWγ vertex).

The total cross section for *$W^{\pm}\gamma$ pair production* is of course formally infinite. Restrictions to specific kinematical regions remove the infrared divergence and allow to test the WWγ vertex. Deviations from standard couplings can also be tested with high sensitivity (see next Section).

3. $W^{\pm}Z^{0}$ AND $W^{\pm}\gamma$ PRODUCTION

3.1 Signal from Standard Model predictions and background studies

To study in some detail the observability of the process $pp \rightarrow W^{\pm}Z^{0} + X$ and $pp \rightarrow W^{\pm}\gamma + X$ at the LHC simulation programs provided by the authors of Ref. [2] and [3] have been used to obtain the results described in the following. Multi-jets from QCD production are produced with substantially higher cross section than the gauge boson pairs. Therefore this background will swamp the purely hadronic signal for gauge boson pair production. Also the W or Z cross sections with associated QCD production are well above the $W^{\pm}Z^{0}$ or $W^{\pm}\gamma$ pair production. Therefore, in the analysis only $W^{\pm}Z^{0}$ or $W^{\pm}\gamma$ pairs with subsequent semi-leptonic decay of the W and the Z in case of WZ production, leading to a final state of three leptons and missing transverse momentum (for $W^{\pm}Z^{0}$) or one lepton, one photon and missing transverse momentum (for $W^{\pm}\gamma$) are considered. The leptons can be either electrons or muons, or both in case of WZ production.

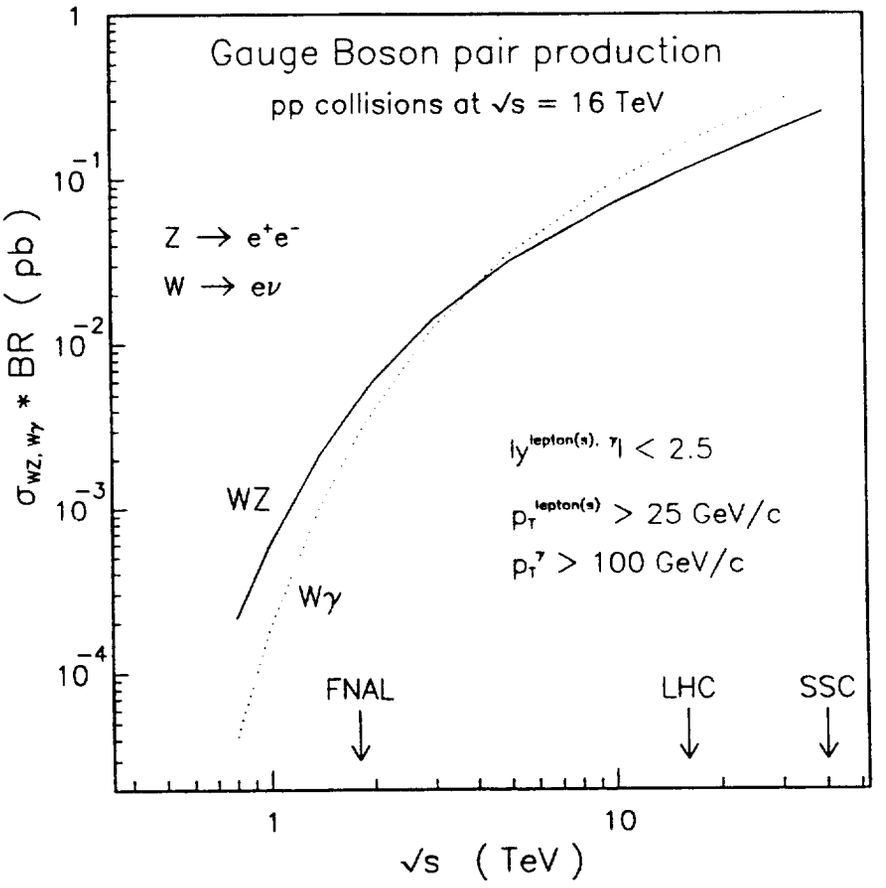


Figure 3

$W^{\pm}Z^{0}$ and $W^{\pm}\gamma$ pair production as a function of $\sqrt{s}$ after cuts

For a realistic simulation of both processes a calorimeter resolution of $\Delta E/E = 15\%/\sqrt{E}$ for electromagnetic showers and of $\Delta E/E = 80\%/\sqrt{E}$ for hadronic showers has been taken into account. The neutrino has been taken as a hadron and has been smeared

with the hadronic resolution. Calorimetry coverage in the pseudorapidity range of $|\eta| < 2.5$ has been assumed. Kinematical cuts on the transverse momenta of the outgoing leptons exceeding 25 GeV/c and of the photon exceeding 100 GeV/c have been applied. The total cross section for WZ and Wγ pair production is shown in Fig. 3 as a function of $\sqrt{s}$ after the above cuts have been applied. A total cross section of 112.4 fb in case of WZ and of 160.6 fb in case of Wγ production is obtained, where the leptonic branching fractions of $BR(W \rightarrow \ell\nu) = 10.88\%$ and of $BR(Z \rightarrow \ell^+\ell^-) = 3.36\%$ have been included and the electron, the muon and in case of WZ production also in the e-μ channels have been taken into account. These cross sections translate into a number of events of ~ 11000 for WZ and of ~ 16000 for Wγ production for 10^5 pb^{-1} which corresponds to one year of running at peak-luminosities of $\mathcal{L} = 10^{34}$ cm^{-2}s^{-1}. These numbers are sufficiently large, even if one assumes peak-luminosities of only 10^{33} cm^{-2}s^{-1}, that one can affort efficiency losses which have not been taken into account yet.

We have found that the signal is well above background by about one order of magnitude for both, the WZ and the Wγ pair production.

For WZ production the main background sources are expected from either $t\bar{t}$ with t or $\bar{t}$ decaying semileptonically and one of the cascaded b's also decaying semileptonically, or from Z + jet (or Z + b) production with the $Z \rightarrow \ell^+\ell^-$ and the jet (b) fragments faking a lepton (electron or muon). The background from semileptonical t or b decays is already reduced by the kinematical cut of $p_T^{leptons}$ exceeding 25 GeV/c [7]. For the suppression of jets faking the electron signature a rejection factor of 10^4 has been assumed, which is rather conservative compared to the rejection of $\geq 5 \cdot 10^5$ obtained by the $\bar{p}p$ collider experiments UA2 and CDF. Taking into account the complexity of the events expected in an LHC environement this seems to be a resonable assumption. Leptons from b decays are expected to be non isolated. Therefore an energy isolation requirement should reduce this background to a small amount. We have assumed a rejection factor of 5, which again is very conservative because it could be as large as 50 depending on the detector performance. Background from $t\bar{t}$ production is much harder to be suppressed, because the subsequent $t \rightarrow Wb$ cascaded by $W \rightarrow \ell\bar{\nu}$ decays produces real, isolated leptons. The constraint that two leptons reconstruct to the Z mass, for which a rejection factor of 10 has been assumed, and an additional isolation requirement on one of the leptons from the b decay reduce this background well below the signal. Table 1 summarizes the expected signal and background rates for WZ production assuming 10^5 pb^{-1}.

For Wγ production the background is mainly due to two different sources: W + jets and heavy flavour production (i.e. $b\bar{b} \rightarrow e\bar{\nu}c$ + jet), where the jet is misidentified as a photon. The experimental technique is mainly based on the signature of the high p_T photon. Since a misidentified jet can fake a photon, the effect of an isolation cut which requires no charged particles in a cone around the photon has been studied. The isolation

cut reduces the background from jet production by a factor ~ 10^4 for $p_T^\gamma > 100$ GeV/c and by $\geq 10^5$ for $p_T^\gamma > 200$ GeV/c [8]. The result for signal and background for $W\gamma$ production is summarized in Table 2 assuming an integrated luminosity per year of $\mathcal{L} = 10^5$ pb^{-1}. Taking into account the rejection factor for the photon and requiring an electron with $p_T^e > 25$ GeV/c the production of $b\bar{b} \rightarrow e\bar{\nu}c$ + jet background is reduced to ~ 0.1 fb for $p_T^\gamma > 100$ GeV/c and is completely negligible for $p_T^\gamma > 200$ GeV/c. A higher cut on p_T^γ clearly reduces the background contribution still keeping the signal at a significant level.

Table 1: $W^\pm Z^0$ pair production, signal and background rates for 10^5 pb^{-1}

$\sqrt{s}$ = 16 TeV	$\sigma_{W^+Z} \cdot B_{\ell\nu}$	$\sigma_{W^-Z} \cdot B_{\ell\nu}$	$\sigma_{W^\pm Z} \cdot B_{\ell\nu}$	# events/year
$W^\pm Z$ $\hookrightarrow \ell^+\ell^-$ $\hookrightarrow \ell\nu$	62.6 fb	48.8 fb	112.4 fb	11240
Z + Jet(s) $\hookrightarrow \ell^+\ell^-$			3.0 fb	300
$Z + b$ $\hookrightarrow \ell\bar{\nu}c$ $\hookrightarrow \ell^+\ell^-$			5.5 fb	500
$t\bar{t}$ (m_{top} = 130 GeV/c^2) $\hookrightarrow \ell\bar{\nu}b$ $\hookrightarrow$ jets			$\leq$ 20 fb	$\leq$ 2000
[$t\bar{t}$ (m_{top} = 150 GeV/c^2)			$\leq$ 14 fb	$\leq$ 1400]
$\lvert\eta^{leptons}\rvert < 2.5$, $p_T^{leptons} > 25$ GeV/c				

Table 2: $W^\pm\gamma$ signal and main background for different p_T^γ thresholds

	$p_T^\gamma > 100$ GeV/c		$p_T^\gamma > 200$ GeV/c	
	$\sigma \cdot B_{e\nu}$	# events/year	$\sigma \cdot B_{e\nu}$	# events/year
$W^\pm\gamma$ $\hookrightarrow e\nu$	160.6 fb	16060	21.7 fb	2170
$W^\pm$ + jets $\hookrightarrow e\nu$	~ 24 fb	2400	~ 0.36 fb	36
$b\bar{b}X$ $\hookrightarrow e\bar{\nu}c$ $\hookrightarrow$ jets	0.1 fb	10		negligible
$\lvert\eta^{lepton,\,\gamma}\rvert < 2.5$, $p_T^{lepton} > 25$ GeV/c, $p_T^\gamma > 100$ GeV/c				

A similar analysis can be performed by looking at $W \rightarrow \mu\nu$ decays with a similar event selection. The observable cross section depends strongly on the muon momentum resolution. Under the assumption of $\Delta p_\mu / p_\mu = \alpha \cdot p_\mu$ the results for different values of α with $p_T^\gamma > 100$ GeV/c are shown in Table 3. To keep a resonable number of events in the muon decay channel after cuts a momentum resolution of about 5% for $p_T^\mu \sim 25$ GeV/c should be aimed at.

Table 3 : $W^+\gamma$ and $W^-\gamma$ cross-sections with $W \rightarrow \mu\nu$ for different values of the muon momentum resolution

	$W^+\gamma \rightarrow \mu\nu$		$W^-\gamma \rightarrow \mu\nu$	
α	$\sigma \cdot B_{\mu\nu}$	# events/year	$\sigma \cdot B_{\mu\nu}$	# events/year
0.001	21.9 fb	2190	16.5 fb	1650
0.003	13.8 fb	1380	10.1 fb	1010
0.005	10.5 fb	1050	7.4 fb	740

3.2 $W^\pm Z^0$ and $W^\pm\gamma$ anomalous couplings

As an example, the sensitivity to deviations from standard couplings have been tested by changing the parameter λ from its SM expectation ($\lambda = 0$) to $\lambda = 0.1$ and 0.04. The total cross section changes very little, but the shape of the total transverse mass distribution of the W and Z pair, M_T^{WZ}, is found to be very sensitive to anomalous couplings. This variable is easily accessed by experiment, because only well measured transverse variables are involved. The total mass M^{WZ} as proposed by Ref. [4] is less sensitive due to the ambiguity of the longitudinal momentum of the neutrino being unknown. The total transverse mass distribution M_T^{WZ} is shown in Fig. 4 for standard couplings (full line), for $\lambda = 0.1$ (dashed line) and for $\lambda = 0.04$ (dotted line). If one defines as sensitivity to have at least 10 events integrated over all events above a certain transverse mass threshold, anomalous couplings can be tested up to $M_T^{WZ} = 1620$ GeV/c^2 ($M_T^{WZ} = 1160$ GeV/c^2) for $\lambda = 0.1$ ($\lambda = 0.04$) assuming 10^5 pb^{-1}.

The presence of anomalies in the WWγ vertex will yield an enhanced number of events at larger p_T^γ or large transverse masses of the Wγ system ($M_T^{W\gamma}$). The photon transverse momentum p_T^γ turns out to be a sensitive variable for different values of the parameters. In case of $\Lambda = 1$ TeV the sensitivity to this anomalous coupling is up to $p_T^\gamma = 800$ GeV/c. Another sensitive variable is $M_T^{W\gamma}$, similarly to the WZ pair analysis (see above). In this case the anomalous couplings can be tested up to values of

$M_T^{W\gamma} \sim 1700$ GeV/c^2. Figure 5 shows the expected deviations in the transverse mass distribution from different anomalous coupling constants for $\Lambda = 2$ TeV.

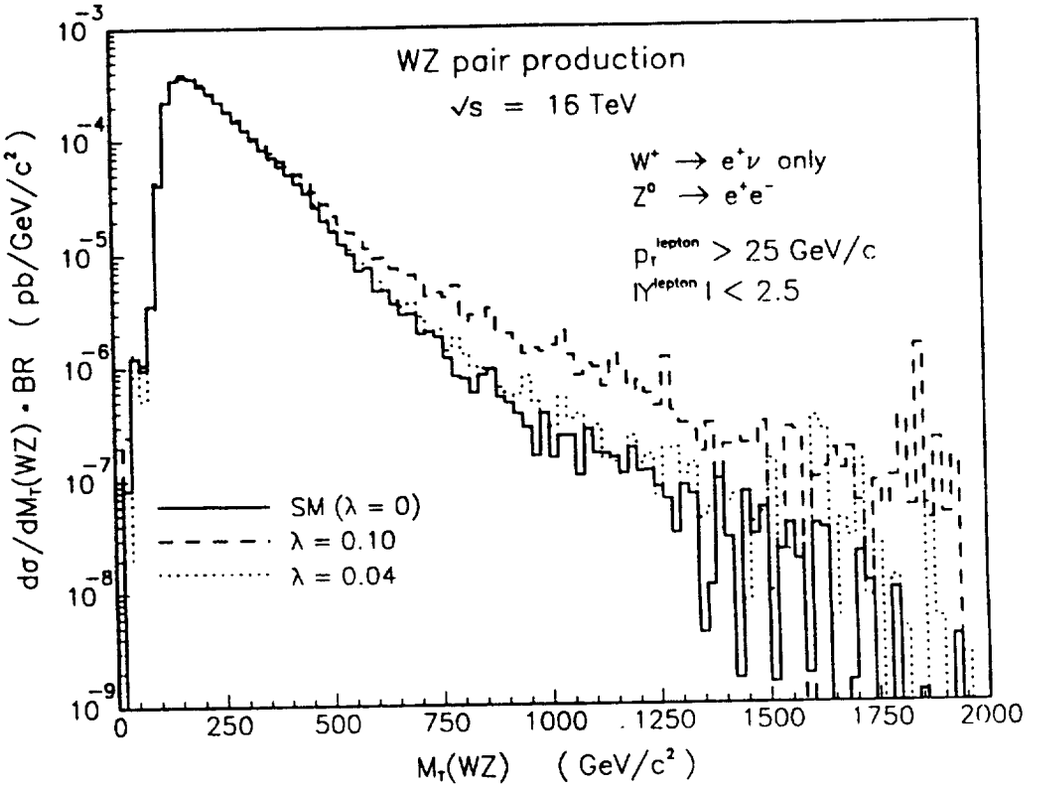


Figure 4

Transverse mass distribution of the W and Z pair, M_T^{WZ}, for standard ($\lambda = 0$) and anomalous couplings ($\lambda = 0.1$ and 0.04)

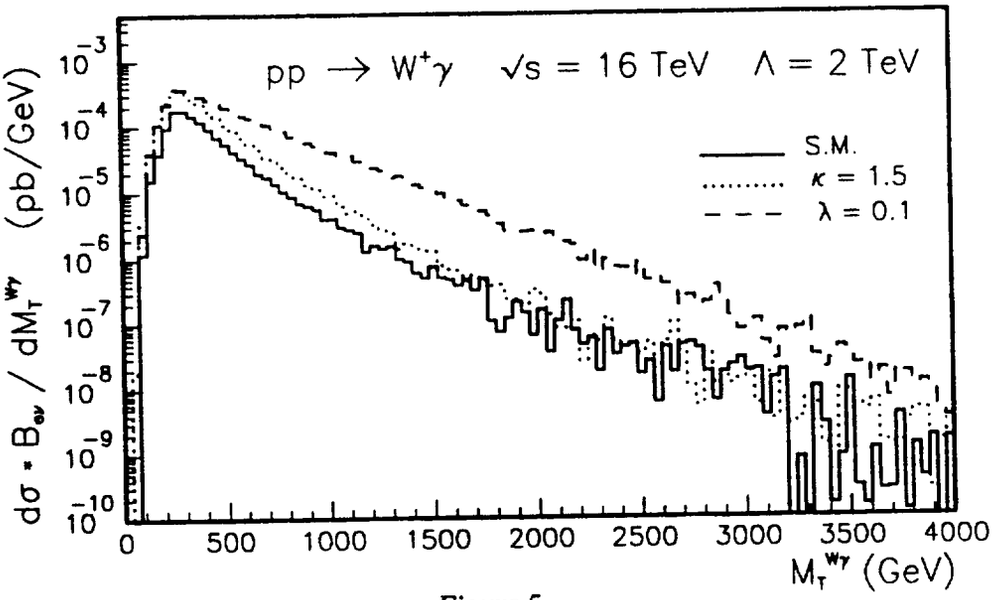


Figure 5

$W^+\gamma$ transverse mass distribution with $\kappa = 1.5$ or $\lambda = 0.1$ for $\Lambda = 2$ TeV compared to Standard Model predictions

As a conclusion we have found that anomalous couplings could be tested to the 2 - 4% level, depending which coupling constant is considered, by comparing the shapes of the transverse mass spectrum of the WZ or Wγ pair, a variable which is easily measurable by experiment and has no ambiguity due to the unknown longitudinal momentum of the neutrino. This gives about one order of magnitude better sensitivity than LEP II.

4. IMPACT ON LEPTON IDENTIFICATION

The M_T^{WZ} and $M_T^{W\gamma}$ or p_T^{γ} distributions will reveal the existence of anomalous couplings if they are sufficiently large. To distinguish between different anomalous couplings angular distributions of the parent Vector Bosons and their decay products are the suitable tools because they allow to determine the Vector Boson helicities, and therefore to identify anomalies in the specific helicity components [4,5]. In the following we give examples only for $W^{\pm}Z^{o}$ pair production. Of cource, $W^{\pm}\gamma$ pair production is equally adequate for such studies.

In the Standard Model the pure V-A structure of the fermion-antifermion-boson coupling produces transversely polarized W^+ of helicity ± 1 which results in a $(1 + \cos\bar{\theta})^2$ angular distribution (where $\bar{\theta}$ is the polar angle of the e^+ or μ^+ with respect to beam direction in the rest frame of the parent W^+). Longitudinally polarized W's result in a $\sin^2\bar{\theta}$ distribution. The different anomalous couplings show different deviations to the SM expectations. Anomalous values of g_1 in case of $W^{\pm}Z^{o}$ production ($g_1 \neq 1$) produce mainly longitudinal polarized W's (within the SM $g_1 = 1$), therefore a dominant $\sin^2\bar{\theta}$ distribution is expected. Anomalous values of λ ($\lambda \neq 0$) enhance transversely polarized W's and Z's giving equal numbers of W's with positive and negative helicities resulting in a symmetric angular distribution around 90°. CP violating contributions such as g_4, $\tilde{\kappa}$ and $\tilde{\lambda}$ may be studied by comparing W^+Z and W^-Z cross sections where the number of events within the SM is expected to be ~ 6200 W^+Z's and ~ 4880 W^-Z's for one LHC year of 10^5 pb^{-1}. To give one example, the decay angular distribution of the charged lepton in its parent rest frame in $pp \rightarrow W^+Z + X$ reaction is shown in Fig. 6 for SM predictions and different choices of anomalous couplings. A cut $M^{WZ} > 600$ GeV/c^2 is imposed on the WZ invariant mass. This figure has been taken from Ref. [4]. Similar decay angular distributions of the charged lepton (μ^+, e^+) from W^+ decays can be obtained for $pp \rightarrow W^+\gamma + X$ production. A detailed study on this subject is in progress.

It is obvious from Figs. 6 that the charge of the W and Z decay products should be measured over a large pseudorapidity range ($|\eta| < 3$) to distinguish between the different anomalous couplings if they exist.

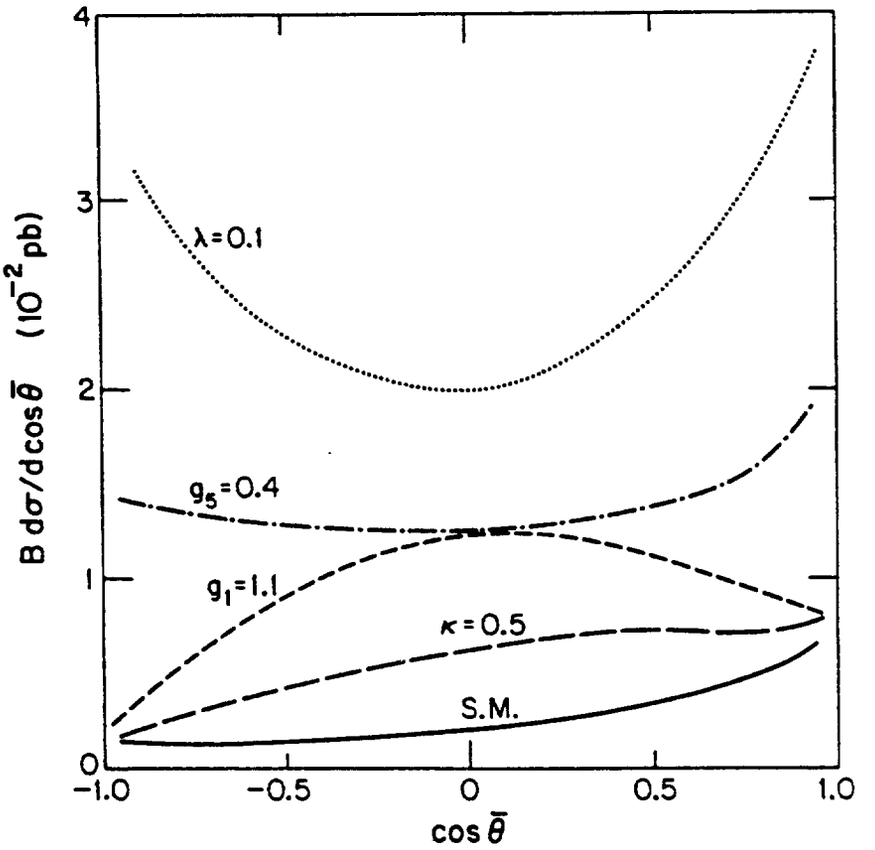


Figure 6

Decay angular distribution of the charged lepton in its parent rest frame for $pp \rightarrow W^+Z + X$

5. CONCLUSIONS

Gauge boson pair production has been found to become an exciting physics topic which can be investigated at the LHC with high sensitivity up to masses exceeding the 1 TeV range. Hadron colliders are capable of producing gauge boson pairs in both, the charged and neutral channels. In pp collisions at LHC energies the structure of the WWZ (WWγ) vertex can be studied by WZ (Wγ) pair production. These channels allow to test the structure of the electroweak theory which predicts the existence of these Intermediate Vetor Boson Self-Interactions.

Both, the $W^{\pm}Z^0$ and $W^{\pm}\gamma$ pair production are easily accessible by experiments after minor cuts. There is a clean signature, for $W^{\pm}Z^0$ three high p_T leptons and significant missing transverse momentum, while for $W^{\pm}\gamma$ one high p_T lepton, one very high p_T photon and missing transverse momentum are the dominant signatures. For an integrated luminosity of 10^5 pb^{-1} which corresponds to one year of running at $\mathcal{L} = 10^{34}$ cm^{-2} s^{-1} ~ 11000 $W^{\pm}Z^0$ events and ~ 16000 $W^{\pm}\gamma$ events are expected in the pseudorapidity range of $|\eta| < 2.5$ for both, the leptons and the photon, and transverse momenta in excess of 25 GeV/c for the leptons and of 100 GeV/c for photon. The main sources of background can be kept well below the $\leq 15\%$ level of the signal.

The presence of anomalous couplings can be tested by comparing the shapes of the M_T^{WZ} or the $M_T^{W\gamma}$ in case of WZ or Wγ pair production, respectively, and in case of $W^{\pm}\gamma$ production also by comparing the behaviour at high values of the observed p_T^{γ} with distributions from the Standard Model predictions. Gauge boson pair production of both, $W^{\pm}Z^0$ and $W^{\pm}\gamma$, allow tests of anomalous couplings up to a sensitivity of 2 - 4%. With 10^5 pb^{-1} of integrated luminosity mass ranges well above > 1600 GeV/c^2 can be tested which gives about one order of magnitude better sensitivity than LEP II. The different anomalous couplings can be distinguished using angular variables which would imply the measurement of the charge of the decay leptons. This statement needs more detailed studies, which have not been made yet.

In conclusion, the WZ and Wγ pair production imply the following requirements on the lepton (electron and muons) identification for a detector at LHC or SSC:

a) moderate electron and good muon identification with lepton transverse momenta exceeding 20 Gev/c,

b) good lepton isolation as an important implication for background suppression and

c) determination of the charge of the leptons over a large pseudorapidity range.

ACKNOWLEDGEMENT

The author would like to thank the conveners, P. Nason and G. Martinelli, and all group members of the Standard Model working group on standard processes, H. Kuijf, T. Matsuura, B. Mele, F. Pastore, M. Pepe, L. Trentadue, D. Wood and D. Zeppenfeld, for the pleasant collaboration resulting in many fruitful discussions.

REFERENCES

[1] H. Plothow-Besch, these proceedings.

[2] F. Pastore and M. Pepe, these proceedings.

[3] R.W. Brown, K.O. Mikaelian and D. Shadev, Phys. Rew. **D20** (1979) 1164;
E. Eichten, I. Hinchliffe, K. Lane and C. Quigg, Rev. Mod. Phys. **56** (1984) 579.

[4] S. Willenbrock and D. Zeppenfeld, Phys. Rev. **D37** (1988) 1775;
U. Baur and E.W.N. Glover, FNAL-PUB-90/75-T.

[5] U. Baur and D. Zeppenfeld, Nucl. Phys. **B308** (1988) 127.

[6] B. Mele, these proceedings.

[7] A. Nisati, these proceedings.

[8] M. Werlen, these proceedings.

Muon Rates at the LHC

Aleandro Nisati
Istituto Nazionale di Fisica Nucleare, Sezione di Roma, Italy.

It is agreed that the lepton identification is a powerful tool for searching for new physics at hadron supercolliders. In particular the muon identification and trigger is of primary importance since muons can be recognized even inside jets, whilst the electrons have to be isolated to be identified.

The muon production cross sections that will be reported have been calculated with the ISAJET [1] Monte Carlo (version 6.24) with the EHLQ structure functions, set I.
QCD higher order corrections are very important for the production of heavy quarks, mainly for beauty and charm quarks. The full $O(\alpha_s^3)$ QCD correction for beauty production is a factor ~ 4 [2], weakly dependent on the p_T of the quark, whilst for the top quark with m_{top} = 150 GeV/c^2 the correction is only for a factor 1.5. The theoretical uncertainties, due to the structure functions, the energy scale μ and Λ_{QCD} are quite large and are discussed in [2].

The ISAJET Monte Carlo incorporates these corrections with the parton shower approach ($g \rightarrow q\bar{q}$; $g \rightarrow gg$; $q \rightarrow qg$). The heavy quarks are then fragmented into hadrons using the independent fragmentation ansatz of Field and Feynman with the Peterson form. More details on this generator and the comparison with other Monte Carlo generators or analytic calculations are reported in [3]. In particular the $b\bar{b}$,$c\bar{c}$ production cross section calculated with ISAJET has been compared with a full calculation of the QCD $O(\alpha_s^3)$ [4]; it turns out that the cross section evaluated with ISAJET is a factor ~ 2 higher at p_T^{μ} = 20 Gev/c and a factor ~ 4 higher at p_T^{μ} = 100 GeV/c.

This generator has been extensively studied by the UA1 Collaboration and the main properties of the heavy quarks production at the CERN proton-antiproton Collider have been found well reproduced by ISAJET [5].

Prompt muon rates

Fig. 1 shows the differential inclusive (prompt) muon cross section in the pseudorapidity region $|\eta| \leq 3$ as a function of p_T^{μ} for several processes at $\sqrt{s}$ = 16 TeV:

$$pp \rightarrow b\bar{b},c\bar{c} + X;$$

$pp \rightarrow t\bar{t} + X$ (for two top masses: 130 GeV/c^2 and 200 GeV/c^2);
$pp \rightarrow Z^{\circ} + X$;
$pp \rightarrow W^{\pm} + X$
$pp \rightarrow \mu^+\mu^- + X$ (Drell Yan)

In fig. 2 the correspondent integral cross section is reported as a function of $p_T^{th.}$. It is possible to see that the muons produced by beauty and charm cascades dominate for a wide range of p_T; only in the region of $p_T \approx 40$ GeV/c the W is competitive (the typical jacobian peak is still visible), whilst for very high transverse momentum a somewhat light top is expected to be competitive. Assuming a luminosity $L = 10^{34}$ cm^{-2} s^{-1} it turns out that by selecting inclusive muons, for instance with $p_T \geq 5$ GeV/c, the rate would be nearly 10^5 Hz. At the Sp$\bar{p}$S CERN Collider the UA1 first level muon trigger rate was only ~ 10^2 Hz (muon $p_T \geq 2$ GeV/c; $|\eta| \leq 2.3$) and was dominated by muons from pion and kaon decays.

For $p_T \geq 20$ GeV/c the prompt muon rate decreases to 10^3 Hz, whilst for $p_T \geq 40$ GeV/c is a factor ~ 10 lower.

Fig. 3 shows the single muon integral cross sections, reported in detail also in Table I; the muons are sorted following the scheme $p_T^{\mu 1} > p_T^{\mu 2} > p_T^{\mu 3} \ldots$.

The background to the prompt muons is essentially constituted by the charged pion and kaon leptonic decays in flight and by the hadronic jets punch-through; it is strongly dependent on the detector geometry and is discussed in detail in [6] and [7].

Fig. 4 shows the dimuon cross section. The beauty and charm production is still dominating in the low p_T region, up to 20 GeV/c. For higher momenta the main contribution comes from Z production, followed by the $t\bar{t}$ processes. At very high p_T the contributions from Z and Drell Yan are equivalent. The dimuon rate (assuming the quoted luminosity) is ~ 30 Hz for $p_T \geq 20$ GeV/c, 50 times lower than the corresponding single muon rate, and it is essentially given by Z decays. In 10^7 s (the usual *one year run*) more than 10^8 muon pairs coming from Z particles can be produced and used for detector calibration.

The level of pile-up effects on the single muon events it is also shown. The "equivalent pile-up cross section" has been calculated as follows. Let us define:

- n the average number of pp inelastic collision
- Δt the resolution time ($\Delta t \geq 15$ ns, the bunch crossing period)
- σ_μ the inclusive muon cross section production with $p_T \geq p_T^{th.}$
- σ_{mb} the inelastic pp cross section

By using the binomial distribution we can define the probability of having one dimuon event by two single muon events pile-up in the time Δt:

$$p^{pile\text{-}up} = n \times \frac{(\sigma_{2\mu}^{pile\text{-}up})}{\sigma_{mb}} = \binom{n}{2} P_\mu^2 \times (1 - P_\mu^2) \qquad (1)$$

$$\text{with } P_\mu = \frac{\sigma_\mu}{\sigma_{mb}} \ll 1 . \qquad (2)$$

By using (2) in (1) we have

$$p^{\text{pile-up}} \approx \left[\frac{n!}{2(n-2)!}\right] \times P_\mu^2 \approx \left(\frac{n^2}{2}\right) \times P_\mu^2 \qquad (3)$$

Now by substituting $n = L\Delta t\sigma_{mb}$ in (3) we obtain the expression of the pile-up "cross section", to be compared with the signal cross section in fig. 4:

$$\sigma_{2\mu}^{\text{pile-up}} = (1/2)\ L\,\Delta t\,\sigma_\mu^2; \qquad (4)$$

for $L = 10^{34}$ cm^{-2} $^{-1}$, Δt= 15 ns and by quoting σ_μ in pb we obtain the expression

$$\sigma_{2\mu}^{\text{pile-up}} = 0.75\times10^{-10}\,\sigma_\mu^2 \qquad (5)$$

From (4) we can see that the pile up rate increases with second power of the luminosity; but, even for the highest luminosity foreseen at LHC (4×10^{34} cm^{-2} s^{-1}) this contribution can be neglected.

The trimuon integral cross section is reported in fig. 5. For $p_T > 40$ GeV/c the main contribution comes from top decays, followed by the production from gauge boson pairs; at lower p_T the beauty and charm hadrons are still the main source of trimuons.

In fig. 6a we show the four muon integral cross section for beauty and charm, top, Zb$\bar{b}$ and for Z^oZ^o (see also Table III). The contribution from pile-up of dimuon events (mainly of b$\bar{b}$, c$\bar{c}$ and inclusive Z events) is also shown and it appears negligible. These curves are compared with those in fig. 6b where the correspondent cross sections for the process $H^o \rightarrow Z^oZ^o \rightarrow \mu^+\mu^-\mu^+\mu^-$ for three values of the Higgs mass: 200, 400 and 700 GeV/c^2 (the top mass has been set to 150 GeV/c^2; see also Table IV) are shown. These distributions suggest a cut on each muon p_T around 20 GeV/c to reduce strongly the level of the background to the Higgs signal.

Finally fig. 7, 8 and 9 show the acceptance curves for detecting the Higgs boson through the process $H^o \rightarrow Z^oZ^o \rightarrow \mu^+\mu^-\mu^+\mu^-$ for n muons (n=1,2,3,4) detected in the pseudorapidity region $|\eta| \leq \eta_{trig}$. The p_T cut applied to all muons is 20 GeV/c (a) and 40 GeV/c (b).

Conclusion

The size of the heavy flavour cross section combined with the enormous luminosity of LHC gives very high muon rates: more than 10^5 Hz for $p_T^\mu > 5$ GeV/c and more than 10^3

Hz for $p_T^{\mu} > 20$ GeV/c; to have a reasonable rate of the order 100 Hz a cut $p_T^{\mu} > 50$ GeV/c is demanded; this request cannot be accepted since much physics is suppressed by demanding such a high p_T cut; in addition it is not an easy task for the trigger system. By demanding two muons with p_T above 20 GeV/c, the rate does not exceed 30 Hz and is largely dominated by Z and heavy quark production.

References

[1] F.E. Paige and S. D. Protopopescu, ISAJET Monte Carlo, BNL 38034 (1986).

[2] J.P. Guillet, P. Nason ans H. Plothow-Besh, these proceedings.

[3] T. Sjostrand, these proceedings.

[4] G. Altarelli *et al.*, Nucl. Phys. B308 (1988) 724.
P. Nason, S. Dawson and R.K. Ellis, Nucl. Phys. B303 (1988) 607.

[5] C. Albajar *et al.* (UA1 Collaboration), Z. Phys. C37, 489-503 (1988)

[6] H. Fesefeldt, "Punch Through Simulation", these proceedings.

[7] M Della Negra, "Muon Trigger and Identification", these proceedings.

$p_T^{th.}$ (GeV/c)	$b\bar{b}$	$t\bar{t}$ (m=130 GeV/c^2)	$t\bar{t}$ (m=200 GeV/c^2)	$W^{\pm}$	Z^o	Drell Yan
8	3.32×10^6	1.37×10^3	2.48×10^2	2.09×10^4	2.42×10^3	5.99×10^3
12	1.05×10^6	1.16×10^3	2.15×10^2	2.02×10^4	2.36×10^3	1.95×10^3
16	3.92×10^5	1.01×10^3	1.89×10^2	1.92×10^4	2.27×10^3	8.91×10^2
20	1.68×10^5	8.89×10^2	1.68×10^2	1.78×10^4	2.16×10^3	5.19×10^2
24	8.11×10^4	7.90×10^2	1.50×10^2	1.60×10^4	2.02×10^3	3.30×10^2
28	4.34×10^4	7.02×10^2	1.35×10^2	1.37×10^4	1.85×10^3	2.15×10^2
32	2.52×10^4	6.24×10^2	1.22×10^2	1.11×10^4	1.65×10^3	1.46×10^2
36	1.57×10^4	5.53×10^2	1.10×10^2	7.94×10^3	1.43×10^3	1.03×10^2
40	1.04×10^4	4.90×10^2	9.94×10^1	3.95×10^3	1.16×10^3	8.28×10^1
44	7.14×10^3	4.33×10^2	9.00×10^1	1.91×10^3	8.77×10^2	5.95×10^1
48	5.08×10^3	3.82×10^2	8.15×10^1	1.17×10^3	4.85×10^2	4.74×10^1
52	3.70×10^3	3.36×10^2	7.39×10^1	8.11×10^2	2.94×10^2	3.79×10^1
56	2.74×10^3	2.96×10^2	6.70×10^1	6.26×10^2	2.04×10^2	3.04×10^1
60	2.05×10^3	2.60×10^2	6.09×10^1	4.77×10^2	1.54×10^2	2.48×10^1
64	1.55×10^3	2.28×10^2	5.52×10^1	3.68×10^2	1.20×10^2	2.06×10^1
68	1.17×10^3	2.00×10^2	5.02×10^1	2.97×10^2	9.36×10^1	1.72×10^1
72	8.95×10^2	1.76×10^2	4.55×10^1	2.46×10^2	7.56×10^1	1.43×10^1
76	6.90×10^2	1.54×10^2	4.13×10^1	2.04×10^2	6.28×10^1	1.20×10^1
80	5.35×10^2	1.34×10^2	3.76×10^1	1.68×10^2	5.28×10^1	1.01×10^1
84	4.18×10^2	1.18×10^2	3.42×10^1	1.47×10^2	4.48×10^1	8.77×10^0
88	3.30×10^2	1.04×10^2	3.10×10^1	1.20×10^2	3.80×10^1	7.54×10^0
92	2.62×10^2	9.15×10^1	2.82×10^1	9.81×10^1	3.21×10^1	6.61×10^0
96	2.10×10^2	8.03×10^1	2.56×10^1	8.48×10^1	2.74×10^1	5.84×10^0
100	1.70×10^2	7.06×10^1	2.33×10^1	7.09×10^1	2.37×10^1	5.15×10^0

Table I. Single muon production integral cross section with $p_T^{\mu} \geq p_T^{th.}$ for different processes in the rapidity region $|\eta| \leq 3.0$. The quoted cross sections are in pb.

$p_T^{th.}$ (GeV/c)	$b\bar{b}$	$t\bar{t}$ (m=130 GeV/c^2)	$t\bar{t}$ (m=200 GeV/c^2)	Z^o	Drell Yan	pile-up (*)
8	2.82×10^4	1.94×10^2	4.70×10^1	1.66×10^3	1.25×10^3	
12	7.76×10^3	1.26×10^2	3.32×10^1	1.62×10^3	3.90×10^2	
16	2.72×10^3	8.82×10^1	2.45×10^1	1.55×10^3	1.58×10^2	1.40×10^0
20	1.11×10^3	6.42×10^1	1.84×10^1	1.47×10^3	9.14×10^1	
24	5.04×10^2	4.83×10^1	1.41×10^1	1.36×10^3	5.69×10^1	
28	2.47×10^2	3.66×10^1	1.10×10^1	1.20×10^3	3.86×10^1	
32	1.28×10^2	2.82×10^1	8.58×10^0	1.01×10^3	2.74×10^1	
36	7.01×10^1	2.19×10^1	6.78×10^0	7.78×10^2	2.02×10^1	
40	3.99×10^1	1.71×10^1	5.41×10^0	5.06×10^2	1.52×10^1	7.00×10^{-3}
44	2.37×10^1	1.35×10^1	4.36×10^0	1.66×10^2	1.18×10^1	
48	1.45×10^1	1.06×10^1	3.51×10^0	3.57×10^1	9.30×10^0	
52	9.20×10^0	8.50×10^0	2.85×10^0	2.05×10^1	7.44×10^0	
56	6.01×10^0	6.82×10^0	2.33×10^0	1.37×10^1	6.03×10^0	
60	4.04×10^0	5.50×10^0	1.92×10^0	1.00×10^1	4.95×10^0	2.70×10^{-4}
64	2.78×10^0	4.47×10^0	1.59×10^0	7.51×10^0	4.14×10^0	
68	1.96×10^0	3.60×10^0	1.33×10^0	5.90×10^0	3.53×10^0	
72	1.42×10^0	2.99×10^0	1.12×10^0	4.81×10^0	3.00×10^0	
76	1.04×10^0	2.46×10^0	9.34×10^{-1}	3.82×10^0	2.56×10^0	
80	7.82×10^{-1}	2.06×10^0	7.88×10^{-1}	3.11×10^0	2.19×10^0	2.20×10^{-5}
84	5.97×10^{-1}	1.69×10^0	6.69×10^{-1}	2.60×10^0	1.87×10^0	
88	4.63×10^{-1}	1.44×10^0	5.64×10^{-1}	2.14×10^0	1.61×10^0	
92	3.63×10^{-1}	1.22×10^0	4.80×10^{-1}	1.77×10^0	1.43×10^0	
96	2.90×10^{-1}	1.03×10^0	4.03×10^{-1}	1.51×10^0	1.24×10^0	
100	2.33×10^{-1}	8.60×10^{-1}	3.50×10^{-1}	1.28×10^0	1.10×10^0	4.60×10^{-6}

Table II. Dimuon production integral cross section with $p_T^{\mu} \geq p_T^{th.}$ for different processes in the rapidity region $|\eta| \leq 3.0$. The quoted cross sections are in pb.
(*) It has been assumed a luminosity $L = 10^{34}$ cm^{-2} $^{-1}$ and a bunch crossing separation $\Delta t = 15$ ns.

$p_T^{th.}$ (GeV/c)	$b\bar{b}$	$t\bar{t}$ (m=130 GeV/c^2)	$t\bar{t}$ (m=200 GeV/c^2)	Z^oZ^o	$Z^ob\bar{b}$	pile-up (*)
8	7.81×10^{0}	6.63×10^{-1}	3.32×10^{-1}	6.38×10^{-3}	3.30×10^{-2}	
10	1.5×10^{0}	3.86×10^{-1}	2.25×10^{-1}	6.21×10^{-3}	2.41×10^{-2}	2.1×10^{-4}
12	5×10^{-1}	2.29×10^{-1}	1.54×10^{-1}	5.96×10^{-3}	1.77×10^{-2}	
14	1×10^{-1}	1.39×10^{-1}	1.07×10^{-2}	5.67×10^{-3}	1.31×10^{-2}	
16	6×10^{-2}	8.58×10^{-2}	7.45×10^{-2}	5.34×10^{-3}	9.75×10^{-3}	
18	1×10^{-2}	5.40×10^{-2}	5.25×10^{-2}	4.95×10^{-3}	7.30×10^{-3}	
20	6×10^{-3}	3.47×10^{-2}	3.73×10^{-2}	4.48×10^{-3}	5.50×10^{-3}	1.6×10^{-4}
22		2.27×10^{-2}	2.67×10^{-2}	3.98×10^{-3}	4.18×10^{-3}	
24	1×10^{-3}	1.51×10^{-2}	1.93×10^{-2}	3.50×10^{-3}	3.19×10^{-3}	
26		1.02×10^{-2}	1.40×10^{-2}	2.98×10^{-3}	2.45×10^{-3}	
28		7.01×10^{-3}	1.03×10^{-2}	2.49×10^{-3}	1.89×10^{-3}	
30	7×10^{-5}	4.90×10^{-3}	7.62×10^{-3}	2.01×10^{-3}	1.47×10^{-3}	9.3×10^{-5}
34		2.51×10^{-3}	4.26×10^{-3}	1.24×10^{-3}	9.06×10^{-4}	
38		1.36×10^{-3}	2.45×10^{-3}	6.90×10^{-4}	5.70×10^{-4}	
42		7.78×10^{-4}	1.45×10^{-3}	3.60×10^{-4}	3.66×10^{-4}	1.6×10^{-5}
46		4.69×10^{-4}	8.83×10^{-4}	2.09×10^{-4}	2.40×10^{-4}	
50		2.95×10^{-4}	5.50×10^{-4}	1.50×10^{-4}	1.61×10^{-4}	5.1×10^{-8}

Table III. Four-muon production integral cross section with $p_T^{\mu} \geq p_T^{th.}$ for different processes in the rapidity region $|\eta| \leq 3.0$. The quoted cross sections are in pb.
(*) It has been assumed a luminosity $L = 10^{34}$ cm^{-2} $^{-1}$ and a bunch crossing separation $\Delta t = 15$ ns.

$p_T^{th.}$ (GeV/c)	H^o, m=200 GeV/c^2	H^o, m=400 GeV/c^2	H^o, m=700 GeV/c^2
8	3.30×10^{-3}	1.45×10^{-3}	3.60×10^{-4}
10	3.24×10^{-3}	1.43×10^{-3}	3.58×10^{-4}
12	3.14×10^{-3}	1.40×10^{-3}	3.54×10^{-4}
14	3.02×10^{-3}	1.37×10^{-3}	3.49×10^{-4}
16	2.84×10^{-3}	1.32×10^{-3}	3.43×10^{-4}
18	2.69×10^{-3}	1.28×10^{-3}	3.39×10^{-4}
20	2.51×10^{-3}	1.23×10^{-3}	3.33×10^{-4}
22	2.32×10^{-3}	1.17×10^{-3}	3.26×10^{-4}
24	2.11×10^{-3}	1.11×10^{-3}	3.20×10^{-4}
26	1.86×10^{-3}	1.06×10^{-3}	3.11×10^{-4}
28	1.62×10^{-3}	9.98×10^{-4}	3.03×10^{-4}
30	1.32×10^{-3}	9.40×10^{-4}	2.95×10^{-4}
34	7.59×10^{-4}	8.25×10^{-4}	2.79×10^{-4}
38	3.40×10^{-4}	7.17×10^{-4}	2.61×10^{-4}
42	7.07×10^{-5}	6.10×10^{-4}	2.46×10^{-4}
46	4.31×10^{-6}	5.09×10^{-4}	2.31×10^{-4}
50		4.13×10^{-4}	2.16×10^{-4}

Table IV. Four-muon production integral cross section with $p_T^{\mu} \geq p_T^{th.}$ from $H^o \rightarrow Z^oZ^o \rightarrow \mu^+\mu^-\mu^+\mu^-$ in the rapidity region $|\eta| \leq 3.0$. The quoted cross sections are in pb. The top mass has been set to 150 GeV/c^2.

(*) It has been assumed a luminosity $L = 10^{34}$ cm^{-2} $^{-1}$ and a bunch crossing separation $\Delta t = 15$ ns.

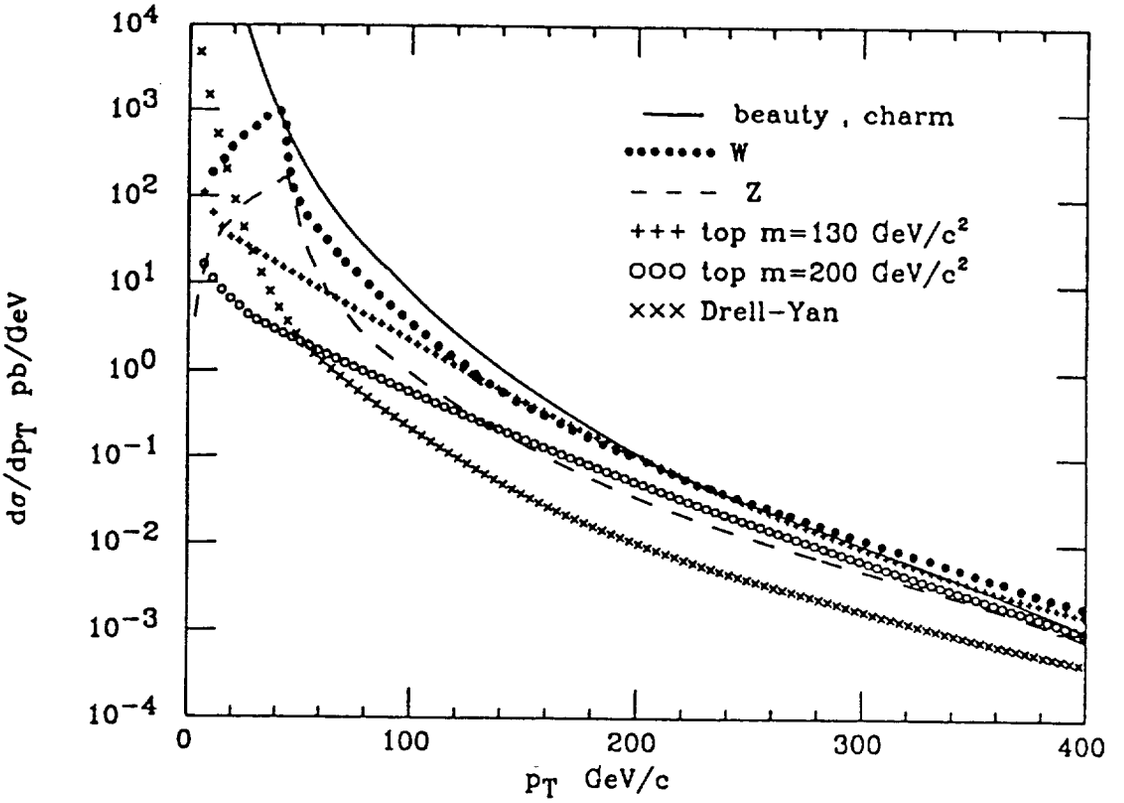


Fig. 1 Differential inclusive muon cross section production in $|\eta| \leq 3$.

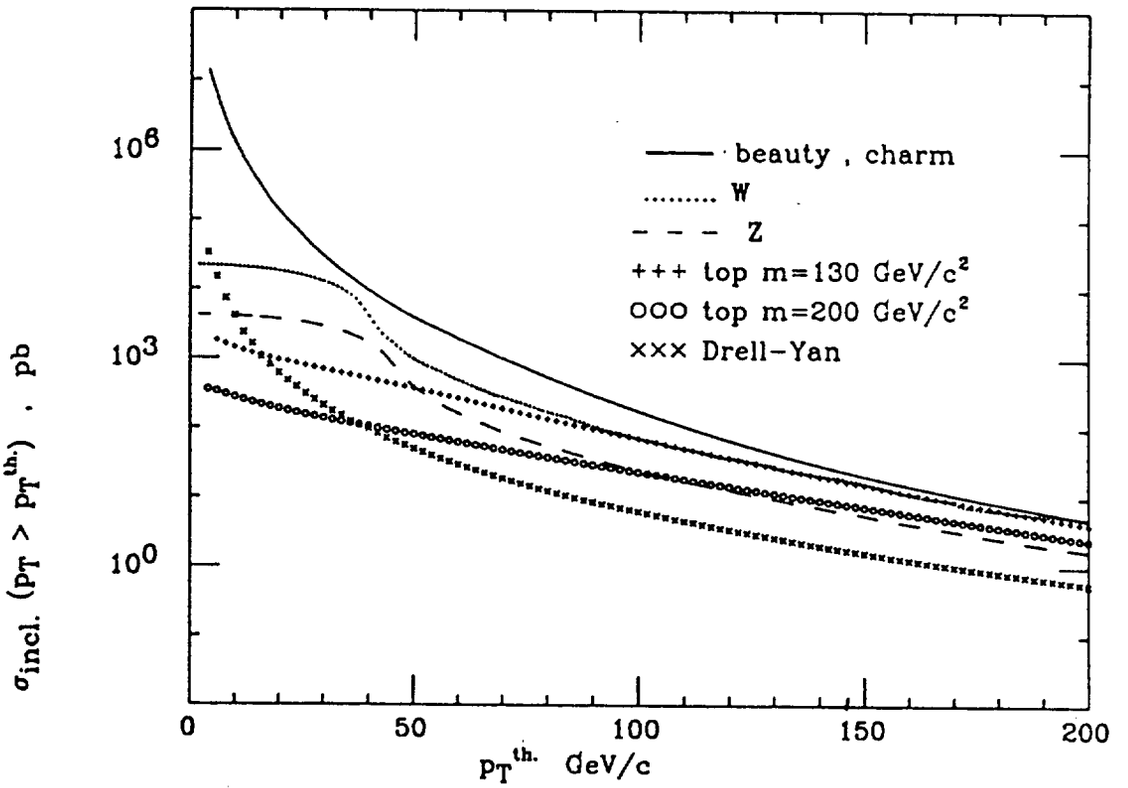


Fig. 2 Integral inclusive muon cross section production in $|\eta| \leq 3$.

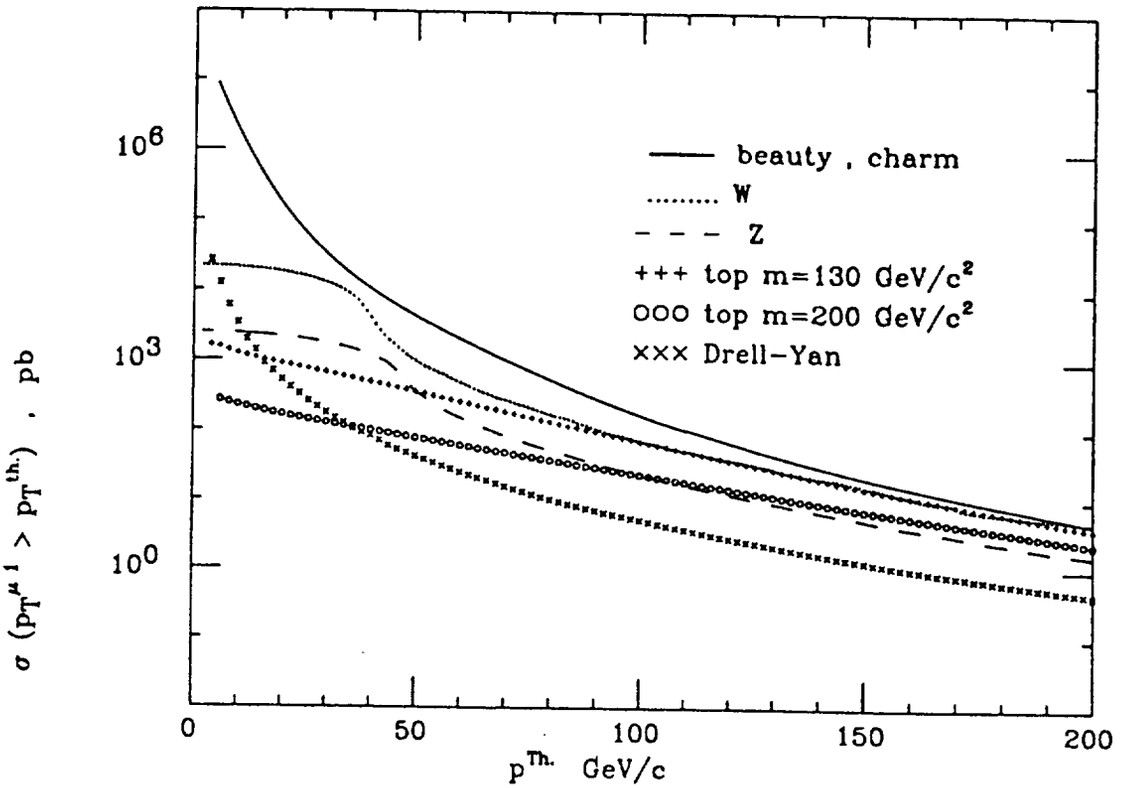


Fig. 3 Single muon production integral cross section in $|\eta| \leq 3$.

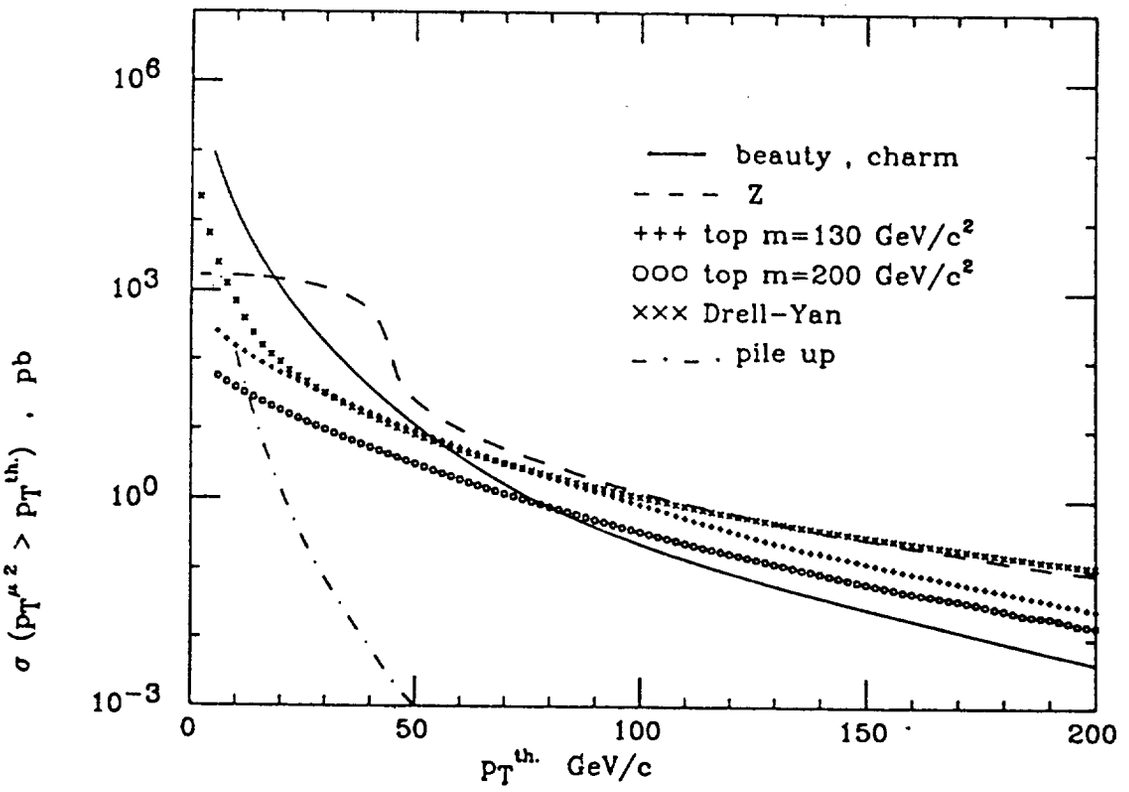


Fig. 4 Dimuon production integral cross section in $|\eta| \leq 3$.

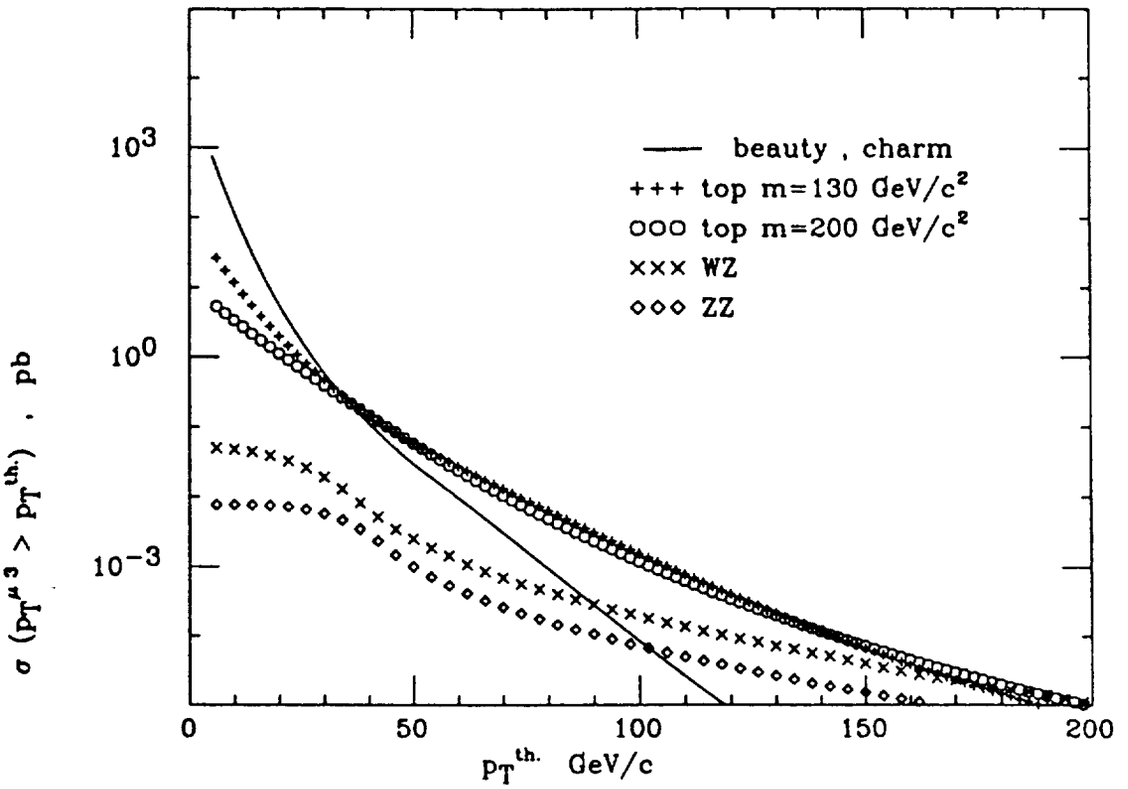


Fig. 5 Trimuon production integral cross section in $|\eta| \leq 3$.

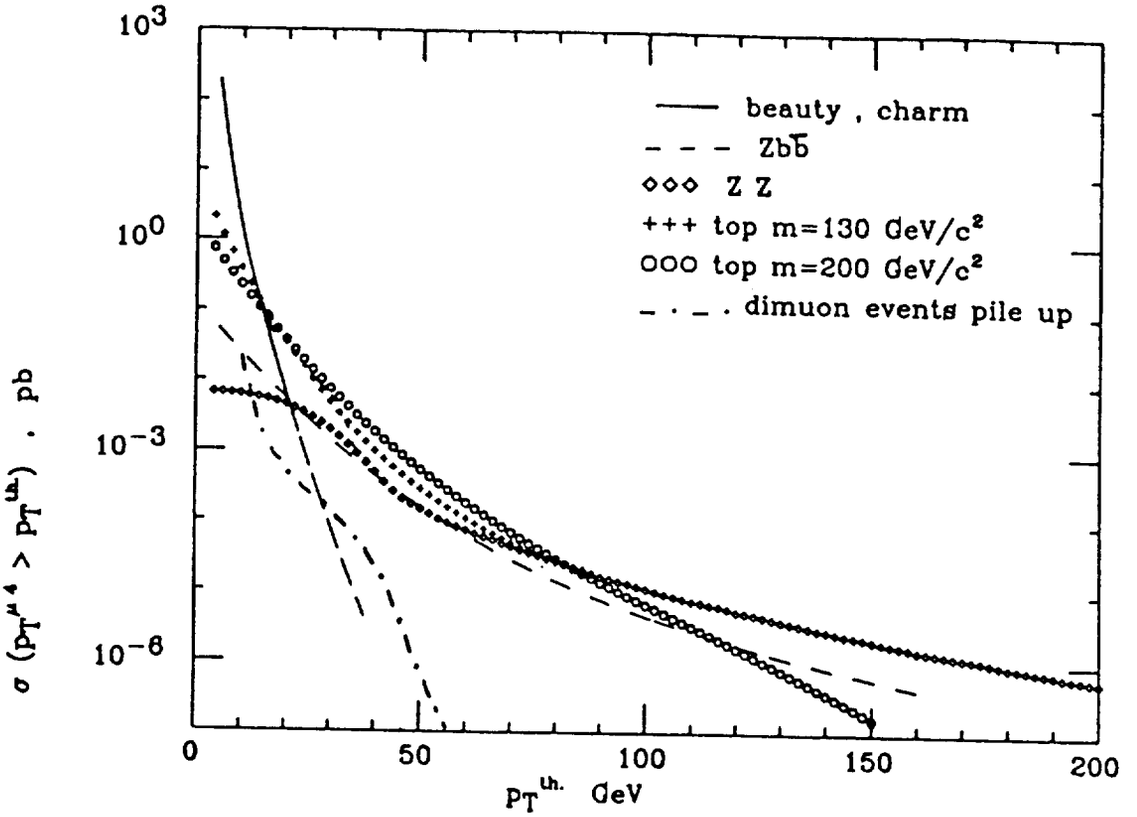


Fig. 6a Four-muon production integral cross section in $|\eta| \leq 3$.

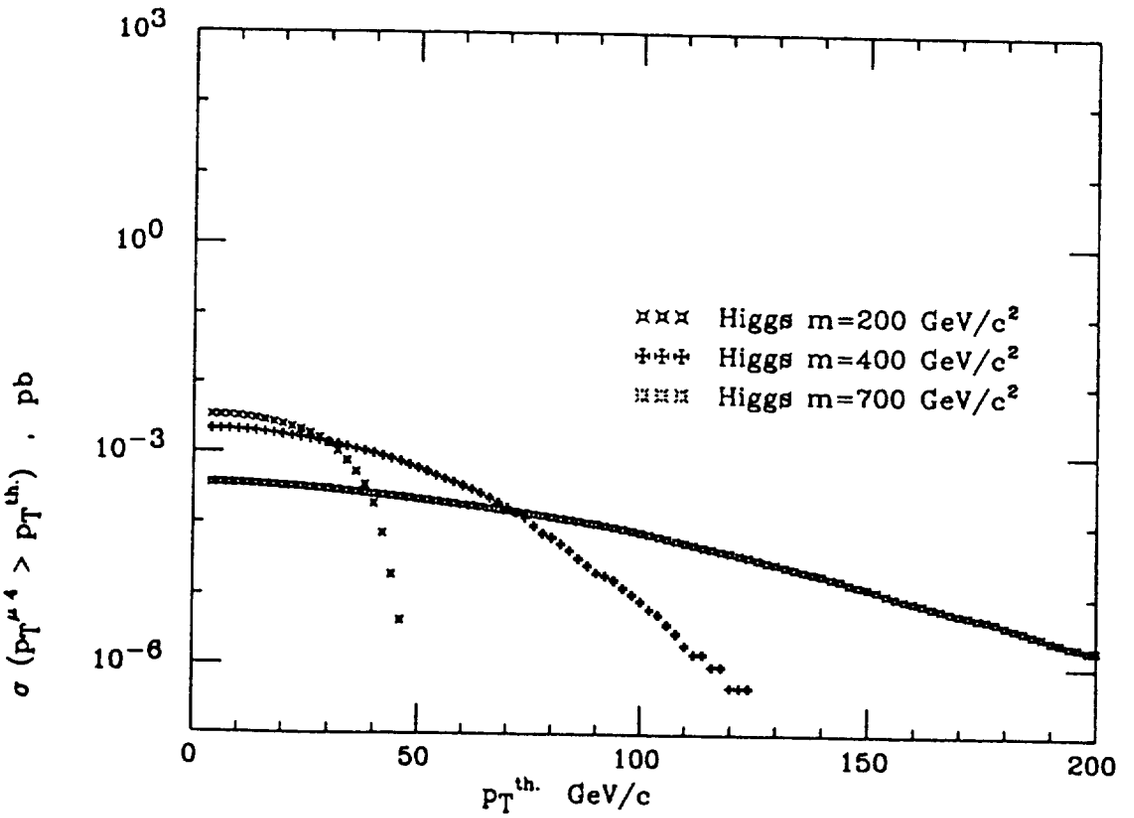


Fig. 6b Four-muon production integral cross section from $H^0 \rightarrow Z^0Z^0 \rightarrow \mu^+\mu^-\mu^+\mu^-$ in $|\eta| \leq 3$. The top mass has been set to 150 GeV/c^2.

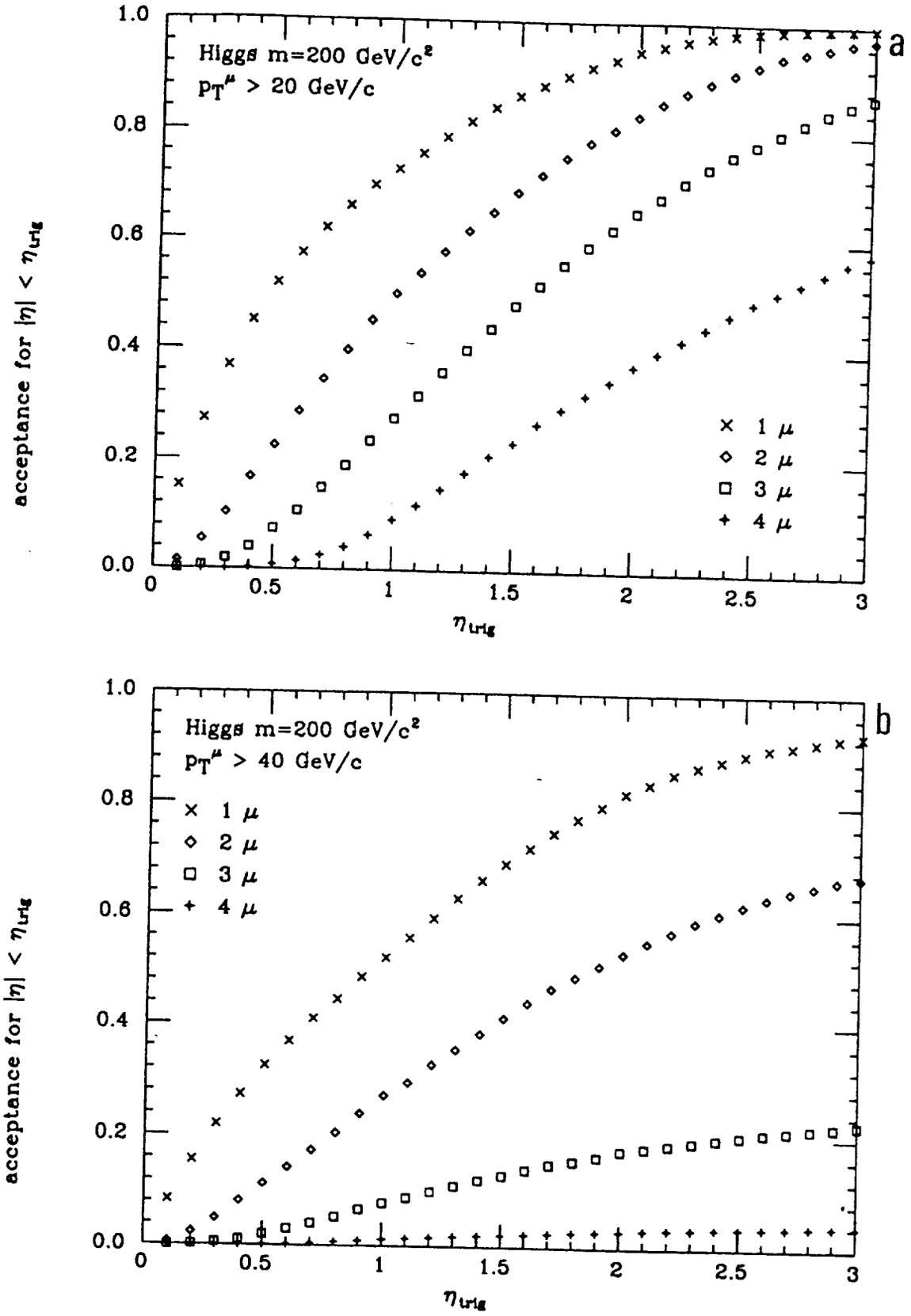


Fig. 7 Acceptance for detecting the Higgs boson through the process $H^o \rightarrow Z^oZ^o \rightarrow \mu^+\mu^-\mu^+\mu^-$ when n muons (n=1,2,3,4) are detected in the pseudorapidity region $|\eta| \leq \eta_{trig}$. The p_T cut applied for all muons is 20 GeV/c (a) and 40 GeV/c (b). The Higgs mass is 200 GeV/c^2.

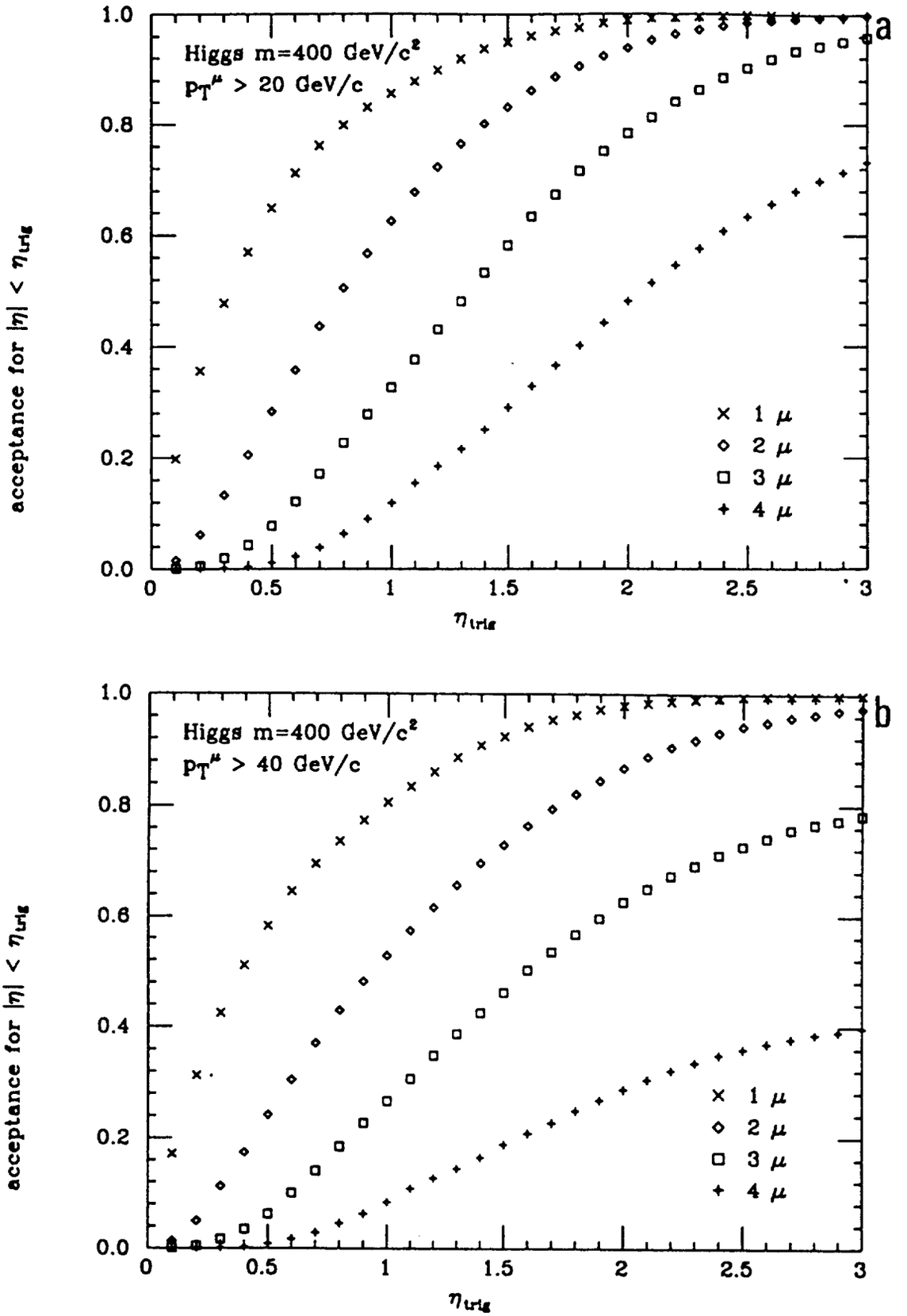


Fig. 8 Acceptance for detecting the Higgs boson through the process $H^o \rightarrow Z^oZ^o \rightarrow \mu^+\mu^-\mu^+\mu^-$ when n muons (n=1,2,3,4) are detected in the pseudorapidity region $|\eta| \leq \eta_{trig}$. The p_T cut applied for all muons is 20 GeV/c (a) and 40 GeV/c (b). The Higgs mass is 400 GeV/c^2.

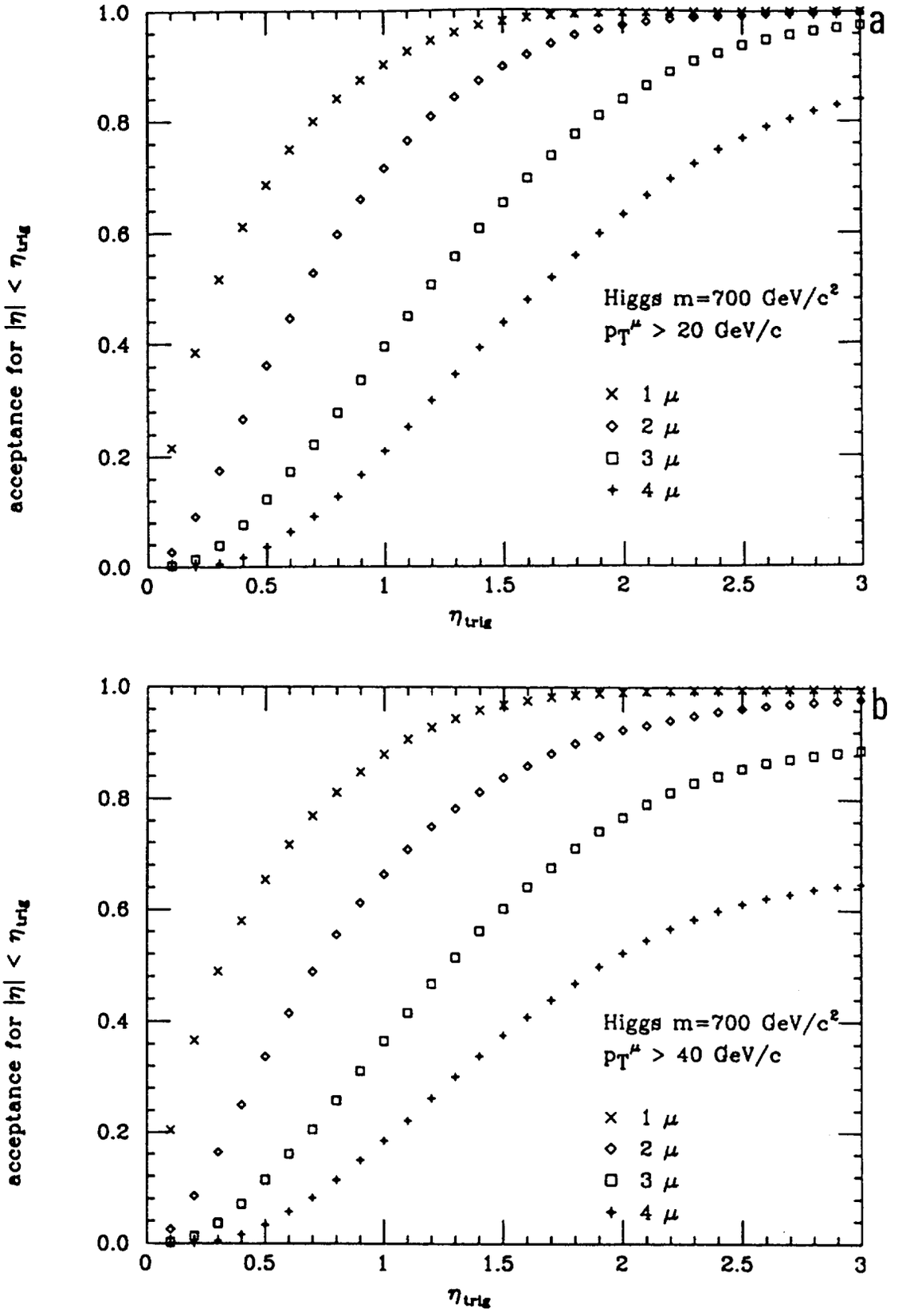


Fig. 9 Acceptance for detecting the Higgs boson through the process $H^o \rightarrow Z^oZ^o \rightarrow \mu^+\mu^-\mu^+\mu^-$ when n muons (n=1,2,3,4) are detected in the pseudorapidity region $|\eta| \leq \eta_{trig}$. The p_T cut applied for all muons is 20 GeV/c (a) and 40 GeV/c (b). The Higgs mass is 700 GeV/c^2.

Punch Through Simulations

H.Fesefeldt
III. Physikalisches Institut, Technische Hochschule Aachen,
D5100 Aachen, Germany

Abstract

Simulations of punch through probabilities at LHC energies are presented. For one of the proposed muon spectrometer (CMS) a detailed analysis of the punch through reduction at the trigger level is discussed.

1 Introduction

The rate of prompt muons at LHC is expected to be large and dominated by muons from charm and bottom decays. Muons lose their energy on the way through matter by ionization. Only at energies much above 10 GeV other processes such as bremsstrahlung, nuclear interactions and electron pair production become sigificant. Apart of these exceptionally catastrophic energy losses, the expected trajectory of a muon is well defined and its fluctuation is determined by multiple scattering and energy loss as described by the continuous slowing-down approximation. The muon signature is thus a deep penetration through matter. To make use of this fact, the leakage of charged particles from hadronic showers in the absorber (secondary decays SD and hadron punch-through HP) must be suppressed and the muons coming from decays of primary mesons (primary decay PD) must be identified. However, for a high rate and high energy enviroment like LHC, it is by no means clear how large the punch through may contribute to the rates of a muon trigger. To this end we have started a project for punch-through simulations on the IBM 3090 at the RWTH Aachen. The aim of this project is to support the experiment builders and to help in optimizing the geometric parameters and the trigger logic.

2 Programs for Punch-Through Simulations

2.1 Full shower simulations

We used for our studies the GHEISHA shower simulation program [3]. The analysis of prompt muons and the estimation of the punch through background were the primary goal for the development of this program in 1978 - 1980 for the MARK J experiment at PETRA [4]. A detailed review of this analysis has been given in ref.[1]. Using a full shower simulation, one obtains as a by-product a simulation of all calorimetric quantities. A very good agreement between simulation and mesurement of the energy flow of jets in e^+e^- interactions has been reported [5]. In 1985 the GHEISHA collision model was interfaced to the general detector simulation package GEANT [6]. This GEANT/GHEISHA version has been validated for punch through simulation in ref.[1]. As example we show in fig.1 the total punch-through probabilities, calculated with GHEISHA and with GEANT/GHEISHA, compared to experimental measurements [7]. The measurements have been obtained with an iron-scintillator calorimeter.

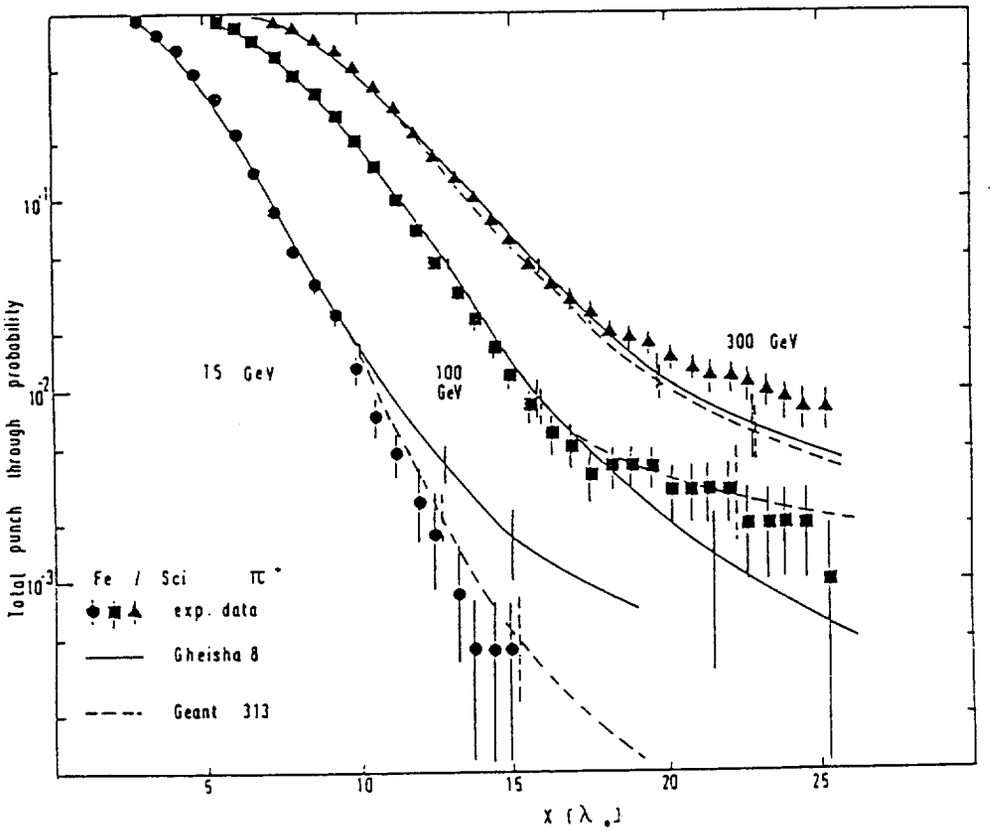


Figure 1: Total punch through probabilities as a function of the longitudinal depth for an iron-scintillator calorimeter. Shown is a comparison between experimental data and Monte Carlo results from GHEISHA and GEANT.

There are other shower simulation programs on the market (FLUKA, HETC e.g.), from which we expect a similar good agreement. As example the same data as in fig.1 have been used to compare with predictions from the FLUKA code [8]. Whereas all simulations seem to be relative precise for absorber thicknesses lower than 20 λ_0 and for punch through probabilities above $\approx 10^{-2}$, an uncertainty of a factor 2 can not be excluded for very thick absorbers ($\geq 20\lambda_0$) or punch through probabilities below 10^{-2}.

A full shower simulation with GEANT is also beeing used by the L3 collaboration in the analysis of prompt muon production in bottom decays of the Z^0 at LEP [9]. In this case the momentum of the punch through particle is measured in the outside muon spectrometer. In general a very good description of the punch through component with momenta above $\approx$ 1 GeV/c has been reported. However, for momenta in the order of a few hundred MeV an underestimation of the punch through could not be excluded.

2.2 Shower Terminators

Whereas at LEP energies it turns out to be still possible to work with full shower simulations, this seems to be a hopeless task at LHC or SSC. Thus we have developed fast shower simulations, based on a very simple terminator for the production of secondary particles. In the full shower simulation we recommend to use constant values for the energy cut-offs (E_C = 10 keV for neutrons, E_C = 100 keV for photons and E_C = 1 MeV for all other particles). The fast shower simulation, on the other hand, is based on an energy cut-off

$$E_C(z) = (1 - \frac{z}{d}) \int_0^d dz \left(\frac{dE}{dz}\right)_\mu ,$$

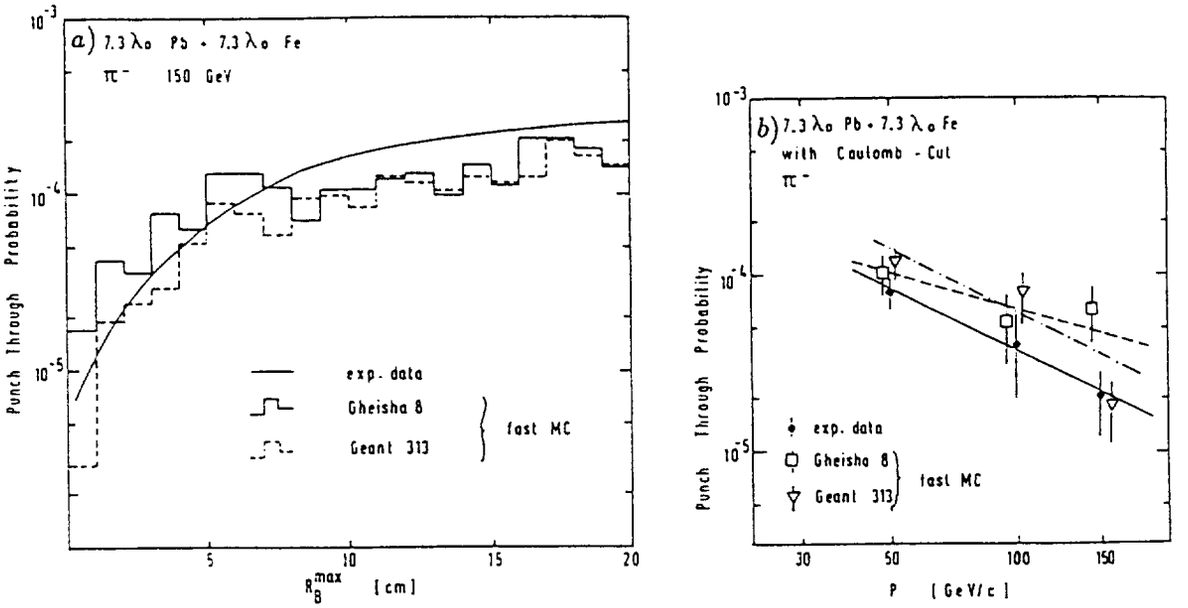


Figure 2: R^{max} distribution after a 14.6 λ_0 absorber, for an incident pion beam with 150 GeV/c momentum (a), and punch through probabilities after application of a Coulomb-cut as function of beam momentum (b). Shown is a comparison between data and predictions of fast Monte Carlo versions.

dependent on the longitudinal position of the interaction along the shower axis. z is the distance of the interaction point with respect to the front face of the absorber and d is the total absorber thickness. The integral can be understood as the total energy loss for minimum ionizing muons traversing the absorber. This fast shower simulation has been validated in detail in ref.[1]. The main conclusions can be summarized as follows. The fast shower simulation underestimates punch through consisting of low energy particles below 300 MeV. All other particles are simulated accurately. Since in most applications such low energy particles will be cut out in the off-line analysis in any case, the fast shower simulation is well suited for applications in muon identification.

An example is given in fig.2a. Shown is the distribution of the quantity

$$R^{max} = \sqrt{(x^{max})^2 + (y^{max})^2},$$

where x^{max} and y^{max} are the largest x and y values from all hits with respect to the beam line. The beam line corresponds to the shower axis. Since in most cases there is only one track, R^{max} can be simply understood as the radial distance from the shower axis. The results shown have been obtained for an incident pion beam at 150 GeV, after an absorber of in total 14.6 λ_0 thickness [10]. Comparisons with fast simulations from GHEISHA and GEANT are shown. We observe some underestimation by the simulations at large distances from the shower axis, which is clearly correlated with missing low energy particles. Close to the shower axis, on the other hand, the GEANT simulation describes very accurate the data, the GHEISHA simulation predicts slightly too high values.

Cutting at the R^{max} values, compatible with multiple scattering of muons, and using a second measurement at an equivalent station after 7.3 λ_0, the punch through probabilities as shown in fig.2b have been obtained.

Another example, which will be quite useful for our later discussions, is a beam dump

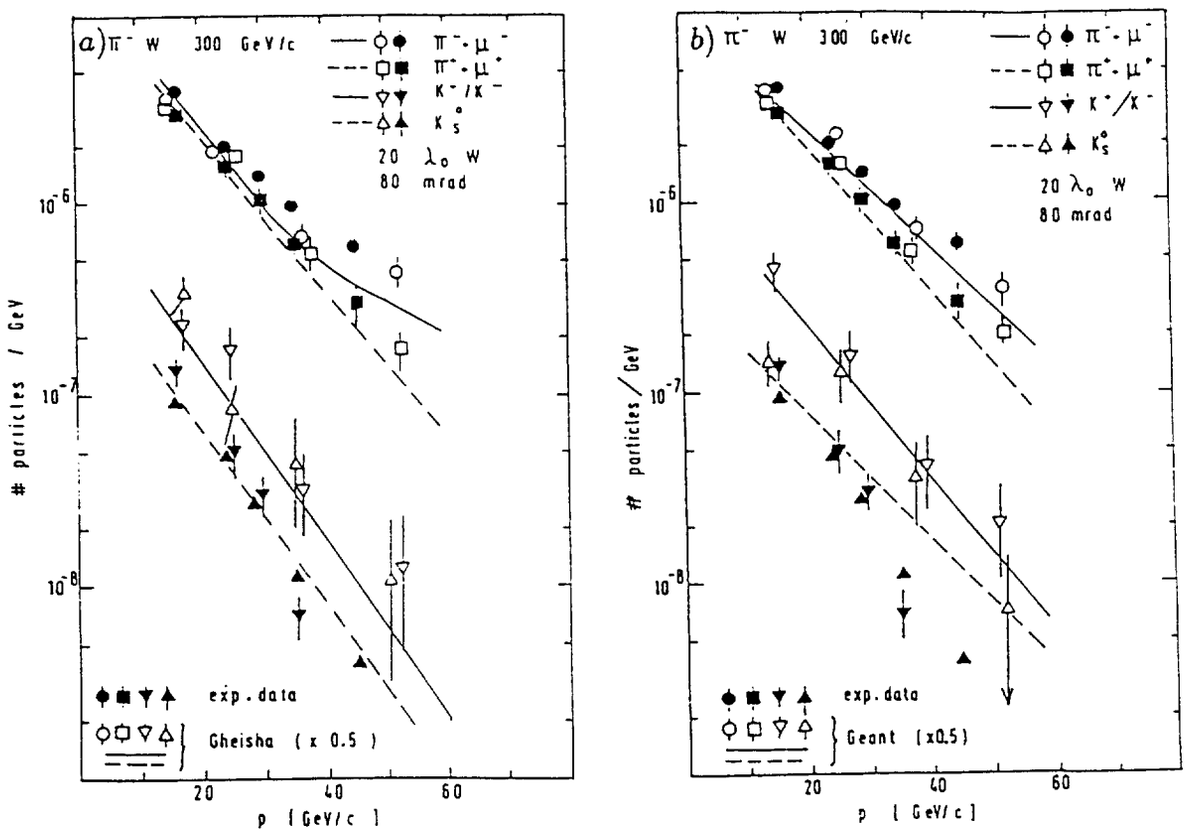


Figure 3: Momentum spectra of secondary particles in a 300 GeV beam dump after a 20 λ_0 tungsten absorber: (a) comparison between data and the results of the GHEISHA Monte Carlo simulation, (b) the same for the GEANT Monte Carlo simulation.

experiment at CERN. The beam dump consisted of a 200 cm long iron target, with a tungsten core of the same length. Thus the punch through is measured at 20 λ_0 absorber thickness. Outgoing particles were measured in the NA3 spectrometer [11]. Due to acceptance limitations, experimental data were only given for momenta above 15 GeV/c and for laboratory production angles of less than 80 mrad with respect to the beam line. With this energy cut-off of $E_C = 15$ GeV we were able to produce ≈ 5 Million showers for each of the two Monte Carlo programs, GHEISHA and GEANT respectively, within reasonable computer time. The results for the energy spectra are shown in fig.3, for the sum of secondary decay muons and pions, for neutral kaons and for the average of charged kaons. Unfortunatively muon/pion seperation was not possible in the experimental analysis. Note that the Monte Carlo results had to be scaled down by a common factor of 2 in order to roughly agree with the data. This is the same degree of uncertainty as was concluded already in the discussion of fig.1. On the other hand, the GHEISHA results (fig.3a) and the results from GEANT (fig.3b) agree perfectly with each other.

Summarizing our results, we may conclude, that the simulation is exact at the 10% level for absorbers not deeper that 10 λ_0. For 20 λ_0 absorbers, on the other hand, we have observed in some comparisons with experimental data an underestimation (see e.g. fig.1), in other comparisons an overestimation (see e.g. fig.2 and fig.3). The uncertainty is in the order of a factor 2.

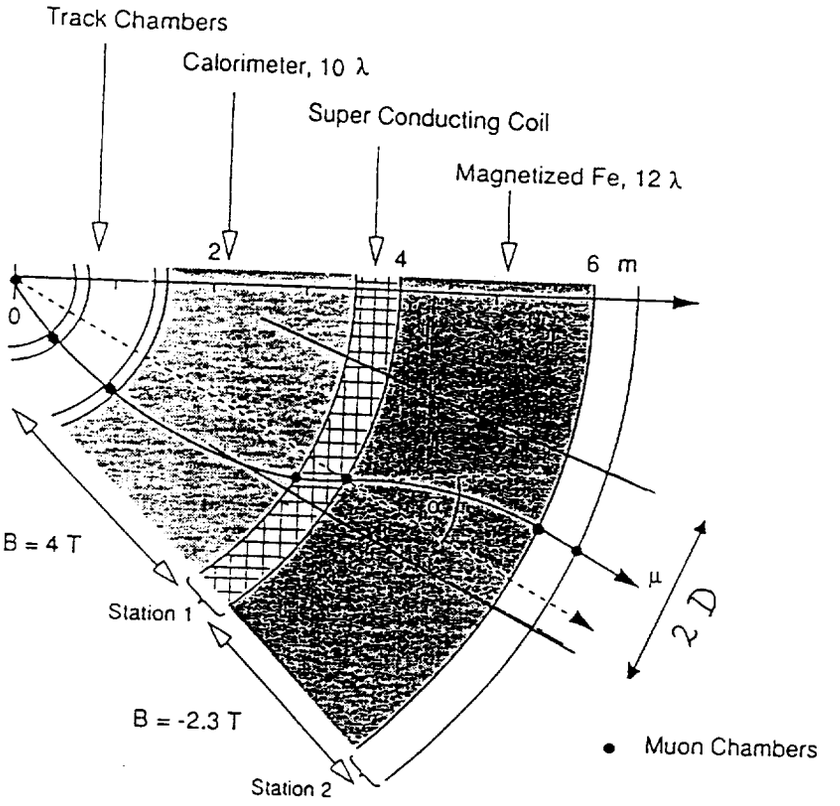


Figure 4: Layout of the CMS muon spectrometer.

3 Simulation Studies for a Compact Muon Spectrometer

3.1 Design concept of the CMS

The fast shower simulation (see section 2.2) has been used for simulation studies of a compact muon spectrometer (CMS) for LHC (see also ref.[2] and the contribution to this conference by M.Della Negra [12] and M.Pimia [13]). The basic concept of this detector is shown in fig.4. It consists of a cylindrical arrangement of a central track chamber, a 10 λ_0 hadron calorimeter, a superconducting coil, which provides a 4 Tesla magnetic field in the inner part of the detector, and a -2.3 Tesla magnetic return field in an additional hadron absorber consisting of magnetized iron. Two stations of muon chambers are located before and behind the coil (station 1) and behind the magnetized iron absorber (station 2) respectively. The deflection α_1 of a track in station 1 is used to measure the momentum and the measurements in station 2 are used to identify the particle as a muon. These two measurements are extremely simple and can thus be analysed already in an on-line trigger. The punch through reduction by such a trigger should be discussed in the following.

Before doing this, we have to discuss two special punch through reduction capabilities of this spectrometer, namely once the strong magnetic field and second the timing between station 1 and station 2. In strong magnetic fields the longitudinal range in shower direction of low energetic secondary particles is strongly reduced, thus giving rise to a considerable reduction of punch through. Examples of comparisons with and without magnetic fields are given in the contribution by M.Della Negra [12]. A second punch through reduction is obtained by a fast time gate in the trigger between station 1 and station 2. As a general observation it turns out, that a fast shower component and a second component, extending to a few hundred nanoseconds, can be clearly distinguished. This fact can be used also for electron/pion separation (see e.g. ref [3]). In all our following studies we have applied a time gate of 50 nsec between the trigger in station 1 and station 2. This trigger cancels the punch through of accidental slow hits in one station in

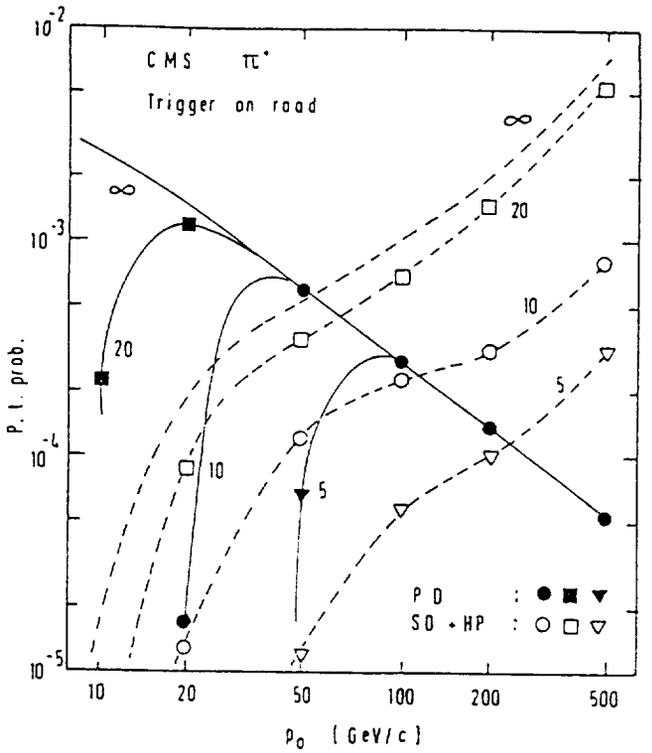


Figure 5: Punch through probabilities without (∞) and with a trigger on all hits within a road of 20, 10 and 5 cm half width respectively.

coincidence with normal fast punch through in the other station. We have estimated, that both effects, the strong magnetic field and the time gate, add up to a punch reduction factor 4.

3.2 Punch through reduction at trigger level

The punch through probabilities in station 2 of the CMS detector are shown in fig.5 by the curves labelled with ∞. Plotted are simulation results for positive pions as function of the incident momentum p_0. The secondary decay component and the hadron punch through is combined. Comparing theses results with the measurements and simulations at 22 λ_0 of fig.1, we may verify the factor 4 of punch through reduction as quoted above in the previous subsection. Thus the results of fig.1 and fig.5 are fully compatible with each other.

A strong further reduction of this punch through rate can be obtained by applying a momentum cut-off. This can be achieved at the trigger level by defining a road, given by the half-width D with respect to the track at station 2 (see fig.4 for explanation). This road is defined in both directions, transverse and along the beam line. We select all hits in stations 1 and 2, enclosed in this road, and demand a trigger in coincidence of all four chambers. The punch through reduction is shown in fig.5, for three half-widths D of the road. It is seen, that a momentum cut-off of $p_0 \approx 15$ GeV/c, 30 GeV/c and 60 GeV/c is obtained for $D = 20$ cm, 10 cm and 5 cm respectively. Here and in all following figures error bars have not been drawn. The statistical errors are always smaller than the systematic errors, which has been estimated to be in the order of a factor 2 for a 22 λ_0 absorber (see section 2.2). Thus there may be an uncertainty of a factor 2 in the vertical scales of all following figures.

A good choice seems to be a half-width $D = 10$ cm. Then the trigger reduces the secondary decay muons and the hadron punch through by approximately one order of magnitude. As can be seen in fig.5, the definition of a road does not introduce a sharp momentum cut-off. Thus

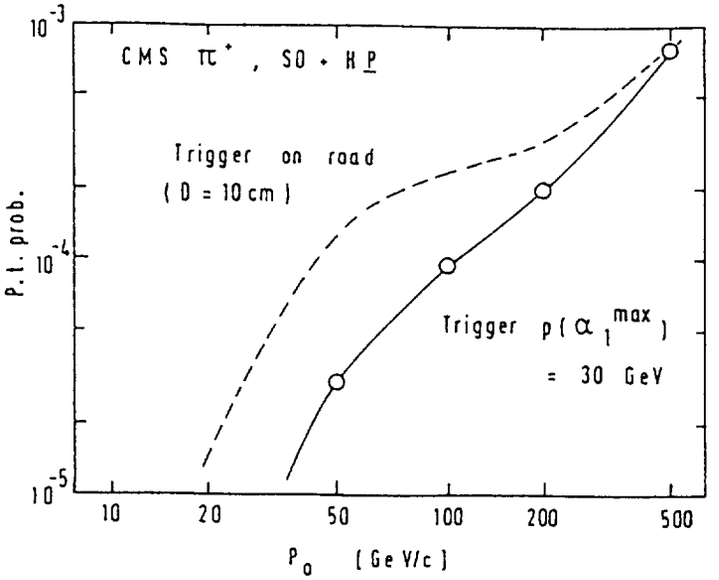


Figure 6: Punch through probability as expected for a road of 10 cm half-width, with an additional cut on the deflection angle α_1, corresponding to 30 GeV/c momentum.

we measure additionally the deflection angle α_1 (see fig.4 for definition), and determine the momentum by the simple formula

$$p_1 = \frac{2.16892}{\alpha_1}.$$

This definition introduces a sign for the momentum, if the deflection angle α_1 is measured with a sign. Thus a positive value for p_1 corresponds to a positive charged particle and negative value of p_1 to a negative charged paricle. For each muon candidate in station 2 there may be more than one corresponding track in station 1. Thus the calculation of the deflection angle α_1 is not unique. We have chosen the minimum value of all combinatorically possible combinations of hits in the two chambers of station 1. In fig.6 we show our results for the cut on the momentum p_1 = 30 GeV, defined by α_1. We observe a further suppression of the punch through by an order of magnitude, especially for low energetic incident pions.

All calculations have been repeated for negative pions and kaons of either charge as incident particles. The results are very similar as for positive pions, with one exception. Kaons show in general a much higher punch through rate as pions, not only for the primary decay component, but also for the secondary decay component and the hadron punch through. As a simple rule it turns out that the punch through probability of all three components, primary decay, secondary decay and hadron punch through combined, is approximately given by $1.5 \cdot 10^{-3}$ for kaons and $5.0 \cdot 10^{-4}$ for pions, nearly independent on the momentum p_0.

We conclude this subsection by the statement, that, combining the effects of strong magnetic fields with a trigger discussed above, the secondary decay muons and the hadron punch through can be reduced by approximately 2 orders of magnitude, compared to the results of fig.1. The determination of this reduction factor is not significantly influenced by the overall uncertainty of the simulation.

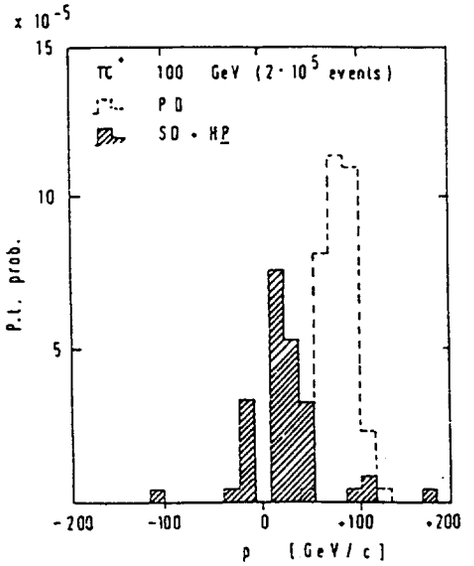


Figure 7: Measured momentum spectra of primary decay muons and secondary decay muons and hadron punch through combined.

3.3 Parametrization of the measured momentum spectra.

The probability for a decay in a free path L can be written as

$$P_{PD}(p_0, x \leq L) \approx \frac{mL}{c\tau p_0},$$

where p_0 is the momentum of the primary particle. The momentum distribution of the decay muons is uniform within fixed limits. The distribution, measured within a trigger road of 10 cm half width, is however distorted and looks more similar to a Gaussian. As illustration we show in fig.7 the measured momentum spectra of primary decay muons and the sum of secondary decays and hadron punch through from 100 GeV pions. From our simulation we get (all units in GeV):

$$P_{PD}(p|p_0) = \frac{1}{\sqrt{2\pi}\sigma_{PD}} exp[-(p - a_{PD}(p_0))^2/2\sigma_{PD}(p_0)],$$

with

$$a_{PD}(p_0) = \begin{cases} q_0(8 + 0.68p_0) & for \quad \pi^{\pm} \\ q_0(10 + 0.56p_0) & for \quad K^{\pm}, \end{cases}$$

and

$$\sigma_{PD}(p_0) = \begin{cases} 0.17p_0 & for \quad \pi^{\pm} \\ 0.25p_0 & for \quad K^{\pm}. \end{cases}$$

q_0 is the charge of the incident pion or kaon.

The total rate for the secondary decays and hadron punch through, as measured in a road of 10 cm half width, can be parametrized by

$$P_{SD+HP}(p_0) = \begin{cases} 5 \cdot 10^{-5} + 1.36 \cdot 10^{-6}p_0 & for \quad \pi^{\pm} \\ 5 \cdot 10^{-5} + 3.40 \cdot 10^{-6}p_0 & for \quad K^{\pm}, \end{cases}$$

with a gaussian momentum distribution, the parameters of which are:

$$a_{SD+HP}(p_0) = \begin{cases} q_0 11.2 & for \quad \pi^{\pm} \\ q_0 19.6 & for \quad K^{\pm}, \end{cases}$$

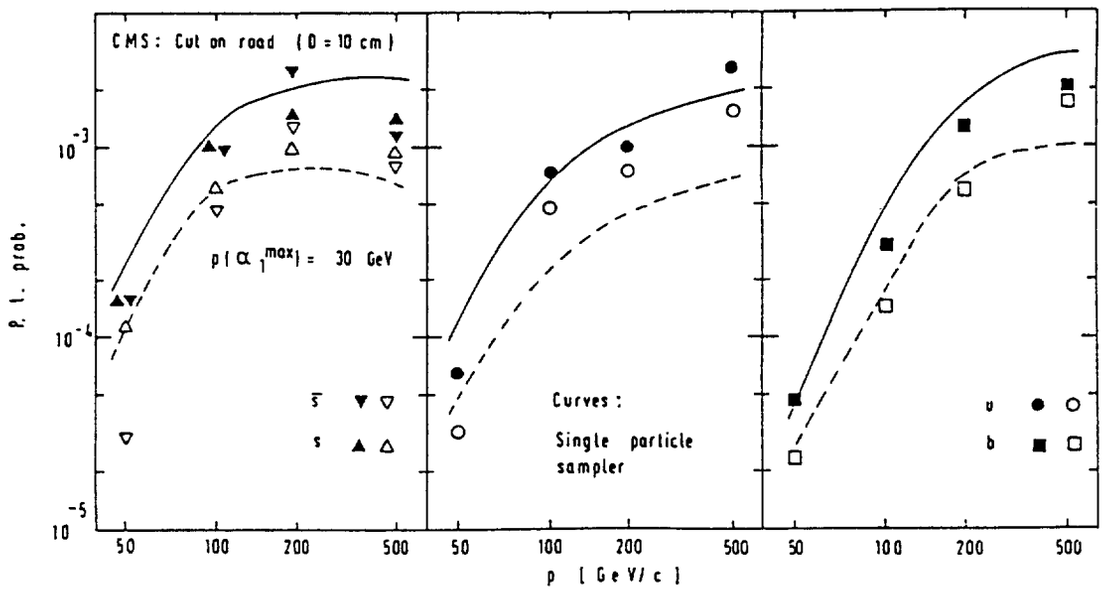


Figure 8: Punch through probabilities for jets as incident particles. Shown are the results with a trigger on hits in a road of 10 cm half width (full points) and additionally with a cut on the deflection angle α_1 corresponding to 30 GeV/c (open points). The curves are explained in the text.

$$\sigma_{SD+HP}(p_0) = 0.36 p_0 \quad for\ \pi^{\pm}\ and\ K^{\pm}.$$

This parametrization indicates, that the average momentum of the secondary decay muons and the hadron punch through does not depend on the incident momentum p_0. Starting from this numbers we have written a small sampler for the probability distribution $P(p, p_0, q_0)$ of the momentum for secondary punch through particles. This sampler will be used in the next subsection to compare with our simulation results for jets.

3.4 Simulation of the punch through in jets

The analysis of section 3.2 has been repeated for jets as incident particles. We have chosen u and b quarks to compare with pions and $\bar{s}$ and s quarks to compare with positive and negative charged kaons respectively. The prompt muons in b quarks have been reconstructed without serious problems. The confusion of punch through hits in station 1 in connection with a prompt muon track in station 2 is negligible small. However, as has been discussed in section 2.2, we used a fast simulation for the shower development in the hadron calorimeter. This simulation underestimates spurious hits from low energetic punch through particles in station 1. A reliable answer of the confusion problem in momentum reconstruction of prompt muons can not be obtained with this simulation.

The results for the total punch through probablities after the trigger condition within a road of 10 cm half width are shown as full points in fig.8. A further cut on the deflection angle α_1, corresponding to a momentum of 30 GeV/c, yields the values as shown as open points in fig.8. The punch through reduction, compared with the total punch through without any trigger conditions, is about a factor 50 at 50 GeV and a factor 10 at 500 GeV jet energy.

As a small exercise we have used a single particle punch through sampler to predict the punch through from jets as incident particles. To this end we assigned to each track of a jet a punch through probability and a measured momentum as calculated by the formulas of section

3.3. The results are shown as curves in fig.8. Without any additional confusion from other tracks of the jets, we would expect agreement between the results of the sampler and the results of the simulation. This agreement is observed for $\overline{s}$ and s quarks (left part of the figure) and for b quarks (right part). Only for u quarks (middle part of the figure) there is a small indication of a confusion problem.

4 Summary

Simulations of punch through probabilities at LHC energies have been presented. Fast Monte Carlo codes with shower terminators, which depend on the distance from the muon chambers, have been used. The uncertainty of such methods for muon identification is in the order of a factor 2. An analysis of the punch through reduction by a fast trigger has been discussed. It was shown that in the CMS muon spectrometer the punch through from secondary decays and hadrons may be suppressed by up to two orders of magnitude, in the energy range from 50 to 500 GeV. Compared to the expected large rate of prompt muons from charm and bottom decay the remaining punch through contribution is negligible.

References

[1] H.Fesefeldt, Th.Hamacher and J.Schug, Nucl. Instr. and Meth. A292 (1990) 279;

[2] M.Della Negra et al., Study of muon triggers and momentum reconstruction in a strong magnetic field for a muon detector at LHC, CERN/DRDC/90-36, August 1990;

[3] H.Fesefeldt, The Simulation of Hadronic Showers -Physics and Applications-, RWTH Aachen Report PITHA 85/02 (1985);

[4] B.Adeva et al., Phys.Rev.Lett. 51 (1983) 443; B.Adeva et al., Phys.Rev. D34 (1986) 681;

[5] J.Schug, PhD thesis, RWTH Aachen 1988, unpublished;

[6] R.Brun, F.Bruyant, M.Maire, A.C.McPherson and P.Zanarini, GEANT3, CERN DD/EE/84-1 (1986);

[7] F.S.Merrit et al., Nucl. Instr. and Meth. A241 (1985) 43;

[8] H.J.Möhring, Proc. International Conference on Calorimeter Simulation, KFA Jülich (1988);

[9] L3-Collaboration, B.Adeva et al., Phys.Lett. 241B (1990) 416;

[10] D.Green et al., Nucl. Instr. and Meth. A244 (1986) 356;

[11] J.Badier et al., Nucl. Instr. and Meth. A249 (1986) 251;

[12] M.Della Negra, Contribution to this workshop (1990);

[13] M.Pimia, Contribution to this workshop (1990);

Muon trigger and identification

DRDC proposal P7

CERN[1]- Helsinki[2] - Kiel[3] - Madrid(CIEMAT)[4] - Padua[5] - Rome(La Sapienza)[6] - Rome(Tor Vergata)[7] - Riverside[8] - UCLA[9] - Vienna[10]

C. Bacci[6], A. Bettini[5], R. Cardarelli[7], S. Centro[5], F. Ceradini[6], G. Ciapetti[6], D. Cline[9], D. Dau[3], M. Della Negra[1], L. Di Lella[1], A. Di Ciaccio[7], K. Eggert[1], A. Ferrando[4], W. Gorn[8], A. Hervé[1], V. Karimäki[2], R. Kinnunen[2], F. Lacava[6], J. Layter[8], S. Lazic[9], R. Martinelli[5], A. Meneguzzo[5], M. Mohammadi[9], A. Nisati[6], J. Park[9], E. Petrolo[6], M. Pimiä[2], L. Pontecorvo[6], R. Santonico[7], B.C. Shen[8], F. Szoncso[10], E. Torrente-Lujan[4], J. Tuominiemi[2], S. Veneziano[6], G. Walzel[10], F. Wittgenstein[1], C.- E. Wulz[10], L. Zanello[6], P. Zotto[5]

presented by M. Della Negra
CERN, Geneva, Switzerland

1. MUON RATES AND PUNCH-THROUGH SIMULATIONS

The inclusive rate from prompt muons is large at LHC and is dominated at all transverse momenta values, P_T, by muons from charm and bottom decays [1]. Such muons are generally contained in jets. At 10^{34} $cm^{-2}s^{-1}$ luminosity and for P_T >5 GeV/c (natural cut due to ranging out in the absorber) the prompt muon rate in the central rapidity region, $|\eta| < 3$, is 10^5 Hz. For $P_T > 40$ GeV/c the inclusive muon rate drops down to 100 Hz. For $P_T > 20$ GeV/c the dimuon rate is dominated by inclusive Z production and is about 10 Hz.

Muon backgrounds associated with beam-beam collisions result from π or K decays before the absorber (primary decays), from decays inside the absorber of shower secondaries (secondary decays) and from leakage of hadron cascades through the absorber (punch-through). Backgrounds associated with beam halo and cosmic rays are not considered here.

To estimate the input rate to the trigger due to background we define a model LHC detector, which consists of a free cylinder for tracking of 1.3m radius and 4.4m in length, followed by a hermetic calorimeter: A barrel calorimeter of 10 interaction lengths (λ) closed by endcap calorimeters of 16λ. The transition between barrel and end-caps is at $|\eta| = 1.3$. With this cylindrical geometry the total thickness of the absorber varies as a function of the polar angle, θ, and reaches a maximum of 20λ at $\theta = 30^o$ (η=1.3). The rate due to primary decays in the inner region follows from the charged hadron rate at LHC. The rate due to secondary decays and hadron punch-

through requires either Monte-Carlo simulations or parametrisations of existing punch-through data.

H. Fesefeldt has shown that a fast version of GEISHA implemented in GEANT can reproduce a variety of punch-through measurements [2]. In Fig. 1 we show the integral punch-through probability of single pions after an absorber of 16.3λ as a function of the pion momentum, predicted by this Monte-Carlo. In this example the absorber starts at a distance L_T = 80 cm from the pion starting point and is operated without magnetic field (Fig. 1a) or with a magnetic field (Fig. 1b, B=4 Tesla). The three components from primary, secondary decays and punch-through hadrons are shown separately. The component from primary decays dominates at low P_T hadrons. Above 40 GeV/c the other two components dominate and are roughly of equal importance. One can also see that the magnetic field has the effect of reducing the contributions from secondary decays and hadrons by an order of magnitude for pions below 20 GeV/c. This can be understood because these two backgrounds are dominated by soft hadrons and muons.

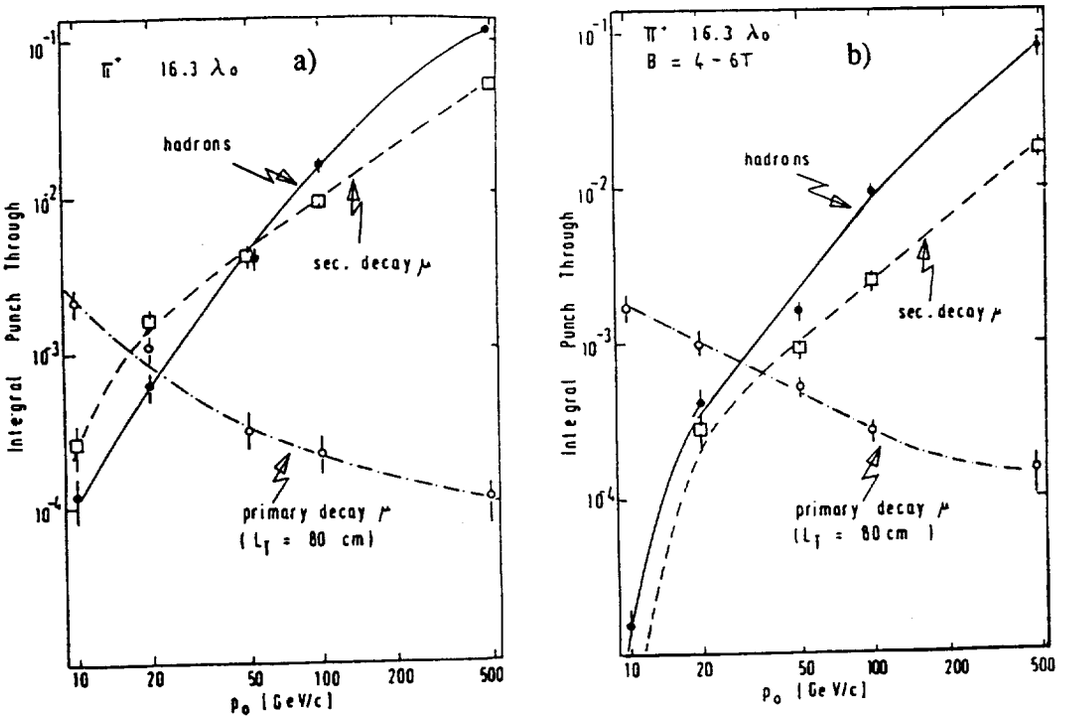


Fig. 1 : Integral punch-through probabilities for pions as a function of incident momentum simulated for a compact muon solenoid detector with B = 4 Tesla,

a) after 16.3 λ_0 of absorber no magnetic field,

b) same with magnetic field switched on.

A parametrisation of the integral punch-through probability as a function of material, input momentum and depth, with separate terms for the hadronic and secondary decay components, has been proposed at this workshop by F. Lacava [3]. As observed experimentally and in agreement with the full shower simulations, the two components have a different dependence on the depth of absorber: After 20λ the hadronic component becomes negligible and only muons from secondary decays can escape the absorber.

Fig. 2 shows the rate of charged hadrons (full line) as a function of the polar angle predicted by ISAJET for two-jet events with P_T^{min} = 5 GeV/c and for a luminosity of 4. 10^{34} $cm^{-2}s^{-1}$. The dashed line is the corresponding decay rate for the model LHC detector previously described. The dotted line is the punch-through rate deduced from the above parametrisation. The dip in the punch-through rate at θ = 30° corresponds to the maximum length of absorber. In the barrel region region the rate is of order 10^6 Hz. The rate is increasing fast in the forward region. If one wants to trigger up to |η| = 3 (θ = 5°) the rate increases to 10^7 Hz.

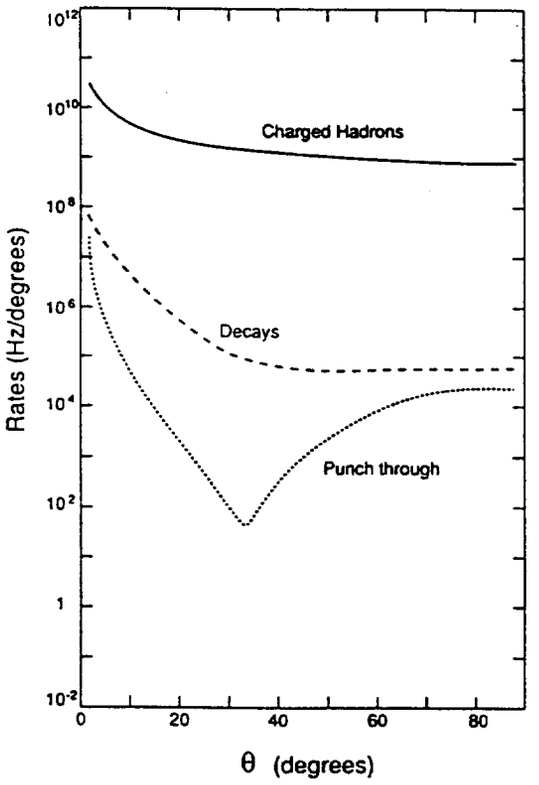


Fig. 2 : Expected rates at $4.x10^{34}$ $cm^{-2}s^{-1}$ luminosity from charged hadrons (full line), π-K decays (dashed line)and hadron punch through (dotted line) as a function of the polar angle.

The energy spectrum of the muons escaping thick absorbers (≥ 20λ), produced by incident hadrons of various momenta, has been measured in neutrino experiments at Fermilab and a parametrisation based on a scaling law in $z = P^{\mu}/P^{h}$ is reported by D.

Green in ref. [4]. Fig.3 shows the predicted energy spectrum of muons escaping an absorber of 16.3λ, with and without magnetic field, produced by pions of 20 GeV/c, using the punch-through simulations of ref. [2]. Two component are clearly visible: The flat hard component, 8 GeV < E < 16 GeV, comes mainly from primary decays. The soft component part of the spectrum (E < 8 GeV) is due to secondary decays and is in agreement with the parametrisation of ref [4] (full curve).

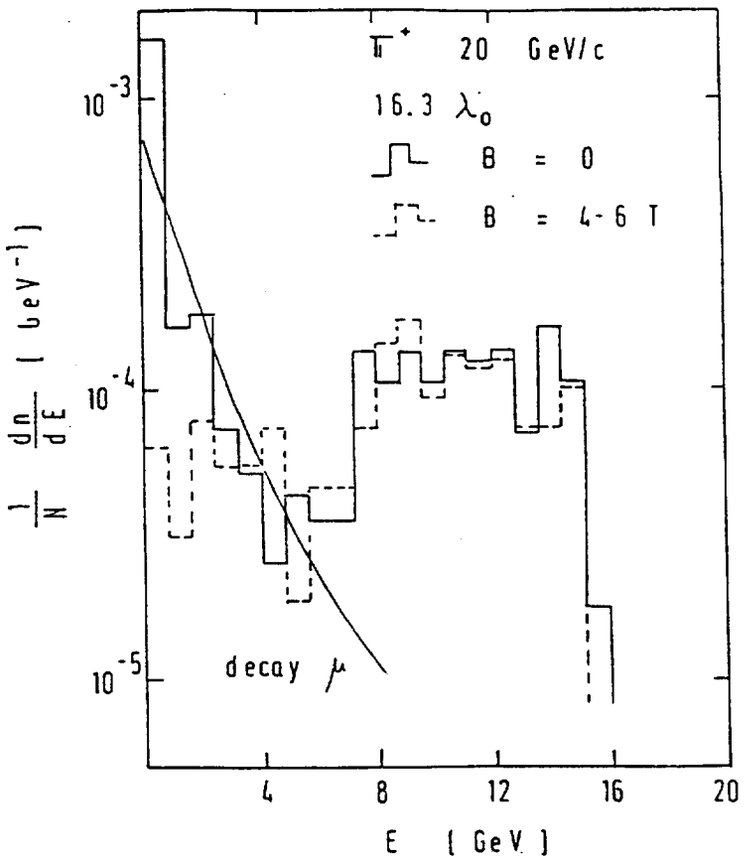


Fig. 3 : Energy spectrum of the decay muons produced by 20 GeV pions after 16.3λ of absorber with magnetic field on (dashed histogram) and off (full histogram). The full line is a parametrization from ref [4].

Fig. 4 shows, for the central region $|\eta| < 3$, the P_T spectrum of jets, mainly responsible for the backgrounds from punch-through and from hadrons decaying into muons. The π and K decay background is compared with the prompt muon rate. For $P_T > 5$ GeV/c the π/K decay rate falls below the prompt muon rate from charm and bottom decays.

The estimate of the surviving punch-through background as a function of P_T is more difficult. Full simulations require too much computer time and existing parametrisations [4] are imprecise for low values of P^{μ} and P^{h}. In Fig. 4 we only indicate by an arrow the integrated punch-through rate, which has been estimated for our model LHC detector, with and without a magnetic field, using the punch-through probabilities of Fig. 1. For $P_T > 5$ GeV/c and at 10^{34} $cm^{-2}s^{-1}$ luminosity, the

contributions to the total rate from prompt muons, primary decays and punch-throughs are roughly of equal importance and of order 10^5 - 10^6 Hz. The P_T spectrum of muons resulting from secondary decays is expected, in general, to be softer than the one from primary decays (dotted curve).

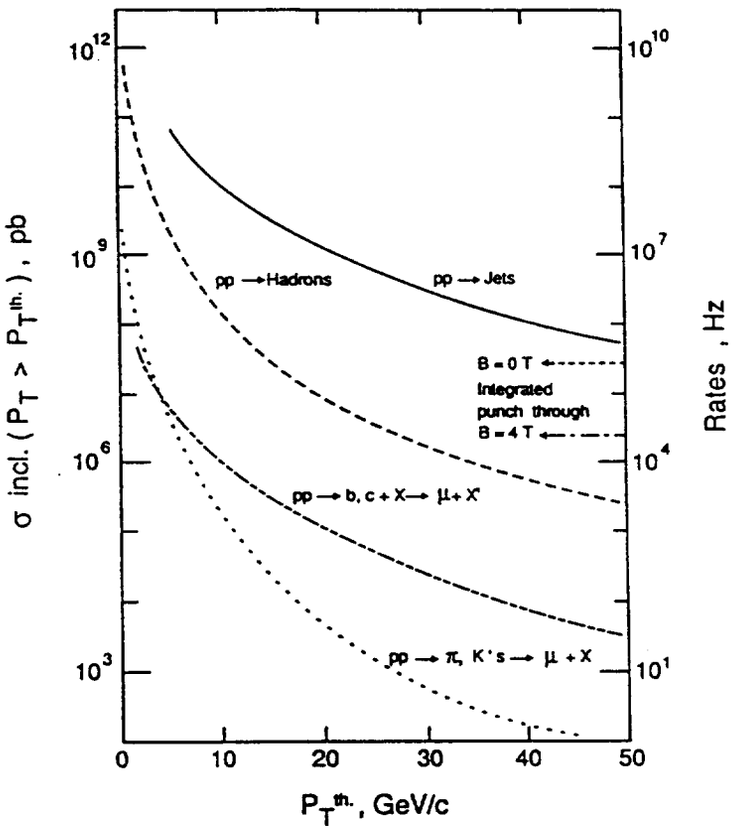


Fig. 4 : Expected cross-sections and rates at 10^{34} $cm^{-2}s^{-1}$ luminosity in $|\eta| < 3$ for jets, single charged hadrons, muons from bottom and charm decays and muons from π, K decays as a function of the threshold, $P_T^{th.}$, on the transverse momentum. The two arrows (for B= 0 T and B = 4 T) indicate the level of the integrated punch-through background for the configuration explained in the text.

The only practical way to reduce this high rate is not by increasing the amount of absorber, since a large fraction of this rate comes from genuine muons, but rather by cutting on the P_T of these muons.

2. MUON TRIGGER IN A STRONG MAGNETIC FIELD

One of the arguments in favour of a strong magnetic field for a muon detector at LHC is to facilitate a cut on P_T at the trigger level, with trigger hodoscopes of modest spatial resolution, $\sigma \approx 1$ cm.

Two possible orientations of the magnetic field can be considered: a toroidal field or a solenoidal field. The solenoidal field is better for triggering in the central region since the bending is in the plane transverse to the beam and the small size of the beam spot ($\pm$ 10μm) provides a very precise point for the momentum determination. Simple

trigger algorithms based on track pointing to the vertex in the R-Φ plane can be implemented.

Fig. 5 shows the transverse view of a possible muon detector based on a strong solenoidal field. The coil is 0.5 m thick and has an inner diameter of 7m. It produces a magnetic field of 4 Tesla in the inner region. A calorimeter of $\approx 10\lambda$ is installed inside the coil starting at R = 1.5 m. The return yoke of the magnet, about 2 m of magnetized iron at 2.3 Tesla, completes the absorber for a total of about 22λ. The detector is very compact and has an overall diameter of only 13 m. M. Pimia [5] will discuss in more details the possible design and performance in momentum resolution of such a Compact Muon Solenoid (CMS) detector. Here we use the CMS only to illustrate the general problem of the trigger.

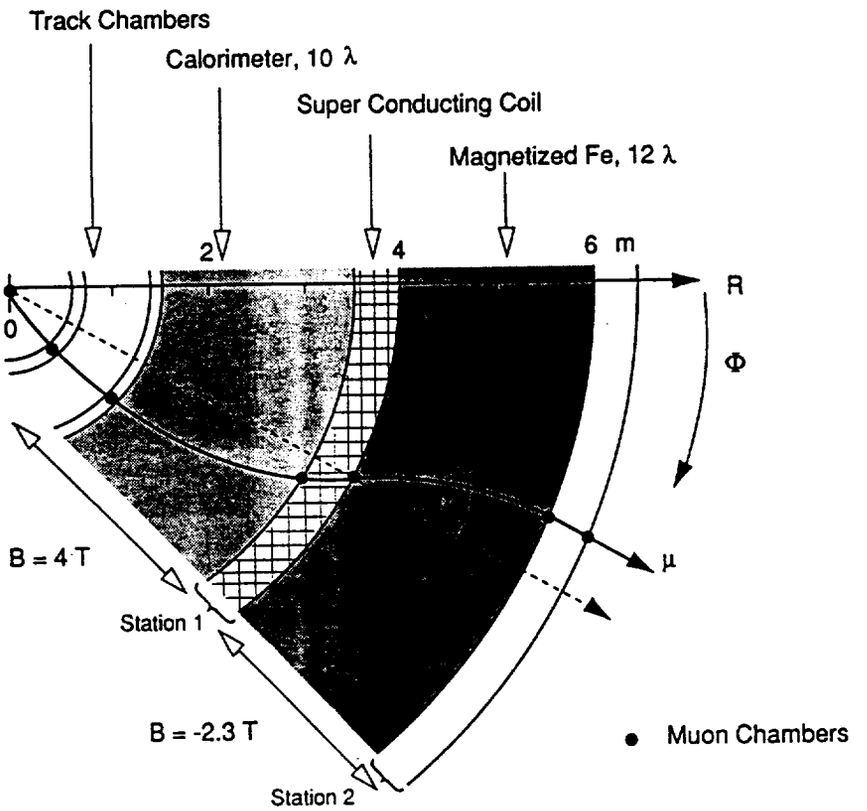


Fig. 5 : Cut in the transverse plane of the Compact Muon Solenoid detector (CMS).

Trigger hodoscopes of granularity $\sigma_{R\Phi}$ = 1cm are placed before and after the coil (station 1) and outside the return yoke (station 2). Pointing of the muon track can be checked by measuring the angle α defined in Fig.5 in two independent triggering stations. Clearly due to the magnetic field configuration, station 1 will be more efficient to cut on P_T than station 2. Station 2 on the other hand will see less punch-through background. A 100 mrad cut in station 1 would allow for example a sharp cut on P_T

with an efficiency of 100% for $P_T > 50$ GeV/c. The same cut in station 2 would impose a cut only around 10 GeV/c. Efficiency curves and trigger rates as a function of the trigger angle are presented in [5].

So far we have ignored the combinatorial background due to multihits in station 1 just behind the calorimeter. There is a potentially serious problem caused by low P_T muons inside jets, due either to π/K or bottom and charm semileptonic decays. This is a general problem for all muon detectors. Station 1 is not expected to be as clean as station 2, because the tail of the accompanying jet and of the hard hadrons of the many overlapping events at high luminosity will produce spurious hits after 10λ in the vicinity of the muon track. A low P_T muon can produce a track in station 2 more or less pointing to the vertex. This is particularly true for the CMS geometry, where the direction of the magnetic field in the return yoke is opposite to the direction of the central field and bends back the outgoing muon in the direction of the vertex. Spurious hits in station 1 in coincidence with the low momentum muon track in station 2 can fake the trajectory of a large P_T muon. In a toroidal geometry the measurement of the bending angle also necessitates two trigger stations. Combinatorial background in station 1 will also spoil the P_T cut at the trigger level. This combinatorial background due to low momentum decay muons inside jets could dominate the large P_T muon trigger. Additional trigger planes between station 1 and station 2 may be necessary to avoid random coincidences and increase the level of redundancy in the muon track definition. To investigate further the muon trigger problem at LHC a proposal (DRDC/P7,[6]) has been submitted to the new Detector R&D Committee (DRDC) set-up at CERN.

3. THE MUON PROPOSAL P7

The main objective of the proposal [6] is to demonstrate the advantage of a strong magnetic field in rejecting efficiently hadron punch-throughs and decays at the trigger level. For this we propose to build a fraction of the compact muon solenoid detector shown in Fig.5. We will expose it to a test beam containing hadrons and muons and record punch-through data.

In parallel we want to study the performance of the plastic resistive plate chambers (RPC) developed by the Rome group [7]. Because of their excellent time resolution these chambers can be used as trigger hodoscopes to apply angular cuts at the first trigger level.

One of the key elements in our proposal is the measurement in a strong magnetic field. We therefore propose to use the EHS magnet which is ideally suited to this purpose. This magnet with coils in a Helmholtz-like arrangement provides a field of 3T

over a free space of about 1.5m x 1.5m x 0.8m. The proposed set-up is shown in Fig. 6.

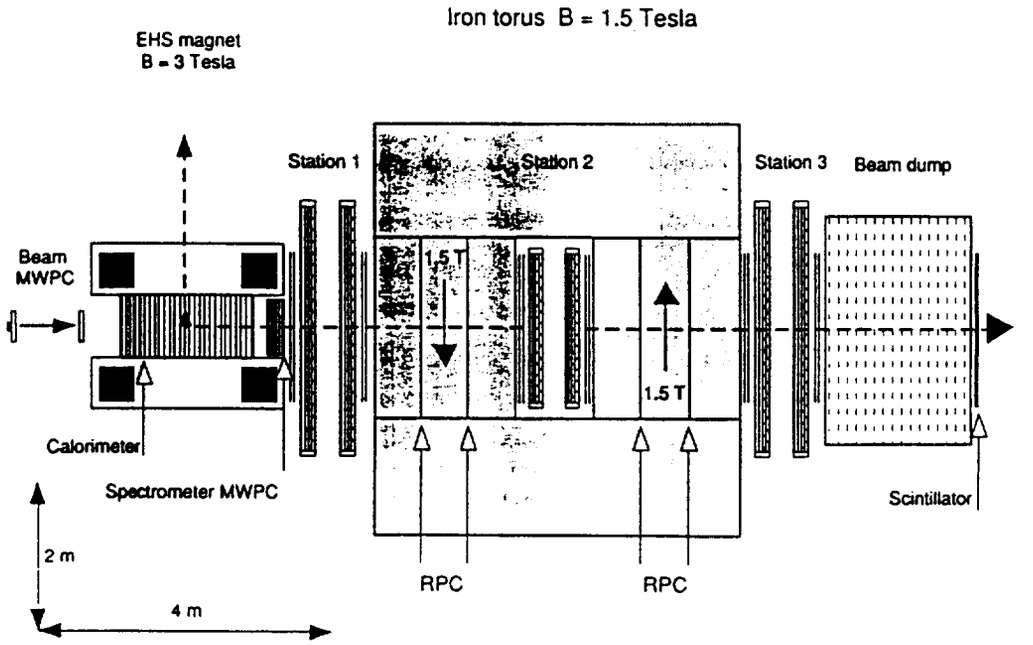


Fig. 6 : Plan view of the experimental set-up for DRDC proposal P7.

A calorimeter acting as a hadron absorber is located in the magnet gap. Its main purpose is to identify hadronic showers, thus rejecting a possible contamination of genuine muons in the beam which would affect the measurement of fake muons from hadron punch-through. In addition, when running with muon beams to study momentum resolution and trigger efficiencies, the calorimeter will provide information on the muon energy loss in the absorber.

The muons are again momentum analyzed in a second magnet which consists of iron plates 2m thick, magnetized to 1.5 T. This magnetised absorber fakes the return yoke of the CMS. As mentioned earlier, it is important to trace the particles in the magnetic field. Hence, we plan to install several layers of track chambers inside the magnetized absorber, as shown in Fig. 6.

Three trigger and chamber stations are located along the beam line, the first behind the EHS magnet, the others inside and behind the iron magnet. The first two correspond approximately to the trigger stations of CMS detector sketched in Fig.5. These stations are composed of muon chambers arranged in the same way as they were used in the UA1 experiment, and of two planes of RPC's which should serve as a fast trigger.

Each trigger plane is made of two layers of RPC's 2x2 m^2 with alternating x-y read out strips of 2-3 cm width. A fast signal from individual strips, or groups of strips, will be available for a fast trigger and tests of first level trigger algorithms.

For a precise measurement of the particle trajectory we propose to use a part of the UA1 muon chambers [8]. Each module consists of two chambers separated by a lever arm of 50 cm thus providing a good determination of the particle direction. The chambers are composed of extruded aluminium tubes, each representing one drift cell. The cells within one chamber are arranged in two double planes which are orthogonal to each other. In order to solve the left - right ambiguities, the tubes of a double plane are staggered. By this tube arrangement a track is measured in two orthogonal projections with four planes per projection. The single point resolution varies from 300 μm near the anode to ~ 500 μm at the edge of the tube.

4. SUMMARY

At LHC the rate from genuine muons in the central muon chambers will be high : 10^6 muons/sec . The muon trigger has to perform a P_T cut of about 50 GeV/c to reduce the trigger rate to an acceptable level.

Leakage of jets after a typical calorimeter of 10 absorption lengths will produce spurious hits causing a confusion in the P_T reconstruction of muons. This combinatorial background will affect the muon trigger and the reconstruction of prompt muons.

Punch through simulations are extremely time consuming. They have large uncertainties and are not adequate to simulate the combinatorial background in the momentum measurement.

Parametrization of existing punch-through measurements cannot be used to study the trigger confusion problem.

The muon proposal P7 will allow realistic trigger studies of general interest for any muon detector system.

In addition the proposed set-up will allow to study the performance of large area muon chambers in magnetized absorbers and the corresponding muon momentum resolution.

REFERENCES

[1] A. Nisati, contribution to this workshop.

[2] H. Fesefeldt, contribution to this workshop.

[3] F. Lacava, contribution to this workshop.

[4] D. Green and D. Hedin, "Muon Rates at the SSC", Fermilab-Pub-90/18

[5] M. Pimia, contribution to this workshop.

[6] "Study of muon triggers and momentum reconstruction in a strong magnetic field for muon detector at LHC", CERN/DRDC/90-36, DRDC/P7

[7] R. Santonico, contribution to this workshop.

[8] K. Eggert et al., Nucl. Instr.Meth. 176 (1980) 217.

Energy loss by muons in dense materials

T. Del Prete and C. Petridou
INFN-Pisa, Italy

presented by T. Del Prete

1 Introduction

There is hardly any need to stress the importance of a muon detector at LHC. Muons from different processes (Higg's particle, additional vector bosons and more conventional sources) will be produced with momentum ranging from few tens of GeV to several hundred GeV. Muons are easy to measure, at least at low energy, where the energy losses are mainly by ionization and the e.m. interactions are suppressed, with respect to electrons, by the factor $(m_e/m_\mu)^2 \simeq 2.3\ 10^{-5}$. At energies above a few hundred GeV radiative processes dominate over ionization in the energy losses of muon in matter. In a fraction of cases muons will lose a significant part of their energy in hard photons and electron pairs that will initiate electromagnetic showers. In the geometry of an experiment at LHC this can occur inside the e.m. or hadronic calorimeters and, if such is the design, in the iron yokes of a muon spectrometer. As a result the measured momentum of the muon will be incorrect. In addition the e.m. shower may overlap with the muon track in the active planes of the detector making precise position measurements impossible. These processes should be studied in depth and taken into account in a design of a muon detector at LHC because, as we will see, they influence the momentum resolution and efficiency and the trigger concepts.

At high muon momentum the energy losses are due to:

- direct pair production [1];
- bremsstrahlung [2];
- nuclear interaction [3];
- knock-on processes [4].

The first three mechanisms have an average energy loss proportional to the muon energy. The average energy loss of muons in matter can then be expressed as:

$$-<\frac{dE}{dx}>= a + b \times ln(E'_{max}/m_\mu) + f \times E_\mu \qquad (1)$$

The first two terms describe the energy loss by ionization [4]. E'_{max} is the maximum energy transfer to a knock-on electron and, at large muon energies, is proportional

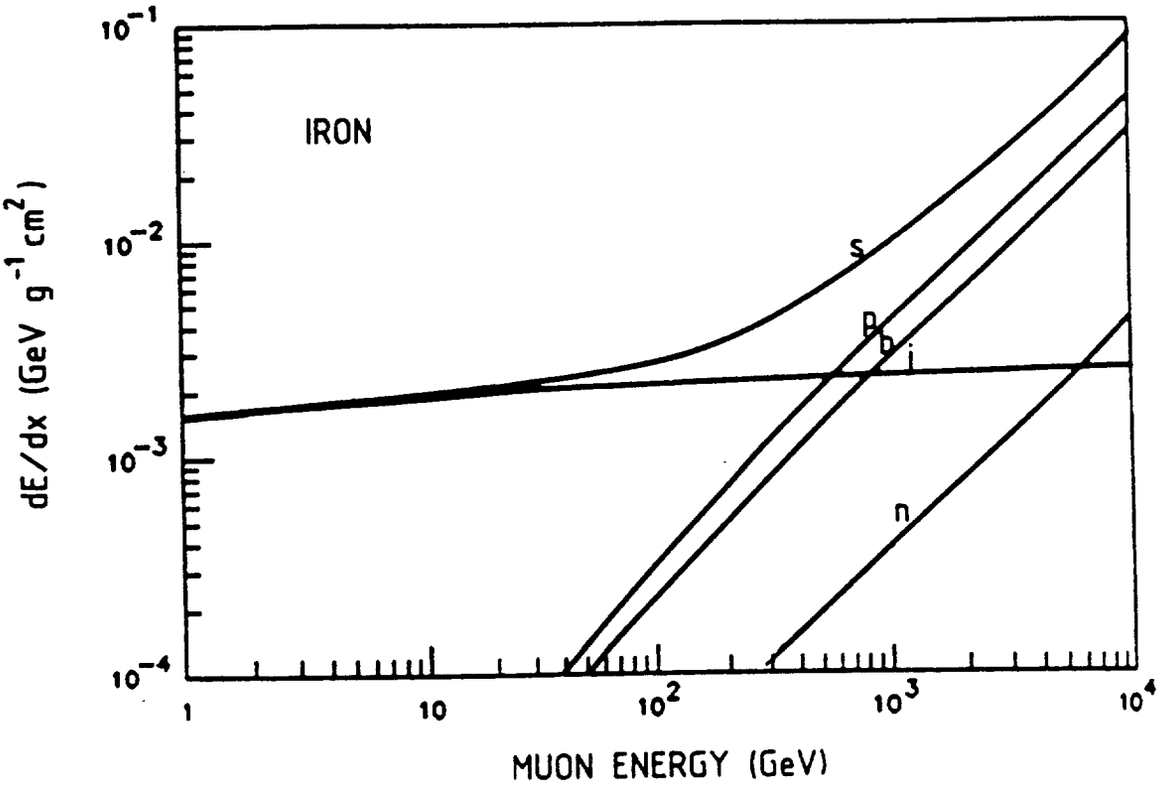


Figure 1: Average energy loss of muons in iron as a function of E_μ[6]. The total energy loss (s) is the sum of ionization (i), bremsstrahlung, (s), pair production (p) and nuclear interactions (n).

to E_μ. The coefficients a, b and f depend on the material of the absorber [5,6]. Fig. 1 shows the energy loss of muons in iron, according to the calculation by W. Lohmann et al [6]. We should notice that, while in principle the contributions of e.m. processes are exactly predictable, different calculations differ up to factors 10-20 % due to uncertainties in the screening effects of atomic electrons, nuclear form factors, cut-offs etc.

It is useful to define, in order to fix the scale of energy, a critical energy E_c, as the muon energy for which the total energy loss is twice the ionization loss. For muons in iron $E_c \simeq 330GeV$ (as can be read from Fig 1), to be compared with $E_c \simeq 25MeV$ for electrons in iron.

Pair production and bremsstrahlung are the dominant processes as can be seen from Fig. 1. Here, as an example, we look at the bremsstrahlung mechanism. The cross section, as a function of the fractional energy loss $v(v = \Delta E_\mu / E_\mu)$ is the Bethe-Heitler formula:

$$\frac{d\sigma}{dv} = \alpha \times (2. \times Z \times r_e \times \frac{m_e}{m_\mu})^2 \times (\frac{1}{v}) \times ln(183/Z^{1/3}) \qquad (2)$$

Where α is the fine structure constant, r_e is the classical electron radius and Z is the atomic number of the absorber. By integrating from a minimum energy loss $v_{min} = 1MeV/E_\mu$ to $v = 1.$, and for an absorber of length L, we get the interaction

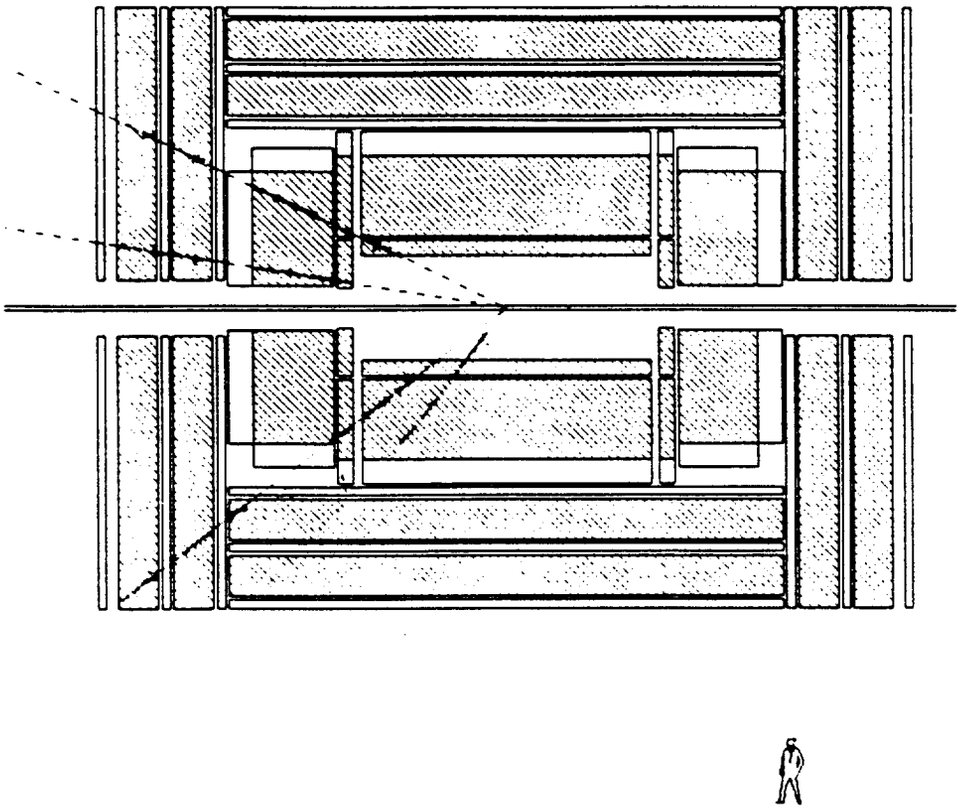


Figure 2: Transverse view of a hypothetical detector at LHC [8]. The muons from the decay of a 500 GeV mass Higgs interact with the calorimeter and the iron toroids of the muon spectrometer, inducing showers (black areas around the μ trajectory)

probability:

$$P \simeq \frac{L}{L_r} \times (\frac{m_e}{m_\mu})^2 \times ln(183/Z^{1/3}) \times ln(\frac{1MeV}{E_\mu}) \qquad (3)$$

(L_r is the radiation length of the absorber.) For a muon of 1TeV in 1m of iron we find a probability of about 7 % which is a small number and justifies the approximations in the previous formulas. However the probability that in a single interaction the muon suffers a fractional energy loss larger than β is:

$$P(v > \beta) = ln(1/\beta)/ln(1/v_{min}). \qquad (4)$$

For $\beta = 0.25$ we compute that the probability that a muon of 1TeV loses 250 GeV in a single interaction is about 10 %. Because of the small interaction cross-section and the large probability of having an important energy loss in a single interaction, these losses are characterized by large fluctuations and have been often called "catastrophic".

These processes have been studied in detail by using the montecarlo program GEANT [7]. Fig 2 shows a longitudinal view of a possible detector at LHC [8] with the two major elements: a dense calorimeter and a muon spectrometer made of iron toroids. The decay of a 500 GeV mass Higg's particle in four muons that interact in the material of the detector illustrates the scope of this study. Before

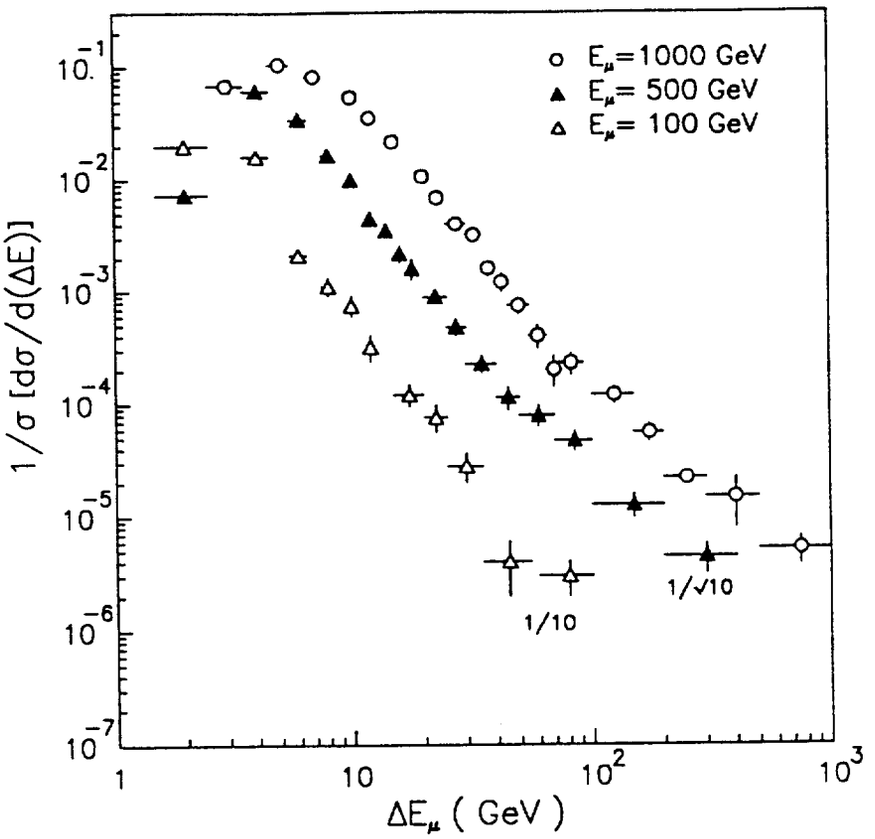


Figure 3: Probability of energy loss for three muon energies. The points for 500 and 100 GeV muon energy are scaled by $1/\sqrt{10}$ and 1/10 respectively.

reaching the spectrometer the muons could interact in the calorimeter (2m of iron = 19 λ) and eventually also in the iron of the spectrometer (3m in this example).

Instead of tackling the complicate problem of the effect of the radiative losses on physics quantities, like the mass and the transverse momentum of the Higgs, we will consider a simpler situation that, however, will allow to draw general conclusions on these effects. Muons of several energies from 10 GeV up to 1 TeV have been traced through 2m of iron and we have studied both the distribution of energy losses and the effects of the e.m. showers initiated by the muon eventually leaking in the tracking detector positioned behind the absorber.

2 Energy losses

Fig. 3 shows the probability of total energy loss ($\frac{1}{\sigma} \times \frac{d(\Delta E_\mu)}{d E_\mu}$) in 2m of iron, for three muon energies. The distribution shows substantial tails at large energy losses. For muon energies larger than the critical energy the fraction of events with ΔE_μ larger than a fixed fraction of $E_\mu$is independent of E_μ. If the energy losses occur in the calorimeter (Fig.2) and the muon is isolated, then in principle we could measure the losses and correct for them. Otherwise the muon momentum

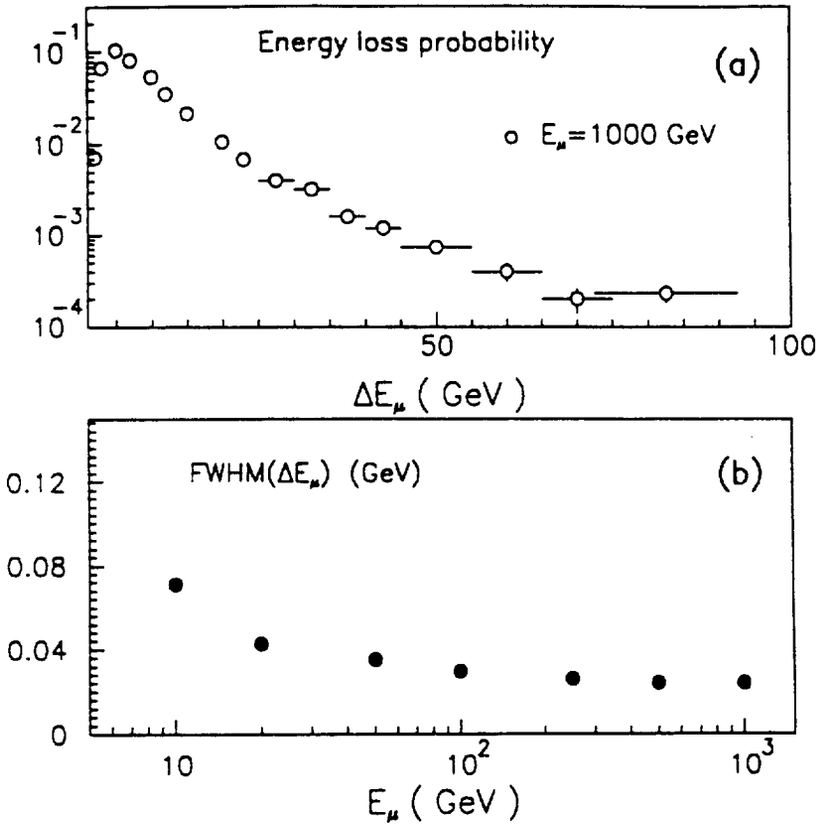


Figure 4: Energy loss distribution of 1 TeV muon (a). Note the long tail on ΔE_μ. The % FWHM of the curve are plotted in (b) as a function of E_μ.

will be mis-measured and eventually the muon could be lost for physics analysis if the losses are too large.

More precisely, the fraction of events with $\Delta(E_\mu) > 0.25 \times E_\mu$ is 0.6 % nearly independent of E_μ. If such is the amount of losses, they are clearly negligible with respect to acceptance etc. [8].

However, even if the energy losses are not so violent, their fluctuation puts a limit on the precision of $E_\mu$measurement. Fig. 4a shows the energy loss spectra of a 1 TeV muon in 2 m of iron. The distribution is not gaussian even for small energy losses and has important tails at large ΔE_μ. We have taken the full width half maximum (FWHM) of the spectra as a measure for the dispersion of the curve. Fig. 4b shows the fractional energy spread ($FWHM(\Delta(E_\mu))/E_\mu$) as a function of E_μ. At $E_\mu$larger than 100 GeV the spread is about 2.4 % but increases to about 7 % at $E_\mu = 10GeV$. These effects are small compared to the resolution of an iron spectrometer [8] but probably represent an absolute limit on the accuracy on the measurement of E_μ.

We have checked the GEANT prediction with the available data in the literature. The cosmic ray experiment MUTRON [9] has collected data in the energy range E_μ= 100 GeV up to 13 TeV, by measuring both $E_\mu$and $\Delta(E_\mu)$. Their data agree with GEANT predictions up to the highest energies and to the largest energy losses, providing a good check on the treatment of cascades in the montecarlo code.

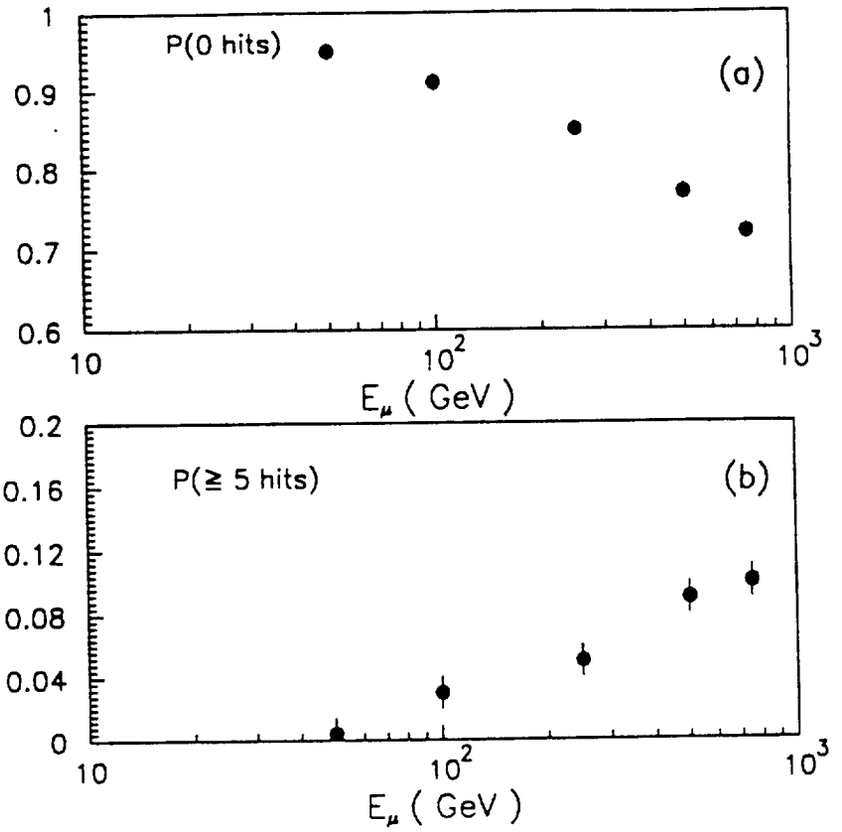


Figure 5: Probability of a clean hit in a detector after 2m of iron (a) as a function of E_μ. The probability of detecting more than 4 hits is plot in (b).

3 Secondary particles

The montecarlo program propagates the e.m. showers initiated by the muon and follows the shower debris up to a minimum cut-off energy. If the e.m. shower is not fully contained in the iron, a tracking detector placed behind the absorber will detect additional hits that could spoil the muon momentum measurement.

GEANT predicts that the charged secondary particles (mainly electrons) have an average energy of 30 MeV. Fig. 5a shows that the probability of clean hit (no secondary charged particle seen in the chambers, after 2m of iron) is .95 for E_μ= 50 GeV decreasing to .72 for E_μ= 750 GeV. The probability of finding more than four particles accompanying the muon (most of the tracking detectors will suffer severe limitations in precision and efficiency in these conditions) increases with the muon energy and reaches 10 % at E_μ= 750 GeV. Also a large number of low energy photons ($< E_\gamma >= 9MeV$) is produced by the e.m. showers and a large fraction will enter the chambers. A muon of 500 GeV will be accompanied by an average of 35 photons and this number is nearly proportional to E_μ.

The NA4 collaboration [10] has studied the influence of soft secondaries on the chamber resolution. Their conclusion was that their chambers, sandwiched between the iron toroids of the muon spectrometer, suffered a worsening of their intrinsic resolution ($\sigma = 1.15mm$) by a "soft" charged particle component ("δ rays"). δ rays contribute with $\sigma = 1.mm$ to the effective chamber resolution

($\sigma = 1.55mm$). However it is clear that these numbers depend strongly on the experimental conditions and cannot be assumed to hold for any set-up.

Also the average number of additional hits accompanying a muon track, predicted by GEANT, agrees with the measurements of NA4. After 2m of iron a muon of 100 GeV has 0, 1, 2 and greater than 2 additional hits with probability 83%, 10%, 4% and 3% respectively, in good agreement with what measured by NA4: 87%, 10%, 2% and .5% respectively for muon energies between 20 and 160 GeV.

GEANT simulation also predicts that secondary particles should cluster around the muon direction with an average distance of about 3 cm. This also is confirmed by the NA4 measurements. This fact could put strong constraints on the triggering schemes based on position measurements inside the spectrometer.

4 Conclusions

The present study confirms and extends the findings of previous investigations [11]. We believe that it should be considered as a guideline to plan experimental studies on these effects and on their implications on the triggering schemes and the momentum measurement in a muon spectrometer at LHC. The measurement of the muon momentum by tracking through iron (toroid and solenoidal schemes have been proposed to this workshop) and the passage of the muons through the calorimeter in any geometry of a LHC experiment, have the intrinsic weakness of the effects of the stochastic, violent interactions of muons in the absorber. As a result the track position measurement will be confused and also the muon will have lost some unpredictable amount of energy before entering the spectrometer. The amount of physics information lost will depend on the detector design and it is possible that a careful offline analysis could recover part of it. It looks wise to provide the muon spectrometer with enough redundancy both in the number of tracking stations (clearly three would suffice but at the cost of large inefficiencies) and in the number of measurements in each station. What still needs a better understanding are the consequences of these processes at the trigger level where a decision has to be made in a very short time (15ns to 1.μs) with a fast algorithm that will not probably be able to exploit all the information of the detector.

References

[1] T. Murota et al: *Prog. Theor. Phys.* **16** (1956) 482.
S. R. Kelner and Yu. D. Kotov: *Can. J. Phys.* **46** (1968) 387.
R.P. Kokoulin and A. A. Petrukin: *Acta Phys. Hung.* **29** Supp.4 (1970) 277.

[2] H. A. Bethe and W. Heitler: *Proc. R. Soc. London Ser.* **A146** (1934) 83.
A. A. Petrukin and V. V. Shestakov: *Can. J. Phys.* **46** (1968) 377.
R. F. Christy and S. Kusaka: *Phys. Rev.* **59** (1941) 405.

[3] K. Daiyasu et al.: *J. Phys. Soc. Jpn.* **17** (1962) 344.
K. Kobayakawa: *Il Nuovo Cimento* **B47** (1967) 156.

L. B. Bezrukov et E. V. Bugaev: *Sov. J. Nucl. Phys.* **33** (1981) 635.

[4] H. J. Bahabha: *Proc. R. Soc. London Ser.* **A164** (1938) 257.
A. M. Bincer: *Phys. Rev.* **107** (1957) 1431.

[5] C. Grupen: *Fortschr. Phys.* **23** (1976) 127.

[6] W. Lohmann et al. : CERN 85-03, Experimental Physics Division, 21 March 1985.

[7] R. Brun et al CERN Data Handling Division DD/EE/84-1, September 1987.

[8] G. Carboni, contribution to this workshop.

[9] K. Mitsui et al: *Nuclear Instr. Meth.* **169** (1980) 97.
K. Mitsui et al: *Il Nuovo Cimento* **73A** (1983) 235.

[10] R. Kopp et al.: *Z. Phys. C Particle and Fields* **28** (1985) 171.
W. Lohmann ad al.: CERN-EP/85-113, August 20th 1985.
A. C. Benvenuti et al.: *Nuclear Instr. Meth.* **226**(1984) 330.

[11] J. J. Eastman and S. C. Loken: LBL-24039 (1987).

A PLASTIC FOIL CHAMBER FOR LARGE AREA MUON DETECTION

Fabio SAULI
CERN, Geneva, Switzerland

The recently developed microstrip gas chamber is a very performing detector of radiation, realized engraving on an glass substrate anode and cathode strips at a very narrow pitch [1-3]. Very promising because of its good localization accuracy at high rates, the microstrip chamber in its present conception is however limited in size and delicate to use due to the possiblity of permanent damage resulting from a discharge between strips.

In the Coated Cathode Conductive Layer (*COCA COLA*) chamber [4] we have attempted to build a similar (though for the time being coarser) geometry on a thin plastic foil; to avoid all together the breakdown problem, we have placed the anode and the cathode strips on opposite sides the sheet (Fig. 1). Apart from a small modification due to the dielectric constant of the support, and before charge-up processes set in, the electric field in the *COCA COLA* chamber is sensibly the same as in the original microstrip detector, and one would expect gaseous amplification to occur. It is conceivable that if a support is chosen with sufficiently low bulk resistivity, charges would neutralize with a time constant smaller than the ions production rate and a stable operating condition could be reached.

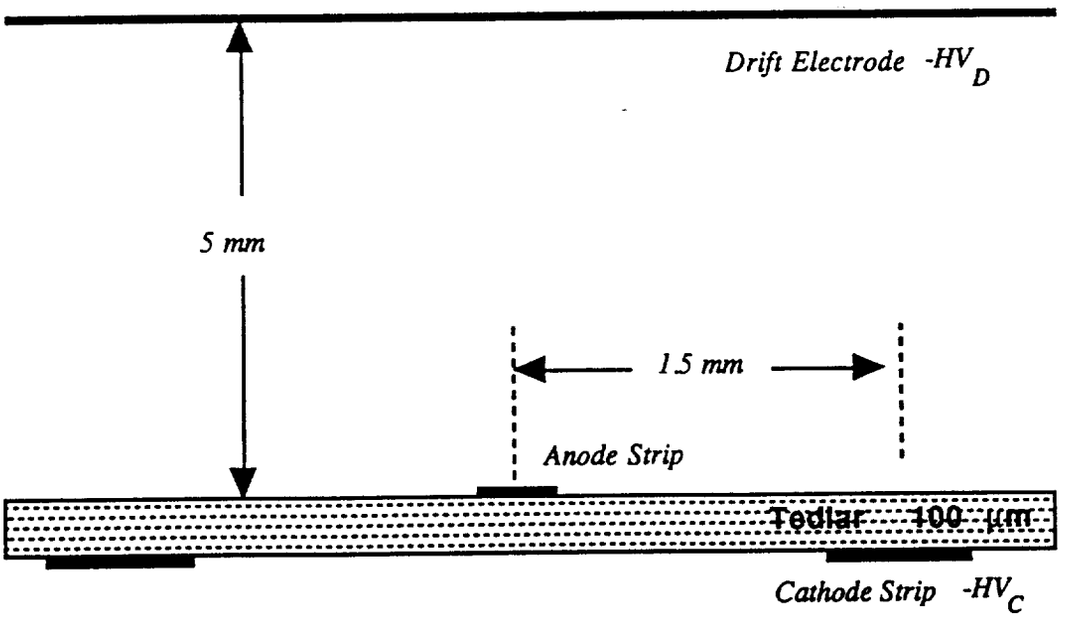


Fig. 1: Schematics of the COCA COLA Chamber. Thin anode and cathode strips are placed on the two sides of a plastic foil.

In our first attempt to realize the chamber we have used as support a 100 μm thick foil of white Tedlar having a bulk resistivity around 10^{12} ohms.cm . The nominal dielectric rigidity of the 100 μm Tedlar foil is 10 kV. Anode strips about 200 μm wide were vacuum evaporated on one side of the sheet at a 3 mm pitch; a printed circuit with wider (500 μm) strips and the same pitch was mounted on the back side of the foil, to realize the geometry sketched in the figure. The active area of the detector was 10x10 cm^2. An 8 mm thick gap, overlaying the plastic foil on the anode side and delimited by an upper electrode served to collect and drift the ionization. For most measurements, we have used an argon-methane (90-10) gas filling.

At moderate detection rates (around hundred hertz per cm^2), the operation of the detector is rather satisfactory. Using a collimated Ru^{106} electron source in coincidence with a small scintillator behind the chamber, we have recorded the pulse height distribution on individual anode strips; an example is shown in Fig. 2. The peak corresponds to a detected charge of about 0.1 pC which, taking into account the ionization loss in the gap (~70 electron-ion pairs) implies a proportional gain of around 10^4.

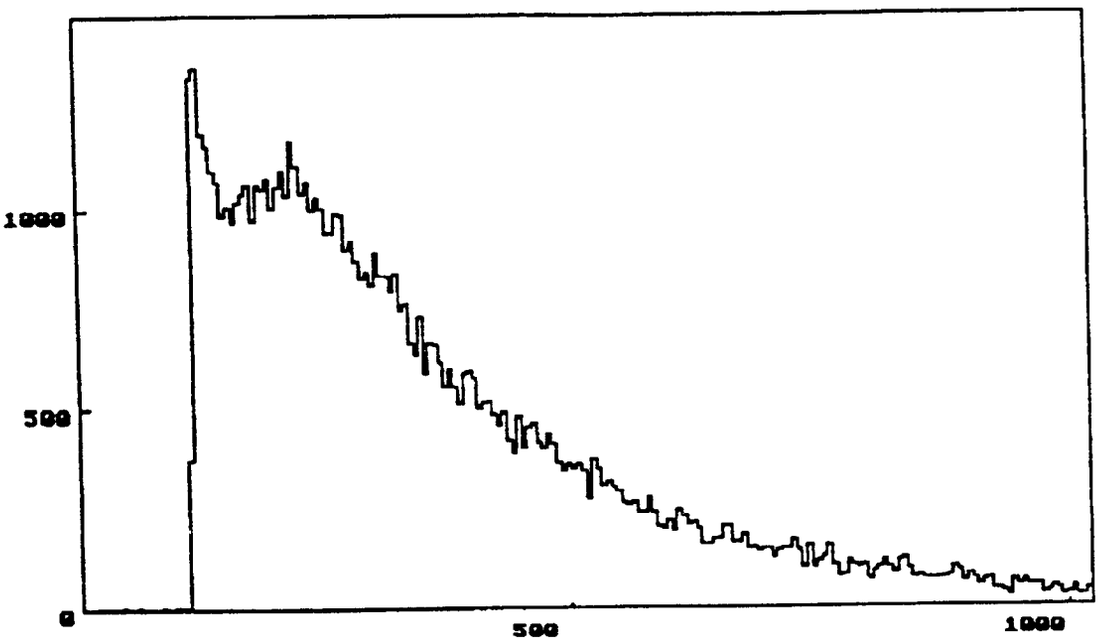


Fig. 2: Pulse height spectrum on one anode strip for minimum ionizing electrons.

In these conditions, for a single strip readout, we have measured the efficiency plateau as a function of cathode voltage (the anode being grounded) shown in Fig. 3. We could not reach 100%, probably because of the poor geometry and to the use of a single scintillation counter as trigger; the fact that the plateau remains constant up to the highest voltages supports this statement. Fig. 4 shows the singles rate with the source in the same range of voltages.

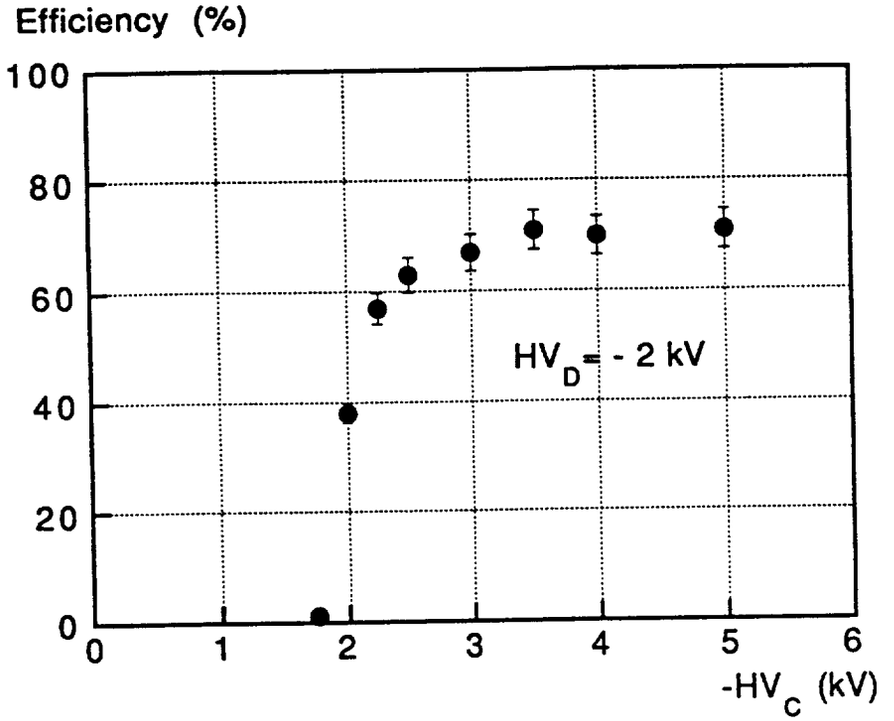


Fig.3: Efficiency plateau for minimum ionizing electrons.

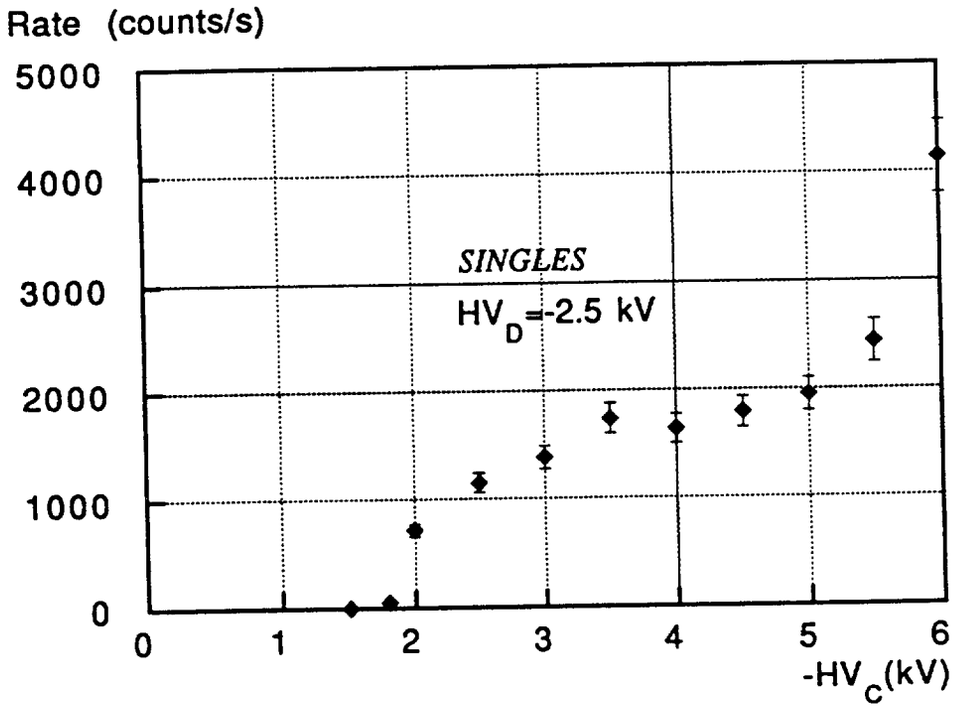


Fig. 4: Singles rate as a function of voltage.

Various phenomena that can be associated to charging up of the insulator have been observed in the detector. The most obvious one is a large drop in efficiency observed whenever the voltage to the cathodes is decreased, even by a few hundred volts. With a time constant of minutes, the efficiency recovers its normal value; there seems to be a slight dependence of the recovery time from the source intensity. When however the voltage is increased by the same amount, no similar effects are observed; full efficiency indeed is measured immediately even when powering the cathodes all the way up from zero potential. We explain the observation as follows: due to the very high resistivity of the foil, ions actually accumulate on the surface until, with their distribution, they oblige the electric field to be parallel to the foil surface for most of the anode-to cathode distance. This is a condition of equilibrium, since it prevents more ions to reach the insulator. When increasing the voltage, ions produced in the avalanches easily attach to the surface to recreate an equilibrium condition. However, when the voltage is decreased, to obtain the same equilibrium one has to actually remove ions from the surface, a much longer process. Similar arguments have been used to explain the behavior of the so-called electrodeless drift chambers [5].

While obviously not suited for high rate applications, the *COCA COLA* chamber may be a valid alternative to existing low-cost devices designed to cover very large surfaces (as for example for muon detection). The exceedingly wide efficiency plateaux, together with complete immunity to spark breakdown, make the detector rather suitable for use in this case.

REFERENCES

[1] A. Oed, Nucl. Instrum. Methods A263 (1988) 351
[2] F. Angelini, R. Bellazzini, A. Brez, M.M. Massai, G. Spandre and M. R. Torquati, Nucl. Instrum. Methods A283 (1989) 755
[3] F. Angelini, R. Bellazzini, A. Brez, E. Focardi, M.M. Massai, G. Spandre, M. R. Torquati, R. Bouclier, J. Gaudaen and F. Sauli, INFN PI/AE 90/6. Pres. at 2d Int. Conf. on Advanced Technology and Particle Physics, Como (1990)
[4] R. Bouclier, J. Gaudaen and F. Sauli, CERN-PPE/90-139. Pres. at 2^{d} London conf. Position Sensitive Detectors, 1990
[5] J. Allison, R.J. Barlow, C.K. Bowdery, I. Duerdoth and P.G. Rowe, Nucl. Instrum. Methods 201(1982) 34

New results on the blade chamber

Presented by F. Bergsma

G. Ambrosi, M. Basile, R. Battiston, J. Berbiers, F. Bergsma,
H. Castro, F. Cindolo, A. Contin, S. De Pasquale, J. Galvez,
P. Gusti, J. C. Labbe, G. Laurenti, G. Levi, G. Maccarone,
R. Nania, F. Rivera, M. Schioppa, A. Sharma, G. Simonet,
J. Solano, G. Susinno and A. Zichichi.

Bologna, CERN, Cosenza, LNF, Perugia, World Lab. collaboration

December 5, 1990

Abstract

The blade chamber here described is a gaseous detector for minimum ionizing particles. Gas amplification takes place around the sharp edge of a thin blade. The use of a blade makes it possible to make round chambers, addapted to the toroidal magnetic field in the forward regions of a detector for a multi-TeV collider. Measurements in proportional mode and limited streamer mode are described using different gas mixtures. The results of calculations are presented, concerning the operation of the blade chamber in a high magnetic field. The construction of a real size prototype and future plans are discussed.

1 Introduction

The "large Area Devices (LAD) Group of the LAA project at CERN is devoted to R and D for muon detection at a future multi-TeV hadron collider. Part of the group activities consist of the development of round chambers for the forward regions of detectors. In these regions muon spectrometers require toroidal magnetic fields. In a toroidal field, polar coordinate readings are desirable to improve trigger capability and momentum measurements. In particular the accurate measurement of the r-coordinate (= distance from the beam axis) is important (see fig. 1). It is clear from this figure that a circular detector would be the ideal configuration. A circular cell can be constructed by replacing the wire of a conventional drift tube by a blade: the chamber can now be bended in the plane perpendicular to that of the blade. Gas amplification takes place around the sharp edge of the blade, where the electrical field strength is maximal. An additional advantage is that such a chamber is very resistive against mechanical shocks. In fig. 2 a side view of a tested blade chamber is given with some characteristic dimensions. The roof is made of an electrical insulator, necessary to divert the electrical force lines from the roof towards the walls and thus increasing detection efficiency(see fig. 10). In addition, an insulating roof makes it possible to apply pick-up strips to determine the phi-coordinate (see fig. 1).

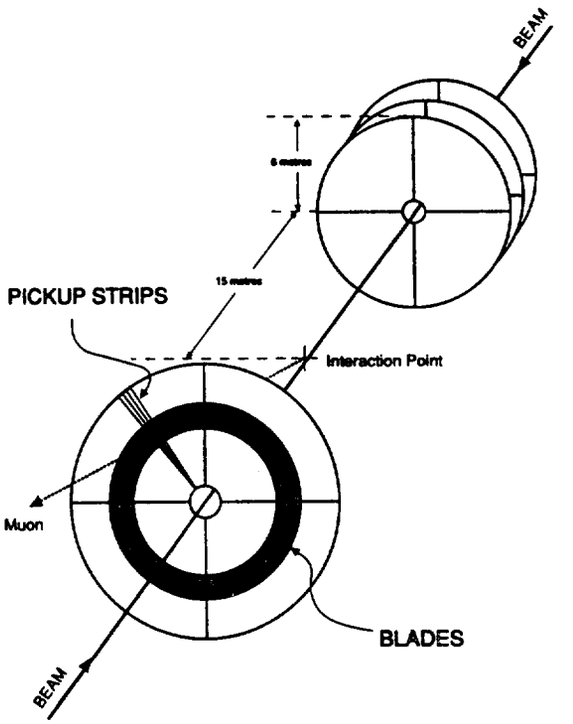


Figure 1: Geometry of blade chambers

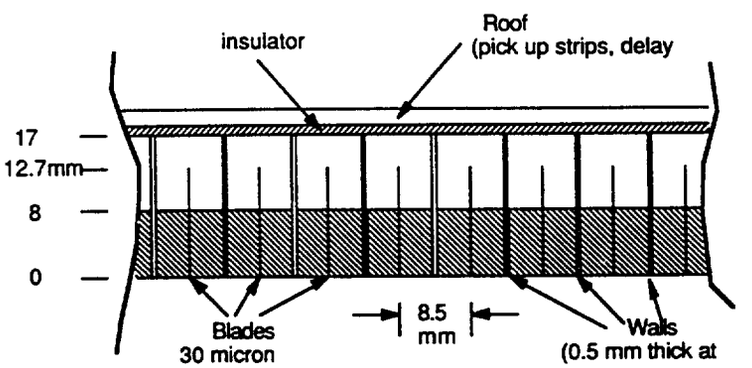


Figure 2: Cross section of insulating roof blad chamber

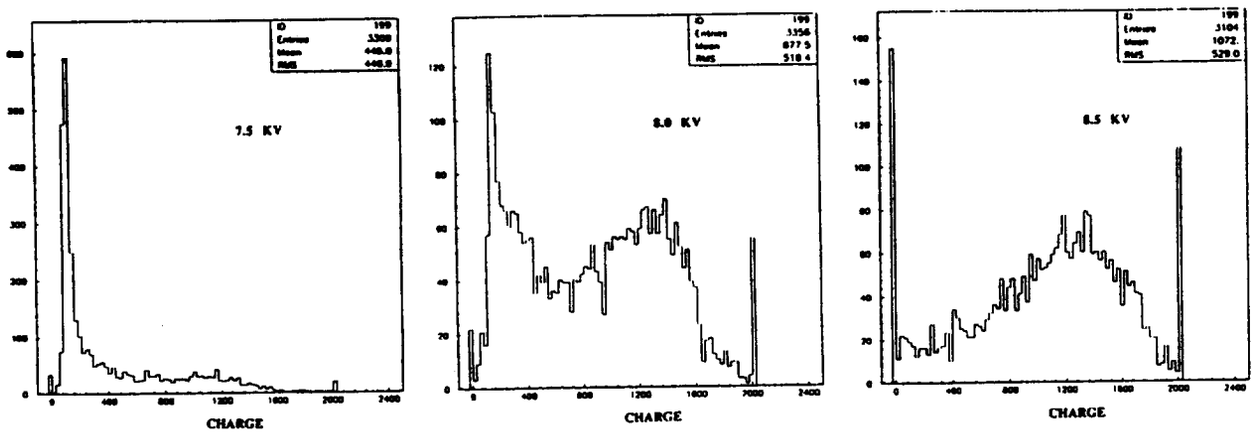


Figure 3: Charge spectra

2 Summary of previously obtained results

Results obtained with blade chambers have been published [ref 1]. The chambers were operated in the limited streamer mode. The left-right ambiguity of traversing tracks could be resolved by using the asymmetry in the signal induced on the two adjacend walls of the fired blade. Thus one chamber is sufficient to determine the coordinates of a track through a plane. Upper limits of sigma=250 μ were obtained for the spatial accuracy in the coordinate orthogonal to the blade, measured through drift time, and sigma=380 μ in the coordinate along the blade, measured with external strips. These numbers are upper limits, because the resolution of the used wire chambers in the test set-up was assumed to be infinite. A rate of about 1 KHz/cm2/sec can be accepted in streamer mode.

3 New Developments

The previous results were obtained with the chambers working in limited streamer mode and the signals were amplified by about a factor of two only, after being transferred by 10 m of coax cable. In order to study the gas amplification around the blade tip with more care, a preamplifier was mounted on the chambers, which made it possible to observe also the proportional mode. A current amplification of about 4 mV/μA was applied. All following results were obtained using chambers with 4 mm distance between walls and blades and of 8 mm distance between the tips of the blades and the roof. The blades were 40 μ thick and 4 mm high. Due to the preamplifier, the beginning of the efficiency plateau for minimum ionizing particles shifted from about 9 KV to 7.5 KV in pure isobutane, compared to the previous results, as can be seen from fig. 7. The charge spectra at the beginning, in the middle and at the end of the plateau are shown in fig. 3. One sees a smooth transition from proportional to streamer mode. In fig. 4 the asymmetry between the signal from the odd and even walls is given as function of the total pulseheight. As one can see, even in proportional mode, the left-right ambiguity of a track can be resolved from the asymmetry between the signals on the walls beside the fired blade. The fact that the asymmetry is not centered around 0 at higher pulse heights is caused by the non-linearity of the used amplifiers. Reducing the high voltage increases the rate capabillity: at 8.0

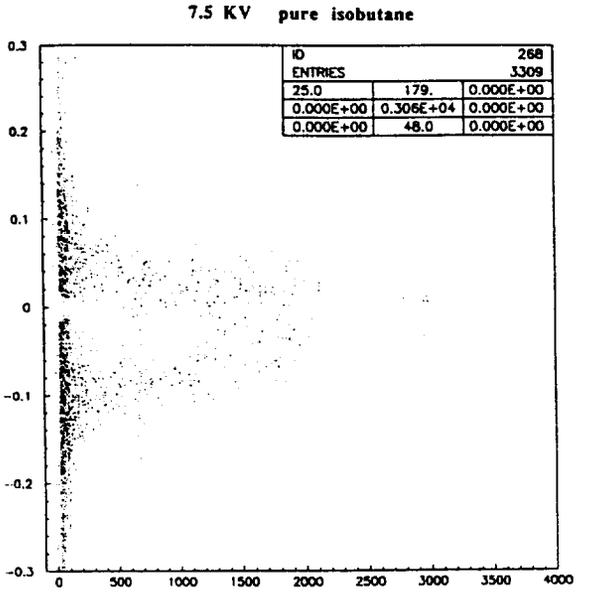


Figure 4: Charge vs asymmetry

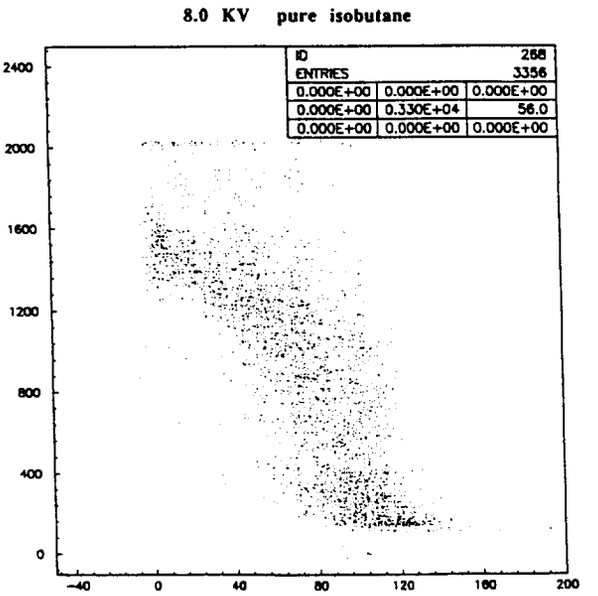


Figure 5: Drift time vs charge

KV the chamber still worked satisfactory at a local rate of 27 KHz/cm2. At 8.0 KV the chamber works halfway between proportional and streamer mode. A peculiarity of a blade chamber is the relation between drifttime and pulse height, shown in fig. 5 for 8.0 KV in pure isobutane: tracks with long driftime, traversing the cell close to the walls, give on average lower pulse heights than tracks that traverse close to the blade. If the voltage is increased, also the late tracks pass over to streamer mode. The explanation can be found looking at the electric fieldlines close to the tip of the blade, as given in fig. 10 and 12: for tracks perpendicular to the roof the path length for electrons drifting towards a low field region of the blade is shorter than for electrons drifting towards a higher field region. In case of a far away track the first ones will make a proportional mode avalanche so close to the high gain region that the field is locally disturbed and the late electrons will not initate the development of a streamer. So if one would cut on a certain pulseheight, only tracks with a short drifttime are selected, which feature could be used in the trigger. If wanted, the drifttime pulseheight correlation can be reduced as is discussed below.

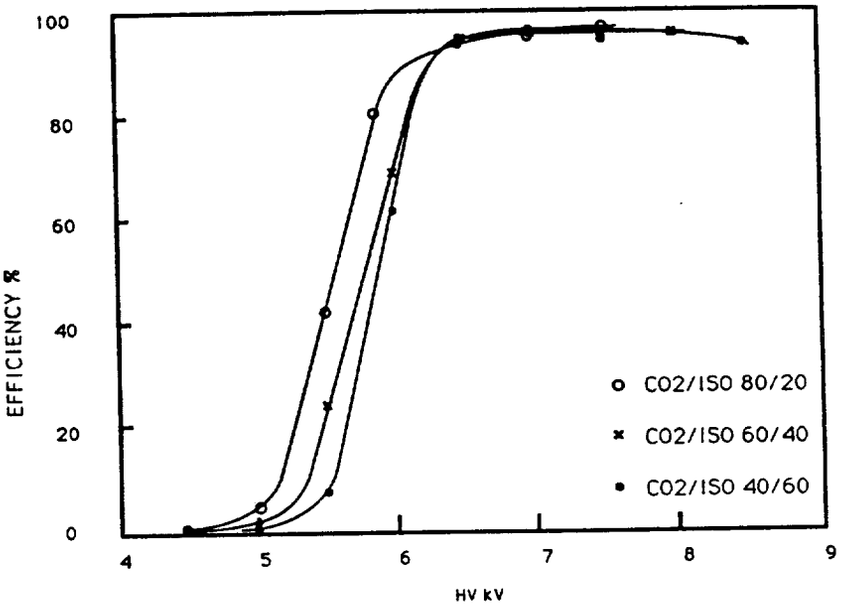


Figure 6: Efficiency curves for cosmics

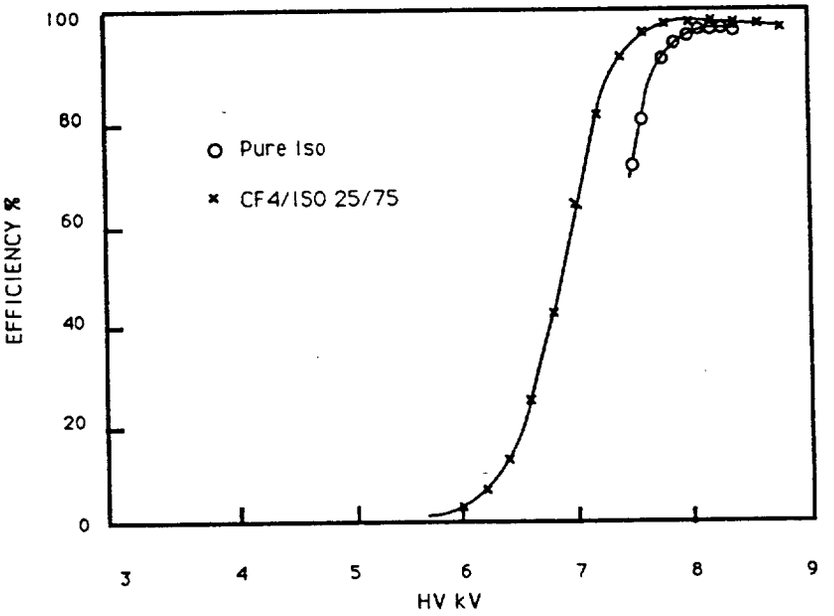


Figure 7: Efficiency curves on beam

Different gas mixtures have been tested. In fig. 6 some plateau curves are displayed using mixtures of CO2 and isobutane. These curves have been obtained with cosmic rays and thus with extremely low rate. With a mixture of 80 % CO2 and 20 % isobutane still a good plateau could be obtained. In fig. 7 plateau curves for pure isobutane and a mixture of 25 % CF4 - 75 % isobutane are compared. With the addition of CF4 the plateau starts at a lower voltage and its length is increased. Addition of CF4 also increases the mean drift speed as can be seen from the drift time spectra shown in fig. 8, taken with the same high voltage: a 25 % CF4 - 75 % isobutane mixture gives a reduction of 25 % in the mean drift time relative to a pure isobutane mixture.

A prototype with curved cells with an inner radius of 1 m and outer radius of 1.8m is under construction and ready for first testing. This prototype (fig. 9) is intended to study construction problems on a real scale and to analize signal response for different cell lengths.

Calculations have been made to predict the chamber behaviour in a magnetic field.

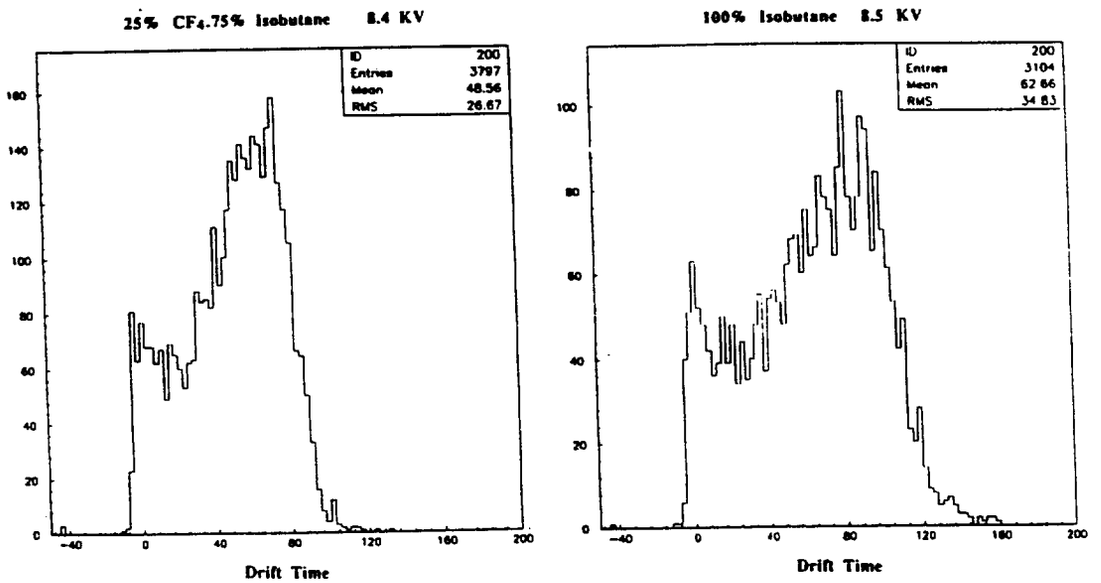


Figure 8: Drift time spectra

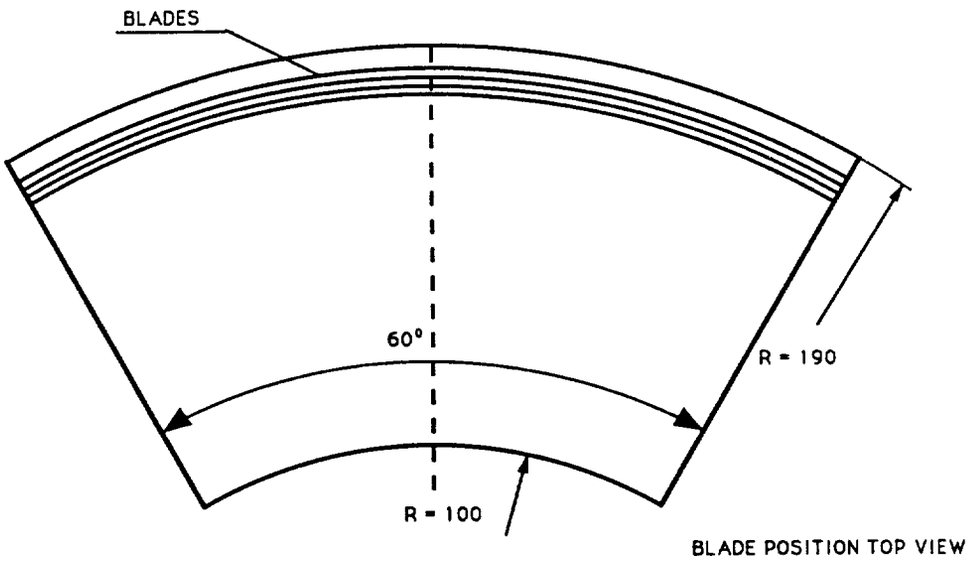


Figure 9: Circular blade chamber

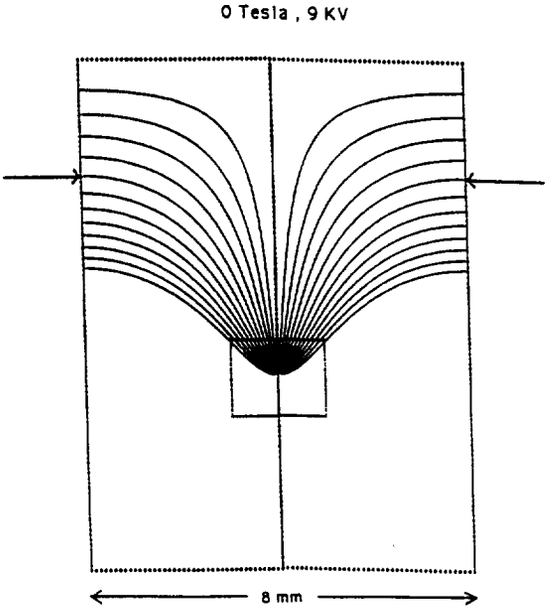


Figure 10: Drift lines without magnetic field

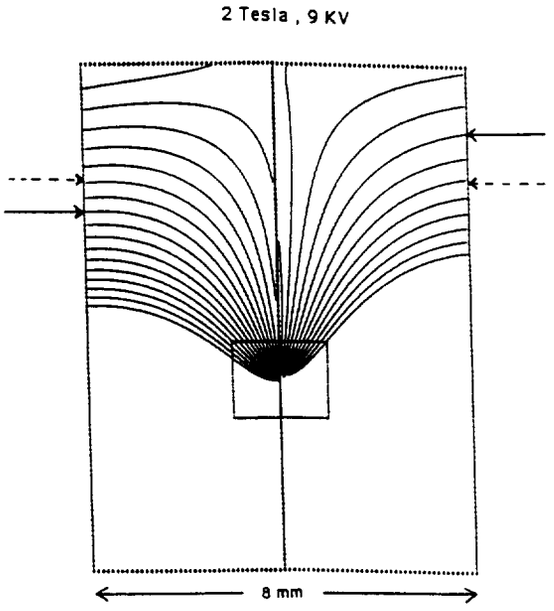


Figure 11: Drift lines with 2 T magnetic field

The gas amplification takes place around the sharp edge of a blade. Applying a high magnetic field will give rise to an asymmetry in the signal of electrons approaching the blade from different sides: from one side the electrons would be pushed towards the region of high electric field, from the other side they would be pushed away from it. This effect is not expected to be prohibitively large. In fact the electric field around the tip of a blade decreases more slowly with distance than around a wire. This means that for the same amplification field on the anode, the electric field along the drift lines is higher in a blade chamber than in a wire chamber, so the Lorentz angle is reduced. The effect has been calculated for a 2 T magnetic field parallel to the blades and a constant electron drift velocity w= 40 μ/ns in the absence of a magnetic field. In fig. 10 and B the drift lines without and with magnetic field are drawn, the active volume of the cell being the one above the arrows. In fig. 12 fieldlines and lines of equal fieldstrength are drawn near the tip of the blade, showing the high field region. Since the electric field is very high in this region, a 2 T magnetic field has a negligible effect on the electron drift lines. The

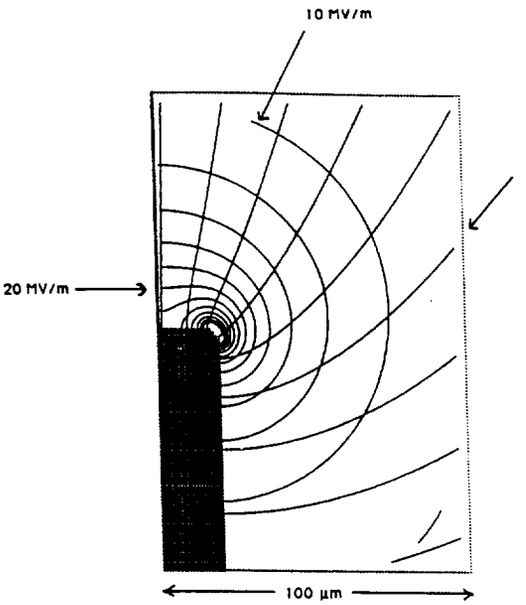


Figure 12: Tip of the blade

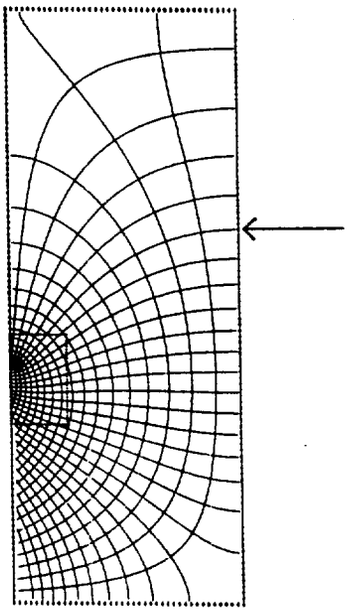


Figure 13: Field lines around conductive tip blade

calculations show that applying a magnetic field reduces the active zone in one side of the cell with respect to the other, but the active zone remains large enough to allow for a good efficiency. The chamber efficiency has to be measured in a test performed in a high magnetic field (1-2 T). If necessary it could be improved by creating some asymmetry in the cell geometry or by the use of a slower gas.

In order to improve the rate capability in streamer mode and to reduce the strong drifttime-pulseheight correlation the use of a insulating blade with conducting tip is investigated. The field configuration around such a blade would be closer to that of a wire chamber, as is shown in fig. 13 for a tension of 9 KV and step of 500 V between equipotential lines. A 40 μ blade of 4 mm height was assumed, with only the last 0.5 mm of the tip conducting. The potential between blade tip and base of the blade was assumed to drop linearly, due to inevitable surface currents. At the same high voltage this type of blade showed a 20 % lower fieldstrength on the walls at the same height as the blade tip and a 20 % higher field at a distance of 50 μ from the tip, as compared to a full metal blade. In

addition the lower boundary of the efficient region is less curved as can be seen from fig. 13, which will reduce the pulseheight drifttime correlation.

4 Conclusions

It has been proven that the blade chamber can work satisfactory also in proportional mode. In this mode the asymmetry in the signal from the two walls beside the hit blade is still large enough to solve the left-right ambiguity of a track. Working in proportional mode has the advantage of an increased rate capability and probably lifetime, because of reduced contamination of the blade tip. On the other hand, the high streamer mode signals require less sophisticated electronics. Probably a working point in between proportional and streamer mode is the most advantageous.

A gas mixture of 25 % CF4 and 75 % isobutane shows interesting features: a lengthening of the efficiency plateau and a reduction of the mean drifttime by 25 %, compared with pure isobutane. Tests using cosmic rays have shown that the chamber can also work with a large amount of CO2 mixed with isobutane.

Field calculations show that the chamber can be used in strong magnetic fields. It was also calculated that an insulating blade with only a conductive tip will improve chamber performance.

For the future we have planned several activities. We will optimize the preamplifiers to gain in linearity and speed. Gas studies will be continued to improve chamber performance and to find a non flamable gas mixture. The resolution will be determined as function of rate and incident angle. Soon measurements on a real size prototype will start. Blade capacity, resolution, gas flow,etc. will be studied. Chamber efficiency and resolution have to me measured in a high magnetic field parallel to the blade. A test cell with metalized blade tip is under construction and will be tested soon. The live time as funtion of charge/cm2 shall be measured.

5 References

[1] G. Ambrosi et al., A new gaseous detector for tracking: the blade chamber, Nucl. Instr. and Meth. A289 (1990) 351.

THE HONEYCOMB STRIP CHAMBER

Harry van der Graaf[a], Paul Rewiersma[a], Adriaan König[b], Thei Wijnen[b], Gerard Faber[c]

a: NIKHEF-H, Amsterdam, The Netherlands
b: NIKHEF & University of Nijmegen, The Netherlands
c: now at ETH, Zürich, Switzerland

The Honeycomb Strip Chamber is a new position sensitive detector. It consists of a stack of folded foils glued together, forming a rigid honeycomb structure. In the centre of each hexagonal cell a wire is strung. Conducting strips on the foils, perpendicular to the wires, pick up the induced avalanche charge. Test results of a prototype show that processing the signals from three adjacent strips nearest to the track gives a spatial resolution better than 64 μm for perpendicular incident tracks. The chamber performance is only slightly affected by a magnetic field.

Principle

In fig.1 the basic element of the chamber is shown: each wire is coaxially surrounded by conducting hexagonal rings [1]. A muon passing the volume inside the rings results in an avalanche on the wire. The (negative) charge signal from the wire equals the total (positive) charge signal on the rings at any time. The charge distribution over the rings is an exclusive function of the avalanche position along the wire and the geometry of wires and rings [2,3,4,5]. In fig.2 the construction of the chamber is shown: folded foils with conducting strips perpendicular to the fold edges are glued together. A stack of these foils form a stiff, rigid and self supporting honeycomb shown in fig.3. In each hexagonal cell a wire is strung: the wire tension is held by the cell walls.The geometry of fig.3 requires conducting strips at both sides of each foil. As a consequence, the mutual capacity between a strip* and its upper and lower neighbour are very high. Since each strip is virtually grounded by its amplifier, the source capacities are far too high and the signal/noise ratio would be poor.This problem is solved in the geometry of fig.4: each layer of cells is covered with an insulating flat foil which acts as a base for the next layer. Odd and even planes are relatively shifted by half a cell pitch. In order to minimize dead volume, the cell pitch within a plane is reduced by shortening the interconnecting plane between two neighbouring cells. In this geometry the capacity between horizontally neighbouring strips dominates the 'vertical' capacity.

Simulation

In order to study the relation between the chamber geometry and the spatial resolution a Monte Carlo simulation program was written (see definitions in fig.5). The following processes were included: generation of points of primary interaction between minimum-ionising particle and argon gas; generation of secondary electron ion-electron pairs; Curran fluctuation in gas gain; the mechanism of induced charge; preamp noise. In fig.6 the spatial resolution is shown as a function of φ, for two cell radii. The spatial resolution can be approached by the expression

$$\sigma^2 = \sigma_0^2 + (\sigma_\varphi \cdot \varphi)^2$$

The best obtainable resolution σ_0 is reached for perpendicular incident tracks ($\varphi = 0$) and is determined by the range of δ-rays. For larger φ the Poisson distribution of the points of primary interaction between the muon and the gas contributes. Values found for σ_0 and σ_φ are 30 and 800 μm, respectively, for a cell radius of 5 mm, in argon at atmospheric pressure.

---

* A strip is defined here as a group of interconnected hexagonal rings.

The optimum in the strip pitch (5 mm for R = 5 mm) tallied with a previous calculation [3].
In order to establish signal/noise ratio demands, a gas gain of 10^5 was assumed; fixing the RMS of the equivalent noise of the preamps at 5000 electrons, a spatial resolution of 100 μm is obtained for $|\varphi| < 0.1$ rad.
The allowed preamp noise limits the length of the strips; a high gas gain may allow strip lengths up to a few meters. The maximum length of a chamber may be twice the strip length by separating the strips in the chamber centre and doubling the number of preamps.

The prototype, the read out system and the experimental set up

The prototype consists of ten identical layers, alternatively shifted by half a cell pitch. Cell radius: 5.77 mm, wire pitch within plane: 13.0 mm, strip width 4.0 mm, strip pitch 5.0 mm. The outer layers have a mere shielding function; in eight planes gold plated tungsten wires (dia. 20 μm) were strung in the cell axis.
Kapton foils with Cu strips were obtained from outside firms. The tolerances of the strip position and strip width were 100 μm. Each chamber layer consisted of 24 cells and 54 strips.
At the open ends of the cells an aluminium profile was glued; nylon plugs, fitting in the chamber cells as well as in holes in the profile defined the position of a chamber plane within the stack. A second aluminium profile formed a sealed gas distribution box with the first one. The second profile was equipped with holes for shrinking tubes that fixed the wires.
The completed chamber was mounted on a solid aluminium plate which acted as support for the preamplifiers and cables.
The strip signals were amplified by 4-channel hybrid charge amplifiers; after this the bipolar signals arrived in the counting room. Here they were filtered, amplified and converted into monopolar signals using 128 channels of 'Analog Line Receivers'. The output signals were guided to the gated, charge-sensitive ADCs.
Twelve adjacent wires of each plane were read out: after a hybrid preamplifier and discriminator the digital signals (96 channels) were transported via 40 m twisted pairs cables to the CAMAC TDCs in the counting room.
We used the secondary SPS beam X3 of the L3 test site in the West Hall at CERN. The beam was tuned for e- and π- of 10 GeV. The electrons were absorbed by inserting 10 mm Pb; per beam spill up to 500 pions passed the chamber.
The chamber was placed in the large L3 test beam magnet. The trigger was obtained from two hodoscopes: one was placed upstream and one downstream the magnet. Each hodoscope consisted of two scintillators with overlapping surface. The geometry of the overlap had the same dimensions as the sensitive area of the chamber. The four-fold coincidence between the scintillators was an efficient trigger with virtually no background.
The gas system consisted of three flow controllers (Brooks 5878); there were no demands on the stability of the mixing rate typical for high-accuracy drift chambers. The used gas mixtures were: A/Ethane 62/38, A/CO_2 80/20 and A/CO_2 50/50.
Positive HV was applied on the wires: the value was adjusted such that the strip signal amplitudes were within the ADC range. The values were 1570, 1700 and 1950 V respectively for the gas mixtures. This corresponds with a gas gain of about 10^5.
Since a honeycomb cell and the wire in its axis form an almost ideal counting tube, the electric field is only strong around the wire. No HV breakdowns occured during the test; a gas gain of 10^6 could be maintained.

Results

For each event the data of 128 ADC channels and 96 TDC channels was written to tape. From the TDC data the angle θ, the Z coordinate and the timing of the track can be obtained [6]; this is not discussed here. The ADC data was first corrected for pedestals. Then the correlated noise was corrected for by subtracting the average value of the ADC readings away from the event.
If the gain of a preamp-ADC channel associated with strip N is relatively high then the positions of the measured tracks through the neighbouring strips N-1 and N+1 are 'pulled' towards strip N. Using this effect and the data, the calibration factors of preamp-ADC channels were obtained by

calculating residuals of position spectra for each strip. An attempt to calibrate using test pulses on wires failed because of the too large spread in strip widths.
For each plane the track position was calculated using the three largest adjacent ADC values after the pedestal and gain correction [6].
Using only 1000 events of perpendicular incident tracks, the relative alignment of the eight chanber planes was obtained: the maximum deviation from perfect alignment was 150 μm.
The relation between spatial resolution and residuals was obtained by a Monte Carlo simulation. Fig.6 shows results for two gases in absence of magnetic field: the performance of the chamber is the same for both gases. The fit of the parameter for the best resolution σ_0 has a value of 90 μm for both gases. Some fine-tuned analyses of runs with small φ gave a value of 64 μm. Parameter σ_φ has the value of 1000 μm. The difference between this figure and the Monte Carlo result is caused by the dependence of the shape of the charge distribution on angle φ, which is not yet included in the analyses
Fig.7 shows the resolution for three values of the magnetic field. The Lorentz angle shift is clearly visible. The fit parameters are the same as in fig.6, indicating that the chamber performance is not affected by the magnetic field. A rotation of the chamber over the Lorentz angle around an axis parallel to the strips fully compensates the shift.

Electronics and trigger for LHC applications

In fig.8 a low-cost read out schema is shown for the strips. Each strip has its own low-noise preamp. The outputs of the preamps are connected with a unit which detects the strip carrying the largest signal. This unit activates three analog switches; three lines Q_{left}, Q_{middle} and Q_{right} are connected with the outputs of the preamps closest to the track. The signals Q_{left}, Q_{middle} and Q_{right} are digitized by two FADCs applied in the divide mode [6].
In this way the main electronic read out circuit is reduced to a preamp and three analog switches per strip and two FADCs per chamber plane. Two coincident tracks within a chamber can be recognized and processed by using some additional electronics [6]. The strip preamps and switches can be integrated in hybrids or ASICs, while the FADCs can be mounted elsewhere on the chamber. Digital communication between the chamber and the outside world could be controlled by a processor on the chamber.
A trigger can be derived from both the strip and the wire signals: they occur within the maximum drift time of 70 - 250 ns (depending on the gas mixture). The principle of the trigger is shown in fig.9: an activated wire or 'maximum strip' activates a FET. A network of FETs, shown in fig.10 is an image of the strips of a four-layer chamber. The resistance measured between the poles drops if a track passes the chamber. The trigger cell, formed by the poles,can activate, in its turn, a FET. This is shown in fig.11 where the resistance drop is a function of the muon momentum. A Monte Carlo simulation must show the feasibility of this trigger.

Conclusions

The test of the prototype of the honeycomb strip chamber shows its potential high resolution: the worsening of the resolution with the angle of incidence was observed, as well as the influence of the magnetic field. Equipped with electronics on the chamber, the price could be much lower than comparable drift chambers. The chamber is extremely light. Its disadvantage is that the spatial resolution depends on the angle of incidence.

Acknowledgements

We would like to thank Wim Gotink, Joost van Echtelt, Tjerk Lopik, Raymond Rosmalen, Hans Kok, Cees Brouwer and Hans Peter van der Klei for various contributions. We thank the L3 Collaboration for the use of the L3 test beam site.

References

[1] H. van der Graaf et al.: The Honeycomb Strip Chamber. Proceedings of the ECFA Study Week on Instrumentation Technology for High-Luminosity Hadron Colliders, Barcelona, 14-21 September 1989. CERN 89-10, ECFA 89-124, vol.2, 24 november 1989.

[2] G. Charpak et al.: Nucl. Instr. & Methods 62 (1968) 262-268

[3] E. Gatty et al.: Nucl. Instr. & Methods 163 (1979) 83-92

[4] E. Mathieson et al.: Nucl. Instr. & Methods 227 (1984) 277-282

[5] H. van der Graaf and J.P.Wagenaar: Nucl. Instr. & Methods A252(1986)311-320

[6] The Honeycomb Strip Chamber: results of the test of a prototype and its application in LHC/SSC experiments. Submitted to Nucl. Instr. & Methods.

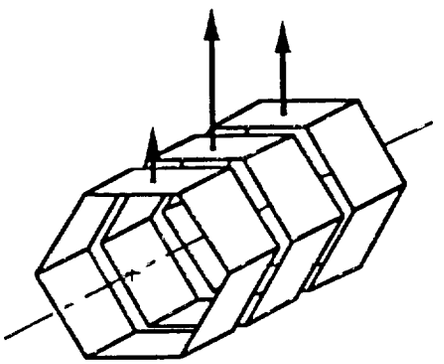


fig.1 Principle

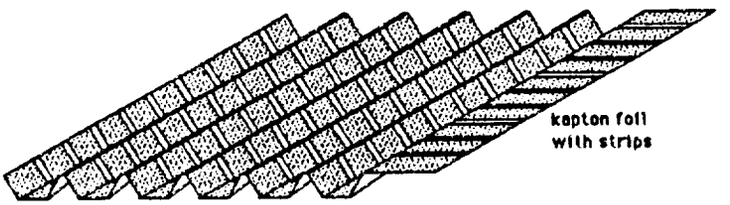


fig.2 Folded and etched kapton/Cu foil

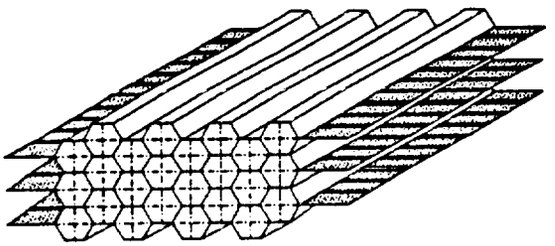


fig. 3 Honeycomb structure

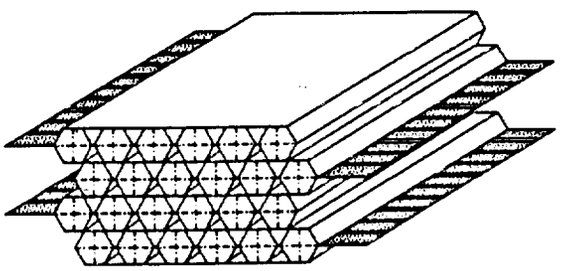


fig. 4 Structure with intermediate flat foil

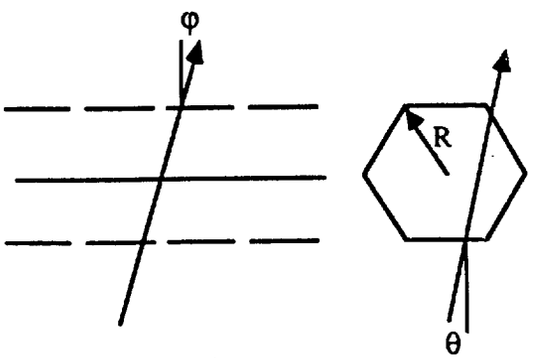


fig.5 Definition of cell geometry and angles

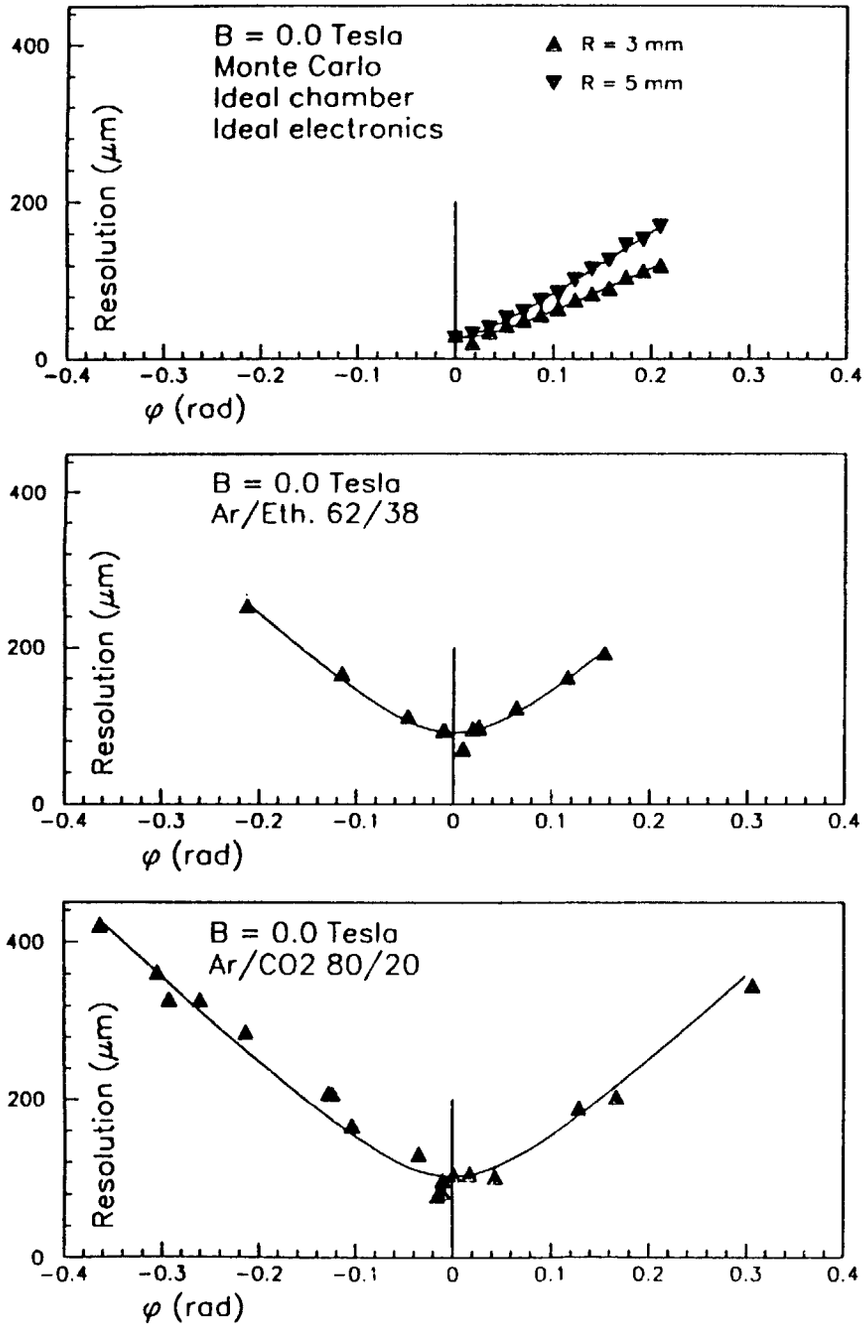


fig 6 Results for B = 0 T. Top: Monte Carlo

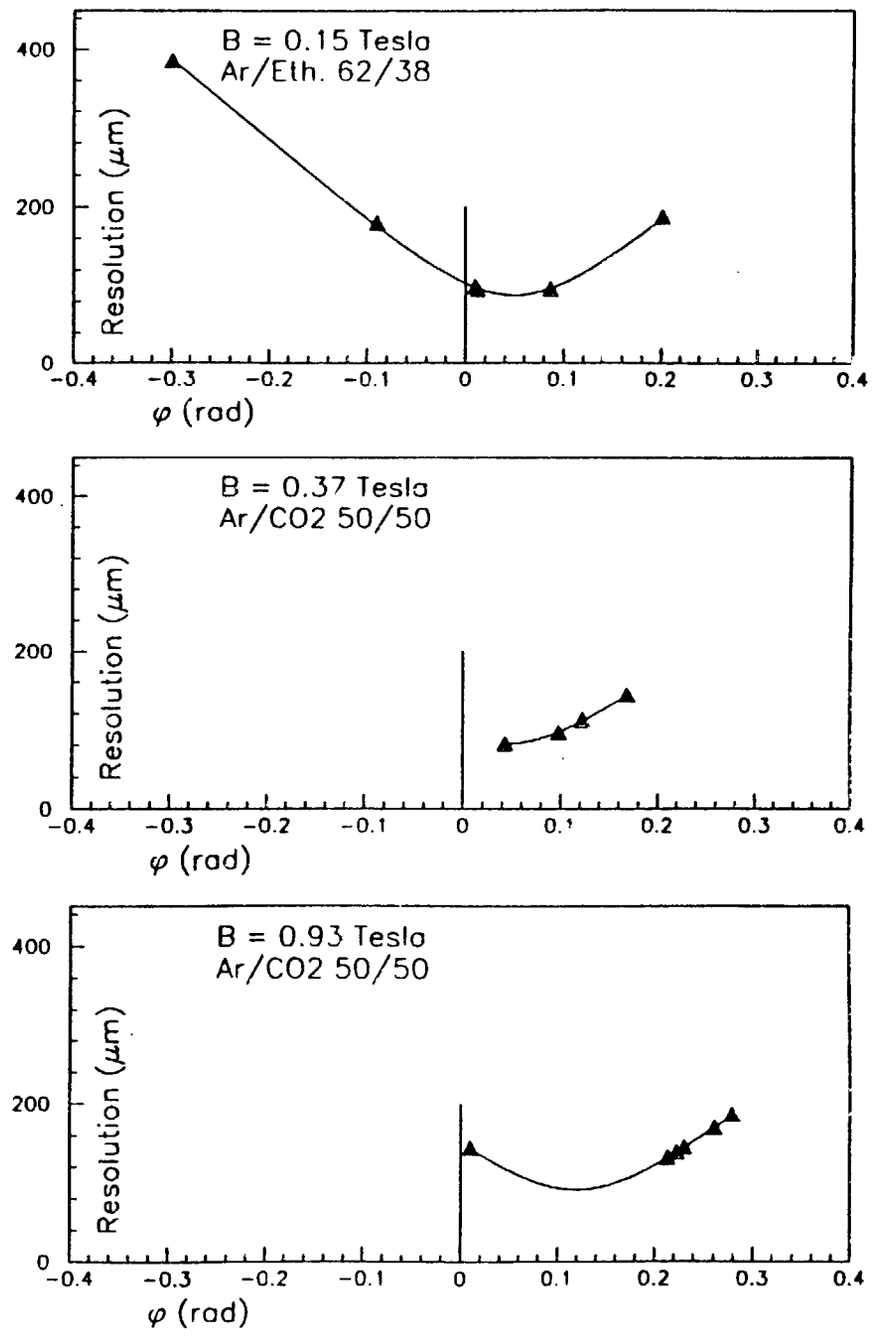


fig.7 Results in magnetic field

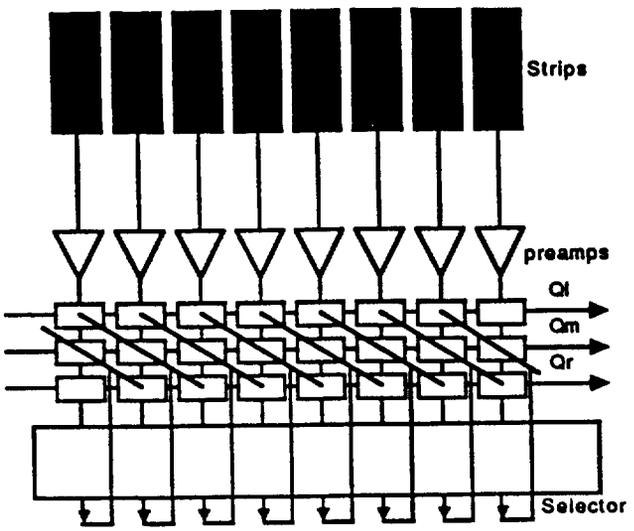


fig.8 Read out system

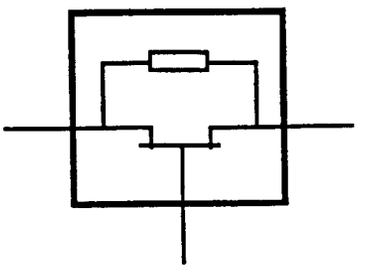
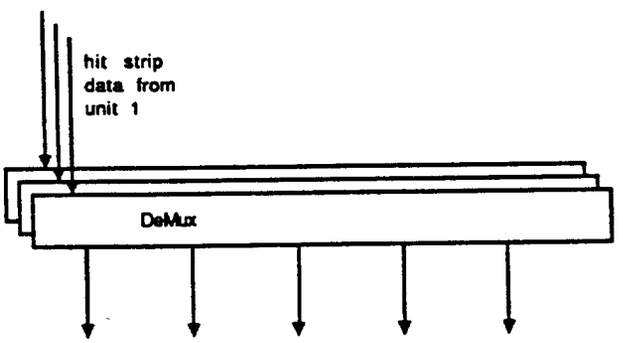


fig.9 Basic trigger element



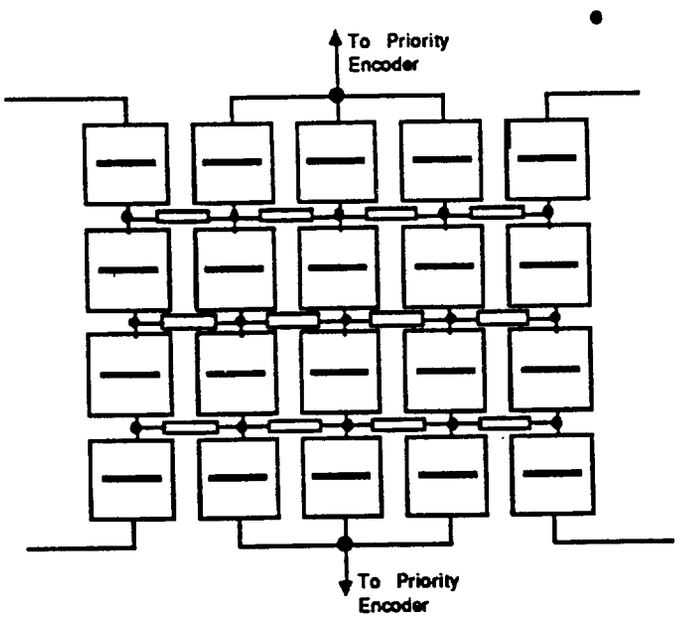


fig.10 Array of FET elements

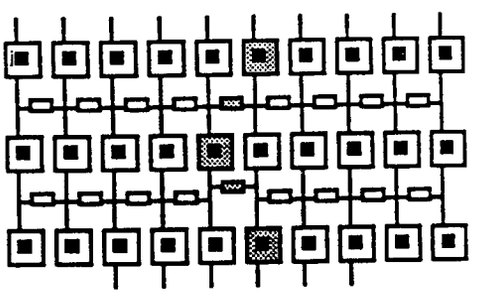


fig.11 Single muon energy trigger

Toroidal Field Geometries for LHC Muon Spectrometers

Ulrich Goerlach
CERN, Geneva, Switzerland

Abstract

Toroidal magnetic field geometries have been discussed frequently as a convenient alternative to solenoidal fields to cover uniformly a wide rapidity interval at large hadron colliders of very high $\sqrt{s}$. A toroidal field leads to a field free-region around the interaction vertex which offers both, advantages and drawbacks. Furthermore, the geometry of the tracking chambers is complicated by the coils which completely surround the field volume.

Several, very different approaches for a conceptual design are presented. The momentum resolution of standard iron toroids is limited to 13–15%. Alternatives to overcome this limitation, such as high-field iron or air toroids are discussed.

Motivation for Toroidal Fields

It is not the purpose of this report, and it is beyond its scope, to discuss in detail the demands for momentum resolution and acceptance. However, let us briefly summarize the arguments. The lepton identification should cover at least the range of $|\eta| \leq 2.5$–3.0 in rapidity and transverse momenta between 10 GeV/c and 2 TeV/c. A wide rapidity range is particularly important for the lighter Higgs and for the asymmetry measurements of new vector bosons. The momentum range is determined at low momenta by the acceptance for the lighter Higgs and at high momenta by the discovery limit for new particles. The question of the required lepton momentum resolution is however more controversial. Whereas for the Higgs search in most of the accessible mass range an excellent momentum resolution is useful but may not be mandatory, it is difficult to judge the necessity of it in the context of new particle searches, where surprises cannot be excluded.

The requirement for an extremely large rapidity acceptance ($\eta = 3 \rightarrow 5.7°$), which is very difficult to cover with a solenoidal field, motivates the use of toroidal field geometries. The field lines of a toroid are circular around the beam axis and so always perpendicular to the particle trajectory. The bending power of the magnetic field increases as $\int B\mathrm{d}l \propto \sin^{-1}\theta$, almost independent of the geometry as indicated in Fig. 1. This is due either to the path length or to the $1/R$ dependence of the field at small angles. As a consequence, the bending power of the magnet follows the increasing momentum for forward rapidities at fixed p_T.

In a solenoidal field, on the contrary, the transverse bending power decreases with $1/\sin\theta$ once the particles no longer traverse the total field volume. It is obvious from this point of view that a toroidal field is the appropriate complement of a solenoidal field in the forward region. However, such a detector will have a complicated transition region between the two magnets. Therefore schemes have been developed to use a toroidal geometry in the whole rapidity range in order to arrive at a more uniform detector.

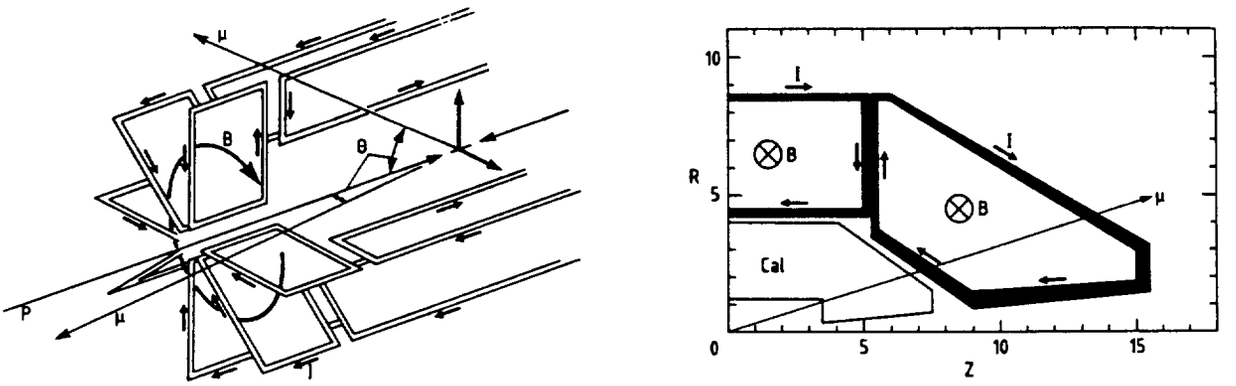


Figure 1: Schematic view of two toroidal field configurations arranged around an interaction region

The Impact of a Toroidal Field

The choice of toroidal fields as the basic magnetic configuration leads to several features in which the layout of the detector will differ significantly from concepts using a solenoid. The most important points will be discussed below.

The Absence of a Central Magnetic Field The most striking feature of toroids is perhaps the absence of a magnetic field around the interaction point. Often this is regarded as an advantage for the detector design for the following reasons:

- All particle trajectories are straight lines, so tracking will be easier.
- Electron pairs from gamma conversions or Dalitz decays are not opened up and can therefore be rejected more easily via a $\mathrm{d}E/\mathrm{d}x$ measurement in a tracking device.
- The jet resolution of the calorimeter is not affected by the deflection of low-momentum particles.
- There is no limitation, due to a magnetic field, in the choice of the read out system and of the electronics for the inner detectors including the calorimeter.

However, the absence of the magnetic field will also result in some important limitations of the apparatus:

- There is no possibility to measure the momentum or the sign of charged particles before the calorimeter. This will, in particular, affect the electron identification.
- The muon momentum will be determined only once after the calorimeter. There is no redundancy in the measurement.
- Low-momentum muons will be measured only w imited precision as they will lose already a very large fraction of their energy in tne calorimeter.
- The high-precision point of the vertex in the transverse plane is not used for the momentum determination of the muons.

These arguments are based upon the assumption that tracking in a magnetic field at high luminosity is feasible. If this is not achievable a central magnetic field is of no use, unless it is very much stronger than the multiple scattering in the calorimeter ($B \geq 2.5$T for $\mathrm{d}p/p \leq 10\%$). The effect of such high fields on the event topology (jets, isolation of leptons, etc.) has not yet been studied.

The Geometry of the Tracking Chambers The field lines in a toroid are completely surrounded by the coils forming a closed magnetic bottle, a property which is exploited in many applications. In order to reach the necessary magnetic fields considerable currents have to be established in the coils. Even modest demands on the uniformity of the field require a large number of coils around the field volume. Furthermore, the net-radial force towards the centre (the beam axis) needs compensation, which is achieved best by a central cylinder supporting and connecting the individual coils. All these conditions lead to a very inaccessible field volume. Therefore, installation and alignment of, and access to the tracking chambers inside the field is in general a very difficult task.

The Size of the Magnet Coil Owing to its more favourable geometry a solenoid with circular coils is a more economical way of generating a field in a given volume. For a toroid the total length of the required conductor will be longer, and therefore costs and the electric power consumption will be higher. The rectangular shape of an individual coil is, in general, not only larger but also mechanically more delicate to stabilize than the circular coil of a solenoid.

Detector Concepts with a Toroidal Field

Let us consider several examples of spectrometer geometries using toroidal fields. Two classes can be distinguished, namely toroids based on magnetized Fe and those based on air-fields.

The use of magnetized Fe has been found to be extremely attractive, as it combines, in an ingenious way, the necessity of a hadron absorber with a very cheap way of generating the magnetic field. The achieved momentum resolution is limited by the multiple scattering of the muons in the Fe. The resolution is given by $\mathrm{d}p/p \approx 0.4/B\sqrt{L}$, where L is the length of the magnetized Fe and B the magnetic field. As we will see later, the practical limit of the magnetization of Fe with normal conducting coils is about 1.8 T. Therefore, 5 m of Fe are necessary to achieve a momentum resolution of 10%. In fixed-target geometries, which cover only a limited solid angle, much better resolutions can be obtained with longer spectrometers. The situation is different in a collider experiment, where a large acceptance close to 4π has to be covered and the total mass of the detector will limit its radial dimensions. Furthermore, the function of the Fe as a hadron absorber is lost after about 2 m thickness. As has been shown both experimentally and in Monte Carlo simulations, after a total thickness of 15 interaction lengths (Λ) the spectrum of punch-through particles is dominated by muons originating from decays in the beginning of the hadronic cascade [1]. Most of the calorimeters discussed for experiments at the LHC have a radial thickness of about 10–12Λ and are not constructed from iron! Only about an additional 5–6Λ would be required by the muon filter. This corresponds to approximately 1–2 m of Fe, much less that necessary for a reasonable momentum resolution!

Ways to overcome the practical limitation of the momentum resolution are either to increase significantly the magnetic field or to use an air-field toroid spectrometer.

In an air-field toroid the magnetic field is solely generated by the very strong electric currents. In this case, the multiple scattering no longer limits the resolution, which is now only determined by the tracking resolution δx according to $\mathrm{d}p/p \propto p \cdot \delta x/BL^2$. As discussed above it is non-trivial to place the tracking chambers in the field of the toroid. Therefore, compromises have been considered, in which only the incident and the exiting direction of the muon track is determined and no tracking is performed in the field volume itself. In this case the thickness D of the coils has to be minimized as it is again the multiple scattering which will limit the resolution: $\mathrm{d}p/p \propto \sqrt{D}/BL$

The clear advantage of the air-field toroids is their superb resolution and their small weight. The challenge is in the construction of the coils and the high-precision tracking chambers.

The Conventional Iron Toroid Given the constraints of a good hadronic calorimeter occupying a cylindrical space with an outer radius of at least 4 m, the total Fe thickness in the central barrel $|\eta| \leq 1$ was limited to 3 m, whereas the intermediate and forward region is 4 m thick, a total mass of approximately 23000 t. Adding a further meter of Fe would increase the weight by 50% but improve the momentum resolution only marginally. For further details see Ref. [2]. Assuming a magnetization of 1.8 T, the electric power consumption has been evaluated to be about 2.6 MW [3].

The theoretical performance with respect to the momentum resolution can be estimated with good confidence following the work of Zupančič et al. [4]. It depends crucially on the precise determination of the direction at the entrance and the exit of the Fe toroid, especially at high momenta.

The multiple scattering limit is ≈12.8%. Assuming tracking only inside the Fe (sagitta measurement) with a 200 μm position resolution in each station, the momentum-dependent contribution to the resolution is $4 \times 10^{-4} \cdot p(\mathrm{GeV}/c)$. This gives, already at 750 GeV/c, an unacceptable resolution of 30% or more; for a 100 μm resolution this limit is at 1.5 TeV/c. A further reduction of the position resolution seems to be far out of reach; already 200 μm is difficult to achieve. The NA4 Collaboration [5] observed a deterioration by 1 mm of their intrinsic chamber resolution owing to the production of delta electrons. Only multi layer chambers with excellent two-track separation can overcome this problem.

A considerable improvement can be obtained if the ingoing and the outgoing trajectory can also be measured with great precision. Assuming 200 μm resolution inside the iron, an angular resolution of 0.1 mrad on one side of the toroid would improve the resolution at high momenta by more than a factor of 2. Such a precision of direction could be achieved by a 50 cm thick multi layer tracker with an intrinsic resolution of about 100 μm. Determining both directions with an accuracy of 0.1 mrad would bring the momentum-dependent term down to 8×10^{-5}, resulting in $\mathrm{d}p/p \approx 15\%$ at 1 TeV/c, or 30% above 3 TeV/c. In this case the momentum resolution is only given by the precision of the outer chambers and not anymore by the position resolution within the Fe. Owing to the need for redundancy, however, these chambers cannot be abandoned.

Clearly, the great importance of a very precise tracking system is obvious, even for this so-called 'modest' muon spectrometer. The total area which has to be covered with tracking chambers is impressive: ≈ 4600 m^2 not including a high-resolution outer tracker which alone has a surface of about 1200 m^2. All these chambers will be difficult to access as they are enclosed by the Fe and the electric coils!

A High-Field Iron Toroid One step towards a considerably improved momentum resolution is to increase the magnetic field and to decrease its thickness. Figure 2 shows the magnetization curve of Fe. Fields up to 1.8 T are easily achievable with relative low currents of $\approx 10^4$A/m. Already the increase to 2 T will require twice the current and thus four times the electric power. Enormous currents, 100 times higher, have to be used to generate fields significantly above the saturation of Fe at 2.16 T. In this regime the additional magnetic field is generated directly by the coil. These currents can only be achieved with superconducting coils. In Fig. 3 an example is given of a detector using compact superconducting Fe toroids arranged around the calorimeter. A 5 T field is generated over a 1.5 m thick Fe core. Thus the multiple scattering limit of the momentum resolution is

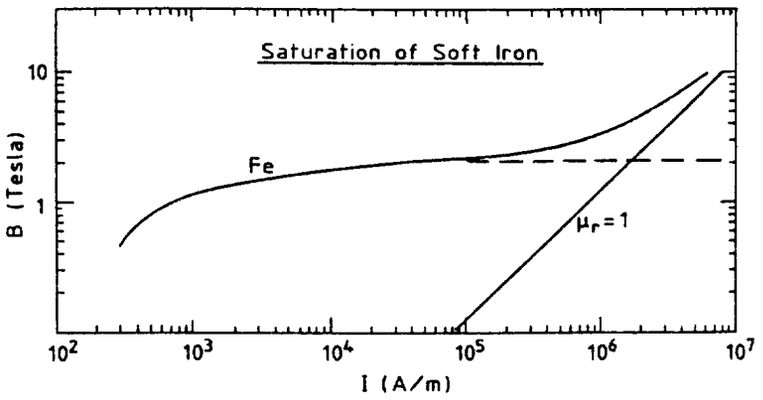


Figure 2: Magnetic induction B inside Fe

6.5%. Assuming precise tracking of 0.1 mrad outside the toroids, the momentum-dependent term amounts to $8 \times 10^{-5} \cdot p(\mathrm{GeV}/c)$

The Fe serves here as an absorber of moderate thickness (8.3 Λ) and as a rigid support structure for the superconductive coils. This necessarily implies that the mass of the Fe, in total 10000 t, has to be cold. The cooling down of this mass is the main challenge of this approach. Further problems are the large size of the coils themselves, and the vacuum vessel, and the large stored energy of 3600 MJ in the barrel.

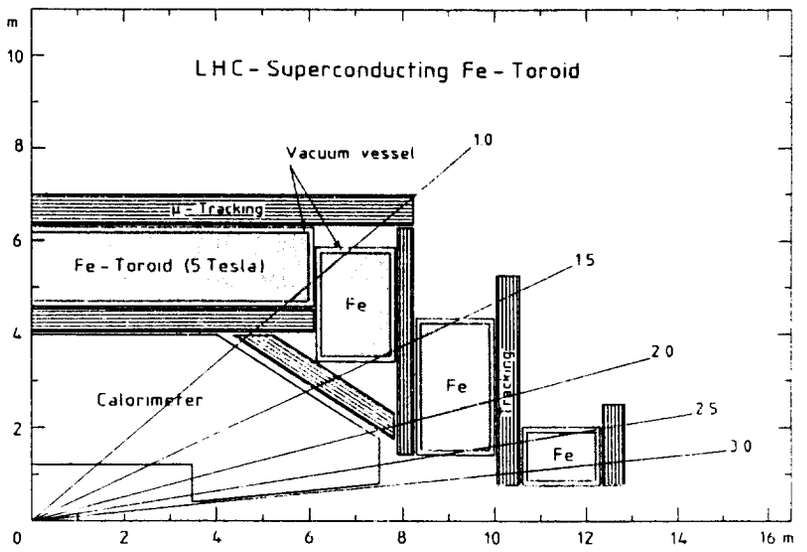


Figure 3: A detector with superconducting Fe-toroids

Owing to the radial field-dependence, which is partially levelled out by the saturation of the Fe, as illustrated in figure 4a, and the technical limit of 10 T for superconductors, the forward toroids have to be split into smaller units providing an almost constant field integral over the rapidity coverage.

The higher the generated field, the smaller the contribution of the Fe to it, which limits the resolution at low momenta by multiple scattering. Replacing it by Al or air can overcome this limitation (Fig. 4) at the cost of the high-momentum range where the resolution will always benefit from the higher bending power of an Fe-filled magnet. Above 2×10^6 ampere-turns per meter the multiple scattering limit of an Al-filled toroid becomes comparable to magnetized Fe despite the lower field. A drastic improvement is obtained for air simulated by Al with an 11% filling factor to account for the material of the coil.Naturally this leads to the proposed air-field toroids.

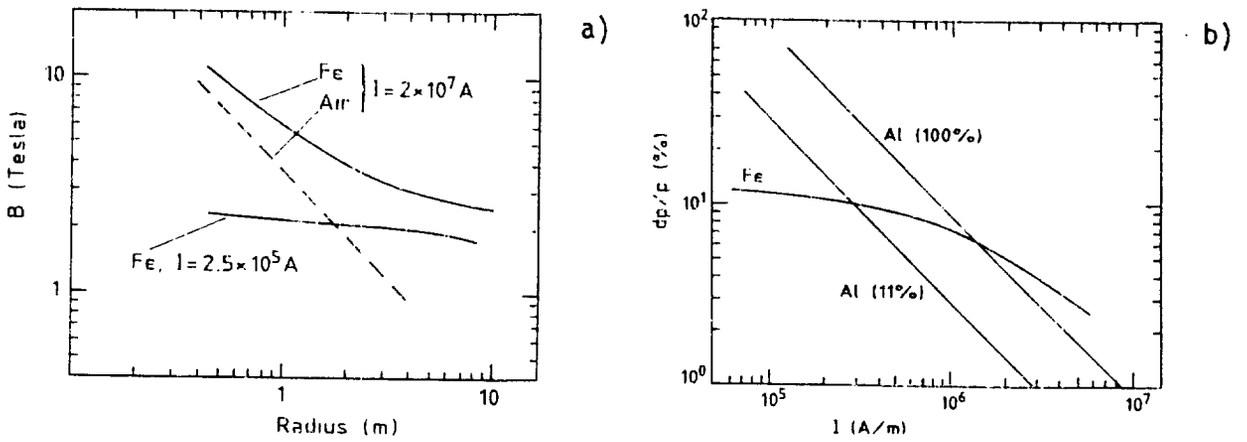


Figure 4: a) The radial field dependence in magnetized Fe b) The multiple scattering limit of magnetized Fe and of Al as a function of the current in the coil

Open Superconducting Coils (LAA) It has been argued above that the requirements of generating the necessary fields, the uniformity, and the mechanical forces occurring between the superconducting coils make it very difficult or even impossible to place the tracking system inside the magnetic field. Nevertheless, an ambitious project has been presented [6] which studies this possibility. Although the estimated performance of this spectrometer is outstanding, serious questions concerning the feasibility still need extensive investigations.

Closed Superconducting Coils (EMPACT) Originally starting with a similar concept for an air toroid detector at the SSC the EMPACT Collaboration is now proposing a solution not using tracking inside the field. Thus, multiple scattering in the material of the vacuum vessel and the superconducting coils has to be optimized by minimizing the total thickness. Extensive engineering studies have been carried out with industry to prove the feasibility of the construction. However, the preliminary cost estimates are high! For further details see Ref. [7].

Large Conventional Coils in a Toroid Geometry In order to reach a good momentum resolution in an air-field a larger volume is more important than a high value of the field. Two such approaches, basically using solenoidal fields [8,9] have been presented at this conference. Very large coils are necessary to cover $|\eta| \leq 3$ in a large air-field of toroidal geometry, preventing the use of superconductors. Studying the possibility of employing warm Al-coils, we have obtained the following result:

Even with a small field of $B \approx 0.25$ T in the central region over a length of 4 m (Fig. 1b) the power consumption was estimated to be $\approx$ 16 MW for the case of conventional Al coils with 8.5×10^6 ampere·turns, weighing 2700 t and completely surrounding the detectors. Access to the tracking chambers is likely to be granted only by interrupting the coils. A very high precision of the chambers, i.e. 30 μm is required to achieve a resolution of $dp/p \approx 2.5 \times 10^{-4} \cdot p \sin\theta$

Comparison and Evaluation of the Different Concepts

In the introduction we summarized the main motivation for a toroidal geometry as follows: the construction of a spectrometer with very wide rapidity acceptance and a momentum resolution uniform in rapidity and dependent only on p_T and not on η.

Momentum Resolution In Fig. 5 we present the momentum resolution at $\eta = 0$ for various designs. As discussed above, Fe-based toroids have a constant resolution (multiple scattering limit) for most of the momentum range, until at high momentum the tracking resolution is dominating. High requirements are imposed on the tracking, the three lines in the figure indicating the improvements due to precise determination of the muon direction for a conventional Fe toroid: 1) tracking (200 μm) inside the Fe only, 2) determining one direction (0.1 mrad) only, and 3) measuring both, entrance and exit trajectories. For the super conducting Fe toroid only the third case is assumed. Despite the shorter magnetic length, this leads a resolution that is twice as good, owing to the high magnetic field.

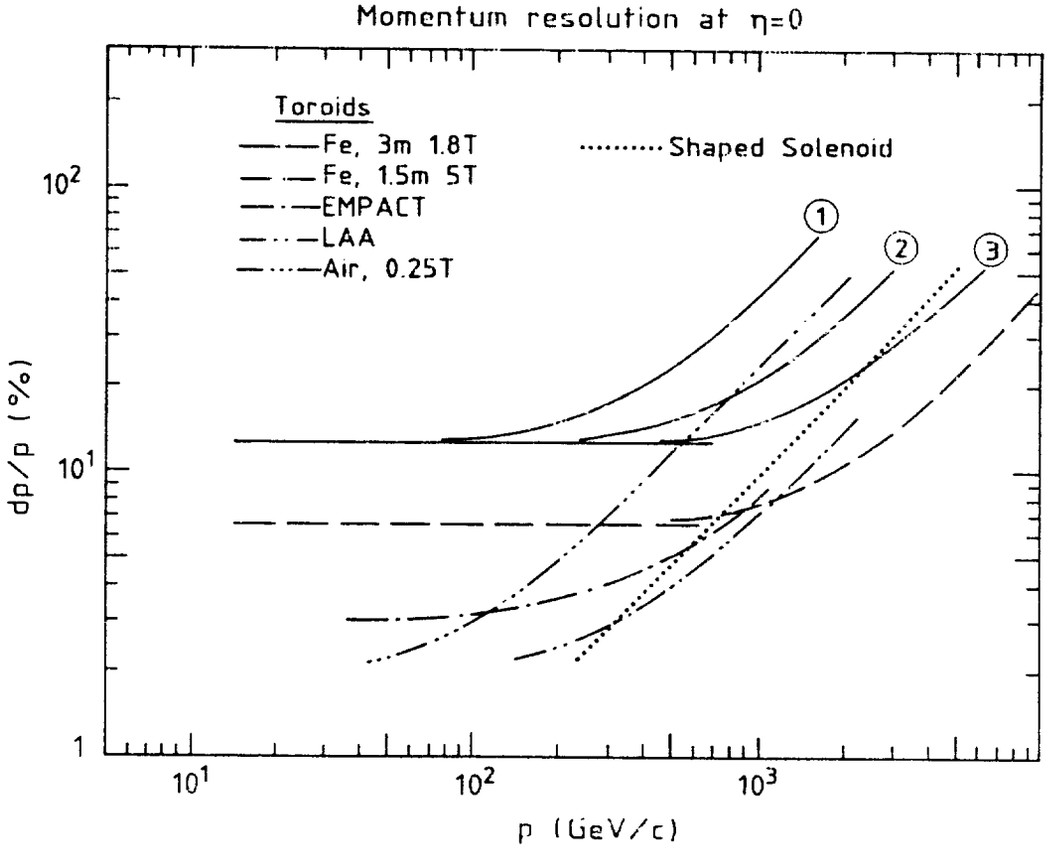


Figure 5: The momentum resolution as a function of momentum

The two air toroids, based on superconducting coils, drastically improve the momentum range below 1 TeV/c; a minimal multiple scattering error of 2% was assumed for Ref. [6]. An air toroid based on conventional coils gives a resolution of better than 10% only below 400 GeV/c.

For comparison, the performance of one solenoid-based design, the large 'Shaped Iron Solenoid', was also included. Assuming 50 μm tracking accuracy it covers the complete momentum range up to 3 TeV/c with good resolution [9] being limited by $\mathrm{d}E/\mathrm{d}x$ fluctuations to $\approx$2% at very low momenta.

To compare the momentum resolution in an unbiased way, it is necessary to test the performance for selected physics topics in a Monte Carlo simulation. As an approximation, we can compare the resolutions within the kinematic acceptance. Figure 6 summarizes the rapidity dependence of the different toroidal configurations at a fixed p_T, here arbitrarily set at 100 GeV/c. The absolute momentum will increase up to 1 TeV/c at $\eta = 3$.

For Fe toroids with very good tracking multiple scattering dominates. The momentum resolution improves like $\sqrt{\sin\theta}$ owing to the increased path in the Fe. For the intermediate and forward rapidity region it changes like $\sqrt{\cos\theta}$ modified by the remaining small $1/R$

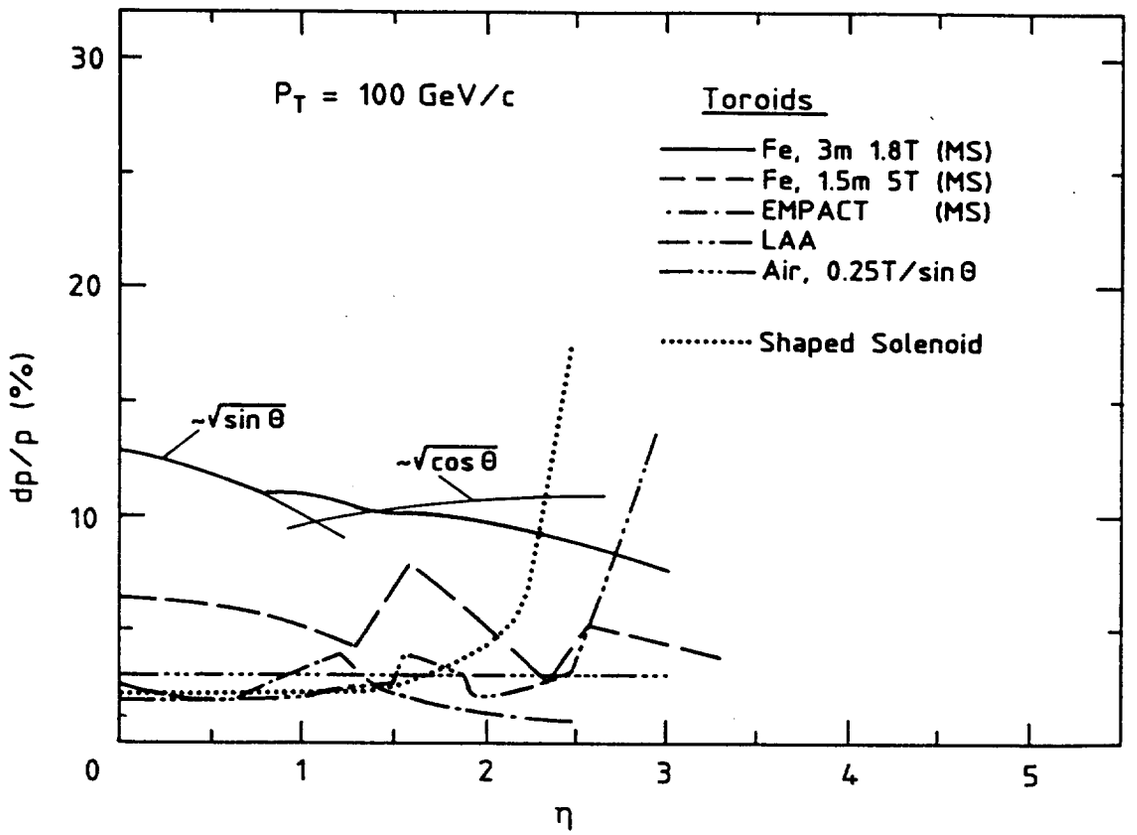


Figure 6: The momentum resolution as a function of rapidity

dependence of the field. In the case of a high-field Fe toroid, the effects of separating it into several modules generates discontinuities. It is important to understand that toroids based on magnetized Fe, in general, will provide an approximately constant field integral over the rapidity acceptance. Therefore, only for those p_T for which p does not exceed the multiple-scattering dominated range will the resolution be independent of rapidity. At high p_T and η, where the resolution depends on p, their performance will deteriorate.

Air-field toroids achieve a rapidity-independent resolution by the increased field integral. The LAA curve [6] shows the Lorentz boost compensation of an air toroid up to 2.5 despite the discontinuity at rapidity 1.5 to 2.0. The compensation of the field-shaped solenoid deteriorates slightly above rapidity 2.0 up to the end of the acceptance at 2.25. For the EMPACT design only the multiple scattering limit is shown [7].

A clear separation between the conventional Fe toroid and the other more ambitious designs is obvious at this transverse momentum.

Summary of Important R&D Items To summarize, for all proposals a tremendous effort both in detector and magnet R&D is required. Very precise large-area tracking is required for the conventional Fe toroid as well as for all air-field configurations. A challenge is posed for the engineers by large superconducting magnets: the solenoid [9] and the toroids, both the air toroids [6,7] and the high field Fe toroid with its large cold mass. Large air toroidal fields seem to be ruled out for the case of conventional coils owing to the high power consumption, and for superconducting coils owing to the enormous size.

References

[1] H. Fesefeldt, Punch-through, these proceedings.
[2] G. Carboni et al., A Fe-toroid for LHC, these proceedings.
[3] F. Wittgenstein, Comments on large magnets, these Proceedings.
[4] Č. Zupančič, Physical and statistical foundations of TeV muon spectroscopy, preprint CERN-EP/85-144(1985).
[5] W. Lohmann et al., Experience with the muon spectrometer.., preprint CERN-EP/85-133(1985).
[6] G. Laurenti et al., Superconducting air toroids, these proceedings.
[7] EMPACT Expression of Interest for SSC, May 1990.
[8] K. Freudenreich et al., L3 converted to LHC, these proceedings.
[9] C. Fabjan et al., Shaped iron solenoid, these proceedings.

AN IRON TOROID FOR LHC

Giovanni Carboni

INFN - Pisa

1. Introduction

The ability to detect and measure leptons with accuracy and efficiency is mandatory in exploiting LHC's discovery potential. Ideally, one would like to combine the best possible performances of muon and electron detectors in the same experiment. In practice, compromises have usually to be reached, with more emphasis on some preferred channels. The extreme case is represented for example by experiments aiming to excellent detection of muons only. When combining electron and muon detection one could sacrifice some resolution and compensate it to some extent with the increase in signal statistics. In that case, one would prefer solutions that can be easily made to coexist. The iron toroid spectrometer that we shall discuss here does not offer the ultimate resolution attainable today because of multiple scattering in iron, but has several advantages that make it a good candidate for a General-Purpose LHC experiment [1]. Moreover, it demands only a limited amount of R&D and is a relatively cheap detector, the cost being dominated by the iron price.

For what the resolution is concerned, a floor of $\Delta p/p$ = 10-12 % is typically achievable for a detector of reasonable size and weight assuming to work with a 1.8 T field (warm coils) [2]. This kind of resolution is considered to be adequate to cover a broad range of physics issues, from the heavy Higgs decay $H \rightarrow 4\,\mu$ to $Z' \rightarrow 2\,\mu$ [3]. For Higgs masses in the range $100 < m_H < 200$ GeV the request of muon isolation is more important than the resolution.

2. A preliminary magnet model

The multiple scattering (MS) contribution to the resolution of a magnetized iron spectrometer only decreases with the inverse square root of the iron length traversed. Going to very large dimensions, the improvement in resolution goes at the expense of an intolerable increase in weight. Keeping also in mind that the maximum diameter of a LHC experimental cavern will be about 24 m [4], we have considered the solution shown in Fig. 1. The increase of thickness in the End Caps (ECs) with respect to the Barrel region is due to the desire to have a better shielding and a better resolution at small angles. The

total mass is about 30,000 tons of iron. We estimate for the coils about 100 tons of Aluminum, and a power consumption of 3 to 5 MW [5]. Cooling the coils to liquid nitrogen temperature (77 K) would result in a drastic cut in power consumption, but at the expenses of an intolerable increase in cooling power. Actual size and placement of the coils, how they influence the assembly of the tracking detectors inside the iron, and what is their effect on muon acceptance have not been taken into account except for assuming 8 dead zones of $\Delta\phi = 5^{\circ}$ .Fig. 2 shows a view of the detector inside a possible experimental area. The ECs can be displaced to access or remove the central detector.

The cost of the detector can be evaluated approximately by assuming 3-4 Sfr/kg for the iron, and 26 Sfr/kg for the coils. One gets:

Iron (includes machining, transport)	:	90 - 120 MSfr.
Aluminum coils	:	2.6 MSfr.
Power supplies, cooling, etc	:	2.4 MSfr.
TOTAL	:	95 - 125 MSfr.

3. Resolution and acceptance

The acceptance of the detector for the $H \rightarrow 4\,\mu$ is shown in Fig. 3 as a function of m_H. To obtain the resolution, we used the GEANT code to simulates muons propagating inside magnetized iron. Then, tracks were fitted to the measurements made by 5 stations each one having 100 μm position resolution. The first station is before the iron, the last is after, and 3 stations are sandwiched between the toroid iron slabs.Only sagitta measurements were considered here. The resulting $\Delta p/p$ vs.p curve for 3 m iron is shown in Fig. 4, showing that the muon sign can be determined up to at least 1 TeV/c momenta. The simulation results have been then parametrized as a function of the iron thickness actually traversed as a function of θ by taking into account the different dependence of the MS and measurement error contributions. These are shown as a function of θ in Fig. 5 for a 0.5 TeV/c muon. Catastrophic energy losses of muons in iron are not important, their contribution to $\Delta p/p$ being 2% at most [6]. The MS contribution decreases at small angles, because of the increased iron thickness in the forward regions. Larger thicknesses there are possible, since the increase in weight would not be large as in the barrel region.

Better momentum resolution could be obtained by introducing muon direction measurement before and/or after the magnetized iron to supplement the sagitta measurement. This would not affect the MS error, and would only be relevant at large muon momenta [1].

4. Muon rates

As it is well known, at LHC the rate of muons having $P_T > 5$ GeV/c is dominated by Heavy-flavours (mainly beauty) decays [7]. Below that cut, the rate is mainly due to muons from hadrons decaying in flight. If the thickness of the absorber in front of the muon detector is large enough (we assumed here to have a 12 Λ calorimeter inside the toroid) the contribution from real punch-through is negligible and what remains are the muons from the hadrons decaying inside the first interaction length of the absorber [8]. For the raw rates, the range cut in the absorber (calorimeter and toroid iron) gives an approximately constant P_T cut down to 53°, after which the cut goes like tan(θ) since the iron thickness start decreasing at small angles. Therefore, muon decays dominate over all the θ range, and their weight relative to prompt muons increases in the EC regions. To compute the rates, weused a parametrized form of the inclusive hadron spectrum extrapolated to LHC energies : $E\, d^3\sigma/dp^3 = A\,(1 + P_T)^{-n}$, A=0.57 barn GeV^{-2}, n = 5.7.The differential rates (in units of μbarn/ 5°) are shown in Fig. 6. Fig. 7 shows the rates corresponding to a luminosity 10^{34} cm^{-2} s^{-1} and integrated from 90° to a given θ. If only the absorption in the calorimeter is considered, these figures become about 10 times larger. Such rates do not result in a significant occupancy in the detector, however they are large and make the design of a trigger system a difficult task especially in the EC regions.

5. Detectors

Required performances are different for tracking and trigger purposes. 1 hit resolution of 1-3 cm is adequate for a muon trigger with a relatively low P_T cut, whereas 100 μm at least are needed for precision tracking at high momenta. 2 hit resolution is more important for tracking, whereas speed is necessary at the trigger level. Finally, a good timing accuracy is needed to resolve bunch crossings spaced of 15 ns. This is necessary at the trigger level to relate the triggering muon(s) to the corresponding bunch crossing. It is unclear, however,that this information would be supplied from a 1st level trigger, since some pattern recognition will probably be needed to extract it. It would be desirable, of course, to use the same detector (or perhaps the same detector technique) for both tracking and triggering. Some dedicated R&D studies have started along this direction.

A complete comparison of possible detector schemes will be needed in order to optimize performances and minimize costs. At the moment, a very crude analysis can be done based on the fact that the BL^2 of this iron toroid is about 4 times the BL^2 of the L3

solenoid, so a system of chambers of the same accuracy as the L3 chambers could be a working solution. Drift chambers would have a relatively small number of channels since one could afford 5 cm cell sizes (1 μs drift time) without occupancy problems, at least in the barrel region. Alternative solutions could be represented by wire chambers with cathode readout.

Assuming a system of drift chambers with about 1 μs drift cells, with 5 stations of 8 wire layers each (40 points on a measured track) to measure in the r-z plane, one would end up with about 64,000 wires, and perhaps 40,000 wires to measure in the r-ϕ plane. This gives 100,000 wires in the barrel region, and probably about the same number of wires would be needed in the ECs. The total cost of the electronics channels could then be estimated at around 40 MSfr, i.e. about 1/4 - 1/3 of the total cost of the spectrometer.

References

[1] see report from U. Goerlach on toroidal field geometries for LHC muon spectrometers, these proceedings.

[2] see e.g. R. Voss and C. Zupancic in "Large Hadron Collider in the LEP tunnel", Vol. I, ECFA 84/85, CERN 84-10, p.228.

[3] see report from the Physics Simulation Group, these proceedings.

[4] see report from L. Leistam on experimental areas, these proceedings.

[5] see report from F. Wittgenstein on large magnets, these proceedings.

[6] A. Van Ginneken,NIM, A251,21 (1986) and T. Del Prete, these proceedings.

[7] see report from A. Nisati, these proceedings.

[8] see report from H. Fesefeldt on Punch-through, these proceedings.

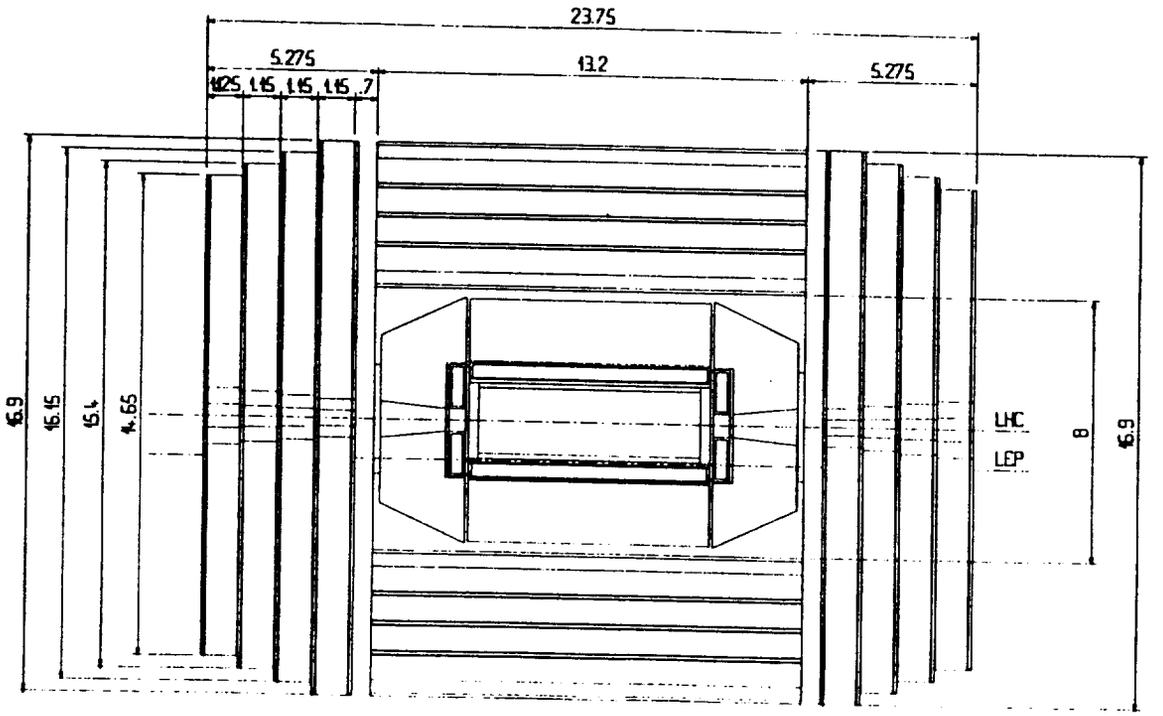


Fig. 1

Longitudinal view of the spectrometer.

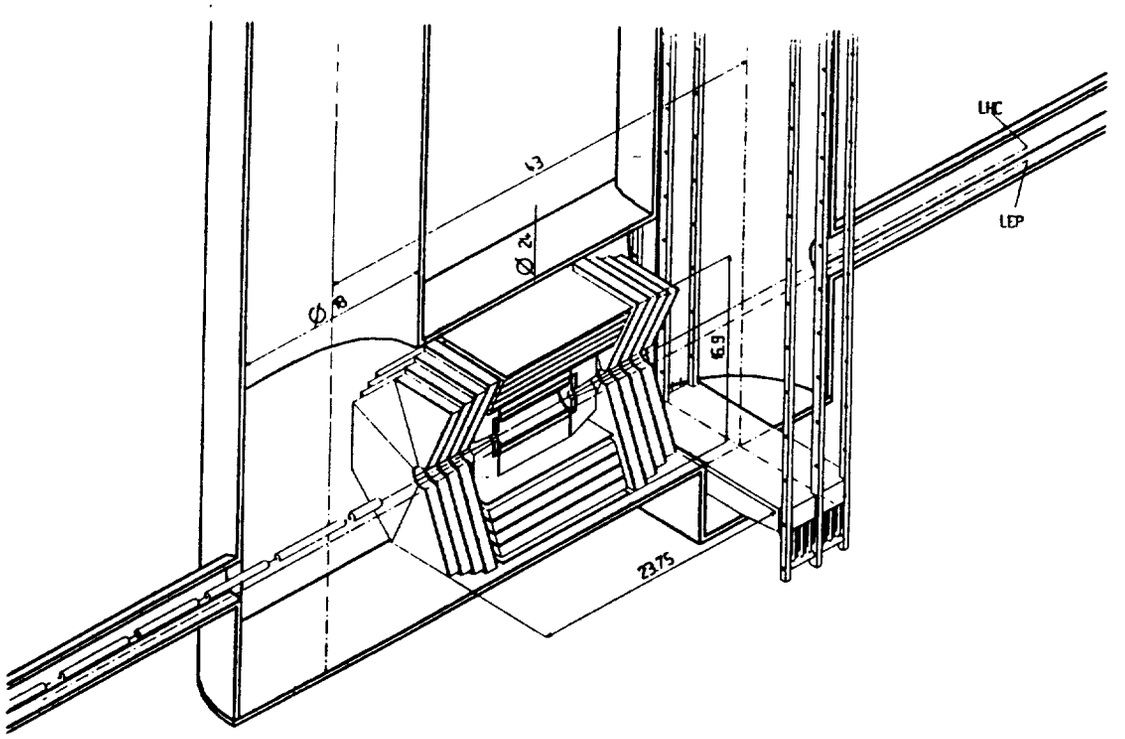


Fig. 2

The spectrometer inside a possible experimental area.

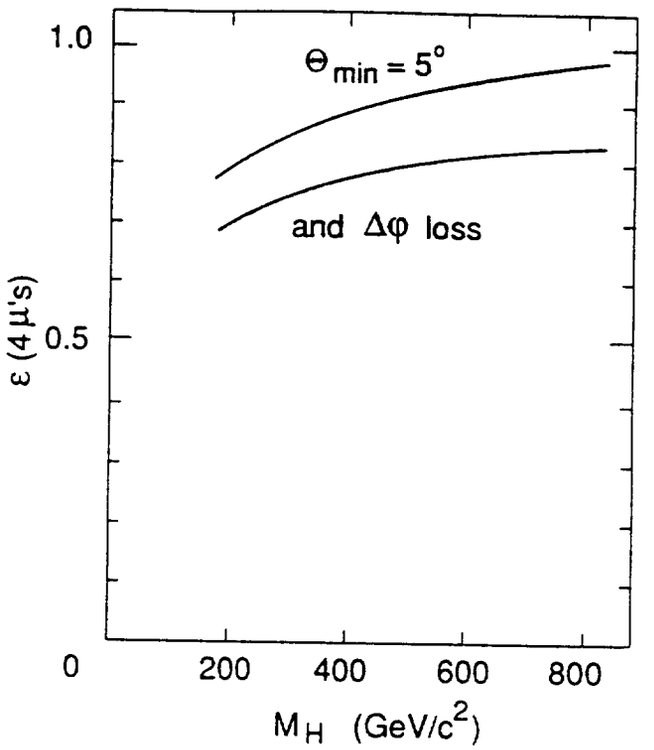


Fig. 3

Detector acceptance for the $H \rightarrow 4\,\mu$ decay as a function of m_H. The lower curve corresponds to 8 dead zones of $\Delta\phi = 5°$ each.

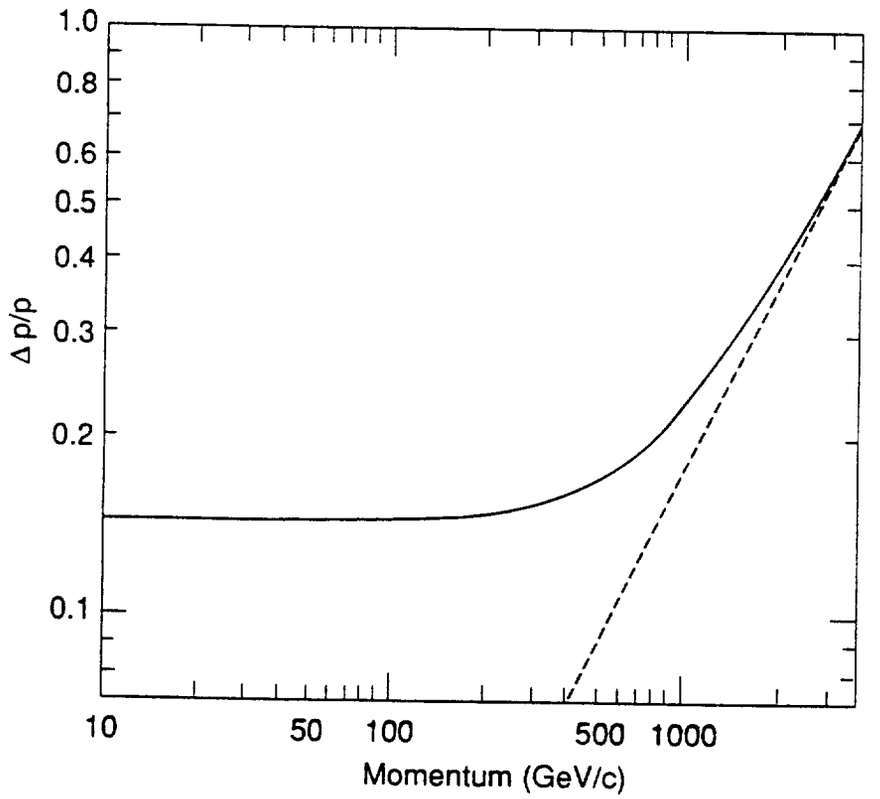


Fig. 4

$\Delta p/p$ vs. p for 90° muon tracks (only sagitta measurement). The dashed line is the contribution from the measurement errors (100 μm chamber accuracy).

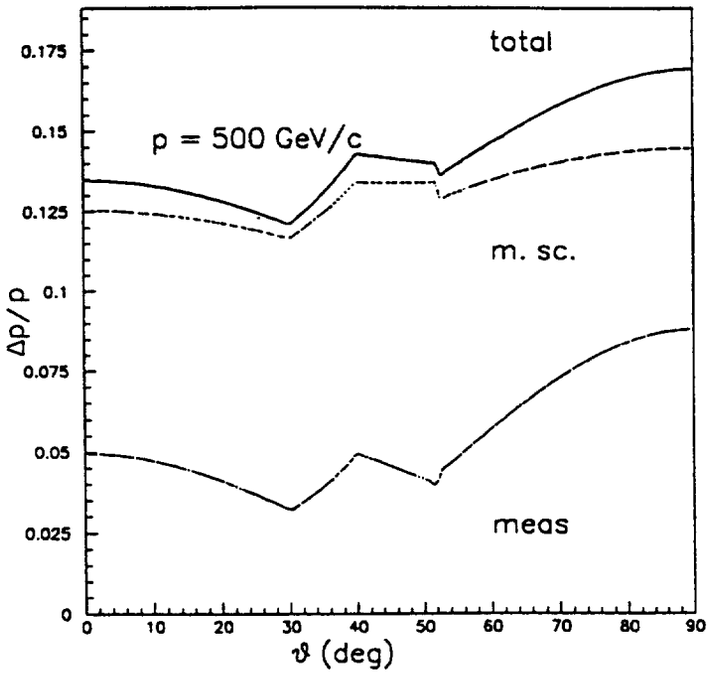


Fig. 5

Δp/p vs. θ for a 0.5 TeV/c muon showing the various contributions.

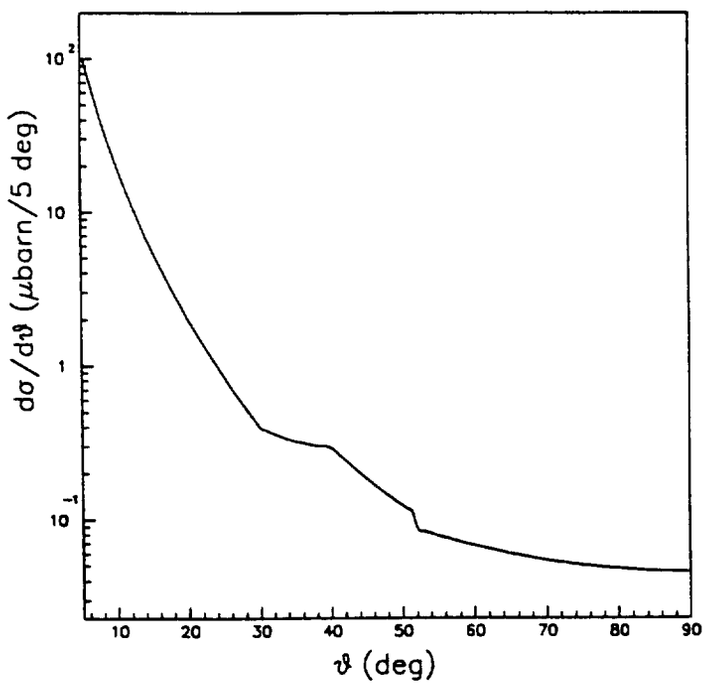


Fig. 6

Differential rate of muons from hadron decays.

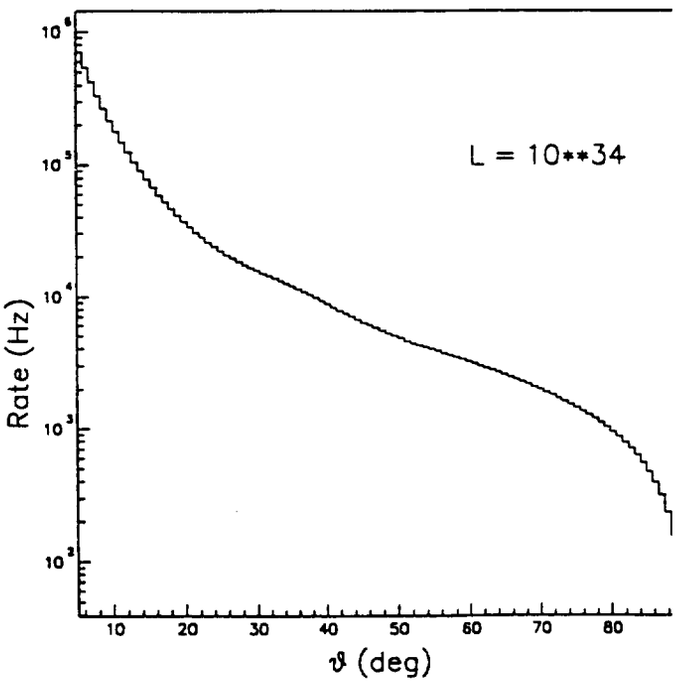


Fig. 7

Actual muon rates integrated from θ = 90° to θ, computed for a luminosity $L = 10^{34}\ cm^{-2}\ s^{-1}$.

CONCEPTUAL DESIGN OF A MUON SPECTROMETER AT HADRON SUPERCOLLIDERS

LAA Project-Large Area Devices Group

F. Bergsma[1)], J. Galvez[4)], G. Laurenti[1)], G. Levi[3)]
Q.Lin[4)], F. Rivera[4)], G. Susinno[4)]

CERN[1)], Cosenza[2)], Perugia[3)] World Lab.[4)]

ABSTRACT

The performances of a muon spectrometer for a hadron supercollider using air core superconducting toroidal magnets are presented. The main construction problems are analised and possible solution are suggested.

INTRODUCTION

A muon spectrometer conceptual design for a multi-TeV Hadron Collider has to have some key features like:

(a) A muon angular coverage down to $\vartheta = 5$ degrees for a good acceptance in Higgs search.

(b) High precision in muon momentum determination, strongly enhancing the signal to noise ratio in Higgs search.

A toroidal magnetic field configuration in the forward and backward regions is a natural choice. However for the barrel region two main options are possible: a solenoidal or a toroidal magnetic field.

The solenoidal field allows for a good vertex constraint in the high-p_T muon trigger. However the transition region between the barrel solenoid and the end cap toroids gives serious limitations for the muon momentum measurement accuracy. An iron core muon spectrometer has limitations in resolution due to multiple scattering, moreover the weight and the cost of the iron, and the power consumption during the operation are relevant.

These considerations have led us to investigate the possibility of designing and constructing a toroidal spectrometer in air using superconducting coils.

This solution presents many interesting features: the toroidal field needs no iron return yoke for the magnetic flux and allows a good continuity in the field geometry, without introducing dead area between the barrel and forward regions. The air core superconducting magnet allows for a good momentum resolution up to a pseudorapidity value around 3.

GENERAL LAYOUT

Our proposed design is of the kind shown in the general scheme of fig. 1 and 2.

A long barrel toroid, with forward and backward toroids inserted inside each end, allows for a very good angular coverage. The general dimensions of the spectrometer depend strongly on the inner part of the detector, we have assumed a region of 3.5 m radius and 10 m length for this purpose.

A modular design of the toroid is proposed: several radial coils inside separated cryostats are assembled together to form the toroidal magnet. In fig. 3 a perspective view of the barrel part is shown. This method is intended to make construction, tests and transport easier. Moreover it permits accessibility to place detectors inside the magnets, increasing the high resolution possibilities.

The same design criteria are used for the barrel, forward and backward parts. The behaviour of the muon spectrometer with toroidal magnetic field was investigated by computer simulation, using the finite element program TOSCA. It shows that a good field uniformity is achievable in the proposed modular design. A more homogeneous coil would require more complicated cryostats and eliminate the accessibility to the inner magnetic volume, without introducing benefits on the momentum measurement accuracy. The set of forward coils is rotated by 11.25 degrees around the beam axis relative to the set of central coils in order to reduce the effect of the inhomogenity of the magnetic field on the momentum resolution and minimize the multiple scattering contribution.

MAGNETIC FIELD SIMULATION

At first glance one might expect that a magnetic field produced by an ensemble of coils as given deviates heavily from the desired uniformity. A detailed evaluation of the field strength was done along radial lines starting from the beam axis.

In fig. 4 the absolute value of the field strength is given along an arc of 45 degrees for different radii in a plane perpendicular to the beam axis and crossing the centre of the spectrometer. To investigate the longitudinal variation of the magnetic field, scans were made along lines parallel to the beam axis inside the coils. For a central coil the result is shown in fig. 5. Scan were made at five different radii: just outside the coil, just inside and at the centre of the coil. The field strength is to a large extent constant. Also here the variations in field strength are small.

MOMENTUM RESOLUTION

To reconstruct muon tracks, detection planes were simulated having a space resolution of 100 μm.

The momentum resolution for 500 GeV/c muon tracks coming from the central interaction region was determined. A polar plot of the resolution is given in fig. 6 (plain line) and the multiple scattering contibution (dashed line). The effect of multiple scattering can only be studied if more design parameters are determined but it can be roughly estimated as following the curve shown in fig. 6.

It has to be stressed that no knowledge from inner detection elements was used, it was only assumed that the tracks cross the beamline . As can be seen the resolution is almost everywhere better than $\Delta p/p = 4\%$, except around 25 degrees at the change from central to forward magnet. In this region the resolution can be improved by optimizing the magnet and detector design.

In fig. 7 the resolution is given in a cartesian $\Delta p/p$ vs ϑ. The full curve and the dotted curve give the resolution for tracks in two different planes through the beam axis rotated by 11.25 degrees one with respect to other. (Lines A and B in fig. 3.) The difference between the two curves is smaller than 0.5% from which one can conclude that the chosen layout with discrete coils is satisfactory.

TRIGGER

A big advantage of the proposed design is that it provides a magnetic shielding of the calorimeter punch-through. Particles of momenta below 1 GeV/c are bent back.

Monte Carlo studies are going on for a precise evaluation of the trigger probabilities at different energies, but it can already be concluded the last detector plane will not be reached by punch-through. The trigger will be defined by hardware roads connecting the intermediate and outer plane to the vertex. A track is accepted if the hit in the outer plane is within a preselected interval from the position of an infinite momentum track passing through the hit in the intermediate position. The method provides tunable transverse momentum cut also taking into account the effects of multiple scattering and the vertex displacement along the beam.

SUPERCONDUCTING CABLES

The magnet current was selected to be 54 or 27 kA for the central coils and 40 kA for the forward coils, after considering a number of factors including: the number of turns and coil layers, the length and cross section of the conductor, the

flexibility of the conductor in the coil windings, the inductance and resistance of the coil, etc.

A large current value has the advantage of simplifying the mechanical structure by reducing the number of turns and layers. It also reduces the coils inductance and resistance, making the quench protection simpler, but it requires a thick conductor, large current leads and a large power supply.

A cable with inner direct cooling has been chosen. The inner direct cooling is achieved by forced flow liquid helium circulating in pipes with a diameter of 6 mm inside the conductor. The conductors are aluminium stabilized $NbTi/Cu$ cables insulated with 0.5 mm thick Kapton foil, as shown in fig. 8.

The current densities are less than half of the critical current at 4.5 K, 2.7 and 3.7 Tesla for this kind of superconducting wire that can be produced with the existing technology. The main parameters of the magnets are listed in table 1.

Table 1. Main parameters of superconducting magnets

	Central detector		Forward detectors	
Number of coil	16		2 × 16	
Coil dimension	4.6 × 19 m^2		2 × 4 m^2	
Current coil (kA)	2700		4000	
Maximum field on the cable (T)	2.7		3.7	
Stored energy/toroid (MJ)	2890		2 × 124	
	Version A	Version B	Version A	Version B
Average current density (kA/cm^2)	4.5	3	4	3.2
Rated current (kA)	54	27	40	40
Cross-section of coil (cm^2)	6 × 100	9 × 100	10 × 30	12.5 × 30
Number of layers per coil	1	2	2	2
Number of turns per layer	50	50	15	15
Number of turns per coil	50	100	30	30

MECHANICAL DESIGN

The forces can be decomposed in an outwards directed pressure on each individual coil, and an inwards force which pushes the coils towards the beam axis. The first part was calculated to be 15 atm, the second 30 atm. The inner and

outer conductor can be connected with cold bars permitting to counterbalance the outer pressure. What remains is an inwards pressure on the inner conductors of 15 atm. A way to support this high pressure is to connect together the inner parts of each coils to form a cylinder. This should permit to keep the heat flow towards the cold parts within limits. A schematic cross section of the barrel coil is shown in fig. 9. The windings are kept inside a stainless steel cage, which is suspended on the outside support by thin rods of a material with low heat conductivity. The support bars have to carry only the weight of this cylinder, connecting it to the cryostat. The total weight of the barrel toroid could be 3500 tons, that of the forward toroids about 300 tons each. Stored energy, forces, and weight decrease rapidly with the size of the muon spectrometer. A good design of the inner part and the use of shaped coils (D-shaped coils, for istance) could also provide some gain in this sense.

DISCUSSIONS AND CONCLUSIONS

From the results one can conclude that the here proposed design is promising: a resolution better than 4% $\Delta p/p$ for 500 GeV/c muons seems to be reacheable, with negligible multiple scattering contributions.

The modularity of the design gives no rise to unacceptable inhomogeneities in the momentum resolution, and symplifies the construction and transport problems, it permit also to use detectors in the magnetic volumes reducing the dimensions of the outers detectors planes.

The main difficulties in this design come from the large amount of stored magnetic energy and the high forces on the superconductors. It is clear that a good design should limit the contact points between the superconductor cold parts and the supporting outer cryostats to maintain heat losses at an acceptable level.

To do that the coils have to be connected with cold chemney in radial direction and a inner structure is necessary to absorb the inward forces. In this early stage many solutions are under study and they do not present unsurpassable problems. In conclusion the complexity of the spectrometer is very well balanced by the level of its performances and makes it worthy of more deep feasibility studies.

BARREL-FORWARD SUPERCONDUCTING AIR CORE TOROIDS

Longitudinal cross section

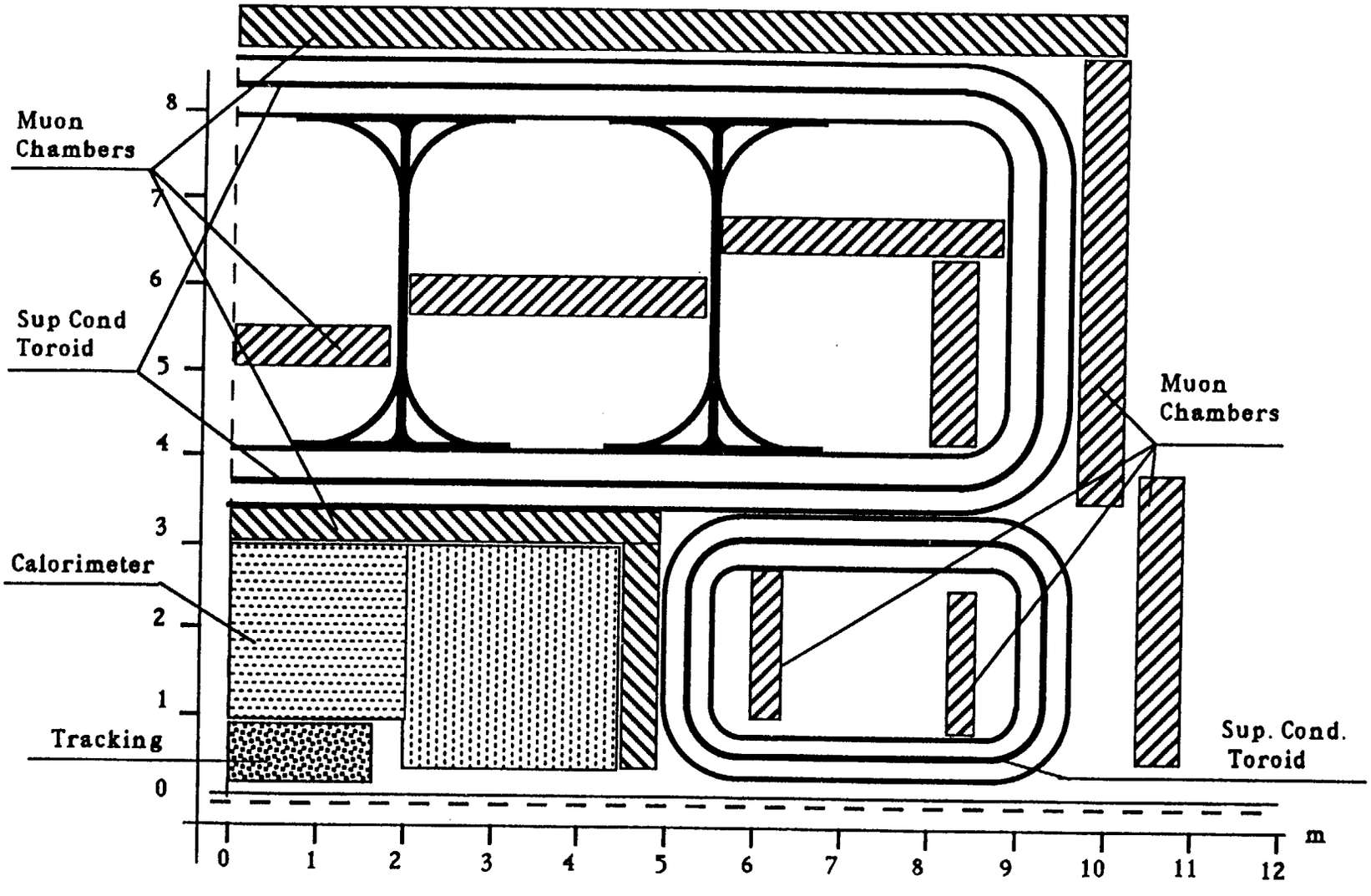


Fig. 1

BARREL FORWARD SUPERCONDUCTING
AIR CORE TOROIDS

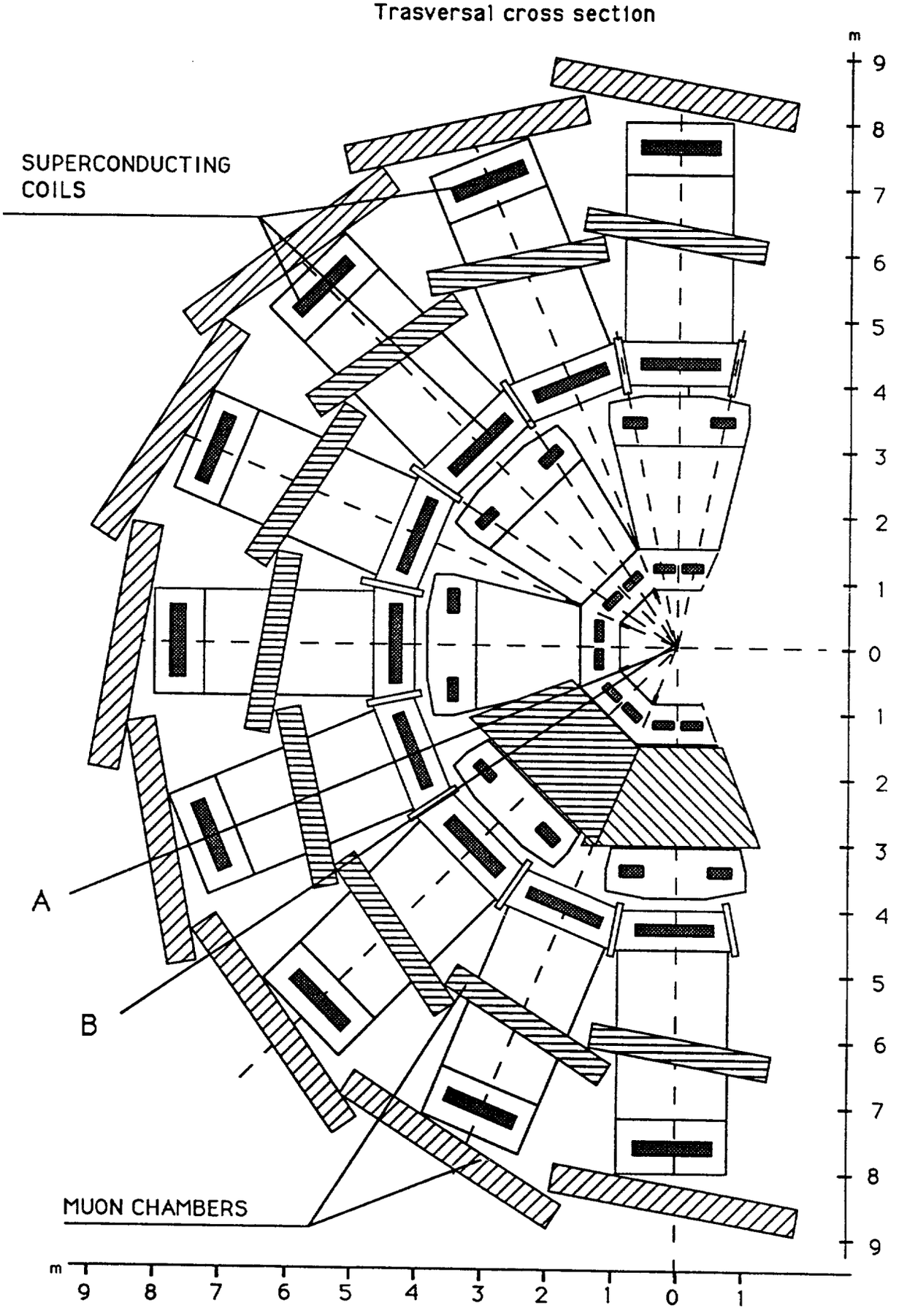


Fig. 2

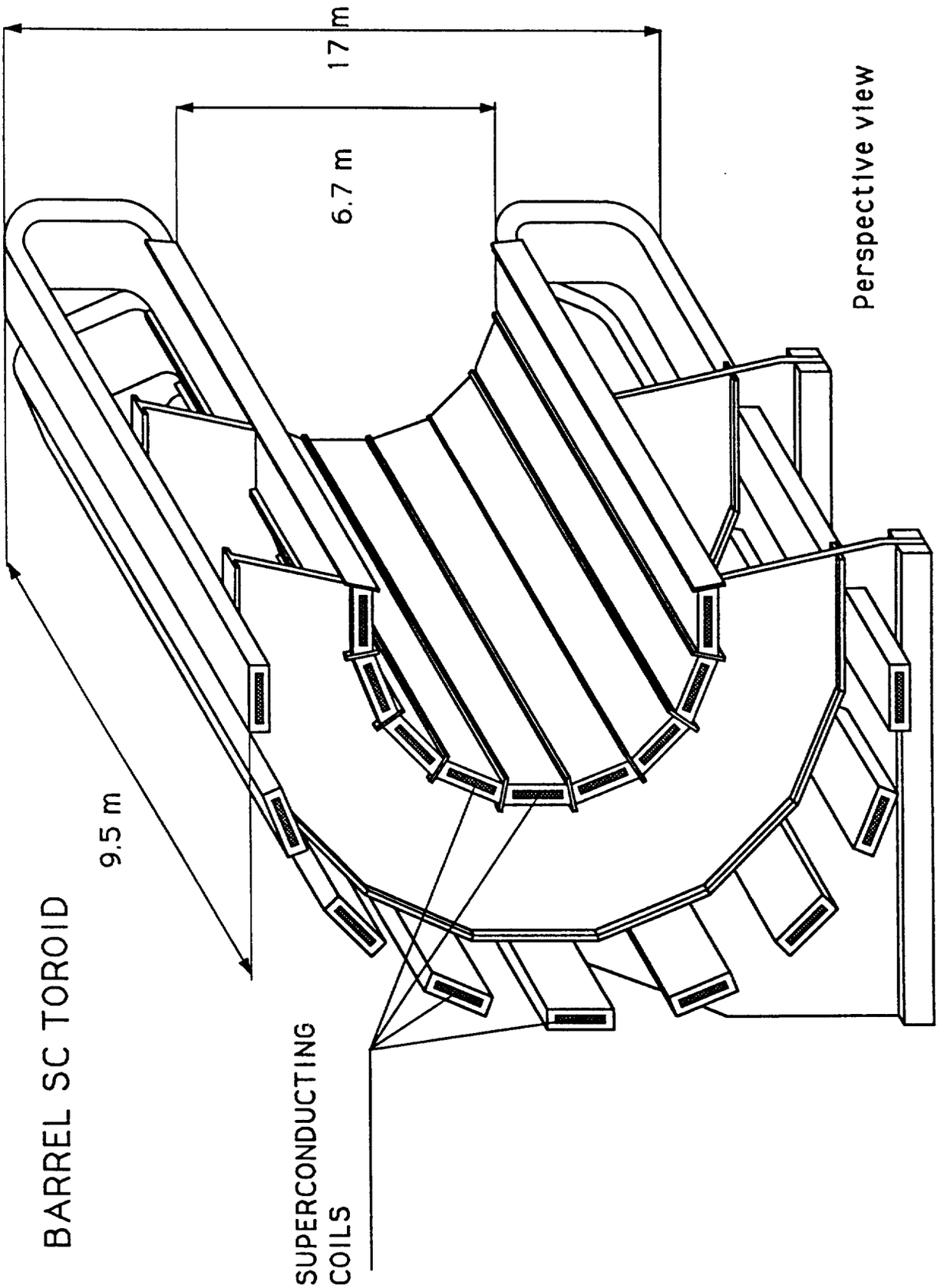

BARREL SC TOROID
SUPERCONDUCTING COILS
9.5 m
6.7 m
17 m
Perspective view

Fig. 3

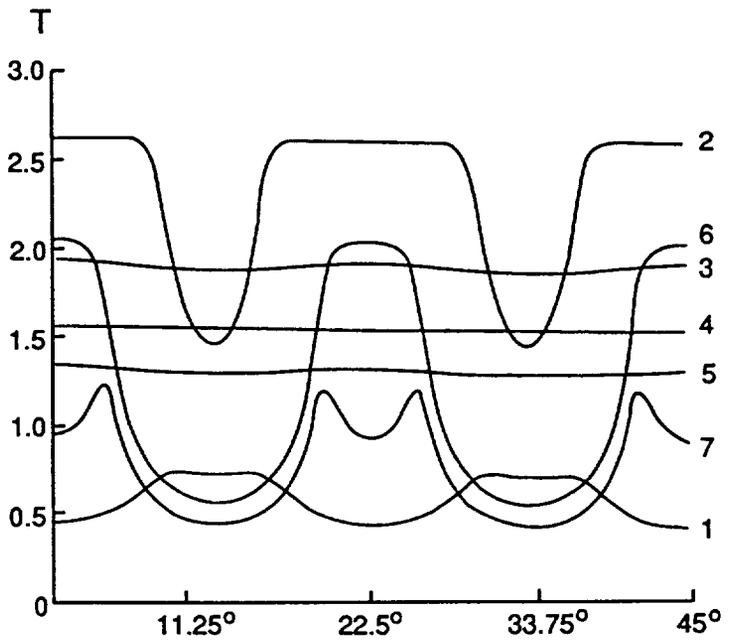


Fig. 4. Scan of the field strength for central coils along an arc of 45^0 at different radii. The arc lies in a plane perpendicular to the beam axis through the centre of the spectrometer. 1: $R = 3.60$ m; 2: $R = 3.80$ m; 3: $R = 4.50$ m; 4: $R = 5.50$ m; 5: $R = 6.50$ m; 6: $R = 8.20$ m; 7: $R = 8.40$ m.

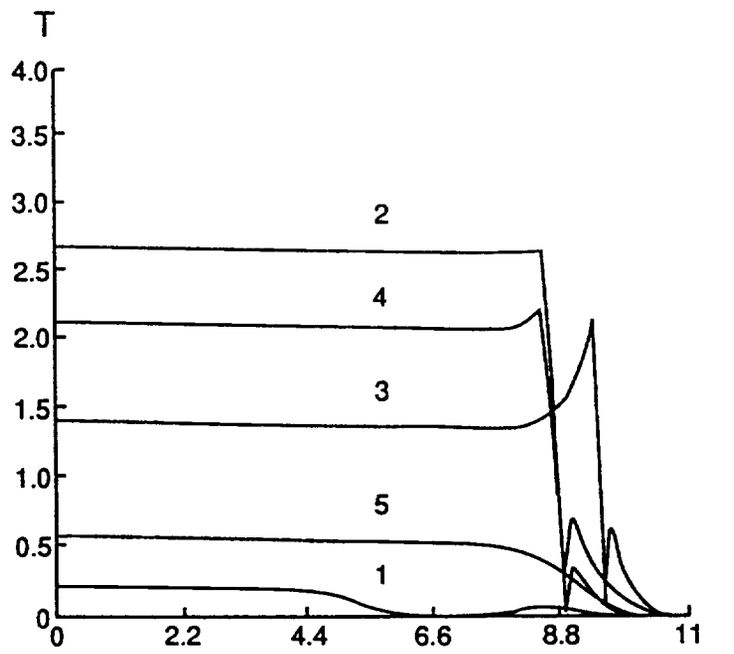


Fig. 5. Longitudinal scan of field strength in central coil. 1: $R = 3.35$ m; 2: $R = 3.75$ m; 3: $R = 6.00$ m; 4: $R = 8.25$ m; 5: $R = 8.65$ m.

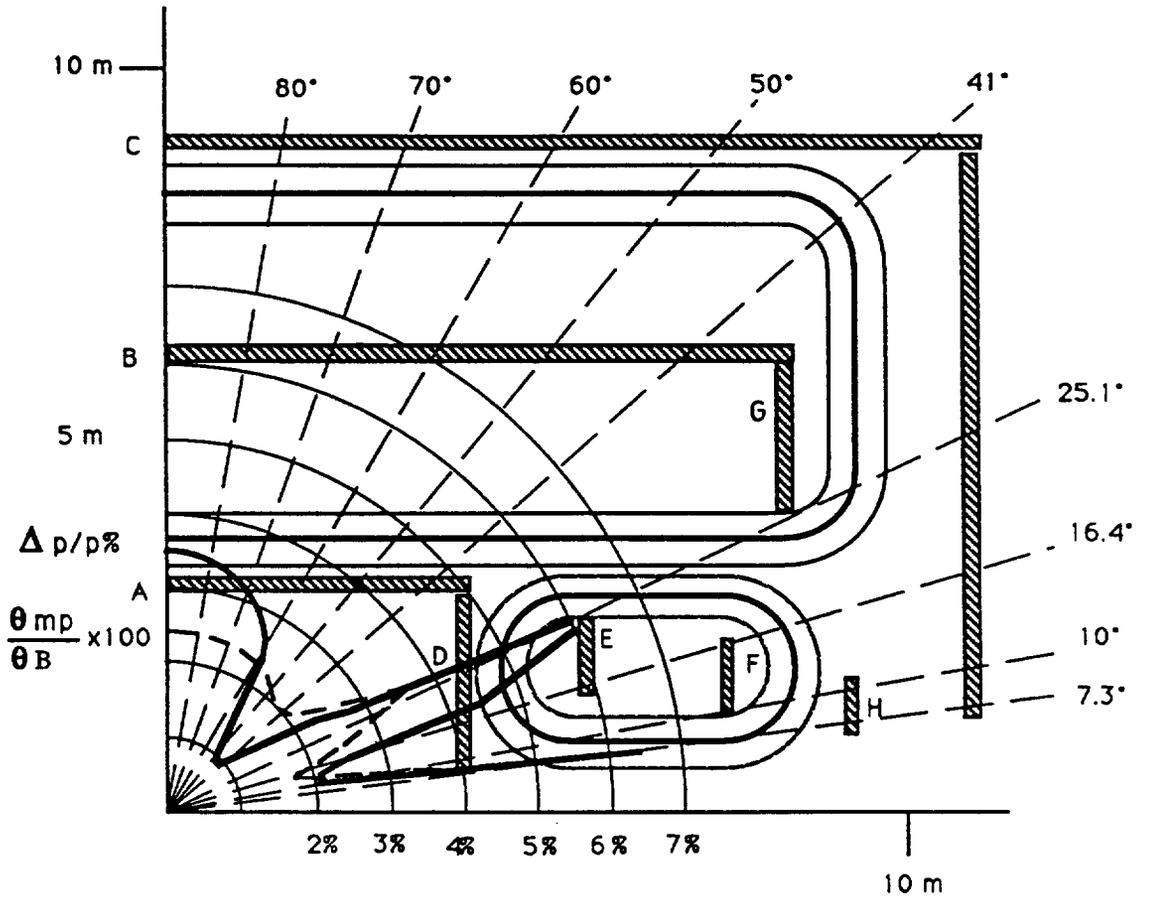

10 m
80°
70°
60°
50°
41°
C
B
5 m
G
25.1°
Δ p/p%
16.4°
A
θmp/θB x100
D
E
F
H
10°
7.3°
2%
3%
4%
5%
6%
7%
10 m

Fig. 6

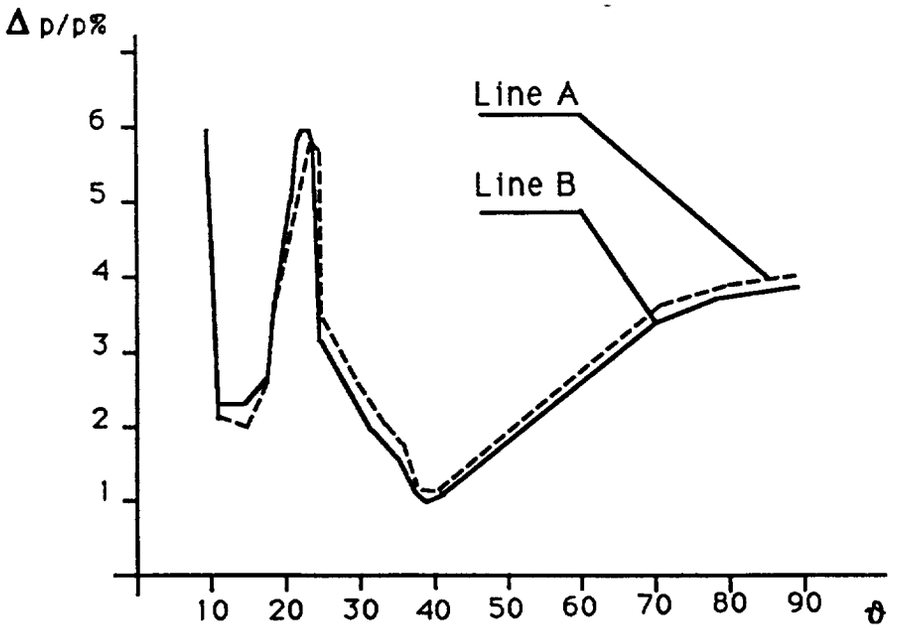
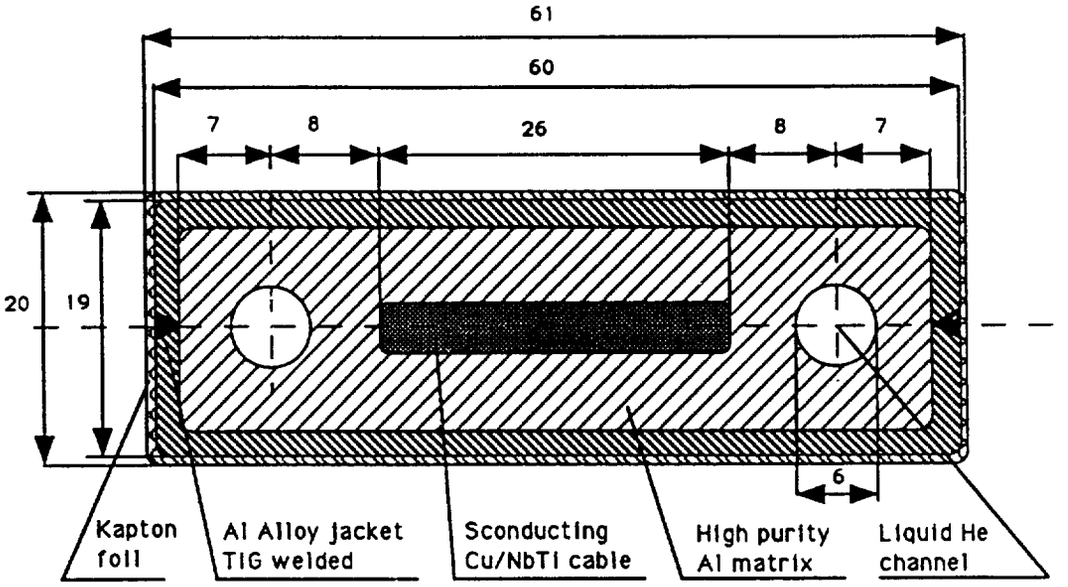

Δ p/p%
6
5
4
3
2
1
Line A
Line B
10
20
30
40
50
60
70
80
90
ϑ

Fig. 7

Super conducting cable 54 KA - 4.5 K
cross section



Super conducting cable 27 KA - 4.5 K
cross section

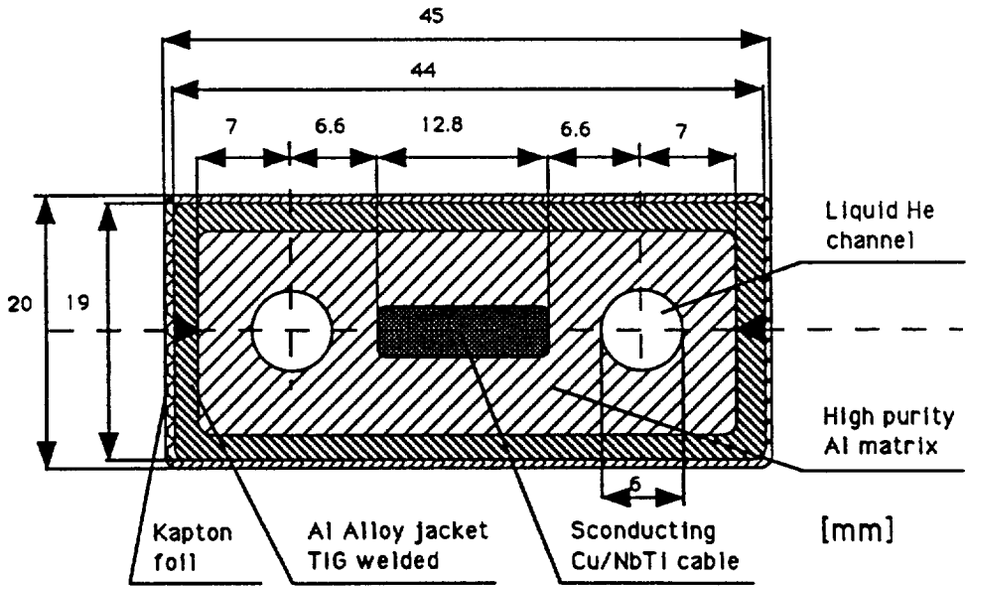


Fig 8

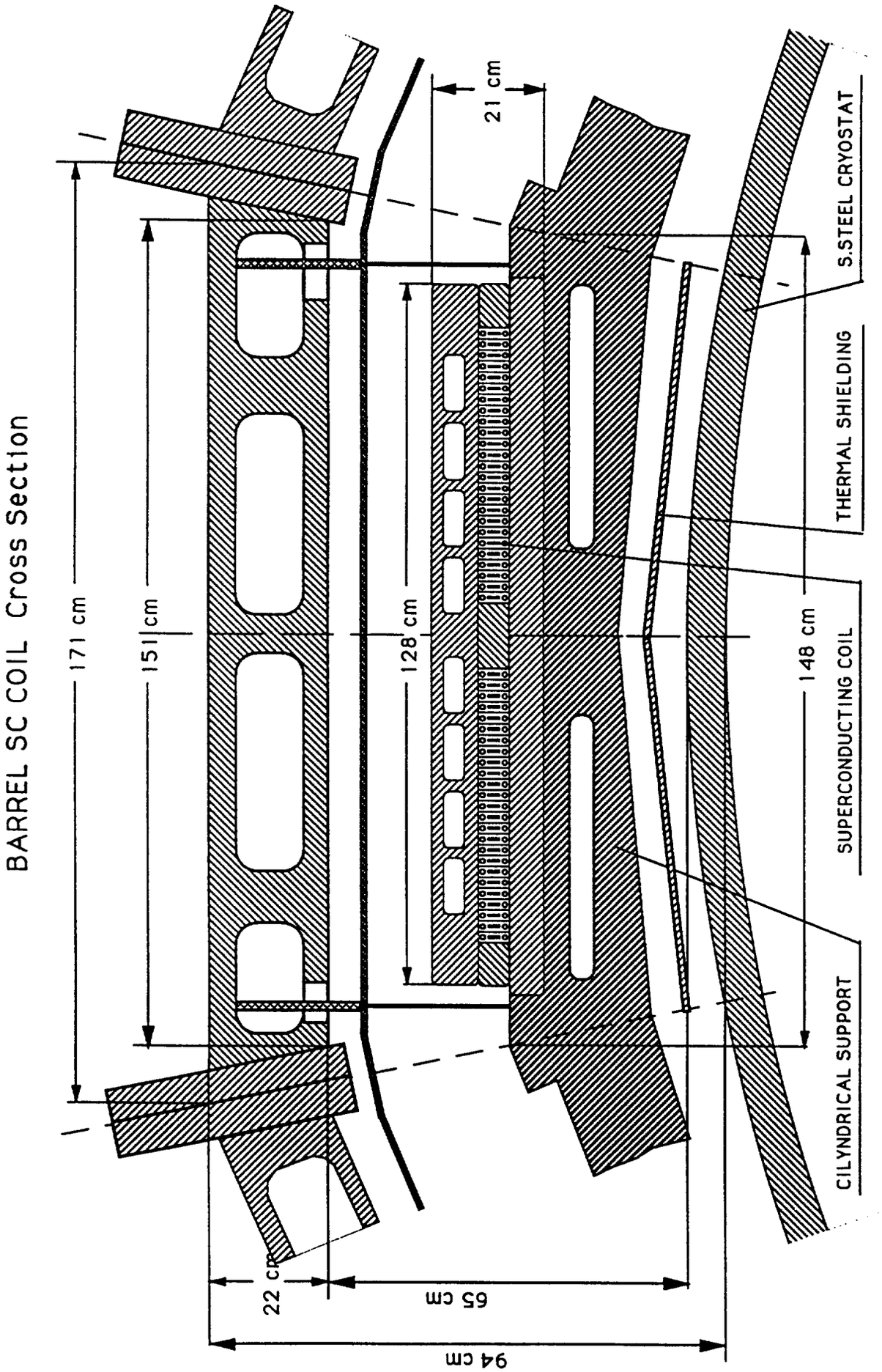

BARREL SC COIL Cross Section
171 cm
151 cm
128 cm
21 cm
148 cm
22 cm
65 cm
94 cm
S.STEEL CRYOSTAT
THERMAL SHIELDING
SUPERCONDUCTING COIL
CILYNDRICAL SUPPORT

Fig. 9

SOME ASPECTS OF TOROID AND SOLENOID DESIGN FOR LHC DETECTORS

C. R. Walters, D. E. Baynham, R. C. Coombs.

INTRODUCTION

To establish a guide order of magnitude for design calculations it is assumed that, at LHC energies, the identification of relevant particles from their tracks requires a total magnetic bending power, perpendicular to the tracks, of around 14 Tesla meters (14Tm). It is desirable to make such a total bending power available along particle paths which are directed at all angles away from the original beams in the LHC. However as the angle between the particle path and the beams is reduced it becomes more difficult to provide the necessary bending so that an angle of around 5 degrees is regarded as a minimum which it would be desirable not to exceed.

A solenoid centred along the LHC beams would provide the required bending at angles greater than about 25 - 30 degrees. However as there is no transverse force on a particle travelling along a magnetic field line and the solenoid field lines are parallel to the beams, bending is reduced, finally to zero, as the angle is reduced to zero.

In contrast, the field lines of a toroidal field centred on and circulating around the beams are always perpendicular to the paths of particles then originating from it's axis. Also the field intensity increases inversely with radius from the beams. This means that, in principle, greater bending becomes available as the angle between the path of the emerging particle and the LHC beams, is reduced.

In practice of course the production of such a field requires windings to be placed adjacent and parallel to the beams where other items such as at least the beam pipe and the magnet cryostat are also required. The boundary at which the full field becomes available is therefore some distance radially away from the beams and low angle bending may only be achieved by placing the torus some distance along them away from the collision point.

Such considerations have led to proposals including not only solenoidal fields which increase in intensity with distance away from the central plane, so called 'magnetic bottles', but also combinations of toroids and solenoids in which a solenoid generally covers the central region around the collision point and a pair of toroids covers the ends of the solenoid.

In this paper, using particular examples, a general view of some of the construction and other technical requirements for both types of magnet is given, together with specification lists.

The example toroid magnet, with a central bore of 6m, was provided by Eggert (private communication). Such a magnet might be constructed, for instance, on the outside of a central solenoid. The forces encountered are greater than those in a toroid that would close the end of a solenoid, otherwise the problems are similar.

The main objective in the case of the solenoid was to assess the practical effectiveness of constructing a 'magnetic bottle' using a solenoid alone. The total bending requirement was met by providing a central field of 4T in a solenoid with a central plane bore of 7m.

THE TOROID

Model specification. (K Eggert)
a. Iron filled: b. Bore of field = 6m: Length = 10m
c. Outside diameter of field = 12m: d. Field at bore = 7T
Note: At 7T the iron will contribute about 2.3T and the winding therefore must produce 4.7T

With an appropiate aspect ratio a toroidal coil can be made self supporting, with the exception of the supported central leg, by winding it such that it's curvature is proportional to the local magnetic field. This is not however possible with the above coil shape which must therefore be externally supported. The options are: 1. Banding, as shown in Fig.1, which leaves the magnetic aperture free of any obstuction; 2. A continuous external cylinder, discounted here because of it's complete lack of radial access; 3. Ties across from the outside to inside of the coil partially obstructing the magnetic aperture.

FIGURE 1. Is a schematic, drawn roughly to scale, of the winding and the stuctural componants required for the first option. The structural sections (modulus 200 GPa), listed in table 1., have been calculated on the basis of an extension of 0.1%, as a suitable match to the probable maximum for the copper (modulus 120GPa) in the superconductor. The magnitude of magnetic forces, particularly longitudinal compression in the central column, disposes towards making the complete structure cold

Fig.1

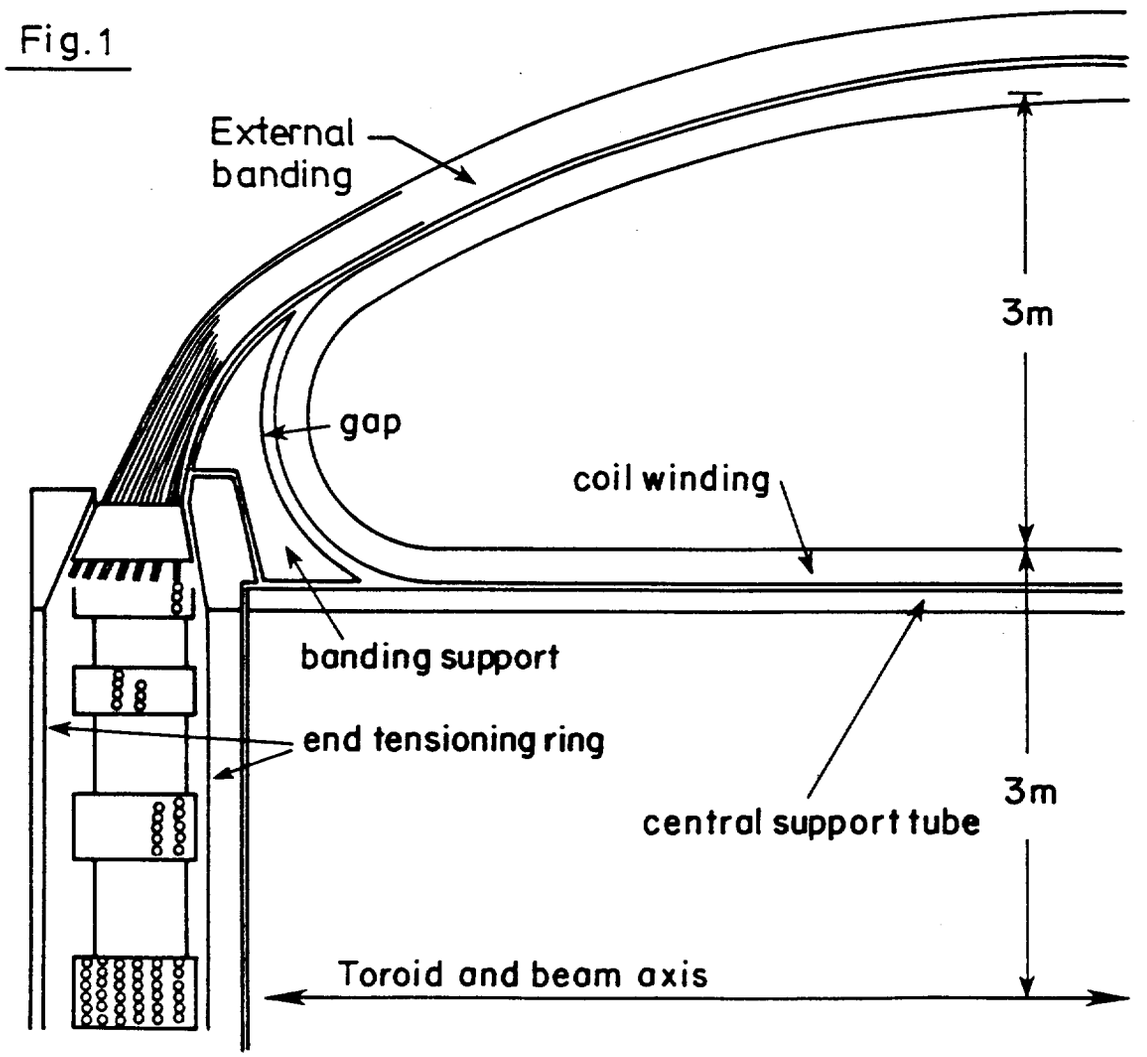


TABLE 1. MAGNETIC FORCES AND SUPPORT STRUCTURE

1. Central column	:		
a. Outside diameter		5.52	m
b. Hoop compression		26.4	MN/m
c. Longitudinal compression		53.3	kTonne
d. Minimum thickness		156	mm
2. Single coil	:		
a. Minimum radius of curvature		1.0	m
b. Total tension		10.4	MN
c. Elastic extension		0.094	%
d. Force to central column		9.29	kTonne
3. External banding	:		
a. Maximum radius of curvature		10.4	m
b. Total tension		39.4	MN
c. Width * thickness		550 * 358	mm * mm
4. End tensioning ring	:		
a. Mean diameter		5.5	m
b. Hoop tension		100	MN
c. Length * thickness		650 * 750	mm * mm
5. Total cold mass	:	1.3	kTonne

The strain in the coil and the adjacent support structure should be matched such that there is no shear between them. Alternatively, either a very strong shear joint is required or an allowance must be made for relative motion between them. In particular such motion could generate heat locally which will cause the coil to quench.

Such a match can and has been achieved on the outer limb of the coils where they are supported by the external banding. It not possible under the banding supports at the ends but the curvature there has been adjusted to make the winding self supporting and a gap must be left as indicated. It is also not possible between the central column, which is in compression holding the end tensioning rings apart, and the winding which, as previously stated, is in tension. Allowance must therefore be made for relative movement to take place between them.

OPTION 3.

The above structure provides an unobstructed magnetic aperture. The third option, of ties spanning from inner to outer limbs of the winding, is much simpler, racetrack coils are possible, the force to the central column is reduced and, possibly of greatest significance for assembly reasons, the axial compression in it is now zero. For example, with ties at 2m intervals the required tie section diameter is 0.26m and the winding can be adequately supported between them by enclosing it in a box beam with 'flanges' 560mm wide by 74mm thick, furthermore this would reduce to 19mm with smaller ties at 1m spacing.

TABLE 2. WINDING PARAMETERS

Notes: 1. A forced flow conductor is envisaged
2. Figures calculated for option 1., option 3. would be similar

1.	Stored energy	9.6	GJ
2.	Operating current	80	MA
3.	Inductance	3.0	H
4.	Maximum dump voltage	2.8	kV
5.	Run down time	85	Sec
6.	Current density in the metal	48	A/sqmm

7.	Volume ratio of metal	70	%
8.	Overall current density	34	A/sqmm
9.	Conductor size over insulation	60 * 36.5	mm * mm
10.	Insulation thickness	2.5	mm
11.	Field in iron at centre	7.0	T
12.	Field at conductor	4.7	T
13.	Total current through the centre	70.5	MA
14.	Number of coils	16	
15.	Ampere turns per coil	4.41	MA turns
16.	Winding section (width * thickness)	550 * 238	mm * mm

TOROID ASSEMBLY

A major problem common to any toroid is how to place massive individual coils for fixing onto the central column. This might be achieved by straightforward horizontal loading if the toroid were to be put together with it's axis vertical, the whole assembly being rotated through 90 degrees on completion. Alternatively, either the coils must be offered up at different angles, or the toroid must be rotated about it's axis as the coils are loaded onto the central column.

In option 1. the individual coils must be mounted directly onto the central column and the cryostat built around the completed structure. This can in principle be achieved by constructing the coil units to include parts of both the support structure, the bands in this case, and the cryostat. Joins are then made at appropiate interfaces.

With option 3., cold support is much lighter because not only is there no banding and therefore no axial compression in the central column but also the load to the central column is reduced by the cross ties. The the possibility of a warm central column now exists, with the coils tied to it through re-entrant columns running in parallel with the ties in order to reduce the heat load. The very real advantage is that the coils can be constructed and assembled as completely separate units.

Warm iron fills the toroid in each case. It is segmented and offered up sequentially between the coils and joined through them in a keystone structure which is self supporting against the radial magnetic forces.

SOLENOIDS

In this paper bending power is defined as the integral of the product of perpendicular field and path length to the solenoid boundary. This boundary is either the bore of the coil or an end plane. At low angles to the axis the bending power of a solenoid is limited by it's length but it can be increased by increasing the field towards the ends. The main objective in this section is to examine this possibility.

Intuitively, bending power is proportional to the number of field lines crossed, from which, until an end is reached, bending power will be independant of the angle of the particle path in a solenoid where the field lines are prevented from leaking through the winding - a constant flux solenoid. Indeed this can be proved analytically in the somewhat artificial case of a uniformly tapered solenoid in which the field has somehow been held constant across the bore at any section.

This model has been used to obtain guideline limits for such solenoids and particular cases have been computed to verify the results and make the predictions more accurate. For the purposes of this exercise a

magnetic field of 7-8 Tesla is regarded as the performance limit of niobium titanium superconductor.

Taking Z as the distance along the axis from the centre of the coil, if B_0,R_0; B_Z,R_Z and B_L,R_L; are the field and radius at Z = 0, Z and the half length of the coil, L, respectively, then:

1. Minimum angle for full bending (phi) is : $\tan^{-1}(R_L/L)$
2. For constant flux : $B_Z R_Z^2 = B_0 R_0^2$
3. Bending power is : $B_0 R_0$

Then if $B_0 R_0$ = 14 Tm, the required coil radius and magnetic field strength at the ends of the solenoids, as a function of the half length, is given in table 3. below:

TABLE 3.

L (metres)	5	6	7	8	9	10
With phi = 20 degrees :-						
R_L (metres)	1.8	2.2	2.6	2.9	3.3	≠ 3.6
B_L (Tesla)	14.8	10.3	7.6*	5.8	4.6	3.7
With phi = 25 degrees :-						
R_L (metres)	2.3	2.8	3.3	≠ 3.7	4.2	4.7
B_L (Tesla)	9.0 *	6.3	4.6	3.5	2.8	2.3

Key:- 1. * = NbTi performance limit. 2. ≠ = Length of straight solenoid

From the table, with phi = 20 the field limit is reached unless the solenoid is at least 7m long and a straight solenoid nearly 10m in length will do the same job. The figures at phi = 25 are 5.5m and 7.5m. It is clearly not possible to achieve the desirable angle of 5 degrees.

COMPUTED CASES

In the following computations the common parameters were: 1. Winding half length = 5.0m. 2. Maximum bore = 3.5m. 3. Bending power = 14Tm. A simple yoke was also included. With these parameters three different solenoids were explored, as follows:

1. A simple straight solenoid
2. A stepped solenoid with currents and geometry adjusted both for constant bending with angle and for minimum bending angle limited by a peak field of 7-8 Tesla.
3. A straight solenoid with length increased to give the same coverage as the stepped solenoid.

The comparative bending of these three solenoids is given in figure 2. below, from which it can be seen that the performance of the stepped solenoid extends to angles which are 15 degrees smaller than that of the short straight solenoid. This can however be made up by a 50% increase in length of the latter. Also the angle is reduced to 14 degrees before the bending power of either is halved.

TABLE 4. Equivalent parameters

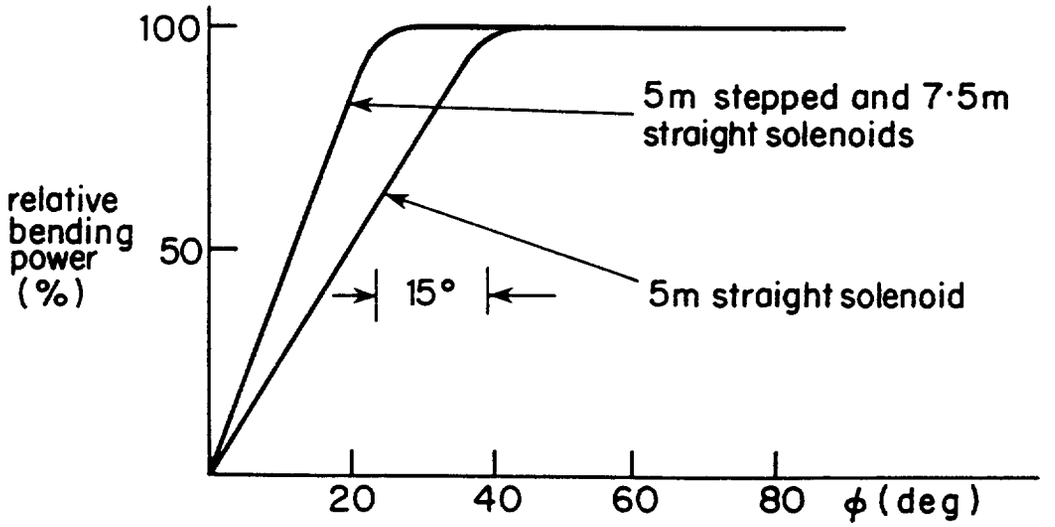
Solenoid	Stored energy (GJ)	Radius*pressure (MN/m)	Axial force (MN)	Cold mass (Tonnes)
5m straight	2.5	22.4	75	280
Stepped	2.9	18 - 88	44 -119	350
7.5m straight	3.7	22.4	75	420

As seen in Table 5. the computed coil is smaller than the constant flux model, probably because the field is not uniform but varies such that the lines are more perpendicular to the tracks than in the latter. However the peak field levels were not dissimilar in the two cases.

TABLE 5. Field levels

Distance from centre (m)	1	2	3	4	5
B in constant flux (T)	4.6	5.3	6.7	7.5	9.0
Peak B in step. sol. (T)	3.4	4.0	5.0	6.5	8.5

FIGURE 2. Comparative bending powers with angle.
(100% = 14%Tm)



CONCLUDING COMPARISON

Compared to the straight solenoid, the advantages and disadvantages of the stepped solenoid are as follows:-

ADVANTAGES :
1. Occupies less space
2. Stores less energy

DISADVANTAGES :
1. Higher field levels - superconductor limits
   - higher stresses
2. Complex cryostat - difficult construction
   - greater volume
   - bore access restricted
3. Complex support structure

COST : The cost of the 7.5m straight solenoid will certainly be less than 50% greater than that of the similar 5m solenoid. Conversely the cost of the more complex 5m stepped solenoid will, with equal certainty, be greater than the 5m straight one. It would not therefore be particularly surprising to find that it was also greater than the 7.5m solenoid.

The Shaped Solenoid for Muon Spectroscopy

C.W. Fabjan
CERN, Geneva, Switzerland

1. Motivation

Most of the LHC physics topics require the identification and momentum measurement of leptons. For the identification of electrons, two approaches –transition radiation and fine–grained pre–shower detection– are being actively developed [1,2]. Conceptually, these approaches should work at luminosities in excess of $L = 10^{34}\ cm^{-2}\ s^{-1}$, but the quality of electron identification near or in the high particle–density core of energetic jets remains to be established. The momentum measurement of electrons may, however, benefit from excellent precision when using the calorimetric approach. Both, homogeneous electromagnetic detectors [3,4] (LXe or BaF_2) or sampling devices [5] will reach $\sigma/E < 1\%$ for electron energies in the 100 GeV range. Muons, on the other hand, when identified as penetrating charged particles behind a calorimeter, are practically inert to the associated particle flux and event topology. For a 'discovery machine', such as the LHC, this could be a life–saving advantage, not to be given up lightly. This ease of identification is unfortunately counterbalanced to some extent by the difficulty of achieving 'good' momentum resolution. In the LHC range of interesting muon momenta –10 GeV to approximately 2 TeV– only magnetic spectroscopy is available, setting the scale for the achievable resolution, which in practical instruments will be considerably worse than then energy resolution for electrons.

Two approaches have been extensively evaluated: iron toroids magnetized at ~ 2 T, provide a robust method using rather conventional tracking methods [6]. The achievable momentum resolution is multiple scattering, limited for $p \leq 500$ GeV/c and is given by $\sigma/p \approx 0.4/B[T] \cdot \sqrt{L[Fe(m)]}$. Alternatively, tracking in air fields, as pioneered by the L3 Collaboration [7], offers the attractive advantage of high–precision momentum analysis over a wide range of muon momenta. Both techniques are at the opposite ends of the performance spectrum: not surprisingly, the challenge of good muon spectroscopy has been met in different ways [8,9].

There has been considerable debate about the 'required' momentum resolution for muons. Typically, the Higgs $\rightarrow$ ZZ at an intermediate mass (~ 300 to 500 GeV/c^2) has been analysed. Indeed, if Nature would obligingly proceed along the lines of present–day event generators, such decays should be visible above the QCD–background, even if the resolution is $\Delta p/p \approx 0.12$. What happens, however, if the branching ratios into ZZ are smaller than assumed [10]? Better resolution would help. There are other cases which argue for better resolution: in the Standard Model the Higgs mass is evaluated to be below $M < 200$ GeV/c^2, and its detection will tax the resolution of any detector. At the high–mass end of the LHC discovery potential, other mechanisms responsible for the breaking of the electroweak symmetry may manifest themselves, e.g. as a WZ final state. Study of this reaction again requires good momentum resolution. There may be several generations of Zs: the mass reach of the LHC is approximately 4 TeV/c^2, limited by the signal–to–background ratio, i.e. the momentum resolution. The list is not complete.

In this note, we comment on the two principal ingredients of air–field spectroscopy: the magnet and the tracking possibilities. Whilst the concept is that of the L3 and L* Collaborations [11], the detailed approach is different and may offer experimental advantages.

High–precision muon spectroscopy is arguably the single most important detection technique to be developed for the LHC: competing concepts should be evaluated to understand their technical and financial dimensions. In my view this is the pre–requisite for an informed decision on the muon systems for our LHC detectors.

2. The Shaped Solenoidal Magnet

One major difficulty, characteristic of LHC experimentation, is the requirement of large rapidity coverage. For electrons and muons, a coverage of $|\eta| < 2.5$ is considered adequate, although by no means generous. The magnetic coverage does not come easily: in the L*–approach, the central solenoid, providing good momentum resolution for $|\eta| < 1.5$, is complemented by additional muon spectrometers covering the larger rapidity regions.

The concept discussed here has a long history: it dates back to the development of the 'Open Axial Field Magnet' conceived by T. Taylor for the Axial Field Spectrometer at the ISR [12], as shown in Fig. 1. This concept was further extrapolated to several interesting magnet configurations, as discussed in Ref. [13]. More recently, the 'shaped solenoid' was adapted to the supercollider requirements [14], as indicated in Fig. 2. A warm solenoidal coil is implied. Field shaping is accomplished, both by increasing the current density at the ends and by extending the yoke into cones for improved flux bending at small polar angles. Considerable bending power is possible with this arrangement, down to $|\eta| \leq 2.5$, see Fig. 3.

A variation of this concept is shown in Fig. 4. Six discrete superconducting coils are distributed to provide field shaping over $|\eta| \leq 2.3$, as can be inferred from the bending power, Fig. 5. Assumed current densities (5 A/mm^2 in the large coils, 20 A/mm^2 in the two small coils) allow for established conductor technology. The overall diameter of the magnet, including the return yoke, is approximately 20 m: it would still fit into a 'standard' longitudinal interaction region for which a maximum diameter of 24 m is considered acceptable [15]. The cylindrical yoke contains approximately 25,000 t of iron; the two forward portions each weigh approximately 4500 t. Hence the total weight is similar to that of a shallow (3 m deep) iron toroid for an inner detector of comparable size [6]. A potential simplification may be achieved in the construction of the central iron yoke: it could be assembled from extruded iron bars, requiring no further machining, and could be part of the structural support of the cylindrical walls of the experimental hall.

3. The Tracking Detector

The requirements on the tracking system can be gauged from Fig. 5. At $\theta = 90^o$, a 1 TeV muon would have a sagitta of ~ 0.6 mm. A 50 μm error on the sagitta measurement would provide 8% resolution at 1 TeV.

The L3 Collaboration has demonstrated that an effective spatial resolution of $\sigma \approx 50$ μm may be achieved with multiple measurements using drift–chamber techniques, where each individual measurement has typically an error of $\sigma \approx 200$ μm [7]. The drift–chamber concept may, however, be quite difficult to implement in the present magnet design, owing to the field shaping as a function of polar angle.

We are attracted by three recent developments in gaseous trackers: microstrip avalanche chambers [16], pad chambers [17] and straw chambers. In the first two techniques, the position is measured by the hit pattern of anode strips [16] or cathode segments [17,18]. Conceptually, control of systematic effects is provided by depositing the sensor elements on inherently stable substrates, e.g. quartz plates.

The microstrip avalanche chambers have not yet been fabricated in large (~ 1 m^2) size, but fabrication techniques (photolithography) used for the present, successfully operated detectors, would allow devices to be constructed in dimensions of up to 40 x 40 cm^2. Assuming anode strip lengths of ~ 50 cm with 200 μm centre spacing (providing a spatial resolution of ≈ 60 μm), the total channel count would reach $N \approx 3 \times 10^7$. The required electronics is very similar to the electronics used at present for Si–strip detectors (with the addition of input spark protection). Strips would be ganged to form 'FAST ORs' available for trigger information. Given the very low occupancy, extensive multiplexing would be used to transfer the hit pattern to the DAQ system.

The second approach uses the interpolation of cathode strips, oriented perpendicularly to the direction of the anode wires. Interpolation accuracies of 1% of the readout spacing have been reported [17,18]. For the muon chambers, we would like to use rather long (~ 50 cm) strips, resulting in a noise penalty and possibly in a reduced interpolation accuracy. Assuming 3 mm wide interpolation, a total of $N \approx 2 \times 10^6$ channels would be required. Fast ORs would provide trigger capability and extensive multiplexing would permit a 'reasonable' ($\approx 10^4$?) channel count of digitization electronics. These chambers would be tilted by the Lorentz angle with respect to normal incidence to achieve approximately perpendicular charge collection, minimizing the effect of Landau fluctuations on the position resolution. It will be advantageous to use $Xe/C0_2$ mixtures, both to increase the collected charge and to benefit from the relatively small Lorentz angle [19] ($\theta_L \approx 16^o$ at 1 T).

The third approach returns to the time–honoured concept of drift chambers, using their modern incarnation of 'drift–straws' [20]. These detector elements have typical diameters of 5 to 10 mm and are frequently thin–walled made from material, such as Mylar or Kevlar. Stable operation is achieved with a variety of gas–mixtures [Ar/Ethane, Ar/C02/CH4, Di–Methyl–ether] (DME). Spatial resolutions of $\sigma \approx 50$ μm at 1 atm, improving to $\sigma < 30$ μm for operation at 4 atm. have been measured. Considerable operational experience has been obtained with vertex chambers operated at several e^+e^- colliders. Several groups have evaluated the use of such detector elements for a large central tracker for SSC experiments. We imagine th euse of thin–walled aluminum tubes, 8 to 10 mm in diameter, operated at a few bars with DME, potentially providing a spatial resolution of $\sigma \approx 30$ μm for a single measurement. Coarse second–coordinate readout may be obtained by measuring the arrival time at both ends of a tube.

Needless to say, the first two concepts would require extensive work before they could be considered as tracking candidates. The third concept is a much more mature technique. Developments would concentrate on fabrication techniques, drift stability and systems aspects.

4. The Muon–Chamber Space Frame

A conceptual detector layout is shown in Fig. 6. The cylindrical yoke is seen to support the central (~ 3000 t) detector on support rods, possibly arranged as spokes of a bicycle wheel. It is a matter of detailed engineering analysis to understand whether the support of the central detector is independent (as in L*) or integrated with the muon–chamber support, as indicated in Fig. 6.

Whether both functions are integrated or not, the muon–chamber space frame is constructed from materials with coefficients of thermal expansion (CTE) = 0 in the temperature range of operation. In recent years, a number of novel composite materials have become available, combining high strength, stiffness, and relatively low atomic number (long radiation length) with zero CTE [19]. In this approach, one would aim for an overall long term (24 h) stability of the space frame of $\sigma \approx 100$ μm, consistent with the measured position stability of the LEP machine components [20]. If this level could be achieved, it would seem adequate to monitor the position of the muon chambers passively and to use the deviations from nominal position as correction terms in the reconstruction programme.

5. Conclusions

High precision muon spectroscopy should be part of an LHC experiment. A magnet concept combined with recently developed gaseous tracking detectors is discussed, which would satisfy the resolution requirements. In a next step, the engineering aspects of the magnet would have to be evaluated. Concurrently, a R&D programme would be needed to study the tracking performance of a module in a magnetic field, using the support techniques briefly outlined.

I would like to thank the many colleagues who discussed these concepts with me and in particular, T. Tortschanoff who carried out the magnetic field calculations for the superconducting version.

References

[1] V.A. Polychronakos et al., Integrated High–Rate Transition Radiation Detector and Tracking Chamber for the LHC; Proposal CERN/DRDC/90–38 (1990).

[2] D.J. Munday et al.: A Proposal to Study a Tracking/Preshower Detector for the LHC; CERN/DRDC/90–27 (1990).

[3] M. Chen et al., Nucl. Instrum. and Methods A267 (1988) 43.

[4] H. Newman et al.: R&D Proposal for Fast and Radiation Hard Crystal Calorimeter at LHC; CERN/DRDC/90–54.

[5] C.W. Fabjan, Sampling Calorimeters vs Homogeneous Total Absorption Calorimeters: a Performance Comparison. Invited talk, Conference on Very High Resolution Electromagnetic Calorimetry, November 1989, Sigtuna, Sweden.

[6] G. Carboni, these proceedings.

[7] B. Adeva et al., Nuclear Instrum. Methods A289 (1990) 35.

[8] M. Della Negra et al., Study of Muon Triggers and Momentum Reconstruction in a Strong Magnetic field, CERN/DRDC/90–26 (1990).

[9] U. Goerlach, these proceedings.

[10] These proceedings.

[11] L. Baksay et al., Expression of Interest by the L* Collaboration.

[12] H. Gordon et al., Nuclear Instrum. Methods 196 (1982) 303.

[13] T. Taylor, Physica Scripta, 23 (1981) 459.

[14] E. Dolgosheina, T. Taylor and W.J. Willis, Field Shaping by Iron for Muon Measurement at Hadron Colliders, to be published in Nuclear Instrum. and Methods, 1990.

[15] L. Leistam, the proceedings.

[16] A. Oed, Nucl. Instrum. Methods A263 (1988) 351;
F. Angelini et al., Particle World 1 (1990) 85.

[17] R. Debbe et al., BNL 43405 (1990).

[18] H. Beker et al., Nucl. Instrum. Methods A283 (1989) 762.

[19] H. Daum et al., Nucl. Instrum. Methods 152 (1978) 541.

[20] W.H. Toki, Review of Straw Chambers, SLAC–PUB–5232 and Proc. 5th Int. Conf. on Instrumentation for Colliding Beam Physics, Novosibirsk, 1990 (to be published).

Figure Captions:

Fig. 1 Vertical cross–section through the open axial field magnet. The magnetic field lines show the direction and level of the field useful for momentum analysis and also the level of 'stray field' in the external detectors [12].

Fig. 2 Cross–section through magnet with shaped iron poles; the field lines are also shown indicating the effect on the magnetic field by the forward cones of the magnet yoke [14].

Fig. 3 Display of BL^2 (Tm^2) for the magnet displayed in Fig. 2 [14].

Fig. 4 Schematic layout of the shaped iron yoke and six superconducting coils.

Fig. 5 Integral $\overline{BL^2}$ of the magnet shown in Fig. 4 (left ordinate and solid line) and the sagitta for 1 TeV particles (right ordinate and dashed line).

Fig. 6 Conceptual layout of a muon spectrometer inside the superconducting shaped solenoid.

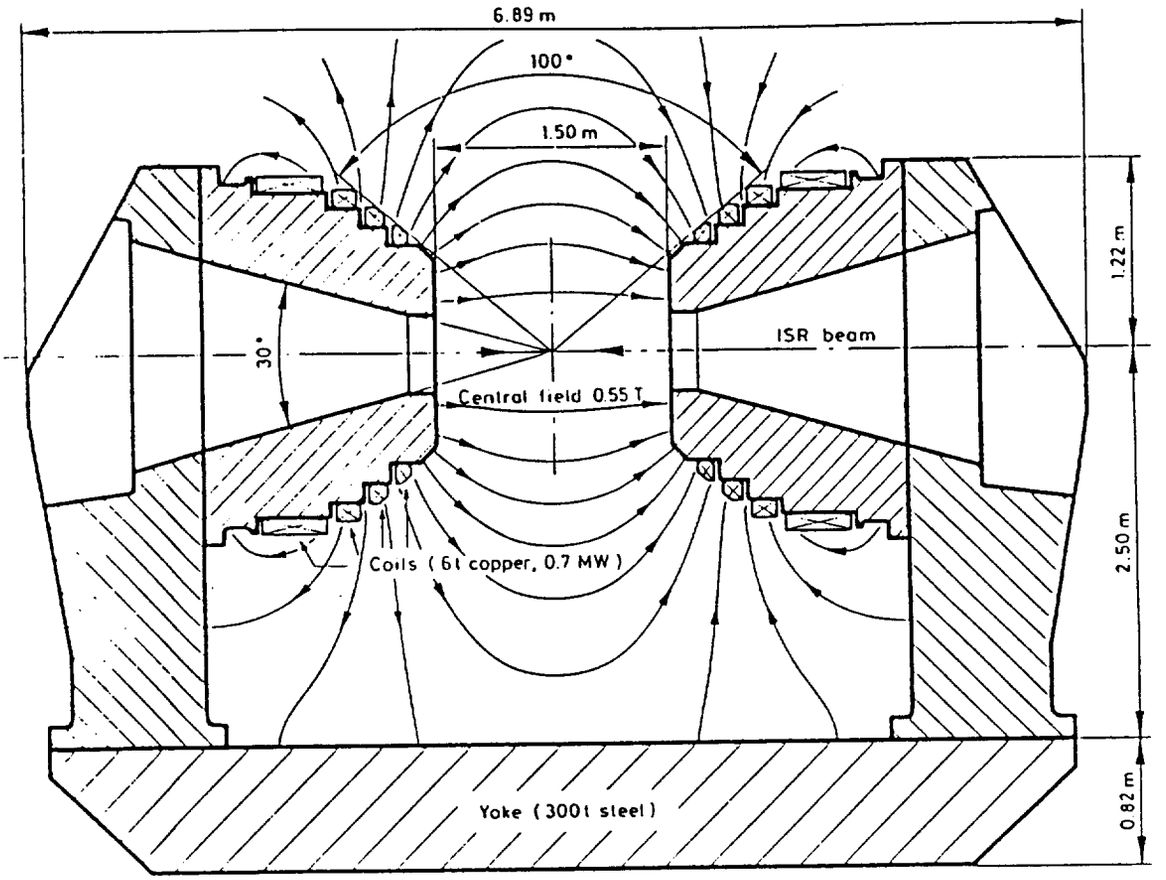

6.89 m
100°
1.50 m
1.22 m
30°
ISR beam
Central field 0.55 T
Coils (6t copper, 0.7 MW)
2.50 m
Yoke (300t steel)
0.82 m

Fig. 1

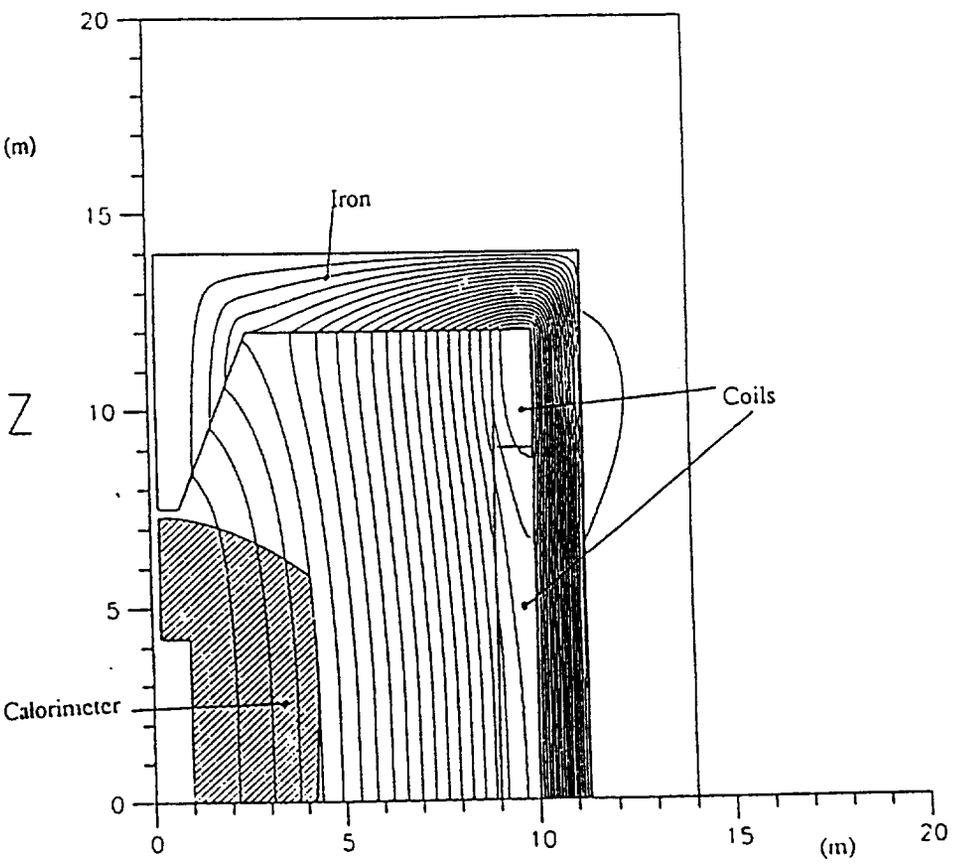

20
(m)
15
Iron
Z
10
Coils
5
Calorimeter
0
0
5
10
15
(m)
20
R

Fig. 2

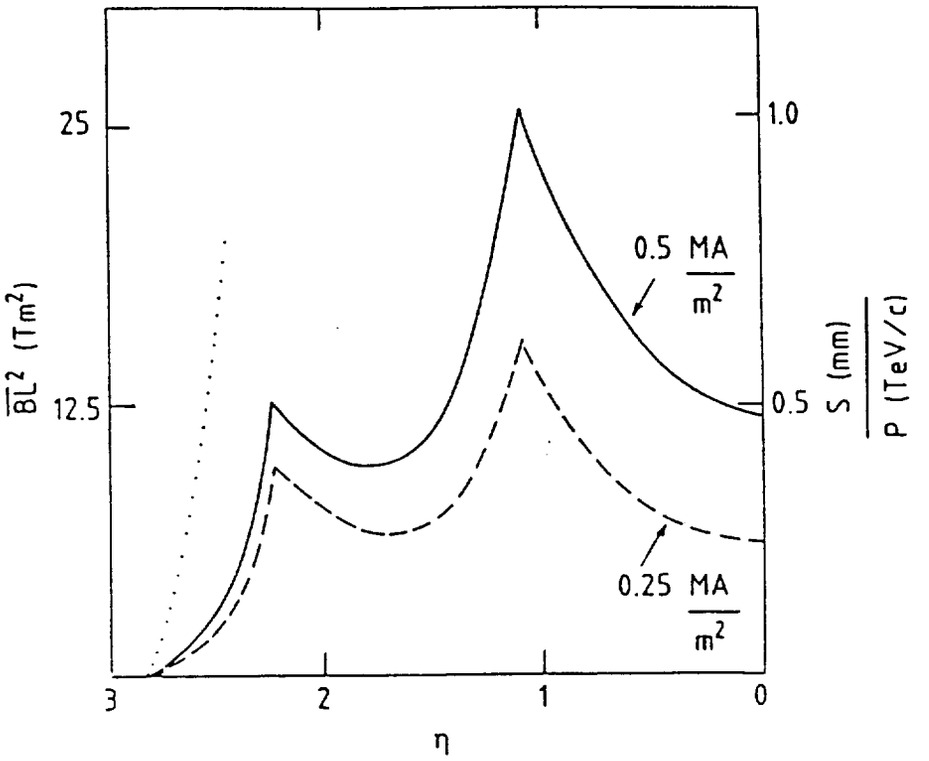

25
12.5
1.0
0.5
$\overline{BL}^2$ (Tm^2)
$\frac{S\ (mm)}{P\ (TeV/c)}$
0.5 $\frac{MA}{m^2}$
0.25 $\frac{MA}{m^2}$
3
2
1
0
η

Fig. 3

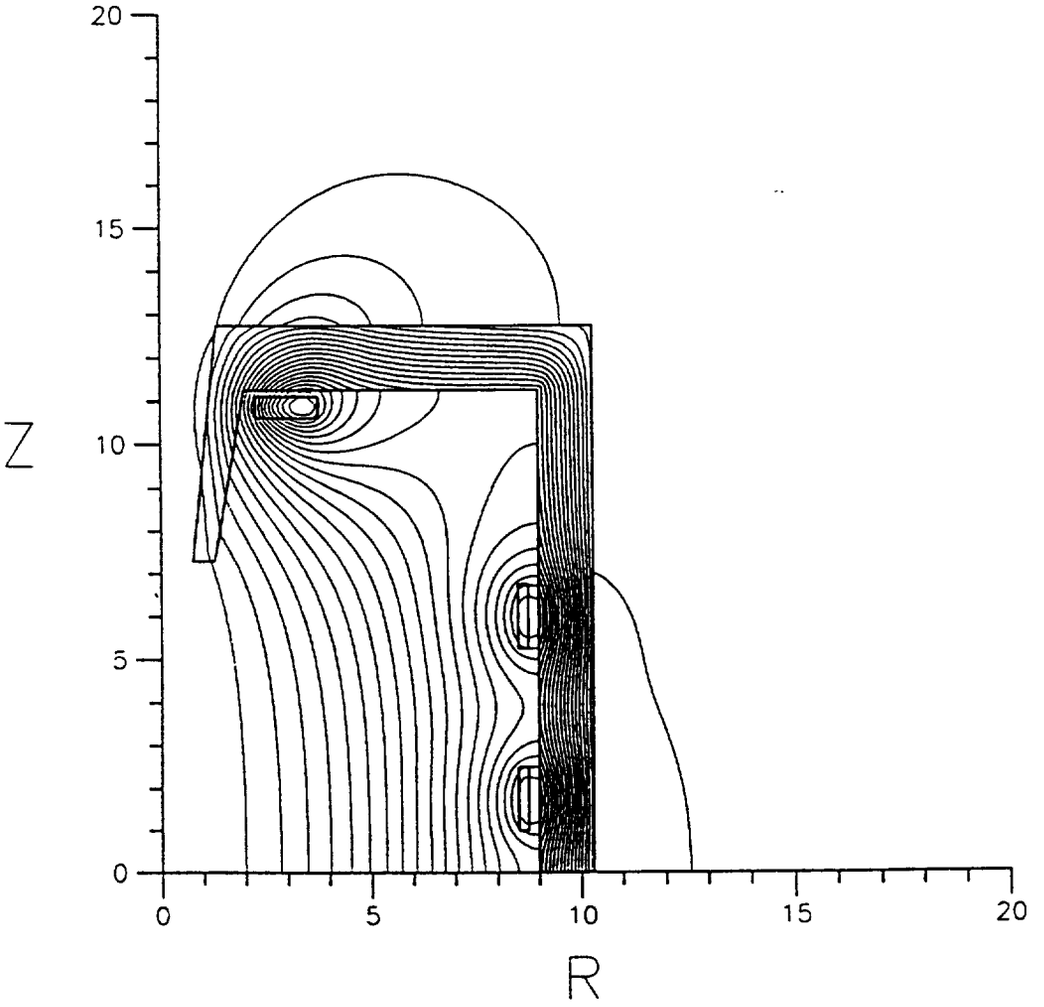

20
15
10
5
0
Z
0
5
10
15
20
R

Fig. 4

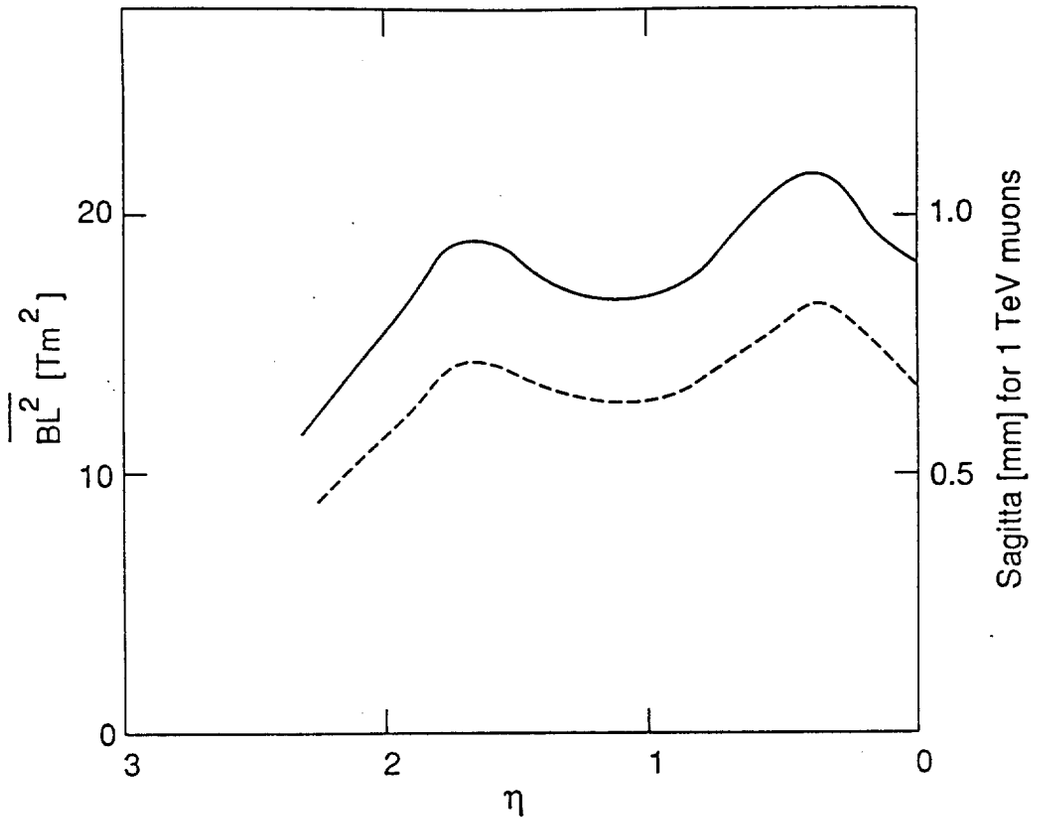

20
10
0
3
2
1
0
η
$\overline{BL^2}$ [Tm^2]
1.0
0.5
Sagitta [mm] for 1 TeV muons

Fig. 5

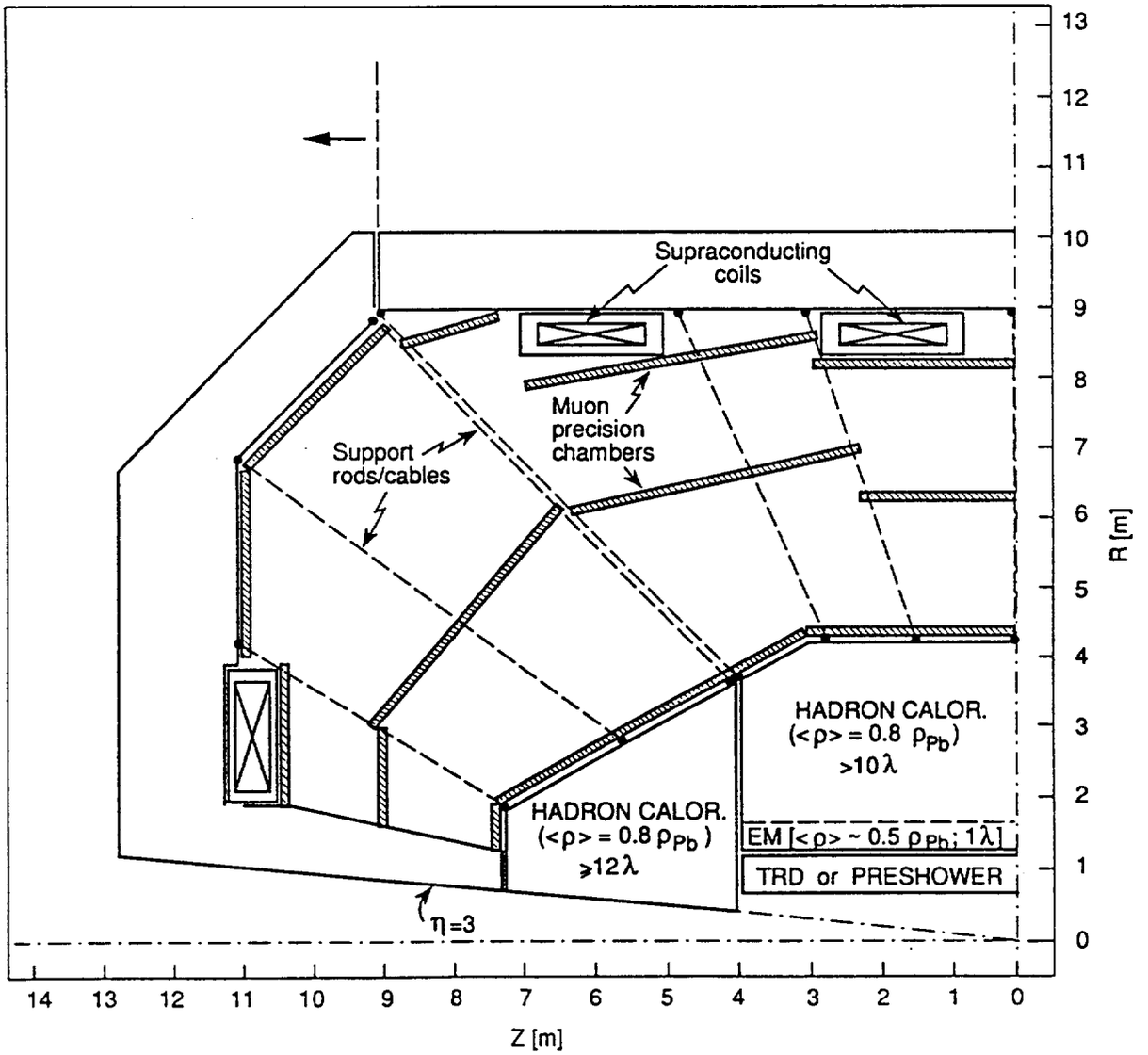

Supraconducting coils
Muon precision chambers
Support rods/cables
HADRON CALOR. (<ρ> = 0.8 ρPb) >10λ
HADRON CALOR. (<ρ> = 0.8 ρPb) ≥12λ
EM [<ρ> ~ 0.5 ρPb; 1λ]
TRD or PRESHOWER
η=3
R [m]
Z [m]
14 13 12 11 10 9 8 7 6 5 4 3 2 1 0
13 12 11 10 9 8 7 6 5 4 3 2 1 0

Fig. 6

Compact Muon Solenoid

M. Della Negra, K. Eggert, M. Lanzagorta, M. Pimiä, F. Szoncso

presented by M. Pimiä

SEFT, University of Helsinki, Finland

Abstract

A compact detector for highest luminosities at LHC is discussed. Muon momentum resolution and muon triggering capability are studied by simulation. Good momentum resolution ($\Delta p/p = 4 \sim 10\%$) is achieved for $|\eta| < 3.5$ up to momenta $p = 1.6$ TeV. Flexible muon triggers providing reasonable trigger rates from a few Hz to a few hundred Hz are shown to be possible.

Muon detection in a strong magnetic field

Figure 1 shows the Compact Muon Solenoid detector.

It has a strong solenoidal field in the central region, completed with forward high field iron toroids. It covers rapidities up to $|\eta| < 4$ and gives good muon identification with thick magnetised absorbers.

The main argument in favour of a strong magnetic field for a muon detector is to achieve a good momentum resolution with a moderate chamber precision, while keeping the size of the detector reasonable. Also the Coulomb multiple scattering limit is less severe for a momentum measurement in an absorber.

A solenoidal field is good for the central region because the bending is in the $r\phi$-plane transverse to the beam. Simple p_t-sensitive trigger algorithms based on track pointing in this plane can be implemented. The small size of the beam spot, $\sigma_{r\phi} = 10\mu m$, provides a very precise point for offline momentum reconstruction.

A toroidal field gives a better momentum resolution in forward regions where the bending power ($\int Bdl$) of the solenoid is limited. For a toroid, the field lines are perpendicular to the muon track and the field is at its strongest near the beam. The main drawback

Compact Muon Solenoid (CMS)

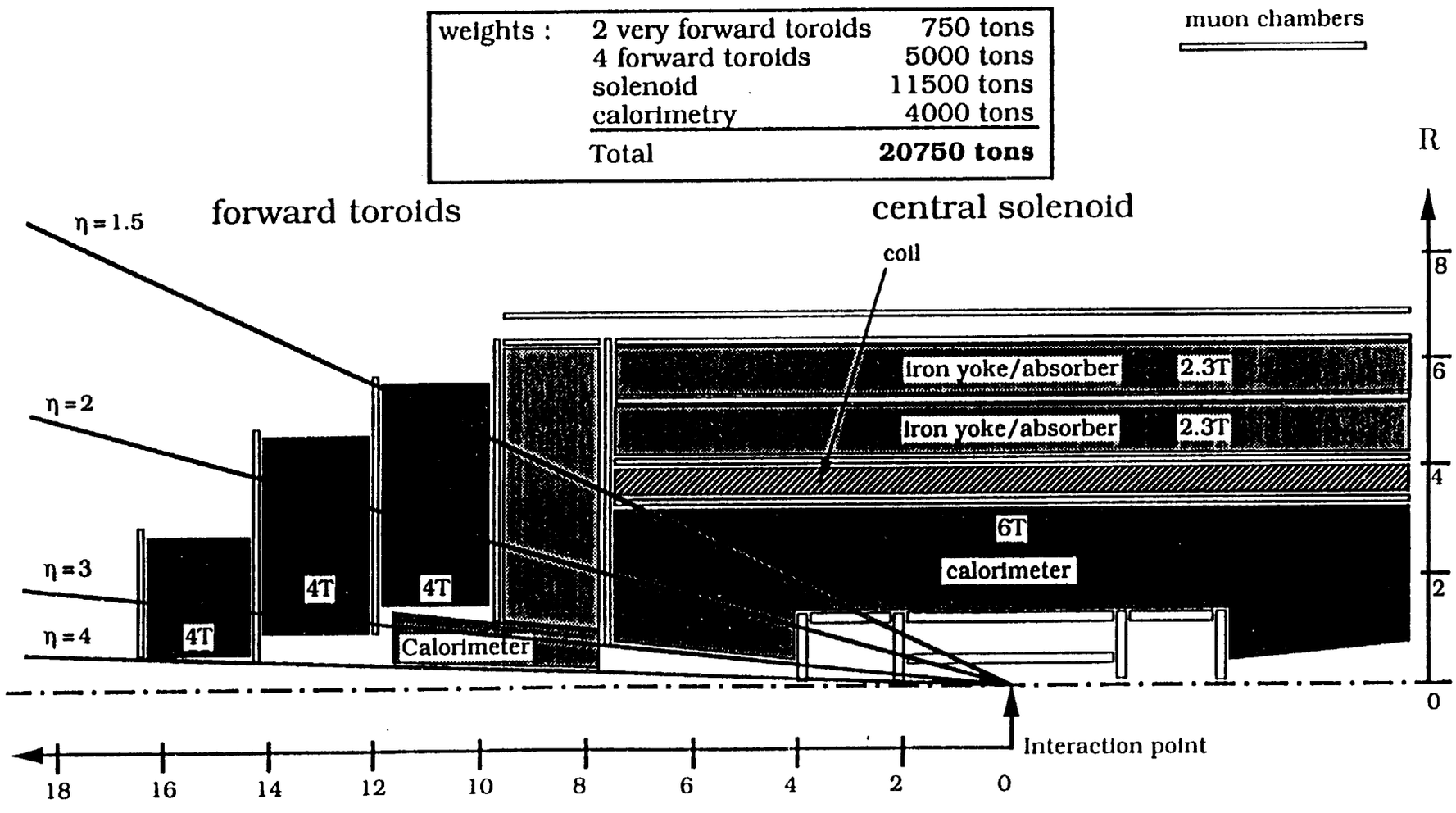


Fig. 1 Longitudinal view of the Compact Muon Solenoid detector.

is that there is no projection where the interaction point is well defined by the beam position. However, for the forward tracks the interaction region can be used as a loose constraint as well as for triggering by pointing.

The dimensions of the detector are small enough to fit well into an experimental hall of the LHC. It has an overall diameter of 13 meters, length of 33 meters and weight of 21000 tons.

Central region

The 15 m long solenoidal coil has an inner diameter of 7 meters. There is no limitations on the coil thickness from calorimetry, as the 10 interaction length calorimeter starts at radius R = 1.5 m and is two meters thick, fully inside the coil. The coil thickness is 0.5 m.

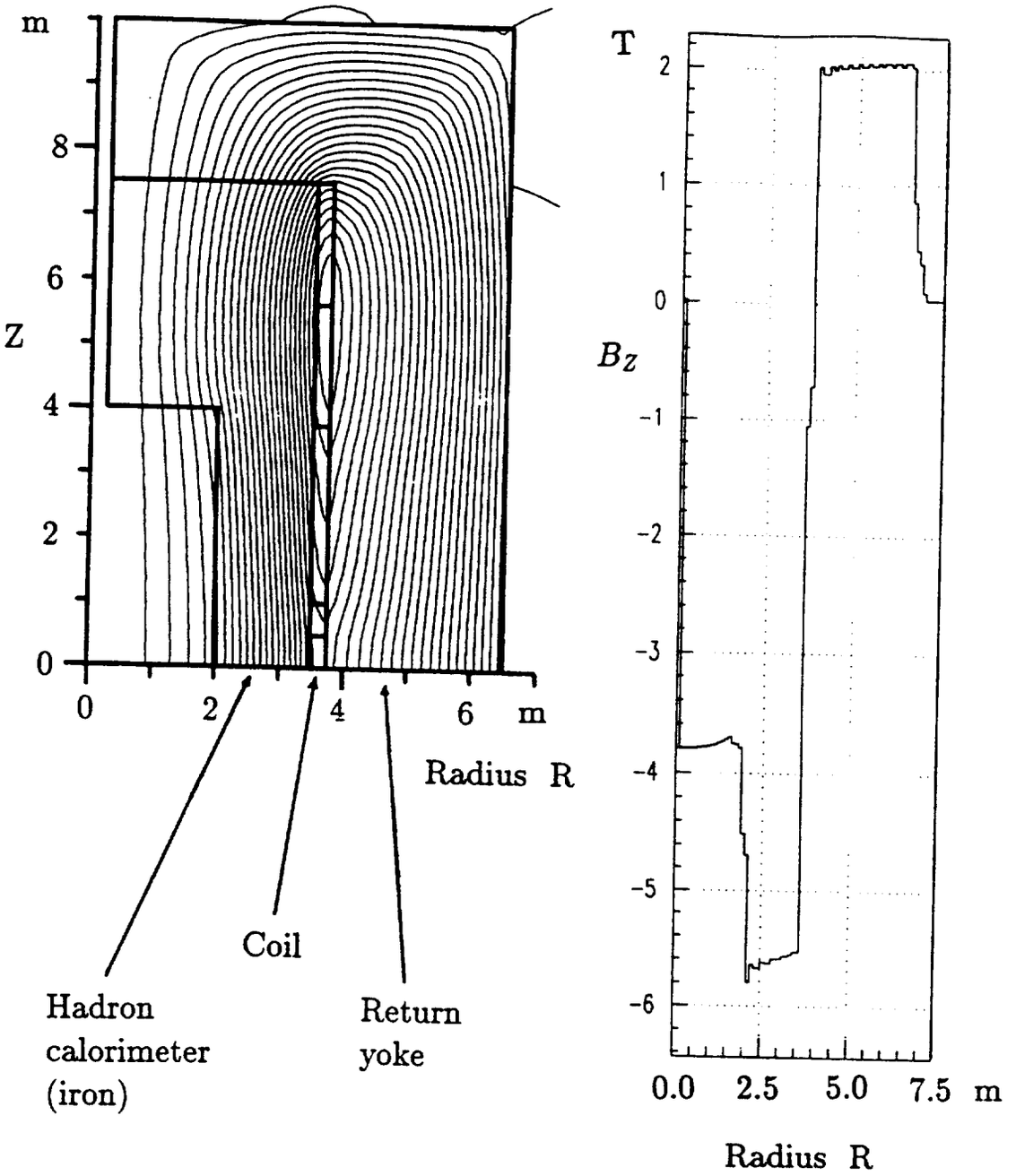
Valuable experience exists for the construction of very large superconducting solenoidal coils. The BEBC magnet was a solenoid producing a central field of 3.5 T with a thick superconducting coil of 5.4 m diameter. The ALEPH magnet has a thin coil with 5.5 m diameter and produces a central field of 1.5 T.

The solenoid consists of two half-solenoids, each 7.5 m long. A design similar to the BEBC 'pancake' design has been found feasible [1]. It produces a central field of 4 T, and the stored energy is ~ 4 GJ.

The field has been calculated for an example current density varying from 8 MA/m^2 at the centre to 13 MA/m^2 at the edges. Figure 2 shows an example of the field configuration with an electromagnetic calorimeter of non-magnetic material (R = 1.5-2.0 m) and a hadron calorimeter of iron (R = 2.0-3.5 m). The calculation shows how the field increases to ~ 6 T in iron while it stays at ~ 4 T in the inner air gap.

The return yoke of the magnet, two meters of iron at -2.3 T field, completes the absorber for a total of about 22 interaction lenghts. As the iron is saturated, some of the field lines escape causing fringe fields around the detector. This could be avoided by adding some iron to the return yoke.

Muon chamber arrays are placed before and after the coil (R = 3.5 m and 4.0 m, $\sigma_{r\phi} = 100\mu$m, $\sigma_z = 0.5$ mm), and outside



Magnetic field lines for a quarter of the solenoid, longitudinal view

Z-component B_Z of the magnetic field in a transverse plane at $Z = 3$ m as a function of the radius R.

Fig. 2 Example of the CMS solenoidal field.

the return yoke (R = 6.0 m and 6.5 m, $\sigma_{r\phi} = 200\mu$m, $\sigma_z = 1$ mm). Given are the effective resolutions when combined from several measurements at each detector plane.

It has been shown that tracking in the proposed 4 T field is feasible [2]. The air gap acts as a p_t cut-off, and the number of hits in the tracking device at a radius R = 0.7 m is not too high for muon observation, and at R = 1.5 m the muon track is very well isolated. Therefore we propose two points from inner tracking, one in the middle of the air gap and another in front of the calorimeter (R = 0.75 and 1.50 m, $\sigma_{r\phi} = 50\mu$m, $\sigma_z = 10$ mm). We think that at least the latter will be available even in complicated events, but we consider also the situation where no information from the inner tracking is available.

Forward region

The ends of the solenoid are closed with 2 meter thick iron end-caps. The forward magnet system consists of three toroids, 2 meters thick each. The toroidal field in the saturated iron varies from 4 T near the inner edge (R = 0.7 m) to 2 T at the outer edge (R = 5.5 m). The forward calorimeter is inside the end-cap and the first toroid. Arrays of muon chambers ($\sigma_{r\phi} = 100\mu$m) are placed inside of the end-cap, before, between and after the three toroids of each forward arm.

Momentum resolution

The momentum resolution in the central rapidity region has been estimated with full reconstruction of carefully simulated tracks. Single muons covering the central part of the detector ($|\eta| < 2.0$) with momenta $p = 25 - 1600$ GeV have been generated and their trajectories followed through the idealised detector.

The Coulomb multiple scattering is treated with the Gaussian approximation using relatively short steps in the heavy absorbers. The beam pipe and the chamber planes contribute to the traversed material by a few percent of a radiation length. The coil is 15 radiation lengths thick.

The energy loss of the muon has been simulated including the 'catastrophic' energy losses mainly due to bremsstrahlung and pair production. These phenomena become increasingly important for muon momenta above 100 GeV.

The beam is very well defined by the LHC machine, and by using data, a good precision in determining the beam position with respect to the detector in the transverse plane can be achieved. It can be measured in about an hour of data-taking with a resolution better than $\sigma_{r\phi} = 20\mu$m, value which is used in this study.

The detectors have been assumed to be fully efficient for muons. Detector resolutions in the simulation are as given before.

A segmented helix fit is applied to reconstruct the muon parameters. The points are weighted according to the detector resolution and the mean multiple scattering. The correlations between measurements due to the nature of the multiple scattering error have not been introduced in the fitting program. The energy loss has not been taken into account in fitting either, the fit result has been corrected for the mean energy loss only.

The calorimeter absorber material has an important role for the muon measurement. As an effective hadronic absorption thickness of ten interaction lengths (10λ) is wanted, the geometrical absorber thickness and the corresponding number of radiation lengths vary considerably with the material: for iron the 10λ thickness is 1.68 meters or 95 radiation lengths, for copper 1.51 m or 106 χ_0, for lead 1.71 m or 305 χ_0 and for uranium 1.05 m or 328 χ_0. The resolution for lead and uranium are about the same, and for the lighter materials as Fe or Cu it is considerably better. Iron has an extra advantage as the magnetic field increases to 6 T whereas copper stays at 4 T.

The muon momentum resolutions $\Delta p/p$ for different calorimeter materials are shown for rapidities $\eta = 0.0,\ 1.0,\ 1.5$ and for momenta $p = 25 - 1600$ GeV in figure 3 for copper and figure 4 for iron calorimeter. The resolution for lead (not shown) is about a factor 1.6 worse than for copper.

The three plots in each of the figures correspond to different inner tracking configurations. The lowest momenta with $\eta = 1.0 \sim 1.5$

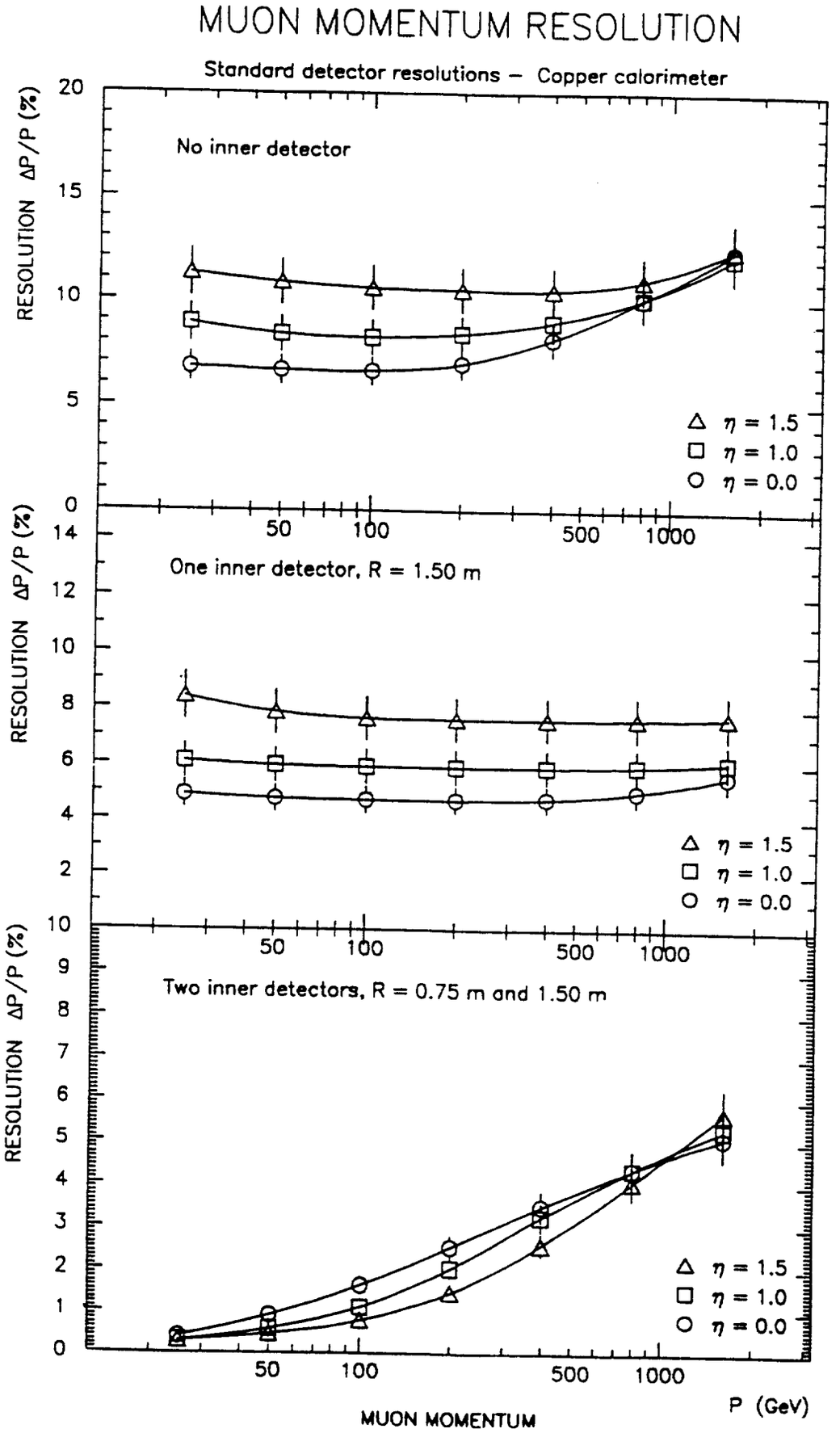


Fig. 3 Momentum resolution as a function of muon momentum for three inner tracking options. Copper 10λ calorimeter.

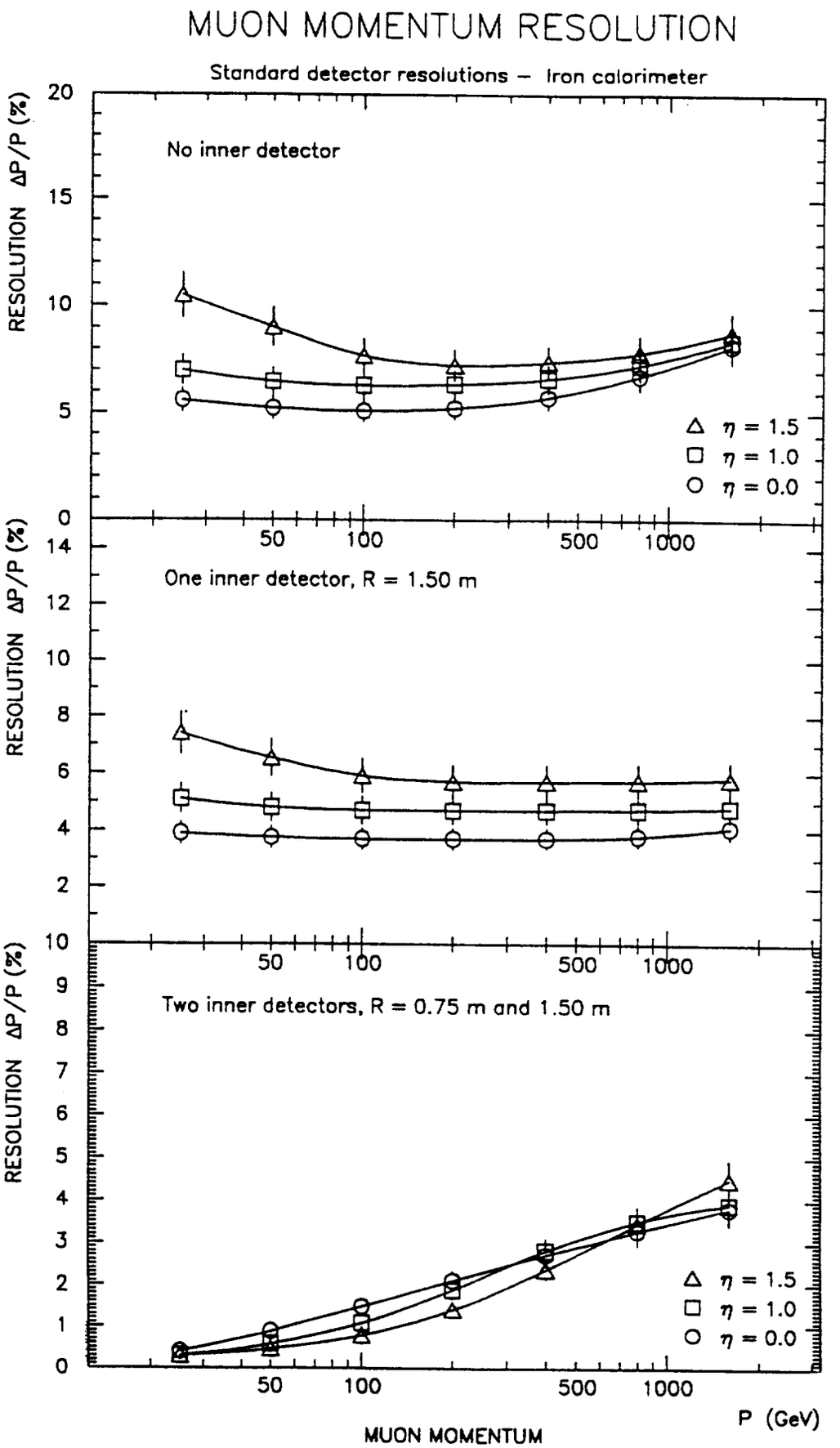


Fig. 4 Momentum resolution as a function of muon momentum for three inner tracking options. Iron 10λ calorimeter.

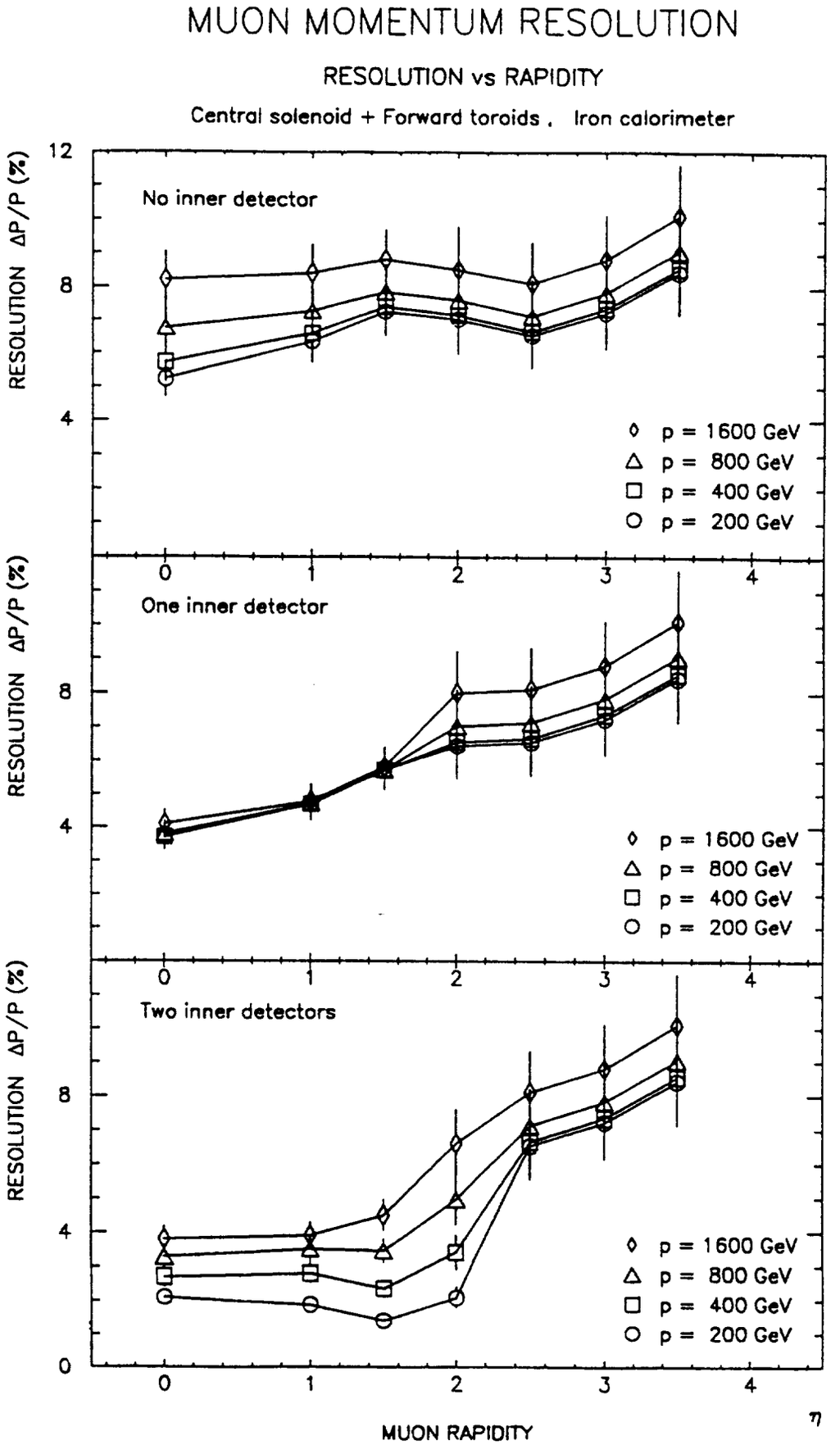


Fig. 5 Momentum resolution as a function of muon rapidity for three inner tracking options. Iron 10λ calorimeter.

suffer from heavy energy loss and multiple scattering as the amount of traversed material is large and the momentum is relatively small. With one inner point at R = 1.5 m and for momenta $50 - 1600$ GeV we get $\Delta p/p = 5 \sim 8\%$ for Cu, $\Delta p/p = 8 \sim 13\%$ for Pb or U, and $\Delta p/p = 4 \sim 6\%$ for Fe.

If the two points from inner tracking are available, the momentum resolution is drastically improved. The momentum is measured before the absorber and thus the random effects of energy loss and multiple scattering are minimal. The muon chambers after absorber improve the resolution only for the high momenta. The resolution below $p < 0.2$ TeV is roughly $\Delta p/p = 0.15 \times p$ (p in TeV).

For the forward regions the field map has not yet been calculated, and therefore a more approximative approach has been used for momentum resolution studies. The resolution limit from multiple scattering for a measurement in the absorber is given by $\Delta p/p \approx 0.5/B\sqrt{l}$ where B is the field in Tesla and l the length of the measured trajectory in meters. This resolution limit is convoluted with the detector resolution $\sigma_{r\phi} = 100\mu$m. For rapidities up to $|\eta| < 2.0$ also the solenoidal field contributes to the momentum measurement.

The momentum resolution for muons with $p = 200 - 1600$ GeV as a function of rapidity is shown in figure 5. The forward toroids extend the rapidity coverage up to $|\eta| < 3.5$ with a momentum resolution $\Delta p/p = 7 \sim 10\%$.

Muon trigger

The muon trigger should allow a fast and efficient cut on the transverse momentum of the muons. The p_t cut at the trigger level is needed to reduce the muon rate to an acceptable level. The required p_t cut value varies with the experimental conditions like luminosity. The muon triggering problems in general have been discussed in detail in this workshop [3].

The pointing of the muon track to the vertex in the transverse projection is a direct measure of the transverse momentum of the muon. The thick absorber of course acts as a passive low momentum filter, as only muons with $p_t > 3$ GeV can cross the full absorber.

Fast trigger hodoscopes with a granularity allowing $\sigma_{r\phi} = 10$ mm are positioned at the same places as the muon chambers, after the calorimeter and outside the return yoke. These hodoscopes provide the information for the first level trigger. No measurement information is needed in the longitudinal or z-direction. The pointing angle α between the vertex direction and the muon track can be checked at two locations: at the coil (station 1, R = 4 m) and outside the yoke (station 2, R = 7 m), see figure 6. The vertex position in the projection, the beam spot, is assumed to be known to 1 mm precision with respect to the detector.

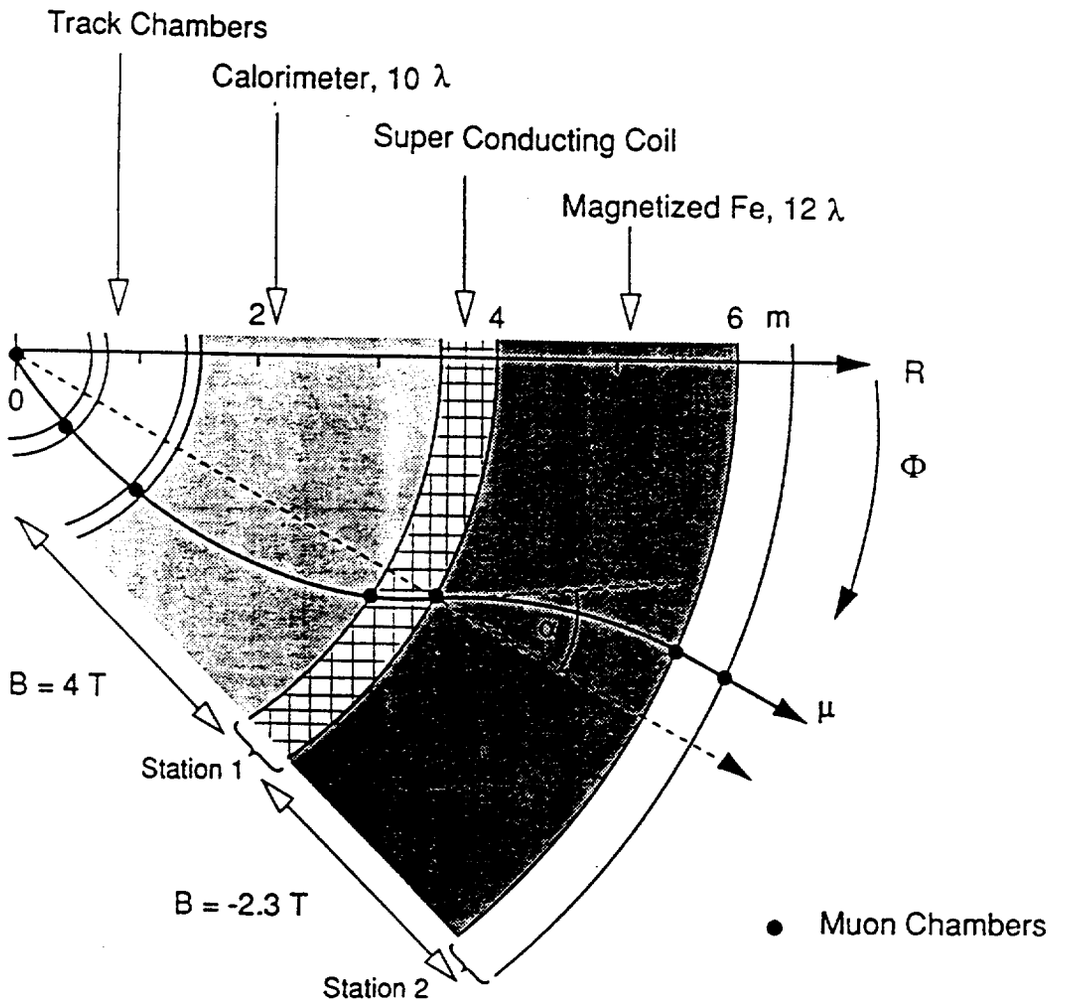


Fig. 6 Transversal view of the Compact Muon Solenoid detector.

A full simulation of muons with $p_t = 3 - 500$ GeV has been performed in the rapidity interval $|\eta| < 2$ in a similar way as for the momentum resolution study. The trigger efficiency curves for different cut angles α as a function of the transverse momentum of the muon are shown in figure 7 for three trigger possibilities:

(i) The cleanest information for a first level trigger is obtained from the hodoscopes at station 2 as it is behind all the absorber. The backgrounds from hadron decays and from punch-through are at reasonable levels already before pointing angle cuts. However, the reversed field in the return yoke decreases the net bending of the muon trajectories. Therefore the efficiency curves are rather flat and only low momentum muons with $p_t < 10 \sim 15$ GeV can be cut, without losing too many of the fast muons. A cut at $\alpha = 80$ (60) mrad gives an efficiency of $\geq 90\%$ for muons with $p_t \geq 17$ (22) GeV, but still 10% of the muons with $p_t = 8$ (9) GeV will be accepted, giving high trigger rate.

(ii) To profit from the full bending power of the magnet the pointing angle at station 1 is used. However, it is after 10λ absorber and might suffer from punch-through if used alone. The trigger selectivity is better than at station 2. A cut at $\alpha = 150$ (100) mrad gives an efficiency of $\geq 90\%$ for $p_t \geq 21$ (36) GeV, and 10% of the muons with $p_t = 12$ (16) GeV are accepted.

(iii) We assume that at the second level trigger, where much more time is available, the trigger information could have a precision $\sigma_{r\phi} = 1$ mm at the station 1. The selectivity is very good up to $p_t = 100$ GeV. A cut at $\alpha = 120$ (50) mrad gives an efficiency of $\geq 90\%$ for $p_t \geq 22$ (50) GeV, and 10% of the $p_t = 16$ (38) GeV muons are accepted.

The efficiency function together with the muon p_t spectra [4] are used to calculate the trigger rate for a given angular cut in each of the discussed trigger options. The rates are given for a luminosity $\mathcal{L} = 2 \times 10^{34} cm^{-2} s^{-1}$ and for the rapidity range $|\eta| < 3$.

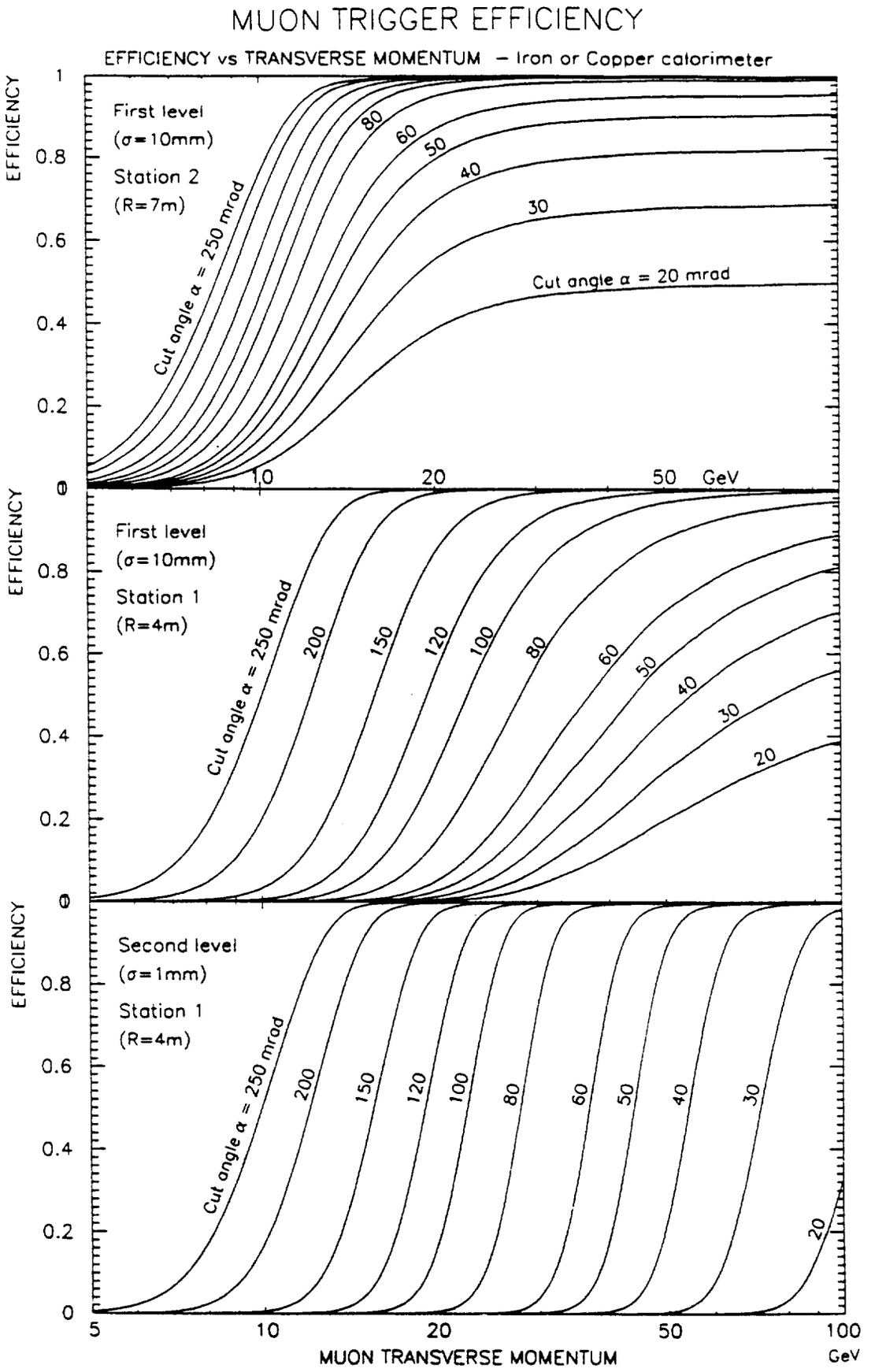


Fig. 7 Muon trigger efficiency as a function of muon transverse momentum for different pointing angle cuts and three trigger options.

In figure 8 is shown the single muon trigger rate as a function of the cut angle α. The different production mechanisms, b or c quark semileptonic decay, W or Z leptonic decay, Drell-Yan mechanism or top quark ($m_{top} = 130$ GeV) production are shown, as well as the total rate.

The background from primary decays of pions and kaons has also been carefully simulated as it could be large. Muonic decays of hadrons have been generated in the air gap of the core of the detector, and the resulting muons have been tracked through the detector. The resulting trigger probabilities have been convoluted with the hadron spectra [4], giving decay muon rates as functions of the cut angles for the three trigger options. As the decay muons are mainly slow, the background is strongly reduced by the p_t cut imposed by the angular cut. The decay rate is also shown in the figure 8, and it is included in the total rate.

The punch-through of hadrons seems not to be a problem because of the thick and strongly magnetised absorber with possible timing and angle cuts. Monte Carlo calculations [5] show that the punch-through rate is below the primary decay background rate in our geometry up to hadron momenta $p < 50$ GeV. Above that, both background rates are negligible in comparison to the b and c induced muon rate. In order to check thoroughly the triggering possibilities and the backgrounds, a study of muon triggers using strongly magnetised absorbers in test beams has been proposed [6].

Figure 9 shows the dimuon trigger rate as a function of the cut angle α. Rates for the different production mechanisms plus the total are shown for the three trigger options.

For the examples discussed above, the single muon and dimuon trigger rates for $\mathcal{L} = 2 \times 10^{34} cm^{-2} s^{-1}$, $|\eta| < 3$ would be

(i) cut $\alpha = 80$ (60) mrad, efficiency $\geq 90\%$ for $p_t \geq 17$ (22) GeV, single muon rate 21000 (19000) Hz, dimuon rate 200 (150) Hz.

(ii) cut $\alpha = 150(100)$ mrad, efficiency $\geq 90\%$ for $p_t \geq 21(36)$ GeV, single muon rate 10000 (3200) Hz, dimuon rate 80 (40) Hz.

(iii) cut $\alpha = 120$ (50) mrad, efficiency $\geq 90\%$ for $p_t \geq 22$ (50) GeV, single muon rate 5000 (200) Hz, dimuon rate 50 (6) Hz.

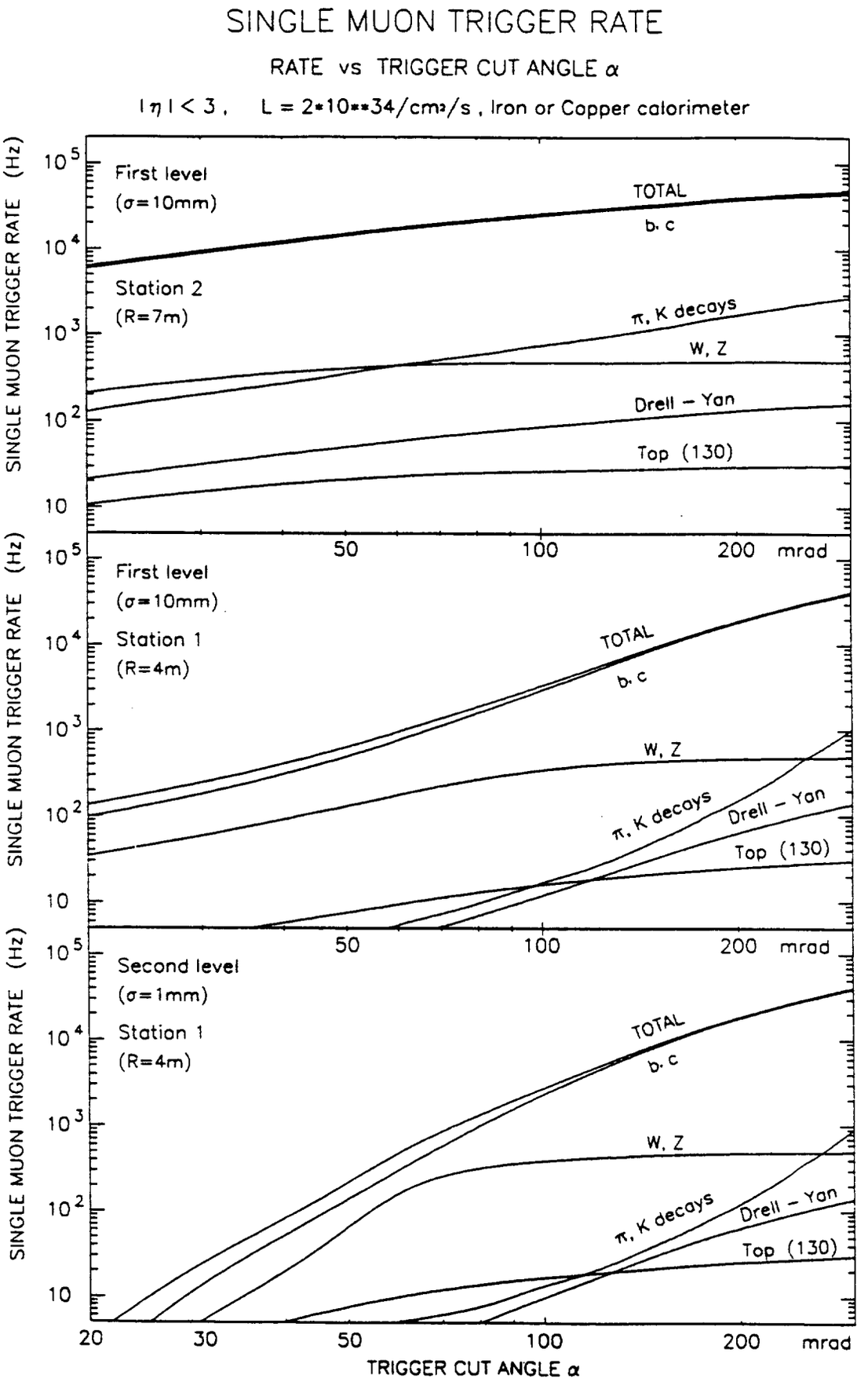


Fig. 8 Single muon trigger rate as a function of the cut angle for three trigger options.

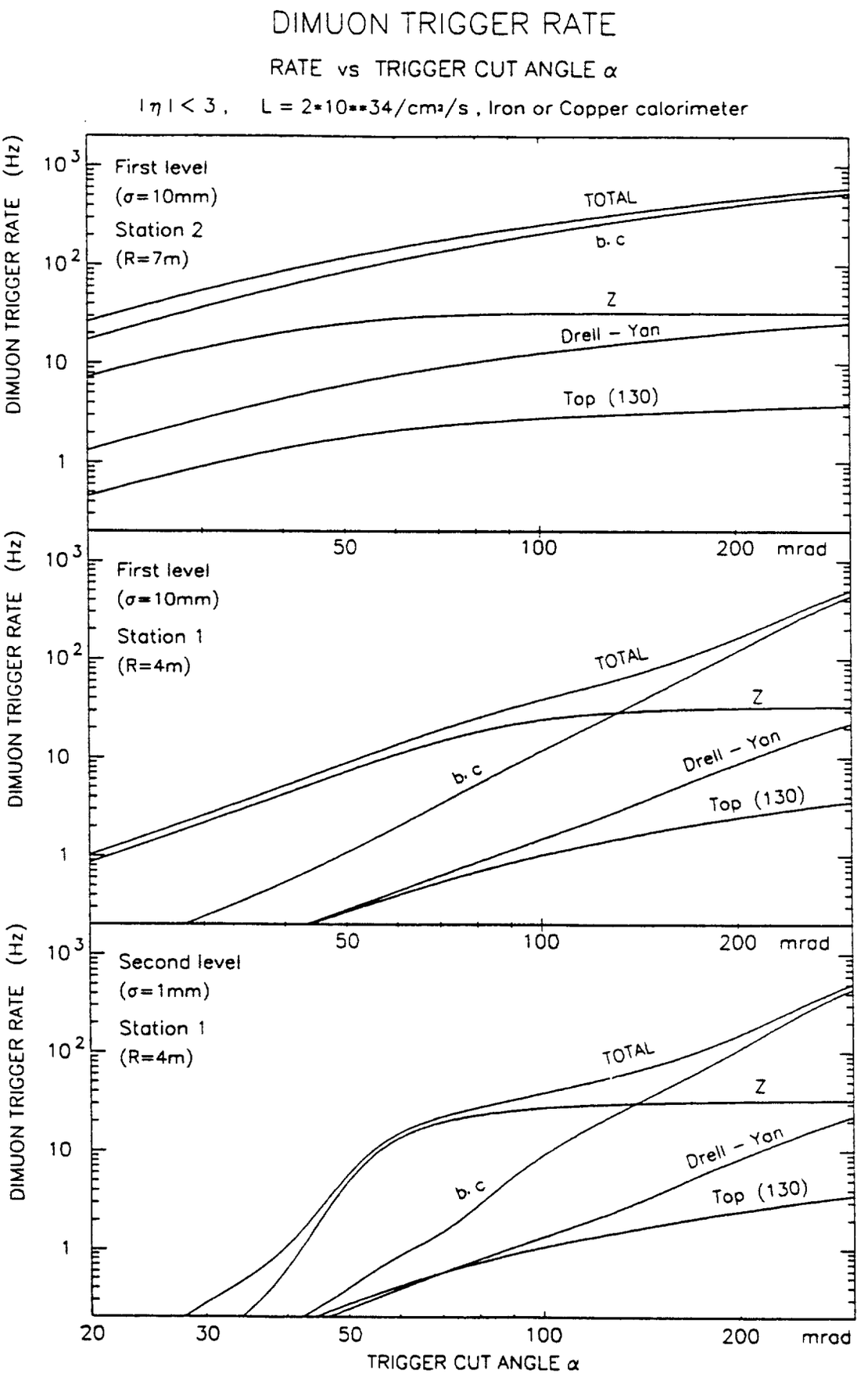


Fig. 9 Dimuon trigger rate as a function of the cut angle for three trigger options.

Conclusions

The Compact Muon Solenoid is shown to be able to cope with the highest luminosities at LHC.

The design has many advantages: It has large $\int Bdl$ for precise muon momentum measurement in high field with moderately precise chambers. The muon can be measured several times: before the absorber, after the calorimeter and in the return yoke. The beam spot can be used as the vertex position, helping pattern recognition, momentum analysis and triggering. The muon trigger based on simple pointing to the vertex is very flexible. For tracking, strong field means p_t cut-off in the inner air gap.

The strong solenoidal field has also disadvantages: Toroids are needed to cover the forward regions. Some of the chambers and the calorimetry are in a strong field. There are lots of spiraling tracks in the vicinity of the beams, making vertex detectors difficult to use.

The design offers a muon momentum resolution $\Delta p/p \leq 6\%$ in $|\eta| < 1.5$ and $\Delta p/p \leq 10\%$ in $|\eta| < 3.5$ up to $p = 1.6$ TeV. Inner tracking allows very precise measurements before absorber, $\Delta p/p = 0.15 \times p \quad (p < 0.2 \text{ in TeV})$ in $|\eta| < 2.0$.

As an example, the trigger rate at $\mathcal{L} = 2 \times 10^{34} cm^{-2} s^{-1}$ is 200 Hz for single muons with $p_t \geq 50$ GeV and 60 Hz for dimuons with $p_t \geq 20$ GeV.

References

1. Desportes, 'Solenoidal magnet with high field', CMS meeting, CERN, 29.5.1990 (unpublished).
2. C. Buttar, T. Sloan, I. Ten Have, 'Occupancy in a magnetic field', contribution to this workshop, Aachen 4.10.1990.
3. M. Della Negra, 'Muon trigger and identification', contribution to this workshop, Aachen 4.10.1990.
4. A. Nisati, 'Muon rates, acceptance and momentum precision', contribution to this workshop, Aachen 4.10.1990.
5. H. Fesefeldt, 'Punch-through simulations', contribution to this workshop, Aachen 4.10.1990.
6. R+D proposal 'Study of muon triggers and momentum reconstruction in a strong magnetic field for a muon detector at LHC', CERN/DRDC/P7, Geneve 30.8.1990.

NEW DOSE CALCULATIONS FOR LHC DETECTORS

G. R. Stevenson
CERN, Geneva, Switzerland
11 October 1990

Abstract

Recent Monte-Carlo cascade simulations are described from which the following parameters can be derived. 1. The maximum dose in the calorimeter, 2. The maximum neutron fluence in the calorimeter, 3. Dose to thin detectors in the central cavity from charged particles and photon conversions, 4. Albedo neutron fluence in the central cavity region. The calculations were made using an idealized detector geometry: that of a hollow lead sphere of 2 metres internal radius where forward and backward cones in the high-rapidity region were removed.

1 Introduction

In recent years there have been a number of studies of dose and neutron fluence within a calorimeter structure which could be used at the new generation of hadron colliders (LHC and SSC). The most extensive of these was the SSC Task-Group report edited by Groom [1], and several shortened versions have been published since then (see [2] for example). The Task Group Report summarized experimental data and Monte-Carlo cascade simulations from which the following parameters could be derived for an idealized detector geometry: that of a hollow sphere of 2 metres internal radius where forward and backward cones in the high-rapidity region had been removed. The parameters of interest are:

1. The maximum dose in the calorimeter,
2. The maximum neutron fluence in the calorimeter,
3. Dose to thin detectors in the central cavity from charged particles and photon conversions,
4. Albedo neutron fluence in the central cavity region, and
5. Photon albedo.

The purpose of this paper is to report on recent data which have appeared since the Task Group met, especially on new Monte-Carlo calculations of the cascade generated by secondary particles from proton–proton collisions at 8+8 TeV within a spherical lead shell.

2 Source Considerations

Evidence was reviewed in the Task Group Report which showed that the the multiplicity of 'minimum bias', 'average' events can be well-approximated by a plateau function of rapidity where the number of particles produced per unit of pseudorapidity η is a constant, H, independent of η and they all have the same transverse momentum, i.e.

$$\frac{\mathrm{d}^2 N_{ch}}{\mathrm{d}\eta \mathrm{d}p_T} \approx H\delta(p_T - < p_T >). \tag{1}$$

Thus, integrating over p_T,

$$\frac{\mathrm{d}N_{ch}}{\mathrm{d}\eta} = H, \quad \text{and} \quad \frac{\mathrm{d}\eta}{\mathrm{d}\theta} = \frac{1}{\sin\theta} \quad \text{or} \quad \frac{\mathrm{d}\eta}{\mathrm{d}\Omega} = \frac{1}{2\pi \sin^2\theta}. \tag{2}$$

This leads to the very simple relations:

$$\frac{\mathrm{d}N_{ch}}{\mathrm{d}\theta} = \frac{H}{\sin\theta}, \quad \text{or} \quad \frac{\mathrm{d}N_{ch}}{\mathrm{d}\Omega} = \frac{H}{2\pi \sin^2\theta}, \quad \text{and} \quad E \approx p = \frac{< p_T >}{\sin\theta}. \tag{3}$$

The constants for use in these relations relevant for p-p collisions at the LHC are: $H = 6.3$ and $p_T = 0.55$ GeV/c.

Many calculations of dose in this spherical geometry have used the DTUJET program [3] as the source of the secondary particles (see [4] for example). The DTUJET program has undergone several revisions during the last few years but none of these has changed the dose estimates by more than a few tens of percent. The latest version [5] has been used for the calculations described in this paper. Figures 1 and 2 show the spectrum of charged hadrons and pions coming from p-p collisions at LHC energies. It will be seen that the number of particles emitted per unit pseudo-rapidity is indeed independent of the pseudo-rapidity interval. The constant H of equation (1) determined from these curves is given in the second column of Table 1. It compares well with the value of 6.3 taken from the Task Group Report. It is to be expected that the constant for pi-zero emission is one-half this value.

The mean transverse momentum is also given in Table 1. There is good agreement with the Task Group value for charged hadrons but the mean transverse momentum of neutral pions is somewhat lower. Finally the last two columns of Table 1 give the DTUJET and Task Group numbers for the average emission in terms of particles emitted per steradian and the DTUJET value of the mean kinetic energy in the different pseudo-rapidity intervals. Apart from ignoring the finite spread in p_T values, the Task Group model is a satisfactory simplification of the source particle spectrum.

Table 1: Parameters for LHC collisions

Rapidity Interval	DTUJET90 H	DTUJET90 $< p_T >$ GeV/c	DTUJET90 ster^{-1}	SSC-SR-1033 ster^{-1}	DTUJET90 GeV
Hadrons					
0.0 to 1.0	5.5	0.50	1.15	1.32	0.41
1.0 to 2.0	6.4	0.46	5.0	5.0	0.90
2.0 to 3.0	6.7	0.43	35.0	32.0	2.4
3.0 to 4.0	6.6	0.41	240.0	240.0	6.6
4.0 to 5.0	5.9	0.40	1630.0	1730.0	18.5
5.0 to 6.0	5.3	0.41	10700.0	12800.0	52.0
Pi-zeros					
0.0 to 1.0	2.7	0.39	0.56	0.66	0.36
1.0 to 2.0	3.1	0.39	2.4	2.50	0.84
2.0 to 3.0	3.0	0.37	15.4	16.2	2.2
3.0 to 4.0	2.8	0.34	103.0	117.0	5.7
4.0 to 5.0	2.5	0.33	690.0	870.0	15.2
5.0 to 6.0	2.0	0.33	4100.0	6400.0	41.0

3 Dose in the Calorimeter

A file containing details of particle type and momentum for approximately 50000 secondaries from 350 interactions was written by DTUJET90 for use in the subsequent analysis. The π^0 mesons were not forced to decay and neutrinos were ignored. The file order was randomized before use in the cascade simulation to avoid effects of only taking part of an event or of single events having unique characteristics.

Particles from the file produced as described above were used as input to the Monte-Carlo Cascade Program FLUKA [6] using recent modifications to the EGS4 part of the code [7]. Energy densities were scored in a spherical shell of lead of inner radius 2 m centred on the p-p collision point. The medium in the inner sphere around the interaction point and within the cones having $|\eta| > 5$ was assumed to be vacuum. EGS4 was used to treat the electromagnetic part of the cascades [8]. Leading-particle biassing was used in both FLUKA and EGS [6] to avoid wasting excessive time in tracking low-energy particles which would not contribute significantly to either cascade propagation or energy deposition.

The dose in lead was calculated by multiplying the energy densities by the standard GeV:joule conversion factor and assuming an integrated luminosity of 10^{41} cm^{-2} with an inelastic p-p cross-section of 60 mbarns. The dose from the electromagnetic cascades initiated by photons, electrons and pi-zeros was scored separately from the hadronic part of the dose. The numerical values of the annual dose rates in the spherical shell are given as a

function of depth and pseudo-rapidity in Tables 2–4 respectively. For two pseudo-rapidity intervals (0–1 and 4–5) the values from the tables have been plotted against depth in the lead sphere in Figure 3. The errors in these histograms represent the standard error on the mean value of the dose obtained from dividing the cascade calculation into five batches each of 10000 secondary particles from the p p interactions. It will be seen that in the inner parts of the sphere the dose from the e-m cascade dominates whereas the hadronic dose is the more important at depths in the sphere greater than 20 cm. It is also important to realize that the variation of dose with depth is very steep especially at lower values of pseudo-rapidity and that different technologies could be used for the construction of the electromagnetic and hadronic parts of the barrel calorimeter. However annual doses to the forward parts of the calorimeter are very large and do not vary very much with depth.

Table 2: Electromagnetic Dose in Gy/year

η interval	0.0 - 1.0	1.0 - 2.0	2.0 - 3.0	3.0 - 4.0	4.0 - 5.0
Radius (m)					
2.000 - 2.025	0.199E+03	0.208E+04	0.335E+05	0.147E+06	0.141E+07
2.025 - 2.050	0.122E+03	0.243E+04	0.540E+05	0.289E+06	0.434E+07
2.050 - 2.075	0.418E+02	0.102E+04	0.220E+05	0.168E+06	0.288E+07
2.075 - 2.100	0.209E+02	0.398E+03	0.108E+05	0.669E+05	0.133E+07
2.100 - 2.150	0.103E+02	0.223E+03	0.605E+04	0.358E+05	0.638E+06
2.150 - 2.200	0.595E+01	0.147E+03	0.371E+04	0.247E+05	0.454E+06
2.200 - 2.300	0.258E+01	0.906E+02	0.265E+04	0.194E+05	0.328E+06
2.300 - 2.400	0.105E+01	0.457E+02	0.151E+04	0.112E+05	0.237E+06
2.400 - 2.600	0.350E+00	0.191E+02	0.702E+03	0.586E+04	0.121E+06
2.600 - 2.800	0.107E+00	0.470E+01	0.251E+03	0.218E+04	0.438E+05
2.800 - 3.000	0.132E-01	0.113E+01	0.126E+03	0.967E+03	0.220E+05
3.000 - 3.400	0.335E-03	0.240E+00	0.215E+02	0.255E+03	0.513E+04
3.400 - 3.800	0.000E+00	0.338E-01	0.188E+01	0.332E+02	0.163E+04
3.800 - 4.200	0.000E+00	0.987E-02	0.199E+00	0.599E+01	0.829E+03
4.200 - 4.600	0.000E+00	0.919E-03	0.292E-01	0.172E+01	0.271E+03
4.600 - 5.000	0.000E+00	0.000E+00	0.000E+00	0.821E+00	0.411E+03

The maximum values of dose (at whichever depth the maximum occurs) taken from the various columns of Tables 2 to 4 are drawn as histograms as a function of pseudo-rapidity in Figures 4, 5 and 6 for the electromagnetic, hadronic and total doses respectively. Also shown in these figures are dashed curves calculated from data in the Task Group Report [1].

The electromagnetic component of the dose was shown to be overestimated by a factor of three in the Task Group Report [9]. The formula relating the maximum e-m dose, D in gray, with photon energy, E in GeV, is now:

$$D \approx 3.2 \times 10^{-9} E^{0.93} \quad (4)$$

Table 3: Hadron Dose in Gy/year

η interval Radius (m)	0.0 - 1.0	1.0 - 2.0	2.0 - 3.0	3.0 - 4.0	4.0 - 5.0
2.000 - 2.025	0.252E+03	0.101E+04	0.134E+05	0.460E+05	0.294E+06
2.025 - 2.050	0.180E+03	0.975E+03	0.147E+05	0.514E+05	0.370E+06
2.050 - 2.075	0.141E+03	0.847E+03	0.157E+05	0.583E+05	0.410E+06
2.075 - 2.100	0.116E+03	0.796E+03	0.161E+05	0.607E+05	0.430E+06
2.100 - 2.150	0.796E+02	0.691E+03	0.159E+05	0.608E+05	0.420E+06
2.150 - 2.200	0.513E+02	0.583E+03	0.141E+05	0.574E+05	0.405E+06
2.200 - 2.300	0.279E+02	0.418E+03	0.117E+05	0.490E+05	0.336E+06
2.300 - 2.400	0.128E+02	0.280E+03	0.833E+04	0.372E+05	0.254E+06
2.400 - 2.600	0.406E+01	0.148E+03	0.501E+04	0.222E+05	0.150E+06
2.600 - 2.800	0.100E+01	0.640E+02	0.237E+04	0.104E+05	0.705E+05
2.800 - 3.000	0.230E+00	0.272E+02	0.113E+04	0.487E+04	0.340E+05
3.000 - 3.400	0.415E-01	0.818E+01	0.340E+03	0.149E+04	0.106E+05
3.400 - 3.800	0.116E-02	0.171E+01	0.625E+02	0.301E+03	0.301E+04
3.800 - 4.200	0.458E-04	0.364E+00	0.170E+02	0.890E+02	0.136E+04
4.200 - 4.600	0.000E+00	0.939E-01	0.477E+01	0.388E+02	0.685E+03
4.600 - 5.000	0.000E+00	0.463E-01	0.162E+01	0.189E+02	0.429E+03

Table 4: Total Dose in Gy/year

η interval Radius (m)	0.0 - 1.0	1.0 - 2.0	2.0 - 3.0	3.0 - 4.0	4.0 - 5.0
2.000 - 2.025	0.451E+03	0.309E+04	0.470E+05	0.193E+06	0.170E+07
2.025 - 2.050	0.303E+03	0.341E+04	0.687E+05	0.340E+06	0.471E+07
2.050 - 2.075	0.183E+03	0.186E+04	0.377E+05	0.227E+06	0.329E+07
2.075 - 2.100	0.137E+03	0.119E+04	0.269E+05	0.128E+06	0.176E+07
2.100 - 2.150	0.899E+02	0.914E+03	0.219E+05	0.966E+05	0.106E+07
2.150 - 2.200	0.573E+02	0.730E+03	0.178E+05	0.821E+05	0.859E+06
2.200 - 2.300	0.305E+02	0.508E+03	0.143E+05	0.684E+05	0.664E+06
2.300 - 2.400	0.139E+02	0.325E+03	0.984E+04	0.484E+05	0.491E+06
2.400 - 2.600	0.441E+01	0.168E+03	0.571E+04	0.281E+05	0.271E+06
2.600 - 2.800	0.111E+01	0.687E+02	0.262E+04	0.125E+05	0.114E+06
2.800 - 3.000	0.243E+00	0.284E+02	0.126E+04	0.584E+04	0.561E+05
3.000 - 3.400	0.418E-01	0.842E+01	0.361E+03	0.174E+04	0.157E+05
3.400 - 3.800	0.116E-02	0.175E+01	0.644E+02	0.335E+03	0.463E+04
3.800 - 4.200	0.458E-04	0.374E+00	0.172E+02	0.950E+02	0.218E+04
4.200 - 4.600	0.000E+00	0.948E-01	0.480E+01	0.406E+02	0.956E+03
4.600 - 5.000	0.000E+00	0.463E-01	0.162E+01	0.197E+02	0.874E+03

This was shown not to depend strongly on material composition [1]. The maximum e-m dose in lead can therefore be calculated by assuming that the number of π^0s coming from the p-p collisions is one-half of the number of charged hadrons, that the mean p_T is the same and that each π^0 gives two photons each carrying one-half of the energy of the π^0.

The hadronic component of the dose can be calculated using the following relation between the maximum dose, D in gray, and the kinetic energy of the hadron, E in GeV [1]:

$$D \approx 3.8 \times 10^{-10} E^{0.89}. \quad (5)$$

The total dose was taken to be the sum of these two components.

It will be seen that there is excellent agreement between the two estimates of maximum electromagnetic dose in the lead calorimeter, but that the hadronic dose is lower at the highest pseudo-rapidity interval considered in the FLUKA simulation (4–5) and higher at the lowest (0–1). The studies reported in [10] suggest that the underestimation is due to lateral diffusion of the cascade and the overestimation is due to hadron albedo. This shows the limitations of idealized geometries such as a sphere in calculations of dose in real calorimeter structures.

It is possible to use the values of Tables 2 to 4 to interpolate values for geometries other than a spherical shell. For the e-m dose, the point of interest is nearly always on the inner surface of the structure and this can be obtained by a simple inverse square correction to the values in the upper rows of Table 2. For the hadronic dose or the total dose, one connects the point of interest to the origin (the p-p collision point), the angle gives the pseudo-rapidity value and the distance through the structure gives the appropriate depth in the spherical shell. The interpolated value for these two coordinates must then be inverse square law corrected using the original distance of the point of interest from the origin and the interpolated spherical radius. This procedure was used for the total dose in a lead cylinder of inner radius 1 metre. Comparisons with a FLUKA plus DTUJET90 calculation in cylindrical geometry of the radial variation of dose for two pseudo-rapidity intervals are shown in Figures 7 and 8. The dose in the FLUKA calculation is averaged over the longitudinal section where the cones corresponding to the limits of the pseudo-rapidity intervals intercept the inner surface of the cylinder. The dashed curves are interpolated from the sphere calculations. It will be seen that at low pseudo-rapidity values the spherical interpolation gives satisfactory values, but at higher values of pseudo-rapidity the spherical interpolation will seriously underestimate the dose at large radii. This is because the source of the dose at large radii is not due to a cascade directed from the p–p collision point but is due to the cascade generated by interactions in the inner surface of the cylinder directly underneath the point of interest. This effect has been known in the shielding of high-energy proton accelerators for some considerable time [11].

4 Neutrons in the Calorimeter

The maximum neutron fluence in a lead calorimeter can be derived from data contained in the Task Group Report [1]. Based on Monte-Carlo calculations and experimental measurements, the area-integrated neutron fluence at cascade maximum is given by an equation of the form:

$$\int \phi da = 31 \times (E_k/1\mathrm{GeV})^{0.67}, \tag{6}$$

where E_k is the incident hadron energy. In scaling from calculations and experiments with different materials the data of Table 5 taken from [1] can be used.

Table 5: Neutron Production in Different Calorimeters

	Scale by
U-LAr or Si	1.8
Pb-LAr or Si	1.0
U-Scint	0.6
Fe-LAr or Si	0.1
Pb-Scint	0.3

Coupling the mono-energetic source model discussed in a previous section with the above formula for neutron production in cascades, and the same reference conditions of the LHC as before (i.e. a luminosity of 10^{34} cm^{-2}, an annual operating time of 10^7 seconds, an inelastic cross-section for p-p interactions of 60 mbarns and a reference calorimeter of a hollow lead sphere having an internal radius of 2 metres with the forward and backward cones at $\eta > 6$ removed), the annual neutron fluence as a function of rapidity will be as shown in Figure 9.

It was shown in an experimental study of neutrons in an iron calorimeter structure [12] that the area-integrated flux of neutrons was directly proportional to the the area-integrated flux of hadrons having an energy above 50 MeV. Thus the variation of neutron fluence within the lead spherical shell idealized calorimeter structure can be obtained from the density of inelastic interactions (stars) calculated using FLUKA (and listed elsewhere in these proceedings [13]). By normalizing in each pseudo-rapidity interval on the maximum neutron fluence taken from Figure 9 the table of star densities can be transformed into a table of neutron fluences. This is given in Table 6.

The effect of hydrogenous material inside the calorimeter-absorber structure on the fluence of low-energy neutrons has long been the subject of debate. In a recent systematic study using computer simulations of cascades induced by 3 GeV/c and 20 GeV/c negative pions in 7.5 mm iron and 5 mm uranium calorimeter structures, Foruno et al showed that the low-energy neutron fluence could be reduced by as much as an order of magnitude

Table 6: Neutron fluence in cm^{-2}/year

η interval Radius (m)	0.0 - 1.0	1.0 - 2.0	2.0 - 3.0	3.0 - 4.0	4.0 - 5.0
2.000 - 2.025	0.485E+13	0.382E+14	0.373E+15	0.424E+16	0.600E+17
2.025 - 2.050	0.342E+13	0.359E+14	0.455E+15	0.527E+16	0.848E+17
2.050 - 2.075	0.283E+13	0.326E+14	0.450E+15	0.596E+16	0.951E+17
2.075 - 2.100	0.227E+13	0.303E+14	0.484E+15	0.691E+16	0.103E+18
2.100 - 2.150	0.150E+13	0.277E+14	0.505E+15	0.721E+16	0.104E+18
2.150 - 2.200	0.107E+13	0.238E+14	0.492E+15	0.702E+16	0.104E+18
2.200 - 2.300	0.555E+12	0.179E+14	0.418E+15	0.616E+16	0.873E+17
2.300 - 2.400	0.274E+12	0.129E+14	0.330E+15	0.487E+16	0.674E+17
2.400 - 2.600	0.104E+12	0.766E+13	0.218E+15	0.308E+16	0.401E+17
2.600 - 2.800	0.261E+11	0.350E+13	0.102E+15	0.149E+16	0.191E+17
2.800 - 3.000	0.682E+10	0.167E+13	0.524E+14	0.688E+15	0.965E+16
3.000 - 3.400	0.126E+10	0.519E+12	0.179E+14	0.230E+15	0.305E+16
3.400 - 3.800	0.553E+08	0.989E+11	0.331E+13	0.449E+14	0.810E+15
3.800 - 4.200	0.000E+00	0.250E+11	0.743E+12	0.136E+14	0.370E+15
4.200 - 4.600	0.000E+00	0.473E+10	0.218E+12	0.429E+13	0.177E+15
4.600 - 5.000	0.000E+00	0.108E+10	0.583E+11	0.220E+13	0.113E+15

by the insertion of polyethylene layers of approximately 1 cm thickness [14]. Their paper also shows the change in neutron spectrum and the change in the predicted damage in silicon as a function of thickness. However the practicability of introducing a hydrogenous material only for reducing the effect of neutrons where it is not required for calorimetric purposes remains open to question.

5 Dose in the Inner Cavity

The dose from charged particles in the central cavity of the detector is derived directly from the charged particle fluence in Equation (3). This shows that the fluence is inversely proportional to the square of the radial off-axis distance. In the Task Group Report [1] the dE/dx of minimum ionizing particles in light materials, 1.8 MeV.cm^2/g, was used to compute the dose from the fluence. The variation with off-axis radius using this value is shown by the dotted line in Figure 10. In the opinion of the author, a more appropriate dE/dx which includes the effect of nuclear interactions would be about 2.5 times the above value. The consequent variation of dose with off-axis distance is given by the solid line in Figure 10. Neither estimation considers the effect of photons converting in the small amount of material assumed to be present. A FLUKA simulation in which a 3 mm thick aluminium shell excluding $|\eta| > 6$ surrounded the p-p interaction point at a radius of

1 metre is shown by the histogram in the same figure. This lies in-between the two simple estimations!

6 Albedo Neutrons

The Task Group Report [1] also summarized estimates of the number of neutrons leaving the front face of a calorimeter assembly as a function of incident hadron energy. No new data have been made available since that time which would lead one to change the relation recommended by the Task Group for estimating the number of albedo neutrons from a lead calorimeter:

$$\int I da = 4.3 \times (E_k/1\mathrm{GeV})^{0.50}, \tag{7}$$

where E_k is the incident hadron energy. This corresponds to the current for an incident hadron fluence of 1 cm^{-2}.

These estimates of the number of neutrons leaving the 'front' face of a calorimeter can be used to estimate the fluence of neutrons inside the inner cavity. For a spherical cavity, $|\eta| < 3$, and assuming isotropic emission of the neutrons from the front face, the average fluence of neutrons for a cavity radius of 2 metres will be 2×10^{13} cm^{-2} for the standard LHC operating conditions. Wilcox has shown that if there is no absorbing material in the inner cavity then the fluence at any point will be higher or lower than this average value by less than a factor of three [15]. If the inner layer were to be lined with 10 cm of polyethylene, then the low-energy neutron fluence in the central cavity would be reduced significantly [16]. Initial results from a recent experiment indicate a reduction factor of four which is consistent with the Monte-Carlo results of Gabriel and Lillie.

The introduction of a neutron absorber will have other effects besides modifying the low-energy part of the albedo spectrum. Due to path-length effects, albedo neutrons from points in the detector far away from the point of interest will be attenuated with respect to those originating nearby. The SSC Task Group Report only considered an 'average' fluence of albedo neutrons in the cavity derived from the total number of neutrons leaving the inner surface of the calorimeter. However the same data can be used to calculate the fluence of albedo neutrons close to the calorimeter surface as a function of rapidity where only that part of the calorimeter close to the point of interest contributes to the albedo fluence. (The area-integrated albedo fluence will be twice the actual number of neutrons, current, leaving the front surface). This is shown in Figure 11 for LHC conditions along with a horizontal line representing the 'average' value of the fluence in a cavity without an absorber. It will be seen that, as expected, the fluence at low rapidities is somewhat lower, but at the higher rapidities the fluence may be significantly higher in small localized regions.

The fluence of albedo neutrons will also depend to some extent on the shape of the calorimeter. Present estimations have been made using a spherical geometry where the

hadrons from the p–p collisions are incident normally on the calorimeter face. Most albedo neutrons will be emitted isotropically from the region of cascade maximum. Thus for a cylindrical geometry, and especially at high rapidities, the cascade maximum will be closer to the surface of calorimeter, so increasing the neutron escape probability. This effect needs to be quantified in future calculations.

7 Summary

An attempt has been made to summarize the main conclusions of the previous sections in Table 7. The first rows give the maximum values of neutron fluence and dose within the spherical lead shell. The inner radius of the shell is 2 metres and a luminosity of 10^{34} $cm^{-2}.s^{-1}$ was assumed for an operational time of 10^7 seconds per year. The inelastic p–p cross-section was taken to be 60 mbarns.

The other rows refer to the neutron dose in the inner cavity. If the point of interest is close to the inner surface of the calorimeter and it is shielded from other parts of the detector, the it will be affected only by neutrons from the region of the calorimeter close to this point. The albedo neutron fluences are then those of the "no cross-talk" model. If on the other hand neutrons from the different rapidity regions are allowed to diffuse throughout the inner detector region, then to within a factor of two the "average" value of neutron fluence is relevant. This value assumes that the calorimeter is open in the region $|\eta| > 3$.

Dose in the inner cavity depends only on the inverse square of the radial distance off-axis and not directly on the pseudo-rapidity. Values of the dose are given in the last row of Table 7.

8 Acknowledgements

The author gratefully acknowledges the value of the help given by many of his colleagues in this work: Don Groom of LBL Berkeley for the long-standing collaboration within the framework of the SSC Task Group, Tejinder Virdee of CERN and Imperial College London and Allan Clark of CERN and Geneva University for many discussions on the meaning of the results and finally my colleagues of the FLUKA collaboration, Alberto Fassò of CERN, Johannes Ranft and Hans-Jorg Mochring of Leipzig University, Alfredo Ferrari of INFN Milan and Pertti Aarnio of the Technical University of Helsinki, without whom it would not have been possible at all.

Table 7: Neutron fluence and Dose per Year

Quantity	η				
	0-1	1-2	2-3	3-4	4-5
Maximum					
n (cm^{-2})	5×10^{12}	5×10^{13}	4×10^{14}	7×10^{15}	1×10^{17}
γ dose (Gy)	200	2.4×10^{3}	5.4×10^{4}	2.9×10^{5}	4.3×10^{6}
h dose (Gy)	250	1.0×10^{3}	1.6×10^{4}	6.1×10^{4}	4.3×10^{5}
Total (Gy)	450	3.4×10^{3}	6.9×10^{4}	3.4×10^{5}	4.7×10^{6}
Albedo					
No cross-talk					
n (cm^{-2})	1×10^{12}	8×10^{12}	8×10^{13}	1×10^{15}	1.2×10^{16}
Albedo					
Average $\lvert\eta\rvert < 3$					
n (cm^{-2})	2×10^{13}	2×10^{13}	2×10^{13}	2×10^{13}	2×10^{13}
Inner cavity					
r off-axis	5 cm	10 cm	20 cm	50 cm	1 m
Dose (Gy)	1.6×10^{5}	4.0×10^{4}	1.0×10^{4}	1.6×10^{3}	400

References

[1] D. E. Groom (Ed.), *Report of the Task Group on Radiation Levels in the SSC Interaction Regions*, SSC Central Design Group Report SSC-SR-1033 (1988).

[2] D. E. Groom, Nucl. Instrum. and Methods A279 (1989) 1.

[3] J. Ranft and K. Hahn, *DTUJET-88, Sampling hadronic events according to the dual topological unitarization of hard and soft hadronic processes*, CERN Divisional Report TIS-RP/218 (1988).

[4] G. R. Stevenson, *Dose to SSC detectors due to p-p collisions*, Appendix 20 in [1].

[5] P. Aurenche, F. Bopp, K. Hahn, M. Maire and J. Ranft, *DTUJET-90, Sampling inelastic p-p and $\bar{p}$-p collisions according to the dual topological unitarization of hard and soft hadronic processes*, CERN Divisional Report *in preparation* (1990).

[6] P. A. Aarnio, A. Fasso, H. J. Mochring, J. Ranft and G. R. Stevenson, *FLUKA86 User's Guide*, CERN Divisional Report TIS-RP/168 (1986).

[7] A. Ferrari, A. Ijspeert, G. R. Stevenson and E. Weisse, *Design of the LHC beam dump*, CERN Divisional Report SL/90-58 and LHC Note 125, paper presented at the 2nd European Particle Accelerator Conference, Nice, June 12-16 (1990).

[8] W. R. Nelson, H. Hirayama and D. W. O. Rogers, *The EGS4 code system*, Stanford Linear Accelerator Center Report SLAC-265 (1985).

[9] D. E. Groom, H. Hirayama and W. R. Nelson, *Erratum to SSC-SR-1033; Radiation levels in the SSC interaction regions*, SSCL Report SSCL-285 (1990).

[10] D. E. Groom and G. R. Stevenson, *Backscatter and lateral diffusion of hadronic cascades in a model calorimeter*, Appendix 21 in [1].

[11] G. R. Stevenson, Liu Kuei-Lin and R. H. Thomas, *Determination of the transverse shielding for proton accelerators using the Moyer model*, Health Physics 43 (1982) 13.

[12] J. S. Russ, G. R. Stevenson, A. Fassò, M. C. Nielsen, C. Furetta, P. G. Rancoita and L. Vismara, *Low-energy neutron measurements in an iron calorimeter structure irradiated by 200 GeV/c hadrons*, CERN Divisional Report TIS-RP/89-02 (1989).

[13] G. R. Stevenson, *Radioactivation in LHC calorimeters*, Proceedings of this conference.

[14] K. Foruno, J. E. Brau and H. Hwang, *Neutron flux suppression with polyethylene moderators in silicon hadron calorimeters*, in ECFA Study Week on Instrumentation Technology for High-Luminosity Hadron Colliders, CERN Report CERN 89-10 (1989) p 325.

[15] T. P. Wilcox, *Neutron reflection in spherical calorimeters*, Appendix 12 in [1].

[16] T. A. Gabriel and R. A. Lillie, *Reduction of the neutron albedo in the vertex detector region of a generic SSC detector*, SSC Central Design Group Internal Note SSC-N-545 (1988).

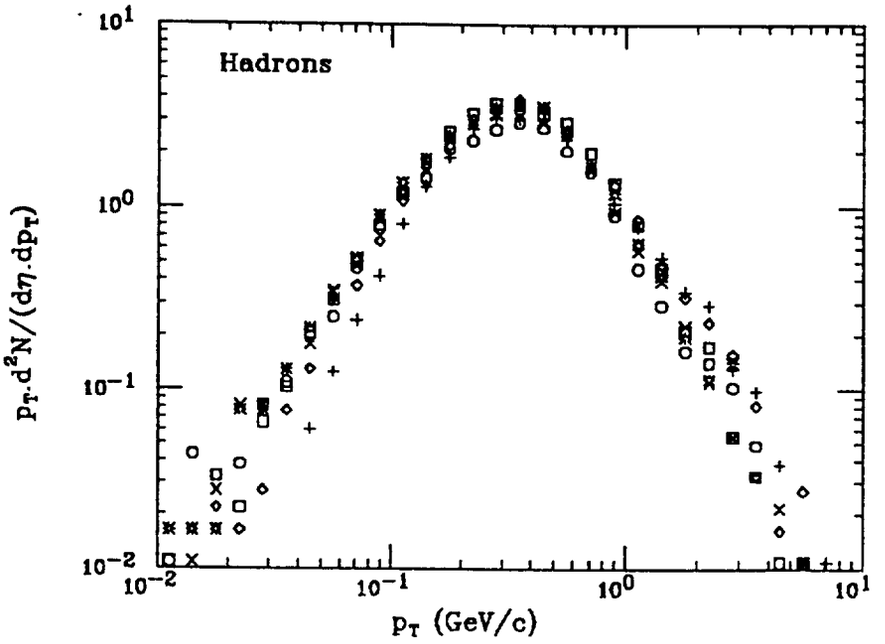


Figure 1: Transverse momentum spectrum of charged hadrons as calculated by DTUJET-90. The symbols correspond to the following pseudo-rapidity intervals. + 0.0–1.0; ◇ 1.0–2.0; □ 2.0–3.0; * 3.0–4.0; × 4.0–5.0; ○ 5.0–6.0.

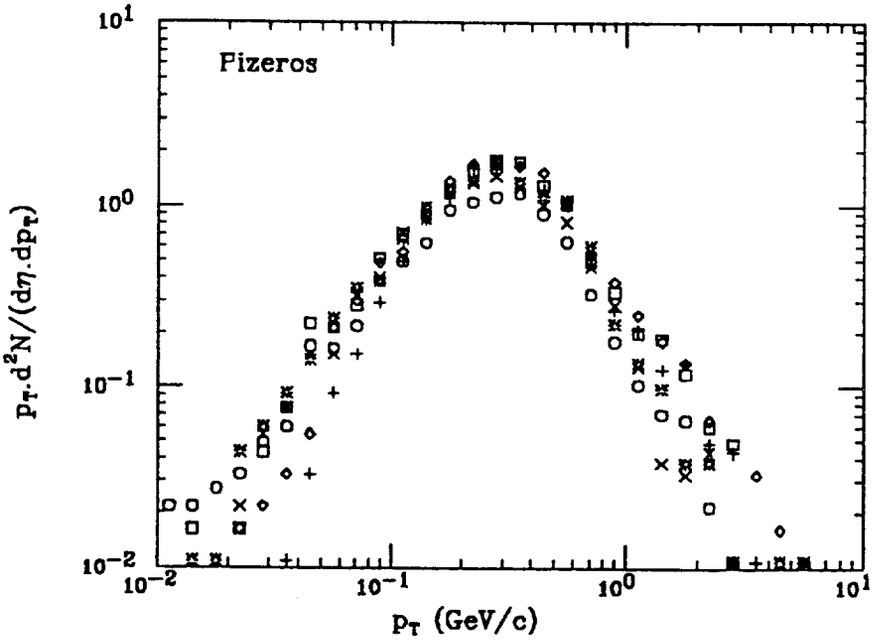


Figure 2: Transverse momentum spectrum of pi-zero mesons as calculated by DTUJET-90. The symbols correspond to the following pseudo-rapidity intervals. + 0.0–1.0; ◇ 1.0–2.0; □ 2.0–3.0; * 3.0–4.0; × 4.0–5.0; ○ 5.0–6.0.

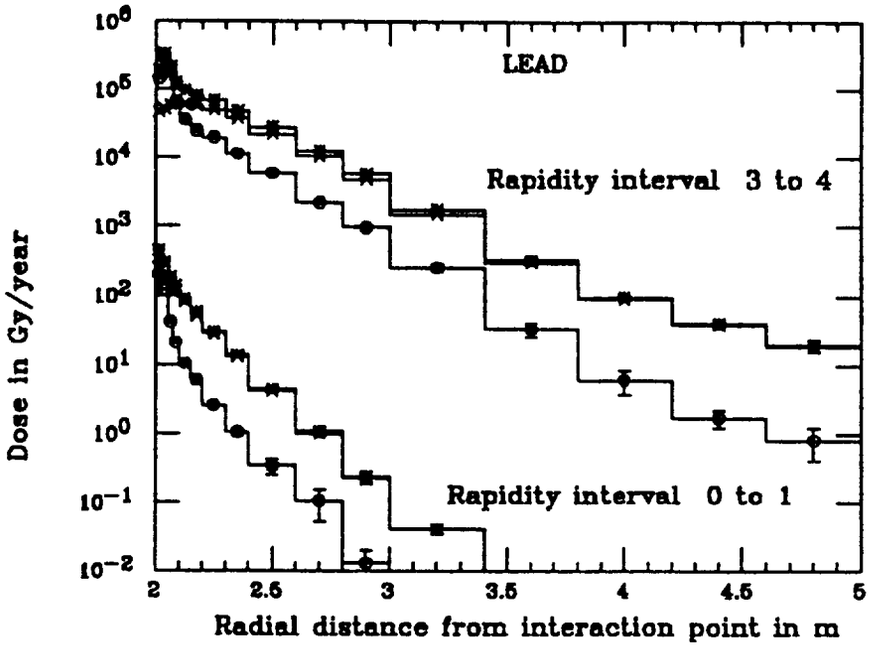


Figure 3: Variation of dose with depth in a spherical lead shell for two rapidity intervals. o e-m dose; × hadron dose; * total dose.

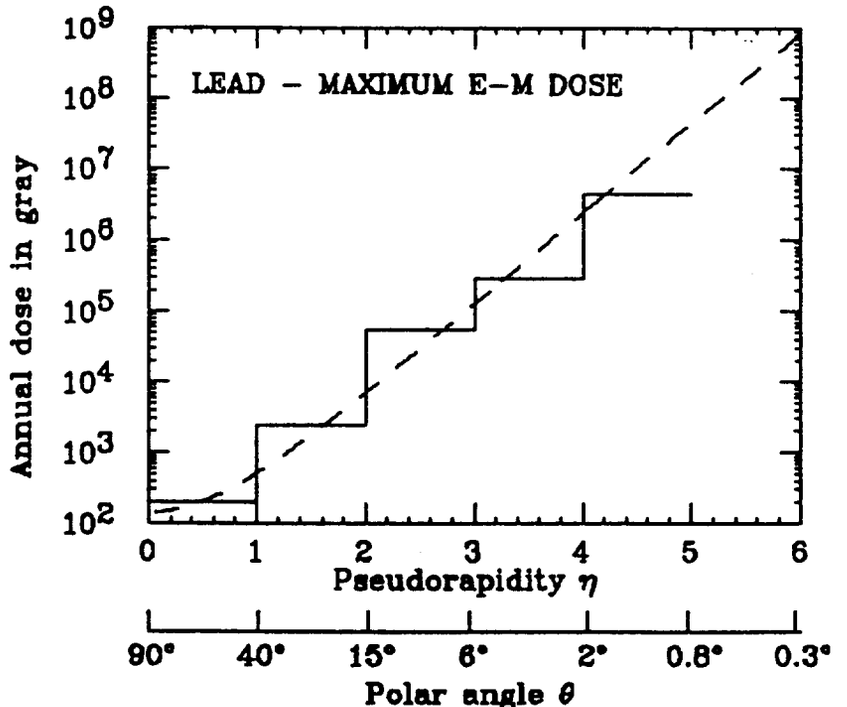


Figure 4: Variation of the maximum value of e-m dose in a 2 m lead shell with pseudo-rapidity. The solid histogram comes from the DTUJET90 plus FLUKA calculations; the dashed curve is derived from the SSC Task Group Report [1].

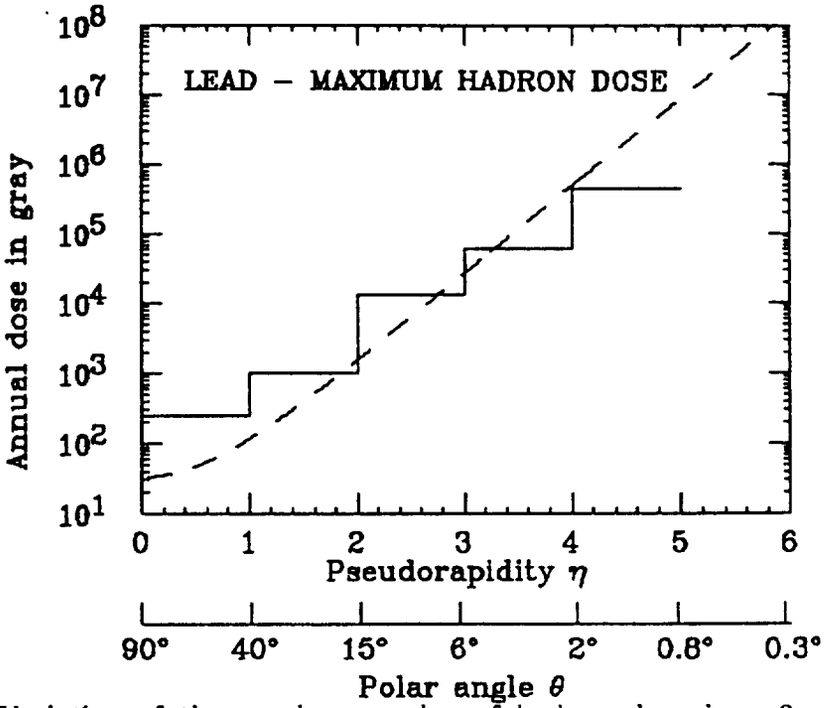


Figure 5: Variation of the maximum value of hadron dose in a 2 m lead shell with pseudo-rapidity. The solid histogram comes from the DTUJET90 plus FLUKA calculations; the dashed curve is derived from the SSC Task Group Report [1].

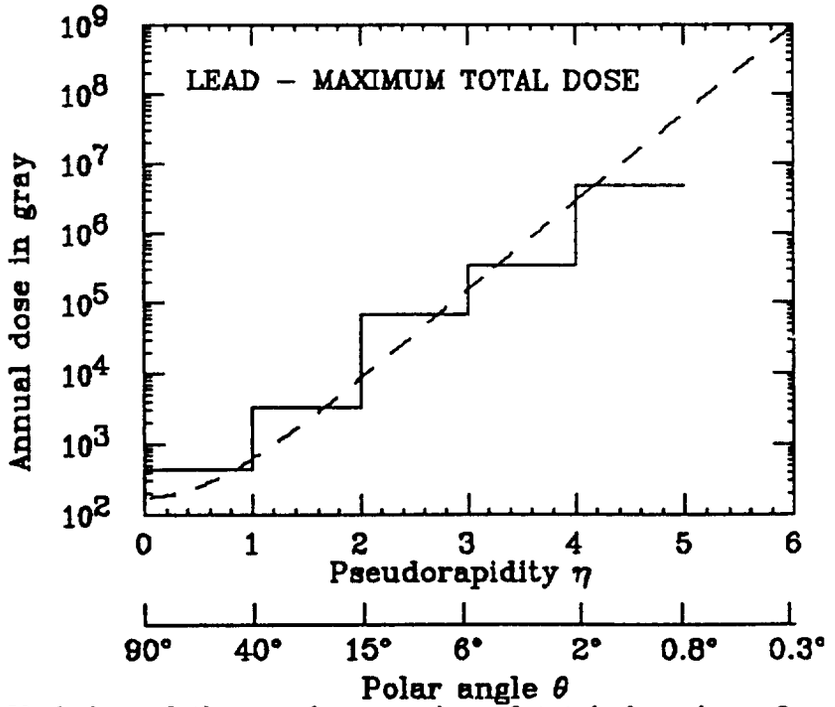


Figure 6: Variation of the maximum value of total dose in a 2 m lead shell with pseudo-rapidity. The solid histogram comes from the DTUJET90 plus FLUKA calculations; the dashed curve is derived from the SSC Task Group Report [1].

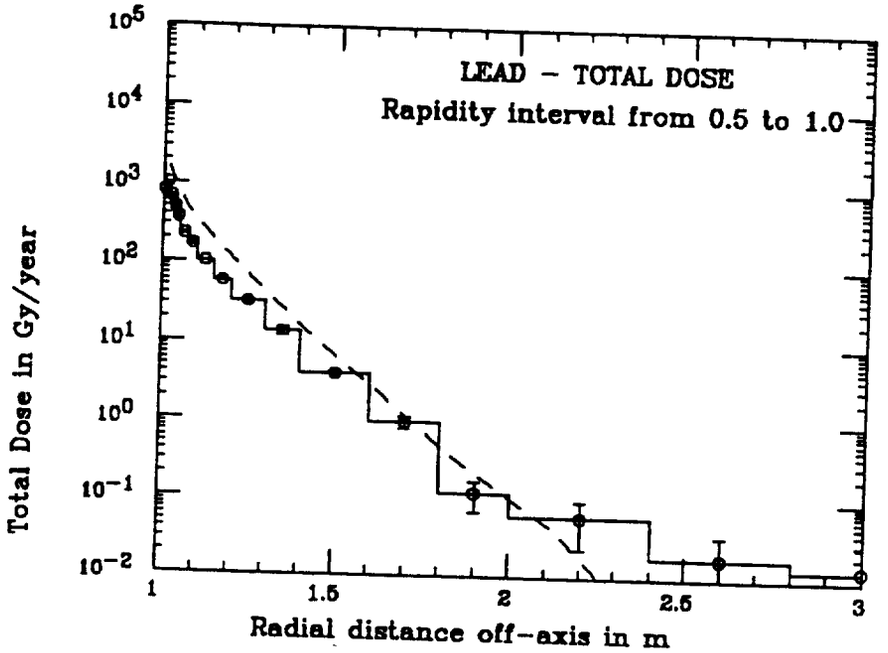


Figure 7: Variation of the total dose in a lead cylinder of inner radius 1 metre with radius off-axis. The solid histogram comes from the DTUJET90 plus FLUKA calculations in cylindrical geometry; the dashed curve is interpolated from the sphere calculations.

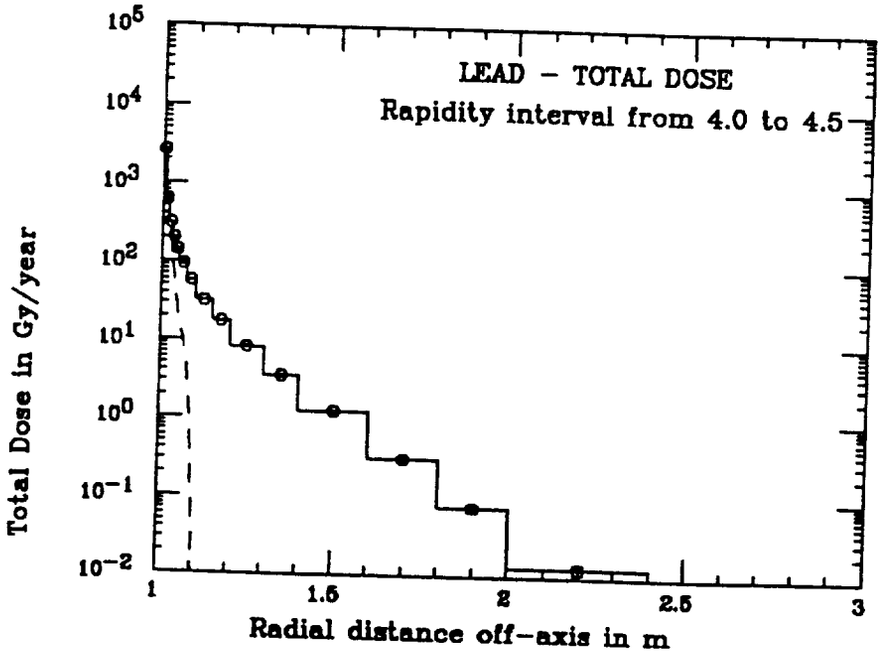


Figure 8: Variation of the total dose in a lead cylinder of inner radius 1 metre with radius off-axis. The solid histogram comes from the DTUJET90 plus FLUKA calculations in cylindrical geometry; the dashed curve is interpolated from the sphere calculations.

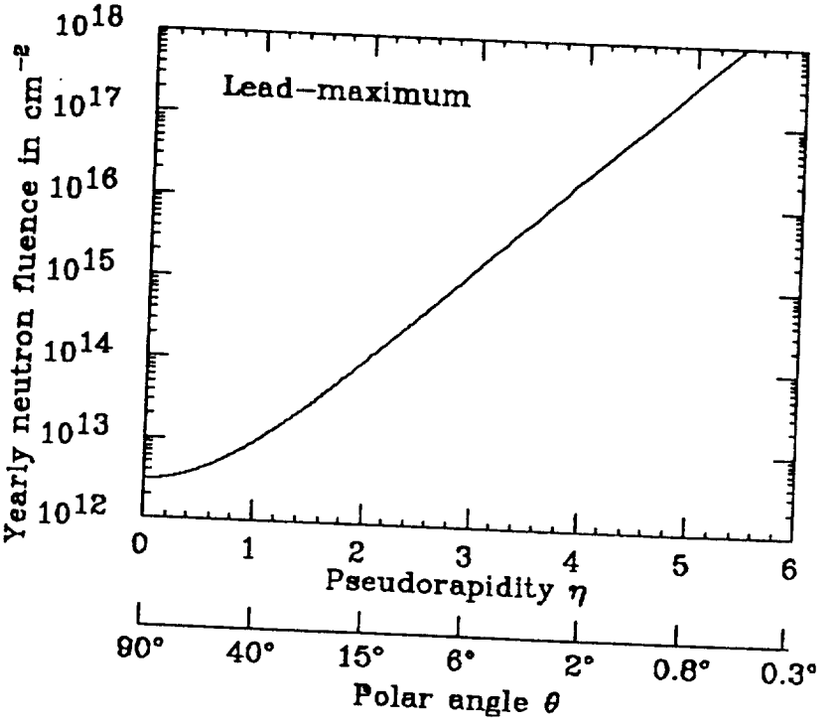


Figure 9: Maximum annual neutron fluences in a spherical lead shell. The sphere has an inner radius of 2 metres. Luminosity etc. are for the reference LHC working conditions (see text).

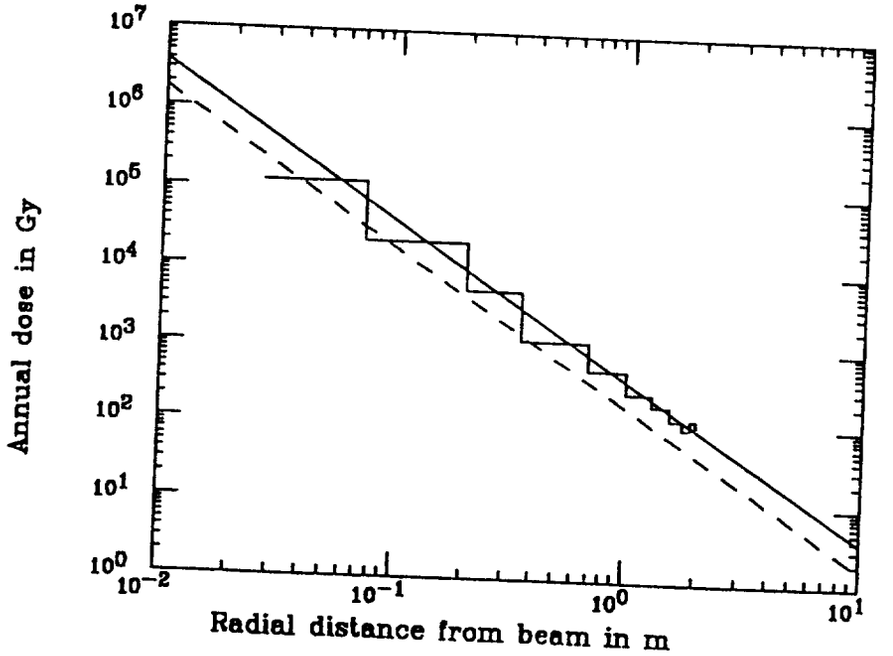


Figure 10: Dose as a function of radial off-axis distance for the inner cavity. The dashed line taken from [1] uses a dE/dx of 1.8 MeV.cm^2/g; the solid line uses a dE/dx of 2.5 times this value. The histogram is from a FLUKA simulation.

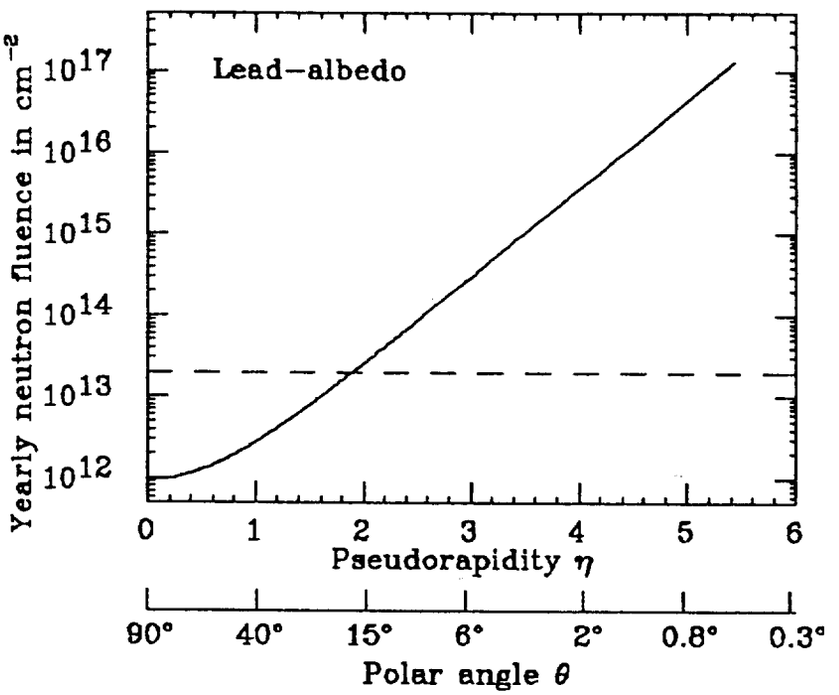


Figure 11: Annual albedo neutron fluences in a spherical lead shell. The sphere has an inner radius of 2 metres. Luminosity etc are for the reference LHC working conditions (see text).

THE RADIATION HARDNESS TEST FACILITY AT RAL

M Edwards, D R Perry
Rutherford Appleton Laboratory,
Chilton, Didcot, Oxon, OX11 0QX, England.

Abstract

The neutron radiation hardness test facility using the spallation neutron source ISIS at RAL is described. The ability to irradiate test structures with neutrons of about 1 MeV energy will be necessary in designing detectors for future high luminosity hadron colliders. This report details the measurements of the neutron energy spectrum and flux available, the requirements placed on devices to be irradiated, and indicates possible ways the facility could be improved in the future should this become necessary.

1 Introduction

Many of the experiments currently being designed for future high luminosity hadron colliders (LHC/SSC) require good quality tracking close to the interaction, where the track density is high. At present the detectors with the best resolution, both in position and double track, are silicon microstrip or pixel devices. However the radiation levels in the cavities of the calorimeters of the experiments will be high, up to several kGy/year. This radiation will originate from two sources; high energy photons and charged particles from the proton-proton interaction, and low energy albedo neutrons from the cascades and showers in the calorimeters.

The annual flux of charged particles has been estimated to be $3 \times 10^{15}/R^2$ per cm^2 for the SSC operating at a luminosity of 10^{33} for 10^7 secs per year. R is the radial distance from the beam lines (in cm). The flux of low energy albedo neutrons will be uniform inside the cavity of the calorimeter, but will depend on the inner radius and composition of the calorimeter. The annual flux from an uranium-scintillator calorimeter of 2m inner radius at the SSC is estimated to be $2.4 \times 10^{12}/cm^2$.[1]

The energy spectrum of these neutrons is expected to be a typical evaporation spectrum, peaking at 1 MeV and falling by a factor 4 or 5 at 0.1 and 10 MeV. This is very similar to the energy spectrum measured by Broome et al[2] in an experiment to study the neutrons emitted from a copper target bombarded with 72 MeV protons. Their work was part of the design study for the collector for ISIS, the 800 MeV proton synchrotron for the spallation neutron source at RAL. The collector is designed to stop the protons from the injector which are not trapped by the RF during the acceleration phase of the ISIS cycle.

The collector in ISIS is a graphite block backed with copper mounted in a rectangular cross section length of beam pipe between the injection and the extraction lines of the synchrotron ring. It is, of course, the most active part of the ring, but access is permitted for short times. The space above the collector is open, with relatively easy access during maching off periods, and available for mounting light objects.

2 The Facility

To take advantage of the copious supply of neutrons produced by the collector of ISIS a lightweight frame was designed and built which could easily be placed on the collector box. This frame is shown in fig. 1. The three shelves hold the samples to be irradiated and are adjustable in height, up to 1m, and width, up to 30 cm. At present the only limitation imposed on samples to be irradiated is that they must be light enough for one man to hold the complete frame out at arms length to place on the collector box. This limitation ensures that mounting the frame does not disturb the alignment of the collector box. The frame can be placed on or removed from the collector box in a few seconds, during which time the dose received by the operator is less than 20μsieverts.

There are power sockets available in the synchrotron hall, hence it is possible, with some limitations, to apply bias voltages to samples being irradiated. To date this has not been done.

3 Method of Energy Spectrum and Flux Measurements

The energy spectra and absolute fluxes are measured by the activation method. Foil materials were chosen after close examination of the nuclide chart and reference data on neutron cross sections. The selection criteria were as follows:

a) The target foil must present no unacceptable handling difficulties.

b) The product nuclide must have a half life greater than 2 hours, so as to reduce errors from corrections for non-uniform flux over a 1 hour irradiation.

c) The decays of the product must produce gammas of energy greater than 100 keV, the lower limit of the accurate calibration range of the counting system used.

d) Little or no confusion with neutron reactions on other isotopes present in the foil.

e) The neutron cross section must be known up to at least 40 MeV incident neutron energy.

f) To obtain energy thresholds spanning as wide a range as possible.

The five metals chosen: aluminium, nickel, cobalt, indium and gold have 13 potentially useful reactions. These are listed, along with their approximate energy thresholds, in table I.

In order to have an independent indication of the very low energy neutron content in the measured flux, 5mm thick containers of boron loaded epoxy have been made. The material of the containers is 55% by weight boron carbide, which, it is estimated, will attenuate thermal neutrons by a factor 10^5. Cobalt foils were placed in these containers and irradiated along with the uncovered foils.

The gamma activity of the foils was measured using a $Ge(Li)$ detector and multichannel analyser located in a low background room, a system in regular use by the Health and Safety Group at RAL. The spectra collected were transferred to the central computer and analysed using the program SAMPO[3]. This finds peaks with greater than a predefined significance, and fits each to a gaussian with exponential tails. The width of the gaussian and exponent of the tails are parameters tuned to the characteristics of the detector. This is done by running SAMPO on a gamma spectrum with good clean peaks using the SHAPEDO option.

The efficiency and energy calibration of the system uses standard sources from Amersham International. The energy calibration of the system is good to $\pm$ 0.3 keV over the energy range of 100 keV to 3.0 MeV. The accuracy of the efficiency calibration is limited by the quoted activity of the sources, typically $\pm$5%.

After exposure to neutrons a foil will emit gammas of energy E_γ at a rate dn/dt given by:

$$dn/dt = [\frac{P.N_A.W.No}{A_T}][(1 - e^{-ti/tm})][e^{-tl/tm}][\frac{tm}{tc}(1 - e^{-tc/tm})][\int_0^\infty \Phi(E)\sigma(E)dE]$$

Where;

P = Probability that the decay of the nucleus will produce a gamma of energy E_γ.
N_A = Abundance of the target isotope in the foil.
W = Weight of the foil (g).
N_0 = Avogadro's number = 6.023×10^{23}.
A_T = Atomic weight of the foil.
tm = Mean life of the product isotope (s) (1.442 × Half Life).
ti = Irradiation time of the foil (s).
tl = Cooling time, i.e. the time between the end of the irradiation and the start of the counting (s).
tc = Count time (s).
$\Phi(E)$ = Differential neutron flux as a function of energy ($n/cm^2/s/MeV$) (assumed constant during the irradiation).
$\sigma(E)$ = Reaction cross section as a function of energy (mbarn).

Hence from the rate of gamma emission it is possible to determine the integral $I = \int_0^\infty \Phi(E)\sigma(E)dE$ for each reaction.

The program LOUHI[4] uses these integrals and the energy dependent cross sections for each reaction to unfold the neutron spectrum and calculate the total neutron flux by an iterative procedure as follows:

1) From an assumed spectrum the program calculates the integral I for each reaction.

2) This is compared to the measured value of the integral I, and the assumed spectrum shape modified.

3) The integral I is recalculated using the modified spectrum, and compared again.

The loop is repeated either 101 times or until the values calculated for the integral I are changing by less than a predetermined amount. Input parameters needed by the program are:

1) The spectrum to be used in the first iteration.

2) The weight to be placed on this spectrum at each iteration.

3) The energy range over which the spectrum will be calculated.

The relevant output of LOUHI consists of:

1) The neutron spectrum in $n/cm^2/s/MeV$ or per logarithmic energy bin (FL/BN/LG in tables 3 and figure 3) in 40 energy steps covering the requested range.

2) The total neutron flux.

3) The fraction of neutrons with energy greater than that of the energy step (percent fluence).

4) The total absorbed dose in tissue or water.

5) The fraction of the total absorbed dose in tissue or water from neutrons with energy greater than that of the energy step.

6) The measured and calculated values of the integral I, and their ratio.

This last gives an indication of the quality of the fit.

The energy dependent cross section for the 12 reactions used, shown in fig. 2, were taken from either [5] or [6].

4 Results of the Energy Spectrum and Flux Measurements

Three sets of foils were exposed to the neutron flux at three heights above the ISIS collector for 1 hour during a machine physics period. The gamma spectra were measured for varying count times over the following three weeks. The sequence and durations of the gamma counting of the foils were determined by the half lives and activities of the nuclides sought. Values of the integral I, in units of $n/cm^2/s/MeV/mbarn$, obtained are given in tables IIA for the foils exposed 8 cm above the base of the frame, IIB for foils at 38 cm, and IIC for foils at 68 cm.

A cobalt foil encased in boron carbide was not used at 8 cm, since only two containers were available. It had been done during an earlier measurement, the results of which are consistent with the results reported here.

The above data was used as input to the program LOUHI with input parameters as follows:

1) The initial spectrum was a $1/E$ spectrum.
2) Minimal weighting to this spectrum.
3) An energy range of 10^{-8} to 1400 MeV.

The resulting energy spectra are shown in fig. 3, and the output from LOUHI in tables IIIA for 8cm height, IIIB for 38cm height, and IIIC for 68cm height.

It is convenient to split the total flux into two components; low energy "background" neutrons, and "1 MeV" neutrons coming directly from the collector. A reasonable energy to make this division is 10 keV, since the spectrum generated by LOUHI contains very few neutrons with energies between 100 eV and 100 keV. The fluxes given by LOUHI are listed in table IV, with the division at 10 keV.

These spectra give good agreement between the calculated and measured values of the integrals I, generally within 10%. The parameters of LOUHI were varied to determine the sensitivity of the calculated spectra to them. It was found that the goodness of fit was not sensitive to the energy range imposed, LOUHI placing all the low energy neutrons in the lowest bins available to it. The calculated fluxes above and below 10 keV remained the same within errors. If a large weighting to a $1/E$ spectrum was demanded, LOUHI produced a $1/E$ spectrum with an excess of neutrons around 1 MeV, however the fit was very poor. The value of the integral I for the indium foil was artificially reduced by a factor two to see the effect of this on the spectrum calculated. As expected the peak value of the spectrum was increased, with fewer neutrons between 10 keV and 1 MeV. This illustrates the importance of the indium measurement in determining the spectrum. The measurement of the integral I for indium is probably the most reliable of the 12 used. It was measured twice, with consistent results, and the gamma line measured was strong and not confused by any other gamma line.

The existence of the low energy neutron "background" in these spectra is qualitatively supported by the marked reduction in the Co^{60} activity of the foils encased in boron carbide. The $Co^{58}, Co^{57}, Fe^{59}$, and Mn^{56} activities of these foils was very similar to that of the foils not encased in boron carbide. Further support is given by the similarity of the Co^{60} and Au^{198} activities of the foils exposed at different heights above the collector.

Alanine and RPL[7],[8] dosimeters have been exposed at various heights on the stand to estimate the gamma contamination of the neutron flux. The measured doses as a function of height are shown in figure 5 for alanine and figure 6 for

RPL. These results are preliminary and will be checked by further irradiations. The alanine and RPL dosimeters have previously[7],[8] been calibrated using a Co^{60} source. The relative sensitivity of alanine to neutrons of approximately 1-5 MeV energy and gammas is 0.5[9]. Using the total absorbed dose, as given by LOUHI, for neutrons of energy greater than 10 keV, the response of the alanine dosimeter to neutrons is calculated to be $2.25 \times 10^2/H^2 \quad Gy/\mu Ah$. This is consistent with the dose measured by the alanine, $2.47 \times 10^2/H^2 \quad Gy/\mu Ah$, indicating little or no gamma contamination. The results of the RPL measurement are not understood at present.

Copper and iron foils have been irradiated for 15 days on the base of the stand. The gamma spectra of these foils showed small amounts of Zn^{65} in the copper foil and Co^{56} in the iron foil. These nuclides can only come from p, n reactions. Using the cross section for these reactions given by Barbier[10], comparison with the measured activities from the reactions $Co^{59}(n,p)Fe^{59}$ and $Ni^{58}(n,p)Co^{58}$, and assuming the energy spectrum of the protons is similar to the energy spectrum of neutrons, the proton contamination of the neutron flux is calculated to be of the order of 0.1%.

5 Irradiation of Samples

Samples to be irradiated are mounted, along with cobalt foils, on pieces of fibreglass board on the shelves of the stand. The height of the shelf is adjusted according to the dose required. The approximate times of the start and end of the irradiation are recorded to determine the irradiation time and the cooling time. The activity of the cobalt foil is measured to obtain the average flux to which the samples have been exposed. Cobalt was chosen as the monitor foil since it has four useful reactions, all with long half life products, with energy thresholds covering the complete range of interest. Thus not only is the integrated flux measured, but also any unexpected large changes in the energy spectrum.

To date samples have been irradiated for periods from 1 hour to 32 days, to fluxes varying from 5×10^8 down to $1.7 \times 10^7 n/cm^2/s$. These fluxes have been calculated using data from all three spectrum measurements with consistent results.

Figure 4 shows the variation of the flux of neutrons above 10 keV energy as a function of height. The data points are from the results of five exposure runs.

6 Limitations of the Facility and Future Plans

In order not to interfere with the normal activity of the ISIS facility, access to the synchrotron hall is restricted to times when the accelerator is off for other reasons (routine maintenance or breakdown). Under these conditions it is not possible to stop the irradiation after exposure to a predetermined flux. However, by placing several samples at different heights on the stand and taking advantage of unscheduled stops of the accelerator, it is possible to get reasonably close to any required integrated flux. If, in the future, this proves to be a serious limitation, then procedures for remote removal of the samples will be implemented.

The weight limitation imposed on the samples is not seen as a disadvantage, since solid state detectors, or electronics, are naturally lightweight.

During the next long shut-down of ISIS, January and February, 1991, it is planned to install a system to apply bias voltages to and monitor the leakage currents of the samples while being irradiated.

Conclusions

This neutron irradiation facility has already proved to be useful in the determination of the radiation hardness of silicon and gallium arsenide test structures. It shows promise as being a valuable source of neutrons for testing detectors and electronics for use with the next generation of particle physics experiments.

Acknowledgements

We would like to thank Mr D A Gray, Mr B Boardman and Dr T A Broome for their invaluable advice and help in starting this project. We are also indebted to the operating crew of ISIS for their willing cooperation and assistance when mounting and removing the samples, and to Rai-Ko Sun of Lawrence Berkeley Laboratory, California, for providing a copy of the LOUHI program, and advice on running it.

References

[1] Radiation Levels in the SSC Interaction Regions, SSC Central Design Group; D E Groom (Editor), SSC-SR-1033 (1988).

[2] Particle Distributions Around a Copper Beam Stop for 72 MeV Protons, T A Broome et al, Health Physics Vol 44 p 487 (1983).

[3] SAMPO, A Fortran IV Program for Computer Analysis of Gamma Spectra from $Ge(Li)$ Detectors, and for other Spectra with Peaks, Jourma T Routti, UCRL-19452 (1969).

[4] Unfolding Neutron Spectra: LOUHI for Pedestrians, A Rindi, LBL- 6413 (1977).

[5] Extrapolated Neutron Activation Cross Sections for Dosimetry to 44 MeV, L R Greenwood, ANL/FPP/TM-115 (1978).

[6] Technical Report Series Vol 273 (1978), International Atomic Energy Association.

[7] Comparison of High-dose Dosimetry Systems in Accelerator Radiation Environments, M. Coche et al, CERN TIS Commission Report TIS- RP/205 (1988).

[8] Alanine Dosimetry as Reference Dosimetric System in Accelerator Radiation Environment, F Coninckx et al, CERN TIS-CFM/216/CF (1989).

[9] Fast Neutron Irradiation Effects-III. Sensitivity of Alanine Systems for Fast Neutron having an Energy of 1 MeV, Y. Katsumura et al, Radiat. Phys. Chem. Vol 28 pp 337-341 (1986).

[10] Induced Radioactivity, Marcel Barbier, pp 189-190, North Holland Publishing (1969) ISBN: 0720401453.

Figure Captions

Figure 1 The frame used for supporting the samples during neutron irradiation.

Figure 2 The energy dependant cross sections used as input to LOUHI.

Figure 3 The neutron energy spectra as calculated by LOUHI.

Figure 4 The flux of neutrons with energy greater than 10 keV per microamp hour of ISIS beam as a function of height.

Figure 5 The response of the alanine dosimeters as a function of height.

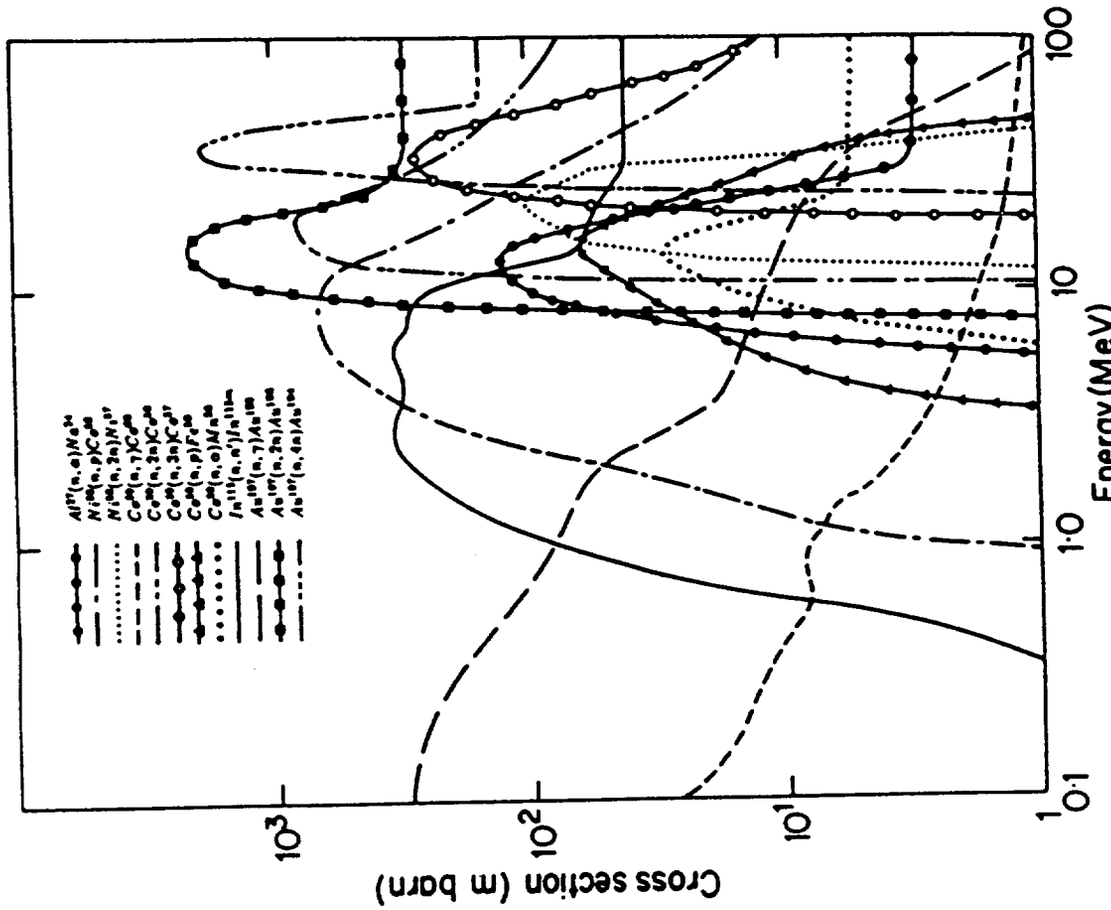


Figure 2

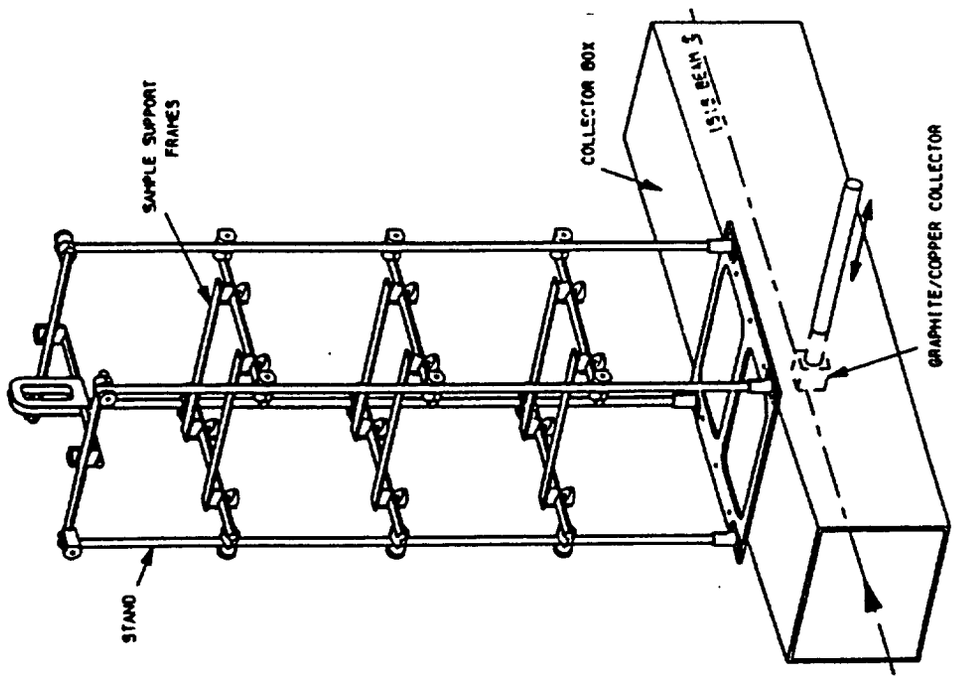


Figure 1.

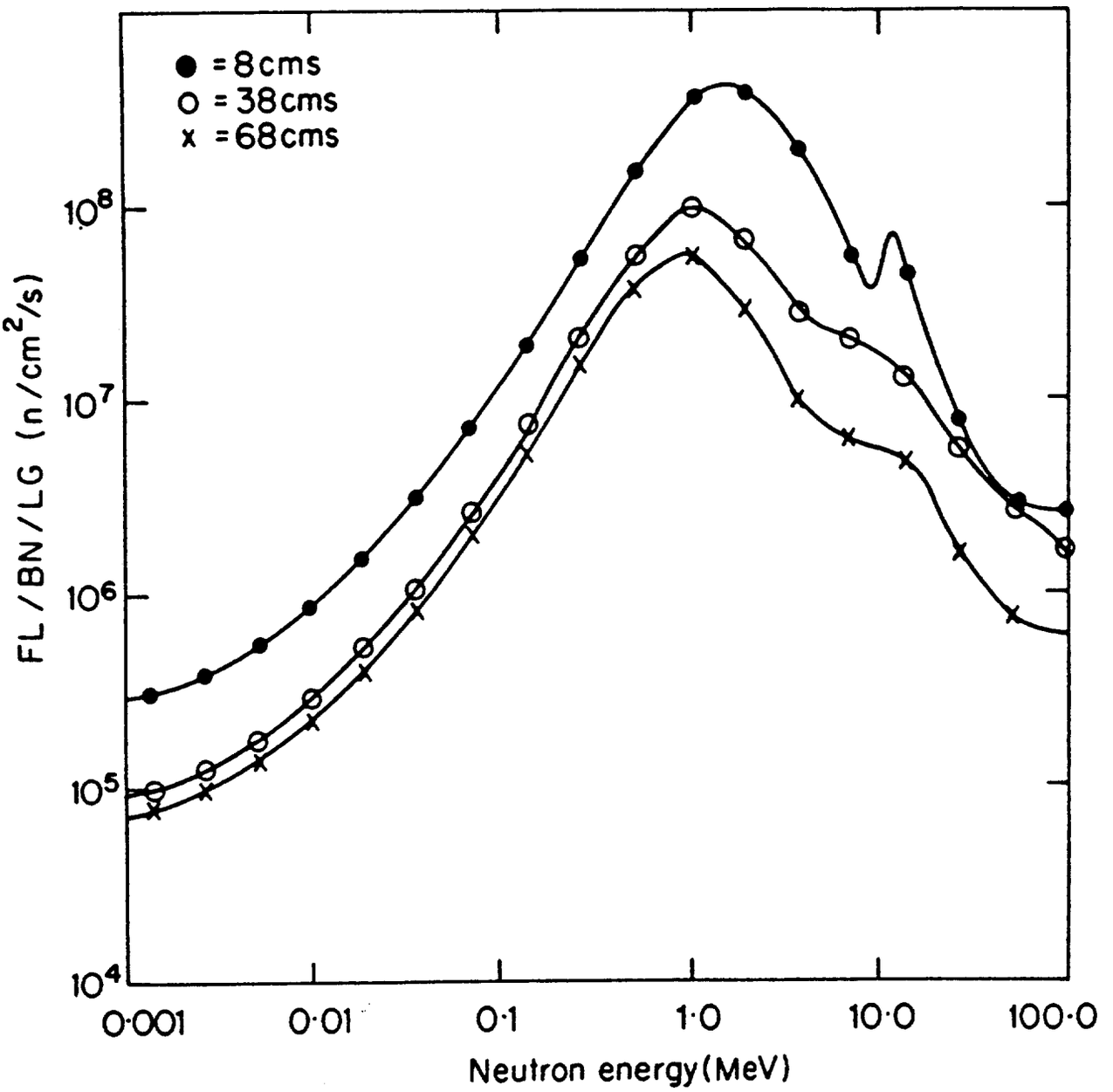

● = 8cms
O = 38cms
x = 68cms
FL/BN/LG (n/cm²/s)
10⁸
10⁷
10⁶
10⁵
10⁴
0·001
0·01
0·1
1·0
10·0
100·0
Neutron energy(MeV)

Figure 3

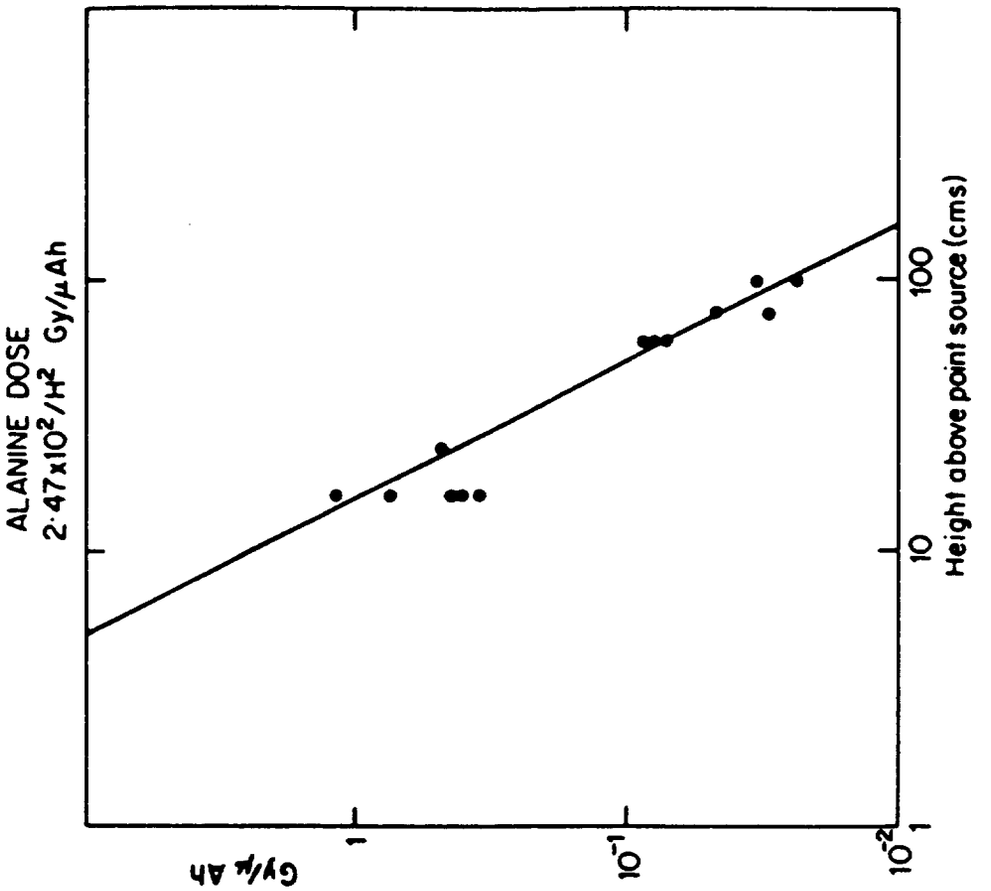


Figure 5

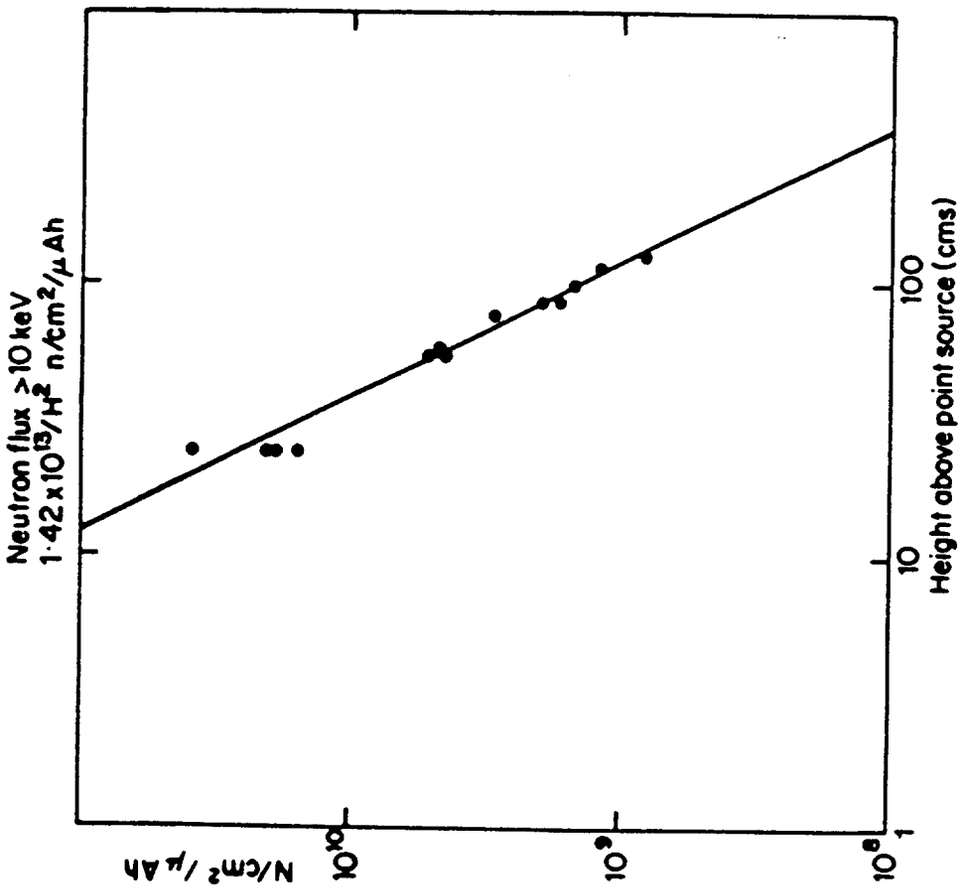


Figure 4

A NEUTRON SOURCE FOR IRRADIATION PURPOSES

B. Merkel
LAL , Orsay (France)

One of the questions for the design of any experimental set-up to be used at very high luminosity Proton-Proton colliders is the stability under severe irradiation levels. The major performance of the detector such as shower energy resolution and absolute calibration, time response, trigger efficiency, have to be fully understood and controlled, so an estimate of the radiation damage effects must be reliable. Electromagnetic showers as well as hadronic cascade showers will produce a copious flux of neutrons. Experimental data obtained with various target materials show that the number of neutrons outside the stopping target is uniformly distributed and that the energy distribution is peaked in the 1 Mev to 2 Mev range [Ref. 1]. One important concern is a good knowledge of the damage induced by the expected neutron fluences. This is particularly true for electronic devices presently available; moreover it is well established that irradiation levels per year are higher than the stability limit for some of the very useful electronic components entering in the amplifier design. It is thus necessary to enter a phase of developments and control of the stability of the new products under irradiation conditions as close as possible to the expectations of rates and radiation types at high luminosity Proton-Proton colliders. In table 1 are presented expectations of dose levels (in Gy) and neutron fluences (in n/cm^2) per year (10^7sec) at luminosity $\mathcal{L} = 10^{34}\ cm^2/s$ at 2.5 cm inside the front face of a lead calorimeter [Ref. 2], extrapolated to a cylindrical detector described in Ref. 3.

Rapidity	Dose (Gy)	Neutron fluence (cm^{-2})
0 to 1	$9.16\ 10^2$	$9.70\ 10^{12}$
1 to 2	$1.36\ 10^3$	$1.53\ 10^{13}$
2 to 3	$1.28\ 10^4$	$9.80\ 10^{13}$
3 to 4	$5.60\ 10^4$	$1.14\ 10^{15}$

Table 1 : expected dose rate and neutron fluence per year
at luminosity $\mathcal{L} = 10^{34}\ cm^2/s$

We tried to find a neutron source giving a satisfactory emulation of the neutron fluence expected at high luminosity Proton-Proton colliders.

The Accelerator

The Orsay Linear Accelerator is currently used as injector for two Synchrotron Radiation facilities, and positrons are stored in the circulating beam. Positron production is done as follows: electrons from the primary source are accelerated up to an energy of 1 Gev, the nominal peak intensity of the beam is 1 ampere with pulse width of 20 ns, 50 Hz repetition rate; this beam hits a thin tungsten target where positrons are produced; after magnetic collimation the positrons are accelerated again to the Synchrotron Radiation facilities. The positron to electron ratio is of the order of 1% to 2%. A diagram of the positron source is shown in Figure 1.

The photon production rate is also very high. Measurements of doses were made with RPL dosemeters at locations in the vicinity of the tungsten target. Results are presented in Figure 1: the radiation levels obtained are rather high, they are representative of the positron gun environment.

Neutron production also occurs, but the rate relative to the primary electron intensity is much smaller than the positron to electron ratio reported above. The integrated flux amounts to 4 10^9 neutrons cm^{-2} s^{-1} for a given position of the neutron detector. Such a neutron intensity is quite satisfactory to be used as the irradiation source.

Such a mixture of high neutron fluence and high dose rate is also better matched to the real conditions of the Proton-Proton Collider environment, although the relative amounts are not quite identical.

Neutron intensity and energy spectra

Measurement of the neutron intensity is made by activation, the energy distribution being unfolded from several measured response on discrete activation detectors. Known cross sections for the production of nuclides are dependent on the neutron energy, this dependence being specific to each nuclide with a particular threshold E_{min}. This feature has been widely used for the determination of the energy distribution of a neutron source. With a Monte-Carlo simulation it is possible to predict the production rate of a daughter nucleus for each activation detector; it is given by the neutron energy distribution $\phi(E_n)$ weighted by the energy dependent cross-section $\sigma_i(E_n)$,

$$A_i = \int_{E_{min}}^{E_{max}} \sigma_i(E_n)\Phi(E_n)dE_n$$

The decay losses are also taken into account, during the irradiation time and before the measurement of the nuclide radioactivity. Putting into the Monte-Carlo simulation the world average determination of the nuclide lifetime, then getting agreement between the Monte-Carlo prediction and the observed decay losses is a good consistency check of the selection of the activated nuclide. The activation detectors used are listed below

1. $^{27}Al \rightarrow {}^{27}Mg$ decay products (γ rays) are counted with an NaI crystal

2. $^{115}In \rightarrow {}^{115m}In$ decay products (γ rays) are counted with an NaI crystal
   $^{115}In \rightarrow {}^{116}In$ is also present and mostly activated by thermal neutrons (total cross section 155 barns). The decay lifetime of ^{116}In is small : 9.5 minutes and it is necessary to wait a few hours before being able to see the other nuclide

3. $^{32}S \rightarrow {}^{32}P$ which is a pure β emitter

4. $^{197}Au \rightarrow {}^{198}Au$ thermal neutrons activation

Given the time dependent counting rate measured on each activation detector the neutron energy distribution can be unfolded. The spectral energy distribution known by experts as the evaporation spectrum gives a very good representation of the rates observed. The energy dependence is described by

$$\Phi(E_n) = E_n \exp(\frac{-E_n}{a}) F$$

where the parameter a is adjusted to describe the relative rates of the nuclides ^{115m}In and ^{27}Mg, and F is a normalisation factor

The activation detectors were exposed for one hour to the neutron flux at nominal intensity. The detectors were installed behind lead 6 cm thick, about 10 radiation lengths, for the full containment of 1 Gev electromagnetic showers. The distance from the primary tungsten target was 2.6 metres, as shown in Figure 1.

Unfolding the spectral energy distribution was then performed as explained above. The best description of the experimental results was obtained with a value a = 2 Mev and a value $F = 5\ 10^8$ neutrons $cm^{-2}\ s^{-1}$. The integrated flux amounts to $4\ 10^9$ neutrons $cm^{-2}\ s^{-1}$. The corresponding spectral distribution is shown in Figure 2. From the

activation of ^{197}Au the flux of thermal neutrons was estimated to be 10^8 neutrons $cm^{-2}\ s^{-1}$.

After one hour's exposure the accumulated flux amounts to 1.510^{13} neutrons $cm^{-2}\ s^{-1}$ and the accumulated dose amounts to 5 Gy; the beam is available four times one hour per day for injection in the two Synchrotron Radiation facilities. Comparing this result with flux estimates shown in table 1, it appears that the irradiation source can be used for a study of irradiation by neutrons, although the dose rate is small.

Installation

We concluded from the neutron flux measurement that it is worth going on, and easy access to the positron source area should be provided for samples under irradiation study. The source is inside a concrete shielding 2 metres thick. Space availability around the target is possible on one side only, the distance between the concrete wall and the accelerator tube is 1.5 metres, leaving 1 metre available, the height is 2 metres and the floor space upstream is 4 metres, nevertheless the neutron flux is far from uniform over this volume. Access from the target area to the laboratory across the concrete shielding has been set up, and it is possible to move in and move out a small printed circuit board (few cm^2) instrumented and powered during irradiation. A test pulse would allow a satisfactory follow-up of the amplifiers under study. A safe area is available, the cable length between target area and safe area being about 15 metres.

Is there any possibility of following the evolution of an amplifier under irradiation at liquid nitrogen or liquid argon temperatures ? Ion mobility has a very strong temperature dependence, and if the aim is to prepare a liquid argon calorimeter it will be very important to know the resistance to irradiation at low temperature. To answer this demand we are presently studying such a possibility: the neutron flux would be partially attenuated by a factor which can be extracted from Monte-Carlo, and which has to be measured. It would be an improvement of the neutron source presented here.

Additional information on the beam

Duty cycle : the electron beam is delivered by a linear accelerator with a 50 Hz repetition rate during setting-up and 25 Hz during positron injection; the spill is short, in the range of 20 ns .

Availability : out of technical stops and critical periods (similar EDF contract as at CERN) there are about four injections every day, one hour each, giving about 6 10^{13} neutrons cm^{-2} every day without disturbing the physics programme of the Synchrotron Radiation facilities.

REFERENCES

1 J.M. Carpenter , Nucl. Instr. and Methods 145 (1977) 91.

2 G.R. Stevenson , Radiation Levels in an idealized Calorimeter , To be presented in this volume

3 G. Carboni Contribution to this ECFA meeting

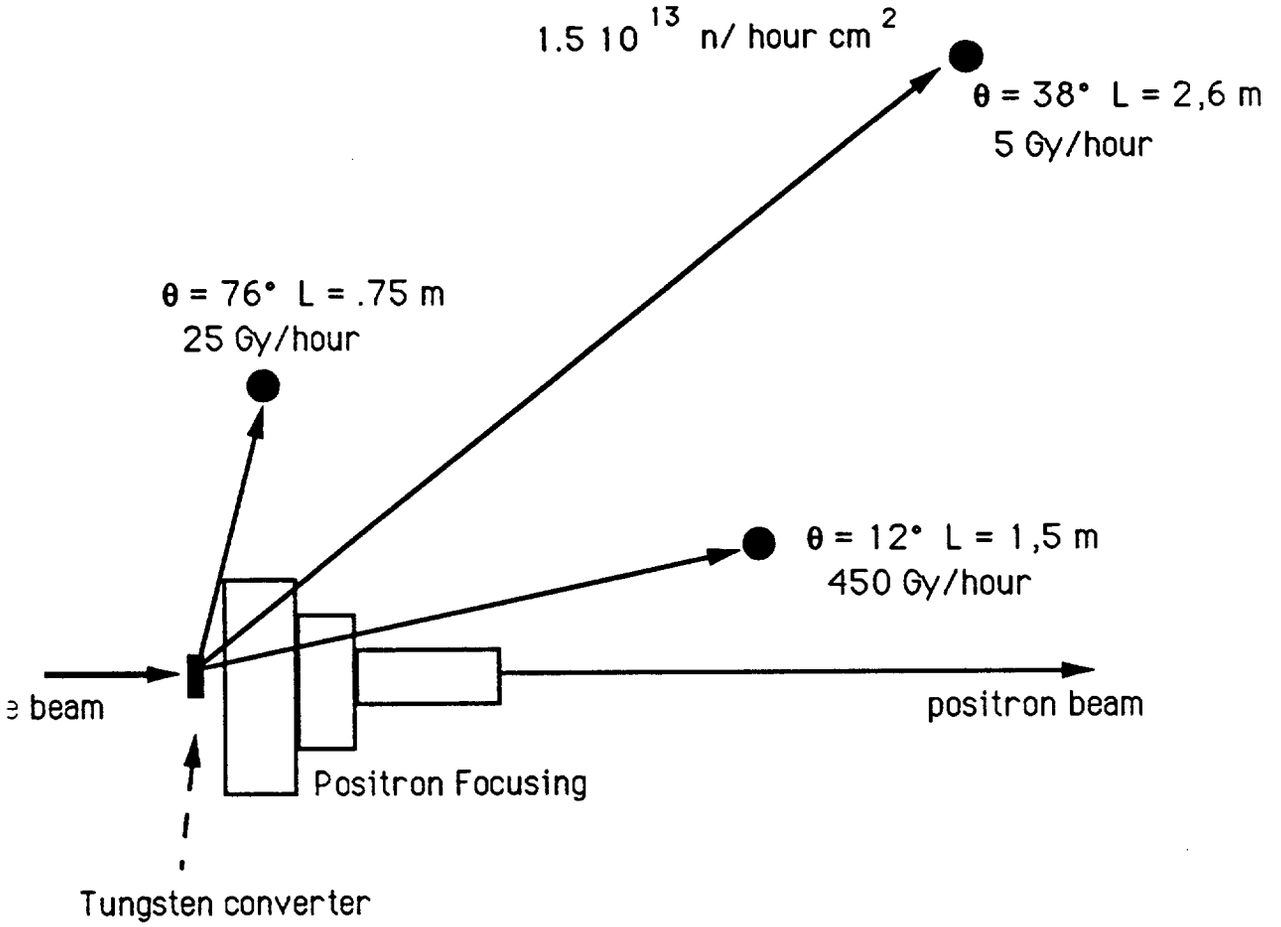


Figure 1 : The Orsay positron source: measured activities (TLD dosemeters) at three positions referenced by the polar angle and distance from the target, neutron flux is measured at one position

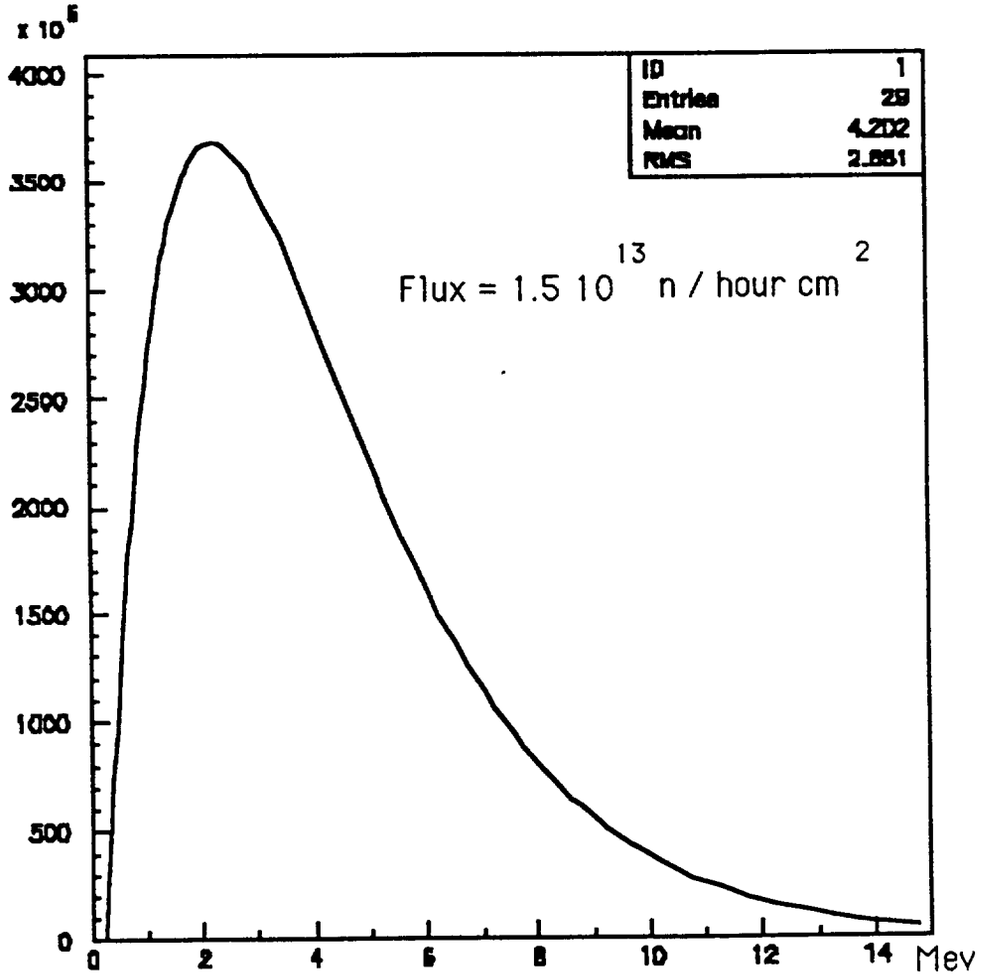


Figure 2 : The neutron energy distribution

Irradiation facilities at CERN

M.Tavlet (CERN-TIS)

Though they produce ionizing radiation, the CERN accelerators are not dedicated to material irradiation. For the purpose of radiation test, our group has been using for many years outside radiation sources such as a research nuclear reactor in Austria and a strong industrial Cobalt source in France. For some months, we operate an industrial X-ray generator, with a maximum high-tension of 80 kV (ref.1). We use also in a parasitic way the target areas of the CERN accelerators. In this case, we are entirely dependant on the machine operation and schedule (ref.2).

From Oktober 1990, we are able to carry out irradiations in a typical accelerator field, in the PS-ACOL target area (ref.3). This facility is presented here.

The components may be irradiated in the target area via a direct access pit from above (see fig.1), the irradiation position is just above the secondary beam line, between the target and the beam-dump (see fig.2). The available diameter for the samples is 15 cm, the length should be limited also to a few dm if homogeneous irradiation is required. The expected dose rate in this position is calculated to be of the order of 2 to 200 Gy/h, depending on the intensity of the proton beam on the target, the height of the irradiation position and the type of material. Precise dose measurements and flux measurements will be carried out in the near futur.

We have also a similar project of an irradiation facility in the future Booster-Isolde target area (ref.4), where a small train will carry the samples near the Isolde 3 target. This facility should be available in 1992.

References:

1. M.Tavlet : Adaptation d'une source de rayons X pour des tests de radiorésistance. TIS-CFM/TM/89-03

2. H.Schönbacher and M.Tavlet : Radiation sources for material testing in Europe. TIS-CFM/IR/90-02

3. M.Tavlet : Project for an irradiation facility in the PS-ACOL target are. TIS-CFM/TM/89-08

4. M.Tavlet : Project for an irradiation facility in the Booster-Isolde target area. TIS-CFM/TM/90-(in preparation)

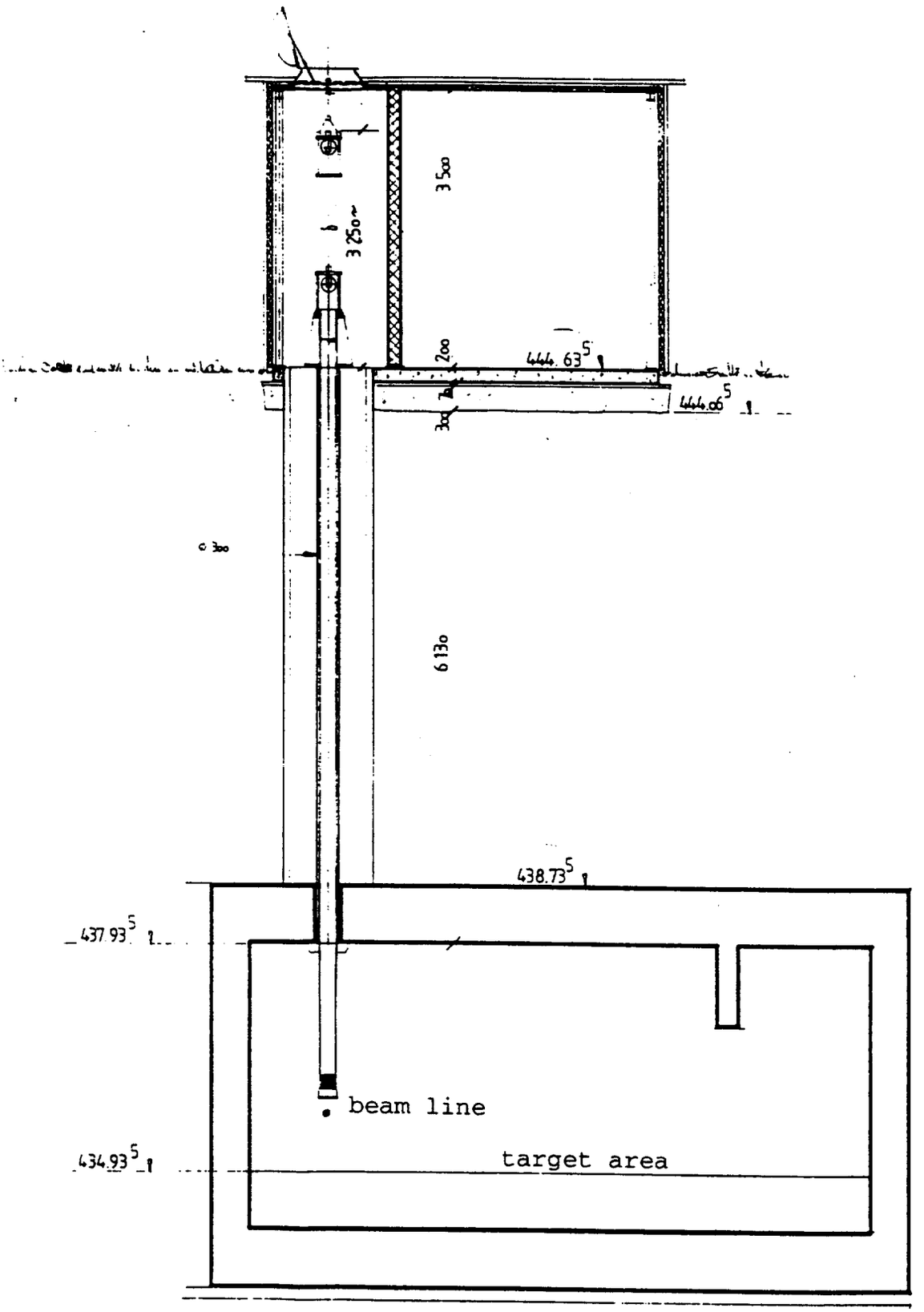


Fig.1 : Irradiation pit, with shanty on top.

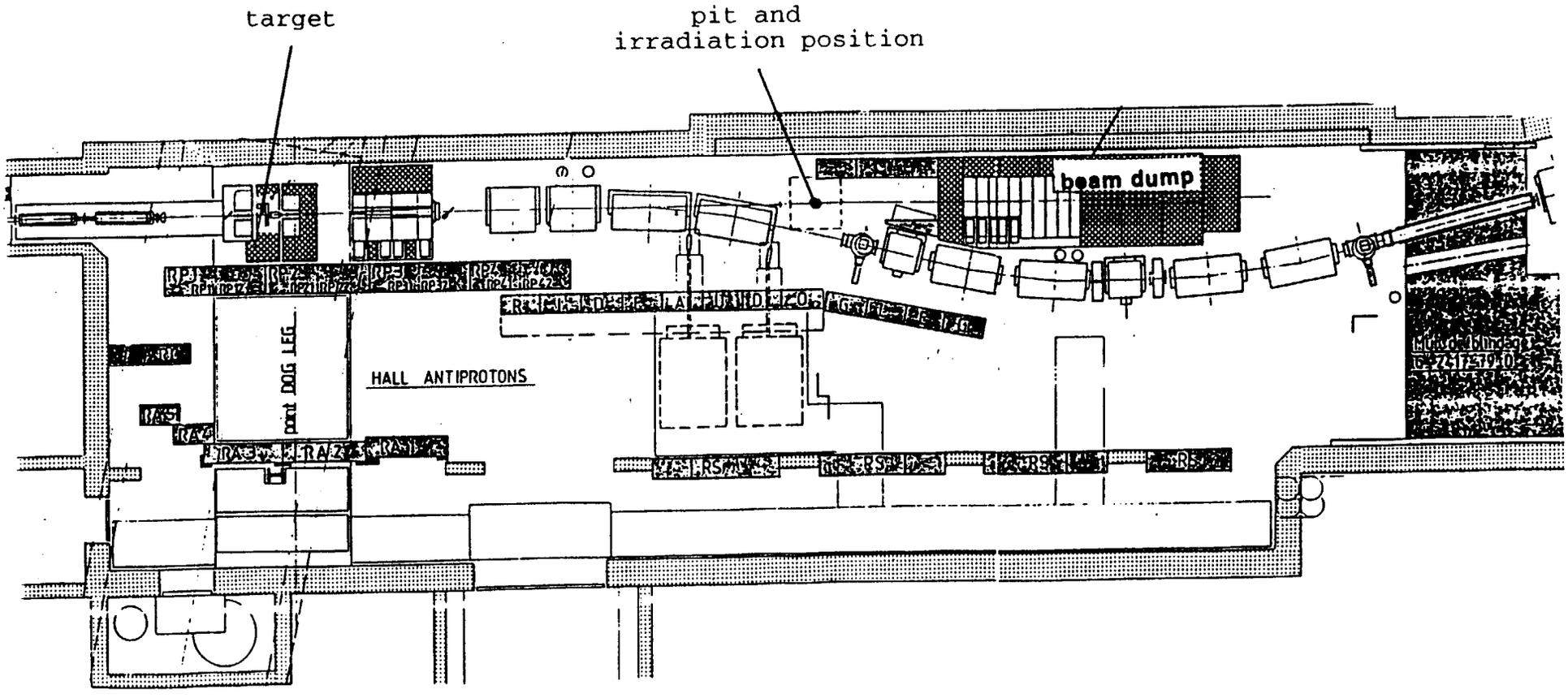


Fig.2 : PS-ACOL target area.

ETHANOL-CHLOROBENZENE DOSIMETRY SYSTEMS FOR HIGH-DOSE DOSIMETRY

Dušan Ražem
"Ruđer Bošković" Institute
41000 Zagreb, Yugoslavia

Introduction

Several physical and chemical phenomena can be used as a basis for dosimetry in the megagray range: ionization, heating and physico-chemical changes in various materials. Ionization and heating are transient phenomena and require a link of the monitoring probe in the radiation field with an external measuring device. On the other hand, the permanent nature of physico-chemical changes induced by irradiation in small portions of various materials makes each piece an autonomous registration device of integrating type. The following presentation shall be restricted to physico-chemical changes in ethanolic solutions of chlorobenzene and corresponding methods of measurement suitable for dosimetry.

Chemical dosimetry is based on the knowledge of the relationship between chemical change induced by radiation in suitable systems and energy absorbed by the systems. In principle, any radiation-induced chemical change can be used for dosimetry, provided the change is reproducible and sufficiently well characterized. Suitable radiation-induced chemical changes may occur in gases, liquids, and solids. Chemical dosimetry is extremely versatile with respect to both space and time: energy absorbed in a volume of any size and shape and at various temporal stages can be measured. By using special fast techniques for the detection and measurement of reactive species ensuing in pulse-irradiated gases and liquids, dosimetry immediately following short radiation pulses can be performed on the time scale of picoseconds. Alternatively, stable products can be measured after the completion of thermodynamic equilibrium, which is obviously the only choice with continuous irradiations.

In irradiated solid systems, on the other hand, chemically reactive species become trapped by impurities or prevented from subsequent reactions by the rigidity of the systems.

In the absence of energy input chemical changes are "frozen" in these systems and persist in them over long periods of time, preserving, also, the dosimetric information. The major interest of chemical dosimetry, however, has been in liquids through the analysis of stable products, while dosimetry methods based on thermoluminescence and lyoluminescence, or ESR measurements of free radicals in solids, have traditionally been parts of the solid-state dosimetry.

The extent of chemical change in an irradiated system at any instant is expressed as the radiation chemical yield, G(X), of the substance X, produced, destroyed, or changed by the mean energy imparted, $\bar{E}$:

$$G(X) = n(X)/\bar{E} \quad \text{mol J}^{-1}$$

where n(X) is the mean amount of substance of a specified entity X.

A related non-SI quantity, G value, has been defined as the mean number of molecules produced, destroyed, or changed by the absorption of 100 eV of energy:

$$G(X) = (X)N_A\ 100/E \quad \text{molecules (100 eV)}^{-1}$$

where (X) is molar concentration of species X, mol dm^{-3}; N_A is Avogadro's number, 6.022×10^{23} molecules mol^{-1}; and E is absorbed energy in eV.

The literature up to the 1980s contains G values expressed per 100 eV. The two quantities are related:

$$1 \text{ mol J}^{-1} = 9.65 \times 10^6 \text{ molecules (100 eV)}^{-1}$$

A dose of 1 MGy will produce 1 mol of chemical change if that change is characterized by a radiation-chemical yield value around 1 μmol/J. Nevertheless, although most radiation-induced changes in solution are characterized by the radiation-chemical yields lower than 1 μmol/J, the amount of change at high doses is large, and it should be taken into account that the irradiated dosimeter at high doses changes its chemical identity. On the deposition of 1 MGy in a rigid system, energy deposition events of an average size, about 30 eV/event, are created only about 1.7 nm apart. The proximity of events enhances the possibility of mutual interactions, rather than fixation of the imparted physico-chemical change, and the dosimeter may reach

saturation. The selection of an appropriate dosimetry system requires matching its performance with the specific application criteria (1). However, irrespective of the selection criteria, the intricacies of any system should be "debugged" by the user himself, and a good and clean procedure should be worked out into routine operation before useful results can be obtained.

Operating Principle

The principle underlying ethanol-chlorobenzene (ECB) dosimetry is the radiolytic formation of hydrochloric acid (HCl) in irradiated aqueous ethanolic solutions of chlorobenzene (CB), coupled with a corresponding analytical method of HCl measurement for readout. A number of analytical methods are available for the measurement of HCl in ethanol. Depending on the readout method, the system can be used as a reference standard or as a routine dosimetry system (1).

The amount of chemical change ensuing in any system in response to irradiation is called the radiation-chemical yield; in this particular case it is the yield of HCl, G(HCl) (moles of HCl formed per 1 J of absorbed energy). G(HCl) primarily depends on the concentration of CB in dosimetric solution, but at any constant CB concentration it is also constant. The system is actually a family of dosimetric solutions, each CB concentration being characterized by its own response, G(HCl).

By varying CB concentration, energy absorption characterics of dosimetric solutions can be matched to energy absorption characteristics of the irradiated material in a broad range of electron densities. The system shows other favourable properties, which make it suitable for high-dose dosimetry in radiation processing, as well as in radiation research.

In the application of a specific dosimetry system the effects of energy spectrum, dose, dose rate and temperature, must be taken into account. This paper describes the effects of these and other variables on the response of the systems. The properties of the system have been particularly thoroughly characterized at several selected CB concentrations: 4, 10, 20, 25 and 40 vol. %, respectively. Correct dosimetry is always possible within the studied range of variables by taking appropriate values of the response, either directly or by interpolation.

ECB dosimetry system provides a means of determining absorbed dose in materials in terms of dose in water.

Absorbed dose in materials other than water may be determined by applying appropriate conversion factors.

ECB dosimetry system requires calibration traceable to national standards.

Composition and Preparation

Components used for the preparation of dosimetric solutions, chlorobenzene and absolute ethanol, are harmless chemicals if handled properly. Commercially available chemicals of sufficient purity are adequate for direct use. "Analytical reagent" (AR), "pro analysi" (p.a.) and "puriss." (-imum) grades are generally satisfactory.

Chlorobenzene of "purum" and "technical" grades requires purification by distillation. Optical absorption in 1 cm cells against water at selected wavelenghts may be used as a criterion of purity of CB: at 300 nm the absorbance should be less than 0.05; at 287 nmn it should not exceed 1. CB is not very volatile (boiling point 131.6 °C) and therefore is easy to handle. It is inert to common nuclophilic reagents and was therefore termed "liquid sand" (2).

Absolute ethanol is used to prepare 96 vol. % ethanol with triply distilled water, and this aqueous ethanol is used for topping dosimetric solutions. Water has no influence on G(HCl) values in the systems between 2.4 and 4 vol. % H_2O. Water enhances the stabilization of radiolytic products by solvation.

Original formulations included 0.02 vol. % benzene and 0.04 vol. % acetone to compensate for the eventual impurities present in ethanol (3,4). However, better control of the (relevant) variables is achieved by using ethanol of adequate purity and without additives.

Triply distilled water is obtained by distillation of ordinary distilled water subsequently from alkaline permanganate, acidic dichromate and without additives (5).

All other chemicals necessary for the evaluation of irradiated dosimeters should be of analytical reagent grade purity and can be used as received.

Dosimeters consisting of 5 mL of dosimetric solution filled into a glass container are usually used, although smaller volumes (e.g. 2 mL) may also be practical.

Corresponding pharmaceutical ampoules without prior treatment are adequate for massive use; chemically cleaned Pyrex ampoules may be used for research purposes.

Dosimeters should be partly deoxygenated immediately before flame sealing the ampoules. Adequate deoxygenation of 5 mL - solutions is accomplished by bubbling nitrogen through a glass capillary for 1 min at approximately 1 bubble per sec. Sealed dosimeters kept in dark are stable for many years, both before and after irradiation.

Mechanism of Response

There is a large number of chemical radiation dosimetric systems described in the literature, which contain some halogenated organic compound in solution or in two-phase systems (6,7). They are based on the well-known property of the halogen-containing hydrocarbons to undergo dissociative electron attachment (8). By this mechanism electrons are converted into halide ions and corresponding hydrocarbons.

Chlorobenzene reacts efficiently with epithermal electrons in the gas phase. The cross-section for dissociative electron attachment peaks at an electron energy of 0.86 eV (9). Events in the liquid phase are influenced by the proximity of molecules, whereby higher density causes faster degradation of electron kinetic energy. The probability of the reaction at any instant is proportional to the overlap between the electron energy distribution function and the attachment cross-section. The probability of the reaction is changed in the condensed phase, as compared with the gas phase, mainly because of the influence of density on the electron energy distribution function. The electron energy distribution function evolves with time after the radiation action. Electron starting with a sufficiently high energy has a finite probability of a resonant attachment by scavenger molecules as it sweeps the range of energies overlapping the cross-section.

The events involving subexcitation electrons take place at a very early stage of radiation action. In polar liquids the high-frequency dielectric constant applies at this stage, which makes the character of the solvent unimportant for early scavenging. There is insufficient time for solvation of reacting species and products, and, consequently, solvent influence on the energy requirement of the reaction can only be negligible: the reaction resembles that in dense inert gases.

Surviving electrons emerge on the low-energy end of the distribution function, and either recombine or become solvated electrons. Thermalized electrons also have a finite probability of reacting with scavengers. The final chemical change on irradiating a liquid is the result of species reacting in early, as well as in subsequent, later stages of radiation action. The contributions of various species to the measured response can be resolved by fast techniques or by scavenging studies.

Fast technique of pulse radiolysis in the nanosecond time window has shown that CB reacts rather efficiently with precursors of solvated electrons in ethanol. The concentration of CB necessary to reduce the yield of solvated electrons to 37 % of the initial value (at 10 ns) in ethanol was found to be 0.3 M (10). This means that the contribution of solvated electrons to the response of dosimetric solutions is about 26 % in solutions containing 4 vol. % CB, not greater than 3 % in solution containing 10 vol. % CB, and negligible at higher concentrations.

Chlorobenzene is only moderately reactive with solvated electrons in ethanol (10); therefore it is easy to find suitable secondary scavengers to suppress the contribution of solvated electrons to the Cl^- ion yield. Scavenging studies have shown that two kinetically distinct populations of electrons are responsible for the response of dosimetric solutions to irradiation, the majority of the response at high concentrations of CB being due to precursors of solvated electrons (11,12).

Energy Absorption Characteristics

The knowledge of the dependence of the response, G(HCl), on the energy of the incident radiation is useful when radiation of known initial energy spectrum is used, and provided that the spectrum does not appreciably change during absorption. On penetrating thick layers of materials, however, the energy spectrum of the incident radiation becomes richer in low energy photons or particles. The probability of energy deposition in the medium is the function of the composition, and the compositions of the dosimeter and of the irradiated material are generally not the same. The dosimeter may be considered a "cavity", having a different composition than the medium. The energy absorbed in the dosimeter would generally not be the same as that absorbed by the medium, had the dosimeter not been there. The relationship between the dose absorbed in the medium, D_M, and that absorbed in the dosimeter, D_D, is given by:

$$D_M = (1/f)\, D_D$$

where f is the correction factor, which depends on the quality of radiation.

The correction factor f for electromagnetic radiation depends also on the size of the dosimeter relative to the range of secondary electons.

When the dimensions of the dosimeter are large as compared to the range of secondary electrons, the exchange of secondary electrons between the medium and the dosimeter has a negligible effect on dose absorbed by the dosimeter. In this case the correction factor is given by the ratio of the corresponding mass energy absorption coefficients for dosimeter and the medium, respectively:

$$f = (\mu_{en}/\rho)_D / (\mu_{en}/\rho)_M$$

By varying CB concentration from 4 to 40 vol. % it is possible to match any mass-energy absorption coefficient in the range from 0.0300 to 0.0289 cm^2g^{-1} at the reference energy, ^{60}Co gamma ray energy 1.25 MeV (TABLE I).

TABLE I.

Energy-absorption characteristics of the ethanol-chlorobenzene dosimeter and of some materials

	Dosimeter			Materials	
CB conc. vol.%	$\rho_{20°C}$ (g/cm^3)	μ_{en}/ρ (cm^2/g)		$\rho_{20°C}$ (g/cm^3)	μ_{en}/ρ (cm^2/g)
4	0.819	0.0300			
10	0.839	0.0299			
20	0.869	0.0296	H_2O	1.000	0.0296
25	0.886	0.0292	muscle	1.127	0.0293
40	0.925	0.0289	poly-styrene	1.060	0.0288
			Lucite	1.190	0.0288

However, as the softening of the incident radiation occurs on penetration through thick layers of materials, the amounts of energy deposited in the dosimeter and in the surrounding material vary proportionally to the energy variation of the respective mass-energy absorption

coefficients. Photoelectric effect is a dominant mode of electromagnetic energy absorption at low photon energies, and its probability increases with the 4th power of the atomic number. Due to its chlorine content the ECB dosimeter would overestimate the dose in water or in other low-Z materials at energies below 0.1 MeV (13,14).

Dependence of the Response on CB Concentration

The concentration of CB is a fundamental variable of the ECB dosimetry. It determines energy absorption characteristics of the system and, to a limited extent, its sensitivity to irradiation, i.e. the response or G(HCl). The dependence of the radiation-chemical yield of Cl^- ions on the concentration of CB is shown in Fig. 1. The influence of the presence of oxygen is also shown.

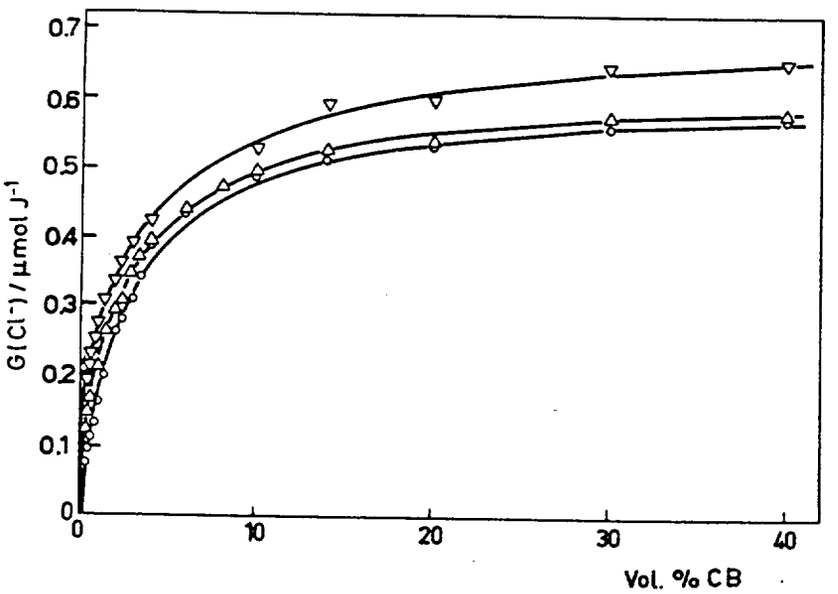


FIGURE 1. Radiolytic yield of chloride as a function of CB concentration. Inverted triangles: evacuated dosimetric solutions; triangles: dosimetric solutions in equilibrium with air; circles: dosimetric solutions in equilibrium with oxygen. Dose rate: 3 kGy/h, the doses applied below 5 kGy.

The curves are typical two-component curves, consisting of the low-concentration part and a high-concentration one. Although it has been claimed that no fundamental significance should be attached to this type of curves, because purely synthetic freehand drawn curves could be

resolved into two components if represented in the coordinates y^{-1} vs. x^{-1}, (15), we have shown that a low-concentration component could be eliminated by the addition of solvated electron scavengers which are more efficient than CB (11). This has also, lent a basis for postulating nonthermal electrons as major precursors of Cl^- ions at higher concentrations.

Dependence of the Response on Oxygen Concentration

The effects of oxygen on the radiation-chemical yields of Cl^- ions in four characteristic formulations of the ECB dosimeter are shown in Fig. 2. (16). The effect of oxygen could not be understood as the competition for solvated

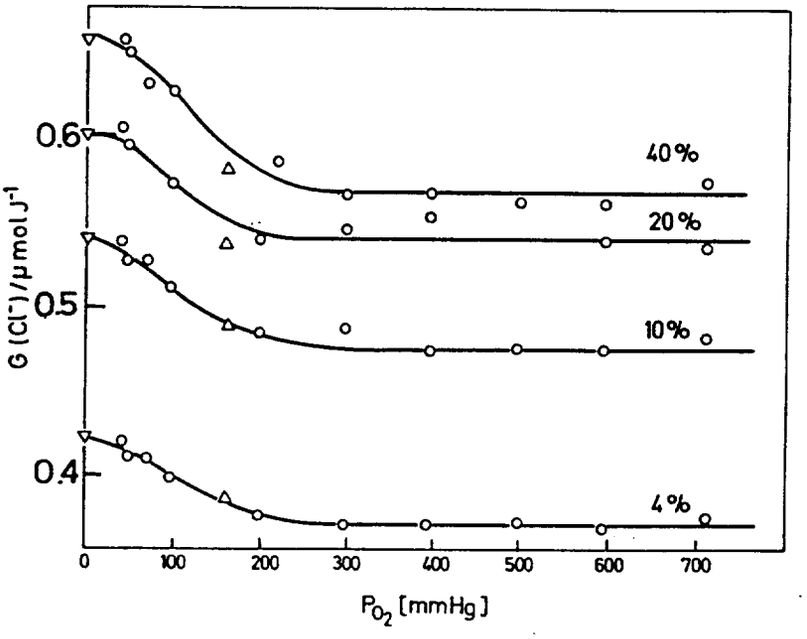


FIGURE 2. Radiolytic yield of chloride as a function of oxygen pressure in dosimetric solutions containing 4, 10, 20 and 40 vol. % CB. Inverted triangles: evacuated dosimetric solutions; triangles: dosimetric solutions in equilibrium with air. Dose rate 3 kGy/h, the doses applied below 5 kGy.

electrons, because at these CB concentrations this is not possible. Moreover, the effect is larger at larger CB concentrations, which is quite opposite of the competitive behavior. This effect is not understood at present. The effect is not saturated in air, the saturation requireing about 50% higher partial pressure of O_2 than it is in air.

Dependence of the Response on Dose

Dose dependence of the response is due to the acccumulation of radiolytic products with dose. The nature of these products depends on the presence of oxygen.

In evacuated dosimetric solutions two dose regions can be resolved: approx. between 3 and 30 kGy, the response decreases a little, while a stronger decrease occurs above 100 kGy (Fig.3).Dosimetric solutions which were initially in

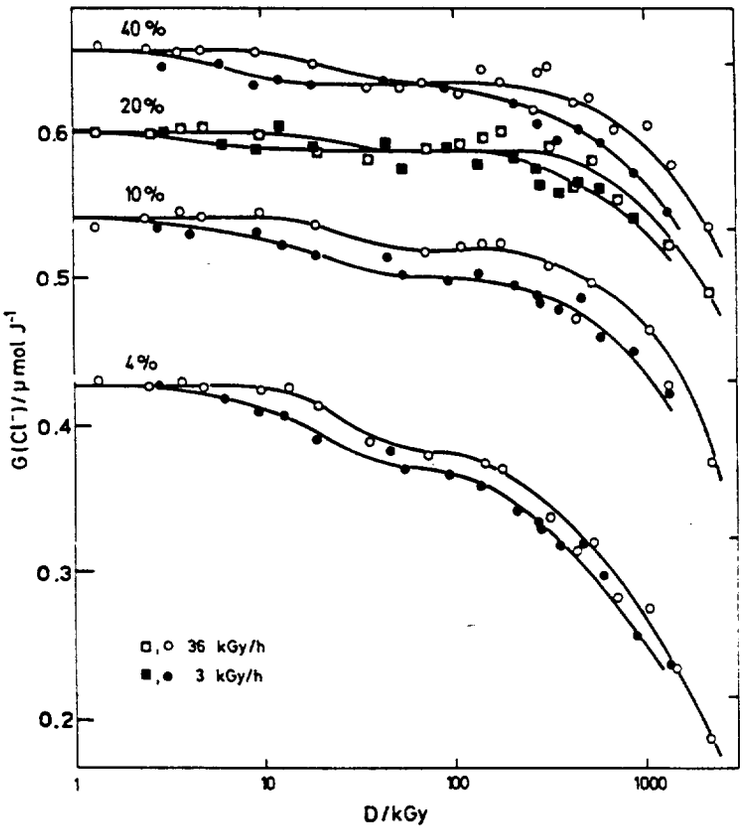


FIGURE 3. Radiolytic yields of chloride as a function of dose and dose rate in evacuated dosimetric solutions containing 4, 10, 20 and 40 vol. % CB. Open circles: 36 kGy/h; filled circles: 3 kGy/h. For better resolution the circles for 20 vol. % CB are inscribed into squares.

equilibrium with air and then sealed off, show only the decrease od $G(Cl^-)$ above 100 kGy. A small increase of the response with dose up to approx. 70 kGy is attributed to the consumption of oxygen. The G values attained upon consumption of oxygen are the same as those attained in

evacuated solutions upon completion of the low-dose (3 - 30 kGy) competition with radiolytic products (FIG. 4) (16).

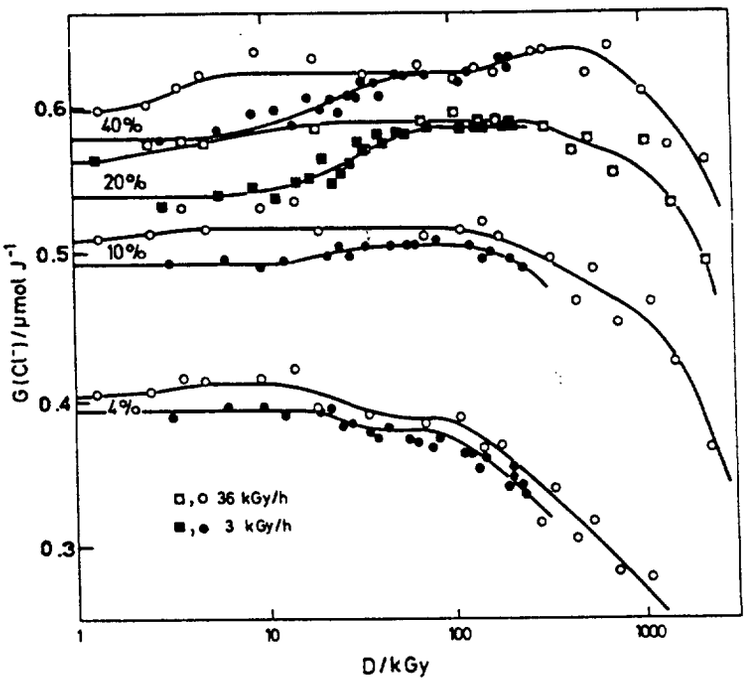


FIGURE 4. Radiolytic yields of chloride as a function of dose and dose rate in dosimetric solutions containing 4, 10, 20 and 40 vol. % CB. Open circles: dosimetric solutions initially brought into equilibrium with air before sealing, dose rate 36 kGy/h; filled circles: dosimetric solutions in ground-glass stoppered test tubes, dose rate 3 kGy/h. For better resolution the circles for 20 vol. % CB are inscribed into squares.

These two effects were combined to accomplish dose-independent response in partially deoxygenated solutions (13). Table II shows the values of the radiation-chemical yields of Cl^--ions in partially doexygenated dosimetric solutions, which are essentially constant in the dose range 0.1 to 100 kGy.

In the presence of oxygen the nature of radiolytic products at high-doses (above 100 kGy) favors the release of HCl, the more so the higher CB concentration (FIG. 5.). The ability of radiolytic compounds produced at low doses to compete with the response does not seem much different from the situation in evacuated solutions. We might speculate that these radiolytic compounds do not include oxygen and are formed in good yield. Stable product analysis would be required to investigate the nature of radiolytic products at

low and high doses and in the absence and presence of oxygen, respectively.

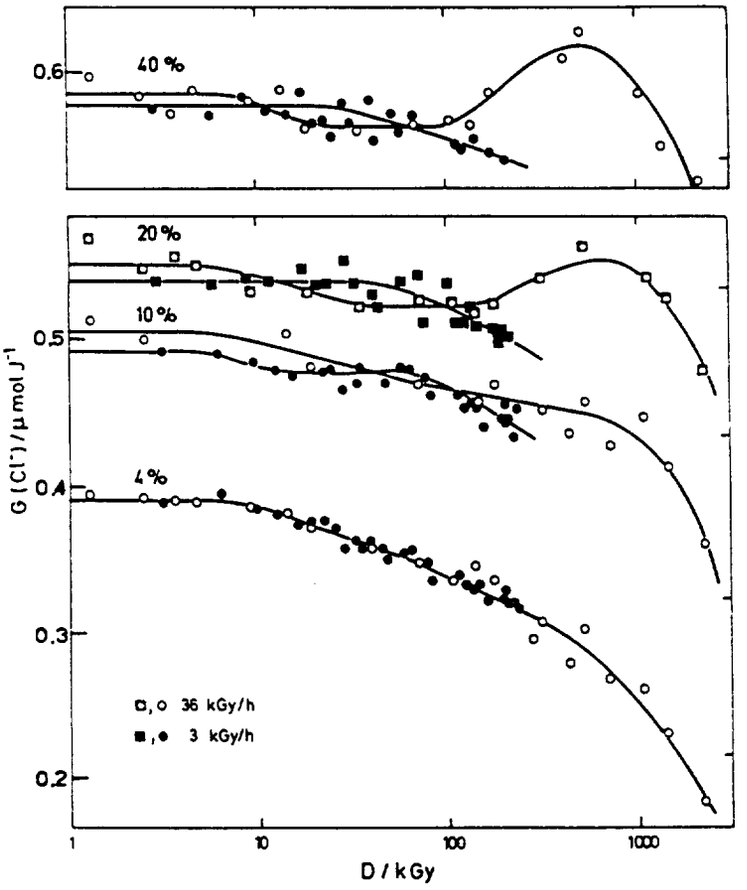


FIGURE 5. Radiolytic yields of chloride as a function of dose and dose rate in dosimetric solutions containing 4, 10, 20 and 40 vol. % CB. Open circles: dosimetric solutions initially brought into equilibrium with oxygen before sealing, dose rate 36 kGy/h; filled circles: dosimetric solutions in loosely covered test tubes, dose rate 3 kGy/h. For better resolution the circles for 20 vol. % CB are inscribed into squares.

TABLE II.

Dose-insensitive radiolytic yields applicable in the dose range 0.1 - 100 kGy

CB conc. (vol. %)	$\rho_{25°C}$ (g cm^{-3})	G(Cl$^-$) (μmol J^{-1})
4	0.819	0.42*
10	0.839	0.52
20	0.869	0.59
25	0.886	0.60
40	0.925	0.63

*dose range 0.1 - 20 kGy

Dependence of the Response on Dose Rate

Dose rate has very little effect on the response to gamma rays between 3 and 36 kGy/h (Figures 3. to 5.)(16). Irradiations with 10 MeV electron at 10^7 Gy/s in pulses gave the response which was only about 5 % lower than the response to gammas (17,18). Taking into account all uncertainties in comparing the irradiations at various locations at various times by various sources, the agreement is rather good.

Dependence on Temperature

ECB dosimeters are generally well protected by their sealed glass containers against most environmental influences except temperature and light. Light effects are not significant (19), and can be minimized by proper handling. The effect of elevated temperature, however, is unavoidable with large radionuclide irradiation facilities and electron-beam facilities.

Dosimetric solutions containing lower concentrations of CB are less susceptible to dose effects at elevated temperatures. The system containing 4 vol. % CB is free of any effect up to 80 °C. Generally, larger temperature

effects are observed at higher temperatures, higher CB concentrations and lower doses (FIG.6.). Dose effects dissappear at higher doses, above 20 kGy at 50 °C and above 25 kGy at 80 °C (20).

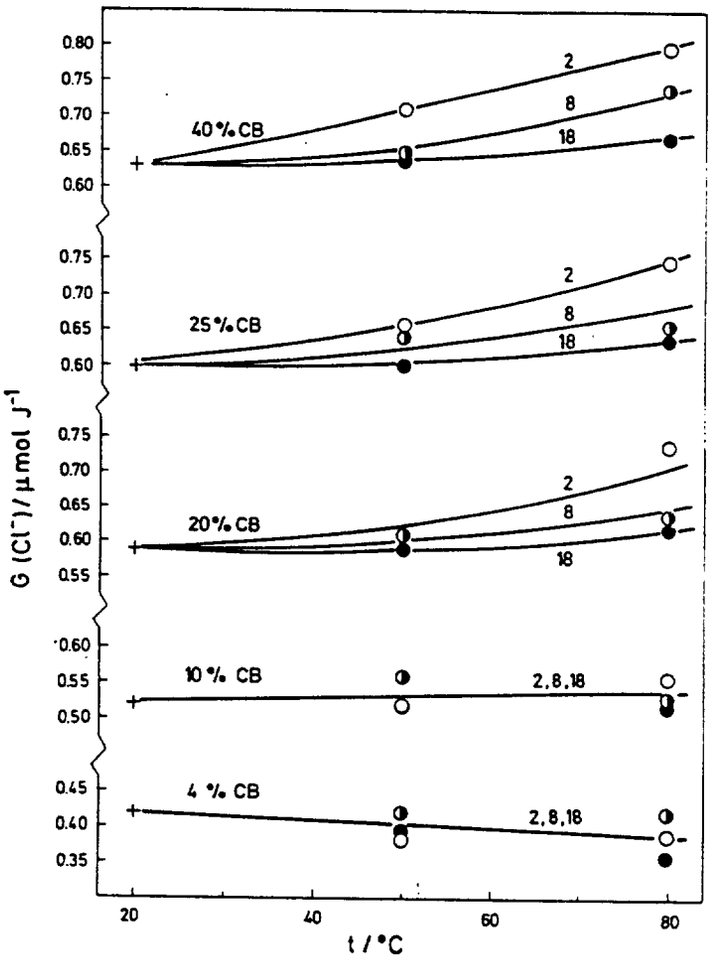


FIGURE 6. Radiolytic yields of chloride as a function of temperature in partially deoxygenated dosimetric solutions irradiated at 2 kGy (open circles), 8 kGy (semi-filled circles) and 18 kGy (filled circles).

Determination of Dose

Determination of dose requires the knowledge of the pertaining value of G(HCl) and of the amount of radiolytically formed HCl. The dose in water (in Gy) is then calculated from the expression:

$$D = 9.65 \times 10^6 \, (HCl) \, / \, G(HCl) \times \rho$$

The selection of the proper value for G(HCl) requires the knowledge of the behavior of the response under given irradiation conditions. The amount of radiolytically formed HCl can be measured by various methods (21), TABLE III.

TABLE III.

The characteristics of employed readout methods

Method	Principle of measurement	Minimum dose (Gy) if G(HCl)=0.5 $\mu mol J^{-1}$
Spectrophotometry	Absorbance of ferric-SCN complex	10
Mercurimetric titration	Diphenylcarbazone color change	100
Alkalimetric titration	Bromophenolblue color change	100
Coulometry	Time-controlled generation of Ag^+ ions	100
Oscillometry	High-frequency conductivity	1000

Spectrophotometric method is based on the reaction of radiolytically generated Cl^- ions with mercury (II) thiocyanate and the subsequent reaction of the liberated thiocyanate ions with iron (III) to give the familiar red colour of the ferric thiocyanate complex. Molar absorptivity of the complex at the maximum optical absorption, 485 nm, was determined as 3990 ± 60 $mol^{-1}cm^{-1}$. The Lambert-Beer law is obeyed in the concentration range 1 x 10^{-6} to 1.5 x 10^{-5} M Cl^- (22).

Mercurimetric titration is based on the formation of insoluble $HgCl_2$ with Hg^{2+} ions in chloride solution (4). When all chlorides have been precipitated, the first excessive mercury reacts with the indicator diphenylcarbazone to form a violet-red complex, and this color change is used for visual observation of the end point. The normality of the mercuric nitrate solution must be checked daily against standard NaCl solutions.

Alkalimetric titration is a straightforward titration of chloride counterions with carbonate or bicarbonate using the indicator bromophenol blue for the visualization of the end point (4). The titrating solutions of carbonate or bicarbonate do not require daily standardization, but $G(H^+)$ is susceptible to invironmental effects, such as alkalinity of the glass container walls, atmosphere etc., more than $G(Cl^-)$. Therefore the values of $G(Cl^-)$ are preferably given in the literature.

Amperometric titration is based on the reaction of silver ions with chloride ions to form insoluble AgCl. The reaction is carried out at a constant rate by passing a fixed direct current between a pair of silver electrodes immersed in an acidic solution. As the equivalence point of the reaction is reached, the current increases and further generation of silver ions is stopped. Since the rate of generation of silver ions is constant, the total titration time is proportional to the number of chloride ions in the sample. The instrument displays this time in milliequivalents of Cl^- per liter (21).

Oscillometric method is based on inserting an irradiated dosimeter in a capacitor of an oscillator circuit resonating at a frequency of 48 MHz (23). As the conductance of the irradiated dosimetric solution has changed due to the radiolytic formation of HCl, the oscillator characteristics of the circuit also change. This change can be compensated for by a variable capacitor in the reference circuit, which is connected in a bridge with the measuring circuit. The amount of compensation is displayed on the instrument scale. The method requires no galvanic contact between the dosimetric solution and the electrodes, so that sealed dosimeters can be kept for a long time after irradiation. The method, however, needs calibration (21).

High-dose Applications

The application of the ECB dosimetry system within the scope of radiation processing doses presents no problems nowadays. The behavior of the whole family of dosimetric solutions has been documented in detail under varying irradiation conditions. Existing data allow correct dosimetry to be made under any conditions within the studied interval of variables by taking appropriate values of the response, either directly or by interpolation.

The application of the dosimeter beyond 25 kGy requires the measurement of more than millimolar concentrations of HCl. The concentration to be measured increases with dose, so that higher and higher doses can be measured at

increasing relative precision. The selection of appropriate values of G(HCl) is critical for accurate dosimetry.

The dosimetric characteristics of the system at doses lower than 25 kGy have been checked many times internally, (24), by comparison with other laboratories, and against the International Dose Assurance Service (IDAS) of the IAEA (25). The behavior of the response above 25 kGy is based on two sets of data at 3 and 36 kGy/h respectively, (16), and one set at 8.6 kGy/h and dose 1.1 MGy. Mutual consistency of these data and their consistency with data below 25 kGy permit the conclusion that the response is adequately characterized up to about 2.5 MGy.

REFERENCES

(1) Standard Guide for Selection and Application of Dosimetry Systems for Radiation Processing of Food. Annual Book of ASTM Standards, Vol. 12.02., E 1261-88, ASTM. Philadelphia, PA (1988).

(2) J.F. BUNNETT, The remarkable reactivity of aryl halides with nucleophiles, J. Chem. Educ., 51 (1974) 312-315.

(3) I. DVORNIK, U. ZEC, F. RANOGAJEC, The ethanol-chlorobenzene aerated system as a new high-level dosimeter for routine measurements, Proc. IAEA Symp. "Food Irradiation", Karlsruhe, 1966; IAEA, Vienna (1966) 81-90.

(4) I. DVORNIK, "The Ethanol-Chlorobenzene Dosimeter" In: Manual on Radiation Dosimetry (N.W. HOLM and R.J. BERRY, Eds.) Marcel Dekker, Inc., New York (1970) 345-349.

(5) N.W. HOLM, Z.P. ZAGORSKI, "Aqueous chemical dosimetry" In: Manual on Radiation Dosimetry (N.W. HOLM and R.J. BERRY, Eds.) Marcel Dekker, Inc., New York (1970) 83-104.

(6) A.K. PIKAEV, "Dosimetry in Radiation Chemistry" (in Russian), Nauka, Moscow (1975).

(7) R. BROSZKIEWICZ, "Chemical Methods of Dosimetry of Ionizing Radiations", (in Polish), Wydawnictwa Naukowo-Techniczne, Warszawa (1971).

(8) L.G. CHRISTOPHOROU, "Atomic and Molecular Radiation Physics", Wiley-Interscience, New York (1971).

(9) L.G. CHRISTOPHOROU, R.N. COMPTON, G.S. HURST, P.W. REINHARDT, Dissociative electron capture by benzene derivatives, J. Chem. Phys., 45 (1966) 536-547.

(10) D. RAŽEM, W.H. HAMILL, Electron scavenging in ethanol and in water, J. Phys. Chem., 81 (1977) 1625-1631.

(11) D. RAŽEM, I. DVORNIK, Scavenging of electrons prior to thermalization in ethanol, Proc. 3rd Tihany Symp. Radiation Chemistry, Balatonfured, Hungary, 1971; (J. DOBO and P. HEDVIG, Eds.), Akademiai Kiado, Budapest (1972) 223-228.

(12) D. RAŽEM, I. DVORNIK, Scavenging of electrons prior to thermalization in ethanol, J. Phys. Chem., 84 (1980) 3577-3581.

(13) D. RAŽEM, I. DVORNIK, Application of the ethanol-chlorobenzene dosimeter to electron-beam and gamma-radiation dosimetry: III. Tissue-equivalent dosimetry. Proc. IAEA Symp. "Radiation Preservation of Food", Bombay, 1972; IAEA, Vienna (1973) 537-547.

(14) A. MILLER, W.L. McLAUGHLIN, Calculation of the energy dependence of dosimeter response to ionizing photons. Int. J. Appl. Radiat. Isot., 33 (1982) 1299-1310.

(15) P.J. DYNE, W.M. JENKINSON, Radiation chemistry of cyclohexane. III. Effect of benzene and iodine on the isotpic composition of radiolytic hydrogen from C_6D_{12} - C_6H_{12} mixtures. Can. J. Chem., 39 (1961) 2163-2170.

(16) D. RAŽEM, I. DVORNIK, Application of the ethanol-chlorobenzene dosimeter to electron-beam and gamma-radiation dosimetry. II. Cobalt-60 gamma rays. Proc. IAEA Symp. "Dosimetry in Agriculture, Industry, Biology and Medicine", Vienna, 1972; IAEA, Vienna (1973) 405-419.

(17) I. DVORNIK, D. RAŽEM, M. BARIĆ, Application of the ethanol-chlorobenzene dosimeter to electron beam dosimetry: pulsed 10 MeV electrons. Proc. IAEA Symp. "Large Radiation Sources for Industrial Processes", Munich, 1969; IAEA, Vienna (1969) 613-622.

(18) A. KOVACS, A. MILLER, Electron dose determination by ethanol-monochlorobenzene dosimeter. Radiat. Phys. Chem., 28 (1986) 531-533.

(19) A. KOVACS, V. STENGER, Environmental effects on the ethanol-monochlorobenzene dosimeter system before, during and after irradiation. Proc. Final Res.

Co-ordinat. Meeting Research in Radiation Processing Dosimetry, Munich 1983, IAEA-TECDOC-321, IAEA, Vienna (1984) 91-139.

(20) M. HOANG HOA, D. RAŽEM, Temperature effects on the ethanol-chlorobenzene dosimeter (Dvornik dosimeter) (submitted for publication).

(21) D. RAŽEM, I. DVORNIK, Ethanol-chlorobenzene dosimetry for absorbed doses below 1 kGy. Appl. Radiat. Isot., 38 (1987) 1019-1025.

(22) D. RAŽEM, G. OČIĆ, J. JAMIČIĆ, I. DVORNIK, Application of the ethanol-chlorobenzene dosimeter to electron-beam and gamma radiation. IV. Spectrophotometry of coloured secondary complexes. Internat. J. Appl. Radiat. Isotopes, 32 (1981) 705-711.

(23) ZS. HORVATH, E. BANYAI, G. FOLDIAK, The radiofrequency, (oscillometric) alcoholic chlor benzene dosimeter. Radiochim. Acta, 13 (1970) 150-152.

(24) D. RAŽEM, L. ANĐELIĆ, I. DVORNIK, Consistency of ethanol-chlorobenzene dosimetry. In: Proc. IAEA Symp. "High-Dose Dosimetry", Vienna, 1984; IAEA, Vienna (1985) 143-156.

(25) J.W. NAM, International standardization of radiation processing dosimetry. In: Proc. Sixth Tihany Symp. Radiation Chemistry, Balatonszeplak, Hungary, 1986, (P. Hedvig, L. Nyikos, R. Schiller, Editors), Academiai Kiado, Budapest (1987) 685-688.

Effects of radiation damage on scintillating fibre calorimetry*

A. Maio

Laboratório de Instrumentação e Partículas -Lisboa

Centro de Física Nuclear da Universidade de Lisboa

Abstract

We report on measurements on radiation hardness of plastic scintillating fibres to be used for scintillating fibre calorimetry. Fibres were irradiated by a ^{60}Co γ-source and the effect on the emission and on the attenuation of scintillation light in the fibres were studied. The influence of the use of optical filters, glue and surrounding atmosphere were investigated. Results are given on the changes in the wavelength spectrum induced by ionizating radiation. A comparative study of radiation damage by neutrons from a fission reactor and γ-rays from a ^{60}Co γ-source has been performed, and dose rate effects have been studied. The results of a Monte Carlo study on the performance of a compensating lead scintillating fibre calorimeter under irradiation were used. We infer from these results that with the best commercially available fibres the effects on calorimeter performance appear to be within acceptable limits up to 10 Mrad doses.

1 Introduction

Detectors operating in future LHC or SSC experiments will encounter a considerable amount of radiation [1]. It is therefore of great importance to study the effect of radiation on the performance of such detectors. Most radiation damage to a calorimeter performance is caused by the production of electromagnetic showers in the calorimeter itself, as all the energy of these showers is deposited in a region of limited depth. Since the most abundantly produced particles near the beam axis of a colliding proton machine are pions, the radiation damage will primarily come from the 2γ decay of π^0's.

Scintillating fibre imbedded in lead have been used at CERN since 1982 in electromagnetic calorimeter prototypes studies, since 1984 in experiments, and since 1986 under rather extreme irradiation conditions of ~ 1Mrad/week in experiment NA38 [10]. Radiation damage studies have preceded the construction of the detectors.

---

* Most of this work has been done in the framework of the LAA project. Extended papers are in preparation to be submitted for publication, including Monte Carlo studies of calorimeter response under irradiation.

The SPACAL collaboration is developing, within the LAA project, prototypes of a scintillating fibre calorimeter intended for the detection of both electromagnetic and hadronic showers in experiments at future multi-TeV hadron colliders. The detectors contain large numbers of 2m long parallel plastic scintillating fibres embedded in a lead matrix at a volume ratio of 1:4 to get compensation [2]. The fibres run almost parallel to the direction of the particles to be detected. A single calorimeter module contains 1141 optical fibres, which are read out by a single photomultiplier. Apart from compensation, the potential advantages of this technique are hermeticity, good energy resolution for electromagnetic and hadronic showers, speed of detector response, linearity, uniformity of detector response as a function of the impact position and angle independent of the degree of segmentation, low noise and sensitivity to minimum ionising particles [3,4,5,6].

To achieve the above list of calorimeter properties, scintillating fibres have to fulfil a number of requirements. The production and attenuation of light in a scintillating fibre is roughly described by an exponential function:

$$I(z) = I_0 \, e^{-z/\lambda_{att}} \qquad (1)$$

where I_0 is the quantity of light produced at a distance z from the light detector, λ_{att} is the attenuation length of the fibre and I(z) is the quantity of light detected. The attenuation of light in the fibre depends on the wavelength and also on the production angle of the light [4,7]. Therefore the mechanism of transmission of light along the fibre would be described more correctly if we replace eq. (1) by a sum of exponential functions. An effective increase of λ_{att} can be achieved with an optical filter that cuts off the short wavelength components (<450nm) [4].

In order to limit the effects of light attenuation on the hadronic energy resolution to an acceptable level, λ_{att} should be at least 7m [4]. By placing a mirror of sputtered aluminium at the far-end of the fibre (reflectivity typically 85%) an effective attenuation length of 6-8m was obtained. Fluctuations in I_0 for fibres read out by the same photomultiplier should be smaller than 6% to maintain a good energy resolution for electromagnetic showers. To prevent pile-up of events in the high rate environment of future hadron colliders (66 MHz), the natural fibre speed, should not be decreased. The stability of the above properties is of major importance, and should be maintained under the high radiation doses expected [1].

We have tested the radiation hardness of a number of commercially available fibres through irradiation by ^{60}Co γ-sources. The wavelength spectra of non-irradiated and irradiated fibres were compared. As the radiation mainly affects the short wavelength components of the light, tests were done with and without a 450nm cut-off yellow optical filter. The influence of glue surrounding the fibres was also studied, since gluing is a relative simple assembly technique.

This paper is divided in several sections. In section 2 of this paper we describe the set-up used for fibre irradiation as well as the different set-ups used to measure the fibre characteristics before and after irradiation. Section 3 starts with an overview of fibres available on the market, followed by results on the wavelength spectra before and after irradiation. Section 4 reports on the influence of the surrounding medium on the radiation

damage to the fibres. In section 5 a comparative study of the radiation hardness for different types of fibres is presented. Section 6 reports on the radiation damage effects on fibres irradiated with neutrons from a fission reactor and γ-rays from a ^{60}Co γ-source; dose rate results are also presented. Conclusions from Monte Carlo calculations [8,9] that simulate radiation damage on a compensating lead scintillating calorimeter are presented, in order to set the limits of radiation damage on the available fibres irradiated at the LHC dose levels. Final conclusions are given in secton 7.

The irradiations both in various ^{60}Co-γ sources and in the Portuguese Research Reactor (R. P. I.) were made possible thanks to I.C.E.N./LNETI, Sacavém, Portugal.

2 Experimental set-up of the irradiation tests.

Two different ^{60}Co-γ sources were used for the irradiation of fibres of 40 cm length . The dose rate profile of the first source, the "normal intensity" source, is shown in fig. 1a. Measurements of the light output of the fibres were normally performed on the less irradiated end (left hand side in fig. 1a). For this source the maximum dose rate of $\approx$30 krad/h is reached at 30 cm from the read out end.

For a second ^{60}Co-γ source appropriate shielding was set up to simulate approximatively the dose rate profile of electromagnetic showers in the calorimeter. The profile of this "very high intensity" source is shown in fig. 1b and reaches a maximum of 1.05 Mrad/h at 27 cm from the read out end.

Fibre measurements were performed before and after irradiation using three different set-ups, which we will call Box1, Box2 and Box3. Box1 was used for comparative studies on 2.3 m long fibres, a length appropriate for use in the calorimeter. A single fibre was placed in a tray. The light was read out trough a plexiglass light guide followed by an XP2081B photomultiplier used in current mode. The photocathode sensitivity peaks at 450 nm and is sensitive up to 650 nm. The read-out end of the fibres was polished by hand using fine sand paper. The opposite end was cut with a knife. Above the fibre a small carriage containing either an ultraviolet light source or a ^{90}Sr-β radioactive source was mounted. While the carriage moved along the fibre the signal of the photomultiplier was measured in current mode under computer control. The 256 nm utraviolet source directly excites one of the secondary emission media in the fibre, unlike to the radioactive source, which excites the fibre base material (polystyrene). For SCSN38 fibres we checked (using Box3) that the detected wavelength spectrum, and therefore the attenuation length of the fibres, is independent of the type of source used. The ultraviolet source has a much higher intensity, and therefore a better signal to noise ratio. The stability of the UV source was checked using a photodiode and appeared to be better than 0.2%. Nevertheless for irradiated fibres the UV lamp is not adequate since the UV light can be absorbed in the irradiated cladding material. The effect of irradiation would be overestimated. Therefore, the UV sorce was used only for the comparative measurements of non-irradiated fibres.A Kodak wratten #3 filter, which cuts off wavelengths below 450 nm was mounted between the light guide and the photomultiplier. For better reproducibility all optical contacts were made in air without using optical grease.

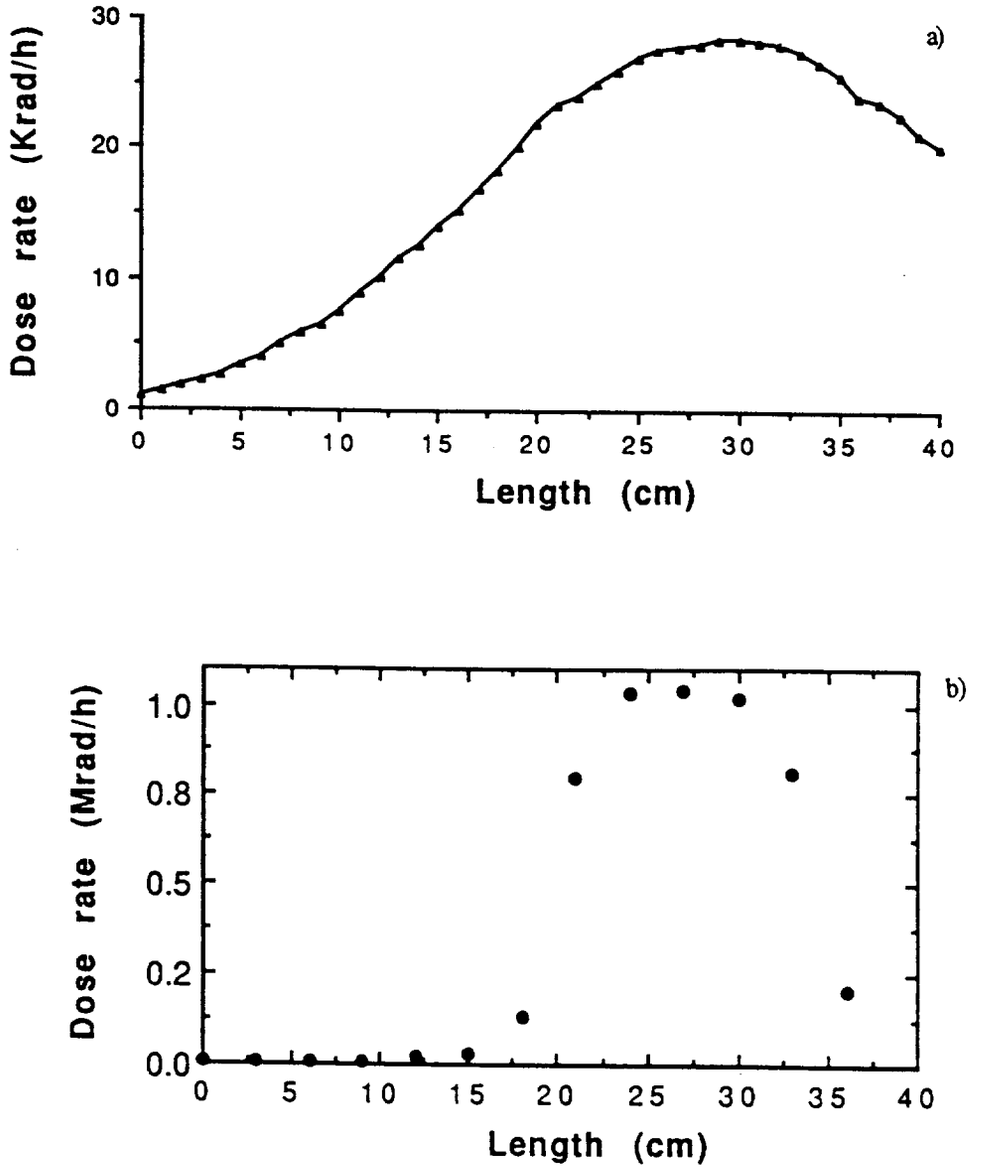


Fig. 1a,b - Dose rate profiles of the two ^{60}Co-γ sources used for the irradiation tests.

In Box2 fibres of 40 cm length were tested. In this set-up the fibre to be tested was placed between two other fibres which were used for trigger purposes. The fibre being tested was held directly against the input window of an RCA 8850 photomultiplier equipped with a photocathode, whose sensitivity peaks at 360 nm and extends up to 600 nm. The box contained a ^{90}Sr-β source could be moved along the fibres. This set-up allowed to perform single photoelectron counting, and is the most suitable when absolute scintillation ligth measurement is wanted, and when the number of photoelectrons produced at the photocathode is small. The efficiency of the set-up was determined from the ratio of the number of coincidences of all three fibres in the set-up and the number of coincidences of the trigger

fibres. It was found to be ≈98% independent of the position along the test fibre.

The third set-up (Box3) was intended to measure the fibre wavelength spectra. It is described in detail in ref. [4]. In this set-up the fibre to be tested was illuminated from the side by a 337 nm Nitrogen laser, which emits light pulses of 0.8 ns duration. The light emitted by the fibre was detected by a photodiode. A fraction of the laser beam was directed to a second photodiode for calibration purposes. The advantage of a laser beam is the large amount of light available (0.7 mJ per pulse), which allows measurements of the wavelength spectrum with a monochromator.

3 Fibre selection and wavelength spectra.

Companies producing or developing scintillating plastic fibres were requested to supply samples. Over the past few years the fibre quality in terms of attenuation length and radiation hardness has improved continuously. We have been including new products each time new tests that were undertaken, which explains the varying choice of fibre types for the different radiation tests described in this paper.

Box1 was used to test the suitability of the different types of non-irradiated fibres for our calorimeter. Fig. 2 shows an attenuation curve as measured in Box1 for a non-irradiated Kyowa SCSN38 fibre[1]. The curve clearly shows a steep attenuation of light in the first 60 cm from the emission point and a slower decrease at longer distances. This phenomenon may come both from the fast absorption of low wavelength components and from the light produced at large angles and reflected on the cladding-air interface[4,7]. In fig. 2 the first effect is almost absent since we are using a yellow filter wich absorbs the short wavelengths (<450nm).

For comparative studies, the light output measurements of a number of polystyrene fibre types were fitted to eq. (1) for distances between 60 cm and 215 cm. The average result for I_0 and λ_{att} as well as the σ_{RMS} of these quantities over samples of 20 fibres are shown in fig. 3. The experimental results depicted in fig. 3 refer to fibres supplied by industry in the first half of 1989. Only fibres with an attenuation length above 3-4m are suitable for use in the calorimeter. The prototypes of our fibre calorimeter described in [3,5,6] contain SCSN38 fibres apart from an additional test module containing polystyrene fibres doped with 3HF + PTP. This choice was mainly dictated by the availability of fibres at the time of the construction.

Fig. 4 shows the wavelength spectra of three types of fibre before and after irradiation with the "very high intensity" dose profile (fig. 1b) . The spectra were measured in Box3 and were corrected for the sensitivity of the photodiode. The laser beam was directed at the point of maximum damage (9.5 Mrad) and the fibres were read out from the end closest to the damaged region. This means that the curves shown in fig.4 represent the emission spectra combined with the transmission effect along 13 cm of the irradiated fibre. No yellow filter was used. In fig. 4a and fig. 4b the measured spectra of SCSN38 and SCSN81 fibres, respectively, are shown. The spectrum of the non-irradiated fibres ranges from 400 to 560 nm (blue fibres).

[1]Kyowa Gas, now Kuraray Co Ltd, Tokyo, Japan.

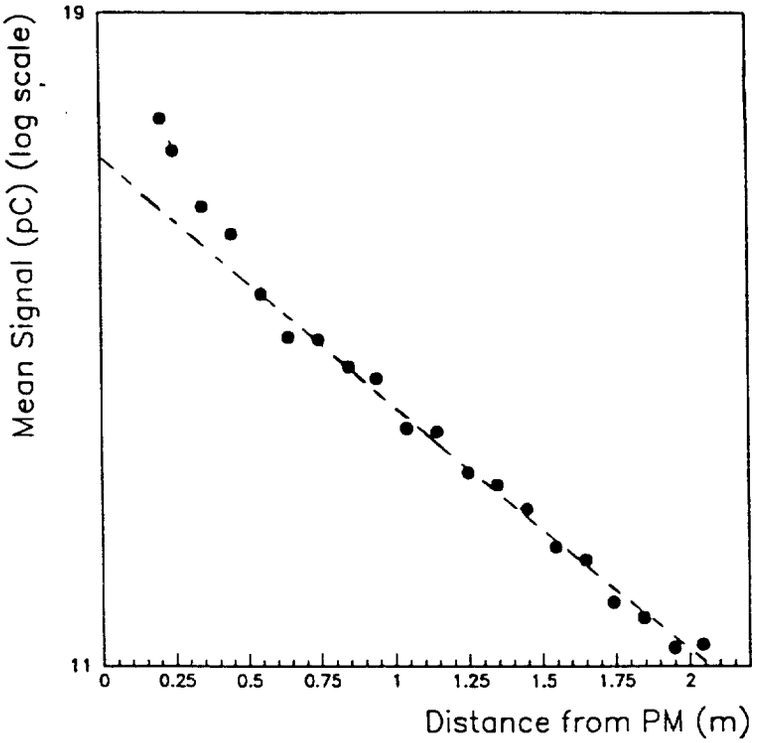


Fig. 2 - Pulseheight of an SCSN38 fibre without mirror as a function of the distance to the photomultiplier. A yellow filter was inserted between the fibre and the photomultiplier.

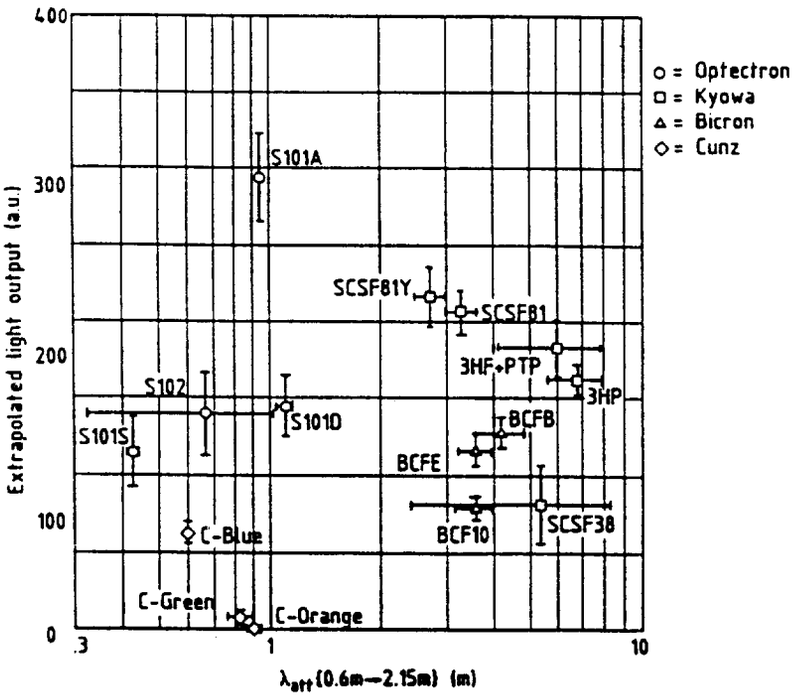


Fig.3- Average light output I_0 versus attenuation length for several types of fibres as obtained from a single exponential fit to the measured pulseheights between 60 cm and 215 cm from the photomultiplier. Each point represents an average of 20 fibres and the error bars give the σ_{RMS} of these quantities. A yellow filter (<450 nm) was inserted between the fibre and the photomultiplier.

From the spectrum of the irradiated fibres, it is seen that the radiation mainly affects the short wavelengths. In fig. 4c the spectra are shown for a polystyrene fibre doped with 0.02% 3HF and 0.01% PTP (yellow fibre). It is seen that the non-irradiated spectrum is centered at a higher wavelength (500nm-650 nm), which makes these fibres much more resistent to radiation. This can be seen from fig. 5 which is derived from the spectra shown in fig. 4. Fig. 5 shows the ratio of the pulseheights of the irradiated and non-irradiated fibres as a function of the wavelength. Above 500 nm this ratio is typically 75% for both SCSN81 and 3HF+PTP fibres and 40% for SCSN38 fibres. Below 500 nm the ratio goes down to 30% for SCSN81 fibres and 15% for SCSN38 fibres at 425 nm.

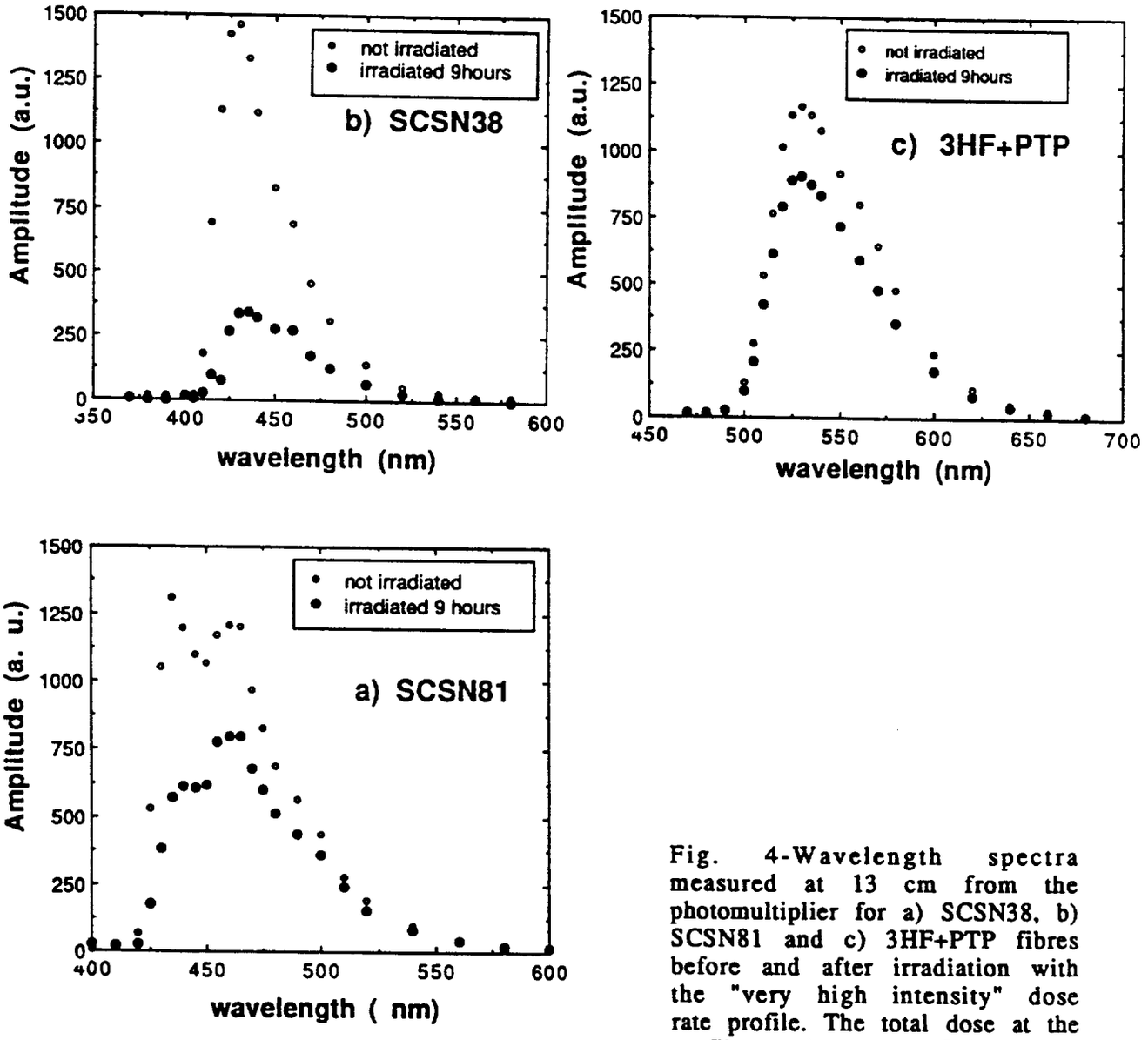


Fig. 4-Wavelength spectra measured at 13 cm from the photomultiplier for a) SCSN38, b) SCSN81 and c) 3HF+PTP fibres before and after irradiation with the "very high intensity" dose rate profile. The total dose at the profile maximum was 9.5 Mrad.

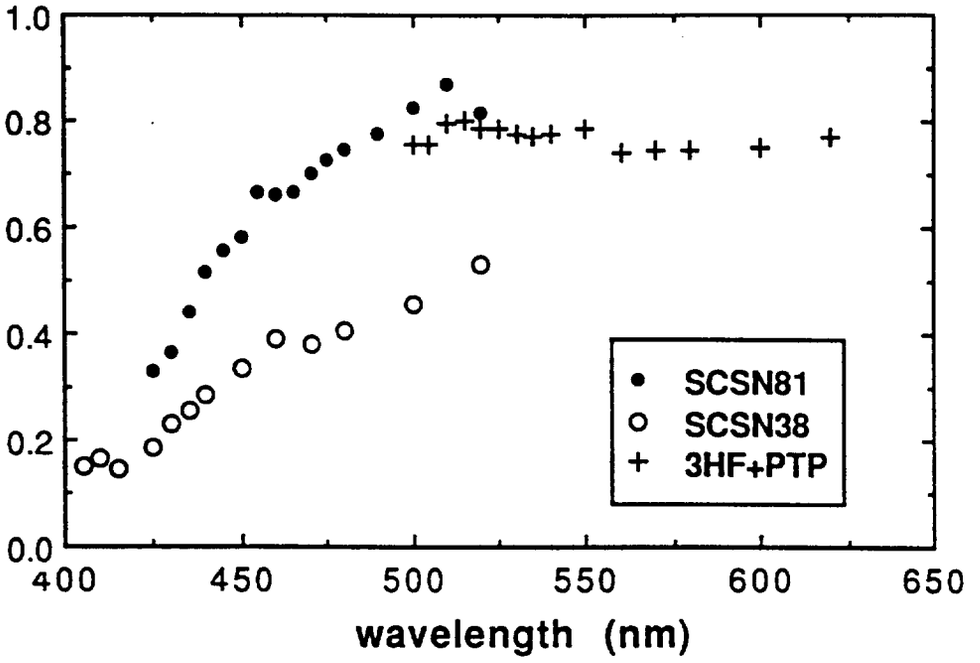


Fig.5-The ratio between the pulseheights of irradiated and non-irradiated fibres as a function of the wavelength for SCSN38, SCSN81 and 3HF+PTP fibres after an applied dose of 9.5 Mrad at the peak of the dose profile.

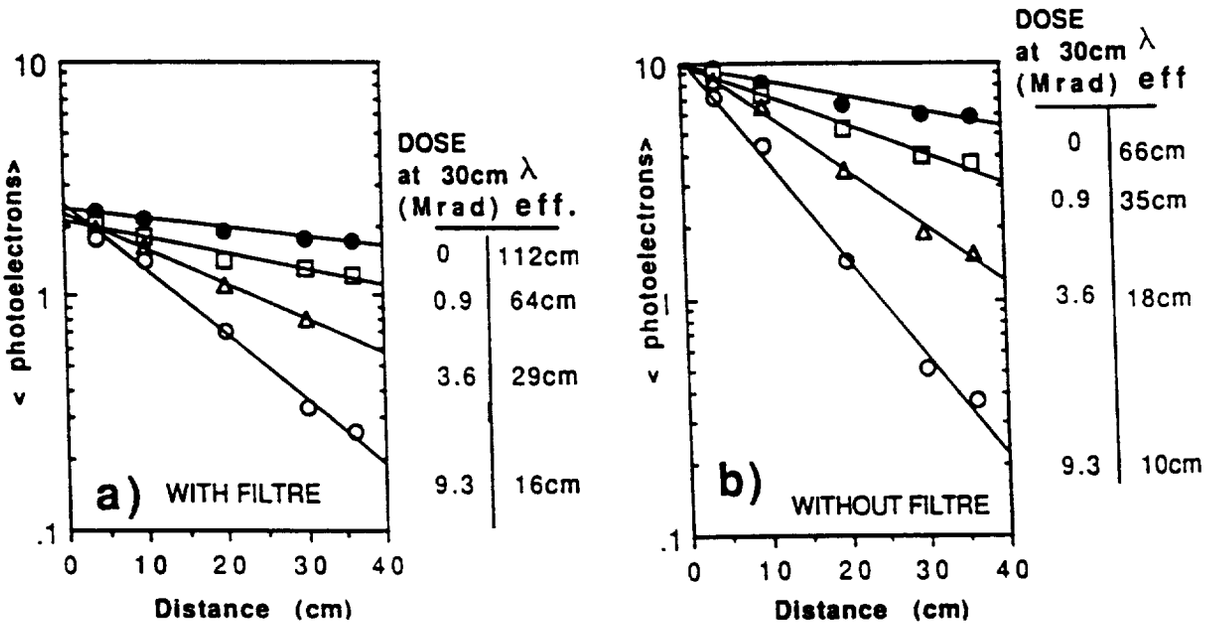


Fig. 6 Number of photoelectrons detected as a function of the position along the fibre a) using a yellow filter between the fibre and the PM b) without filter. the filter (wratten #3) cuts roughly 77% of the scintillation spectrum but roughly doubles the effective light attenuation length.

The use of a yellow optical filter will result in an artificial improvement of the radiation hardness of the blue fibres (SCSN38, SCSN81, S101A) at the expense of the total quantity of light observed (not a critical parameter in our design). This effect is shown in fig. 6 for SCSN38 fibres irradiated in the "normal intensity" source (Fig. 1a) at doses at the peak of the profile during 31, 119 and 311 hours. This corresponds to doses at the peak of the profile of 0.9, 3.6 and 9.3Mrad respectively. Although the irradiation is not uniform along the fibre, single exponential fits were used. The extrapolation to z=0 shows that the wratten #3 filter cuts roughly 77% of the emission spectrum, mainly in the blue region. The transmitted (yellow) light is however less attenuated, roughly by a factor of 2 both before and after irradiations.

4 The influence of the medium surrounding the fibres.

The fibre damage due to radiation and in particular an eventual recovery of the damage is influenced by environmental effects. In existing lead scintillating fibre calorimeters, like the calorimeters Omega and NA38 [10], glue (Araldite F) was used to aggregate fibres to preformed lead sheets. As the use of glue may facilitate the construction of calorimeter modules, the influence of glue surrounding the fibres was tested at an early stage. For these tests S101A and S101(UA2)[2] fibres were used. The manufacturer informed us that these two types of fibres differ only in their cladding composition. For these tests fibres covered with Araldite F glue were compared with fibres without glue. The glue was applied on the central part of 40 cm long fibres, from a distance of 17 cm to the PM to a distance of 34 cm. The light output was measured in Box2 at distances of 10 cm and 36 cm from the PM, outside the region of the glue. We observed that the glue does not influence the transmission for non-irradiated fibres. The fibres were irradiated by the "normal intensity" source during a total of 115 hours, which corresponds to a dose of 2.8 Mrad at 36 cm from the end read by the PM. The irradiation was interrupted several times for about 10 minutes to remeasure the light output. The light output after irradiation was compared to the light output before irradiation and the results for the point at 36cm from the PM are shown in fig. 7a,c. After irradiation the fibres were left in air and the light output was remeasured several times. For the point 10cm away from the PM the fibres do not present any difference in light detected, as expected.

From fig. 7 we can conclude that this glue enhances the damage to the fibres under irradiation. This effect is much more important for S101(UA2) fibres than for S101A fibres. Furthermore the S101A fibres show recovery effects, which are absent for the S101(UA2) fibres. We observed that the S101(UA2) fibres covered with glue turned brown under irradiation, whereas the S101A fibres became only a bit yellow. This colouring effect did not disappear for the S101(UA2) fibre after the irradiation, while the colouring of the S101A fibre seemed to fade away. As the two fibre types differ only in the cladding material, the impact of the glue has to be attributed to its interaction with the cladding. The above results made us decide to refrain from using glue around the fibres in the construction of the calorimeter.

---

2 Optectron , France

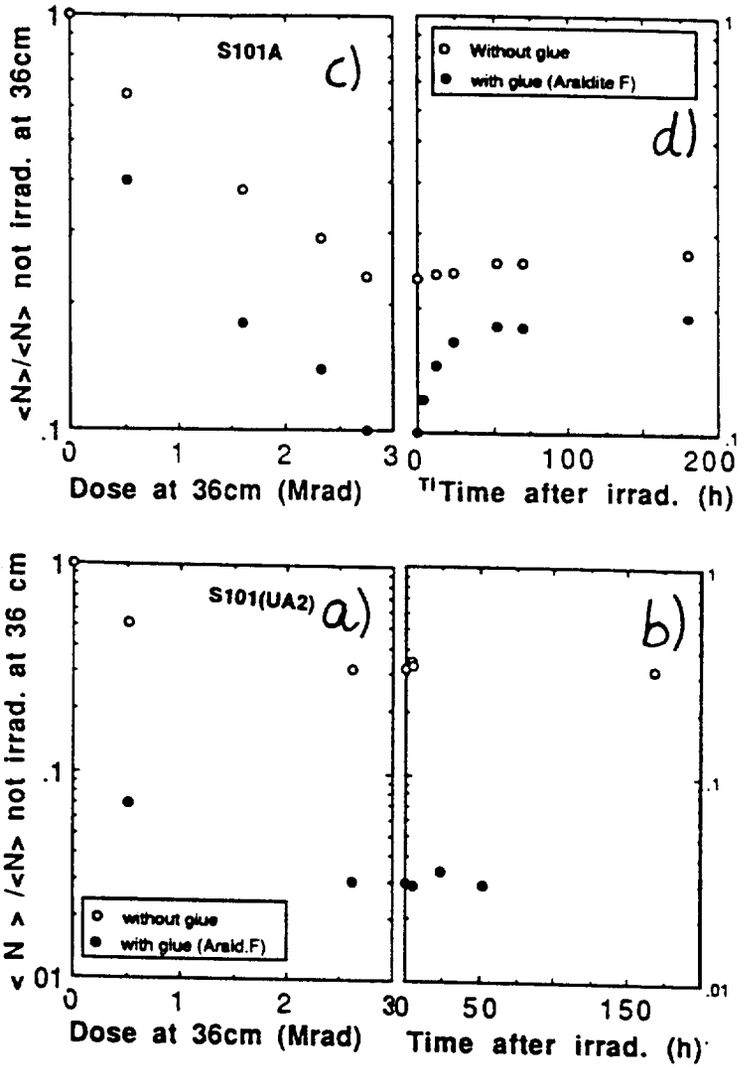


Fig. 7-The effect on light transmission for fibres with (0) and without (0) glue (Araldite F) before and after irradiation. The average number of photoelectrons <N> at 36 cm from the PM divided by the number before irradiation is given as a function of the dose (at 36 cm) for two types of fibres, a) S101A and c) S101A(UA2). After 2.6 Mrad (at 36 cm) the fibres b) S101A and d) S101A(UA2), were taken away from the source and were removed from the source and were remeasured several times. The light output rom the S101A fibre covered with glue shows some recovery, with a time constant of ~ 10 h.

Further tests on environmental effects concern the influence of the surrounding gas. For this purpose, S101A fibres were irradiated with the "normal intensity" source (fig.1a) in either air or a vacuum. The total dose at the maximum of the profile amounted to 3.5 Mrad. The light output at 10 cm from the dose maximum was measured in Box2 before and after irradiation as shown in fig. 8. The response of the fibres irradiated in air dropped by 20%. Those fibres show no recovery effect after irradiation. The fibres irradiated in vacuum initially lost 95% of their response, but recovered most of it when exposed to air, after the end of the irradiation.

After 45 minutes of recovery in air, the response rose to 28% of the value before irradiation, and 5 days later we measured 75%, after which the recovery process seemed to stop. From these results we conclude that fibres

irradiated in air recover continuously from some of the radiation damage in such a way that for dose rates inferior to 30 krad/h an equilibrium situation holds. After the irradiation is stopped the observable fraction of the loss is stable and does not recover further. Fibres irradiated in vacuum did not recover during the irradiation and even after a later recovery in air the final fractional loss was bigger.

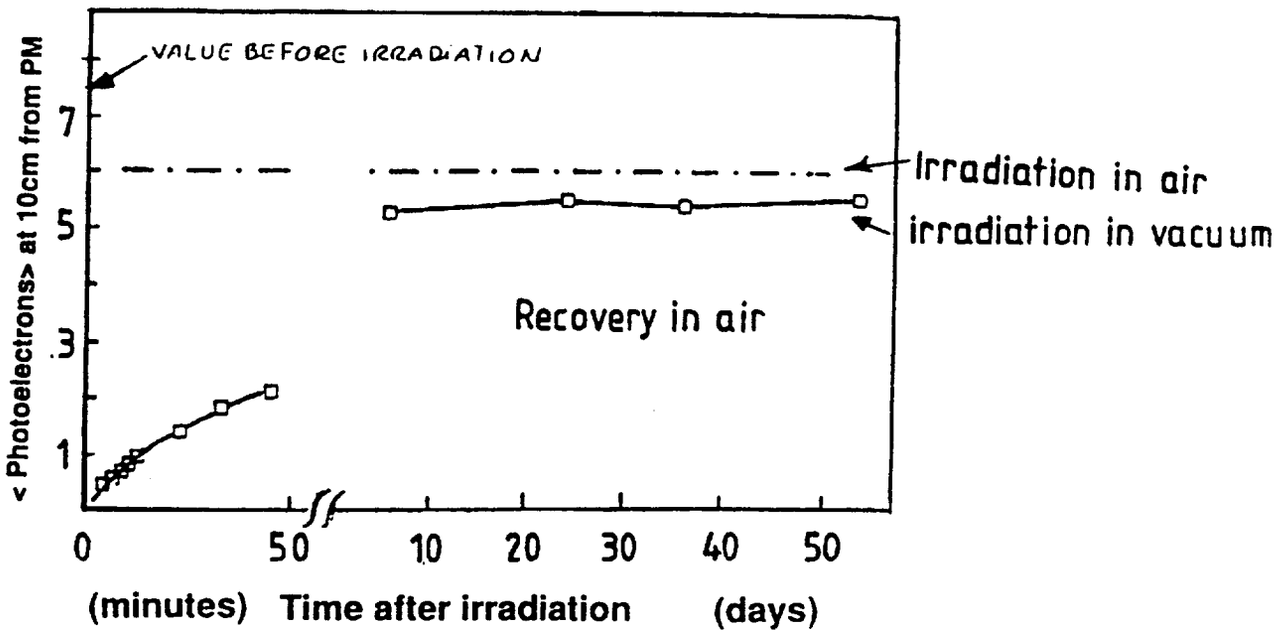
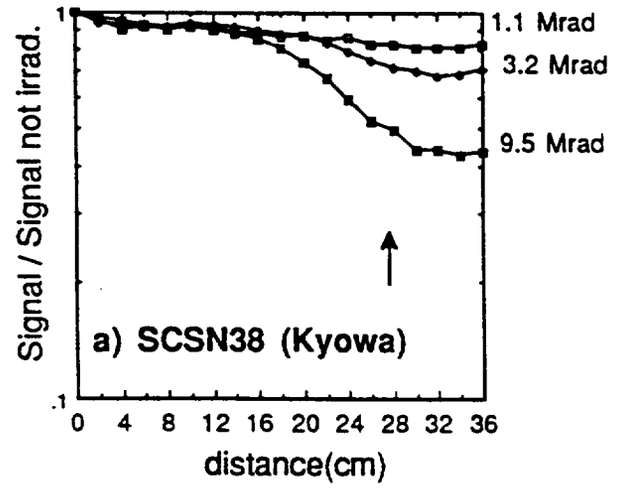


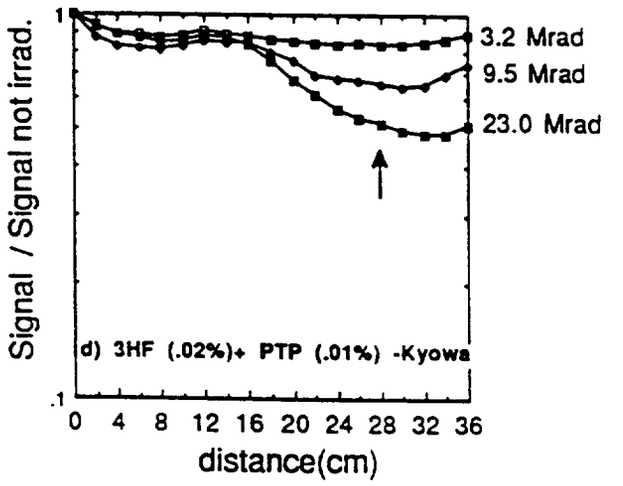
Fig. 8-The effect of the gas surrounding the irradiated fibre. The average number of photoelectrons <N> at 10 cm from the light detector is given as a function of the recovery time after a 2.8 Mrad dose for two S101A fibres, one irradiated in air and one in a vacuum. The recovery took place in air for both fibres.

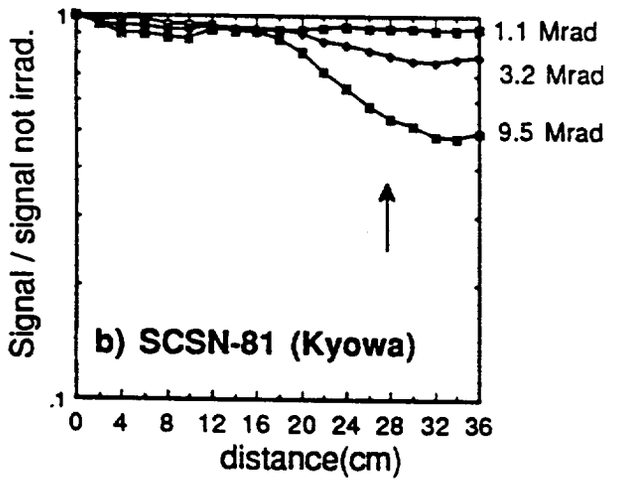
5 Comparative studies of radiation hardness.

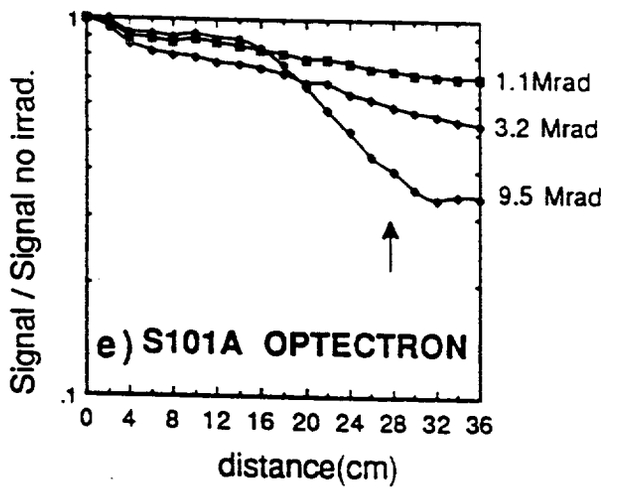
In this section we present a comparative study of the radiation hardness for 5 types of fibres. The fibres were irradiated according to the "very high intensity" radiation profile (fig 1b) with a maximum dose rate of 1.05 Mrad/h at 30 cm from the PM. Total doses of 1.1, 3.2, 9.5 and 23 Mrad were applied. The measurements were carried out in Box2. A yellow filter was used for the measurements. Fig 9 shows the attenuation curves for 5 types of fibres: SCSN38, SCSN81, S101(UA2), 3HF and 3HF+PTP. The curves were normalised at each position to the response for non-irradiated fibres. From fig. 9 we see that the 3HF+PTP fibres are the least damaged. To quantify the local loss in light emission and light transmission for the different types of fibre as a function of the dose we apply a very simple mathematical model which roughly fits the data.

It assumes that the scintillation light produced in the fibre decreases exponentially with the local dose:









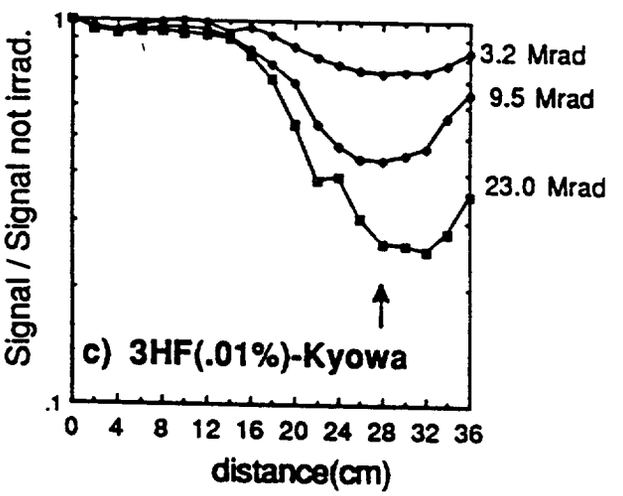


Fig. 9. Pulseheight as a function of the distance to the light detector for five different types of fibres, a) SCSN38, b) SCSN81, c) S101A, d) 3HF and e) 3HF+PTP. The curves measured after irradiation by doses up to 23 Mrad at the maximum of the profile are normalised at each position to the response of the same fibre before irradiation. The lines are meant to guide the eye.

$$I(0,D) = I_0\, e^{-D(z)/\gamma}\,, \qquad (2)$$

where D(z) is the dose at position z along the fibre, and I(0,D) is the light emission in the absence of radiation.

The local loss in transmission is parametrised as:

$$k(z) = k_0 + \alpha\, D(z), \qquad (3)$$

where $k(z) = 1/\lambda_{att}(z)$, and $k_0 = 1/\lambda_{att}$ in the absence of radiation, as in eq.(1). We then use the following expression to fit the measured light output:

$$I(z,D) = I_0\, e^{-D(z)/\gamma}\, .e^{-k0z}\, .e^{-\alpha\int_0^z D(z')dz'} \qquad (4)$$

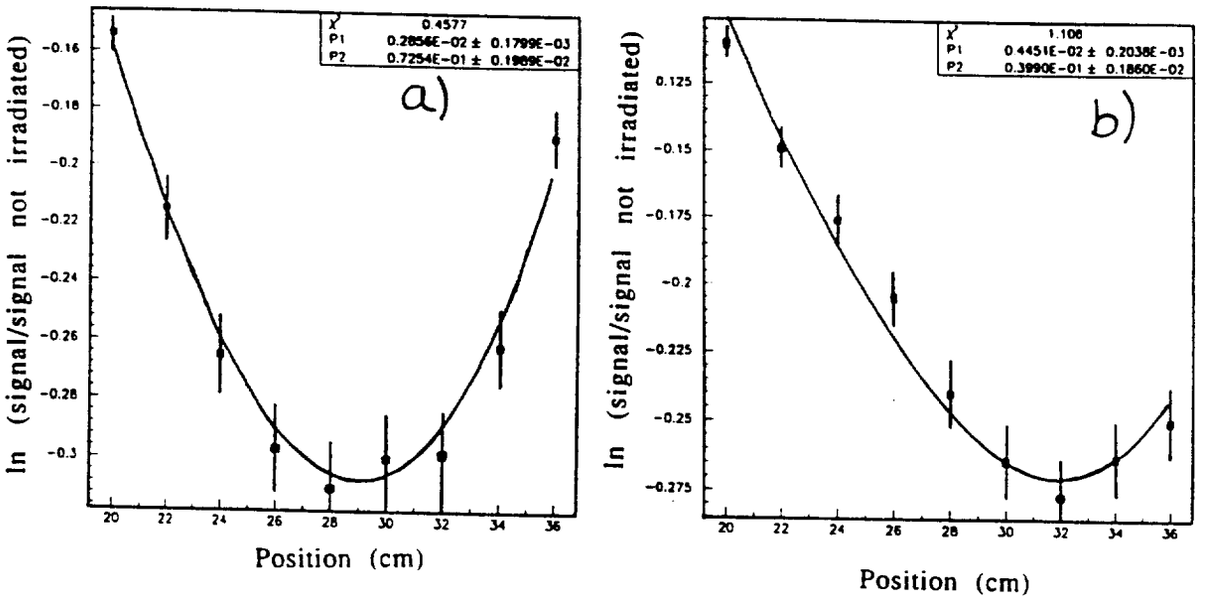


Fig. 10-Example of two fibres irradiated with a dose of 3.15 Mrad at the peak of the profile, a) 3HF losing essentially emission and b) SCSN81 losing essentially transmission. The curves represent the best fit to a model describing the decrease in light emission (γ) and in light transmission (α) as a function of the dose.

The very inhomogeneous dose of Fig. 1b rendes the coefficients of $1/\gamma$ and α, i.e. dose D(z) and its integral from the point of light emission to the phototube, respectively, sufficiently different to estimate separately the light emission and transmission effects. γ is the dose for wich light emission is reduced to 1/e. α is related to the light absorption caused by irradiation.

In this simplified model, if the loss in transmission is negligible (α=0), the logarithm of the light output scales with the dose profile. This is illustrated in fig. 10 for two types of fibres, 3HF and SCSN81, both irradiated by a 3.2 Mrad dose. The 3HF fibre has a small transmission loss, and shows mainly an emission loss after irradition correspondingly, the fractional loss in output follows closely the irradiation profile D(z). The SCSN81 fibre has a

better emission resistance but a worse transmission and the maximal loss in light output (at z~32cm) occurs well beyond the dose maximum (z~27cm). In general one observes that the yellow fibres (3HF and 3HF+PTP) lose more in emission meanwhile the blue fibres (SCSN38, SCSN81, S101A) lose essentially on transmission.

In table 1 are presented the fitted values α and γ when only the data points in the irradiated region are considered (z>15cm) and in a first approach the light output values are normalised to 1 at the point closest to the photomultiplier. However looking at fig.9 one observes that the non irradiated fibre region (z<15cm) is also damaged. This effect is so far not understood and does not seem to scale with the applied dose. So, in a second aproach the base line for each fibre was redefined as the average ratio in the non-irradiated part (0-15cm), and a new set of α and γ values (table 2) was obtained. Although for each fit the typical errors on α and γ are in the 5%-10% range, by comparing table 1 and table 2 one sees that the uncertainty on γ due to the unknown baseline is much bigger, up to a factor of 1.8, when the 1/e dose γ is much larger than the delivered dose D.

	SCSN38		SCSN81		S101A		3HF		3HF+PTP	
$Dose_{peak}$ (Mrad)	α (Mrad-1cm-1)	γ (Mrad)	α (Mrad-1cm-1)	γ (Mrad)	α (Mrad-1cm-1)	γ (Mrad)	α (Mrad-1cm-1)	γ (Mrad)	α (Mrad-1cm-1)	γ (Mrad)
3.2	6.5×10^{-3}	20.0	4.5×10^{-3}	25.1	-	-	2.8×10^{-3}	13.7	1.2×10^{-3}	18.2
9.5	5.1×10^{-3}	28.9	4.6×10^{-3}	39.4	6.5×10^{-3}	21.3	1.8×10^{-3}	14.5	1.4×10^{-3}	27.9
23.0	-	-	-	-	-		2.3×10^{-3}	25.8	1.4×10^{-3}	51.9

Table 1 - Values of α and γ obtained for several types of fibres using a mathematical model for the damage on the transmission and emission of light. Each kind of fibre was irradiated 1, 3, 9 hours (SCSN38, SCSN81, S101A) or 3, 9, 22 hours (3HF, 3HF+PTP) corresponding to 1.1, 3.15, 9.5, 23.0Mrad at the maximum of the dose profile.

	SCSN38		SCSN81		S101A		3HF		3HF+PTP	
$Dose_{peak}$ (Mrad)	α (Mrad-1cm-1)	γ (Mrad)	α (Mrad-1cm-1)	γ (Mrad)	α (Mrad-1cm-1)	γ (Mrad)	α (Mrad-1cm-1)	γ (Mrad)	α (Mrad-1cm-1)	γ (Mrad)
3.2	6.1×10^{-3}	37.4	4.1×10^{-3}	54.7	-	-	2.6×10^{-3}	16.3	-	-
9.5	5.0×10^{-3}	38.5	4.5×10^{-3}	71.4	6.3×10^{-3}	26.5	1.7×10^{-3}	15.7	1.0×10^{-3}	52.4
23.0	-	-	-	-	-	-	2.3×10^{-3}	28.0	1.3×10^{-3}	71.8

Table 2 - Values of α and γ as obtained in table 1 but corrected to the base line shift in the non-irradiated part (from 0-15cm).

In table 1 and table 2 one observes a systematic increase of γ with increasing dose. Since the simplified model described by eq. 2 and 3 does not take in account any wavelength dependence, it is expected that α and probably also γ [11, 12] vary with dose due to the fact that the irradiated fibre spectra are shift to larger wavelengths (fig.4).

A problem which is not fully taken care of in the results shown so far, all based on short (~40cm) fibres, is the possible contribution of a light component of short attenuation length which is negligible in long fibres. As we saw from fig. 2, a non irradiated 2m fibre shows a steeper decrease of light in the first 50 cm than in the last 1.5m, even when a yellow filter is used. The points of fig. 2 are well described by the sum of the two exponentials, with attenuations lengths of 0.166m and 4.7m respectively. If a fit to a single exponential (eq.1) is done from 0 to 60 cm and from 60 to 200 cm, we obtain λ_{att}=2.4 m and λ_{att}=4.7 m respectively. Clearly, there is a light component which is fully absorbed after typically 0.5 m and is also less radiation hard as we will see in fig. 11.

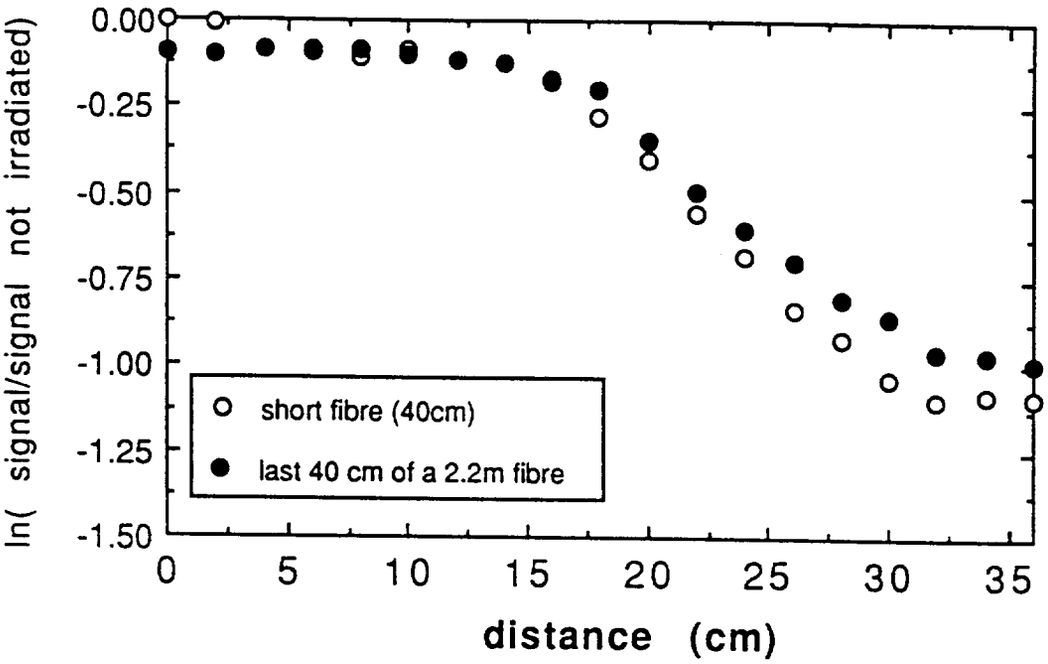


Fig. 11 Comparison of the irradiated region of a S101A fibre when the light produced on irradiated region has to travell a) a long way through a non irradiated region of the fibre or b) is detected imediately after the irradiated region. The last 20 cm of the fibre were irradiated in the inhomogeneous dose profile of fig.1b with 9.5 Mrad at the maximum of the peak.

The last 40 cm of a long (2.2m) S101A fibre were irradiated in the inhomogeneous dose profile of fig.1b. The rest of the fibre got a negligible dose. The signal measured in the last 40 cm of the fibre (180 cm - 220 cm) normalized to the non-irradiated signal is presented in fig. 11 (closed circles). *The measurement was done with a yellow filter and without mirror.* The fibre was then cut at 180 cm from the PM and the last 40 cm were

remeasured (open circles). For the long fibre the fitted values of α and γ in the irradiated region are 0.0057 $Mrad^{-1}cm^{-1}$ and 24.8 Mrad respectively. After cutting the fibre the values obtained for the remaining 40 cm are α=0.0065 $Mrad^{-1}cm^{-1}$ and γ=21.3 Mrad respectively. So for the long fibre the results are typically 15% better. This can be due to two effects. First, the light emitted at short wavelength is less radiation hard (see section 3) and is absorbed faster than the light emitted at high wavelength, even for the non irradiated fibre. As the light produced close to the PM has a higher short wavelength content it is therefore less radiation hard. This effect is partially reduced when a yellow filter is used. The second effect originates from the light travelling in the cladding. If the cladding becomes more opaque under irradiation, the cladding light will be absorbed even more quickly. This effect will be enhanced in short fibre.

This study emphasises the importance of performing radiation damage studies in realistic conditions. For hadronic calorimetry the fibres under study should be about 2m long. If the S101A fibre are taken as a representative example the results described in table 1 are pessimistic by about 15%.

6. Comparative study of radiation damage from neutrons and γ-rays

Several samples of S101 OPTECTRON fibres, 47 cm long, have been irradiated uniformly in a ^{60}Co γ-source and in the R. P. I. nuclear reactor. The dose distribution in the Co source was not uniform, and the fibres were therefore curled around circles of 15cm diameter and turned around periodically in order to achieve a homogeneous dose over the full fibre length. The total doses ranged from 250Krad to 2Mrad. For uniform irradition in the pool type reactor fibres curled around a 15cm circle were inserted into a water-proof box made of vaulinex material. The reactor flux composition in the place where the fibres were irradiated was the following:

Thermal neutrons:		$F_{thn} = 5.5 \times 10^9$ kW^{-1} cm^{-2} s^{-1}
Epithermal neutrons:	(E~1 eV)	$F_{epn} = 2\%\ F_{thn}$
Fast neutrons:	(E>1MeV)	$F_{fn} = 7.0 \times 10^8$ kW^{-1} cm^{-2} s^{-1}
Gamma rays:	(E~1 MeV)	$DR_\gamma = 3.4 \times 10^4$ kW^{-1} rad h^{-1}

where F and DR stands for flux and dose rate. The following flux-dose rate conversion factors for hydrocarbons have been used:

Thermal neutrons:	$DR_{thn} = 1.67 \times 10^{-6}\ F_{thn}$
Epithermal neutrons:	$DR_{epn} = 2.4 \times 10^{-5}\ F_{epn}$
(0.5 eV < E < 0.1 MeV)	
Fast neutrons:	$DR_{fn} = 1.54 \times 10^{-5}\ F_{fn}$

The flux and dose rate are given in $cm^{-2}\ s^{-1}$ and rad h^{-1} respectively and the total dose rate is 57 kW^{-1}krad h^{-1} (15.8 kW^{-1} rad s^{-1}) with 17 % of thermal neutrons, 5% of epithermal neutrons, 19% of fast neutrons and 59% of photons. Since the irradiations have been made at 1 kW, 10 kW and 100 kW, the total absorbed dose rates were 57 krad/h, 570 krad/h, and 5.70 Mrad/h. The total absorbed doses ranged from 44 krad up to 8.8 Mrad.

Fibre measurements were carried out in box 2 and all the results presented in this section were obtained from *measurements without filter*. In order to compare all the results, experimental values for the number of photoelectrons N(z,D) are divided by the values before irradiation. Fig. 12 shows the light output for z=15cm, as a function of dose, for a wide range of dose rates ranging from 30 Krad/h for the ^{60}Co γ-source to 5700 Krad/h for the reactor mix of neutrons and photons at the highest reactor power level.

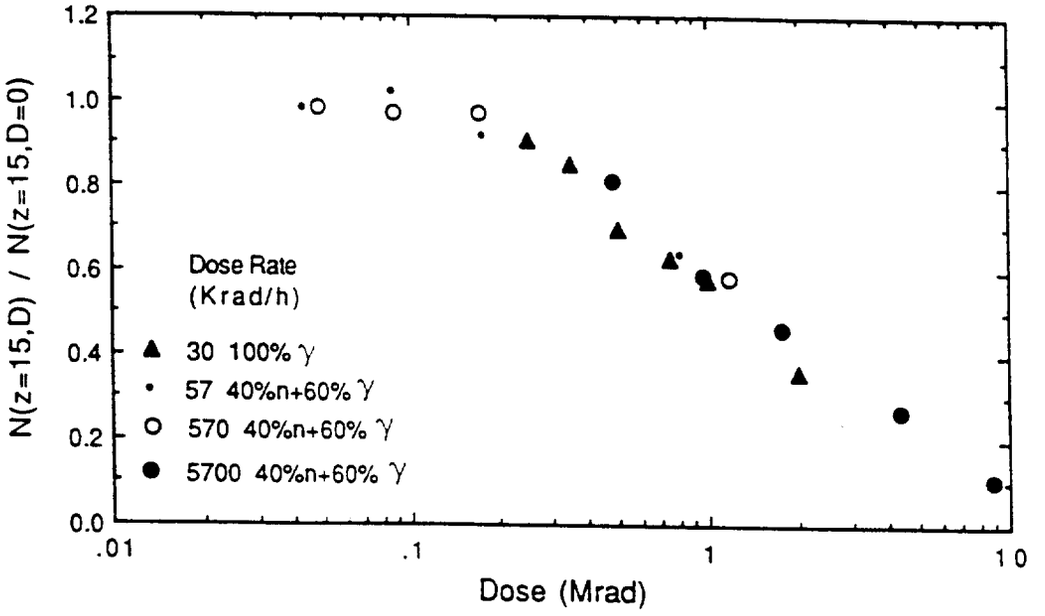


Fig. 12 - Average number of photoelectrons N(z,D) at 15 cm from the PM divided by the values before irradiation N(z,0) versus the dose. Fibres were irradiated in a reactor (n+γ) at different dose rates and in a ^{60}Co γ-source.

This figure shows firstly that the radiation damage, for S101 fibres for rather high dose rates, is remarkably independent from dose rate. This is borne out in particular for 1 Mrad total dose which was covered by the four dose rates used, all yielding the same 40% loss in light output. It further shows that the neutrons are not more harmful than photons, for the same fibre and range of dose rates. ^{60}Co photons even appear to produce slightly more damage than the reactor n+γ mix at the same total dose.

We proceed to try and separate light emission and ligth transmission damages. The method is still based on eqs 1 to 4, with the difference of the dose being homogeneous in space: D(z)=D, and of the approximation of wavelength independent α and γ beeing less justified without using a yellow

filter. The z-dependence of the light output is nicely exponential for each condition within the measured range 15cm <z< 40cm. The extrapolation to z=0cm is therefore interpreted as the light emission N(0,D). As fig. 13 shows, it decreases exponentially with dose D, and is reduced to 1/e for a dose $\gamma = 7$ Mrad, with good compatibility between photons and the reactor n+γ mix. The 1/e dose is noticeably smaller than the values of γ=20 Mrad (Table 1, 2) found for fibres of the same type exposed to inhomogeneous radiation fields and measured with yellow filter.

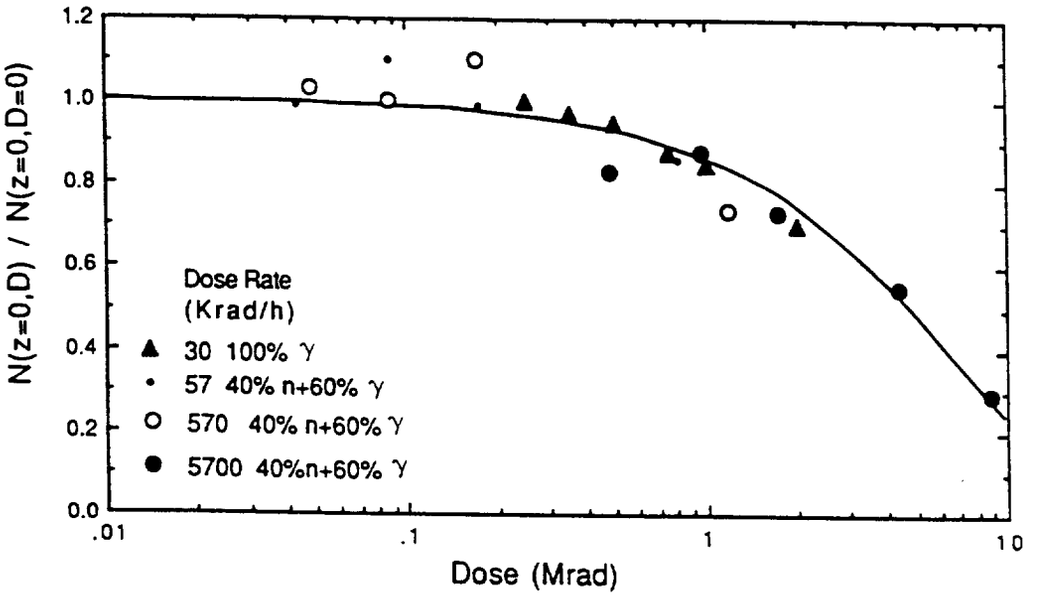


Fig. 13 - Average number of photoelectrons N(0,D) divided by the values before irradiation versus the dose. The values are taken from the extrapolation to z=ocm of the exponentials [N(z,D))/(N(0,D)] = exp(-kz) (eq.4), from z=15cm to z=35cm. Fibres were irradiated in a reactor (n+γ) at different dose rates and in a ^{60}Co γ-source.

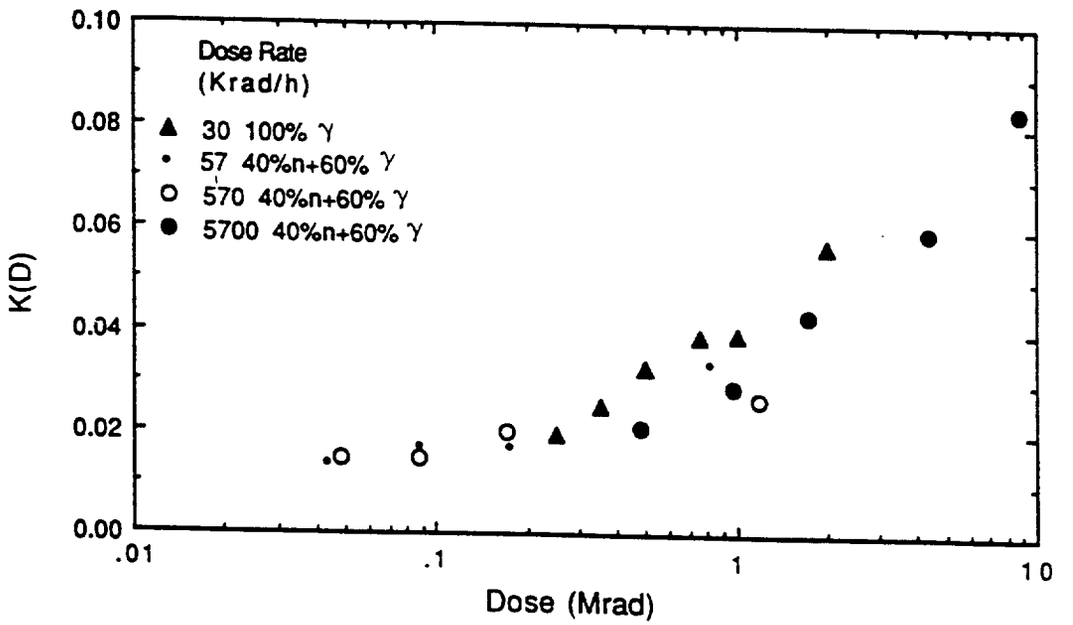


Fig. 14 - K=1/λatt versus the dose for fibres irradiated in a reactor (n+γ) at different dose rates and in a ^{60}Co γ-source. K(D) are the slopes of the exponentials in z [N(z,D))/(N(0,D)] = exp(-kz) (eq.4), from z=15cm to z=35cm.

The slopes of the exponentials $[N(z,D))/(N(0,D)] = \exp(-kz)$ (see eq.4) give k_0 and αD as a function of D. In fig. 14 we can see that α is not constant, but decreases with increasing D, and probably more for the reactor n+γ mix than for the ^{60}Co γ's. At 10 Mrad (n+γ) dose α is $0.007 Mrad^{-1}cm^{-1}$, while it is $0.02 Mrad^{-1}cm^{-1}$ for 2 Mrad γ's. We conclude at this stage that the method used does not really allow to separate the radiation effects on light emission and transmission.

7 Conclusions

We have measured the radiation damage in polystyrene based scintillating fibres under a number of different conditions. From these measurements we conclude that the radiation mainly affects the short wavelength components of the light and thereby the effect can be reduced by using a suitable optical filter. The use of Araldite F glue surrounding the fibres deteriorates the radiation hardness. Fibres irradiated in air show less radiation damage than fibres irradiated in a vacuum.

The radiation damage of fibres by γ-rays from a ^{60}Co γ-source and neutrons and γ-rays from a fission reactor was compared for the first time and found to be very similar. In the n+γ irradiations, where the dose rate was varied by a factor of 100, those effects are found not to depend on the dose rate.

For 5 types of fibres the loss in light output after irradiation with doses up to 23 Mrad was measured, and tentatively separated into a loss in light transmission and a loss in light emission. The 3HF and 3HP+PTP fibres have the smallest loss in light transmission, whereas the SCSN81 fibres show the smallest loss in light emission.

Two papers [8,9] study the degradation of the response to electrons and hadrons of a large SPACAL fibre calorimeter to be used in an LHC or SSC experiments. We infer from [8] that both for 3HF+PTP and SCSN81 fibres the energy resolution for 10 GeV electrons, which is of ~5.5% at 10 GeV and 2% at 150 GeV [3] before irradiation, would increase by~2-3% at both energies after irradiation by a maximum local dose of 10 Mrad. With more conventional fibres which were also studdied, the degradation in energy resolution would be several times worse. These studies are preliminar and consider only the dominating damage due to the neutral energy deposition, mainly π0's.

References

[1] - Radiation Levels in SSC Interaction Regions, report SSC-SR-1033, D.E. Groom, editor (1988).
[2] - R. Wigmans, Nucl. Instr. and Meth. A259 (1987) 389.
[3] - D.Acosta et al., Nucl. Instr. and Meth.. A294 (1990) 193
[4] -F.G. Hartjes and R. Wigmans, Nucl Instr. and Meth. A277 (1989) 379.
[5] - DeSalvo et al., Nucl. Instr. and Meth. A279 (1989) 467.
[6] - D.Acosta et al. "Electron Pion Discrimination with a Scintillating Fibre Calorimeter" CERN/LAA/HC/89-004, submitted to Nucl. Instr. and Meth.
[7]- C.M. Hawkes et al., Nucl. Instr. and Meth. A292 (1990) 329.

[8] - D. Acosta, "The Effects of Radiation Damage on a Scintillating Plastic Fiber Calorimeter", LAA preprint, (1989)
[9] - J.Badier "Electromagnetic Shower Resolution in a Scintillating Fiber Calorimeter", Proceedings of the Workshop on Radition Damage of Plastic Scintillators, Tallahassee (1990).
[10] - P.Sonderegger, Nucl. Instr. and Meth. A257 (1987) 523.
[11] - S. Majewski, Radiation damage in plastic scintillators, in proceedings of the ECFA Study Week on instrumentation Technology for High-Luminosity Hadron Colliders, Barcelona September 1989.
[12] - K. Wick et al., Radiation Resistance of Scintillators, Wave-length Shifters and Light Guides, ZEUS - Note 87-045.

Acknowledgments

We thank the SPACAL/LAA collaboration, and the LIP/Lisbon group for permission to use unpublished data, and the Director and Staff of ICEN Lisbon for making the irradiations possible. We are very much indebted to the LAA project leader, Prof. A. Zichichi, for his warm interest and encouraging support for this project. This project is supported in part by Junta Nacional de Investigação Cientifica-JNICT.

HIGH AND LOW DOSE RATE IRRADIATIONS OF SCINTILLATORS AND WAVE LENGTH SHIFTERS

A.Dannemann, U.Holm,T.Marckmann,K.Wick
I.Inst.f.Experimentalphysik, Universität Hamburg,
Luruper Chaussee 149, D-2000 Hamburg 50 and
M.Rohde
Deutsches Elektronen-Synchrotron DESY,
Notkestr. 85, D-2000 Hamburg 52

1 Introduction

The calorimeter of the ZEUS detector[1] at the HERA collider consists of depleted uranium (DU) plates interleaved with plastic scintillators (SCI) SCSN-38[2]. The SCI are read out via wavelength shifters (WLS) Y-7 in PMMA with a UV absorber[2]. Both plastic materials have to withstand a radiation background from the collider, especially hadrons hitting absorbers, which has been estimated for stable machine operating conditions to about 100 Gy/a. Additionally they are exposed to the low dose rate of several ten Gy/year from the DU. Both the yield of the scintillation light and also the transmission through the material may decrease with an increasing dose and so lead to a degraded calorimeter resolution and homogeneity. Even the low DU radiation dose may strongly affect the quality of the optical components[3]. Therefore various investigations concerning the radiation stability of SCI and WLS have been carried out. The SCI have been irradiated with ^{60}Co-sources, a 25 MeV proton beam and, for very low dose rate investigations, plates of DU. The applied doses were 1, 10 and 24 kGy, the latter with dose rates between 30 and 1000 Gy/h. The DU radiation dose was 42 Gy with 1.6 mGy/h. The samples have been irradiated and stored under different atmospheres(e.g. air, oxygen, nitrogen, argon).

Diagnostic tools for the change in absorption length and loss in light yield were a spectrophotometer, and a movable UV lamp, witch can excite the different fluors seperately.

2 Short-term irradiations

The results of the short-term high dose rate proton and ^{60}Co irradiations show a very similar behaviour for quite different materials. The radiation induces additional absorption centers (free radicals) which shorten the absorbtion length of the scintillation light. No influence of the surrounding gas atmosphere on the type and concentration of the radicals was seen for dry air, nitrogen and argon[4]. Under an inert gas (Ar, N_2, CO_2) atmosphere after irradiation, one has a slow decrease of the density of the induced absorption centers (recovery) in the SCI SCSN-38, while for the WLS Y-7 and K-27 in PMMA no recovery at all is observed. In the presence of oxygen the free radicals form peroxide radicals which do not absorb the emitted light and one generally has a strong recovery of SCI and WLS to a permanent damage which is much smaller than the initial one. The recovery time constant strongly depends on the oxygen pressure, the thickness of the sample and the base material(diffusion constant, radical concentration) and is quite different for the polystyrene based SCSN-38 ($\sim$ 1 day, 2mm thick) and the acrylic WLS ($>$ 1 year, 2 mm thick). This can be well understood by a simple oxygen diffusion model [11]: the diffusion constant of polystyrene is about a factor ten higher whereas the created radicals per dose are 60 times more for PMMA (see chapter 5). Another radiation effect is the destruction of the dye molecules which leads to a reduced fluorescence efficiency.

The radiation induced additional absorption coefficient $\Delta\mu$, measured with a xenon lamp device, can be described by a sum of a time dependent term (recovery) and a constant term which describes the permanent damage. Both are proportional to the applied dose D (at least for our doses):

This work was supported by the German Federal Minister for Research and Technology (BMFT) under the contract number 05 5 HH 171.

$$\Delta\mu(D,t) = a \cdot D \cdot f(t) + b \cdot D, \quad (1)$$

where t is the time after the end of the short-term irradiation. The function *f(t)* with $f(t=0) = 1$ and $f(t=\infty) = 0$ describes the decay of the initial damage by diffusion of oxygen. The change $\Delta\mu(\lambda)$ of the spectral absorption coefficient , measured with a spectrophotometer, behaves in the same way.

Table 1 shows a summary of the high dose rate low term irradiations of SCSN-38, Y-7 and K-27. Irradiations with ^{60}Co and 25 MeV protons and measurements with the xenon lamp and the photospectrometer are compared. The results are compatible especially if one takes into account that the induced additional absorption coefficient $\Delta\mu$, measured with the xenon lamp, depends on thedifferent dimensions of the sample and on the fits to the attenuation curves, which also had been different.

For the ZEUS calorimeter follows that 10 years after operation in air the attenuation length of the SCI will change for about 5% which is unnoticeable for the only 20 cm long SCI. For the WLS Y-7 one expects in the direct vicinity of the beam pipe a loss of light transmission of < 17% for the longest (2 m) WLS.

The loss in SCSN-38 fluorescence light yield due to destroyed fluors is $(5-9) \times 10^{-4}\%$ Gy^{-1} for irradiation in dry air, measured with different methods and SCI thicknesses. In argon the loss is only half as big [12].

Table 1: *Summary of the high dose rate irradiations (see eq. 1 and 2). The applied doses were 24 kGy for the ^{60}Co exposure with rates of 1 - 10 kGy/h and 10 kGy with rates of 2 - 10 kGy/h for 25 MeV protons. The irradiation and storage has been performed in (dry) air. The fluor concentration of the WLS was 30 ppm Y-7 in PMMA and 100 mg/l K-27 in PMMA - except for the p irradiations where we had 47 ppm or 150 mg/l. The spectral absorption coefficient $\Delta\mu(\lambda)$ is shown for λ = 430 nm (SCSN-38) and 510 nm (WLS). All quantities are given in $10^{-6}cm^{-1}Gy^{-1}$*

		^{60}Co photospect.	^{60}Co xenonl.	25 MeV p xenonl.
SCSN-38	a or a (λ)	33 ± 3		(18 ± 1)
	b or b(λ)	2.4 ± 1.7	2.0 ± 0.2	1.1 ± 0.1
Y-7	a or a(λ)	5 ± 1	3.8 ± 0.5	5 ± 0.3
	b or b(λ)	1 ± 1	0.4 ± 0.1	$< (0.2 + 0.1)$
K-27	a or a(λ)	5 ± 1.2	4.7 ± 0.6	5 ± 0.3
	b or b(λ)	0.8 ± 0.8	0.7 ± 0.1	$< (0.2 + 0.1)$

3 Series investigations on radiation hardness

The SCI material for the ZEUS calorimeter has been produced in many production cycles (mixtures). To ensure that there are no differences in the radiation stability we have always investigated two samples (dimensions: $200 \times 50 \times 2.6mm^3$) of 38 production units. They have been exposed in air to 40 Gy from a ^{60}Co-source with a high dose rate of about 2 kGy/h and measured before and 4 weeks afterwards, when total recovery in air was reached, with the movable xenon lamp. Fig.1 shows the ratio of the light yields after recovery and before irradiation. From this curve the radiation induced additional absorption coefficient $\Delta\mu$ and the loss in light yield can be extracted. We have not tried to understand this curve completely and to develop a formula which describes its (non exponential) behaviour. Our only aim was to compare the different samples. For this we

have fitted all the curves in two different regions I and II (where they all could be fitted very well) with the functions:

$$L_i = A_i \cdot (e^{-\Delta\mu_i x} + Re^{-\Delta\mu_i(400mm-x)}) \; , i = \mathrm{I}, \mathrm{II} \tag{2}$$

R = 0.29 is the reflexion factor for an open SCI end. The only two parameters A and $\Delta\mu$ describe the reduced flourescence yield or the additional absorption coefficient.

Fig.2 shows the induced absorption coefficients $\Delta\mu$ for region I (upper curve) and region II. The "error bars" represent the difference of the two samples of one cycle. The variations of the absorption coefficient $\Delta\mu$ between the cycles are comparable to the spreads within the cycles. The mean value and the spread of all cycles are for region I (near the read-out edge):
$\Delta\mu_{\mathrm{I}} = (3.6 \pm 0.4) \cdot 10^{-3} mm^{-1}$
and for region II:
$\Delta\mu_{\mathrm{II}} = (2.3 \pm 0.3) \cdot 10^{-3} mm^{-1}$ for a dose of 40 kGy.
The ratio $b = \Delta\mu_{\mathrm{I}}/D = 0.9 \cdot 10^{-6} cm^{-1} Gy^{-1}$ (see eq.1) is in good agreement with the previous measurements performed with much smaller SCI samples[7].
The radiation-caused reductions in light yield have been calculated by extrapolating the fits of region I (fig.1) to x=0 mm. Here also no essential differences could be seen. The mean loss in fluorescense light yield for all these samples is about $7 \cdot 10^{-4}\%$ Gy^{-1}.

4 Dose rate investigations of radiation damage

As pointed out, the high dose rate investigations may underestimate the real radiation damage in the calorimeter[3], where SCI and WLS are exposed to relatively low dose rates . This seems to be especially valid if oxygen is present during the irradiation. Zorn[5] has discussed this item in more detail. We have studied the radiation damage of SCIs and WLSs at medium and high dose rates (30 - 1000 Gy/h) and very low dose rates (2 mGy/h). The results will be presented in sections A and B.

A Medium and high dose rate exposures

SCSN-38 scintillators (thickness 2.8mm , size$(26 \cdot 2) cm^2$) have been exposed in air to γ rays of different ^{60}Co sources. The total absorbed dose (D = kGy) was kept constant , while the mean dose rates were 30, 100 and 1000 Gy/h, respectively . The corresponding exposure times were T = 1, 10.5 and 31.5 days.

To detect radiation damage the scintillators were excited using a xenon flash lamp. The fluorescence light was absorbed by a WLS (30 ppm Y7 in PMMA) transmitting the light to a photomultiplier tube. In this case a black coverage at the open end of the scintillator suppressed the reflection of light. The results for irradiations in dry air are presented in fig.4. The light yield ratio $L_{irr}(x)/L_{unirr}$ of irradiated and unirradiated samples has been determined.

Directly after the end of a short term irradiation (fig.3) one observes a strong initial radiation damage. Recovery of polysterene base materials in air is very fast. The permanent radiation damage remaining after (1-2) days storage in air is much weaker than the initial damage. The data plotted in fig.3b,c show that the behaviour during long term irradiations differs considerably from that described above. Samples of 2.8 mm thickness recover during irradiation if the dose rate is less than 100 Gy/h. After the end of the long term irradiations practically no further changes of radiation damage have been observed. A second result is that we find no dependence of the permanent damage on the dose rate within the experimental errors. The important consequence for the scintillator is that the radiation damage expected after long term irradiations in air can be determined from short term irradiations with subsequent recovery in air.

The above statements confirm with higher accuracy the results obtained using a spectrophotometer [4].Quantitatively the observed effects can be described in terms of the diffusion model [11,12]. The radiation creates free radicals which act as absorption centers so that the SCI appears yellow-brown. When the samples are stored in contact with air, the oxygen diffuses into the SCI and forms peroxides which do not absorb visible light. Therefore, for recovery in air after short term high dose rate irradiations, bleached zones with thickness z at both surfaces of the SCI can be observed, where z increases with time after the end of the irradiation due to the subsequent delivery of oxygen from the outside by diffusion. In the case of a thin sample with d = 2.8 mm at dose rates below 100 Gy/h the diffusion delivers enough oxygen to recover nearly all created

absorption centers at once, so that the sample is completely transparent (totally recovered) at the end of the irradiation.

B Low dose rate irradiations

A SCSN-38 SCI of 60 cm length and 5cm width has been irradiated in between DU plates. Together with a shielded (not exposed to DU) sample of the same dimensions, cut out of the same larger plate and machined in one process, it has been fixed via light guides to a photomultiplier. The absorbtion coefficients (AC) and light yields of both SCI have been measured by placing a ^{106}Ru source always at the two ends of the scintillators. The same set-up was used for pairs of SCI with thicknesses of 2.6 and 5 mm.

As a result fig.4 shows the AC for the 5 mm thick samples over a period of 478 days , corresponding to a totally accumulated dose of 14.3 Gy. Both SCI behave in the same way. The AC increases by about 14% within this period and seem to converge to a constant value of about 1.05 - 1.06 $m^{-1}m$. This increasure apparently is due to normal ageing. Within the errors no radiation effect is to be seen.

Fig.5 shows the AC of the 2.6 mm thick SCI, measured over 1100 days, corresponding to a dose of about 42 Gy. Here the AC of the non-irradiated sample increases only by about 3% while the SCI exposed to DU shows an increase of 9%. If this difference would be caused by the radiation it would be a very large effect. The radiation-induced additional absorption coefficient $\Delta\mu$ would be a factor 20 higher than expected from the high dose rate irradiations (table 1). But there are some hints that this difference is not caused by the radiation: Both curves converge with increasing time to constant nearly identical AC. One might deduce that the non-irradiated sample had a different "pre-ageing" when the measurement started. It is not clear why this should happen but we have seen similiar effects for two identical WLS K-27 in PMMA which were not exposed to any radiation [6]. The fact that both AC of the 5 mm thick samples (fig.6) show a growth (normal ageing) which is similiar to the 2.6 mm irradiated SCI also indicates that the non-irradiated 2.6 mm thick sample behaves differently from the others. Furthermore one would not expect a convergence to a constant AC of the irradiated SCI but a nearly linear increase with time if the effect would be caused by radiation.

The ratios of the light yields of the DU-exposed and non-exposed SCI showed within the errors no changes with time.

For the DU irradiation of WLS K-27 in PMMA we have seen strong changes of the absorption coefficient[6] which probably have to be explained by normal ageing.

No radiation damage effect has been seen when a SCSN-38 plate has been exposed in air to 230 Gy from a ^{90}Sr-source with a dose rate of 0.25 Gy/h [9]. In contrast to this an "Altulor" SCI already showed a strong damage effect for half the dose [3].

On the other hand studies at the Tevatron collider[10] have shown that there are already strong damages of SCSN-38 and other SCI after an exposure to 150 - 200 Gy with rates of about 0.5 Gy/a.

A possible strong dose rate effect has been seen for the CDF beam counters made of 25.4 mm thick SCSN-23 SCI [8]. SCSN-23 has a twice as high concentration of the first fluor b-PBD and another second fluor (BBOT) compared with SCSN-38.After a one year run of the collider the AL decreased from 109 to 15 cm and the light yield was reduced for 40%. In the first two months of the run the dose unfortunately was not measured, afterwards the SCI have accumulated only 40 Gy. Consequently either there is a strong dose rate effect or the SCI have seen a very strong dose within the first two months of the run.

5 Summary

The results can be summarized as follows:

(1) The low term high dose rate (1 - 10 kGy/h) irradiations of SCSN-38 and Y-7 and K-27 up to 24 kGy with subsequent storage in air and inert gases resulted in the same induced permanent absorption coefficients $\Delta\mu$ and $\Delta\mu(\lambda)$ for exposure to ^{60}Co or 25 MeV protons. Series investigations on 38 production cycles showed no larger deviations. The reduction in light yield of SCSN-38 was stronger for irradiation in air than in argon. The radiation stability of the investigated materials is high enough for 10 years of ZEUS operation.

(2) At medium dose rates of $\dot{D}$ = 30 - 100 Gy/h in air the SCI SCSN-38 of 3 mm thickness is always in the totally recovered state and the damage can be calculated from the short-term experiments. The damages are higher than expected from the accumulated dose due to the fact

that the diffusion of oxygen into the interior of the material is not fast enough. For the WLS the situation is more complicated and critical due to an initial blocking of the recovery.

(3) At very low dose rates (some mGy/h) in air some experiments show a much stronger damage of SCI and WLS than expected from the applied dose from short-term irradiations. On the other hand it is not totally excluded that these effects are caused by other reasons than radiation, e.g. ageing or chemical reactions of oxygen with shorter lived radicals. Especially the ageing may be responsible for strong changes of the attenuation length.

6 References

[1] ZEUS Collaboration,"The ZEUS detector", Status Report 1989, March 1989.

[2] Manufactured by KYOWA GAS CHEMICAL INDUSTRY, see T. Kanon, K. Kondo, A. Yamashita, T. Shimizu, L. Nodulman, "A new scintillator and wavelength shifter", *Nucl. Instr. and Meth.*, vol. 213,(1983) 261

[3] Y.Sirois and R.Wigmans , *Nucl. Instr. and Meth.* vol. 213,(1985) 262.

[4] D.Paul, P.Schröder, V.Stieber, K.Wick, proceedings of the ECFA *Study Week on Instrumentation of High Luminosity Hadron Colliders* ed. E.Fernandez,G.Jarlskog,vol.1(1989) 159

[5] C. Zorn, *IEEE Trans. Nucl. Sc.*, vol. 37 (1990),504

[6] U. Holm, see ref.[4] , p. 163.

[7] U. Holm and K. Wick, *IEEE Trans. Nucl. Sc.*, vol. 36,(1989) 579.

[8] N. Giokaris, private communication

[9] J. Straver and R.Wigmans, private communication

[10] C. S. Lindsey, E. W. Anderson, C. Hojvat, F. Turkot, A. Bujak, *Nucl. Instr. and Meth.*, vol. A 254,(1987) 212.

[11] K.Wick,G.Riedel,D.Paul,V.Stieber, *Nucl. Instr. and Meth.*,vol.A 227,(1989) 251

[12] D.Paul,P.Schröder,V.Stieber,B.Bicken,K.Wick, to be published in *Nucl. Instr. and Meth.*

7 Figures

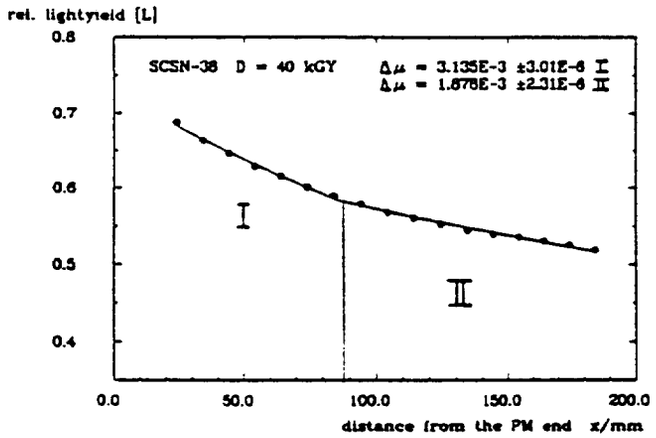


Figure 1: *Light yield ratio, measured with a zenon lamp, of a SCI sample after total recovery and before irradiation. The solid lines represent two fits with the functions of eq.2 in Regions* I *and* II.

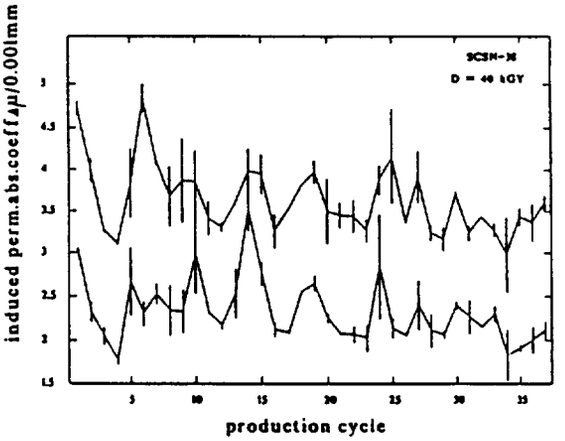


Figure 2: *Radiation induced permanent absorbtion coefficients* $\Delta\mu$ *for region* I *(upper curve) and region* II *for 38 production cycles.*

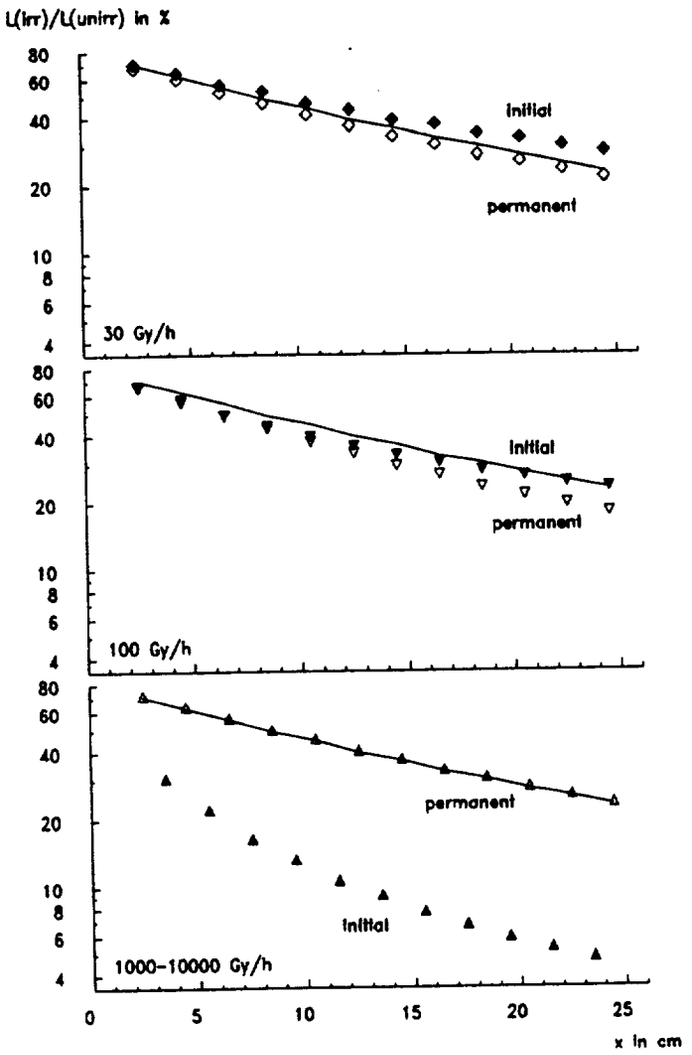


Figure 3: *Light yield ratios of irradiated and unirradiated SCSN-38 scintillators measured after exposure to a fixed dose D = 24 kGy at different dose rates* $\dot{D}$. *The solid and open symbols refer to measurements performed directly or more than 100 days after irradiation (initial and permanent radiation damage).The solid lines indicate the permanent damage measured at a high dose rate.*

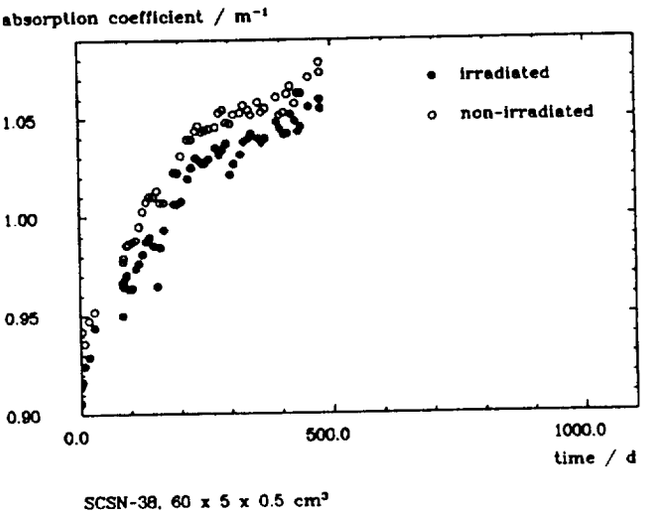


Figure 4: *Absorption coefficients of a SCI SCSN-38 (thickness 5mm), exposed to DU ,as a function of the exposure time.For comparison the AC of an identical non-irradiated sample is shown.*

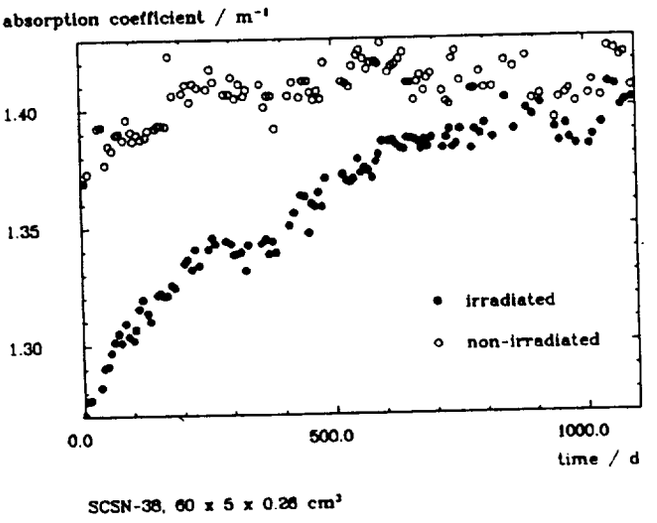


Figure 5: *The same as in fig.4 but the SCI thicknesses are 2.6 mm .*

RADIATION RESISTANCE OF CRYSTAL SCINTILLATORS HOW TO STUDY IT? HOW TO IMPROVE IT? THE EXAMPLE OF THE BGO

P. LECOQ CERN / PPE

1- Introduction :

The understanding of the radiation damage mechanism in crystal scintillators has considerably improved in the last few years [1] , and new fast scintillators , particularly fluorides crystals like BaF_2 or CeF_3 , are now recognized as being radiation hard up to several Mrads per year [2] .

After irradiation , neither the fluorescence spectrum nor the efficiency of luminescent centres is modified [3] , but the light transmission of monocrystals decreases , mainly in the blue , as a consequence of the formation of colour centres . Several methods can be used to study the properties of these colour centres , and to try to relate them to some impurities in the raw material . The absorption , thermoluminescence and thermoconductivity spectra are studied for different kinds of irradiation , different doses and at different temperatures . The example of the BGO is given here , where doped samples were also tested , showing the role of impurities , mainly iron , in the process of damage . A particular effort was undertaken to remove iron from the raw material , which led to a considerable improvement of the BGO radiation hardness . Finally a model is proposed which explains all the experimental results .

Similar efforts are on the way for other scintillators , which are now studied for a high performance electromagnetic calorimeter at LHC .

2. Optical transmission :

After irradiation with different radiation sources (UV xenon lamp with a filter at 320 nm , excimer laser at 308 nm , cobalt 60 source at 1.17 Mev and 1.33 Mev , 18 Mev linac) , the transmission spectrum of the crystals is recorded , from which the absorption coefficient is calculated . This parameter is directly proportional to the density of colour centres , and is therefore more usefull for a quantitative analysis .

The behaviour is qualitatively the same for all the crystals , for the different radiation sources and at different doses . The absorption gradually decreases from UV to the red (Fig 1). Measurements on very thin samples , where the lattice self-absorption is smaller , show that this tendency probably continues in the ultraviolet . No clear structure is visible in this very large absorption band , suggesting either a large number of families of traps , or a large number of energy levels for one or a few types of traps .

In order to determine the activation energy of the colour centres , we irradiated one crystal with photons of increasing energies , using the Xenon lamp and a monochromator . The light intensity at the crystal level was monitored with a photodiode , and the exposure time adjusted so that for each wavelength the energy dose was the same , and far below saturation . Once again , no difference was seen in the shape of the absorption spectrum as a function of the irradiation photon energy , suggesting that one type only of colour centre was created . However , the intensity of the damage is a function of the wavelength (Fig 2) . The right part of the curve results from the minimum energy needed to create the damage , whereas the left part reflects the BGO absorption of UV photons , which cannot penetrate and damage the crystal in depth . From this curve it can be seen that the activation energy of the colour centres is about 3.6 eV , which means that the traps are quite close to the conduction band (or to the valence band if they are hole traps) . Furthermore , photons from the fluorescence light of the BGO (emission peak centred at 480 nm) are not energetic enough to damage the crystal . There is no self damaging .

It has been shown that already at room temperature the thermal energy is sufficient to release trapped charges , and the BGO spontaneously recovers. This recovery process goes faster at increasing temperatures [3]. For a given temperature , the kinetics of this process gives important information on how the traps are emptied . If P is the probability for an electron to escape a trap at a given temperature , and to recombine immediately (localized mode) , the density n of the colour centres will decrease according to :

$$- dn / dt = P . n$$

and the absorption will have the following time dependence :

$$\mu(t) = W . n(t) = W . n_0 . \exp (-P . t)$$

where W is the absorption probability of the colour centre .

If , on the other hand , there is a diffusion of the trapped electrons or holes , via the conduction or valence band , the differential equation is of the second order :

$$- dn / dt = P' . n^2$$

and

$$\mu(t) = W . n(t) = W . n_0 / (1 + n_0 . P' . t)$$

All the crystals have been studied at room temperature after a cobalt irradiation of 1000 Rads . For all the crystals , the absorption coefficients at different wavelengths decrease at the same speed at all times , which means that the shape of the absorption spectrum does not change during the bleaching . A quick analysis shows that there is no direct correlation between the initial damage and the recovery characteristics . This suggests that the initial damage is a function of the number of charges trapped by the crystal defects , whereas the bleaching efficiency results from the type of traps , through the release mechanism offered to the charges . When plotted on a semi-logarithmic graph over a long period of time (Fig 3), the decrease of the absorption coefficient clearly shows two regimes . The first one is fast , with a time constant of 10 to 20 hours , is similar for all crystals and corresponds to a first order mechanism . The second regime is much slower , and very different for crystals from different origins (300 hours to 5000 hours). It is much more difficult to conclude anything about the order of the kinetics for this second regime .

By heating the crystals in the spectrophotometer , we then studied the recovery kinetics between 40° C and 80° C in steps of 10° C . The recovery is much faster at higher temperatures where two regimes clearly appear , suggesting either two types of colour centre or two different recovery mechanisms . A careful analysis of the second regime shows that it decreases less rapidly than exponentially, which is the sign of a second order kinetics [4]. The first regime on the other hand is exponential , and the time constants can be derived from the Fig 4 .

Several crystals have been irradiated with increasing doses . The shape of the absorption spectrum remains constant . For small doses the absorption increases almost linearly with the dose , but saturation occurs after a few thousand Rads , with a kinetics independent of the type of radiation (Fig 5) . The energy necessary to create colour centres is certainly much too small (3.6 eV) to create crystal defects . Very likely , the effect of the radiation is to liberate charges which are then trapped by already existing crystal impurities or defects .

The kinetics of the colour centre formation results from the rate at which charges are trapped , compared with the rate at which the thermal bleaching occurs . On all the crystals , 2 saturation time constants were found with time constants of about 6 mn and 33 mn . By comparing the saturation time constants to the thermal bleaching time constant (10 to 20 hours for the fast one) , it is clear that the origin of the saturation cannot be explained by thermal recovery . Similarly , the identical behaviour of the saturation with UV or gamma rays of very different energy leads to the conclusion that optical bleaching cannot explain the saturation . It is therefore very likely that the saturation simply reflects the limitation of the number of crystal defects . When saturation is reached , all the defects are occupied by trapped charges .

3 Thermoluminescence :

When a crystal is irradiated , electrons and holes are freed by the ionizing radiation and migrate in the conduction or valence band . Most of them directly recombine in a short time , but some are trapped by impurities or defects in metastable states between the valence and conduction bands . When the crystal is heated , these trapped electrons or holes are thermally excited and can recombine in specific centres . If this recombination is radiative , a thermoluminescent signal is emitted (TL) .

When the temperature increases , the probability of untrapping charges goes from 0 to 1 following the exponential Boltzmann law . At the same time the density of trapped charges decreases , because more and more start to recombine . This produces the typical thermoluminescence peak , the size and the shape of which depend on the intrinsic characteristics of the trap (energy depth) , but also of the irradiation dose and of the recombination mechanism) . For a temperature cycle , several peaks can be found corresponding to several traps . Once annealed , the crystal is left with all the traps emptied , and a new temperature cycle will not produce TL , without further irradiation .

The symmetry of the thermoluminescence peak is an important parameter which determines whether the kinetics is of the first or of the second order . On the low temperature side of the peak , the shape is an increasing exponential , giving , via the Boltzmann law , the number of charges escaping the trap as a function of temperature . On the high temperature side , the shape is defined by the charges left in the traps . If there are more

recombination centres than traps , this population decreases rapidly as charges escaping the traps have a low probability of being trapped again . In this case the kinetics is of the first order and the peak is very asymmetric . If , on the other hand , there are more traps than recombination centres , charges escaping traps can easily be trapped again , so that the total population of trapped charges decreases at a lower rate . In this case the kinetics is of the second order and the peak is much more symmetric . A detailed mathematical description of these phenomena can be found in the literature [5] .

For the BGO crystals , 2 thermoluminescence peaks are systematically observed ; one at ≈ 100°C , large and assymetric , corresponds to a first order kinetics , whereas the second peak is much smaller, centered at ≈ 170°C with a symetry reflecting a second order kinetics (Fig 6) . As can be seen on this plot , increasing doses do not modify the shape of the peaks and their relative intensity . The shape of each peak is also not changed when the traps are partialy depopulated , when the sample is annealed by steps at increasing temperatures . The characterization of the thermoluminescence signals by different methods gives the same trap depth of ≈ 0.7 eV for both peaks . When the crystal is irradiated with photons of increasing energy , an activation energy of ≈ 3.6 eV is found for the traps responsible of the 2 thermoluminescence peaks , exactly the same as for the traps responsible of the optical absorption . Moreover , the optical absorption , when monitored duri g the thermoluminescence experiment , recovers in 2 steps correlated with the 2 thermoluminescence peaks .

All these results strongly suggest the existence of one trap only , responsible of the optical absorption and the 2 thermoluminescence peaks .

As far as the saturation is concerned , it can be split in 2 regimes for both the absorption and the TL . In both cases it seems to be related to the limitations in the number of the crystal defects . But there is a significant difference between the time constants of the absorption saturation (6 mn and 33 mn) and the TL saturation (23 mn and 20 hours) . This can be explained if there are 2 types of centres ; the first one can trap electrons (or holes) , and becomes a colour centre ; the second one can trap holes (or electrons) and produces the recombination centres . The phosphorescence decay , as well as the absorption recovery are governed by the untrapping kinetics .They have therefore the same time constants . The absorption is determined by the number of colour centres . On the other hand the TL signal is function of the number of recombination centres which have no reason to be filled at the same rate as the colour centres .

This result is confirmed by the spectral distribution of the TL signal , which was analysed with a monochromator for the 2 peaks . shows that the spectrum is similar for the 2 peaks , centred in the red at 600 nm , and completely different from the BGO fluorescence spectrum . It seems therefore that the thermoluminescence recombination centres are different from the fluorescence centres , and that the Bi^{3+} centres normally associated with the BGO fluorescence are not activated .

4- Doped samples :

A series of doped samples has been prepared from a very pure (3 times recrystallized) BGO crystal . The undoped purified plate has no thermoluminescence signal, which means that impurities are directly responsible for the damage . Most of the other samples have an asymmetric

peak at around 100° C with sometimes a small contribution at 70° C . The asymmetric peak at 100° C is very similar to the first peak observed in the production crystals . It is especially large for the iron-doped samples , with an area directly proportional to the iron content in the crystal (Fig 7) . It is therefore very likely that the first asymmetric peak observed in most of the production crystals is caused by the presence of iron . Traces of iron probably exist in the other doped samples and could explain the more or less pronounced peak at 100° C .This idea is reinforced by the chemical analysis of BGO pieces , made by 2 Swiss firms , ANALUB (plasma emission) and SCITEC (atomic absorption) , which almost systematically detected a few ppm of iron . For crystals having a deviation from the stœchiometry (excess of Ge or Bi) , a second peak appears at about 140°C .

All the crystals are grown with a slight excess of germanium to prevent the strong chemical reaction between the bismuth and the platinum from the crucibles . This deviation from the stœchiometry will produce vacancies on bismuth sites , which will be electrically compensated by the oxidation of some Bi^{3+} into Bi^{5+} ions . If impurities exist in the melt , they will have a tendency to occupy a fraction of these vacancies , which is energetically favourable . Therefore , an initial stœchiometric deviation (systematic or accidental) , will favour the introduction of impurities , and the creation of 2 types of defects : the impurities themselves and the Bi^{5+} ions .

It is important to notice that doping can be sometimes a usefull way to create some energy levels in the crystal which will ease the release of the charges trapped by crystal defects . This has been successfully experienced with BGO , where a few ppm of europium were enough to reduce by a factor of about 2 the initial damage after irradiation , and to considerably reduce the recovery time constant [6,7] .

5- Thermocurrents :

It is interesting to see whether the trapped charges are thermally released through the bands (conduction for electrons or valence for holes) or not . Therefore we have measured thermoconductivity spectra on BGO samples using the apparatus described by Rogemont [8] .

To record the thermoconductivity spectrum , the current is first measured when the crystal is heated after an irradiation . After cooling , a new temperature cycle is applied (without new irradiation) , and the thermoconductivity spectrum is obtained by subtraction of the 2 curves . This method of noise subtraction is very important because of the very small currents involved. Fig 8 shows on the same plot the TL and the thermoconductivity spectra for a production crystal . No current is associated to the first TL peak . On the other hand a clear correlation exists between the second TL peak and the thermoconductivity signal . When the experiment is repeated on an iron-doped sample , for which only the first asymmetric TL peak is seen , no current can be detected .

From the preceding results , it is very likely that the first asymmetric TL peak is associated with a localized transition which does not involve the conduction band . The trapped charges are first thermaly excited to an intermediate level in the forbidden band , from which the transition to a recombination centre is possible . This of course implies a close connection between the trap and the recombination centre . On the other hand, the second TL peak is associated to a non localized transition , through the

conduction (or valence) band . In this case the recombination centre can be quite far from the trap .

6- Proposed model :

The transmission experiments have shown that the absorption spectrum keeps the same shape for different irradiation sources and doses , and during the recovering process . This indicates that probably one kind only of colour centre is produced by irradiation . On the other hand , the 2 recovery regimes , as well as the 2 thermoluminescence peaks , suggests 2 different modes of charge untrapping , one localized and the second through the valence band (Fig 9) .

The most probable defect is the substitution of an Fe^{3+} ion on a Ge^{4+} site . Fe^{3+} can be oxidised by trapping holes , and create the colour centres . The electrical neutrality implies the oxidation of Bi^{3+} in Bi^{5+} on some sites . Bi^{5+} ions can trap electrons and are the recombination centres . If the Bi^{5+} ion is close to the Fe^{3+} trap , the trapped hole can be neutralized via a localized transition . Otherwise , a larger thermal activation E_2 is necessary , to allow the hole to transit via the valence band to the recombination centres. This explains the 2 TL peaks , the first one at low energy is asymmetric of the first order , and corresponds to the localized transition , and the second one with an higher order and a larger energy reflects the non localized transition . This model with only one type of trap , also explains why the shape of the absorption and the TL spectra do not change with the irradiation dose .

The iron-doped sample has only the first TL peak and no thermoconductivity peak . This implies that only localized transition exist in this crystal . As the BGO was previously purified before being doped , it is probable that the only impurity in this sample is iron . In this case , it is energetically favourable that the Bi^{5+} ions are created in localized groups with the Fe^{3+} trap . On the other hand , the production crystal certainly have other impurities than iron , which can electrically stabilize some of the Fe^{3+} defects . It should also be remembered that Bi^{5+} defects are randomly created by deviation from the ideal stœchiometry . Therefore , a fraction of the Fe^{3+} and Bi^{5+} defects are not necessarily associated , and are at the origin of the second TL peak . The intensity ratio between the first and the second peak gives the proportion of localized Fe^{3+} and Bi^{5+} defects .

7- Conclusions :

It was shown on the example of the BGO , that rather simple methods can be used to study the radiation damage in scintillator crystals . The correlation of the results obtained by the different methods is a very powerfull tool to have a decent understanding of the damage mechanism . This is a fundamental step if one wants to have a feedback at the crystal production level . At least , it was a very important breakthrough for the BGO quality .

The same process is now on the way to understand the damage mechanism of BaF_2 and CeF_3 crystals . For BaF_2 , lead has been already identified as a critical impurity . More generally it has been established that interstitial or substitution impurity ions play a major role in the creation of colour centres . From this point of view , fluoride crystals , because of their high chemical stability , and their compact lattice (fluoride ion is large and deformable) , are good candidates for a compact and radiation hard electromagnetic calorimeter at LHC [9] .

REFERENCES

/1/ P. LECOQ , P.J. LI , B. ROSTAING " BGO radiation damage effects : optical absorption , thermoluminescence and thermoconductivity
To be published in NIM

/2/ G. CHARPAK et al. CERN-EP/90-41 ; D. ANDERSON , private communication

/3/ C. LAVIRON and P. LECOQ , Nuclear Instruments and Methods , 227 , 45-53 (1984)

/4/ B. ROSTAING , thèse de doctorat INPG , Grenoble , in french

/5/ Y. S. HOROWITZ , "Thermoluminescence and thermoluminescent dosimetry" , CRC Press, Inc. Boca Raton, Florida 1984

/6/ M.CHEMARIN , P. LECOQ , P. J. LI , M. SCHNEEGANS "Tests on doped BGO crystals" L3-655 , March 1989

/7/ Z. W. YIN et al "A new BGO crystal with higher radiation hardness" NIM A275 , 273-276 (1989)

/8/ F. ROGEMOND , Thèse , LYON I (1986) , in french

/9/ P. LECOQ , M. SCHNEEGANS , "A fast and radiation hard crystal calorimeter for the LHC" , contribution to this workshop

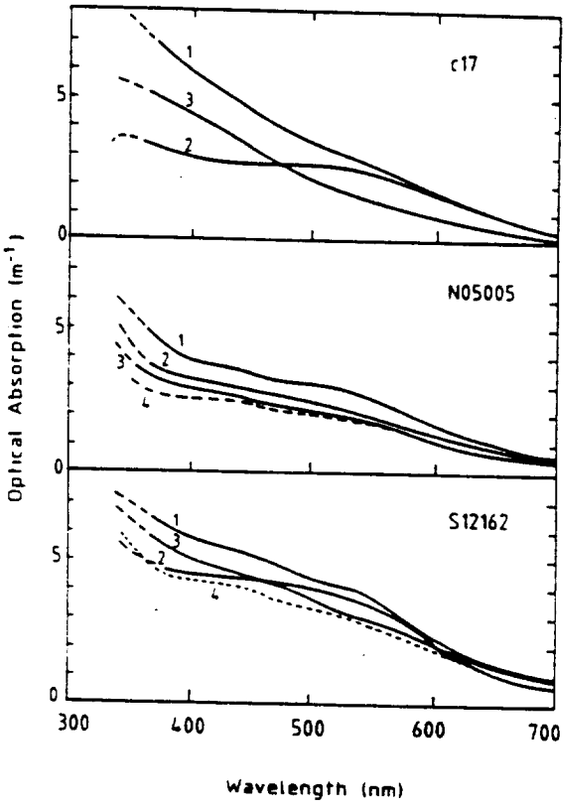


Fig. 1 Absorption spectra for different irradiation sources: 1: 1000 rad cobalt source (1.17 and 1.33 MeV); 2: 500 rad electrons from linac (18 MeV); 3: 15 h UV from the xenon lamp (320 nm); 4: 60 pulses from the excimer laser (200 mJ, 308 nm).

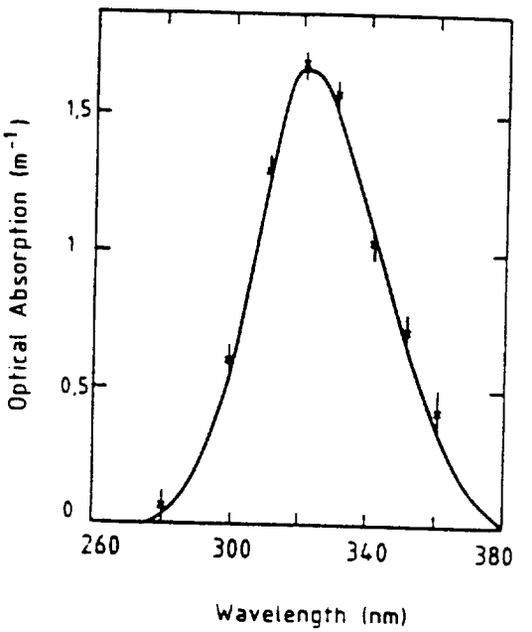


Fig.2 Total absorption between 400 and 600 nm as a function of the irradiation photon wavelength for the same energetic dose.

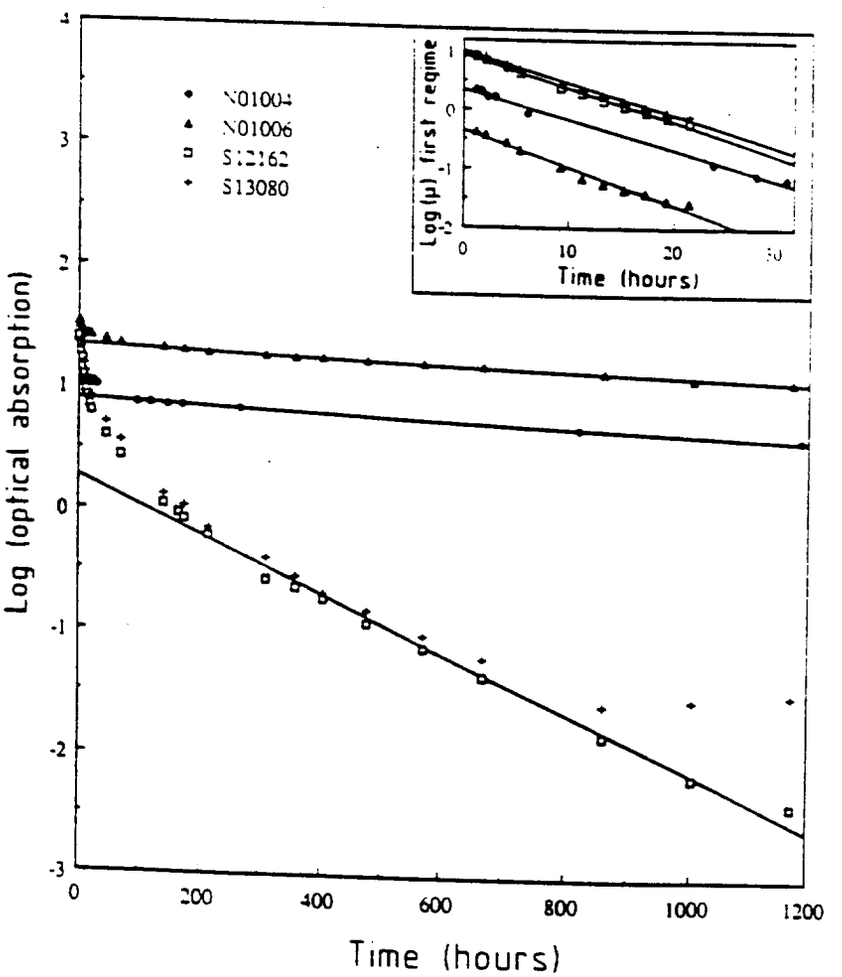


Fig.3 . Recovery over 2 months for four production crystals.

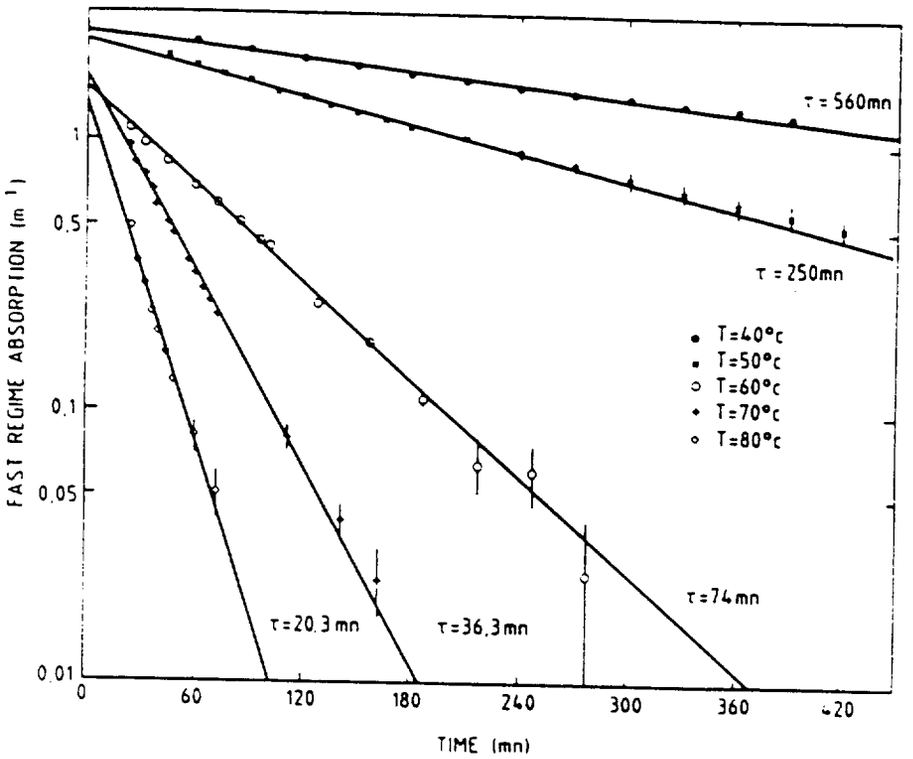


Fig. 4 Time dependence of the total absorption recovery between 440 and 500 nm after a 15 h irradiation from the xenon lamp, for different temperatures (crystal S72).

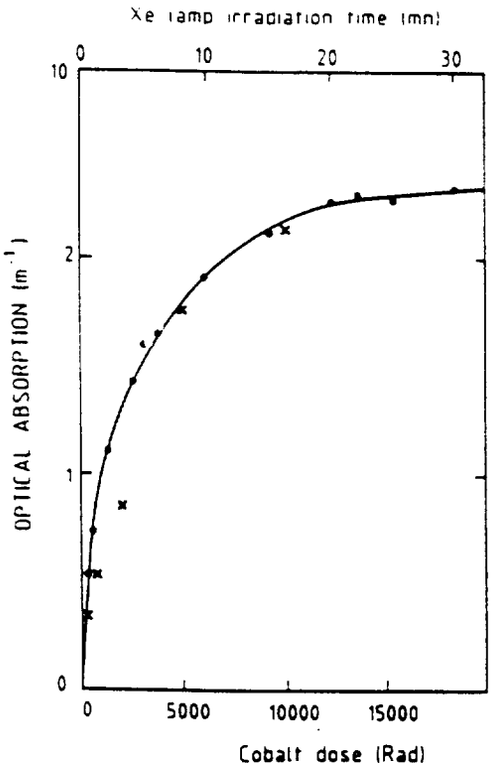


Fig. 5. Total absorption between 400 and 600 nm as a function of total dose (crystal S02046) for ● UV irradiation (xenon lamp 320 nm) and × cobalt source.

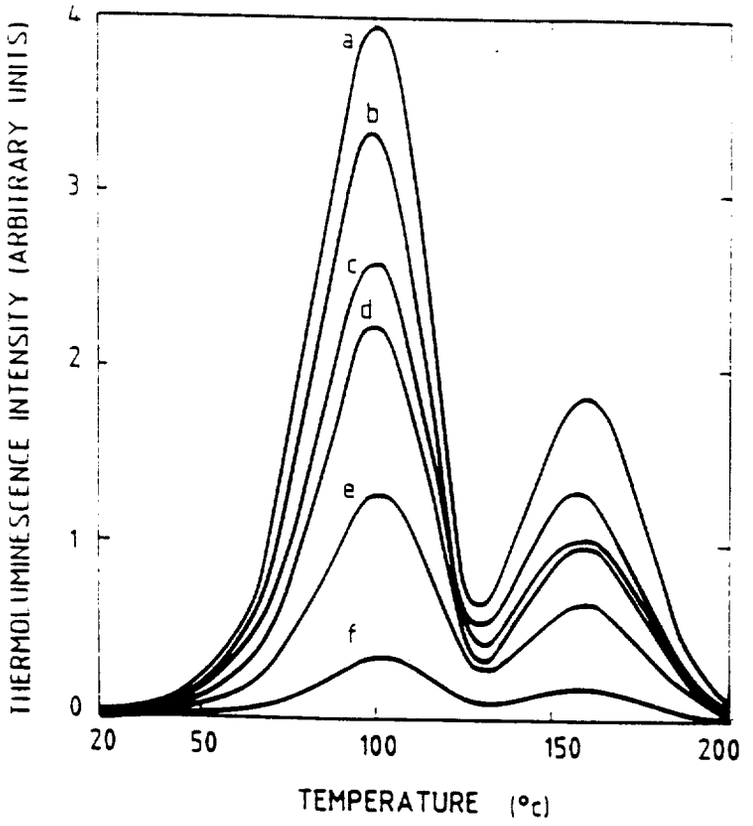


FIG. 6

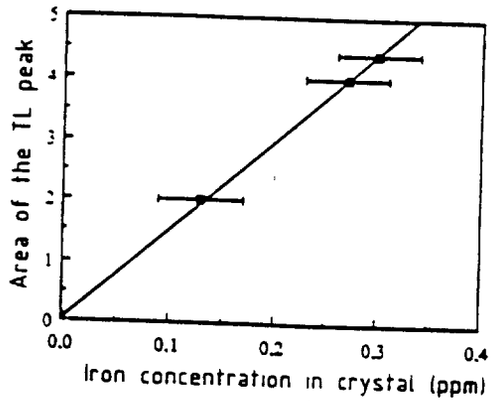


Fig. 7 . Correlation between the TL signal and the amount of Fe measured by neutron activation.

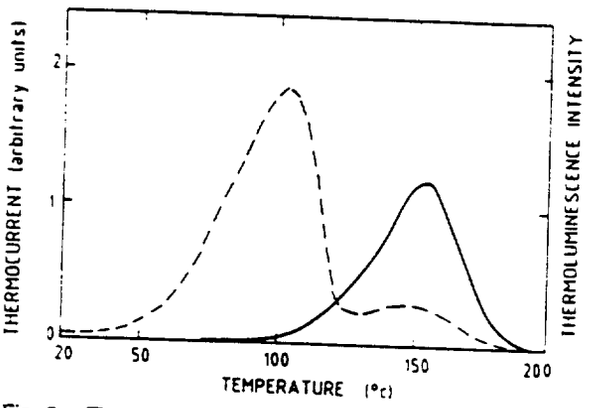


Fig. 8 . Thermoconductivity (full line) and thermoluminescence (dashed line) spectra for crystal S02046.

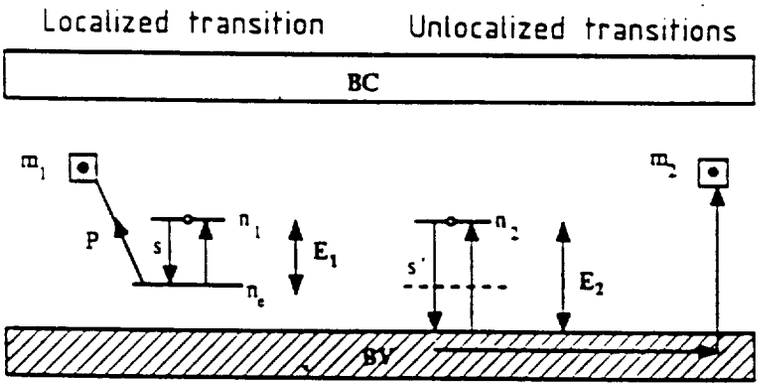


Fig. 9. Proposed model of the colour centres and the thermoluminescence centres in the BGO.

Radiation damage and resolution loss in scintillating fibers calorimeters

J.Badier
Ecole Polytechnique , LPNHE
Palaiseau , F - 91128

Abstract

Radiation damage affects the precision of a scintillating plastic fiber calorimeter. The inhomogeneity of the dose distribution induces a non linearity and a resolution degradation in electron energy measurements. Taking independently into account the light emission loss and the increase in attenuation length one finds that at LHC, over ten years, with presently available fibers, the precision of measured energy for electrons may be kept within 1%, out of the directions close to the beam axis.

1 Introduction

The scintillating fibers calorimetry is an attractive solution to measure and identify electrons and gammas at LHC. All the radiation damage effects have to be investigated. Aside from their light yield loss which may be corrected, using an appropriated calibration, there is a non linearity of the energy and a resolution degradation which cannot be corrected in any case. They are due to the conjonction of two effects :
- One third of the energy coming from the interaction point is due to the gammas of the neutral pions decays; that concentrates the dose distribution in a few centimeters region at the calorimeter entrance (fig. 1).
- The mean profile of the electromagnetic showers depends on their energy (fig. 2) and at a given energy they have big fluctuations (fig. 3).

2 Showers parametrisation

Fast and simple calculations may be performed from a parametrisation of the longitudinal shape of a shower. One uses the mean value m and the r.m.s. σ of the longitudinal distribution, expressed in radiation lengths units. It is an experimental observation [1] that $1/m$ and σ^2/m^2 are uncorrelated and are gaussianlike parameters describing the large fluctuations of the individual cascades. The following numerical values were obtained from [2] and corrected using a scaling law for a lead scintillator medium.

$$m = 5.51 + 1.04 \ln(E) \tag{1}$$

$$\sigma^2/m = 1.87 + 0.04 \ln(E) \tag{2}$$

$$[d(1/m)/(1/m)]^2 = 0.018 + 0.021/E \tag{3}$$

$$[d(\sigma^2/m^2)/(\sigma^2/m^2)]^2 = 0.057 + 0.066/E \tag{4}$$

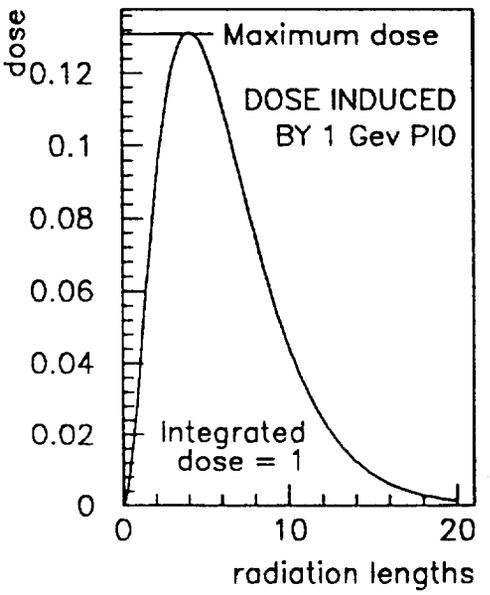


Figure 1

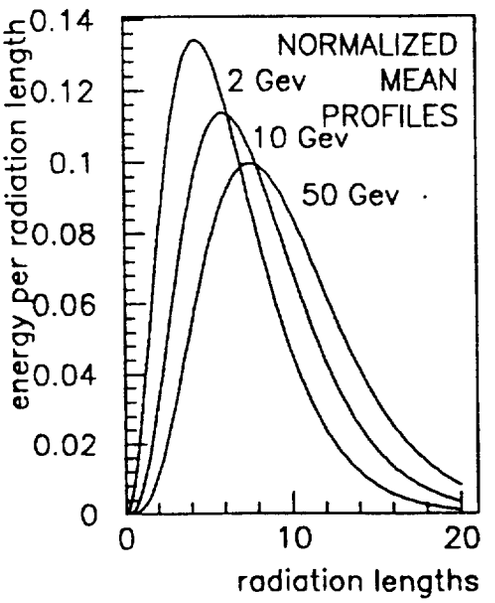


Figure 2

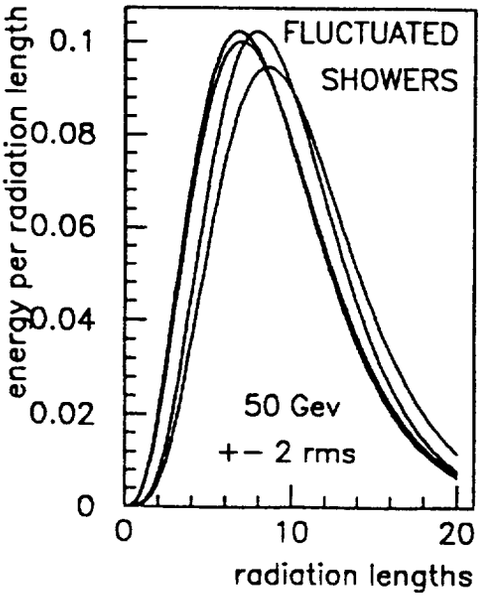


Figure 3:

3 Emission loss of light.

The irradiation of a point of the scintillator decreases the emitted light :

$$s(z) = s_0(z)exp(-Dose(z)/\gamma) \tag{5}$$

The light yield before irradiation $s_0(z)$ is like the shower energy profile. The dose profile induced by the π_0s is obtained by applying the parametrisation (1),(2),(3),(4) to the final electrons and positrons, asuming an exponential momentum distribution. The scintillator life γ depends of the fiber type and varies from 10 to 100 Mrad . The total emitted light S after irradiation is obtained by integrating $s(z)$ over z. The variations of S lead to an estimation of the errors. Choosing as a parameter the maximum value of the dose (fig.1), it appears that the errors are weakly dependent on the others parameters. The resolution degradation $\Delta S/S$ and the non linearity are proportional to the ratio of the maximum dose to γ. In order to express numerically the non linearity one uses the relative difference between an asymmetric and a symmetric electron pair coming from a gamma materialisation. One obtains :

$$\Delta S/S = .07\ Dose_{max}/\gamma \tag{6}$$

$$1 - 2S(E/2)/S(E) = .04\ Dose_{max}/\gamma \tag{7}$$

A fiber with a coefficient $\gamma = 100$ Mrad withstands a radiation level of 15 Mrad at the maximum of the dose.

4 Localised absorption.

The effect of the radiation on the absorption can be described at the first order by :

$$K(z) = K_0 + \alpha Dose(z) \tag{8}$$

The α coefficient depends on the recuperation conditions for a given fiber type, it varies from 10^{-2} to $10^{-3} cm^{-1} Mrad^{-1}$. The best parameter is the integral of the dose due to the π_0s (Σ_{Dose}). Putting aside the constant term, one defines a transmission factor :

$$T = exp(-\alpha \Sigma_{Dose}) \tag{9}$$

The calculations lead to estimations of the resolution and of the linearity degradations, they depend of the reflection r of the mirror at the fiber entrance :

$$\Delta Q/Q = .1\ (1-T)(1-Tr) \tag{10}$$

$$1 - 2Q(E/2)/Q(E) = .06\ (1-T)(1-Tr)/(1+r) \tag{11}$$

$(1-T)(1-Tr) < .1$ insures good linearity and resolution . Assuming a fiber with $\alpha = 10^{-3} cm^{-1} Mrad^{-1}$ one finds that 400 Mrad cm with r = 1 and 100 Mrad cm with r = 0 are acceptable.

5 Uniform absorption.

The absorption coefficient K of a non irradiated fiber is the inverse of its attenuation length. A uniform radiation dose increases this coefficient. The distance to the photomultiplier is such that the transmission by the cladding has not to be taken in account. Calling L the fiber length, the transmitted light q is :

$$q = s_0(z) \exp(-KL)\ [\exp(-Kz) + r \exp(Kz)] \tag{12}$$

$$q = s_0(z) \exp(-KL)\ (1+r)\ [1 + Kz(1-r)/(1+r) + K^2 z^2/2] \tag{13}$$

We have expended the exponentials because Kz is small. The integrations over z of $s_0(z)$, $z s_0(z)$ and $z^2 s_0(z)$ are respectively equal to Q_0 ,mQ_0 and$(m^2+\sigma^2)Q_0$. The total transmitted light Q is :

$$Q = Q_0 exp(-KL)\ (1+r)\ [1 + Km(1-r)/(1+r) + K^2(m^2+\sigma^2)/2] \tag{14}$$

Aside the mean loss $exp(-KL)(1+r)$ the dependance of m and σ on the energy induces a non linearity. By derivation of the formula (14) with respect to m and σ/m and using (3) and (4) one finds the resolution degradation. K is expressed in cm^{-1} . When r=1 or r=0 , one has respectively :

$$\Delta Q/Q = 1.5\ K^2\ or\ .8\ K$$

$$1 - 2Q(E/2)/Q(E) = 2.5\ K^2\ or\ .5\ K$$

The attenuation length has to be greater than 16 cm with r=1 and than 80 cm with r=0 .

6 Dose rate estimation

The doses are calculated using a total cross section of 85 mb . One produces 3 π_0s per interaction and per rapidity interval with a mean transverse momentum of .6 Gev/c .The LHC luminosity is assumed to be $10^{34} cm^{-2} sec^{-1}$ during 10^7 sec per year. The integrated dose Σ_{Dose} and the maximum dose are functions of the polar angle θ and of the distance D to the interaction point:

$$\Sigma_{Dose} = .42\ 10^{10}/D^2 sin^3\theta\ \ rad\ cm \tag{15}$$

$$Dose_{max} = \Sigma_{Dose}\ (.2 - .04 \ln(.6/sin\theta)\ \ rad \tag{16}$$

The figure 4 is obtained for an ellipsoidal calorimeter whose equatorial radius is 2 meters and the half axis along the beam is 4 meters.

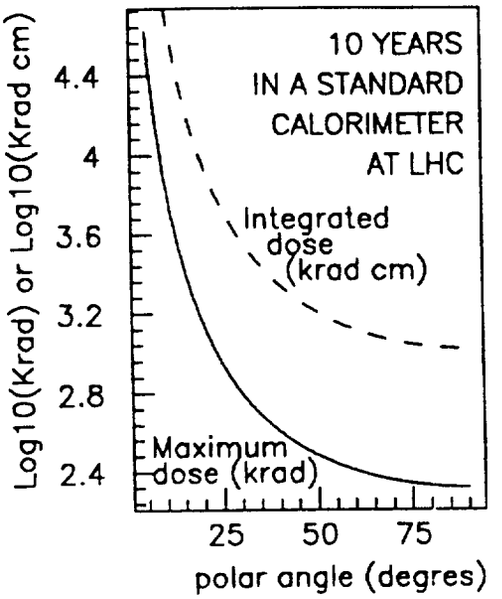


Figure 4

7 Conclusion.

The influence of the radiation damage on the resolution and linearity in electron measurements with a scintillating fibers calorimeter agrees with precedent studies [3,4]. With presently available fibers, the dose at the peak of irradiation has to be smaller than 15 Mrad . The decrease in the attenuation length gives a limitation to the integrated dose which has to be smaller than 400 Mrad cm assuming an entrance reflector. The first condition is the more restrictive, it imposes a polar angle greater than 5° ($\eta < 3$) over 10 years at LHC.

8 References

[1] J.Badier,ALEPH 87-09,(1987)
[2] M.Bardadin,ALEPH 89-1,(1989)
[3] H.P.Paar,ECFA 89-124,226,(1989)
[4] D.Acosta,LAA preprint,(1989)

SILICON ON INSULATOR FOR ULTRA-HARD APPLICATIONS

- CEA SOI TECHNOLOGIES -

A cooperative work from three CEA institutes :
CEA-DAM, B.P. 12, 91680 Bruyères-Le-Châtel, France
J.L. Leray, E. Dupont-Nivet, T. Garié, J.L. Martin, J. Montaron, J.F. Péré, A. Tissot
CEA-DTA/LETI, B.P. 85X, 38019 Grenoble, France
A.J. Auberton-Hervé, M. Bruel, E. Delevoye, J. Gauthier, B. Giffard, R. Truche, J. De Poncharra
CEA-DSM, Saclay, France
P. Borgeaud, R. Aleksan, E. Beuville

INTRODUCTION

Hardened technologies have been initially developed for the space or military purposes only. As a result, a large stream of studies have been proceeded since the first radiation-induced failure in Telstar communication satellite (1962). A considerable knowledge and practice has been accumulated since then. Recently, studies lead at CEA have exhibited an extra-high hardness behavior in one of the most questionable variety of integrated technology : the CMOS on Insulator (S.I.M.O.X. type) [1,2,3].
Other SOI devices, relevant to linear functions (Junction FET and bipolar transistors) have been developed [4] and are also very promising.

SOI STRUCTURE AND ASSETS

SOI has been first developed for the sake of military and space applications, in which the reduction of active MOS silicon volumes is the only practical way to harden circuits versus transient radiation induced photocurrents : gamma ray pulses and cosmic ion strike. Figure 1 depicts the MOS/SOI transistor structure used in CEA hardened technologies, versus standard "bulk" ones.
In a second analysis, it has been found that this complete insulation has some important side-effects, that give unique advantages for advanced neutron and total dose hardened products :

- full isolation of transistors among each others prevents any leakage current, commonly encountered in bulk technologies after total dose irradiation. The number of parasitic transistors is drastically reduced, as shown in figure 2.
- the buried oxide allows a direct control of the transistor body, suppressing latch-up, improving MOS and bipolar characteristics, improving JFET structure by easily forming a dual-gate transistor, lowering capacitance in transistors and cross-talk between them.

This structure is therefore naturally committed to high-frequency, high-linearity, low noise and high hardness applications.
Finally, a synergistic effect is found for the first time between military, space and civilian applications and market (including research physics and nuclear power plant instrumentations), converging on a unique "technology of choice".

1. LOGIC TECHNOLOGY AND APPLICATIONS

Structures. The logic-oriented bimetal technology allows 1.2 µm design rules and is high-speed high-integration oriented. The MOS on Insulator structure is shown on fig. 3. The process flow is stabilized since 1988 and provides 70-95% fabrication yield for the 16 bit microprocessor test structure. This process is industry transferred.

Results. The high dose tolerance was studied at 3 levels :

- transistor and oxide physics
- elementary cell (200 MHz cut-off frequency, 250 ps/gate propagation delay)
- 16 bit-slice microprocessor (compatible with 29101 commercial Cypress part, 30 MHz cycle time)

Figures 4 and 5 summarize the very good behavior of elementary devices (N and P transistors threshold voltages, divide-by-16 logic cell up to 700 Mrad(SiO_2)). Interesting *room temperature* recovery characteristics have been observed, allowing increased tolerance levels in radiation is slowly delivered (fig 5).

This behavior has been confirmed in an adequate number of lots (7 up to now), including complex bimetal-poly full process (fig. 6 and 7).

2. LINEAR ORIENTED APPLICATIONS

Structures. The JFET/SOI structure is seen on fig. 8. Very good transfer characteristics have been obtained from the first try (fig. 9 and 10).

Results. This JFET device is inherently hard to megarad levels as can be seen on fig. 11 and 12. The J-FET noise figure is found to be close to the expected value, as can be noticed on figure 11. The 1/f noise figure defines a *corner frequency of 20 Hz* when extrapolated to the white noise background. Due to this excellent noise figure, the JFET could be preferably used as low noise device input stages. 1 MeV neutron irradiation has been performed up to 5 10^{14} neutrons/cm^2 (fig 13).

Bipolar transistors have also been made using the JFET masks. Super-beta NPN has an Early voltage of 4-5 volts (β=5000), whereas it is 20-30 volts for standard NPN (β= 100).

CONCLUSIONS

The future trend might be a marriage between logic and linear ultra-hard technologies, allowing a true high speed signal processing at the chip level.

Fast linear circuits are attainable in SOI. Inherently low capacitance and low cross-talk in SOI structures could be a unique asset.

For the logic parts, we must finally add that greater total dose tolerance could reasonably be expected by varying some technological parameters that have not been ultimately optimized yet up to now. The circuits design have not been specifically optimized either. This could open the way for CMOS circuit technology and architectures for the purpose of levels exceeding largely 100 megarad(SiO_2).

REFERENCES

1. Les technologies de circuits intégrés silicium sur isolants SOI : état de l'art et perspectives, J.L. Leray, E. Dupont-Nivet, P. Lalande, O. Musseau, conference RADECS, Université des sciences et techniques du Languedoc, Montpellier, 11-14 sept. 1989. Editions de Physique.

2. Les technologies de circuits intégrés silicium sur isolants SOI pour le Durcissement en environnement Nucléaire ou Spatial, J.L. Leray, E. Dupont-Nivet, O. Musseau, Y.M. Coïc, A.J. Auberton-Hervé, M. Bruel, B. Giffard, 6-8 février 1990, Journées Information Electronique CEA, Institut National des Sciences et Techniques Nucléaires, Centre d'études de Saclay, 91-Gif-sur-Yvette

3. CMOS/SOI Hardening above 100 Megarad(SiO_2) : Limits and Liabilities, J.L. Leray, E. Dupont-Nivet, J.F. Péré, Y.M. Coïc, M. Raffaelli, A.J. Auberton-Hervé, M. Bruel, B. Giffard, J. Margail, IEEE International Conference on Nuclear Science and Radiation Effects, Reno, Nevada 17-20 juillet 1990

4. P. JFET On SIMOX for Rad-Hard Analog Devices, J.P. Blanc, J. Bonaimé, E. Delevoye, J. De Poncharra, R. Truche, E. Dupont-Nivet, J.L. Martin, J. Montaron, IEEE International Conference on S.O.S/S.O.I. Technology, Key West, Florida, Octobre 1990

For additional contacts : Tel. 33 1 69 26 47 90 / 33 1 69 26 60 27/ Fax. 33 1 69 26 60 17

Figure 1. SOI versus bulk technologies.

SOI is obtained by burying oxide layer underneath the top silicon active volume.

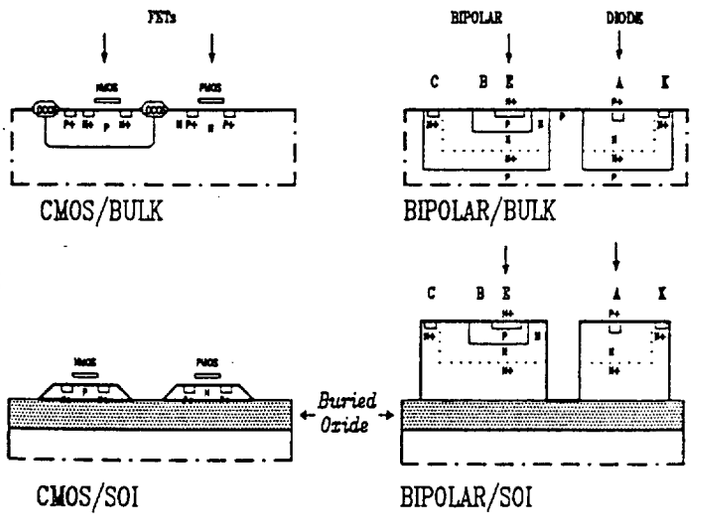
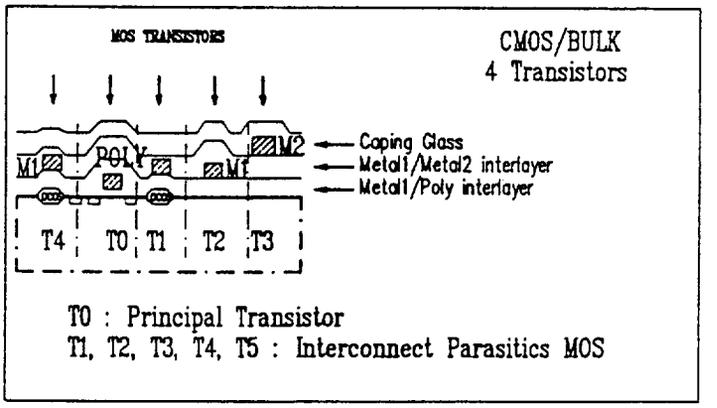


Figure 2. Advantages of SOI structures in term of parasitic transistors and capacitances reduction.



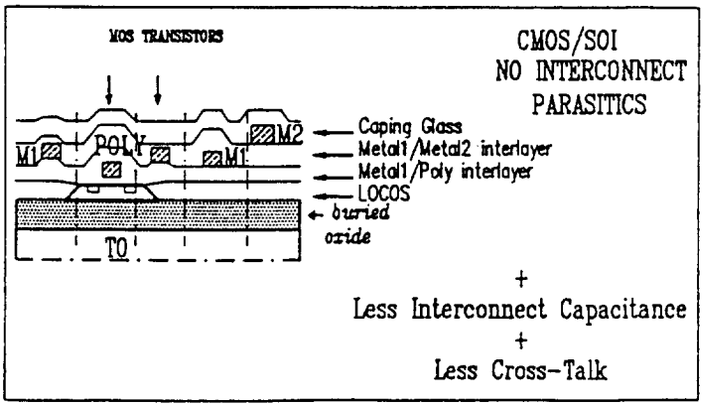
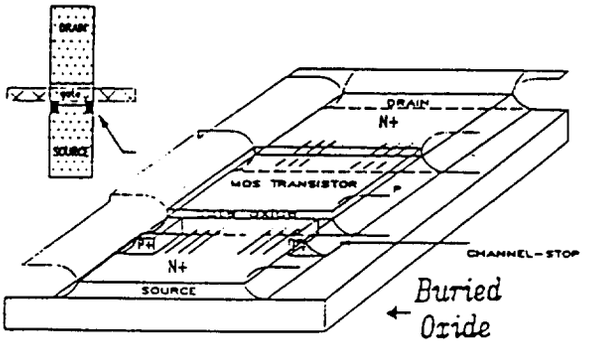


Figure 3. Hardened MOS/SOI Transistor



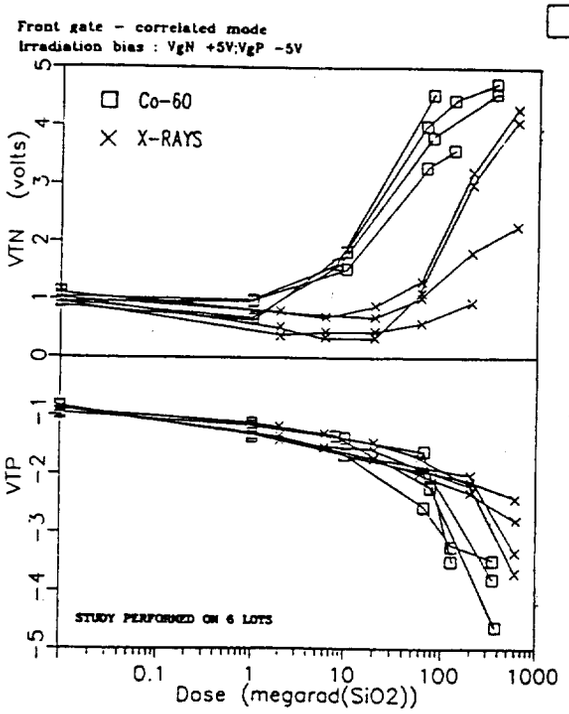


Figure 4. Threshold Voltages vs. dose

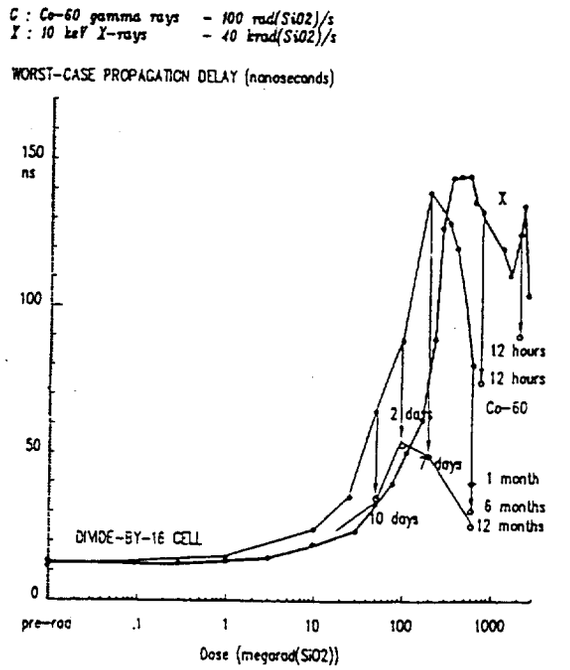


Figure 5. Simple Cell vs. dose

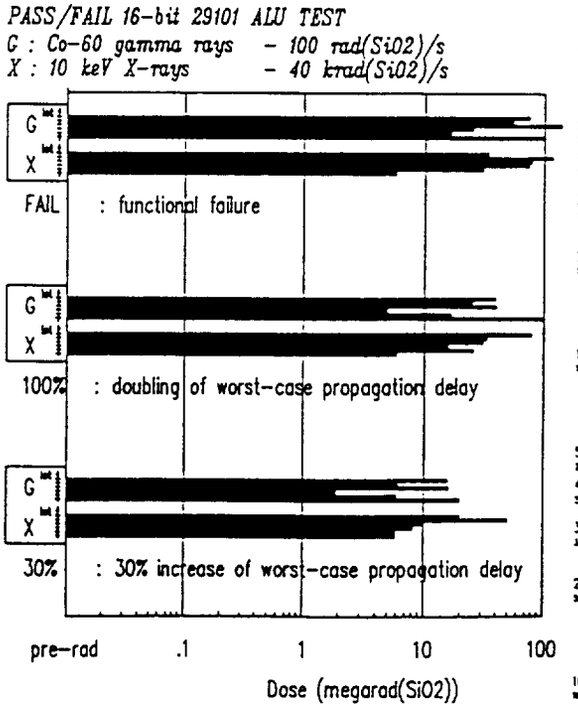


Figure 6. Dose Statistics

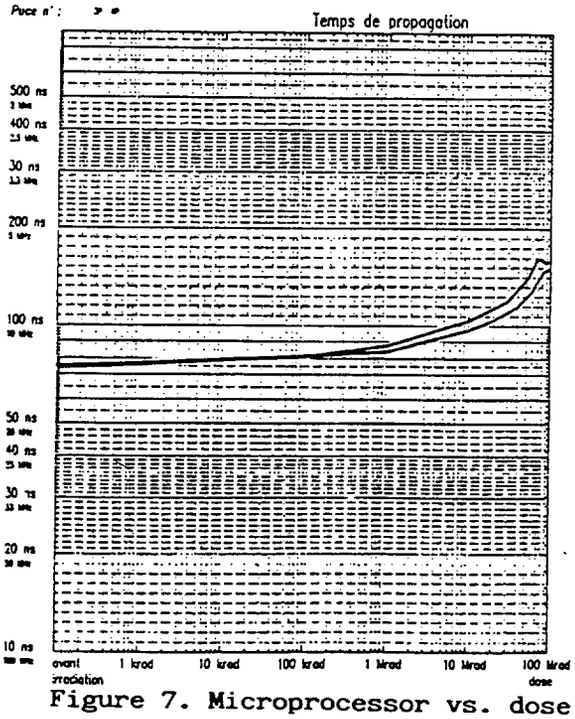
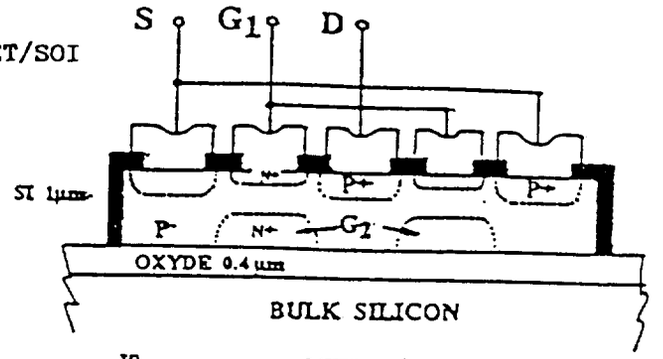


Figure 7. Microprocessor vs. dose

Figure 8. Hardened JFET/SOI Transistor



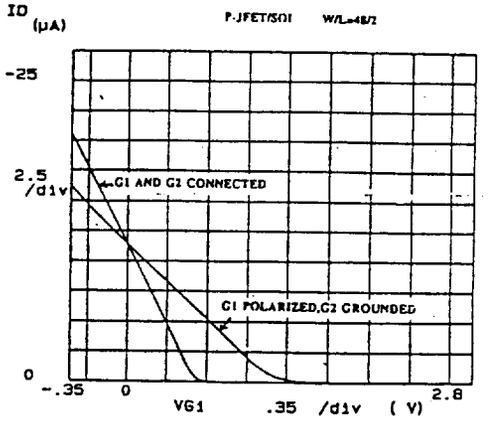


Figure 9. JFET Id(VG1) characteristics

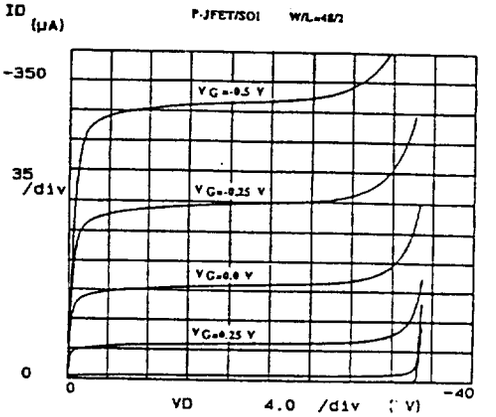


Figure 10. JFET Id(Vds) characteristics

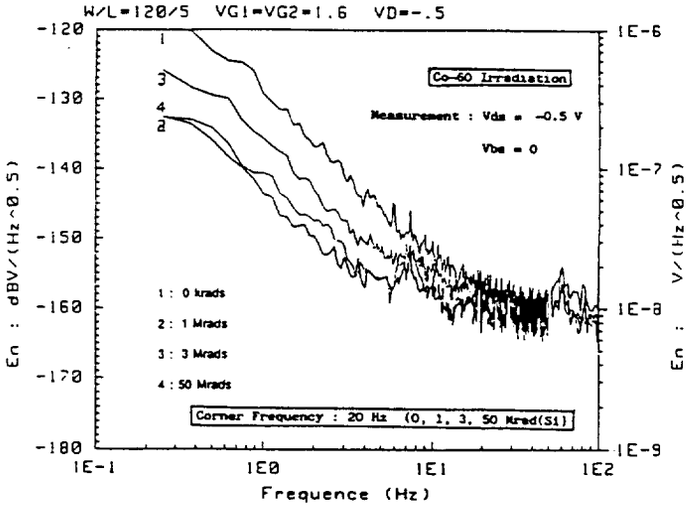


Figure 11. JFET noise figure vs. dose

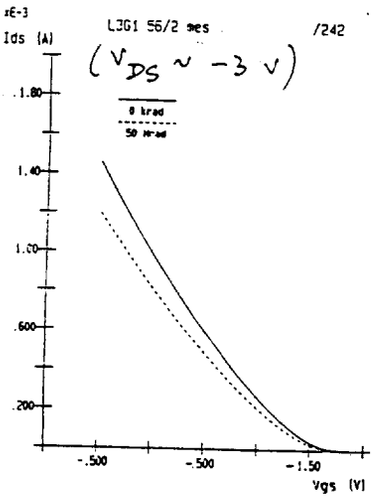


Fig. 12. JFET Id(Vg) at 0 and 50 Mrad(Si)

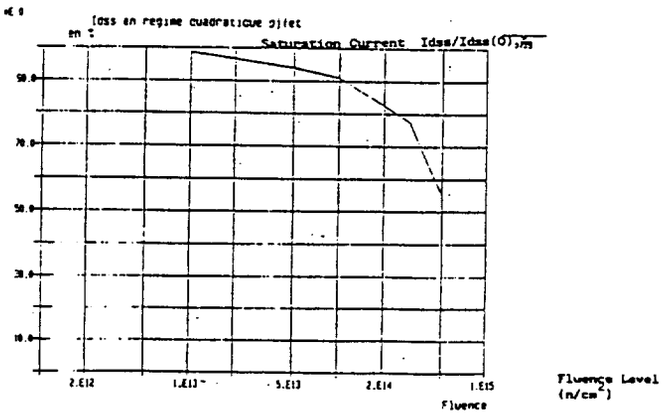


Fig. 13. JFET Saturation Current Idss vs. 1 MeV neutron fluence

RAD HARD AND RAD TOLERANT IC's DEVELOPED TO SATISFY THE EXTREME SPACE AND LHC REQUIREMENTS.

Gilles DURAND, Space Business Development Manager
Jean-Michel MAUREL, Space Products Development Manager

TEXAS INSTRUMENTS
European Military & Space Products Departement
BP 5, Avenue Bel-Air, F-06271 Villeneuve-Loubet cedex, France
Tel. (33) 93.22.20.01, Fax. (33) 93.20.30.11, Tlx. 470127 F

1- ABSTRACT

As the European space market flies to new successes and experiences fast sustained growth, new challenges and opportunities are developing for Europe to be a leader in the conquest of the space frontier.
The challenges of the future point towards new levels of integration in complex systems and higher price performance ratios for European space products. New requirements in quality and reliability and more radiation performance are fast becoming standard needs of the European space clients.

In order to better satisfy the radiation requirements and care-abouts of its customers, the European Military & Space department of Texas Instruments has particularly emphasized the studies on the radiation performances of its high reliability products.
The following article will show the radiation behavior of the Texas instruments IC's, independant of the specification system to which these components are procured.

2- HISTORY AND REFERENCES

For over 20 years, Texas Instruments in Europe has manufactured and supplied high reliability integrated circuits for space and strategic military applications under the European Space Agency (ESA) / Space Component Committee (SCC) specification system.

As a unique ESA/SCC qualified source for bipolar logic families, Texas Instruments has supplied approximately one million components to all the European Space Programmes for :

Communication satellites, Olympus, Eutelsat, Inmarsat, Telecom 1, Skynet iv, DFS, Italsat, Insat II, TDF, Tvsat, TeleX, Gimpel, Telecom 2, ECS, Intelsat...

Observation satellites, Spot, Argos/Sarsat, Meteosat, ERS, Hipparcos, Rosat, ISO...

Scientific satellites, Eureca, Topex/Poseidon, Tethered, Sigma, Exosat...

Space station, Spacelab

Launcher, Ariane (1,2,3,4)

3- MARKET COMMITMENT

Texas Instruments provides a dedicated facility in Villeneuve-Loubet, France, for engineering and manufacturing of European space products. Personnel are assigned for marketing, engineering, production, and quality assurance functions.

This manufacturing line is qualified by the ESA and is quarterly controlled through the Process Identification Document by the ESA and the CNES.

4- SPACE PRODUCTS RANGE

Approximately 200 device types are included in the ESA qualified part list. (bipolar logic families : ALS - LS - S).
HCMOS ESA qualification is progressing nicely and will be completed by december 1990.

Because of the extremely high demand for advanced products and thanks to the capability of the T.I. Villeneuve Loubet space operation, the space group is dedicating its effort to offer in space level the following components : AC/ACT, BICMOS (JTAG), F, AS, DSP 320C25, 320C30, 1-4 MEG DRAM, SIMOX SRAM, Asic's, GaAs MMIC's.

5- TECHNOLOGY AVAILABLITY / QUALIFICATION

TECHNOLOGY	SPACE FLOW AVAILABILITY	ESA QUALIFICATION
LS	yes	yes
S	yes	yes
ALS	yes	yes
AS	yes	1991
54 F	yes	1991
55xxx	yes	no
TTL	yes	no
HCMOS (HC/HCT)	yes	4Q90
BICMOS (JTAG)	yes	planned
ACL (AC/ACT)	yes	1991
320C25SCB	yes	project qual
ASIC & FPGA	yes	planned
GaAs	yes	planned

6- RADIATION ASSURANCE

Texas Instruments has evaluated the radiation performance of most of its products.
Tests have been performed by the radiation laboratory of Texas Instruments in Dallas, Texas, and also by Customers, in the frame of cooperation with T.I.

Radiation hardening programmes have been run to improve the performances of some families. An example is for the HCMOS family where T.I. has improved the radiation tolerance from 10 to 20 krads.

Important : in every case the eventual wafer process modifications are set up on the complete wafer fab production, this allows users of T.I. components to take benefit of improved radiation performances even when buying non space specification like military or commercial levels.

7- RADIATION GUIDELINES OF T.I. PRODUCTS

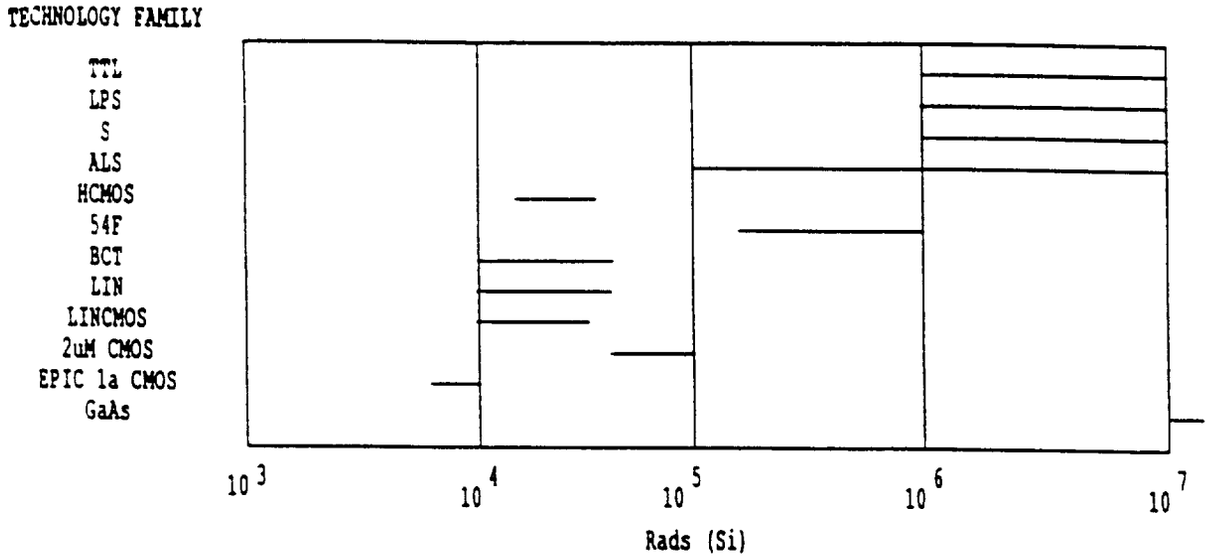
FAMILY	FEATURES	QUAL. STATUS	TECHNOLOGY	TOTAL DOSE PERFORMANCE (TYPICAL) RADS(SI)	TRANSIENT UPSET PERFORMANCE (TYPICAL) RADS(SI)/S
54 LS		ESA/SCC JAN-S CECC 883C	BIPOLAR	> 10E6	> 3 10E8
54 S		ESA/SCC JAN-B CECC 883C	BIPOLAR	> 10E6	> 3 10E8
54 ALS		ESA/SCC JAN-B 883C	BIPOLAR NESTED 2.5 u	> 10E6	> 10E8
54 AS		883C	IMPACT tm (1)	> 2 10E5	> 10E8
54 F		JAN-S 883C	IMPACT tm (1)	> 2 10E5	> 10E8
54 TTL		JAN-B CECC 883C	BIPOLAR	> 10E6	> 3 10E9

FAMILY	FEATURES	QUAL. STATUS	TECHNOLOGY	TOTAL DOSE PERFORMANCE (TYPICAL) RADS(SI)	TRANSIENT UPSET PERFORMANCE (TYPICAL) RADS(SI)/S
HC/HCT		ESA/SCC JAN-S CECC 883C	CMOS 3u	2 10E4	> 10E8
AC/ACT		883C	EPIC tm (2)	10E4	> 10E8
54 BCT	BUS INTERFACE LOGIC JTAG	883C	BIPOLAR-CMOS	10E4	> 10E8
ASIC	G.A./S.C.	883C	EPIC tm (2)	10E4	> 10E8
320C25	DSP	CECC 883C	CMOS TW 1.8u EPITAXIAL	10E4 (FUNCTIONAL)	> 10E8
GaAs	CATALOG DEV. FOUNDRY	883C	GaAs	10E7	> 10E9
SIMOX	SRAM 64K/256K ASIC, AD/DA, DSP PLANNED	883C	CMOS/SOI	> 10E6	> 6 10E9

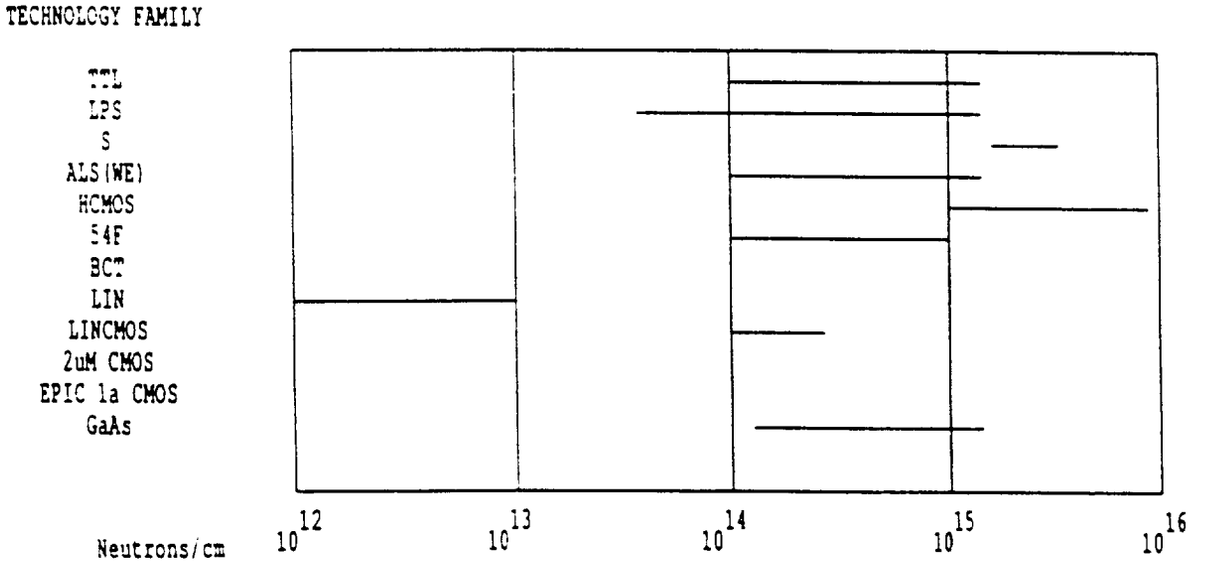
(1) : IMPACT is a trademark of Texas Instruments. (2u bipolar oxide isolated nested emitter technology)

(2) : EPIC is a trademark of Texas Instruments. (1u enhanced performance implanted cmos. twin well. epitaxial substrate)

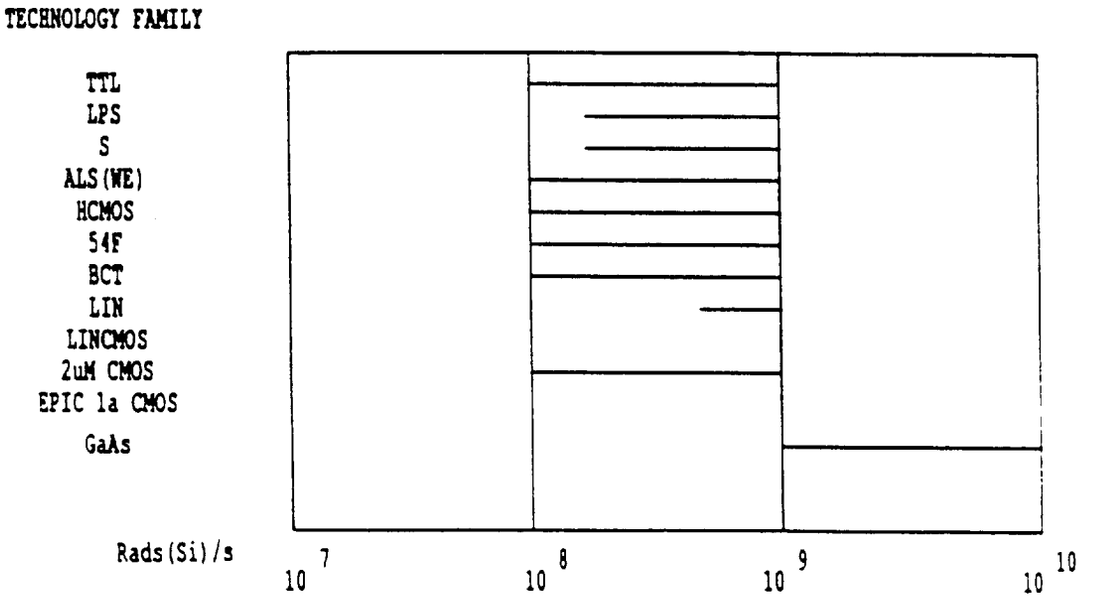
TOTAL GAMMA DOSE PERFORMANCE



NEUTRON FLUENCE PERFORMANCE



GAMMA DOSE RATE PERFORMANCE



8- CONCLUSION

Since the creation of its dedicated team in 1969, Texas Instruments Europe has been committed to providing its European partners with quality products and services for space and radiation applications with best performance price solutions.

Priority has been given to support radiation needs of customers by evaluating and enhancing performances of the products. This has resulted in offering a wide range of rad hard and rad tolerant products available in space grade, but also in military and commercial specification levels.

TI Europe reaffirms its commitment to European partnership with its dedicated European space team, 100-strong, and space semiconductor facilities in France with a 1200 sqm clean room. Enhancing its high levels of investment in the most up-to-date manufacturing equipment (MegaOne, IDS 5000,...), Texas Instruments has achieved new levels in quality and service with consistent on-time delivery. All this is backed by TI's European space organization and personnel and their commitment to total customer satisfaction through complete Statistical Process Control and a unique Total Quality Culture.

Objective is to be the preferred European supplier for all rad hard and rad tolerant IC based solutions in Advanced Logic Families, Memories, Processors, ASICs and FPGA, GaAs and MMICs.

Henning LARSEN[1], and Tom MASSAM[1]

LPS Radiation Tests on Service Electronics

Abstract

This describes the main results of radiation tests for the read–out and support electronics for the Leading Proton Spectrometer prototype in the frame–work of the LAA project[1]. The tested compo–nents are 8 bit digital TTL buffers, Fuse Programmable Logic Device and quad twisted pair drivers and receivers. The main aim was to give some indication of which family of TTL devices is the best suited.

[1] CERN, LAA, Swizerland.

1. Radiation test of TTL logic

1.1 Introduction

A High Energy Physics Experiment like the LPS consists of the following main elements.

Detectors very close to the beam.
Associated signal amplifiers, D/A converters etc.
Read-out and control typically located in regions with insignificant radiation. This part is often based on standard bus architectures like VME, Fastbus, Camac etc.
Support electronics: Power supply, monitoring etc.
Finally one needs a transport media to bring signals between those two regions

With decreasing bunch time separation as the accelerators becomes more and more performant, the distance between the detector and the front-end electronics becomes smaller. This is due to many factors for example the bandwidth requirements per channel, but also the large number of channels makes cabling bulky. The proximity with the beam, increases the radiation hardness requirements of the front-end electronics. This is the subject of many other contributions here in Aachen. We will concentrate on the data transport and service electronics in the experiment.

Front-end circuits are becoming more and more complex VLSI circuits. Typically they have very poor output drive capabilities, in order to keep the power consumption low. This means they can only drive short signal lines. As the experiments get bigger the distances for the signals grow. As consequence one need to put some driver electronics between the front-end and the transport media.

Likewise the front-end needs power supplies which can tolerate a certain radiation. This problem will not be addressed in this paper.

1.2 LPS topology

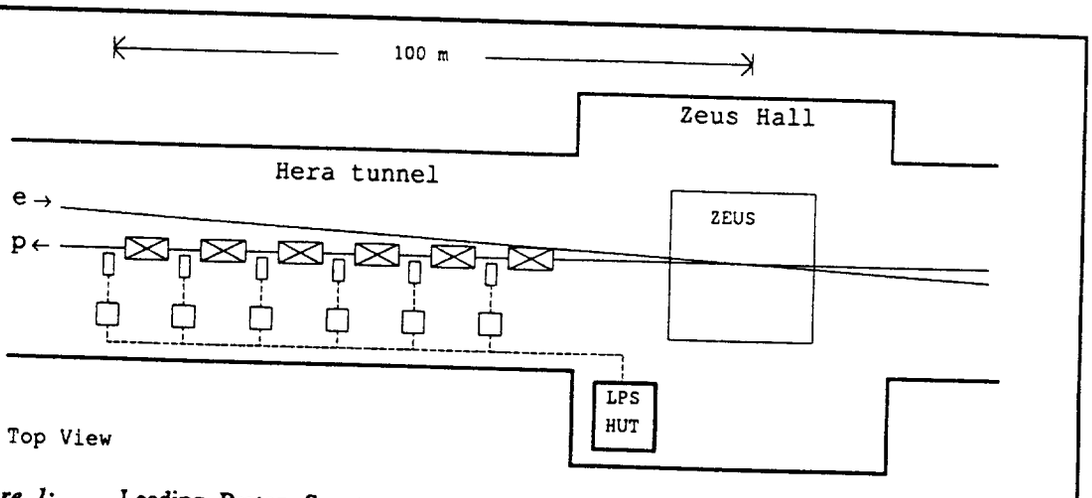


Figure 1: Leading Proton Spectrometer topology. The LPS shown in the context of the HERA collider at DESY in Hamburg.

Figure 1 shows the topology of the Leading Proton Spectrometer at the HERA proton electron collider. The ZEUS main detector is located around the interaction point. The aim of the LPS is to measure the momentum of the forward scattered protons. For this reason the Si–strip detectors of the LPS are located downstream the interaction point few mm's from the p–beam

The total number of strips in the LPS of about 50000 are partitioned between 6 stations at distances from 24 to 90 m from the interaction point. The intermediate magnets are used as bending magnets for the low Xt protons. As can be seen on Figure 1 on page 1 the detectors and front–ends are located in the accelerator tunnel, and consequently exposed to radiation. It also can be seen that the read–out and control signals has to pass over a distance of up to 110 m before low level radiation is reached.

It turned out to be useful to put the main part of the tunnel support electronics at locations in the tunnel where the radiation is at a minimum. Under the concrete constituting the walkway along the accelerator, there was found both room and minimum radiation.

The expected dose in the sheltered region over the experiment life is less than $10^{13} n/cm^2$ and a synchroton radiation of less than 500 Gy. These numbers are apparently modest, but they are very difficult to estimate, because they depend on how the accelerator is operated. I.e. a single beam accident can give rise to a large dose, or when machine trials are being made.

The expected dose at the detector region is $10^{13} n/cm^2$ and a synchroton radiation of 10K Gy.

1.3 Choice of standard commercial components

Many different components are involved in a read–out and support electronics like the LPS. One would like to avoid the expense of using special rad hard electronic components for relatively primitive functionality. Such can easily cost from 100 to 1000 times and have a delivery delay of 10 months.

Therefore we were forced to adopt the philosphy of using cheap commercial components which can be thrown away when they start failing. Adopting this philosophy also means that one must be particularly careful to include suitable monitoring and test facilities in order to compensate for a lower reliability.

We then started a search of suitable components among the vast product range. Contacts with Hahn Meitner Institute, Berlin confirmed that in general bipolar is more radiation resistant than their CMOS counter–parts[2]. The price to pay is increased power consumption, which in our case is not of primary concern. It turned out that exact results on radiation tolerance is concentrated around the lower power CMOS parts.

As media for data transport one finds..

Coax: Expensive, Bulky, High bandwidth
Fibers: Expensive, Not radiation hard in standard version[3], High bandwidth, Very Compact.
Twisted pair: Cheapest, Compact, Many support chips available (EIA Standards RS–422–A, RS–485)

For those reasons we have chosen twisted pair cables as our primary medium.

As general glue and buffer logic we have chosen the TTL family which has a vast number of different components in many different technologies. We could have chosen the ECL family, which is faster, but more difficult to interface to our front–end, and the twisted pair line receivers has poor common mode rejection. I.e. more suceptible to noise. Incidently the ECL family is one of the most radiation hard digital circuits even in commercial version[2].

As versatile TTL logic building block the vast family of Programmable Logic Devices had our interest.

1.4 Irradiation procedures

TTL logic circuits evaluated and tested at CERN were irradiated in the manner shown on Figure 2.

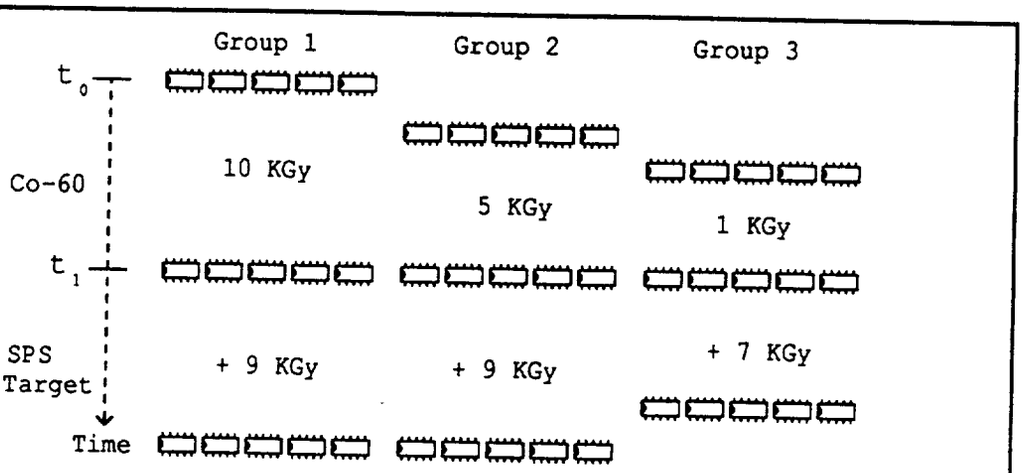


Figure 2: Irradiation procedures. 3 groups of TTL circuits were first irradiated with Co-60, then afterwards in the SPS accelerator target area.

Each type of circuit was divided in 3 groups of 5 pieces each. Those 5 in a group were all exposed in the same manner. First they received a dose of Co-60 gamma rays with a rate of 106 Gy/h (Si)(Perspex). This was done in the commercial irradiation facilities Conservatome-Montluel in Lyon. By putting in the circuits at different moments one obtained that they all had got their final dose at the same time t_1. This facilitated the tranport back to CERN where the test was done. The doses were 1070 Gy, 5400 Gy and 10 KGy. All circuits were irradiated under electrical power and with all inputs grounded and outputs open. To irradiate under power constitutes a significant complication when using commercial facilities which is not normally used for electronics.

The circuits were tested before and after irradiation. We have not looked for any annealing effects, because the testing took plase some weeks after irradiation.

It turned out, that all circuits worked perfect without measurable degradation on the tested parameters. For that reason we decided to continue irradiation in the SPS accelerator North target area, when such an occasion came. The three groups of circuits were put on top of the beam pipe down-stream the target. Group 3 was taken out after 17 days and group 1 and 2 after 34 days.

The neutron fluence in the 34 days of irradiation is estimated to have been $310^{11} n/cm^2$ (E > 2.3 MeV) plus an unknown dose of thermal neutrons and high energy particles with E > 40 MeV. An inconvenience in such an irradiation facility, is that the dose is very difficult to control, because it depends on the machine operation, and on the restriction of access. This is why the two last groups

got almost the same dose. The first group got 7 KGy and the last two 9.5 KGy measured with RPL–glass[1].

Another serie of devices was irradiated at HMI's 2.5 MeV electron accelerator source. HMI is equipped with very powerful test equipment, so several parameters were tested and only the main results can be presented here.

1.5 Radiation test on TTL 74X244 and 74X241 family

The two devices 74X244 and 74X241, are the digital buffers in families Low power Schottky, Advanced Low power Schottky and Fast. Functionally they are both non–inverting buffers, except 74X241 has one of the two enables active high, so they are all very alike.

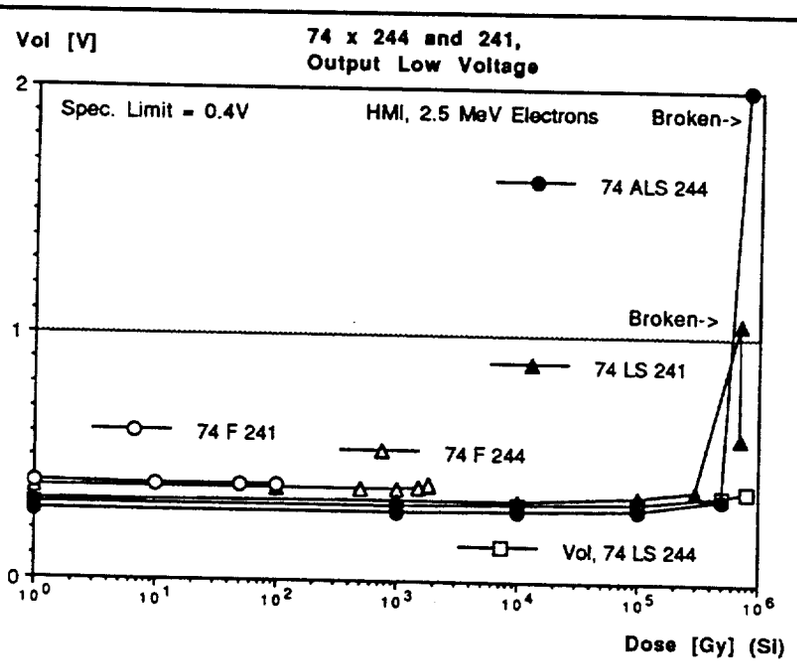


Figure 3: Output low voltage. V_{ol} at the rated load current for each devices family versus accumulated dose in Gy (Si)

On Figure 3 we have plotted the output low drive voltage for the different devices versus the accumulated dose in Gy. It must be remarked that the load current is the specification limit current for each device, which is not the same for each family, but the voltage limit of 0.5V is common for all. Note also that the maximum dose is not the same for all devices. It can be seen that 74ALS244 and the 74LS241 are effectively breaking down after about 300 KGy, whereas the 74LS244 is still fine at 700 KGy. The Fast types were still within their specification limit at the doses tested. Later we will se why they were not tested to higher doses.

On Figure 4 we compare the output high drive voltage for the 74X244 and 74X241 devices. All devices are seen to stay well above the specification limit of 2.0 V.

[1] Radio Photo Luminescent

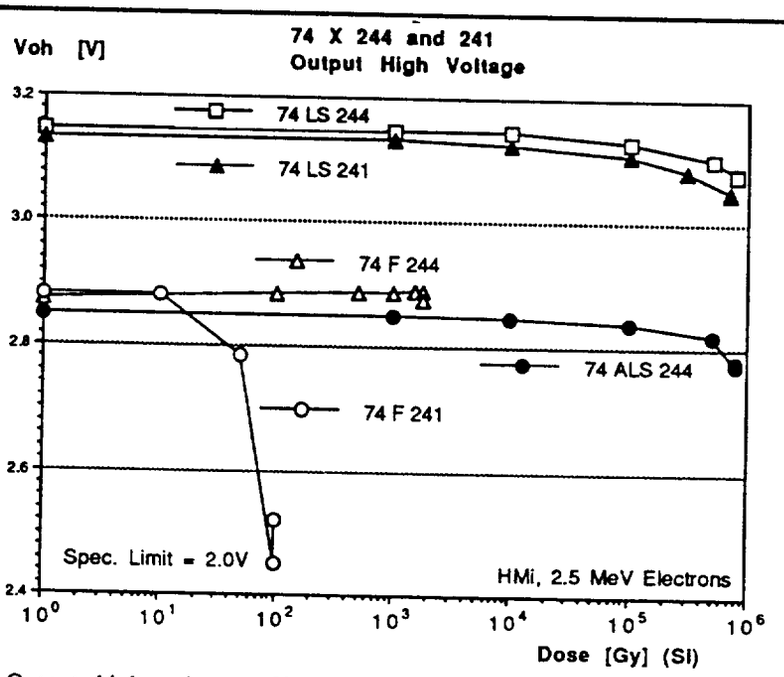


Figure 4: Output high voltage. V_{oh} at the rated load current for each devices family versus accumulated dose in Gy (Si)

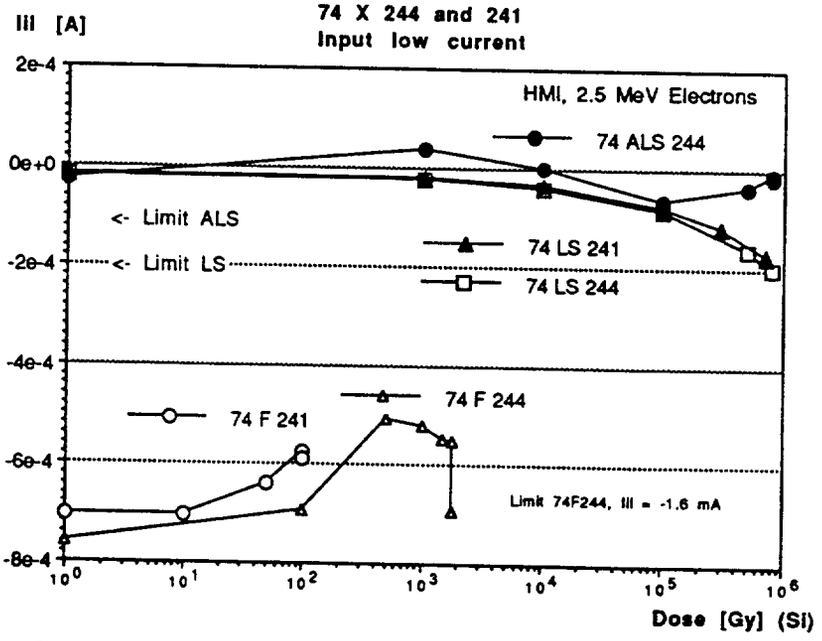


Figure 5: Input low current. I_{il} at rated input low voltage versus accumulated dose in Gy (Si)

Figure 5 on page 4 shows the input current needed to pull the input down to 400 mV. The two

LS devices are seen to track and they stay within their specification limit of 200 µA, up to 700 KGy.

The 74ALS244 also stays within its -100 µA range. Normally one has to pull current **out** of the input in low state, but for the 74ALS244 it changes sign some times. This is probably due to balancing leakage current effects which change with dose.

The two F devices are seen to be more sensitive to radiation, yet they still are within the -1.6 mA specification. Of the two points at the end of the F curves the lower is the performance after 15 days of annealing at room temperature.

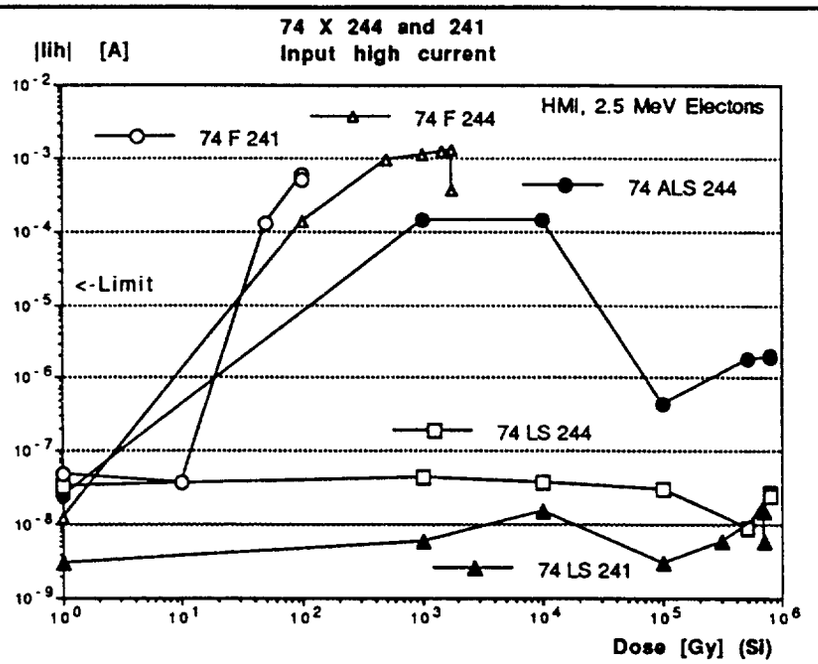


Figure 6: Input high current. I_{ih} at rated input high voltage versus accumulated dose in Gy (Si)

The curves on Figure 6 show the current necessary to drive the input high to 2.4 V The only device which stays within the specification limit of 20 µA is again the 74LS244 and 74LS241 devices. The others pass the limit with upto 1 mA for even modest doses.

It must be noted that this does not mean that the device fails in an application. This depends on whether there is sufficient drive current present to compensate the increased leakage current. Normally the fan-out of a typical family of TTL is 10 or more, but most applications uses only a few inputs per output. Busses, on the other hand, in general have a higher fan-out count than 10, but there one generally uses special bus drivers like the '244 and '241 which hve a large fan-out margin of 100 to 700 inputs per output.

The Figure 7 on page 7 shows the propagation delay which as opposed to previous static performances represent a dynamic characteristic. Only the 74ALS244 is seen to fail this dynamic test and that at the highest dose of 700 KGy.

In all these tests, the F device was showing high sensitivity at the leakage currents, and for that reason they were only irradiated up to a limit where this parameter passed standard specs. What is

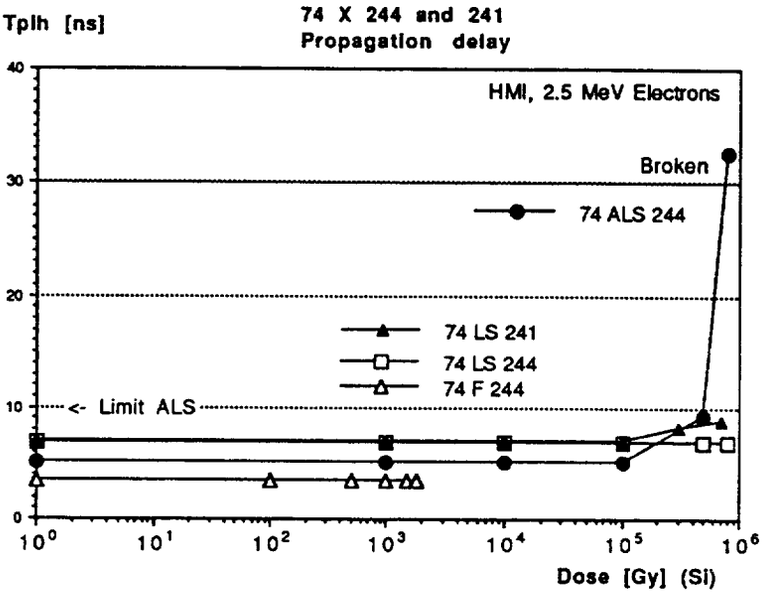


Figure 7: Propagation delay. T_{plh}, the delay from input to output of a low to high transition versus accumulated dose in Gy (Si)

clearly seen is that the old–timer standard LS series shows better irradiation tolerance, than the more recent F and ALS families.

Other items of the same devices we irradiated first with Co–60. As this was found to have neglegible effect on the measured parameters, the same chips were put into the SPS target for further irradiation as explained in 1.4 on page 3. Figure 8 on page 8 shows the output high drive current supplied when the output voltage is at the specification limit of 2.4 V. All devices are seen to degrade only slightly up to the measured dose of 20 KGy (Perspex). It has to be noted that the accelerator irradiation contains among other a lot of neutrons, for which bipolar circuits are known to be vulnerable. The input leakage currents was not measured.

1.6 Balanced line drivers and receivers

Balanced driver 74ALS194, µA96172 and balanced receiver µA96173 from Texas instruments and Fairchild meeting the RS–422–A standard were tested. In order to make the most realistic measurement for our application and facilitate the result evaluation, we tested the performance of the irradiated device in an application ressembling our final as much as posible.

Measured were the maximum data rate over 100 m of twisted pair shielded cable with pseudo random binary sequence of data. The measurements were all done with the same un–irradiated reference device in the other cable end, so we had one reference driver and one reference receiver.

There were no significant degradation up to 10K Gy of Co–60 gamma rays. The same devices after irradiation in the SPS target show still no significant change in the 74ALS194 driver performance as seen on Figure 9. The Fairchild drivers and recievers series start to degrade and brake down at the higher doses of 15–20KGy. Our application limit is 10 MHz.

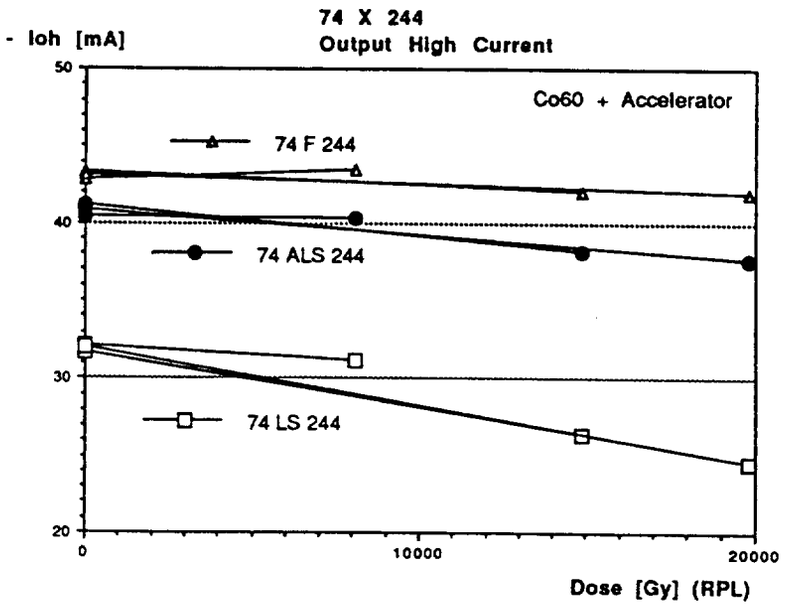


Figure 8: Output high current. I_{oh} at rated output high voltage versus accumulated dose in Gy (SPS Accelerator and Co–60).

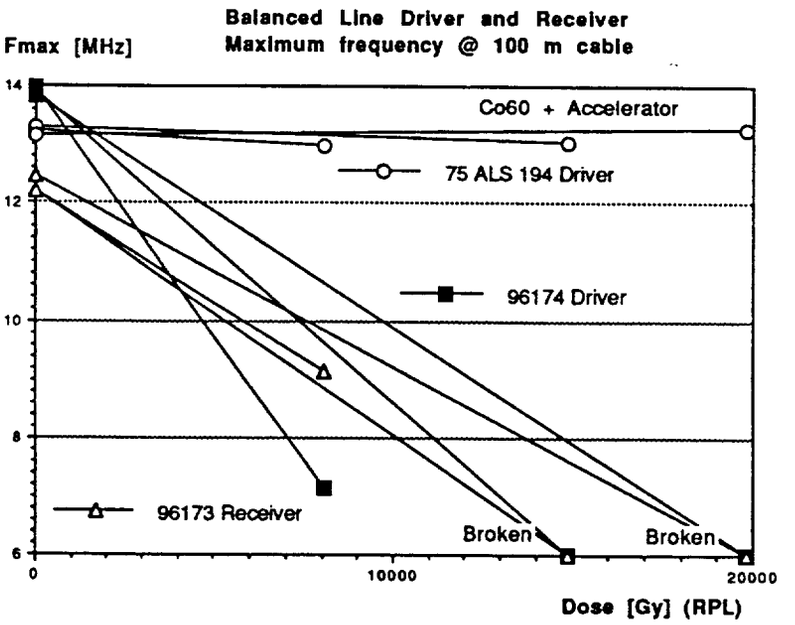


Figure 9: Maximum data rate. F_{max} on 100 m of multipair twisted screen cable versus accumulated dose in Gy (Si)

Note that with a very application oriented test–setup like this, one greatly simplifies the test and

result evaluation. In general this is a very effective method if one has a unique application of the circuit. The results are less useful for other applications. Note for instance, that we do not know anything about which specific parameter degraded. Our application tolerates a big increase in leakage currents for example, so perhaps this is why it worked at rather high doses.

1.7 Fuse Programmable Logic Device

Significant interest in radiation hardness is related to progammable logic devices, because they are very versatile logic building block. It can be programmed to perform many logic functions, and in case of system upgrades, it can be reprogrammed.

It was programmed as a 6 bit binary counter, in order to test the maximum of the device internals. A serie of 4 devices was irradiated with electrons of 2.5 MeV at HMI. The maximum count frequency is seen to degrade slowly up to around 30 KGy. After that dose, catastrophic failures occured in the V_{oh} output drive capability. The input and output leakage currents stayed within the devices specification limits even up to a dose of 100 KGy.

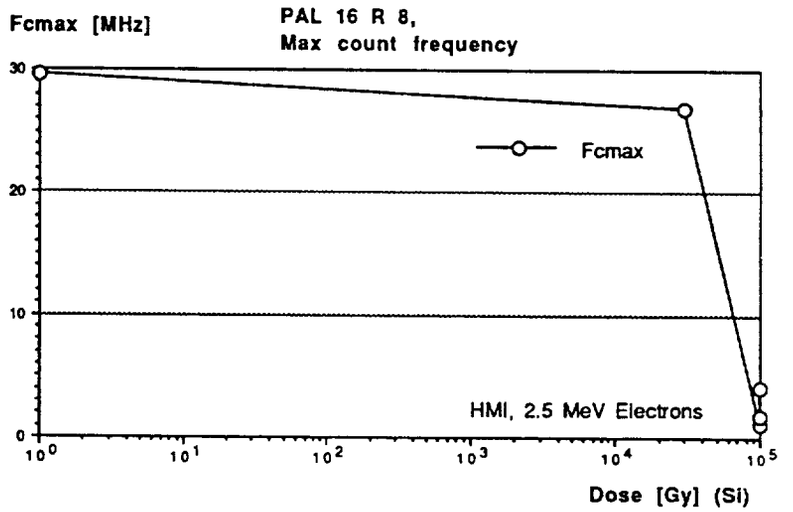


Figure 10: FPLD maximum clock rate. Fc_{max} is the maximum clock rate of a 6 bit binary counter versus accumulated dose in Gy (Si)

1.8 Conclusion

The old well proven 74LS family shows good radiation resistance.

It is dangerous to make conclusions within the same family between chips with different functions. One type of device may be good, the other type bad.

Generally one must expect an increase in leakage and input currents, and eventually a minor drive loss, but the speed is less affected. As a consequence one can make circuits which still works with some radiation damage if one takes those effects into account during design. This means for instance

that one should avoid bus line with many taps, and be more conservative with the number of inputs driven by a given output.

We want to warn that the radiation testing is very time consuming, especially if you only have simple test equipment and limited access to suitable radiation sources. If it is posible to test the devices in a go–no go test for your particular application, then this can save you some time in testing and frustrating result evaluations.

One must keep in mind that radiation resitance is very dependent on process quality, a quality which in general is not of importance to non radiation qualified components. This means one device can show good radiation resitance, and another bad, just because they come from a different diffusion batch. So if you want realy to be very serious you have to buy a complete diffusion batch, test it and take it or reject it all. The problem in this is of course that you have to buy the whole batch or at least as many as you will need from a batch. The date–code being the same does not guarantee that the batch is the same!.

1.9 Acknowledgements

This work was only possible with the cooperation of several people from CERN. Francois CONINCKX, Mark TAVLET looked after the irradiations and dosimetry. Jan SCHIPPER made all the tedious measurements at CERN, and Helmuth SCHÖNBACHER arranged the contacts with Hahn Meitner Institute from where Mr. D. BRÄUNIG, A. BODEN and in particular Mr. F. WULF are acknowledged for numerous fruitful advises and of course the comprehensive tests.

Bibliograpy

1. Zichichi, A. *'The LAA Project', CERN–LAA 89–1 1989.*

2. WULF, F. et al. *'Electronic Components in a High–Dose Environment', ECFA Study Week, 14–21 Sep. 1989, CERN 89–10, ECFA 89–124, Vol. 1, 24 Nov. 1989.*

3. FRIEBELE, E. J. et al. *'Effects of ionizing radiation on the optical attenuation in doped silica and plastic fiber–optic waveguides'. Appl. Phys. Lett. 32, pp. 619–621 (1978)*

Radiation-hard SOS-VLSI for detector electronics

Presented by
Nils Bingefors, Universtity of Uppsala[1]

Abstract

Preliminary results of radiation tests on SOS circuits are presented in this paper. The importance of operating conditions and circuit design is underlined.

Introduction

Within the LAA project, an evaluation of the SOS4 process of ABB-Hafo (Järfälla, Sweden), is being performed. Silicon On Sapphire in this process has previously been extensively used for radiation hard digital electronics, e g for satellite use.

It has however not been evaluated for analogue preamplifier circuits before. Traditionally SOS has had a reputation of having very poor transistor characteristics for analogue use. Recent process developments by ABB-Hafo has however changed this.

Careful process design and a technique to contact the deep implantation layer under the transistor channel eliminates the problems with floating substrate. The so called kink-effect is also eliminated and short channel phenomena are substantially reduced. This makes the SOS-transistor useful in analogue designs.

First prototype chip

In order to evaluate this process for use in the field of high energy physics a prototype charge preamplifier was designed and manufactured. It was decided to place the emphasis of the evaluation on circuit effects caused by radiation; the effects caused on single transistors were already being investigated by the industry. It was also supposed that the useful life of a circuit exposed to radiation is to a high degree dependent on circuit design and operating conditions, as was indeed seen in the early results of this project.

The first prototype manufactured contained errors in the biasing network causing high levels of excess noise and reduced bandwidth in the circuit. The noise of the signal path, a crucial parameter in this type of application, was thus masked and could not be evaluated with any accuracy. However, measurements with probes directly on internal nodes in the chip indicate that tolerable noise levels could be reached. This prototype was used anyway in some preliminary radiation tests in order to test the radiation and measurement facilities and to confirm that the SOS technology had a radiation tolerance high enough to motivate a second

[1] The following persons have worked in this project: At University of Uppsala/CERN — Tord Ekelöf, Nils Bingefors. At the Institute of Micro Electronics/Catella_Generics — Anders Sjölund, Göran Mörk, Antoni Fertner, Göran Lundström, Göran Stille. At ABB Hafo — Christer Eriksson, Magnus Paulsson.

prototype design and manufacture cycle. The results of these very preliminary tests will be presented here. It should be stressed that these results are not final and only serve to indicate some typical phenomena encountered when a circuit of this type is subjected to radiation.

Irradiation with a Cobalt-60 source

Samples of the chip were irradiated in a Cobalt-60 source at a dose rate of approximately 200 Rad/min. The irradiation cycle was 20 hours of irradiation plus 4 hours for measurements. This was repeated until a total dose of approximately 1.4 MRad had been reached. The samples were then annealed, first at room temperature for 5 days, then 2 days in 90 °C followed by 4 days in 120 °C.

One preamplifier was biased with 2.75 V during irradiation and the annealing at 25 °C. A second preamplifier was left unbiased during the entire test.

The gain of the preamplifier stage was measured as an indication of the functionality of the circuit. The measurements were performed at 2.75 V bias, i e the minimum bias for proper function of an unirradiated chip, and at 3.5 V bias, i e the expected optimum bias for irradiated chips. Figures 1 and 2 show these measured gains of the two samples at different points in the irradiation/annealing cycle.

It is interesting to note that the functionality of the circuit, as indicated by the gain, continues to decrease after irradiation has stopped. The suggested explanation for this is that while the degradation of the transistors during irradiation is quite well matched between PMOS and NMOS, the annealing processes for PMOS and NMOS follow different time constants. This results in an increase in mismatch during the initial part of annealing, which is later recovered when annealing approaches completion.

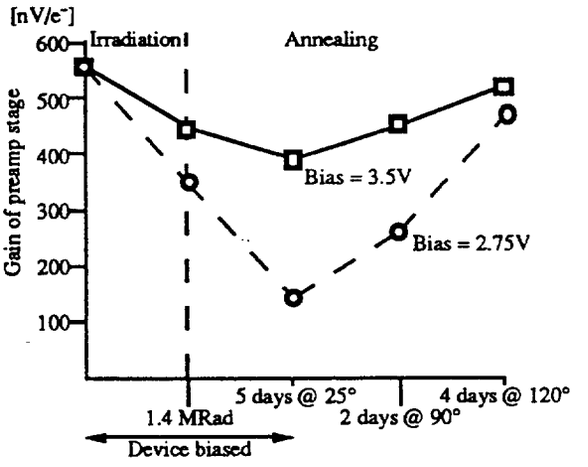


Fig. 1

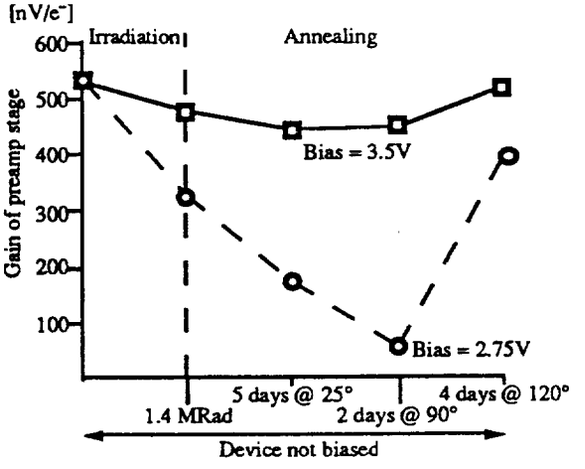


Fig. 2

Also the clear dependence on bias voltage is noteworthy. This further demonstrates the high influence of operating conditions on a circuit's life time in radiation. It becomes clear that a circuit operated under the optimum conditions determined by "normal" design procedures, i e leaving the effects of radiation to "be dealt with later", may fail unnecessarily after relatively low doses and that proper margins have to be designed and built into the circuit from the beginning.

Neutron irradiation

The status of the evaluation of SOS with regards to tolerance to neutrons is very much "work in progress". Preliminary tests to use a spallation source for neutron irradiation of electronic chips have been made. A sample of the SOS preamplifier chip together with a set of activation foils were placed 18 mm from a 10 mm thick Tungsten target irradiated by a 72 MeV proton beam of 3 μA for 405 minutes. Only minor effects on amplifier performance were noticed after irradiation. Other samples of test transistors placed at different distances from the target also showed only very small changes.

Due to software problems a definite total dose has not yet been determined. A separate run with the samples replaced by TLD dosimeters has been made to determine the background of gamma radiation and presently awaits analysis.

The mechanical system for neutron irradiation is now being redesigned to allow more flexibility in sample positioning, connection of cooling media, bias voltages etc.

Second prototype

A second SOS-chip is expected to leave the processing house in November 1990. This new circuit has a redesigned bias network, an improved layout of the input transistor to eliminate inactive gate capacitance and to substantially reduce the chip area occupied while keeping gate length and width virtually unchanged and incorporates several variations in layout solutions for switch transistors to study effects of transistor geometry on radiation tolerance.

Also the input protection circuitry has been redesigned to minimize its noise contribution.

It is expected that this new chip shall provide the answer to the crucial question encountered when designing analogue circuits in SOS: Is it possible to overcome the higher 1/f-noise in Silicon On Sapphire material?

Radiation-hard Bipolar and CMOS Front-end Electronics

K. O'Shaughnessy, J. DeWitt, D. E. Dorfan, B. Hubbard, D. Pitzl,
W. A. Rowe, H. F.-W. Sadrozinski, A. Seiden, E. Spencer
Santa Cruz Institute for Particle Physics,
University of California, Santa Cruz, CA 95064

H. J. Ziock, P. Ferguson, E. C. Milner, W. F. Sommer
Los Alamos National Laboratory,
P. O. Box 1663, Los Alamos, NM 87545

J. Ellison
University of California, Riverside, CA 92521

The Leading Proton Spectrometer (LPS) in ZEUS at HERA consists of planes of silicon detectors close to the beamline in the forward proton direction (the first plane is 20 m from the interaction point). The front-end electronics for the system must respond to the following design constraints:

- 100 μm pitch (to match detector)
- high speed operation at HERA (10.4 MHz collision frequency)
- data storage during LEVEL 1 trigger decision (5μs)
- data storage during LEVEL 2 trigger decision ($> 100\mu$s)
- high radiation exposure
- low power consumption.

To respond to these needs it was decided to build a digital system. The first stage of electronics is an amplifier and comparator, built in bipolar technology for low noise. The digital stage of electronics, built using 1.2 μm CMOS technology for low power consumption, is a buffer system to allow data storage during trigger decisions. Both stages have been designed and are in the prototyping phase. We report here studies of radiation hardness of components.

The design of the Analog Amplifier Comparator Chip (AACC) has been previously discussed [1]. The amplifier has a peaking time of 20 nsec for pulses from silicon-strip detectors and the power consumption is estimated at 1.6 mW/channel. The comparator threshold can be set as low as 30% of the pulse due to minimum-ionizing particles. The equivalent noise charge is 700 electrons. The design is being fabricated using Dielectric Isolated (DI) bipolar technology and components produced by this process were irradiated to determine their performance. The transistors were exposed to 1 MeV neutrons produced in a beam

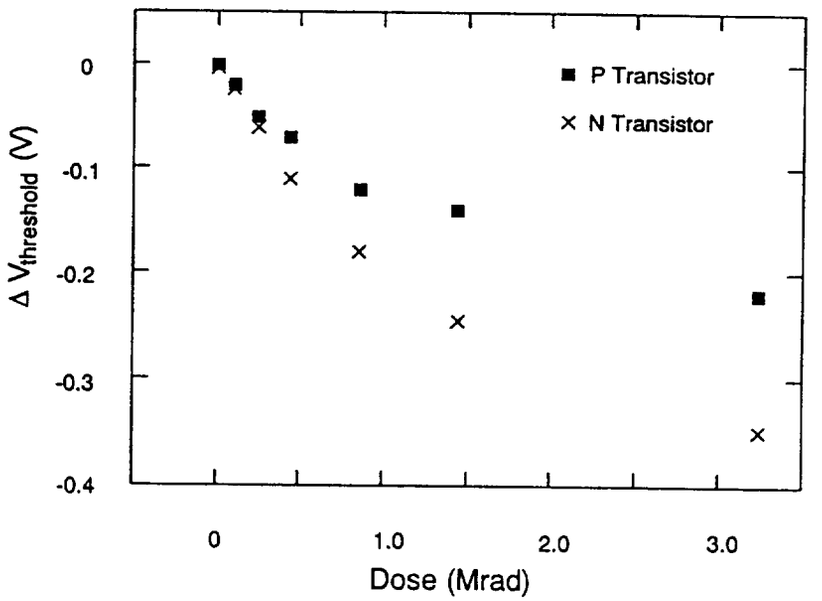


Figure 1: Variation of threshold voltage as a function of photon dose.

dump at LAMPF. The transistor β decreased by approximately 12% after a dose of 5×10^{13} n/cm^2. Transistors were also exposed to 500 and 800 MeV protons up to a flux of 7×10^{14} protons/cm^2 at LAMPF. The dose was approximately 25 Mrad(Si) and is much larger than the estimated dose for the LPS. In this case the β decreased from 85 to 35. Although a significant decrease, it should be possible to operate the chip at these levels.

The design of the Digital Time Slice Chip (DTSC) has been described in reference 2. The first buffer is a 64-stage shift register which stores the data during the LEVEL 1 trigger decision. If a LEVEL 1 valid signal is received then the data is written into a 32-word queue to wait for LEVEL 2. A test version of the chip has been manufactured in a radiation-hard 1.2 μm CMOS process by UTMC[3]. Included on the wafer were some test structures which have been irradiated with photons from a ^{60}Co source at UC Santa Cruz. For both p- and n-transistors, the shift in threshold voltage was measured as a function of dose. The results are shown in Figure 1 and are less than 0.4V for approximately 3 Mrad dose (the operating voltage is 1 V). The test structures also included combinations of transistors to produce inverter and NAND circuits. These were also irradiated and show even smaller shifts as the changes in the p- and n-transistors compensate. After the performance of other structures is evaluated, they will also undergo radiation tests.

We have a design and are working on prototypes for the analog and digital stages of a front-end system for the Leading Proton Spectrometer. We have performed irradiation studies on transistor components produced using radiation-hard bipolar and CMOS technologies. Exposure to 5×10^{13} n/cm^2 of 1 MeV neutrons caused the bipolar transistor current gain, β, to decrease by approximately 12%. The decrease due to 7×10^{14} p/cm^2 was more severe, but still tolerable. The CMOS transisitors and logic circuits showed small changes in threshold voltage ($< 40\%$ of the operating voltage) after exposure to 3 Mrad(Si) of ^{60}Co photons. Our future work includes the irradiation of the functional chips when available with neutrons and photons.

References

1. D. E. Dorfan, NIMA**279** (1989) 186.

2. J. DeWitt, NIMA**288** (1990) 209.

3. United Technologies Microelectronics Center, Boulder CO.

Radiation resistance of semiconductor detectors and associated electronics

G. Hall
Blackett Laboratory
Imperial College
London SW7 2AZ, UK

Abstract

A review of the basic damage mechanisms in semiconductor devices is given, with an emphasis on silicon. Some estimates are made of the potential degradation of detectors when operated in an LHC environment.

1. Introduction

In terms of radiation damage, at least, LHC experiments will represent the most challenging environment in which detectors have yet operated. It is now well known that the flux of particles will comprise two important components: neutrons and charged particles. Both of these have important consequences for semiconductor devices and in the case of silicon many of the important mechanisms of damage are well studied[1-4], if not always completely understood. Other potentially interesting materials, such as gallium arsenide, are less well studied and less well known to this author. However some of the damage mechanisms are similar for different materials and it is possible to draw conclusions about likely advantages compared to silicon even if these benefits will require further R&D to realise.

2. Radiation doses

Since the detectors are not yet designed and semiconductor devices, in particular the electronics, will be distributed throughout the entire detector volume it is difficult to generalise about the radiation doses to be encountered. They will depend on the composition, shape and dimensions of the experiment. For example in a spherical lead calorimeter with a 4m diameter internal cavity [5-8] annual neutron fluences near shower maxima are expected to vary from ~10^{12} cm^{-2} at $\eta = 0$ to ~10^{17} cm^{-2} at large η with corresponding total hadron and gamma doses of ~500 Gray to ~5x 10^6 Gray in the calorimeter. In the central cavity, which will probably be used for tracking detectors, the charged particle dose will depend (as $1/r^2$) on radial distance from the beam while the neutron fluence will be practically

isotropic. Here annual neutron fluences of ~10^{13} cm^{-2} will be typical while a charged particle dose of 10^4 -10^5 Gray at 10cm radius may be expected.

Simulations carried out so far are expected to have uncertainties of order 2 [5]. It is also important to note that the fluences depend, at least to factors of 2-3, on the decisions which are made on calorimeter design and thus estimates of the performance of semiconductor detectors, in particular, need to be made using realistic assumptions. It can also be expected that there will be local regions of higher than average doses caused by the finer details of detector construction which need to be taken into account.

The basic damage mechanisms in semiconductors are conveniently separated into two categories [1-3] - bulk effects and surface damage. In general the simplest types of semiconductor detectors, like diodes, are most affected by bulk damage while many important electronic devices in MOS technology are most adversely affected by surface effects. For more complex modern detectors this simple rule may not hold.

3. Bulk damage

To displace an atom from its site in the crystalline lattice requires ~15eV of kinetic recoil energy. This immediately sets a limit to the damage caused by some particles expected to be present, for example electrons and thermal neutrons. Neutrons of the ~1MeV energy typical of nuclear boil-off reactions, and therefore present as a result of hadron collisions in the calorimeter[9], are particularly effective in generating displacement damage. For simple kinematic reasons, it can be estimated that a neutron requires more than ~110 eV to remove an atom from its site. From these considerations and knowledge of neutron-Si cross-sections [10] the relative damage of neutrons as a function of incident energy can be calculated (fig.1); it shows a substantial increase at ~200keV but then remains relatively constant.

There is evidence from studies of electronic devices that displacement damage is proportional to non-ionising energy loss. This can also be calculated and Van Ginneken[11] has extended previous estimates to energy ranges of interest to particle physicists for all particle types (fig.2). Although, as yet, difficult to confront with experimental data this indicates at least that high energy muons and electrons should not be used as the standard with which to measure average ionising particle bulk damage.

An energetic displaced atom initially loses energy by ionisation but towards the end of its range creates multiple further displacements, ultimately leading to ~10^3 displacements in a highly disordered region only a few hundred Angstroms in linear dimensions. The simplest lattice defects are point defects, like vacancies at a lattice site or interstitial atoms located between normal lattice positions. These are normally unstable at room temperature and may migrate from their point of origin - either

annihilating, being trapped at a surface or forming a stable defect complex. Since the semiconductor properties depend critically on lattice symmetry both of the latter cases imply adverse consequences for the material since unwanted energy levels in the band gap are formed.

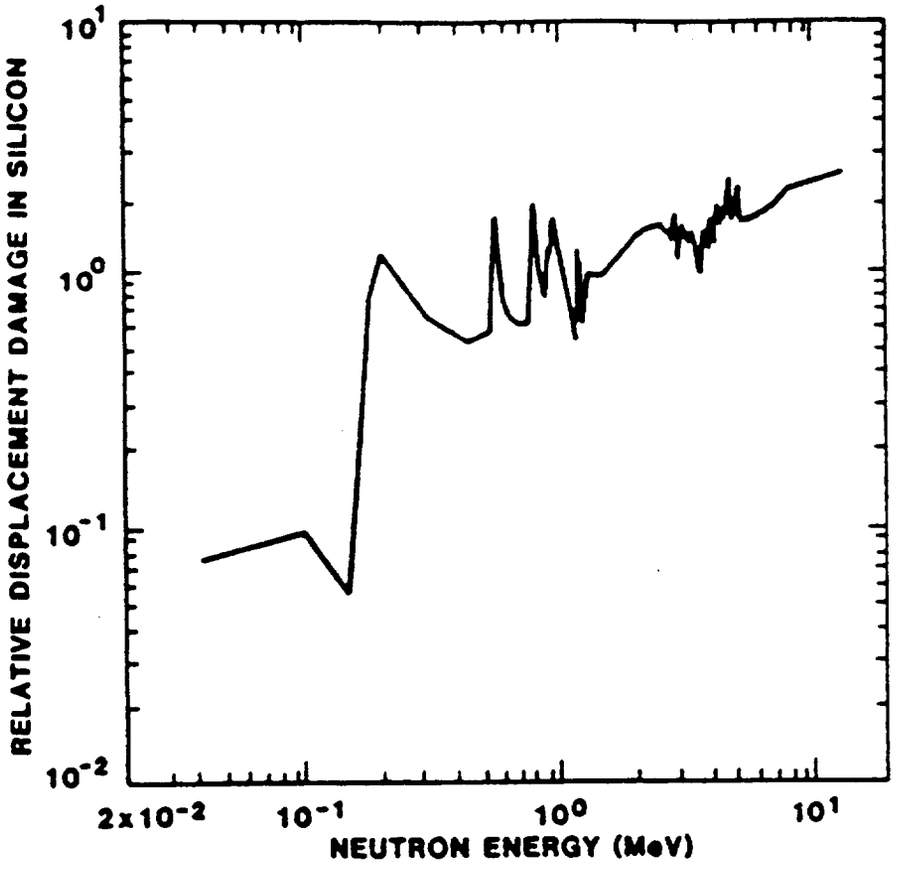


Fig.1 Relative displacement damage by neutrons in silicon [1].

The most well known effect of energy levels in the band gap is an increase in leakage current in depleted detectors since the ease with which a mobile carrier can traverse the gap is greatly enhanced by intermediate levels. There are other important effects however: trapping of carriers can degrade the signal either by incomplete charge collection or by increasing the duration of the signal current pulse. Degradation of minority carrier lifetime is a related effect. An effect of particular concern is compensation of the material by defects which are charged and thus behave effectively as ionised doping atoms; this will change the electric field in the device.

Many of the defect structures present after irradiation have been identified. The complexity of the defects, which can have several charge states as well as energy levels, requires a variety of correlated techniques to characterise them completely[4]. Nevertheless, in the case of silicon, there is some consensus on the most important observations. A vacancy-phosphorus complex has been observed in several studies [4,12,13,19e] and is thought to be responsible

for much of the leakage current increase in neutron irradiated detectors [12]; this would also explain the observed temperature dependence of the leakage current[19a,n]. Other complexes which have been identified as important are vacancy-oxygen and vacancy-vacancy in several charge states.

An important side effect of charged defect formation is compensation of the substrate material. It has now been established in several measurements that during irradiation donor removal occurs in n-type detector material which eventually inverts and becomes p-type. The measurements are not yet sufficiently detailed to show if this phenomenon continues indefinitely but at fluences up to about a few $x10^{12}$ $n.cm^{-2}$ there seems to be a roughly linear change of effective doping concentration with fluence. Inversion probably occurs for detector grade material at neutron fluences of ~10^{13} cm^{-2} [19e,n].

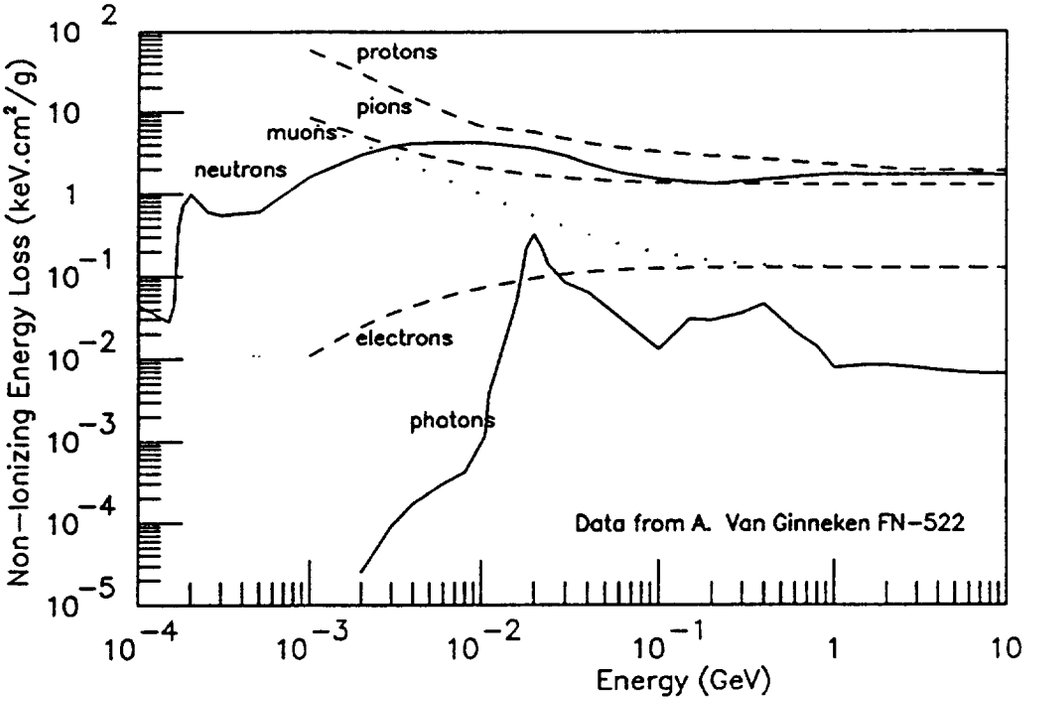


Fig.2 Calculated non-ionising energy loss for different particles [11].

There is a large flux of thermal neutrons expected to be present and it is interesting to note one of their possible effects although, as noted, they cannot directly cause displacement damage. Neutron transmutation doping [14] is a method for obtaining highly uniform n-type silicon for electronics applications. Thermal neutrons undergo capture reactions in silicon but, with the exception of the 3% of ^{30}Si atoms present, the resulting silicon isotopes are stable. ^{31}Si beta decays with a 2.6h half life to ^{31}P which contributes donor dopants. However estimation of the reaction rate demonstrates that fluences of 10^{13} thermal $n.cm^{-2}$ produce only ~10^{9} cm^{-3} phosphorus atoms which is insignificant in comparison to the doping concentration of high resistivity silicon.

4. Surface damage

Surface damage effects are well studied in silicon where the usual oxide-silicon interface plays an important role in the operation of some important electronic devices. During the high temperature oxidation procedure, which is one of the first fabrication steps, charge is unavoidably incorporated into the oxide in several forms. While mobile charges introduced by the presence of sodium are normally avoided by scrupulous cleanliness and gettering techniques several varieties of charges fixed in the oxide are created.

Close to the interface [15] resides the positive fixed charge which results from the transition from silicon to silicon dioxide over atomic layer dimensions; typical densities are 10^{10}-10^{12} cm^{-2}. Interface states, which represent surface mid-gap energy levels, are also formed; these are mobile and play an important role in surface leakage currents. Bulk fixed trapped charge can be present from defects in the bulk oxide. All of these are enhanced by irradiation, most importantly by ionising particles.

Typically, after mobile charges are generated by ionisation a certain fraction rapidly recombines. Electrons then diffuse or migrate in any oxide field to a surface while holes, which are several orders of magnitude less mobile, move slowly in the opposite direction. In many cases this can be the oxide-silicon interface and holes are trapped there, enhancing the fixed charge or the interface states. The dynamics of this process are quite complicated [16] and the mobility of defects created by ionisation appears to depend strongly on processing conditions, for example the presence of hydrogen. An enormous research effort has been devoted to developing radiation hard oxides for MOS electronics with considerable success and some of this information is in the public domain, for example the well known dependence of gate voltage threshold shifts on oxide thickness[1,2].

Typical consequences of oxide damage are therefore increased surface leakage currents, and decreased carrier mobility, as a result of carrier scattering from traps. Gate voltage threshold shifts in MOS transistors are caused by the need to compensate extra charge accumulated at the Si-SiO_2 interface before inducing carriers in the channel for device conduction. Another potentially important effect is the creation of conducting surface channels by inversion layers. In p-type silicon additional positive oxide charge at the oxide interface causes a high density of negative charge to be accumulated there; n-type regions can therefore be connected together by low resistance paths produced by electron layers.

In the electronics industry many years of research have been repaid with the ability to control most of these effects by special processing and careful design; fabrication of detectors is a relatively primitive technology in comparison.

5. Consequences of radiation damage for detectors

Some of the effects caused by radiation damage have already been mentioned. Here they are summarised, along with important side effects. Most silicon detectors are operated at room temperature but it should be noted that the effects of damage may be different at lower temperatures. Annealing effects on detector leakage currents have only been studied carefully under ambient conditions and different defect complexes are likely to be stable at reduced temperatures. Certainly, less annealing is expected although bulk leakage currents have an exponential dependence on temperature and will be reduced substantially by cooling. The consequences for compensation and trapping are less clear. It is also well known[15] that hole mobility in the oxide is substantially reduced at low temperature and thus a different distribution of oxide charge, compared to room temperature, may result.

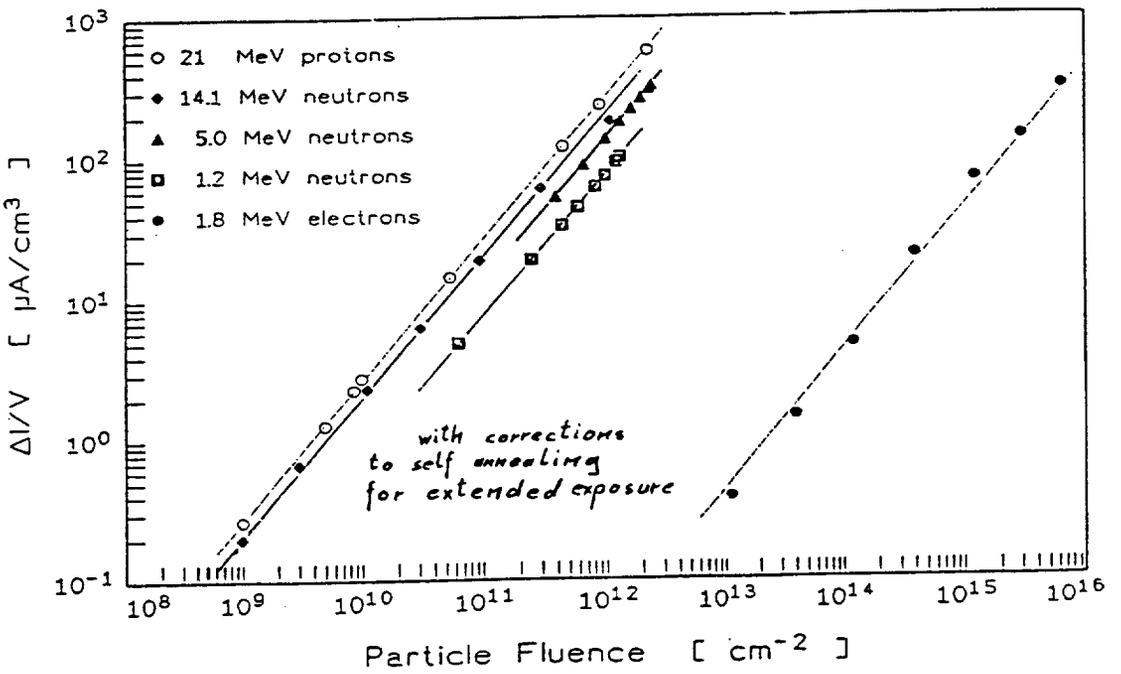


Fig.3. Change of leakage current density after irradiation [19e].

5.1 Increased leakage currents.

These lead to increased electronic noise and increased power consumption, neither of which will be trivial for any silicon detector operating in the LHC environment. Gallium arsenide detectors show a much lower increase in leakage current after extremely large neutron fluences[17]. This is probably because the substrate material is of relatively poor quality compared to silicon and the band gap is already heavily populated with intermediate levels. However since the initial leakage current is comparable with good quality silicon devices gallium arsenide is a promising material for LHC

applications provided large area detectors with uniform (even if incomplete), high speed charge collection can be produced.

More systematic studies (a good example is that of ref [19e]) are still needed but for silicon it is well established that the increase in current density is proportional to particle fluence: $\Delta J = \alpha \phi$ (fig.3). The damage constant is not well defined for all types of particle and most of the available data, acquired under a range of conditions[1], are shown in Table 1. From these it is possible to extract damage constants for neutrons and charged particles[2]. I estimate [18] 6.9×10^{-17} A.cm^{-1} for neutrons and 2.9×10^{-17} A.cm^{-1} for charged particles. Given these it is possible to calculate the leakage current increase for a given detector configuration at LHC .

Table 1 **Leakage current damage constant**

Experimenters	Irradiation	α (nA/cm)	Ref
NA32	200 GeV hadrons	$1.3\ 10^{-8}$	19a
Nakamura	800 GeV p	$2.9\ 10^{-8}$	19b
Lindström	14 MeV n	$15\ 10^{-8}$	19d
Lindström	21 MeV p	$21\ 10^{-8}$	19d
Lindström	1.2 MeV n	$7.9\ 10^{-8}$	19d
Lindström	5 MeV n	$14\ 10^{-8}$	19d
Lindström	1.8 MeV e	$4\ 10^{-11}$	19d
Vismara	^{252}Cf n	$4.5\ 10^{-8}$	19e
Borgeaud	hadrons	$9.1\ 10^{-8}$	19f
NFM	reactor n	$15\ 10^{-8}$	19c,d
NFM	GeV μ + shower	$0.6\text{-}9\ 10^{-8}$	19c,d
NFM	GeV μ + shower	$0.18\ 10^{-8}$	19c,d
Korde	^{252}Cf n	$5.8\ 10^{-8}$	19g
Ohsugi	12 GeV p	$3.0\ 10^{-8}$	19h
Hasegawa	reactor n	$6.6\ 10^{-8}$	19i
Djikstra	β electrons	$\sim 0.5\ 10^{-9}$	19j
Chilingarov	1.5 MeV e^- ,~10keV γ	$0.8\text{-}7.0\ 10^{-9}$	19k
Mishra	0.8 GeV p	$1.8\ 10^{-8}$	19e
Ziock	800MeV p	$3.9\text{-}4.4\ 10^{-8}$	19m
Edwards	~1MeV n	$>3.1\ 10^{-8}$	19n

As an example I consider a detector consisting of cylindrical layers of 300μm thickness silicon in the inner cavity of a uranium-scintillator calorimeter

[1]Few of these are dedicated experiments and most extract the damage constant from a single measurement.

[2]The reader is invited to form his own opinion as to the merit, or otherwise,of the values I have chosen.

with 2m inner radius[3]. The three inner layers could be part of a microstrip tracker; the outer layer could be one part of a pre-shower detector (not necessarily simultaneously present).

For a luminosity of 2×10^{34} $cm^{-2}.s^{-1}$ and $10^7 s.yr^{-1}$ the fluences are $\approx 4\times10^{16}/R^2$ minimum ionising particles.cm^{-2} and $\approx 3\times10^{13}$ n.cm^{-2}[5,8]. The annual rate of increase of leakage current, assuming room temperature operation, can be written

$$\Delta I = 62 + 3.5\ 10^4/R^2\ (\mu A.cm^{-2})$$

The results for layers at different radii, including the extra power need to sustain the increased leakage current, are shown in Table 2.

Table 2 Annual rate of leakage current increase for $L = 2 \times 10^{34}\ cm^{-2}\ s^{-1}$

Layer	R(cm)	L(cm)	$\Delta I(\mu A cm^{-2})$	$\Delta I_{layer}(A)$	$\Delta P(kW)$ (at 100V)
1	10	50	410	1.3	0.13
2	30	130	100	2.5	0.25
3	50	200	75	4.7	0.47
4	200	400	63	32	3.2

Electronic noise depends on detector segmentation. As an example consider a microstrip 25μm x 9cm (or a pad 1.5mm x 1.5mm) in each layer. After five years of operation, assuming CR-RC shaping with a 15nsec time constant, the strip or pad currents and shot noise are given in Table 3. Increased noise at these levels may just be tolerable for the outer layers but for the inner layers increased segmentation is surely required to ensure a reasonable lifetime for detection of minimum ionising particle signals of ~25000 electrons, often shared between strips.

Table 3 Microstrip leakage currents and shot noise contribution after 5 years operation

Layer	ΔI_{strip} (μA)	ENC_{shot} (e)
1	46	2900
2	11.3	1430
3	8.4	1230
4	7.1	1130

[3]U-scintillator is a median case; other materials change the neutron fluence up or down by a factor 2-3 [5]. More optimistic or pessimistic assumptions regarding several factors could be made; those chosen are not claimed to be optimal, merely realistic.

It is clear that leakage currents alone represent a significant heat load and need to be allowed for - in addition to the 1-2mW/channel required for front end electronics. For detectors at larger distances from the beam it would clearly be advantageous to reduce significantly the neutron flux if this can be achieved, by the use of moderating material at the calorimeter face for example. Unfortunately there are potentially even more serious problems.

5.2 Change of effective doping concentration

As n-type material gradually becomes intrinsic and then inverts to p-type the electric field in the detector changes. This will have the effect of changing the speed at which the carriers are collected and thus the time development of the signal current pulse. It has already been stressed [22] that it is important to operate the detectors well over-depleted to ensure that the full signal is observed within the electronic shaping time; otherwise further signal to noise degradation occurs. This will become more important after inversion of the substrate. Then the junction side, where the electric field is maximum, moves from the p-type surface to the n-type surface. Holes will then be collected more slowly, probably leading to extended tails on the signal pulse.

A second effect, not so far observed, is the likely interconnection of p-type regions after the substrate becomes inverted. In double sided strip detectors a considerable effort has been devoted to solving the problem of isolation of n-type strips on n-type silicon. It is not yet clear how serious a problem this will be for p-type areas on p-type silicon. It should be noted that it applies to multi-pad detectors as well as microstrips.

For microstrip detectors the change in electric field within the detector is likely to lead to degradation in position resolution, especially if the radiation is significantly non-uniform. Such an effect was observed already in the NA32 experiment[19a] where field distortions caused carrier trajectories to be non-normal to the wafer surface.

5.3 Surface damage

Many microstrip detectors presently in use now incorporate integrated capacitors and resistors. Some of these, for example polysilicon resistors and capacitors, are quite clearly radiation hard[19n]. Others, such as punch-through and accumulation layer resistors[20] may be radiation tolerant but, for operation, depend strongly on conditions at the surface of the silicon. The magnitude of resistor values is known to change with leakage currents drawn by the detectors and measurements are required to demonstrate that this can be tolerated at LHC. Interstrip isolation is also dependent on surface fields in some designs [21] and needs evaluation.

6. Consequences of radiation damage for electronics

Summarising the radiation resistance of electronics is made difficult by the range of technologies available. In practice hardness depends on choice of technology, details of design and processing, and fabrication techniques specially aimed at very high radiation hardness specifications have been developed for military and space applications.

Table 4 **Selected hardness levels of LSI circuits (after Dressendorfer)**

Technology	Total dose (rads (Si))	Neutrons (n/cm^2)
NMOS	$10^3 - 10^4$	$>10^{15}$
CMOS		
Commercial	$10^3 - 10^4$	$>10^{15}$
Hardened	$10^5 - 10^6$	
CMOS/SOS		
Commercial	$10^3 - 10^4$	$>10^{15}$
Hardened	$10^5 - 10^6$	$> 10^{15}$
Bipolar		
Older technologies	$10^6 - 10^7$	$10^{14} - 10^{15}$
Newer technologies	$10^4 - 10^5$	$10^{14} - 10^{15}$

Two of the most interesting technologies for general HEP and, specifically, LHC requirements are CMOS and bipolar. Variations on simple hardened CMOS processing include silicon on insulator (SOI) [26,27] technologies and demonstrations have recently been provided of circuits hardened to 1MGray levels using SIMOX processes [23-25]. The radiation resistances achieved have been summarised by Dressendorfer [29] (Table 4) and the principal requirements to achieve radiation hardening are explained below.

6.1 MOS technologies

The main cause of damage is from ionisation within the oxide which leads to accumulation of charge and traps at the oxide interface; thus total dose is of greater concern than neutron fluence. The most important parameters changed are gate voltage thresholds and carrier mobility in the conducting channel of the transistors. Bulk damage is of much less importance but leads to increased leakage currents, decreased minority carrier lifetimes and reduced mobility. In CCDs bulk effects reduce charge transfer inefficiencies but surface damage dominates in non-hardened devices.

An example of a radiation hard bulk CMOS process is that of UTMC [27] where the technical description guarantees that circuits in a 1.2μm process

will meet specifications to 10^6 rads and at least $5x10^{14}$ n.cm^{-2} and function to doses greater than 10^7 rads. Measurements have confirmed the small expected threshold changes [19m]. What is not yet clear, and is of great interest to analogue designers, is the noise behaviour of the transistors.

6.2 Bipolar technologies

In contrast to MOS devices, bulk damage is of great importance in bipolar transistors. Enhanced carrier recombination in the base due to displacement damage effects is an important cause of gain degradation since transistor gain is determined by the fraction of carriers which traverse the base from emitter to collector. Leakage currents also increase because of bulk damage. Surface effects are most important for relatively low doses but a general statement of the hardness of bipolar circuits depends on details of the technology and design of the devices. Certainly useful analogue electronics can be designed to accommodate significant changes in transistor gain so reduction need not be fatal.

7. Conclusions

Estimates can already be made of the radiation tolerance of detectors in an LHC environment and potential weak points can be identified. It is still possible to imagine the use of silicon strips or pixels in regions even quite close to the beam but close attention needs to be paid to charge collection speed, total leakage current and shot noise to ensure adequate detector lifetimes. Gallium arsenide detectors could be a promising alternative to simple silicon diodes in some circumstances to avoid these problems if better quality detectors can be developed in the near future.

The consequences of damage induced compensation of bulk silicon are a serious concern and further investigations are certainly required. Complex microstrip detectors with integrated components need further development and evaluation of the different technologies available to ensure sufficient radiation tolerance.

Radiation hard electronics technologies based on silicon appear to be commercially available with adequate levels of radiation resistance to read out signals from semiconductor detectors at LHC. There are important questions concerning noise and performance which will only be answered by detailed evaluation of circuits produced for high energy physics applications.

References

Basic radiation damage mechanisms

1. J.E.Gover and J.R.Srour. Basic radiation effects in nuclear power electronics technology. Sandia Labs Report SAND85-0776 (1985)
2. T.P.Ma and P. Dressendorfer. Ionising Radiation Effects in MOS Devices and Circuits. J.Wiley (1988).
3. V. A. J. Van Lint. Nucl. Instr. and Meths. A253 (1987) 453.
4. E. Heijne. CERN Yellow Report 83-06 (1983).

Radiation doses

5. D. Groom. 1988 Snowmass Summer Study Proceedings, p711.
6. Radiation Levels in the SSC Interaction Regions. SSC Central Design Group, D. Groom, ed. SSC -SR-1033 (1988).
7. G. Stevenson. Proceedings of ECFA Study Week on Instrumentation Technology for High Luminosity Hadron Colliders, p173. CERN 89-10 (1989).
8. G. Stevenson, this meeting.
9. T.A.Gabriel et al. SSC report, SSC-110 (1987).
10. D.I. Garber and R.R.Kinsey. Brookhaven National Laboratory Report BNL 325 (1976).
11. A. Van Ginneken. Fermilab Note. FN-522 (1989).
12. E. Borchi, M. Bruzzi, M.S.Mazzoni. London Conference on Position Sensitive Detectors (1990). University of Florence preprint (1990).
13. C. Furetta, L.Vismara. This conference.
14. A.J.R. De Kock. Handbook on Semiconductors, Vol.3, 318. North-Holland (1983).
15. E. Nicollian and J. Brews. MOS Physics and Technology. J. Wiley (1982).
16. B. Magorrian and N.M. Allinson. Nucl. Instr. and Meths. A273 (1989) 599.
17. K. Smith, this conference.
18. G. Hall. Prospects for silicon detectors in the 1990s. Topical Seminar on Experimental Apparatus for High Energy Physics, San Miniato. IC/HEP/90/2 (1990)

19. *Experimental references on damage constants*

a. H. Dietl et al. Nucl. Instr. and Meths. A253 (1987) 460.
b. M. Nakamura et al. Nucl. Instr. and Meths. A270 (1988) 42.
c. E. Heijne. CERN Yellow Report 83-06 (1983).
d. E. Beuville et al. CERN/EF 89-4 (1989).
e. G. Lindström et al. DESY Report 90-109 (1990).
f. P. Borgeaud et al. Nucl. Instr. and Meths 211 (1983) 363.
g. R. Korde et al. IEEE Nuclear Science Symposium 1990.
h. T. Ohsugi et al. Nucl. Instr. and Meths. A265 (1988) 105.
i. M. Hasegawa et al. Nucl. Instr. and Meths. A277 (1989) 395.
j. H. Dijkstra et al. 1988 Snowmass Summer Study Proceedings,p 727.
k. A.Chilingarov et al. Nucl. Instr. and Meths. A288 (1990) 62.

l. C.S.Mishra et al. Fermilab-Conf-90/107 (1990).
m. H.J.Ziock et al. IEEE Trans. Nucl. Sci. 37 (1990) 1238.
n. M. Edwards, G. Hall, S. Sotthibandhu. London Conference on Position Sensitive Detectors (1990). IC/HEP/90/3

20. P. Holl et al. IEEE Trans. Nucl. Sci. 36 (1989) 251.
21. B. S. Avset et al. IEEE Trans. Nucl. Sci. 37 (1990) 1153.
22. M. Turala, this conference.
23. J.L.Leray, (CEA). This conference.
24. C. Terrier, (Thomson). This conference
25. G. Durand, J.Maurel, (Texas Instruments). This conference
26. T. Davies, (Marconi) This conference
27. T. Ekelöf, N.Bingefors. This conference
28. United Technologies Microelectronics Centre. Radiation Hard CMOS. Technical Description. (1988).
29. P. Dressendorfer, IEEE Nuclear Science Symposium (1988).

RADIATION DAMAGE OF SILICON DETECTORS BY MONOENERGETIC NEUTRONS AND ELECTRONS *)

R. WUNSTORF, M. BENKERT, E. FRETWURST, G. LINDSTRØM, T. SCHULZ
University of Hamburg, D 2000 Hamburg, Fed. Rep. Germany

N. CROITORU, R. DARVAS, M. MUDRIK
Tel-Aviv University, 69978 Ramat Aviv, Israel

R. BØTTGER, H. SCHØLERMANN
PTB, D 3300 Braunschweig, Fed. Rep. Germany

The effects of radiation damage produced by monoenergetic neutrons and electrons in silicon detectors are studied. With respect to the detector performance detailed measurements of the leakage current increase, charge collection deficiency and change of the effective donor concentration are investigated as function of energy and particle fluence. A first set of results obtained by using the method of deep level transient spectroscopy leads to preliminary conclusions for the observed radiation induced point defects.

1. INTRODUCTION

Silicon detectors have gained increasing interest for the application in high energy physics experiments. They allow easy operation at low voltages and in normal ambients, offer the most compact design and combine a direct charge read out with an excellent signal to noise ratio and fast response. Thus they are in many respects best suited for the challenge imposed by future colliding beam machines (SSC in the United States, LHC at CERN and UNK in the Soviet Union). However, the very intense radiation fields connected with their high luminosity make radiation hardness the priority demand for all components. It has therefore to be proven that the superior performance of silicon detectors can be maintained over extended periods of operation. In most applications the neutron flux will play a dominant role. As an example, for the SSC with a luminosity of 10^{33} $cm^{-2}s^{-1}$ a neutron fluence of 10^{13} neutrons per cm^2 and year has been estimated in an Iron/Silicon-calorimeter at forward angles (η = 2) and moderate distances (r = 2 m) [1,2]. If detectors are to be placed close to the interaction point the high energy charged hadron component may have a considerable effect, too. In both cases the detector performance is affected mostly as a consequence of bulk damage. On the other hand even low energy electrons may cause defects in the oxyde passivation layers of silicon detectors and thus lead to a deterioration of their properties.

In continuation of earlier studies[3-7] we describe here results of our ongoing systematic investigations of damage effects, induced by monoenergetic neutrons between 1 and 14 MeV and 1.8 MeV electrons. The primary damage effect in silicon detectors is governed by the generation of PKA's (primary knock on atoms) and thus depends on the type of the particle interaction with the lattice atoms. For neutrons the predominant nuclear scattering leads to high maximum energy transfers and thus could cause recoil cascades. Hence a mixture of point defects and clusters is to be seen. Electrons interact only by Coulomb-scattering, the average energy transfer is very low. Therefore in this case only point defects are generated in the detector bulk. A comparison of results obtained with neutron and electron irradiation should consequently offer a possibility to distinguish between cluster and point defects. An additional motivation for the electron irradiation was the above mentioned surface effect

*) work supported in part by BMFT, contr. no. 05 5HH19 I

which is due to ionization in the oxyde layer. Details of the used irradiation sources and experimental conditions are summarized in chapter 2.

In our investigations of the radiation damage we concentrated so far on the deterioration of the detector performance. Here the strong increase of the leakage current is the most pronounced effect (chapter 3). However, its consequence for the detector operation may be considerably reduced by a moderate cooling or by possible annealing methods. Therefore we have shifted our attention to the other aspects of radiation damage. Here we regard the influence on the charge collection efficiency to be most important as it would directly affect the stability of the energy calibration (chapter 4). On the other hand our previous measurements have also shown that the effective impurity concentration in n-type silicon is decreasing as function of the neutron fluence. As this will change the electric field distribution and hence influence the charge collection process, this effect was studied in more detail, too (chapter 5). It should be noticed that in all cases self annealing at room temperature is very important. Its consequences are nonavoidable for all detector employment purposes and play in many respects a favorable role. For a better understanding of the physical processes responsible for the deterioration of the detector performance it is essential to use additional experimental techniques which allow the characterization of the involved defects. In a first attempt we have employed the DLTS-method for this purpose (chapter 6). The detectors used throughout these experiments were produced by a process, which combines planar and surface barrier techniques using n-type FZ - silicon with a nominal resistivity of 3 resp. 5 kΩcm [3,4].

2. IRRADIATION

Relevant parameters for the irradiation sources and conditions are summarized in table 1. All irradiations were performed at room temperature and without applied bias. It was the aim of our experiments to use as short exposure times as possible for each given fluence and energy. This enables the possible separation between damage and self annealing. It should be pointed out that the results obtained in this way may therefore be considerably different from the work of other authors, in which long exposure times were used. However, taking the detailed knowledge of self annealing effects into account we are able to calculate the resulting effect at room temperature and for long exposures even if the flux is depending on time as in normal operation in a collider experiment. The neutron energy spectrum in e.g. a calorimeter set up is peaking at about 1 MeV but stretches out even beyond 10 MeV [1,2]. We therefore thought it useful to study the damage at different neutron energies. The choice of the 1.8 MeV electron energy was rather pragmatic. However, it ensured a homogeneous damage in the silicon bulk, since the mean energy loss in our 400 μm thick detectors is only 160 keV. In addition to the irradiation facilities displayed in table 1, a few exposures were also done within the SICAPO collaboration at CERN, technical details are described in another paper of this conference [8].

3. LEAKAGE CURRENT

Fig. 1 summarizes all results of our present work together with previous data as function of particle fluence respectively dose [4-6]. It should be emphasized that in the case of neutron and proton irradiation the current increase is practically only due to bulk damage. This was shown in detail in a previous paper [4]. In the case of electron damage surface effects contribute to the observed total current by only about 20%. Therefore we can extract a current

related damage rate α according to equation (1).

$$\Delta I = \alpha \cdot V \cdot \Phi \qquad (1)$$

Here ΔI is the current increase, V the depleted volume and Φ the particle fluence. In order to compare data obtained with various exposure times and at different intervals between irradiation and measurement it has been shown that the correction for self annealing is essential [4,5,7]. With the detailed knowledge on its time dependence one can then derive α-values which would correspond to short exposures. The final results for neutrons, summarized and compared to the work of other authors in table 2, are normalized to a temperature of 20°C. It is quite interesting to compare these findings with the energy dependent displacement cross section σ_D, which has been recently calculated again by Lazo et al. [14]. Assuming that the density of the radiation induced generation centers, responsible for the bulk current increase, is proportional to the displacement cross section σ_D we would expect that the damage rate α has the same energy dependence. For verification we define a ratio r according to equation (2).

$$r = \frac{\alpha(E_n)/\alpha(14.1\,\mathrm{MeV})}{\sigma_d(E_n)/\sigma_d(14.1\,\mathrm{MeV})} \qquad (2)$$

These values are also included in table 2. One can see that α is really proportional to σ_D for the three different neutron energies between 1.2 and 14.1 MeV (r = 1 !). Consequently we may then fold $\sigma_D(E_n)$ with the known neutron spectra for the other cases and derive the r-values in an equivalent way. Taking the given experimental errors into account also in these cases the expected value of r = 1 is very nicely reproduced.

For the 21.1 MeV protons we get a damage rate of $\alpha = (2.09 \pm 0.10) \cdot 10^{-16}$ Acm^{-1} and for the 1.8 MeV electrons $\alpha = 4 \cdot 10^{-20}$ Acm^{-1}. This means that the equivalent 1.8 MeV electron fluence, resulting in the same damage rate as that produced by 21 MeV protons is 5000. From a graph reported by van Lint et al.[15] we would expect a value of about 2000.

4. CHARGE COLLECTION

The charge collection efficiency in a totally depleted silicon detector depends on the ratio of the trapping time constant τ^+ and the transit time t_c for the respective charge carriers. This effect was measured for electrons and holes separately using monoenergetic α-particles incident on the front and rear side of the detector. Details of this method can be found elsewhere [4]. As described there, the charge collection deficiency $\Delta Q/Q_0$ is a linear function of the carrier transit time t_c. $1/\tau^+$ can be derived from the slope of this curve, taking a geometry factor into account. Examples for such measurements are given in fig. 2. If the density of the effective trapping centers N_t is proportional to the neutron fluence Φ one expects $1/\tau^+$ to be proportional to Φ, too. Results, supporting this expectation are shown in fig. 3 for a 5 MeV neutron damage up to a fluence of $2.4 \cdot 10^{12}$ n/cm^2. With respect to applications in high energy physics the consequences of charge trapping are most important for the detector response to minimum ionizing particles. However, a direct measurement of this effect would be very difficult. From known values of the trapping time constants one can however calculate the resulting charge loss for mip's according to:

$$\frac{\Delta Q}{Q_0} = \frac{1}{6}\left[\frac{t_{c,e}}{\tau_e^+} + \frac{t_{c,h}}{\tau_h^+}\right] \qquad (3)$$

Taking τ_e^+ and τ_h^+ from our α-particle measurements we arrive at the results displayed in fig. 4. Again we see a linear dependence on the neutron fluence. Therefore we define a damage rate γ, related to charge trapping by equation (6) as in reference [6].

$$\frac{\Delta Q}{Q_0} = \gamma \cdot \Phi \qquad (4)$$

For γ we get a value of $3 \cdot 10^{-15}$ cm^2. With respect to eq. (3) it should be noticed that due to the different carrier velocities the transit time for the holes is about a factor of 3 larger than that for the electrons. Therefore the hole trapping contribution to the total charge loss is enhanced accordingly. As mentioned above the results shown in fig. 4 are obtained after 5 MeV neutron damage. The displacement cross section with respect to 1 MeV is 1.7 (see chapter 3). Hence extrapolating the curve of fig. 4 and taking this energy dependence into account, for a 1 MeV irradiation we would expect a relative charge loss of 2% at 10^{13} n/cm^2. For a detector irradiated in a calorimeter set up at CERN within the SICAPO collaboration [8,16], we measured at about that fluence 1.5%. The small discrepancy between the experimental and expected value may be easily attributed to self annealing since the measurement with the α-particles was performed more than one year after irradiation.

The influence of self annealing on the trapping effect was so far only studied in one particular case. A detector with a nominal resistivity of 6 kΩcm was irradiated with a neutron fluence of $2.4 \cdot 10^{12}$ n/cm^2 at 5 MeV. Before irradiation the measured values for the electron and hole trapping constants were $\tau_e^+ = 28$ μs and $\tau_h^+ = 36$ μs. For the damaged detector we found a few days after irradiaton $\tau_e^+ = 0.44$ μs and $\tau_h^+ = 0.58$ μs. After a 150 days storage at room temperature we got $\tau_e^+ = 0.87$ μs and $\tau_h^+ = 0.61$ μs. Though more elaborate experiments are needed for further substantiation this behaviour indicates that a considerable improvement can be expected only for the electron components.

In addition to self annealing, taking place at room temperature, we studied also the influence of an enhanced heat treatment. A heating cycle of 1 hour at 200°C was used. An example for such measurements after repeated irradiations and heat treatments is included in fig. 9. The respective values for the trapping time constants are compiled in table 3. Also here we observe a nice recovery effect for the electron trapping constant as a consequence of the heat treatment. The hole trapping is even worsened or not affected (as for self annealing see above).

5. IMPURITY CONCENTRATION

In this chapter we will deal only with those effects of damaged induced defect centers, which influence the depletion voltage, since this is most relevant for the practical application of detectors. If no shallow donors or acceptors in the lower half of the band gap are created, this change is dominated by the donor removal. For n-type silicon it is due to the formation of vacancy-phosphorus (V-P) centers as discussed in chapter 6. The other deep negatively charged states as measured by DLTS can be disregarded to first order since they will influence the net charge distribution only in a small transition region at the very end of the depletion zone. A more detailed discussion is given e.g.

in reference 17 and literature cited there.

According to this approach we performed capacity voltage measurements at room temperature and extracted the depletion voltages in the same way as described already in a previous paper [4]. From these values we can derive the effective donor concentration N_{eff} directly using the well known relation between depletion thickness and voltage. In an alternative method N_{eff} is extracted from the slope of the C-V characteristic. It should however be mentioned that in this case the absolute effective detector area is needed, which may be much influenced by edge effects especially at low voltages. We therefore prefer the first method.

Also the measured values of the effective donor concentration are influenced by self annealing at room temperature. Examples of relevant measurements for detectors with $N_{eff} = 9 \cdot 10^{11}$ cm^{-3} before and $N_{eff} = 8 \cdot 10^{11}$ cm^{-3} after irradiation are shown in fig. 5. The self annealing obviously reduces the initial change in the effective donor concentration by roughly a factor of 2 within the first hours after irradiation. In contrast to the situation for the current change (see reference 4) no longer time constants have been observed. All further measurements of N_{eff} were performed at a time at least 33 hours after the end of the irradiation cycle. According to fig. 5 this ensures saturation of the self annealing. According to a simple assumption for the donor removal we would expect $dN_D = - c \cdot N_{D,0} \cdot d\Phi$ where $N_{D,0}$ is the concentration before irradiation. From this we get

$$N_D = N_{D,0} \cdot e^{-c\Phi} \qquad (5)$$

as already given in reference 4. However one has to take into account that N_D can be obtained from the measured value of N_{eff} only if the acceptor concentration N_A is known. This value has unfortunately the same order of magnitude as N_D [18]. In addition the acceptor concentration can also be affected by radiation damage, e.g. via the formation of complex defects envolving silicon interstitials and the boron impurities[19]. It would be therefore very difficult to perform any analysis according to eq. (5). Instead we have plotted in fig. 6 the ratio of the effective donor concentrations after and before irradiation as function of Φ in a rather pragmatic way. Here we have included measurements for several different detectors with initial values of the material resistivity between 3 and 6 kΩcm. The experimental data for all three neutron energies were included and the fluences corrected with respect to the energy dependence according to chapter 3. One observes a general decrease suggesting a possible inversion of the conduction type at about $8 \cdot 10^{12}$ n/cm^2. But with respect to the discussion given above it is by far not clear whether this extrapolation is valid.

In order to clarify the situation special measurements have been undertaken for detectors, which were either irradiated with a very high fluence or for which inversion due to a heat treatment was expected. The relevant C-V characteristics are shown in fig. 7. For the detector 8814B3 irradiated at CERN we observe a depletion voltage, which is much lower than before irradiation, indicating at least a near total compensation. The drastic decrease of the capacitance at low bias voltage, observed before irradiation and attributed to the field plate (MOS like edge zone, see reference 4) is completely lost after irradiation. This may indicate that the electric field starts from the rear electrode as expected for inversion. We also notice a deviation of the slope in the C-V characteristic from the normally expected one ($C^{-2} \propto V$ as before irradiation). A similar behaviour is observed for detector 8813B4, which had under-

gone subsequent heat treatments at 200° C of 1 hour after 14 MeV neutron irradiations. The possible inversion of the conduction type was further substantiated by measurements with monoenergetic α-particles as described in chapter 4. For n-type silicon the depletion zone starts at the gold electrode (front side). Therefore the short ranged α-particles incident on this side will give rise to a nearly complete charge collection already at low bias voltages. With incidence on the rear electrode we expect a full signal amplitude only when almost total depletion is reached. The ratio of the respective signal amplitudes for rear and front incidence as shown in fig. 8 (case before irradiation) is therefore understandable. For the damaged detectors we observe an opposite effect. Rear incidence yields higher signal amplitudes than front bombardement for the same bias values below depletion voltage. This is regarded to be a strong indication for real inversion of the conduction type. A proof of this result could only be obtained with measurements of the Hall-effect, which are planned for further studies. It should be mentioned that, regardless of this inversion, the detectors are still operable though the leakage current is higher than would otherwise be expected. For the detector 8813B4, irradiated and annealed in successive steps, the different effects with respect to the effective donor concentration, leakage current and charge collection are summarized in fig. 9.

6. DLTS-MEASUREMENTS

For a selected set of detectors irradiated with 14 MeV neutrons at fluences up to $1 \cdot 10^{11} n/cm^2$ DLTS-measurements were performed. By the DLTS method the reemission of majority carriers after being trapped in deep levels during a filling pulse is measured via the capacitance transient. From an appropriate plot of the emission rate versus the temperature (Arrhenius plot) one can extract the corresponding activation energies. Varying the fill pulse width up to values for which complete saturation is achieved the values for the capture rates are obtained. If the effective donor concentration is known at the same temperature one may also calculate the corresponding capture cross section. From the capacitive transient immediately after the end of the fill pulse and the capacitance at the same bias and temperature the impurity concentration can be deduced. This method was originally introduced by Lang and is widely used [20-24].

Preliminary results obtained for detectors irradiated with different neutron fluences are summarized in table 4. The listed activation energies for the defects, labeled E1, E2 and E3,. are in good agreement with values found by other authors[21-24]. In addition a fourth level E4 at about 0.47 eV was found in the DLTS spectra, which is well separated from the E3 peak and occurs with a quite small amplitude compared to the E3 level. The defects E1 and E2 can be attributed to the well known vacancy-oxygen ($V\text{-}O^-$) center and the double negatively charged state of the divacancy ($V\text{-}V^=$). For the defect E3 Tokuda et al.[22] as well as the Milano/Florence group[12,23] suggest that this defect contains two contributions, which are associated with the single negatively charged state of the divacancy ($V\text{-}V^-$, 0.39 eV) and the vacancy - phosphorus level ($V\text{-}P^-$, 0.44 eV). It is therefore by far not clear whether the level observed by us at 0.47 eV can be associated with the $V\text{-}P^-$ center.

So far capture cross-sections were extracted for the defects E1 and E3 only (see table 4). While the value measured by us for E3 is in quite good agreement with recent results reported by Vismara et al.[12] a much lower cross section was found for E1. However also this result has to be verified in additional studies. For E1 and E3 the concentrations are plotted as function of the

neutron fluence in fig. 10. Only one value was measured for E4 so far. The formation of E1 seems to be proportional to the neutron fluence whereas we observed a nonlinear behaviour for E3. This latter result is in contrast to the observation reported by Borchi et al.[23]. It should however be noticed that in our case the same neutron fluence was obtained in a much shorter time. The possible influence of different neutron fluxes has still to be investigated. As mentioned in chapter 5 the radiation induced change of N_{eff} may be interpreted by a donor removal due to the formation of V-P centers. For comparison we have therefore included in fig. 10 the respective results from our C-V measurements. Again, it is at least quite interesting that the concentration of E4 coincides pretty well with ΔN_{eff}. Hence it could be tentatively attributed to the V-P center. As stated above this interpretation is however questionable.

7. CONCLUSIONS

Radiation damage experiment performed with monoenergetic neutrons of 1.2, 5 and 14 MEV and 1.8 MeV electrons have shown that the major effect with respect to the detector performance is associated with the creation of generation/recombination centers in the bulk material. As expected from the different types of primary interactions the current related damage rate α is much larger for neutrons than for electrons. For a neutron energy of 1 MeV we get $\alpha = 8 \cdot 10^{-17}$ Acm^{-1}. The measured energy dependence of α is in quite good agreement with theoretical calculations of the displacement cross section.

In contrast to the current increase, which can be handled e.g. by moderate cooling, the deterioration caused by charge trapping and donor removal may become much more relevant for higher fluences. As the charge collection deficiency directly affects the energy response, detailed investigations of the trapping effect were undertaken. Our experiments have shown that the charge collection deficiency for mip's is less than 2% for a 1 MeV neutron fluence up to 10^{13} n/cm^2. As in the case of the damaged induced current we observed also here a self annealing effect. A temperature enhanced annealing leads however to a worsening of the charge collection. Further investigations are under way in order to clarify the possible dependence on the shaping time.

As was already observed in our previous papers we measured a decrease of the effective donor concentration as expected from the creation of V-P centers. This effect increases with neutron fluence in a complicated way. An extrapolation of the general behaviour suggests a possible inversion from n- to p-type at about $8 \cdot 10^{12}$ n/cm^2 for a neutron energy of about 1 MeV. Another indication for such an inversion was also obtained from detailed studies of charge collection. This result has to be proven by e. g. Hall effect measurements. Self annealing was found only to be relevant within about 2 days after irradiation and as for charge collection a heat treatment leads to a further worsening.

Preliminary results of DLTS-measurements were obtained after 14 MeV neutron irradiation up to $1 \cdot 10^{11}$ n/cm^2. As observed by other authors the DLTS-spectra are dominated by the vacancy related complex defects V-O$^-$, V-V$^=$ and V-V$^-$. Though we could identify a fourth defect level at about the energy to be expected for the V-P center it is not quite clear yet, whether this assignment is really valid. More detailed studies on its annealing and other properties are needed. In addition to the extracted activation energies we have measured the capture cross sections and concentrations for the V-O$^-$ and V-V$^-$ centers. While the defect density of the V-O$^-$ center depends linearly on the neutron fluence, non linear effects seem to be relevant for the V-V$^-$ defect. It should be repeated again, that the DLTS- results are based on a first set of

measurements, which have to be continued in a elaborate way, before a more reliable correlation with the detector performance can be undertaken.

ACKNOWLEDGMENTS

Thanks are due to A. Hess at the University Hospital Hamburg for providing the 14 MeV neutron irradiation facility. The possibility to use the electron accelerator at Telefunken- System-Technik (Wedel) and the assistance by B. P. Offermann is greatly appreciated. Special thanks are due to A. Seidman (Tel Aviv University) and P. G. Rancoita (INFN Milano) for extensive discussions.

REFERENCES

1. D.E. Groom, in: Proc. Workshop on Calorimetry for the SSC, Tuscaloosa 1989, World Scientific, Singapore 1990, pp. 77-89.
2. K. Furuno et al., in: ECFA Study Week Barcelona 1989, CERN 89-10, ECFA 89-124 (1989), pp. 325-335.
3. E. Fretwurst et al., NIM A253 (3) (1987) 467.
4. E. Fretwurst et al., NIM A288 (1) (1990) 1.
5. G. Lindström et al., in: Proc. Workshop on Calorimetry for the SSC, Tuscaloosa 1989, World Scientific, Singapore 1990, pp. 659-672. 6.
6. R. Wunstorf et al., in: ECFA Study Week Barcelona 1989, CERN 89-10, ECFA 89-124 (1989), pp. 321-323.
7. G. Lindström et al., in: Proceedings of the V. Intern. Conf. on Instrumentation for Colliding Beam Physics, Novosibirsk, USSR (1990), in print; DESY 90-109.
8. SICAPO Collaboration, P. Giubellino et al., Como Conference, June 1990
9. D. Pitzl et al., Como Conference, June 1990
10. H.W. Kraner et al., NIM A279 (1989) 266.
11. T. Ohsugi et al., HUPD - 8903 (1989).
12. SICAPO Collaboration, L. Vismara et al., Como Conference, June 1990
13. H. Kröger, Diploma Thesis Univ. of Hamburg, ZEUS Collaboration, in preparation.
14. M.S. Lazo et al., Techn. Rep. SAND - 0098 Vol.1, 1986, 85 - 103.
15. V.A.J. van Lint et al., Mechanismus of Radiation Effects in Electronic Materials, Vol.1 (John Wyley & Sons, New York, 1980).
16. SICAPO Collaboration, to be published.
17. R. Grube, PhD Thesis, Univ. of Hamburg (1978).
18. P. Dreier, NIM A288 (1) (1990) 272.
19. K. Schmalz, PhD Thesis, Akademie der Wissenschaften der DDR, Frankfurt/Oder (1990).
20. D.V. Lang, J. Appl. Phys. 45 (1974) 3023.
21. G.L. Miller et al., Ann Rev. Mat. Sci. 30 (1977) 377.
22. Y. Tokuda et al., IEEE Trans Nucl. Sci. NS-28 (1981) 3564.
23. E. Borchi et al., NIM A279 (1989) 277.
24. L. Tulach et al., Phys. Status Solidi (a)100 (1987) K13.

Tab. 1 Parameters of the radiation sources used for the present experiments.

Radiation Source	intensity range [$cm^{-2} s^{-1}$]	fluence range [cm^{-2}]	fluence error
neutrons			
14.1 MeV	$1 \cdot 10^6 - 6 \cdot 10^8$	$1 \cdot 10^9 - 3 \cdot 10^{12}$	5 %
5.0 MeV	$7 \cdot 10^6 - 1.5 \cdot 10^7$	$4 \cdot 10^{11} - 2.4 \cdot 10^{12}$	3 %
1.2 MeV	$7 \cdot 10^6 - 1 \cdot 10^7$	$7 \cdot 10^{10} - 1.3 \cdot 10^{12}$	4 %
protons			
21.1 MeV	$6 \cdot 10^6 - 5 \cdot 10^8$	$1 \cdot 10^9 - 2 \cdot 10^{12}$	1 %
electrons			
1.8 MeV	$1 \cdot 10^{11} - 3 \cdot 10^{12}$	$1 \cdot 10^{12} - 6.4 \cdot 10^{15}$	2 %

Tab. 2 Comparison of radiation induced damage rate α and normalized ratio to displacement cross section (see text).

Ref.	neutron source	E_n[MeV]	α_{corr} (20 °C) [10^{-16} A cm^{-1}]	r
this work	T(p,n)	1.2	0.79 ± 0.03	1.17
this work	D(d,n)	5.0	1.36 ± 0.04	1.08
this work	T(d,n)	14.1	1.47 ± 0.09	1.00
9	LAMF	5.0	0.79 ± 0.40	1.33
10	PuBe	4.8	1.10 ± 0.10	0.99
11	reactor	2.1	0.79 ± 0.08	0.95
12	^{252}Cf	2.1	1.26 ± 0.20	1.50
13	^{252}Cf	2.1	0.95 ± 0.10	1.14

Tab. 3 Trapping time constant for electrons and holes after successive irradiation and annealimg steps (compare fig. 9).

	τ_e^+ [μs]	τ_h^+ [μs]
before irradiation	11.00	13.00
after 1. irradiation ($0.44 \cdot 10^{12}$ n/cm^2)	1.86	1.92
after 1. heat treatment (200 °C, 1 h)	2.64	1.03
after 2. irradiation ($1.61 \cdot 10^{12}$ n/cm^2)	0.65	0.51
after 2. heat treatment (200 °C, 1 h)	1.20	0.40

Tab. 4 Activation energies and capture cross sections for different defects observed by DLTS measurements after 14 MeV neutron damage.

Defect	$E_c - E_t$ [eV]	σ_n [cm^2]
E 1	0.16 ± 0.01	$1 \cdot 10^{-15}$
E 2	0.24 ± 0.01	—
E 3	0.41 ± 0.02	$4 \cdot 10^{-16}$
E 4	0.47 ± 0.03	—

FIGURE CAPTIONS

Fig. 1 Increase of measured bulk generation current as function of particle fluence.

Fig. 2 Charge collection deficiency versus transit time bewith 5.805 MeV α-particles, incident on the rear electrode.

Fig. 3 Dependence of the trapping rate $1/\tau^{+}$ for electrons and holes on the 5 MeV neutron fluence.

Fig. 4 Estimated charge collection deficiency for mip's as function of 5 MeV neutron fluence.

Fig. 5 Self annealing of effective donor concentration.

Fig. 6 Relative impurity concentration versus neutron fluence for different neutron energies normalized to 1 MeV (see text).

Fig. 7 Capacitance-voltage characteristics for : (a) detector 8813B4 before irrad. and after final step of successive damage annealing (compare fig.9), (b) detector 8814B3 before and after irrad. with about 10^{13} n/cm^2.

Fig. 8 Ratio of observed response to α-particles incident on the rear and front side of highly damaged detectors in comparison to the normal behaviour before irradiation (see text)..

Fig. 9 Effect of successive 14 MeV neutron damage and annealing (1h, 200 °C) for detector 8813B4 (see text). 1st irradiation: $4.4 \cdot 10^{11}$ n/ cm^2, 2nd irradiation: $1.61 \cdot 10^{12}$ n/cm^2.

Fig. 10 Defect concentration as function of 14 MeV neutron fluence as extracted from DLTS measurements. For comparison values of of the effective donor concentration as measured by C-V characteristics are induced (see text).

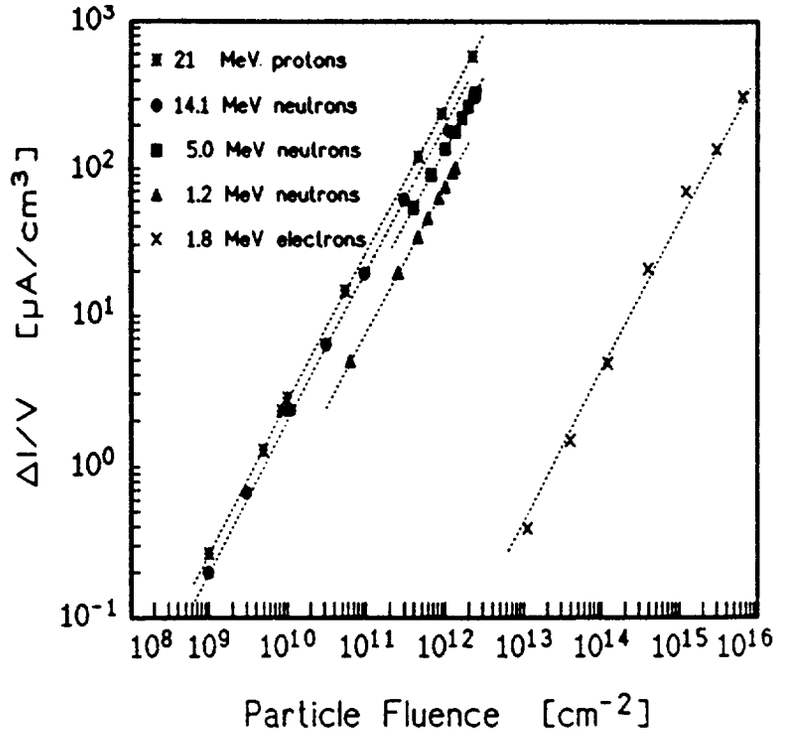

21 MeV protons
14.1 MeV neutrons
5.0 MeV neutrons
1.2 MeV neutrons
1.8 MeV electrons
ΔI/V [μA/cm³]
Particle Fluence [cm⁻²]

Fig. 1

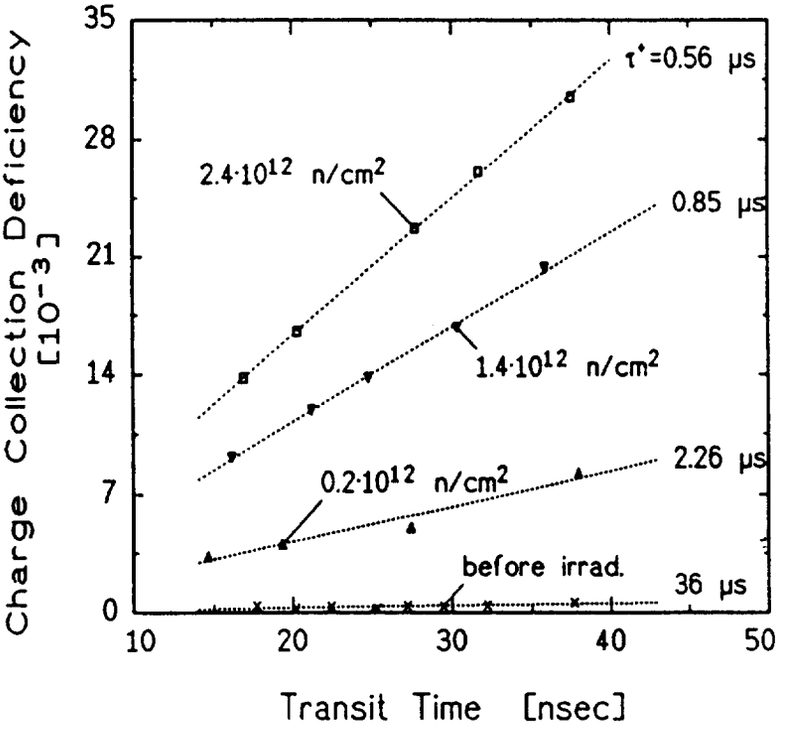

τ*=0.56 μs
2.4·10¹² n/cm²
0.85 μs
1.4·10¹² n/cm²
2.26 μs
0.2·10¹² n/cm²
before irrad.
36 μs
Charge Collection Deficiency [10⁻³]
Transit Time [nsec]

Fig. 2

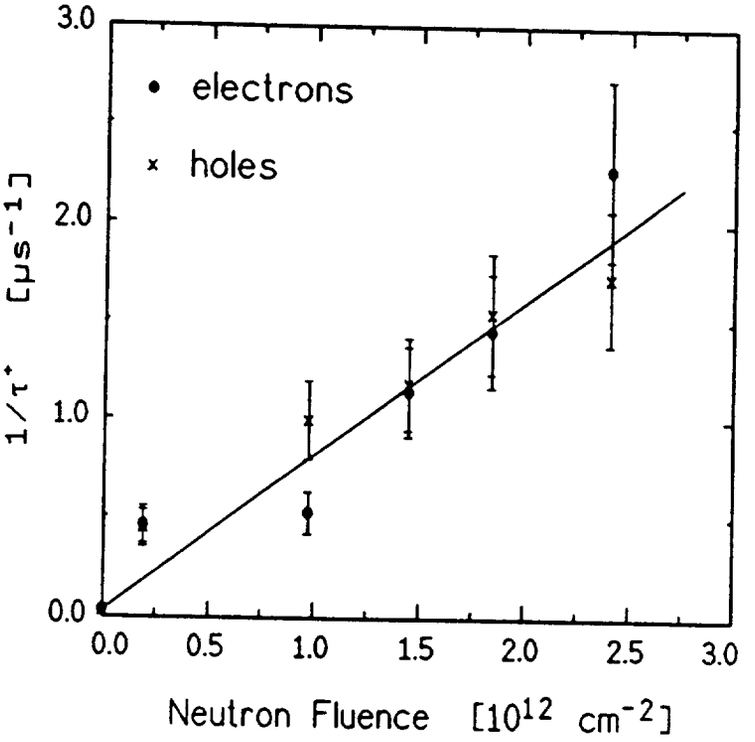

3.0
2.0
1.0
0.0
• electrons
× holes
1/τ⁺ [μs⁻¹]
0.0
0.5
1.0
1.5
2.0
2.5
3.0
Neutron Fluence [10¹² cm⁻²]

Fig. 3

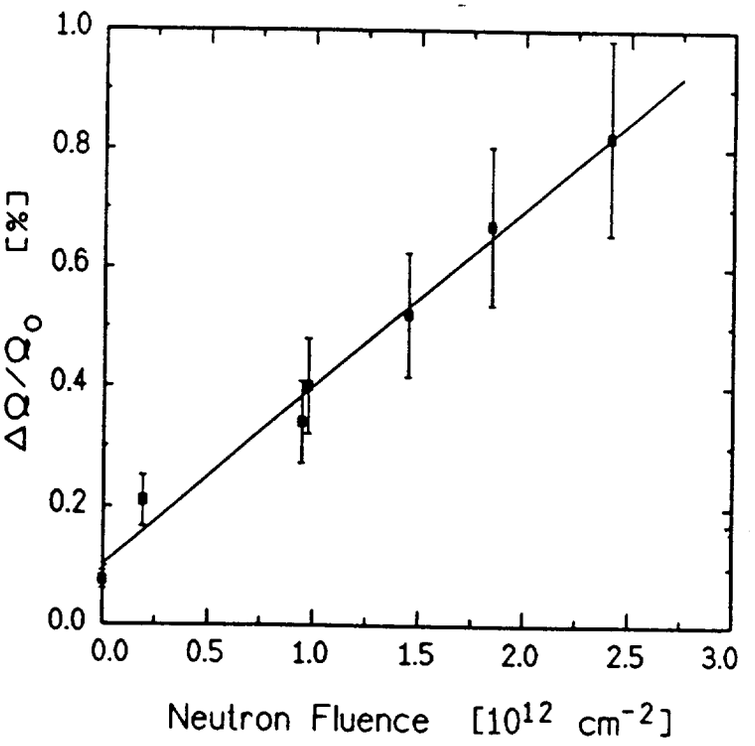

1.0
0.8
0.6
0.4
0.2
0.0
ΔQ/Q₀ [%]
0.0
0.5
1.0
1.5
2.0
2.5
3.0
Neutron Fluence [10¹² cm⁻²]

Fig. 4

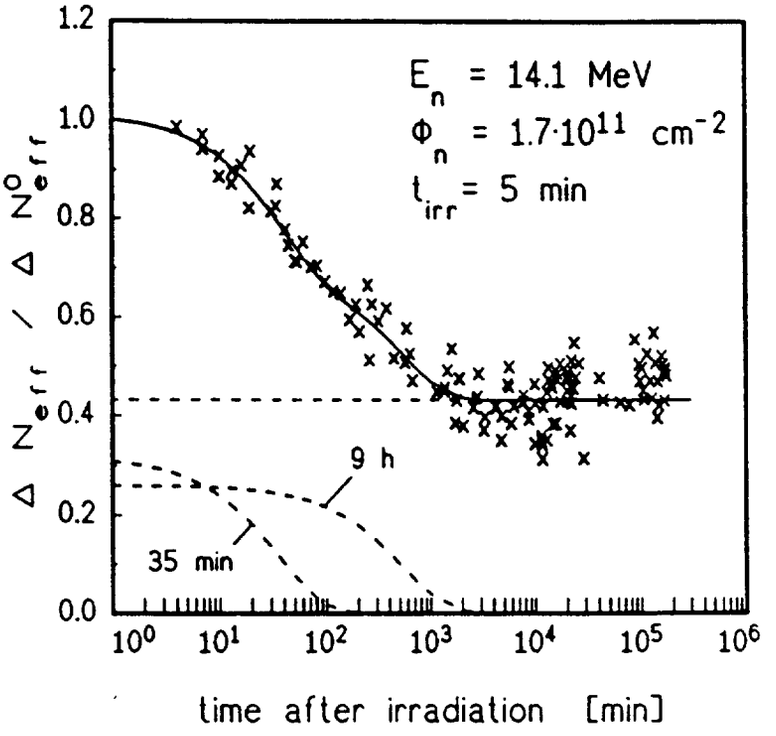

1.2
1.0
0.8
0.6
0.4
0.2
0.0
E_n = 14.1 MeV
Φ_n = 1.7·10^{11} cm^{-2}
t_{irr} = 5 min
9 h
35 min
$\Delta N^{o}_{err} / \Delta N_{err}$
10^0 10^1 10^2 10^3 10^4 10^5 10^6
time after irradiation [min]

Fig. 5

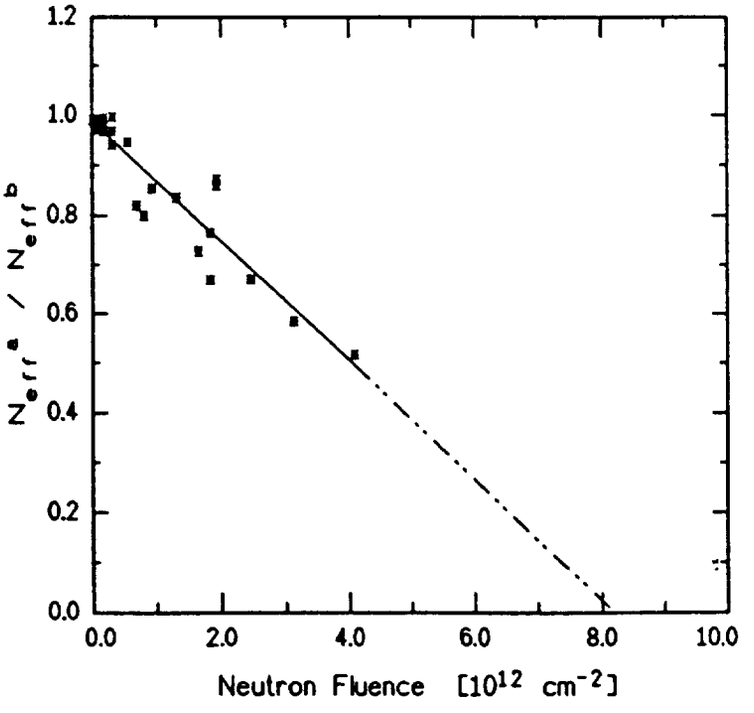

1.2
1.0
0.8
0.6
0.4
0.2
0.0
$N^{a}_{err} / N^{b}_{err}$
0.0 2.0 4.0 6.0 8.0 10.0
Neutron Fluence [10^{12} cm^{-2}]

Fig. 6

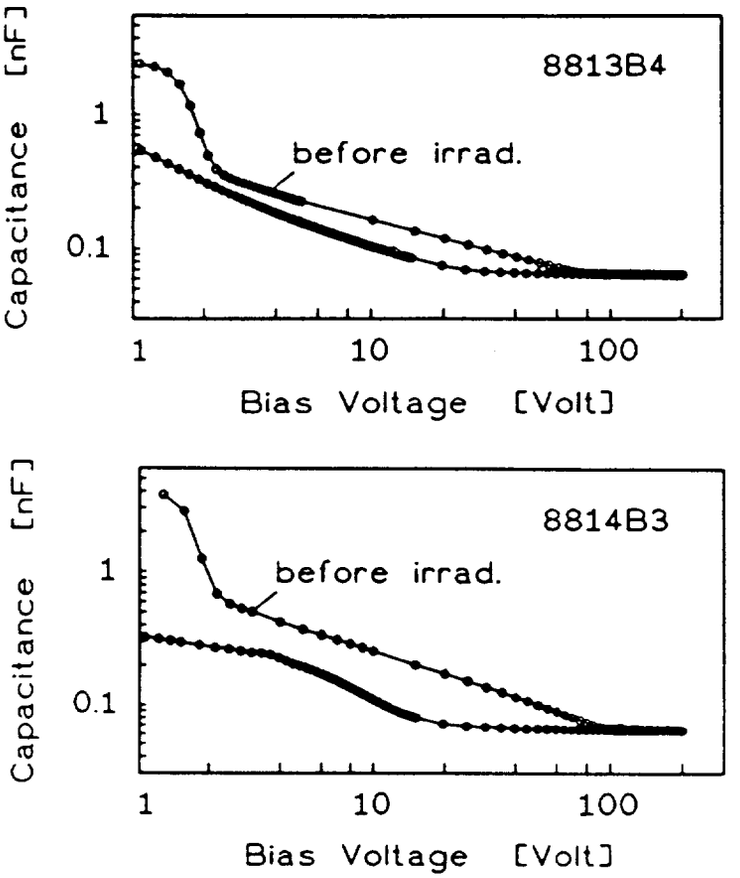

8813B4
before irrad.
Capacitance [nF]
1
0.1
1
10
100
Bias Voltage [Volt]
8814B3
before irrad.
Capacitance [nF]
1
0.1
1
10
100
Bias Voltage [Volt]

Fig. 7

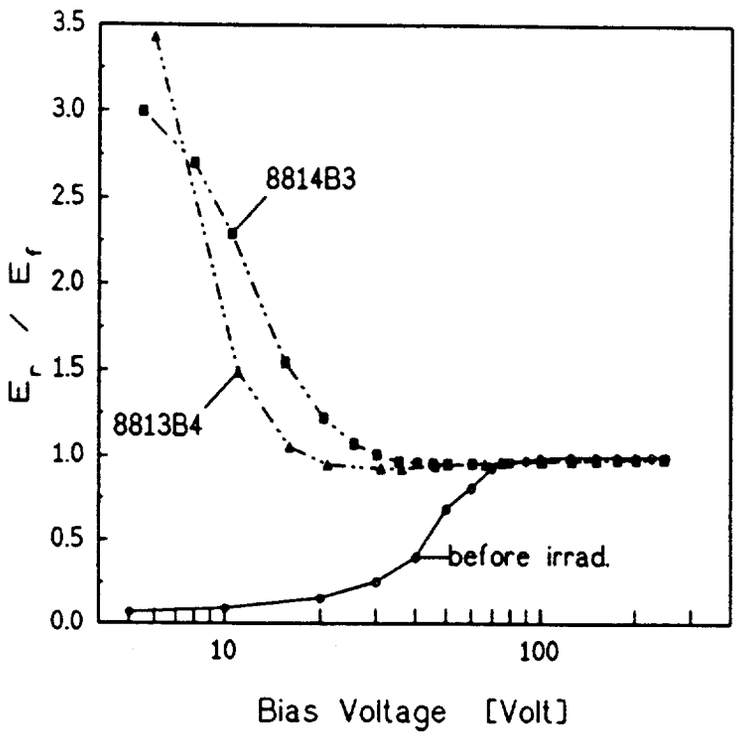

3.5
3.0
2.5
2.0
1.5
1.0
0.5
0.0
E_r / E_f
8814B3
8813B4
before irrad.
10
100
Bias Voltage [Volt]

Fig. 8

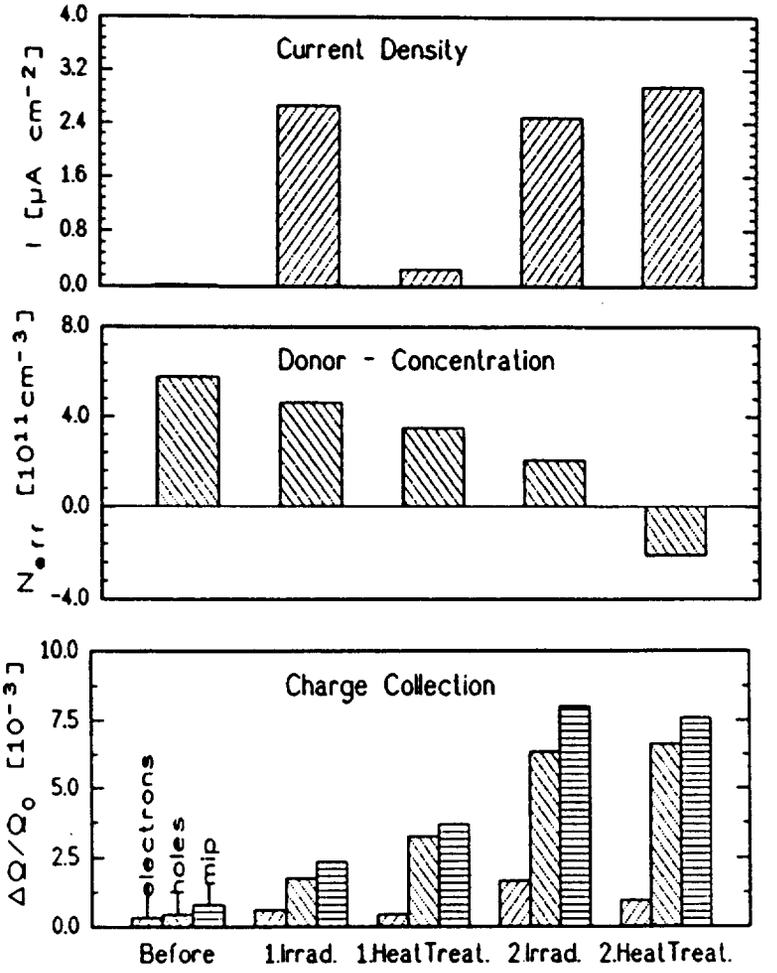

Current Density
I [μA cm⁻²]
4.0
3.2
2.4
1.6
0.8
0.0
Donor - Concentration
N_eff [10¹¹cm⁻³]
8.0
4.0
0.0
-4.0
Charge Collection
ΔQ/Q₀ [10⁻³]
10.0
7.5
5.0
2.5
0.0
electrons
holes
mip
Before
1.Irrad.
1.HealTreat.
2.Irrad.
2.HealTreat.

Fig. 9

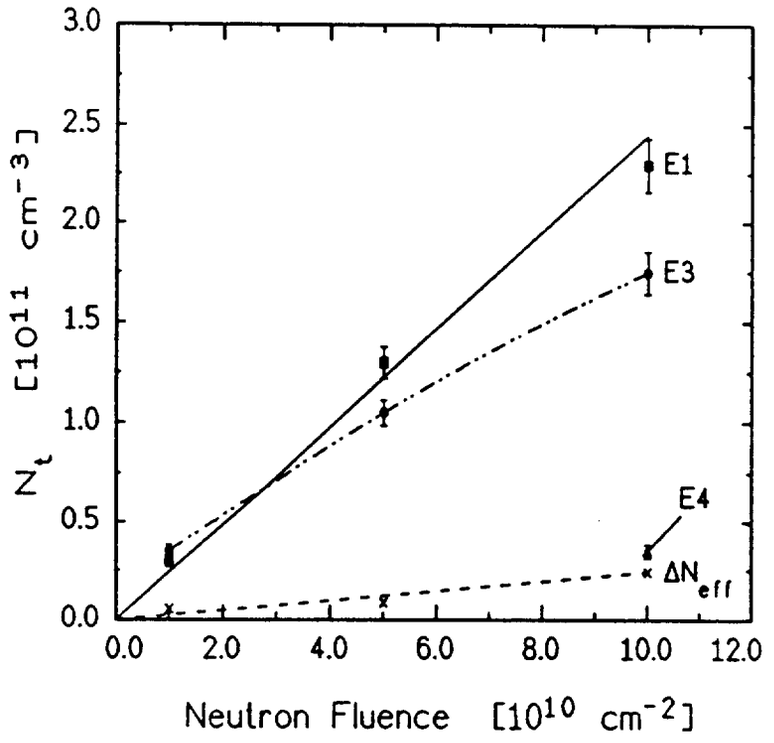

N_t [10¹¹ cm⁻³]
3.0
2.5
2.0
1.5
1.0
0.5
0.0
E1
E3
E4
ΔN_eff
0.0
2.0
4.0
6.0
8.0
10.0
12.0
Neutron Fluence [10¹⁰ cm⁻²]

Fig. 10

STUDY OF OPERATING CONDITION OF SEMICONDUCTORS FOR CALORIMETRY

E. Borchi[1], M. Bosetti[2], C. Furetta[2*], C. Leroy[3], R. Macii[1], R. Paludetto[2], S. Pensotti[2@], G. Pessina[2], P. G. Rancoita[2], A. Seidman[3+], G. Terzi[2] and L. Vismara[2]

[1] University of Florence and INFN, Florence, Italy
[2] INFN Milan, Milan, Italy
[3] University of Montreal, Montreal, Canada
[*] and University of Rome "La Sapienza", Rome, Italy
[@] and University of Milan, Milan, Italy
[+] and Tel-Aviv University, Tel-Aviv, Israel

Abstract

The choice of silicon detectors as active medium of calorimeters to be used at the future hadron colliders, such as SSC and LHC, satisfies several special experimental requirements. Appropriate front-end readout electronics has been especially developed for the applications in calorimetry.

1. INTRODUCTION

In the past years, the development of semiconductor detectors in view of their use in various scientific applications has been both rapid and widespread. Recently, interest of silicon detector applications in high energy physics has been displayed in several papers presented at various conferences [1-5]; in particular, the usefulness of silicon detectors in calorimetry has been stressed. A calorimeter based on silicon as active medium is able to satisfy the requirements of compactness, granularity, fast charge collection, easy calibration, good energy resolution and the achievement of the compensation condition. However, the silicon detectors have to satisfy the further requirement of radiation hardness.

Estimates of the neutron fluence existing at the future hadron colliders have been recently reported and a value of several

$$10^{13}\ n\ cm^{-2}\ yr^{-1}$$

has been given [6].

Neutrons produced during proton beam interaction with the calorimeter constitute the main problem when using silicon as active medium in hadron colliders. It has also been proved that the fast neutron energy spectrum has a maximum around 1 MeV of energy [7]. The neutrons being the main source of damage in silicon detectors, it is then necessary to carry out a detailed study in order to understand the defect growing process and the changes of the electrical properties as a consequence of the amount of neutrons generated in a hadron cascade inside a calorimeter.

The interactions of fast neutrons by elastic scattering with silicon atoms, induces deep defect levels in the silicon band gap as vacancies, multivacancies, vacancy-impurity pairs and clusters of defects.

All these deep levels in the bulk of detectors induce changes in their electrical characteristics.

The present work reports studies on neutron irradiated silicon detectors which include leakage current measurements before and after irradiation, defect identification carried out using DLTS (Deep Level Transient Spectroscopy) and TSC (Thermally Stimulated Current) analysis, effect of various annealings after irradiation to check a possible recovery of detectors in terms of leakage currents. Also the effect of the leakage current increase on the Equivalent Noise Charge (ENC) for a VLSI preamplifier is also reported.

2. EXPERIMENTAL METHOD

The p^+-n silicon detectors used for this study had a nominal area of 5x5 mm^2 and 10x10 mm^2, 400 μm of thickness and a resistivity ranging from 2 to 6 $K\Omega\ cm$.

The irradiations of detectors have been performed at CERN, using a ^{252}Cf neutron source whose energy spectrum has a maximum around 1 MeV. The value of the measured fluxes were between $3.4 * 10^3$ and $9.9 * 10^4$ $n\ cm^{-2}\ sec^{-1}$. To simulate one year of operation in a SSC or LHC apparatus, a maximum irradiation time of 10^7 *sec* has been used, with a corresponding maximum fluence of 10^{12} $n\ cm^{-2}$.

The irradiations have been carried out without bias applied to the detectors according to the observation of Kraner [8].

2.1 Leakage current measurements

The increase of the leakage current after the irradiation is expected to be a linear function of the neutron fluence according to the expression:

$$\Delta I = \alpha \Phi V$$

where:

α $[A\ cm^{-1}]$ is the leakage current constant,

Φ $[n\ cm^{-2}]$ is the neutron fluence,

V $[cm^3]$ is the detector volume,

ΔI $[A]$ $= I_i - I_0$ is the difference between the leakage current after irradiation (I_i) and before irradiation (I_0).

The measurements have been carried out at 20°C and the experimental value of α was found to be:

$$\alpha = (4.8 \pm 0.9) * 10^{-17} A\ cm^{-1}$$

It must be noted that the α value is affected by the self annealing effect which takes place during the very long irradiation performed.

A second irradiation has been carried out on the silicon detectors placed in an iron calorimeter. The detectors were inserted in the calorimeter at different positions and the Fe - calorimeter itself was irradiated with the primary 24 *GeV* proton beam at the CERN-PS. The irradiation lasted three hours. The neutron fluences were measured with indium foils placed near the silicon samples and the maximum fluence observed was $7 * 10^{12}$ $n\ cm^{-3}$. In this case the observed leakage currents of detectors are in a good agreement with those expected from measured neutron fluences; this fact confirms that the damages in silicon are mainly due to the evaporative neutrons generated in the hadronic shower.

2.2 DLTS and TSC measurements

DLTS and TSC techniques allow to detect the deep defect levels produced in the silicon device bulk as a consequence of irradiation and to obtain the activation energy values of the traps themselves.

DLTS uses the measure of the capacitance transient variations due to the slow carriers emissions from the filled traps, as a function of the temperature. A plot of DLTS measurements is shown in fig. 1, where three different peaks can be easily observed. These peaks can be related to different defects as shown in Table 1.

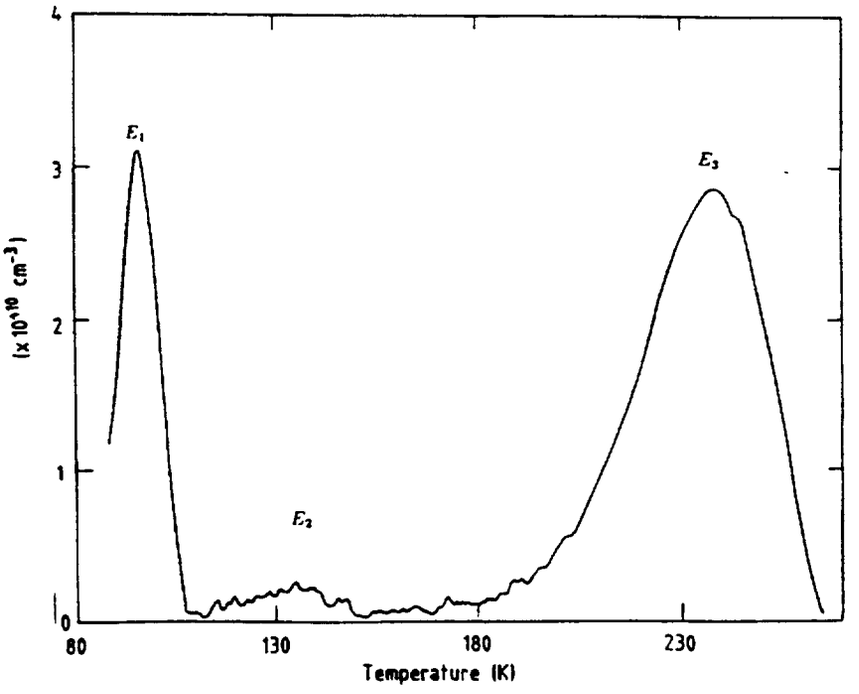


fig. 1 DLTS spectrum

Peak	Activation Energy [eV] DLTS	Activation Energy [eV] TSC	Capture Cross Section [cm^2]	Lattice defect
E_1	$E_c - (0.16 \pm 0.001)$	- - - -		
E_2	$E_c - (0.25 \pm 0.002)$	$E_c - (0.25 \pm 0.002)$	$(1.4 \pm 0.2) \cdot 10^{-14}$	vacancy oxigen complex
E_3	$E_c - (0.40 \pm 0.002)$	$E_3' - E_c - (0.39 \pm 0.001)$	10^{-16}	double minus divacancy
		$E_3'' - E_c - (0.42 \pm 0.002)$	$(0.7 \pm 0.4) \cdot 10^{-15}$	single minus divacancy
				vacancy phosphorous complex

Tab. 1 Activation Energies

With TSC technique, instead, one measures the leakage current of the sample during a thermal scan and after a filling of the traps present in the silicon band gap. The detrapping of carriers during the thermal scan causes a current peak.

The delayed heating method [9] has been used in TSC measurements. This method allows to resolve overlapped peaks and, from this point of wiew, it is more sensitive than DLTS method.

The TSC measurements gave the same results obtained with DLTS. Moreover, the delayed heating method allows to resolve the E_3 peak in two well defined components (fig. 2). The results are given in the same tab. 1. The TSC technique has also been used with the silicon detectors irradiated in the Fe - calorimeter and the same E_3 defect level has been detected.

2.3 Annealing effect

In order to study the annealing effect on the irradiated silicon detectors various thermal annealings have been performed. It has to be noted that the leakage current observed immediately after irradiation is lower than the expected one owing to the self annealing effect which takes place during the long irradiation itself. After an annealing at 100°C a recovery of 50% is observed. However an 80% of recovery is obtained after annealing at 150°C. A further increase of temperature does not seem to lead to a better recovery. The behaviour of the trap concentration for E_3 defect level has also been studied as a function of the annealing temperature. The ratio N_T/N_{T_o}, where N_T and N_{T_o} are the E_3 trap concentrations after and before annealing, as a function of the temperature, shows a decrease of more than 90% at 250°C. A certain number of the irradiated-annealed detectors have been irradiated again and then subjected to a new annealing. The results obtained in this experiment are similar to those found after the first irradiation, i.e. the same recovery after a 150°C thermal annealing.

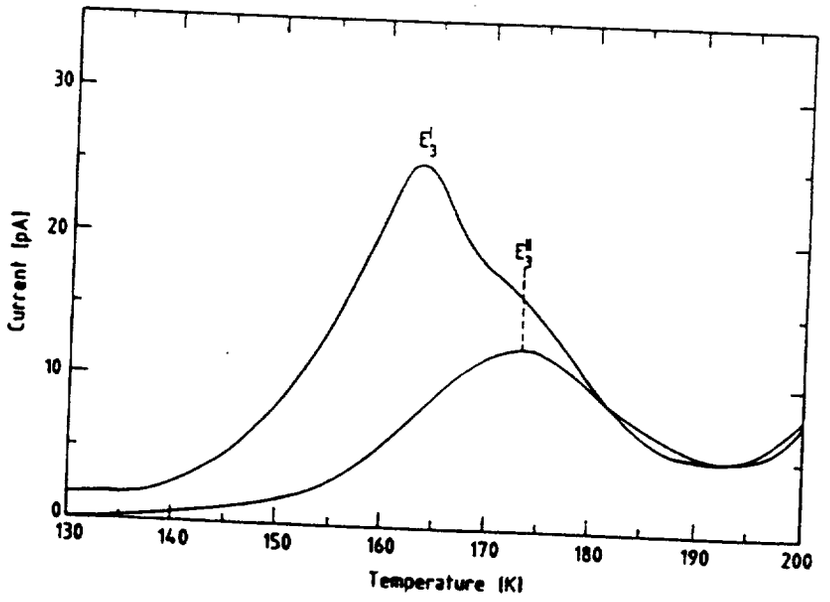


fig. 2 The resolved E_3 peak components

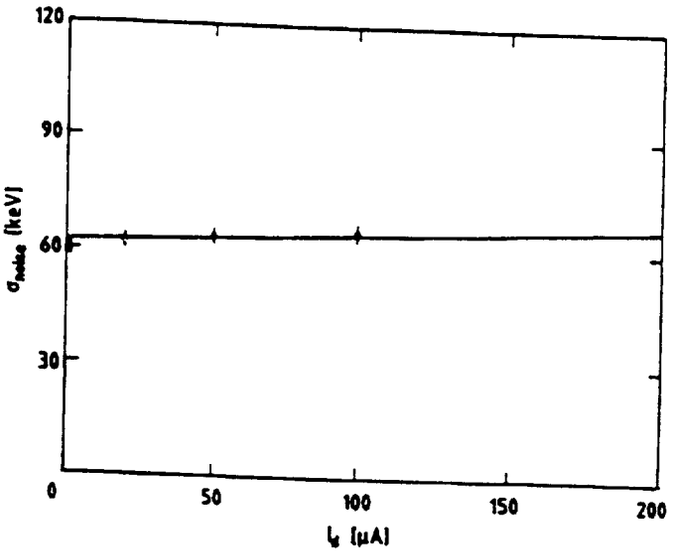


fig. 3 The noise expressed as a function of detector leakage current

2.4 VLSI preamplifier

A VLSI preamplifier has been developped and built to match the requirements of silicon calorimetry applications at the next generation of hadron colliders. The preamplifier has been designed in Milan by INFN and built by SGS-Thomson with a new process in mixed technology, bipolar-CMOS (HF2CMOS). The preamplifier's characteristics are a rise time of 7 *nsec* for a 5 *V* output swing with 150 *pF* of input capacitance, a linear range above 1 *GeV*, with $C_f = 10\ pF$ and an equivalent noise charge (ENC) of 17 ke_{rms} for a RC-CR shaping time, τ_m, of 20 *nsec* and an input capacitance of 150 *pF*. The ENC equation [10] shows two noise components, the series and the parallel one. The series noise is proportional to the input capacitance and to the inverse of τ_m, while the parallel noise is proportional to τ_m. So, at low τ_m value and high input capacitance, the parallel noise contribution to ENC may become negligible. In fact the effect of the detector leakage current, I_d, on the noise can be expressed by adding the quantity $\overline{i^2}_d = 2qI_d$ in the parallel noise term of the ENC equation. With the use of a fast front-end electronics, the noise behaviour is then almost independent from the leakage current values being the parallel noise directly proportional to the shaping time. Fig. 3 shows the σ value, expressed in dimension of energy, as a function of I_d.

3. CONCLUSIONS

Silicon detectors, irradiated with fluences of up about $10^{12} n\ cm^{-2}$, showed a linear increase of leakage current versus the fluence of irradiation with a proportionality constant of $(4.8 \pm 0.9) * 10^{-17} A\ cm^{-1}$ for an irradiation duration of up to about 120 days at 20°C. The leakage current increase caused by neutron irradiation of the order of magnitude expected at the future colliders is considerably ameliorated by the new VLSI preamplifier. This fast preamplifier which was especially developed for its use in silicon sampling calorimeters, has a noise performance which is almost independent on the leakage current values.

REFERENCES

1. Int. Conf on Advanced technology and Particle Physics, Como, Italy, June 13-17, 1988. Nucl. Inst. Meth. A279 (1989).
2. 1990 IEEE Nuclear Science Symposium, Arlington, VA, October 23-27, 1990.
3. Proc. Workshop on Calorimetry for the SSC, Tuscaloosa 1989
4. E.C.F.A. Study Week Barcellona 1989, CERN 89-10, ECFA 89-124 (1989).
5. Proc. of the *V* Intern. Conf. on Instrumentation for Colliding Beam Physics, USSR (1990).
6. D. E. Groom, ECFA Study Week Barcellona 1989, CERN 89-10, ECFA 89-124.
7. D. E. Groom, Int. Conf on Advanced technology and Particle Physics, Como, Italy, June 13-17, 1988. Nucl. Inst. Meth. A279 (1989), 1.
8. H. W. Kraner, Z. Li, K. U. Posnecker, Int. Conf on Advanced technology and Particle Physics, Como, Italy, June 13-17, 1988. Nucl. Inst. Meth. A279 (1989), 266.
9. C. Schrager, J. C. Muller, R. Stuck, P. Siffert, Phys. St. Solidi (a) 31 (1975), 247.
10. A. Gola, G. Pessina, P. G. Rancoita, Nucl. Inst. Meth. Phys. Res. A 292 (1990), 648.

Results of radiation hardness tests of GaAs solid-state detectors+

Presented by S. D'Auria

S.P. Beaumont[4], R. Bertin[2], S. D'Auria[1], C. del Papa[1], M. Edwards[6], F. Fiori[1], J. C. Linch[5], B. Lisowski[1], M. Nuti[3], V. O'Shea[1], P.G. Pelfer[3], C. Raine[5], I.O. Skillicorn[5], K. M. Smith[5], R. M. Turnbull[5], and A. Zichichi[2]

1- Dipartimento di Fisica dell'Universita' and INFN Bologna, Italy

2- CERN, Geneva, Switzerland

3- Dipartimento di Fisica dell'Universita' and INFN Firenze, Italy

4- Dept. of Electrical and Electronic Engineering, University of Glasgow, U.K.

5- Dept of Physics and Astronomy, University of Glasgow, U.K.

6- Rutherford-Appleton Lab., Chilton, Didicot, U.K.

Abstract

GaAs solid state detectors have been tested before and after 1 MeV neutron and ^{60}Co irradiation at levels expected in LHC. The test fully confirms the intrinsic radiation hardness of this material.

Introduction

It is shown elsewhere in these proceedings and in [1,2,3] that Semi Insulating (S.I.) Gallium Arsenide is a good material for particle detectors, with a full detection efficiency of m.i.p.s. The charge collection efficiency is incomplete, due to the presence of traps, but shows a plateau with full electron collection. The main attractive of these devices is the intrinsic radiation hardness and the potential speed, which make GaAs competitive with Si in high radiation and high rate environments. Here we present the results on the effects of gamma and neutron irradiation on several diodes, all made of S.I., undoped, LEC-grown GaAs.

The main radiation damage to semiconductor detectors is due to displacement of atoms, that gives rise to lattice defects and isolated levels in the forbidden gap, and to generation of charges which are permanently trapped in insulating parts and at interfaces.

These two effects can be separated by irradiating samples with different radiations, namely neutrons and gamma rays. The latter give rise mainly to ionization damage, the former to displacement.

+ *This work has been done in the framework of the LAA project*

Gamma ray test

GaAs has no native oxide and either SiO_2 or Si_3N_4 can be used as passivating layer; however the samples we tested have no passivation; thus they are expected to be very resistent to ionization damage.

Eight Schottky diodes, 600 μm thick, were irradiated with γ from ^{60}Co at the Conservatome facility at Dagneau-Montluel (F) with a composite 150 kCi source. As the damage is generally dependent on applied bias, four of the samples were reverse biased at a working voltage (100 V). The temperature during irradiation was 18 °C. The dose was measured with a perspex dosimeter; the detector characteristics have been measured after each of three irradiation runs, at 4.8, 8.3 and 16 Mrad (Si equivalent). We found no appreciable effect either in reverse current, in noise (fig. 1), or in charge collection efficiency (fig. 2). Also no difference can be found between biased and unbiased diodes. The minimum electron energy to displace an As atom in a head-on collision is about 400 keV, a factor 2 more than for Si, so the lattice regularity is not much affected by 1.3 MeV γ irradiation. Small displacements, which give rise to vacancy-interstitial defects, are rapidly recombined, especially in the Ga sublattice, even at low temperature [4].

Neutron irradiation

Energetic neutrons, on the other hand, can displace atoms, which in turn can travel a distance of many lattice constants displacing other atoms, especially at the end of their path. Thus permanent defects are formed and they introduce isolated deep levels in the forbidden gap.
As GaAs has a band gap 310 meV wider than Si, a much bigger concentration of intermediate levels can be tolerated without increasing dramatically the reverse current. In bulk LEC-grown GaAs the typical concentration of traps is 10^{16} cm^{-3} (mainly EL2 type, 820 meV level). This fact changes the charge transport mechanism, here dominated by trapping and fast release of electrons, but nevertheless the reverse current still stays at an acceptable level.
Besides, the energy transfer in collision with Ga or As atoms is 40 % w.r. t. Si, which partially compensates the higher neutron cross section. Ga As may therefore tolerate a high neutron flux without dramatic change in reverse current. To prove this we have irradiated six other Schottky diodes, 600 μm thick, with ≈ 1 MeV spallation neutrons of the ISIS facility at RAL. The characteristics of the source and the techniques of dosimetry can be found elsewhere in these proceedings [5,6]. During irradiation the samples were not biased. An integrated flux of $7 * 10^{14}$ n/cm^2 was reached, and samples were tested one week after the end of irradiation, at 27-28 °C room temperature. No annealing procedure was used.

After irradiation we noticed that the peak position in β spectra moved, i.e. charge collection efficiency decreased roughly by a factor of two (fig. 3). This means that the trap concentration increased. However, we don't see an effect on noise: the increment, if any, is very small (fig. 4). The signal over noise ratio does change, but the signal still remains well separed from noise (fig. 5), without changing bias or shaping time. The diodes are still operational as detectors.

Conclusions

The radiation hardness of solid-state detectors made of S.I. GaAs has been tested with γ and neutron exposure, up to the levels foreseen in next hadron colliders. Very little effect is noticed in detector performance with γ irradiation up to 16 Mrad. Neutron irradiation of $7 * 10^{14}$ n/cm^2 does not affect the noise, but lowers the charge collection efficiency by creating electron traps.

Detectors remain operational without any change in the amplification chain.

These results are encouraging, and further study on transport mechanism, also in irradiated material, may enable further improvements in the performances of GaAs detectors.

References

[1] R. Bertin et al., *A preliminary study of GaAs solid-state detectors for high energy Physics* Nucl. Instr. and Meth. A294, (1990), 211.

[2] C. del Papa, C. Raine et al., *New results on GaAs solid-state detectors for high energy Physics*, Contribution to the 4th San Miniato topical seminal on experimental apparata for high energy Physics and Astrophysics, June 1990.

[3] K. M. Smith, these proceedings

[4] D. Pons and j. Bourgoin, *Irradiation-induced defects in GaAs*, Journal of Physics C, vol. 18 n 20, (1985), 3839.

[6] M. Edwards and D. R. Perry *The radiation hardness test facility*, RAL report, RAL-90-065 , August 1990

[7] M. Edwards, these proceedings.

Figure captions

Fig. 1:Noise variarion with gamma dose (Si eq.) for the diode array #11, 600 μm thick, at 300 V bias voltage.

Fig. 2: Charge collection efficiency for different gamma doses, for the same array as in fig. 1, at the same conditions.

Fig. 3: Noise (e.n.c.) at 300 V bias voltage, 302 °K, for the diode array #29, 600 μm thick, before and after neutron irradiation by $7*10^{14}$ n/cm^2.

Fig. 4: Charge collection efficiency variation for the same diode array as in fig.3, at the same conditions, before and after neutron irradiation.

Fig. 5: Pulse height spectrum from ^{106}Ru source, corresponding to minimum ionizing particles, before (a) and after (b) the neutron irradiation.

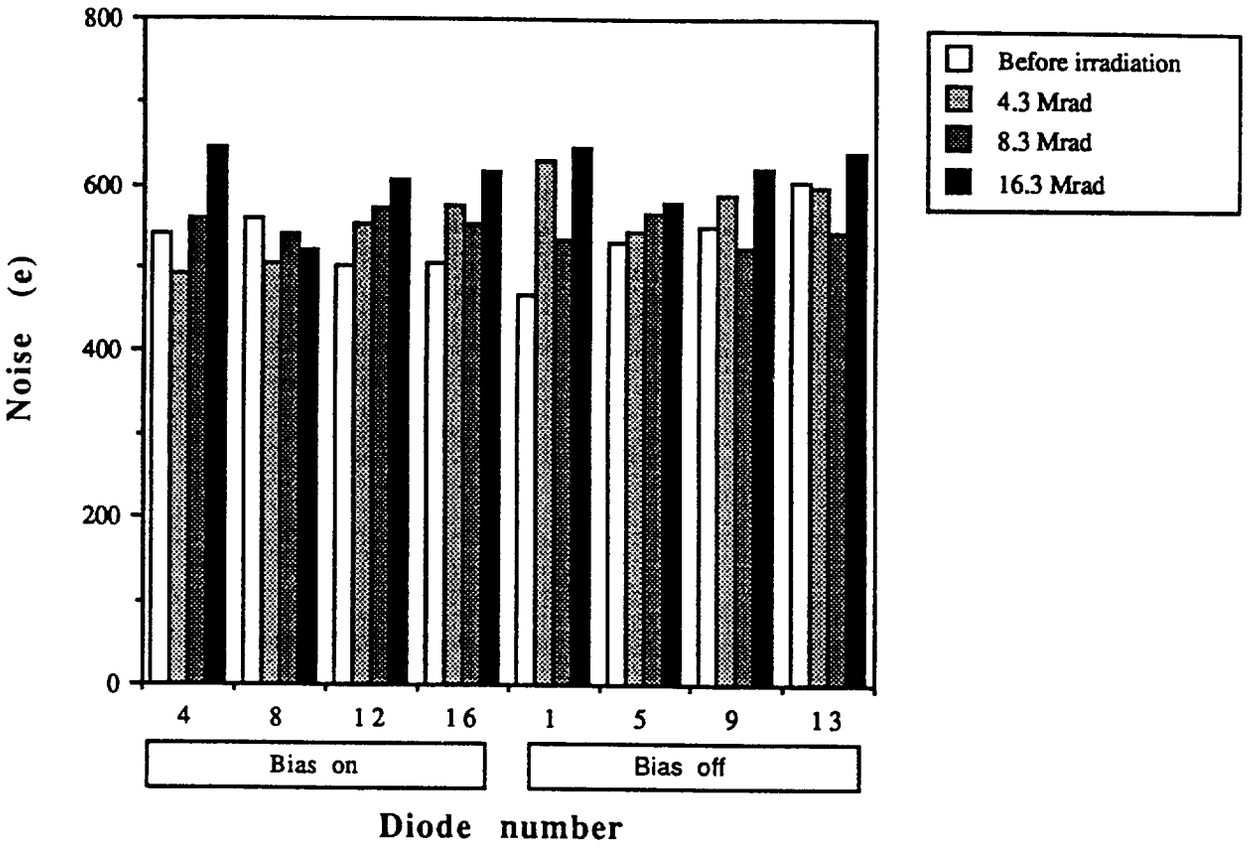

800
600
400
200
0
Noise (e)
Before irradiation
4.3 Mrad
8.3 Mrad
16.3 Mrad
4
8
12
16
1
5
9
13
Bias on
Bias off
Diode number

Fig. 1

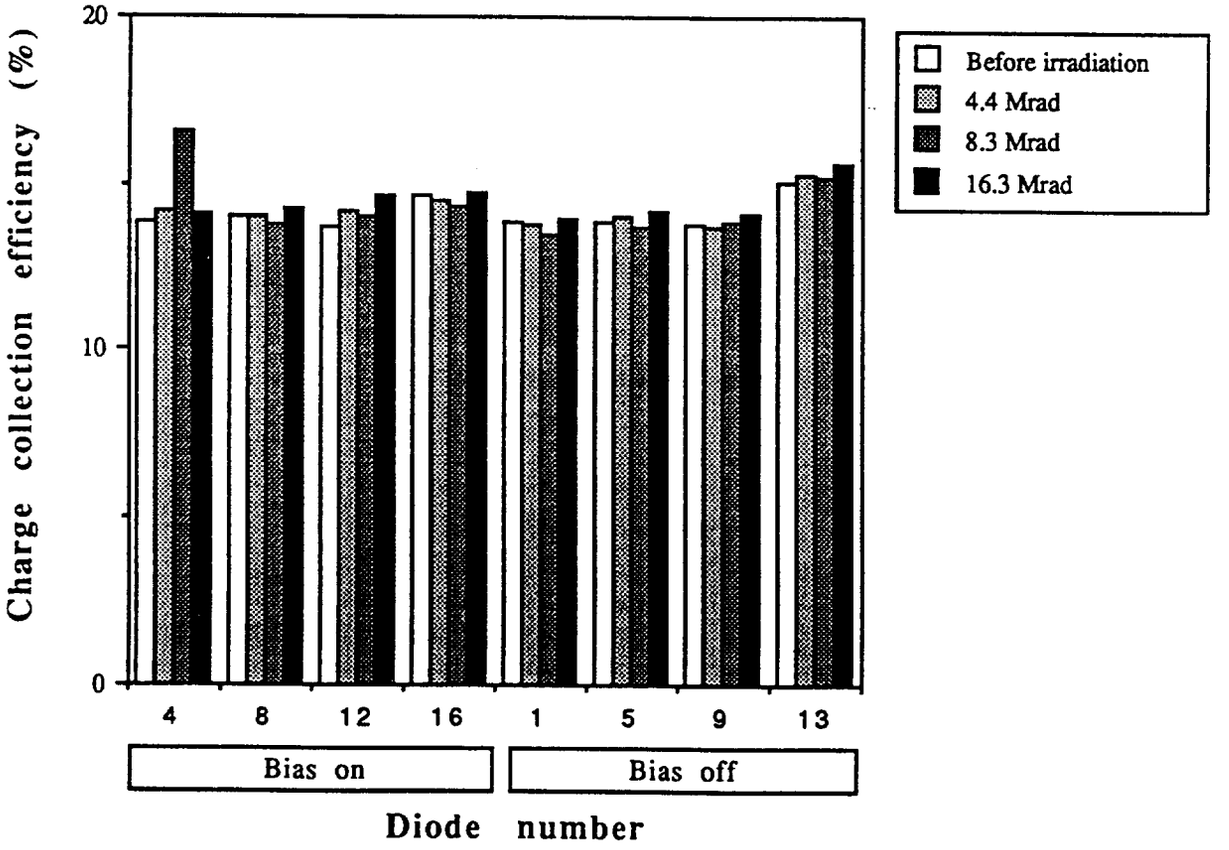

20
10
0
Charge collection efficiency (%)
Before irradiation
4.4 Mrad
8.3 Mrad
16.3 Mrad
4
8
12
16
1
5
9
13
Bias on
Bias off
Diode number

Fig. 2

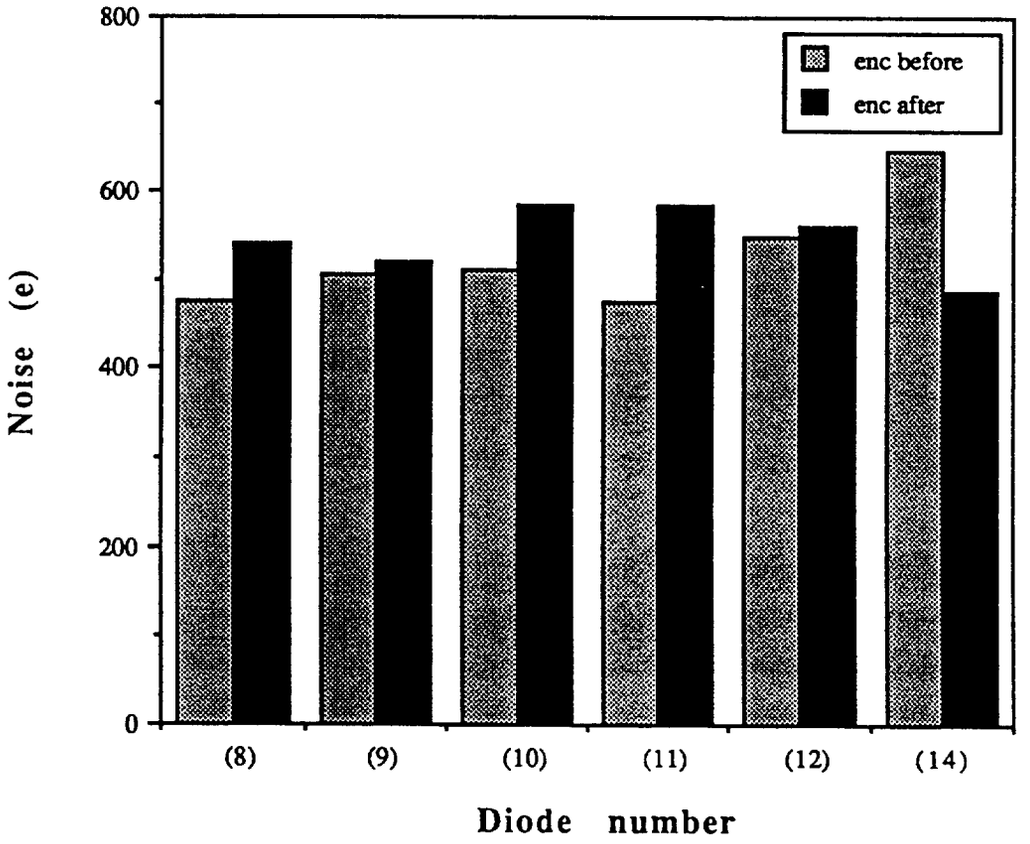

800
600
400
200
0
Noise (e)
enc before
enc after
(8)
(9)
(10)
(11)
(12)
(14)
Diode number

Fig. 3

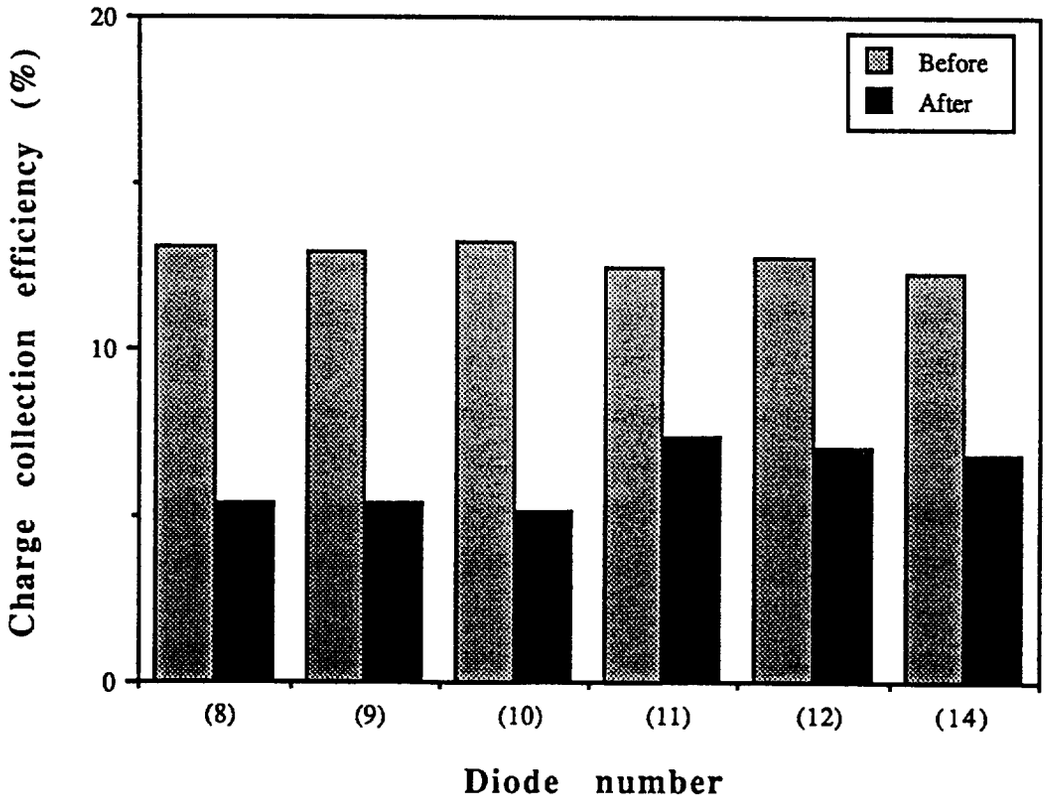

20
10
0
Charge collection efficiency (%)
Before
After
(8)
(9)
(10)
(11)
(12)
(14)
Diode number

Fig. 4

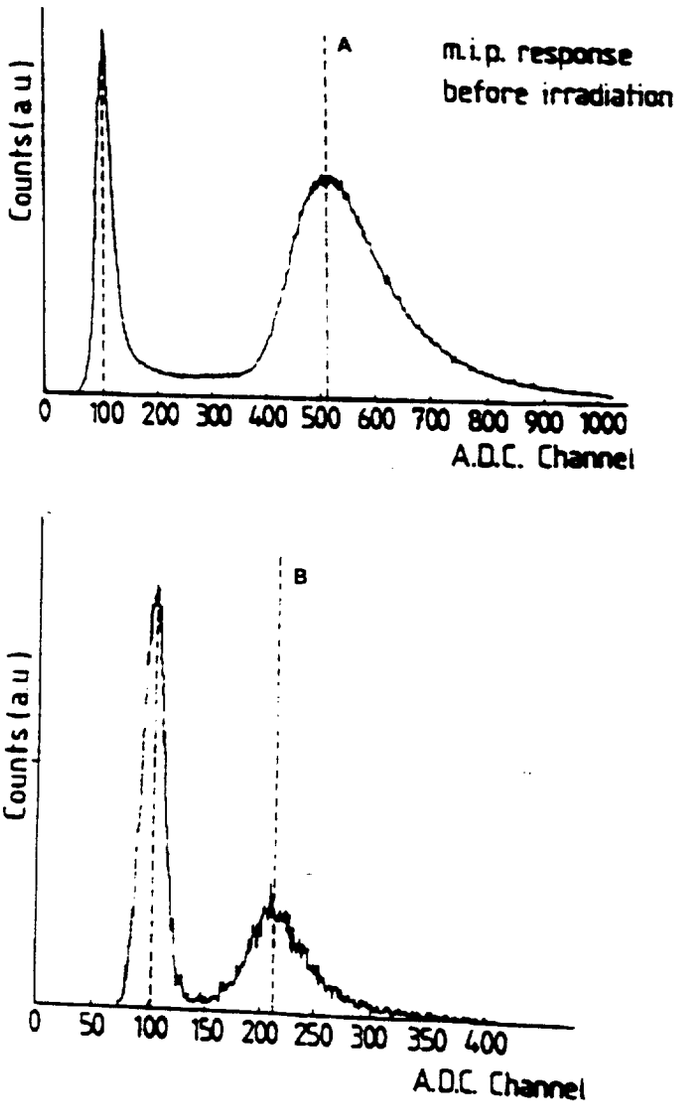

A
m.i.p. response
before irradiation
Counts (a u)
0 100 200 300 400 500 600 700 800 900 1000
A.D.C. Channel
B
Counts (a u)
0 50 100 150 200 250 300 350 400
A.D.C. Channel

Fig. 5

Radiation testing of optical fibres and typical results

H. Henschel, Fraunhofer-INT, D-5350 Euskirchen

1. INTRODUCTION

It is no longer necessary to list up the advantages of optical fibres. But they exhibit also a severe drawback, compared with conventional copper coax cables. That is their increased sensitivity against ionizing radiation.

The most important radiation effect is an increased light attenuation (radiation induced loss; see, e.g., refs. 1, 2). A second disturbing effect can be the luminescence light. It is caused by the Čerenkov effect and can prevent signal identification for a certain time in presence of high radiation dose rates (e.g. pulsed irradiation). With a graded index multimode fibre we also observed a decrease of bandwidth from 1.4 to 1 GHz during a continuous irradiation up to 10^5 rd.

The magnitude of the radiation induced loss depends on fibre type as well as on the test parameters. The fibre type is mainly determined by the preform manufacturing process, the concentration of dopants and impurities, and the fibre drawing parameters.

The major test parameters that might influence the induced loss are total radiation dose and dose rate, wavelength and intensity of the conducted light ("photobleaching"), and fibre temperature.

In order to simulate certain radiation environments, the Fraunhofer-INT has three major irradiation facilities: a ^{60}Co irradiation facility, a flash X-ray facility, and a 14 MeV neutron generator.

2. TYPICAL TEST RESULTS

Figure 1 compares the increase of loss with radiation dose for three different fibres. Fibre 1 is a graded index fibre whose core is doped with 11.9% Ge and 0.13% P. The P atoms seem to form very effective, extremely long living colour centres. As a consequence, the induced loss shows a linear increase with dose up to extremely high values.

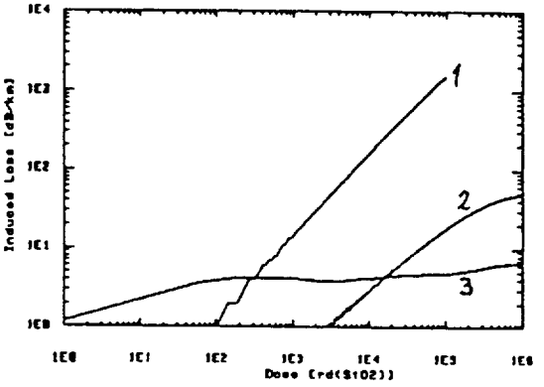
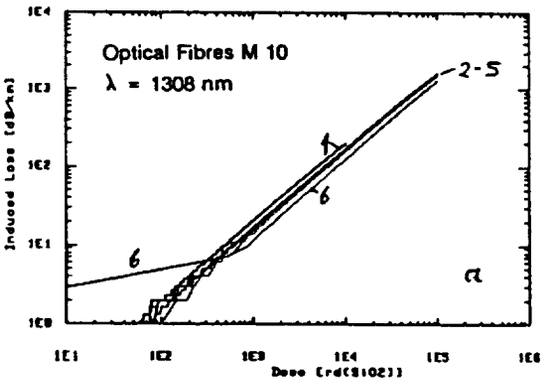


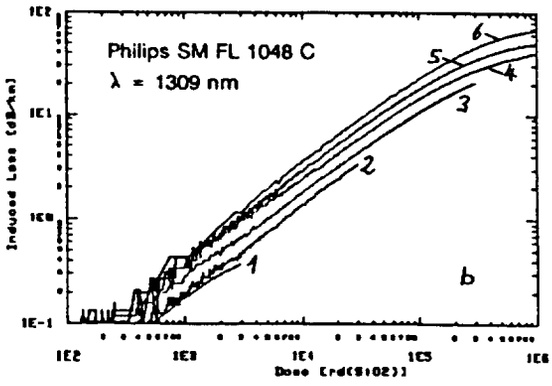
Figure 1: Induced loss as a function of dose. 1: "Optical Fibres M 10" (λ = 1308 nm), 2: "Philips SM FL 1048C" (λ = 1309 nm), 3: "Heraeus SS 1.2 152/90" (λ = 865 nm). $\dot{D}_\gamma \approx 20$ rd/s, T = 22°C.

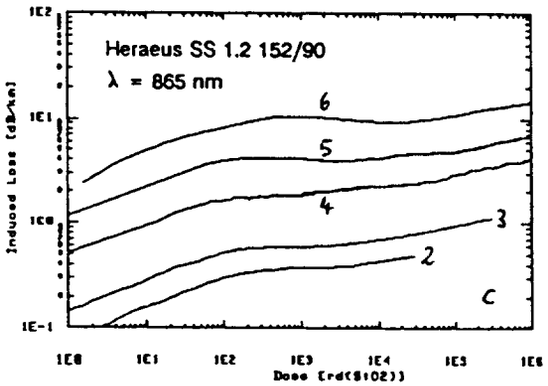
Fibre 2 is a single mode fibre with Ge (and eventually also F) as doping material within the core. This type of fibre exhibits a relatively good annealing of the colour centres, so that the induced loss is much lower, compared with the P containing fibre. The saturation at high dose values can be explained by the beginning of an equilibrium of colour centre formation and colour centre decay rates.

Fibre 3 has a pure SiO_2 core, but with very high OH content ($\gtrsim$ 800 ppm). This high OH content is responsible for the very fast annealing of the colour centres especially at late times after continuous irradiations. With high annealing rates, the equilibrium between colour centre formation rate and annealing rate is reached at very low levels of the induced loss.

Figures 2a-c show the increase of induced loss with dose for the same fibres than Fig. 1, but measured with different dose rates, ranging from 0.05 rd/s up to about 175 rd/s. One can see that the influence of dose rate is strongly dependent on the annealing behaviour of the different fibre types: the faster the annealing, the stronger the influence of dose rate.







Figures 2a-c: Induced loss as a function of dose for six different dose rates: $\dot{D}_\gamma$ = 0.05 rd/s (1), 0.25 rd/s (2), 1 rd/s (3), ≈ 5 rd/s (4), ≈ 20 rd/s (5), and ≈ 175 rd/s (6). T = 22°C.

The radiation induced loss shows, in principle, for most of the fibres the same strong decrease with wavelength as the initial loss (attenuation before irradiation), see fig. 3. The results are nearly indentical for all Ge doped fibres. The increase of the $1.4 \cdot 10^6$ rd curve at longer wavelengths suggests the formation of a new type of colour centre.

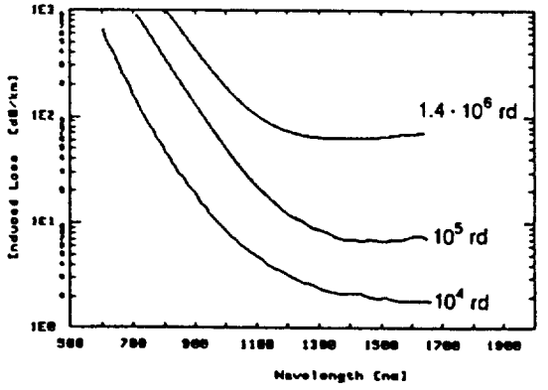


Figure 3: Induced loss as a function of wavelength for three different radiation dose values; $\dot{D}_\gamma$ = 21.7 rd/s, T = 22°C.
Fibre: Graded index "AT&T MM Rad Hard 3A".

It is well known that light intensity can reduce the radiation induced loss of optical fibres ("photo bleaching"). The highest influence of light power we ever found exhibited low OH fibres with undoped core fabricated by Schott with the PICVD process (see Figure 4).

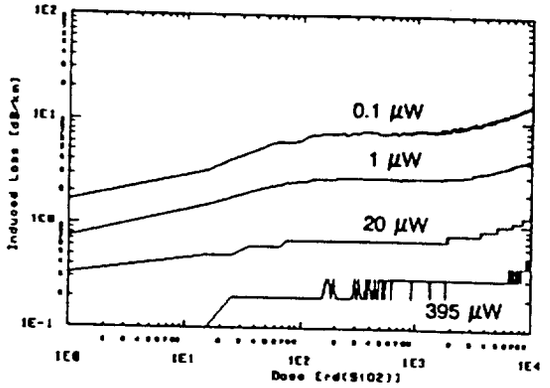


Figure 4: Influence of light power on radiation induced loss; λ = 1545 nm, T = 22°C. Fibre: Single mode "Schott P928/11".

Most of the fibres show a more or less pronounced decrease of the induced loss with increasing temperature (see Fig. 5).

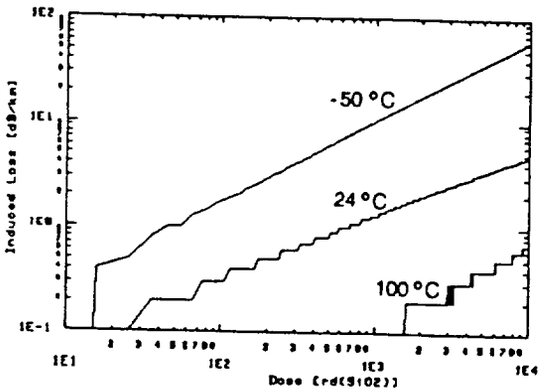


Figure 5: Influence of fibre temperature on radiation induced loss; $\lambda \approx$ 1300 nm, $\dot{D}_1$ = 5 rd/s, P = 20 µW. Fibre: Fujikura SM 10/125 04.

3. CONCLUSIONS

In the meantime there exist a variety of radiation hard optical fibres. Nevertheless it is necessary to select by specific irradiation tests the optimum fibre for each intended application.

REFERENCES

1) H. Henschel, O. Köhn, H.U. Schmidt; "Induced loss after pulsed and continuous irradiation of single mode and graded index fibres"; SPIE Vol. 992 Fiber Optics Reliability: Benign and Adverse Environments II (1988), p. 96-108

2) H. Henschel, O. Köhn, H.U. Schmidt; "Radiation damage and radiation induced loss in optical fibres"; SPIE Vol. 1174 Fiber Optics Reliability: Benign and Adverse Environments III (1989), p. 46-59

PRODUCING RADIATION HARD ALL SILICA FIBERS – STATE OF THE ART AND FUTURE ASPECTS –

H. Fabian, U. Grzesik
Heraeus Quarzglas GmbH, 6450 Hanau, FRG

K.–F. Klein
Fachhochschule Gießen Friedberg, 6360 Friedberg, FRG

Abstract

Fiber optic waveguides show a high degree of reliability in transmitting data even under adverse conditions like ionizing radiation. Nevertheless there is still some radiation induced additional loss which can cause problems for some specific applications.

A review on intrinsic and radiation induced defects in all silica fibers with undoped core is given to understand the radiation induced loss in different types of fibers. Measurements on fibers with special refractive index profiles are presented to elucidate the contribution of the core material and the cladding material.

The influence of production parameters on the performance of fibers is demonstrated for pulsed electron and continuous γ–irradiation.

The state of the art is summarized and an outlook for the production of radiation hard fibers is presented.

1. Introduction

The development efforts in the field of fiber optic waveguides have led to dramatic improvements especially in attenuation over the last two decades.

Because of the chemical inertness of silica it is an ideal material to be applied in adverse environments. One of the challenging fields of applications is data or power transmission in the presence of ionizing radiation. In this case the material may show substantial values of induced attenuation after exposure to high radiation doses. Though a number of research and development groups have made substantial contributions in the last decade, the understanding of the behaviour of silica under ionizing radiation is still a field of research (1–5).

2. Defects in the silica network

Since the work of Zachariasen in 1932 (6) the structure of silica is known to be "built up of oxygen tetrahedra which surround silicon atoms. ... The oxygen tetrahedra share corners with each other in such a manner that the oxygen atom is linked to two silicon atoms". This structure still has some degrees of freedom leading to a "continuous random network". Disturbances of the network will be referred to as a "defect", "defect center", or "color center".

Defects are caused by contamination, broken chemical bonds, and missing or delocated atoms. Defect centers always cause changes in the electronic states or even create new states, sometimes leading to dramatic changes of the optical properties of a silica sample.

2.1 Intrinsic defects

Directly after the production process, characteristic absorption bands may be observed. They are attributed to so–called "intrinsic" defect structures. The most important defects and the correlated absorption bands are shown in table 1.

Note that some defects are believed to cause two absorption bands and that absorption bands located in the same spectral region (325 nm) are correlated to different types of defects. Because of their large number bands caused by hydrogen compounds or metallic impurities (7,8) are not included.

2.2 Radiation induced defects

Under exposure of ionizing radiation new absorption bands are "induced" in optical fibers or bulk samples. The mechanisms of this type of defect creation are not well understood and depend on the type of radiation, dose, dose rate, temperature, type of material, and doping elements.

Griscom identified three different types of E'–centers by their behaviour under different irradiation and annealing conditions (fig. 1, 2). The detailed experimental parameters are described in the literature (9).

Generation of E'_{β}– and E'_{γ}–centers starts from specific glass network configurations or defects like a threefold coordinated silicon atom or an oxygen vacancy. These network distortions are called "precursors" or "precursor defects". The precursor density mainly determines the increase of radiation induced loss.

3. Test equipment

The radiation measurements shown in this paper were performed at Fraunhofer INT in Euskirchen (FRG). A detailed description of the measurement set–up is given in the literature (10,11). For pulsed electron irradiation the induced loss is measured as a function of time after the radiation pulse. The measurement intervall covers times from 100 ns to 10 s. For continuous γ–irradiation a ^{60}Co–source is used and the induced loss is measured during and after irradiation as a function of dose. All results were obtained at room temperature.

4. Influence of OH–content on radiation hardness of undoped silica core optical fibers

The operating wavelength is very important because radiation induced loss is strongly wavelength dependent, which is shown for a low OH–content fiber in fig. 3. The fiber was exposed to a 10 krd continuous γ–irradiation.

Synthetic silica used as core material for optical fibers is devided into two different groups depending on whether the OH–content is high or low. In telecommunication systems fibers with low OH–content core materials are needed because attenuation values have to be small at standard operating wavelengths around 850 nm, 1300 nm, and 1550 nm. Applying fibers with high OH–content core material data transmission becomes restricted to 850 nm wavelength because of strong OH–absorption bands at higher wavelengths.

In order to make a "fair" comparison of radiation hardness the right wavelength choice should be done. Therefore, comparing radiation hardness of OH–rich and OH–poor core materials one should chose the most common operating wavelength for each material, that is 850 nm and 1300 nm for high and low OH–content materials, respectively.

In fig. 4 the dose dependence of radiation induced loss during γ–irradiation is shown for fibers with high and low OH–content core materials at their optimal operating wavelength. At low dose values the performance of the OH–poor fiber is slightly better. For dose levels above 500 rd, however, the induced loss becomes significantly higher compared to the fiber with OH–rich core material. The same result is obtained for radiation induced loss after pulsed irradiation (fig. 5). Again the radiation hardness of OH–rich fibers is better.

An explanation for the differences in radiation hardness can be inferred from the UV–attenuation spectra of the fibers (fig. 6). The OH–poor material is showing absorption bands at 325 nm and in the region of 265 nm and 245 nm wavelength. This indicates that there is a variety of precursor defects. These can be converted by ionizing radiation into color centers causing an increase in attenuation at 1300 nm.

In contrast to the OH–poor material the OH–rich material does not show any absorption bands. The glass network seems to have very few precursor defects and so the radiation induced attenuation is quite small.
As a result we can state that fibers having core materials with high OH–content are more radiation hard than fibers with low OH–content cores. This is valid even when the comparison is performed at the most favorable operating wavelength of the materials.

5. Influence of core material production process on radiation hardness of high OH–content undoped silica core fibers

To get a deeper insight into radiation effects on fibers with OH–rich core material we produced two fibers having different core material quality. UV–attenuation spectra of these fibers are shown in fig. 7. OH–content, preform production process, and fiber drawing parameters were kept about the same for both samples.

The difference between the fiber samples is introduced by the production process of the core material. Producing samples with improved quality process parameters were controlled in order to minimize the number of precursor defects. As can be seen by the UV–attenuation curves significantly improved UV–performance was obtained.

Investigating the radiation hardness of these two fiber samples (fig. 8 and fig. 9) we found that the improved UV–attenuation is correlated with higher radiation hardness. The lower the UV–attenuation is the lower the radiation induced loss will be during γ–irradiation or after pulsed irradiation.

6. Radiation hardness of F–doped silica cladding

In the literature different methods are decribed to measure radiation induced loss in F–doped silica (12, 13, 14).

A direct method for testing F–doped material will be discussed in the following sections. A special step–index fiber (14) is used having three different fluorine levels in the cladding.

The measured refractive index profile of the preform is shown in fig. 10. The core material of the preform consists of SUPRASIL–W (15) having an OH–content less than 5 ppm.

In the second cladding because of the higher refractive index in comparison to the first and the third ones, the condition of total reflection is fulfilled. Light guidance in the second cladding is possible, but with a higher attenuation due to bending losses. Using selective mode excitation at the fiber front face either the modes of the core or of the second cladding are excited (fig. 11). In this configuration the radiation induced loss difference of undoped and F–doped silica can be measured with only one fiber sample.

Some results obtained with this fiber type are being presented in fig. 12 and fig. 13. Induced loss and recovery characteristics after pulsed irradiation are about the same for F–doped cladding and undoped core material. During continuous γ–irradiation the F–doped cladding is even more radiation resistant than the undoped low OH–content core material. With increasing dose the difference between F–doped and undoped material becomes bigger.

7. Summary

Using optical fibers for data transmission under ionizing radiation those with undoped silica core having a high OH–content show the best performance regarding radiation induced loss. This is attributed to the small number of precursor defects.

UV–absorption bands in optical fibers indicate a high concentration of precursor defects and correlate to high radiation induced loss. Users of optical fibers might use UV–attenuation in a fiber sample to predict the radiation induced loss.

For future improvement a better understanding of the mechanisms of defect generation will be essential. Knowing the precursor defects one needs a method like UV–attenuation measurements on optical fibers to determine their concentration. As a final step process parameters have to be adjusted to minimize precursor defect concentration

8. Acknowledgements

We gratefully acknowledge the performance of all radiation measurements by the Fraunhofer INT. Especially we would like to thank Dr. H. Henschel and O. Köhn (Fraunhofer INT) for their cooperation and valuable discussions.

Literature:

1. G.H. Sigel, Jr., M.J. Marrone, J. Non–Cryst. Solids, 45, (1981), 235
2. E.J. Friebele, C.G. Askins, M.E. Gingerrich, K.J. Long, Nucl. Instr. Meth. Phys. Res., B1, (1984), 355
3. D.L. Griscom, J. Non–Cryst. Solids, 68, (1984), 301
4. R.A.B. Devine, Phys. Rev. B, Vol. 35, No. 18, (1987), 9783
5. K. Nagasawa, M. Tanabe, K. Yahagi, Jap. J. Appl. Phys., Vol. 23, No. 12, (1984), 1608
6. W.H. Zachariasen, J. Am. Chem. Soc., 54, (1932), 3841
7. P.C. Schultz, J. Am. Ceram. Soc., 57, 7, (1974), 309
8. J.U. Stone, J. Lightwave Techn., LT–5, 5, (1987), 712
9. D.L. Griscom, J. Non–Cyst. Solids, 73, (1985), 51

10. K.–F. Klein, A. Mühlich, K.–H. Wörner, H. Henschel, O. Köhn, H.U. Schmidt, Proc. SPIE Vol. 867, Cannes 1987, 17
11. H. Henschel, Internal report of the Fraunhofer INT Nr. 10/87
12. T. Gozen, H. Tanaka, A. Utsumi, T. Maeda, S. Okamoto, Conf. Electr. Insul. Dielectr. Phenom., IEEE Piscataway, NY 1984, 65
13. H. Fabian, K.–F. Klein, H. Henschel, O. Köhn, H.U. Schmidt, P. Lyons, L. Looney, Proc. SPIE Vol 1314, London 1990, to be published
14. H. Fabian, K.–F. Klein, A. Mühlich, K.–H. Wörner, H. Henschel, O. Köhn, H.U. Schmidt, Proc. SPIE Vol. 992, Boston 1988, 129
15. Reg. trademarks of Heraeus Quarzglas GmbH

Figures:

Fig. 1: Different types of E'–centers induced by ionizing radiation
Fig. 2: Thermal annealing of different types of E–centers
Fig. 3: Wavelength dependence of radiation induced loss in fibers having low OH–content core material
Fig. 4: Radiation induced loss at working wavelength of fibers having high and low OH–content core materials
Fig. 5: Recovery characteristics at working wavelength of fibers having high and low OH–content core materials
Fig. 6: UV–attenuation of fibers having high and low OH–content core materials
Fig. 7: UV–attenuation of fibers having high OH–content core materials of different quality
Fig. 8: Recovery characteristics of fibers having high OH–content core materials of different quality
Fig. 9: Radiation induced loss of fibers having high OH–content core materials of different quality
Fig.10: Refractive–index profile of a TC–preform
Fig.11: Nearfield–pattern of TC–fiber endface with selectively excited core (left) or second cladding (right) modes
Fig.12: Influence of F–doping on recovery characteristics at 1300 nm wavelength
Fig.13: Influence of F–doping on radiation induced loss at 850 nm wavelength

Fig. 1:

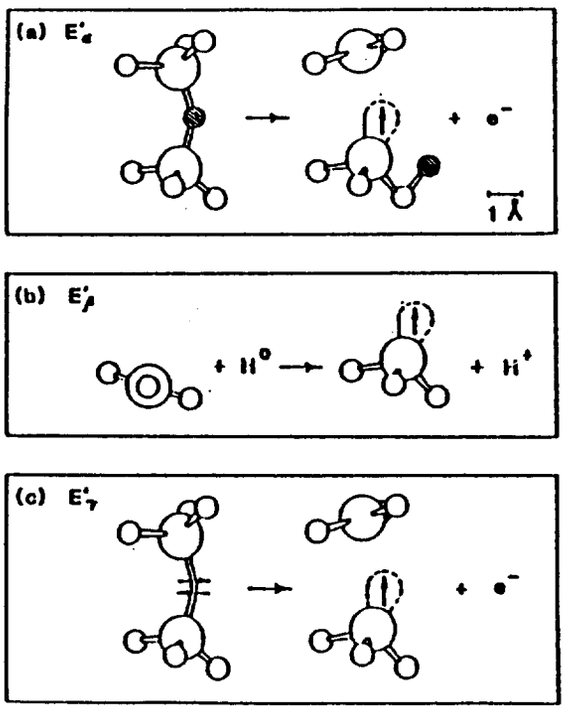


Fig. 2:

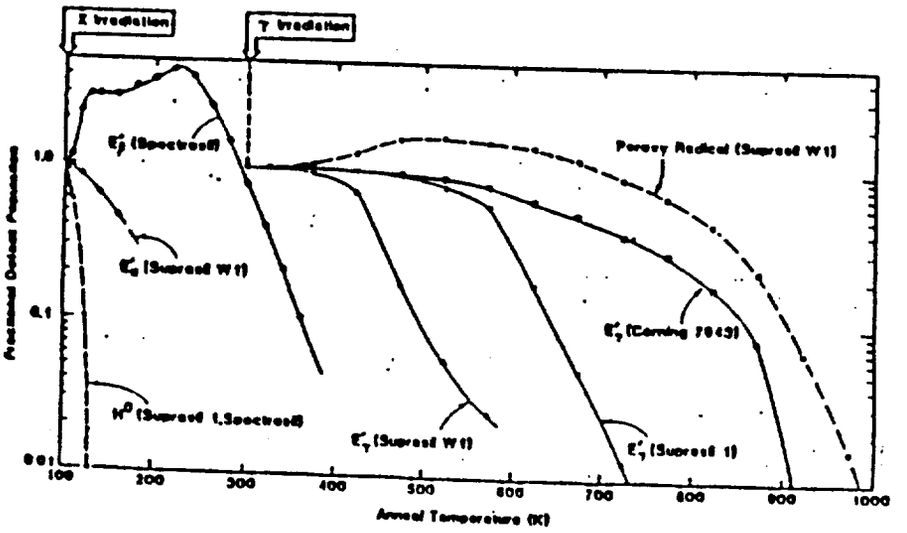


Fig. 3:

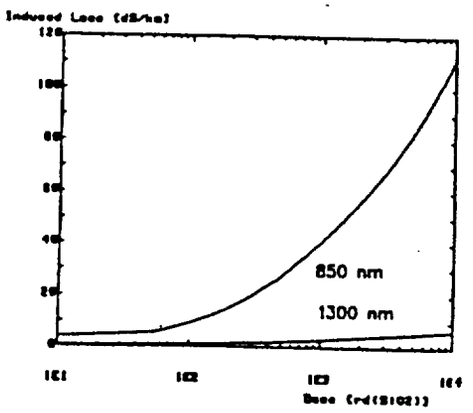


Fig. 4:

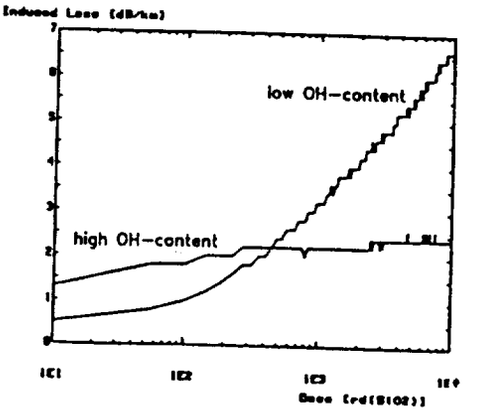


Fig. 5:

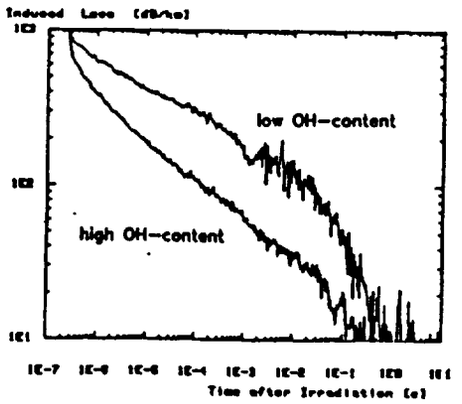


Fig. 6:

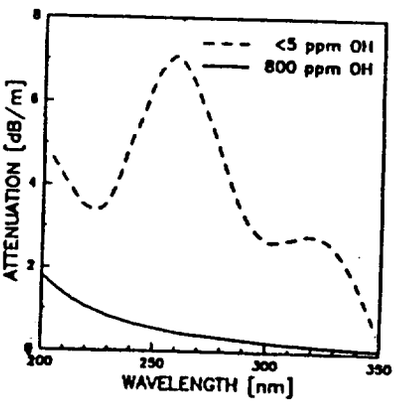


Fig. 7:

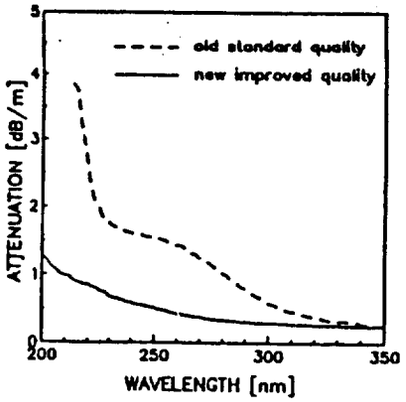


Fig. 8:

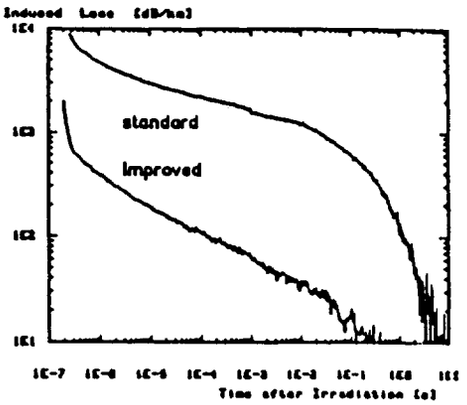


Fig. 9:

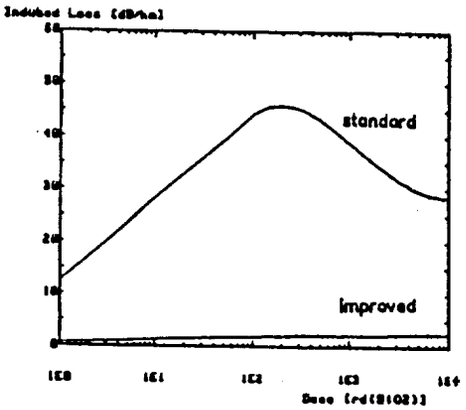


Fig. 10:

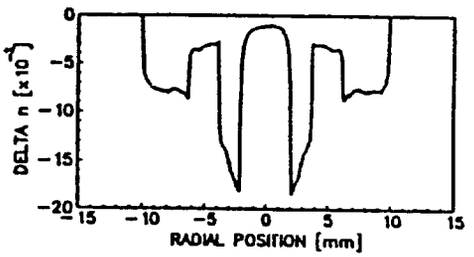


Fig. 11:

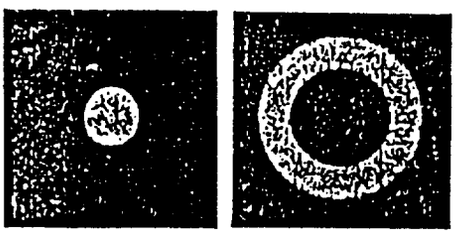


Fig. 12:

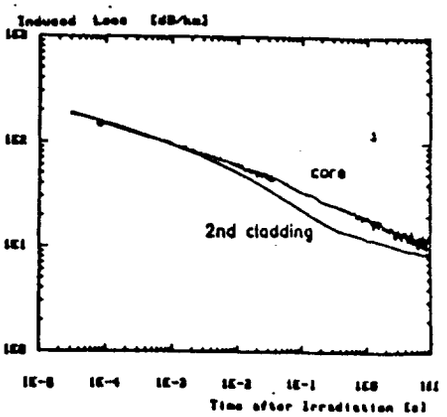


Fig. 13:

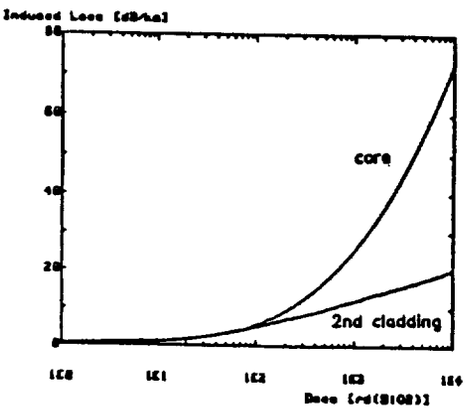


TABLE 1: ABSORPTION BANDS AND DEFECTS

≡Si°	E'-CENTER	215 nm
≡Si–Si≡	OXYGEN VACANCY	163 nm 247 nm
—O–Si°–O—	TWOFOLD COORDINATED SILICON	243 nm
≡Si–O–O–Si≡	PEROXY LINKAGE	325 nm
≡Si–Cl Cl–Si≡	CHLORINE CENTER	328 nm
≡Si–O°	NBOH-CENTER	265 nm 630 nm

+ BANDS DUE TO HYDROGEN COMPOUNDS

+ BANDS DUE TO METALLIC IMPURITIES

Radiation resistance of insulators and structural materials.

M.Tavlet, H.Schönbacher
CERN-TIS

Introduction

From the very beginning of CERN, attention was given to the effects of ionizing radiation, notably on organic materials. Our present knowledge is based upon hundreds of experimental irradiation tests as well as upon special research carried out in conjonction with outside institutes and industries. Over the past 20 years, many experimental data have become available. Results are published for a large variety of commercial materials; cable insulations and sheaths, thermoplastic and thermosetting resins, and other materials and components used around high-energy accelerators, such as hoses, connectors, switches, etc.

This paper summarises the radiation effects on the polymer materials, it presents a general classification of radiation resistant products, and it gives a list of available data compilations and publications (in appendix).

Radiation effects on polymers

Polymers' macromolecules are strongly affected by radiation. The first fondamental effect after ionization and excitation is the radical formation. The radical may react with another chain, by branching, it is called the cross-linking; it may lead to chain-scission and degradation. It may also leave unsaturations in the chain and give rise to gaz evolution.

Chain scission and cross-linking have some opposite effects on the mechanical properties of the polymer. They both make the material more brittle, with less elasticity.

Oxidative degradation is an important factor to be considered. It explains that many polymers are sensitive to dose-rate effect. The presence of oxygen during irradiation promotes chain-scission and accelerates the degradation.

The temperature may also be an important factor; the synergistic effect of temperature and irradiation accelerates the degradation of the material.

Insulators or structural materials are never made of pure polymer. The radiation resistance of a materials depends of the base polymer and of the additives and/or fillers and/or charges, copolymers and compounds may also be used. As additive, stabilyzers and antioxidants are much used to

improve the radiation resistance, dyes do not change the radiation resistance. Mineral fillers are often used to improve the fire- or flame-resistance of the materials, they usually decrease their radiation resistance. Charges such as glass mat or glass fibres increase the radiation resistance of the resins.

Test methods, presentation of results

For the purpose of our radiation resistance tests, the materials are usually irradiated in a strong source (reactor or Cobalt, at dose rates above 1 Gy/s). They undergo mechanical tests based on the IEC standard 544.

The rigid thermoplastics and the thermosetting resins undergo flexural tests. The flexural strength is usually the most sensitive property of the resins and the strongly cross-linked materials, the deflection at break may be more sensitive for others. According to the recommandation of the IEC 544, the end-point criterion is based on the reduction of the flexural strength.

The soft thermoplastic materials and the rubbers undergo tensile tests. The elongation at break is their most sensitive property, and therefore chosen as the critical property. The end-point criterion is based on the reduction of this elongation at break.

A classification of these two types of materials is given in tables 1 and 2; it is based on the reduction of their critical property. The classification gives only an order of magnitude of the limit-dose of usability of the materials; for some materials, the dose-rate effect is important.

To check the dose-rate effect in the materials, they are also irradiated at low-dose rate (0.03 Gy/s) in a cobalt source, and tested. Some tests are also carried out on materials which have been exposed to life condition in a CERN accelerator for several years. These last tests allow to estimate the life time of the materials in real environment. An example of test result and of the dose-rate effect on a polyolefin-based material is shown in Figure 1.

Conclusions and evolution of the studies

Radiation degradation of organic materials depends on material type and composition, dose, and dose rate, as well as on mechanical, electrical and other stresses. Our experience and knowledge about the phenomena become more complete.

Some materials and components are very sensitive to ionizing radiation: PTFE, optical fibres and electronics. These two latter as well as scintillating materials and semiconductor detectors have to be used in detectors; significant results have been reported at this workshop.

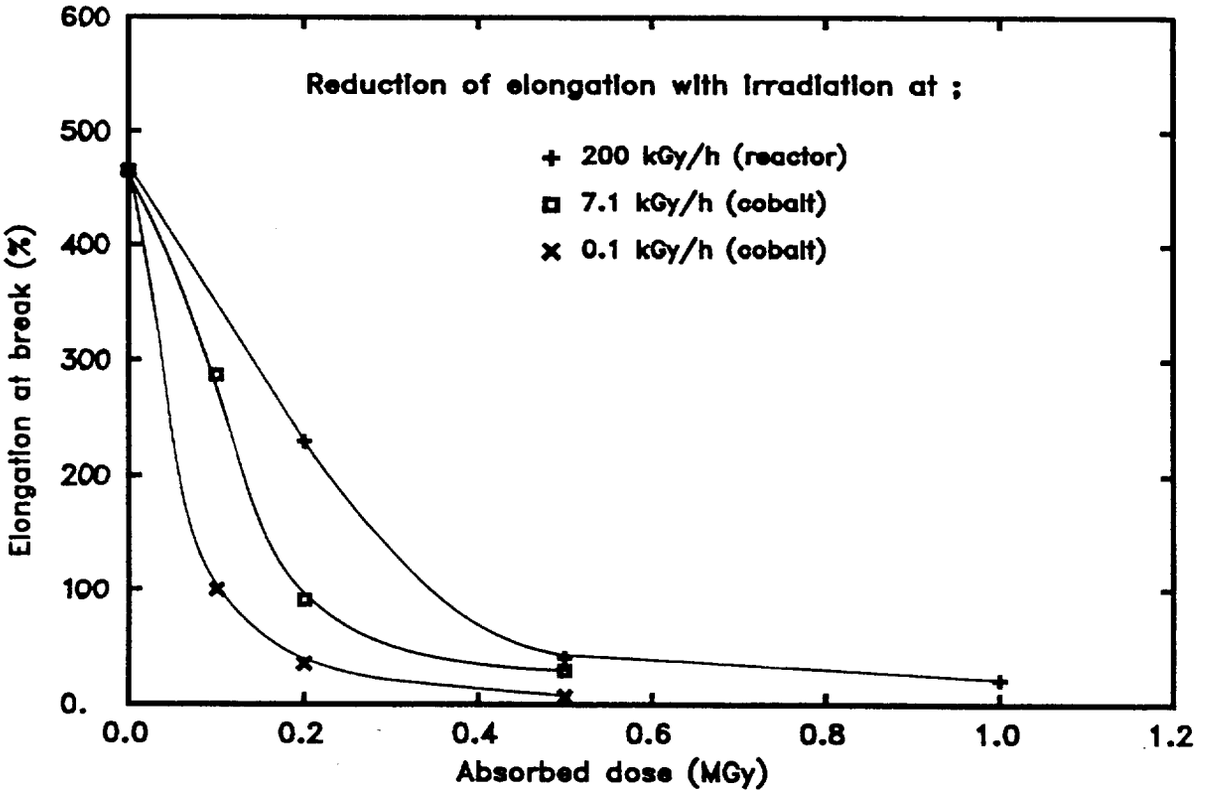


Figure 1 : Dose-rate effect in a Polyolefin material

Experience has shown that, for most of the applications in radiation environment around the CERN accelerators, standard products can be found on the market; this should also be possible for future detectors. We may assume that for a detector-radiation environment:

- conventional cable insulating materials (polyolefin-based) show no degradation below 10 kGy and may be used to doses up to 0.1 or 0.3 MGy;

- EPR- and PUR-based insulations, hoses, and gaskets do not present important dose-rate effect and may be used to doses up to 1 to 3 MGy;

- new performant materials such as PEEK and polyimides may be used until 3 to 10 MGy;

- glass-reinforced epoxy resins mainly used as magnet-coil insulations show no dose-rate effect and could withstand doses as high as 10 to 30 MGy;

- metals and most of the ceramics do not suffer from radiation damage at usual accelerators dose levels.

For the past 5 years, our efforts concentrate on the study of special parameters such as radiation types and dose rates. This was done in collaboration with international institutes such as IAEA and IEC.

Appendix : Selected publications.

Compilation of radiation damage test data;
Part I: **cable** insulating materials CERN 79-04

Compilation of radiation damage test data;
Part II: insulating **resins** CERN 79-08

Epoxy resins in radiation environments CERN 81-05

Radiation resistant magnets CERN 82-05

Compilation of radiation damage test data;
Part III: **miscellaneous materials** CERN 82-10

Radiation effects on rare-earth cobalt permanent magnets.
CERN/TIS-RP/IR/83-07

Long-term radiation effects on commercial cable-insulating materials irradiated at CERN. CERN 83-08

Radiation tests on selected electrical **insulating materials** for high-power and high voltage application. CERN 85-02

Radiation damage to organic scintillation materials.
CERN 85-08

Strahlenbestandigkeit von epoxidformassen (Ciba-Geigy)
Kunststoffe 76 (1986) CERN/TIS-RP/170/pp

Effects of radiation types and dose rates on selected cable-insulating materials. CERN/TIS-RP/191/pp
Radiat.Phys.Chem. Vol.30,No1,pp1-9 (1987)

Review of radiation damage on scintillating materials.
CERN/TIS-RP/201 (1987)

Review of radiation effects in optical fibres.
CERN/TIS-RP/IR/88-21 (1988)

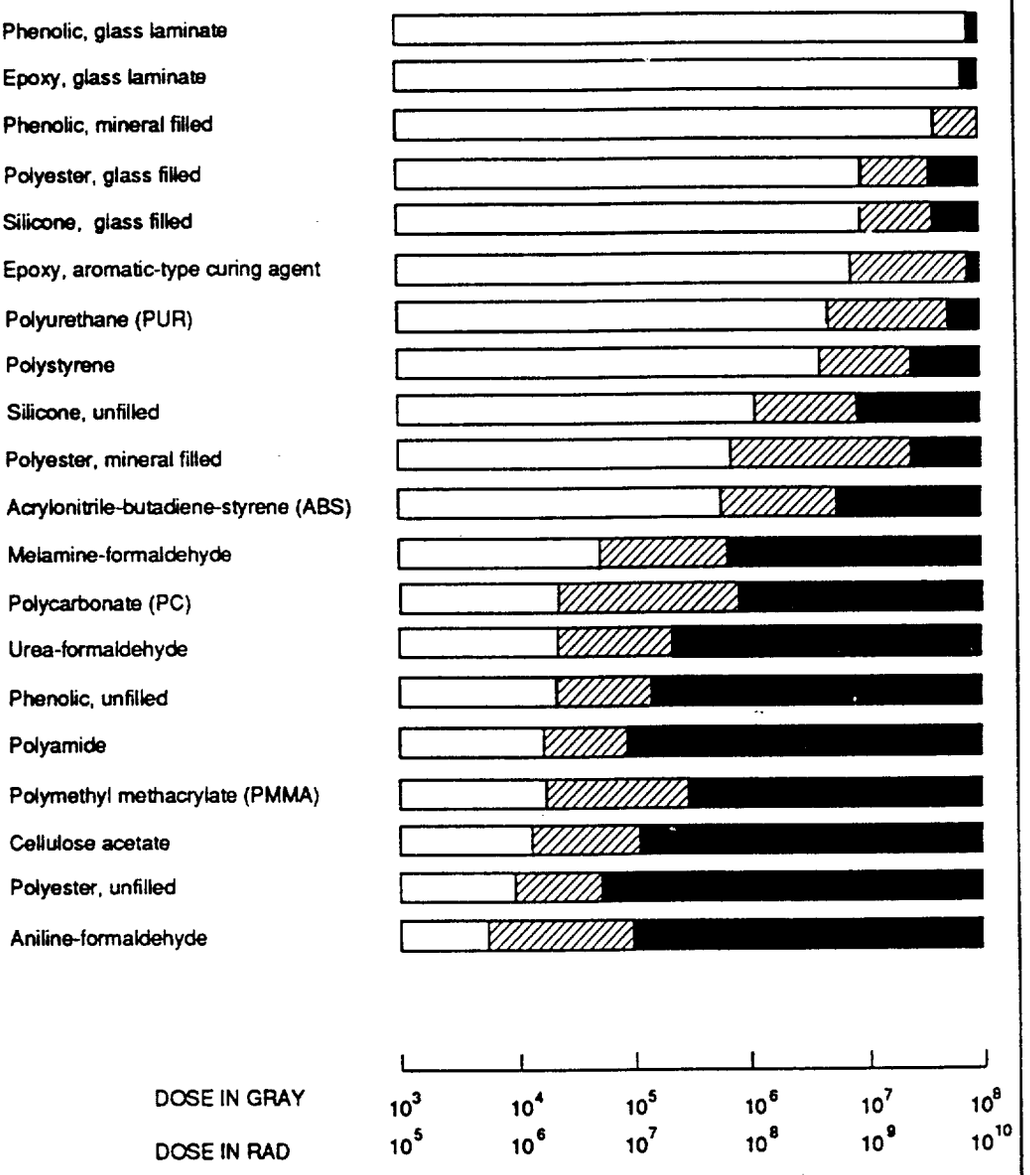
Ageing of organic materials in ionizing radiation environments of high energy particles accelerators.
IAEA CRP 4319 CERN/TIS-CFM/89-11

Compilation of radiation damage test data;
Part I-2: **cable** insulating materials CERN 89-12

Compilation of radiation damage test data;
Part II-2: insulating **resins** CERN 91-..

Table1

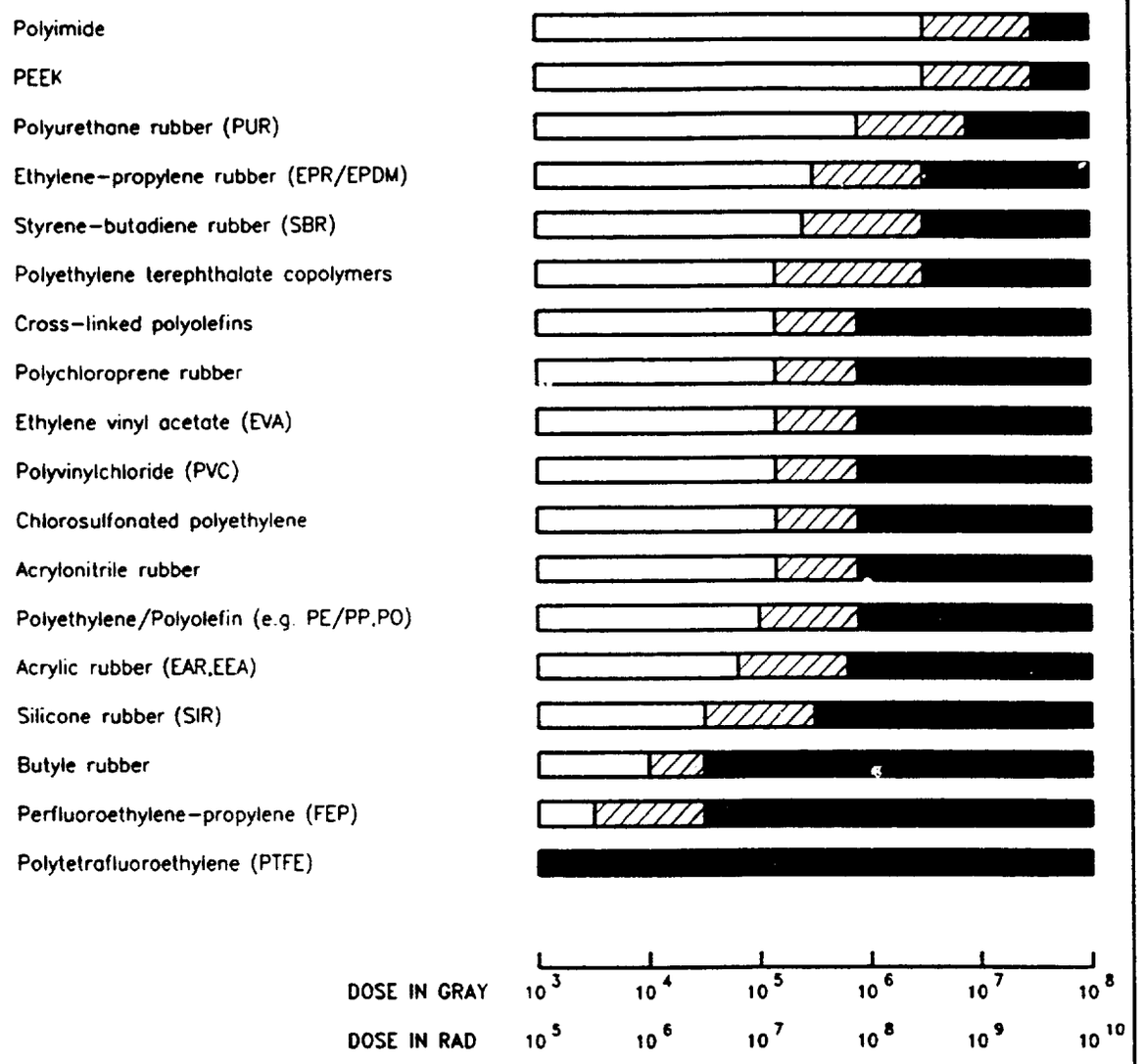
Classification of thermosetting and thermoplastic resins according to their radiation resistance.



Damage	Tensile strength (in % of initial value)	Utility
Incipient to mild	70-100 %	Nearly always usable
Mild to moderate	25- 75 %	Often satisfactory
Moderate to severe	< 25 %	Not recommended

Table 2

Classification of materials according to their radiation resistance



Appreciation of Damage	Elongation	Utility
Incipient to mild	75–100 % OF IN. VALUE	Nearly always usable
Radiation index area	25–75 % OF IN. VALUE	Often satisfactory
Moderate to severe	< 25 % OF IN. VALUE	Not recommended

Radiation hardness of semiconductor detectors and read out electronics for the ALEPH minivertex detector

Paolo Walter Cattaneo
Max-Planck-Institut für Physik und
Astrophysik, 8000 München 40, FRG

December 7, 1990

Abstract

In ALEPH at the LEP $e^+ - e^-$ collider, a double sided silicon microstrip detector has been installed as minivertex detector [1, 2]. Its read out electronics consists of a custom designed VLSI amplifier CAMEX 64 [3], a digital steering chip running the CAMEX and a line driver driving the output line [4].
Two different types of detector wafer have been designed for it by Max Planck Institut für Physik, Munich and INFN Pisa, respectively.
The read out electronics and the detector wafer designed in Munich relevant source of radiation damage is the synchroton radiation, the radiation tests have been carried on with X-ray machines and a Co_{60} γ source. This types of radiations are hardly able to generate bulk defects in the silicon but, through the photoelectrons produced in photoelectric and Compton interactions, they are effective in damaging the silicon dioxide used on the surface of the devices. Therefore in the study of the detector the attention has been concentrated on the carachteristics dependent on the $Si - SiO_2$ surface.
The radiation sources employed are a 200 keV X ray machine with an average energy of $\approx$ 80 keV, a Co_{60} γ ray source and a 80 keV X ray machine.
The sources have been calibrated using a PIN diode and the absorbed dose is expressed as rad in silicon [5].

1 ALEPH minivertex electronics

The detector front end read out consists of the custom designed VLSI chip CAMEX 64 based on a $3.5\mu m$ CMOS technology and switched capacitor technique, employing a n-channel MOSFET as input transistor and CMOS as switches.
It includes amplification, shaping and multiplexing of 64 channels. It is followed by a line driver able to drive the output line, while a digital steering chip supplies both with the required clock signal [6]. The last two chips have been designed in $2\mu m$ technology. In Fig. 1 the scheme of the CAMEX, based on the principle of multiple correlated sampling, is sketched. The CAMEX technological parameters relevant to radiation damage are: gate oxide thickness 400Å, field oxide thickness 7500Å, polysilicon gate thickness 7500Å, passivation glass 10000Å.

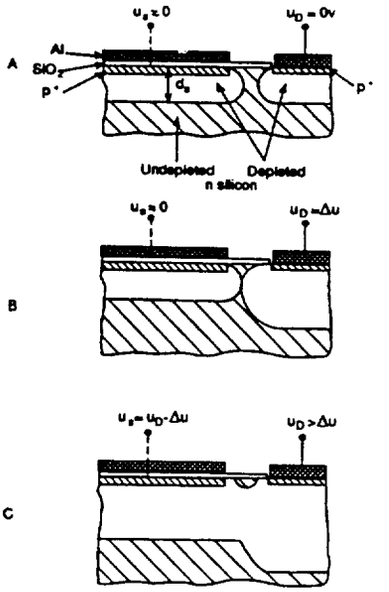


Figure 1: Single channel scheme of the CAMEX64 and timing diagram

2 ALEPH minivertex detector

The ALEPH minivertex detector is a double sided silicon microstrip detector [7] AC coupled to the read out electronics with a strip pitch of $25\mu m$ on the phi side and of $50\mu m$ on the z side. On the p-side, the biasing of the strips is obtained through an adiacent p^+ contact as shown in Fig. 2.

On the n-side, the bias is obtained through a conductive channel due to the electron accumulation layer under the oxide, delimited by a p^+ implantation Fig. 2. On the edges of the wafers produced for the ALEPH minivertex detector several test structures have been integrated to simulate the behaviour of different parts of the detector. These structures include MOS diodes with or without guardring and p^+ implantation pattern simulating the bias scheme of Fig. 2.

3 Irradiation of the electronics

What is known about radiation damages in silicon electronics is summarized in [8, 9], while for detectors [11] gives a good overview.
The electronics has been irradiated under diverse bias conditions; the results have been already reported in [12], so that only a summary is reported here.
The CAMEX 64 has been irradiated unpowered, with D.C. power but without digital signals and in fully operational condition with both D.C. power and digital signals. The steering chip has been irradiated unpowered or in full operational regime. The steering chip only in full operational condition.
The results of the irradiation with power off with the 200 keV X-ray machine source is plotted in Fig. 3

The most noteworthy feature is the doubling of noise at approximately 140 krad. The same irradiation with the γ ray source shows that the noise increases till 440 krad, where the chip breaks down.
If the chip is biased either D.C. or in operation the noise changes very little till the chip crashes. That happens at about 10 krad for D.C. bias and 20-30 krad for chip in operation.

In Fig. 3 the curve noise versus dose is plotted for a chip irradiated in operation.
A qualitative explanation of the measurements can be obtained on the basis of the known

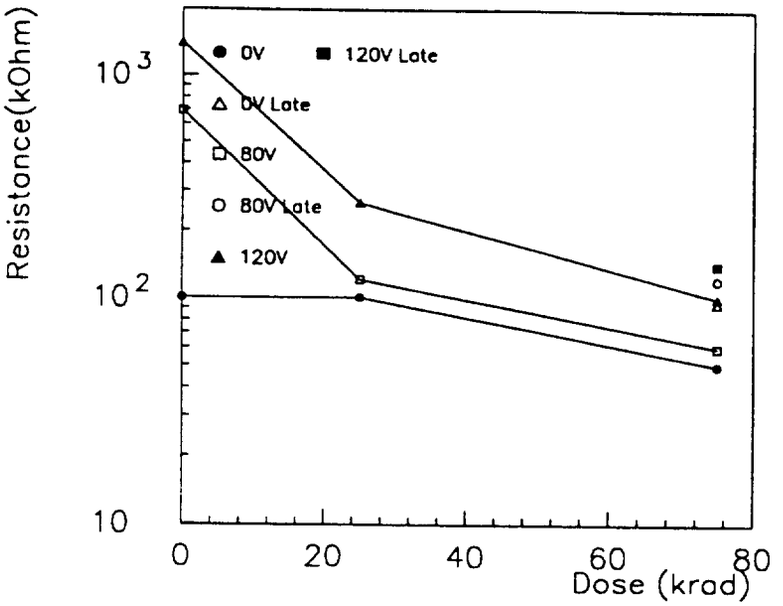


Figure 2: Schematic sequence of the p-side biasing. A: no bias voltage is applied. B: the voltage ΔU is just sufficient to cause the depletion zone around the right p^+ bias contact to touch the depletion zone of the floating p^+-strip. C: for still higher bias the voltage with an almost constant difference of ΔU

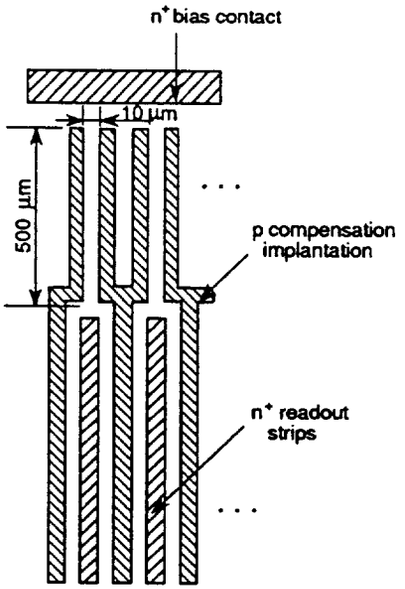


Figure 3: Geometry of the n^+ side with p^+ implantation defining a channel acting as bias resistance for the strips the n^+ strips

properties of radiation effects on MOS structures. A higher sensitivity to radiation under bias condition is expected and therefore the chip in operation, for which many components are biased only part of the time, gives an intermediate result.
A careful analysis of all the data, including irradiation on single components (see also [10]) lets draw the following conclusions: for powered chip, when the threshold voltage shift is large enough, the switches can't be closed anymore and the chip stop working. For the unpowered chip, there is a gradual increase of the interface trap density, which brings a related increase in 1/f noise.
The line driver [4], in the two versions for positive and negative signals, has been irradiated with the 80 keV machine with power off and in operation. Of all the parameters measured, power consumption, risetime, closed loop amplification of the circuit and output voltage offset V_0, only the last one is subject to changes. With power off the negative line driver experienced a gradual increase of the output offset(more negative) till 400mV at 150krad and then it crashes at 200 krad; the positive has a small increase (more positive), approximatively 50mV, up to 400 krad and then crashes at 500 krad. With power on in operation, the negative stands without modification till 25 krad and with increasing voltage offset till it crashes at 50 krad; the positive stands without modification till 50 krad and with increasing offset till it crashes 85 krad.
For the line driver *crash* means that the output voltage becomes comparable to the maximum output signal steerable by the chip $\pm 1V$.
These results are consistent with the previous ones on the CAMEX, because it is evident that the output voltage offset is very sensitive at the threshold voltage of the transistors and also the order of magnitude of the dose the chip can withstand are comparable to the ones of the CAMEX under the same bias conditions.
The steering chip has been irradiated in operation with the 80 keV machine. It is stable till 650 krad, when the output lines don't switch anymore. No test at power off has been tried.

4 Test structures

Before irradiating the detector wafers, a few test structures integrated on the same wafers have been irradiated to test separately some of the features of the detector. The irradiation was carried out with bias on up to 500 krad and off up to 1Mrad. Bias on means that the bulk was biased at the depletion voltage, while each single device was biased appropriately as explained in the following.
The leakage current was measured both for diode with and without guard ring. For the diodes with guardring there is no increase of the current in both cases; in absence of guardring the current of the diode irradiated with power off increases from 8nA to 12 nA, while with power on it has a very irregular behaviour starting from 5nA and increasing up to $10\mu A$ at 40 krad and then decreasing again down to 8nA. The conclusion is that the increase in bulk current is very small, while large contribution may arise from surface current.
MOS capacitors have been tested measuring the threshold voltage shift. The MOS were irradiated unbiased and biased. The bias was obtained with a +2V voltage on the capacitor.

In Fig. 4 the threshold voltage is plotted versus radiation. The results show a strong sensitivity of the oxide to the radiation.

Another test structure is shown in Fig. 4, it consists of a p^+ guard ring surrounding three p^+ pads. If the n^- backside is at ground, the guard ring is set at an increasing negative voltage and the pads are floating, the voltage on the pads follows the guardring at 0V for a few volts but, when the depletion zone from the guardring touchs the pads, it starts following the guardring voltage with an almost constsnt difference.

In Fig. 4 the guardring voltage required to bring one of the pads to 20V is plotted versus

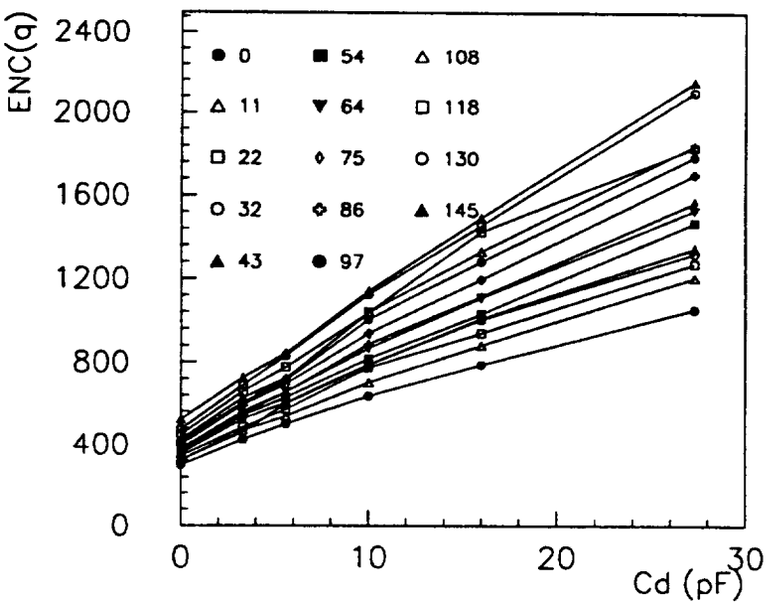


Figure 4: Noise in ENC versus input capacitance with dose in krad as parameter for an unbiased chip

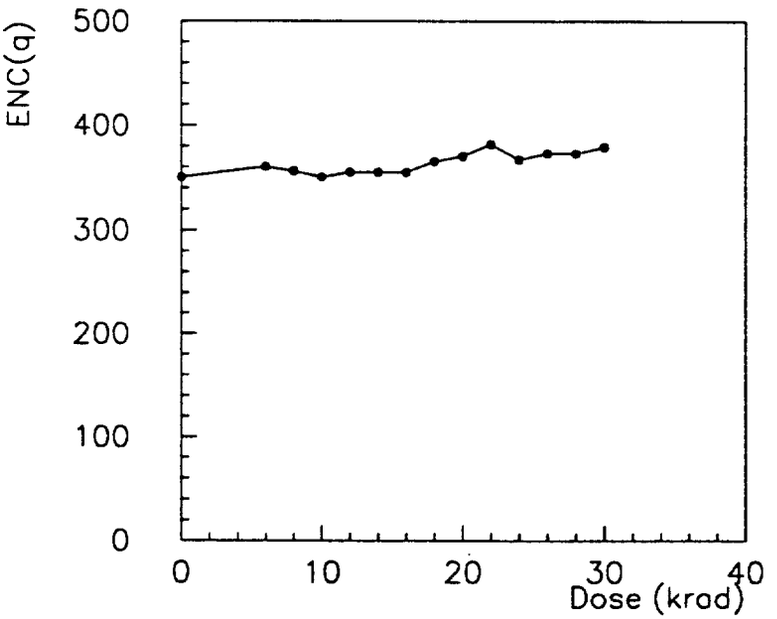


Figure 5: Noise in ENC versus dose in krad for chip irradiated in operation (The plot is not ENC versus capacitance as in because the mild dependance of ENC on the radiation would make the plot unreadable)

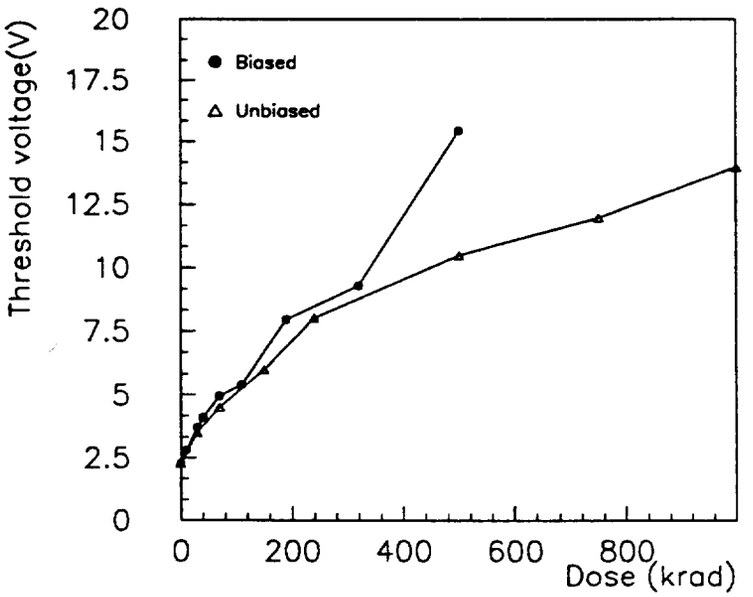


Figure 6: Threshold voltage of the MOS capacitor integrated on the test structure versus radiation dose in krad

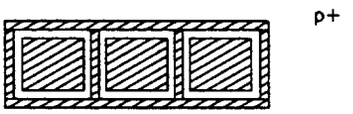


Figure 7: Layout of the pad-guardring test structure described in the text

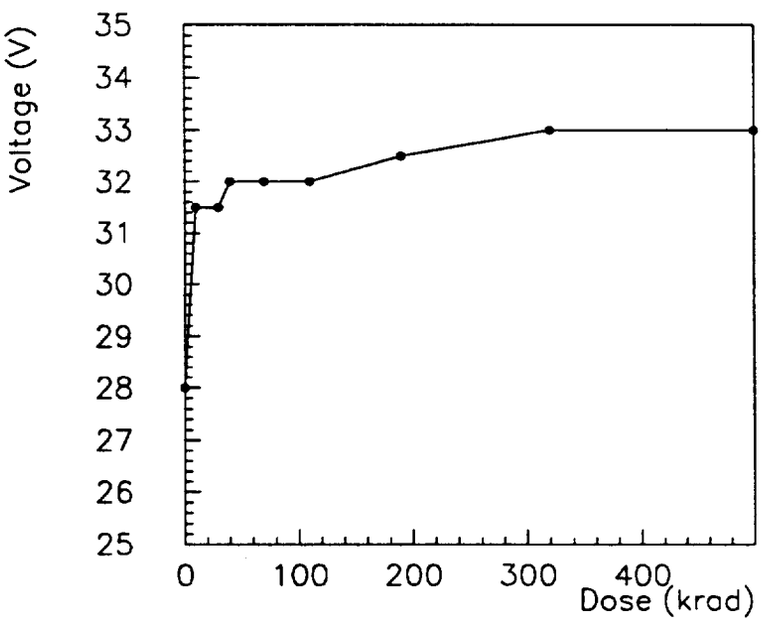


Figure 8: Dependance on the radiation dose of the pad voltage with 50 V on the guard ring

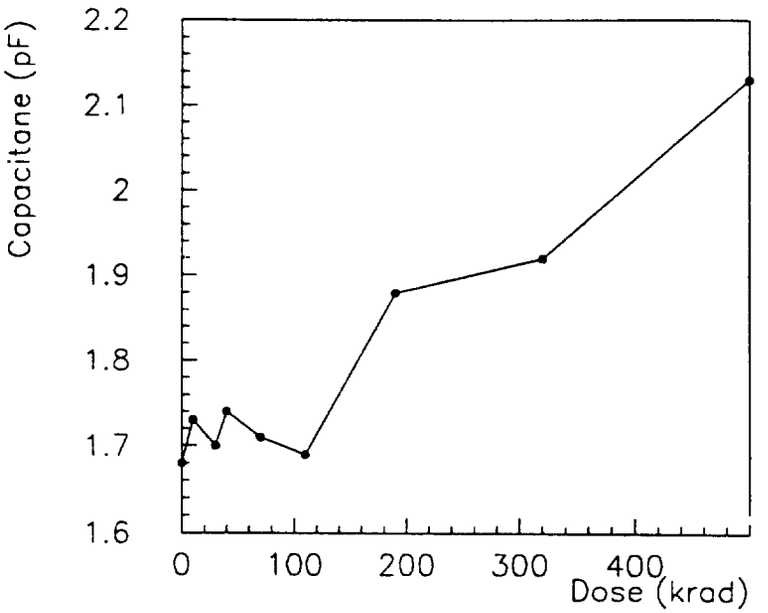


Figure 9: Pad-guard ring capacitance as a function of the dose in krad

the dose.

For the same structure the capacitance between pads and guardring has been measured. It is sensitive to the expansion of the accumulation layer under the oxide between the p^+ implantations, which tends to increase the capacitance. In Fig. 4 the capacitance is plotted versus the dose.

5 Detector

Preliminary tests have been carried out also on the detector wafer, irradiating it with the 80 keV X ray machine up to 75 krad.For the reason already explained previously the measurements have been concentrated on the features of the detector surface, also because a few damaged strips were drawing a quite large current, masking any possible increase due to radiation.

The AC coupling capacitors have been irradiated in two conditions: with the metal on the top of the oxide floating and with a -2.5V on it simulating the input voltage of the electronics. The C_{AC} increase from 128 pF to 133 pF for the unbiased case and from 131 pF to 138 pF for the biased case.

The interstrip capacitance on the p^+ is also measured to gauge the increase of the accumulation layer underneath the field oxide and its value is constant at 8-9 pF (5cm long strip) without appreciable variation within the 10-15% precision of the measurements.

More relevant are the modification of the bias resistor on the n^+ side. From the geometry shown in Fig. 3, the bias is supplied to the strip n^+ through an accumulation layer of a channel $500\mu m$ long and $10\mu m$ wide. Its resistance is measured for strip with pin-holes that allow to contact the strips through the metal. The measurements have been done at three different bias voltage $V_B = 0, 100, 150V$, so to distinguish the resistance component coming from the bulk from the one from the surface layer. The same measurements have been repeated 4 weeks later and an increase of the resistances is observed.

In Fig. 5 the bias resistance versus dose plus the delayed measurement is plotted for one strip.

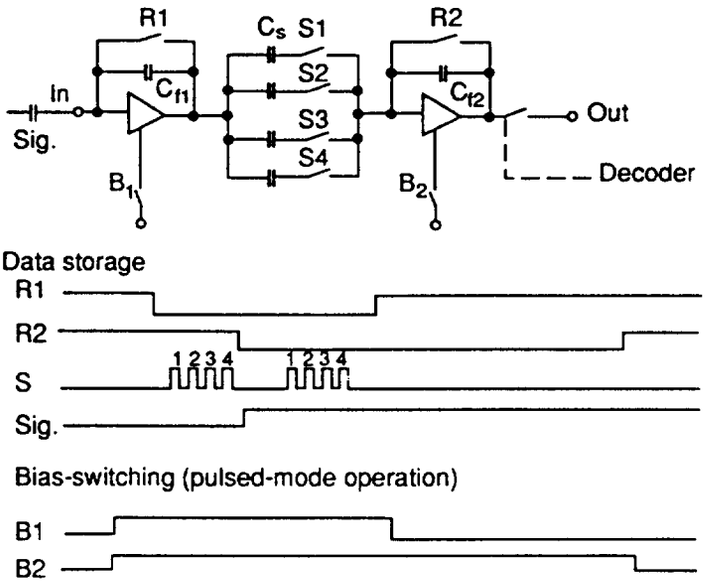


Figure 10: Bias resistor on the n^+ side for three bias voltage vesus radiation dose in krad. It is also plotted the value messured after 4 weeks

6 Conclusion

The entire readout electronics of the ALEPH minivertex detector has been irradiated. The weakest part of the readout is the CAMEX 64, that stands in operation till 20-30 krad and power off till 150-200 krad with noise doubled. These values are well suited for the actual generation of $e^+ - e^-$, but not for the next one of hadron collider (UNK-SSC-LHC). For those harsh condition a new version in JFET-CMOS technology has already been developed [10].

Irradiation of test structures and of a detector wafer of the double sided strip detector designed for ALEPH shows that the far most sensitive part is the bias resistor on the n^+ side. Again that is not a problem for the LEP experiment but this design is inappropriate for the future hadron colliders.

References

[1] P. Holl et al., IEEE Transaction on Nuclear Science, Vol. 36, No. 1, 1988, 251.

[2] H. Becker et al., Contribution to the 2nd London Conference on positive sensitive detectors, London, UK, 4-7 September 1990, to be published in Nucl. Instr. & Meth. A.

[3] W.Buttler et al., ICFA Instrumentation bulletin, No.5, September 1988.

[4] W. Buttler et al., Contribution to the ESSIRC conference, Sept. 14–18, 1985 in Toulouse, France.

[5] P.Cattaneo, Calibration procedure for irradiation tests on silicon devices silicon strip detectors, MPI-PE/Exp. El. 223 May 1990, IEEE transaction for nuclear science, in print.

[6] H. Becker et al., IEEE Transaction on Nuclear Science, Vol. 36, No. 1, 1988, 246.

[7] P. Holl et al., Nucl. Instr. & Meth. A257 (1987) 587.

[8] E.H. Nicollian et J.R. Brews, MOS (Metal Oxide Semiconductor) Phisics and technology, (John Wiley & sons) pp. 549-577.

[9] W.R. Dawes, Nucl. Instr. & Meth. A288 (1990) 54.

[10] W. Buttler et. al., Nucl. Instr. & Meth. A288 (1990) 140.

[11] E. Heijne: Muon flux measurement with silicon detectors in the CERN neutrino beams, CERN 83-06 1983.

[12] P.W. Cattaneo et al., Radiation hardness tests on the read out electronics chain of the aleph minivertex detector, Contribution to the 2nd International Conference on advanced technology and particle physics, Como, Italy, 11-15 June 1990, to be published in Nuclear Instruments and Methods A.

EXPERIMENTAL INSERTIONS FOR THE LHC

by

Walter Scandale,
CERN, div SL, Geneva.

Luminosity and number of interactions.

In a hadron collider the most important parameters are the luminosity and the beam energy.

For round beams and head-on collisions, the luminosity L is given by:

$$L = \frac{kN_b^2 f_0 \gamma}{4\pi\varepsilon^* \beta^*}$$

where k is the number of bunches in each beam,
N_b is the number of particles per bunch,
f_0 is the revolution frequency,
γ is the energy divided by the rest mass of the particles,
$\varepsilon^* = \gamma\sigma^2/\beta^*$ is invariant emittance,
β^* is the betatron function at the crossing point.

The most fundamental limitation to the performances of the LHC comes from the beam-beam interaction, which has two components, the head-on interaction which occurs at the wanted interaction points, and the long range interactions, which occur on either side of the interaction region in the portion of the beam pipe which is common to both beam. The importance of these effects is determined by the beam-beam tune shift parameter ξ

$$\xi = \frac{N_b r_p}{4\pi\varepsilon^*}$$

where r_p is classical radius of the proton.

The studies of the CERN SppbarS and at the Fermilab Tevatron have shown that the total tune spread due to the beam-beam interaction and to the magnetic imperfections has to be limited to below 0.02.

By assuming a contribution of the lattice non-linearities to the tune-spread smaller than 0.005, as assured by the lattice design, the permissible total beam-beam tune spread ΔQ is 0.015. This quantity has to be shared by the different interaction regions, and it determines the ultimate performance of the collider.

The total beam current might be limited by the increasing difficulties of controlling the particle losses in the superconducting magnets and of dumping the beams, as well as by the heat load on the cryogenic system due to the synchrotron radiation.

Using the parameters of Table 1, the LHC has been optimized for three simultaneous pp collision with a maximum luminosity of $1.65\ 10^{34}\ cm^{-2}\ s^{-1}$, and a total energy in the center of mass of 14.4 TeV.

Table 1

Nominal parameters of the LHC

Maximum energy for B = 10 T	7.7 TeV
Number of bunch N_b	4725
Bunch spacing	15 ns
Number of interaction points n_x	3
ß*	0.5 m
Normalized emittance ε*	3.75 μm
Particles per bunch N_b	10^{11}
Revolution frequency f_0	11.2454 kHz
Circulating current	0.85 A
Beam-beam tune shift ξ	0.0032

Other ways of optimizing the performances of the LHC are conceivable.

In the case of a single collision, the luminosity can be increased by a factor of three, i.e. up to 5 10^{34} cm^{-2} s^{-1}, without any major modification to the machine design. In fact, by multiplying by three the number of protons per bunch N_b, the beam-beam-tune spread is unchanged. By increasing by a factor of three the bunch spacing, from 15 to 45 ns, the total current is unchanged in the LHC as well as in the injectors, and therefore the nominal emittance is preserved.

In the case of more than three collisions, in order to leave unchanged the beam–beam tune shift, the number of protons per bunch N_b has to be reduced in the ratio $3/n_x$, where n_x is the number of simultaneous collision. As a consequence of that, the luminosity is reduced by the factor $(3/n_x)^2$.

In the case of three collision, by changing the value of ß*, it is possible to lower the luminosity in only one collision, without affecting the two others. No beneficial side effects have to be expected, since the beam-beam tune shift is independent of ß*.

Experimental insertions

The lattice of the LHC is made of eight arcs of regular cells, and eight insertions, where the two proton ring cross each other. There are thus the eight possible interaction points for pp collisions.

The assignment of the insertions for the various functions has not yet been finalized. The present design of the LHC is based on the assumption that there are three experimental insertions and five machine insertions, two of which are dedicated to special purpose, i.e. to dump the beam and to clean the halo particles. The layouts in Fig 1 are used. They are interchangeable, so that any insertion can be located around any crossing point.

The two counter-rotating proton beams will be injected in the insertions 1 and 8 respectively.

The general purpose insertion is such that the value of ß* can be tuned between 0.5 and 15 m. The free space around the interaction point is ± 20 m long. A part of it is required for the cryogenic infrastructure, as well as for the radioprotection of the superconducting quadrupoles nearby. A space of ± 16 m thus is reserved to the experimental set-up. The crossing angle of the two proton beam is 200 μrad.

A special insertion has been studied, with a free space of ± 10 m around the crossing point, by which values of ß* of 0.3 m can be reached. The crossing angle is 230 μrad.

In a preliminary analysis, an insertion has been designed to reach quite large values of ß*. Using a layout derived from that of the dump insertion, with a free space around the crossing point of ± 80 m, one can vary ß* between 160 and 750 m. This is not yet adequate to study the pp elastic scattering, since the beam envelope is too small at the location of the experimental set-up.

Non standard use of the LHC

During this workshop a number of questions have been raised on non-standard use of the LHC. A very preliminary answer is given here to some of them.

Antiprotons

It seems not impossible to have ppbar collisions in the LHC. Due to the limited aperture of the magnets, it seems excluded to separate the beams in the arcs, and no more than four bunches per beam have to be used, with a consequent limitation of the luminosity to about few 10^{30} cm^{-2} s^{-1}. Additional transfer lines will be needed in the injector complex, and in one of the injection point of the LHC, the injection devices have to be moved from one ring to the other, since the protons and the antiprotons have to circulate in the same LHC ring.

Gas jet

From the experience of the SppbarS, the operation of a gas jet device in the LHC is expected to be compatible with simultaneous pp collision operation.

A possible location for the gas jet is the free space of about 100 m between D2 and Q4 in one of the general purpose insertions (Fig. 1). Choosing an odd point of the LHC lattice seems preferable as in the even points the infrastructure of the LEP supercunducting RF cavities is expected to be incompatible with the installation of an experimental set-up. The advantages of this choice are that the excavations required for the experimental cavern are expected to be of a moderate cost, that there is no need of a dedicated insertion, and that by intercepting with the target the outgoing proton beam no background is expected to be produced in the nearby collision region. The drawback is that in this location the two counter-rotating proton beams are horizontally separated by 180 mm and are contained in two distinct vacuum chambers with an inner diameter of 50 mm. It is thus impossible to make available for the experimental apparatus a symmetric volume around the interacting beam, unless the gas jet is operated in a dedicate time, during which the non interacting beam is stopped and its vacuum chamber dismounted where necessary.

Solid target intercepting the beam halo

It has been suggested to intercept with a solid target the halo of one of the proton beams, in order to provide high luminosity internal fixed target collisions in the LHC, simultaneously with pp collisions.

This seems to be possible provided that the level of the induced background can be made tolerable.

The location recommended for a gas jet device is also adequate for a solid target, with the same limitations discussed above: for a parasitic operation, the two vacuum chambers of the two counter-rotating beams have to be imbebbed in the experimental set-up; in a dedicated operation, the experimental set-up can be made symmetric around the direction of the incoming

proton beam. The longitudinal free space available of about 100 m seems to be largely adequate for the experimental requirements. To have a symmetric apparatus, in a parasitic mode of operation, a dedicated insertion has to be made available.

Extracted beam

It has been suggested to study the feasibility of a controlled slow extraction in the LHC, in order to provide an external proton beam of about 8 TeV energy and at least 10^8 particles/s flux.

Because of the lack of aperture and of the quite large field imperfections expected in the LHC magnets, a classical resonant extraction of the beam seems unlikely to be feasible, even in a dedicated mode of operation. Problems may arise also for the conception of the extraction septum, by which the extracted beam has to be separated from the circulating beam and deflected into the extraction channel. Standard electrostatic septa are in fact not suitable for the LHC, since the required length is likely to be incompatible with the free space available along the circonference. Non-standard modes of extraction have thus to be studied.

In the LHC there are natural diffusive mechanisms by which the particles in the halo of the circulating beams are rapidly pushed towards the vacuum chamber, so that a special set of collimators is required to capture them before they are lost in the superconducting magnets. Since these particles are useless for pp collisions, one can imagine to deflect them towards a fixed target, just before they are lost in the collimators. The useful depth of the halo is expected to be of the order of 1 to 2 μm, and flux hitting the collimators of the order of a few 10^9 protons/s. To handle it one can imagine to use a bent monocrystal, located at the edge of the circulating beam. This has never been tried before, and it is very difficult to predict in which regime a monocrystal can work as an extraction septum, or if it may provoke disturbing effects on a simultaneous pp collision operation.

Provided an appropriate crystal can be made available, and all the problems of beam interaction with the crystal are mastered, a dedicated insertion is required in order to implement the slow extraction in the LHC. Extracting in the horizontal plane seems to be more favorable, since the deflection of the extracted protons can be enhanced by an appropriate design of the separation recombination dipoles D1 and D2 in the insertion. The extracted particles have to be directed outside the LHC circle, in order to avoid interferences between the main tunnel and the experimental cavern. The extraction insertion has thus to be located in an odd point. A layout similar to that of the dump insertion appears adequate for preliminary considerations and can be carefully optimized later. The crystal is assumed to be located in the section between Q3 and Q4, and has to provide a deflection not in excess of 0.7 mrad (a small deflection corresponds to a large channeling efficiency). The extracted beam is assumed to be deflected by about 20 mrad at a location about 250 m downstream the crossing point. A transport channel with an appropriate set of superconducting dipoles is expected to be necessary. Increasing the size of the halo is expected to enhance the extraction efficiency and this may be made possible in the LHC by an appropriate matching of the beam envelope at the location of the crystal, without perturbing the optics of the other insertions.

Additional studies and experimental tests have to be planned to give more structured answers to the issues considered here.

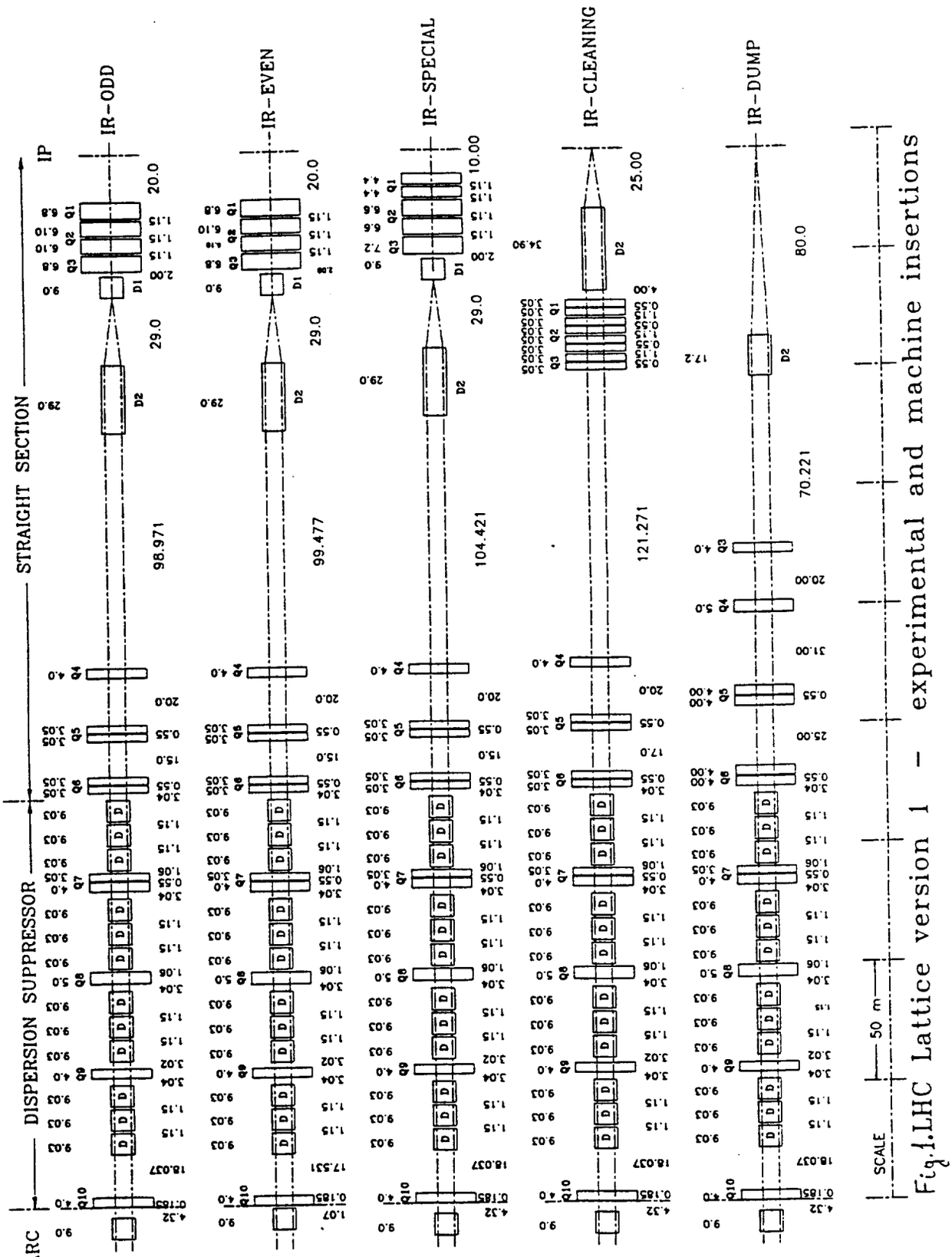


Fig.1.LHC Lattice version 1 - experimental and machine insertions

LHC Interaction Regions

K. Potter, CERN

Introduction

The geometry of the LHC interaction regions as given by the machine parameters can be reasonably clearly defined, but many details - the interaction region vacuum pipe for instance - have not been fully studied and will also depend on the experiments which will be installed. The following is nonetheless an attempt to present a coherent picture of the machine experiment interface, but it should be borne in mind that certain parameters are no more than proposals and at the limit best guesses.

Interaction Rates and Beam Sizes

The standard interaction region described below will offer a luminosity ranging from 5.5×10^{32} to 1.7×10^{34} $cm^{-2}s^{-1}$, by varying the β parameter at the interaction point, that is to say the local beam focusing. It should be noted that with the standard parameters for pp operation, notably bunch crossings every 15 ns, this luminosity means 0.7 to 19 events per bunch crossing (assuming σ inelastic = 60 mb). At the collision point, the transverse σ of the round beams varies from 0.015 mm at high luminosity to 0.082 mm at low luminosity as the focusing is adjusted within the range given above. Elsewhere in the machine the beam tails will be limited to 6 σ with collimators. The interaction region volume is further defined by the bunch length of 75 mm giving an interaction length of ~ 50 mm; the beam crossing angle of only 200 μrad having a negligible effect. It should be noted that it will be possible to separate the two beams vertically and hence luminosity calibrations of the "Van der Meer" type will be possible. In any case vertical beam steering will be needed, in order to bring the beams into collision and optimise the luminosity.

Vacuum Chamber

In spite of the very small interaction volume outlined above, the diameter of the vacuum chamber will normally be similar to that required in the adjacent machine quadrupoles, in order to be certain that beam halo particles can never strike the vacuum chamber in the centre of an experiment. The vacuum chamber diameter will thus be around 50 mm in order to accommodate the two beams throughout the single bore region, taking into account the crossing angle and vertical separations of the two beams of up to 10 σ which will be necessary during injection and other machine operations when collisions must be avoided.

It may be possible to reduce the diameter of the vacuum pipe in the central area while still ensuring that it is not a source of background due to

halo particles. The presence of a thin-walled chamber in the centre of the very long vacuum chamber (40 m) passing through the experiment will also need to be taken into account for the support structure. A number of supports in the detector region will in any case be needed, and these must also take the additional loading of the vacuum getter pumps which will be required every few metres to ensure an acceptable vacuum in the presence of the beams. The cleaning of the vacuum chamber walls will require an in situ bakeout to a temperature of ~ 200°C.

Geometry of the Interaction Region

The parameter list of the standard physics interaction region providing the luminosities mentioned above indicates that there will be a 40 m drift length between the final quadrupoles or ± 20 m on each side of the crossing point. However, this 20 m is the distance from the collision point to the magnetic face of the quadrupole and the truly free space will be much less, ~ 16 m. The final quadrupole will be a high gradient superconducting magnet with a relatively large aperture, ~ 50 mm. The outside diameter of the cryostat will be around 1.0 m with the outside face some 30 cm beyond the magnetic face. Space will then be needed for vacuum sector valves and a substantial vacuum pump. The flux of forward particles from the interaction region itself will be far too high to allow it to strike directly the superconducting coils of the magnet and most of the energy will need to be absorbed in a 3 m long copper block surrounding the vacuum tube, in order to avoid quenching the magnet. Hence the reduction to a genuinely free vacuum chamber length of ± 16 m.

In a longitudinal experimental cavern, the first machine elements will probably be inside the cavern itself and will therefore have to be supported some 10 m above the floor, as far as possible on cantilevered supports to give maximum space for opening of the experiment and access to central detectors. The weight of the copper absorber alone will be around 20 t.

An impression of a possible layout is shown in Figure 1, where the position of the LEP beam, 1.20 m below the LHC, is also indicated but where the LEP shielding described in the contribution of H. Taureg to this workshop [1] is not shown.

It is important to note that the forward LHC elements described above will all become radioactive to a greater or lesser extent after running at high luminosity. G.R. Stevenson has given estimates in session D8 of this workshop of induced activity levels which will lead to dose rates of several mSv/h with an average luminosity of 10^{34} $cm^{-2}s^{-1}$. More than enough to require very careful control of access and work in this region.*

* the CERN safety rules do not allow a personal accumulated dose of more than 15 mSv/year

Finally it should be noted that the alignment of the interaction region quadrupoles is extremely critical in all colliders. At the LHC the relatively long distance between these quadrupoles (40 m) with a large experiment between them and the requirement for good performance of alignment to a few hundredths of a millimeter will give the surveyors a particularly difficult task. A method of ensuring the relative alignment of the two quadrupoles through the experiment must be found, a survey wire through a tube passing longitudinally right through the experiment being one possibility [2].

References

1 G.R. Stevenson, H. Taureg, Shielding of LEP Experimental Areas during LHC Operation, TIS-RP/90-16 (LHC Note 135), September 1990

2 M. Mayoud (CERN Survey Group), private communication.

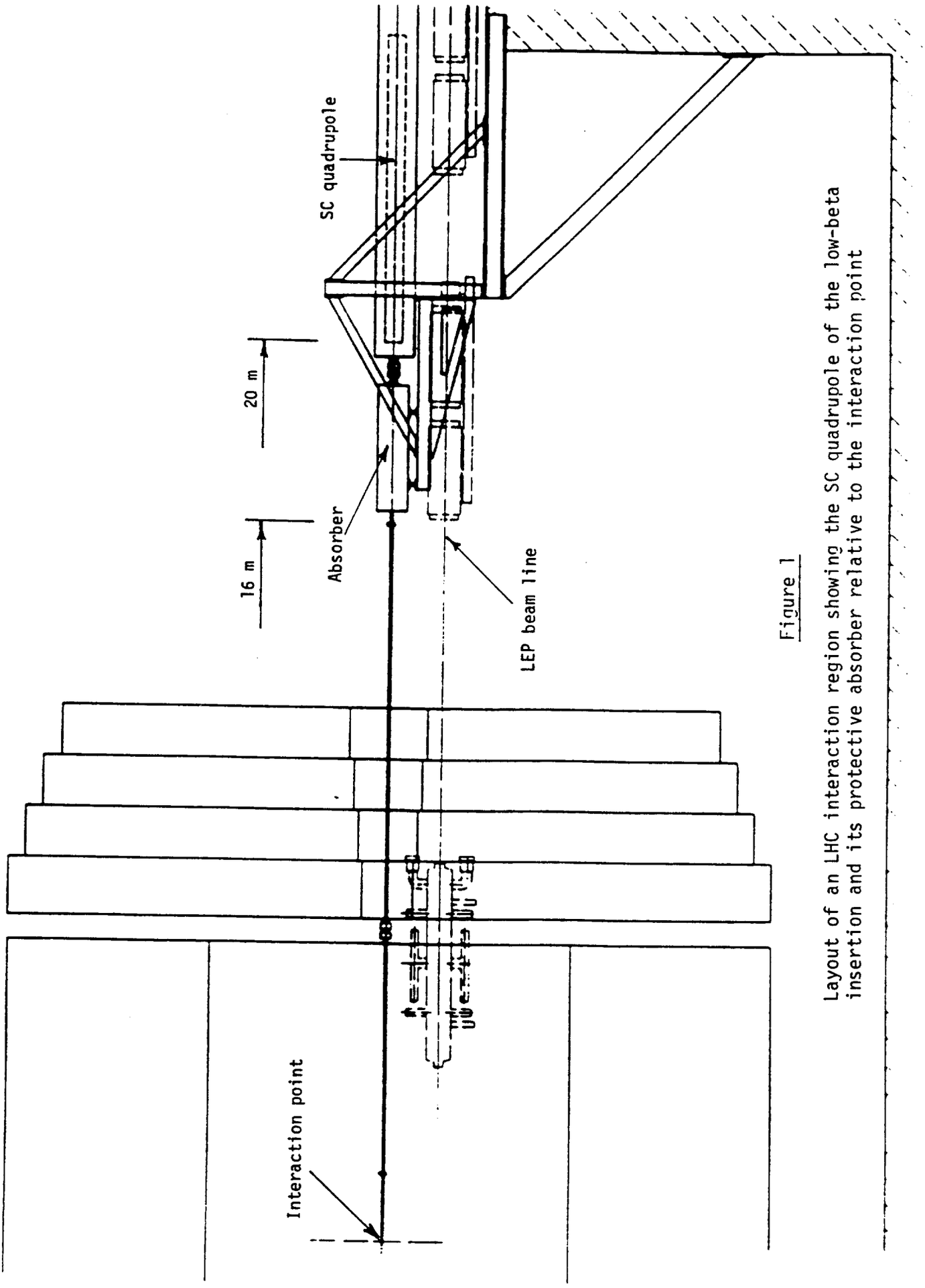


Figure 1

Layout of an LHC interaction region showing the SC quadrupole of the low-beta insertion and its protective absorber relative to the interaction point

Beam pipe size and impact parameter resolution

Presented by
F. Bedeschi, INFN - Pisa

December 4, 1990

The feasability of ~10 μm resolution silicon microstrip detectors has been demostrated by many groups [1]. Vertex detectors based on this tecnique are now considered for hadron colliders: the CDF vertex detector (SVX) is being built right now and the SDC collaboration is proposing a large volume silicon tracker for SSC [2]; the goal being that of tagging b quarks by the observation of their decay vertex. Though worries have been expressed about the radiation resistance of these detectors in a high luminosity environment, many progresses are being made on this issue and, also, pixel detectors, which are intrinsically more radiation hard, are being developed both in Europe and in the USA. Our considerations apply also to this class of detectors.

The radial size of the beam pipe defines the minimum distance of a vertex detector from the beam line. This in turn has a strong effect on the attainable impact parameter resolution, in particular for low momentum tracks, due to multiple scattering effects. We have studied, as an example, how the impact parameter resolution of the SVX is affected by a global shift in radius for tracks at 90° polar angle, the result is summarized in the approximate formula (p = track momentum, L = transverse distance of the first layer from the beam):

$$\sigma_D(\mu m) = (6.5 + 1.2L(cm)) + (\tfrac{15.8}{p(GeV)}L(cm)),$$

where the first term is the asymptotic resolution ($p \to \infty$), which depends only on the intrinsic detector resolution and its geometry, and the second term is the multiple scattering contribution. We notice that, apart from a small constant term the resolution is essentially proportional to L.

It can be shown [3] that good b tagging efficiencies can be obtained in top events, for $L \approx 3cm$, with a vertex detector installed at LHC. Given that the typical impact parameter of b decay prongs is in the order of a few hundred μm and their average mumentum about 5 GeV, we expect a severe degradation of these efficiencies should the beam pipe radius be much larger than a couple of centimeters.

References

[1] F. Bedeschi et al., IEEE Trans. on Nucl. Sci., **NS-36**, 35 (1989)
H. G. Moser, "The ALEPH minivertex detector", II London Conference on Position Sensitive Detectors, London, 4-7 Sept. 1990.

[2] Expression of Interest by the Solenoidal Detector Collaboration, March 1990.

[3] F. Bedeschi, "Top Quark Physics with B Tagging at LHC", these proceedings.

LEP/LHC Alternate Operation and Shielding

Hans Taureg, CERN-PPE

Abstract

The shielding requirements for experimental areas during LHC and LEP operation are discussed and the access conditions to these areas are explained. The difference in beam height between LEP and LHC requires special measures by the experiments during the operation of one or the other machine. Several possibilities are outlined for passing the LEP beam through LHC experimental areas.

1. Introduction

The installation of LHC in the LEP tunnel brings with it severe shielding requirements if access to the underground areas should be allowed. Areas, where permanent access is permitted have to be shielded by about 4.5 m of concrete from the proton beam. The shielding of the LEP beams will require only about a meter of concrete. Nevertheless, access will not be possible to the LHC experiments during LHC operation.

The design of the LHC experiments and experimental areas has to take into account that for a number of years LHC and LEP will operate alternately. The experiments associated with one machine have also to let the beams of the other machine pass. The two machines differ more than a meter in the beam height above floor level. Consequently the LHC experiments have to roll out of the beam position or provide a large enough passage for the LEP beam. Several possibilities are discused.

2. Shielding Requirements

The basic assumption for the design of shielding is that a loss of one full proton beam ($5\ 10^{14}$ protons) should be attenuated by the shielding to a dose of 50 mSv at the outside surface of the shielding under the most pessimistic conditions. This corresponds to a dose of $1.0\ 10^{-16}$ Sv/proton and translates to a concrete shielding of 4.3±0.3 m thickness transverse to the beam direction and starting at 2 m distance from the beam line for the main ring of the accelerator, see figure 1. Details about the shielding of the LHC beams can be found in references [1] and [2].

In the case of LEP beams the shielding consists of a concrete shielding of 1.2 m thickness as outlined in the LEP design report [3].

3. Access Conditions

The design of the LHC experimental areas does not allow access to the LHC experiment during operation of the proton beams. In contrast to most LEP areas there is no shielding linking the experiment and the machine tunnel, see figure 1. It is not considered very practical to construct a mobile shielding similar to the LEP case. Furthermore, induced radioactivity along the beam line may favour a more open layout which allows easy access with remotely controlled devices for work on beam elements and forward detector parts if necessary. Only when the detailed designs of the experiments are known will it be possible to assess if they could be considered as selfshielding.

When LEP is operating a shielding of 1.2 m concrete equivalent is required if access to the experimental cavern should be permitted. The magnet return yoke of a LHC experiment is very likely sufficiently thick to function as shielding for the LEP beams provided there are no holes and a tight

connection can be established to the shielding in the forward regions between the experiment and the machine tunnel.

In reference [2] the shielding and access conditions are outlined for the present LEP experimental areas.

4. LHC/LEP alternate operation

The beam lines of the LHC and LEP accelerators are located about a meter apart in the vertical direction as shown in figure 2. This difference in beam height above the floor level will be kept in the experimental caverns as well. Consequently, the experiments associated with one accelerator have to make room for the beam line of the other accelerator when the latter one is operating. Different possibilities are discussed for a LHC experiment to let the LEP beam pass.

a) A transverse cavern with a movable LHC experiment is preferred solution. It allows the largest flexibility for the operation of the machine and work on the experiment. The change over from one machine to the other promises to be easier and faster with this solution. The experiment is rolled to a garage position during LEP operation. There it can stay in its data taking configuration for cosmics running or be opened for maintenance. The shielding arrangement for the LEP beam is relatively easy.

b) In a longitudinal cavern parallel to the beam line presumably the available space will not allow to roll the experiment to one side and install the LEP beam line and shielding along side the experiment. The experiment has to be split along its axis and moved apart, see figure 3, making room for the LEP beamline and the shielding. Or the experiment is lowered by 1.2 m to the level of the LEP beam passing the beam through the center of the experiment, see figure 4. Then, however, work on the LHC experiment will be severely restricted during LEP operation.

c) If an experiment can not be moved from the LHC beam line because of weight or space restrictions a sufficiently large passage has to be cleared through the experiment for the LEP beamline and, possibly, the associated shielding, see figure 5. This entails the removal of the central detector and, at least, parts of the end caps for LEP operation and their reinstallation prior to LHC running.

As can be see from figure 5 some beam elements of LEP are located relatively close to the intersection point. Therefore a passage has to be cleared around the LEP beam axis of at least 1 m in radius. The beam elements and the vacuum pipe require a support of sufficient strength and stability within the LHC experiment.

5. Change-over Time

A first, very preliminary estimate of the time needed for a change over from LEP to LHC or LHC to LEP operation gives about three months. A proper design of the experimental areas and the experiments may reduce this time considerably for the LHC experiments if a frequent change over is taken into account from the start The time span taken for the change over may then be determined by the LEP experiments especially if a LHC shielding is installed.

References

[1] G.R.Stevenson and R.H.Thomas, Ed., Radiological Considerations for the Environment around LHC, CERN LHC Note 115, 1989

[2] G.R.Stevenson and H.Taureg, Shielding of LEP Experimental Areas during LHC Operation, CERN LHC Note 135, 1990

[3] LEP Design Report, CERN LEP/84-01 Vol. II

Figure Captions

Fig. 1 Conceptual layout of a LHC experimental hall

Fig. 2 Cross section of the machine tunnel with the LEP and the LHC beamline

Fig. 3 LHC experiment split vertically to let the LEP beam pass

Fig. 4 LHC experiment lowered by 1.2 m for the passage of the LEP beam

Fig. 5 Cut through a LHC experimental cavern, showing the LEP beamline trough an experiment and through a concrete shielding

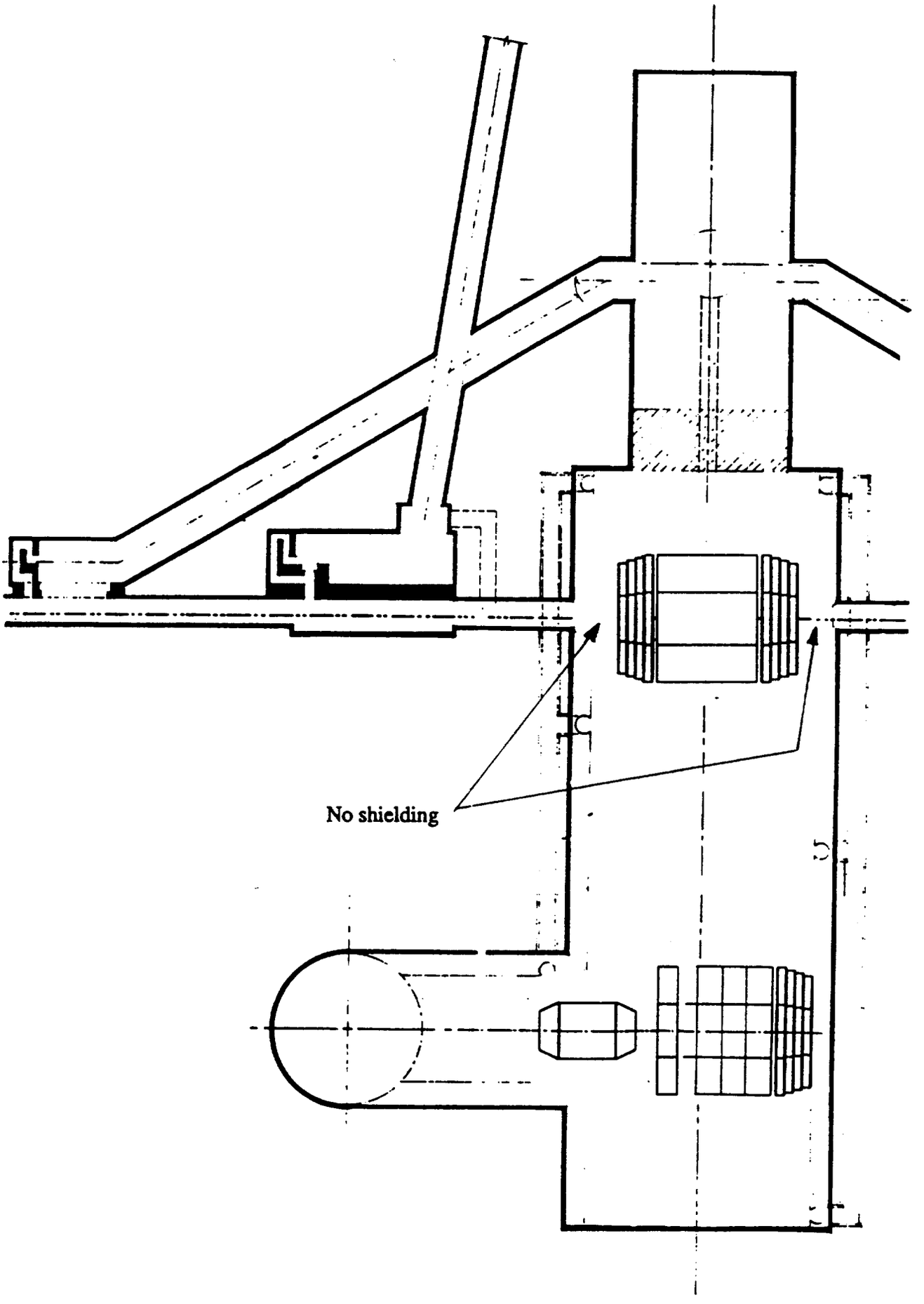


Fig. 1

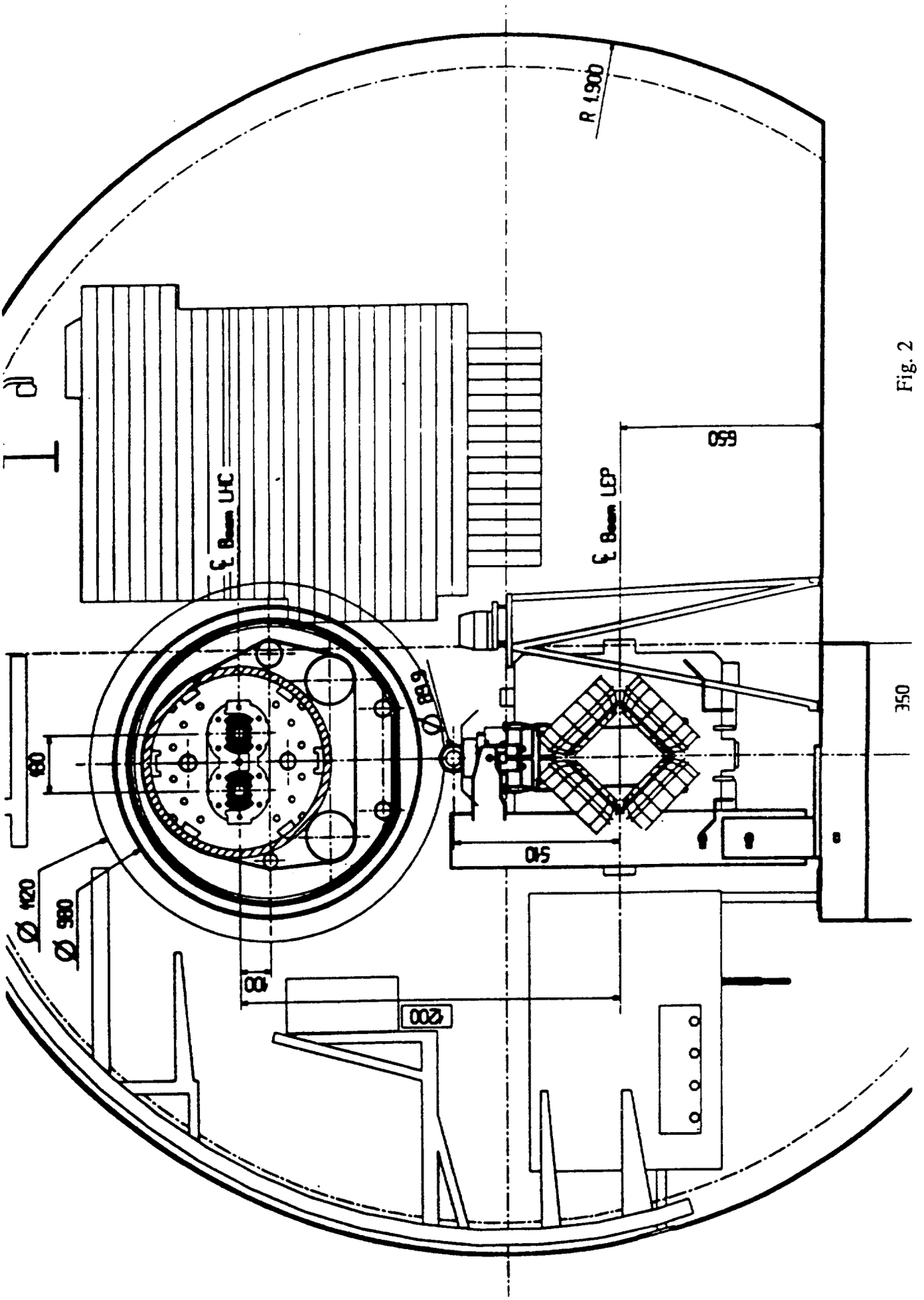


Fig. 2

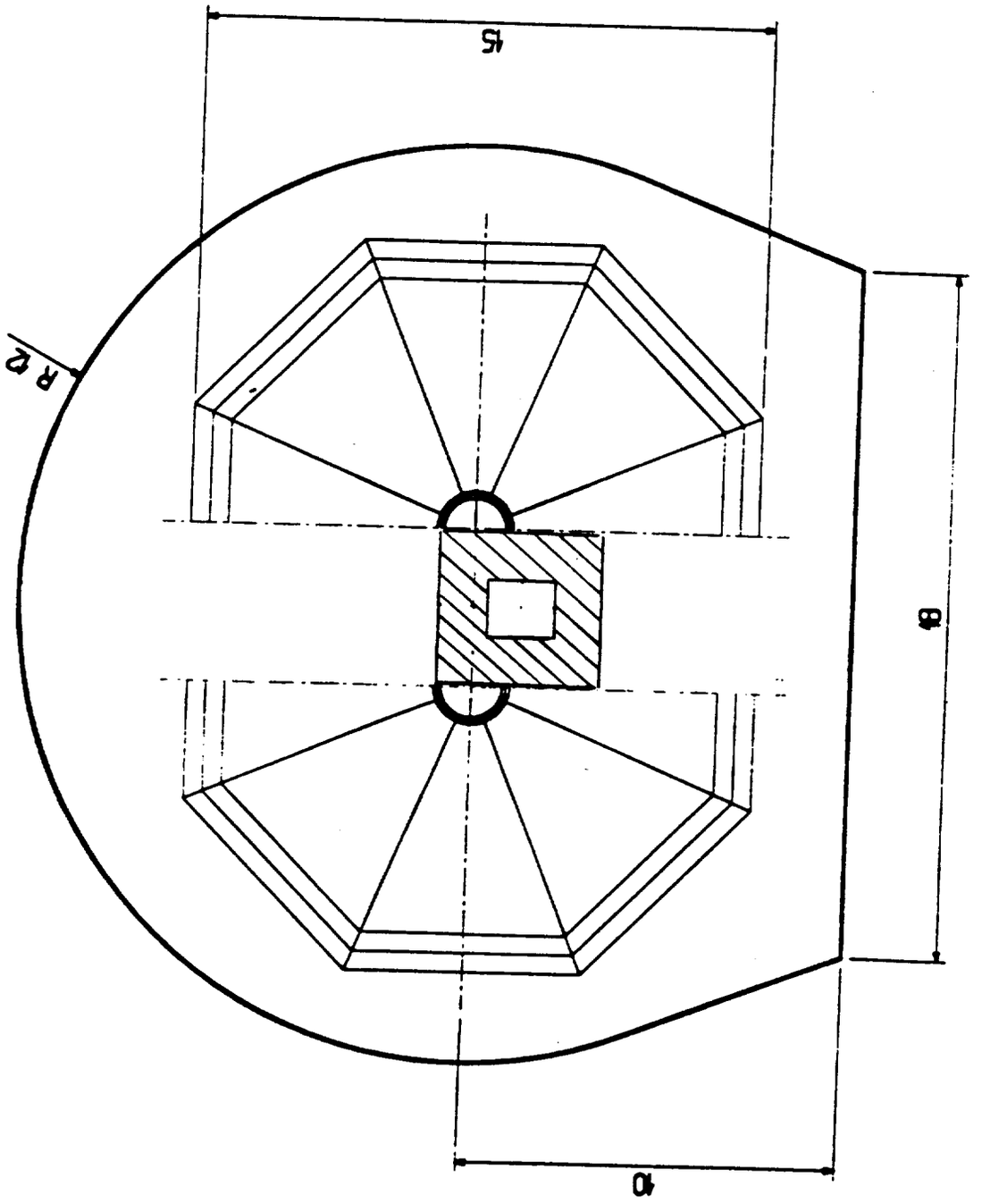


Fig. 3

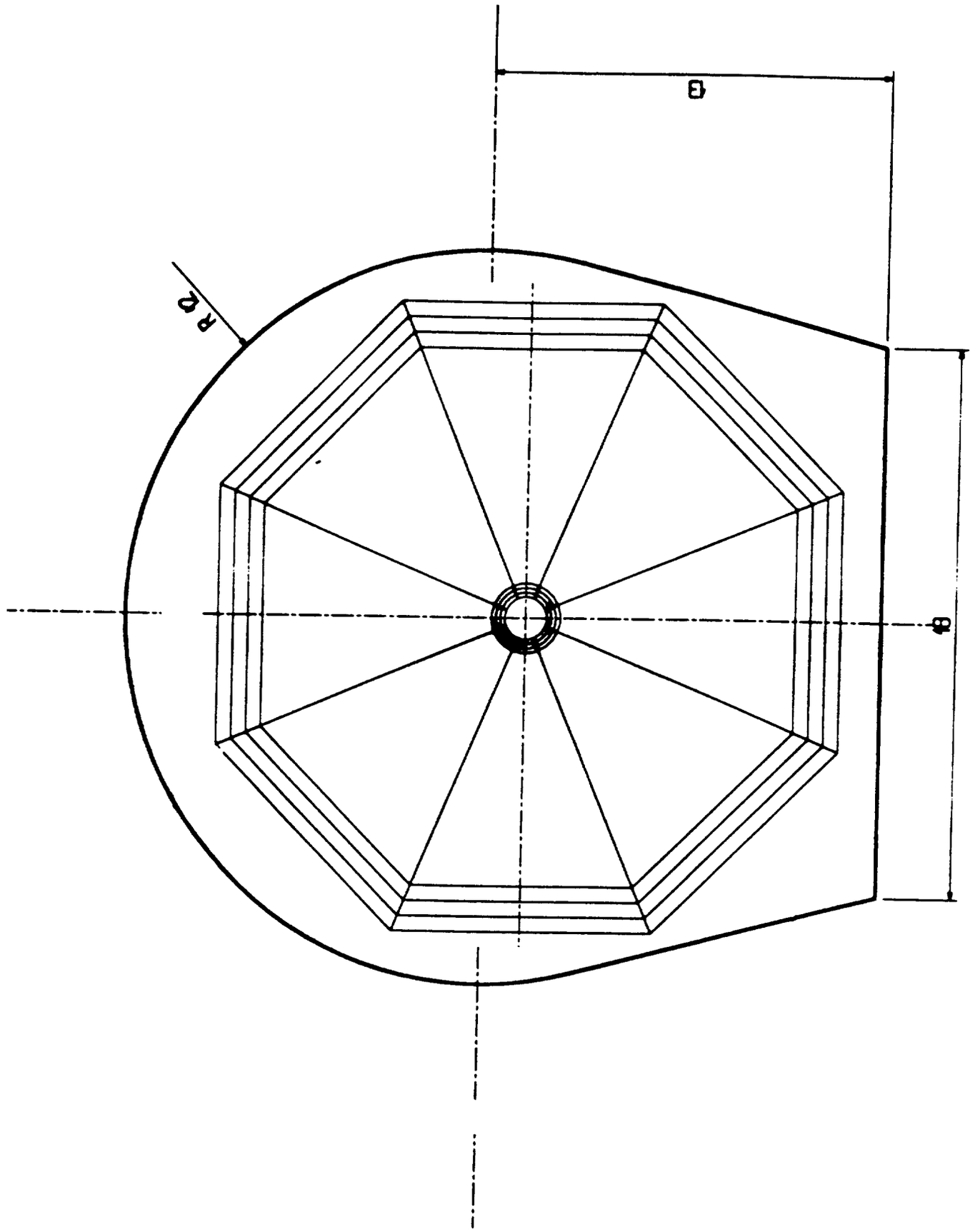


Fig. 4

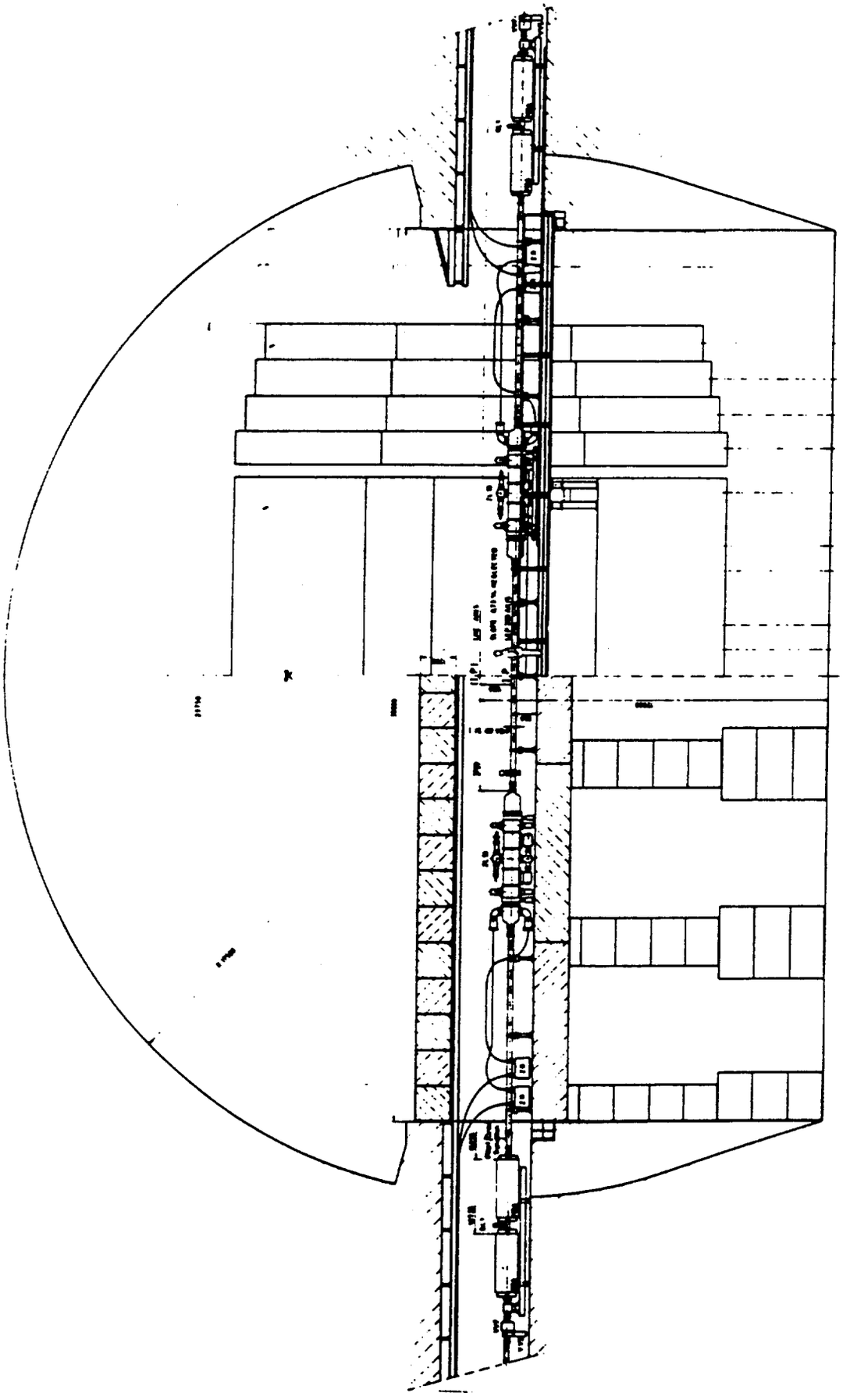


Fig. 5

Remarks on large magnets

François Wittgenstein
CERN, PPE Division,1211 Geneva23, Switzerland

Introduction

Large volume magnets are a major component of the High Energy Physics detectors. International and national laboratories pioneered in the beginning of the sixties in the development of multi-megajoules magnet .
As the energy of new accelerators increases, the constraints of the tracking systems are becoming more severe. The future magnets have to offer large improvements expressed in $B*L^2$ or $B*\sqrt[2]{L}$ imposing new limits for the magnetically stored energies and the dimensions.
Henry M.Noad reports [1] that a horse-shoe magnet of extraordinary power was constructed in 1830 for the Academy of Sciences at Paris by M.Pouillet. Each horse shoe was wrapped with 10000 feet of copper wire and with a current of modest intensity,this apparatus supported a weight of several tons.[2]
This demonstrates that the evolution of this ancient machine is running since nearly 200 years and that the definition of new goals is a tradition for magnet builders.

Basic layouts.

To compare new style magnets to existing detectors magnets we resume in table 1 some definition parameters:

	ALEPH	BEBC
Amperturns in Mat	10	20
Stored Energy in MJ	130	750
Cold mass in t	60	200
Fe yoke in t	3000	2000
Power in MW	.75	1.5
Central Induction in T	1.5	3.5

Table1. Detector magnet definition parameters

Several lay-outs of magnets for LHC detectors are briefly described and the main parameters are presented .

---

1 Henry M. Noad,Manual of Electricity ,,Part 2, p668, Georges Knight and Co,London, 1857

2 Sturgeon's Electro-magnetic engine for turning machinery."Annals of Electricity",vol. 1, p75

The first figure , SYMBOLIC 1, includes a superconducting solenoid imbedded in an iron yoke absorber and surrounding a calorimeter.

According to the permeability of the calorimeter, two can be considered :

SYMBOLIC 1

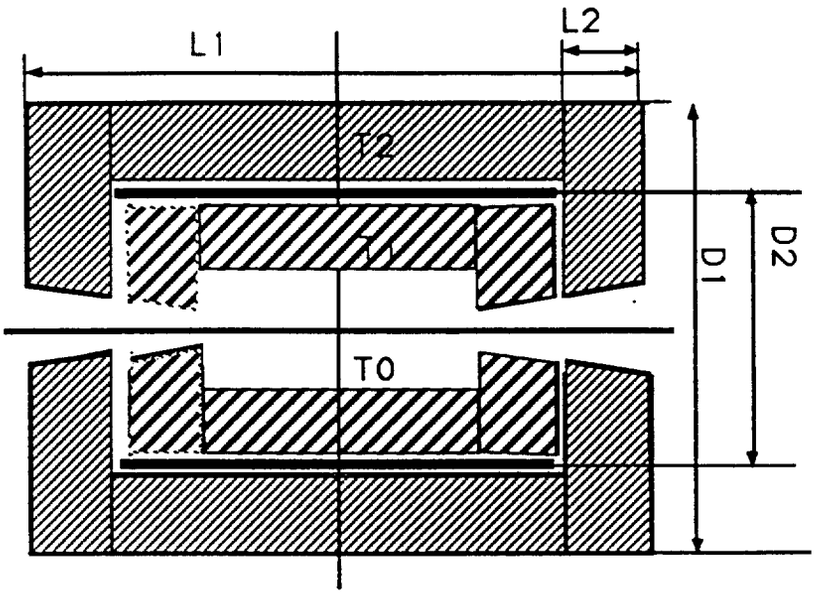


Fig1. Symbolic of a compact μ Solenoid
T0=field in centre
T1=field in calorimeter
T2=field in iron yoke

	Calorim.permeability r=1	Calorim.permeability r>1
Amperturns in Mat	50	50
Stored Energy in MJ	4500	4500
Cold mass in t		
Fe yoke in t	12000	12000
Power in MW		
Central Induction inT	4.0 (T0)	6.0 (T0)
Calorim.Induction in T	4(T1)	4 (T1)
Yoke Induction in T	2.3 (T2)	2.3 (T2)
Total length in m; L1	20	20
Pole thickness in m; L2	2.2	2.2
Overall Diameter in m; D1	12	12
Solen.Diameter in m; D2	7	7

Table2 . Parameters of symbolic 1

The 2 alternatives presented in Table2, show the important impact of the iron , also when saturated, on the analyzing power of the detector magnet. Therefore, in fig 2, we show the relative permeability factor of the iron above 1.8T .

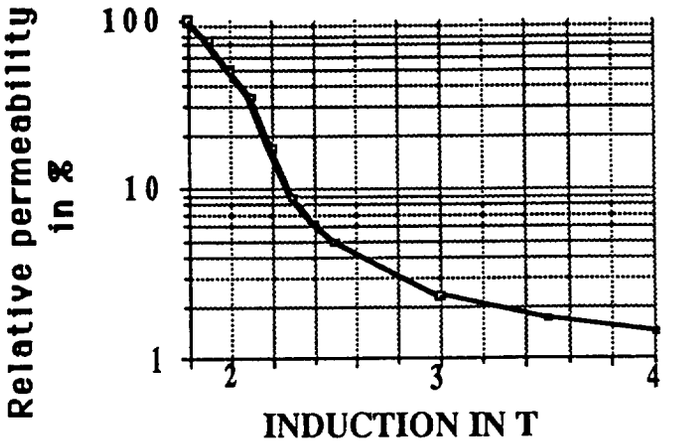


Fig2. Relative permeability (100=1.8T) valid for standard Iron.
$\mu r_{(1.8T)} = 144$

The use of saturated iron allows a reduction of the magnetically stored energy. The gain is shortly given in fig.3 :

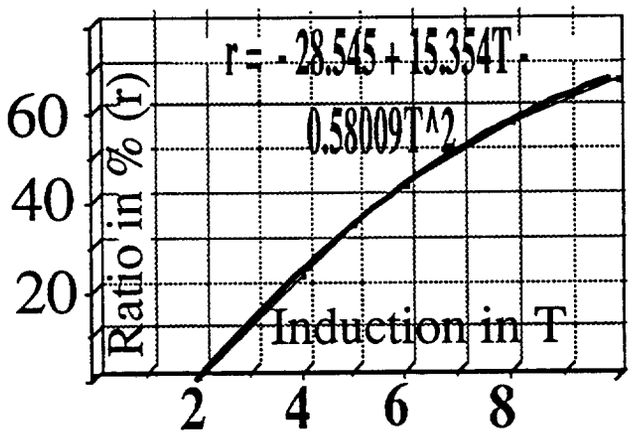


Fig3. Ratio of the magnetic stored energy in iron to the magnetic stored energy in air.
Same induction value.

The next lay-out , SYMBOLIC 2, presents a warm magnet with less analyzing power but with a reduced investment in capital cost. The coils distributed on the barrel and on the poles could be manufactured with standard hollow bus-bars made of Aluminium with a simplified insulation.

SYMBOLIC 2

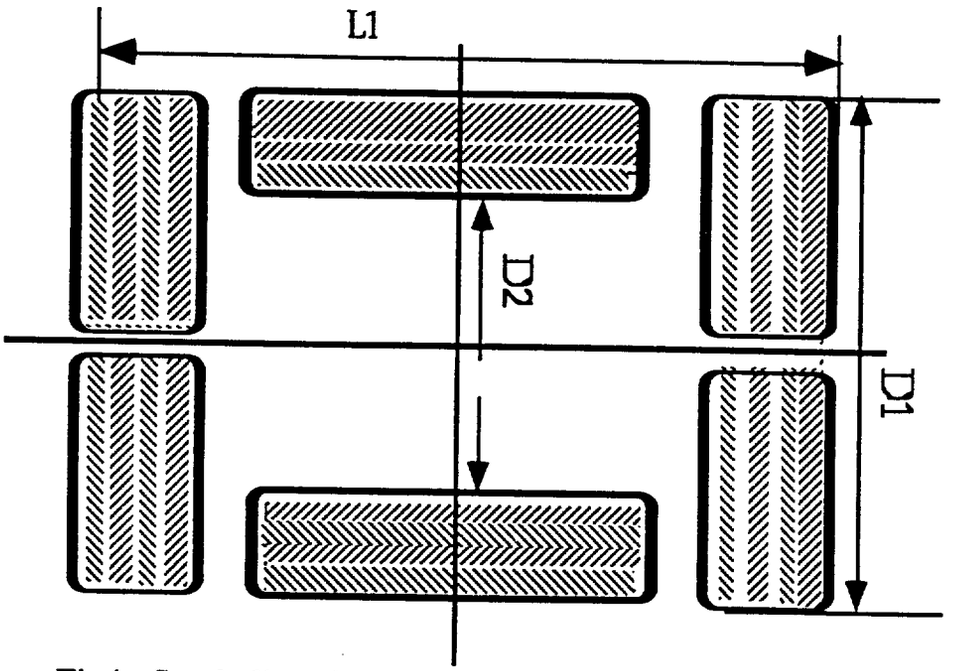


Fig4. Symbolic of a toroidal warm magnet detector

This solution would require twice the weight of iron, relatively to the fig1. ,but would be very simple to manufacture at low power consumption and have practically no stored energy. The calorimeter is a field free region and the tracking chambers are embedded in the iron.

Amperturns in Mat	1.1(1.8T);1.9(2.0T)
Stored Energy in MJ	<10MJ
Coils weight in t	150(1.8T);260(2.0T)
Fe yoke in t	23000
Power in MW	2.6(1.8T;4.6(2.0T)
Central Induction inT;T0	0
Calorim.Induction in T;T1	0
Yoke Induction in T;T2	2.0
Total length in m; L1	24
Pole thickness in m	4
Overall Diameter in m; D1	24
Internal Diameter in m; D2	8

Table3. Parameters of symbolic 2

The following sketch, SYMBOLIC 3, shows a strong superconducting analyzing magnet with front and backwards toroids :

Amperturns in Mat	400
Stored Energy in MJ	6000
Coils weight in t	150(1.8T);260(2.0T)
Fe yoke in t	7500
Power in MW	
Central Induction inT;T0	0
Calorim.Induction in T;	0
Yoke Induction in T;	5 - 10
Total length in m; L1	26
Pole thickness in m	4
Overall Diameter in m; D1	14
FreeDiameter in m;	

Table4. Parameters of symbolic 3

SYMBOLIC 3

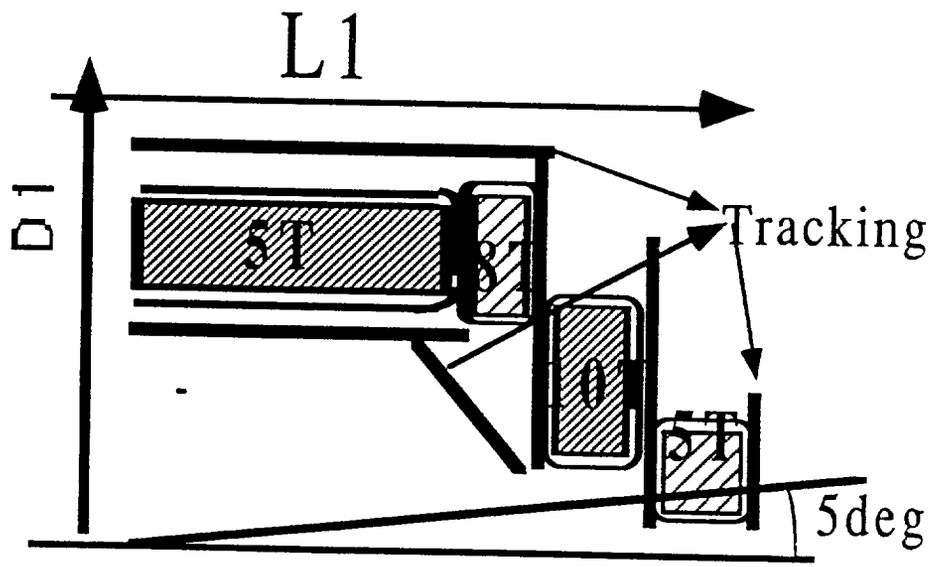


Fig5. Symbolic of a superconducting toroidal magnet with front and backward toroids

The last sketch , SYMBOLIC 4, shows an extension of a large solenoid magnet with an additional nose to bend the barrel flux lines in the forward/backward regions :

SYMBOLIC 4

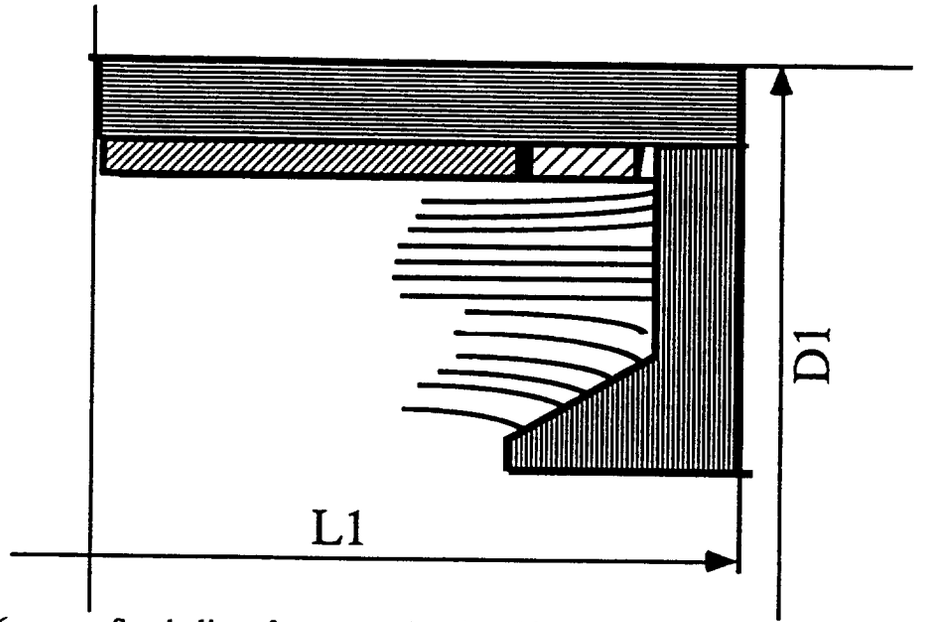


Fig6. Symbolic of a normal solenoid magnet with bent flux lines

Amperturns in Mat	12
Stored Energy in MJ	300
Coils weight in t	3500
Fe yoke in t	30000
Power in MW	10
Central Induction inT	.55
Calorim.Induction in T	.55
Yoke Induction in T	2
Total length in m; L1	28
Pole thickness in m	2
Overall Diameter in m; D1	23
FreeDiameter in m;	23

Table5. Parameters of symbolic 4

An increase of the current density in the end coils reinforce the bending effect of the pole extensions.

General features.

High Energy Physics detectors of today include big volumes and operate in a continuous mode.Therefore, pulsed magnets are not considered. The choice between superconducting coils and normal coils is determined by the technical aspects (manufacturing, assembly , dissassembly transport, power capabilities , operations duty cycles), financial considerations (capital, running costs) and in case of

international collaborations, the real delivery and support capabilities of the contributors.
In the following we proposed some general aspects of both technics. For a magnet requesting a magnetic flux circulation the following simple relations are always valid :

FIELD = AMPERTURNS = STORED ENERGY = FORCES
AMPERTURNS = MANPOWER • CURRENT = WEIGHT • POWER

Normal Magnets.

The first criteria is the definition of the operation temperature.
The interest in low temperature is based on the resistivity reduction at low temperature . Therefore higher fields at lower heat losses per unit weight can be generated. However, for big volumes, large investments in refrigeration plants restrict considerably this advantage.
Ultra-pure material, with resistivity ratio of more than 10000 from 300k to 4.2K are available. However ultra-pure metals have poor mechanical strength and adequate reinforcement will be necessary in case of an application. For the same power the central field is proportional to the square root of the resistivity and for the same field and the same geometry, the power reduction is proportional to the ratio of the resistivities.
In addition, if the resistivity of aluminium at very low temperatures saturates with the field at about 3T, this saturation is absent for copper which loses 50% of the cold effect between 0T and 8T.[3]

Resistivity at (0T)	300K	77K	20K
Cu (OFHC)	100	18	0.8
Al 99.95	100	15	0.1

Table6. Ratio of resistivities for commercially available conductors relatively to the room temperature.

For the envisaged systems, the operation at the hydrogen temperature should be avoided. According to Table 6, a ratio of ρ_{300}/ρ_{77} =6 could be considered as normal for copper and aluminium at the liquid nitrogen temperature .
This gain is however not compensating the overprice of the cryogenic liquid estimated to about Sfrs 0.2/l and .016 l/W.
In water-cooled magnets, the main concern is the power requirement to generate a given magnetic field. A simple relation shows that :

3 H.Brechna. Superconducting magnet systems,Spriger Verlag,Berlin ,1973.

$$P = \text{weight} * J^2 \text{lamda} * \rho_0 / \text{density}$$

At 60 C the ratio are as follows for Aluminium and copper :

	Al	Cu
ρ_0/density(ohm*cm^4/g)	1.296 E06	0.235 E06

This shows that if the cooling conditions could be supplied, an Aluminium magnet would be more than 5 times lighter than a copper magnet for the same power.
However the operation conditions require generally to reduce the power consumption. Therefore the dissipated power per cm3 is of the order of 10 to100mW/cm3,i.e 30 to 300t Aluminium or 100 to 1000t Cu per MW.
The heat losses imply the operation of an adequate cooling circuit of demineralized water which should be carefully operated to limit the electrolytic and chemical corrosion of the magnet circuits.
This circuit should be capable to circulate about 40m3 of water per MW. A first order estimate of the pressure drop in the cooling pipe is given by the relation

$$\frac{\text{Delta p}}{L} = .64 * 10^{-3} * \frac{\text{Power}^{1.75}}{\text{Diameter}^{4.75}}$$

With L expressed in m, the hydraulic diameter D in cm, the power in kW and the pressure drop in bar. In this expression the temperature rise is assumed to be 20K in the cooling channels. Additional temperature rise in the section should be considered according to the conductor geometry as well as temperature drop from the conductor to the coolant. Some typical flow lines are given in fig. 7.

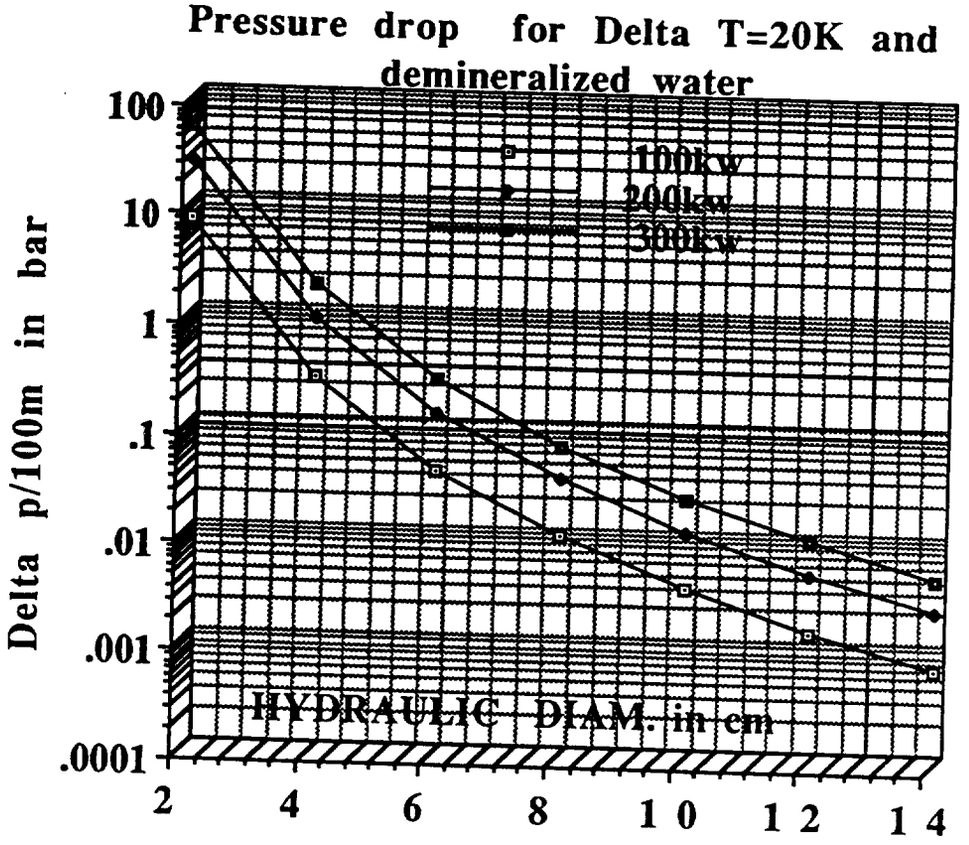


Fig 7. Pressure drop in water cooled conductor

Superconducting Magnets.

A superconducting magnet[4] must be structurally strong to withstand very large electromagnetic forces, thermally stable to keep the conductor at its operating temperature , and protected from permanent damage in the event of a magnet quench. Superconductivity is confined within the phase surface bounded by magnetic field, temperature and current. Of these three parameters, the temperature is neither completely controllable or predictable, because the energy stored in the magnet, both magnetic and mechanical, can easily be converted into heat, upsetting the thermal equilibrium within the winding. Therefore in magnet operation, the thermal behavior of the conductor is the most important.

No matter[3] how stable a superconductor is, there is always a chance that a disturbance may occur which could lead to a quench. The heat may propagate along the conductor or remain locally at the spot of disturbance.In any case the protection of the coil against local heating, loss of helium cooling, voltage breakdown of the insulation requires that the stored energy must be transferred from the cold region to an external dumping body and that the temperature of any part of the magnet should not

[4] IEEE Transactions on Magnetics,vol 24,No2,March88, p1211,Y.Iwasa

exceed a certain specified value dictated by the characteristics of the cold part of the magnet. The energy dissipation takes place in the substrate of the composite conductor and the dissipated energy should be balanced by the thermal capacity of the substrate. In this approximation the contribution of the superconductor and of the helium (in case of a direct cooling) are considered as negligible. Therefore if c_p is the heat capacity of the substrate :

$$F j^2 dt = F c_p / p \, dT$$

Fig.8 gives the behavior of this ratio for two typical substrate.
If we write $Fc_p/p = g(T)$, we see that with J_1 =the initial current density in the substrate and
t= the discharge time constant :

$$0.5 * j_1^2 * t = g(T)$$

Therefore the operation current density of the magnet is well defined by its protection conditions and the development of this relation gives :

$$j_1 = 0.034 \sqrt[5]{g(T) * U * E}$$

In this expression we suppose that :
Sn= being the cooled perimeter per unit length and A= Total conductor cross-section, the following relation is valid :

$$S_n = 3\sqrt{A}$$

In fig.9 we show the overall current density of the magnet for the max. temperature of 100K and for two maximum voltages at the magnet taps of 250V and 500V. This graph demonstrate that for large magnets, the safety conditions determine an overall current density of the order of 3000A/cm^2.

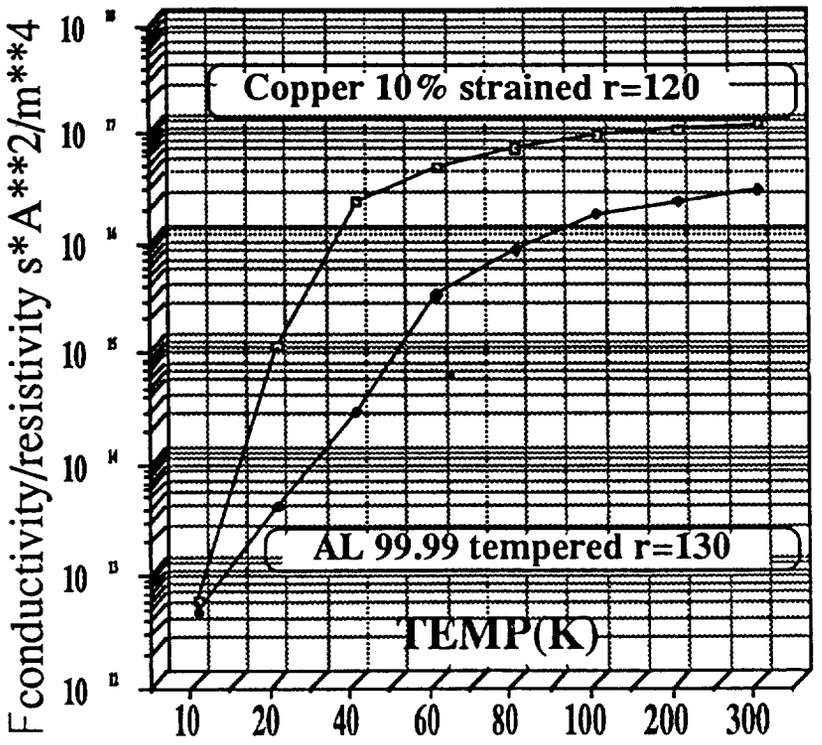


Fig8. $F c_p / p$ as function of the temperature

As the ratio of the heat capacity to the resistivity is less favorable for an Aluminium substrate, the overall current density defined by the operational conditions is only 90% of the copper values.

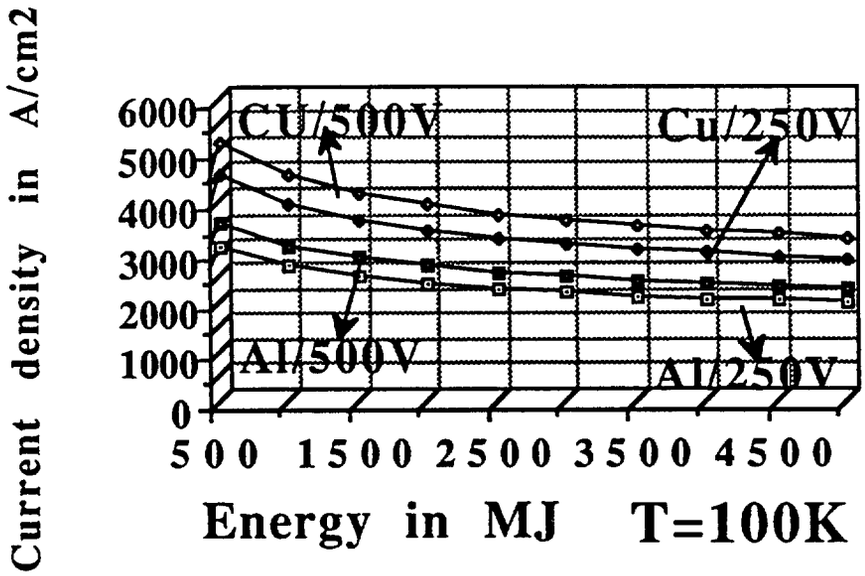


Fig9. Current optimization

For big magnets, the cooling conditions are essential because the total enthalpy of the system requires important masses of cooling fluids.
The table 7 compare the enthalpy of the elements generally used in the construction of magnets and the heat of vaporization of the cryogenics fluids :

K	300/77	77/4	Enthalpy
Al	180	6	j/g
Cu/Fe	80	4	j/g
K	300/77	300/4	heat of vap.
Nitrogen	200		j/g
Helium	------- --	21	j/g

Table7. Enthalpies and heat of vaporization of substrates and cooling fluids

This table show that the cooling of 1000t Fe and 1000t Al requests about 1300 t N2 or 50 containers of $20m^3$. This result can be slightly changed taking into account the direct cooling through the gas.
The heat losses occur as a result of three modes of heat transport :
Heat conduction Heat convection Heat radiation
As a rough approximation, we propose to take into account the following values :

$1m^2$ at 4K= .2.....5 W_{4K} + 5...10 W_{77K} = 400.....500 W_{300K}

1pair of current leads = 25 W_{4K} per KA

$1000m^2$ +2*30kA =1MW $_{300K}$

In solenoid magnets[5], the current flows at right angles to the field, and the Lorentz-force interaction between the current and the field results in stresses within the coil which tend to burst the coil radially outward and to crash it axially. In superconducting magnets additional forces are created by the thermal stresses . An easy way to eliminate the body forces assume that the field is generated by the inner diameter current sheet and that this lay out is equivalent to a thick walled cylinder supporting an internal pressure :

$$p=4*B^2 \quad (atm.T)$$

5 D.B.Mongomery.Solenoid magnet design.Wiley-Interscience.1969.

The stresses resulting from an internal pressure in a thick-walled tube are given by the expression:

$$s=p*(R+1)/(R-1) \quad \text{with } R=(R_{out}/R_{in})^2$$

This expression is generally pessimistic in a bracket of 10 to 50%.

For toroidal geometry the non-uniform field distribution increase the complexity of the calculation. A first rough approach could be made taking a uniform field distribution and a calculation taking into account the maximum value of the induction on the small value of the torus

L3+1 at LHC

by
the L3 Collaboration

presented by K. Freudenreich (ETHZ), A. Hervé (CERN) and Y. Kamyshkov (ITEP)

1 Introduction

It is a natural question to ask if and how the L3 detector can be used at the high energy CERN proton-proton collider LHC presently under discussion. We present here a preliminary feasibility study aimed to answer main technical questions and to elucidate unavoidable limitations. The basic assumptions of this study can be listed as follows:

- The experiment must be fully operational the first day of LHC beams.
- Civil engineering work should be strictly limited to lifting the magnet and shielding for the radiation protection of the counting rooms.
- The new set-up must be compatible with LEP beams crossing at "zero luminosity".
- The present muon spectrometer should be kept for the central region.
- The final detector should aim to specific performances to limit the cost.

Under these conditions we propose to complement the central detector with two forward muon spectrometers of similar values of $B \cdot L^2$ which will be presented in sections 2 and 3. Since the present central calorimeter has not the proper thickness measured in absorption lengths we are investigating two possible options: the first one aimed to maintain the existing mechanical structure with uranium plates (see section 4.1) and the second one aimed to design a new calorimeter with better performance (see section 4.2). No attempt to optimize any of these solutions has been pursued yet, as ample space and time is still available.

The modified L3 detector (L3+1) clearly can be used to study multimuon events within $\pm$ 4 units of rapidity. Both versions of the calorimeter have good capabilities to detect high p_T jets as well as electrons and photons. We can anticipate that the results of the above mentioned studies will compare favourably with detectors specifically designed for LHC.

2 Experimental Hall and Magnets

2.1 Description of L3

The L3 experiment [1] is installed at interaction point 2 of the LEP storage ring. A 7800 ton octagonally shaped solenoid houses all the detectors. The poles of the magnet are split into doors to give access to the field volume. The maximum field is 0.5 T and the effective field volume is 11.4 m across and 11.9 m along the beam. The detectors are supported by a 32 m long and 4.45 m diameter steel tube which rests at both extremities on adjustable jacks placed on concrete pillars (see Fig. 1 + 2).

The 21.4 m diameter, 40 m long experimental hall is oriented longitudinally with respect to the LEP beam line which enters the hall with a slope of 1.39%. The hall is equipped with a 40 t overhead crane and an 11 t monorail fixed to the ceiling. The 23 m diameter and 52 m deep access shaft connected to one end of the experimental hall serves as access for the experimental equipment and personnel, for hall services and provides

in its upper half space for four counting rooms directly above the LEP beam line and protected from radiation by a 1.7 m thick shielding of concrete beams. A "blockhouse" at the bottom of the access shaft provides shielded space for electronics near the detectors.

The 4 MW magnet has been built in a fixed position on the LEP beam, without the need of a garage position, in a way which will be very similar for the future LHC experiments. The construction of the magnet is described in detail in Ref [1]. Basically, the magnet has been built "in situ", aligned on the beam, then concrete was poured under it. The coil is a 1000 ton aluminium solenoid resting on two rails supported by the lower octant of the magnetic structure. This structure is a 6600 ton iron shield 15.8 m across and 14.1 m long. The complete assembly is tilted at 1.39% to follow the LEP beam.

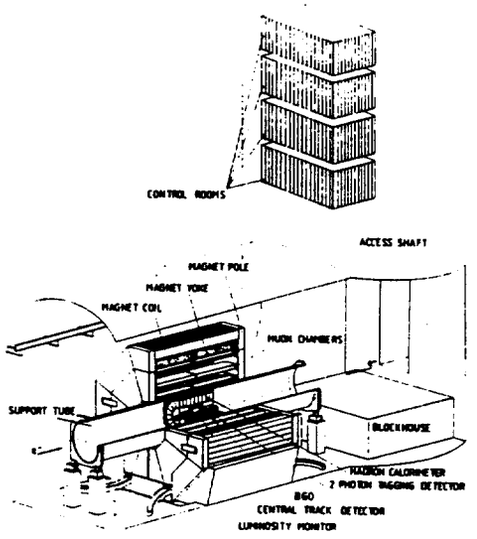


Fig. 1: Perspective view of the L3 experiment

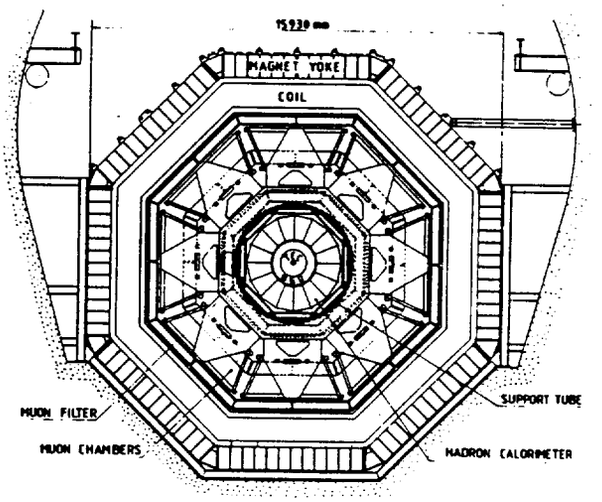


Fig. 2: Transverse view of L3

2.2 General lay-out of L3+1

To be converted to LHC, as described in the introduction, the following operations must be performed in the experimental area and around the main magnet once all detectors have been removed:

- Remove the 32 m long support-tube and replace it by a shorter one to give room for the forward/backward magnets
- Raise the magnet by 1.2 m to bring it to the level of the LHC beam.
- Replace the existing 10 t ceiling monorail by a 30 t one, as access of the 40 ton crane to the far end of the experimental area will be greatly limited once the magnet has been raised to the level of the LHC beam.
- Complement the main magnet by two forward spectrometers to achieve better muon detection for angles smaller than 42°.
- Complement the radiation shielding in order to meet the requirements of LHC.

The general lay-out of L3+1 is shown in Fig. 3, together with the various acceptance angles. The new forward-backward magnets assembly occupies ± 15 m around the intersection point, thus fitting nicely in the ± 16 m of free space left between the passive scrapers protecting the last LHC mini beta magnets which are separated by ± 20 m in a

standard insertion (L. Leistam, these proceedings). The two forward-backward magnets can be moved on linear rails along the beam by 4 m to give access to the muon spectrometer, and allow the removal of the hadronic end-caps and the new hadronic insert, using the 30 t ceiling monorail. This last operation, which is a shut-down activity, will require the removal of the passive scrapers, but not of the mini beta magnets, thus the beam line will not be affected. As swinging doors are not compatible anymore with the forward-backward magnets, the main magnet doors (minus the bottom which will be used to support the new support-tube) will be carried by these magnets and handled like conventional end-caps on other LEP detectors.

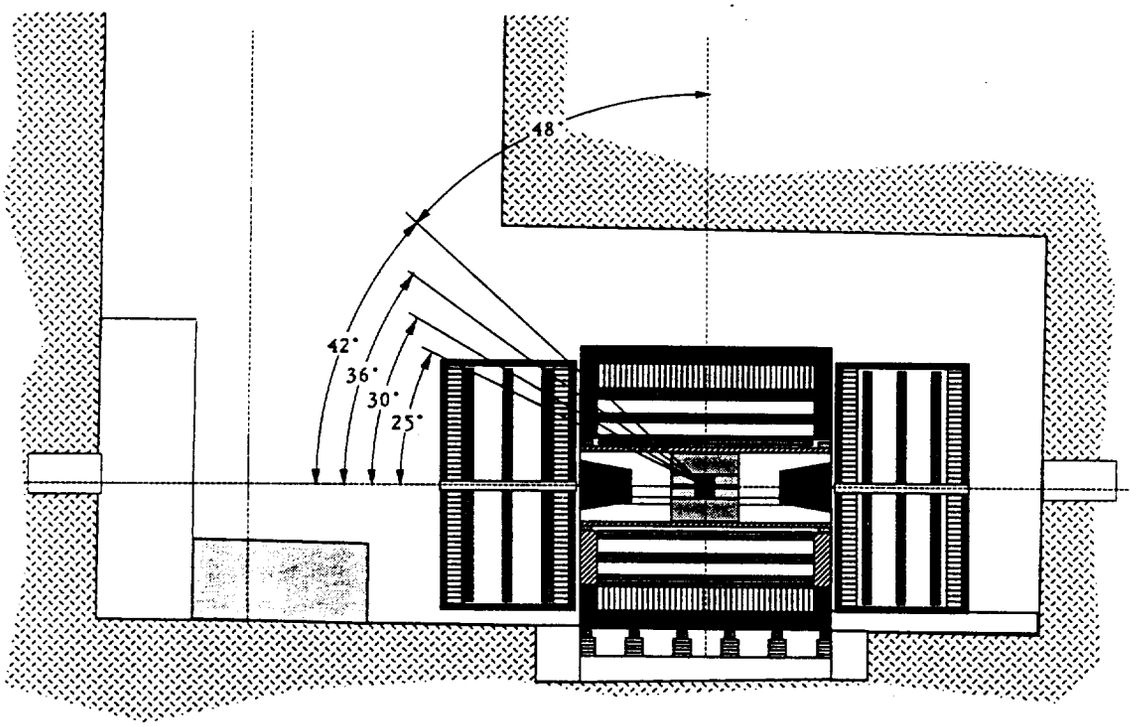


Fig. 3: General Lay-out of the L3+1 set-up

2.3 Remove the 32 m long support-tube and replace it by a shorter one

Prior to this operation, all detectors will be removed and stored on the surface for possible repair and amelioration to the muon spectrometer and modifications to the hadronic barrel. The present support tube will be cut in 3 pieces in the underground hall, in order that the central piece which is in stainless steel could be refitted and used as the new shorter support-tube. This new support tube will be supported by metallic pillars, which will be in effect an integral part of the main magnet poles (see Fig. 4). In fact they can be made from parts removed from the present swinging doors. With this solution, the existing

muon barrel spectrometer will use exactly the same supporting structure as in present L3.

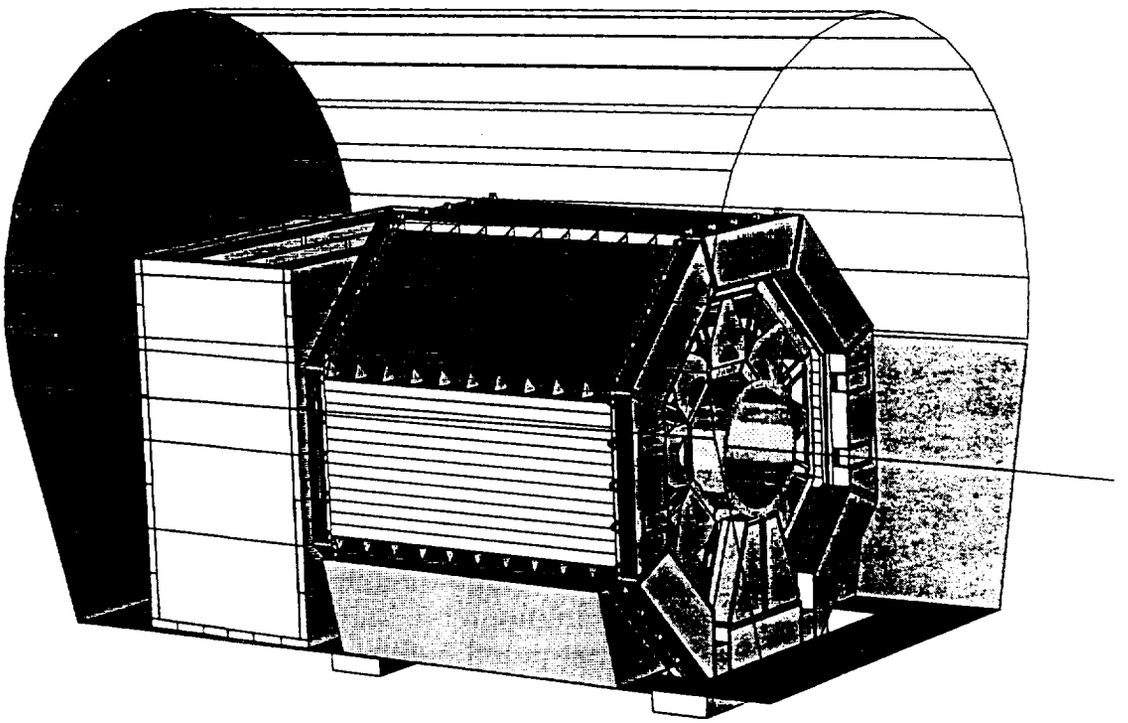


Fig. 4: Perspective view of the L3+1 set-up with one vertical solenoid not yet installed.

2.4 Raise the magnet by 1.2 m

The lifting operation although certainly difficult to engineer is in essence not very different to other spectacular lifting operations which have already been performed on buildings or on oil sea platforms. However, making room under the magnet to place the necessary jacks, and performing the actual separation of the main magnet from its concrete berth is clearly a bigger unknown. For this reason, a feasibility study was requested already one year ago from a firm specialized in concrete destruction. This feasibility study has been very positive, and a possible scenario has been drafted. It relies mainly on drilling holes with a core cutter, then sawing the concrete between holes with a diamond covered wire. The main stages of this operation are the following:

- Temporary stiffening of the magnetic structure.
- Cutting an access trench under the magnet and separate the magnet from the concrete berth.
- Inserting the 24 necessary hydraulic jacks.
- Lifting proper.

To make sure that the new L3+1 set-up will stay compatible with e-p physics at CERN which requires the running of LEP and LHC concurrently (at zero luminosity for our insertion), the main magnet will have to stay on jacks in order to be brought down by 60 cm to let both beams go through the inner hole of the hadronic barrel (this clearly requires that the hadronic end-caps and hadronic insert are removed).

2.5 Complementing the main magnet by two forward spectrometers

The forward-backward spectrometers have been designed as two simple magnets using the L3 construction technique, having for 0^o tracks the same analysing power $B \cdot L^2$ as the main magnet at 90°. The magnetic axis is vertical in order to have a good access from the top to load the muon chamber assemblies using the ceiling monorail and ease the long muon chamber manufacturing by aligning wires with gravity. The coil is split in two halves with a gap of 20 cm to allow the LHC beam pipe to go through. The internal volume of the magnet is protected from the coil heat losses by a thermal shield similar to the one used on the main magnet.

The limited maximum acceptance angle of these magnets (25° for the full 3 planes of muon chambers) comes from the fact that the outside width of these magnets have been chosen equal to the actual width of the main magnet (15 m) to nicely fit in between existing gangways and inside the present experimental hall (Fig. 5).

Parameter	Value
B	0.2 T
Power (per side)	2.5 MW
Analysing power at 0 degree	5 T.m2
Position of front face from IP	7.5 m
Free aperture along beam	5.75 m
Free aperture perp to beam	13.6 m
Outside length along beam	7.3 m
Weight of coil	290 t
Weight of iron	1500 t
Thickness of coil	21 cm
Thicknes of barrel	24 cm
Thickness of pole	27 cm
Current	9100 A
Inductance	455 mH
Stored energy	19 MJ
Distance between layers of chambers	5 m

Table 1: Parameters of the forward/backward magnets.

2.6 Strengthening of the shielding against radiation

It is clear that safety wise shielding for LHC is more demanding that for LEP (Ref[2] and also G. Stevenson and H. Taureg, these proceedings). The first clear implication is that the "blockhouse" containing the fast electronics will not be accessible during LHC beam. However, controlled access will certainly be possible between fills for quick repair. More important is the fact that the shielding of the plug (presently 1.7 to 2.5 m of concrete) will have to be increased at least to 3.5 m to protect the existing counting rooms in the access pit. Also the two existing "chicanes" giving access to the LEP machine zone US-25 will have to be modified and a known weak point between the experimental area and one LEP by-pass will have to be strengthened. It is worth noting that all these improvements on the radiation protection and shielding would have to be done anyway, L3 being converted or not to LHC, otherwise the L3 counting rooms, surface halls, LEP US-25 and by-pass

zones at point 2 would not be accessible during LHC running.

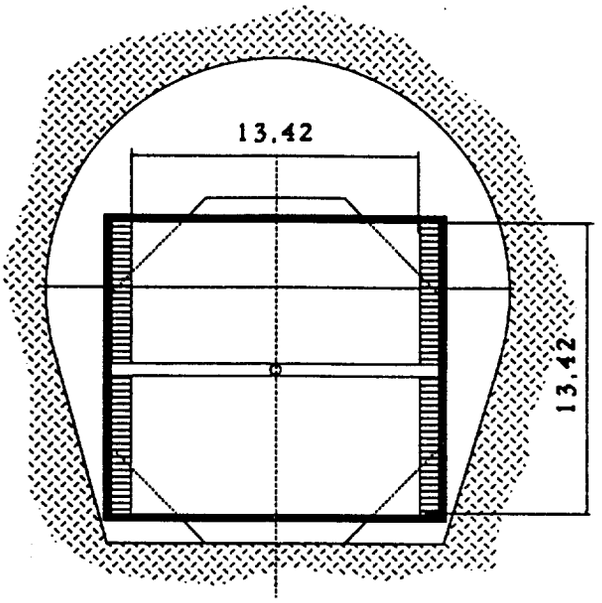


Fig. 5: Cross-section of the L3+1 magnets inside the hall.

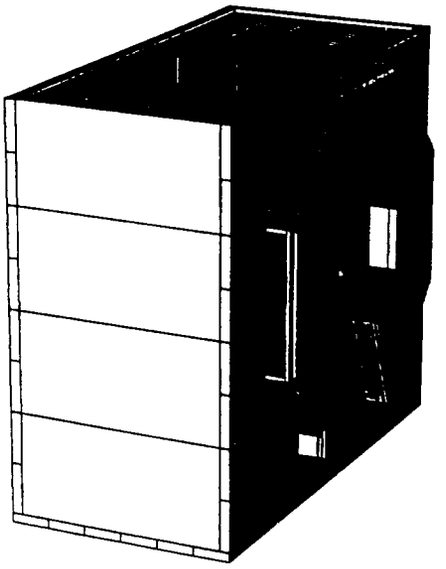


Fig. 6: Perspective view of one forward magnet.

2.7 Planning of operation

Operations will go in the following order, once physics with LEP has been discontinued.

1) Removal of the detectors, and modification of the support tube and its new supports will progress in parallel with the creation of the bottom trench. It is to be noted that the cutting of this trench could start during the previous LEP shut-downs if requested. 2) Assembly of the backward magnet has to be done before the magnet is raised to take full advantage of the coverage by the existing 40 t crane. 3) Once the assembly of the backward magnet is finished, the main magnet can be raised to its new position after temporary strengthening of the magnetic structure. The swinging doors will be opened. 4) Then the muon barrel, the hadron barrel and other hadronic detectors can be put in position inside the main magnet using temporary tooling. 5) The magnet doors will be disconnected from the main magnet and the assembly of the forward magnets can proceed. 6) The muon chambers can be loaded into the forward/backward magnets. 7) Then the forward-backward magnets can be closed towards the main magnet, and the main door fixed onto them (see Fig. 6 + 7).

From the start of the operations, we estimate that after 6 months the main magnet could be in position . Then 3 months later (9 in total) the mounting of the muon barrel can start. Then from our experience from L3, 6 more months are needed to complete the

detector. Thus a total of 15 months are needed in UX-25 to convert L3 to L3+1.

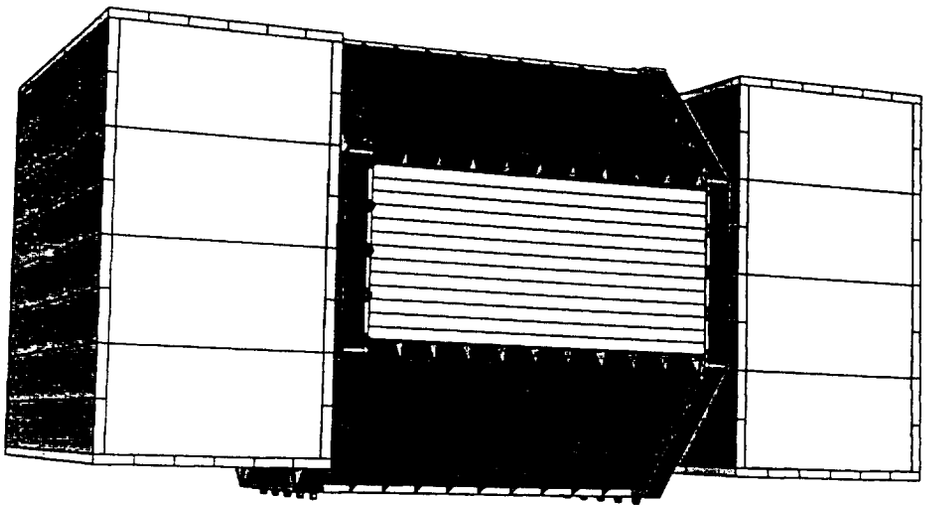


Fig. 7: Perspective view of the completed L3+1 set-up

3 Muon Spectrometer

The system of muon spectrometers will be composed of the existing central L3 magnet and drift chambers complemented by the two forward/backward magnets where three drift chambers will be inserted into each. One immediate advantage of this geometry is the fact that the wires will be vertical thus avoiding sagging.

3.1 Momentum Resolution

All L3+1 magnets are solenoids. Solenoids are known for their well behaved field properties which allows to install tracking detectors like drift chambers **inside** the useful volume. The L3 muon spectrometer is based on the fact that the momentum resolution improves quadratically with the measured track length L and only linearly with the field strength B:

$$\Delta p/p \sim p_T/(B \cdot L^2) \tag{1}$$

The parameters of the forward/backward spectrometers were choosen to yield the same values of $B \cdot L^2$ as in the barrel region, i.e. 5 Tm^2. Clearly one could run both the central solenoid and the forward/backward solenoids with a higher field (e.g. 0.75T) and obtain a higher resolution. However, for this preliminary study we concentrated on an economic solution, i.e. $B_{central} = 0.5T$ and $B_{forw/backw} = 0.2T$. Another property of the L3 muon spectrometer is the fact that the tracks are measured in three chambers which consist of many planes reducing in this way the single wire resolution by $\sigma_{s.wire}/\sqrt{N_{planes}}$. We assumed for the forward/backward spectrometers the same number of drift chamber planes as in the existing barrel system, viz. 16 planes close to interaction point, 24 planes in the middle and 16 planes at the outside. If it turns out in the future that the so-called "honeycomb strip chambers" as presented by H. van der Graaf [3] will yield the same or higher resolution at lower cost we clearly would envisage such a solution. For this study, however, we assumed for the single wire resolution the **measured** value of $\sigma_{s.wire} = 250\mu$. Since in a test beam $\sigma_{s.wire} = 150\mu$ has been obtained there is again room for improvement. As can be seen from Fig. 3 the proposed L3+1 set-up is hermetic down to 1.5° for muon detection. Nevertheless, there are regions in the set up (between 25° and 42°) where

the muons traverse either three sets of chambers with one being separated from the others by iron or the third chamber is not fully traversed. For these regions we need to study the resolution in more detail. The resolution presented here for this angular region must be considered as preliminary. It was calculated using only two chambers and a vertex constraint. We shall study whether equally spaced chambers will improve the resolution in this region. Fig. 8 shows the momentum resolution $\Delta p/p$ as a function of θ for p = 50 GeV/c. The region between 36° and 42° has been left out because there the calculation of the resolution is not yet done. This gap corresponds to 0.2 units of rapidity and was taken into accout in the acceptance calculation.

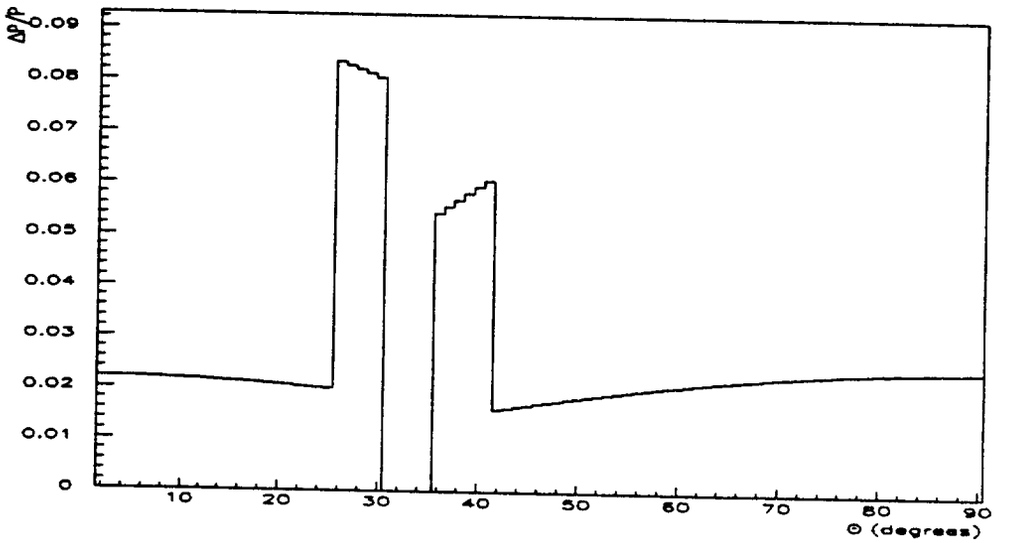


Fig. 8: Momentum resolution as a function of θ for p = 50 GeV.

Fig. 9 shows $\Delta p/p$ as a function of p for an angle of 90°.

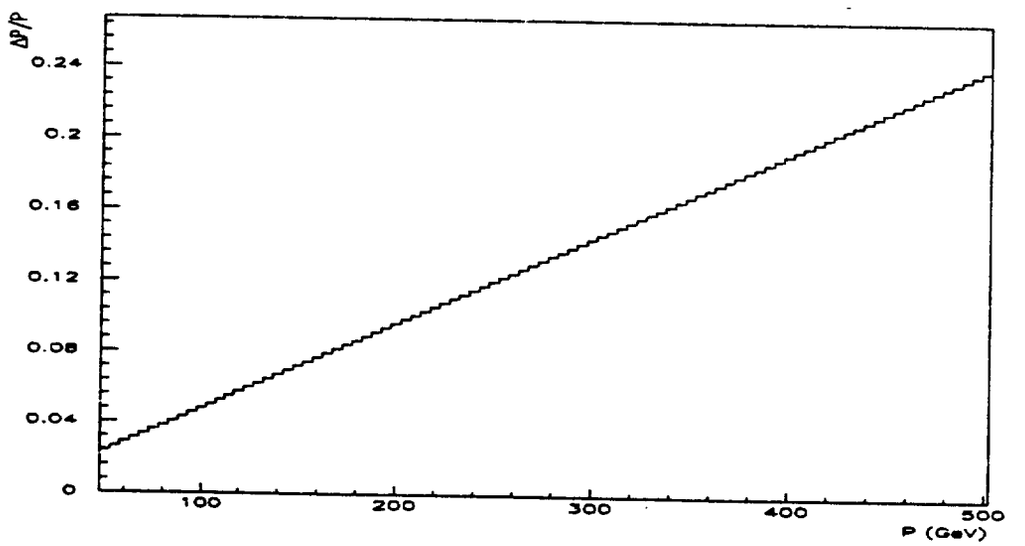
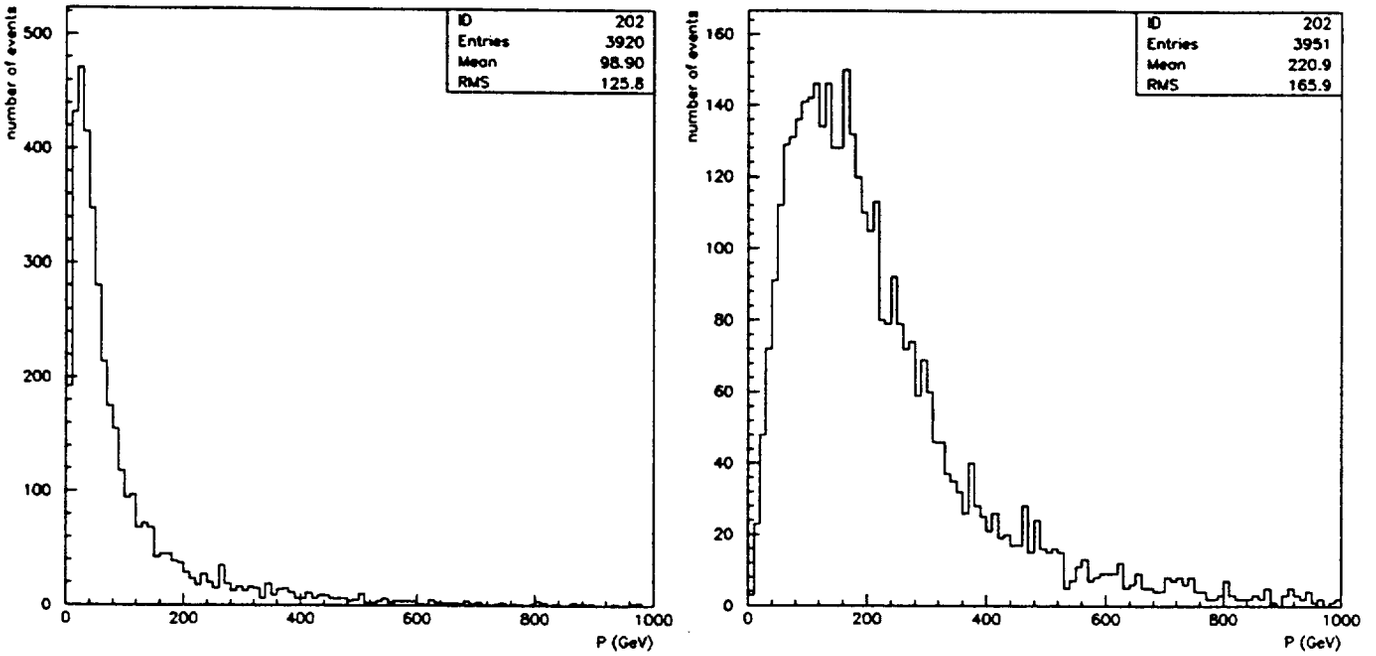


Fig. 9: Momentum resolution as a function of p for $\theta = 90°$.

Even at LHC energies the muon momenta expected from $H \rightarrow 4\mu$ decays are mostly below 200 GeV/c as can be seen from Fig. 10 and 11 where the muon momentum distribution from $H \rightarrow 4\mu$ decays is shown for the two extreme cases: In Fig. 10 originating

from a Higgs of M = 130 GeV and in Fig. 11 from a Higgs of M = 600 GeV (using the ISAJET Monte Carlo). The L3+1 resolution seems to be, therefore, quite adequate to detect multimuon decays of heavy particles. Fig. 12 shows the smeared mass spectrum from $H \rightarrow 4\mu$ of $M_{Higgs} = 400 GeV/c^2$ together with the most important 4 μ background from standard $Z^0 Z^0$ production. The L3+1 resolution clearly allows to resolve the resonance.



Muon momenta from Higgs $\rightarrow 4\mu$ decays.
Fig. 10: $M_{Higgs} = 130 GeV$ Fig. 11: $M_{Higgs} = 600 GeV$

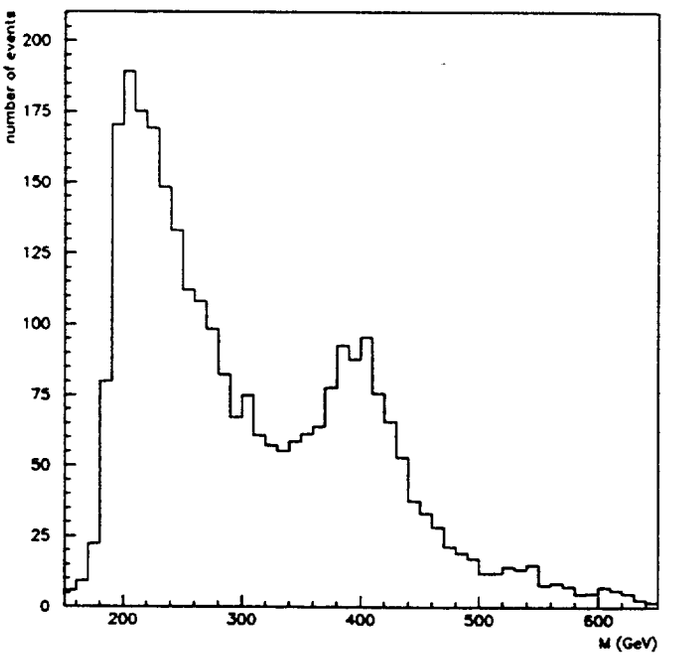


Fig. 12: Smeared 4μ mass spectrum from Higgs(M = 400 GeV) and $Z^0 Z^0$ production.

3.2 Acceptance

The $H \rightarrow 4\mu$ decay was again used to calculate the geometric acceptance for the proposed L3+1 set-up. For $130GeV < M_{Higgs} < 600GeV$ it is $\geq 70\%$. If one considers only the high resolution part of the spectrometer the acceptance is reduced by a factor two.

3.3 Future studies

In addition to the above mentioned studies of the momentum resolution we have to study single rates and trigger rates as well. Since more than 13 λ of absorption length are protecting the muon chambers the single rates should not be a problem. For triggering purposes we are studing the possibility to install planes of resistive plate counters (RPC) at each standard muon chamber layer[4]. RPC with their associated electronics provide a low cost method of instrumenting large areas. They provide a very fast discharge after the passage of a ionizing particle and the read-out is done by pick-up electrodes providing a time resolution of 2-3 ns, adequate for the bunch crossing time foreseen at LHC.

4 Calorimeter

4.1 Introduction

Precise calorimetric measurements are expected to be of great importance in experiments at the LHC. In the L3+1 experiment at LHC the calorimeter will be used as a precision instrument for searching for new physics through lepton and quark channels. The performance criteria for a calorimeter should include hermiticity, good lateral and longitudinal segmentation, e/h as close to one as possible (which implies good linearity), ability to contain most of the shower and capability for precise calibration. The LHC is a very high luminosity machine with very short bunch crossing times. Hence, it is imperative that the detectors be able to withstand high radiation doses and have short response times in order to handle the high data rates. Short response time also enables a suitably designed calorimeter to contribute to the first level trigger - an important consideration given the particle production rate of the LHC. The proposed calorimeters can be a means to separate electrons from hadrons by measuring shower shape. In the context of muon detection their primary purpose is of course to separate muons from other particles by total absorption of the hadronic component. Muon bremsstrahlung will be detected and will provide a correction to the muon energy measurement obtained from the muon detector.

4.2 Uranium Calorimeter

The calorimeter meeting the above requirements on the energy resolution and the short response time is a uranium/plastic scintillator calorimeter [5]. In view of the high event rate at the LHC and consequently possible radiation damage problems we propose an uranium/liquid scintillator calorimeter instead of an uranium/plastic one. It will be an adaptation of the existing L3 calorimeter to the operation at LHC.

Inherently liquid scintillators are more resistant to radiation damage than plastics [6]. Moreover they can be replaced conveniently therefore the radiation damage of the scintillator is no longer a problem.

The calorimeter for the L3+1 experiment makes use of the mechanical structure of the existing L3 hadron calorimeter [7]. Thus in the modules of the barrel (Fig. 13) every second chamber is replaced by a Uranium sheet of 7 mm thickness. The rest of the proportional chambers is substituted by the containers filled with liquid scintillator(LS). The thickness of the liquid in the containers is 5 mm. Similar changes are made in the

modules of the endcap.

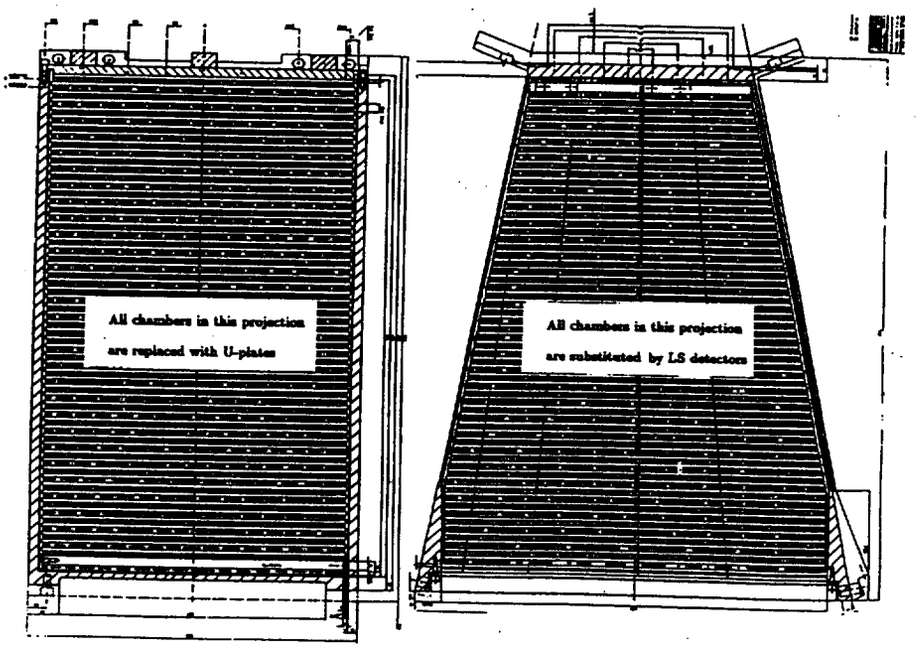


Fig. 13: Side view of the module of the L3 hadron calorimeter barrel. All chambers in one projection are replaced with uranium plates.

The BGO electromagnetic calorimeter is replaced by a central barrel calorimeter. This calorimeter is divided into 16 modules in the plane perpendicular to the beam and in two halves in the beam direction (Fig. 14). The sampling structure of the calorimeter is 5 mm uranium sheet followed by a liquid scintillator container similar to those used in the outer calorimeter.

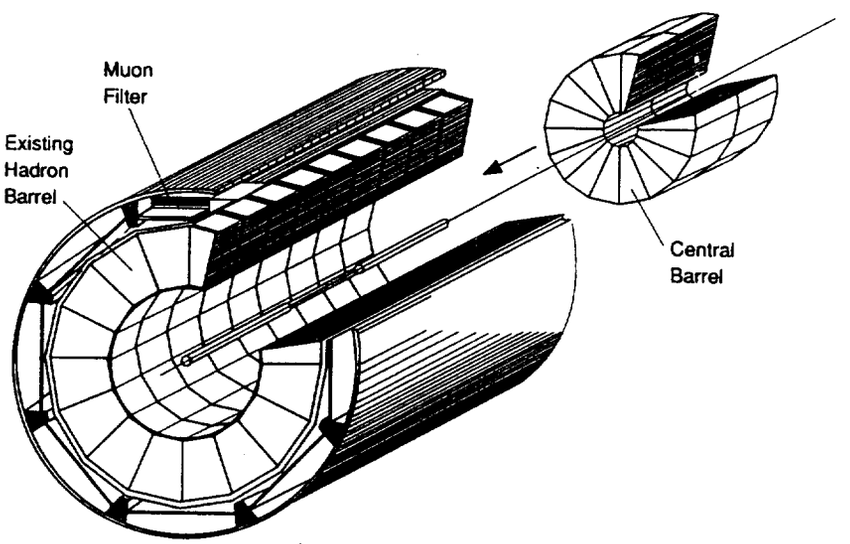


Fig. 14: Integration of the L3+1 hadron calorimeter into the existing L3 structure.

The forward region is coverd by two calorimeters with absorber/detector structure similar to that of the barrel but with layers oriented perpendicular to the beam as in the existing

endcap. To improve filtering capacity of the calorimetric system at 90° the Muon Filter of the L3 detector is replaced by a block of tungsten. The resulting calorimeter structure is summarized in Table 2. The numbers given in the table correspond to the direction perpendicular to the beam axis and therefore reflect a minimal absorbtion and filtering capacity of the calorimeter.

Material	Differential length (λ)
New barrel	
55 uranium plates of 5 mm	2.62
56 containers (2 mm brass)	0.76
56 layers of 5 mm LS	0.33
Module supporting structure (st.steel)	0.30
Subtotal	4.01
Old barrel	
Existing 60 uranium plates of 5 mm	2.94
Additional 28 uranium plates of 7 mm	1.92
30 containers (2 mm brass)	0.41
30 layers of 5 mm LS	0.17
Supporting structure (St.steel)	0.37
Subtotal	5.81
Passive material	
Muon filter (210 mm of W)	2.19
Support tube	0.67
TOTAL	**12.68**

Table 2: L3+1 hadron calorimeter thickness in units of nuclear interaction length.

In Fig. 15 the results of a Monte-Carlo study of the proposed calorimeter are shown. The jet energy resolution is calculated to be almost independent of the angle of incidence of a jet and to fit to $\approx 41\%/\sqrt{E}$ with a constant term of $\approx 1\%$. The electromagnetic energy resolution is estimated to be of the order of $20\%/\sqrt{E}$ at 90°.

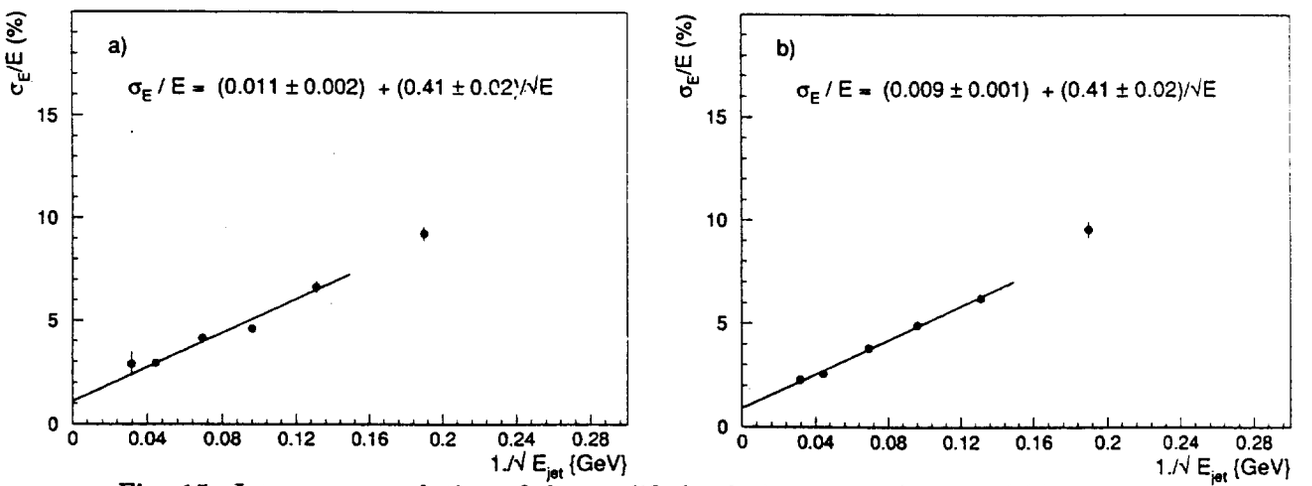


Fig. 15: Jet energy resolution of the modified calorimeter at a) 90° and b) 45° to the beam axis.

To exploit the full potential of the high energy resolution of the calorimeter one has to reduce systematic effects of the energy measurement to the lowest possible level. The cell

structure of the detectors of the proposed calorimeter and the possibility of intercalibration of these cells using the natural radioactivity of uranium absorbers provides a good tool to keep the systematic errors of the energy measurement low.

The spatial resolution of the calorimeter is determined by the structure of the read-out cells in the liquid scintillator detectors which is adapted to match the size of the object(jets,photon/electrons showers) to be measured.

4.2.1 Liquid scintillator detectors

A liquid scintillator detector consists basically of a container for the LS and a means for obtaining the information from the scintillation light. A possible LS detector design is shown in Fig. 16.

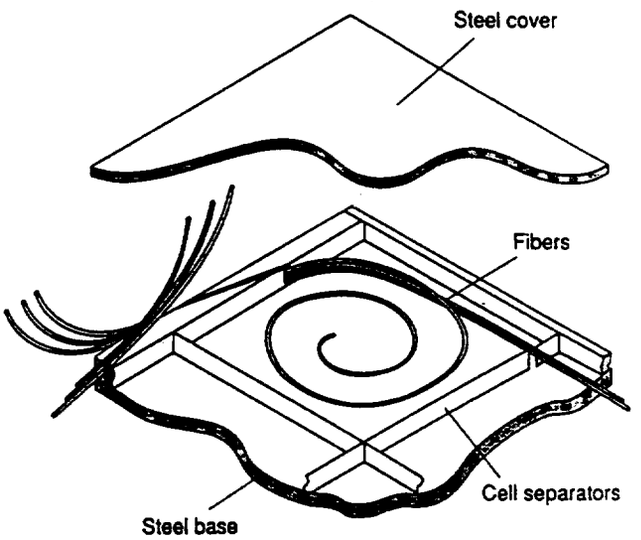


Fig. 16: Perspective view of one of the liquid scintillator cells.

The basic detector element is a rectangular cell filled with LS. The light resulting from particles crossing the cell is collected by a spiral shaped wavelength shifting (WLS) optical fiber which is 1mm in diameter and is immersed in the liquid. Only the part of the fiber immersed in the liquid has a wavelength shifter admixture. The inner walls of the cell are painted with white reflecting paint. In a calorimeter the cells belonging to one layer between two absorber sheets of a module are combined together in a detector which is a sealed rectangular vessel. The fibers pass through a seal in the container wall and run along the module sides, reaching photodetectors mounted at the module base. Several consecutive cells in depth would be connected to one photodetector. Because of reflecting walls and relatively small cells, the light is absorbed mainly by the fiber and should make the response within a cell uniform. The light collection efficiency for the cell with the size 6x6x0.5 cm^3 was estimated by Monte Carlo and the result is given in Table 3.

There are several photo detector candidates such as multi-anode PMs (produced by Hamamatsu, ITT, Phillips, and others) and solid state detectors (Solid State Photomultipliers by Rockwell International, Avalanche Photodiodes by RCA). The final choice of photo detector will be made taking into account the pertinent requirements on the stability, dynamic range, capability of operation in the magnetic field and cost.

	Light fraction	$N_{photons}$
Scintillator light output		9900
Reemitted by WLS 1 mm fiber	0.45	4455
Collection of reemitted light	0.07	312
Pass trough fiber,turn 90°	0.56	174
Transport to photo detector through 1 m clear fiber	0.84	146
90° turn of fiber	0.64	94

Table 3: Monte Carlo evaluation of the light collection efficiency. For liquid scintillator $< dE/dx >$=1.8MeV/cm, i.e. for dx=5mm,$< dE >$=0.9MeV. Light output for BC-517S (66% antracene):11000 photons/Mev.

4.3 Silicon calorimeter

In this section we consider as an alternative option the possibility to replace all the detectors inside the support tube by a completely new calorimetric device. This new detector has to cope with few stringent constraints: its external radius must be less than 2.17 m, while the internal one will be dictated by the radiation hardness of the sensitive material. In addition this calorimeter must provide an amount of material sufficient to dump to a reasonable value the background of charged tracks entering the muon system. In order to deal with high P_T jets, good energy and direction resolution is requested at 90°, while in the forward regions the detector should mainly serve as hadron filter with muon tracking ability.

A silicon calorimeter with dense absorbing material, integrating the functions of EM and Hadron detector, seems a well suited solution. In order to preserve the linearity of the energy response the e/π ratio must be close to one. This feature can be obtained combining Fe and W plates with a fractional length of 74% and 26% respectively. The ratio of the thicknesses (measured in radiation length) is 0.56. In [8] it is shown that the e/*mip* value can be decreased using passive sampling consisting of low and high-Z materials (Fe and Pb, whose critical energies are about 21.0 and 7.4 MeV, respectively). A e/*mip* value of about 0.6 is reached for a ratio of thicknesses (measured in radiation length) of the two materials of 0.56. A similar effect is expexted when W absorbers (whose critical energy is about 8.1 MeV) replace the Pb ones. This way, the Si/Fe+W hadron calorimeter is tuned to reach the compensation condition (the h/*mip* is expected to be about 0.6).

With this component ratio, the effective radiation length is X_0 = 8.6 mm and the effective interaction length is λ =14 cm.

A tentative design is proposed, using a readout system of 3 mm silicon active samplers (2.6 mm thick supporting structure and 0.4 mm thick silicon detectors). The electromagnetic section will have a sampling every radiation length for a total of 20 X_0. This corresponds to 1.23 λ or 23.2 cm. The expected resolution of this part for electromagnetic showers is $18\%/\sqrt{E}$ [9]. The hadronic section covers a depth of 5.77 λ or 89.2 cm with 28 silicon sampling planes (corresponding to 4.9 sampling/λ, or 1 sampling every 3 X_0). This configuration provides a single particle resolution of $65\%/\sqrt{E}$ with negligible constant term. In fact, the ratio of thicknesses, in unit of interaction length, of the Fe and W absorbers is about 1.7. Thus the contribution to the total energy resolution of the binding energy losses is dominated by the low value (about (18-20)%/$\sqrt{E}$) of the Fe absorber. The expected contribution to the overall energy resolution due to the sampling fluctuation is about $56\%/\sqrt{E}$.

As a whole the calorimeter is 7 λ deep, containing about 95% of shower energies up to 300 GeV.

The calorimetric part can be complemented by a hadron dump, instrumented to provide some muon tracking capability. It can be made by 6 λ of tungsten, interspersed with 4 active readout planes, with a depth of 58.6 cm.

The total detector depth is then 13 λ (in passive absorber plates, to which an additional 0.3 interaction length is provided by the active samplers) or 171 cm. Allowing up to 6 cm of clearance for services at the end, the inner radius can be set at 40 cm. The hadron calorimeter part starts at 63.2 cm and goes up to 152 cm. In order to cover at least the angle of the barrel inner muon chamber, an angular range from 26.6° to 153.4° is needed for the central calorimeter.

In [10] it is given the maximum annual (10^7 s) neutron fluence for the case of a spherical Pb calorimeter covering up to 0.3° with an inner radius of 2 m, operating at LHC for an average luminosity of 10^{34} $cm^{-2}s^{-1}$ and σ_{in} about 60 mb. The maximum annual neutron fluence is at the beginning of the e.m. section of the calorimeter. In the proposed design, the distance of the calorimeter from the beam crossing point goes from 40 cm at 90° to 90 cm at 26.5°. However, the use of iron in the absorber reduces the neutron fluence of about a factor of 2 respect to Pb [11]. Furthermore, it has been shown [12] that an effective suppression factor of 6 has to be taken into account ewhen two 1 mm polyethylene sheets (which have the same properties of the usual G10 plates in tuning the e.m. response [13]) are located as supporting structure of the silicon planes in the e.m. section. This way, the expected maximum annual neutron fluence is about 6.3 $10^{12}cm^{-2}$ at 90° and does not exceed 10^{13} cm^{-2} at 26.6°. No major effects on charge collection is expected for these neutron fluences [14]. Systematic investigations of silicon detector performances for neutron fluences between 10^{12} and 10^{14} n/cm^2 are presently carried out by few different groups (SICAPO coll., BNL, Hamburg Univ., UT-ORNL-ISI). Furthermore, at 26.6° the effect of the boundary region (where a reduced neutron fluence is expected) is not included in the extimations. The overall neutron fluence as a function of the calorimeter depth can be further suppressed by optimizing the use of polyethylene in the hadronic section of the calorimeter.

In the forward region the radiation problem must be investigated in more details. However the constraints from the existing structure are less stringent, so that also a completely different device could fit there.

An overall design of the structure in the barrel region is presented in Fig. 18. From this design, an exstimate of the total silicon surface can be derived, as shown in Table 4. The sensitive part of the hadron dump is not included in this figures.

E.M. Section	20 planes 280 cm long	181 m^2
Hadron section	10 planes 380 cm long	189 m^2
	18 planes 490 cm long	686 m^2

Table 4: Silicon surfaces.

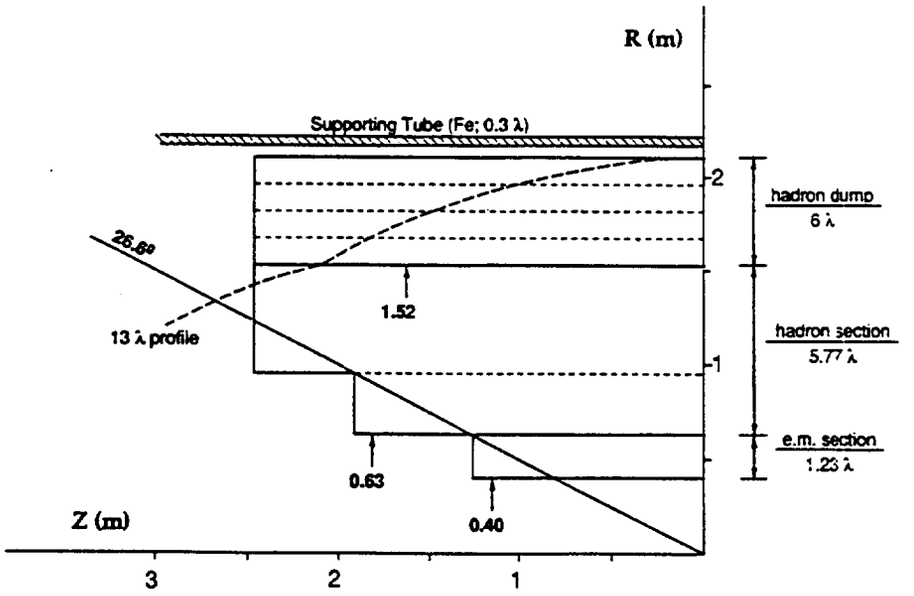


Fig. 18: Silicon calorimeter in the barrel region.

5 Conclusions

From the preliminary study of the L3+1 detector concept at LHC we conclude:

- The necessary lifting of the L3 magnet by 1.2 m is feasible.
- A full coverage muon detector can be achieved by adding two forward/backward magnets.
- The calorimeter can be transformed to yield good energy resolution and acceptable rates in the muon chambers.
- The L3+1 detector should be able to detect with sufficient precision the expected multimuon states.
- The L3+1 detector concept allows substantial savings. It could be ready right at the start of LHC.

Acknowledgement

We would like to aknowledge J.L. Benichou, who contributed to the mechanical studies, and W. Scandale for several fruitful discussions on the LHC project. Special thanks are due to P.G. Rancoita, who contributed intensively to the study of the Silicon Calorimeter option.

The L3 Collaboration:
B.Adeva[15] O.Adriani[13] M.Aguilar-Benitez[23] H.Akbari[5] S.Aksouh[16] J.Alcaraz[23] A.Aloisio[25] G.Alverson[9] M.G.Alviggi[25] Q.An[16] H.Anderhub[39] A.L.Anderson[12] V.P.Andreev[14] T.Angelov[12] L.Antonov[34] D.Antreasyan[7] G.Anzivino[7] P.Arce[23] A.Arefiev[24] F.Arzarello[7] R.Ayad[16] T.Azemoon[3] T.Aziz[8] P.V.K.S.Baba[16] P.Bagnaia[30] J.A.Bakken[29] L.Baksay[32] R.C.Ball[3] S.Banerjee[8,16] J.Bao[5] G.Barbagli[7] G.Bari[7] T.Barillari[7] L.Barone[30] A.Bay[17] M.Basile[7] U.Becker[12] J.Behrens[39] S.Beingessner[4] L.Bellagamba[7] Gy.L.Bencze[10] J.Berdugo[23] P.Berges[12] B.Bertucci[30] B.L.Betev[34] A.Biland[39] R.Bizzarri[30] J.J.Blaising[4] P.Blömeke[1] B.Blumenfeld[5] G.J.Bobbink[2] M.Bocciolini[13] W.Böhlen[37] A.Böhm[1] T.Böhringer[19] B.Borgia[30] D.Bourilkov[34] D.Boscherini[7] M.Bourquin[17] D.Boutigny[4] B.Bouwens[2] J.G.Branson[31] I.C.Brock[28] G.Bruni[7] P.Bruni[7] F.Bruyant[15] C.Buisson[22] A.Bujak[36] J.D.Burger[12] J.P.Burq[22] J.Busenitz[35] X.D.Cai[16] C.Camps[1] M.Capell[20] L.Caputi[7] G.CaraRomeo[7] F.Carbonara[25] F.Carminati[13] A.M.Cartacci[13] M.Cerrada[23] G.Castellini[7] H.Castro[16] F.Cesaroni[30] Y.H.Chang[12] U.K.Chaturvedi[16] M.Chemarin[22] A.Chen[41] C.Chen[6] G.M.Chen[6] H.F.Chen[18] H.S.Chen[6] M.Chen[12] M.C.Chen[27] M.L.Chen[3] G.Chiefari[25] M.Chiarini[7] C.Y.Chien[5] F.Chollet[4] L.Cifarelli[7] F.Cindolo[7] F.Ciralli[7] C.Civinini[13] I.Clare[12] R.Clare[12] H.O.Cohn[26] G.Coignet[4] E.Colavita[7] N.Colino[15] V.Commichau[1] G.Conforto[13] A.Contin[15] A.Contin[7] F.Crijns[2] X.Y.Cui[16] T.S.Dai[12] R.D'Alessandro[13] M.Dardo[7] S.D'Auria[7] R.de Asmundis[25] A.Degré[15,4] K.Deiters[15,38] E.Dénes[10] P.Denes[29] F.DeNotaristefani[30] S.DePasquale[7] C.DelPapa[7] M.Dhina[39] D.DiBitonto[35] M.Diemoz[30] F.Diez-Hedo[15] H.R.Dimitrov[34] C.Dionisi[30] F.Dittus[27] R.Dolin[12] M.Th.Dova[7] E.Drago[25] T.Driever[2] D.Duchesneau[17] P.Duinker[2,15] I.Duran[15,23] H.El Mamouni[22] A.Engler[28] F.J.Eppling[12] F.C.Erné[2] E.Eskut[16] P.Extermann[17] R.Fabbretti[39] G.Faber[12] S.Falciano[30] Q.Fan[16,6] S.J.Fan[33] M.Fabre[39] O.Fackler[20] J.Fay[22] J.Fehlmann[39] H.Fenker[9] T.Ferguson[28] G.Fernandez[23] F.Ferroni[30,15] H.Fesefeldt[1] J.Field[17] F.Filthaut[2] G.Finocchiaro[30] F.Fiori[7] I.Fiori[7] P.H.Fisher[5] G.Forconi[17] T.Foreman[2] F.Frasconi[7] K.Freudenreich[39] W.Friebel[38] M.Fukushima[12] M.Gailloud[19] Yu.Galaktionov[24] E.Gallo[13] J.Galvez[16] S.N.Ganguli[8] P.Garcia-Abia[23] S.S.Gau[41] S.Gentile[30] P.Guisti[7] M.Glaubman[9] S.Goldfarb[3] Z.F.Gong[16,18] E.Gonzalez[23] A.Gordeev[24] P.Göttlicher[1] D.Goujon[17] G.Gratta[27] C.Grinnell[12] M.Gruenewald[27] M.Guanziroli[16] A.Gurtu[8] H.R.Gustafson[3] L.J.Gutay[36] H.Haan[1] S.Hancke[1] K.Hangarter[1] W.Hao[16] M.Harris[15] A.Hasan[16] D.Hauschildt[2] C.F.He[33] T.Hebbeker[1] M.Hebert[31] T.Hernandez-Benavides[16] G.Herten[12] U.Herten[1] A.Hervé[15] K.Hilgers[1] H.Hofer[39] H.Hoorani[16] L.S.Hsu[41] G.Hu[16] G.Q.Hu[33] B.Ille[22] G.Iacobucci[7] M.M.Ilyas[16] V.Innocente[25,15] E.Isiksal[39] E.Jagel[16] B.N.Jin[6] L.W.Jones[3] Yu.Kamyshkov[24] Y.Karyotakis[4,15] M.Kaur[16] R.A.Khan[16] S.Khokhar[16] V.Khoze[14] M-N.Kienzle[17] W.Kinnison[21] D.Kirkby[27] W.Kittel[2] A.Klimentov[24] A.C.König[2] O.Kornadt[1] V.Koutsenko[24] R.W.Kraemer[28] T.Kramer[12] V.R.Krastev[34] W.Krenz[1] J.Krizmanic[5] A.Kuhn[37] K.S.Kumar[11] V.Kumar[16] A.Kunin[24] A.Kuzucu[16] A.van Laak[1] I.laakso[7] V.Lalieu[17] G.Landi[13] K.Lanius[15] D.Lanske[1] S.Lanzano[25] G.Laurenti[7] P.Lebrun[22] P.Lecomte[39] P.Lecoq[15] P.Le Coultre[39] D.Lee[21] I.Leedom[9] J.M.Le Goff[15] L.Leistam[15] R.Leiste[38] M.Lenti[13] E.LeonFlorian[16] J.Lettry[39] P.M.Levchenko[14] X.Leytens[2] C.Li[wl,18] H.T.Li[6] J.F.Li[16] L.Li[39] P.J.Li[33] Q.Li[16] X.G.Li[6] J.Y.Liao[33] Q.Lin[7,16] Z.Y.Lin[18] F.L.Linde[28] D.Linnhofer[15] B.Lisowski[7,16] R.Liu[16] Y.Liu[16] W.Lohmann[38] S.Lökös[32] E.Longo[30] Y.S.Lu[6] J.M.Lubbers[2] K.Lübelsmeyer[1] C.Luci[15] D.Luckey[7,12] L.Ludovici[30] X.Lue[39] L.Luminari[30] W.G.Ma[18] G.Maccarone[7] M.MacDermott[39] R.Magahiz[32] M.Maire[4] C.Maidantchik[16] P.K.Malhotra[8] R.Malik[16] A.Malinin[24] C.Maña[23] D.N.Mao[3] Y.F.Mao[6] M.Maolinbay[39] P.Marchesini[16] A.Marchionni[13] A.Margotti[7] J.P.Martin[22] L.Martinez[15] F.Marzano[30] Th.Massam[7] G.G.G.Massaro[2] T.Matsuda[12] K.Mazumdar[8] P.McBride[11] T.McMahon[36] D.McNally[39] Th.Meinholz[1] M.Merk[2] L.Merola[25] M.Meschini[13] W.J.Metzger[2] Y.Mi[16] M.Micke[1] U.Micke[1] G.B.Mills[21] Y.Mir[16] G.Mirabelli[30] J.Mnich[1] M.Möller[1] B.Monteleoni[13] G.Morand[17] R.Morand[4] S.Morganti[30] V.Morgunov[24] N.-E.Moulai[16] R.Mount[27] E.Nagy[10] R.Nania[7] M.Napolitano[25] H.Newman[27] M.A.Niaz[16] L.Niessen[1] V.O'Shea[7] N.Ozdes[16] E.Pallante[7] F.Palmonari[7] D.Pandoulas[1] F.Plasil[26] G.Passaleva[13] G.Paternoster[25] S.Patricelli[25] Y.J.Pei[1] P.G.Pelfer[7] D.Perret-Gallix[4] J.Perrier[17] A.Pevsner[5] D.Piccioni[7] M.Pieri[13] P.A.Piroué[29] V.Plyaskin[24] M.Pohl[39] V.Pojidaev[24] N.Produit[17] J.M.Qian[12,16] S.Quian[7,16] K.N.Qureshi[16] R.Raghavan[8] G.Rahal-Callot[39] P.Razis[39] K.Read[29] D.Ren[39] Z.Ren[16] S.Reucroft[9] O.Rind[3] C.Rippich[28] F.Rivera[16] H.A.Rizvi[16] B.P.Roe[3] M.Röhner[1] S.Röhner[1] U.Roeser[38] Th.Rombach[1] L.Romero[23] J.Rose[1] S.Rosier-Lees[4] R.Rosmalen[2] Ph.Rosselet[19] T.Ruan[16] J.A.Rubio[15,23] W.Ruckstuhl[17] H.Rykaczewski[39] M.Sachwitz[38] J.Salicio[15,23] J.M.Salicio[23] G.Sanders[21] G.Sartorelli[7,16] G.Sauvage[4] A.Savin[24] V.Schegelsky[14] M.Schioppa[7] D.Schmitz[1] P.Schmitz[1] M.Schneegans[4] M.Schöntag[1] H.Schopper[40] D.J.Schotanus[2] H.J.Schreiber[38] R.Schulte[1] S.Schulte[1] K.Schultze[1] J.Schütte[11] J.Schwenke[1] G.Schwering[1] C.Sciacca[25] M.Scioni[7] I.Scott[11] R.Sehgal[16] P.G.Seiler[39] J.Seixas[16] J.C.Sens[2] A.Sharma[16] P.Sharma[16] I.Sheer[31] V.Shevchenko[24] S.Shevchenko[24] X.R.Shi[28] K.Shmakov[24] V.Shoutko[24] E.Shumilov[24] N.Smirnov[14] C.Solano-Salinas[16] A.Sopczak[27,31] C.Spartiotis[5] T.Spickermann[1] B.Spiess[37] P.Spillantini[13] R.Starosta[1] M.Steuer[7,12] D.P.Stickland[29] W.Stoeffl[20] B.Stöhr[39] H.Stone[17] K.Strauch[11] B.C.Stringfellow[36] K.Sudhakar[8,1] G.Sultanov[15] R.L.Sumner[29] L.Z.Sun[18] G.C.Susinno[7] H.Suter[39]

R.B.Sutton[28] J.D.Swain[16] A.A.Syed[16] X.W.Tang[6] E.Tarkovsky[24] L.Taylor[9] E.Thomas[16] R.Timellini[7] C.Timmermans[2] Samuel C.C.Ting[12] S.M.Ting[12] Y.P.Tong[41] F.Tonisch[38] M.Tonutti[1] S.C.Tonwar[8] J.Tòth[10] G.Trowitzsch[38] K.L.Tung[6] J.Ulbricht[37] L.Urbàn[10] U.Uwer[1] E.Valente[30] R.T.Van de Walle[2] H.van der Graaf[2] I.Vetlitsky[24] G.Viertel[39] P.Vikas[16] U.Vikas[16] M.Vivargent[4,12] H.Vogel[28] H.Vogt[38] M.Vollmar[1] G.Von Dardel[15] I.Vorobiev[24] A.A.Vorobyov[14] An.A.Vorobyov[14] L.Vuilleumier[19] M.Wadhwa[16] W.Wallraff[1] C.R.Wang[18] G.H.Wang[28] J.H.Wang[6] Q.F.Wang[11] X.L.Wang[18] Y.F.Wang[13] Y.Y.Wang[16] Z.Wang[16] Z.M.Wang[16,18] J.Weber[39] R.Weill[19] T.J.Wenaus[12] J.Wenninger[17] M.White[12] R.Wilhelm[2] C.Willmott[23] F.Wittgenstein[15] D.Wright[29] R.J.Wu[6] S.L.Wu[16] S.X.Wu[16] Y.G.Wu[6] B.Wysłouch[12] G.Xexeo[16] C.Xu[16] Y.D.Xu[6] Z.Z.Xu[18] Z.L.Xue[33] D.S.Yan[33] B.Z.Yang[18] C.G.Yang[6] G.Yang[16] K.S.Yang[6] Q.Y.Yang[6] Z.Q.Yang[33] C.H.Ye[16] J.B.Ye[39] Q.Ye[16] S.C.Yeh[41] Z.W.Yin[33] J.M.You[16] K.You[16] M.Yzerman[2] C.Zaccardelli[27] Y.ZamoraGarcia[16] L.Zehnder[39] M.Zeng[16] Y.Zeng[1] D.Zhang[31] D.H.Zhang[2] Z.P.Zhang[18] J.F.Zhou[1] R.Y.Zhu[27] H.L.Zhuang[6] A.Zichichi[7,15,16]

---

1 I. Physikalisches Institut, RWTH, Aachen, Federal Republic of Germany*
III. Physikalisches Institut, RWTH, Aachen, Federal Republic of Germany*
2 National Institute for High Energy Physics, NIKHEF, Amsterdam; NIKHEF-H and University of Nijmegen, Nijmegen, The Netherlands
3 University of Michigan, Ann Arbor, Michigan, United States of America
4 Laboratoire de Physique des Particules, LAPP, Annecy, France
5 Johns Hopkins University, Baltimore, Maryland, United States of America
6 Institute of High Energy Physics, IHEP, Beijing, China
7 INFN-Sezione di Bologna, Italy
8 Tata Institute of Fundamental Research, Bombay, India
9 Northeastern University, Boston, Massachusetts, United States of America
10 Central Research Institute for Physics of the Hungarian Academy of Sciences, Budapest, Hungary
11 Harvard University, Cambridge, Massachusetts, United States of America
12 Massachusetts Institute of Technology, Cambridge, Massachusetts, United States of America
13 INFN Sezione di Firenze and University of Firenze, Italy
14 Leningrad Nuclear Physics Institute, Gatchina, Soviet Union
15 European Laboratory for Particle Physics, CERN, Geneva, Switzerland
16 World Laboratory, FBLJA Project, Geneva, Switzerland
17 University of Geneva, Geneva, Switzerland
18 Chinese University of Science and Technology, USTC, Hefei, China
19 University of Lausanne, Lausanne, Switzerland
20 Lawrence Livermore National Laboratory, Livermore, California, United States of America
21 Los Alamos National Laboratory, Los Alamos, New Mexico, United States of America
22 Institut de Physique Nucléaire de Lyon, IN2P3-CNRS/Université Claude Bernard, Villeurbanne, France
23 Centro de Investig. Energeticas, Medioambientales y Tecnologicas, CIEMAT, Madrid, Spain
24 Institute of Theoretical and Experimental Physics, ITEP, Moscow, Soviet Union
25 INFN-Sezione di Napoli and University of Naples, Italy
26 Oak Ridge National Laboratory, Oak Ridge, Tennessee, United States of America
27 California Institute of Technology, Pasadena, California, United States of America
28 Carnegie Mellon University, Pittsburgh, Pennsylvania, United States of America
29 Princeton University, Princeton, New Jersey, United States of America
30 INFN-Sezione di Roma and University of Roma, "La Sapienza", Italy
31 University of California, San Diego, California, United States of America
32 Union College, Schenectady, New York, United States of America
33 Shanghai Institute of Ceramics, SIC, Shanghai, China
34 Central Laboratory of Automation and Instrumentation, CLANP, Sofia, Bulgaria
35 University of Alabama, Tuscaloosa, Alabama, United States of America
36 Purdue University, West Lafayette, Indiana, United States of America
37 Paul Scherrer Institut, PSI, Würenlingen, Switzerland
38 High Energy Physics Institute, Zeuthen-Berlin, Federal Republic of Germany
39 Eidgenössische Technische Hochschule, ETH Zürich Switzerland
40 University of Hamburg, Federal Republic of Germany
41 High Energy Physics Group, Taiwan, China
* Supported by the German Bundesministerium für Forschung und Technologie

References

[1] The construction of the L3 experiment, B.Adeva et al., NIM A289 (1990) 35-102.

[2] G. Stevenson and H. Taureg, Shielding of LEP experimental areas during LHC operation, CERN-TIS-RP/90-16.

[3] H. van der Graaf et al., Proceedings of the ECFA conference on instrumentation, Barcelona October 1989, Part 2; H. van der Graaf et al., "The honeycomb strip chamber: its application in SSC/LHC experiments and the test results of a prototype", submitted to Nucl.Instr.Meth..

[4] R. Santonico and R. Cardarelli, Nucl.Instr.Meth. 187 (1981),377; R. Cardarelli et al., Nucl.Instr.Meth. A236 (1988),20; M. Bertino et al., Nucl.Instr.Meth. A283 (1989),654.

[5] T.Akesson et al. Nucl.Instr.Meth. A241 (1985) 17, Nucl.Instr.Meth. A262 (1987) 243; B.Anders et al. DESY 86-105 (1986); E.Bernard et al. Nucl.Instr.Meth. A262 (1987) 229; G.. d'Agostini et al. Nucl.Instr.Meth. A274 (1989) 134; G.Drews et al. Nucl.Instr.Meth. A290 (1990) 335.

[6] BICRON Application Note SC-115 and references therein.

[7] B.Adeva et al. Nucl.Instr.Meth. A289 (1990) 35.

[8] E.Borchi et al. (SICAPO coll.), Phys. Lett. B 222 (1989),525

[9] G.Barbiellini et al. (SICAPO coll),NIM A235 (1985),55; G.Barbiellini et al. (SICAPO coll.), NIM A236 (1985),316; A.Nakamoto et al., NIM A238 (1985),53; A.Nakamoto et al., NIM A251 (1986), 275; M.Bormann et al.,NIM A240 (1986); SICAPO collaboration, Longitudinal and transverse development of electromagnetic showers using silicon detectors, CERN-EP/89-27, presented at the Int. Conf. on Advanced Technology and Particle Physics (Como, 13-16 June 1988).

[10] G. R. Stevenson, Calorimetry with silicon, presented at this workshop.

[11] J.Kirby et al., Report of the compact detector subgroup, Proc. of the Workshop on Experiments, Detectors and Experimental Areas for the Supercollider (Berkeley July 7-17, 1987), p. 388.

[12] K Furund et al., Neutron flux suppression with polyethylene moderators in the EMPACT silicon E.M. Calorimeter, presented at the Symposium on Detector R&D for the SSC (Fort Worth, 14-18 october 1990).

[13] SICAPO collaboration, Study of the local hardening effect from different low Z materials, paper in preparation.

[14] G. Lindstroem, Calorimetry with silicon, this workshop. P.G. Rancoita et al., Compensating silicon calorimetry for SSC/LHC colliders, presented at the Symposium on Detector R&D for the SSC (Fort Worth, 14-18 october 1990).

NEUTRINO PHYSICS AT LHC

Leslie Camilleri
CERN
(for the LHC Neutrino Working Group[1])

I. Introduction.

It has been pointed out[2] that a neutrino beam could be produced at LHC from the decay of charmed particles produced very abundantly in pp collisions at these energies. The advantages are

(i) the possibility to study ν_μ's and ν_e's at high energy (in excess of 500 GeV)

(ii) as many ν_e's as ν_μ's (unlike conventional neutrino beams obtained from π and K decay).

(ii) The possibility to discover the ν_τ.

Instead of beam-beam collisions at 16 TeV, a neutrino beam could also be obtained from $c\bar{c}$ production in interactions between one of the circulating beams and a gas-jet target (or an internal target such as the beam scrapers already planned for reducing the beam halo). Yet another possibility would be to extract continuously a fraction of the circulating beam and direct it to a beam dump to produce $c\bar{c}$ pairs.

II. Gas-jet in LHC.

The hydrogen jet[3] currently being used by UA6 in the SPS collider has a density of 4×10^{14} protons/cm^3 and a length of 0.8 cm. When coupled with the 4.8×10^{14} protons/beam planned for LHC, and the 11.246 kHz revolution frequency, a 1 cm long jet would yield a luminosity of

$$4 \times 10^{14} \text{ (protons/cm}^3\text{)} \times 1 \text{ cm} \times 4.81 \times 10^{14} \text{ (protons/beam)} \times 11246 \text{ (Hz)}$$
$$= 2.2 \times 10^{33} \text{ cm}^{-2} \text{ s}^{-1}.$$

If a heavy gas such as Xenon were to be used instead of hydrogen the luminosity could probably be increased substantially. However it is unlikely, for luminosity lifetime reasons, that a luminosity in excess of that available in an interaction region ($\sim 4 \times 10^{34}$ cm^{-2} s^{-1}) would be tolerated. Therefore this makes the use of a gas-jet somewhat questionable as the $\sqrt{s}$ of an LHC beam incident on a gas-jet is 123 GeV as opposed to 16 TeV. The $c\bar{c}$ production cross sections are therefore lower by a factor of 10 - 20 making the neutrino beams correspondingly less intense.

III. Extracted proton beam in a beam dump.

Here the idea is to peel off ~ 10^{10} protons/sec through, for instance, crystal channeling[4]. This extracted beam would be then directed into a beam dump. The luminosity would be given by

$$L = N/\sigma = 10^{10} / (50 \times 10^{-27}) = 2 \times 10^{35} \text{ cm}^{-2} \text{ s}^{-1}.$$

This very high instantaneous luminosity would be partly offset by the lower $c\bar{c}$ production cross sections at $\sqrt{s}$ = 123 GeV. The technical problems in the production of such a beam in a collider environment are of course formidable.

In view of the above the rest of this note will focus on $c\bar{c}$ production through beam-beam collisions.

IV. Production cross sections for $c\bar{c}$ production.

The production cross sections and x-distributions for $c\bar{c}$ production were estimated using the Quark-gluon String Model[5] (QGSM) of Kaidalov et al. The processes are described in figs. 1a, b, c). The following facts emerge from this computation.

(i) Process 1b) in which a D^0 or D_s is produced through the combination of two quarks within the ladder dominates over process 1a) in which the light quark in the D is one of the valence quark of the proton. As a result D production is a central process in this model; no "leading particle" effect is to be expected. The x-distribution is consequently soft.

(ii) At high energies, as at the LHC, there are as many s quark pairs as u or d pairs deep in the ladder. The c quark is therefore as likely to combine with an s as with a u quark resulting in similar cross sections for D^0 and D_s production.

(iii) The production cross sections are found to be 5 mb for $D\bar{D}$ production and 75 μb for $B\bar{B}$.

The processes included in Pythia[6] are shown in fig. 2. The production cross sections are found to be 0.75 mb for $c\bar{c}$ production, considerably lower than with QGSM. However a comparison of the x-distribution of D mesons obtained with the two methods shows them to be very similar when the difference in absolute cross sections is normalised out (fig. 3). It is found that

$$d\sigma/dx \sim (1 - x)^{12}$$

The probability of interaction of a neutrino in a detector is proportional to the neutrino energy. It is therefore useful to plot the energy weighted energy spectrum of the neutrinos from charm decays. This is shown in fig. 4 for muon neutrinos. Note that 15% of the interacting neutrinos have an energy greater than 500 GeV. The energy spectrum for tau neutrinos is shown in fig. 5. Here there are two components. The neutrinos coming directly from the D_s decay are soft because of the large mass of the

accompanying tau. The tau neutrinos from the decay of the tau have a harder spectrum and therefore are the main source of high energy neutrinos.

The angular distribution of neutrinos is also an important parameter as it determines the transverse size of a detector. This is shown in fig. 6 for electron neutrinos of more than 500 GeV. It can be seen that these neutrinos are peaked sharply forward and that it is therefore important for a detector to have a good acceptance at less than 5 mrad.

V. Detector.

(i) General.

Tau neutrinos would be detected through the reaction

$$\nu_\tau N \rightarrow \tau^- X$$

where the tau would be identified through its finite travel and subsequent decay. The signature would be to look for tracks with kinks or tracks with non-zero transverse impact parameters (fig. 7). Very good spatial resolution (~ 10 μm) and granularity (~ 100 μm) are needed. The technologies being envisaged[7] are silicon strips, liquid argon TPC or scintillating fibers.

For a ν_τ detector there are definite advantages in being as close to the interaction region as possible in order to minimize the physical dimensions, and therefore the cost, of this highly instrumented detector.

For a high energy ν_μ and ν_e detector the detection of the recoil hadrons require large calorimeters and therefore a large hall. On the other hand the granularity can be coarser thus allowing a bigger detector to be built. A location far from the interaction region would therefore be acceptable.

(ii) Location of Detector.

There are two alternatives as to the location of a neutrino detector. The first is to place the detector as close as possible to the interaction region. The advantage is that, for a given angular coverage, this minimizes the size of the detector. The disadvantages are that the background from interactions and from the beam halo can be considerable. Furthermore space is limited and in particular there is little room for shielding. The second alternative is to place the detector far enough away from the interaction region that the machine lattice has already curved the circulating beams away from the detector. This location would have a reduced background from beam-beam interactions, a reduced effect of the beam halo due to adequate room for shielding plus the sweeping of machine magnets and finally more space.

It may be that both solutions would be adopted : a close detector for ν_τ studies and a far detector for ν_μ and ν_e interactions.

(iii) Constraints from the LHC and LEP lattice.

The LHC magnets are 1.2 m above the LEP magnets. In principle the LEP quadrupoles in the straight section can be removed during LHC operation such that the

only constraints on placement of detectors come from the LHC lattice. The separation of the two proton beams is 18 cm up to magnets D2 (fig 8) at which point they start coming together to collide at the IP. The radius of the beam pipes is 2.5 cm which leaves 13 cm free space between beams for the placement of a detector. The main free areas are 99 m between Q4 and D2 and 29 m between D2 and D1. Any installation of a large ν_μ or ν_e detector in these two free areas would almost surely necessitate enlarging the tunnel to allow for the co-existence of the detector, cable tray, monorail etc. On the other hand it would be conceivable to install a small ν_τ detector between and surrounding the two beams either just before or just after D2. At 100 m a 2.5 mrad acceptance implies a 25 cm radius detector which is less than an LHC dipole. Of course, it would be traversed by the two beam pipes.

The other alternative is to place the detector far enough away that the curvature of the machine has already bent the LHC beams away from the 0^o line at that point. The minimum distance, L, at which this happens is a function of

θ = the maximum angular acceptance of the detector = 0.005 rad

d_i = the dead space between the edge of the detector and the beam due to cable trays etc.

L_B = the distance between the end of the straight section and the detector

θ_B = the bending angle per m = 0.006 rad/23 m.

Then, d, the distance between the 0^o line and the LHC beam at the detector is given by

$$d = \theta L + d_i \qquad [1]$$

and also by

$$d = \theta' L_B \qquad [2]$$

where θ' = angle between the 0^o line and the line joining the end of the straight section and the edge of the detector.

Equating[1] and [2]

$\theta_{L+} d_i = \theta' L_B = (1/2\ \theta_B L_B)\ \ L_B = 1/2\ \theta_B\ L_B^2$

$0.005\ (L_B + 248) + 1 = 0.006\ L_B^2$

using the length of the straight section as 248 m.

This gives L_B = 152 m, L = 400 m and a detector radius of 2 m.

It is of great interest to note that 497.2 m away from point 1 is a hall and access shaft, PM18, near the entry of one of the LEP injection lines. The 0^o line is 8.15 m from the beam at that point and is in the surrounding rock (fig. 9). It would be relatively easy to enlarge the existing hall to allow the installation of a neutrino detector in the 0^o line. One could then create a neutrino laboratory at moderate cost since all the needed infrastructure (electricity, water, ventilation, access shaft, lift....) already exists today.

VI. Event Rates.

The following assumptions have been made to calculate event rates : -

1) A luminosity of 4×10^{34} cm^{-2} s^{-1}
2) A run lasting 10^7 secs.
3) An angular coverage of $\pm$ 2.5 mrad.

(i). ν_τ detector.

Here a 10 m long detector with a radius of 25 cm and a density of 2 gm cm^{-3} has been assumed. The total weight is 4 tons and it would be located 100 m from the interaction region.

A total of 15400 ν_τ interactions in the detector are to be expected. In addition 72000 ν_μ and 72000 ν_e interactions would be observed.

(ii) ν_μ, ν_e Detector.

In this case a 15 m long detector with a density of 7.86 gm cm^{-3} and a total weight of 24 tons, has been assumed. A total of 430000 ν_μ and 430000 ν_e interactions are to be expceted of which 58000 of each type involve neutrinos of more than 500 GeV.

VII. Gas-jet revisited.

It was mentioned earlier that the use of a gas-jet to produce neutrinos would probably not be useful because of the smaller neutrino fluxes. However it could be that a jet would allow placing the detector in the 0^o line at distances smaller than 500 m. This would have definite advantages as far as detector size.

For instance a jet placed at the end of straight section 1 would halve the distance between the production point and PM18 thus reducing the detector size correspondingly.

Another attractive possibility would be to place the jet between magnets D_1 and D_2 on the outgoing beam from the IP (fig. 10). Magnet D_2 would then sweep the LHC beam away from the 0^o neutrino production line allowing the installation of a detector at 0^o in a cave excavated as shown in the figure.

Finally it is envisaged to install scrapers near the D_2 magnets near an interaction point to clean the beam continuously. These could potentially replace the gas-jet in the above discussion.

VIII. Outstanding problems.

1) ν Flux measurement.

Any neutrino measurement (other than the ν_τ discovery) needs an estimate of neutrino flux incident on the detector. Computing it with a Monte Carlo program is

problematic as $c\bar{c}$ production cross sections are relatively uncertain. One possibility would be to measure the flux of prompt muons also coming from $c\bar{c}$ decay. However the background from π, K decays could make this very difficult.

2) Background.

Is the background from muons through the detector excessive ? Can it be reduced through shielding ? Or through sweeping using either the machine magnets or dedicated iron torroids ?

3) Physics.

Quantify what would be learnt from a high energy $\nu_\mu + \nu_e$ beam ?

4) Detector size.

How big a ν_τ detector can be built realistically ?

5) Gas jet.

Can a gas jet or a scraper be competitive in the production of a neutrino beam ?

IX. Conclusion

The cross sections for $c\bar{c}$ production at LHC energies are large enough to envisage the production of a neutrino beam from $c\bar{c}$ decays. This beam would contain an equal number of ν_μ's and ν_e's unlike conventional beams. The energy spectrum of such a beam is such that more than 50000 interactions of each type of neutrinos with energy in excess of 500 GeV can be envisaged in a 24 ton detector in a one year run. The beam would also contain an appreciable number of ν_τ's resulting from D_s decays. This would allow the observation, and possibly the discovery, of the ν_τ.

An excellent location for a ν_μ, ν_e detector would be at the existing PM18 shaft, 500 m from point 1. A ν_τ detector could conceivably be located between and around the beams near the D2 bending magnet, about 100 m from an interaction point.

Although the $c\bar{c}$ production cross sections are at least an order of magnitude smaller at $\sqrt{s}$ = 123 GeV than at 16 TeV, a gas-jet or scraper could be competitive in the production of a neutrino beam as the detector could be close to the source and therefore smaller than for beam-beam collisions.

REFERENCES

1. Working group on neutrino physics : L. Camilleri, A. Capone, A. De Rujula, U. Dore, A. Erediddato, E. Fernandez, J. Gomez, A.B. Kaidalov, P.F. Lovere, V. Palladino, F. Pietropaolo, L. Rolandi, R. Santacesaria, S. Schlenstedt, F. Vanucci, K. Winter.
2. A. De Rujula and B. Rückl, Neutrino and Muon physics in the collider mode of future accelerators in Large Hadron Collider in the LEP Tunnel, Lausanne 1984, ECFA 84/85, CERN 84-10, Vol. II, p. 571.
3. L. Dick and W. Kubischta, Physics with jet targets at the SPS $p\bar{p}$ collider in Hadronic Physics at Intermediate Energy, T. Bressani, R.A. Ricci (Editors) Elsevier Science Publishers, B.V. 1986, p. 209.
4. H.W.A.Atherton et al., Crystal channeling at LHC, CERN SL/EA /Note 90-06
5. A.B. Kaidalov, Phys. Lett. 116B (1982) 459 and
   O.I. Piskounova, Inclusive distribution and Cross-Sections for hadroproduction of Heavy Flavoured Particles in Quark-Gluon Strings Model, Moscow 1990.
6. H.U. Bengtsson, T.Sjostrand LU-TP 86-22 (Pythia 5.3). Pythia 5.4 courtesy of T. Sjostrand.
7. For a more detailed discussion of detectors see the report by K. Winter on Neutrino Physics in the Standard Cross Sections part of these proceeding

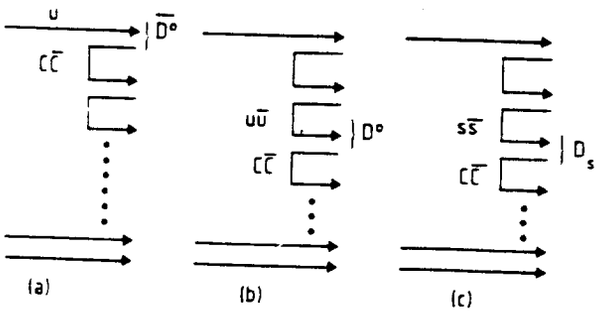


Fig. 1 The contributions to heavy quark production in the Quark-gluon-String Model (ref. 5)

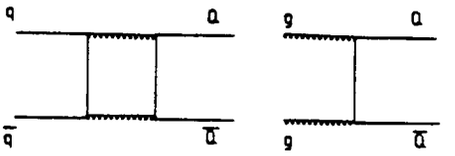


Fig. 2 The contributions to heavy quarkproduction used in the (ref. 6)Pythia Monte Carlo

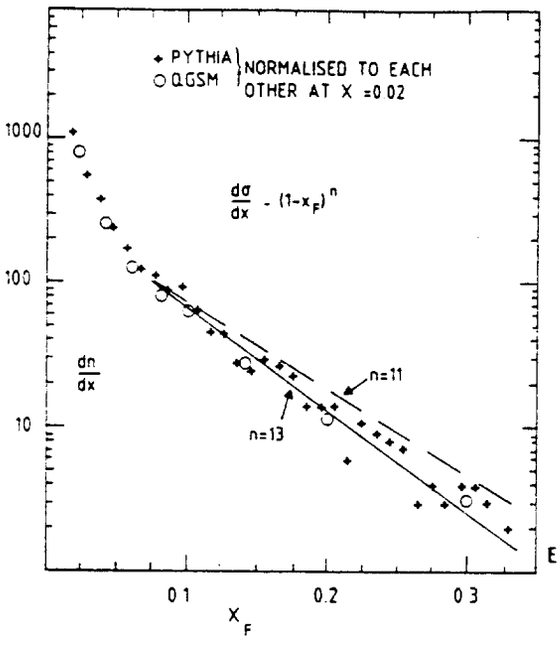


Fig. 3 The x distributions obtained using the QGSM (open circles) and Pythia (crosses) normalised to each other at x = 0.02.

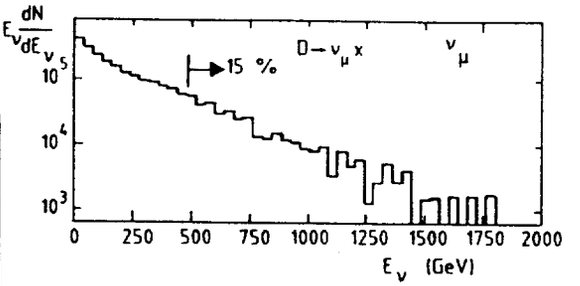


Fig. 4 The energy weighted energy spectrum of ν_μ's.

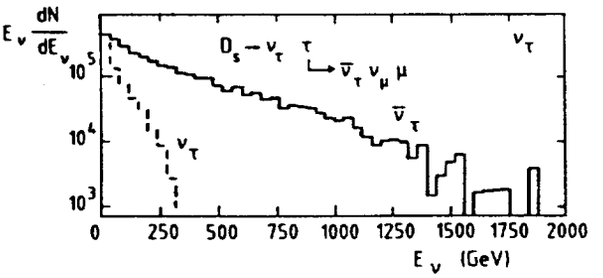


Fig. 5 The energy weighted energy spectrum of ν_τ's. The dashed curve is the contribution coming directly from D_s decays.

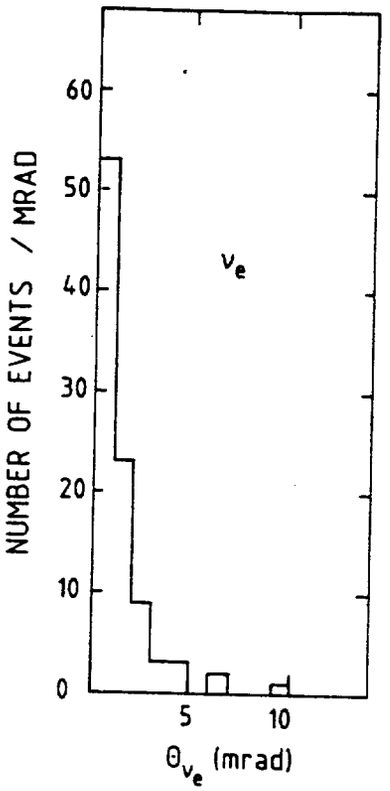


Fig. 6 The angular distribution of ν_e's of energy greater than 500 GeV.

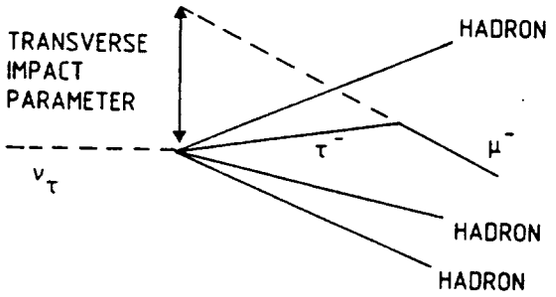


Fig. 7 A schematic representation of a ν_τ interaction, showing a kink in a track and a non-zero transverse impact parameter due to the τ decay.

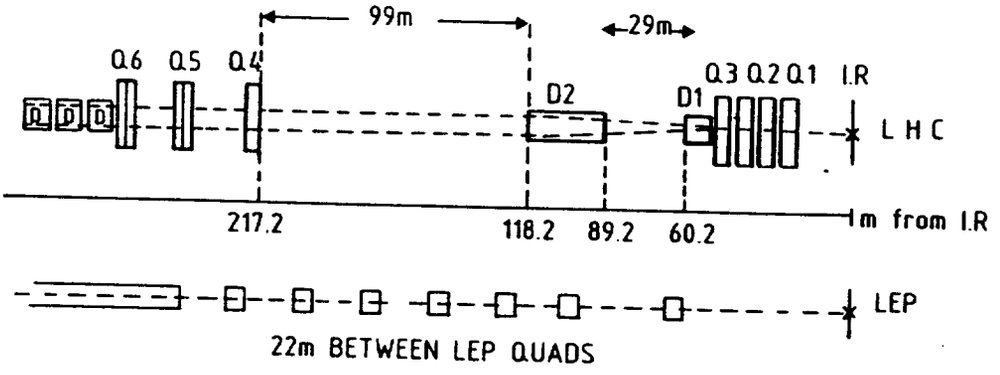


Fig. 8 The LHC lattice near an interaction point.

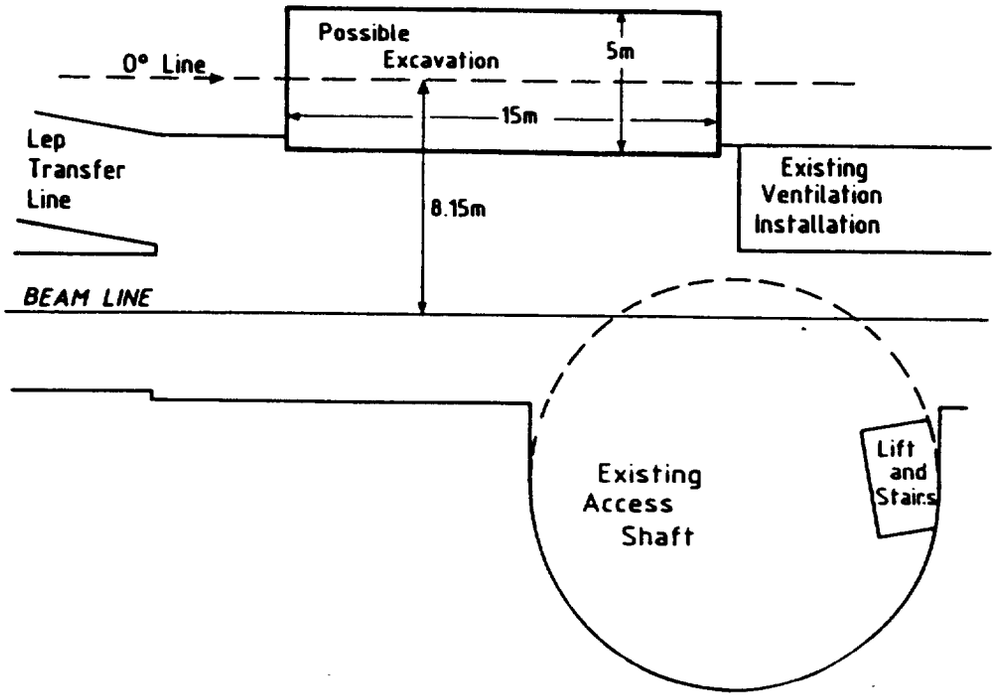


Fig. 9. The layout of the underground cavern near PM18, showing a possible excavation to include a neutrino detector along the 0^0 line from point 1 (~ 500 m away).

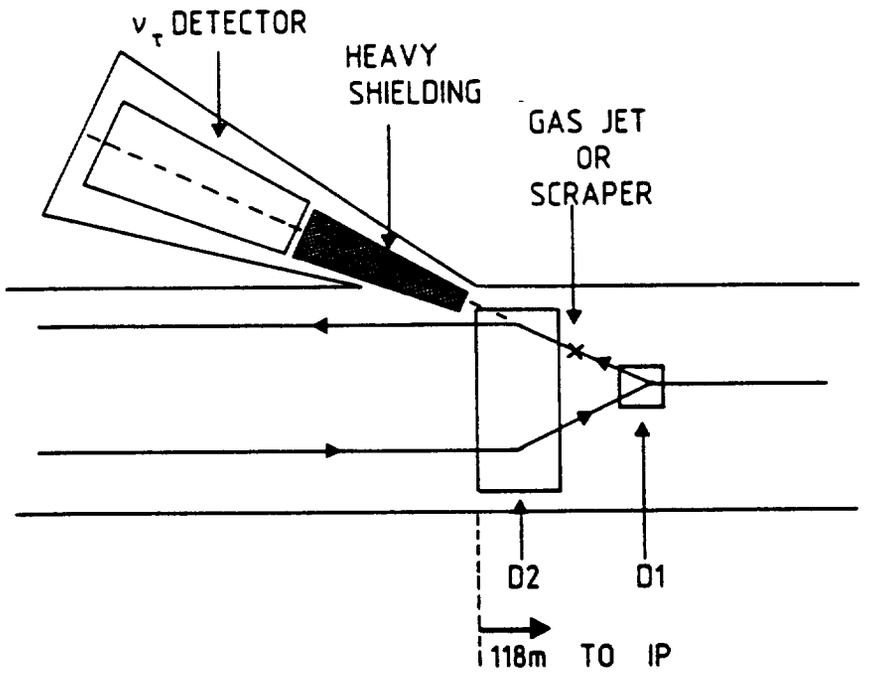


Fig. 10 A schematic representation of a gas-jet on the outgoing beam from an interaction region and just before the D2 bending magnet.

An e-p insertion for LHC and LEP

André Verdier
(CERN / SL Division)

1 e-p insertion

In order to obtain collisions with protons and electrons using LEP and LHC, the electron beam is steered towards the LHC plane and then deflected in order to make head-on collisions, the proton beam being kept in its plane. The topology of this arrangement is shown in fig. 1. The upwards deflection of the electron beam is done by dipole magnets

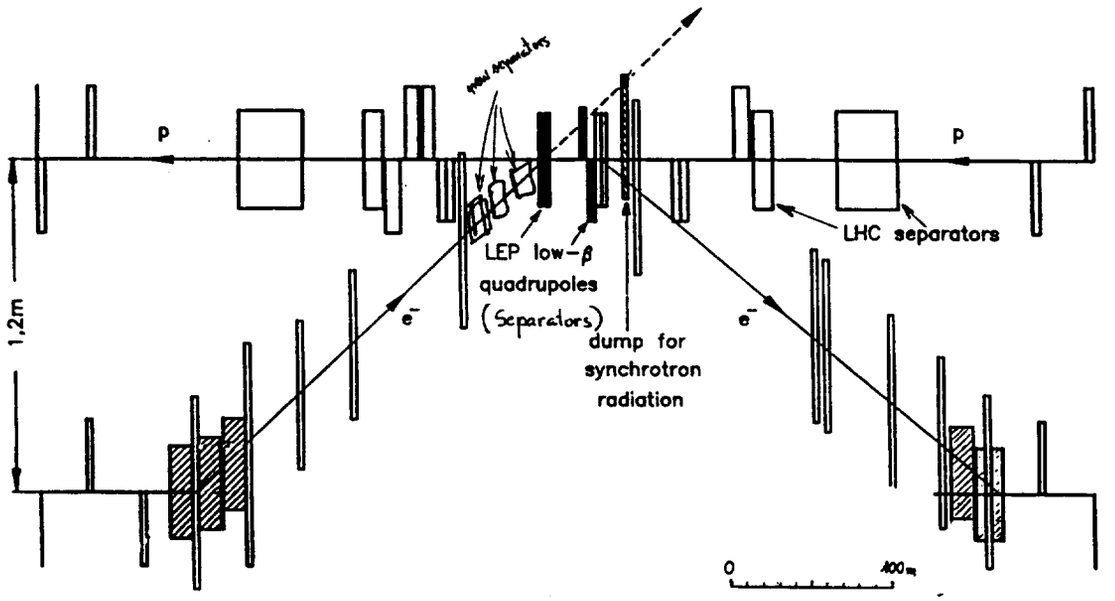


Figure 1
Layout of the e-p insertions in LEP and LHC

sitting close to the dispersion suppressor of LEP. The deflection which makes it come in head-on collision with the proton beam circulating in LHC is obtained by means of dipole magnets sitting close to the interaction region. After collision, the electron beam is deflected downwards with other dipole magnets and then steered into the LEP plane by means of dipole magnets sitting close to the next dispersion suppressor of LEP. The dipole magnets close to the insertion are called separators because they separate the electron beam from the proton beam thanks to the large difference between their momenta.

The synchrotron radiation emitted by the electron beam when passing in the separators poses a serious problem because it may disturb the experiment. In the presented scheme it was assumed that the synchrotron radiation emitted by the upstream separators had to pass through the hole of the forward calorimeter (see fig 2) so that no photon hits any element in the region around the crossing point. Such an arrangement has a serious drawback : for a given position of the aperture restriction due to the forward calorimeter, the length of the separators is a strongly decreasing function of the length of the calorimeter. This leads to use small bending radii which results in hard synchrotron radiations.

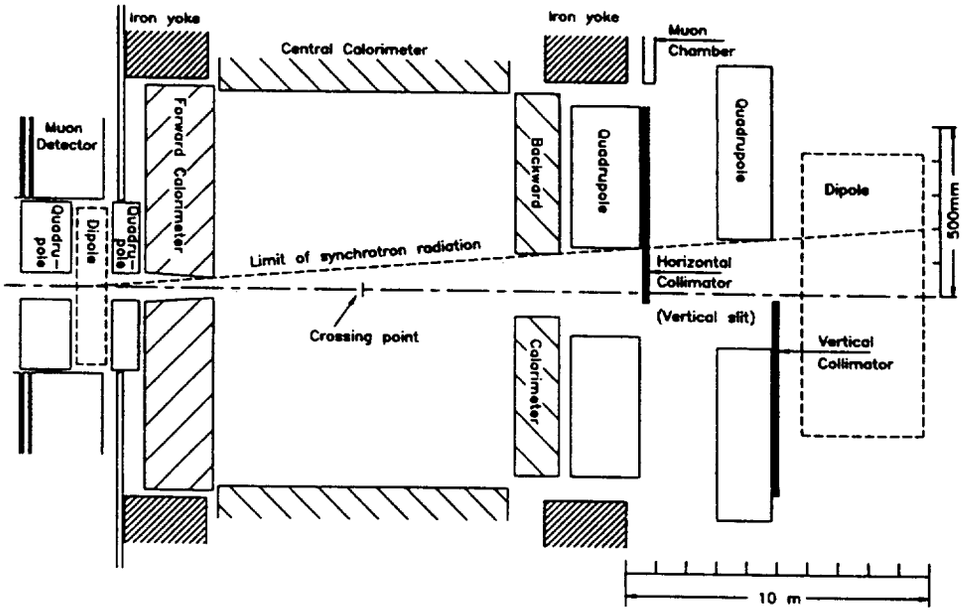


Figure 2

Layout of the e-p detector and low-β quadrupoles of LEP. The upstream separators consist of the two quadrupoles and the dipole inbetween, on the left of the figure. Their length of about 3.5m is such that the synchrotron radiation fan passes through the hole of the forward calorimeter of radius 30mm. Their deflection is 7mrad, leading to an average radius of 500m and a critical energy of about 1MeV.

With the geometry of the presented scheme the critical energy of the photons emitted by the upstream separators is around 1MeV and the synchrotron power around a quarter of a megawatt. Furthermore the length of the forward calorimeter has to be kept as small as possible. The radiation problem was seriously questionned. Such a big critical energy leads to a substancial creation of pairs of electrons and positrons which produces background in the experimental detector. This was such a concern to the experimentalists that an alternative solution was sought after the meeting. It was admitted that if the critical energy of the photons is below 50keV, most of the photons are easily absorbed and, for instance, the vacuum chamber in the forward calorimeter is sufficient to protect it against the radiations emitted by the upstream separator (W. Bartel). The separators consist then of low field dipoles upsteam and downstream the insertion. These are reffered to as 'new separators' on fig 1. This new arrangement suppresses the condition previously imposed on the length of the forward calorimeter : it can be made long enough to detect perfectly the hadronic showers. Another fortunate consequence of the lengthening of the separators is the reduction of the vertical emittance. The emittance of the electron beam can then be set at its optimum value. The luminosity gain with respect to the presented scheme was estimated after the meeting to be about 20% for the nominal energy of the electron beam of 60GeV.

However, as the critical energy of the synchrotron radiation varies with γ^3, the design of the separator scheme depends strongly on the working energy. It has been clearly established at the ' la Thuile ' worshop that, with the variation of the luminosity with energy obtained with the presented scheme, the most favourable conditions are low electron energy and high luminosity. This has been confirmed at the present meeting. Therefore the design of the separators will be done for an energy of the electrons of 60GeV.

2 Collision of electrons with deuterons

The deuteron nucleus is made from 3 u-quarks and 3 d-quarks. This quark system has a symmetry which makes the computation of the structure functions easier than for the case of protons. This is why collisions of electrons with deuterons are attractive.

Deuterons have been used at CERN for a long time. From the most recent experience, we can expect 10^{11} proton per bunches with the same emittance as that of protons. The intensity is smaller than that of protons because the acceleration of deuterons in the LINAC is less efficient. The emittance is the same : the normalised emittance of the deuterons is twice as small because their speed is half that of protons when they enter the booster which has a given admittance, then in the LHC the γ Lorenz factor of deuterons is half that of protons.

With this emittance and intensity it is then possible to optimise the LHC low-β insertion, so that finally the luminosity with deuterons is smaller than that with protons by only 10%. This is possible because the electron emittances can be made small enough with the separation scheme made with low-field dipoles, as well as the β^*-values in the LHC insertion. However making small β^*'s implies that large, although acceptable, β-values appear in the low-β quadrupoles of LHC. This makes the background due to the hadron beam potentially larger for the deuteron operation than for proton operation.

3 Callibration of the detectors with Z_0

The absolute callibration of the energy measured by the detector is necessary for a good determination of the differential cross sections. Setting the LEP enegy at 46.2GeV and using four bunches of electrons and positrons, it is possible to detect Z_0 events, the energy of which has already been measured within some 10^{-4}, to make this callibration. The positron beam will make synchrotron radiation in the forward calorimeter, which is not a problem since the callibration is necessary only for the central calorimeter.

The luminosity needed for this purpose is about $10^{30} cm^{-2} s^{-1}$. This makes a production of about 3000 Z_0 per day at the peak. The formula for the luminosity, is :

$$L = \frac{f_{rev} k_b N^2}{2\pi \sigma_h \sigma_v} \tag{1}$$

N is the number of leptons per bunch that we have to compute to obtain this luminosity, k_b is the number of bunches i.e. 4 here. The LEP optics used is the same as that used for e-p collision, i.e. the β^* values are 0.26m and 0.85m in the vertical plane and the horizontal plane respectively. The LEP horizontal emittance is taken to be the natural one for a 90° lattice at 46.2GeV, i.e. 11.9nm. The vertical emittance is taken to be a tenth of this, as presently achieved, since the contribution of the separators made with low-field dipoles is negligible. Putting those numbers in formula 1 we compute a needed number of leptons per bunch of 4.97×10^{10}, i.e. a current per bunch of 89.6μA. This has already been achieved in LEP with a 90° lattice.

The synchrotron power deposited in the forward calorimeter due to the electron beam is 21W. The beam-beam tune-shift parameters are respectively 0.017 and 0.03 in the horizontal and vertical plane.

The callibration of the central calorimeter by means of Z_0 events is then extremely easy.

4 Conclusion

The discussion about the proposed e-p insertion led to a complete redesign of the insertion optics. The basic solution was in fact obtained during the meeting thanks to the links with the CERN computer which was extremely effective.

The final design and performance analysis of the e-p insertion can be found in the CERN Divisionnal report : CERN SL/90-105(AP). The insertion described here has the maximum possible luminosity compatible with the maximum beam-beam tuneshift parameters. For an electron energy of 60GeV and a proton energy of 7.7TeV, it amounts to $2.8 \times 10^{32} cm^{-2} s - 1$. This relies on the fact that the parasitic mode losses in the superconducting cavities are non-resonant.

e-p Experiments in LEP / LHC Interaction Regions.

W.Bartel, DESY

Working Group: W.Bartel, E.Lohrmann, K.Potter, H.Taureg, A.Verdier

Abstract.

The requirements on the experimental areas and the LHC/LEP machine for e-p operation are investigated. Dedicated e-p running periods have to be allocated, because parasitic e-p operation appears not to be a viable option. Longitudinal lepton polarisation would enlarge the physics scope of the LHC/LEP collider. In order to control the relative normalisation of different experiments an overlap with HERA data is necessary. This overlap and a measurement of longitudinal structure functions would require running the proton beam at a lower energy of the order of 2 TeV. Certain isospin combinations of structure functions call for e-p and e-d collisions under the same kinematic conditions. In order to calibrate the calorimetry of an e-p experiment, e^+ e^- running on the Z^0 pole will be required. For some physics investigations it is desirable to accumulate data also on e^+-p interactions with the positrons circulating in the same sense as electrons. The size of an e-p experiment is such that it would fit into one of the standard LHC underground tunnels with a radius of about 15 m.

1 Introduction

Once a hadron collider is installed in the LEP tunnel, collisions between electrons or positrons stored in the LEP ring and protons from the LHC will become available, by steering the lepton beams head on against the proton beam. Interactions between 60 GeV electrons and 7.7 TeV protons will then considerably enlarge the kinematic range accessible to experiments as compared with HERA, where 30 GeV electrons will collide with 820 GeV protons [1].

By the time of this workshop the HERA experiments are in the middle of the installation phase and the work of the LHC e-p study groups was to a large extent inspired by the work performed for HERA. Any experimental experience

is, however, still missing and the e-p option for the LEP/LHC collider should be reviewed after a few years of HERA operation.

The main purpose of the present study is to evaluate the prevalent features of e-p experiments at LEP/LHC, to point out special measures which have to be taken to make these experiments feasible and to indicate open questions and areas of concern.

2 Machine Requirements

It is planned to install the LHC ring 1.2 m above the LEP ring. Therefore, in order to collide electrons with protons, the electron beam has first to be deflected upward before it is steered against the protons for head-on collisions. Finite crossing angles as in the case of proton proton collisions should be avoided in the e-p option, because the different shapes of the electron and proton bunches and the different tunes of the two machines may interfere and cause the proton beam to blow up. Therefore the coupling between the two beams has to be minimised.

Experiments are primarily affected by the synchrotron radiation generated in the vertical bends of the electron beam for which two off-axis quadrupoles and dipole magnets are employed. Fig. 1 shows a sketch of the magnet configuration close to the interaction point with a set of masks to protect the detector components around the interaction point. In the present design study, which was updated after the Aachen meeting, the last dipole magnet has a length of 25 m, providing a 2.5 mrad deflection [2]. Upstream masks limit the size of the synchrotron radiation cone such that it will pass through the beampipe inside the detector and the downstream quadrupoles. Behind the interaction region the synchrotron radiation photons are dumped into a low albedo absorber. Additional synchrotron radiation is emitted in the downstream bends, part of which is directed towards the superconducting LHC magnets, which have to be well protected.

The level of synchrotron radiation one has to face at LEP/LHC will be of the same order of magnitude as at HERA and it should be possible to design a system of masks, which is capable of reducing the rate of synchrotron radiation penetrating into the sensitive parts of the detector to a tolerable rate of about 10^8 photons per second.

The technical implications in designing the required set of masks and absorbers together with an appropriate deflection scheme should not be underestimated. The vertical bending has to be performed in steps with a large radius bend close to the interaction point as proposed. There may, however, be interference between the beam elements of the electron ring and the proton ring necessitating the design of special magnets.

The measurement of structure functions requires a precise knowledge of the absolute normalisation when combining data from different experiments. By the time LEP/LHC is in operation the majority of the data involved in such combi-

nations will be that recorded by the HERA experiments. It is therefore desirable that there should exist an overlap of the kinematic regions covered by the two machines. For this purpose operation at a reduced proton energy of about 2 TeV are requested at a luminosity not worse than that at 7.7 TeV.

The determination of structure functions is not only sensitive to the absolute normalisation of cross sections but also to the energy calibration of the calorimetry. Recording the decay products of Z^0's with an e-p detector offers a unique opportunity for an in situ calibration. Therefore, an option should be kept open to collide electrons and positrons on the Z^0 pole with a moderate luminosity of some 10^{29} cm^{-2} sec^{-1}. Of course an e^+ e^- operation will require a special beam pipe with appropriate synchrotron radiation masks.

At a later stage of e-p experimentation it will be desirable to also collide deuterons with electrons in order to access neutron structure functions and to separate isoscalar and isovector components in the nucleon structure.

A precise measurement of the proton structure function, F_2, as well a systematic study of radiative corrections involves a comparison of e^+-p with e^--p cross sections under the same kinematic conditions. Therefore an operation of LEP with electrons and positrons circulating in the same sense would be desirable.

Due to a mismatch of the RF systems in LEP and LHC, only 510 electron and proton bunches can be collided. This corresponds to a time between crossings of 164 nsec with a spatial bunch separation of nearly 50 m. Therefore there is sufficient space to separate the electron beam from the proton beam and also the detector performance profits from the long time, which is available for making trigger decisions. This feature of the e-p version is highly welcomed by experimenters.

Only dedicated e - p running should be considered, because parasitic modes of operation have distinct disadvantages and may even not be possible for technical reasons.

- Running the LHC in the p-p collision mode at the same time will lead to additional unwanted e-p collisions in the straight section, where electrons and protons are still on the same orbit.
- The circulation of additional beams will increase the background in an e-p detector.
- Running LEP in the e^+ e^- mode at the same time causes synchrotron radiation entering the interaction region from the 'wrong' side.

3 Detector Requirements

The aim of the detector considerations is not to design an e-p detector for LEP/LHC but rather to get a feeling for the size of such a detector with an estimate of the floor space required and the space in the interaction zone. Such a detector is sketched in Fig. 2.

An e-p detector has to be hermetic in order not to confuse NC and CC events from deep inelastic scattering. The two types of reactions are discriminated by missing transverse momentum measurements and in order to maintain a high resolution for missing p_t the angular coverage of the detector has to extend to very small angles w.r.t. the beam in particular in the proton (forward) direction, where one should aim for angles of about 10 mrad. In the backward hemisphere 30 mrad would be sufficient.

Due to the energy difference between the electron beam and the proton beam, the center of mass is not at rest in the laboratory frame and all secondary particles undergo a boost into the proton direction. As a consequence, the energy to be recorded is a function of the angle w.r.t. the beam line. Typical energies in the backward hemisphere (outgoing electron) are of the order of the electron beam energy. At around 90°, energies of the order of 100 GeV are expected and in the forward cone, 3 TeV of hadronic energy will enter the calorimeters. The depth of the hadron calorimeters will thus vary between about 6 interaction lengths in the backward hemisphere and 10 interaction lengths in the forward. A first guess of the space occupied by calorimetry may be obtained by assuming an effective interaction length $\lambda = 25$ cm plus half a meter for readout and cabeling. Adequate calorimeters for e-p detectors at LEP/LHC will be high density compensating calorimeters with an energy resolution of the order of $30\% / \sqrt{E}$ for hadrons and about $10\%/\sqrt{E}$ for electrons and photons. The granularity of the calorimeters is limited by the natural width of electromagnetic and hadronic showers i.e. by the Moliere radius and the effective interaction length. Typical cell sizes are 3×3 cm^2 for the electromagnetic section and 20×20 cm^2 for the hadronic section.

A tracking device inside a solenoidal magnetic field of typically 1.5 Tesla is needed for momentum measurements of individual particles, to support particle identification and jet reconstruction and for event reconstruction of low multiplicity events. The kinematic asymmetry of e-p interactions is accounted for by special tracking chambers in the forward cone. The space occupied by the tracking system and the solenoid is typically a cylinder with a diameter between two and three meters and a length of three meters in the proton direction and about 2 m in the backward hemisphere. Individual particle momenta are estimated to increase on the average by about a factor between 3 and 4 as compared with HERA, assuming some softening through increased gluon emission. A transverse momentum resolution of $\sigma\ (p_t)/p_t^2 = 0.2\%$ should be sufffficient. The central tracking system should be complemented by a vertex detector in order to tag long lived particles.

The instrumented iron yoke of the superconducting solenoid serves three purposes. It serves as a magnetic flux return, as a backup calorimeter to record hadronic showers leaking through the rear face of the central calorimeter, and it is also the main component of a muon spectrometer. The amount of steel necessary to serve these aspects of the yoke will be deterimened by the calorimetric and muon spectrometer properties. A total thickness of 2 m with a segmentation into 10 cm steel plates with 3 cm gaps for the active elements seems to be adequate.

In order to improve the momentum resolution for muons, additional magnetisation could be considered. The instrumentation will consist of large area detector planes, which are capable of serving as active elements in a calorimeter and at the same time record spatial coordinates for muon tracking.

In the forward direction the iron thickness of the magnet yoke is not sufficient to measure the charge of energetic muons. Therefore a toroid of magnetized iron interleaved with tracking chambers is installed around the first elements of the machine. The forward toroid can be considered as a fixed installation which does not move out of the interaction region together with the experiment.

4 Experimental Area

The e-p detector which has been sketched in the previous section represents a box about 17 m long and 15 m high. It is not centered in the interaction region. The total weight of the detector is estimated to be 15,000 tonnes. As demonstrated in Fig. 3 such a detector would fit into one of the standard LHC halls with a radius of 15 m. The length of the underground tunnel perpendicular to the beamline should be about 70 m to enable the experiment to be assembled outside the interaction region during LHC operation. The two positions of an e-p experiment, active position and garage position, are indicated in Fig. 3. With the experiment in the parking position there will be sufficient space for a shielding wall to separate LHC from the rest of the hall. As already mentioned, the muon toroid should be considered as a permanent installation. The design of the toroid has to allow for access to the machine components.

5 Summary and Conclusion

The investigations into an e-p experiment at LEP/LHC have shown that the standard infrastructure provided for LHC collider experiments is sufficient to accommodate an e-p experiment.

The requirements for e-p physics at LEP/LHC on the machine are such that only dedicated e-p running should be considered.

- The electron beam has to be deflected upward to the height of the proton beam. The absorption of the synchrotron radiation emitted in the bends has to be carefully studied.
- In order to fully exploit the physics capability of LEP/LHC it would be desirable to operate the LEP machine with electrons and positrons circulating in the same sense.
- In order to exploit as large a kinematic region as possible, LHC running at low energy of about 2 TeV is required. It is anticipated that the luminosity will be the same as for 7.7 TeV running.

- At a later stage of the e-p program electron deuteron-collisions could be considered as a useful complement of the physics program.
- Longitudinally polarized electrons would enlarge the physics scope of e-p experiments.
- In order to calibrate calorimeters in situ, e^+e^- running on the Z^0 pole would be desirable.

References

[1] J. Feltesse, These Proceedings, Vol. 1
R. Rueckl, These Proceedings, Vol 1
[2] A. Verdier, These Proceedings, Vol. 3

Figure Captions.

Fig.1 Synchrotron radiation profile in the interaction zone.
Fig.2 Sketch of an e - p experimental set up.
Fig.3 Accommodation of an e - p experiment in an LHC under ground hall.

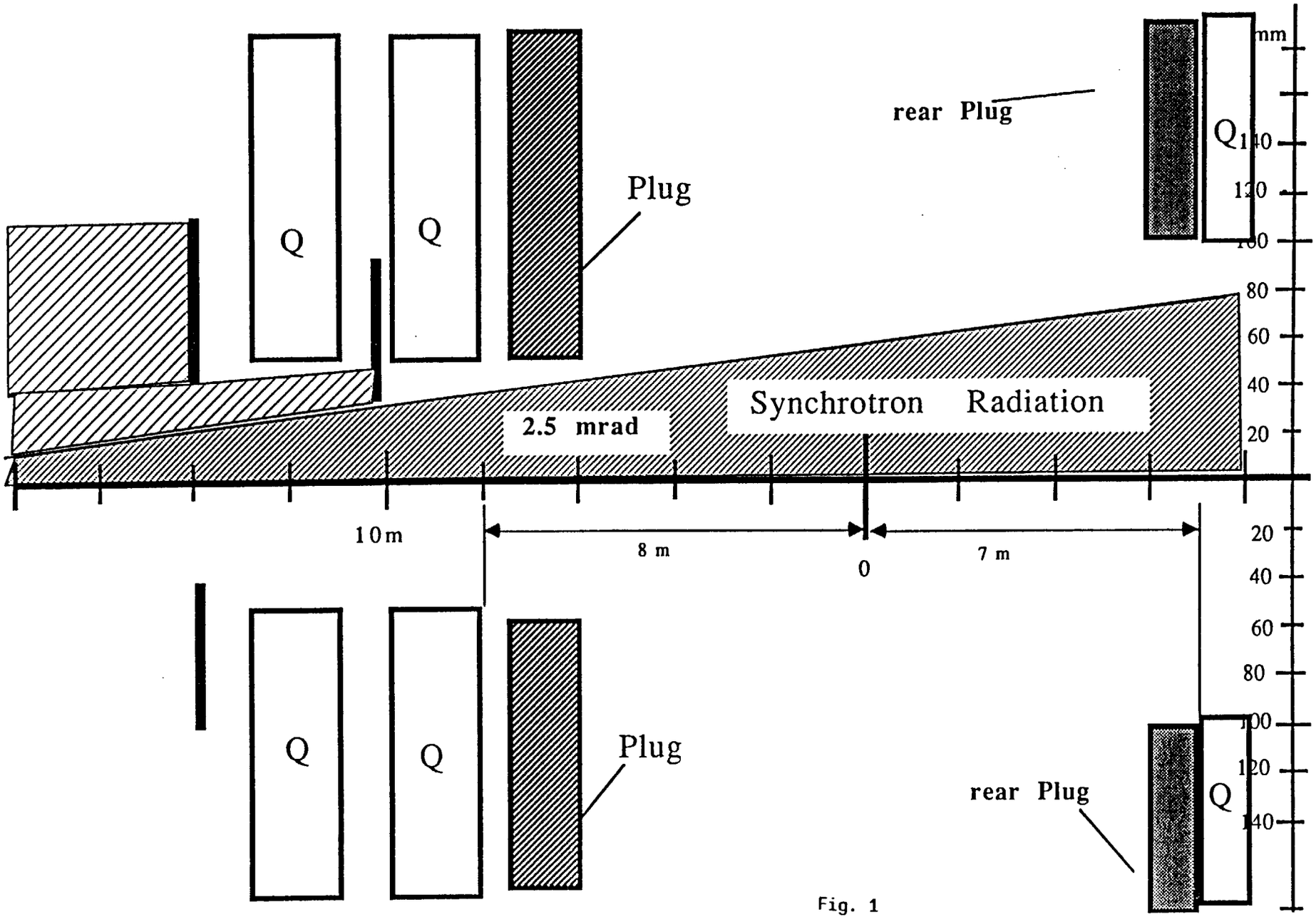

Q
Q
Plug
rear Plug
Q
mm
80
60
40
20
2.5 mrad
Synchrotron Radiation
10m
8 m
0
7 m
20
40
60
80
100
120
140
Q
Q
Plug
rear Plug
Q

Fig. 1

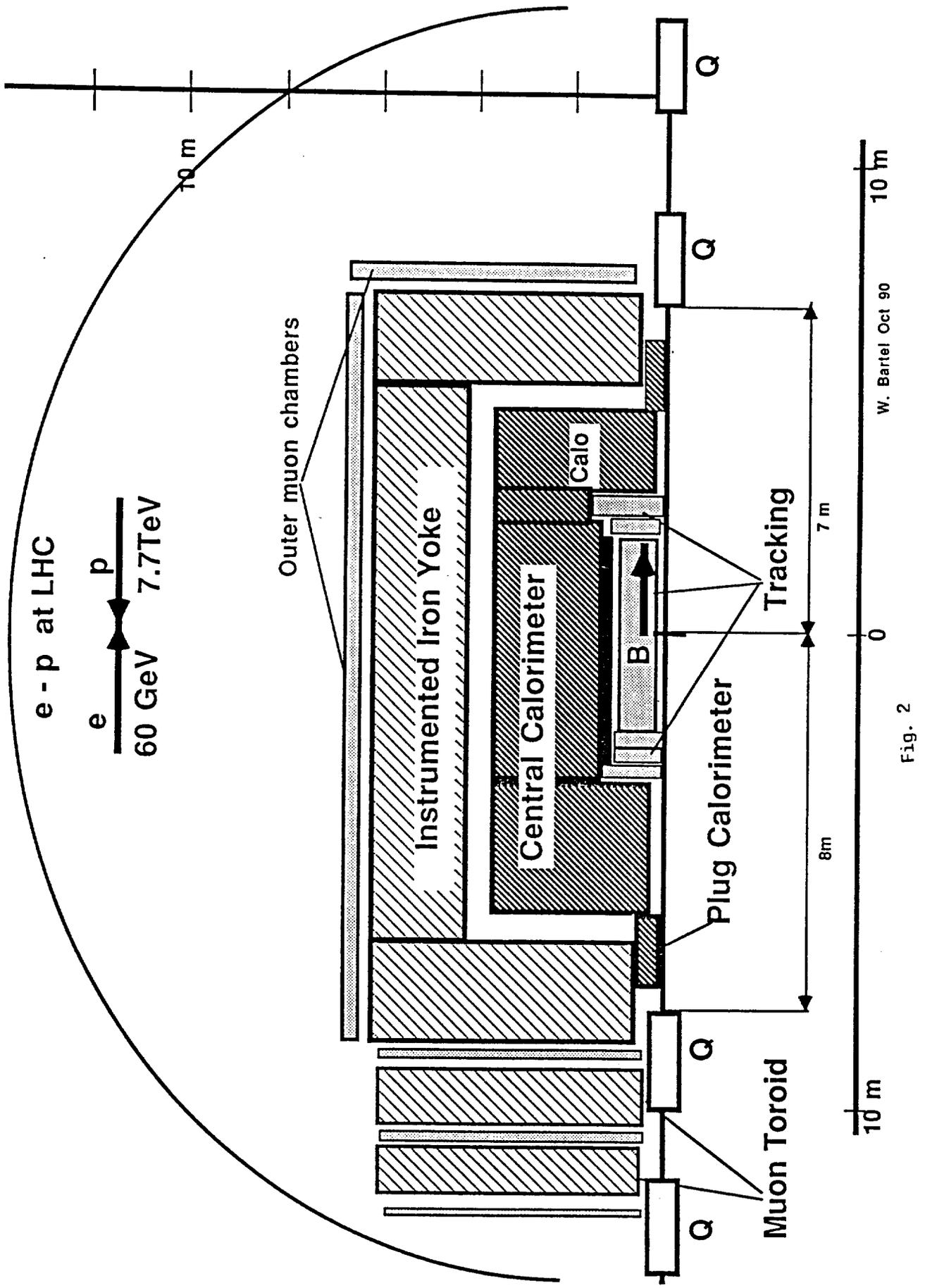
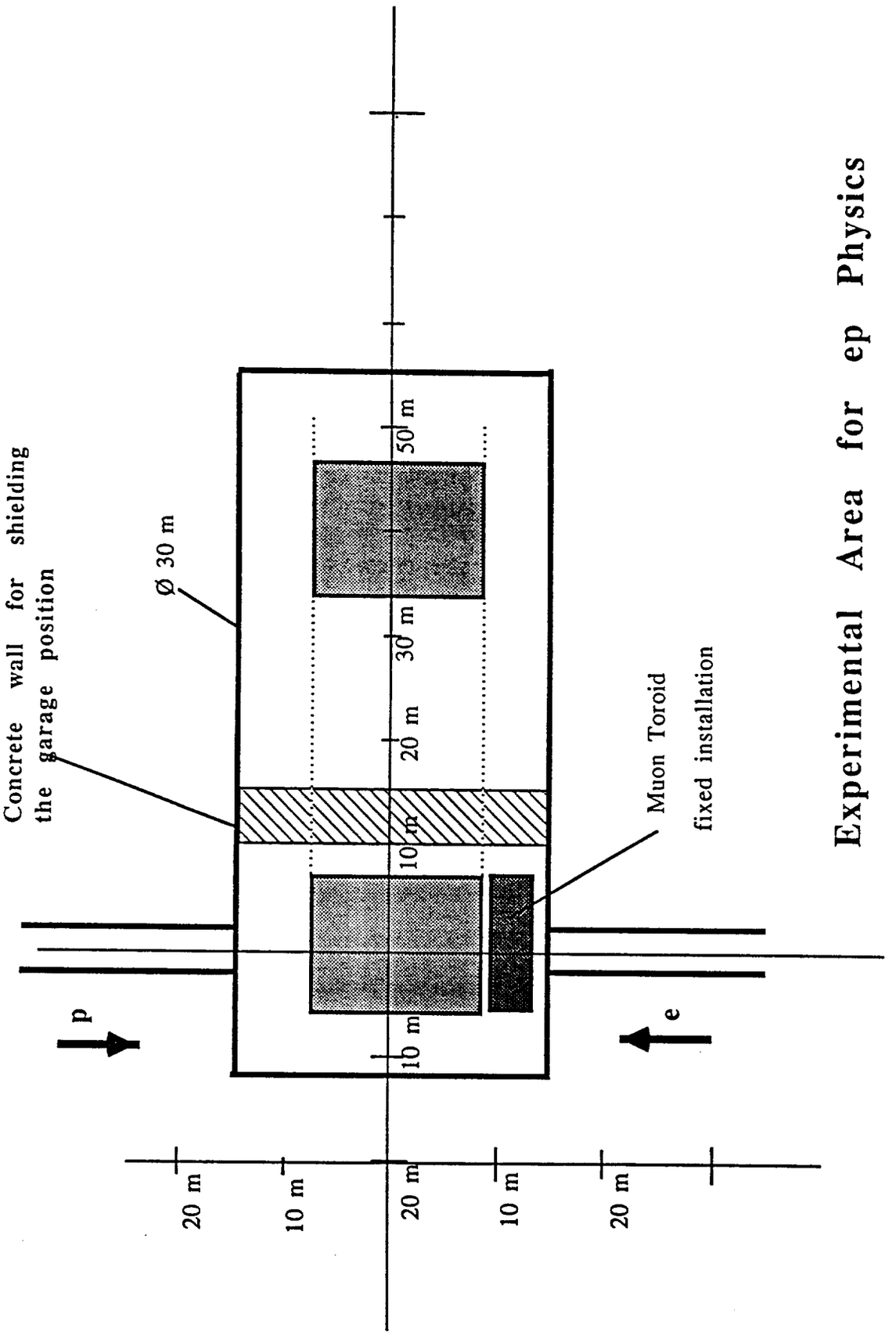

e - p at LHC
e
60 GeV
p
7.7TeV
10 m
Outer muon chambers
Instrumented Iron Yoke
Central Calorimeter
Calo
B
Tracking
7 m
Plug Calorimeter
8m
Muon Toroid
Q
Q
Q
Q
10 m
0
10 m
W. Bartel Oct 90

Fig. 2



Experimental Area for ep Physics

Fig. 3

ION COLLISIONS AT LHC

P. Sonderegger, CERN

Abstract

Ion-ion collisions at LHC energies are an urgent priority in view of assessing the Quark-Gluon Plasma and studying its properties. The emphasis is on low $p_\perp$ and the experiments will therefore be somewhat smaller and less heavy than p-p experiments. For A-A collisions, the energy density, the parameter which is relevant for QGP, is almost independent on the transverse energy, and has to be varied by varying the ion atomic number and/or the collision energy. An experimental programme based on usage of p-p detectors, plus a dedicated low $p_\perp$ detector located in a medium sized interaction region, should start right at the beginning of LHC operation.

1 Introduction

While we refer to H. Satz's and H. Specht's Plenary Session talks for a broad picture of the physics of the Quark-Gluon Plasma (QGP), whose study is the aim of ultrarelativistic ion collisions, and to H. Specht's talk for current ideas on detector layout, we recall in Section 2 those features which dictate the experimental effort. Section 3 states why the LHC option is first priority for QGP physics. Section 4 discusses the run strategy acknowledging that physics results are not really expected from a single Pb-Pb run, but rather from the atomic number and energy dependence of signals. In Section 5 we conclude.

2 Ion Collisions means Low $p_\perp$ Physics

Particle production has been found to follow a Boltzmann distribution, with $< p_\perp > \approx 2\ T$ and $T \approx 200$ MeV, all the way from the old PS data to the most recent Tevatron collider results. This is the principal experimental support of the idea of a first order transition between the QGP and the Hadron Gas at a temperature $T_c \approx 200 MeV$: Hadrons would be formed, at the energies explored so far, near and at the constant temperature and pressure characteristic of a mixed QGP - HG phase. The first goal of an LHC experiment with ion beams is then to follow this trend to the highest energy densities by measuring number and $p_\perp$ distributions (up to a few GeV/c) of the wealth of produced particles. The ratio of strange to non-strange particles, the correlation between pairs of identical particles of similar momenta ("interferometry"), and the comparison of baryon and meson $p_\perp$ distributions are among the main QGP signatures.

The $p_\perp$ distributions of direct photons and the mass distributions of thermal dileptons are in principle of even greater interest, since they are produced by the QGP itself in the earliest phases of the reaction, and leave the interaction region without reinteracting. Again, these are low $p_\perp$ particles; the experimental problem comes from the enormous background of photons and leptons from ordinary sources which must be understood and subtracted first — a task which may well turn out not to be feasible.

A different type of signature, known presently under the name of "J/Ψ suppression", concerns the heavy quarkonia, which cannot survive in a hot plasma (initial temperature $T \geq 1.2 \cdot T_c$). At LHC energies, most J/Ψ's come from b's decaying far away from the interaction region. One will rather look for the survival of the Υ's, over a $\sim$ 10-20 GeV $p_\perp$ range. This requires a measurement of the leptons (e or μ) into which they decay, in a comparable $p_\perp$ range, with reasonably good resolution such as to measure pair invariant masses to 100 MeV precision.

All these signatures require rather more conventional detectors than those envisaged for p-p reactions, except for the granularity which must be adequate for several thousand particles per unit of rapidity, as anticipated for central Pb-Pb reactions. Some of the p-p detector designs now under study may be adequate for the hard signatures, such as the Υ survival.

3 LHC is Highest Priority for QGP Search

The heavy ion physics is governed by a unique variable, the energy density ϵ, which measures the initial reaction temperature, as well as the probability to form a QGP. Following Bjorken, it is expressed as

$$\epsilon = \frac{dE_T}{dy} \cdot \frac{1}{A_\perp \cdot c\tau_0} \tag{1}$$

where E_T is the total transverse energy of all produced particles, $A_\perp$ is the transverse area of the collision, and $c\tau_0 \approx 1$ fermi the formation time of quarks or hadrons. The maximal energy density is obtained as a function of the nucleon-nucleon c.m. energy $\sqrt{s}$ and the atomic number A of the colliding nuclei as

$$\epsilon_{max} \simeq 0.2 \cdot ln\sqrt{\frac{s}{1GeV^2}} \cdot A^{\frac{1}{3}} \tag{2}$$

where a conservative $ln\sqrt{s}$ energy dependence of the particle rapidity density and a constant $< p_\perp > \simeq .4\ GeV/c$ have been used.

Table 1 shows various machines with the attainable energy densities. JACEE stands for the cosmic ray experiment which sent a calorimeter to the stratosphere [1] and found half a dozen events at energies 1 to 2 orders of magnitude above the SPS ions exhibiting high and quickly rising values of $< p_\perp >$. This is still the only — and scanty — evidence, even after 4 years of ion experiments at SPS and AGS, for a possible hot QGP phase manifesting itself beyond the

Accelerator	Cosmic	SPS	Tevatron	RHIC	LHC	LHC	LHC
Particle	C..Si..	S,Pb	$p\bar{p}$	Au-Au	Pb-Pb	d-d	Pb-Pb
$\sqrt{s}$ (GeV)	JACEE	20	1800	200	6400	6400	360
ϵ_{max} (GeV/fm^3)	$\sim$7	3.6	$\sim$6	6.4	10.4	$\sim$ 2.2	7

Table 1: **Nucleon-nucleon c.m. energies and maximal energy densities.**

$< p_\perp >$ plateau indicative of the mixed phase. Only the LHC, not RHIC, will clearly exceed the JACEE energy densities. A further and handsome advantage of LHC over RHIC is the expected increase by three orders of magnitude in the event rate for Υ's (see [2]).

4 Studying QGP is Varying A and/or $\sqrt{s}$

The existence of an absolute signature for QGP is very unlikely. All QGP searches done so far have consisted invariably in plotting signals against the energy density ϵ, or a related variable. In collisions between light beam ions and heavy targets, this was mostly achieved by varying the transverse energy E_T . It is not always realized that in collisions between identical ions, say Pb-Pb, E_T is *not* a measure of ϵ, since when one moves from central (impact parameter zero) collisions to less central collisions, the overlap area $A_\perp$ in eq. (1) decreases at first *faster* than dE_T/dy; overall, the energy density ϵ is almost constant and equal to ϵ_{max} for almost the full E_T range. It will obviously be interesting to check the E_T independence of the potential signals. But the main goal, *varying* ϵ, will only be achieved for A-A collisions at LHC by *varying the atomic number A and/or the nucleon-nucleon c.m. energy* $\sqrt{s}$. The last columns of Table 1 exemplify the two possibilities.

Varying A from deuterons to Pb opens up a wide range in ϵ (almost a factor 5). Event rates can even increase with decreasing A, since the cross section decrease for rare events ($\sigma \propto A^2$ for, say, Υ production), is more than offset by the increase in luminosity with the more intense ion beams available at lower Z. The only drawback on a strategy based on varying A is the fact that the reaction volume, which is clearly related to thermalization, varies at the same time.

Varying ϵ *at constant volume* can in principle be obtained by varying $\sqrt{s}$. The span in ϵ is small, a mere factor 1.5 from injection to maximal energy. Running a superconducting collider at energies much below nominal is difficult and the luminosity is expected to decrease with decreasing energy faster than the beam energy [3]. It may then be preferable to compare LHC with RHIC and SPS results, taking into account the differences in apparatus. Last not least, the underlying physics has a natural tendency to get richer with increasing energy; e.g. the J/Ψ production goes through a totally different mechanism at the LHC than at the SPS. To summarize, varying ϵ at constant volume is not only impractical, but in some cases meaningless.

The possibility of collisions of ion beams with fixed gas jet targets (from Hydrogen to Xenon) has not aroused strong interest. The potential bonuses of a point-like, immaterial target, of a handsome luminosity with relatively little cost to the lifetime, and of a moving centre-of-mass do not appear to outweigh the severe loss in c.m. energy.

Finally, asymmetric collisions, in particular p-A, appear to be in principle possible in LHC. These are being advocated on the grounds that the physics may, even in the present SPS and AGS data, manifest itself in the *difference in A behaviour* in A-A as compared to p-A. More work is needed here.

5 Conclusions

Ion collisions at LHC are *the* way to *study the QGP phase well beyond transition temperature*. Some of the most promising signatures (the Υ's; jets) accessible at LHC are possibly beyond reach at RHIC.

Most relevant signatures and quantities to be measured should be within reach of a detector of moderate size and weight (albeit immoderate complexity). An interaction region like No. 5 (Cessy), whose geology makes it somewhat uncomfortable and costly for large p-p experiments, is well suited to accomodate, right from the start of LHC operation, a dedicated detector for ion-ion collisions to be debugged on minimum bias p-p events, exploited with ions during a small fraction of the year, and possibly rolled away from the beam for the rest of the time. First designs are appearing [4], at a time when the understanding of the accumulated data is growing and practical experience with more daring concepts is starting.

The "hard" signatures are hoped to be accessible also for some of the forthcoming p-p detectors. The explorative nature of the search for the Quark-Gluon Plasma and its properties, and the breakthrough to be expected at LHC energies, call for short runs right from the beginning of LHC operation, rather than for long runs later.

References

[1] T. Burnett et al., Ph.Rev.Lett. 57 (1986) 3249.

[2] P. Sonderegger, Dilepton Physics with Ion Beams at LHC, these Proceedings.

[3] I am indebted to D. Brandt and W. Scandale for enlightening me on the non-desirability of running the LHC below maximum energy.

[4] H. Specht, Ion-Ion Collisions at LHC (Experiment), Plenary Talk, these Proceedings.

FAST MUON TRACKING WITH RESISTIVE PLATE CHAMBERS

R. Santonico
INFN - Sezione di Roma " Tor Vergata "
Via E. Carnevale, Rome, Italy

ABSTRACT

The possibility to use Resistive Plate Chambers for the muon detection at the future accelerators is considered. Experimental results on muon tracking are presented.

The Resistive Plate Chambers (RPC) [ref 1], whose sketch is shown in fig. 1, are gaseous detectors working with a uniform field of about 5 KV/mm generated by two parallel electrode plates of a plastic phenolic material with a bulk resistivity ranging in the interval $10^{10} - 10^{12}$ $\Omega \times$ cm. The electrode plates are separated by a 2 mm gap filled with a argon-butane mixture, usually in the ratio 60/40 in volume, and a small amount of freon. Construction details of a RPC are visible in the photograph of the fig.2.

The discharges developing in the gas are quenched by the high resistivity of the electrodes whose effect is to extinguish the field in a limited area of a few mm^2 around the discharge point, producing a local dead time of about 10 ms but leaving the rest of the chamber active.

Electric signals originating in the discharges are induced in a system of pick-up electrodes which can be shaped, with the required precision, e.g. on a printed board of high mechanical standard pressed against the external surface of the chamber. The reconstruction of a muon track can be related in this way to the position of a few such boards and turns out to be independent on the mechanical accuracy of the chamber itself.

The most actractive feature of the RPC concerning the muon physics at the future accelerators is their capability to identify the bunch crossing in which a given event has been generated. The low signal intrinsic delay, of the order of 10 ns,

with respect to the time in which the gas has been ionized and the time resolution, of about 1 ns, should make this identification possible even for interbunch times as short as 16 ns as expected for LHC.

On the other hand, it has been shown [ref 2] that even a low resolution tracking based only on the read-out electrode segmentation of the RPC, would allow to realize a simple, very fast muon multiplicity trigger capable to discriminate high energy muons through their low magnetic bending, allowing to eliminate soft muon background.

A much higher spatial resolution can be obtained from the barycenter of the charge induced in a few contiguous read out strips. Although it has not yet been proved so far that this method would allow to obtain with RPC the resolution required for a good muon tracking, i.e. a few hundreds of microns or better, this is an extremely interesting possibility to study, with the purpose to unifie in a single detector both the triggering and tracking functions.

Finally the RPC are built of standard commercial plastic materials. This makes them unexpensive, easy to be industrially produced, and suitable to realize even very large detectors such as those presumably needed for the muon detection at the future accelerators.

RPC are already in use in accelerator and cosmic ray experiments. As an example their use in the Fermilab E771 experiment [ref 3] is described. Fig.3 shows the lay-out of the experiment searching for beauty particles produced by a proton beam in a fixed silicon target.

Three planes of RPC shielded by iron absorbers are used as a very fast, coarse muon tracker giving a first level trigger signal for events with one or more muons coming from the target. Each plane of sensitive area 18 m^2 consists of 10 chambers, as shown in fig.4, read-out by squared (12×12 and 6×6 cm^2) and rectangular (6×12 cm^2) pads. The detection efficiency and the time resolution vs. the applied voltage are given in fig.5a and 5b respectively. An example of dimuon event is shown in fig.6.

Specific tests of RPC have been recently carried out at the H2 and X1 beams of the CERN [ref 4] with the purpose to:

a) Track high energy muons

b) Measure the punch through of pions in iron

In the test at the H2 beam, eight chambers of 2×1 m^2 (fig.7) read out by pick-up strips 3 cm wide and interleaved with five iron absorbers 40 cm thick were installed downstream of the UA2 calorimeter, about 6 λ thick, and irradiated with muon and pion beams.

The hit patterns of a 220 GeV muon and a 40 GeV pion are shown in fig.8. The punch through measured at various iron depths for 70 GeV pions is compared in fig.9 with the Geant 3 simulation of the test.

Finally the detection efficiency vs. the applied voltage is given in fig.10 for the chambers utilized at the X1 beam. The above tests showed that the chambers were fully efficient at the rate of 50 particles/cm^2 sec.

REFERENCES

1- R. Santonico, R. Cardarelli: N.I.M. 187, 377(1981)

R. Cardarelli et al: N.I.M. A263 ,20(1988)

M. Bertino et al: N.I.M. A283, 654(1989)

NADIR - G. Bressi et al: N.I.M. A261, 449(1987)

FENICE Collaboration: LNF-87/18 (1987)

2- E. Petrolo: Contribution to this workshop

3- F. Grancagnolo: Private communication

4- C. Bacci, R. Cardarelli, F. Ceradini, A.Di Ciaccio, G. Ciapetti, F. Lacava, E. Petrolo, R. Santonico, L. Zanello and S. Veneziano: "Test of resistive plate counters with pion and muon beams", to be published

FIGURE CAPTIONS

Fig 1- Sketch of a RPC.

Fig 2- Photograph of a RPC sectioned at one corner. The internal spacers, the graphite painted electrodes and the PVC film insulating the pick-up strips from high voltage are clearly visible.

Fig 3- Lay out of the Fermilab E771 experiment.

Fig 4- Detailed view of one of the RPC planes utilized by the muon trigger system of the experiment.

Fig 5- a) Efficiency versus high voltage for a RPC of the Fermilab E771 experiment. Butane/Argon = 0.8, Freon = 3%, discrimination threshold = 90 mV. Pad of 12×12 cm^2.

Fig 5- b) Time resolution vs. voltage. Butane / Argon = 0.67 , Freon = 5%.

Fig 6- Example of a dimuon event.

Fig 7- Lay out of the test carried out at the H2 beam of the CERN.

Fig 8- Hit pattern of a 220 GeV muon (8a) and a 40 GeV pion (8b).

Fig 9- Punch through measurements for 70 GeV pions in iron and comparison with the Geant 3 simulation of the test.

Fig 10- Efficiency vs. voltage for the chambers utilized in the test at the X1 beam.

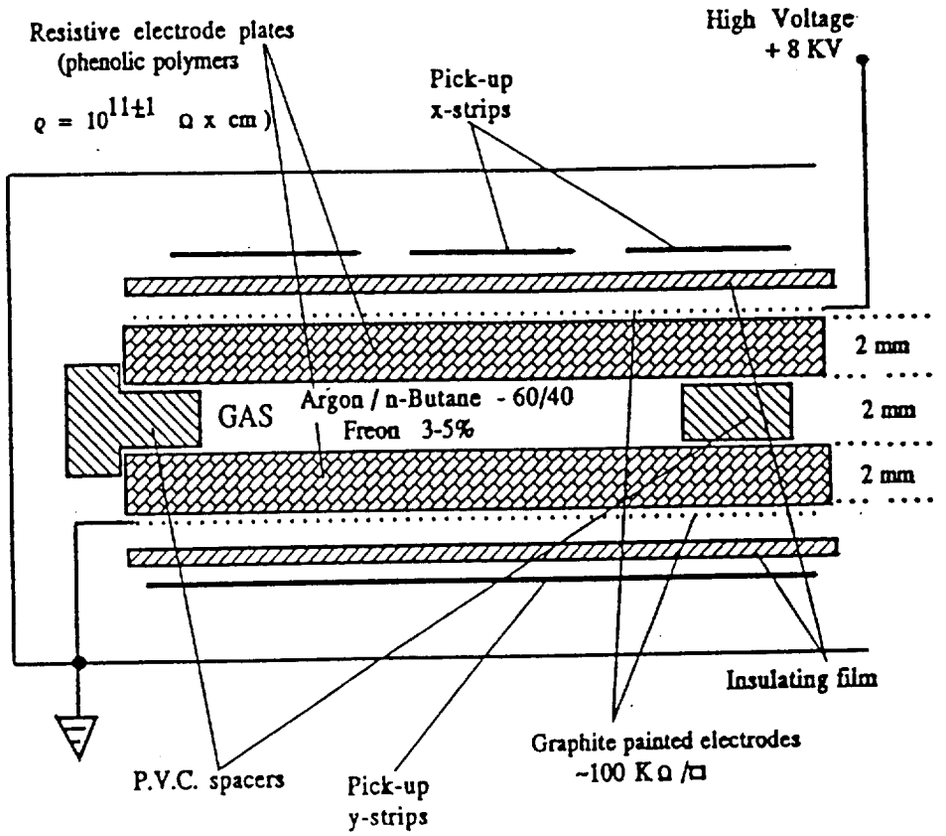

Resistive electrode plates
(phenolic polymers
ρ = 10^11±1 Ω x cm)
High Voltage
+ 8 KV
Pick-up
x-strips
2 mm
GAS
Argon / n-Butane - 60/40
Freon 3-5%
2 mm
2 mm
Insulating film
Graphite painted electrodes
~100 KΩ /□
P.V.C. spacers
Pick-up
y-strips

FIG 1

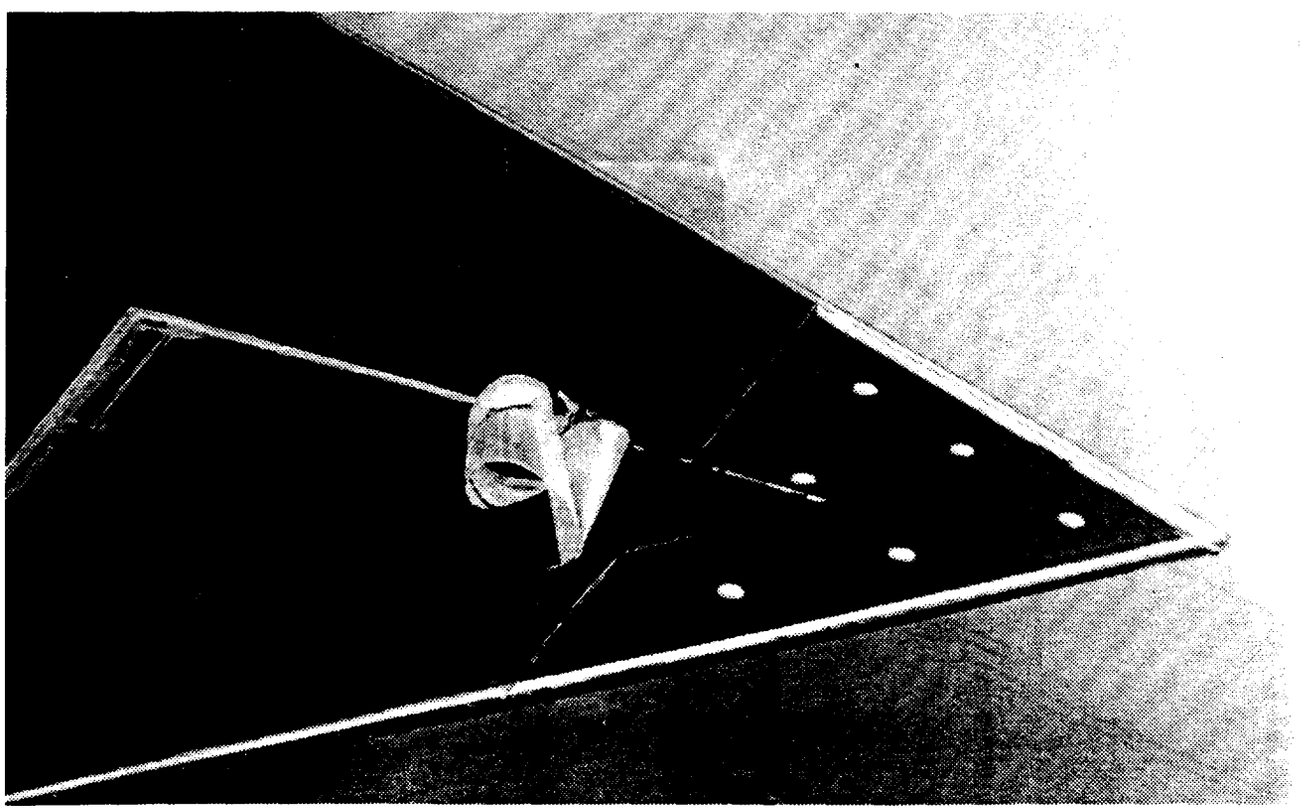


FIG 2

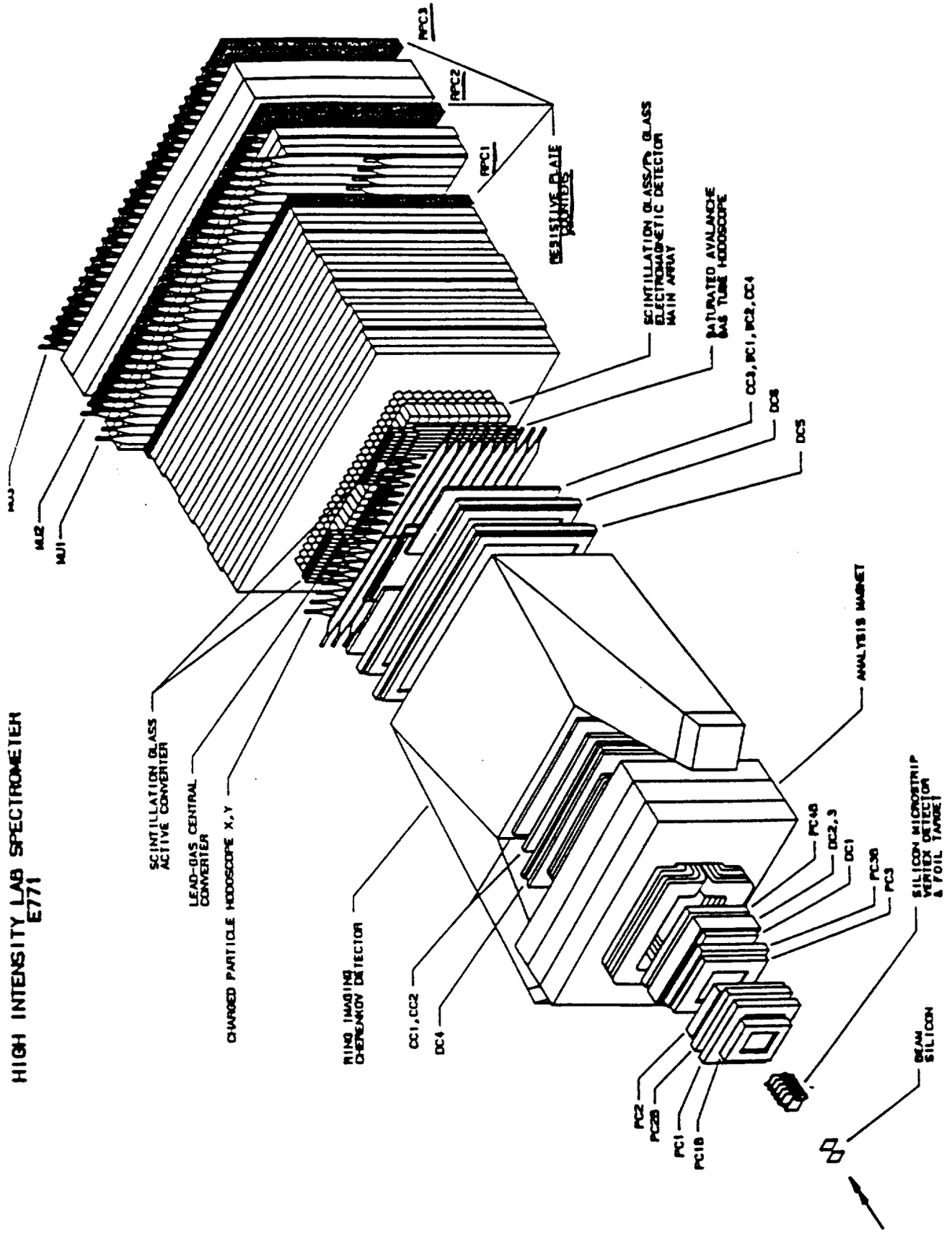

HIGH INTENSITY LAB SPECTROMETER
E771
RPC3
RPC2
RPC1
RESISTIVE PLATE COUNTERS
SCINTILLATION GLASS/PB GLASS ELECTROMAGNETIC DETECTOR MAIN ARRAY
SATURATED AVALANCHE GAS TUBE HODOSCOPE
CC3, PC1, PC2, PC4
DC6
DC5
MU3
MU2
MU1
SCINTILLATION GLASS ACTIVE CONVERTER
LEAD-GAS CENTRAL CONVERTER
CHARGED PARTICLE HODOSCOPE X,Y
RING IMAGING CHERENKOV DETECTOR
CC1, CC2
DC4
ANALYSIS MAGNET
PC4B
DC2,3
DC1
PC3B
PC3
SILICON MICROSTRIP VERTEX DETECTOR & FOIL TARGET
PC2
PC2B
PC1
PC1B
BEAM SILICON

FIG 3

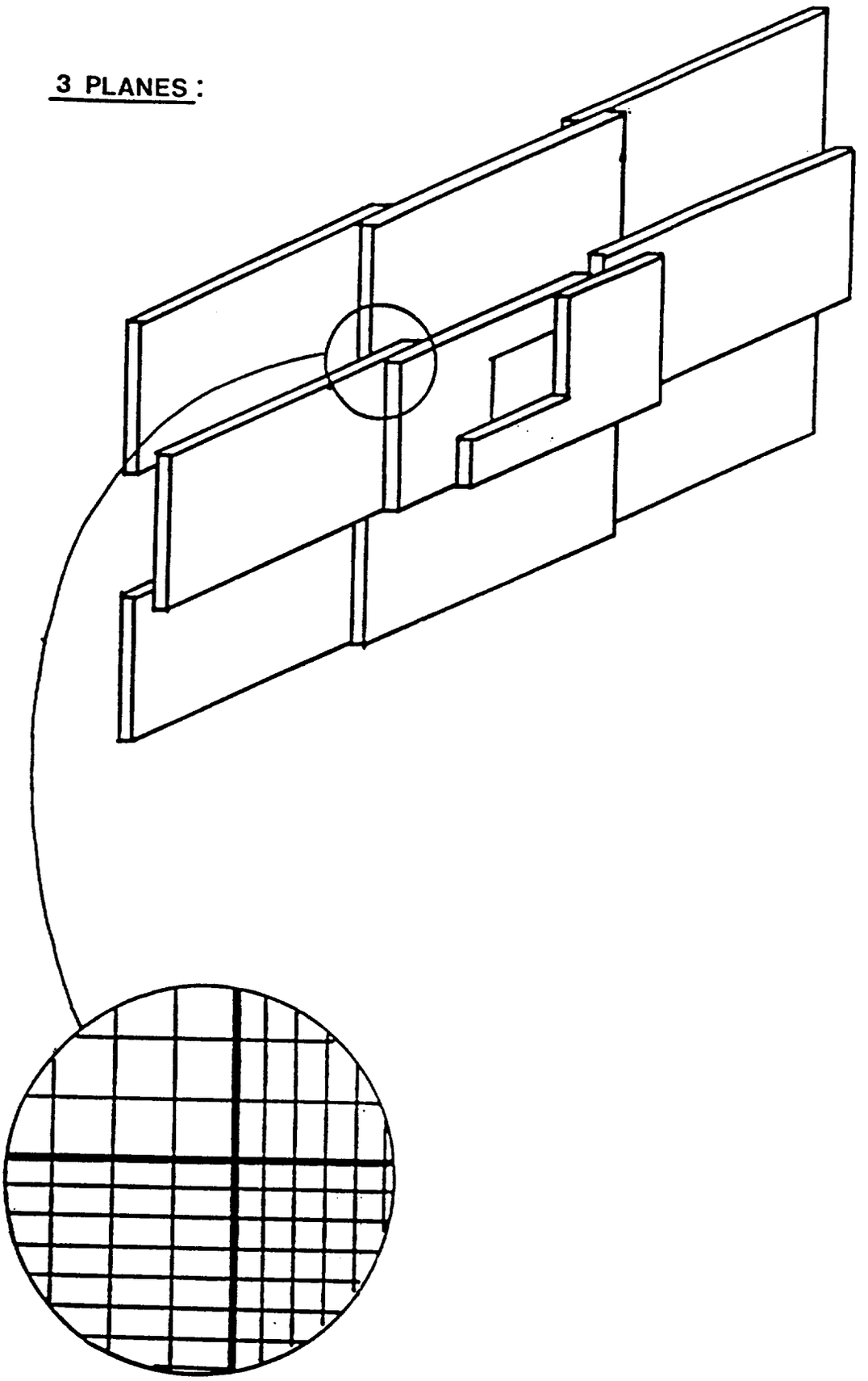


FIG 4

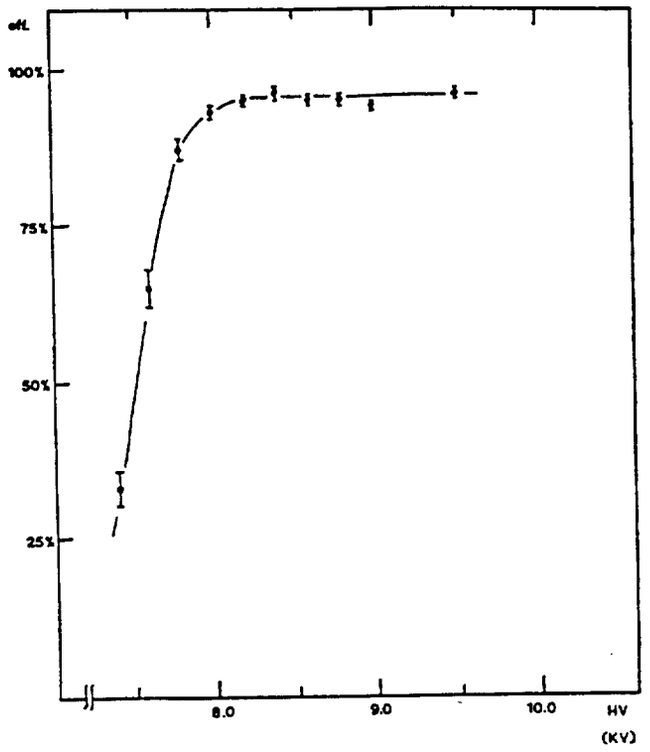


FIG 5a

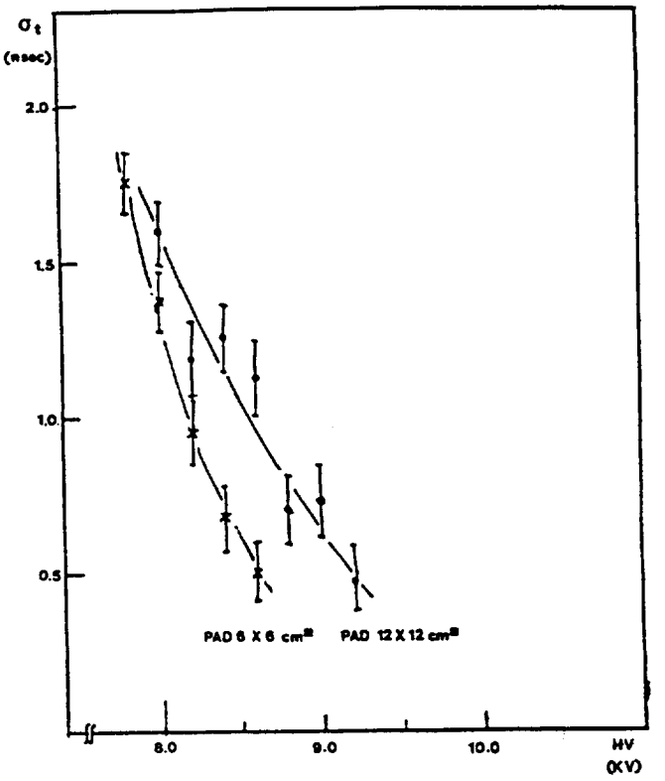


FIG 5b

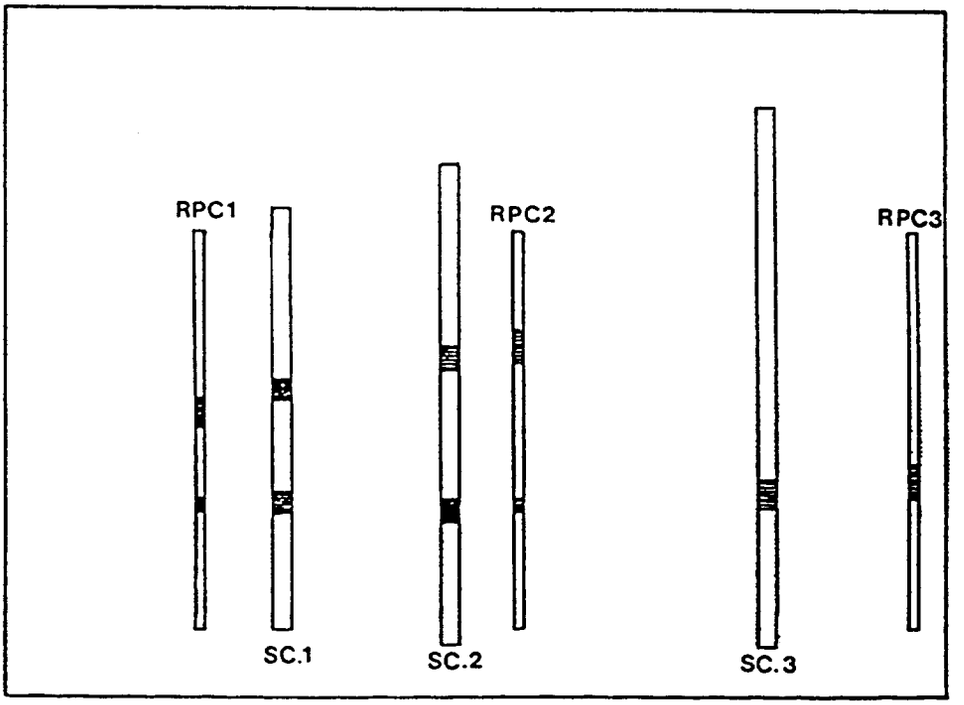


FIG 6

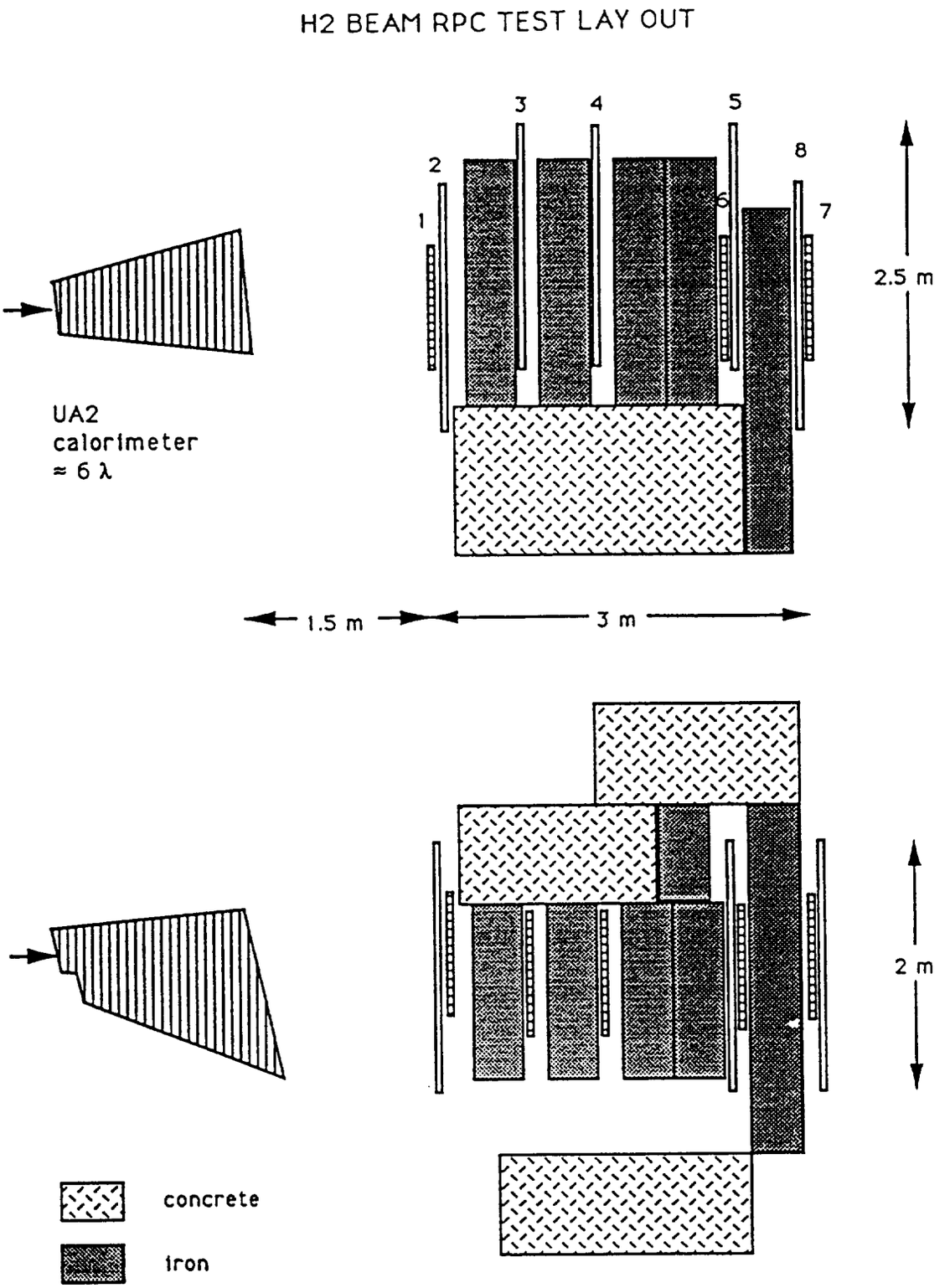

H2 BEAM RPC TEST LAY OUT
UA2
calorimeter
≈ 6 λ
1
2
3
4
5
6
7
8
2.5 m
1.5 m
3 m
2 m
concrete
iron

FIG 7

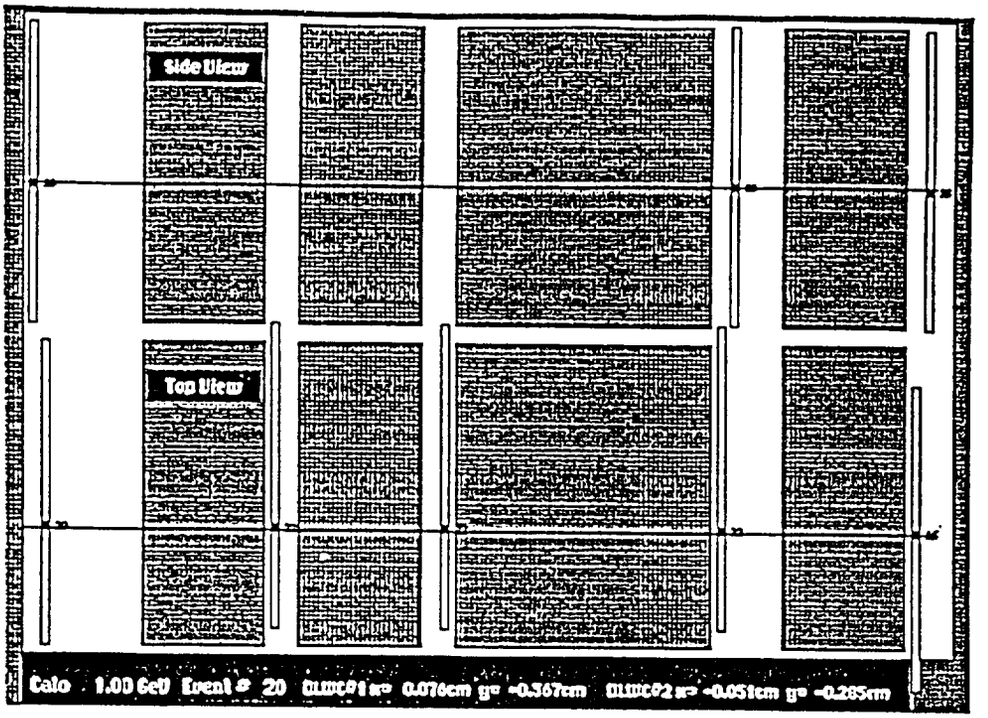

Side View
Top View
Calo 1.00 GeV Event # 20

FIG 8a

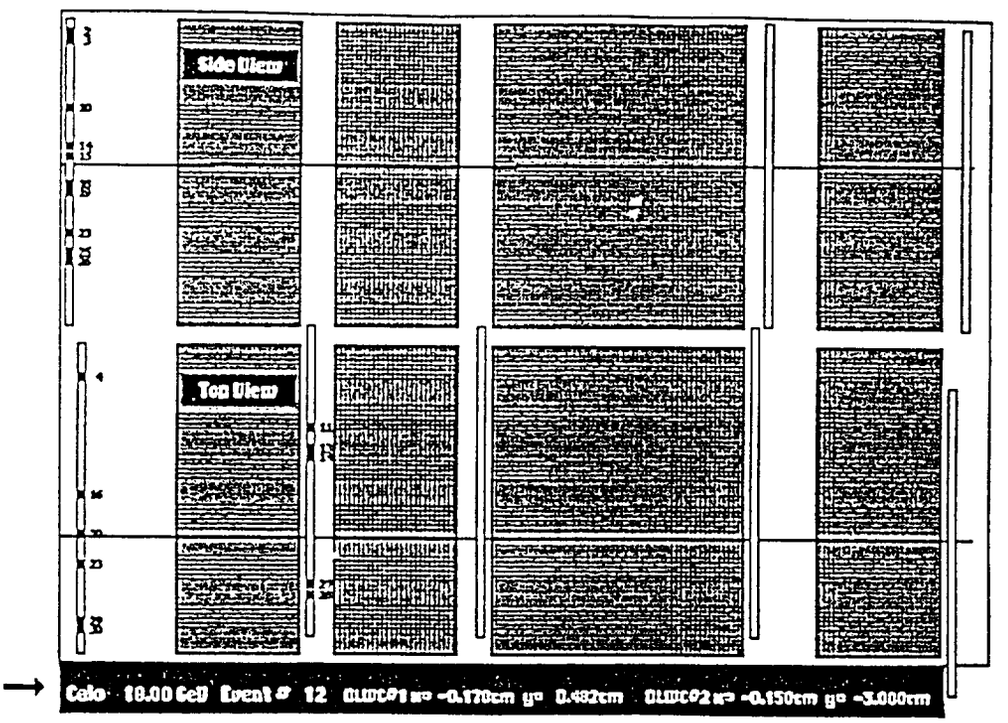

Side View
Top View
Calo 18.00 GeV Event # 12

FIG 8b

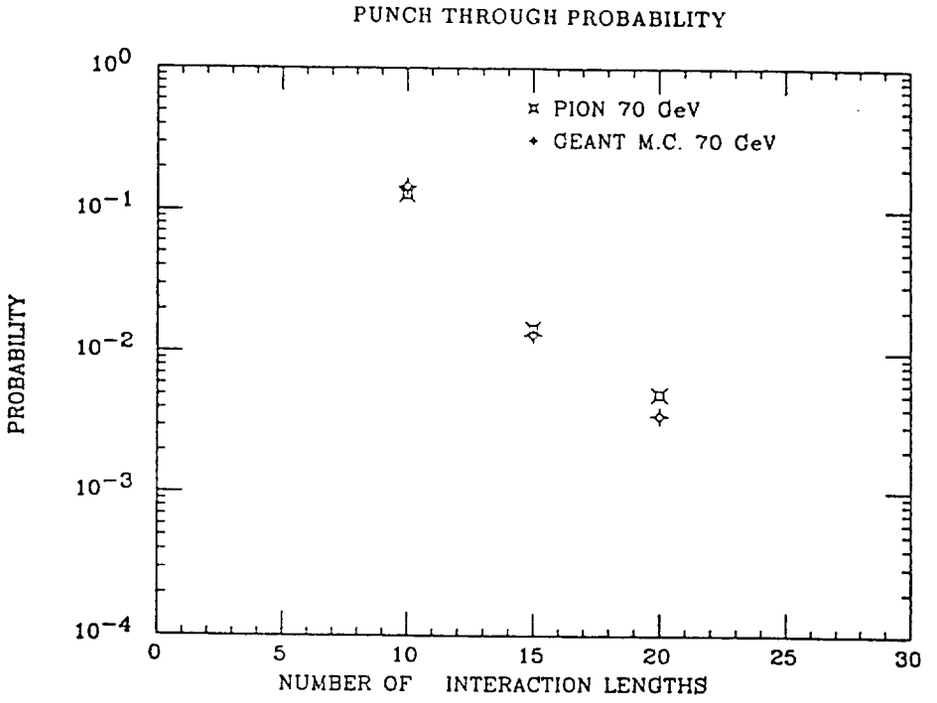

PUNCH THROUGH PROBABILITY
PION 70 GeV
GEANT M.C. 70 GeV
PROBABILITY
10^0
10^{-1}
10^{-2}
10^{-3}
10^{-4}
0
5
10
15
20
25
30
NUMBER OF INTERACTION LENGTHS

FIG 9

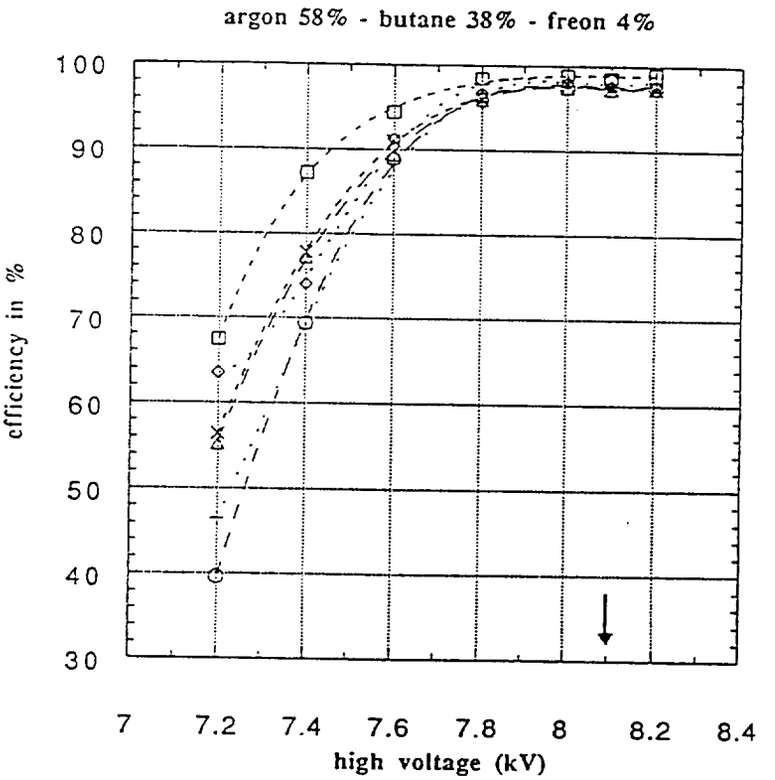

argon 58% - butane 38% - freon 4%
efficiency in %
100
90
80
70
60
50
40
30
7
7.2
7.4
7.6
7.8
8
8.2
8.4
high voltage (kV)

FIG 10